UTIAS
UNIVERSITY OF TORONTO
INSTITUTE FOR AEROSPACE STUDIES

FINAL CONTRACT REPORT

on

# STUDY OF INTERNAL BALLISTICS OF A CLOSED VESSEL

for the

DEFENCE RESEARCH ESTABLISHMENT VALCARTIER
COURCELETTE, QUEBEC, CANADA

DREV Scientific Authority: Dr. L.-S. Lussier
DSS Contracting Officer: Mrs. Genevieve Arcand
DSS Contract Number W7701-O-0001/01-XSK
DSS File Number XSK90-00030-(303)

by

**Professor James J. Gottlieb**
Principal Investigator

Institute for Aerospace Studies, University of Toronto
4925 Dufferin St., Downsview, Ontario, Canada

June 2000

FINAL CONTRACT REPORT

on

# STUDY OF INTERNAL BALLISTICS OF A CLOSED VESSEL

for the

DEFENCE RESEARCH ESTABLISHMENT VALCARTIER
COURCELETTE, QUEBEC, CANADA

DREV Scientific Authority: Dr. L.-S. Lussier
DSS Contracting Officer: Mrs. Genevieve Arcand
DSS Contract Number W7701-O-0001/01-XSK
DSS File Number XSK90-00030-(303)

by

Professor James J. Gottlieb
Principal Investigator
Institute for Aerospace Studies, University of Toronto
4925 Dufferin St., Downsview, Ontario, Canada

June 2000

# OVERVIEW OF FINAL CONTRACT REPORT

The original objectives[1] of this contract work can be summarized in general terms as follows:

> *to carry out a research project involving the development of several numerical models and analyses along with computer codes based on chemical equilibrium principles with different relevant equations of state for the burning of propellants in DREV's closed vessel,*

with more specific details outlined in the contract.

This final report summarizes the work done for this DREV contract. The objectives of this research were originally set too high and fulfillment of the research goals were not satisfied in the time frame of the original and extended contract.

The first part of this report provides a summary of the type of work and reasons for undertaking the work and accomplishments, in order to put the contract work into context and provide perspective. The second part of this report is a set of appendices, each one self-contained on a particular topic, in order to provide additional details on the individual studies.

---

[1] The objective as stated in the contract: "DREV Technical Specification 1412-90-01."

## Table of Contents

Title Page .......... i

Overview of Final Contract Report .......... ii

Table of Contents .......... iii

Summary of Contract Work .......... 1

1. Introduction .......... 1
2. Chemical Equilibrium Analysis for Gaseous and Condensed Combustion Products .......... 2
3. Motions of Gases and Particles Inside a Closed Vessel .......... 5
4. Heat Transfer in a Closed Vessel .......... 6
5. Study of Equation of State for Combustion Products .......... 6
6. Reproduction of JANAF Thermochemical Data .......... 8
7. Distributed Particle Surface Model for Gas-Particle Flows and Particle-Particle Collisions .......... 10
8. Appendices:
   - Appendix 1: Chemical Equilibrium Analysis for Gaseous and Condensed Combustion Products at Constant Volume (Ph.D. Thesis) .......... 13
   - Appendix 2: Chemical Equilibrium Analysis for Gaseous and Condensed Combustion Products at Constant Volume (Journal Paper) .......... 181
   - Appendix 3: Numerical Model for Gas and Particle Motions in a Closed Vessel .......... 249
   - Appendix 4: Prediction of Heat Transfer from Propellant Burning at the Walls of a Closed Vessel .......... 343
   - Appendix 5: Some Notes on Radiative Heat Transfer in a Closed Vessel .......... 455
   - Appendix 6: Study of Equations of State for Combustion Products in a Closed Vessel .......... 475
   - Appendix 7: Spline Reproduction of Thermochemical Data for Flow Computations for a Closed Vessel .......... 573
   - Appendix 8: Computational Model for Gas-Particle Flows Using Particles with Distributed Surfaces .......... 625
   - Appendix 9: Numerical Study of Particle-Particle Collisions Using Particles with Distributed Surfaces .......... 691

# SUMMARY OF CONTRACT WORK

## 1. INTRODUCTION

The Defence Research Establishment Valcartier in Quebec, Canada, has two constant-volume closed vessels that are used to evaluate the characteristics of old and new propellants used for military guns and projectile launchers. New propellants include LOVA and HELOVA. Similar research and developments are in progress in other countries. The proper use of these closed vessels can result in the determination of, most importantly, the *(a)* adiabatic flame temperature $T_f$ and propellant force constant $RT_f$, and *(b)* the constants $\alpha$ and $\beta$ in the assumed burning rate law $r = \alpha P^{\beta}$, for different propellants having various grain shapes (e.g., multiperforated cylinders, strips, ball).[2] However, sophisticated computer codes based on modern chemical equilibium principles and advanced curve-fit techiques are needed to perform meaningful determinations. These codes must incorporate a suitable equation of state, with co-volume as a minimum and preferably with multiple virial coefficients, to properly handle high-pressure and high-temperature dense gases typical of explosion conditions. At the present time, no computer codes of this type have been developed in Canada and simplified and older codes from other countries are currently used at DREV. For example, in use are the Blake-Tiger code,[3] the SIMPCB and CBRED codes from BRL,[4] and the Bagheera code from France.[5]

The objective of the present contract work was to advance information and analyses for computer equilibrium codes at DREV, and they should be constructed on modern advances in chemical, mathematical and computing techniques. These modified codes should be more efficient, flexible, robust, user-friendly, and documented than previously existing codes to serve DREV's needs, and they should be capable of evaluating effectively new propellants like LOVA and HELOVA. Our work was aimed at improving, complementing or replacing the Blake-Tiger and Bagheera codes, which compute complicated equilibrium properties of a mixture of a limited number of gaseous and condensed species at high densities with and without melting of some substances, for which advanced equations of state are needed to properly handle the dense gaseous species and compressible condensed phases. Our work was also directed at improving, complementing or replacing the SIMPCB and CBRED codes for evaluating propellant burning rates, flame temperature and force constants (e.g., $\alpha$, $\beta$, $RT_f$) from experimental data. The goal in this latter work was an attempt to incorporate a better heat transfer model at the vessel walls.

---

[2] Grune, D., 1987, The influence of the variation of combustion chamber volume under pressure load on the determination of thermodynamic characteristics of solid propellants in closed bombs, Propellants, Explosives and Pyrotechniques, Vol. 12, pp. 8–12.

[3] Freedman, E., 1982, "Blake–A Thermodynamic Code Based on Tiger: User's Guide and Manual," Technical Report ARRL–TR–02411, Ballistic Research Laboratory, US Army Armament Research and Development Command (AD/A–121 2590).

[4] Price, C.F. and Juhasz, A.A., 1977, A versatile user-oriented closed bomb data reduction program CBRED, Ballistic Research laboratory, Aberdeen Proving Ground, Md., Report 2018.

[5] The Bagheera code was developed at the Le Bouchet Research Center of the SNPE Group in France, starting in the late 1970s or early 1980s. Since 1991 to 1992 it has been the NATO standard code for analysing the thermodynamic properties of military propellants.

## 2. CHEMICAL EQUILIBRIUM ANALYSIS FOR GASEOUS AND CONDENSED COMBUSTION PRODUCTS

The primary contribution of this contract is the work on the chemical equilibrium analysis and computer program for computing the equilibrium composition of a complicated mixture of numerous gaseous and condensed species (e.g., hundreds to thousands), even though most of the reaction products are trace species that exist in small amounts. These calculations can include a substance that exists in the gaseous phase simultaneously with the liquid phase (e.g., steam and water, lead vapor and lead liquid) and gaseous phase simultaneously with multiple solid phases (e.g., red and yellow lead), as well as including the transition of condensed phases (e.g., liquid and solid lead). Furthermore, these calculations can be done at high pressures and densities typical of those conditions occurring in the burning of propellant in experimental projectile launchers and guns, the combustion of rocket-motor propellants, and the detonation of primers, igniters and explosives.

Computer codes such as those called NASA, Blake and Bagheera have been developed in the past for computing such equilibrium compositions. However, they have algorithm deficiencies, computer-programming and logic problems, and computer-running disadvantages. These have been largely overcome and circumvented by the new code developed for this work. The disadvantages of previous computer codes and the advances made with the new code are now mentioned briefly. More details can be found in Wong's Ph.D. thesis, which is attached as appendix 1 starting on page 13.[6]

The NASA, Blake and Bagheera codes were all developed primarily on the basis of a nonstoichiometric formulation, and they use the Newton-Raphson method to solve iteratively a set of nonlinear equations that minimizes either the Helmholtz free energy at a specified total energy and vessel volume or the Gibbs free energy at a specified system pressure and temperature, in order to obtain the equilibrium composition of the reaction product mixture. In the nonstoichiometric formulation one essentially uses an approximate set of linear equations $Ax = b$ to the nonlinear equations, and solves these in a set of steps, each iterative, to determine an equilibrium composition of a mixture. The inversion of matrix $A$ to obtain the composition $x$ at each step becomes increasingly difficult when the numbers of gaseous and condensed species increases, when the number of melting substances increases, when nonideal equations of state are used to describe the pressure-volume-temperature relationships of the gaseous and condensed species, and when the products are mostly condensed species. When more than one solid phase of a substance is included, matrix $A$ is outrightly singular.[7] In some cases when matrix $A$ is nearly computationally singular and its inversion seems impossible from a computational viewpoint, the entries of matrix $A$ are adjusted (fudged) so that a solution for composition $x$ can be forced to occur, and there is evidence

---

[6] The appendices have their own table of contents and page numbers (bottom center) for internal consistency. However, the contract report has a separate set of consecutive page numbers at the bottom side of the pages for convenience.

[7] Hence, for two phases of one substance, one must solve the problem at least twice, once with only one phase, and then choose the most appropriate solution, that is the solution with the lowest Helmhols or Gibbs free energy.

(see appendix A) to show that these adjustments make the amounts of some trace species highly erroneous (orders of magnitude incorrect). In other cases when matrix $A$ is almost computationally singular, the code simply fails to find a converged solution for the reaction products at equilibrium.

The Blake code has a limit on the number of gaseous species, less than thirty, and also has a limit on the number of condensed species, probably in an effort to avoid or circumvent failures in determining converged solutions. The NASA code fails often when the number of condensed species in a calculation is large, especially when no information regarding the condensed species present at equilibrium is used to start the calculation, and it fails also when converged solutions are sometimes altered (fudged). Previous codes fail to yield converged solutions for some formulations of black powder used by the military, and most of the previous codes fail in the case of fuses (where the majority of the combustion products are condensed species with only relatively small amounts of gases). Such difficulties are well explained and documented in appendix 1 on "Chemical Equilibrium Analysis of Gaseous and Condensed Combustion Products" by Fred Wong.

The chemical equilibrium anaysis and algorithm originally developed by a number of people (Villars, Cruise, Smith and Missen)[8,9,10,11,12,13,14] has been called the VCS algorithm after some of the developers. This algorithm is based on a stoichiometric rather than nonstoichiometric formulation, and it involves the minimization of Gibbs free energy at a specified system pressure and temperature.[15] However, there are some good advantages of using the stoichiometric formulation, as pointed out in detail in appendix 1.

The formulation is elegantly set up in a final form as an algorithm which uses a second variational method for solving an unconstrained minimization problem involving the Gibbs free energy, in order to obtain the equilibrium composition. The algebraic equations are nonlinear, but an iteration on an approximate linear set $Ax = b$ is solved at each step of

---

[8] Villars, D.S., 1959, A Method of Successive Approximations for Computing Combustion Equilibria on High Speed Digital Computers, J. Physical Chemistry, Vol. 63, No. 4, pp. 521–525.

[9] Villars, D.S., 1960, Computation of Complicated Combustion Equilibria on a High Speed Digital Computer, in G.S. Bahn and E.E. Zukoski, editors, Kinetics, Equilibria and Performance of High Temperature Systems, Proc. First Conference, Los Angeles, 2–5 November, 1959, Western States Section, The Combustion Institute, Butterworths, London, pp. 141–151.

[10] Cruise, D.R., 1964, Notes on the Rapid Computation of Chemical Equilibria, The Journal of Physical Chemistry, Vol. 68, No. 12, pp. 3797–3802.

[11] Smith, W.R., 1976, Some Remarks on the Calculation of Complex Chemical Equilibria by General Methods, Industrial and Engineering Chemistry Fundamentals, Vol. 15, No. 3, pp. 227–229.

[12] Smith, W.R., 1980, Computational Aspects of Chemical Equilibrium in Complex Systems, Theoretical Chemistry: Advances and Perspectives, H. Eyring and D. Henderson, editors, Vol. 5, pp. 185–259, Academic Press, Inc., New York.

[13] Smith, W.R., and R.W. Missen, 1967, On the Two-Derivative Method of Optimization, Canadian Journal of Chemical Engineering, Vol 45, No. 6, pp. 346–348.

[14] Smith, W.R., and R W. Missen, 1968, Calculating Complex Chemical Equilibria by an Improved Reaction-Adjustment Method, Canadian Journal of Chemical Engineering, Vol. 46, No. 4, pp. 269–272.

[15] To produce a final equilibrium composition of the reaction products at an initially unknown system pressure and temperature for a given amount of energetic material burned in a vessel of a given volume requires a further iterative loop.

the iteration. Although one still has to solve $Ax = b$ without constraints at each iterative step to obtain the composition $x$, matrix $A$ is not inverted. Instead, a clever method is used whereby matrix $A$ and vector $b$ are iteratively adjusted such that $A$ becomes an identity matrix, thereby producing the solution $x = b'$, where $b'$ is the alterned $b$, even in the case of problems with a singular matrix $A$.

As a consequence of this procedure, one can effectively eliminate any restrictions on the numbers of gaseous species and number of condensed species, although computational run times increase as the number of species increases. Solutions to problems with 550 gaseous species and 220 condensed species have been obtained without much difficulty, although including the melting of condensed species and the transition between solid phases increase the computational effort. Furthermore, the solution of the reaction products have routinely been obtained for difficult problems of energetic materials like black powder and fuses, as illustrated in appendix 1.

Previous codes for solving equilibrium problems have been limited by submodels used inside these programs. The NASA code, for example, is quite limited in that it is written on the basis of a perfect-gas mixture model with condensates having no volume.[16] The Bagheera code is slightly less limited because it is written for an ideal mixture of imperfect gases with condensates that are incompressible (fixed molar volume). The Blake code is based on better submodels, including a nonideal mixture of imperfect gases with condensates that are compressible (have a variable volume molar volume).

The new code has been written to handle all of the previous situations, that is the cases of perfect or imperfect gaseous and condensed species, perfect or imperfect mixtures, and condensates that are incompressible or compressible or have no volume, as selected by the code user. Furthermore, for even more generality the equation of state can be selected from the perfect-gas, Redlich-Kwong-Soave, Bennedict-Webb-Rubin-Starling, truncated virial and modified virial equations of state. This new code has been developed both for comprehensiveness and flexibility for engineering applications, and also to facilitate direct and convenient comparisions of solutions with those of the previous codes. At this time the new code is still a research tool, rather than a production code that users can use blindly, and more work is required to complete the code and make it easily usable by other researchers, scientists and engineers.

In the case of the constant-volume closed vessel, one might think that the best procedure is to minimize the Helmholtz free energy for a specified total energy and volume, which at first appears to involve only one iterative procedure. This is true for the case of the NASA code which has a fixed vessel volume for the gaseous species, because the NASA code simply ignores the subvolume taken by the condensates. For the more realistic Blake and Bagheera codes, which include the condensates as incompressible and compressible, respectively, and does not ignore their subvolumes, the volume for the gaseous species is no longer constant or known ahead of time, and another iteration is required to adjust the gaseous into their initially unknown volume. Hence, the process in the VCS method of minimizing the Gibbs free energy iteratively for a specified system pressure and temperature, with another iteration to adjust these conditions to match a particular closed vessel volume is not a disadvantage of the VCS method.

---

[16] This makes the NASA code predictions for fuses highly questionable or impractical, because fuses produce mainly condensates which have a significant volume fraction of the mixture

Villars, Cruise, Smith and Missen have applied their VCS theory and algorithm to solving chemical equilibrium problems at a specified constant temperature and pressure. Their computed examples involved fairly small problems with tens of gaseous and condensed species as reaction products, and without melting and phase transitions. These were solved primarily to prove that their algorithm was functional and their claims of advantages over previous codes were proven. The new VCS theory and algorithm, and the new code developed in this work, have been applied for the first time to problems at constant energy and vessel volume with a really large number of reaction-product species, including the extra features of melting and phase transitions of pure condensed phases. Most of these applications involve explosives, propellants, ignitors, primers and fuses, and they are thereby important to military research and development in this field. The VCS method and its advantages are essentially unknown today in civilian and military research communities that have interests in such energetic materials. However, the VCS theory and algorithm as developed today are probably the best ones for solving such equilibrium problems, so the spread of knowledge in this regards is important.

Part of the work described above, in this section and appendix 1, on the theory and algorithm for computing chemical equilibrium has been prepared as a separate paper for submission for publication in a scientific journal. The theory and algorithms for the condition of the melting of a phase of a substance has not been included in the draft paper. This separate paper is reproduced in appendix 2, although it has not yet been finalized and submitted for publication.

## 3. MOTIONS OF GASES AND PARTICLES INSIDE A CLOSED VESSEL

When propellant grains are burned inside a closed vessel, the propellant grains shrink during combustion. The grains also burn more quickly as the pressure increases, and the maximum vessel pressure occurs as the particles disappear (burn out). Heat transfer from the hot reaction products to the cooler vessel walls limits the pressure maximum and thereafter the pressure drops slowly, until the reaction products and the vessel attain the same temperature. The propellant grains, and the reaction gases and condensates stemming from grain burning, are all in motion during the combustion process. The vigorousness of their motions affects and influences the time-dependent heat transfer from the reaction products to the vessel walls.

The proper use of a closed vessels can result in the determination of, most importantly, the *(a)* adiabatic flame temperature $T_f$ and propellant force constant $RT_f$, and *(b)* the constants $\alpha$ and $\beta$ in the assumed burning rate law $r = \alpha P^{\beta}$, for different propellants having various grain shapes (e.g., multiperforated cylinders, strips, ball). This determination is affected by the heat transfer between the hot combustion products and cooler vessel walls, with various *ad hoc* assumptions used to account for heat transfer.

To improve our understanding of the heat transfer, to relax *ad hoc* assumptions on heat transfer and to obtain better determinations of the adiabatic flame temperature and burning rate constants, some studies were set in motion to predict the motions of propellant grains and reaction products inside the closed vessel and predict the amount of heat transfer. The first study was a M.A.Sc. thesis by Grant Tisdall, "Numerical Model for Gas and particle Motions in a Closed Vessel," and this work is included as appendix 3.

This work started as a straightforward review of various gas-particle models that are relevant to predicting the three-dimensional gas-particle motions in an axisymmetric vessel. This review revolved around the Navier-Stokes equations with Reynolds-averaged turbulence, and how they could be used. These equations were summarized, without numerical computations, for Grant Tisdall's M.A.Sc. degree, and this work is well done.

Grant Tisdall started his Ph.D. program on doing predictions for the gas and particle motions inside the closed vessel during propellant combustion. However, the work proved very difficult, partly because Grant Tisdall increased the complexity of the problem and partly because the particle grains can be closely spaced (packed) and the previous computational models simply did not apply for predicting accurately the grain motions. After four years of work, he took a job in a Toronto patent office and became a Canadian wage earner.

## 4. HEAT TRANSFER IN A CLOSED VESSEL

Simultaneously with Grant Tisdall's work in his M.A.Sc. and Ph.D. programs, I employed Florence Berger to do a M.A.Sc. degree on "Heat Transfer from Propellant Burning in a Constant-Volume Vessel." Her work was focussed on a simple two-dimensional computational flow model of the gas flow around a single, stationary, burning particle, with the intent of determining an approximate heat-transfer coefficient for the heat losses from the gases to the vessel walls. This heat transfer was assumed to occur as a result of conduction and free or forced convection. Her study was quite surprising in that it showed clearly that there were highly nonuniform gaseous flows with vortical gas motions, high-speed jets in some places, and high-temperature regions or 'hot spots' in others places resulting from the compression of reaction product produced earlier by the reaction products produced later. These nonuniform effects can lead to abnormally large amounts of heat transfer in localized wall regions; in wall regions of very low speed flow the dominant heat transfer mechanism is by free convection, whereas in regions of jet flows the dominant heat transfer mechanism is by forced convection. Her two-dimensional computational work is too limited to be definitive or conclusive, but the effects of vorticies, jets and hot-spots are highly likely to be found in in realistic three-dimensional computations of the flow inside the closed vessel. Hence, this was a major impetus for Grant Tisdall's Ph.D. program on the motion of gases and particles in the closed vessel.

Florence Berger's work stimulated thoughts on how important radiative heat transfer was inside the vessel. This lead to a seperate study by Berger and Gottlieb called "Some Notes on Radiative Heat Transfer in a Closed Vessel," which is included as appendix 5. Most of the heat transfer appears to be in the realm of the grey-body type.

## 5. STUDY OF EQUATIONS OF STATE FOR COMBUSTION PRODUCTS

Most of the past work involving the interior ballistics of closed vessels and guns use either the Clausius equation of state or a truncated virial equation of state. The Clausius equation of state,[17,18]

$$p = \frac{1}{1 - b\rho}\rho RT \,,$$

is the ideal equation of state ($p = \rho RT$) modified slightly to include the effect of co-volume (using a constant $b$) for application in the case of moderately high gas pressures and densities. The three-term virial equation of state,[19,20]

$$p = \rho RT \left[A + B(T)\rho + C(T)\rho^2\right] ,$$

has $A = 1$ and two temperature dependent coefficients: $B(T)$ includes mainly the effects of repulsion (i.e., co-volume) and partly the effects of attraction between molecules associated with binary collisions, and $C(T)$ includes the overall effects of repulsion and attraction of molecules associated with trimolecular collisions. These equations of state are fairly simple, compared to others that might be used, partly to help make computations more simple and partly because more complicated equations have unknown constants for combustion products occurring in the firing of closed vessels and guns.

The main problem in using these equations of state for the interior ballistics of closed vessel and guns is that they do not model accurately the behaviour of gases at high pressures and densities near their critical point, and they also fail completely to model the behaviour of compressible liquids. These restrictions limit our current analyses of the interior ballistics of closed vessels and guns, in which the pressures and densities are often sufficiently high that some of the gases in the mixture exist in the vicinity of their critical point and other substances in the mixture exist as condensed species (in their liquid state). Some computer codes on interior ballistics have a separate equation of state for condensed species; however, this equation of state is normally limited to incompressible liquids at higher temperatures because compressibility data is still unavailable. Nonetheless, a single equation of state to simultaneously cover both the compressible gas and liquid ranges of densities is highly desirable. Cubic equations of state[21] given by

$$p \;=\; \frac{1}{1 - b\rho}\rho RT \;-\; \frac{a\rho^2}{1 + ub\rho + wb^2\rho^2}$$

---

[17] Krier, H., and Adams, M.J., 1979, "An Introduction to Gun Interior Ballistic and a Simplified Ballistic Code," AIAA Journal, Vol. 17. pp. 1–40.

[18] Gough, P., 1979, "Modelling of Two-Phase Flow in Guns," Progress in Astronautics and Aeronautics, Vol. 66, pp. 176–196.

[19] Robbins, F.W., and Horst, A.W., 1976, "Numerical Simulation of Closed Bomb Performance Based on Blake Code Thermodynamic Data," Naval Ordnance Station, Indian Head, Maryland, U.S.A

[20] Dymond, J.H., and Smith, E.B., 1980, "The Virial Coefficients of Pure Gases and Mixtures," Clarendon Press, Oxford.

[21] Eliezer, S., 1986, "An Introduction to Equations of State: Theory and Applications," Cambridge University Press, Oxford.

with different values of the constants $a$, $b$ and $u$ and $w$ yield slightly different but some worthwhile equations of state due to Van der Waals,[22] Redlich and Kwong, [23] Soave,[24] and Peng and Robinson.[25] These equations and some later variations on Soave's all simultaneously cover both the gaseous and liquid ranges, but they have not yet been used in closed vessel analyses mainly because of limitations on their accuracy and applicability.

I initiated a study of various equations of state by my student Ilja Hauss, and this study is included in this contract report as Appendix 6 with the report title "Study of Equations of State for Combustion Products in a Closed Vessel," although his Master of Applied Science thesis has the somewhat different title "A Study of Equations of State for the Density Range from Dilute Gases to Compressed Liquids." The objectives of this work were to study past and present equations of state for gases and liquids, covering the range of densities from dilute gases to compressed liquids which are encountered in the applications of interior ballistics of closed vessels and guns, in order to determine if a more appropriate equation of state has become available in more recent times, or if older equations with new techniques could be put to better use. Furthermore, I wanted to see if we could combine or blend two equations of state for gases and liquids into a single equation of state for convenient usage in closed vessel computations.

Ilja Hauss reviewed many equations of states for gases including the ideal gas law, Clausius' equation, a extended Clausius' equation, three virial equations of state, Beattie and Bridgeman's equation, and a number cubic equations of state (including that of Soave for combined liquids and gases). He also reviewed Hankinson, Brobst and Thompson's equation of state for compressible liquids,[26] one of the best ones available today (recognized as better than Tait's various equations of state), but this equation of state was found to be too limited for closed vessel applications, because it application is restricted only to the temperature range below the critical point temperature.

Ilja Hauss' results of the study of various equations of state, and his blending of two different equations for gases and liquids into a single equation of state, are incomplete and therefore inconclusive. The behaviours of gases and liquids near the critical point are much more complicated than we originally anticipated, and they depend on the classes of various molecules (e.g., nonpolar, polar), and more work is likely required to make significant advancements. Nonetheless, Ilja Hauss' study moves us in the right direction, and it provided significant insight into the problems that would have to be overcome. One good idea could easily reverse this situation.

---

[22] For Van der Waals' equation of state, $a = 27R^2T_c^2(64p_c)^{-1}$, $b = RT_c(8p_c)^{-1}$, $u = 0$ and $w = 0$.

[23] For Redlich and Kwong's equation of state, $a = 0.42748R^2T_c^2p_c^{-1}(T_c/T)^{1/2}$, $b = 0.08664RT_cp_c^{-1}$, $u = 1$ and $w = 0$.

[24] For Soave's equation of state, $a = 0.42748R^2T_c^2p_c^{-1}\left[1 + f_\omega\left\{1 - (T_c/T)^{1/2}\right\}\right]^2$, $b = 0.08664RT_cp_c^{-1}$, $u = 1$, $w = 0$ and $f_\omega = 0.480 + 1.574\omega - 0.176\omega^2$.

[25] For Peng and Robinson's equation of state, $a = 0.45724R^2T_c^2p_c^{-1}\left[1 + f_\omega\left\{1 - (T_c/T)^{1/2}\right\}\right]^2$, $b = 0.07780RT_cp_c^{-1}$, $u = 2$, $w = -1$ and $f_\omega = 0.37464 + 1.54226\omega - 0.26992\omega^2$.

[26] Reid, R.C., Parausnitz, J.M., and Poling, B.E., 1987, "The Properties of Gases and Liquids," fourth edition, McGraw-Hill Book Company.

## 6. REPRODUCTION OF JANAF THERMOCHEMICAL DATA

Thermochemical data for gases and condensed species have been available for over fourty years in the form of tabulations of data. In addition to physical constants for numerous atoms and molecules,[27,28] there exists data for enthalpy, entropy, Gibbs free energy, and specific heat at constant pressure, which are tabulated as a function of temperature for atoms and molecultes which can be in gaseous, liquid and solid form.[29,30,31,32,33] These sets of tablulated data are derived from complex and long calculations based on our knowledge of atomic constants, atomic and molecule force fields, and statistical or quantum mechanics.

Thermochemical data are needed as part of our computer codes to compute the type and amount of various gaseous and condensed species in chemical equilibrium mixtures, and to compute the total energy, enthalpy, pressure and temperature of propellant and explosive reaction products in a constant-volume vessel, or for some other processes. The engineering custom has been to include such tabulated thermochemical data directly in the form of interpolation tables or indirectly in the form of curve fits or data splines into our general purpose computer codes. Noboby uses the original complex computations to recalculate the thermochemical properties from first principles, because this reproduction process has thus far been too complex and long.

One has to be careful, however, in regards to the use of your own curve fits or the curve fits of others, so that the reproduced thermochemical data is accurate. To the end of the 1980s, most curve fits were often inaccurate (e.g., localized errors larger than 10%), and some curve fits were too limited in the temperature range and forced extrapolations were simply inaccurate. For example, the enthalpy $h$ and specific heat at constant pressure $C_p$ might be represented by the two polynomials

$$h = a + bT + cT^2 \qquad \text{and} \qquad C_p = \alpha + \beta T + \delta T^2\,,$$

with separately evaluated coefficients. These low-degree polynomials may fit data smoothly (in contrast to high-degree polynomials with oscillations) but are likely limited to a small temperature range (e.g., 300–800 K versus 250–6000 K), so the unfortunate use of sets of splined polynomials are required to cover the full temperature range. In addition, the polynomials for $h$ and $C_p$ are inconsistent because

$$C_p \;=\; \frac{\mathrm{d}h}{\mathrm{d}T} \;=\; b + 2cT \;\neq\; \alpha + \beta T + \delta T^2\,.$$

As a consequence of encountering such problems in the 1950–1980s, I initiated a project by the student Antonio Mandatori to use a spline method for reproducing accurately the JANAF

---

[27] Anon, 1995, "Atomic Weights of the Elements."

[28] Anon, 1993, "Journal of Physical and Chemical Reference Data, Vol. 24, No. 4, pp. 1561–1576.

[29] Chase, M W., Jr., ed., 1985, "JANAF Thermochemical Tables," 3rd edition, Pts. 1 & 2

[30] Anon, 1985, Journal of Physical and Chemical Reference Data, Vol. 14, Suppl. 1.

[31] Barin, I., 1993, "Thermochemical Data of Pure Substances," VCH Verlagsgesellschaft mbH, Pts. 1–5.

[32] Gordon, S., and McBride, B.J., 1999, "Thermochemical Data to 20,000 K for Monatomic Gases," NASA, Glenn Research Center, NASA/TP–1999–208523.

[33] McBride, B.J., Gordon, S., and Reno, M.A., 1993, "Thermodynamic Data for Fifty Reference Elements," NASA, NASA Technical Paper 3287.

termochemical data. His work is included as part of this contract report as Appendix 7 with the report title "Spline Reproduction of Thermochemical Data for Flow Computations for a Closed Vessel," although his actual Master of Applied Science thesis title is "A Spline Method of Reproducing JANAF Thermochemical Data."

Antonio Mandatori reviewed the literature and learned which thermochemical data would be most advantageous to be reproduced and which data should be obtained from the original reproduction. As illustrated previously, if one reproduces the enthalpy $h$ by a curve-fit or spline method, then the specific heat at constant pressure $C_p$ can be obtained by differentiation, because $C_p = \mathrm{d}h/\mathrm{d}T$. This should be done to make the data consistent. In the process of doing his studies, Antonio Mandatori discovered that Bonnie McBride and Sanford Gordon of NASA were revisiting their previous work on curve fits to thermochemical data, and that they were obtaining much more accurate curve fits of thermochemical data. There interpolant was normally taken to be

$$C_p = \sum_{i=1}^{8} a_i T^{i-5}$$

and the enthalpy, entropy and Gibbs free energy can then be obtained from the curve-fit results for $C_p$ (see Appendix 7 for full details). These were significant steps to improving the curve-fit accuracy and using a fairly wide temperature interval.

Antonio Mandatori followed the recent course of McBride and Gordon and completed his studies for a Masters degree, although he used interconnecting splines to cover large temperature ranges. His thesis provides results for only a few examples of different few gases, and the splined interpolants for a set of smaller temperature ranges will produce a better accuracy than one interpolant. However, his one-man effort could not compete with NASA's ongoing efforts. As a consequence, we now recommend that NASA's curve-fit work of the thermochemical tables be adopted.[34,35,36,37] You can purchase their curve fit package, or you can purchase their curve-fit program from which you can attempt your own curve fits, although the latter is recommended only when you need special curve fits to new data that are not provided by NASA.

## 7. DISTRIBUTED PARTICLE SURFACE MODEL FOR GAS-PARTICLE FLOWS AND PARTICLE-PARTICLE COLLISIONS

The motions of the combustion gases and burning propellant grains or particles in closed vessels and guns is complicated. The combustion gases evolve from the burning

---

[34] Gordon S., and McBride, B.J., 1994, "Computer Program for Calculation of Complex Chemical Equilibrium Compositions and Applications, I. Analysis," NASA Reference Publication 1311

[35] McBride, B.J., and Gordon, S., 1996, "Computer Program for Calculation of Complex Chemical Equilibrium Compositions and Applications, II. Users Manual and Program Description," NASA Reference Publication 1311.

[36] McBride, B.J., and Gordon, S., 1992, "Computer Program for Calculating and Fitting Thermodynamic Functions," NASA Reference Publication 1271.

[37] McBride, B.J., and Gordon, S., 1993, "Coefficients for Calculating Thermodynamic and Transport Properties of Individual Species," NASA Technical Memorandum 4513.

propellant particles around which a combustion flame yields heat transfer by conduction, convection and radiation that further volatizes the particle surface as part of the combustion process. The combustion products that flow through the flame, away from grain, reaches the walls of the closed vessel or gun, which results in conductive, convective and radiative heat transfer to these walls. The flow of combustion products away from the particle at which they originate also produces pressure forces and aerodynamic drag on the surrounding burning particles, and such forces sets these particles into motion. During combustion the particles are lofted throughout a closed vessel or propelled along the combustion chamber and barrels of guns. The resulting motion of the particles is not uniform locally and particle-particle jostlings and particle-wall collisions occur frequently when the particles are numerous, concentrated, or stacked.

Current computations of gas-particle mixtures assume that gas and particles are separate continuum phases, each phase governed by the conservation of mass, momentum, energy and total volume (gas and particle volumes), and all interactions between the phases are in the form of source terms for mass (combustion products transfer from burning particles to gases), momentum (combustion product momentum transfer from particles to gases, aerodynamic drag, particle and gas friction at walls, viscous effects due to particle beds) and energy (combustion product heat transfer).[38,39,40] This model is deficient in two respects: the drag model for particle motions is insufficient and the handling of particle-particle collisions is missing.

These deficiencies can be overcome by using a continuum model for the gas and a noncontinuum model for the particles, that is by computing the gas flow within the closed vessel or gun but around the particles as individual moving objects, akin to computing the flow over a moving airfoil (unsteady).[41,42] Today, this is practical only for the case of a few particles, because of the large computer information storage associated not only with tracking all particles but also with being able to reproduce their surfaces when required by using a local particle coordinate system and surface information, and also by doing boundary conditions around all particles to evaluate lift, drag and torque. To overcome this horrendous storage problem, and to eliminate the use of cut cells at gas and particle boundaries, I have proposed a new model of particles with slightly distributed and porous boundaries.

Each particle has a slightly distributed surface through which the gas can flow, but the relative motion between the gas and particle is impeded by viscous forces which increase rapidly into the particle. Particles are therefore porous with most of the flow going around the particles (outside and in the distributed region), and very little through the core of

---

[38] Rudinger, G., 1980, "Fundamentals of Gas-Particle Flow," Elsevier Scientific Publising Company, New York.

[39] Hetsroni, G., 1982, "Handbook of Multiphase Systems," McGraw-Hill Book Company, New York.

[40] Soo, S.L , 1967, "Fluid Dynamics of Multiphase System," Blaisdell Publishing Company, Ginn and Compayn (Xerox Corporation), Lexington, Massachusetts (formerly Blaisdell, Waltham, Massachusetts

[41] Powell, K.G., Roe, P., and Quirk, J., 1993, "Adaptive-Mesh Algorithms for Computational Fluid Dynamics," in "Algorithmic Trends in Computational Fluid Dynamics," Springer-Verlag, New York.

[42] Bayyuk, S.A., Powell, K.G , and Van Leer, B., 1993, "A Simulation Technique for 2-D Unsteady Flows Around Arbitrary Moving and Deforming Bodies of Arbitrary Geometry," AIAA Paper 93–1930.

the particle. A particle is mapped into three-dimensional space as a porosity distribution and moves in translation and rotation determined by the viscous forces of the relative flow primarily through its surface distribution. Particle-particle collisions are handled by letting the distributed surfaces overlap and generate repulsion forces and torques from the degree of overlap and relative motion in translation and rotation. This model eliminates the needs for tracking individual particles and knowing where the surfaces are, by tracking only their porosity distributions on the grid. Computational updates of the gas and particle motions are done on all cells outside and inside particles.

Chak M. Tsui was my first student on this project, and he studied the reflection of a shock wave from the end wall of a shock tube that was slightly distributed and porous. His work is reported in Appendix 8, "Computational Model for Gas-Particle Flows using Particles with Distributed Surfaces," although his exact thesis title is "A Computational Model for Gas-Particle Flows with Distributed Phase Interfaces." We encountered some difficulties in integrating the final set of Ordinary Differential Equations with the ODE solver called VODE, so the project did not proceed quickly and the results are inconclusive. The primary problem that I found later in his written report was that the pressure derivative was evaluated by a central difference technique, which made the equations marginally stable and very stiff. With this problem corrected, results can be obtained more easily. However, his results could not be reworked in the time available, and this first project has to be repeated.

At the same time as Chak Tsui's work was progressing, I asked Vlad Vainberg to study particle-particle collisions without the presence of a gas. His work is reported in Appendix 9, "Numerical Study of Particle-Particle Collisions using Particles with Distributed Surfaces," and his exact thesis title was "The Numerical Study of Particle-Particle Collisions using a Distributed Particle Surface Model." He showed that a particle could be represented as a porosity distribution in space and propagated with little spreading or dispersion. He also showed that a particle with a distributed interface could be bounced off a wall which also had a distributed interface.

The work on gas flow through particles interfaces and that on particle-particle collisions is presently being developed further with the intent of applying these concepts to helping to solve the gas-particle flows occurring in the closed vessel. The objective is to obtain more realistic results for the case with particle-particle collisions.

# APPENDIX 1

# CHEMICAL EQUILIBRIUM ANALYSIS FOR GASEOUS AND CONDENSED COMBUSTION PRODUCTS AT CONSTANT VOLUME (Ph.D. Thesis)

by

**Frederick C. H. Wong**

# CHEMICAL EQUILIBRIUM ANALYSIS OF COMBUSTION PRODUCTS AT CONSTANT VOLUME

by

Frederick C. H. Wong

A thesis submitted in conformity with the requirements
for the degree of Doctor of Philosophy
Graduate Department of Aerospace Science and Engineering
University of Toronto

Copyright © 2000
by Frederick C. H. Wong

# Abstract

A new computational code was developed to determine the high-temperature and high-pressure combustion products of energetic materials inside a constant-volume vessel with the assumptions of chemical equilibrium and adiabatic vessel walls. The product mixture was modelled as an equilibrium mixture of gases with pure condensates dispersed uniformly. The Villar-Cruise-Smith minimization algorithm that is optimized, based on a stoichiometric formulation, uses chemical equations and does not require matrix inversions was applied to solve this chemical equilibrium problem. The resulting computational code is versatile, robust and easy to use, and different models and complicated equations of state can be used for describing the mixture of gases and the condensates. Solutions to extremely difficult problems involving many gaseous and condensed products, problems that previous major computational codes have difficulty solving, were easily and straightforwardly obtained by this new code. New procedures were also implemented to handle the special case of phase transitions of condensed substances; the new code can consequently obtain solutions to problems with phase transitions for which previous major codes failed. The new code can also routinely handle large systems involving hundreds of gaseous and condensed product species.

# Acknowledgements

I wish to express my deepest gratitude to Prof. J. J. Gottlieb, my thesis supervisor, for his guidance, encouragement and support throughout the course of the present study. His continual interest in this study is very much appreciated.

I would also like to thank Profs. A. A. Haasz and P. A. Sullivan, the other members of my doctoral committee, for their interest and advice regarding this study.

Many thanks should go to Dr. L.-S. Lussier for numerous discussions on chemical equilibrium computational work on constant-volume combustion conducted at the Defence Research Establishment at Valcartier (DREV), and also for supplying me with results of closed-vessel experiments. The discussions on the NASA computational code with Mr. R. Stowe at DREV is also gratefully acknowledged. My gratitude is extended to Dr. J. Lavigne at DREV, the contract monitor during the initial phase of this project, for his interest in the project.

I am grateful to Dr. E. Freedman for providing me with a copy of the Blake chemical equilibrium computational code, and for discussions with him on some code applications.

My appreciation is extended to Judy Mills and Nora Burnett of the UTIAS library for their timely and unfailing assistance in obtaining the necessary technical documents for the present research.

Financial support in the form of UTIAS student assistantships stemming from a DREV contract with the University of Toronto and from NSERC operating grants (OGP0003539) to my supervisor are acknowledged with thanks.

# Contents

**Abstract** ii

**Acknowledgements** iii

**Nomenclature** v

**1 Introduction** 1

**2 Summary of Chemical Equilibrium Theory and Solution Practices** 5

- 2.1 Chemical Equilibrium Theory . . . . . 5
  - 2.1.1 Definitions . . . . . 5
  - 2.1.2 Characteristics of Chemical Equilibrium . . . . . 6
  - 2.1.3 Constraints . . . . . 8
  - 2.1.4 Conservation of Mass Constraint . . . . . 8
  - 2.1.5 Nonnegativity Constraint . . . . . 9
  - 2.1.6 Thermodynamic State Constraints . . . . . 9
  - 2.1.7 Thermodynamic Potential Functions and Equilibrium Criteria . . . . . 10
  - 2.1.8 Chemical Stoichiometry . . . . . 10
  - 2.1.9 Equilibrium Formulations for a Given Temperature and Pressure . . . . . 16
  - 2.1.10 Chemical Potentials for Gaseous and Condensed Species . . . . . 18
  - 2.1.11 JANAF Tables of Thermochemical Properties . . . . . 28
  - 2.1.12 Equations of State for Gaseous and Condensed Species . . . . . 29
  - 2.1.13 Implications of the Nonnegativity Constraint . . . . . 36
  - 2.1.14 Phase Rule and Chemical Equilibrium Solutions . . . . . 37
- 2.2 Numerical Methods and Equilibrium Solution Algorithms . . . . . 39
  - 2.2.1 Second Variation Method for Unconstrained Minimizations . . . . . 39
  - 2.2.2 Newton-Raphson Method for Nonlinear Equations . . . . . 40
  - 2.2.3 Nonstoichiometric Algorithms . . . . . 41
  - 2.2.4 Numerical Singularities in Equilibrium Computations . . . . . 44

2.2.5 Stoichiometric Algorithms . . . . . . . . . . 47

2.2.6 Relative Merits of BNR Nonstoichiometric Algorithms and VCS Stoichiometric Algorithm . . . . . . . . . . 47

2.3 Major Computational Codes for Chemical Equilibrium . . . . . . . . . . 50

2.3.1 NASA Code . . . . . . . . . . 50

2.3.2 Bagheera Code . . . . . . . . . . 51

2.3.3 Blake Code . . . . . . . . . . 52

2.3.4 Potential Numerical Difficulties . . . . . . . . . . 54

**3 Adaptation of VCS Algorithm** **55**

3.1 Basic VCS Algorithm for a Given Temperature and Pressure . . . . . . . . . . 55

3.2 Treatment of Condensed Species . . . . . . . . . . 59

3.3 Inclusion of Thermodynamic Data and Selection of Condensed Species . . . . . . . . . . 60

3.4 Initial Estimates . . . . . . . . . . 64

3.5 Equilibrium Iterative Procedures . . . . . . . . . . 65

3.6 Treatment of Trace Gaseous Species . . . . . . . . . . 67

3.7 Inclusion of Different Gaseous Mixture Models . . . . . . . . . . 69

3.7.1 Perfect-Gas Mixture . . . . . . . . . . 69

3.7.2 Ideal Mixture of Imperfect Gases . . . . . . . . . . 69

3.7.3 Nonideal Mixture of Imperfect Gases . . . . . . . . . . 70

3.8 Inclusion of Different Equations of State for Gaseous Species . . . . . . . . . . 71

3.8.1 Redlich-Kwong-Soave EOS . . . . . . . . . . 71

3.8.2 Benedict-Webb-Rubin-Starling EOS . . . . . . . . . . 73

3.8.3 Truncated Virial EOS . . . . . . . . . . 75

3.8.4 Modified Virial EOS . . . . . . . . . . 76

3.8.5 Truncated Virial EOS (rigid sphere model for third coefficients) . . . . . . . . . . 76

3.9 Inclusion of Different Compressibility Models for the Condensed Species . . . . . . . . . . 77

3.10 Inclusion of Different Equations of State for Condensed Species . . . . . . . . . . 79

3.10.1 Polynomial Type Empirical Equation of State . . . . . . . . . . 79

3.10.2 Redlich-Kwong-Soave EOS for Liquid Species . . . . . . . . . . 79

3.10.3 Approximate Equation of State for Solid Species . . . . . . . . . . 79

3.11 Treatment of Melting . . . . . . . . . . 80

3.11.1 Procedures Based on the NASA and Bagheera Models of Phase Transition Curves . . . . . . . . . . 80

3.11.2 Procedure Based on the Blake Model of Phase Transition Curves . . . . . . . . . . 84

3.12 Inclusion of Numerous Gaseous and Condensed Species . . . . . . . . . . 90

**4 Computational Code, Validation, Capability and Robustness** **91**
4.1 Computational Code . . . . . . . . . . . . . . . . . . . . . . . . . . . . . . . . 91
4.2 Some Validations . . . . . . . . . . . . . . . . . . . . . . . . . . . . . . . . . . . 92
  4.2.1 Hydrazine Combustion Problem . . . . . . . . . . . . . . . . . . . . . . 92
  4.2.2 Blast Furnace Problem . . . . . . . . . . . . . . . . . . . . . . . . . . . . . 93
  4.2.3 Hydrogen-Oxygen Reaction Problem . . . . . . . . . . . . . . . . . . . . 94
4.3 Demonstration of Treatment of Condensed Species . . . . . . . . . . . . . . . . . 98
  4.3.1 Capability to Precisely Determine the Presence and Absence of Condensed Species . . . . . . . . . . . . . . . . . . . . . . . . . . . . . . . . . . 98
4.4 Demonstration of Treatment of Melting . . . . . . . . . . . . . . . . . . . . . . . 106
  4.4.1 Results Based on the NASA Models . . . . . . . . . . . . . . . . . . . . . 106
  4.4.2 Results Based on the Blake Models . . . . . . . . . . . . . . . . . . . . . 109
4.5 Demonstration of Inclusion of Numerous Gaseous and Condensed Species . . . . . . 111

**5 Critical Assessment of Computational Codes** **113**
5.1 Equilibrium Calculations for a Moderate Number of Species with No Melting . . . . 113
  5.1.1 Test Cases and Procedure . . . . . . . . . . . . . . . . . . . . . . . . . . . 113
  5.1.2 Comparison of Results of the NASA and New Codes . . . . . . . . . . . . . . 118
  5.1.3 Comparison of Results of the Bagheera and New Codes . . . . . . . . . . . . 124
  5.1.4 Comparison of Results of the Blake and New Codes . . . . . . . . . . . . . . 126
5.2 Equilibrium Calculations for a Moderate Number of Species with Melting . . . . . . 130
  5.2.1 Comparison of Results of the NASA and New Codes . . . . . . . . . . . . . . 130
  5.2.2 Comparison of Results of the Bagheera and New Codes . . . . . . . . . . . . 138
  5.2.3 Comparison of Results of the Blake and New Codes . . . . . . . . . . . . . . 141
5.3 Equilibrium Calculations for a Large Number of Species Without and With Melting 144

**References** **149**

# Nomenclature

**Alphanumeric**

$\mathbf{0}$ → null vector

$a$ → number of atoms of an element in a species molecule

→ polynomial coefficients from fitting thermodynamic data (equations 2.89 to 2.91)

→ parameter for evaluating temperature-dependent coefficients of empirical equation of state for condensed species (equations 2.147 to 2.149)

$\mathbf{a}$ → formula vector of a species

$A$ → molecular formula of a species

→ temperature-dependent coefficients of empirical equation of state for condensed species (equation 2.146)

$\mathbf{A}$ → formula matrix of a system

$b$ → total number of moles of an atomic element in a system

→ polynomial coefficients of from fitting thermodynamic data (equations 2.90 and 2.91)

$\mathbf{b}$ → elemental-abundance vector of a system

$B$ → second virial coefficient

$c_p$ → molar heat capacity at constant pressure of a species

$C$ → rank of formula matrix $\mathbf{A}$

→ third virial coefficient

$g$ → molar Gibbs function of a species

$G$ → total Gibbs function of a system

$\delta G$ → change in total Gibbs function of a system

$\Delta G$ → change of Gibbs function across a chemical reaction

$h$ → molar enthalpy of a species

$lq$ → liquid phase of a substance

$\mathcal{L}$ → Lagrangian of a system

$M$ → number of atomic elements involved in a system

$n$ → number of moles of a species

$\mathbf{n}$ → species-abundance vector of a system

$\delta\mathbf{n}$ → species-abundance-change vector of a system

$n_t$ → total number of moles of species in a multispecies phase

$n_{t_g}$ → total number of moles of gases in a mixture which comprises gases and pure condensates

$n_z$ → number of moles of inert gases in a gaseous mixture

$N$ → number of species in a system

$\mathbf{N}$ → stoichiometric matrix of a system

$N_c$ → number of condensed species in a system

$N_g$ → number of gaseous species in a system

$p$ → pressure

→ partial pressure of a gaseous species

$P$ → system pressure

$\mathbf{Q}$ → matrix whose elements are zeros, except that $Q_{11}$ is equal to $-n_g$

$R$ → maximum number of linearly independent chemical equations for species in a system

→ universal gas constant

$s$ → molar entropy of a species

→ solid phase of a substance

$T$ → temperature

→ system temperature

$T_t$ → trial equilibrium system temperature

$u_c$ → molar internal energy of a condensed species

$u_g$ → molar internal energy of a gaseous species

$U_c$ → total internal energy of condensed products

$U_g$ → total internal energy of gaseous products

$U_p$ → total internal energy of products

$U_r$ → total internal energy of reactants

$\Delta U$ → difference between total internal energy of products and reactants $(U_p - U_r)$

$v$ → molar volume

$\bar{v}$ → partial molar volume of a species

$V$ → volume of a gaseous mixture

$x$ → mole fraction of a species in a gaseous mixture

$\mathbf{x}$ → species mole fractions vector of a gaseous mixture

$z$ → compressibility factor

**Greek**

$\alpha$ → phase designator

→ parameter in modified virial equation of state (equation 2.180)

$\beta$ → phase designator

→ parameter in modified virial equation of state (equation 2.180)

$\boldsymbol{\beta}$ → coefficient matrix of linearized equations of BNR algorithms

$\delta_{ij}$ → Kronecker delta; $\delta_{ij} = 1$ if $i = j$ and $\delta_{ij} = 0$ if $i \neq j$

$\delta_k$ → phase related parameter; $\delta_k = 1$ if the $k^{\text{th}}$ species is gaseous and $\delta_k = 0$ if the $k^{\text{th}}$ species is condensed

$\phi$ → fugacity coefficient

$\lambda$ → Lagrange multiplier

$\lambda$ → Lagrange multipliers vector
$\Lambda$ → diagonal matrix whose diagonal elements are $\{n_1, n_2, \ldots, n_{N'}\}$
$\mu$ → chemical potential of a species
$\boldsymbol{\mu}$ → chemical potentials vector of species in a system
$\nu$ → stoichiometric coefficient
$\boldsymbol{\nu}$ → stoichiometric vector
$\pi$ → total number of phases in a system
$\xi$ → reaction extent parameter
$\boldsymbol{\xi}$ → reaction extent vector
$\delta\xi$ → change in reaction extent parameter
$\boldsymbol{\delta\xi}$ → reaction extent change vector

### Subscripts

$i$ → index for species and also chemical equations
$j$ → index for chemical equations and also species
$k$ → index for elements, Lagrange multipliers and also species
$l$ → index for species
$m$ → mixture (gaseous)
→ melting condition

### Superscripts

$-1$ → inverse of a scalar or of a matrix
$0$ → standard quantity at reference pressure of one unit
$m$ → index of iteration steps
$T$ → transpose of a vector or of a matrix
$*$ → standard quantity at system pressure $P$
$'$ → first derivative of temperature

### Chemical Formulae (some examples)

$H_2O$ → gaseous phase (water vapor) of substance water
$H_2O(lq)$ → liquid phase (water) of substance water
$H_2O(s)$ → solid phase (ice) of substance water
$Na_2S(s\text{-}1)$ → solid phase '1' of substance disodium sulfide
$Na_2S(s\text{-}2)$ → solid phase '2' of substance disodium sulfide
$PbO$ → gaseous phase of substance lead oxide
$PbO(lq)$ → liquid phase of substance lead oxide
$PbO(s\text{-}yw)$ → solid phase 'yellow' of substance lead oxide

# Chapter 1

# Introduction

Materials that burn or combust at rapid rates and in the process release exothermically significant amounts of heat are often called energetic materials. The applications of energetic materials range from the simple lighting of a match, artistic displays of colourful fireworks, demolition of buildings, fracturing of rocks for mining and road building, propulsion of rockets, to military devices used to generate explosions. As the applications become more sophisticated the required level of understanding of the characteristics of energetic materials also increases.

Depending on the applications, energetic materials can be divided into a variety of categories; for example, primers, igniters, propellants, explosives and fuses. Primers are sensitive exothermic mixtures mainly responsible for the ignition of some other energetic materials, usually an igniter. Once an igniter starts burning, it normally produces large amounts of gases at high temperature, which will then ignite a propellant or an explosive. Alternatively, propellants and explosives are primary energy releasing agents which normally perform tasks. Propellants will usually have much longer burning times then explosives. Finally, fuses while burning emit insignificant amounts of gases and form mainly condensed liquid and solid products. They are often used to provide time-delayed ignitions.

The present project was initiated as a result of the development program on low vulnerability propellants for military guns being undertaken at the Defence Research Establishment Valcartier (DREV), Courcelette, Quebec. Such new propellants are not as easily ignited comparing to previous conventional propellants, with the specific intent of reducing the possibility of accidental ignition and increasing the level of safety during ammunition transportation and handling. While new propellant ingredients are being tested to reduce ignition sensitivity for safety reasons, there are energetic requirements that such propellants must meet to fulfill objectives. To evaluate the burning characteristics of a particular propellant, sample grains of the propellant are combusted inside a sealed, almost rigid, container and the pressure change inside the container is recorded during the experiment.

Explosive containers are frequently referred to as closed vessels. DREV has two such experimental vessels, one with a chamber volume of 200 cm$^3$ and the other with a volume of 700 cm$^3$, which conforms to NATO standards. The schematic of a typical closed vessel is shown in figure 1.1. Normally, such a vessel will consist of a thick-walled, hollow, steel cylindrical body; two threaded plugs, one at each end; and an inner replaceable steel liner. The chamber can be filled by propellant grains to various amounts to simulate different loading conditions in guns. Two firing electrodes are mounted inside, on one of the end plugs, with the firing pins protruding into the chamber for ignition. Often the grains are not ignited directly, but rather an igniter (such as black powder)

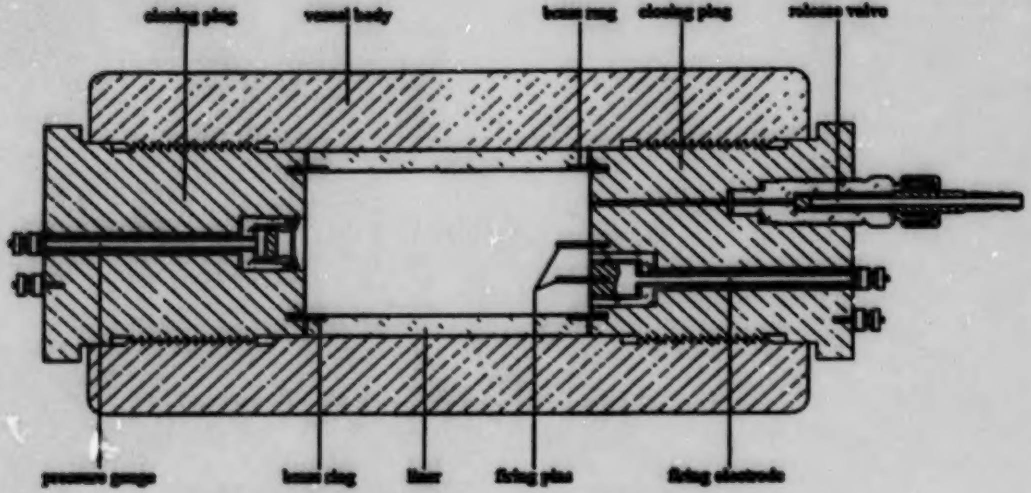

Figure 1.1: Schematic diagram of a typical closed vessel.

will be ignited first. The heat of the burning igniter in turn ignites the propellant grains. A piezoelectric gauge is installed in the other end plug, with the gauge surface almost flush with the inner plug wall, for measuring the pressure changes of the reactant gases inside the chamber during combustion. In the end plug containing the firing electrode, a channel and valve are provided to allow the release of the high temperature and pressure products at the completion of combustion. The end plugs are thread fitted for easy assembly and disassembly, and sometimes to facilitate a chamber volume adjustment. The 200 cm$^3$ vessel at DREV can sustain a maximum pressure of 850 MPa, while the 700 cm$^3$ NATO standard vessel can sustain a maximum of 325 MPa.

Shown in figure 1.2 is an example time-history signature of the pressure changes occurring during a closed-vessel experiment. Once combustion has started, the pressure inside the vessel rises rapidly with time to some maximum value and then decreases gradually due to heat losses to the vessel wall. Had there been no heat losses to and no gas leakage through the vessel walls, the maximum pressure would remain constant with time.

From the pressure signature recorded during a closed-vessel firing, certain parameters such as the burning rate of a particular propellant and the force and co-volume constants of a co-volume equation of state can be deduced. However, there are time and economical reasons that it would be advantageous if the burning properties of a propellant can be determined numerically with the use of computational programs and analytical models. Such programs can be useful tools in the developmental stage of new propellants. At the present time, no complete modelling of the process of burning large number propellant grains in a closed vessel has been done. Such a process would be quite complicated because the motion of propellant grains, burning at grain surfaces, combustion chemistry, turbulent mixing of product species and heat transfer to the vessel wall would all need to be taken into account. Computational codes have been developed to analyse the combustion products in a closed vessel by assuming that adiabatic combustion occurs and that chemical and mechanical equilibrium of the gaseous and condensed products species exist.

Currently, there are several computational codes available for propellant analysis based on the assumptions mentioned previously. These include the Blake and Bagheera codes, which are

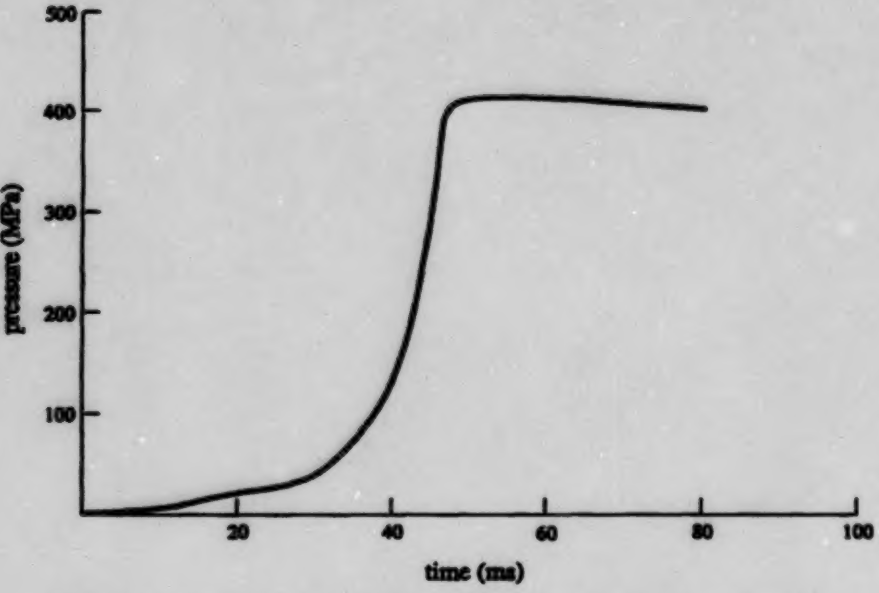

Figure 1.2: Pressure-time signature from a closed-vessel experiment.

the previously and presently agreed standard codes, respectively, for propellant research among the NATO countries. Difficulties in achieving convergence with Blake, particularly for cases involving a large number of condensed products, have been reported by Lussier [1991]. The primary objective of the present work was to develop a new chemical equilibrium computational code with improved convergence capability. During the course of this work the Bagheera code was adopted as the new standard computational code for NATO countries; consequently, it was also studied in this work.

The chemical equilibrium problem is a difficult minimization problem. At equilibrium, for a given temperature and pressure, the Gibbs free energy of a system is at a minimum. The formulations of the equilibrium problem can be broadly classified into two fundamental categories, stoichiometric and nonstoichiometric. All of the major computational codes that are currently in use for propellant analysis are based on nonstoichiometric formulations. Numerical iterative procedures for solving the equilibrium problem formulated by using this category of formulation require the inversion of a matrix at each iteration step in the minimization. Occasionally, such a matrix may become singular, especially with the occurrence of condensed species in a system, and this often causes convergence difficulties. The present project includes work to adapt a numerical algorithm, which is based on a stoichiometric formulation, to obtain equilibrium solutions to closed-vessel problems. The new algorithm is named after the three original workers as the Villar-Cruise-Smith (VCS) algorithm, who contributed to its various stages of development. The new algorithm does not require the inversion of a matrix; hence, it does not have the singularity problem inherent in previous algorithms based on nonstoichiometric formulations. The new algorithm is also more robustness.

A summary of chemical equilibrium theory and solution methods is given in chapter 2, and a review of the major computational codes for the propellant analysis is also presented. The adaptation of the VCS numerical algorithm to chemical equilibrium calculations at constant volume is described next in chapter 3. The versatility, capabilities and robustness of the new code were demonstrated with many exemplary calculations, and these results are presented in chapter 4. Results of a critical comparison between the previous major codes and the new code are presented next in chapter 5.

# Chapter 2

# Summary of Chemical Equilibrium Theory and Solution Practices

Solutions to complicated equilibria of a mixture of gaseous and pure condensed species in an adiabatic and constant-volume vessel are sought for in the present study. In this chapter the basic concepts and information which are important to the understanding of this study are presented. Many aspects of chemical equilibrium theory are described first. A survey of chemical equilibrium solution methods is presented next. Previous major computational codes for equilibrium analysis are introduced last.

## 2.1 Chemical Equilibrium Theory

### 2.1.1 Definitions

To facilitate the following discussions, some terms and symbols are defined in this section, even though some of the terms have already been used.

**Phase:** A phase is a quantity of matter that is homogeneous in its properties. Examples of phases are a gas or a mixture of gases, a liquid or a liquid solution, and a solid crystal. A phase need not be continuous. For the present study, pure solids and liquids, which are condensed phases, are assumed as dispersed throughout a continuous phase of gases.

**Species:** A species is a chemical entity which is distinguished from another one by its molecular formula, the phase in which it exists, and its molecular structure. Therefore, carbon dioxide gas and water vapour, liquid water and water vapour, as well as the alpha and beta forms of solid potassium sulphate, are examples of different species. In this report, species are also referred to by their molecular formulae. Since most of the species that were dealt with were gaseous species, the phase designation of gaseous species has been omitted. Otherwise, a phase designation is provided together with the molecular formula. For example, $CO_2$ and $H_2O$ stand for carbon dioxide gas and water vapour, respectively, $H_2O(lq)$ and $H_2O(s)$ denote liquid water and solid water (ice), respectively, and $K_2SO_4(s\text{-}\alpha)$ and $K_2SO_4(s\text{-}\beta)$ denote the alpha and beta forms of solid potassium sulphate, respectively.

**Substance:** A substance is a chemical entity distinguished from another by its molecular formula. Therefore, $H_2O$, $H_2O(lq)$ and $H_2O(s)$ are the same substance, and $K_2SO_4(s\text{-}\alpha)$ and $K_2SO_4(s\text{-}\beta)$ are also the same substance.

**System:** The system investigated herein involves a collection of $N$ species formed from a group of $M$ elements, with $N$ being larger than $M$. ($N$ must be larger than $M$ for a meaningful problem.) Such a system can be expressed as

$$\{(A_1, A_2, \ldots, A_i, \ldots, A_N), (E_1, E_2, \ldots, E_k, \ldots, E_M)\},$$

where $A_i$ is the molecular formula of the $i^{\text{th}}$ species, with appropriate phase and structural designations if necessary, and $E_k$ is the $k^{\text{th}}$ type of element. A system is said to be closed if it does not interchange matter with its surroundings. A system is said to be adiabatic if it does not interchange heat with its surroundings. If it does not interchange both heat and matter with its surroundings, then it is said to be isolated. The system in this investigation is of this latter type.

### 2.1.2 Characteristics of Chemical Equilibrium

When a thermodynamic system is left alone, initial changes in its properties may occur. The system is said to have reached an equilibrium state, when all its properties have ceased to change, usually after a long enough period of time. Sometimes the more complete term, thermodynamic equilibrium, is used to mean that thermal, mechanical as well as chemical and/or phase equilibrium have been reached by the system.

Thermal equilibrium has been attained when temperature is equalized, as a result of heat transfer, everywhere within a system. On the other hand, mechanical equilibrium has been attained within a system when all the forces are balanced. This does not necessarily mean that pressure is the same everywhere within the system. Consider the example of a vertical column of fluid under the influence of a gravitational field. The pressure in the fluid will decrease with increasing elevation, and each fluid element in the column is in mechanical equilibrium under the action of its own weight and the buoyancy force due to the difference in pressure at its upper and lower surfaces [Sears and Salinger, 1975, pp. 16–17].

If the system under consideration is a chemically reacting one, then chemical equilibrium is reached when the system composition does not change any further with time. Or if there are nonreacting substances existing in more than one phase in a system, then phase equilibrium has occurred when the composition, as a result of internal mass transfer, becomes constant throughout each phase (compositions of different phases are different). Of course, there are cases when chemical reactions as well as phase transitions take place among the various species in a system. In this report, the term chemical equilibrium denotes cases where phase equilibrium exists in a system as well, and thermodynamic equilibrium is implied.

There are several characteristics of chemical equilibrium [Mahan, 1975, pp. 174–178] that are worth noting. Such characteristics can be illustrated by considering the example of thermal decomposition of calcium carbonate ($CaCO_3(s)$). When calcium carbonate, which is a solid at atmospheric condition, is heated inside an enclosed, constant-volume vessel, decomposition occurs giving rise to calcium oxide $CaO(s)$ and carbon dioxide $CO_2(g)$. As the amounts of calcium oxide and carbon dioxide continue to increase, they recombine to form calcium carbonate again. After some time no further changes in the amounts of the three species are observed, and an equilibrium situation is reached. The decomposition and recombination reactions and the equilibrium situation can all be expressed as

$$CaCO_3(s) \rightleftharpoons CaO(s) + CO_2(g). \tag{2.1}$$

The right pointing arrow is used to indicate calcium carbonate decomposes into calcium oxide and carbon dioxide, and the left pointing arrow is used to indicate calcium oxide combines with carbon dioxide to form calcium carbonate.

The first characteristic of chemical equilibrium is that there is a natural tendency for a system to undergo changes in composition on approaching an equilibrium state. When a system is left alone long enough, an equilibrium state will eventually be attained. The composition of the system will then remain unchanged with time, as long as there is no change from influencing factors such as the temperature and pressure.

Consider the above example again. If the temperature of the contents of the vessel and the volume of the vessel (which would imply a certain value of pressure will be exerted by the carbon dioxide) are kept constant, and the contents of the vessel are left alone long enough, the system will eventually approach an equilibrium state.

The second characteristic is that the same equilibrium state will always be attained once the system defining parameters are fixed, regardless of the initial composition of the system.

Consider the above example once again. Given the same amount of matter (to be elaborated further in section 2.1.4) to begin with inside the vessel, if the temperature is held constant, then the same equilibrium composition will be obtained, regardless of whether calcium carbonate is allowed to form calcium oxide and carbon dioxide, or the reverse. As a matter of fact, the initial condition is not limited to these two species, there can be a certain amount of each species to begin with and the same equilibrium composition will still be obtained.

The first and second characteristics combined has the implication that a system that has reached chemical equilibrium is stable with respect to fluctuations in system defining parameters. That is, once the fluctuations decay and the original values of the parameters have been restored, the same equilibrium composition will eventually be attained. This, of course, is related to the fact that the state of a thermodynamic system is fixed once the value of the system defining parameters are specified.

The third characteristic is that the state is not static but rather dynamic, meaning that even though the composition does not appear to change at the macroscopic level, at the microscopic level there are ongoing reactions occurring among the various species in the system. At equilibrium, reactions are proceeding in such a way that the rates of depletion and production of each species are equal, thereby resulting in no net change in the amount of each species.

In the previous example, calcium carbonate decomposes to form calcium oxide and carbon dioxide, but at the same time calcium carbonate is formed when calcium oxide recombines with carbon dioxide. At equilibrium, the rate of decomposition and rate of recombination are equal; the abundance of each of the three species, therefore, remains unchanged.

The fourth characteristic is that the state arises as a result of a balance between two opposing tendencies. The first being the tendency to assume a state of minimum energy and the second being the tendency to attain a state of maximum molecular disorder or entropy.

Refer to this example again. When calcium carbonate (a solid) decomposes into calcium oxide (another solid) and carbon dioxide (a gas), greater molecular disorder occurs because the gaseous molecules are free to move within the vessel. However, energy is absorbed in this process and this indicates that the resulting products, calcium oxide and carbon dioxide, have a higher total energy content than the lone reactant, calcium carbonate. Therefore, the tendency to attain a state of maximum molecular disorder will favour the decomposition reaction, whereas the tendency to assume a state of minimum energy will favour the combination reaction. Equilibrium occurs when the two tendencies reach a compromise.

### 2.1.3 Constraints

Chemical equilibrium analyses are done in general for a system with a number of constraints that can be classified as given below [Smith and Missen, 1982, pp. 4–5]:

**Overriding Constraints** These include tensile, surface, field, acceleration and nuclear effects. In this study these effects were assumed either absent or their influence small enough to be neglected; only the chemical thermodynamics of the system is considered. If, under such an assumption, the effect of gravity on the equilibrium mixture was ignored, then the pressure of the mixture would be constant throughout the vessel, and the pressure would be due entirely to the random motions of gaseous molecules and their intermolecular force fields.

**Mandatory Constraints** These are thermodynamic equilibrium criteria involving the conservation of mass constraint and the nonnegativity constraint. In the latter case the mole number of a species at equilibrium should either be positive (the species exists in a finite amount) or zero (the species does not exist).

**Specific Constraints** These are particular problem parameters, such as the temperature and pressure of the system, the kind of species involved, the molar amount of each element inside the system (for conservation of mass consideration), and if there are any inert species.

### 2.1.4 Conservation of Mass Constraint

The system investigated consisted of a mixture of combustion products enclosed in a constant volume. No mass transfer across the system boundary was assumed; the mass of the system was conserved. This implied that the mass of the products must equal that of the reactants. In addition, the system mass would also be conserved throughout the process in approaching equilibrium.

Mathematically, such a constraint can be defined by a set of equations relating the total atomic abundances of the chemical elements making up the product species to some stipulated values [Smith and Missen, 1982, pp. 15–16], which can be written as

$$\sum_{i=1}^{N} a_{ki} n_i = b_k, \quad \text{with} \quad k = 1, 2, \ldots, M. \tag{2.2}$$

In this equation, $a_{ki}$ is the subscript of the $k^{\text{th}}$ element in the molecular formula of the $i^{\text{th}}$ product species, which is the number of atoms of the $k^{\text{th}}$ element involved in forming a molecule of the species, $n_i$ is the number of moles of the $i^{\text{th}}$ product species postulated, $b_k$ is the number of moles of atoms of the $k^{\text{th}}$ element in the system, which is assigned and fixed for a given problem, $M$ is the number of element types in the system and $N$ is the number of product species considered.

The set of $b_k$ stipulates the amount of substances or matter (mass) enclosed in the system, which is fixed and determined when the amounts of reactants are specified for a problem. At the same time the set of $n_i$ represents the composition of the product mixture and take on different values as the system evolves towards the equilibrium state. What equation 2.2 requires is that for a set of $n_i$ to be a possible solution of the equilibrium composition the set must give the specified amount of matter. They therefore specify the law of conservation of mass.

Equations 2.2 can be written in vector-matrix notation as

$$\mathbf{A}\mathbf{n} = \mathbf{b}, \tag{2.3}$$

where $\mathbf{A}$ and $\mathbf{b}$ are called the formula matrix and element-abundance vector of the system, respectively, and $\mathbf{n}$ is a species-abundance vector.

The matrix A has a dimension of $M$ by $N$ and with each column composed of $a_{ki}$ from the same species. Each of these columns can be considered as a vector and is call a formula vector (for the reason that its entries are the subscripts to the elements in the molecular formula of a species). Hence, if the formula vector of the $i^{th}$ species is denoted as $\mathbf{a}_i$, then

$$\mathbf{A} = [\mathbf{a}_1, \mathbf{a}_2, \ldots, \mathbf{a}_N], \tag{2.4}$$

and it is clear why A is called a formula matrix. (An example of A is given in section 2.1.8.)

Alternatively, equation 2.3 may be rewritten to become a constraint on the changes in compositional states as

$$\mathbf{A}\,\delta\mathbf{n} = 0, \tag{2.5}$$

where $\delta\mathbf{n}$ is called the species-abundance-change vector. Its elements $\delta n_i$ are the differences or changes in the number of moles of the $i^{th}$ species between two compositional states of the system. When solving for the equilibrium composition numerically in this study, equation 2.5 is used when the composition of the product species is corrected in an iterative manner.

### 2.1.5 Nonnegativity Constraint

The nonnegativity constraint illustrates that species considered in the system must either be present in some finite amount or absent at equilibrium; therefore, all the $n_i$ must be nonnegative real numbers. It will be seen that, when applied to pure condensed phases, this constraint poses a difficult challenge for previous algorithms. The mathematical form

$$n_i \geq 0, \qquad \text{where} \qquad i = 1, 2, \ldots, N \tag{2.6}$$

expresses the nonnegativity constraint.

### 2.1.6 Thermodynamic State Constraints

Assuming the absence or negligible effects of any overriding constraints, the state of a system in thermodynamic equilibrium is usually determined by specifying two independent intensive properties of the system. However, it can also be determined by specifying the mass and two independent extensive properties of the system. Examples of intensive properties are temperature, $T$, and pressure, $p$, and examples of extensive properties are total volume, $V$, and total internal energy, $U$, of the system. These properties are also referred to as state functions, because their values depend only on the state of a system and not its history. Also, since the values of these properties do not depend on the system history, they are said to be path independent.[1]

In addition to specifying the mass of a system through the element-abundance vector, the specification of the values of two state functions defines the type of thermodynamic state constraints imposed on an equilibrium problem. The most common state constraints are temperature and pressure. This is related to the widely encountered problems of this type in engineering practices. Consequently, most of the numerical algorithms for equilibrium analysis had been developed for problems with these constraints.

---

[1] In this report, lower case letters denote intensive properties and upper case letters denote extensive properties, with the exception of temperature and pressure. Capital $T$ denotes temperature and, while the lower case $p$ denotes pressure in general, the upper case $P$, with or without a corresponding subscript or superscript, denotes some specific pressure such as the system pressure or the vapour pressure of a condensed phase of a substance.

The state constraints for the system investigated were total internal energy and total volume; however, the algorithm used to solve the problem is developed based on the constraints of temperature and pressure. The total volume of the system was assumed the same as that before combustion and also constant throughout the process in approaching equilibrium. The system boundary was assumed adiabatic and allow no heat loss to the surroundings. Hence, the total internal energy of the product mixture must have the same value as that of the reactants. This advantageous features of the algorithm and how it was adapted to solve the problem is described later. From here on, the discussion is centered around equilibrium solutions of problems under temperature and pressure constraints, and the basic concepts leading up to the introduction of the algorithm, which include in particular chemical stoichiometry, chemical potentials and numerical methods.

### 2.1.7 Thermodynamic Potential Functions and Equilibrium Criteria

For the thermodynamic state constraints of temperature and pressure, and assuming no work other than that involving volume changes done on a closed system, the second law of thermodynamics provides a statement regarding the conditions for spontaneous changes and at equilibrium [Denbigh, 1981, pp. 82–83]. Such conditions make use of the Gibbs potential function $G$, where $G = H - TS$ and $H$ and $S$ are the total enthalpy and entropy of the system, respectively. The statement is

$$\mathrm{d}G_{T,P_s} \leq 0, \tag{2.7}$$

where $\mathrm{d}G_{T,P_s}$ is the total differential change in $G$ of the system at constant a system temperature $T$ and pressure $P_s$. The condition of decreasing $G$ is for spontaneous changes and the equality condition is what holds at equilibrium. Therefore, at equilibrium, when all possible changes have ceased, the Gibbs function of such a system must be a minimum. This criterion is used for determining the equilibrium composition, and the problem of finding such a composition is one of minimization.

The state of chemical equilibrium represents a balance between the tendency to assume a minimum energy and that to achieve a maximum randomness in the system, as mentioned earlier. The Gibbs function $G$ is equal to $H - TS$. The term $H$ can be interpreted as a measure of the energy contents of the products, whereas the term $TS$ can be interpreted as a measure of the randomness of the products. Therefore, by considering $G$, both of these two tendencies are considered, and at a minimum $G$ these two tendencies are balanced [Denbigh, 1981, pp. 83–84].

A statement similar to equation 2.7 is also given by the second law of thermodynamics for the state constraints of temperature and total volume. The statement is based on the Helmholtz potential function $A$, where $A = U - TS$, and it is stated as follows:

$$\mathrm{d}A_{T,V} \leq 0. \tag{2.8}$$

Hence, at equilibrium the Helmholtz function of a system governed by these constraints is at a minimum. This condition was also used for the present study on several occasions.

### 2.1.8 Chemical Stoichiometry

Before going on to discuss different mathematical formulations of the chemical equilibrium problem with constant temperature and pressure as the constraints, the concepts of chemical stoichiometry need to be introduced first. Only a summary of the concepts is given below, detailed discussions can be found in Smith and Missen [1979; 1982, pp. 18–27] and Missen and Smith [1989].

Chemical stoichiometry are constraints on the compositional changes in a closed system, requiring that elemental abundances be conserved during physiochemical change within a system. Application of the principles of chemical stoichiometry enforce the mass constraint conservation.

Central to chemical stoichiometry is the concept of chemical equations. It will be shown below that chemical equations, in the stoichiometric sense, are simply conservation statements. They do not necessarily have any implication with regard to the actual reactions or reaction mechanisms that take place. Furthermore, a set of chemical equations, which is not unique, relating all the product species can be determined, once the list of species has been specified.

#### 2.1.8.1 Stoichiometric Vectors and Chemical Equations

Equation 2.3 is a set of $M$ linear algebraic equations in the $N$ unknowns of species mole numbers $n_i$. If the equations are consistent (the rank of the augmented matrix [A, b] equals that of A, which must occur for a meaningful problem), then for $M < N$ (which occurs for this study), they process an infinity of solutions. The general solution of equation 2.3 may then be expressed as

$$\mathbf{n} = \mathbf{n}^0 + \sum_{j=1}^{R} \boldsymbol{\nu}_j \xi_j, \tag{2.9}$$

where $\mathbf{n}^0$ is any solution (e.g., an initial composition), the $\boldsymbol{\nu}_j$ (having dimensions $N$ by 1) is any set of $R$ linearly independent solutions of the homogeneous equation corresponding to equation 2.3 (i.e., equation 2.5) and $\xi_j$ is a set of real parameters [Noble, 1969, pp. 90–92, 119–120].

Each $\boldsymbol{\nu}_j$ is called a stoichiometric vector, it is nonzero and satisfies

$$\mathbf{A}\boldsymbol{\nu}_j = 0 \qquad (j = 1, 2, \ldots, R). \tag{2.10}$$

The symbol $R$ denotes the maximum number of linearly independent solutions of equation 2.5;

$$R = N - C, \tag{2.11}$$

where $C$ is the rank of A which is less than or equal to $M$, or

$$C = \mathrm{rank}(\mathbf{A}) \le M. \tag{2.12}$$

Usually, but not always, $C$ is equal to $M$.

The set of $\xi_j$ are $R$ values of variables that are free to be selected to solve for the remaining $C$ variables in equation 2.5. They are also referred to as the extents of reactions.

The significance of equation 2.9 is that any compositional solution of the system $\mathbf{n}$ can be written in terms of any particular solution $\mathbf{n}^0$ and a linear combination of a set of $R$ linearly independent vectors $\boldsymbol{\nu}_j$. Hence, equation 2.9 may be regarded as essentially a linear transformation from the $N$ independent variables $n_i$ to the $R$ independent variables $\xi_j$. However, the variables $n_i$ are constrained by the mass conservation equation 2.3, whereas the variables $\xi_j$ are not.

Premultiplication of equation 2.9 by A gives

$$\mathbf{A}\mathbf{n} = \mathbf{A}\mathbf{n}^0 + \sum_{j=1}^{R} \xi_j \mathbf{A}\boldsymbol{\nu}_j = \mathbf{b}. \tag{2.13}$$

The terms $\mathbf{A}\boldsymbol{\nu}_j$ are equal to zero by virtue of equation 2.10. Hence, the conservation of mass constraint is automatically satisfied by the variables $\xi_j$. It is, therefore, of advantage to work with the $\xi_j$ instead, which is done in this work.

If equation 2.9 is rewritten as

$$n_i = n_i^0 + \sum_{j=1}^{R} \nu_{ij}\xi_j \quad \text{with} \quad i = 1,2,\ldots,N, \tag{2.14}$$

then for a fixed $\mathbf{n}^0$

$$\left(\frac{\partial n_i}{\partial \xi_j}\right)_{\xi_{k\neq j}} = \nu_{ij} \quad \text{with} \quad i = 1,2,\ldots,N \quad \text{and} \quad j = 1,2,\ldots,R. \tag{2.15}$$

The element $\nu_{ij}$ is called the stoichiometric coefficient of the $i^{\text{th}}$ species in the $j^{\text{th}}$ stoichiometric vector. It is the change in $n_i$ for a unit change in $\xi_j$ while keeping the other $\xi_j$ constant.

Now, equation 2.10 can be written for the $R$ stoichiometric vectors $\boldsymbol{\nu}_j$, by using the column formula vectors $\mathbf{a}_i$ of $\mathbf{A}$, as

$$\sum_{i=1}^{N} \mathbf{a}_i \nu_{ij} = \mathbf{0} \quad \text{with} \quad j = 1,2,\ldots,R. \tag{2.16}$$

A set of chemical equations is obtained from equations 2.16 when the formula vectors $\mathbf{a}_i$ of the species are replaced by the corresponding molecular formulae $A_i$ and the vector $\mathbf{0}$ by 0 so that

$$\sum_{i=1}^{N} A_i \nu_{ij} = 0 \quad \text{with} \quad j = 1,2,\ldots,R. \tag{2.17}$$

Two points should be noted: (1) such a set of chemical equations is not unique as suggested by the fact that the set of stoichiometric vectors is not unique, (2) the equations are statements only of the law of mass conservation, they are determined solely on the list of product species considered and do not imply any knowledge of actual reactions or reaction mechanisms that take place.

The linearly independent set of $R$ stoichiometric vectors is called a complete set of stoichiometric vectors of the system with formula matrix $\mathbf{A}$. The corresponding chemical equations obtained from a complete set of stoichiometric vectors is then a complete set of chemical equations of the system. The method of finding a complete set of stoichiometric vectors and thereby a complete set of chemical equations, followed by an example illustrating the procedure, is given below.

### 2.1.8.2 Complete Stoichiometric Matrix

A complete stoichiometric matrix of a system is a matrix whose columns are composed of a complete set of stoichiometric vectors. Denoting such a matrix by $\mathbf{N}$, then

$$\mathbf{N} = [\boldsymbol{\nu}_1, \boldsymbol{\nu}_2, \ldots, \boldsymbol{\nu}_R]. \tag{2.18}$$

Other than the linearly independent requirement, the choices of the stoichiometric vectors $\boldsymbol{\nu}_j$ and $\mathbf{N}$ are entirely arbitrary, and these can be used to gain certain computational advantages. $\mathbf{N}$ is usually specified such that it is in what is called the canonical form; a set of $C = \text{rank}(\mathbf{A})$ species with linearly independent formula vectors are selected from the $N$ species and formula vectors of each of the remaining $R$ species is expressed as a linear combination of the formula vectors of the $C$ species, resulting in $R$ stoichiometric vectors, one for each of the $R$ remaining species.

This is equivalent to separating the species into two groups, the $C$ species with linearly independent formula vectors called the component species (which means basic block), and the remaining $R$ species called the noncomponent species. The stoichiometric vectors have the form now described. Each of them would have at least one nonzero element in the first $C$ elements, the remaining $R$ elements are zero with the exception that for the $j^{th}$ ($j = 1$ to $R$) stoichiometric vector, and the $(C + j)^{th}$ element is unity. Hence, the portion of $\mathbf{N}$ below row $C$ is an identity matrix of dimension $R$. Written in full in canonical form,

$$\mathbf{N} = \begin{bmatrix} \nu_{11} & \nu_{12} & \cdots & \nu_{1R} \\ \nu_{21} & \nu_{22} & \cdots & \nu_{2R} \\ \vdots & \vdots & \vdots & \vdots \\ \nu_{C1} & \nu_{C2} & \cdots & \nu_{CR} \\ 1 & 0 & \cdots & 0 \\ 0 & \ddots & \ddots & \vdots \\ \vdots & \ddots & \ddots & 0 \\ 0 & \cdots & 0 & 1 \end{bmatrix}_{N\times R} . \tag{2.19}$$

When converted into a chemical equation, each of the stoichiometric vectors in $\mathbf{N}$ is equivalent to requiring that one mole of the noncomponent species, with unity stoichiometric coefficient, be formed from the component species, to be shown below.

Storage and computational advantages with this form of stoichiometric matrix exist. Savings of computer memory are achieved because only the storage of $RC$ rather than $RN$ coefficients is required. ($C$ is usually equal to $M$ which in turn is usually much smaller than $N$, because the number of species that can be formed from a certain number of elements is in general much larger than the number of elements itself.) The algorithm for this study also makes use of this form.

Making use of $\mathbf{N}$ and equation 2.9, the species-abundance vector can be expressed as

$$\mathbf{n} = \mathbf{n}^0 + \mathbf{N}\boldsymbol{\xi}, \tag{2.20}$$

where $\boldsymbol{\xi}$ is a column vector with its $j^{th}$ element, $j$ equals 1 to $R$, being the $\xi_j$ parameter.

#### 2.1.8.3 Generation of Stoichiometric Matrix and Chemical Equations

To apply the concept of stoichiometry in the present study, the determination of a complete stoichiometric matrix in the canonical form, which consists of a set of $R$ linearly independent stoichiometric vectors $\boldsymbol{\nu}_j$, was required. A systematic approach for performing such a task is a matrix method. The procedure is similar to that used in the solution of linear algebraic equations by the Gauss-Jordan reduction technique [Noble, 1969, pp. 65–66, 119–120]. This procedure is outlined by the following three steps:

1. Form an $M$ by $N$ formula matrix $\mathbf{A}$ for the given system, with each column identified at the top with the chemical species that it represents.
2. Form a unit matrix as large as possible in the upper left portion of matrix $\mathbf{A}$ by elementary row operations [Noble, 1969, p. 81], and column interchange when necessary. If two columns are interchanged, the designation of the species at the top of the columns must also be interchanged. When this is done a matrix called $\mathbf{A}^*$ is obtained, which has the following form

$$\mathbf{A}^* = \begin{bmatrix} \mathbf{I}_C & \mathbf{Z} \\ \mathbf{0} & \mathbf{0} \end{bmatrix}, \tag{2.21}$$

where $\mathbf{I}_C$ is the identity matrix of dimension $C$, the rank of $\mathbf{A}$, and $\mathbf{Z}$ is a $C$ by $R$ matrix that has at least one nonzero element. The number of components is $C$ and a set is given by the $C$ species forming the unity matrix. The maximum number of linearly independent stoichiometric vectors is $R = N - C$. Normally the $\mathbf{0}$ submatrices are absent and $C = M$.

3. A complete stoichiometric matrix **N** in canonical form is formed from $\mathbf{A}^*$ by appending the identity matrix $\mathbf{I}_R$ below $-\mathbf{Z}$; that is

$$\mathbf{N} = \begin{bmatrix} -\mathbf{Z} \\ \mathbf{I}_R \end{bmatrix}. \tag{2.22}$$

A set of chemical equations for the given system is obtained by using the columns of **N** and equations 2.17, taking into account any change in the order of species as a result of column interchange in step 2. The equations can be put into the usually recognized form by following the convention that species names with negative stoichiometric coefficients are written on the left side of the equations and those with positive coefficients on the right side.

Once again it must be emphasized that such a set of chemical equations is not unique. (Consider the case that, for example, a different order of the species is used in forming **A**.) As a matter of fact, it will be seen later that the components and therefore the stoichiometric vectors would change during the numerical iterative solution of a problem, which imply that there can be more than one set of chemical equations relating the species.

When a set of components, that is species with linearly independent formula vectors, is chosen *a priori* and placed at the left end of matrix **A** at the beginning, then **A** could be reduced to $\mathbf{A}^*$ by using the method of row reduction alone and no column interchange would be necessary. This is what is done in the present study, after the rank of **A** has been determined at the initial stage of a calculation. The choices of the component species and the linear independence of the formula vectors were established by using the Gram-Schmidt orthogonalization method [Cruise, 1964; Noble, 1969, pp. 314–315].

### 2.1.8.4 Illustration of the Procedure

To illustrate the procedure for generating a complete stoichiometric matrix and a complete set of chemical equations for a given system, consider the example that is adopted from Smith and Missen [1979]:

$$\{(CO_2, H_2O, H_2, CH_4, CO), (H, C, O)\}.$$

For this system the number of species $N = 5$ and the number of elements $M = 3$.

The species are denoted from 1 to 5, in the order that they appear in the list, and expressing the species formula vectors using the order H, C and O for the elements, the formula matrix **A** for the system is

$$\mathbf{A} = \begin{array}{c} \begin{array}{ccccc} (1) & (2) & (3) & (4) & (5) \end{array} \\ \begin{bmatrix} 0 & 2 & 2 & 4 & 0 \\ 1 & 0 & 0 & 1 & 1 \\ 2 & 1 & 0 & 0 & 1 \end{bmatrix} \end{array}. \tag{2.23}$$

Matrix **A** can be reduced to

$$\mathbf{A}^* = \begin{array}{c} \begin{array}{ccccc} (3) & (1) & (2) & (4) & (5) \end{array} \\ \begin{bmatrix} 1 & 0 & 0 & 4 & 1 \\ 0 & 1 & 0 & 1 & 1 \\ 0 & 0 & 1 & -2 & -1 \end{bmatrix} \end{array} \tag{2.24}$$

by doing a row reduction and interchanging columns. Note the new order of the species.

The rank of A is equal to the dimension of the identity matrix (which is three); hence, $C$ is equal to three and is equal to $M$. The set of components is $H_2$ (3), $CO_2$ (1) and $H_2O$ (2), and the maximum number of linearly independent stoichiometric vectors, $R = N - C$, is equal to two. The two noncomponent species are: $CH_4$ (4) and CO (5).

On application of equation 2.22, the corresponding complete stoichiometric matrix is

$$\mathbf{N} = \begin{array}{c} \begin{bmatrix} -4 & -1 \\ -1 & -1 \\ 2 & 1 \\ 1 & 0 \\ 0 & 1 \end{bmatrix} \end{array} \begin{array}{c} (3) \\ (1) \\ (2) \\ (4) \\ (5) \end{array} \tag{2.25}$$

in canonical form. The stoichiometric coefficients are associated with the species according to the order given by $\mathbf{A}^*$, which is shown next to N.

Substituting for the formula vectors of the species and taken into account the changes in the order of the species, equations 2.16, with $j$=1 and 2, can be written out in full as

$$-4\begin{bmatrix} 2 \\ 0 \\ 0 \end{bmatrix} - 1\begin{bmatrix} 0 \\ 1 \\ 2 \end{bmatrix} + 2\begin{bmatrix} 2 \\ 0 \\ 1 \end{bmatrix} + 1\begin{bmatrix} 4 \\ 1 \\ 0 \end{bmatrix} = \begin{bmatrix} 0 \\ 0 \\ 0 \end{bmatrix} \tag{2.26}$$

and

$$-1\begin{bmatrix} 2 \\ 0 \\ 0 \end{bmatrix} - 1\begin{bmatrix} 0 \\ 1 \\ 2 \end{bmatrix} + 1\begin{bmatrix} 2 \\ 0 \\ 1 \end{bmatrix} + 1\begin{bmatrix} 0 \\ 1 \\ 1 \end{bmatrix} = \begin{bmatrix} 0 \\ 0 \\ 0 \end{bmatrix}. \tag{2.27}$$

By replacing the formula vectors of the species with their corresponding molecular formulae (see equations 2.17) and after some rearrangement, the particular form of the stoichiometric vectors implies that one mole of a noncomponent species can be considered as formed from a combination of the component species. That is,

$$4H_2 + 1CO_2 - 2H_2O = 1CH_4, \tag{2.28}$$

$$1H_2 + 1CO_2 - 1H_2O = 1CO. \tag{2.29}$$

The equal sign '=' stresses that these two equations are mass conservation statements, rather than representations of reactions in equilibrium, for which the sign '$\rightleftharpoons$' (see equation 2.1) is more appropriate.

For the convention that species names with negative stoichiometric coefficients are written on the left side and those with positive coefficients on the right, and omitting the unity coefficients, then

$$4H_2 + CO_2 = 2H_2O + CH_4, \tag{2.30}$$

$$H_2 + CO_2 = H_2O + CO. \tag{2.31}$$

are two chemical equations in the normally recognized format.

### 2.1.9 Equilibrium Formulations for a Given Temperature and Pressure

At equilibrium, the Gibbs state function of a system at constant temperature and pressure is at a minimum, as stated earlier. Mathematically, the chemical equilibrium problem with these constraints may be formulated in several different ways, and each of the formulations suggests different numerical methods for its solution. Four different mathematical formulations of such a problem are to be presented below, with the emphasis that they can be classified into two categories [Smith and Missen, 1988; Smith, 1980]:

1. The nonstoichiometric formulation, in which chemical stoichiometry are not used and the conservation of mass constraint is treated separately.
2. The stoichiometric formulation, in which the conservation of mass constraint is treated by means of chemical stoichiometry so that the result is an essentially unconstrained problem.

In addition, within each category the formulations may result in a minimization problem or one that involves solving a set of nonlinear equations. The four possible formulations are denoted as F1 to F4 for future usage.

#### 2.1.9.1 Nonstoichiometric Formulation

To keep the following formulations general the mass conservation constraint has been restated as

$$\mathbf{A}'\mathbf{n} = \mathbf{b}' \tag{2.32}$$

instead. The augmented matrix $[\mathbf{A}', \mathbf{b}']$ has the dimension of $C$ by $N + 1$ and has the full rank of $C$, which is the rank of $\mathbf{A}$ and is less than or equal to $M$. Furthermore, it is row equivalent to $[\mathbf{A}, \mathbf{b}]$, that is equations 2.3 and 2.32 have the same solution set [Noble, 1969, p. 78]. What these two requirements mean is that equation 2.32 is a reduced version of equation 2.3 and consists of the maximum number of independent equations in equation 2.3. (Since there is more than one sequence of elementary row operations that can perform the reduction, the matrix $\mathbf{A}'$ and vector $\mathbf{b}'$ are not unique.) The elements of $\mathbf{A}'$ and $\mathbf{b}'$ are denoted as $a'_{ki}$ and $b'_k$, respectively, with $k$ equal to 1 to $C$ and $i$ equal to 1 to $N$. This change is to allow for the uncommon cases whereby $C$ is less than $M$. When $\mathbf{A}$ has the full rank of $M$, equation 2.32 is simply equation 2.3.

**F1.** As a constrained optimization problem the system Gibbs state function $G$ is minimized for fixed $T$ and $P$ in terms of $N$ mole numbers, subject to the conservation of mass constraint. Hence,

$$\text{minimise } G(\mathbf{n}) = \mathbf{n}^T \boldsymbol{\mu}, \tag{2.33}$$

such that

$$\mathbf{A}'\mathbf{n} = \mathbf{b}' \quad \text{and} \quad \mathbf{n} \geq 0, \tag{2.34}$$

where $G(\mathbf{n})$ indicates that $G$ is a function of $\mathbf{n}$ (for a given $T$ and $P$), $\mathbf{n}^T$ is the transpose of $\mathbf{n}$ and $\boldsymbol{\mu}$ is a column vector with its $i^{\text{th}}$ element being the chemical potential of the $i^{\text{th}}$ species denoted as $\mu_i$ and defined as

$$\mu_i \equiv \left(\frac{\partial G}{\partial n_i}\right)_{T,P,n_{j\neq i}} \quad \text{and} \quad i = 1, 2, \ldots, N. \tag{2.35}$$

Based on the definition, it can be seen that $\mu_i$ is the partial molar Gibbs function of the system due to the $i^{\text{th}}$ species, which is the change in $G$ for a unit change in $n_i$. The chemical potential of a pure species is the molar Gibbs function of the species itself.

**F2.** This formulation is related directly to formulation F1 and the method of Lagrange multipliers is used to include the conservation of mass constraint. The Lagrangian $\mathcal{L}$ as a function of $\mathbf{n}$ and $\boldsymbol{\lambda}$, where $\boldsymbol{\lambda}$ is a column vector of $C$ unknown Lagrange multipliers, $\lambda_1, \lambda_2, \lambda_3, \ldots, \lambda_C$, is given by

$$\mathcal{L}(\mathbf{n},\boldsymbol{\lambda}) \equiv \sum_{i=1}^{N} n_i\mu_i + \sum_{k=1}^{C}\lambda_k\left(b'_k - \sum_{i=1}^{N} a'_{ki}n_i\right). \tag{2.36}$$

Then, the Kuhn-Tucker conditions [Walsh, 1975, pp. 35–39] for the minimum $\mathcal{L}$ are also the necessary conditions for determinang a solution to problem F1. There are precisely $N+C$ conditions involving the $N+C$ unknowns $n_1, n_2, \ldots, n_N$ and $\lambda_1, \lambda_2, \ldots, \lambda_C$. Firstly, for the $i^{\text{th}}$ species, with $i = 1, 2, \ldots, N$,

$$\mu_i - \sum_{k=1}^{C} a'_{ki}\lambda_k = 0 \quad \text{if} \quad n_i > 0, \tag{2.37}$$

or

$$\mu_i - \sum_{k=1}^{C} a'_{ki}\lambda_k \geq 0 \quad \text{if} \quad n_i = 0. \tag{2.38}$$

Secondly, for the conservation of mass

$$\mathbf{A}'\mathbf{n} = \mathbf{b}', \tag{2.39}$$

which is a set of $C$ equations. This is the formulation that other major computational codes for chemical equilibrium analysis are based upon.

#### 2.1.9.2 Stoichiometric Formulation

**F3.** As an essentially unconstrained optimization problem, for which the conservation of mass constraint has been incorporated by means of chemical stoichiometry, $G$ is minimized, for fixed $T$ and $P$, in terms of the $\xi_j$ parameters. That is

$$\text{minimize } G(\boldsymbol{\xi}) = \mathbf{n}^T\boldsymbol{\mu} = [\mathbf{n}^0 + \mathbf{N}\boldsymbol{\xi}]^T\boldsymbol{\mu} \tag{2.40}$$

such that

$$\mathbf{n} \geq \mathbf{0}. \tag{2.41}$$

The problem is only essentially unconstrained because the nonnegativity constraint still holds. This is the formulation used in the present study.

**F4.** The nonlinear equations resulting from the first-order necessary conditions for a minimum $G$, as a function of the $\xi_j$ parameters, can be written as

$$\left(\frac{\partial G}{\partial \boldsymbol{\xi}}\right)_{T,P} = \mathbf{N}^T\boldsymbol{\mu} = \mathbf{0}, \tag{2.42}$$

for which $\mathbf{N}^T$ is the transpose of $\mathbf{N}$. Furthermore, equation 2.42 is a set of $R$ equations which are the same as the chemical equations relating the species, except that chemical potentials of the species are in the place of molecular formulae and can be recognized as the classical criteria for specifying chemical equilibrium.

The nonnegativity constraints are included by the application of the Kuhn-Tucker necessary conditions. With the stoichiometric matrix expressed in canonical form, the $R$ noncomponent species are given by

$$\mu_{j+C} + \sum_{k=1}^{C} \nu_{kj}\mu_k = 0 \quad \text{if} \quad n_{j+C} > 0 \tag{2.43}$$

or

$$\mu_{j+C} + \sum_{k=1}^{C} \nu_{kj}\mu_k \geq 0 \quad \text{if} \quad n_{j+C} = 0, \tag{2.44}$$

where $j = 1, 2, \ldots, R$. These $R$ equilibrium conditions are equivalent to the $N$ equilibrium conditions obtained by using equations 2.37 and 2.38 (see Smith and Missen, 1982, p. 48).

The solution of the chemical equilibrium problem for all four different formulations requires the appropriate expressions for the chemical potential ($\mu_i$) of each specie, and these are discussed next.

### 2.1.10 Chemical Potentials for Gaseous and Condensed Species

Regardless of which aforementioned formulation is used, chemical potentials of the product species remain the most important properties that need to be evaluated. In this section the forms of the chemical potentials, as a function of temperature and pressure, are introduced for a pure gaseous, liquid or solid species, and for species in a gaseous mixture.

The product mixture was modelled for this study as a mixture of gases with pure liquids and/or solids dispersed throughout the vessel volume. The gases may be modelled as perfect or imperfect. Furthermore, the mixture of gases itself may be modelled as an ideal or a nonideal mixture. For the liquid and solid species, they can be assumed to occupy no volume or have finite volume. In addition, they can be incompressible or compressible. Depending on the models incorporated, the form of the chemical potential of a species varies. Alternatively, all of the information regarding the models utilized for the mixture and species is reflected through or embodied in a single property—the chemical potential. However, before the various expressions of chemical potentials for the species are discussed, some information regarding the phases of a pure substance and the condition for its phases to be co-existing in equilibrium need to be provided to aid the understanding of the expressions.

#### 2.1.10.1 Phases of a Pure Substance and Phase Equilibrium Conditions

References have been made to the various phases of a substance without dwelling on the conditions at which such phases would exist by themselves or possiblely co-exist in interactions with others. Such conditions in terms of temperature and pressure can be depicted by using what is normally called a phase diagram. Such a diagram helps to relate the various phases of a substance and to illustrate appropriate expressions for the chemical potentials of pure condensed species (phases).

Figure 2.1 is a temperature versus pressure plot defining the regions of temperature and pressure conditions at which the solid, liquid or vapour phase of a pure substance would exist as a stable phase. (Some substances have more than one solid phase; however, for illustrative purposes only one solid phase has been shown.) The regions are divided by curves marking the conditions at which phase transitions can occur and that two phases can co-exist. The curves for solid-liquid, liquid-vapour and solid-vapour transitions are denoted respectively as fusion, vaporization and sublimation curves. While the fusion curve continues to rise, the vaporization curve terminates at the critical point (c.p.). The three phase transition curves meet at the triple point (t.p.) and at the corresponding temperature and pressure conditions all the three phases can co-exist. There is a continuous change in substance properties when following a path of change in conditions, for instance, in going from point $A$ to point $B$.

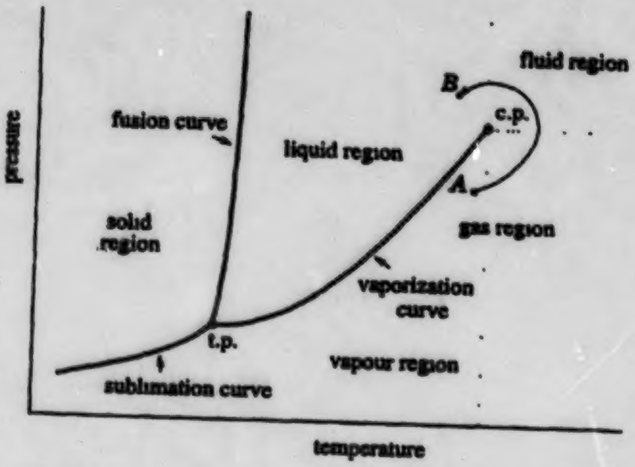

Figure 2.1: Phase transitions for a pure substance for pressure versus temperature.

If the definitions that a liquid is one which can be vaporized by reduction of pressure at constant temperature and that a gas is one which can be condensed by cooling at constant pressure are followed, then the fluid region is in between that of liquid and gas. The boundaries are denoted by dotted lines because no discontinuous changes in properties are involved. A gas existing at conditions defined by the region to the left of the critical temperature is also referred to as a vapour which can be condensed by compression at constant temperature in addition to by cooling at constant pressure [Smith and Van Ness, 1987, pp. 54–55]. Since no discontinuous change in properties occurs when a gas is compressed into a fluid at constant temperature, their properties can be modelled as if they are one continues phase. For discussions in this report, what is meant by gases includes fluids as well, unless mentioned otherwise.

As a direct consequence of the application of the equilibrium criterion given by equation 2.7 to phases of a pure substance co-existing in equilibrium at constant temperature and pressure, it can be shown that the molar Gibbs function, or the chemical potential, has the same value in all the phases [Sears and Salinger, 1975, pp. 190–191; Denbigh, 1981, p. 86]. Therefore, for example, at conditions corresponding to any point along the vaporization curve, the liquid phase and the vapour phase will have the same chemical potential. In addition, at the triple point the chemical potentials of all the three phases are equal. The property of equal chemical potential between a vapour and a condensed phase at transition conditions can be used as a basis for evaluating the chemical potential of a condensed phase, which will be shown in the next section.

### 2.1.10.2 Pure Species

Based on a relation for the differential change of the molar Gibbs function in terms of differential changes in $T$ and $P$, the following dependence of chemical potential on pressure for a pure species can be obtained [Van Wylen and Sonntag, 1965, pp. 329–330]:

$$\left(\frac{\partial \mu}{\partial P}\right)_T = v, \tag{2.45}$$

where $v$ is the molar volume. Hence, at constant $T$, the molar volume of a pure species can be integrated from a reference pressure $P^0$ to $P$ giving the change in its chemical potential. The chemical potential $\mu(T, P)$ at the mixture temperature $T$ and pressure $P$, is then given by

$$\mu(T, P) = \mu(T, P^0) + \int_{P^0}^{P} v \, \mathrm{d}P, \qquad (2.46)$$

where $\mu(T, P^0)$ is the chemical potential at the mixture temperature $T$ and reference pressure $P^0$. This general equation applies to all cases of a perfect gas, an imperfect gas, a liquid or a solid.

### 2.1.10.2.1 Perfect gas

A perfect gas consists of gaseous molecules that are assumed to have negligible volume and no interactions among them except during collisions. When the equation of state of a perfect gas

$$Pv = RT \qquad (2.47)$$

is substituted into the right-hand side of equation 2.46, and choosing a reference or standard-state pressure $P^0$ to have a value of unity, results in

$$\mu(T, P) = \mu^0(T) + RT \ln(P), \qquad (2.48)$$

where $P$ is in the same units as $P^0$, usually chosen as one atmosphere or one bar. Note that $\mu(T, P^0)$ has been rewritten as $\mu^0(T)$, which is called the standard chemical potential, and it is now a function of temperature only. Note that the value of $\mu^0(T)$ can be assigned in several ways by making use of various thermodynamic properties of the gas, a perfect gas, which in turn can be determined using statistical thermodynamics [McBride and Gordon, 1992].

Consistent with earlier comments, the expressions given for a gas are also applicable to a fluid. The same equation of state describes the properties of the gas and fluid, and the numerical or analytical integration can be performed to the corresponding pressure $P$.

### 2.1.10.2.2 Imperfect gas

The gaseous molecules for an imperfect gas are assumed to occupy finite volumes and interaction forces are included. The equation of state of an imperfect gas has the form

$$Pv = zRT, \qquad (2.49)$$

where $z$ is the compressibility factor which is different from unity. (For a perfect gas, $z = 1$.) By adding and subtracting the term $RT \ln(P/P^0)$, equation 2.46 can be rewritten as

$$\mu(T, P) = \mu(T, P^0) - RT \ln(P^0) + RT \ln(P) + \int_{P^0}^{P} \left(v - \frac{RT}{P}\right) \mathrm{d}P. \qquad (2.50)$$

In the limit of $P^0$ going to zero, the gas then approaches the behaviour of a perfect gas and its chemical potential $\mu(T, P^0)$ is therefore given by equation 2.48. As a consequence, the first two terms on the right-hand side of equation 2.50 can be replaced by $\mu^0(T)$ (the standard chemical potential of the gas in the idealized state of a perfect gas) and equation 2.50 then reduces to

$$\mu(T, P) = \mu^0(T) + RT \ln(P) + \int_{0}^{P} \left(v - \frac{RT}{P}\right) \mathrm{d}P, \qquad (2.51)$$

as shown by Smith and Missen [1982, pp. 49–50].

By comparing equation 2.51 with equation 2.48, the deviations for an imperfect gas from a perfect gas is contained in the integral term in equation 2.51. This term is related to the ratio of the fugacity $f$ of the gas to the pressure $P$, that is the fugacity has the form

$$RT \ln\left(\frac{f}{P}\right) = \int_0^P \left(v - \frac{RT}{P}\right) \mathrm{d}P \,. \tag{2.52}$$

The ratio of $f$ to $P$ is also defined to be the fugacity coefficient, $\phi$, of the gas. Hence,

$$\phi \equiv \frac{f}{P} \tag{2.53}$$

and

$$RT \ln(\phi) = \int_0^P \left(v - \frac{RT}{P}\right) \mathrm{d}P \,. \tag{2.54}$$

Equation 2.51 can be considered to be valid for all gases, imperfect as well as perfect, since for perfect gases, the extra term is equal to zero and equation 2.48 is recovered. Therefore, equation 2.51 should be the equation of choice for pure gases in general.

### 2.1.10.2.3 Liquid and solid

For a pure condensed species, either liquid or solid, there are two similar methods of evaluating chemical potential of condensed species, each resulting from a different choice of the reference pressure $P^0$. This is illustrated in figure 2.2 for a the case of a liquid; the same approaches can be utilized for a solid.

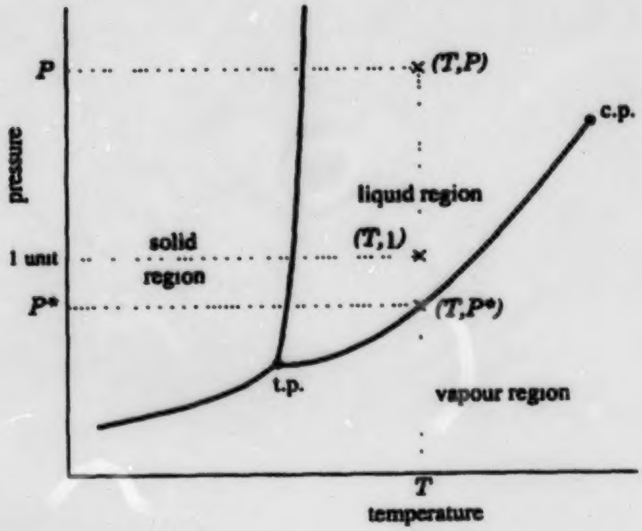

Figure 2.2: Two approaches for the evaluation of the chemical potential of a pure liquid at temperature $T$ and pressure $P$, based on two choices of $P^0$, one being equal to one unit, the other being equal to its vapour pressure $P^*$ at $T$.

### $P^0$ equals one unit.

The first approach one can take involves choosing a value of $P^0$ equal to one unit, such as one atmosphere or one bar, and use a straightforward application of equation 2.46. There are a further three different models that can be employed when assigning values to the molar volume $v$ for a pure condensed species.

### Zero molar volume.

In this case the condensed species is assumed to occupy no volume or its volume is simply neglected. Therefore, the second term in equation 2.46 does not contribute and

$$\mu(T,P) = \mu(T,P^0) \quad \text{with} \quad P^0 = 1 \text{ unit.} \tag{2.55}$$

### Constant molar volume.

The condensed species is assumed in this case to have finite volume and be incompressible. Thence, $v$ is nonzero and constant and the second term of equation 2.46 can be integrated to give

$$\mu(T,P) = \mu(T,P^0) + v(P - P^0) \quad \text{with} \quad P^0 = 1 \text{ unit.} \tag{2.56}$$

When the value of $P$ is much larger than unity and the term $P^0$ can be neglected,

$$\mu(T,P) = \mu(T,P^0) + vP \quad \text{with} \quad P^0 = 1 \text{ unit.} \tag{2.57}$$

### Variable molar volume.

The condensed species in this case is assumed to have finite volume and also that it is compressible. The molar volume $v$ is a function of temperature and pressure and generally an equation of state is required for the evaluation of the second term in equation 2.46.

### $P^0$ equal to $P^*$.

The second approach involves choosing $P^0$ as $P^*$, the vapour pressure of the liquid or solid at $T$, and using of the condition that the chemical potential of the liquid or solid equals that of its vapour at $T$ and $P^*$. The chemical potential of the liquid or solid at $T$ and $P^*$ can then be obtained by applying equation 2.51 to the vapour at these conditions, and it is [Smith and Missen. 1982, p. 50]

$$\mu(T,P^*) = \mu^0(T) + RT\ln(P^*) + \int_0^{P^*} \left(v_g - \frac{RT}{P}\right) \mathrm{d}P, \tag{2.58}$$

where $v_g$ is the molar volume of the vapour. When letting $P^0$ to be equal to $P^*$ in equation 2.46 and substituting for $\mu(T,P^*)$, the chemical potential of the liquid or solid at $T$ and $P$ is

$$\mu(T,P) = \mu^0(T) + RT\ln(P^*) + \int_0^{P^*} \left(v_g - \frac{RT}{P}\right) \mathrm{d}P + \int_{P^*}^{P} v\,\mathrm{d}P, \tag{2.59}$$

where $v$ is the molar volume of the liquid or solid.

The three models described previously for assigning values to $v$ (zero, constant, variable) also apply here. Depending on the mode, the last term in the above equation may vanish or require an integration. In any case, the values of the last two terms are often small in comparison to the first two. If they are neglected, then the chemical potential of the liquid or solid becomes

$$\mu(T,P) \approx \mu^0(T) + RT\ln(P^*) \tag{2.60}$$

as an approximation. Similar to the case of an imperfect gas,

$$RT\ln\left(\frac{f}{P}\right) = \int_0^{P^*}\left(v_g - \frac{RT}{p}\right)\mathrm{d}p + \int_{P^*}^{P} v\,\mathrm{d}p \tag{2.61}$$

is the fugacity of a liquid or solid.

#### 2.1.10.3 Gaseous Mixture

A mixture of gases can be modelled rather simply as an ideal mixture or in the most general manner as a nonideal mixture.

##### 2.1.10.3.1 Ideal mixture

An ideal mixture is one whereby the chemical potential of every species in the mixture is a linear function of the logarithm of its mole fraction in the form [Denbigh, 1981, p. 249]

$$\mu_i(T,P,x_i) = \mu_i^*(T,P) + RT\ln(x_i), \tag{2.62}$$

where the subscript $i$ is used to denote properties of the $i^{\text{th}}$ species. The term $\mu_i^*(T,P)$ is a function of temperature and pressure only. It is the chemical potential of the $i^{\text{th}}$ pure species in the gaseous state at the mixture $T$ and $P$. The mole fraction $x_i$ is given as $n_i/n_t$, where $n_i$ and $n_t$ are the number of moles of the $i^{\text{th}}$ species and the total number of moles of gases, respectively.

The ideal mixture model is highly idealized; it is an approximation that can be good. In general a mixture will be close to this ideality limit when volumes of species molecules are about equal, and when the intermolecular forces are very similar [Smith and Missen, 1982, pp. 153–154; Denbigh, 1981, pp. 244–249].

An ideal mixture is one that follows Amagat's law; at fixed temperature and pressure the volume of the mixture is equal to the sum of the volume of the component species as pure gases at the mixture conditions—the gases have a zero volume change of mixing and

$$V = \sum_i n_i v_i, \tag{2.63}$$

where $V$ is the total volume of the mixture and $v_i$ is the molar volume of the $i^{\text{th}}$ pure species. Defining the partial molar volume of the $i^{\text{th}}$ species as

$$\bar{v}_i \equiv \left(\frac{\partial V}{\partial n_i}\right)_{T,P,n_{j\neq i}}, \tag{2.64}$$

and differentiating equation 2.63 with respect to $n_i$, then

$$\bar{v}_i = v_i \tag{2.65}$$

is obtained.

An ideal mixture has a partial molar volume of the $i^{\text{th}}$ species equal to the molar volume of a pure gas. This occurs directly from the definition of the ideal mixture. Omit the notation for the functional dependence and differentiate equation 2.62 with respect to the pressure to get

$$\left(\frac{\partial \mu_i}{\partial P}\right)_{T,\mathbf{n}} = \left(\frac{\partial \mu_i^*}{\partial P}\right)_T . \tag{2.66}$$

The left-hand side of this equation is $\bar{v}_i$ (see equation 2.45) and the other side is $v_i$, since $\mu_i^*$ is the chemical potential of the $i^{\text{th}}$ pure species [Prausnitz, Lichtenthaler and Azevedo, 1986, p. 30; Denbigh, 1981, pp. 128–130].

In the category of an ideal mixture, the most specific of the simplest types of gaseous mixtures is the perfect-gas mixture. All of the other mixtures in this category then fall under the type of an imperfect-gas mixture. Each of these two mixture types is discussed below.

### Perfect-gas mixture

In the case when species molecules in a mixture are assumed to have negligible volume and no interaction among them until they collide, as in the case of a perfect single gas, a perfect-gas mixture is resulted. Each gas in such a mixture behaves as if no other gas were present; consequently, the equation of state of a perfect-gas mixture has the same form as a perfect single gas, equation 2.47 [Denbigh, 1981, pp. 114–116; Smith and Missen, 1982, p. 51].

The form of the chemical potential of each species in a perfect-gas mixture in accordance with the assumptions and characteristics of such a mixture is as follows:

$$\mu_i(T,P,x_i) = \mu_i^0(T) + RT\ln(P) + RT\ln(x_i). \tag{2.67}$$

The above equation is valid for values of $x_i$ up to the case of unity, therefore, $\mu_i^0(T)$ is simply the standard chemical potential of the $i^{\text{th}}$ species as a perfect pure gas. The function $\mu_i^*(T,P)$ for a perfect-gas mixture then has the form $\mu_i^0(T) + RT\ln(P)$, which is the chemical potential of the $i^{\text{th}}$ pure species at $T$ and $P$, as a perfect gas.

Equation 2.67 can be expressed more compactly by combining the last two terms to give

$$\mu_i(T,P,x_i) = \mu_i^0(T) + RT\ln(p_i), \tag{2.68}$$

where $p_i$ is the partial pressure of the $i^{\text{th}}$ species in the mixture and is defined to be

$$p_i \equiv x_i P. \tag{2.69}$$

Therefore, the chemical potential of a species in a perfect-gas mixture (given by equation 2.68) has the same form as that of the species when it exists as a single perfect gas (given by equation 2.48) except that its partial pressure in the mixture is used instead.

### Imperfect-gas mixture

For an imperfect-gas mixture the gaseous molecules in the mixture are assumed to occupy finite volumes and the forces of interaction among them are taken into account, as in the case of an imperfect pure gas. The chemical potential of a species in such a mixture has the form

$$\mu_i(T,P,x_i) = \mu_i^*(T,P) + RT\ln(x_i), \tag{2.70}$$

as given by equation 2.62. The term $\mu_i^*(T,P)$ is the chemical potential of the $i^{\text{th}}$ pure species as an imperfect gas at the mixture temperature and pressure, and it has a form different than $\mu_i^0(T) + RT\ln(P)$ for a perfect gas.

Alternatively, the chemical potential of the $i^{\text{th}}$ species in an imperfect-gas mixture can be expressed in terms of the fugacity as

$$\mu_i(T,P,x_i) = \mu_i^0(T) + RT\ln[f_i(T,P,x_i)], \tag{2.71}$$

where $\mu_i^0(T)$ is the standard chemical potential of the $i^{\text{th}}$ pure species in the idealized perfect gas state as a function of temperature only, as defined before, and the fugacity $f_i$, indicated explicitly as a function of $T$, $P$ and mole fraction $x_i$, is given in a way similar to that for a pure species by

$$RT\ln\left(\frac{f_i}{x_iP}\right) = \int_0^P \left(v_i - \frac{RT}{P}\right) \mathrm{d}P. \tag{2.72}$$

Since $v_i$ is the molar volume of the $i^{\text{th}}$ pure species, when comparing the above equation with equation 2.52, it can be seen that

$$f_i = x_i f, \tag{2.73}$$

which is a relation commonly known as the Lewis and Randall's fugacity rule. That is the fugacity of the $i^{\text{th}}$ species in an ideal mixutre is simply its fugacity as a pure gas at the temperature and pressure of the mixture multiplied by its mole fraction in the mixture.

The fugacity coefficient of the $i^{\text{th}}$ species, $\phi_i$, is defined as

$$\phi_i \equiv \frac{f_i}{x_iP} \tag{2.74}$$

and

$$RT\ln(\phi_i) = \int_0^P \left(v_i - \frac{RT}{P}\right) \mathrm{d}P. \tag{2.75}$$

Making use of equation 2.72 and substituting for $f_i$, equation 2.71 becomes

$$\mu_i(T,P,x_i) = \mu_i^0(T) + RT\ln(P) + \int_0^P \left(v_i - \frac{RT}{P}\right) \mathrm{d}P + RT\ln(x_i). \tag{2.76}$$

The first three terms on the right in the above equation can be recognized to be the chemical potential of the $i^{\text{th}}$ pure species as an imperfect gas, which is what $\mu_i^*(T,P)$ was defined to be. Consequently, the two forms of $\mu_i(T,P,x_i)$ given by equations 2.70 and 2.71 are equivalent.

If equation 2.75 is used and the integral term in equation 2.76 is replaced, then $\mu_i(T,P,x_i)$ can also be expressed as

$$\mu_i(T,P,x_i) = \mu_i^0(T) + RT\ln(P) + RT\ln[\phi_i(T,P)] + RT\ln(x_i), \tag{2.77}$$

in which the fugacity coefficient has been indicated explicitly as a function of mixture temperature and pressure.

#### 2.1.10.3.3 Nonideal mixture

The most general way to model a gaseous mixture is as a nonideal mixture. Such a mixture is similar to an ideal imperfect-gas mixture in the sense that the gaseous molecules in the mixture are assumed to occupy finite volumes and the forces of interaction among them are taken into account. (Note that a nonideal mixture must be a mixture of imperfect gases.) However, the requirement that the chemical potential of every species in the mixture be a linear function of the logarithm of its mole fraction is relaxed. The chemical potential of the $i^{\text{th}}$ species in a nonideal mixture is then general and can be expressed as [Denbigh, 1981, pp. 270–271; Smith and Missen, 1982, pp. 54–55]

$$\mu_i(T,P,\mathbf{x}) = \mu_i^*(T,P) + RT\ln(\gamma_i(T,P,\mathbf{x})x_i), \tag{2.78}$$

where $\gamma_i$ is the activity coefficient of the $i^{\text{th}}$ species and has been indicated explicitly as a function of the mixture temperature and pressure and the mole fractions of all the species in the mixture, the mixture composition, represented by the elements of the vector $\mathbf{x}$.

The activity coefficient $\gamma_i$ would approach unity when the mole fraction $x_i$ approaches unity. Under this condition the logarithmic term vanishes and therefore $\mu_i^*(T,P)$ is the chemical potential of the $i^{\text{th}}$ pure species at the mixture temperature and pressure and in the gaseous state, the same as in the definition for the chemical potential of a species in an ideal imperfect-gas mixture.

The chemical potential of a species in such a mixture can also be expressed in terms of fugacity as in the case of ideal imperfect-gas mixture, so that

$$\mu_i(T,P,\mathbf{x}) = \mu_i^0(T) + RT\ln[f_i(T,P,\mathbf{x})], \tag{2.79}$$

where $f_i$ has also been indicated explicitly as a function of the mixture temperature and pressure and the composition of the mixture. The fugacity $f_i$ is now given by

$$RT\ln\left(\frac{f_i}{x_i P}\right) = \int_0^P \left(\overline{v}_i - \frac{RT}{P}\right) \mathrm{d}P, \tag{2.80}$$

where $\overline{v}_i$ is the partial molar volume of the $i^{\text{th}}$ species, as defined earlier.

If the fugacity coefficient $\phi_i$ is defined in the same way as in the case of ideal perfect-gas mixture by using equation 2.74 then

$$RT\ln(\phi_i) = \int_0^P \left(\overline{v}_i - \frac{RT}{P}\right) \mathrm{d}P, \tag{2.81}$$

and the chemical potential of the $i^{\text{th}}$ species can be expressed as

$$\mu_i(T,P,\mathbf{x}) = \mu_i^0(T) + RT\ln(P) + RT\ln[\phi_i(T,P,\mathbf{x})] + RT\ln(x_i), \tag{2.82}$$

which has a form similar to that for an ideal imperfect-gas mixture except that $\phi_i$ is now a function of mixture temperature and pressure and the composition of the mixture, as explicitly indicated.

### 2.1.10.4 Evaluation of Chemical Potentials

#### 2.1.10.4.1 Pure Gas

When evaluating the chemical potential of a pure gas, perfect or imperfect, the determination of the standard chemical potential $\mu^0(T)$ is needed. For an imperfect gas the fugacity or fugacity coefficient of the gas also needs to be determined, which is usually done by assuming a certain equation of state for the gas. For this study, the product gases exist in the form of a mixture; however, the evaluation of the chemical potential of a species in a gaseous mixture is similar, as outlined below.

### 2.1.10.4.2 Pure condensed species

When evaluating the chemical potential of a pure condensed species, liquid or solid, two approaches can be used, as noted above. When the first approach is used, the standard chemical potential of the species at $T$ and the reference pressure $P^0$, $\mu(T, P^0)$, is required. Then depending on whether the species is modelled to be incompressible or compressible, a single value of the its molar volume or an equation of state giving its molar volume as a function of temperature and pressure is also needed. (See equations 2.55, 2.56 and 2.46.)

When the second approach is used, the standard chemical potential of the gaseous phase of the substance as a perfect gas at $T$ and the reference pressure $P^0$, $\mu^0(T)$, is required. In addition, the vapour pressure of the condensed phase at the temperature $T$ and an equation of state for the molar volume of the vapour are also needed. Lastly, a single value of the molar volume of the condensed phase or an equation of state giving its molar volume as a function of temperature and pressure may be necessary, depending on the model used for assigning values to its molar volume, as in the first approach. (See equation 2.59.)

### 2.1.10.4.3 Species in a gaseous mixture

When evaluating the chemical potential of a species in a gaseous mixture, be it ideal or nonideal, the determination of the standard chemical potential $\mu_i^0(T)$ is required. (See equations 2.67, 2.71, 2.77, 2.79 and 2.82. Equations 2.62 and 2.78 are not used for the present study.) In addition, for species in an ideal imperfect-gas mixture, the determination of the fugacity or the fugacity coefficient of the gas is also needed, which is usually done by assuming a certain equation of state for the gas. Generally, each gas in such a mixture is assumed to follow the same equation of state, in which species specific parameters are used. Finally, for a species in a nonideal mixture, the fugacity or the fugacity coefficient of the gas becomes mixture composition dependent and usually a certain equation of state is applied to the mixture as a whole using mixture parameters. That is the mixture is modelled as if it is a single gas. The mixture parameters used in the equation are determined based on the parameters of the gases forming the mixture.

Equations for determining the fugacities or fugacity coefficients of gaseous species are given later in section 3.8, in the discussion of different equations of state for gaseous species in the new computational code. The assignment of values to standard chemical potentials is discussed in the next section.

### 2.1.10.4.4 Assignment of values to standard chemical potentials

Three ways of assigning values to standard chemical potentials, $\mu_i^0(T)$ for gases and $\mu(T, P^0)$ for condensed species (with $P^0$ equal to one unit), are described below [Smith and Missen, 1982, pp. 65–69]. In the following, the symbol $\mu_i^0$ is used to denote the standard chemical potential of the $i^{\text{th}}$ pure species, gaseous or condensed, and other thermodynamic properties denoted as standard properties are also properties at the reference pressure $P^0$.

Molar enthalpy and entropy

The chemical potential of a pure species is the molar Gibbs function of the species, as mentioned earlier. The standard chemical potential of the $i^{\text{th}}$ pure species, $\mu_i^0$, is then given by its molar Gibbs function at the reference pressure $P^0$, denoted as $g_i^0$. However, $g_i^0$ is given by $h_i^0 - Ts_i^0$ in turn, where $h_i^0$ and $s_i^0$ are the molar enthalpy and entropy of the $i^{\mathrm{th}}$pure species at $P^0$, respectively. Therefore,

$$\mu_i^0 = g_i^0 = h_i^0 - Ts_i^0 . \tag{2.83}$$

Like $\mu_i^0$ itself, $g_i^0$, $h_i^0$ and $s_i^0$ are all functions of temperature only.

### Thermal function

The molar Gibbs function of the $i^{\mathrm{th}}$ pure species at the reference pressure $P^0$, $g_i^0$, can be given in terms of a thermal function in the form

$$-\frac{g_i^0 - h_i^0(T_r)}{T},$$

where $h_i^0(T_r)$ is the molar enthalpy of the $i^{\mathrm{th}}$ pure species at $P^0$ and at the reference temperature $T_r$, which is assigned to have the value of the standard enthalpy of formation of the $i^{\mathrm{th}}$ pure species at $T_r$, $\Delta h_{f_i}^0(T_r)$. The function is usually given with $T_r$ chosen to be 298.15 K (25°C). Hence, $g_i^0$ for a given $T$ can be determined from the function with the use of $\Delta h_{f_i}^0(298.15\ K)$.

### Gibbs function of formation

The use of molar Gibbs function at $P^0$ is the usual way of obtaining the standard chemical potential of a pure species. An alternate way is to make use of its Gibbs function of formation. The standard Gibbs function change of a reaction, denoted by $\Delta G^0$, is related to the standard chemical potentials of individual species, $\mu_i^0$, that take part in the reaction on one hand and their standard Gibbs functions of formation, $\Delta G_{f_i}^0$, on the other hand as

$$\Delta G^0 = \sum_i \nu_i \mu_i^0 = \sum_i \nu_i \Delta G_{f_i}^0 , \tag{2.84}$$

where $\nu_i$ is the stoichiometric coefficient of the $i^{\mathrm{th}}$ species that takes part in the reaction. Therefore, $\Delta G_{f_i}^0$ can be identified as $\mu_i^0$. That is

$$\mu_i^0 = \Delta G_{f_i}^0 . \tag{2.85}$$

Values of $\mu_i^0$ determined by using $\Delta G_{f_i}^0$ would differ from those determined by using $g_i^0$. However, they would give same results when applied to equilibrium calculations [Smith and Missen, 1982, p. 69].

### 2.1.11 JANAF Tables of Thermochemical Properties

Thermodynamic properties such as $h^0$ and $s^0$, thermochemical properties such as $\Delta h_f^0(298.15)$ and $\Delta G_f^0$ and thermal function such as $-[g^0 - h^0(T_r)]/T$ (properties in general are referred to and subscript $i$ has been omitted here) can be found in various references [Marsh, Frenkel, Gadalla and Wilhoit, 1996; Barin, Sauert, Schulze-Rhonhof and Wang, 1993; Gurvich, Veyts and Alcock, 1989; Wagman, Evans, Parker, Schumm, Halow, Bailey, Churney and Nuttall, 1982]. However, the most widely used reference on thermodynamic data in chemical equilibrium computational codes is the JANAF Thermochemical Tables [Anon., 1960–1970; Chase, Davis, Downey, Frurip, McDonald and Syverud 1985]; it is used by all major such computational codes. Data for over a thousand chemical species are given in the tables, and they are tabulated, basically, at intervals of one hundred degrees Kelvin, as functions of temperature.

A huge amount of data are included in these tables, and it is not practical to incorporate them directly into a computational code for use. Rather, such data are usually curve fitted by using analytical functions with a few unknown coefficients. Such coefficients are then stored in a computational code for evaluating thermodynamic properties at various temperatures. As a result, there is a tremendous reduction in the amount of data that need to be stored for each species.

Extensive curve fitting of JANAF thermodynamic data, $c_p^0$, $h^0$ and $s^0$, where $c_p^0$ is the standard molar heat capacity at constant pressure, has been done by McBride [1992] and McBride and Gordon [1967]. The following curve-fit function was assumed for the heat capacity:

$$\frac{c_p^0}{R} = \sum_{i=1}^{r} a_i T^{q_i}, \tag{2.86}$$

where the exponent $q_i$ may be zero or either a positive or negative whole or fractional number. The enthalpy and entropy are related thermodynamically to the heat capacity by means of

$$\frac{h^0}{RT} = \frac{b_1}{T} + \frac{1}{T}\int \frac{c_p^0}{R}\,\mathrm{d}T \tag{2.87}$$

and

$$\frac{s^0}{R} = b_2 + \int \frac{c_p^0}{RT}\,\mathrm{d}T, \tag{2.88}$$

where $b_1$ and $b_2$ are integration constants.

Curve fits had been obtained by using a set of functions generated with $r$ equal to 5 and $q_i$ assume the values of 0, 1, 2, 3 and 4 as given below:

$$\frac{c_p^0}{R} = a_1 + a_2 T + a_3 T^2 + a_4 T^3 + a_5 T^4, \tag{2.89}$$

$$\frac{h^0}{RT} = a_1 + \frac{a_2}{2}T + \frac{a_3}{3}T^2 + \frac{a_4}{4}T^3 + \frac{a_5}{5}T^4 + \frac{b_1}{T}, \tag{2.90}$$

and

$$\frac{s^0}{R} = a_1 \ln(T) + a_2 T + \frac{a_3}{2}T^2 + \frac{a_4}{3}T^3 + \frac{a_5}{4}T^4 + b_2. \tag{2.91}$$

A simultaneous least-squares technique [Zeleznik and Gordon, 1961; Burcat, 1984] was used to fit these equations to thermodynamic data to determine $a_1$ to $a_5$, and find $b_1$ and $b_2$.

### 2.1.12 Equations of State for Gaseous and Condensed Species

When evaluating the fugacity or fugacity coefficient of an imperfect gaseous species in an ideal mixture, or when evaluating the chemical potential change between $P^0$ and $P$ (see equation 2.46) for a pure condensed species, assuming it is compressible, the molar volume of pure species as a function of temperature and pressure is required, which is usually provided by an equation of state. Furthermore, generally, the same equation of state is assumed for each gas in an ideal mixture, except that parameters specific to each gas are used in the equation.

Usually one equation of state is assumed for each phase of a substance, because of differences in characteristics of $P$-$v$-$T$ properties of phases and discontinuities in such properties across phases. The latter is particularly true in the case of the solid phase, which can only be transformed into the liquid or the vapour phase by going through abrupt changes in $P$-$v$-$T$ properties. However, the transformation between the gaseous and liquid phases is different. They can be transformed into each other both through discontinuous or continuous changes in $P$-$v$-$T$ properties, as shown in figure 2.1. Thus, there are equations which could model the gas, which includes the vapour, the fluid and liquid phases together. In particular, they could model the $P$-$v$-$T$ properties of both the liquid and vapour phases at vaporization (or condensation) conditions.

For gaseous species in a nonideal mixture, an equation of state describing the $P$-$v$-$T$ properties of the mixture is required for determining their fugacities or fugacity coefficients. Usually, the same equation of state assumed for the gaseous species in an ideal mixture is also assumed for the nonideal mixture; however, the mixture instead of species parameters are used. That is the mixture is modelled as if it is a single gas. The mixture parameters used in the equation are determined based on the parameters of the gases forming the mixture, as mentioned before.

No single equation of state can model accurately the $P$-$v$-$T$ properties of a phase of a pure substance or a gaseous mixture over a wide range of values of temperatures and pressures. An equation may be accurate for a certain range of temperature and pressure but not others. Depending on the system temperature and pressure of interest, one equation of state may be more accurate than another and should be used in the analysis. It is then highly desirable that equations of state incorporated in a computational code can be easily substituted, so that less accurate equations can be replaced by more accurate ones. This is one of the important attributes of the new computational code developed. In the following, some equations of state for gases, which are also applicable to gaseous mixtures, for liquids and solids are described. Results of calculations using these equations will be presented in chapter 4 to illustrate such attributes of the new code.

#### 2.1.12.1 Gaseous Species

##### 2.1.12.1.1 Redlich-Kwong-Soave EOS

This is a cubic equation of state (EOS) applicable to both the gaseous and liquid phases of a substance and has the following form [Soave, 1971; Redlich and Kwong, 1948]:

$$p = \frac{RT}{v-b} - \frac{a}{v(v+b)}\,, \tag{2.92}$$

where $p$ is the pressure, $T$ is the temperature, $v$ is the molar volume and $R$ is the universal gas constant. Parameter $a$ is temperature dependent and accounts for the attractions among the molecules, while parameter $b$ is constant and accounts for the repulsions. The equation is cubic in $v$ when expressed in plynomial form by clearing fractions, which is what is usually determined for a given temperature and pressure. At temperatures below the critical temperature (temperature at the critical point of the substance, see figure 2.1), the molar volume of the liquid phase is given by the smallest root to the cubic and that of the gas (vapour) phase by the largest. At temperatures above the critical temperature, there is only one root and it is the molar volume of the gas phase. This equation can also be applied to the case of a pure gas or to a nonideal gaseous mixture. (The $P$-$v$-$T$ properties of individual pure gases are required when calculations are performed by using the model of ideal mixture of imperfect gases. See section 2.1.10 for a discussion.

For a pure gas the parameters $a$ and $b$ are determined by using the critical temperature $T_c$, the critical pressure $P_c$ (pressure at the critical point of the substance), and the acentric factor $\omega$ (a constant representing the nonsphericity of the molecules of the substance). The results are

$$a = 0.42747\alpha R^2T_c^2/P_c, \tag{2.93}$$

$$\alpha = \left[1 + m\left(1 - \sqrt{T/T_c}\right)\right]^2, \tag{2.94}$$

$$m = 0.48 + 1.574\omega - 0.176\omega^2, \tag{2.95}$$

$$b = 0.08664RT_c/P_c. \tag{2.96}$$

The relation for $\alpha$ was determined by using vapour pressure data of hydrocarbons and that for $m$ was determined by correlation against values of $\omega$.

For a nonideal gaseous mixture the parameters $a$ and $b$ are calculated by using

$$a = \sum_{i=1}^{N}\sum_{j=1}^{N} x_i x_j a_{ij}, \tag{2.97}$$

$$b = \sum_{i=1}^{N} x_i b_i, \tag{2.98}$$

as the two mixing rules; where $x_i$ and $x_j$ are the mole fractions of the $i^{\text{th}}$ and $j^{\text{th}}$ species in the mixture, respectively, $b_i$ is the parameter $b$ of the $i^{\text{th}}$ pure species (from equation 2.96), and the summation extends over the total number of mixture species $N$. Parameter $a_{ij}$ is determined by using the following combined rule:

$$a_{ij} = \sqrt{a_i a_j}\,(1 - k_{ij}), \tag{2.99}$$

where $a_i$ and $a_j$ are the parameter $a$, given by equation 2.93, of the $i^{\text{th}}$ and $j^{\text{th}}$ pure species, respectively.

The parameter $k_{ij}$ is the binary interaction parameter of the $i^{\text{th}}$ and $j^{\text{th}}$ species, which can be found from a curve fit to experimental vapour-liquid equilibrium data of the binary. It is equal to zero for $i$ equal to $j$ ($i^{\text{th}}$ and $j^{\text{th}}$ species are the same) and $a_{ij}$ is equal to $a_i$; for $i$ not equal to $j$ ($i^{\text{th}}$ and $j^{\text{th}}$ species are different), it is in general a small positive or negative number close to zero providing a slight adjustment to the geometric mean $\sqrt{a_i a_j}$.

### 2.1.12.1.2 Benedict-Webb-Rubin-Starling EOS

This BWRS equation of state is a virial EOS which is also applicable to the gaseous and liquid phases of a substance. This EOS has the following form [Starling, 1971; Benedict, Webb and Rubin, 1940]:

$$\begin{aligned} P = \rho RT &+ \left(B_0RT - A_0 - C_0T^{-2} + D_0T^{-3} - E_0T^{-4}\right)\rho^2 \\ &+ \left(bRT - a - dT^{-1}\right)\rho^3 + \alpha\left(a + dT^{-1}\right)\rho^6 \\ &+ cT^{-2}\left(1 + \gamma\rho^2\right)\rho^3 \exp\left(-\gamma\rho^2\right), \end{aligned} \tag{2.100}$$

where $\rho = 1/v$ is the molar density and $A_0, B_0, C_0, D_0, E_0, a, b, c, d, \alpha$ and $\gamma$ are eleven empirical constants. This equation of state can be rearranged in terms of the compressibility factor given by $z = Pv/RT$ to give

$$z = 1 + B/v + C/v^2 + D/v^5 + (C'/v^2)(1 + \gamma/v^2)\exp(-\gamma/v^2), \tag{2.101}$$

with

$$B = (RT)^{-1}(B_0RT - A_0 - C_0/T^2 + D_0/T^3 - E_0/T^4), \tag{2.102}$$

$$C = (RT)^{-1}(bRT - a - d/T), \tag{2.103}$$

$$D = (RT)^{-1}\alpha(a + d/T), \tag{2.104}$$

$$C' = (RT)^{-1}(c/T^2). \tag{2.105}$$

This equation applies to both pure gas and gaseous (nonideal) mixtures.

For a pure gas the eleven parameters in equation 2.100 are obtained from the critical temperature $T_c$, critical molar density $\rho_c$ and acentric factor $\omega$, using relationships taken from Starling and Han [1972]:

$$\rho_c B_0 = A_1 + B_1\omega, \tag{2.106}$$

$$\rho_c A_0/(RT_c) = A_2 + B_2\omega, \tag{2.107}$$

$$\rho_c C_0/(RT_c^3) = A_3 + B_3\omega, \tag{2.108}$$

$$\rho_c^2 \gamma = A_4 + B_4\omega, \tag{2.109}$$

$$\rho_c^2 b = A_5 + B_5\omega, \tag{2.110}$$

$$\rho_c^2 a/(RT_c) = A_6 + B_6\omega, \tag{2.111}$$

$$\rho_c^3 \alpha = A_7 + B_7\omega, \tag{2.112}$$

$$\rho_c^2 c/(RT_c^3) = A_8 + B_8\omega, \tag{2.113}$$

$$\rho_c D_0/(RT_c^4) = A_9 + B_9\omega, \tag{2.114}$$

$$\rho_c^2 d/(RT_c^2) = A_{10} + B_{10}\omega, \tag{2.115}$$

$$\rho_c E_0/(RT_c^5) = A_{11} + B_{11}\omega\exp(-3.8\omega), \tag{2.116}$$

where the two sets of eleven coefficients, $A_1$ to $A_{11}$ and $B_1$ to $B_{11}$, are determined by a simultaneous curve fits to $P$-$v$-$T$ data and enthalpy and vapour-pressure data of normal paraffin hydrocarbons. Some results are given in table 2.1. This equation had been well tested for hydrocarbons, it was applied herein to some other, mainly inorganic, substances. Values of $A_i$ and $B_i$ used are listed for reference in table 2.1.

Table 2.1: Coefficients $A_i$ and $B_i$.

| $i$ | $A_i$ | $B_i$ | $i$ | $A_i$ | $B_i$ | $i$ | $A_i$ | $B_i$ |
|---|---|---|---|---|---|---|---|---|
| 1 | 0.443690 | 0.115449 | 5 | 0.528629 | 0.349261 | 9 | 0.0307452 | 0.179433 |
| 2 | 1.28438 | −0.920731 | 6 | 0.484011 | 0.754130 | 10 | 0.0732828 | 0.463492 |
| 3 | 0.356306 | 1.708710 | 7 | 0.0705233 | −0.044446 | 11 | 0.006450 | −0.022143 |
| 4 | 0.544979 | −0.270896 | 8 | 0.504087 | 1.322450 | | | |

For a nonideal gaseous mixture, the eleven parameters in equation 2.100 are found with eleven mixing rules and by using the corresponding parameters of the pure substances involved in the mixture. The rules are

$$B_0 = \sum_{i=1}^{N} x_i B_{0i}\,, \tag{2.117}$$

$$A_0 = \sum_{i=1}^{N}\sum_{j=1}^{N} x_i x_j \sqrt{A_{0i} A_{0j}}\,(1 - \bar{k}_{ij}), \tag{2.118}$$

$$C_0 = \sum_{i=1}^{N}\sum_{j=1}^{N} x_i x_j \sqrt{C_{0i} C_{0j}}\,(1 - \bar{k}_{ij})^3, \tag{2.119}$$

$$\gamma = \left[\sum_{i=1}^{N} x_i \gamma_i^{1/2}\right]^2, \tag{2.120}$$

$$b = \left[\sum_{i=1}^{N} x_i b_i^{1/3}\right]^3, \tag{2.121}$$

$$a = \left[\sum_{i=1}^{N} x_i a_i^{1/3}\right]^3, \tag{2.122}$$

$$\alpha = \left[\sum_{i=1}^{N} x_i \alpha_i^{1/3}\right]^3, \tag{2.123}$$

$$c = \left[\sum_{i=1}^{N} x_i c_i^{1/3}\right]^3, \tag{2.124}$$

$$D_0 = \sum_{i=1}^{N}\sum_{j=1}^{N} x_i x_j \sqrt{D_{0_i} D_{0_j}}\,(1 - \overline{k}_{ij})^4, \tag{2.125}$$

$$d = \left[\sum_{i=1}^{N} x_i d_i^{1/3}\right]^3, \tag{2.126}$$

$$E_0 = \sum_{i=1}^{N}\sum_{j=1}^{N} x_i x_j \sqrt{E_{0_i} E_{0_j}}\,(1 - \overline{k}_{ij})^5. \tag{2.127}$$

Similar to the binary interaction parameter $k_{ij}$ used for determining the parameter $a$ for a mixture (see equations 2.97 and 2.99), described by the Redlich-Kwong-Soave (RKS) EOS, the binary interaction parameter $\overline{k}_{ij}$ used in the above mixing rules equals zero when $i = j$ and is a small number close to zero when $i \neq j$, which is also determined by a fit to vapour-liquid equilibrium data of the binary. In the latter case, however, the value of $\overline{k}_{ij}$ would be different from that of $k_{ij}$, because the curve-fit equations or models used to determine them are different. In theory it is possible to calculate one from the other; in practice this is not done [Reid, Prausnitz and Poling, 1987, p. 86, pp. 76–77].

#### 2.1.12.1.3 Truncated virial EOS

This EOS is the pressure-explicit form of the virial equation of state, truncated after the third term, and given by

$$z = 1 + \frac{B}{v} + \frac{C}{v^2}, \tag{2.128}$$

in which $z$ is the compressibility factor and $B$ and $C$ are the second and third virial coefficients, respectively, which are functions of temperature only. This EOS is applicable only to gases. The second virial coefficient takes into account deviations from the perfect gas behaviour which resulted from interactions between two molecules, whereas the third virial coefficient takes into account such deviations resulted from the interaction of three molecules.

Similar to the previous two equations, this equation is also applicable to a pure gas and a gaseous mixture (nonideal). For a pure gas the coefficients $B$ and $C$ were determined by assuming the molecules were spherical and nonpolar, and by using the Lennard-Jones (6-12) intermolecular potential for interactions between two molecules of this type [Hirschfelder, Curtis and Bird, 1954, pp. 162–173],

$$\phi(r) = 4\varepsilon\left[\left(\frac{\sigma}{r}\right)^{12} - \left(\frac{\sigma}{r}\right)^{6}\right], \tag{2.129}$$

where $r$ is the intermolecular separation, and $\sigma$ and $\varepsilon$, which have the dimensions of length and energy, respectively, are the force constants characteristic of the species. (The third virial coefficient was determined based on the pairwise additivity assumption, which states that the potential energy of the interaction of three molecules is the sum of the potential energy of the interaction between each pair of the three possible pairs of the three molecules.)

Defining the following quantities:

$$b \equiv \frac{2}{3}\pi N_A \sigma^3 \quad \text{and} \quad T^* \equiv kT/\varepsilon, \tag{2.130}$$

where $N_A$ is the Avogadro number and $k$ is the Boltzmann constant, then $B$ and $C$ can be rewritten in the form

$$B = bB^* \quad \text{and} \quad C = b^2 C^*, \tag{2.131}$$

where $B^*$ and $C^*$ are nondimensional second and third virial coefficients, respectively, as functions of the nondimensional temperature $T^*$.

With the use of the Lennard-Jones (6-12) potential, $B^*$ is obtained as an infinite series

$$B^* = \sum_{j=0}^{\infty} b_j (T^*)^{-(2j+1)/4}, \tag{2.132}$$

where the coefficients $b_j$ are given as

$$b_j = -\frac{2^{j+\frac{1}{2}}}{4j!}\Gamma\left(\frac{2j-1}{4}\right), \tag{2.133}$$

with $\Gamma$ being the gamma function. Similarly, $C^*$ is obtained as

$$C^* = \sum_{j=0}^{\infty} c_j (T^*)^{-(j+1)/2}, \tag{2.134}$$

where the coefficients $c_j$ are fairly complicated integrals. These integrals were evaluated by Kihara [1948, 1951] and Bird, Spotz and Hirschfelder [1950]. Recently, Hauss and Gottlieb [1997] improved the accuracy. The summations in equations 2.132 and 2.134 converge fairly rapidly. Only thirty terms for $B^*$ are normally sufficient for an accuracy of five significant digits; fewer terms are required for $C^*$.

When evaluating or calculating the internal energy of a pure gas for the purposes of energy conservation, the first derivatives of $B$ and $C$ with respective to the temperature, denoted as $B'$ and $C'$, respectively, are required. They were determined according to the equations

$$B' = \frac{b}{T}B_1^* \quad \text{and} \quad C' = \frac{b^2}{T}C_1^*, \tag{2.135}$$

where $B_1^*$ and $C_1^*$ are given as

$$B_1^* = T^*\frac{dB^*}{dT^*} = -\frac{1}{4}\sum_{j=0}^{\infty}(2j+1)b_j(T^*)^{-(2j+1)/4}, \tag{2.136}$$

and

$$C_1^* = T^*\frac{dC^*}{dT^*}, = -\sum_{j=0}^{\infty}\frac{(j+1)}{2}c_j(T^*)^{-(j+1)/2}, \tag{2.137}$$

with the use of equations 2.132 and 2.134.

For a nonideal gaseous mixture, the second and third virial coefficients for the mixture, $B_m$ and $C_m$, are given by the following mixing rules:

$$B_m = \sum_{i=1}^{N}\sum_{j=1}^{N} x_i x_j B_{ij} \tag{2.138}$$

and

$$C_m = \sum_{i=1}^{N}\sum_{j=1}^{N}\sum_{k=1}^{N} x_i x_j x_k C_{ijk}\,. \tag{2.139}$$

The coefficient $B_{ij}$ describes the interaction between molecules $i$ and $j$, which may belong to the same or two different species. In the particular cases of $B_{ii}$ and $B_{jj}$, they are simply the virial coefficients of the $i^{\text{th}}$ and $j^{\text{th}}$ pure species, respectively. On the other hand, $B_{ij}$ is a cross-coefficient involving two species if $i$ is different from $j$. Similarly, the coefficient $C_{ijk}$ describes the interaction of the three molecules $i$, $j$ and $k$, which may belong to one, two or three different species. The coefficients $C_{iii}$, $C_{jjj}$ and $C_{kkk}$ are pure-species coefficients; the other coefficients with at least two indices being different are cross-coefficients.

The coefficient $B_{ij}$ was calculated in the same way as for a pure species, except with the use of force constants $\sigma_{ij}$ and $\varepsilon_{ij}$ determined by using the corresponding constants of the the $i^{\text{th}}$ and the $j^{\text{th}}$ pure species and the following combining rules:

$$\sigma_{ij} = \frac{1}{2}(\sigma_i + \sigma_j) \tag{2.140}$$

and

$$\varepsilon_{ij} = \sqrt{\varepsilon_i \varepsilon_j}\,. \tag{2.141}$$

For the present study, the coefficient $C_{ijk}$ was evaluated by using the approximation suggested by Orentlicher and Prausnitz [1966]

$$C_{ijk} = \left(C_{\{ij\}} C_{\{jk\}} C_{\{ik\}}\right)^{1/3}, \tag{2.142}$$

where $C_{\{ij\}}$ (similar to $C_{\{jk\}}$ and $C_{\{ik\}}$) is the third virial coefficient of a hypothetical pure species with force constants $\sigma_{ij}$ and $\varepsilon_{ij}$ determined from the combining rules of equations 2.140 and 2.141.

When evaluating or calculating the internal energy of a nonideal gaseous mixture for the purposes of energy conservation, the first derivatives of $B_m$ and $C_m$ with respective to temperature, $B'_m$ and $C'_m$, were required. They were determined according to the equations

$$B'_m = \sum_{i=1}^{N}\sum_{j=1}^{N} x_i x_j B'_{ij} \tag{2.143}$$

and

$$C'_m = \sum_{i=1}^{N}\sum_{j=1}^{N}\sum_{k=1}^{N} x_i x_j x_k C'_{ijk}\,, \tag{2.144}$$

where $B'_{ij}$ and $C'_{ijk}$ are the first derivatives of $B_{ij}$ and $C_{ijk}$ with respective to temperature.

The determination of the derivative $B'_{ij}$ was similar to that of the derivative $B'$ of a pure species, except that the force constants $\sigma_{ij}$ and $\varepsilon_{ij}$ were used instead. By differentiating equation 2.142 with respective to temperature, $C'_{ijk}$ was determined to be

$$\begin{aligned} C'_{ijk} = {} & \frac{1}{3}(C_{\{ij\}} C_{\{jk\}} C_{\{ik\}})^{-2/3}(C'_{\{ij\}} C_{\{jk\}} C_{\{ik\}} \\ & + C_{\{ij\}} C'_{\{jk\}} C_{\{ik\}} + C_{\{ij\}} C_{\{jk\}} C'_{\{ik\}})\,, \end{aligned} \tag{2.145}$$

where $C'_{\{ij\}}$ is the first derivative of $C_{\{ij\}}$ with respective to temperature and was determined like the derivative $C'$ but by using $\sigma_{ij}$ and $\varepsilon_{ij}$. $C'_{\{jk\}}$ and $C'_{\{ik\}}$ are similarly defined and obtained.

#### 2.1.12.2 Liquid Species

##### 2.1.12.2.1 RKS and BWRS EOS

The molar volume of a pure liquid species can be obtained by using these equations of state which are applicable both to gases and liquids.

##### 2.1.12.2.2 Empirical EOS of polynomial type

In this case the molar volume of a pure liquid species is obtained as

$$v = A_1 + A_2P + A_3P^2, \tag{2.146}$$

where the constants $A_1$, $A_2$ and $A_3$ are given by

$$A_1 = a_1 + a_2T + a_3T^2, \tag{2.147}$$
$$A_2 = a_4 + a_5T + a_6T^2, \tag{2.148}$$
$$A_3 = a_7 + a_8T + a_9T^2. \tag{2.149}$$

The nine coefficients $a_1$ to $a_9$ are determined empirically.

#### 2.1.12.3 Solid Species

##### 2.1.12.3.1 Simple approximate EOS

This equation has the following form:

$$v = v_0[1 + \beta(T - T_0) - \kappa(P - P_0)], \tag{2.150}$$

where $v_0$ is the molar volume at reference conditions of $T_0$ and $P_0$, $\beta = (1/v)(\partial v/\partial T)_P$ is the coefficient of volume expansion and $\kappa = -(1/v)(\partial v/\partial P)_T$ is the isothermal compressibility. Both $\beta$ and $\kappa$ are assumed constant. As such, this is more of an approximate equation and lower accuracy is expected for conditions more different from the reference one.

##### 2.1.12.3.2 Empirical EOS of polynomial type

The molar volume of a pure solid species can also be obtained by the polynomial type equation for a pure liquid species stated above.

### 2.1.13 Implications of the Nonnegativity Constraint

Two relations, equation 2.38 for the nonstoichiometric formulation and equation 2.44 for the stoichiometric formulation, had been given in section 2.1.9, stipulating the conditions at which a species would be absent ($n_i = 0$) at equilibrium. For the present study for which a product mixture consisting of a gaseous mixture plus a number of pure condensed species had been assumed, this can only happen in essence to the latter, because for a species in a multi-species phase to be absent the entire phase would have to be absent [Smith and Missen, 1982, pp. 57–58].

An alternate form of the most general form of chemical potential of a species in a mixture, that of a species in a nonideal mixture, at fixed temperature and pressure can be written as

$$\mu_i = \mu_i^* + RT\ln[\gamma_i(\mathbf{x})] + RT\ln\left(\frac{n_i}{n_t}\right), \tag{2.151}$$

where $\mu_i^*$ is the standard chemical potential of the $i^{\text{th}}$ species as defined before, and $\gamma_i$ is the activity coefficient as a function of the mixture composition. Also, from the definition of $\mu_i$,

$$\mu_i = \left(\frac{\partial G}{\partial n_i}\right)_{T,P,n_j \neq i}. \tag{2.152}$$

Assuming that $\gamma_i$ is finite for all possible compositions, which is certainly true for the case of an ideal mixture for which $\gamma_i = 1$, then $\mu_i$ would tend towards negative infinity if $n_i$ approaches zero and $n_t$ does not approach zero. Based on the definition of $\mu_i$, it then follows that $G$ may be lowered by increasing an infinitesimal amount of the $i^{\text{th}}$ species. This then implies that $n_i$ vanishes at equilibrium if, and only if, $n_t$ also vanishes.

Although in theory no gaseous species can vanish, for numerical reasons gaseous species present in trace amounts are often omitted in the main calculations. More details follow in the next chapter.

### 2.1.14 Phase Rule and Chemical Equilibrium Solutions

The phase rule is a general statement giving the number of degrees of freedom of a system existing at equilibrium which is the number of intensive variables whose values are free to be chosen before the system is in a determinate state. The number is obtained as a difference between the total number of intensive variables required to specify the state of a system in general and the total number of independent equations relating such variables when the system is at equilibrium. For a system where chemical as well as phase equilibrium can take place, the form of the phase rule is given by [Denbigh, 1981, pp. 184–187; Sears and Salinger, 1975, pp. 214–216]

$$f = C + 2 - \pi, \tag{2.153}$$

where $f$ is the number of degrees of freedom, $C$ is the number of components of the system, as defined earlier, and $\pi$ is the number of phases present in the system.

As an example, consider the system of liquid water in equilibrium with its vapour. In this case, the number of components is one. This is because the number of species $N$ is two, the number of independent stoichiometric equations $R$ is one and $C$ is equal to $N - R$ (see equation 2.11). The single stoichiometric equation states that the chemical potential of water in the liquid phase is equal to that in the vapour phase. Since the total number of phases is two, the number of degrees of freedom is one. The temperature and pressure of the system cannot be independently varied; when one is chosen the other is fixed. For instance, if the value of temperature is chosen, then the value of the pressure would have to be that of the vapour pressure.

Next, suppose that all three phases of water, which have the same chemical potential, are co-existing at the triple point. In this case the number of species has increased by one, but so does the number of independent stoichiometric equations. For the three species, there are two independent stoichiometric equations expressing the equality of their chemical potentials. Therefore, the number of components is again equal to one. Because the total number of phases is three, the number of degrees of freedom is then zero for the triple point. With this being the case, as the triple point of a pure substance occurs at a characteristic set of values of temperature and pressure, this characteristic set is not free and cannot be specified.

Consider another example that involves two substances. Suppose that the liquid and vapour phases of a mixture of oxygen and nitrogen is in equilibrium for this two-substance system [Van Wylen and Sonntag, 1965, pp. 479–480]. Then the number of species is four, liquid oxygen and nitrogen plus gaseous oxygen and nitrogen, and the number of independent stoichiometric equations is two, oxygen and nitrogen have equal chemical potentials in their two phases. The number of components is two and, as a result, the number of degrees of freedom is also two. Therefore, once the temperature and pressure of the system have been specified, the system is in a determinate state and the compositions of the two phases can be solved. Alternatively, if the temperature and mole fraction of one of the species in one of the two phases are specified, then the pressure of the system and the mole fractions of the other three species are fixed and can be determined.

Lastly, consider an example which involves a chemical reaction. This is one of the examples used to validate the new computational code. Results of calculation for this example will be presented in chapter 4. This example involves four species: gaseous oxygen, hydrogen and water, and liquid water. In the system, the oxygen gas reacts with the hydrogen gas to form water vapour, which condenses to form liquid water. The number of independent stoichiometric equations is two, representing the water-forming chemical reaction and phase equilibrium between liquid and gaseous water. Hence, the number of components is two. Since the number of phases existing in the system is two, the gaseous mixture and pure liquid water, the number of degrees of freedom is two. The two independent intensive variables whose values are specified could be the temperature and pressure of the system or the temperature of the system together with the mole fraction of one of the species in the gaseous mixture. (The composition of the liquid phase which consists of pure water only requires no evaluation.) The state of the system is determined once the values of two independent intensive variables are chosen.

It should be noted that what the phase rule refers to is the state of a system but not its size. For example, in the above system, while that the mole fractions of the species in the gaseous mixture become determinate once the temperature and pressure of the system are fixed, and that liquid water exists as a pure condensed phase, the exact amount of each species will not be known. To find out the abundance of each species, the amount of materials in the system would have to be taken into account, which is usually done when the abundance of each element in a system is specified in a chemical equilibrium calculation.

When carrying out a chemical equilibrium calculation, the initial species abundances in terms of number of moles are specified so that the amount of materials in a system is fixed. The species mole numbers, instead of mole fractions, at equilibrium are the quantities determined. Each of the four formulations described in section 2.1.9 provides the right number of equations, either directly or indirectly, for solving such mole numbers. For the nonstoichiometric formulations, the species mole numbers are solved for by minimizing the system Gibbs function (formulation F1), or the species mole numbers together with the Lagrange multipliers are solved for by using a set of nonlinear equations (formulation F2). For the stoichiometric formulations, the mass conservation constraint is automatically satisfied when switching to the $R$ reaction extent parameters. The species mole numbers can be determined by minimizing the system Gibbs function in terms of such parameters (formulation F3), or by a set of nonlinear equations (formulation F4).

Another point worth remembering is that the phase rule provides the number of degrees of freedom for a given number of phases. For a system in general the number of phases that exist at equilibrium is not known in advance. A chemical equilibrium analysis is required to allow the determination of the composition of a system at equilibrium, and this would include the number of phases present.

## 2.2 Numerical Methods and Equilibrium Solution Algorithms

There are many general purpose algorithms developed for solving the chemical equilibrium problem with the constraints of constant temperature and pressure, which are motivated by one of the two formulations: nonstoichimetric and stoichiometric. The formulations can also involve either function minimization or solution of nonlinear equations. Various numerical methods are available for solving each of these two types of problems [Walsh, 1975; Rabinowitz, 1970]. In this section, however, only those that are directly related to the algorithms and computational programs to be discussed will be covered.

Following an introduction to numerical methods is a discussion on some algorithms which are based on the nonstoichiometric formulation. Intrinsic difficulties of these algorithms are discussed next. The algorithm used for the present study which is based on the stoichiometric formulation is then introduced, followed by a summary of comparision between this algorithm and those just mentioned, at the end of this section.

The chemical equilibrium problem is solved iteratively. Starting from an initial estimate of the mole numbers $\mathbf{n}^{(0)}$, the estimate is corrected in a sequence of steps until a prescribed accuracy is achieved. In general

$$\mathbf{n}^{(m+1)} = \mathbf{n}^{(m)} + \omega^{(m)}\delta\mathbf{n}^{(m)} \tag{2.154}$$

for the $(m+1)^{\text{th}}$ iteration, with $m$ equal to 0, 1, 2 and so on. The scalar quantity $\omega$ is called the step-size parameter, which can be chosen to limit the amount of corrections defined by the vector $\delta\mathbf{n}^{(m)}$ to fulfil certain conditions. Equation 2.154 is used in general, but how $\delta\mathbf{n}^{(m)}$ is determined would be different for different algorithms.

In the following discussion on numerical methods, the symbol x used for denoting the independent variables is not to be confused with the symbol $x$, which is used for mole fractions. The set of independent variables are collectively referred to by the vector $\mathbf{x}$. The function to be minimized is denoted by $f$ and, the set of nonlinear functions the zeros of which are to be found are denoted by $g_i$ or more concisely by the vector $\mathbf{g}$.

### 2.2.1 Second Variation Method for Unconstrained Minimizations

To be in line with the discussion on the application of this method given later, let $f$ be a function of $R$ independent variables. The problem is to

$$\text{minimize } f(\mathbf{x}), \tag{2.155}$$

where $\mathbf{x}$ is a vector of $R$ real numbers, $\mathrm{x}_1$ to $\mathrm{x}_R$. Let the vector $\mathbf{x}^{(m)}$ be the estimate to the solution vector after the $m^{\text{th}}$ iteration. In order to solve for $\mathbf{x}^{(m+1)}$, $f$ is approximated near $\mathbf{x}^{(m)}$ by a quadratic function and the minimum of this function is sought. The local quadratic approximation to $f(\mathbf{x})$ at $\mathbf{x}^{(m)}$ is given by the first three terms of the Taylor-series expansion of $f(\mathbf{x})$ about $\mathbf{x}^{(m)}$.

Denoting the quadratic function by $Q(\mathbf{x})$, then

$$Q(\mathbf{x}) = f(\mathbf{x}^{(m)}) + \sum_{i=1}^{R} \frac{\partial f}{\partial \mathbf{x}_i}\bigg|_{\mathbf{x}=\mathbf{x}^{(m)}} (\mathbf{x}_i - \mathbf{x}_i^{(m)}) + \frac{1}{2}\sum_{i=1}^{R}\sum_{j=1}^{R} \frac{\partial^2 f}{\partial \mathbf{x}_i \partial \mathbf{x}_j}\bigg|_{\mathbf{x}=\mathbf{x}^{(m)}} (\mathbf{x}_i - \mathbf{x}_i^{(m)})(\mathbf{x}_j - \mathbf{x}_j^{(m)}), \tag{2.156}$$

where the symbol $|_{\mathbf{x}=\mathbf{x}^{(m)}}$ means that the quantity on the left is to be evaluated at $\mathbf{x}^{(m)}$.

The first-order necessary conditions for a minimum $Q$ then yields

$$\frac{\partial f}{\partial \mathbf{x}_i}\bigg|_{\mathbf{x}=\mathbf{x}^{(m)}} + \sum_{j=1}^{R} \frac{\partial^2 f}{\partial \mathbf{x}_i \partial \mathbf{x}_j}\bigg|_{\mathbf{x}=\mathbf{x}^{(m)}} \delta \mathbf{x}_j = 0 \quad \text{with} \quad i = 1, 2, \ldots, R, \tag{2.157}$$

where $\delta \mathbf{x}_j$ equals $\mathbf{x}_j - \mathbf{x}_j^{(m)}$. Equation 2.157 consists of $R$ linear equations can be written concisely in the form

$$\delta \mathbf{x}^{(m)} = -\left[\frac{\partial^2 f}{\partial \mathbf{x}^2}\right]^{-1}_{\mathbf{x}^{(m)}} \left[\frac{\partial f}{\partial \mathbf{x}}\right]_{\mathbf{x}^{(m)}}, \tag{2.158}$$

where $\partial^2 f/\partial \mathbf{x}^2$ is the so-called Hessian matrix, the subscript $\mathbf{x}^{(m)}$ indicates an Hessian matrix evaluation at $\mathbf{x}^{(m)}$, and the superscript $-1$ denotes the inverse of the Hessian matrix that has been evaluated at $\mathbf{x}^{(m)}$.

### 2.2.2 Newton-Raphson Method for Nonlinear Equations

Let the number of unknowns be $N$ so there are $N$ nonlinear equations to be solved. Denoting the set of nonlinear functions by $\mathbf{g}$ and the set of independent variables by $\mathbf{x}$,

$$\mathbf{g}(\mathbf{x}) = 0. \tag{2.159}$$

is the set of equations that needs to be solved. Let $\mathbf{l}^{(m)}(\mathbf{x})$ be the set of local linear approximations to $\mathbf{g}(\mathbf{x})$ at $\mathbf{x}^{(m)}$, given by the first two terms of the Taylor-series expansion of $\mathbf{g}(\mathbf{x})$ around point $\mathbf{x}^{(m)}$. That is

$$l_i^{(m)}(\mathbf{x}) = g_i(\mathbf{x}^{(m)}) + \sum_{j=1}^{N} \frac{\partial g_i}{\partial x_j}\bigg|_{\mathbf{x}=\mathbf{x}^{(m)}} (x_j - x_j^{(m)}) \quad \text{with} \quad i = 1, 2, \ldots, N. \tag{2.160}$$

By setting all of the linear functions $l_i^{(m)}(\mathbf{x})$ to zero, one can obtain the following set of equations:

$$\sum_{j=1}^{N} \frac{\partial g_i}{\partial x_j}\bigg|_{\mathbf{x}=\mathbf{x}^{(m)}} \delta x_j^{(m)} = -g_i(\mathbf{x}^{(m)}) \quad \text{with} \quad i = 1, 2, \ldots, N, \tag{2.161}$$

which can be rewritten as

$$\delta \mathbf{x}^{(m)} = -\left[\frac{\partial \mathbf{g}}{\partial \mathbf{x}}\right]^{-1}_{\mathbf{x}^{(m)}} \mathbf{g}(\mathbf{x}^{(m)}) \tag{2.162}$$

for the correction vector $\delta \mathbf{x}^{(m)}$.

### 2.2.3 Nonstoichiometric Algorithms

Mathematical formulations of the chemical equilibrium problem with constant temperature and pressure constraints can be classified into the nonstoichiometric and stoichiometric categories, depending on whether the conservation of mass constraint is treated by means of chemical stoichiometry, as mentioned in section 2.1.9. Chemical equilibrium algorithms based on nonstoichiometric formulations are termed as nonstoichiometric algorithms and those based on stoichiometric formulations are termed as stoichiometric algorithms. The most representative nonstoichiometric algorithms for ideal systems, systems consist of phases which are either pure phases, or ideal mixtures or solutions, are discussed below.

#### 2.2.3.1 The Brinkley, NASA and RAND Algorithms

The Brinkley, NASA and RAND algorithms, denoted by BNR for brevity, are closely related [Smith and Missen, 1982, pp. 122–136]. All three can be derived by incorporating explicitly the conservation of mass constraint using Lagrange multipliers, before the minimum of the system Gibbs function is sought; that is by using equilibrium formulation **F2** and applying the Newton-Raphson method to the resulting set of equations. They differ only in how the mole-number variables are treated and how the equilibrium conditions and conservation of mass constraint are satisfied.

In the following discussion,

Reference is made to a single multispecies phase that would normally be a gaseous mixture. Results that are related to single-species phases are noted seperately. Also, the formula matrix $\mathbf{A}$ is assumed to be of full rank $M$, that is $C = \text{rank}(\mathbf{A}) = M$. Equation 2.39 which expresses the mass conservation constraint is then simply equation 2.3.

Equation 2.37 when applied to individual species in the multispecies phase gives a set of equilibrium conditions. All three algorithms can be derived by applying the Newton-Raphson method to this set of equilibrium conditions and to the mass conservation constraint given by equation 2.39, but they differ slightly in the way they numerically treat the mole-number variables. (Mole numbers of species in a single multispecies phase are always greater than zero, as dicussed in section 2.1.13, and equation 2.38 does not apply in this case.) The RAND algorithm [Zeleznik and Gordon, 1962; Levine, 1962] uses the variables $n_i$, whereas the $\ln(n_i)$ are used in the algorithms of Brinkley [1947] and NASA [Huff, Gordon and Morrell, 1951; Gordon, Zeleznik and Huff, 1959].

The RAND algorithm was originally formulated by White, Johnson and Dantzig [1958] as a constrained minimization problem, which requires the conservation of mass constraint be satisfied at each step and iteratively minimizes the Gibbs function of the system. It was later modified so that the mass conservation constraint need not be satisfied at each step, and then iterations are done to satify the equilibrium conditions and conservation of mass constraint simultaneously.

Contrary to the original RAND algorithm, the Brinkley algorithm requires that the equilibrium conditions be satisfied at each step and iterations be done to satisfy the conservation of mass constraint. When the restriction that the equilibrium conditions be satisfied at each step is relaxed, the NASA algorithm resulted. Hence, the NASA algorithm complements the Brinkley algorithm in a similar manner that the modification to the RAND algorithm complements its original version. Computationally, there is little difference in the performance of the three algorithms [Zeleznik and Gordon, 1960].

Nonstoichiometric algorithms make use of equations 2.37 and 2.39, and the number of variables involved in general is $N + M$ (assuming $C = M$), which include $N$ mole number related variables and $M$ Lagrange multipliers. However, for an ideal system the number could be reduced. For the case of a single multispecies phase, the number can be reduced to $M+1$. Such a reduction will be illustrated below, where the RAND algorithm is derived as an example.

#### 2.2.3.2 The RAND Algorithm Derivation

The derivation shown in this section is due to Smith and Missen [1982, pp. 123–127]. The algorithm is first derived by considering that systems consist of a single multispecies phase; results for multiphase systems are then quoted. The derivation begins with a general nonideal mixture and later introduces simplifications as a result of the ideality assumption.

Smith and Missen included the possibility of having the presence of inert species in the mixture by means of the following equation

$$n_t = \sum_{i=1}^{N'} n_i + n_z, \tag{2.163}$$

in which $n_t$ is the total number of moles of species in the mixture, $N'$ is the number of species other than inert species in the mixture, and $n_z$ is the total number of moles of inert species in the mixture.

In this case, $N'$ has taken the place of $N$, and a set of $N'$ equations is obtained from equation 2.37, by setting $i$ equal to 1 to $N'$, for the $N'$ species in the mixture which are not inert. Dividing such equations by $RT$, $R$ being the universal gas constant, and applying the Newton-Raphson method to the resulting equations gives

$$-\frac{1}{RT}\sum_{j=1}^{N'}\left(\frac{\partial \mu_i}{\partial n_j}\right)_{\mathbf{n}^{(m)}} \delta n_j^{(m)} + \sum_{k=1}^{M} a_{ki}\,\delta\psi_k^{(m)} = \frac{\mu_i^{(m)}}{RT} - \sum_{k=1}^{M} a_{ki}\psi_k^{(m)} \quad \text{with } i = 1,2,\ldots,N', \tag{2.164}$$

where

$$\delta n_j^{(m)} = n_j - n_j^{(m)}, \tag{2.165}$$

$$\delta\psi_k^{(m)} = \psi_k - \psi_k^{(m)} \tag{2.166}$$

and

$$\psi_k = \frac{\lambda_k}{RT}, \tag{2.167}$$

which is a nondimensional Lagrange multiplier, and $m$ is an iteration index. Equations 2.164 are obtained by linearization about an arbitrary estimate of the solution $(\mathbf{n}^{(m)}, \boldsymbol{\psi}^{(m)})$, where $\mathbf{n}^{(m)}$ is a vector of the $N'$ mole numbers $n_1^{(m)}$ to $n_{N'}^{(m)}$, and $\boldsymbol{\psi}$ is a vector of the $M$ nondimensional Lagrange multipliers $\psi_1$ to $\psi_M$.

When the Newton-Raphson method is applied to equation 2.39, an additional set of equations is obtained as follows:

$$\sum_{i=1}^{N'} a_{ki}\,\delta n_i^{(m)} = b_k - b_k^{(m)} \quad \text{with} \quad k = 1,2,\ldots,M, \tag{2.168}$$

where

$$b_k^{(m)} = \sum_{i=1}^{N'} a_{ki} n_i^{(m)} \quad \text{with} \quad k = 1,2,\ldots,M. \tag{2.169}$$

Equations 2.164 and 2.168 are a set of $N' + M$ linear equations in the $N'$ unknowns $\delta n_1^{(m)}$ to $\delta n_{N'}^{(m)}$ and the $M$ unknowns $\delta\psi_1^{(m)}$ to $\delta\psi_M^{(m)}$. However, for ideal mixtures, the number of linear equations can be reduced and for the present case of a single multispecies phase the number can be reduced to $M + 1$. The reduction is accomplished by eliminating the variables $\delta n_1^{(m)}$ to $\delta n_{N'}^{(m)}$ in equations 2.164 and 2.168 and introducing a new variable which is related to the total number of moles of species in the mixture. This is possible because of the particular form of the chemical potential of a species in an ideal mixture given by equation 2.62.

By differentiating equation 2.62, the rate of change of the chemical potential of the $i^{\text{th}}$ species with respect to the number of moles of the $j^{\text{th}}$ species is determined to be

$$\frac{1}{RT}\left(\frac{\partial \mu_i}{\partial n_j}\right) = \frac{\delta_{ij}}{n_j} - \frac{1}{n_t}, \tag{2.170}$$

where $\delta_{ij}$ is the Kronecker delta, which is equal to one when $i$ is equal to $j$ and is equal to zero when $i$ is different from $j$. Making use of equation 2.170, equations 2.164 can be rearranged to give

$$\delta n_i^{(m)} = n_i^{(m)}\left(\sum_{k=1}^{M} a_{ki}\psi_k + u - \frac{\mu_i^{(m)}}{RT}\right) \quad \text{with} \quad i = 1, 2, \ldots, N', \tag{2.171}$$

where the new variable $u$ is defined as

$$u = \frac{\sum_{j=1}^{N'} \delta n_j^{(m)}}{n_t^{(m)}} \equiv \frac{\delta n_t^{(m)}}{n_t^{(m)}}. \tag{2.172}$$

Changing the index $k$ to $j$ in equations 2.168 and substituting for $\delta n_i^{(m)}$ with $i$ equal to 1 to $N'$ yields a new set of equations as

$$\sum_{k=1}^{M}\psi_k \sum_{i=1}^{N'} a_{ki}a_{ji}n_i^{(m)} + b_j^{(m)}u = \sum_{i=1}^{N'} a_{ji}n_i^{(m)}\frac{\mu_i^{(m)}}{RT} + b_j - b_j^{(m)} \quad \text{with} \quad j = 1, 2, \ldots, M. \tag{2.173}$$

By summing equations 2.171 and making use of equation 2.163, an additional equation can be obtained from equation 2.172, which is

$$\sum_{k=1}^{M} b_k^{(m)}\psi_k - n_z u = \sum_{j=1}^{N'} n_j^{(m)}\frac{\mu_j^{(m)}}{RT}. \tag{2.174}$$

Consequently, the number of iteration equations is $M + 1$.

At each iteration step, the RAND algorithm involves solving the set of $M+1$ linear equations given by equations 2.173 and 2.174, for the $M$ nondimensional Lagrange multipliers $\psi_1$ to $\psi_M$ and the variable $u$, and using equations 2.171 to determine $\delta n_1^{(m)}$ to $\delta n_{N'}^{(m)}$. Let $\delta \mathbf{n}^{(m)}$ be the vector which consists of the elements $\delta n_1^{(m)}$ to $\delta n_{N'}^{(m)}$. The new estimates of the number of moles of the species can then be obtained according to equation 2.154.

The RAND algorithm can be extended to include any number of single-species phases and to more than one multispecies phase. In the general case, when there are $\pi_m$ multispecies phases and $\pi_s$ single-species phases, equations 2.171, 2.173 and 2.174 become, respectively,

$$\delta n_i^{(m)} = \begin{cases} n_i^{(m)}\left(\sum_{k=1}^{M} a_{ki}\psi_k + u_\alpha - \frac{\mu_i^{(m)}}{RT}\right) & \text{for species in multispecies phases} \\ u_\alpha n_i^{(m)} & \text{for species in single-species phases} \end{cases} \tag{2.175}$$

$$\sum_{k=1}^{M} \psi_k \sum_{i=1}^{N'} a_{ki} a_{ji} n_i^{(m)} + \sum_{\alpha=1}^{\pi} b_{j\alpha}^{(m)} u_\alpha = \sum_{i=1}^{N'} a_{ji} n_i^{(m)} \frac{\mu_i^{(m)}}{RT} + b_j - b_j^{(m)} \quad \text{with} \quad j = 1, 2, \ldots, M, \tag{2.176}$$

$$\sum_{k=1}^{M} b_{k\alpha}^{(m)} \psi_k - n_{s\alpha} u_\alpha = \sum_{j=1}^{N'} n_{j\alpha}^{(m)} \frac{\mu_{j\alpha}^{(m)}}{RT} \quad \text{with} \quad \alpha = 1, 2, \ldots, \pi, \tag{2.177}$$

where the subscript $\alpha$ has been used to identify a phase and $\pi = \pi_m + \pi_s$. Therefore, in general, the RAND algorithm consists of iteratively solving the set of $M + \pi$ linear equations given by equations 2.176 and 2.177, for the $M$ nondimensional Lagrange multipliers and the $\pi$ variables related to the total number of moles in each phase. The reduction from $N' + M$ equations to $M + \pi$ equations is possible only because of the ideality assumption. Equations 2.176 and 2.177 can be reduced to equations 2.173 and 2.174, for the case $\pi_s = 0$ and $\pi_m = 1$.

Despite the seemingly straightforward solution of equations 2.176 and 2.177, numerical problems may sometimes be encounted. These problems arise when the coefficient matrix of these linear equations becomes singular at some point in a calculation. Conditions at which singularities may occur are to be discussed in fair detail in the following section.

### 2.2.4 Numerical Singularities in Equilibrium Computations

For the nonstoichiometric equilibrium algorithms that require the solution of a system of linear equations for each iteration, there can arise situations in which the coefficient matrix of these equations becomes singular in the course of the computations. In such cases, the algorithm will normally fail, unless appropiate corrective actions are taken. In this section we shall briefly illustrate the sources of such difficulties, by using the problem involving an ideal mixture of gaseous species plus any number of pure condensed solids and liquids; this is a gas-solids problem.

The coefficient matrices of the linear equations in the BNR algorithms at a given iteration is

$$\beta = \begin{pmatrix} \mathbf{A}_1 \Lambda \mathbf{A}_1^T & \mathbf{b}_1 \quad \mathbf{A}_2 \\ \mathbf{b}_1^T & \\ \mathbf{A}_2^T & \mathbf{Q} \end{pmatrix}$$

where $\mathbf{A}_1$ and $\mathbf{A}_2$ are parts of the formula matrix $\mathbf{A}$ referring to the multispecies phase and pure condensed phases, respectively. $\Lambda = \mathrm{diag}(n_1, n_2, \ldots, n_h)$ is the number of species in the multispecies phase and $\mathbf{b}_1$ is the current elemental-abundance vector in the multispecies phase. Now, $\mathbf{b}_1 = \mathbf{A}_1 \mathbf{n}_1$ where $\mathbf{n}_1 = (n_1, n_2, \ldots, n_h)^T$, and $\mathbf{Q}$ is the null matrix of order $\pi \times \pi$, except that $Q_{11} = -n_z$, where $\pi$ is the total number of phases and $n_z$ is the total number of moles of inert species.

Now $\beta$ is always singular for problems with only pure condensed phases. This occurs because all the entries in $\beta$ with subscript 1 are absent. Such equilibrium problems are linear programming problems, because the logarithm term is absent in equation 2.62. Also, $\beta$ is singular whenever the block of zeros (given by $\mathbf{Q}$) in the lower right-hand corner is too large. This problem is circumvented by keeping $\pi_s \leq C - \pi_m$, where $\pi_s$ is the number of single-species phases and $\pi_m$ is the number of multispecies phases.

Since $\mathbf{A}_1 \Lambda \mathbf{A}_1^T$ can be expressed as the product of a nonsingular matrix and its transpose, it is never singular when the multispecies phase has all $n_i > 0$. Thus, for problems consisting of only one single multispecies phase, $\beta$ is never singular. However, finite computer word lengths can cause $\beta$ to be numerically singular in some cases.

It can be shown in general when no inert species are present ($n_s = 0$) in the multispecies phase, $\beta$ can in principle be singular only if the columns of $(\mathbf{b}, \mathbf{A}_2)$ are linearly dependent. When inert species exist in the mixture, singularity occurs only if the columns of $\mathbf{A}_2$ are linearly dependent. However, similar to an earlier discussion, $\beta$ can also appear numerically singular even when these conditions do not hold. Apart from these, the difficulty with a singular $\beta$ is associated with the presence of pure condensed species in the calculation. Even when $\beta$ is nonsingular, the nonnegativity constraint on these species must be handled carefully. Different types of situations are discussed that can produce a singular coefficient matrix $\beta$ in the context of a gas-solids problem.

#### 2.2.4.1 Numerical Singularity when $\pi_s = 0$

A numerical singularity of $\beta$ for $\pi_s = 0$ occurs when $\mathbf{b}$ is nearly all contained in fewer than $C$ species. Consider the system $\{(O_2,H_2,H_2O),(H,O)\}$ with $\mathbf{b} = (2,1)^T$; the temperature and pressure can be such that the only species present in a mole fraction greater than $10^{-8}$ is $H_2O$. Then

$$\beta = \begin{pmatrix} 4+\epsilon_1 & 2+\epsilon_2 & 2 \\ 2+\epsilon_2 & 1+\epsilon_3 & 1 \\ 2 & 1 & 0 \end{pmatrix},$$

where $\epsilon_i$ are small numbers of the order of magnitude of $10^{-8}$. In a numerical calculations, computer rounding can sometimes cause $\beta$ to appear singular.

#### 2.2.4.2 Columns of $(\mathbf{b}, \mathbf{A}_2)$ Linearly Independent

The solution to the equilibrium problem is unique for this case; we focus our attention primarily on how to handle the pure condensed species. If the columns of $(\mathbf{b}, \mathbf{A}_2)$ are linearly independent, two cases occur: (1) the system is composed of the species in the multispecies phase only, that is the set $W = \{\mathbf{n}_1 : \mathbf{A}_1\mathbf{n}_1 = \mathbf{b}, n_{1i} > 0\}$ is nonempty, and furthermore (2) the system cannot occur in this way, that is $W$ is empty.

*W* nonempty. Equilibrium is first calculated assuming that all of the pure condensed species are absent. Consequently,

$$\Delta G_i = \mu_i^* - \sum_{k=1}^{M} a_{ki}\lambda_k \tag{2.178}$$

are calculated for each pure condensed species. If any $\Delta G_i < 0$, the condensed species with the smallest $\Delta G_i$ value is inserted into the calculation, and the equilibrium composition is computed again, and for the resulting composition the test is done again. This procedure is repeated until all absent condensed species have $\Delta G_i \geq 0$. Equation 2.178 essentially tests whether or whether not the inclusion of the condensed species marginally lowers the value of the system Gibbs state function.

*W* empty. If $W$ is empty, then the system cannot be composed of the species in the multispecies phase alone. Hence, at least one pure condensed species must exist at equilibrium. However, which of these may not be known *a priori*. Difficulties arise because there is no explicit procedure in the BNR algorithms for ensuring $n_i > 0$ for the pure condensed species. If a pure condensed species is incorrectly assumed to exist, the equilibrium $n_i$ are calculated with negative values. When $\pi_s$ is small, it may be feasible to insert or remove pure condensed species in the course of a calculation in accordance with equation 2.178, but this is tedious. Each problem is then a special case.

Numerical singularity. For the above two cases, numerical singularities may occur as described in section 2.2.4. If portions of b are linearly dependent on one or more than one columns of $A_2$, all but a very small amount of those portions may be combined in the condensed species, resulting in $\beta$ appearing numerically singular. As an example, for the system consisting of $Al_2O_3$ together with several gaseous species containing the elements oxygen and hydrogen, when $(b_{Al}, b_O) = (2,3)$, we may have

$$\beta = \begin{pmatrix} \tau & \epsilon_2 & 0 & b_H & 0 \\ \epsilon_2 & \epsilon_3 & 0 & \epsilon_1 & 3 \\ 0 & 0 & 0 & 0 & 2 \\ b_H & \epsilon_1 & 0 & 0 & 0 \\ 0 & 3 & 2 & 0 & 0 \end{pmatrix},$$

where $\tau$ is a relatively large number. The second and third columns/rows of $\beta$ can result in numerical singularities, depending on the size of the computer roundoff errors.

### 2.2.4.3 Columns of $(b, A_2)$ Linearly Dependent

In this case when $n_z = 0$ the solution to the chemical equilibrium problem need not be unique. The following four cases need to be discussed: (1) the columns of $A_2$ are linearly independent and $W$ is nonempty, (2) the columns of $A_2$ are linearly independent and $W$ is now empty, (3) the columns of $A_2$ are linearly dependent and $\pi_m > 0$, and (4) the columns of $A_2$ are linearly dependent and now $\pi_m = 0$.

**The columns of $A_2$ are linearly independent and $W$ is nonempty.** Provided that $n_z \neq 0$, this case may be treated in the same way as in the case described in section 2.2.4. When $n_z = 0$, if any subset of the pure condensed phases with formula vectors that are linearly dependent on b is included in the calculation, $\beta$ may be singular. This would occur at some stage of the calculations when a fraction of the element-abundance vector is distributed among the species in the multispecies phase and the remainder is distributed among the condensed phases. In this situation $b_1$ is linearly dependent on the columns of $A_2$, so that $\beta$ is singular, and the algorithm then fails.

**The columns of $A_2$ are linearly independent and $W$ is empty.** In this case the situation is similar to that described in section 2.2.4. The difference here is that $\beta$ is singular if all the condensed species are included in a calculation.

**The columns of $A_2$ are linearly dependent and $\pi_m > 0$.** In this case $\beta$ is singular if more than $C-1$ single-specie phases are included in the calculation. If $W$ is nonempty, it may be feasible to use the procedure discussed in section 2.2.4. If $W$ is empty, at least one condensed species must be removed, and the difficulties with this type is described in section 2.2.4 apply in addition.

**The columns of $A_2$ are linearly dependent and $\pi_m = 0$.** In this case $\beta$ is always singular, and the difficulty becomes a linear programming problem, to which the BNR algorithms are simply not applicable.

Although we have discussed in detail only the case $\pi_m = 1$, the results essentially apply when $\pi_m > 1$, provided that all multispecies phases are actually present at equilibrium. The stoichiometric algorithms are ideally suited to problems involving pure condensed species since they do not give rise to numerical singularities.

### 2.2.5 Stoichiometric Algorithms

These are algorithms based on stoichiometric formulations which eliminate the conservation of mass constraint by transforming the set of mole-number variables to a new set of reaction-extent variables. Viewing the system Gibbs function as a function of the set of reaction-extent variables, the chemical equilibrium problem may be treated numerically from either the minimization or nonlinear equations point of view, that is by formulations F3 or F4.

### 2.2.6 Relative Merits of BNR Nonstoichiometric Algorithms and VCS Stoichiometric Algorithm

The major differences between the BNR algorithms and the VCS algorithm are discussed in this section, with the emphasis on their relative merits. The differences are listed in table 2.2, with relative merits indicated by the symbol ⊛ and discussed in the order they appear in the table.

In these algorithms, corrections in mole numbers are obtained from the corrections in the reaction extents. Denoting these corrections by the vectors $\delta\mathbf{n}$ and $\delta\boldsymbol{\xi}$, respectively, and following

Table 2.2: Major differences between and relative merits of the BNR nonstoichiometric algorithms and the VCS stoichiometric algorithm.

| | attributes compared | BNR nonstoichiometric algorithms | VCS stoichiometric algorithm |
|---|---|---|---|
| 1) | use of chemical stoichiometry | no | yes |
| 2) | mass conservation constraint | $\mathbf{A}\,\mathbf{n}=\mathbf{b}$ | $\mathbf{n}=\mathbf{n}^0+\mathbf{N}\boldsymbol{\xi}$,<br>where $\mathbf{A}\mathbf{n}^0=\mathbf{b}$ |
| 3) | equilibrium conditions | $\boldsymbol{\mu}-\mathbf{A}^T\boldsymbol{\lambda}=\mathbf{0}$ | $\mathbf{N}^T\boldsymbol{\mu}=\mathbf{0}$ |
| 4) | numerical technique | Newton-Raphson method for nonlinear equations | second variation method for minimization problems |
| 5) | number of variables | ⊛ $M+\pi$ | $N-M$ |
| 6) | mass conservation satisfied automatically at each iterative step | no | yes |
| 7) | equilibrium conditions satisfied automatically at each iterative step | yes for Brinkley,<br>no for NASA,<br>no for RAND | no |
| 8) | matrix singularities | possible | ⊛ never |
| 9) | nonnegativity constraint | not easily handled | ⊛ easily handled |
| 10) | if $C < M$ | A must be reduced | ⊛ no change required |
| 11) | comparison variables conditions | iterative equations must be rederived | ⊛ minor changes required |

⊛ relative merit

equation 2.20, then

$$\delta \mathbf{n} = \mathbf{N}\,\delta\boldsymbol{\xi}, \tag{2.179}$$

where N is a complete stoichiometric matrix. Provided that the mole numbers which satisfy the mass conservation constraint are used to start the iterations, adjusted mole numbers at each iteration step will continue to satisfy the constraint. In addition, N is not unique and can be chosen to fulfil certain computational advantages.

#### 2.2.6.1 The Villars-Cruise-Smith (VCS) Algorithm

This is the algorithm chosen for the development of the new computational code. It is particularly well suited for solving chemical equilibrium problems involving pure condensed phases [Smith and Missen, 1982, p. 144]. Villars [1959, 1960] originally viewed this algorithm as a way of using the Newton-Raphson method on the equilibrium conditions equation 2.42. He used an arbitrarily chosen stoichiometric matrix N and adjusted these equations one at a time repeatedly until convergence was achieved. Cruise [1964] later incorporated the use of an optimized N and advocated adjusting all equations simultanoeusly. Smith and Missen [1968] finally reformulated the algorithm from the minimization point of view and introduced the use of the step-size parameter $\omega$, resulting in improved convergence properties.

While matrix singularities may be encountered when using the BNR algorithms, which cause convergence difficulties, the VCS algorithm eliminates the need for matrix inversion, thus avoiding the problem of singular matrices [Smith and Missen, 1982, p. 145]. Furthermore, the presence or absence of pure condensed species can be handled straightforwardly by this algorithm [Smith and Missen, 1982, p. 211]. The formulation of this algorithm will be given in where the adaptation of this algorithm to the solution of chemical equilibrium problems with constant volume and internal energy as the constraints are discussed in detail. In the mean time, to help to see why this algorithm was preferred, a summary of the major differences between and relative merits of the BNR algorithms and the VCS algorithm is given in the next section.

1) and 2) In nonstoichiometric algorithms, the conservation of mass constraint $\mathbf{A}\mathbf{n}=\mathbf{b}$ is handled directly, whereas in stoichiometric algorithms this constraint is treated by using chemical stoichiometry, which relates the species-abundance vector $\mathbf{n}$ to the vector of reaction extents $\boldsymbol{\xi}$ by $\mathbf{n} = \mathbf{n}^0 + \mathbf{N}\boldsymbol{\xi}$ (equation 2.20). Now, $\mathbf{n}^0$ is a particular vector of species mole numbers satisfying the mass conservation constraint, usually consisting of the vector of initial estimates of the species mole numbers.

3) For nonstoichiometric algorithms which make use of Lagrange multipliers to incorporate the mass conservation constraint, such as the BNR algorithms, the equilibrium conditions to be satisfied are obtained by applying equations 2.37 and 2.38 to the species in a system, which are Kuhn-Tucker necessary conditions for a constrainted minimized problem. On the other hand, for stoichiometric algorithms, such as the VCS algorithm, the equilibrium conditions are first-order necessary conditions for an essentially unconstrainted minimization problem, see equations 2.42 to 2.44. For presentation simplificity only equality conditions are stated in the table, which is equivalent to the assumption that all species exist at equilibrium (with mole numbers greater than zero). These conditions may appear different but they are equivalent, as noted before.

4) In the BNR algorithms the Newton-Raphson method is utilized to solve the equation set corresponding to equilibrium conditions and the mass conservation constraint. In the VCS algorithm, the second variation method is utilized to solve an essentially unconstrainted minimization problem.

5) In general, the total number of variables to be determined in nonstoichiometric algorithms which make use of Lagrange multipliers to incorporate the mass conservation constraint and involve solving sets of nonlinear equations is $N + M$, where $N$ is the total number of species in a system (assuming there is no inert species) and $M$ is the number of elements involved in the same system (assuming $C = M$). When an ideal system is assumed, this number can be reduced to $M + \pi$, where $\pi$ is the total number of phases. In the case of stoichiometric algorithms, the number of variables is always $R$ ($= N - M$, see equation 2.11). For ideal systems involving multispecies phases with many species, nonstoichiometric algorithms of this type usually have fewer variables than stoichiometric algorithms, and the difference could be quite large, depending on the number of species present in the multispecies phases. An example of this case is that between the BNR algorithms and the VCS algorithm. However, for nonideal systems, stoichiometric algorithms always have fewer variables than this type of nonstoichiometric algorithms, even though the difference may be small, depending on the values of $N$ and $M$.

6) At each iteration step, the BNR algorithms may satisfy the conservation of mass constraint and iterate to satisfy the equilibrium conditions (original version of RAND), or may satisfy the equilibrium conditions and iterate to satisfy the conservation of mass constraint (Brinkley), or may satisfy neither and iterate to satisfy both simultaneously (later modified version of RAND, derivation of which shown above, and NASA). The VCS algorithm satisfies the conservation of mass constraint at each step and iterates to satisfy the equilibrium conditions.

7) In the BNR algorithms, during the course of a calculation, the coefficient matrix of the linear iteration equations may become mathematically singular, or numerically singular due to computer roundoff errors, causing convergence problems. On the other hand, in the VCS algorithm, no matrix inversion is necessary thus eliminating these problems.

8) The determination of the presence or absence of pure condensed species at equilibrium can be done more easily by the VCS algorithm than by the BNR algorithms. The coefficient matrix of the iteration equations in the BNR algorithms will become singular if too many pure condensed species are considered at the same time, as noted in section 2.2.4. If the conservation of mass constraint can be satisfied by the gaseous species alone, than the testing for the inclusion of one condensed species is done after convergence has been achieved by the main calculation. The procedure is repeated for each condensed species included. However, if the mass conservation constraint cannot be satisfied by the gaseous species alone, than at least one condensed species would have to be included in the main calculation at the outset, and additional assumptions regarding the presence or absence of condensed species would have to be made. The trial and error process could be quite tedious when the number of condensed species is large. On the contrary, in the VCS algorithm, the presence or absence of condensed species at equilibrium can be determined by considering all of the condensed species together, without the need of any assumptions. Details of such a procedure will be presented in chapter 3.

9) On the occasions when $C$ is less than $M$, the reduced matrix $\mathbf{A}'$, as described in section 2.1.9, instead of $\mathbf{A}$ must be used, and the coefficients as well as the number of the iteration equations in the BNR algorithms must be modified, otherwise singular coefficient matrices will result. However, this situation is not a concern in the case of the VCS algorithm, because in this algorithm, when determining the complete stoichiometric matrix, $\mathbf{A}$ would have to be reduced anyway, and this situation is automatically handled.

10) The last difference is mentioned for information only; it did not affect the analysis of systems that consist of a multispecies gaseous phase and a number of pure condensed species. This happens because mole fractions as composition variables were used in developing the BNR and

VCS algorithms, which are the appropiate composition variables of the gaseous phase. However, in the case of solutes in electrolyte solutions, composition variables such as molarities are often used. In such cases the iterative equations in the BNR algorithms need to be rederived, whereas the changes required for the VCS algorithm are minor [Smith and Missen, 1982, pp. 147–148].

## 2.3 Major Computational Codes for Chemical Equilibrium

In this section three major current computational codes for constant-volume chemical equilibrium analysis are introduced. These are the computational codes which had been critically assessed together with the new code. (Results of the assessment are left until chapter 5.) All these three codes use the same product mixture model: a mixture of gases with pure condensates dispersed throughout; however, they use different models for the the gaseous species, the condensed species and the gaseous mixture. As a result, the codes are introduced in the order of increasing complexity of the models used.

### 2.3.1 NASA Code

The NASA code [Gordon and McBride, 1971] was developed at the NASA Lewis Research Center over a period of twenty years starting in the early fifties. It is a general purpose chemical equilibrium computational code, with applications not only limited to equilibrium computations for assigned thermodynamic states, but also to rocket performance, shock wave calculations and Chapman-Jouguet detonations. For the present study it was used to carry out constant-volume and constant-energy type of calculations.

The code was written by assuming that the gaseous products form a perfect-gas mixture and that the pure condensed species occupy no volume. (These are simple models but can provide a quick and straightforward answer to a problem, albeit an approximate one at times.) Its solution algorithm is of the nonstoichiometric type and makes use of Lagrangian multipliers when treating the conservation of mass constraint. It uses the Newton-Raphson method to solve a set of nonlinear equations.

The NASA code also has a library of polynomial coefficients, for evaluating the standard state thermodynamic properties of a numerous product species. These coefficients were obtained by curve fits to data in the third edition of the JANAF Thermochemical Tables [Chase *et al.*, 1985], which uses 0.1 MPa (1 bar) as the standard reference pressure, by using the polynomials introduced in section 2.1.11. To facilitate the discussions given in the next two chapters, it is necessary to describe the phase transition curves of the condensed phases of a product substance used in the code and the temperature range over which a condensed phase of a substance is considered the stable one of the others.

Shown in figure 2.3 is a diagram of the phase transition curve of the solid phase and liquid phase of a product substance, which is a vertical line, used by the NASA code. In the region to the left of the transition curve, the solid phase is the stable phase, and in the region to the right the liquid phase is the stable phase. The plot has been done for a lower bound in pressure of 0.1 MPa (1 bar), which is the standard reference pressure. In the NASA code, the lower limit of the temperature range over which polynomial coefficients for evaluating thermodynamic properties of the condensed phases at 0.1 MPa are given is 300 K, and the upper limit is usually 5000 K. This is why the pressure axis together with a vertical line drawn at 5000 K have been used to indicate the left and the right boundary of the stable region of the solid and liquid phases, respectively.

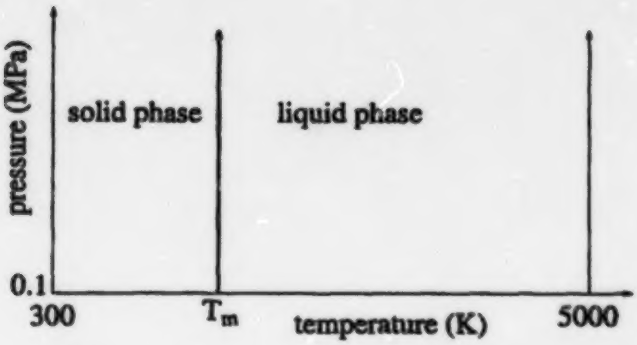

Figure 2.3: The phase transition curve of the solid phase and liquid phase of a product substance and the regions in which one of these two phases is the stable phase as modelled in the NASA code.

At the melting temperature $T_m$ at 0.1 MPa, the chemical potentials of the solid phase and the liquid phase are equal. However, because a zero molar volume is assumed for these phases, their chemical potentials become pressure independent and are equal to their standard state values at 0.1 MPa (compare equations 2.45 and 2.46). Consequently, their transition curve is a vertical line; that is $T_m$ is their melting temperature for all pressures.

Only one solid phase has been shown in figure 2.3. For a substance which has more than one solid phase, each of the transition curve of two neighbouring solid phases is also a vertical line. Finally, the stable regions referred to here are with respect to the other condensed phases, nothing has been said with respect to the gas phase. The limit of 5000 K may also seem to be unrealistic in many cases. Hence, it should really have been said that in the high-temperature region the liquid phase is only considered, or modelled, to be stable with respect to the solid phase(s).

### 2.3.2 Bagheera Code

The Bagheera code was developed at the Le Bouchet Research Center of the SNPE Group in France over a period of about a decade, starting at the beginning of the eighties or in the late seventies. Since 1991 to 1992 it has been the NATO standard code for analysing the thermodynamic properties of military propellants. It can only perform constant-volume and constant-energy type of calculations.

The solution method of the Bagheera code is similar to that of the NASA code. It is of the nonstoichiometric type and makes use of Lagrangian multipliers to incorporate the mass conservation constraint. It also uses the Newton-Raphson method to solve a set of nonlinear equations.

The programming logic of the Bagheera code also bears a strong resemblance to that of the NASA code. (Some of the variable and subroutine names in the former are even the same as those in the latter.) In addition, the library of polynomial coefficients for evaluating species thermodynamic properties for the Bagheera code is essentially that of the NASA code.

The Bagheera code is different from the NASA code in that for the Bagheera code the gaseous species are assumed to follow a modified virial equation of state—while the gaseous mixture itself is still modelled as an ideal mixture—and the condensates are assumed to have a finite, constant molar volume. (The Bagheera code does provide the option to use the perfect gas equation of state for the gases.) Because the Bagheera and the NASA codes used different models for the species, the resulting nonlinear equations of the two codes are also different.

The modified virial equation of state used in the Bagheera code is volume explicit and given by

$$v = \frac{RT}{p} + \frac{\beta_1}{1+\alpha_1 p} - \frac{\beta_2}{1+\alpha_2 p}. \tag{2.180}$$

The parameters $\beta_1$, $\beta_2$, $\alpha_1$ and $\alpha_2$ are defined in terms of the second and third virial coefficients $B$ and $C$ which are obtained by assuming the Lennard-Jones (6-12) potential [Hirschfelder, Curtiss and Bird, 1954, pp. 162–173, p. 1119] and

$$\beta_1 = \text{positive part of } B = 1.733001b(T^*)^{-1/4}, \qquad \beta_2 = \beta_1 - B,$$

$$\alpha_1 = \frac{{\beta_2}^2 + B^2 - C}{\beta_1 RT}, \qquad \text{and} \qquad \alpha_2 = \frac{\beta_2}{RT}. \tag{2.181}$$

Because so many things are in common between the Bagheera and NASA codes, one may expect that the model used for the transition curve(s) of the condensed phases of a substance in the Bagheera code would be similar to that used in the NASA code. As a matter of fact, the same model is used, vertical line(s)—even though constant molar volume as opposed to zero molar volume condensates has been assumed in the Bagheera code. This is because in the Bagheera code, in addition to assuming the condensates are having finite, constant molar volume, condensed phases of a substance are assumed to have the same density, or molar volume. (In the Bagheera code, a density value of 2 gm/cm$^3$ is assigned to the condensed phases of any substance for which density data are not available.)

As an example, consider the case of the transition curve of melting of the solid phase and the liquid phase of a substance. At the melting temperature $T_m$ at 0.1 MPa, the chemical potentials of the two phases are equal. Since the same molar volume has been assumed for both phases, according to equation 2.46, the changes in their chemical potentials as a function of pressure above 0.1 MPa at $T_m$ are the same. That is their chemical potentials would be the same at all pressures, which implies the phase transition curve is a vertical line.

### 2.3.3 Blake Code

The Blake code [Freedman, 1982] was the previous NATO standard code for military propellant thermodynamic properties analysis. It was adapted from the Tiger code [Cowperthwaite and Zwisler, 1974], which was first developed during 1966 to 1968 at the Ballistic Research Laboratory of the US Army Armament Research and Development Command. The adaptation is believed to have started in the later part of the sixties or early seventies; however, the user guide, which is the only documentation on the Blake code, was published in 1982.

Applications of the Blake code involve only calculations for assigned thermodynamic states. For the present study, the code was used to carry out calculations for combustions at constant volume and energy. Furthermore, the Blake code uses the most general models for the gaseous mixture and the species themselves. The gases are not only assumed to be imperfect gases, they are also assumed to form a nonideal mixture; in addition, the condensates are assumed to have finite, variable molar volume.

There is a choice of four equations of state in the Blake code for describing the $P$-$v$-$T$ properties of the gaseous mixture: the perfect gas, the truncated virial, the Becker-Kistiakowsky-Wilson (BKW) and the Powell-Wilmot-Haar-Klein (PWHK) [1979] equations of state. (When the perfect gas equation of state is used, it is equivalent to modelling the gaseous mixture as a perfect-gas mixture, which is a specific case of the general nonideal mixture.) For the present study, calculations were performed only by using the truncated virial equation of state. Furthermore, in the Blake code the polynomial type, empirical equation of state discussed in section 2.1.12 is used for describing the $P$-$v$-$T$ properties of the condensates.

The classification of the solution algorithm of the Blake code, or the Tiger code for that matter, is not so well defined; the algorithm does use component species, but not in the sense of using chemical stoichiometry, and it does not use extent-of-reactions as independent variables. The algorithm uses a set of independent variables, the number of which is always the number of elements in the system (which would normally be the number of Lagrangian multipliers) plus two. The foundation of this algorithm was laid by Dr. S. R. Brinkley, and Smith and Missen [1982, p. 140] classified the Brinkley algorithm as a nonstoichiometric algorithm. This is the classification followed in this report for the Blake code. The set of nonlinear equations in the independent variables is also solved by using the Newton-Raphson method.

The Blake code uses a set of functions for the evaluation of standard species thermodynamic properties different from that used by the NASA and Bagheera codes, which is given as follows:

$$\frac{c_p^0}{R} = b_1 + b_2\theta + b_3\theta^2 + b_4\theta^3 + \frac{b_5}{\theta} + \frac{b_6}{\theta^2} + \frac{b_7}{\theta^3}, \tag{2.182}$$

$$\frac{h^0}{RT} = b_1 + \frac{b_2}{2}\theta + \frac{b_3}{3}\theta^2 + \frac{b_4}{4}\theta^3 + \frac{b_5\ln(\theta)}{\theta} - \frac{b_6}{\theta^2} - \frac{b_7}{2\theta^3} + \frac{b_8}{RT}, \tag{2.183}$$

and

$$\frac{s^0}{R} = b_1\ln(\theta) + b_2\theta + \frac{b_3}{2}\theta^2 + \frac{b_4}{3}\theta^3 - \frac{b_5}{\theta} - \frac{b_6}{2\theta^2} - \frac{b_7}{3\theta^3} + \frac{b_9}{R}, \tag{2.184}$$

where

$$\theta = T/1000.$$

The constants $b_1$ to $b_7$ were obtained most likely by using a least-squares fit to standard species heat capacity data (i.e, $c_p^0$ versus $T$) from the second edition of the JANAF Thermochemical Tables [Stull and Prophet, 1971], which uses one atmosphere as the standard reference pressure. The additional coefficients $b_8$ and $b_9$ stem from the integration $\int c_p^0\,\mathrm{d}T$ to give $h^0$ and the integration $\int (c_p^0/T)\,\mathrm{d}T$ to give $s^0$, respectively, in conjunction with matches to tabulated data for $h^0$ and $s^0$ at some reference temperature. The library of coefficients of the Blake code is much more limited than those of the NASA and Bagheera codes, both in terms of the number of product species and the number of elements involved.

In the Blake code, if a substance is assumed to have any solid phases, meaning that if the curve-fit coefficients are provided in the library, it is assumed to have only one. As shown in figure 2.4, the model of the transition curve of the solid phase and liquid phase of a substance is more realistic in this case. The transition curve is determined by making use of the curve-fit coefficients of both phases, which are assumed in both cases to be valid from 100 to 10,000 K. Beginning at the melting temperature $T_m$ at a presure of 1 atm (the standard reference pressure for which the thermodynamic data gave the least-squares curve fits), the transition curve is not only sloped but also curved. This occurs because the molar volume of the two phases are assumed different. Hence, for different temperatures the pressures are different at which the chemical potentials of the two phases become equal.

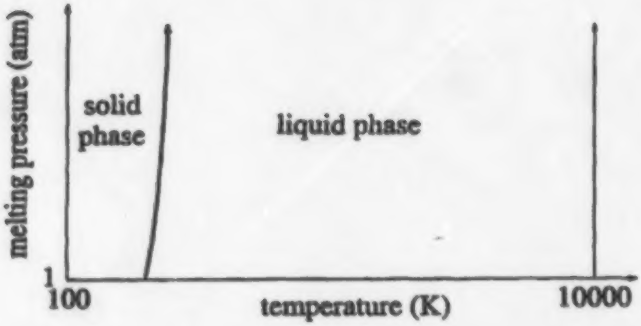

Figure 2.4: The phase transition curve of the solid phase and the liquid phase of a product substance as modelled in the Blake code.

### 2.3.4 Potential Numerical Difficulties

The potential difficulties of a singular coefficient matrix of the BNR algorithms for constant temperature and pressure problems had been described in section 2.2.4. These algorithms were developed by assuming a product mixture modelled as a perfect-gas mixture together with zero molar volume condensates. For the present study, constant-volume and constant-energy type of problems were considered. And while the NASA code retains the same models used for the gaseous mixture and the condensates, the Bagheera code and the Blake code assume more general ones. However, the solution formulations for all three codes are all of the nonstoichiometric type and require matrix inversions. Hence, it was expected that these codes might encounter singularity problems and probably would have difficulties in obtaining a solution for systems involving many condensed species. Some of the difficulties encountered will be addressed in chapter 5, in which the results of assessment of these three codes and the new code are presented.

# Chapter 3

# Adaptation of VCS Algorithm

The combustion of energetic materials was assumed to take place at constant volume in the development of the new chemical equilibrium computational code. Furthermore, heat losses to the surroundings were neglected and the total energy of the products was assumed equal to that of the reactants. Consequently, the chemical equilibrium problem was studied with the thermodynamic state constraints of constant energy and volume. However, the VCS algorithm was developed for systems with a constant temperature and pressure as state constraints. To apply this algorithm to a constant-volume and constant-energy system, some changes were needed. Such adaptations are described in this chapter. Some of these changes were due solely to this new set of thermodynamic constraints, some are more of the consequence of this new set of constraints, and some simply result from the possibility of using different models for the gaseous mixture and product species. A description of the VCS algorithm and its working equations are given, and then the changes are described.

## 3.1 Basic VCS Algorithm for a Given Temperature and Pressure

Because the VCS algorithm eliminates the need for matrix inversion and handles the nonnegativity constraint for condensed species straightforwardly, it is particularly well suited for solving chemical equilibrium problems involving many pure condensed phases [Smith and Missen, 1982, p. 144]. This algorithm was developed for ideal systems at constant temperature and pressure; however, for this study, it was applied to both ideal and nonideal systems at constant volume and internal energy.

The VCS algorithm uses the stoichiometric formulation given by equations 2.40 and 2.41 and is named after several workers (Villars, 1959, 1960; Cruise, 1964; Smith and Missen, 1968) who contributed to the development. It is intermediate between a first- and second-order method. In the following description the possibility of the presence of inert species in the multispecies phases of a system is allowed. In this case, the complete stoichiometric matrix $\mathbf{N}$ is formed only among the noninert species. If $N'$ is the total number of noninert species in a system, then $R = N' - M$ is the number of reaction-extent parameters that can be defined for the system, which are the number of elements in the vectors $\delta\mathbf{n}$ and $\delta\boldsymbol{\xi}$.

In its final form the algorithm uses the second variation method for solving the unconstrained minimization problem, which involves finding the minimum of the quadratic approximation to the system Gibbs state function at the current estimate of the equilibrium composition. The quadratic approximation is obtained by a Taylor-series expansion of the system Gibbs state function as a function of the reaction extent parameters and with terms higher than the second order neglected, which can be written as

$$\delta G = \left.\frac{\partial G}{\partial \xi}\right|^{T}_{\mathbf{n}^{(m)}} \delta\xi + \frac{1}{2}\,\delta\xi^{T} \left.\frac{\partial^2 G}{\partial \xi^2}\right|_{\mathbf{n}^{(m)}} \delta\xi, \tag{3.1}$$

where $\delta G$ is the change in $G$, $\partial G/\partial\xi$ and $\delta\xi$ are column vectors whose $j$ elements ($j$ equals 1 to $R$) are the partial derivative $\partial G/\partial\xi_j$ and the change in $\xi_j$, respectively, the subscript $\mathbf{n}^{(m)}$ indicates that the entity on the left is evaluated at the current estimate of the equilibrium composition, and the superscript $T$ denotes the transpose of a vector. In addition, $\partial^2 G/\partial\xi^2$ is the Hessian matrix whose $j^{\text{th}}$ element in the $i^{\text{th}}$ row is the double partial derivative $\partial^2 G/\partial\xi_i\partial\xi_j$, and both $i$ and $j$ can assume values from 1 to $R$. Finally, all changes are with respect to current values.

The amounts of reaction extents that must be adjusted to reach the minimum $\delta G$ are obtained through the first-order necessary conditions and given as

$$\delta\xi^{(m)} = -\left.\frac{\partial^2 G}{\partial \xi^2}\right|^{-1}_{\mathbf{n}^{(m)}} \left.\frac{\partial G}{\partial \xi}\right|_{\mathbf{n}^{(m)}}, \tag{3.2}$$

where $m$ ($\geq 1$) is the iteration-step index and the superscript $-1$ denotes an inverse. The corresponding adjustments in mole numbers, $\delta\mathbf{n}^{(m)}$, are obtained from equation 2.179. Once the new estimate of the equilibrium composition is obtained the process is repeated until convergence is achieved.

For a single multispecies phase, such as a gaseous mixture, the elements of the Hessian matrix can first be written as

$$\frac{\partial^2 G}{\partial\xi_i\partial\xi_j} = \frac{\partial}{\partial\xi_j}\left(\sum_{k=1}^{N'} \nu_{k_i}\mu_k\right) \quad \text{with} \quad i,j = 1,2,\ldots,R, \tag{3.3}$$

and $N'$ is the total number of species in the phase. Equation 3.3 is obtained by applying the chain rule of differentiation, since $G$ is a function of the species mole numbers which in turn are dependent on $\xi_i$, and by using equations 2.15 and 2.35. Assuming an ideal solution, equation 2.62 applies. When similarly applying the chain rule for differentiating $\mu_k$ with respect to $\xi_j$ and using of equation 2.62, the right-hand side of equation 3.3 becomes

$$RT\sum_{k=1}^{N'}\sum_{l=1}^{N'} \nu_{k_i}\nu_{l_j}\left(\frac{\delta_{kl}}{n_k} - \frac{1}{n_t}\right), \tag{3.4}$$

where $\delta_{kl}$ is the Kronecker delta which equal to unity when $k$ and $l$ have the same value and equals zero when $k$ and $l$ are different. Further simplification yields

$$\frac{1}{RT}\frac{\partial^2 G}{\partial\xi_i\partial\xi_j} = \sum_{k=1}^{N'}\frac{\nu_{k_i}\nu_{k_j}}{n_k} - \frac{\bar{\nu}_i\bar{\nu}_j}{n_t} \quad \text{with} \quad i,j = 1,2,\ldots,R, \tag{3.5}$$

where

$$\bar{\nu}_i = \sum_{k=1}^{N'}\nu_{k_i} \quad \text{and} \quad \bar{\nu}_j = \sum_{k=1}^{N'}\nu_{k_j}. \tag{3.6}$$

Since the choice of $\mathbf{N}$ is arbitrary, this can be effected so that the inversion of the Hessian matrix is avoided. Firstly, if $\mathbf{N}$ is chosen to be in the canonical form, for a noncomponent species, the product $\nu_{k_i}\nu_{k_j}$ is equal to one when $i$ equals $j$, otherwise it is equal to zero, since each noncomponent species has a stoichiometric coefficient of value unity only in one stoichiometric vector and zero in the others. Therefore, when the component species are numbered from 1 to $M$ and the noncomponent species from $M+1$ to $N$, the elements of the Hessian matrix become

$$\frac{1}{RT}\frac{\partial^2 G}{\partial\xi_i\partial\xi_j} = \frac{\delta_{ij}}{n_{j+M}} + \sum_{k=1}^{M}\frac{\nu_{ki}\nu_{kj}}{n_k} - \frac{\bar{\nu}_i\bar{\nu}_j}{n_t}; \quad \text{with} \quad i,j = 1,2,\ldots,R, \tag{3.7}$$

where only the diagonal elements will have the first term on the right-hand side.

Secondly, if the component species are chosen to be the most abundant species, the second term on the right-hand side of equation 3.7 tends to be small compare to the first, because $n_k$ are larger than $n_{j+M}$. The last term will also generally be small, because of the presence of the term $n_t$ in the denominator; it may even vanish if either $\bar{\nu}_i$ or $\bar{\nu}_j$ equals zero.

When **N** is formed meeting the above two requirements, the Hessian matrix will become diagonally dominant. Finally, if the off-diagonal terms are neglected, it can be approximated as being diagonal and be inverted directly to give

$$\frac{\partial^2 G}{\partial\xi^2}^{-1} \approx \left[\frac{1}{RT}\left(\frac{1}{n_{i+M}} + \sum_{k=1}^{M}\frac{\nu_{ki}^2}{n_k} - \frac{\bar{\nu}_i^2}{n_t}\right)^{-1}\delta_{ij}\right] \quad \text{with} \quad i,j = 1,2,\ldots,R. \tag{3.8}$$

At the end of each iteration step, the new species mole numbers are examined to ensure that the component species remain to be the most abundant species. If this is untrue, a new set of component species is selected and a new stoichiometric matrix is formed before carrying out the next iteration step.

With the inversion of the Hessian matrix eliminated, equation 3.2 can be rewritten giving straightforwardly corrections to the reaction extent parameters as

$$\delta\xi_j^{(m)} = -\left(\frac{1}{n_{j+M}^{(m)}} + \sum_{k=1}^{M}\frac{\nu_{kj}^2}{n_k^{(m)}} - \frac{\bar{\nu}_j^2}{n_t^{(m)}}\right)^{-1}\frac{\Delta G_j^{(m)}}{RT} \quad \text{with} \quad j = 1,2,\ldots,R, \tag{3.9}$$

where the superscript $-1$ now stands for the reciprocal of a scalar quantity and

$$\Delta G_j^{(m)} = \left.\frac{\partial G}{\partial\xi_j}\right|_{\mathbf{n}^{(m)}} = \sum_{i=1}^{N'}\nu_{ij}\mu_i^{(m)}. \tag{3.10}$$

For systems involving an ideal multispecies phase plus a number of single-species phases, equation 3.9 has a slightly different form. In its final form for a system consists of an ideal gaseous mixture and a number of pure condensed species, equation 3.9 becomes

$$\delta\xi_j^{(m)} = -\left[\frac{\delta_{j+M}}{n_{j+M}^{(m)}} + \sum_{k=1}^{M}\frac{\nu_{kj}^2\delta_k}{n_k^{(m)}} - \frac{(\sum_{k=1}^{N'}\nu_{kj}\delta_k)^2}{n_{tg}^{(m)}}\right]^{-1}\frac{\Delta G_j^{(m)}}{RT}, \quad \text{with} \quad j = 1,2,\ldots,R, \tag{3.11}$$

where $\delta_{j+M}$ is unity if the $(j+M)^{\text{th}}$ species is a gaseous species and is zero if it is a condensed species, the same conditions apply to $\delta_k$, and $n_{tg}^{(m)}$ is the total number of moles of gases in the gaseous phase. This is the equation used in the present code for determining the corrections to the reaction extent parameters.

After $\delta\xi_j$ have been determined, changes to species abundances are obtained from equation 2.179. However, such changes are modified twice before they are applied [Smith and Missen, 1967, 1968]. The first modification is to take into consideration the nonnegativity constraint, which is handled by multiplying the changes to the species abundances obtained from equation 2.179 by a scaling parameter, $\kappa$, such that

$$\delta\mathbf{n} = \kappa \mathbf{N}\,\delta\xi \quad \text{with} \quad 0 < \kappa \leq 1\,, \tag{3.12}$$

and all $n_i$ are kept greater than zero. Because the exact procedure for the determination of $\kappa$ was not stated in the original papers by Smith and Missen [1967, 1968], the author's procedure described below is implemented in the new code.

The value of $\kappa$ is determined by first finding the maximum of the ratios

$$-\frac{\delta n_i}{x_i} \quad \text{for} \quad i = 1, 2, \ldots, N'$$

for positive $x_i$. If the maximum ratio is greater than or equal to unity, it identifies a limiting case for which the amount of a species is reduced to zero, when changes determined by equation 2.179 are applied and while the abundances of all other species stay positive. To avoid such a case, $\kappa$ is set equal to 0.99 divided by the maximum ratio. However, if the maximum ratio is less than one, then no species has an amount that is reduced to zero. Then, $\kappa$ is set equal to one, and full corrections obtained from equation 2.179 are applied.

The second modification is due to the application of a convergence forcer, which in essence is a one-dimensional minimization of the system Gibbs state function in the direction defined by the vector $\delta\mathbf{n}$ given by equation 3.12. Denoting this vector as $\delta\mathbf{n}'$ instead, then the actual corrections at each iteration step are given as

$$\delta\mathbf{n} = \lambda\delta\mathbf{n}' \quad \text{with} \quad 0 < \lambda \leq 1, \tag{3.13}$$

and the system Gibbs state function $G$ has become a function of $\lambda$. The $\lambda$ value is chosen such that the minimum of $G$ has not been passed or the minimum is obtained. To accomplish this, the value of the directional derivative of $G$ with respect to $\lambda$, $\mathrm{d}G/\mathrm{d}\lambda$, is checked. We write

$$\frac{\mathrm{d}G}{\mathrm{d}\lambda} = \frac{\partial G}{\partial \mathbf{n}}^T \delta\mathbf{n}' = \boldsymbol{\mu}^T \delta\mathbf{n}', \tag{3.14}$$

by noting that $G$ depends on the species mole numbers which in turn depend on $\lambda$, where $\boldsymbol{\mu}$ is evaluated at the adjusted mole numbers determined by $\lambda$, that is at $\mathbf{n}$ equal to $\mathbf{n}^{(m)} + \lambda\delta\mathbf{n}'$.

At first $\partial G/\partial\lambda$ is evaluated for $\lambda$ equals to one, that is a full correction as given by $\delta\mathbf{n}'$ is applied. If $\partial G/\partial\lambda$ is nonpositive, the corrections are accepted and iterations continue. If $\partial G/\partial\lambda$ is positive, then $\lambda$ is determined by assuming $G$ is a parabolic function of $\lambda$ and giving a zero value to $\partial G/\partial\lambda$; hence,

$$\lambda = \frac{\left.\dfrac{\mathrm{d}G}{\mathrm{d}\lambda}\right|_{\lambda=0}}{\left.\dfrac{\mathrm{d}G}{\mathrm{d}\lambda}\right|_{\lambda=0} - \left.\dfrac{\mathrm{d}G}{\mathrm{d}\lambda}\right|_{\lambda=1}}. \tag{3.15}$$

The zero gradient criterion is for finding the minimum to the parabolic $G$, which is an approximation to that of the true $G$. Species mole numbers are then readjusted based on this value of $\lambda$ and iterations continue.

## 3.2 Treatment of Condensed Species

Through the application of two procedures, the VCS algorithm can consider practically as many condensed species as required. The first procedure is for handling the nonnegativity constraint for noncomponent condensed species. (Condensed species which are component species cannot have zero molar amounts; otherwise they would not have been chosen as components in the first place.) The Kuhn-Tucker condition for the stoichiometric formulation for a noncomponent condensed species being absent at equilibrium is used to determine the deletion or introduction of such a species from or into the main calculation [Smith and Missen, 1982, p. 208]. This condition is similar to equation 2.38 and is given as

$$\frac{\partial G}{\partial n_i} \equiv \frac{\partial G}{\partial \xi_j} = \mu_i^{\circ} + \sum_{k=1}^{M} \nu_{kj}\mu_k \geq 0 \quad \text{if} \quad n_i = 0, \tag{3.16}$$

where $i$ equal to $j + M$. Equation 3.16 is based on N being expressed in the canonical form. $\mu_i^{\circ}$ is the standard chemical potential of the pure condensed species, which is independent of the composition of the product mixture. The quantity on the right is also recognized to be the free energy change across the $j^{\text{th}}$ reaction denoted as $\Delta G_j$. The first two terms are identical because the stoichiometric coefficient of a noncomponent species is unity. This condition implies that if the value of the system Gibbs state function will decrease with the addition of an infinitesimal amount of a condensed species (i.e., $\Delta G_j$ is negative) that is absent, the species will form. Therefore, the sign of $\Delta G_j$ is checked for determining whether such a condensed species should be introduced into the main calculation.

During the course of a calculation, when the adjusted mole number (based on equation 2.179) of a noncomponent condensed species present in minute amount becomes negative at an iteration step, it is set to zero. At a subsequent step the sign of $\Delta G_j$, $j = i - M$ (based on the reaction for this species) is examined. Should $\Delta G_j$ becomes negative, the species is reintroduced in the calculation. Therefore, the pure condensed species readily enter or exit the main calculation during iterations.

In the new code, a noncomponent condensed species is considered present in minute amount if its molar abundance is less than one thousandth (0.1%) of that of its least abundant forming components. This criterion prevents premature deletion of a condensed species. Checking on the deletion of trace condensed species is done after the reaction-parameter changes are first obtained. If there is any species that needed to be deleted, the corresponding reactions forming these trace species are adjusted first. Instead of using the original values determined, the changes in the reaction parameters of these reactions are taken to be the negative of the abundances of the trace species, so that their application would reduce the amounts of the trace species to zero. After these new reaction-parameter changes have been applied to adjust the corresponding reactions, they are set to zero (no more adjustments to the trace condensed-species-forming reactions), and the remainder of the reactions are then adjusted by equations 3.12 and 3.13.

The second procedure is for handling reactions which involve pure condensed species only [Cruise, 1964]. These cases occur occasionally when many condensed species are considered together. They may involve species of different substances, but they may also involve, for example, only the solid phase and the liquid phase of the same substance, at conditions other than the melting conditions of the substance. (The special case of melting is discussed in section 3.11.) These are situations of phase-rule violations. When such a reaction arises, at least one of the species in the reaction must not be present and should be deleted. Hence, the reaction is adjusted by an amount $\delta\xi_j$ which takes the sign of $-\Delta G_j$ and has a magnitude which reduces the amount of the limiting species to zero. That is

$$\delta\xi_j = \mathrm{sign}(-\Delta G_j) \cdot \mathrm{minimum}\left[\frac{n_j, n_1}{|\nu_{1j}|}, \ldots, \frac{n_k}{|\nu_{kj}|}, \ldots, \frac{n_M}{|\nu_{Mj}|}\right], \tag{3.17}$$

where $n_j$ is the mole number of the $j^{\text{th}}$ noncomponent species, $n_1$ to $n_M$ are the mole numbers of the component species and $|\nu_{1j}|$ to $|\nu_{Mj}|$ are the absolute values of the stoichiometric coefficients of the component species for this $j^{\text{th}}$ reaction. In this way a phase is deleted and a degree of freedom is gained. With this phase-deletion procedure included, the case when only pure condensed species exists in the product mixture and no gaseous phase is postulated can also be treated. This is a linear programming problem that cannot be handled by the BNR algorithms, as noted before.

## 3.3 Inclusion of Thermodynamic Data and Selection of Condensed Species

For the present study, a comparison between the new code and the three major previous computational codes was performed. In order to have valid comparisons, when comparing with the current codes, the same models of the gaseous mixture and the condensed species as used in the current codes were used in the new code. In addition, the same libraries of coefficients for the evaluation of thermodynamic properties at standard reference pressure were used. These properties are for the evaluation of standard chemical potentials as a function of temperature.

The curve-fit functions employed to obtain the curve-fit coefficients given in the NASA library had already been presented in section 2.1.11; they are repeated below:

$$\frac{c_p^0}{R} = a_1 + a_2T + a_3T^2 + a_4T^3 + a_5T^4, \tag{3.18}$$

$$\frac{h^0}{RT} = a_1 + \frac{a_2}{2}T + \frac{a_3}{3}T^2 + \frac{a_4}{4}T^3 + \frac{a_5}{5}T^4 + \frac{b_1}{T}, \tag{3.19}$$

and

$$\frac{s^0}{R} = a_1\ln(T) + a_2T + \frac{a_3}{2}T^2 + \frac{a_4}{3}T^3 + \frac{a_5}{4}T^4 + b_2. \tag{3.20}$$

Two sets of seven coefficients, that is $a_1$ to $a_5$ and $b_1$ and $b_2$, are given in the library for each product species. The first set is for the evaluation of thermodynamic properties above 1000 K, and the second set is for properties below 1000 K. Curve fits were obtained such that there is continuity in the properties between the two sets of curve-fit coefficients at 1000 K.

In addition, associated with the curve-fit coefficients of each product species is a specific temperature range. For the gaseous phase of a substance the range is always from 300 to 5000 K. For the condensed phases the temperature ranges correspond to the ranges over which the solid and liquid phases are considered to be stable, and a condensed phase can be selected for consideration only if the trial temperature is within this stable range of the phase. If the substance has only one solid phase and a liquid phase, the temperature range of the solid phase is from 300 K to the melting temperature of the substance. The range for the liquid phase is usually from the melting temperature to 5000 K. However, the upper limit for the liquid phase can be below 5000 K, occasionally. If the substance has more than one solid phase, the ranges for these solid phases are set by their transition temperatures. There are also some cases when coefficients of only the

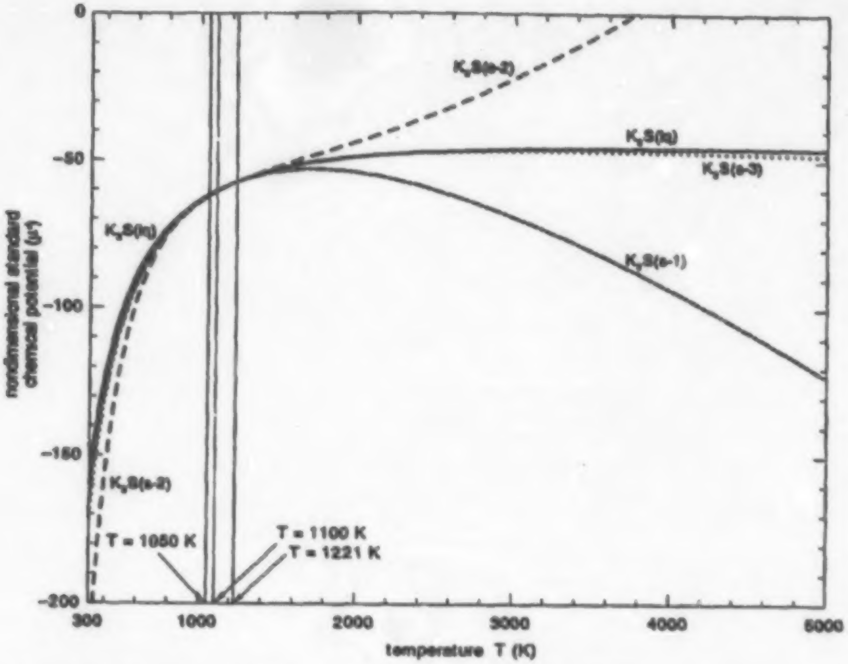

Figure 3.1: Nondimensional standard chemical potentials at 1 bar of the four condensed phases of $K_2S$, determined by using their polynomial coefficients for evaluating thermodynamic properties given in the NASA code, as a function of temperature from 300 to 5000 K.

solid or the liquid phase of a substance are listed. For such cases usually the upper limit of the temperature range is much lower than 5000 K.

Shown in figure 3.1 is a plot of the nondimensional standard chemical potentials of the four condensed phases of $K_2S$ from 300 to 5000 K, evaluated by making use of their polynomial coefficients given in the NASA library. A small scale has been used for the chemical potential in order to show some of the small differences in this property of the phases. Vertical lines have also been added at the transition temperatures of the phases to help to identify the stable range of each phase. Transitions from $K_2S(s\text{-}1)$[1] to $K_2S(s\text{-}2)$, from $K_2S(s\text{-}2)$ to $K_2S(s\text{-}3)$, and from $K_2S(s\text{-}3)$ to $K_2S(lq)$, occur at 1050, 1100 and 1221 K, respectively. Hence, below 1050 K, $K_2S(s\text{-}1)$ should have the lowest chemical potential of the four. However, both $K_2S(s\text{-}2)$ and $K_2S(s\text{-}3)$ have lower chemical potentials. On the other hand, above 1221 K, $K_2S(lq)$ should have the lowest chemical potential, but this is not true either. Its chemical potential is only below that of $K_2S(s\text{-}2)$.

The details in the regions from 1050 to 1100 K and from 1100 to 1221 K are shown in figure 3.2. In the former, $K_2S(s\text{-}2)$ should have the lowest chemical potential. While it is clear

---

[1] The convention for substance names and identification used herein differs somewhat but is similar to that used in the NASA code. in this report '(lq)' denotes the condensed liquid phase—in contrast to '(l)' in the NASA code, '(s)' denotes the condensed solid phase—when there is only one phase, and '(s-1)', '(s-2)', '(s-α)', etc., denote condensed solid phases of different types when more than one type can occur, in contrast to using only '(1)', '(2)', '(α)', etc , in the NASA code.

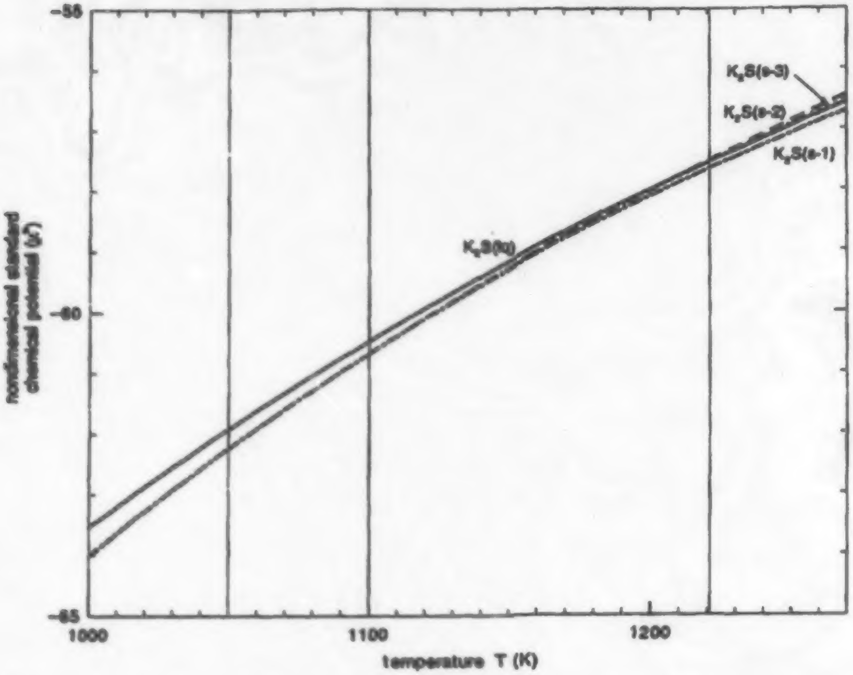

Figure 3.2: Nondimensional standard chemical potentials at 1 bar of the four condensed phases of $K_2S$, determined by using their polynomial coefficients for evaluating thermodynamic properties given in the NASA code, as a function of temperature from 1000 to 1270 K.

that $K_2S$(s-2) has lower chemical potential than $K_2S$(lq), it appears that $K_2S$(s-1), $K_2S$(s-2), and $K_2S$(s-3) have the same potentials. Actually, based on numerical results, $K_2S$(s-2) has a higher chemical potential than $K_2S$(s-1); on the other hand, the potential of $K_2S$(s-2) is lower than that of $K_2S$(s-3), except towards the end of the region where the reverse becomes true. From 1100 to 1221 K the chemical potential of $K_2S$(s-3) is always lower than those of $K_2S$(s-2) and $K_2S$(lq) but higher than that of $K_2S$(s-1). $K_2S$ has been used as an example here, similar inconsistencies has been observed for condensed phases of other substances. The inconsistencies arise because the polynomial coefficients were obtained by curve fitting available data (largely in the stable region) of the phases and they are not well suited for extrapolation outside the range.

The VCS algorithm is capable of considering more than one condensed phase of a substance simultaneously. Referring to the above example of $K_2S$, had the chemical potential data been consistent, calculations can be done at any temperature between 300 and 5000 K and involving all of the four phases. The phase which is the stable phase at the trial temperature under consideration should have the lowest value in chemical potential and will be retained while the other three will be deleted. However, because of the inconsistencies in the data, a straightforward inclusion of all four phases would lead to erroneous results. In any case, for comparison purposes, in the new code only stable phases at the trial temperature would be chosen for consideration, as in the NASA code. What has been pointed out is the inconsistency of the chemical potential data, nothing has been said regarding their correctness. The ability of the coefficients in reproducing the original data will be discussed in chapter 5.

Atmosphere is the unit of pressure used in the NASA code; hence, the standard state pressure should be chosen to be one atmosphere (see section 2.1.10). Furthermore, tje thermodynamic properties used for curve fits of polynomials should be the properties at this pressure. Coefficients in an earlier version of the NASA library were obtained based on thermodynamic properties given in the second edition of the JANAF Thermochemical Tables [1979] which uses one atmosphere as the standard state pressure. However, coefficients in the current NASA library were obtained based on more recent thermodynamic properties given in the third edition of the JANAF Thermochemical Tables [Chase *et al.*, 1985] which is the SI edition and has chosen one bar (0.1 MPa) as the standard state pressure. In essence, in the NASA code when the standard state pressure was switched from one atmosphere to one bar, the unit of pressure in general was unfortunately left unchanged at one atmosphere.

In the NASA code, a perfect-gas mixture is assumed for the product mixture. The chemical potential of a gaseous species in a perfect-gas mixture is given by equation 2.48. The effect of changing the pressure unit from atmosphere to bar will introduce a small difference in the logarithm of pressure term, that is ln(1.01325). This difference is usually small in comparison to the standard chemical potential of the species. (Chemical potentials of condensed species considered in the NASA code only have the standard chemical potential parts.) Furthermore, this difference is applicable to all the gaseous species in the mixture. However, the overall effect of this change in pressure unit on the equilibrium composition of the product mixture is believed to be small. For comparison purposes, the unit of atmosphere is kept in the new code.

The Bagheera code uses the same polynomials used by the NASA code for the evaluation of species thermodynamic properties. In addition, the Bagheera library of polynomial coefficients is essentially that of the NASA code. Hence, the same procedure with regard to the selection of condensed phases for consideration followed when comparing with the NASA code was followed again when comparing with the Bagheera code.

The Blake code uses a different set of functions for the evaluation of thermodynamic properties at standard reference pressure, which are given as follows:

$$\frac{c_p^0}{R} = b_1 + b_2\theta + b_3\theta^2 + b_4\theta^3 + \frac{b_5}{\theta} + \frac{b_6}{\theta^2} + \frac{b_7}{\theta^3}, \tag{3.21}$$

$$\frac{h^0}{RT} = b_1 + \frac{b_2}{2}\theta + \frac{b_3}{3}\theta^2 + \frac{b_4}{4}\theta^3 + \frac{b_5\ln(\theta)}{\theta} - \frac{b_6}{\theta^2} - \frac{b_7}{2\theta^3} + \frac{b_8}{RT}, \tag{3.22}$$

and

$$\frac{s^0}{R} = b_1\ln(\theta) + b_2\theta + \frac{b_3}{2}\theta^2 + \frac{b_4}{3}\theta^3 - \frac{b_5}{\theta} - \frac{b_6}{2\theta^2} - \frac{b_7}{3\theta^3} + \frac{b_9}{R}, \tag{3.23}$$

where $\theta = T/1000$. It is believed that only the constants $b_1$ to $b_7$ were obtained by least-square fits to standard heat capacity data; the constants $b_8$ and $b_9$ were likely taken directly from tables and are recognized to be valid. Most of the coefficients were obtained based on the data of the second edition of the JANAF Thermochemical Tables; hence, the use of atmosphere as the unit of pressure in the code is consistent.

The evaluation of standard thermodynamic properties is quite different in the Blake code. Firstly, at most only one solid phase is assumed for a product substance. Secondly, if either the solid or the liquid phase of a product substance can be a stable phase and coefficients are given for both phases (as oppose to cases for which coefficients are given only for either the solid or the liquid phase), then both phases would be selected for consideration and their coefficients would be used for evaluating the properties of the two phases, for any temperature within the range from 100 to 10000 K. What this latter aspect implies is that which phase is more stable is determined entirely by their properties evaluated by using the coefficients. That is no selection of phases based on stable ranges is done, such as in the case of the NASA code. When comparing with the Blake code, the same species coefficients and procedure for the inclusion of both condensed phases of a product substance for consideration are used in the new code.

## 3.4 Initial Estimates

The VCS algorithm requires initial estimates of species abundances which satisfy the conservation of mass constraint. Smith and Missen [1968] also devised a systematic mean in determining a set of such initial estimates. This procedure is based on solving a linear programming problem directly related to the actual problem to be solved, obtained by neglecting the composition dependent logarithmic terms in the chemical potentials and defined as follows:

$$\text{minimize } G(\mathbf{n}) = \mathbf{n}^T \mu^*, \tag{3.24}$$

subject to the linear constraints

$$\mathbf{A}\mathbf{n} = \mathbf{b} \tag{3.25}$$

and for

$$n_i \geq 0 \quad \text{with} \quad i = 1, 2, \ldots, N'. \tag{3.26}$$

The $\mu^*$ are constant at constant temperature and pressure.

There are three possible outcomes to this linear programming problem. The first is that a solution exists with $M$ of the mole numbers being nonzero while the rest are. In this case the mole numbers of the remaining gaseous species are determined from the $M$ solution mole numbers. By using these $M$ species as components and the remaining $R(N' - M)$ species as noncomponents, a complete stoichiometric matrix in the canonical form can be formed. The mole numbers of the gaseous noncomponents are determined by firstly assuming that their forming reactions have reached equilibrium, that is by setting the $\Delta G_j$ of the corresponding reactions to zero, and by secondly retaining the mole numbers of the component species. Thus

$$n_j = n_{t_g} \exp\left(-\mu_j^* - \sum_{k=1}^{M} \nu_{kj}\mu_k\right) \tag{3.27}$$

where $j$ takes on values that fall within the range from 1 to $R$ and $n_{t_g}$ is the total number of moles of the gaseous components.

These $n_j$ are then taken to be reaction extents. Adjustments to the mole numbers of the components and the gaseous noncomponents are then made, such that the nonnegativity constraint is observed and a one-dimensional minimization is achieved, much like that for the adjustments in the main calculation. This procedure is also described in the original reference by Smith and Missen [1968] and is not repeated here. The mole numbers of the noncomponent pure condensed species are left at zero, and they are introduced into the main calculation by following the procedure described in the previous section.

The second outcome is that a solution exits but with fewer than $M$ of the mole numbers being nonzero. In this case, all the remaining gaseous species are assigned with an arbitrarily small mole number ($1\times10^{-26}$ is used in the new code), while the remaining condensed species are left at zero. This case happens infrequently. The last outcome is that no feasible solution is found. This means that the mass conservation constraint defines an impossible situation.

## 3.5 Equilibrium Iterative Procedures

In this section the iterative procedures for determining equilibrium compositions used in the new code are described. For the present study, the VCS algorithm has been applied to systems at constant internal energy and volume. While the product mixture is modelled to consist of a gaseous mixture with pure condensed species dispersed throughout, the gaseous mixture can be assumed to be an ideal mixture such as in the NASA and Bagheera codes, or a nonideal mixture such as in the Blake code. To apply the VCS algorithm, which is an ideal-system algorithm, to a nonideal mixture, the intermediate approach [Smith and Missen, 1982, p. 169] is used. This approach involves retaining the use of equation 3.11, but the chemical potentials of the gaseous species are replaced by their nonideal values.

To satisfy the constant internal energy constraint, an iteration on temperature is required. A calculation is first done for a certain trial equilibrium temperature, $T_t$. Based on the equilibrium composition found for this trial temperature, the total internal energy of the reaction products, $U_p$, is determined. If this energy does not equal to that of the reactants, $U_r$, a new temperature is chosen. A higher temperature is assumed if $U_p$ is lower than $U_r$, and a lower temperature is assumed if the reverse is true.

The equilibrium temperature is solved by first bracketing it and then applying Brent's root-finding method [Press, Flannery, Teukolsky and Vetterling, 1986, pp. 251–254]. The total internal energy of the product mixture is a monotonically increasing function of the trial equilibrium temperature and hence the difference between the total internal energy of the products and reactants, $\Delta U(= U_p - U_r)$. The equilibrium temperature can be determined by finding the root of

$$\Delta U(T_t) = 0 \tag{3.28}$$

and root bracketing is detecting a sign change in $\Delta U$. The default initial bracket used is 2300 to 2700 K. The bracket limits and, if necessary, the temperature range, 400 K in this case, can be adjusted until the root is bracketed.

The total internal energy of the product mixture consists of contributions from the gaseous mixture and the condensed species. Thus

$$U_p = U_g + U_c, \tag{3.29}$$

where $U_g$ and $U_c$ are total internal energies of the gaseous mixture and condensed species. For an ideal gaseous mixture, the internal energy of the mixture is equal to the sum of the internal energy of the individual species as pure gases at the system conditions. That is,

$$U_g = \sum_{i=1}^{N_g} n_i u_{g_i}, \tag{3.30}$$

where the summation is done for the $N_g$ gaseous species in the mixture and $u_{g_i}$ is the molar internal energy of the $i^{th}$ species, as a pure gas at system conditions. In the case of a nonideal gaseous mixture, the entire mixture is treated like a single gas. Also, the internal energy contributed by the condensed species is the sum of the internal energy of the individual species at system conditions. Hence,

$$U_c = \sum_{i=1}^{N_c} n_i u_{c_i}, \tag{3.31}$$

and the summation is done for $N_c$ condensed species in the product mixture and $u_{c_i}$ is the molar internal energy of the $i^{\text{th}}$ species, as a pure condensed species at system conditions.

The Brent method is used because it has two nice features. Firstly, it combines the sureness of the bisection method with the speed of inverse quadratic interpolation. Convergence is guaranteed provided the root is first bracketed. Secondly, the method requires only functional values and not the derivative or the form of the function, which for $\Delta U$ in this case are not readily available. The subroutines given by Press *et al.* [1986, p. 245, pp. 253–254] for root bracketing and the Brent method had been incorporated into the new code.

To satisfy the constant volume constraint, a similar iteration on pressure can be nested within the iteration on temperature. However, this is not the approach followed. The approach followed is to determine a new pressure which will satisfy the constant volume constraint at each iteration step. This is because the former approach takes more time (computations using the two approaches had been tried). In the former case, for every trial temperature, an equilibrium composition would have to be determined for each trial pressure, until the constant volume constraint is satisfied; however, in the later case only one equilibrium composition is required for every trial temperature.

The idea of the second approach was conceived based on the fact that standard chemical potentials of gaseous species in a nonideal mixture need to be re-evaluated at each iteration step. Based on equations 2.67 and 2.77 it can be seen that the standard chemical potentials of the gaseous species in an ideal mixture of gases need only be evaluated once for any given pair of trial temperature and pressure. However, because of the composition dependent characteristic of these quantities (see equation 2.82) for a nonideal mixture, they need to be re-evaluated at each iteration step. The new pressure is determined either directly or by iteration, depending on the models used for the gaseous mixture and pure condensed species. The procedures followed when comparing results from current codes are now described.

For comparison with the NASA code, when a perfect-gas mixture and zero molar-volume condensates are assumed, the new pressure at each iteration step is determined directly by applying the perfect equation of state. For comparison with the Bagheera code, when an ideal mixture of imperfect gases and constant molar-volume condensates are assumed, the volume that is supposed to be occupied by the gaseous mixture is first obtained by subtracting the volume occupied by the condensed species from the constraint volume. The new pressure is then determined iteratively so that at which the sum of the volume occupied by each gaseous species, as a pure gas at this pressure and the current trial temperature, is equal to the pre-determined volume of the mixture.

For comparison with the Blake code, when the gaseous mixture is modelled as a nonideal mixture and the condensed species are assumed compressible, the new pressure would have to be determined once again iteratively. In this case even though the entire gaseous mixture can be treated like a single gas, the new pressure cannot be evaluated directly. This is because the volume occupied by the gaseous mixture cannot be determined by a straightforward subtraction as in the previous case. The new pressure is that at the current trial temperature the sum of the volume occupied by the gaseous mixture and by each pure condensed species is equai to the constraint volume. When determining the new pressure iteratively, the Brent method is again used.

Note that for calculations done at the start for validating the new code, by using the RKS, BWRS and truncated virial equations of state for gases of the polynomial type and the simple equa-

F2

tions of state for condensates, iterative determination of the new pressure was required whenever the ideal mixture of imperfect gases model was used. This was also true in the case of the nonideal gaseous mixture model, if the presence of variable molar-volume condensates were assumed.

Once a trial equilibrium temperature has been decided, an iterative solution to an equilibrium composition can begin if no evaluation of initial estimates is needed. Other than the first trial temperature, initial estimates are evaluated for a new trial temperature only if it differs from the previous one by more than 400 K (see the next section); otherwise, results for the previous trial temperature are used as the initial estimates. At the beginning of each iteration step, a new pressure and the chemical potentials of the species are evaluated. The $\Delta G_j$ are then determined and the re-introduction of condensed species is checked.

Next is a check on reactions involving pure condensed species entirely. This includes the case involving a noncomponent condensed species being re-introduced. The case involving a noncomponent condensed species which would continue to be absent is not a problem. The phase-deletion procedure is applied to the first reaction of such a type encountered during the check which begins with the first reaction and continues consecutively through to the last reaction. A new iteration step is taken after a deletion.

If there is no reaction involving entirely pure condensed species, adjustments in the reaction extent parameters are then calculated by using equation 3.11. The deletion of noncomponent condensed species is checked next. If there is any trace noncomponent condensed species that needs to be deleted, adjustments to the corresponding reactions are done first. Adjustments to the other reactions are then performed based on equation 2.179—this also includes the re-introduction of noncomponent condensed species. Changes to species abundances are modified twice before they are applied, to take into consideration the nonnegativity constraint and to effect a one-dimensional minimization, as mentioned before.

At the end of each iteration step the convergence of the equilibrium composition is checked. The convergence criterion is based on fractional changes in mole numbers. If the absolute value of the correction in mole number divided by the new mole number, after the correction has been applied, is less than or equal to $5\times10^{-6}$ for each of the product species, convergence is deemed to have been achieved. This check is skipped for species which are absent at the end of the iteration step, which is to avoid any division by zero. (Noncomponent trace condensed species are deleted when they become less than one thousandth of its least abundant forming component. This would in general imply fractional changes in the component species greater than $5\times10^{-6}$. In addition, the deletion of trace condensed species would take place at some point during the iterations and is generally not expected to occur towards the end of the iterations, when equilibrium composition is nearly reached. Therefore, the skipping of convergence check for deleted trace condensed species is not a problem. There is another point regarding the skipping of convergence check for species which are absent at the end of an iteration step, which will be cover in the next section.)

## 3.6 Treatment of Trace Gaseous Species

During the course of iterations, many of the gaseous species would often tend to exist in very trace amounts, such as below the order of $10^{-20}$ kg-mole/kg-mixture.[2] Corrections to these trace gaseous species would be very small because of the nonnegativity constraint, which will limit the corrections to the other more abundant species and slow down the convergence of the iterations. Smith and

---

[2] The unit kg-mixture means kilogram of product mixture

Missen [1982, pp. 217–218] indicated that they removed these species from the main calculation and adjusted their abundances separately. A simpler procedure is used in the new code.

In the new code, the procedure proposed by Smith and Missen is used to determine initial estimates of the equilibrium mole numbers for a trial equilibrium temperature, but with a modification to include the handling of trace gaseous species: the noncomponent gaseous species whose estimated amounts given by equation 3.27 that are below a pre-defined lower limit are not considered from the outset; deletion and introduction of trace gaseous species are done only after convergence of the main calculation occurs.

After the first convergence is achieved, all gaseous species whose molar amounts fell below the pre-defined lower limit are deleted. Otherwise, those gaseous species that have been left out at the beginning, but whose estimated amounts based on the converged mole numbers are now above or equal to the lower limit are introduced. (The full corrections as given by equation 3.27 are used.) If no deletion or introduction is necessary, final convergence is assumed achieved; otherwise, the components are adjusted to reflect such changes and iterations are continued.

From the second convergence onward no deletions are done, only gaseous species that have been left out at the start and those that have been deleted after previous convergences are checked for introduction. In this way, some gaseous species present in amounts slightly smaller than the lower limit will be included, because the amounts of gaseous species are often overestimated by equation 3.27. This ensures that no gaseous species that should be included are missed. Eventually no more gaseous species has to be introduced and the equilibrium solution is then obtained by doing one final deletion of gaseous species that exist in amounts smaller than the lower limit, and the iterations are done one more time. Usually no more than two to three additional convergences after the first convergence of the main calculation are needed to reach an equilibrium solution.

The final deletion step is taken only for matching the same number of gaseous species that have been considered by a major current code when carrying out comparisons. In the major current codes, some gaseous species with amounts slightly smaller than the specified lower limits are allowed. Because of this, the lower limits specified in the new code are not equal to those specified in the current codes, but are actually just below the molar amounts of the least abundant gaseous species considered in the current codes. This way all the species considered by a major current code will be considered by the new code.[3]

For different trial equilibrium temperatures, the initial estimates of the equilibrium mole numbers are different. However, if the temperatures do not differ very much, the initial estimates should also not differ very much. At the present moment, a new set of initial estimates is evaluated only when a new trial equilibrium temperature is different from the previous one by more than 400 K; otherwise, the results determined for the previous temperature are used as the initial estimates for the new temperature. This is also why the trial temperatures of the initial bracket for root searching is 400 K apart.

On rare occasions, there are components present also in very minute amounts and whose amounts would be rendered to become nonpositive (actually negative for condensed components and nonpositive for gaseous components), after corrections as a result of deletion and/or introduction of trace gaseous species have been made. Such occurrences are possible *only* when no initial estimates of the equilibrium mole numbers are evaluated for a trial equilibrium temperature because it is close to a previous one. Hence, for these cases, the calculation for that trial temperature would be repeated with a set of initial estimates evaluated first. If the same situation happens again, a message is printed calling for the use of a smaller pre-defined lower limit and adjustments of the trace gaseous species and of the components are reverted. Equilibrium composition for that trial temperature is deemed to have been achievd and the equilibrium calculation continues.

---

[3] In the NASA and Bagheera codes, besides the lower limits used for handling trace gaseous species, there are also lower limits specified for printing results, abundances of the gaseous species, which are below the latter limits will not be printed. The limits for printing are normally chosen to be greater than the limits for handling trace species.

Mentioned in the last section is that convergence check is skipped for species that are absent at the end of an iteration step. This would be true for those trace gaseous species that are set to zero molar because their initial estimates are below the pre-defined lower limit. As described above these trace gaseous species are taken care of by a separate procedure.

## 3.7 Inclusion of Different Gaseous Mixture Models

The use of different mixture models in the new code for the product gases is reflected in two aspects: the chemical potential form used for the species and the way the total internal energy of the mixture is evaluated. These two aspects are discussed below for all three models. Some of the equations presented earlier are repeated here for completeness.

### 3.7.1 Perfect-Gas Mixture

The chemical potential of a species in a perfect-gas mixture is given as

$$\mu_i(T, P_m, x_i) = \mu_i^0(T) + RT\ln(P_m) + RT\ln(x_i). \tag{3.32}$$

The total internal energy of an ideal mixture of product gases is given in general by

$$U_g = \sum_{i=1}^{N_g} n_i u_{g_i}, \tag{3.33}$$

where $u_{g_i}$ is the molar internal energy of the $i^{\text{th}}$ species as a pure gas at the mixture (system) conditions. For a perfect gas, the molar internal energy is a function of temperature only and can be given by its value at the standard reference pressure. That is

$$u_{g_i} = u_i^0. \tag{3.34}$$

Furthermore,

$$u_i^0 = h_i^0 - RT. \tag{3.35}$$

### 3.7.2 Ideal Mixture of Imperfect Gases

The chemical potential of a gaseous product as an imperfect gas in an ideal mixture has an additional fugacity coefficient term which depends only on the mixture conditions and not its composition. This term is

$$\mu_i(T, P_m, x_i) = \mu_i^0(T) + RT\ln(P_m) + RT\ln[\phi_i(T, P_m)] + RT\ln(x_i). \tag{3.36}$$

Two equations can be used for evaluating the fugacity coefficient of such a species, depending on the independent variables used in the equation of state used for describing its *P*-*v*-*T* properties. For independent variables $T$ and $p$, equation 2.75 is used in the form

$$RT\ln(\phi_i) = \int_0^{P_m} \left(v_i - \frac{RT}{p}\right) \mathrm{d}p. \tag{3.37}$$

If the independent variables $T$ and $v$ are used in the equation of state, then the following equation [Prausnitz *et al.*, 1986, p. 38] alternate to equation 3.37 is used:

$$RT\ln(\phi_i) = \int_V^{\infty} \left(\frac{p}{n_i} - \frac{RT}{V}\right) \mathrm{d}V - RT\ln(z_i) + RT(z_i - 1), \tag{3.38}$$

where $V$ is the total volume of the mixture and $z_i = P_m v_i / RT$ ($v_i = V/n_i$) is the compressibility factor of the $i^{\text{th}}$ pure species at the mixture conditions.

The corresponding equations for determining the molar internal energy of the $i^{\text{th}}$ species as a pure gas at the mixture conditions are

$$u_{g_i} = \int_0^{P_m} \left[v_i - T\left(\frac{\partial v_i}{\partial T}\right)_{p,n_{i_g}}\right] \mathrm{d}p - P_m v_i + h_i^0 \tag{3.39}$$

and

$$u_{g_i} = \frac{1}{n_i}\int_V^{\infty} \left[p - T\left(\frac{\partial p}{\partial T}\right)_{V,n_{i_g}}\right] \mathrm{d}V + u_i^0 \tag{3.40}$$

(see Prausnitz *et al.*, 1986, p. 38).

### 3.7.3 Nonideal Mixture of Imperfect Gases

The fugacity coefficient of a product gas as an imperfect gas but in a nonideal mixture depends not only on the mixture conditions but also its composition, and the chemical potential of such a species is given by

$$\mu_i(T, P_m, x) = \mu_i^0(T) + RT\ln(P_m) + RT\ln[\phi_i(T, P_m, x)] + RT\ln(x_i)\,. \tag{3.41}$$

Again, there are two ways to evaluate the fugacity coefficient, this time depending on the independent variables used in the equation of state used for describing the $P$-$v$-$T$ properties of the mixture. For independent variables $T$ and $p$,

$$RT\ln(\phi_i) = \int_0^{P_m} \left(\bar{v}_i - \frac{RT}{p}\right) \mathrm{d}p, \tag{3.42}$$

and for independent variables $T$ and $v$,

$$RT\ln(\phi_i) = \int_V^{\infty} \left[\left(\frac{\partial p}{\partial n_i}\right)_{T,V,n_{j\neq i}} - \frac{RT}{V}\right] \mathrm{d}V - RT\ln(z_m), \tag{3.43}$$

where $z_m$ is the compressibility factor of the mixture.

The total internal energy of the mixture is now evaluated directly as an extensive property. Two equations are available for this purpose, corresponding to the two sets of independent variables. However, the one only for the variables $T$ and $v$ is listed, because in all the cases studied involving a nonideal mixture, the $P$-$v$-$T$ properties of the mixture were described by an equation of state given in terms of these two variables. Thus,

$$U_g = \int_V^{\infty} \left[p - T\left(\frac{\partial p}{\partial T}\right)_{V,n_{i_g}}\right] \mathrm{d}V + \sum_{i=1}^{N_g} n_i u_i^0 \tag{3.44}$$

[Prausnitz *et al.*, 1986, p. 38].

## 3.8 Inclusion of Different Equations of State for Gaseous Species

Depending on which equation of state is used for describing the *P-v-T* properties of the gases in an ideal mixture or of a nonideal mixture, different equations for evaluating the fugacity coefficient of a gaseous species in the mixture will result. A similar situation applies to the internal energy of a gaseous species, except that in the case of a nonideal mixture no evaluation of the internal energy of individual gases is required. The resulting equations used for evaluating fugacity coefficients and internal energy based on the equations of state used for the present study are listed below. Equations based on the equations of state used for the validation of the new code are listed first, followed by those based on the equations of state used in the current codes which were needed when comparing the new code with the current codes. (Equations for a perfect-gas mixture are simple, have been presented earlier and they are not repeated here.)

### 3.8.1 Redlich-Kwong-Soave EOS

This is the first equation of state that describes the *P-v-T* properties of imperfect gases used in calculations to validate the new code. For the ideal mixture model, the fugacity coefficient of the $i^{th}$ gaseous species in a mixture was obtained by applying equation 2.92 to equation 3.38. On evaluating the integral by using partial fractions and then recombining terms, equation 3.38 can be written as

$$\ln(\phi_i) = z_i - 1 - \ln\left[\frac{P_m}{RT}(v_i - b_i)\right] - \frac{a_i}{b_i RT}\ln\left(\frac{v_i + b_i}{v_i}\right), \tag{3.45}$$

where $a_i$ and $b_i$ are the parameters $a$ and $b$ of the $i^{th}$ pure species at the mixture conditions.

Similarly, the internal energy of the species was obtained by applying equation 2.92 to equation 3.40 to give

$$u_{g_i} = \frac{Ta_i' - a_i}{b_i}\ln\left(\frac{v_i + b_i}{v_i}\right) + u_i^0, \tag{3.46}$$

where $a_i'$ is the temperature derivative of $a_i$.

By differentiating equations 2.93 and 2.94, then $a_i'$ can be obtained as

$$a_i' = 0.42747\alpha' R^2 \frac{T_c^2}{P_c}, \tag{3.47}$$

where $\alpha'$ is now the temperature derivative of $\alpha$ and is given as

$$\alpha' = -\frac{m}{\sqrt{TT_c}}\left[1 + m - m\sqrt{\frac{T}{T_c}}\right]. \tag{3.48}$$

Demonstration calculations using this equation were performed for a gaseous mixture consists of 14 species. For an ideal mixture, the system pressure is determined iteratively by summing volume of individual gases. Molar volume of each gas was determined by finding the largest root to the nondimensional equation in the form

$$z^3 - z^2 + z(A - B - B^2) - AB = 0, \tag{3.49}$$

where $z$ is the compressibility factor, and $A$ and $B$ are defined as

$$A \equiv \frac{ap}{(RT)^2} \qquad \text{and} \qquad B \equiv \frac{bp}{RT}. \tag{3.50}$$

The root was first bracketed and then determined by using the bisection method. When solving for $v$ using an iterative method, it is easier to do this in terms of $z$ instead of $v$, because variations in the $z$ values are much more limited.

For the nonideal mixture model, the fugacity coefficient of the $i^{\text{th}}$ gaseous species in a mixture was obtained by applying equation 2.92 to equation 3.43, but with $a$ and $b$ in equation 2.92 replaced by their mixture counterparts which are determined by using equations 2.97 and 2.98. Once again, on evaluating the integral by partial fractions and then recombining terms, equation 3.43 becomes

$$\begin{aligned}\ln(\phi_i) = {} & \frac{b_i}{b_m RT}(P_m v - RT) - \ln\left[\frac{P_m}{RT}(v - b_m)\right] \\ & - \frac{1}{b_m RT}\left[2a_i^{1/2}\sum_{j=1}^{N_g} x_j a_j^{1/2}(1 - k_{ij}) - \frac{b_i a_m}{b_m}\right]\ln\left(\frac{v + b_m}{v}\right), \qquad (3.51)\end{aligned}$$

where $v$ equals $V/n_{g_t}$ is the molar volume of the mixture and can be used to calculate $P_m$ directly from the equation of state itself.

When evaluating parameter $a_m$, determination of the $a_{ij}$ parameters by using equation 2.99 requires a knowledge of the $k_{ij}$ parameters. Because of the lack of data on the $k_{ij}$ parameters for many of the species pairs used in the sample calculations, they had been neglected and set to zero for all pairs. For such cases, $a_m$ becomes $\sum_{i=1}^{N_g} x_i a_i^{1/2} \sum_{j=1}^{N_g} x_j a_j^{1/2}$ and $\sum_{j=1}^{N_g} x_j a_j^{1/2}$ equals $a_m^{1/2}$. When factoring out $a_m$ from the third term, equation 3.51 becomes

$$\begin{aligned}\ln(\phi_i) = {} & \frac{b_i}{b_m RT}(P_m v - RT) - \ln\left[\frac{P_m}{RT}(v - b_m)\right] \\ & - \frac{a_m}{b_m RT}\left[2\left(\frac{a_i}{a_m}\right)^{1/2} - \frac{b_i}{b_m}\right]\ln\left(\frac{v + b_m}{v}\right). \qquad (3.52)\end{aligned}$$

The total internal energy of the mixture was evaluated by applying equation 2.92 together with mixture parameters $a_m$ and $b_m$ to equation 3.44. After carrying out an integration similar to the case of a gaseous species in an ideal mixture, the total internal energy of the mixture is

$$U_g = n_{t_g}\frac{Ta_m' - a_m}{b_m}\ln\left(\frac{v + b_m}{v}\right) + \sum_{i=1}^{N_g} n_i u_i^0, \qquad (3.53)$$

where $a_m'$ is the derivative of $a_m$ with respect to temperature $T$.

By differentiating equations 2.97 and 2.99, $a_m'$ can be obtained as

$$a_m' = \sum_{i=1}^{N_g}\sum_{j=1}^{N_g} x_i x_j a_{ij}', \qquad (3.54)$$

where $a_{ij}'$ is the temperature derivative of $a_{ij}$ and is given as

$$a_{ij}' = \frac{1 - k_{ij}}{2\sqrt{a_i a_j}}[a_i a_j' + a_j a_i'], \qquad (3.55)$$

and $a_i'$ and $a_j'$ are derivatives of $a_i$ and $a_j$ of the $i^{\text{th}}$ and the $j^{\text{th}}$ pure species with respect to temperature, respectively. When $k_{ij}$ is set to zero, $a_{ij}'$ becomes

$$a_{ij}' = \frac{1}{2\sqrt{a_i a_j}}[a_i a_j' + a_j a_i']. \qquad (3.56)$$

Critical constants were not available for four of the 14 species used for the demonstration calculations. For these species, the constant were estimated by using the approximate relations given by Hirschfelder *et al.* [1954, p. 244–247],

$$\varepsilon/k = 0.77T_c \tag{3.57}$$

and

$$b = 18.4T_c/P_c. \tag{3.58}$$

which are based on the principle of corresponding states. These relations were originally proposed for estimating the Lennard-Jones (6-12) force constants based on the critical constants, but they had been used in the reverse order. The force constants were estimated in turn by following the procedure used in the Bagheera code (to be mentioned again in the section on the modified virial equation used by the Bagheera code to follow). The acentric factors of these species were set to zero, which is a reasonable choice for three of the four species, which are monoatomic molecules.

### 3.8.2 Benedict-Webb-Rubin-Starling EOS

This is the second equation of state describing the *P-v-T* properties of imperfect gases used in calculations to validate the new code. Equation 2.100 was used with the molar density $\rho$ first converted to molar volume $v$. Equations for evaluating chemical potentials and internal energy of product gases were obtained in a way similar to that for the RKS equation, except that integration by parts was used to handle the exponential term in equation 2.100.

The fugacity coefficient of the $i^{th}$ species was determined using

$$\begin{aligned}\ln(\phi_i) = {} & \frac{2}{RT}\left(B_{0i}RT - A_{0i} - \frac{C_{0i}}{T^2} + \frac{D_{0i}}{T^3} - \frac{E_{0i}}{T^4}\right)\rho_i \\ & + \frac{3}{2RT}\left(b_iRT - a_i - \frac{d_i}{T}\right)\rho_i^2 + \frac{6\alpha_i}{5RT}\left(a_i + \frac{d_i}{T}\right)\rho_i^5 \\ & + \frac{c_i}{\gamma_i RT^3}\left[1 - (1 - \frac{1}{2}\gamma_i\rho_i^2 - \gamma_i^2\rho_i^4)\exp(-\gamma_i\rho_i^2)\right] + \ln\left(\frac{\rho_i RT}{P_m}\right),\end{aligned} \tag{3.59}$$

for the ideal mixture model, which can be rewritten as

$$\begin{aligned}\ln(\phi_i) = {} & 2B_i\rho_i + \frac{3}{2}C_i\rho_i^2 + \frac{6}{5}D_i\rho_i^5 \\ & + \frac{C_i'}{\gamma_i}\left[1 - \left(1 - \frac{1}{2}\gamma_i\rho_i^2 - \gamma_i^2\rho_i^4\right)\exp\left(-\gamma_i\rho_i^2\right)\right] + \ln\left(\frac{\rho_i RT}{P_m}\right),\end{aligned} \tag{3.60}$$

where the coefficients $B_i$, $C_i$, $D_i$ and $C_i'$ are the coefficients $B$, $C$, $D$ and $C'$ of the $i^{th}$ species, defined by equations 2.102 to 2.105.

On the other hand, the molar internal energy of the $i^{th}$ species was determined as

$$\begin{aligned}u_{g_i} = {} & \left(-A_{0i} - \frac{3C_{0i}}{T^2} + \frac{4D_{0i}}{T^3} - \frac{5E_{0i}}{T^4}\right)\rho_i - \left(\frac{a_i}{2} + \frac{d_i}{T}\right)\rho_i^2 \\ & + \frac{\alpha_i}{5}\left(a_i + \frac{2d_i}{T}\right)\rho_i^5 + \frac{3c_i}{\gamma_i T^2}\left[1 - \left(1 + \frac{\gamma_i\rho_i^2}{2}\right)\exp\left(-\gamma_i\rho_i^2\right)\right] + u_i^0.\end{aligned} \tag{3.61}$$

Demonstration calculations of the same problem was also done by using this equation. When determining the system pressure iteratively for the ideal mixture, molar volume of each gas was determined by solving for the largest root (which can also be used to evaluate the molar density of a gas) to the following nondimensional form of equation 2.101:

$$z^6 - z^5 - \overline{B}z^4 - \overline{C}z^3 - \overline{D} - \overline{C'}z\left(z^2 + \overline{\gamma}\right)\exp\left(-\frac{\overline{\gamma}}{z^2}\right) = 0, \tag{3.62}$$

where

$$\overline{B} = \left(\frac{p}{RT}\right)B, \quad \overline{C} = \left(\frac{p}{RT}\right)^2 C, \quad \overline{D} = \left(\frac{p}{RT}\right)^5 D,$$
$$\overline{C'} = \left(\frac{p}{RT}\right)^2 C', \quad \overline{\gamma} = \left(\frac{p}{RT}\right)^2 \gamma. \tag{3.63}$$

Again, the root was first bracketed and then solved for using the bisection method. The same critical constants and acentric factors used for calculating the RKS parameters were also used for calculating the eleven parameters of a pure species.

For the nonideal mixture model, the fugacity coefficient of the $i^{\text{th}}$ species becomes

$$\begin{aligned}
\ln(\phi_i) = {} & \rho(B_{0m} + B_{0i}) + \frac{2\rho}{RT}\sum_{j=1}^{N_g} x_j \Big[-(A_{0i}A_{0j})^{1/2}(1-\overline{k}_{ij}) \\
& -\frac{(C_{0i}C_{0j})^{1/2}}{T^2}(1-\overline{k}_{ij})^3 + \frac{(D_{0i}D_{0j})^{1/2}}{T^3}(1-\overline{k}_{ij})^4 - \frac{(E_{0i}E_{0j})^{1/2}}{T^4}(1-\overline{k}_{ij})^5\Big] \\
& +\frac{\rho^2}{2RT}\left[3(b_m^2 b_i)^{1/3}RT - 3(a_m^2 a_i)^{1/3} - \frac{3(d_m^2 d_i)^{1/3}}{T}\right] \\
& +\frac{\alpha_m \rho^5}{5RT}\left[3(a_m^2 a_i)^{1/3} + \frac{3(d_m^2 d_i)^{1/3}}{T}\right] + \frac{3\rho^5}{5RT}\left(a_m + \frac{d_m}{T}\right)(\alpha_m^2 \alpha_i)^{1/3} \\
& +\frac{3(c_m^2 c_i)^{1/3}\rho^2}{RT^3}\left[\frac{1-\exp(-\gamma_m\rho^2)}{\gamma_m\rho^2} - \frac{1}{2}\exp(-\gamma_m\rho^2)\right] + \ln\left(\frac{\rho RT}{P_m}\right) \\
& -\frac{2c_m}{\gamma_m RT^3}\left(\frac{\gamma_i}{\gamma_m}\right)^{1/2}\left[1 - \exp(-\gamma_m\rho^2)(1 + \gamma_m\rho^2 + \frac{1}{2}\gamma_m^2\rho^4)\right],
\end{aligned} \tag{3.64}$$

where $\rho$ equals $n_{g_t}/V$ is the molar density of the mixture and was used to calculate $P_m$ directly from the equation of state itself.

Because of the lack of data on the $\overline{k}_{ij}$ parameters for many of the species pairs used in the sample calculations, they had also been neglected and set to zero for all pairs. When $\overline{k}_{ij}$ were neglected, the fugacity coefficient of the $i^{\text{th}}$ species became

$$\begin{aligned}
\ln(\phi_i) = {} & \rho(B_{0m} + B_{0i}) + \frac{2\rho}{RT}\Big[-(A_{0i}A_{0m})^{1/2} - \frac{(C_{0i}C_{0m})^{1/2}}{T^2} + \frac{(D_{0i}D_{0m})^{1/2}}{T^3} \\
& -\frac{(E_{0i}E_{0m})^{1/2}}{T^4}\Big] + \frac{\rho^2}{2RT}\left[3(b_m^2 b_i)^{1/3}RT - 3(a_m^2 a_i)^{1/3} - \frac{3(d_m^2 d_i)^{1/3}}{T}\right] \\
& +\frac{\alpha_m \rho^5}{5RT}\left[3(a_m^2 a_i)^{1/3} + \frac{3(d_m^2 d_i)^{1/3}}{T}\right] + \frac{3\rho^5}{5RT}\left(a_m + \frac{d_m}{T}\right)\left(\alpha_m^2 \alpha_i\right)^{1/3} \\
& +\frac{3(c_m^2 c_i)^{1/3}\rho^2}{RT^3}\left[\frac{1-\exp(-\gamma_m\rho^2)}{\gamma_m\rho^2} - \frac{1}{2}\exp(-\gamma_m\rho^2)\right] + \ln\left(\frac{\rho RT}{P_m}\right) \\
& -\frac{2c_m}{\gamma_m RT^3}\left(\frac{\gamma_i}{\gamma_m}\right)^{1/2}\left[1 - \exp(-\gamma_m\rho^2)\left(1 + \gamma_m\rho^2 + \frac{1}{2}\gamma_m^2\rho^4\right)\right],
\end{aligned} \tag{3.65}$$

and

$$U_g = n_{gt}\left[\left(-A_{0m} - \frac{3C_{0m}}{T^2} + \frac{4D_{0m}}{T^3} - \frac{5E_{0m}}{T^4}\right)\rho - \left(\frac{a_m}{2} + \frac{d_m}{T}\right)\rho^2 + \frac{\alpha_m}{5}\left(a_m + \frac{2d_m}{T}\right)\rho^5 + \frac{3c_m}{\gamma_m T^2}\left\{1 - \left(1 + \frac{\gamma_m \rho^2}{2}\right)\exp(-\gamma_m \rho^2)\right\}\right] + \sum_{i=1}^{N_g} n_i u_i^0. \tag{3.66}$$

was determined to be the total internal energy of the mixture.

### 3.8.3 Truncated Virial EOS

The third equation of state used for describing the *P-v-T* properties of imperfect gases for sample calculations by using the new code was the truncated virial equation of state, equation 2.128. When using the ideal gaseous mixture model, the chemical potential and the molar internal energy of the $i^{\text{th}}$ species in a mixture were determined as

$$\ln(\phi_i) = \frac{2B_i}{v_i} + \frac{3C_i}{2v_i^2} - \ln(z_i) \tag{3.67}$$

and

$$u_{g_i} = -n_i RT^2\left(\frac{B_i'}{v_i} + \frac{C_i'}{2v_i^2}\right) + u_i^0, \tag{3.68}$$

where $B_i'$ and $C_i'$ are the temperature derivatives of the second and the third virial coefficients of the $i^{\text{th}}$ species, respectively.

Demonstration calculations using this equation was performed for a number of cases, which include the case of an ideal gaseous mixture only and the case of a nonideal gaseous mixture together with a number of variable molar-volume condensates; both these two cases require iterative determination of system pressure. This time, as a trial of an alternative approach, the molar volume of each gas was solved analytically, as the largest root to the cubic equation. Formulae given in Press *et al.* [1987, p. 146] for the roots were used. Most force constants for the evaluation of the second and third virial coefficients of the 14 gases for calculations were taken from Hirschfelder *et al.* [1954, pp. 1110–1111]. Values from the Bagheera and Blake codes were also used.

For nonideal gaseous mixtures, the chemical potential of the $i^{\text{th}}$ species and the total internal energy of the mixture were obtained as

$$\ln(\phi_i) = \frac{2}{v}\sum_{j=1}^{N_g} x_j B_{ij} + \frac{3}{2v^2}\sum_{j=1}^{N_g}\sum_{k=1}^{N_g} x_j x_k C_{ijk} - \ln(z_m) \tag{3.69}$$

and

$$U_g = -n_{t_g} RT^2\left(\frac{B_m'}{v} + \frac{C_m'}{2v^2}\right) + \sum_{i=1}^{N_g} n_i u_i^0, \tag{3.70}$$

where $B_m'$ and $C_m'$ are the temperature derivatives of the mixture virial coefficients given by equations 2.143 and 2.144.

For demonstration calculations for a nonideal gaseous mixture only or a nonideal gaseous mixture with a number of zero molar-volume condensates, $v$ is simply equal to the constraint volume divided by the total number of moles of gases in the mixture and was used for calculating $P_m$ directly from the equation of state itself. For the case in which constant molar-volume condensates were assumed, volume of the gaseous mixture was obtained by subtracting the volume of the condensates from the constraint volume, so that $v$ and then $P_m$ could be evaluated.

### 3.8.4 Modified Virial EOS

For comparison with the Bagheera code, equation 3.37 was used to determine the fugacity coefficient of the $i^{\text{th}}$ species, because the Bagheera code uses the ideal mixture model and a volume-explicit equation of state. On substituting equation 2.180 into equation 3.37 and doing two easy integrations

$$\ln(\phi_i) = \frac{\beta_{1_i}}{\alpha_{1_i}} \ln(1 + \alpha_1 P_m) - \frac{\beta_{2_i}}{\alpha_{2_i}} \ln(1 + \alpha_2 P_m). \tag{3.71}$$

The molar internal energy of the $i^{\text{th}}$ species was obtained by applying equation 2.180 to equation 3.39, which resulted in several standard integrals, and is given as

$$\begin{aligned} u_{g_i} = {} & \frac{\beta_{1_i} - T\beta'_{1_i}}{\alpha_{1i}} \ln(1 + \alpha_{1_i} P_m) - \frac{\beta_{2_i} - T\beta'_{2_i}}{\alpha_{2_i}} \ln(1 + \alpha_{2_i} P_m) \\ & + \frac{T\beta_{1_i}\alpha'_{1_i}}{\alpha_{1_i}^2} \left[\ln(1 + \alpha_{1_i} P_m) + \frac{1}{1 + \alpha_{1_i} P_m} - 1\right] - RT - \frac{\beta_{1_i} P_m}{1 + \alpha_{1_i} P_m} \\ & - \frac{T\beta_{2_i}\alpha'_{2_i}}{\alpha_{2_i}^2} \left[\ln(1 + \alpha_{2_i} P_m) + \frac{1}{1 + \alpha_{2_i} P_m} - 1\right] + \frac{\beta_{2_i} P_m}{1 + \alpha_{2_i} P_m} + h_i^0, \end{aligned} \tag{3.72}$$

where

$$\beta'_{1_i} = -\frac{1.733001 b_i}{4} (T_i^*)^{-5/4} - \frac{k}{\varepsilon_i}, \qquad \beta'_{2_i} = \beta'_{1_i} - B'_i,$$

$$\alpha'_{1_i} = \frac{2(\beta_{2_i}\beta'_{2_i} + B_i B'_i) - C'_i - \alpha_{1_i} R(\beta_{1_i} + T\beta'_{1_i})}{\beta_{1_i} RT}, \qquad \text{and} \qquad \alpha'_{2_i} = \frac{\beta'_{2_i}}{RT} - \frac{\beta_{2_i}}{RT^2}.$$

In the Bagheera code, the virial coefficients and their temperature derivatives, $B_i$, $C_i$, $B'_i$, and $C'_i$ required for the evaluation of the above quantities are determined by linearly interpolating the $B^*$, $C^*$, $B_1^*$, and $C_1^*$ values tabulated in Hirschfelder *et al.* [1954, pp. 1114–1117]. Furthermore, values of force constants $\sigma$ and $\varepsilon$ (in terms of $\varepsilon/k$) of gases species are listed together with their polynomial coefficients in the library of Bagheera. However, when values of these constants are not available, they are either assigned or calculated. If the number of atoms in the molecules of a gas is greater than three, then 3.5 Å and 100 K are assigned to $\sigma$ and $\varepsilon/k$, respectively. If the number is three or less, then they are calculated based on the atomic types and by using several averaging schemes. The same procedures are followed in the new code when comparing with the Bagheera code.

### 3.8.5 Truncated Virial EOS (rigid sphere model for third coefficients)

Calculations done with the Blake code use the truncated virial equation of state. To evaluate the third virial coefficients of pure species, the Blake code uses the rigid sphere model and molecules are assumed to have a radius 0.81 times the Lennard-Jones force constant $\sigma$ [Hirschfelder *et al.*, 1954, p. 157]. Also, interactions among species are neglected when determining the third virial coefficient of the mixture. The mixing rule (linearly weighted sum) is given first in the Blake code's user guide for evaluating $C_m$ as

$$C_m = \sum_{i=1}^{N_g} x_i C_i. \tag{3.73}$$

However, given expressions for various derivatives of $P$-$v$-$T$ and chemical thermodynamic properties that are used in the Blake code, the use of the mixing rule

$$C_m = \sum_{i=1}^{N_g} x_i^3 C_i \tag{3.74}$$

seems obvious, in which is the simplified result of equation 2.139 when neglecting interactions among species and replacing $C_{iii}$ by $C_i$ [Freedman, 1982, pp. 9–14]. A check into the source code revealed that equation 3.73 had been used for evaluating the compressibility factor and equation 3.74 had been used in many of the expressions of derivatives of $P$-$v$-$T$ and chemical thermodynamic properties. The check also revealed that some of these expressions may actually be in error.

Because equation 3.74 is a natural consequence of equation 2.139 which has a sound theoretical basis, equation 3.74 is used in the new code. However, it is likely that the contributions of the third virial coefficients are small, and no big differences in results were found when the Blake code was compared with the new code. Based on equation 3.74, equation 3.69 becomes

$$\ln(\phi_i) = \frac{2}{v}\sum_{j=1}^{N_g} x_j B_{ij} + \frac{3x_i^2 C_i}{2v^2} - \ln(z_m). \tag{3.75}$$

$C_m$ is temperature independent due to the rigid sphere model and equation 3.70 becomes

$$U_g = -\frac{n_{t_g} R T^2 B'_m}{v} + \sum_{i=1}^{N_g} n_i u_i^0. \tag{3.76}$$

For $B_{ij}$ the Blake code uses equation 2.140 for $\sigma_{ij}$, but the combining rule for $\varepsilon_{ij}$ given by

$$\varepsilon_{ij} = \frac{\sqrt{\sigma_i^3 \sigma_j^3}}{\sigma_{ij}^3}\sqrt{\varepsilon_i \varepsilon_j} \tag{3.77}$$

is used. The quantity $b$ is determined as defined by equation 2.130. The $B^*$ and $B_1^*$ values are evaluated by cubic spline interpolation based on those tabulated in Hirschfelder *et al.* [1954, pp. 1114–1117] and by using an IMSL cubic spline subroutine. As for the third virial coefficient,

$$C = \frac{5}{8} b_{rs}^2, \tag{3.78}$$

and

$$b_{rs} = \frac{2}{3}\pi N_A \sigma_{rs}^3, \tag{3.79}$$

where $\sigma_{rs}$ is equal to $0.81\sigma$. When values of $\sigma$ and $\varepsilon$ (in terms of $\varepsilon/k$) of a species are not available, the Blake code assigns 3.5 Å and 100 K to $\sigma$ and $\varepsilon/k$, respectively. The same relations and procedures were used in the new code when carrying out the comparison.

## 3.9 Inclusion of Different Compressibility Models for the Condensed Species

The compressibility model (three possible cases) for the condensed species is also reflected in the form of the chemical potential and of the molar internal energy used for the species. The chemical potentials of condensed species can be evaluated based on one of two choices of the reference state pressure, $P^0$ or $P^*$, as mentioned in section 2.1.10. Expressions of chemical potentials and molar internal energy based on $P^0$ will be given first, followed by those based on $P^*$.

### 3.9.1 $P^0$ Equals One Unit

The chemical potential of a pure condensed species is given in this case by equation 2.46 which can be rewritten for the $i^{\text{th}}$ condensed species in a product mixture as

$$\mu_i = \mu_i^0 + \int_1^{P_m} v_i \, dp. \tag{3.80}$$

The corresponding equation for evaluating the molar internal energy is given similarly by

$$u_{c_i} = u_i^0 + \int_1^{P_m} du_i. \tag{3.81}$$

Making use of the combined first and second laws of thermodynamics and the Maxwell's relations, equation 3.81 can be expressed alternatively as

$$u_{ci} = u_i^0 - \int_1^{P_m} \left[ T\left(\frac{\partial v_i}{\partial T}\right)_p + p\left(\frac{\partial v_i}{\partial p}\right)_T \right] dp. \tag{3.82}$$

(The subscript $c$ has been used here only to comply with equation 3.31.)

### 3.9.2 Zero Molar Volume

In this case the second terms in equations 3.80 and 3.82 contribute nothing and the chemical potential and the molar internal energy of the $i^{\text{th}}$ condensed species are summarized as

$$\mu_i = \mu_i^0 = h_i^0 - Ts_i^0 \qquad \text{and} \qquad u_{c_i} = u_i^0 = h_i^0. \tag{3.83}$$

### 3.9.3 Constant Molar Volume

When $v_i$ is assumed constant it can be taken out of the integral in equation 3.80 to give

$$\mu_i = \mu_i^0 + v_i(P_m - 1). \tag{3.84}$$

In the Bagheera code it assumed that $P \gg 1$ and the above equation is replaced by

$$\mu_i = \mu_i^0 + v_i P_m. \tag{3.85}$$

This is the equation used for evaluating the chemical potential of a condensed species when comparing with the Bagheera code. In this case, the second term of equation 3.82 also vanishes and the molar internal energy of the $i^{\text{th}}$ condensed species is given by

$$u_{c_i} = u_i^0 = h_i^0 - v_i^0. \tag{3.86}$$

The $pv$ term is in general small in comparison with the enthalpy term and can be ignored; hence,

$$u_{c_i} = u_i^0 = h_i^0. \tag{3.87}$$

This equation is used in the Bagheera code and when a comparison is made with this code.

### 3.9.4 Variable Molar Volume

When condensed species are assumed compressible a full evaluation of the integrals in equations 3.80 and 3.82 is required. The equations for determining the chemical potentials and molar internal energy of the condensed species, derived for three equations of state, are given next.

## 3.10 Inclusion of Different Equations of State for Condensed Species

### 3.10.1 Polynomial Type Empirical Equation of State

Equation 2.146 is applicable to both liquid and solid species. When it is applied to equation 3.80 the chemical potential of the $i^{\text{th}}$ condensed species is given by

$$\mu_i = \mu_i^0 + A_{1i}P_m + \frac{A_{2i}}{2}P_m^2 + \frac{A_{3i}}{3}P_m^3 - \left(A_{1i} + \frac{A_{2i}}{2} + \frac{A_{3i}}{3}\right). \tag{3.88}$$

Similarly, the molar internal energy of the $i^{\text{th}}$ condensed species is obtained by applying equation 2.146 to equation 3.82 and is given by

$$\begin{aligned} u_{c_i} = h_i^0 \; + \; (B_{1_i} - A_{1_i}) + \frac{B_{2_i} - A_{2_i}}{2} \; + \; \frac{B_{3_i} - A_{3_i}}{3} \\ - \frac{2A_{3i} + B_{3_i}}{3}P_m^3 + \frac{A_{2i} + B_{2_i}}{2}P_m^2 \; + \; B_{1_i}P_m\,. \end{aligned} \tag{3.89}$$

### 3.10.2 Redlich-Kwong-Soave EOS for Liquid Species

The molar volume of the liquid phase of a substance described by the RKS equation is the smallest root of the cubic, as noted in section 2.1.12, which can be obtained analytically [Press *et al.*, 1987, p. 146] using a cosine function whose argument is system pressure dependent. The Gauss-Legendre integration [Press *et al.*, 1987, pp. 121–126] was used to numerically evaluate the integral in equation 3.80, giving the chemical potential of the $i^{\text{th}}$ condensed species (presumably a liquid).

For the RKS equation of state, equation 3.82 becomes

$$\begin{aligned} u_{c_i} \;=\; u_i^0 - \int_1^{P_m} \Bigg[ & T\frac{[a_i'(v_i - b_i) - Rv_i(v_i + b_i)]v_i(v_i^2 - b_i^2)}{a_i(2v_i + b_i)(v_i - b_i)^2 - RTv_i^2(v_i + b_i)^2} \\ & + p\frac{v_i^2(v_i^2 - b_i^2)^2}{[a_i v_i(v_i - b_i) - (v_i^2 - b_i^2)](v_i - b_i) - RTv_i^2(v_i + b_i)^2}\Bigg]\,\mathrm{d}p. \end{aligned} \tag{3.90}$$

The complicated integral in the above equation was also evaluated by using Gauss-Legendre integration, giving the molar internal energy.

### 3.10.3 Approximate Equation of State for Solid Species

Equation 2.150 is more suitable for solid species. The chemical potential and molar internal energy of the $i^{\text{th}}$ condensed species (supposedly a solid) are obtained by applying equation 2.150 to equations 3.80 and 3.82, and the results are given by

$$\mu_i = \mu_i^0 + v_{0_i}\,[\,1 + \beta_i(T - T_0) - \frac{\kappa_i}{2}(P_m - 1)\,]\,(P_m - 1) \tag{3.91}$$

and

$$u_{c_i} = h_i^0 - v_{0_i}\,[\,1 + \beta_i(T - T_0) - \beta_i T(P_m - 1) + \frac{\kappa_i}{2}(P_m^2 - 1)\,]. \tag{3.92}$$

## 3.11 Treatment of Melting

It is possible that two neighbouring condensed phases, such as the solid and liquid phases, of a pure substance both exist and are in transition at the equilibrium conditions of the product mixture. A special procedure is required to handle this type of situations. In the following discussion, the transition between the solid and liquid phases, melting, is referred to as an example, but the arguments and procedures apply to the transition between two solid phases as well. The procedures adopted depend very much on the models of phase transition curves used which in turn depend on the models of molar volume of condensed phases used. Because the idea was to eventually have a comparison between the new code and the major current codes, the procedures developed were based on the models of the phase transition curves used in the major current codes. In addition, because the models of molar volume of condensed phases used in the NASA and the Bagheera codes lead to the same model for the phase transition curves, very similar procedures were developed to be used for comparison with these two codes. Consequently, the procedures for these two codes will be described first, followed by that developed for the Blake code.

### 3.11.1 Procedures Based on the NASA and Bagheera Models of Phase Transition Curves

In the case of the NASA code, because condensed phases are assumed to occupy no volume, the phase transition between two condensed phases of a pure substance becomes independent of pressure and occurs at a fixed temperature. The phase transition curves are then vertical lines in a pressure-temperature plot, as shown in figure 2.3. When iterating on the equilibrium temperature of a problem involving a melting substance, either its solid or its liquid phase is selected depending on the trial temperature falls on which side of the melting temperature. However, neither of these two cases can satisfy the constant internal energy constraint; in order to satisfy this constraint part of the condensed amount of the substance would have to be in the solid form and part in the liquid form. (The constant volume constraint can always be satisfied because condensed species occupy no volume and the specified volume is assumed to be filled entirely by the gaseous products.)

When the trial temperature is below the melting temperature, the solid phase is selected and the total internal energy of the product mixture will be below the value set by the reactants, because the internal energy of the solid phase of a pure substance is lower than its liquid phase. A temperature higher then the melting temperature is then tried; the liquid phase is selected and the total internal energy of the product mixture becomes higher than the specified value, which results in selecting a trial temperature lower than the melting temperature. This causes the trial temperature to oscillate about the melting temperature.

During iterations, the switching between temperatures lower or higher than the melting temperature does not necessarily occur on alternate trials. It is quite possible that the trial temperature may remain below or above the melting temperature for more than one trial before it switches side. In any case, even though the internal energy constraint may not have been satisfied, convergence would be achieved when the difference between two trial temperatures becomes smaller than a certain tolerance. (This is one of the convergence criteria used for finding the equilibrium temperature.) However, the converged trial temperature is expected to be very close to the melting temperature, and this is the condition used for testing the possible existence of a melting substance.

Before describing the procedure any further, a few notes regarding transition temperatures are needed. In the NASA code, the polynomial coefficients, for evaluating thermodynamic properties, of some pure substances do not reproduce their designated transition temperatures. There are also cases the polynomial coefficients of a pure substance fail to predict any transition temperature at all. In general, based on the designated transition temperature of a pure substance, either the phase stable below or the phase stable above it is selected for consideration. However, when considering the possible transition of a pure substance, both these two phases are selected and their polynomial coefficients used. If the substance is truly in transition than the equilibrium temperature would ended up to be the transition temperature determined by the polynomial coefficients of the two phases. All these would mean problems with the NASA code.

One example of each of the two aforementioned problems with the polynomial coefficients in the NASA code is given below. Both these two examples are related to $N_2S$ which has three condensed phases: $N_2S$(s-1), $N_2S$(s-2), and $N_2S$(lq). $N_2S$(s-1) and $N_2S$(s-2) are solid phases and the transition from $N_2S$(s-1) to $N_2S$(s-2), at 1 bar, occurs at 1276 K. The melting temperature of $N_2S$(s-2) at 1 bar is 1445 K. Results of calculations illustrating the difficulties encountered by the NASA code in these two cases will be given in chapter 5, in which findings of an assessment of the new and the major current codes are presented.

Figure 3.3 is a plot of the nondimensional standard chemical potentials of $N_2S$(s-2) and $N_2S$(lq), determined by using their polynomial coefficients, as a function of temperature from 1440 to 1460 K. Below its melting temperature $T_m$, $N_2S$(s-2) is the stable phase and should have a lower chemical potential than that of $N_2S$(lq); above the melting temperature the reverse is true. The two curves should cross at 1445 K because at melting the chemical potentials of $N_2S$(s-2) and $N_2S$(lq) are equal. However, the crossing occurred at 1452.17 K. The melting temperature from the polynomial coefficients, which may be different from the designated value, is denoted by $T'_m$. (Transition temperatures given by polynomial coefficients are quoted to six significant digits.)

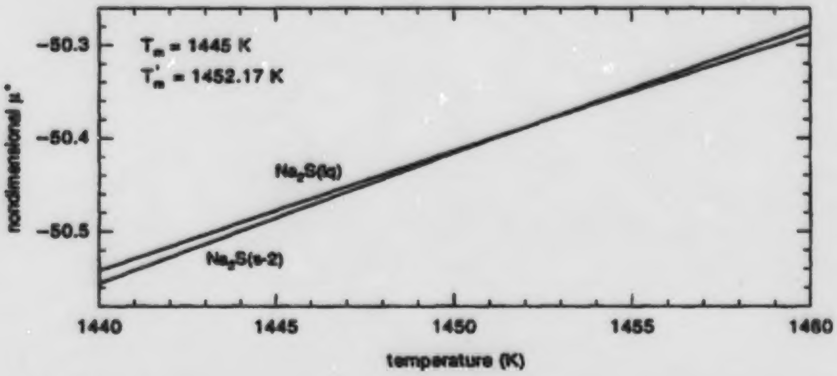

Figure 3.3: Nondimensional standard chemical potentials of $Na_2S$(s-2) and $Na_2S$(lq), determined by using their polynomial coefficients for evaluating thermodynamic properties, given in the NASA code, as a function of temperature from 1440 to 1460 K.

In figure 3.4, similar nondimensional standard chemical potentials of $N_2S$(s-1) and $N_2S$(s-2) are plotted in the vicinity of their transition temperature $T_t$ = 1276 K. In this case, the two curves never cross. The chemical potential of $N_2S$(s-1) is always slightly lower than that of $N_2S$(s-2).

For comparison purposes, in the new computer code, the transition temperatures of all neighbouring condensed phases considered in a calculation, dictated by the polynomial coefficients were

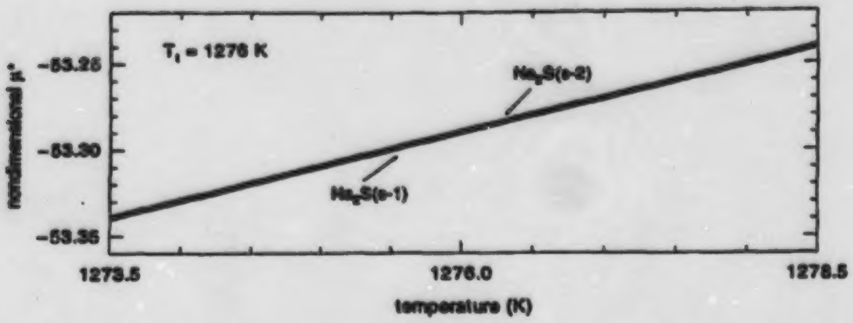

Figure 3.4: Nondimensional standard chemical potential of $Na_2S$(s-1) and $Na_2S$(s-2), determined by using their polynomial coefficients for evaluating thermodynamic properties, given in the NASA code, as a function of temperature in the vicinity of their transition temperature, 1276 K.

determined and used to replace the designated values, before carrying out the calculation. This is because if a substance in transition is present at equilibrium the NASA code would converge to the transition temperature dictated by the polynomial coefficients. An error message is printed for two neighbouring condensed phases, if a transition temperature cannot be found within 10 K from their designated value, asking for a check on their polynomial coefficients. This includes cases where the transition temperature is different from the designated value by more then 10 K or like that of $N_2S$(s-1) and $N_2S$(s-2). In these cases the original designated temperatures were retained.

The use of transition temperatures dictated by polynomial coefficients is in line with the programming logic of the new code. At the convergence of the iteration on equilibrium temperature, if the converged temperature is not near the transition temperature of any substance, it is taken to be the equilibrium temperature. If it is close to the transition temperature of a substance, a transition test is performed. The transition temperature would be the equilibrium temperature if transition does occur; otherwise, the converged temperature is the equilibrium temperature. In this way, the case that at equilibrium there is no transition but the product mixture is at a temperature close to the transition temperature of a substance is covered. It also means that in the new code selection of condensed phases for consideration is based on transition temperatures which are consistent with the predictions of their polynomial coefficients.

To identify neighbouring condensed phases that may be in transition, at the convergence of the iteration on equilibrium temperature, all neighbouring condensed phases the transition temperatures (determined based on polynomial coefficients) of which are within 3 K from the converged temperature are recorded. The value of 3 K is arbitrarily chosen to represent a small temperature difference. It is possible that the converged trial equilibrium temperature is actually close to the transition temperatures of more than one substance. An example based on the phase transition curves for transitions from $Na_2SO_4$(s-I) to $Na_2SO_4$(lq) and from PbO(s-yw) (yellow lead oxide) to PbO(lq) which were determined to occur at 1157.00 and 1159.00 K, respectively, is illustrated in figure 3.5, where the converged trial equilibrium temperature is arbitrarily chosen as 1156.5 K. In this case, the melting temperatures based on polynomial coefficients agree with the designated values of 1157 and 1159 K. (In chapter 5, results of calculations involving this example performed by using the NASA code will be presented, showing that the NASA code has difficulties in analysing transition conditions of substances when their transition temperatures are close.)

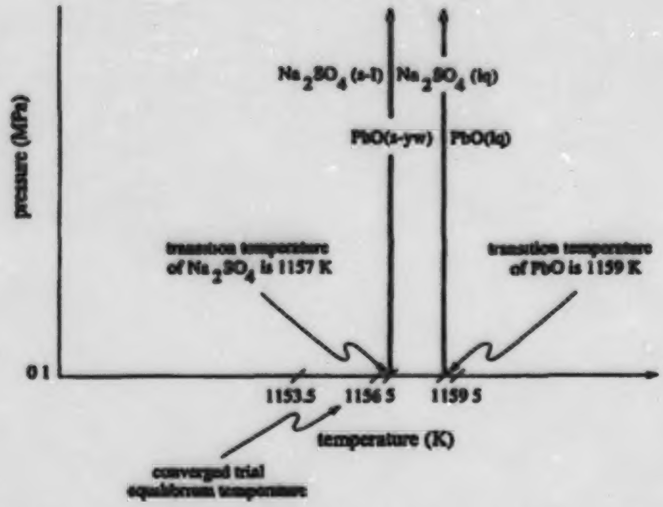
pressure (MPa)
$Na_2SO_4$ (s-I)
$Na_2SO_4$ (lq)
PbO(s-yw)
PbO(lq)
transition temperature of $Na_2SO_4$ is 1157 K
transition temperature of PbO is 1159 K
0 1
1153.5
1156 5
1159 5
temperature (K)
converged trial equilibrium temperature

Figure 3.5: An example illustrating that two substances the transition temperatures of which are within 3 K from the converged trial equilibrium temperature, based on the phase transition curves for transitions from $Na_2SO_4$(s-I) to $Na_2SO_4$(lq) and from PbO(s-yw) to PbO(lq) which occur at 1157 and 1159 K, respectively. The converged trial equilibrium temperature is arbitrarily chosen as 1156.5 K.

A pair of neighbouring condensed phases is considered to be in possible transition, if at least one of the two phases is determined to be present at the converged trial equilibrium temperature. That is even though the converged trial equilibrium temperature is close to the transition temperature of two neighbouring condensed phases, the two phases cannot be in transition if neither of them is present at this temperature. If the converged temperature falls on either side of the transition temperature of two neighbouring condensed phases, only the presence at equilibrium of the phase selected for consideration needed to be tested. In the unlikely event that the converged trial equilibrium temperature happens to be the transition temperature of two neighbouring condensed phases and both phases were selected for consideration, the test of presence at equilibrium of the two phases are required. In this case, if the phase stable below the transition temperature is present at equilibrium, then the two phases are considered to be in possible transition, regardless whether the phase stable above the transition temperature has been predicted, and the checking of the presence of the phase stable above the transition temperature is not required. However, if the phase stable below the transition temperature is absent at equilibrium, then the presence of the phase stable above the transition temperature would have to be checked. If it is present, then the two phases are still considered to be in possible transition.

The case of a converged trial equilibrium temperature happening to be the transition temperature of two neighbouring condensed phases has never occurred. Nevertheless, the new code have been tested for this case by specifying trial equilibrium temperatures as transition temperatures, or by assigning equal chemical potentials to two neighbouring condensed phases at the same temperature. In these tests, either one of the two phases or neither was determined to occur at equilibrium. The case of both phases existing at equilibrium has not been found; however, even if it happens it is doubtful that the amounts of the two phases will satisfy the constant internal energy constraint. A special procedure is required to treat the transition case.

Using melting as an example again, the melting problem is solved based on the fact that the two phases in melting will have equal chemical potentials. To all other species they are the same, and therefore their total amount can be obtained by considering only one of them. Thus, the equilibrium problem is re-solved by considering the solid phase alone at the transition temperature. When the solid phase amount at equilibrium has been determined, it is divided iteratively between the solid and liquid phases, until the constant internal energy constraint is satisfied.

The search of the amounts of the two phases is a root finding problem of the difference between the total internal energy of the product mixture and that of the reactants, with the root being the fraction of liquid of the total amount of both phases. An attempt is first made to bracket the root by finding this difference of total internal energy when no melting (solid phase only) is assumed and when complete melting (liquid phase only) is assumed. If the differences for these two cases have the same sign, then the substance under consideration is not in transition. If they are of opposite sign, then a root is bracketed, and it is solved by Brent's method.

A calculation like that described above is done for each pair of neighbouring condensed phases that are in possible transition, that is including those between two solid phases as well. In the case that if two or more pairs satisfy the transition condition, the pair which gives the lowest value of the system Helmholtz state function is taken to give the correct product mixture composition. (Nevertheless, it is not sure if such a case can actually happen.) If not a single pair satisfies the transition condition, then the converged trial equilibrium temperature determined before the transition test is the equilibrium temperature, and a recalculation is performed using this temperature to obtain the product mixture composition. The procedure for testing and treating transitions of neighbouring condensed phases is summarized in flow chart form in figure 3.6.

### 3.11.2 Procedure Based on the Blake Model of Phase Transition Curves

In the Blake code condensed species are assumed to have finite and variable molar volume. Because the molar volume of the solid phase of a substance is smaller then that of its liquid phase, their transition curve would be sloped and in general be curved as shown in figure 2.4. Melting of a substance can occur only if the system temperature falls within the temperature range spanned by its transition curve. For example, if the system is considered for system pressures above 1 atm, then melting of a substance can only occur if the system temperature is higher than its normal melting temperature. In addition, for a system temperature which falls within such a range, the liquid phase should be the stable phase if the system pressure is below the corresponding melting pressure of the given temperature, and the solid phase should be the stable phase if the system pressure is above the melting pressure. For the comparison with the Blake code, the new code used the same equation of state and fitted functional coefficients given in the library of the Blake code; hence, the new code used the same model of phase transition curves as used in the Blake code. The finding of the final solution to a problem which involves melting requires in general the solution of a series of problems for trial temperatures falling on either side of the final system temperature, with each of the problems involving either melting or close to melting conditions.

The new code detects a melting condition by detecting an oscillation in the system pressure when it changes from iteration step to iteration step. Suppose a trial system temperature falls within the temperature range covered by the transition curve of a substance and the substance is in melting, then during iterations an inconsistent iteratively determined system pressure would result if only one of the two phases is included. Because the molar volume of the solid phase is smaller than the liquid phase, when the entire amount of the melting substance is considered to be

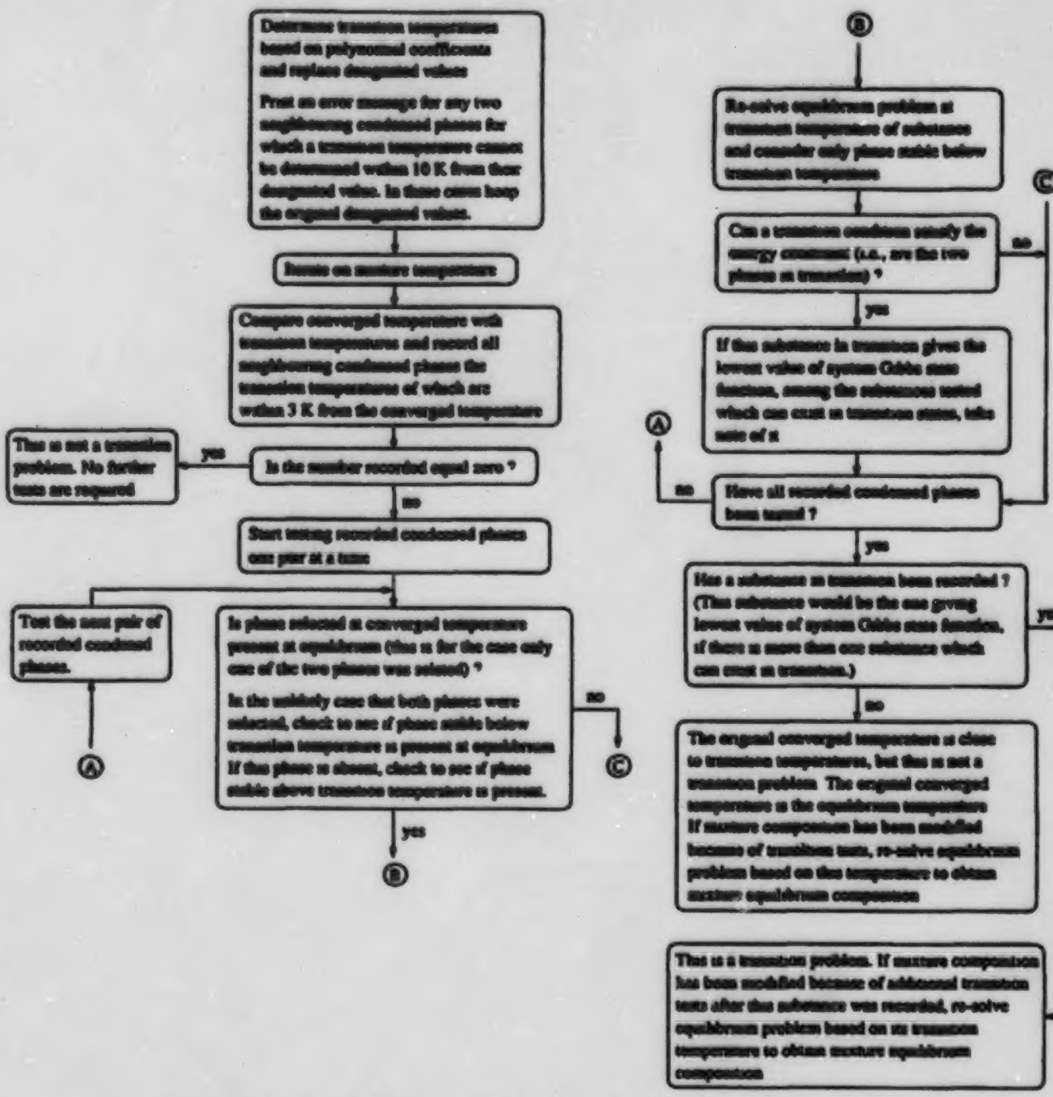
Determine transition temperatures based on polynomial coefficients and replace designated values
Print an error message for any two neighbouring condensed phases for which a transition temperature cannot be determined within 10 K from their designated value. In these cases keep the original designated values.
Iterate on mixture temperature
Compare converged temperature with transition temperatures and record all neighbouring condensed phases the transition temperatures of which are within 3 K from the converged temperature
This is not a transition problem. No further tests are required
yes
Is the number recorded equal zero ?
no
Start testing recorded condensed phases one pair at a time
Test the next pair of recorded condensed phases.
Is phase selected at converged temperature present at equilibrium (this is for the case only one of the two phases was selected) ?
In the unlikely case that both phases were selected, check to see if phase stable below transition temperature is present at equilibrium If this phase is absent, check to see if phase stable above transition temperature is present.
no
yes
Ⓐ
Ⓑ
Ⓒ
Re-solve equilibrium problem at transition temperature of substance and consider only phase stable below transition temperature
Can a transition condition satisfy the energy constraint (i.e., are the two phases at transition) ?
no
yes
If this substance in transition gives the lowest value of system Gibbs state function, among the substances tested which can exist at transition state, take note of it
Have all recorded condensed phases been tested ?
no
yes
Has a substance at transition been recorded ? (This substance would be the one giving lowest value of system Gibbs state function, if there is more than one substance which can exist at transition.)
yes
no
The original converged temperature is close to transition temperatures, but this is not a transition problem The original converged temperature is the equilibrium temperature If mixture composition has been modified because of transition tests, re-solve equilibrium problem based on this temperature to obtain mixture equilibrium composition
This is a transition problem. If mixture composition has been modified because of additional transition tests after this substance was recorded, re-solve equilibrium problem based on its transition temperature to obtain mixture equilibrium composition

**Figure 3.6: Flow chart for testing and treating transitions of neighbouring condensed phases, based on the NASA models of phase transition curves and molar volume of condensed phases.**

**present in the solid phase a system pressure below the melting pressure would be determined, which implies that the liquid phase is the stable phase and should really be present. The reverse is true when the entire amount of the melting substance is considered to be present in the liquid phase. Hence, an oscillation in the system pressure about the melting pressure occurs as the iterations continue, with the substance being considered to be present in the solid phase at some steps and in the liquid phase at the others. The only way to rectify this situation is by assuming the system**

to be at the melting pressure of the substance and the substance is in melting with part of it being present in the solid phase and part in the liquid phase.

There are two ways which can give rise to an oscillation in the system pressure. The first is when the melting substance is a component. At the beginning the entire amount of the melting substance will be present in only one of its two phases, while the other phase will be absent. However, whether the solid or the liquid phase happens to be present and in an amount large enough to be chosen as a component, there is a reaction representing a phase equilibrium between the chosen phase and the other phase (which is a noncomponent and is absent). Such a reaction is one which involves entirely condensed species. Thus, for example, when the solid phase is chosen as a component at a certain iteration step and the system pressure is determined to be below the melting pressure and the liquid phase becomes the stable phase, the special procedure for handling reactions involving entirely condensed species will lead to the deletion of the solid phase and transfer the entire amount of the substance to the liquid phase. For the next iteration step, the liquid phase will then be chosen as a component and the system pressure will be determined to be higher than the melting pressure, making the solid phase the stable phase. Consequently, the liquid phase will be deleted and the entire amount of the substance will be transferred back to the solid phase. The cycle repeats itself and gives an oscillation in the system pressure as the iterations continue.

The second way an oscillation can happen is when the melting substance is present in small amount and both its solid and liquid phases are noncomponents. This time there is no direct reaction relating the two phases, but rather each one of them is related to the components by a reaction in the same way, and mass transfer between the two phases would have to occur through changes in the components. The arising of the oscillation in the system pressure is similar to the case when the melting substance is a component, in the sense that the system pressure would fall below the melting pressure when the entire amount of the substance is considered to be present in the solid phase and the reverse is true with regard to the liquid phase. However, there is one difference, the switching between the two phases does not happen at each iteration step. Because the melting substance is present in small amount, the system pressure will be very close to the melting pressure whether the solid or the liquid phase is considered. Hence, the difference in the chemical potentials of the two phases will be small and the driving force for driving the mass transfer ("through the components") from one phase to the other will also be small. As a result, when one of the two phases is considered and there is an inconsistent system pressure determined indicating that the other phase should be the stable phase, many iterations is required to transfer materials to the stable phase, often exceeding the maximum number allowed for the equilibrium calculation. This situation may also arise in a case close to melting conditions, when the system pressure is also close to the melting pressure and the transfer of materials from the unstable to the stable phase is required. A special step is taken to rectify this situation.

For a given trial temperature, the new code prepares for the possibility of a melting problem by first determining the melting pressures of all those condensed substances selected for the problem and for which equation of state and fitted functional coefficients are available for both the solid phase and the liquid phase. However, not necessary a melting pressure can be determined for each of these substances, because only melting pressures from atmospheric to 15000 atm are determined. The former was chosen as a lower limit because it seems to be logical. The latter was chosen to represent an exceptionally large system pressure. Thus, if the given trial temperature falls below the normal melting temperature or higher than that at 15000 atm of a substance, a melting pressure will not be found for the substance at that temperature. Consequently, the possibility of melting needs only to be checked for those substances for which melting pressures are found, and these are the substances the following discussion will focus on. The melting pressure of a substance is determined by first bracketing and then by applying the Brent method to find the root to the difference in the chemical potentials of the two phases as a function of pressure.

It is possible that the system conditions are close to the melting conditions of more than one condensed substance. In this case, a wrong substance could be detected. As a conservative check, after one substance that is possibly in melting has been detected, all other condensed substances whose melting conditions are close to the one detected will also be recorded and possible melting of these other substances are tested as well. Such a check is done by making use of an upper limit in pressure above and a lower limit in pressure below the melting pressure of the substance first detected. In figure 3.7, such pressure limits has been plotted schematically for a substance's melting pressure from atmospheric pressure and up. (A more gentle slope of the transition curve has been used to make the illustration more visual.) The melting conditions of a second substance is considered to be in the proximity of that of the first detected, if its melting pressure is within the limits of that of the latter. The upper limit is defined to be three per cent or 15 atm, which ever is greater, higher than the melting pressure. The lower limit is similarly defined, and in the case the melting pressure is below 16 atm, it is taken to be 1 atm. A percentage based difference is used because at higher system pressures the fluctuations in pressure due to the switching between the solid and the liquid phase of a substance are also higher. As another conservative check, even if no oscillation is detected and an equilibrium calculation at a trial temperature has converged, if the converged system pressure falls within the pressure limits of any condensed substances, possible melting of these substances is checked as well.

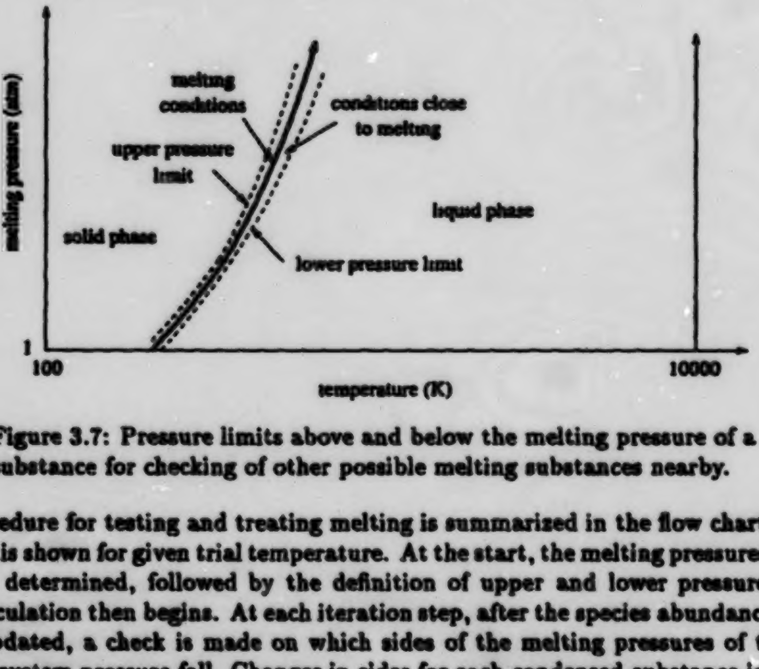

Figure 3.7: Pressure limits above and below the melting pressure of a substance for checking of other possible melting substances nearby.

The procedure for testing and treating melting is summarized in the flow chart in figure 3.8. This procedure is shown for given trial temperature. At the start, the melting pressures of condensed substances are determined, followed by the definition of upper and lower pressure limits. The equilibrium calculation then begins. At each iteration step, after the species abundances and system pressure are updated, a check is made on which sides of the melting pressures of the condensed substances the system pressure fall. Changes in sides for each condensed substance is tracked. The system is deemed to have possible melting conditions when changes in sides for one of the substances reaches seven times, and control is transferred out of the equilibrium calculation. Any additional condensed substances the melting pressures of which falls within the pressure limits of the first substance detected are then recorded, to prepare for the testing of possible melting conditions.

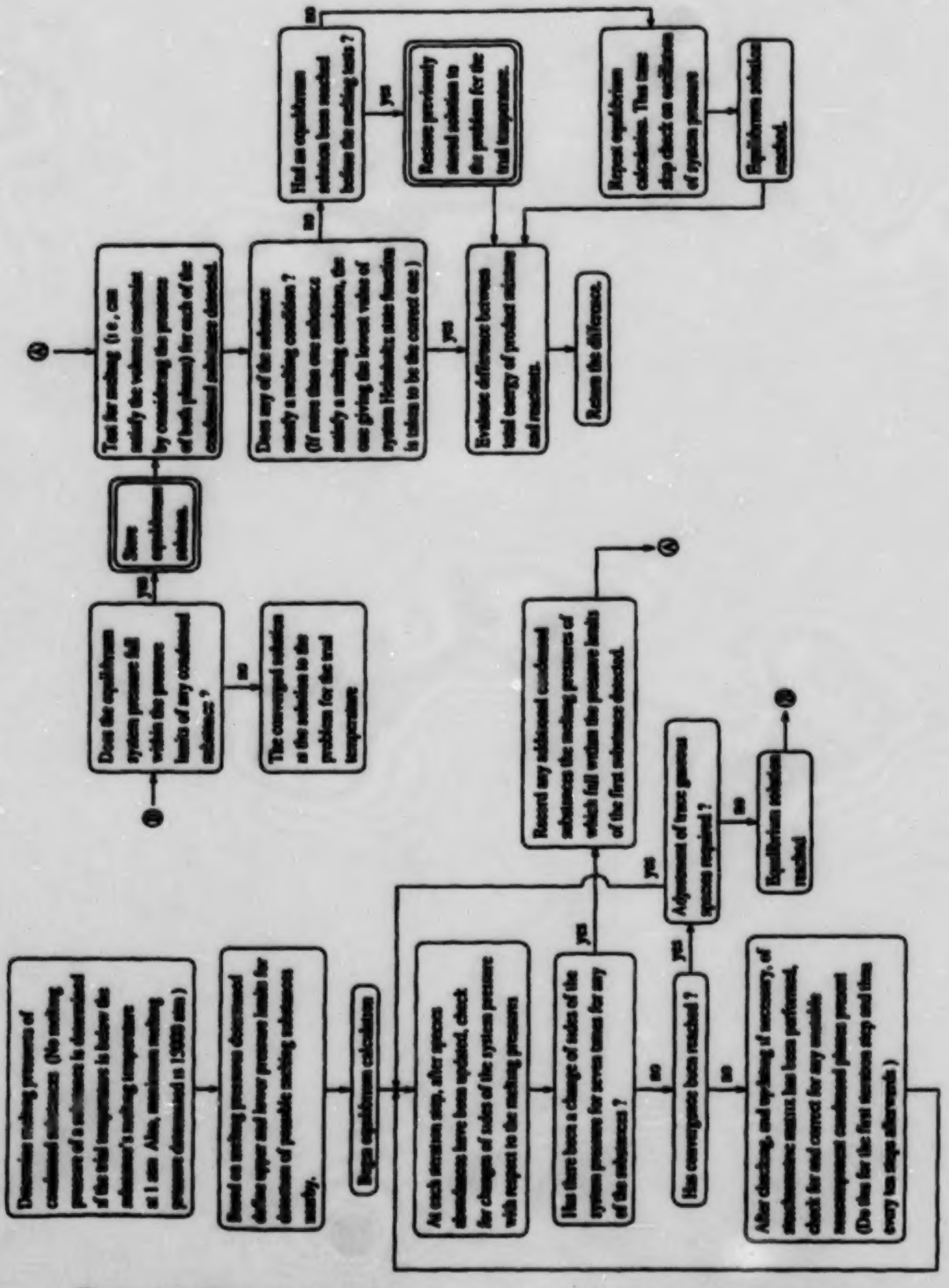

Determine melting pressures of condensed substances (No melting pressure of a substance is determined if the trial temperature is below the substance's melting temperature at 1 atm Also, maximum melting pressure determined is 15000 atm )
Based on melting pressures determined define upper and lower pressure limits for detection of possible melting substances nearby.
Begin equilibrium calculation
At each iteration step, after species abundances have been updated, check for changes of sides of the system pressure with respect to the melting pressures
Has there been a change of sides of the system pressure for seven times for any of the substances ?
yes
no
Has convergence been reached ?
yes
no
After checking, and updating if necessary, of stoichiometric matrix has been performed, check for and correct for any unstable noncomponent condensed phases present (Do this for the first iteration step and then every ten steps afterwards )
Record any additional condensed substances the melting pressures of which fall within the pressure limits of the first substance detected.
A
yes
Adjustment of trace gaseous species required ?
no
Equilibrium solution reached
B
B
Does the equilibrium system pressure fall within the pressure limits of any condensed substance ?
yes
no
Store equilibrium solution.
The converged solution is the solution to the problem for the trial temperature
A
Test for melting (i e , can satisfy the volume constraint by considering the presence of both phases) for each of the condensed substance detected.
Does any of the substance satisfy a melting condition ? (If more than one substance satisfy a melting condition, the one giving the lowest value of system Helmholtz state function is taken to be the correct one )
no
yes
Had an equilibrium solution been reached before the melting tests ?
no
yes
Restore previously stored solution to the problem for the trial temperature.
Evaluate difference between total energy of product mixture and reactants.
Return the difference.
Repeat equilibrium calculation. This time skip check on oscillation of system pressure
Equilibrium solution reached.

Figure 3.8: Flow chart procedure for a given trial temperature for testing and treating of melting of condensed substances, based on the Blake models of phase transition curves and molar volume of condensed phases.

Next, convergence of the calculation is checked. If convergence has not been achieved, the program will then check for the necessity of the updating, and update, if necessary, the stoichiometric matrix. After which, a special step is taken to rectify the situation of minor condensed species occurring at inconsistent system pressure, as mentioned above. If both phases of a substance are absent, no check is necessary; otherwise, the substance is tested for whether it is a noncomponent. If it is, then if any of its two phases is present as a unstable phase at an inconsistent system pressure, the amount is transferred to the stable phase. At melting or close to melting conditions, it is quite possible that both of the two phases of a noncomponent condensed substance occur at some iterations steps, and this transfer is performed whether the stable phase exists or not.

Such a check is performed at the end of the first iteration step of an equilibrium calculation and this is usually sufficient to correct a potentially inconsistent situation. After the initial check, checking is only performed every ten iteration steps. This is to give the abundances of the two phases a chance to settle in through the usual iterative procedure and to avoid unnecessary transfers. If the system has a noncomponent substance in melting, the presence of unstable phases and the side switching of the system pressure will continue until the seven counts is up, and control will be transferred out of the equilibrium calculation, as mentioned above. After this step, calculation proceeds to the next iteration.

If convergence of the main calculation has been reached then a check on the necessity of the adjustment of trace gaseous species is performed (more on this in the following section). If adjustment of trace gaseous species is required, then iterations will continue. Otherwise, a solution has converged, which normally would be an equilibrium solution. However, if the system pressure falls within the pressure limits of any condensed species, all such substances are recorded and a check on possible melting conditions is still done. Also recorded is the converged solution which is to be reassigned as the equilibrium solution for the trial temperature, in case no melting conditions are found. This saves the time for reevaluating the equilibrium solution after the tests.

In both cases, whether there has been an oscillation or a solution has actually been reached, possible melting of the recorded substances is tested one by one. A substance is in melting if the volume constraint can be satisfied by considering a portion of the substance to be in the solid phase and a portion in the liquid phase. The melting test is a constant temperature and pressure problem, at the trial temperature and the corresponding melting pressure of the substance. The determination of the total amount of the substance again makes use of the fact that at these conditions the chemical potentials of the two phases are equal and is done by assuming the entire amount to be present in the solid phase first. The absence of the liquid phase is guaranteed by making its chemical potential to be higher than that of the solid phase, again by adding two additional units to its nondimensional standard chemical potential, which is the basis for evaluating the chemical potential. After the total amount of the substance has been determined, a check on whether the two system total volume evaluated by assuming the entire amount of the substance to be present in the solid phase or in the liquid phase will bracket the constraint volume is performed. If the constraint volume is bracketed, the system is at the melting conditions of the substance. The portion of each phase present is determined by finding the root to the function of difference between the system total volume and the constraint volume, as a function of the fraction (valued from 0 to 1) of the liquid phase. Otherwise, the calculation will proceed, and test of melting of another condensed substance is done if necessary.

At the moment, only one substance in melting is assumed, the case more than one substance are simultaneously in melting (which would probably imply a nonunique solution) is excluded. (The Blake code also only deals with one substance in melting.) If more than one substance satisfies melting conditions, the one giving the maximum system entropy is taken to be the correct one.

If a solution at melting conditions is found, it is used for evaluating the difference between the total internal energy of the product mixture and the reactants at the trial temperature. Otherwise, depending on whether a converged solution was found and there is a prestored solution, which can be reassigned, or control was transferred out of the equilibrium calculation after oscillations were found, the calculation has to be repeated. (In figure 3.8 the step of storing a converged solution and the step of reassigning this solution have been shown in double boxes to indicate their link.) Either way the solution is then used for determining the difference in total internal energy at the trial temperature. The same subroutine used for the equilibrium calculation at the beginning is used for calculations for testing of melting and for repeating the equilibrium calculation after melting tests have failed, except that the check on oscillation in system pressure is skipped. In addition, in the former case, no updating of system pressure is required at each iteration step, as such the part in the subroutine for the evaluation of species chemical potentials corresponding to this step can be skipped, and the chemical potentials are evaluated at the fixed trial temperature and the fixed melting pressure of the substance under test.

A final remark regarding the aforementioned procedure is that for some cases, if initial oscillation in the system pressure suggests the possible existence of melting which, however, is not detected by the melting tests, and oscillation in the system pressure persists when a regular equilibrium solution is sought afterwards, a solution to this problem will not be found. It is most possible that such cases happen when the system condition is close to the melting conditions of two or more substances (which is a special condition); however, how likely, it is not sure, because calculations involving substances with melting conditions close to each other has only been done for one system (solutions were found for all cases attempted, except for one case which involves the possibility of the melting of two substances which is beyond the basic assumption of the present procedure).

Such cases occur when both phases of a condensed substance are considered simultaneously, which causes an oscillation. In retrospect, the equilibrium solution could have included an explicit iteration with the system pressure. This makes the constant-energy and constant-volume problem into a set of constant-temperature and constant-pressure problems. Stable phases can then be chosen on the basis of the trial system pressure and the current melting pressures, similar to the case of selecting stable phases in the NASA model for equilibrium solutions. However, this approach wastes CPU time, which is also why the approach of updating the system pressure at each iteration step was adopted. Also, the majority of problems do not involve melting. More work is needed to assess if this approach is a viable and better alternative for handling melting.

## 3.12 Inclusion of Numerous Gaseous and Condensed Species

In developing new formulations for energetic materials, uncommon elements are often tried and a large number of elements are may be included. This results in the simultaneous consideration of numerous possible product species. It is therefore desirable to ascertain if the new code can handle such cases. A second reason why such an investigation is worthwhile is that all the systems studied and reported in the literature for the VCS algorithm fall within the small to medium range.

A system was considered large if the number of species involved was four hundreds or more. To prepare for this, the variable arrays in the new code simply had to be dimensioned accordingly. Of the three major current codes, the NASA code is the one that can handle the largest number of species. It is six hundred, which is approximately one-third of the total number of species listed in the JANAF Thermochemical Tables. Consequently, for later comparisons, the new code was also dimensioned to handle this same maximum number of species.

# Chapter 4

# Computational Code, Validation, Capability and Robustness

Computational codes for solving equilibrium compositions of gaseous and condensed products of complicated combustion reactions at constant volume should be capable of handling a large number of gaseous and condensed species, including multiple condensed phases of the same substance (liquid and various solid phases) with a precise determination of which if any of these multiple phases exist at equilibrium. Such codes should also apply to high-pressure applications and handle nonideal gaseous mixtures with compressible condensates. In addition, it is desirable that such codes have the capability and versatility of using different equations of state for describing the $P$-$v$-$T$ properties of the various gaseous and condensed species, because, depending on the application, some state equations give a more accurate representation of such properties. Two last characteristics that are desirable of such codes are robustness and efficiency in achieving converged equilibrium solutions, which determine to a large extend how widely these codes are used.

A comprehensive computer code was developed in this study for chemical equilibrium analysis. A general description of the code is given first, followed by some code validations, detailed illustrations of code capabilities, demonstrations of code robustness, and some comparisons of predicted and experimental results.

## 4.1 Computational Code

A general description is given herein of the computational code that was written for this work to determine the equilibrium compositions of combustion products in a constant volume. A detailed description of the principles, models, procedures and mathematical equations used to develop the code was given in the previous chapter. The code is general in its application to a wide variety of chemical equilibrium problems, solving for the equilibrium compositions of the combustion products in a closed vessel.

The volume of the vessel is assumed constant and no heat loss is assumed to occur from the product mixture to the vessel walls. The latter assumption implies that the total internal energy of the products is constant and equal to that of the reactants before combustion. Therefore, the main problem solved by this code is a chemical equilibrium problem with constant total volume and internal energy as constraints. The solution is obtained by adapting the VCS algorithm for chemical equilibrium problems with constant temperature and pressure as the constraints. Note that this code can handle a large number of product species (gaseous and condensed). At this time, the code has been dimensioned to include seven hundred species in the calculation.

Different models for the gaseous mixture can be used in the code. The gaseous products can be assumed as a mixture of perfect gases, an ideal mixture of imperfect gases or a nonideal mixture of imperfect gases, which is the most general model for a gas mixture. If the gaseous mixture is assumed to be a mixture of perfect gases than the perfect gas equation of state should be used to describe the *P-v-T* properties of the gases. Otherwise, an equation of state for imperfect gases is needed for describing such properties.

Depending on the temperature and pressure ranges that a product mixture in an application may experience, one equation of state may describe the *P-v-T* properties of the gases more accurately than others and should be used. This code has the versatility that the equation of state used to describe such properties can be changed by modifying or replacing the subroutine for determining the chemical potentials of product species and the subroutine for finding the difference between the total internal energy of the product mixture and that of the original reactants. The guidelines for incorporating a new equation of state had been given in section 3.8.

Similarly, different compressibility models can be used for the condensed species. These species can be considered as compressible or incompressible. If they are considered incompressible, they can further be considered to have no volume or a constant volume. If the condensed species are assumed compressible, then an equation of state is required to describe their *P-v-T* properties. Again, the code has the versatility to allow different equations of state be used, depending on the application or preference. This is also achieved through modifications (or replacement) to existing subroutines for determining the chemical potentials of product species and the difference between the total internal energy of products and reactants, as in the case of gaseous species.

The greatest advantage of the present code is that no specific knowledge is required of which possible condensed species may exist at equilibrium and should be included, or be included in a particular order such that convergence can be achieved, in a calculation; all possible condensed species for an application can be included and the code can consider all of them and determine the amount of each condensed species present at equilibrium, which may be zero or nonzero.

## 4.2 Some Validations

Validations of the new computational code were carried out to ensure that it was written properly in terms of using chemical equilibrium principles correctly and avoiding programming errors. They were achieved by comparing results predicted by the new code with published data. Problems of the constant-temperature and constant-pressure type were used. The solution of this type of problem was checked because they are the actual chemical equilibrium minimization problems to be solved when solving constant volume problems, as described in section 3.5.

Three problems were considered which included: a hydrazine combustion problem, a blast furnace problem and a hydrogen-oxygen reaction problem. For the first two problems, values of abundances of species were compared. For the third, equilibrium constants, which can be evaluated once the abundances of species are known, were compared.

### 4.2.1 Hydrazine Combustion Problem

The first problem that was solved is related to the combustion of hydrazine, which was originally investigated by White *et al.* [1958]. Only gaseous species are involved in this problem. Combustion of an equimolar mixture of hydrazine ($N_2H_4$) and oxygen ($O_2$) was considered. Following the problem definition of White *et al.*, the combustion of one mole of the initial mixture was assumed to occur at 3500 K and 51 atm, and ten gaseous products forming a perfect-gas mixture were included. The original input data for standard chemical potentials and estimates of species abundances at equilibrium were also used. The composition of the gaseous products at equilibrium conditions was determined. The results given by the new programme and those listed in the book of Smith and Missen [1982, p. 146] are presented in table 4.1. Agreement to six or seven significant digits was obtained for most of the species.

Table 4.1: Comparison of species abundances at equilibrium for hydrazine combustion determined by using the Smith and Missen's and Wong's computational codes of the VCS algorithm.

| species | abundance determined by using computational codes of the VCS algorithm (mole) | | agreement in abundance computed by the two codes (significant digits) |
|---|---|---|---|
| | Smith and Missen's code | Wong's code | |
| $H_2O$ | $7.8314153\times10^{-1}$ | $7.8314158\times10^{-1}$ | 7 |
| $N_2$ | $4.8524622\times10^{-1}$ | $4.8524623\times10^{-1}$ | 7 |
| $H_2$ | $1.4773739\times10^{-1}$ | $1.4773736\times10^{-1}$ | 7 |
| OH | $9.6876244\times10^{-2}$ | $9.6876179\times10^{-2}$ | 6 |
| H | $4.0672719\times10^{-2}$ | $4.0672747\times10^{-2}$ | 6 |
| $O_2$ | $3.7316404\times10^{-2}$ | $3.7316441\times10^{-2}$ | 6 |
| NO | $2.7400034\times10^{-2}$ | $2.7400000\times10^{-2}$ | 6 |
| O | $1.7949382\times10^{-2}$ | $1.7949357\times10^{-2}$ | 6 |
| N | $1.4143465\times10^{-3}$ | $1.4143466\times10^{-3}$ | 7 |
| NH | $6.9318773\times10^{-4}$ | $6.9318879\times10^{-4}$ | 5 |

### 4.2.2 Blast Furnace Problem

The second problem involves a blast furnace that was studied by Madeley and Toguri [1973a, 1973b]. The blast-furnace problem requires the treatment of pure condensed species as well as gaseous species. The blast furnace problem involved six pure solids and nine gaseous species; however, only a subset of the six solid species were present at equilibrium. The species were formed of the five elements: C, O, H, Fe and Ca. Nitrogen as an inert gas was also present in the product mixture. When solving this problem, the solid species were assumed to have zero molar volume and the model of perfect-gas mixture was applied to the gaseous species. Using the original input data for standard chemical potentials [Smith, 1976] and initial estimates of number of moles, the composition of the product mixture at equilibrium at 1050 K and 1 atm was determined. The results given by the new programme and those listed in the book of Smith and Missen [1982, p. 210] are presented in table 4.2.

First of all, the amount of nitrogen as an inert gas in the product mixture remained unchanged from the initial to the equilibrium state; therefore, the two programmes must predict the same amount at equilibrium. In addition, the new programme did give the same predictions that only Fe(s) and CaO(s) existed at equilibrium. Comparison of number of significant digits in agreement was not needed for nitrogen and for the four solid species that were absent at equilibrium. Otherwise, an agreement to six or more significant digits in the results was achieved for most of the species. If fact, the species abundances at equilibrium obtained by the two programmes were the

Table 4.2: Comparison of species abundances at equilibrium for blast furnace problem determined by using the Smith and Missen's and Wong's computational codes of the VCS algorithm.

| species | abundance determined by using computational codes of the VCS algorithm (mole) | | agreement in abundance computed by the two codes (significant digits) |
|---|---|---|---|
| | Smith and Missen's code | Wong's code | |
| $N_2$ (inert) | $1.8710000\times10^{2}$ | $1.8710000\times10^{2}$ | † |
| CO | $8.1623915\times10^{1}$ | $8.1623915\times10^{1}$ | 8 |
| $CO_2$ | 6.6635330 | 6.6635332 | 7 |
| $H_2$ | 6.4270838 | 6.4260841 | 3 |
| $H_2O$ | $4.4381579\times10^{-1}$ | $4.4381556\times10^{-1}$ | 6 |
| $CH_4$ | $6.5487405\times10^{-3}$ | $6.5487176\times10^{-3}$ | 5 |
| $CH_2O$ | $2.3581110\times10^{-6}$ | $2.3581077\times10^{-6}$ | 6 |
| CHO | $1.0516532\times10^{-6}$ | $1.0516525\times10^{-6}$ | 7 |
| OH | $7.9295075\times10^{-11}$ | $7.9295822\times10^{-11}$ | 4 |
| $O_2$ | $1.7303566\times10^{-19}$ | $1.7303591\times10^{-19}$ | 6 |
| Fe(s) | $4.2827000\times10^{1}$ | $4.2827000\times10^{1}$ | 8 |
| CaO(s) | $7.5620000\times10^{-1}$ | $7.5620000\times10^{-1}$ | 8 |
| FeO(s) | 0 | 0 | – |
| $Fe_3O_4$(s) | 0 | 0 | – |
| $CaCO_3$(s) | 0 | 0 | – |
| C(s) | 0 | 0 | – |

† No determination of agreement in abundance in terms of number of significant digits was required.

same for both Fe(s) and CaO(s). Therefore, it was concluded that the understanding and coding of the VCS algorithm was both correct and verified, with particular reference to the treatment of the condensed species. Furthermore, the capability of the new programme to include inert species was considered to be demonstrated.

Even though the two programmes are based on the same solution algorithm, there will be small and even large differences in the coding of the algorithm. Furthermore, the verification is for the model of the product mixture that is assumed composed of a gaseous mixture and a number of pure condensed species. As noted in section 2.1.10, the models for the product mixture and species are separate entities. The former was fixed and the latter was varied. Although a perfect-gas mixture and zero molar-volume condensates was used as models for the gaseous and condensed species, respectively, the verification is valid for the other species models, which had been described in section 2.1.10. Finally, comparisons for more examples would have been done, had more output results from the original VCS programme been available in the Missen's book, but these were the only ones available.

### 4.2.3 Hydrogen-Oxygen Reaction Problem

Next, to obtain some indication and validation that the VCS algorithm was solving chemical-equilibrium problems correctly, the equilibrium compositions of a fairly simple system which involved the formation of water by the combination of hydrogen and oxygen was determined with the new programme. The calculated results that were obtained were then used to evaluate the equilibrium constants for the formation reaction and the values of the equilibrium constants determined were compared with those tabulated in the JANAF Thermochemical Tables [Chase *et al.*, 1985], and agreement to four significant digits was obtained.

Both gaseous and liquid water were considered in the system, which then consisted of the following four species: $H_2$, $O_2$, $H_2O$ and $H_2O(lq)$. An initial amount of one mole of hydrogen and oxygen was assumed. Two system conditions were considered. The first was 400 K and 1 bar, and the second was 298.15 K (25° C) and 1 bar. (SI units were used wherever possible.) The pressure unit of one atmosphere was used in the previous two examples because that was used in the original calculations. A system pressure of 1 bar was assumed for this and several other examples that follow, for the reason that thermodynamic properties of chemical species at this pressure are readily available from the JANAF Thermochemical Tables.) The vapour pressure of water at the two temperatures were determined, by linear interpolation of values in the ASME Steam Tables [Anon., 1967], as 2.457 and 0.03168 bar, respectively. The two conditions were chosen so that in the one case all the water existed in the vapour phase, that is, there was no liquid water at equilibrium and in the other case the water was existed in both the vapour and the liquid phases. (The reasoning for this inference will become clear after the discussion in the following section.) A perfect-gas mixture was assumed for the gases, and equation 2.60 was used to approximate the chemical potential of liquid water.

A complete set of stoichiometric equations relating the four system species are given as

$$H_2 + \frac{1}{2}O_2 = H_2O \tag{4.1}$$

and

$$H_2O = H_2O(lq). \tag{4.2}$$

Equation 4.1 represents the formation reaction of gaseous water from its elements. The system composition at equilibrium was solved with the new programme and the results are presented in table 4.3. Besides the abundances, the chemical potentials of the species at equilibrium are also listed for discussion. (Results were provided in five significant digits so that the precision of the resulting calculations can be maintained and that calculations and conclusions can be verified, in case the reader so wishes.) Mole fractions of the species are not listed because their actual values do not enter into the discussion. Because there was no liquid water present at equilibrium at the system temperature of 400 K, the discussion of the results at this temperature is simpler and therefore given first.

The results for the equilibrium conditions of a temperature of 400 K and a system pressure of 1 bar show that the initial one mole of hydrogen reacted completely with a half of a mole of oxygen

Table 4.3: Species abundances and chemical potentials at equilibrium of the hydrogen-oxygen reacting system determined by using the Wong's computational code of the VCS algorithm.

| species | system temperature | | | |
|---|---|---|---|---|
| | 400 K | | 298.15 K | |
| | abundance (mole) | chemical potential ($\mu/RT$) | abundance (mole) | chemical potential ($\mu/RT$) |
| $H_2$ | $1.0002\times10^{-29}$ | $-67.180$ | $1.4932\times10^{-42}$ | $-95.647$ |
| $O_2$ | $5.0000\times10^{-1}$ | $-1.0986$ | $5.0000\times10^{-1}$ | $-0.032193$ |
| $H_2O$ | 1.0000 | $-67.730$ | $1.6358\times10^{-2}$ | $-95.663$ |
| $H_2O(lq)$ | 0 | $-66.425$ | $9.8364\times10^{-1}$ | $-95.663$ |

to form one mole of water, which agrees with stoichiometry conditions as stated by equation 4.1. At equilibrium, even though the amount of water formed may not be exactly one mole and the oxygen left may not be exactly half a mole, these were the values assumed, because the amount of hydrogen remaining at equilibrium was practically zero. Furthermore, the value of number of moles of hydrogen left was retained for the computation of the equilibrium constant for the formation reaction. If the amount of hydrogen left was set to zero, then the value of the equilibrium constant would become infinite and indeterminate. In addition, the results show that the water formed would remain in the vapour state.

Another indication that the VCS algorithm had solved the problem correctly was verified by checking the chemical potentials of the species. The values of these potentials listed are nondimensional. The first check of the chemical potentials was done by means of the equilibrium condition. Equation 2.42 is a set of equations for the equilibrium conditions obtained from a complete set of stoichiometric equations of a system. Based on equations 4.1 and 4.2, they were applied to the system. Taking the chemical potentials as their non-dimensional values and putting the reactants and products on the opposite sides, the the equilibrium conditions are specified by

$$\hat{\mu}_{H_2} + \frac{1}{2}\hat{\mu}_{O_2} = \hat{\mu}_{H_2O} \tag{4.3}$$

and

$$\hat{\mu}_{H_2O} = \hat{\mu}_{H_2O(liq)}, \tag{4.4}$$

where $\hat{\mu}_{H_2}$ and similarly others are nondimensional chemical potentials. Equations 4.3 and 4.4 are similar to equations 4.1 and 4.2, except that chemical potentials are involved in one case and molecular formulae in the other. When the non-dimensional values of chemical potentials taken from table 4.3 were substituted in equation 4.3, the results for both equations sides agreed to four significant digits. The second check involving chemical potentials was in accordance with what was described about the determination of the presence and absence of a pure condensed species in section 3.2. The value of the chemical potential of liquid water was greater than that of gaseous water did agree with the prediction that liquid water could not exist at equilibrium.

The third indication that the VCS algorithm had solved the problem correctly was obtained by checking on the value of the equilibrium constant of the formation reaction of water. When the gaseous species, $H_2$, $O_2$ and $H_2O$ are assumed to form a perfect-gas mixture, the equation relating the equilibrium constant for the formation reaction, represented by equation 4.1, and their mole fractions can be written as follows [Reynolds and Perkins, 1977, p. 467]:

$$K_{eq_{H_2O}} = \frac{x_{H_2O}}{x_{H_2}\, x_{O_2}^{1/2}} \left(\frac{P_{sys}}{P^0}\right)^{-1/2}, \tag{4.5}$$

where $K_{eq_{H_2O}}$ is the equilibrium constant, $x_{H_2O}$ is the mole fraction of gaseous water and similarly for the others, $P_{sys}$ is the system pressure and $P^0$ is the standard reference pressure.

In this case, $P_{sys}$ had been chosen to be equal to 1 bar. Furthermore, the standard reference pressure used in the JANAF Thermochemical Tables [Chase *et al.*, 1985] is equal to 1 bar, and because the data for the calculation were taken from the JANAF Thermochemical Tables, $P^0$ would also have the value of 1 bar. Thus, the second term in the product on the right hand side of equation 4.5 involving $P_{sys}$ and $P^0$ is equal to one and was eliminated.

When values of the mole fractions of the gaseous species were substituted into equation 4.5, the value of the logarithm of the equilibrium constant to the base 10, $\log_{10}(K_{eq_{H_2O}})$, was determined to be 29.24, which agreed to four significant digits with the value for the same reaction that was tabulated in the JANAF Thermochemical Tables. In other words, the equilibrium constant for the formation reaction of gaseous water at the equilibrium conditions of 400 K and 1 bar, as determined from results obtained by the VCS programme, agreed with the tabulated value in the JANAF Thermochemical Tables.

For the system temperature and pressure of 298.15 K and 1 bar the discussion is similar. Firstly, the initial amount of one mole of hydrogen was found to react completely with half a mole of oxygen to form one mole of water. However, a large amount of water that formed condensed into liquid. At equilibrium, both gaseous and liquid water existed, and the two phases constituted one mole.

A check on some chemical-potential equations was also done. When values of the chemical potentials of the gaseous species were substituted into equation 4.3, once again the results on both sides of the equation was found to agree to four significant digits. In addition, this time, water in the gaseous mixture was in equilibrium with pure liquid water in the system, and the chemical potential of gaseous water was equal to that of liquid water. In other words, equation 4.4 held true. Finally, when values of the mole fractions of the gaseous species were substituted into equation 4.5, the value of $\log_{10}(K_{eq_{H_2O}})$ was determined to be equal to 40.05, which once again agreed to four significant digits with the tabulated value in the JANAF Thermochemical Tables for the same reaction.

In summary, the check that was made on the equilibrium constant, the value of $\log_{10}(K_{eq_{H_2O}})$ for the formation reaction of water, as determined by the new code based on the VCS algorithm and from those taken from the JANAF Thermochemical Tables, are repeated for convenient reference in table 4.4.

Table 4.4: Calculated and tabulated values of the logarithm to the base 10 of the equilibrium constants at 298.15 and 400 K of the formation reaction of water.

| state condition of system | | $\log_{10}(K_{eq_{H_2O}})$ | |
|---|---|---|---|
| temperature (K) | pressure (bar) | based on results from VCS algorithm | tabulated in JANAF tables |
| 298.15 | 1 | 40.05 | 40 05 |
| 400 | 1 | 29.24 | 29 24 |

Note that there should be no surprise that the calculated and tabulated values agree so well. Equilibrium constants are evaluated from standard free energy data [Reynolds and Perkins, 1977, p. 468] which are the same data used for determining the standard chemical potentials of species when carrying out equilibrium calculations. The check on the values of the equilibrium constants is qite similar to the case when the solution to an equation is back substituted into another equation which can be recasted from the original one. Therefore, the two equations contain the same information, and the solution also satisfies the second equation as expected. As a matter of fact, the use of equilibrium constants had been the traditional approach for solving equilibrium problems in the past. However, further details on this approach are skipped in order to focus on the present discussion.

The comparison of calculated results for two examples had been presented in this section, verifying that the VCS algorithm was understood and coded correctly. In addition, the results of calculations on the formation of water has also been reported, providing good indications that the

VCS algorithm is solving the chemical equilibrium problem properly. The part of the computational code which was written based on the VCS algorithm formed the basis for solutions of the closed-vessel problem. Calculated results for demonstrating the capability of the VCS algorithm in treating pure condensed species are presented in the next section. The example on the formation of water will appear again late.

## 4.3 Demonstration of Treatment of Condensed Species

Calculated results are presented in this section for some calculations that demonstrate the effectiveness of the VCS algorithm in handling pure condensed species. These calculations were done, once again, for systems at constant temperature and pressure conditions. The first capability to be demonstrated is the precise determination of the presence and absence of condensed species. The second capability to be demonstrated is the selection of stable condensed species. The third is the capability to handle many condensed species concurrently, and the fourth is the capability to handle systems that are composed solely of condensed species, that is the usual gaseous mixture in a system is not postulated.

### 4.3.1 Capability to Precisely Determine the Presence and Absence of Condensed Species

Two examples would be used for showing the first capability (presence). The first example is the formation of water from the reaction of hydrogen and oxygen, which we had used in the previous section. The second example involves a mixture of nitrogen gas, benzene vapour and toluene vapour, in which nitrogen was taken as an inert gas.

To illustrate the first example, reference is made to figure 4.1, in which equilibrium states of the hydrogen-oxygen reacting system held at temperature $T$ and pressure $P_{sys}$ are shown. Depending on the value of $P_{sys}$, there may or may not be liquid water present at equilibrium. When $P_{sys}$ has a value less than or equal to some particular value, $P_{sys}^{con}$, no liquid water will be present. On the other hand, if $P_{sys}$ has a value larger than $P_{sys}^{con}$, condensation of liquid water will occur and

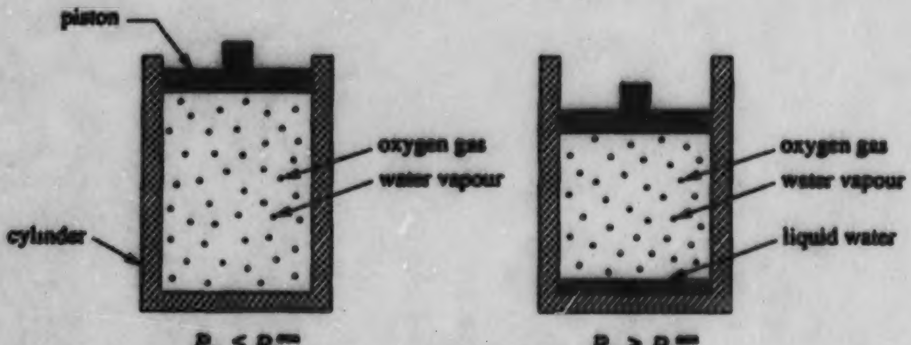

$P_{sys} \leq P_{sys}^{con}$ $P_{sys} > P_{sys}^{con}$

Figure 4.1: Equilibrium states of hydrogen-oxygen reaction system at temperature $T$ and pressure $P_{sys}$, where $P_{sys} \leq P_{sys}^{con}$ for one case and $P_{sys} > P_{sys}^{con}$ for the other.

liquid water will be present at equilibrium. At first the value of $P^{\mathrm{con}}_{\mathrm{sys}}$ is shown related to the vapour pressure of liquid water at $T$ and, the mole fraction of gaseous water in the equilibrium mixture in which only gaseous and no liquid water is present. After which, the VCS algorithm is then shown to predict the presence of liquid water at the right conditions.

The system of water formation from the reaction of hydrogen and oxygen, as discussed in the previous section, can be represented by equations 4.1 and 4.2. At equilibrium, the condition as stated by equation 4.3 holds true among the substances hydrogen, oxygen and gaseous water. If liquid water exists, then the additional condition of phase equilibrium between the gaseous and liquid water as stated by equation 4.4 is true. In other words, the chemical potential of gaseous water has to equal that of the liquid water. Assuming a perfect-gas mixture for the gaseous species, the chemical potential of gaseous water is then given by equation 2.68. Furthermore, if equation 2.60 for approximating the chemical potentials of pure condensed species is applied to the liquid water, equation 4.4 then becomes

$$\mu^0_{H_2O} + RT \ln p_{H_2O} = \mu^0_{H_2O} + RT \ln p^*_{H_2O(liq)} \,. \tag{4.6}$$

When equation 4.6 is simplified, the relation

$$p_{H_2O} = p^*_{H_2O(liq)} \tag{4.7}$$

is obtained. At equilibrium, if liquid water exists, then the partial pressure of gaseous water will have a value equal to that of the vapour pressure of liquid water.

Such a relation holds true only for the particular models used for gaseous and liquid water. The relation would be slightly different (some extra terms will be involved) when other models are used. In the case that the partial pressure of gaseous water is less than the vapour pressure of liquid water at the system temperature, there will be no liquid water present in the mixture. It turns out that the system pressure would have to be larger than a certain value before liquid water will form. Such a value is denoted as $P^{\mathrm{con}}_{\mathrm{sys}}$. And when liquid water exists, the partial pressure of gaseous water would be equal in value to the vapour pressure of liquid water. This situation is similar to that in which dew is formed in saturated air. These points will become clearer after some numerical results are given.

As a side note, the two conditions (a) that if the partial pressure of gaseous water has a value lower than that of the vapour pressure of liquid water, no liquid water will be present at equilibrium, and (b) that if liquid water is present at equilibrium, the partial pressure of gaseous water would be equal in value to the vapour pressure of liquid water, should be compared with those in the case where water is the only substance in a system. For such a case, as long as the pressure of gaseous water is less than the vapour pressure of liquid water, no condensation of liquid water will take place, and if there is condensation, the gaseous water will be at the vapour pressure of liquid water. The difference between the former and latter cases is that in the former case the partial pressure of gaseous water is involved whereas in the latter case the pressure of pure gaseous water is involved. Once again, the relation as stated by equation 4.7 does not hold in general. This parallelism stems from the fact that only an perfect-gas mixture has been assumed for the gases, and the simplified formula given by equation 2.60 for evaluating the chemical potential of liquid water was employed.

In the following, the results of a sample calculation for the system are presented. The system temperature was assumed to be 359.82 K (188.0 °F). At first, how the value of $P^{\mathrm{con}}_{\mathrm{sys}}$ was determined is shown. The partial pressure of gaseous water, $p_{H_2O}$, in the perfect-gas mixture at equilibrium is given by $P_{sys} x_{H_2O}$, where $x_{H_2O}$ is the mole fraction of gaseous water in the mixture. Substituting for $p_{H_2O}$, equation 4.7 becomes

$$P_{sys} x_{H_2O} = p^{\circ}_{H_2O(liq)}. \tag{4.8}$$

There was initially one mole each of hydrogen and oxygen in the system, and one mole of water was formed from the reaction between hydrogen and oxygen, with half a mole of oxygen left (see table 4.3). Hence, the mole fraction of gaseous water in the final gaseous mixture, without the presence of liquid water in the system, was 2/3. (The in-essence zero amount of hydrogen left at equilibrium had been neglected.) The vapour pressure of liquid water at 359.82 K was taken as 0.6169 bar fro the ASME Steam Tables [Anon., 1967]. Substituting the corresponding values of $x_{H_2O}$ and $p^{\circ}_{H_2O(liq)}$ into equation 4.8 and solving for $P_{sys}$, the value 0.92535 bar was obtained. This pressure was designated as $P^{max}_{sys}$. Because there is a one to one correspondence between $T$ and $p^{\circ}_{H_2O(liq)}$, there is also a one to one correspondence between $T$ and $P^{max}_{sys}$.

The pressure of 0.92535 bar was the highest system pressure at a temperature of 359.82 K for which no formation of liquid water occurred. Below this pressure, the mole fraction of gaseous water remained at the value of 2/3. The partial pressure of gaseous water was lower than the vapour pressure of liquid water, and no formation of liquid water occurred. Above this value the formation of liquid water was expected. The partial pressure of gaseous water remained equal to the vapour pressure of liquid water. Because the amount of water formed was shared between the gaseous and liquid phases, the amount of gaseous water existing at equilibrium was less than one mole. At the same time, the amount of oxygen left was unchanged, and the mole fraction of gaseous water decreased below 2/3.

The results given by the new programme did follow these trends. Calculations were done for the temperature value of 359.82 K and for values of pressure ranging from 0.9 to 1 bar. Selected results are given in table 4.5. The results of 0.9 and 0.92535 bar show that no liquid water was present at equilibrium at pressures below 0.92535 bar; however, the calculations for 0.9253501 and 1 bar show that liquid water was present at pressures above 0.92535 bar. Therefore, it can be seen that for pressures (e.g., 0.9253501 bar) which are only slightly higher than 0.92535 bar the VCS algorithm already predicted the presence of a minute amount of liquid water at the equilibrium conditions.

Table 4.5: Species abundances in the hydrogen-oxygen reacting system at equilibrium.

| | system pressure (bar) | | | |
|---|---|---|---|---|
| | 0.9 | 0.92535 | 0.9253501 | 1 |
| species | abundance (mole) | abundance ($\mu/RT$) | abundance (mole) | abundance ($\mu/RT$) |
| $H_2$ | $3.088342\times10^{-38}$ | $3.045745\times10^{-39}$ | $3.045744\times10^{-39}$ | $2.200405\times10^{-39}$ |
| $O_2$ | $5.000000\times10^{-1}$ | $5.000000\times10^{-1}$ | $5.000000\times10^{-1}$ | $5.000000\times10^{-1}$ |
| $H_2O$ | 1.000000 | 1.000000 | $9.999997\times10^{-1}$ | $8.051423\times10^{-1}$ |
| $H_2O(lq)$ | 0 | 0 | $3.242016\times10^{-7}$ | $1.948577\times10^{-1}$ |

To give a more complete presentation, the results of calculations were plotted in figure 4.2. In addition to the number of moles of species, the partial pressure of water in the gaseous mixture at equilibrium was also plotted. It can be seen that below 0.92535 bar, the partial pressure of water is lower than the vapour pressure of liquid water at 359.82 K, and no liquid water was formed. At

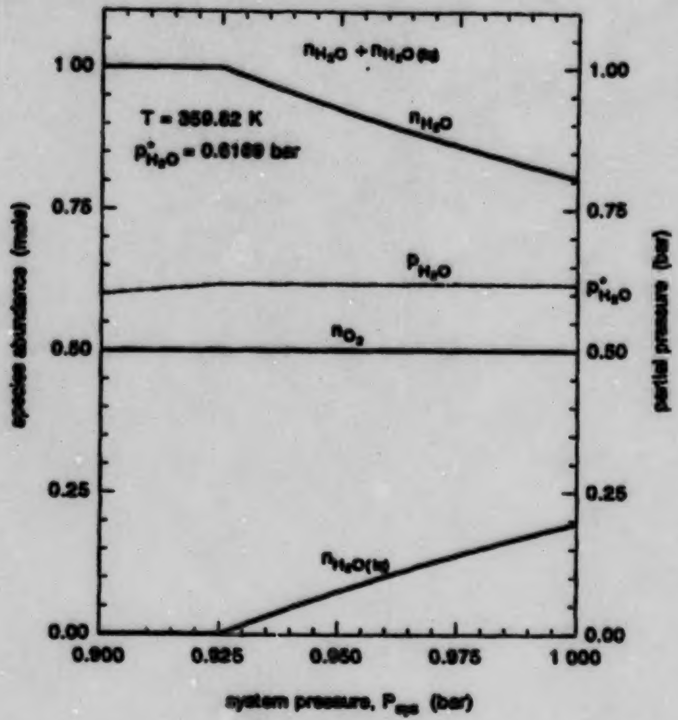

**Figure 4.2: Number of moles of $H_2O$, $H_2O(lq)$ and $O_2$, and partial pressure of $H_2O$, in the hydrogen-oxygen reacting system at equilibrium, at 359.82 K and system pressures ranging from 0.9 to 1 bar.**

pressures above 0.92535 bar, liquid water was present and the partial pressure of gaseous water remained equal in value to the vapour pressure of liquid water. In fact, as the system pressure increased above 0.92535 bar the amount of liquid water formed also increased. However, the total number of moles of gaseous and liquid water present at the equilibrium conditions has to equal unity. Hence, the amount of gaseous water that formed decreased by an equal amount. Also shown in the figure is the number of moles of oxygen existing at equilibrium, which stayed at 1/2 mole.

In the previous example, the determination of the absence or presence of the liquid phase of one substance was shown. One more example is given, showing the determination of the absence and presence of the liquid phases of two substances, and providing additional insights into the implications of the equilibrium condition between the liquid and vapour phases of a substance. Although the liquid phases of two substances were considered in this second case, the underlying chemical principles apply to an even larger number of liquids in equilibrium with their vapours.

In this second example, a mixture of nitrogen gas, benzene vapour and toluene vapour was considered. In the mixture, nitrogen was taken to be an inert gas, and only phase equilibria of benzene and toluene liquids with their own vapours were allowed. Using the same models for the gaseous and liquid phases, as employed in the first example, liquid benzene and liquid toluene were each found, once again, to condense at the condition when the partial pressure of the gaseous phase became equal in value to its vapour pressure.

The species involved were $N_2$, $C_6H_6$, $C_6H_6(lq)$, $C_7H_8$ and $C_7H_8(lq)$, where $C_6H_6$ and $C_6H_6(lq)$ represent the gaseous and liquid phases of benzene, respectively, and $C_7H_8$ and $C_7H_8(lq)$ represent the gaseous and liquid phases of toluene, respectively. The two phase-equilibrium processes assumed to occur inside the system can be represented as

$$C_6H_6 = C_6H_6(lq) \tag{4.9}$$

and

$$C_7H_8 = C_7H_8(lq). \tag{4.10}$$

The initial amounts of one-half of a mole of nitrogen and one mole each of benzene and toluene were assumed in this problem. The system temperature was taken as 298.15 K. The vapour pressure of benzene at such a temperature was evaluated to be 0.127 bar and that of toluene as 0.038 bar [Reid *et al.*, 1987, pp. 699, 705]. Calculations were done for values of system pressure ranging from 0.05 to 0.3 bar.

A plot of the results is given in figure 4.3. The amount of nitrogen stayed at half of a mole. It can be seen that the condensation of toluene vapour occurred before that of benzene vapour. This is because liquid toluene has a lower vapour pressure than liquid benzene and, toluene and benzene vapours had the same initial (before any condensation occurred) molar fractional amounts. When an analysis similar to the one done for water vapour in the previous example and based on the initial mole fraction of 0.4 was done for each of the two vapours, it was found that $P_{sys}^{con}$ of toluene vapour had a lower value than that of benzene vapour. The values for toluene and benzene vapours were 0.095 and 0.3175 bar, respectively.

Now, consider a slight twist to what had been said. The value of system pressure denoted by $P_{sys}^{con}$ was defined as the value above which the liquid phase of a substance would be present. In other words, it is the value of pressure at which condensation of the vapour of a substance is just about to occur. Thus, strictly speaking, the value 0.3175 bar was not the value of $P_{sys}^{con}$ for benzene vapour, because the vapour was not actually about to condense at such a value. This value was a working number, it was presented as a mean to explaining why toluene vapour was the first to condense.

The determination of the actual value of system pressure $P_{sys}^{con}$ of the benzene vapour was not as straightforward as that of the toluene vapour, which was the first vapour to condense. In fact, this would always be true for a system with two or more substances which might condense. This occurs because the mole fractions of the vapours do not stay constant in such problems, once the first condensation has occurred.

Before the condensation of toluene vapour had begun, the molar amounts of nitrogen, toluene and benzene vapours were constant, and so were their mole fractions. After condensation of toluene vapour occurred, its molar amount decreased, while that of nitrogen and benzene vapour remained the same. Therefore, the mole fraction of toluene vapour was decreasing, while that of benzene vapour was increasing. A relationship similar to equation 4.8 was still valid which relates to the system pressure, the mole fraction of benzene vapour and the vapour pressure of liquid benzene when liquid benzene was in equilibrium with its vapour. However, the value of $P_{sys}^{con}$ could not be determined by means of a straightforward substitution of the constant value of the initial mole fraction of benzene vapour, as was done for the water vapour in the previous example and the toluene vapour in this example.

When the value of system pressure $P_{sys}$ was increased, the mole fraction of benzene vapour was also increased, until their product, the partial pressure of benzene vapour, became equal in value to the vapour pressure of liquid benzene (0.127 bar), then for a further increase in $P_{sys}$

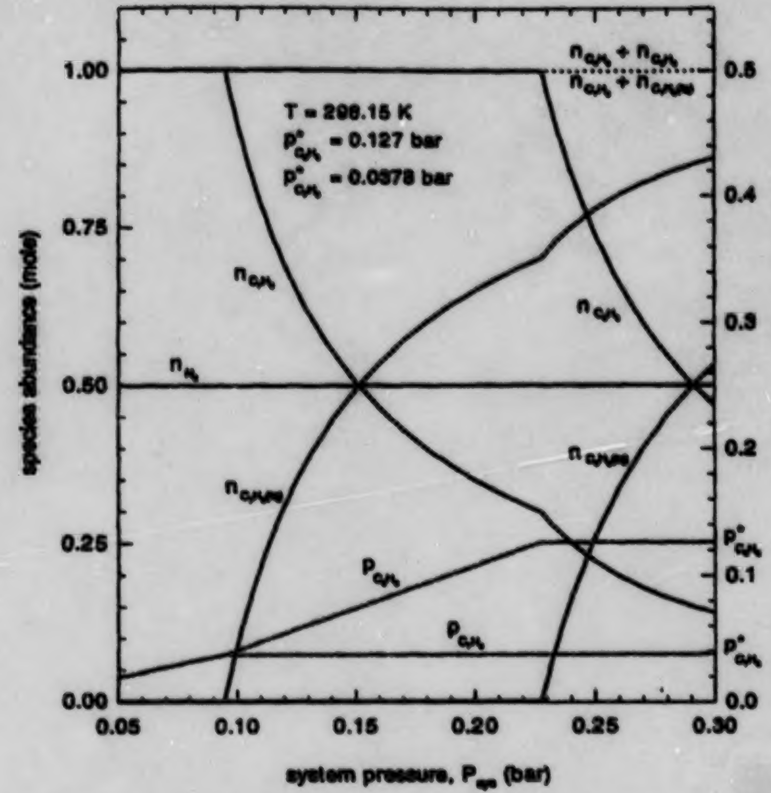

Figure 4.3: Number of moles of various species and partial pressures of $C_6H_6$ and $C_7H_8$ in the benzene-toluene-nitrogen phase equilibrium system, for $T = 298.15$ K and system pressures ranging from 0.05 to 0.3 bar.

the condensation of benzene vapour would occur and liquid benzene would become present at equilibrium conditions.

Once again, the value of system pressure $P_{sys}$, above which the condensation of benzene vapour was to occur, was designated as the symbol $P^{con}_{sys}$ for the benzene vapour. Such a value was determined to be 0.2285 bar. At the pressure 0.228501 bar, a minute amount of liquid benzene was determined to be present in the mixture.

At system pressures below 0.095 bar, the partial pressures of benzene and toluene vapours were equal but below the vapour pressures of their respective liquid phases. No liquid existed at equilibrium, both benzene and toluene vapours maintained their initial amounts (one mole). As the system pressure was increased, the partial pressures of benzene and toluene vapours increased.

At a system pressure of 0.095 bar the partial pressure of toluene vapour became equal in value to the vapour pressure of liquid toluene, so liquid toluene was about to condense. However, the partial pressure of benzene vapour was below the vapour pressure of liquid benzene, so no formation of liquid benzene occurred, and the benzene and toluene vapours stayed at their initial one mole amounts.

When the system pressure was increased just above 0.095 bar, liquid toluene was formed. As the system pressure was kept increased, the amount of liquid toluene present also increased, and an equal amount of toluene vapour was depleted. At the condition that half a mole of liquid toluene was present at equilibrium, there must also be half a mole of toluene vapour present in the mixture. This can be seen that the two curves representing the number of moles of liquid and vapour toluene crossed at the value of 0.5. The partial pressure of toluene vapour remained at the value of the vapour pressure of liquid toluene.

Because the mole fraction of toluene vapour was inversely proportional to the system pressure (see equation 4.8), the number of moles of toluene vapour also decreased in some inverse fashion. While the number of moles of toluene vapour decreased, the number of moles of nitrogen and benzene vapour remained unchanged, the mole fraction of benzene vapour in the gaseous mixture was therefore increasing. The partial pressure of benzene vapour was then increasing linearly. At 0.2285 bar, the partial pressure of benzene vapour reached the vapour pressure of liquid benzene, and liquid benzene was about to condense.

Above 0.2285 bar, condensation of benzene vapour occurred, and liquid benzene appeared at equilibrium. The partial pressure of benzene vapour also became remained at the value of the vapour pressure of liquid benzene. The changes in the numbers of moles of benzene vapour and liquid were similar to that of toluene. There was an increase in the rate of depletion of benzene vapour as the system pressure was increased. This occurs because its amount was inversely related to the system pressure and the amount of benzene vapour was decreasing.

Based on the results of the above two examples, summarized in figure 4.2 and figure 4.3, the effectiveness of the VCS algorithm in determining the absence and presence of pure liquid species had been clearly demonstrated. Even though, pure liquids had been used in the examples, the effectiveness applies equally well to pure solids.

A relation similar to equation 4.8 can also be obtained between the vapour and the solid phases of a substance. Hence, implications of such an equilibrium condition on the condensation of liquids are also valid in the case of solids.

The second capability of the VCS algorithm to be demonstrated is the selection of stable phases. The best advantage of this algorithm is its excellent capability in handling pure condensed species. No specific knowledge or guessing of which condensed species will exist at equilibrium is required. A list of chemically possible condensed species needs to be included only for consideration in an equilibrium calculation. At the end, the condensed species from the list that should be present at equilibrium, if there is any, will be retained. The determination of which condensed species would or would not exist at equilibrium follows the requirement of minimum system Gibbs free energy. That is, the combination of condensed species retained, should allow the system to have the lowest possible value of Gibbs free energy at a given state. Results of calculation of a equilibrium system for two different states will be presented, showing that the VCS algorithm was able to retain species representing stable condensed phases of substances and delete species of metastable condensed phases of substances, which had higher Gibbs free energies than the stable phases.

The system considered involved ten gaseous species and four condensed species formed from the four elements—carbon (C), sulphur (S), oxygen (O) and potassium (K). The species represented by their respective molecular formulae were give as follows: $CO_2$, CO, $SO_2$, K, SO, $O_2$, S, C, $K_2SO_4$, $K_2$, $K_2CO_3$(s), $K_2CO_3$(lq), $K_2SO_4$(s) and $K_2SO_4$(lq). The system pressure was assumed to have a value of 1 bar. Two different temperatures values were assumed, the first was set at 700 K and the second was taken as 1500 K. At 700 K, the solid species are the stable species and the liquid species are the metastable species. At the temperature of 1500 K, the opposite is true. The model of a perfect-gas mixture was applied to the gaseous species. For the condensed species, the model of zero molar-volume condensates was employed. Thermodynamic data were taken from the JANAF Thermodynamic Tables [Chase *et al.*, 1985]. The initial number of moles of each gaseous species was assumed to be unity. For the condensed species it was one tenth of a mole.

The number of moles of the species at equilibrium determined by using the VCS algorithm are shown in figure 4.4. It can be seen that the changes were fair in the number of moles of the abundant gaseous species, CO and S, when the system temperature was increased from 700 to 1500 K. On the other hand, the increases for the less abundant species like $CO_2$, $SO_2$, K, $K_2SO_4$ and $K_2$ were quite significant. The numbers of moles of C and $O_2$ were too small to be illustrated in the figure.

Shown in the lower shaded area are the numbers of moles of the condensed species. At 700 K, $K_2SO_4(s)$ and $K_2CO_3(s)$ were the stable species and retained. At the same time, $K_2SO_4(lq)$ and $K_2CO_3(lq)$ were the metastable species and were deleted. With the stable instead of the metastable species retained, the system Gibbs free energy was less at equilibrium. AT 1500 K, the stable and the metastable species were reversed. This time, $K_2SO_4(lq)$ and $K_2CO_3(lq)$, instead of $K_2SO_4(s)$

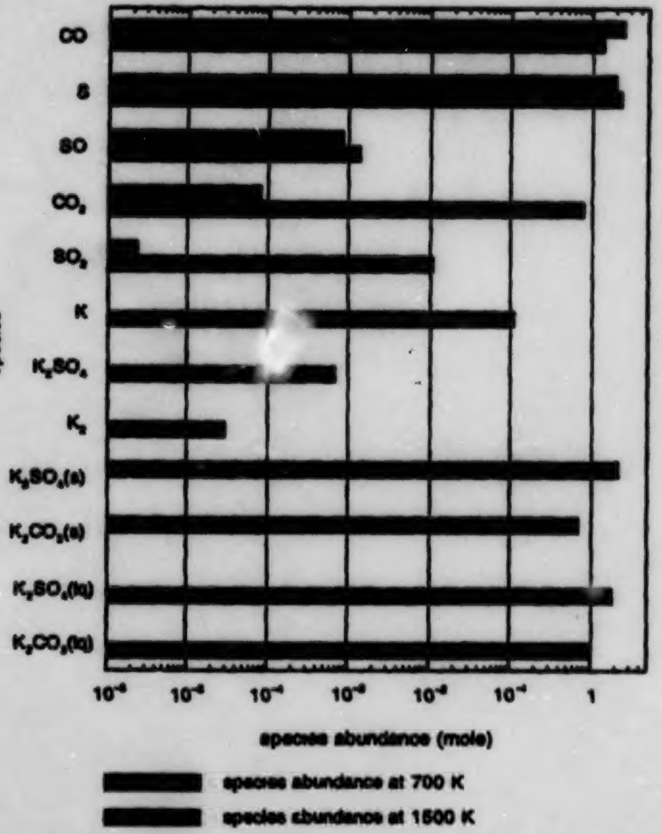

Figure 4.4: Numbers of mole of species at equilibrium of a system involving stable and metastable species, at $P_{sys}$ = 1 bar and $T$ = 700 and 1500 K.

and $K_2CO_3(s)$ were retained. The amount of $K_2SO_4(s)$ present at equilibrium at 700 K was larger than that of $K_2SO_4(lq)$ at 1500 K. However, the amount of $K_2CO_3(s)$ present at equilibrium at 700 K was smaller than that of $K_2CO_3(lq)$ at 1500 K. Because of the closed-system constraint, the abundance of each element was conserved. Hence, the increases in the numbers of moles of $SO_2$, K, $K_2SO_4$ and $K_2$, when the system temperature was increased from 700 to 1500 K, were due mainly to the decrease in the number of moles by the process of changing from $K_2SO_4(s)$ to $K_2SO_4(lq)$. Otherwise, the increases in the number of moles of $CO_2$ and in number of moles from going from $K_2CO_3(s)$ to $K_2CO_3(lq)$ must be related to the decrease in the number of moles of CO.

## 4.4 Demonstration of Treatment of Melting

In this section, results of calculations of problems involving melting obtained using the procedures described in section 3.11 are presented. Results obtained by using the procedure developed based on the NASA models of phase transition curves and molar volume of condensed phases are given first, followed by those based on the Bagheera models and the Blake models.

### 4.4.1 Results Based on the NASA Models

To demonstrate the capability of the new code in handling problems involving melting of a pure substance, calculations were done for a black powdrer of the following composition. Historically, black powders were used as propellants; however, in modern days they are often used as igniters to other propellants of more superior characteristics.

Ingredients listed in table 4.6 are the stable phases of substances at atmospheric conditions (298.15 K, 1 atm), and no separate phase designations are given. An ingredient may have a chemical name (e.g., potassium nitrate) or a common name (e.g., charcoal). Abbreviated names appear in brackets, as used by Freedman [1988], from which the formulae and enthalpies of formation of ingredients were taken. (Within experimental accuracy, standard enthalpies of formation of condensed phases are the same for a reference pressure of 1 atm or 1 bar.) The formula for charcoal involves summation; the ratios among the types of atoms forming the ingredient are given, and scaling for different bases applies. This explains the high numbers. Points regarding the ingredients of this formulation apply to the others given elsewhere in this report. The weight percentages were obtained by trials to produce melting conditions; they may not seem realistic.

Table 4.6: Composition of black powder used for calculations demonstrating the treatment of melting based on the NASA models of phase transition curves and molar volume of condensed phases.

| ingredient | formula | enthalpy of formation at 298.15 K (cal/mole) | percentage by weight |
|---|---|---|---|
| potassium nitrate (KN) | $K_1N_1O_3$ | −117,760 | 45 |
| susquehanna charcoal (SUSQ) | $C_{1331}H_{872}S_{6}N_{4}O_{100}$ | −4,490,000 | 23 |
| sulphur (S) | $S_1$ | 0 | 17 |
| liquid water (H2O) | $H_2O_1$ | −68,315 | 0.5 |
| ash (ASH, potassium carbonate) | $K_2C_1O_3$ | −274,900 | 14.5 |

The total number of species involved in this problem is 185. Of them 156 are gaseous species and 29 are condensed species. Out of the 29 condensed species, there are 12 neighbouring pairs. For three of these twelve pairs the transition temperatures cannot be determined within 10 K from their designated values. The pairs are as follows: $K_2S$(s-1) and $K_2S$(s-2), $K_2S$(s-2) and $K_2S$(s-3), and S(s) and S(lq).

The first calculation for this problem was carried out for a loading density of 0.1 gm/cm$^3$, and some calculated results are presented in table 4.7. When chemical equilibrium was obtained, melting between $K_2S$(s-3) and $K_2S$(lq) was discovered to occur. The designated melting temperature of $K_2S$(s3) is 1221 K, but the value dictated by the polynomial coefficients for the melting of $K_2S$(s-3) and $K_2S$(lq) was 1222.24 K, which is the equilibrium temperature. The equilibrium pressure was 15.56 MPa, and only the gaseous species having abundances larger than $10^{-10}$ kg-mole/kg-mixture are included in the table.

Table 4.7: Species abundances at $T = 1222.24$ K and $p = 15.56$ MPa from calculations for black powder at a loading density of 0.1 gm/cm$^3$, demonstrating the treatment of melting based on the NASA models of phase transition curves and molar volume of condensed phases.

| gaseous species | abundance (kg-mol/kg-mix) | gaseous species | abundance (kg-mol/kg-mix) | condensed species | abundance (kg-mol/kg-mix) |
|---|---|---|---|---|---|
| CO | $4.892\times10^{-3}$ | formic acid | $1.814\times10^{-8}$ | C(s-gr) | $6.765\times10^{-2}$ |
| $CO_2$ | $3\ 408\times10^{-3}$ | HNCO | $7.633\times10^{-9}$ | $K_2CO_3$(lq) | $1.653\times10^{-3}$ |
| $H_2$ | $2.782\times10^{-3}$ | $S_2O$ | $5.844\times10^{-9}$ | $K_2S$(s-3) | $9.430\times10^{-4}$ |
| $N_2$ | $2.250\times10^{-3}$ | KCN | $5.090\times10^{-9}$ | $K_2S$(lq) | $6\ 791\times10^{-4}$ |
| COS | $8.539\times10^{-4}$ | $SO_2$ | $5.030\times10^{-9}$ | | |
| $H_2O$ | $5.150\times10^{-4}$ | ethylene | $3.606\times10^{-9}$ | | |
| $H_2$ | $5.091\times10^{-4}$ | ethane | $2.177\times10^{-9}$ | | |
| $CS_2$ | $5.108\times10^{-5}$ | CS | $9.203\times10^{-10}$ | | |
| $CH_4$ | $3.599\times10^{-5}$ | K | $9.024\times10^{-10}$ | | |
| $S_2$ | $8.192\times10^{-6}$ | ketene | $6\ 323\times10^{-10}$ | | |
| $NH_3$ | $9.614\times10^{-7}$ | methanol | $3.879\times10^{-10}$ | | |
| SH | $2.702\times10^{-7}$ | SO | $3.556\times10^{-10}$ | | |
| HCN | $9.980\times10^{-8}$ | methyl cyanide | $1.830\times10^{-10}$ | | |
| KOH | $3.892\times10^{-8}$ | acetaldehyde | $1.260\times10^{-10}$ | | |
| formaldehyde | $2.571\times10^{-8}$ | $CH_3$ | $1.036\times10^{-10}$ | | |

To further illustrate the treatment of melting by the new computer code, additional calculations were performed for loading densities ranging from 0.095 to 0.105 gm/cm$^3$. As the loading density was increased, the condensed amount of $K_2S$ changed from being entirely in the solid phase, through an increasing melted portion, to being entirely in the liquid phase. Selected calculation results are plotted in figure 4.5 for loading densities ranging from 0.096 to 0.105 gm/cm$^3$. Calculations that were done for this case were lower than 0.096 gm/cm$^3$ for a direct comparison to the results from the NASA code.

Before melting occurred, the equilibrium temperature of the product mixture was rising with an increase in loading density. Once melting started, the equilibrium temperature remained constant at 1222.24 K until melting was complete and the entire condensed amount of $K_2S$ existed in the liquid phase only. Then the equilibrium temperature started to rise again. The rise in equilibrium temperature appeared as linear both before and after melting. However, the two segments representing the rises are plotted over very small ranges of the loading density and equilibrium

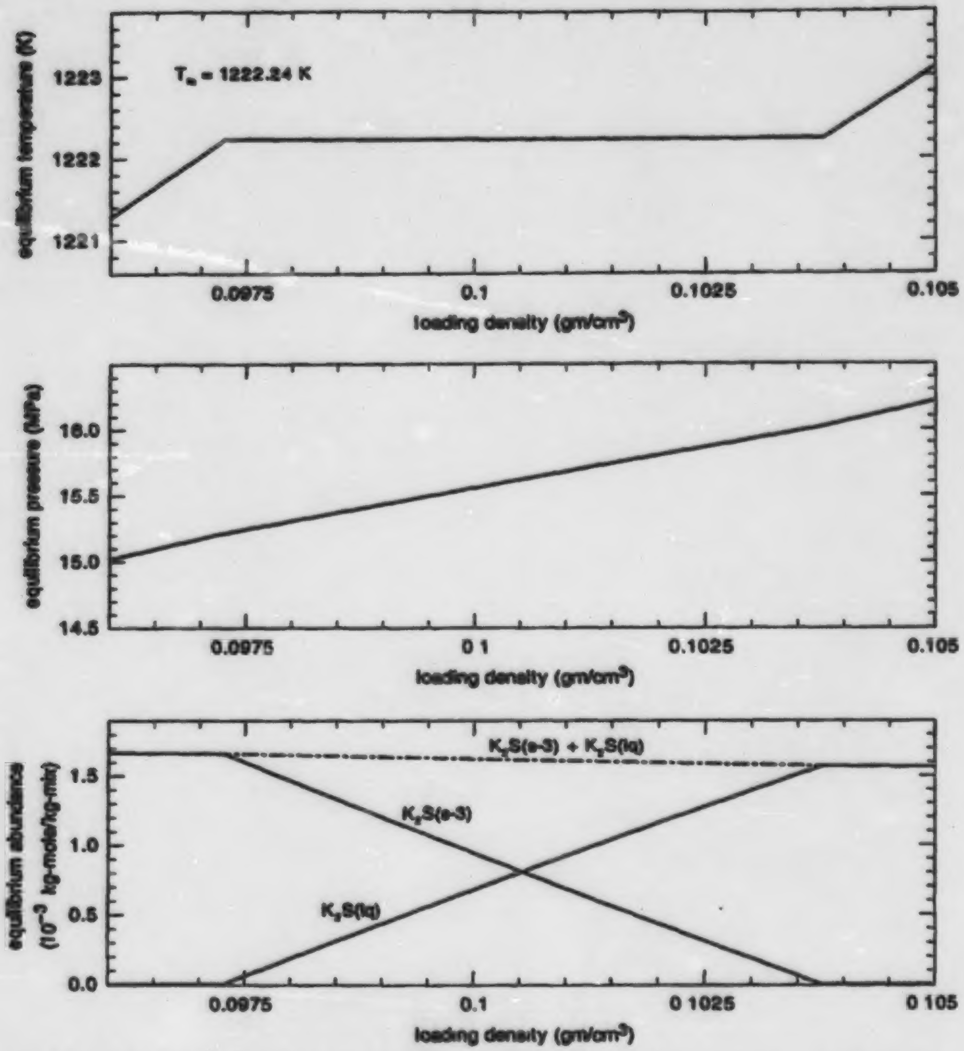

**Figure 4.5: Selected results of additional calculations of black powder problem for further illustration of the treatment of melting: equilibrium temperature and pressure of product mixture; equilibrium abundances of $K_2S$(s-3), $K_2S$(lq), and $K_2S$(s-3) and $K_2S$(lq) added together.**

**temperature. The equilibrium pressure of the product mixture was rising for the entire range of loading densities plotted. This rise was essentially linear, with two very slight changes in slope at the points where the melting started and stopped, a decrease in the former slope and an increase in the latter slope.**

**The total amount of condensed $K_2S$ decreased slightly over the range of the loading densities considered. The decrease was basically linear, with two very slight changes in the rate at where**

melting began and ended. There was an increase in the former slope and a decrease in the latter slope. Once melting commenced, the portion of $K_2S$(s-3) out of the total amount of condensed $K_2S$ started to diminish, while the portion of $K_2S$(lq) increased; both the decrease and increase were linear. Eventually, no more $K_2S$(s-3) existed at equilibrium and only $K_2S$(lq) remained. The results given in this figure demonstrate that the new code can handle the melting problem very well. Numerical values of some of the results plotted in this figure will be presented in chapter 5, in which the comparison of the treatment of melting between the NASA and new codes is discussed further.

### 4.4.2 Results Based on the Blake Models

To demonstrate that the new code can also treat problems involving a melting condensed product, for the Blake models of phase transition curves and molar volume of condensed phases, calculations were performed for two black powder formulations. The first one produced conditions involving a melting component and the second one involving a melting noncomponent. These two formulations in terms of weight percentages are tabulated in table 4.8.

Table 4.8: Compositions of black powder used for calculations demonstrating the treatment of melting based on the Blake models of phase transition curves and molar volume of condensed phases.

| ingredient | composition for demonstrating melting of a component (percentage by weight) | composition for demonstrating melting of a noncomponent (percentage by weight) |
|---|---|---|
| potassium nitrate (KN) | 54 | 49.3 |
| susquehanna charcoal (SUSQ) | 20 | 24 |
| sulphur (S) | 15 | 17 |
| liquid water (H2O) | 0.5 | 2 |
| ash (ASH, potassium carbonate) | 10 5 | 7.7 |

A total of 45 possible product species were selected from the library of the Blake code. There consisted of 36 gases and nine solids and liquids. Among the nine condensed species, eight of them were solid-liquid pairs of four substances. The truncated virial equation of state with the rigid sphere model was used to evaluate the third virial coefficients of the gases. The curve-fit coefficients used the evaluation of the standard thermodynamic properties of the product species, the force constants for the evaluation of the virial coefficients, and the coefficients used in the polynomial type of equation of state for describing the condensed species, were taken directly from the library in the Blake code.

In the first case, $K_2S$ was the component in melting. Nine calculations were carried out, and the equilibrium temperatures and pressures and the equilibrium abundances of $K_2S$(s) and $K_2S$(lq) are tabulated in table 4.9. Unlike the cases of the NASA and Bagheera codes, in which the melting temperature of a substance is constant, there was a small increase in the melting temperature, in agreement with the upward sloped trend of the transition curve. Furthermore, starting from $K_2S$ existing entirely in the solid form, there was a gradual increase in the proportion of liquid $K_2S$ determined by the new computer code, until finally the entire amount was in liquid form. The equilibrium abundances of the other five components for the loading density of 0.00085 gm/cm$^3$

Table 4.9: Selected results of calculations for the black powder problem for the formulation demonstrating the treatment of a melting component based on the Blake models of phase transition curves and molar volume of condensed phases.

| loading density (gm/cm$^3$) | equilibrium temperature (K) | equilibrium pressure (MPa) | equilibrium abundance (kg-mole/kg-mixture) | |
|---|---|---|---|---|
| | | | $K_2S$(s) | $K_2S$(lq) |
| 0.00085 | 1391 | 0.18 | $3.422\times10^{-3}$ | absent |
| 0.00086 | 1392 | 0.18 | $3.416\times10^{-3}$ | $6.424\times10^{-6}$ |
| 0.0009 | 1392 | 0.19 | $3.372\times10^{-3}$ | $5.030\times10^{-5}$ |
| 0.0015 | 1392 | 0.31 | $2.883\times10^{-3}$ | $5.424\times10^{-4}$ |
| 0.005 | 1392 | 1.02 | $1.746\times10^{-3}$ | $1.682\times10^{-3}$ |
| 0.021 | 1394 | 4.26 | $5.242\times10^{-4}$ | $2.905\times10^{-3}$ |
| 0.042 | 1396 | 8.60 | $5.548\times10^{-5}$ | $3.374\times10^{-3}$ |
| 0.0458 | 1396 | 9.40 | $5.371\times10^{-6}$ | $3.424\times10^{-3}$ |
| 0.0465 | 1396 | 9.55 | absent | $3.430\times10^{-3}$ |

were comparable to that of $K_2S$. They are quoted here in kg-mole/kg-mixture as additional information: $CO_2$ at $6.391\times10^{-3}$, CO at $4.892\times10^{-3}$, $N_2$ at $2.687\times10^{-3}$, $H_2O$ at $1.347\times10^{-3}$, and $S_2$ at $8.428\times10^{-4}$.

In the second case, $K_2CO_3$ was the noncomponent species in melting. Seven calculations were carried out in this case, and the equilibrium temperatures and pressures and the equilibrium abundances of $K_2CO_3$(s) and $K_2CO_3$(lq) are tabulated in table 4.10. This time, because $K_2CO_3$ was present in very small amount, the entire transition was completed with very little change in the equilibrium conditions. The equilibrium abundances of the six components for the loading density of 0.0876 gm/cm$^3$ are also quoted here in kg-mole/kg-mixture as additional information: CO at $5.359\times10^{-3}$, $CO_2$ at $4.883\times10^{-3}$, $H_2S$ at $3.037\times10^{-3}$, $K_2S$(s) at $2.662\times10^{-3}$, $N_2$ at $2.456\times10^{-3}$, and COS at $1.802\times10^{-3}$.

Table 4.10: Selected results of calculations for the black powder problem for the formulation demonstrating the treatment of a melting noncomponent based on the Blake models of phase transition curves and molar volume of condensed phases.

| loading density (gm/cm$^3$) | equilibrium temperature (K) | equilibrium pressure (MPa) | equilibrium abundance (kg-mole/kg-mixture) | |
|---|---|---|---|---|
| | | | $K_2CO_3$(s) | $K_2CO_3$(lq) |
| 0.0876 | 1199 | 16.85 | $3.335\times10^{-4}$ | absent |
| 0.08764 | 1199 | 16.86 | $3.292\times10^{-4}$ | $4.862\times10^{-6}$ |
| 0.088 | 1199 | 16.92 | $2.791\times10^{-4}$ | $6.067\times10^{-5}$ |
| 0.0887 | 1199 | 17.05 | $1.827\times10^{-4}$ | $1.681\times10^{-4}$ |
| 0.0895 | 1199 | 17.20 | $7.404\times10^{-5}$ | $2.893\times10^{-4}$ |
| 0.09 | 1199 | 17.29 | $6.939\times10^{-6}$ | $3.642\times10^{-4}$ |
| 0.091 | 1200 | 17.49 | absent | $3.775\times10^{-4}$ |

## 4.5 Demonstration of Inclusion of Numerous Gaseous and Condensed Species

To demonstrate that the new code can handle large systems, results of calculations of two formulations of an 18-element system obtained by using the new code are presented in this section. Because only comparisons with the NASA code were going to be done, the calculations were performed by using the same models of gaseous mixture and condensates used by the NASA code. In addition, fitted coefficients for the evaluation of species standard thermodynamic properties were taken from the NASA library.

Results for the two formulations are shown in table 4.11. There were twelve ingredients taken from several formulations used for comparison calculations to be discussed in chapter 5. The 18 elements were Ba, Cr, O, K, Cl, N, Na, Al, F, C, H, S, Pb, Mg, Ti, Li, B and Zr. The enthalpies of formation of $BaCrO_4$, $BaN_2O_6$ and $Na_3AlF_6$ were taken from the Bagheera code library of ingredients. The enthalpies of formation of $KClO_4$, PbO, $MgCO_3$, $TiO_2$ and LiH come from the JANAF Thermochemical Tables. The enthalpy of formation for $C_{11}F_{14}H_8$ was provided by DREV, and that for $MgCO_3$ comes from Freedman's article [1988]. The total number of product species considered was 587; 395 of them gaseous and 192 of them condensed.

Table 4.11: Two formulations of an 18-element system used for calculations demonstrating the handling of large systems by the new code. (Listed below the table are the numbers of gaseous and condensed species in the system.)

| ingredient | formula | enthalpy of formation at 298.15 K (cal/mole) | percentage by weight, composition number 1 | 2 |
|---|---|---|---|---|
| barium chromate | $Ba_1Cr_1O_4$ | −342,200 | 45 | |
| potassium perchlorate | $K_1Cl_1O_4$ | −102,800 | 5 | 5.5 |
| barium nitrate | $Ba_1N_2O_6$ | −238,280 | 1 | 1 |
| sodium cryolite | $Na_3Al_1F_6$ | −758,470 | 1 | 1 |
| Viton A fluoroelastomer | $C_{11}F_{14}H_8$ | −737,170 | 5 | 5 |
| magnesium carbonate | $Mg_1C_1O_3$ | −265,700 | 15 | 15 |
| potassium sulphate (KS) | $K_2S_1O_4$ | −342,660 | 5 | 5 |
| lead oxide | $Pb_1O_1$ | −52,440 | 8 | 8 |
| titanium oxide | $Ti_1O_2$ | −225,800 | 5 | 5 |
| lithium hydride | $Li_1H_1$ | −21,660 | 1 | 1 |
| boron | $B_1$ | 0 | 8 | 8 |
| zirconium | $Zr_1$ | 0 | 1 | 1 |

395 gaseous species, 192 condensed species, 587 species in total.

Results of calculations for the 18-element system for a loading density of 0.2 gm/cm$^3$ are presented in table 4.12. Equilibrium temperatures and pressures of the product mixtures and equilibrium abundances of the 14 most abundant gaseous species along with those of the condensed species are listed therein. However, the first case is a fairly regular problem with a moderate number of species and does not involve melting, so only the abundance of Cr(s) is listed. On the other hand, the second case involves numerous gaseous and condensed species and includes the melting of

**Table 4.12: Equilibrium temperatures and pressures and selected species abundances obtained by the new code for the 18-element system.**

| mixture properties | | |
|---|---|---|
| | composition 1 | composition 2 |
| T (K) | 2123 | 2130 |
| p (Mbar) | 16.54 | 16.87 |

| species abundances (kg-mole/kg-mixture) | | | | | |
|---|---|---|---|---|---|
| gases | composition 1 | composition 2 | condensates | composition 1 | composition 2 |
| $LiBO_2$ | $1.343\times10^{-3}$ | $1.243\times10^{-3}$ | $B_2O_3$(lq) | $2.487\times10^{-3}$ | $2.468\times10^{-3}$ |
| CO | $1.145\times10^{-3}$ | $1.152\times10^{-3}$ | C(s-gr) | $1.923\times10^{-3}$ | $1.910\times10^{-3}$ |
| $H_2$ | $1.068\times10^{-3}$ | $1.068\times10^{-3}$ | Cr(s) | $1.776\times10^{-3}$ | $8.399\times10^{-4}$ |
| $KBO_2$ | $9.189\times10^{-4}$ | $9.544\times10^{-4}$ | Cr(lq) | absent | $9.167\times10^{-4}$ |
| $NaBO_2$ | $1.395\times10^{-4}$ | $1.395\times10^{-4}$ | $BaF_2$(lq) | $9.983\times10^{-4}$ | $9.981\times10^{-4}$ |
| Pb | $4.627\times10^{-5}$ | $4.769\times10^{-5}$ | MgO(s) | $5.916\times10^{-4}$ | $5.431\times10^{-4}$ |
| HBO | $2.868\times10^{-5}$ | $2.999\times10^{-5}$ | $Mg_2TiO_4$(lq) | $5.814\times10^{-4}$ | $6.056\times10^{-4}$ |
| $CH_4$ | $1.220\times10^{-5}$ | $1.202\times10^{-5}$ | BaO(s) | $3.552\times10^{-4}$ | $3.175\times10^{-4}$ |
| LiCl | $1.076\times10^{-5}$ | $1.070\times10^{-5}$ | Pb(lq) | $3.114\times10^{-4}$ | $3.100\times10^{-4}$ |
| $HBO_2$ | $1.036\times10^{-5}$ | $1.071\times10^{-5}$ | BaS(s) | $2.869\times10^{-4}$ | $2.869\times10^{-4}$ |
| $BaCl_2$ | $9.495\times10^{-6}$ | $9.934\times10^{-6}$ | $BaCl_2$(lq) | $1.602\times10^{-4}$ | $1.776\times10^{-4}$ |
| KCl | $8.363\times10^{-6}$ | $8.651\times10^{-6}$ | $ZrO_2$(s-II) | $1.096\times10^{-4}$ | $1.096\times10^{-4}$ |
| K | $5.262\times10^{-6}$ | $5.497\times10^{-6}$ | BN(s) | $6.690\times10^{-5}$ | $6.654\times10^{-5}$ |
| $B_2O_3$ | $4.196\times10^{-6}$ | $4.485\times10^{-6}$ | TiC(s) | $4.453\times10^{-5}$ | $2.031\times10^{-5}$ |
| BOF | $3.677\times10^{-6}$ | $3.876\times10^{-6}$ | $MgAl_2O_4$(s) | $2.380\times10^{-5}$ | $2.380\times10^{-5}$ |

Cr, so the abundances of both of Cr(s) and Cr(lq) are listed. These results help demonstrate that the new code based on the VCS algorithm can handle a large system including numerous species and melting.

# Chapter 5

# Critical Assessment of Computational Codes

## 5.1 Equilibrium Calculations for a Moderate Number of Species with No Melting

### 5.1.1 Test Cases and Procedure

Five sample energetic materials were used as test cases, in order to help compare the capabilities of the new computational code in handling condensed species without melting to those of major codes developed previously (BLAKE, NASA, Bagheera). The first energetic material is a LOVA propellant; the second is a propellant for which DREV [Lussier, 1991] found that the Blake code would not converge; the third is a primer; the fourth is a black powder that can be used as an igniter; and the fifth is a delay (or fuse). Primers, igniters and propellants are normally used in sequence, with a primer initiating an igniter and an igniter initiating a propellant. Delays have relatively slow burning rates and are used for introducing time lapses between stages in pyrotechnic processes. These five test materials were chosen such that there is an increasing number and amount of condensed products present in the equilibrium product mixtures. In all cases the combustion of the energetic materials was assumed to occur in a constant-volume vessel under adiabatic conditions.

The compositions and thermodynamic data of the five energetic materials are listed in tables 5.1 to 5.5. The compositions of the first four energetic materials were provided by DREV; the fifth composition was taken with modification from the book *Chemistry of Pyrotechnics* by Conkling [1985, p. 130]. These tables provide the name, molecular or summation formula, enthalpy of formation and percentage by weight of each ingredient of the energetic material.

The name of an ingredient listed in the tables is a chemical name (e.g., potassium nitrate), common name (e.g., graphite), or trade name (e.g., Viton A), whichever seemed most appropriate. Many of the ingredients of the five samples were listed previously in Freedman's article [1988], in which they were assigned abbreviated names. These abbreviated names of some ingredients are also provided in the tables (in capital letters in brackets).

The formulae and enthalpies of formation were taken from different sources. Those for the LOVA propellant were used by DREV and were taken mainly from the library of ingredients of the Bagheera code. Those for the second propellant and black powder were also used by DREV and taken mainly from the library of ingredients of the Blake code and from Freedman's article.

Table 5.1: Composition of the LOVA propellant used for code comparisons.

| ingredient | formula | enthalpy of formation at 298.15 K (cal/mole) | percentage by weight |
|---|---|---|---|
| 1,3,5-trinitrohexa-hydro-s-triazine (RDX) | $C_3H_6O_6N_6$ | 16,760 | 76.0 |
| cellulose acetate butyrate (CAB) | $C_{4883}H_{6827}O_{3411}$ | −159,400,000 | 12.0 |
| ATEC | $C_{14}H_{22}O_8$ | −400,000 | 7.6 |
| nitrocellulose, 12.6% of nitration (NC1260) | $C_{22037}H_{27718}O_{36363}N_{8994}$ | −619,617,000 | 4 0 |
| ethyl centralite (EC) | $C_{17}H_{20}O_1N_2$ | −35,840 | 0.4 |

Table 5.2: Composition of the propellant with lead oxide used for code comparisons.

| ingredient | formula | enthalpy of formation at 298.15 K (cal/mole) | percentage by weight |
|---|---|---|---|
| nitrocellulose, 13.15% of nitration (NC1315) | $C_{6000}H_{7364}O_{10272}N_{2636}$ | −164,650,000 | 89.217 |
| amyl phthalate (AMYLPH) | $C_{18}H_{26}O_4$ | −220,900 | 6.499 |
| potassium sulphate (KS) | $K_2S_1O_4$ | −342,660 | 1.280 |
| ethyl centralite (EC) | $C_{17}H_{20}O_1N_2$ | −25,100 | 1.231 |
| diphenylamine (DPA) | $C_{12}N_1H_{11}$ | 31,070 | 0.985 |
| graphite (C) | $C_1$ | 0 | 0 591 |
| lead oxide (PbO) | $Pb_1O_1$ | −103,500 | 0.197 |

Table 5.3: Composition of the primer used for code comparisons.

| ingredient | formula | enthalpy of formation at 298.15 K (cal/mole) | percentage by weight |
|---|---|---|---|
| potassium nitrate (KN) | $K_1N_1O_3$ | −117,760 | 75 |
| magnesium carbonate | $Mg_1C_1O_3$ | −265,700 | 10 |
| boron | $B_1$ | 0 | 8 |
| Viton A fluoroelastomer | $C_{11}F_{14}H_8$ | −737,170 | 7 |

For the primer the enthalpy of formation of potassium nitrate was taken from the Blake library and that of magnesium carbonate from the JANAF Thermochemical Tables [Chase *et al.*, 1985], and the formula and enthalpy of formation of Viton A were provided by DREV. In the case of the delay the enthalpy of formation of barium chromate was taken from the Bagheera library and that of potassium perchlorate from the JANAF Thermochemical Tables.

Enthalpies of formation of ethyl centralite used for the LOVA and second propellant are different, because they were obtained from two sources. The formulae for ingredients such as cellulose, nitrocellulose and charcoal are summation formulae. They essentially give the ratios among the types of atoms involved in forming the ingredient and could be scaled based on different

Table 5.4: Composition of the black powder used for code comparisons.

| ingredient | formula | enthalpy of formation at 298.15 K (cal/mole) | percentage by weight |
|---|---|---|---|
| potassium nitrate (KN) | $K_1N_1O_3$ | −117,760 | 73.849 |
| susquehanna charcoal (SUSQ) | $C_{1831}H_{872}S_6N_4O_{100}$ | −4,490,000 | 15.746 |
| sulphur (S) | $S_1$ | 0 | 9.966 |
| liquid water (H2O) | $H_2O_1$ | −68,315 | 0.299 |
| ash (ASH, potassium carbonate) | $K_2C_1O_3$ | −274,900 | 0.140 |

Table 5.5: Composition of the delay used for code comparisons.

| ingredient | formula | enthalpy of formation at 298.15 K (cal/mole) | percentage by weight |
|---|---|---|---|
| barium chromate | $Ba_1Cr_1O_4$ | −342,200 | 80.0 |
| zirconium | $Zr_1$ | 0 | 8.5 |
| nickel | $Ni_1$ | 0 | 8.5 |
| potassium perchlorate | $K_1Cl_1O_4$ | −102,800 | 3.0 |

bases giving different sets of numbers of atoms. The bases used for the formulae in the Bagheera and Blake codes are obviously different; this explains why the numbers of atoms for the 12.6% nitrocellulose are so much larger than those for the 13.15% nitrocellulose. Even though formulae and enthalpies of formation of the five samples were taken from different sources, this would not affect the consistency of the comparisons, because ingredient information of an individual sample was kept the same when doing the comparisons.

The enthalpies of formation were required for energy considerations. When treating the conservation of energy constraint, the total internal energies of the energetic materials were needed, and they were obtained by summing the internal energies of the ingredients. Before combustion took place, the energetic materials, and thus their ingredients, were assumed to be at 298.15 K (25° C) and 1 atm. At these conditions, the internal energies of the ingredients, which are solids, can be approximated by their enthalpies, because their product terms between pressure and volume are small by comparison. In addition, their enthalpies at these conditions were taken to be their enthalpies of formation at the same conditions, which is common practice. This is why enthalpies of formation were required as input data.

According to DREV, the Blake code could not solve the second propellant problem because floating point errors occurred. However, if lead oxide was removed from the formulation, the code determined the equilibrium composition. Hence, it is important to keep the original composition, including lead oxide, and their enthalpies of formation for the comparison tests. In particular, the enthalpy of formation of lead oxide was found to be in error, the value quoted in the JANAF Thermochemical Tables [Chase *et al.*, 1985] is −52,440 cal/mole. The value −103,500 cal/mole was found both in the ingredient library of the Blake code and Freedman's article [1988].

The composition of the black powder is very close to that of Du Pont 3814 black powder quoted by Freedman [1988]. The original formulation of the delay given by Conkling [1985, p. 130] consisted a 17% by weight of a 50/50 zirconium-nickel alloy. Owing to the difficulty in obtaining the enthalpy of formation of this uncommon alloy, the formulation was altered to include elemental zirconium and nickel instead, for which the enthalpies of formation are simply zero. Also, for simplicity, an equal percentage by weight of 8.5% of each element was assumed.

The major objective of the present comparison was to demonstrate the robustness and efficiency of the new code relative to previously developed codes (NASA, Bagheera and Blake codes). In order to be sure that comparisons were between algorithms and to eliminate any uncertainties which may arise due to the use of different models and input data, the same gaseous mixture model, condensate model, equations of state, and species property and thermodynamic data were all kept the same when comparing the new code with a previous code. Hence, if a previous code has difficulties or fails to solve a problem while the new code succeeds, it can be attributed directly to the superiority of the solution algorithm of the new code. For comparison purposes, most calculations were performed for a loading density of 0.2 gm/cm$^3$.

Besides the capabilities of handling condensed species, the speeds of the solution algorithms of the new and previous codes were also compared in terms of central processor unit (CPU) times. The CPU times compared were times required for the actual solution of equilibrium problems, they were the times from the initial estimation of equilibrium compositions to the convergence of iterations determining the equilibrium compositions. The times taken for the processing of ingredients data, the selection of possible product species, and the processing and printing of final outputs were not included. Furthermore, all the codes were compiled with same compiling options and run on a Hewlett-Packard 9000 series model 433s workstation. In particular, no optimization of the codes performed by the compiler was specified.

Another aspect which would affect the CPU times is the number of product species considered for a problem. In order to have a proper comparison, when solving a problem, the number of species considered by the new code was kept the same as that considered by the previous codes. However, the meaning of keeping the same number of species requires some elaboration.

Ingredients of an energetic material are compounds composed of elements. In the NASA and Bagheera codes the variable arrays are large enough such that all the product species that may form from a subset of the elements defined by the ingredients and available in its thermodynamic library (curve-fit coefficients for various thermodynamic properties) are selected for a calculation. This is the basic list of product species considered. For each condensed product species there is an associated temperature range, with a temperature within which the species is considered as a stable phase and outside an unstable phase. (For example, liquid water in the NASA code is considered stable between 273.15 and 500 K.) The condensed species in the basic list, which are unstable for a trial equilibrium temperature under consideration are eliminated (not considered). Consequently, the condensed species considered at any one time are in general a subset of those in the basic list. The new code uses the same basic list of product species and selects the same stable condensed species as the NASA or Bagheera code.

The libraries of the NASA and Bagheera codes are very large; the number of gaseous species included in their lists can easily exceed a hundred when six to seven elements occur in a system. However, many of these gaseous species exist only in trace amounts, and their abundances in these codes are set to zero for computational efficiency and robustness. Specific cut-off limits in these two codes differs. However, the new code has an option so that the user can set the cut-off limit, which facilitates matching the number of gaseous species with nonzero abundances in the NASA and Bagheera codes.

In the Blake code, at most 29 gaseous species and the condensed species of ten substances can be selected for equilibrium calculations. (If data for both solid and liquid phases of a substance are available, they are selected together.) In general, not all of the possible product species in the library can be selected. Species are selected in the order that they appear in the library; and by specifying which species to omit, selection control is exercised. In general there are no guidelines, and one relies on experience. This certainly is the case when new or uncommon energetic materials are analysed for the first time. Gaseous species existing in significant amount and condensed species that should exist at equilibrium can be missed. The Blake code usually has great difficulties in choosing a set of components when condensed phases of a few substances are selected. Therefore, for comparison purposes when selecting product species, reference was made to the NASA or new code results, so that gaseous species selected would be the most abundant gaseous species if all the possible products were considered, and the condensed phases of substances for which one of the two phases was present at equilibrium were selected.

The use of the results of the NASA code to aid the selection of product species was suggested by Freedman [1982, p. 41]. However, the NASA and Blake codes use different models and data, the species abundances predicted by the two codes would be different. Therefore, the most abundant gaseous species predicted by the two codes were not necessarily the same. (Usually the same condensed species were predicted, except that the Blake code had difficulties in solving the problems which included condensed species of a few substances for consideration.) To achieve the above objective, calculations were performed by using the new code (using the same models and data as the Blake code), in which *all* possible product species that could be selected from the library of the Blake code were considered.

The library of the Blake code is much smaller than that of the NASA code; hence, it is possible for some gaseous species, which occur in fair amounts according to the NASA results, do not exist in the Blake library. It was the most abundant gaseous species which were also found in the library of the Blake code that were selected. If these selected most abundant gaseous species were different from those selected based on the results of the new code, the latter was followed. The two selections were considered to be different only when the two sets of species selected were different, the amounts of individual species selected could be different.

Even though selection of species based on the results of other computational codes was done to aid the achievement of solutions in the case of the Blake code, the selection did not base on the results of the new code at the outset. This was to avoid giving the impression that results of the new code which was to be compared with the Blake code were used directly to help to obtain the results of the Blake code.

For the final comparison, especially of the CPU times, the new code was rerun using the same list of species selected for the Blake code. Furthermore, in the Blake code, all the condensed species, after they were selected from the library, were considered between 300 and 5000 K, making no further selection based on whether the phases were stable or unstable for a given trial equilibrium temperature, as in the cases of the NASA and Bagheera codes. That is which of the two condensed phases, or none, of a substance would be present at equilibrium was determined through minimization. The new code followed the same procedure.

The CPU time taken by the new code to solve a problem is dependent on the initial temperature bracket for bracketing the equilibrium temperature. Since the equilibrium temperatures for many energetic materials lie between 2300 and 2700 K, these were the nominal values chosen for the initial temperature bracket. However, two of the sample energetic materials had equilibrium temperatures lower than 2300 K; for these two cases, additional runs were performed by using initial temperature brackets with temperature limits at approximately 200 K above and below the equilibrium temperature.

### 5.1.2 Comparison of Results of the NASA and New Codes

Equilibrium calculations were done for the previously defined five energetic materials using the NASA and new codes. For each test case, the new code was used to do calculations using the models, number of species and input data matching those of the NASA code. Values of the equilibrium temperatures and pressures of the product mixtures and the CPU times for computer runs, as determined by the NASA and new codes are summarized in table 5.6. These calculations were performed by assuming that the gaseous species were perfect gases and that the condensed species had zero molar volumes.

The LOVA propellant consisted of the four elements C, H, N and O. The seven condensed species considered was small in comparison to the 133 gaseous species. At equilibrium, only the gaseous species were present (no condensed species). Note that the number of system elements, number of gaseous and condensed species considered, number of condensed species present at equilibrium, and some other data are summarized in the table (see the table footnotes).

The propellant with lead oxide consisted of the seven elements C, H, O, N, K, S and Pb. In this case the number of gaseous species considered was 160, and the number of condensed species considered at 38 was much larger than that for the LOVA propellant. However, again, only gaseous species existed at equilibrium.

Table 5.6: Comparison of the equilibrium temperatures and pressures and CPU times for the NASA and new codes for five sample energetic materials all at a loading density of 0.2 gm/cm$^3$.

| energetic material | mixture properties and CPU time | NASA code | new code | CPU ratio | temperature range (K) |
|---|---|---|---|---|---|
| Lova propellant (4, 133, 7, 0, 0%, 0%)[†] | $T$ (K) | 2551 | 2551 | | |
| | $P$ (MPa) | 204.0 | 204.0 | | |
| | CPU time (s) | 0.29 | 1.67 | 5.8 | 2300–2700[‡] |
| propellant with lead oxide (7, 160, 38, 0, 0%, 0%) | $T$ (K) | 2421 | 2421 | | |
| | $P$ (MPa) | 178.6 | 178.6 | | |
| | CPU time (s) | 0.46 | 3.91 | 8.5 | 2300–2700 |
| primer (8, 214, 37, 2, 6.3%, 6.4%) | $T$ (K) | 2538 | 2538 | | |
| | $P$ (MPa) | 73.37 | 73.37 | | |
| | CPU time (s) | 1.32 | 9.97 | 7.6 | 2300–2700 |
| black powder (igniter) (6, 156, 29, 2 17.9%, 45.1%) | $T$ (K) | 2153 | 2153 | | |
| | $P$ (MPa) | 58.61 | 58.61 | | |
| | CPU time (s) | 1.09 | 19.12 | 17.5 | 2300–2700 |
| | CPU time (s) | 1.09 | 8.80 | 8.1 | 2000–2400 |
| delay or fuse (7, 27, 29, 6, 79.7%, 94.0%) | $T$ (K) | 361.1 | 361.1 | | |
| | $P$ (MPa) | 1.12 | 1.12 | | |
| | CPU time (s) | 2.93 | 2.55 | 0.9 | 2300–2700 |
| | CPU time (s) | 2.93 | 2.19 | 0.7 | 300–500 |

[†] The six numbers in brackets denote *(1)* number of system elements, *(2)* number of gaseous species considered, *(3)* number of condensed species considered, *(4)* number of condensed species present at equilibrium, *(5)* percentage of condensates by mole, *(6)* percentage of condensates by weight.

[‡] Temperature range used in the new code to start the equilibrium calculations.

The primer consisted of the eight elements B, C, F, H, K, Mg, N and O. This was the system involving the largest number of elements; hence, the number of gaseous species at 214 and condensed species at 37 were also the largest. Only two condensed species were present at equilibrium, that is liquid $MgF_2$ and solid MgO.

The black powder consisted of the six elements K, N, O, S, C and H. Even though the number of elements involved was one less than that of the propellant with lead oxide, the numbers of gaseous species at 156 and condensed species at 29 considered in these two cases were very close. This is a result of the type of elements involved. At equilibrium, two condensed species were present, liquid $K_2CO_3$ and liquid $K_2S$, but they exist in higher percentages than the two liquids for the primer.

For the four energetic materials cases just discussed, the NASA code obtained results without any difficulty, and so did the new code. The equilibrium temperatures and pressures and the equilibrium abundances obtained by using the two codes agreed to four significant digits. However, the species abundances are too numerous to list. Even though the equilibrium temperatures of the product mixtures of the first three materials were roughly equal, the equilibrium pressures decreased by fairly large percentages. This was due to a decrease in the predicted amount of gases present in the product mixtures.

The delay consisted of the seven elements Ba, Cr, O, K, Cl, Zr and Ni. Although a fair number of elements were involved, for this combination of elements, the number of possible product species from the library of the NASA code that could be selected was not large; 27 gaseous and 29 condensed species. The new code was able to consider all of them together, in particular all 29 condensed species, and determine at equilibrium that six condensed species were present. In descending order of abundances the six condensed species were BaO(s), $Cr_2O_3$(s), Ni(s-$\alpha$), $ZrO_2$(s-$\alpha$), KCl(s), and $BaCl_2$(s-$\alpha$).

Even though the NASA code predicted the same equilibrium temperature and pressure given by the new code, the solution of the problem itself was not straightforward. It was affected by factors such as whether condensed species were specified for consideration right from the beginning, the order these condensed species were specified, and whether multiple loading densities were considered. The NASA code also required more iterations than normal. In addition, even if a solution was reached, singular matrices were often encountered. The problem for the delay or fuse is a good test case because, firstly, there are a fair number of condensed species present at equilibrium, and, secondly, many of the species including one condensed species are present in trace amounts. The consideration of these trace species helps to illustrate some difficulties that can be encountered by the NASA code when solving a problem involving many condensed species.

Some selected results from a variety of runs with the NASA code for the delay problem will be presented in tables 5.7 to 5.10 for discussion. Most of these results are at a loading density 0.2 $gm/cm^3$. These tables include the number of coefficient and derivative matrix singularities encountered during the courses of iterations, and include the abundances of the trace species $BaCl_2$(s-$\alpha$), $NiCl_2$ and ClO. Each run gave the same equilibrium temperature and pressure and the abundances of the major species other than $BaCl_2$(s-$\alpha$), $NiCl_2$ and ClO, so only the abundances for $BaCl_2$(s-$\alpha$), $NiCl_2$ and ClO are listed and discussed.

The effects on the NASA calculations of the initial specification of condensed species to be considered from the start, in order to obtain a solution, are now discussed. These results are given in table 5.7. The main differences in starting the NASA calculations are the initial specification of the condensed species. The four runs start with zero, four, five or six condensed species, listed in the table, and included in the descending order of their equilibrium abundances determined by the new code. Note that the results for the cases of one, two or three initially specified condensed

Table 5.7: Selected NASA code results for the delay with 0, 4, 5 and 6 condensed species† at a loading density of 0.2 gm/cm$^3$.

| condensed species | none | BaO(s), $Cr_2O_3$(s), Ni(s-$\alpha$), $ZrO_2$(s-$\alpha$) | BaO(s), $Cr_2O_3$(s), Ni(s-$\alpha$), $ZrO_2$(s-$\alpha$), KCl(s) | BaO(s), $Cr_2O_3$(s), Ni(s-$\alpha$), $ZrO_2$(s-$\alpha$), KCl(s), $BaCl_2$(s-$\alpha$) |
|---|---|---|---|---|
| number of coefficient matrix singularites | 0 | 3 | 1 | 2 |
| number of derivative matrix singularites | 0 | 1 | 0 | 0 |
| $BaCl_2$(s-$\alpha$) abundance (kg-mole/kg-mixture) | f.p. error | not predicted | $1.265\times10^{-21}$ | $4.466\times10^{-21}$ |
| $NiCl_2$ abundance (kg-mole/kg-mixture) | f.p. error | not predicted | $1.914\times10^{-32}$ | $1.914\times10^{-32}$ |
| ClO abundance (kg-mole/kg-mixture) | f.p. error | not predicted | $2.326\times10^{-38}$ | $2.326\times10^{-38}$ |
| CPU time (s) | | | 2.93 | 1.26 |

† The condensed species in the header of this table are included in descending order of their equilibrium abundances as determined by the new code.

species are not included, because the results are the same as those given for the case when no condensed species was included.

In addition, the inclusion of the condensed species according to the descending order of their equilibrium abundances as determined by the new code is entirely arbitrary. Also, equilibrium compositions are typically obtained in three to twelve iterations [Gordon and McBride, 1971, p. 73] in the NASA code and the maximum allowable number of iterations had been set to fifty. However, the results in table 5.7 were obtained by setting the maximum allowable number of iterations to be 20,000, an arbitrary chosen large number, because convergence was not achieved in the cases of four, five or six initally included condensed species when only a maximum of fifty iterations was allowed.

In the NASA code, for a problem involving condensed species and their possible presence at equilibrium, if no condensed species is specified for the initial consideration of a solution, the default is to seek a solution by first assuming that the product mixture is a mixture of perfect gases only. Upon achieving this first solution, condensed products are then tested for incorporation. However, there are occasions that when only a perfect-gas mixture is considered, a very low temperature is reached. For such cases, an error message will be printed by the code, calling for the inclusion of condensed species for the initial consideration. This was the case for the delay problem when no condensed species was included for consideration from the start as well as when one, two or three condensed species were included, in the descending order of their equilibrium abundances determined by the new code, when the maximum number of iterations was set to fifty. Hence, one concludes that when the maximum number of iterations was set to fifty, the inclusion of condensed species was called for when zero, one, two or three condensed species were included, and convergence was not achieved when four, five or all six condensed species predicted by the new code were included.

In order to test if convergence was achievable, equlibrium calculations were done by setting the maximum allowable number of iterations at 20,000. Run-time floating-point (f.p.) errors were encountered and the jobs were aborted for the cases with no condensed species up to three condensed species included for consideration. A solution was obtained first when four condensed species were included. In this case, a singularity of the iteration matrix was encountered three times and a singularity of the derivative matrix was encountered once. The species $BaCl_2(s\text{-}\alpha)$, $NiCl_2$ and ClO were not predicted. Convergence was also achieved when five or six condensed species were included. Singularities of the coefficient matrix were encountered, once in the former case and twice in the latter. The species $BaCl_2(s\text{-}\alpha)$, $NiCl_2$ and ClO were predicted to exist in trace amounts; however, the trace amount of $BaCl_2(s\text{-}\alpha)$ is different for the two cases, being $1.285\times10^{-21}$ kg-mole/kg-mixture in the former case and $4.466\times10^{-21}$ kg-mole/kg-mixture in the latter case. Also, a longer CPU time of 2.93 s versus 1.26 s was required for a converged solution to occur when only five condensed species were included.

Whenever an iteration matrix singularity is encountered during the course of an iteration the NASA code may alter the elemental abundances slightly to circumvent this problem and proceed with the iteration. This slight change in elemental abundances may affect the prediction of trace species like $BaCl_2(s\text{-}\alpha)$, $NiCl_2$ and ClO, and thereby explain why these species were not predicted in the case when four condensed species were included for consideration and why the amounts of $BaCl_2(s\text{-}\alpha)$ were different when five or six condensed species were included, because the iteration matrix singularity was encountered in all these three cases.

An example of the equilibrium species abundances from the NASA and new codes is given in table 5.8. These abundances were determined for the case when five condensed species were included. Only seven of the 27 gaseous species considered were above the cut-off abundance limit, and after convergence there are six condensed species. Compared to the previous four energetic materials, fewer gaseous species in smaller amounts were formed at equilibrium for this delay, and the gaseous mixture was composed essentially entirely of oxygen.

The agreement of results for the two codes was to four significant digits for all species except $BaCl_2(s\text{-}\alpha)$. An abundance of $4.498\times10^{-29}$ kg-mole/kg-mixture was predicted by the new code in contrast to $1.285\times10^{-21}$ kg-mole/kg-mixture for the NASA code. Since both of these abundances

Table 5.8: NASA and new code abundance predictions for the delay at a loading density of 0.2 gm/cm$^3$, for which the NASA code included the five most abundant condensed species determined by the new code.

| product species | NASA code abundance (kg-mole/kg-mixture) | new code abundance (kg-mole/kg-mixture) |
|---|---|---|
| $O_2$ | $1.870\times10^{-3}$ | $1.870\times10^{-3}$ |
| $O_3$ | $3.695\times10^{-27}$ | $3.695\times10^{-27}$ |
| KCl | $1.870\times10^{-28}$ | $1.870\times10^{-28}$ |
| $K_2Cl_2$ | $1.042\times10^{-31}$ | $1.042\times10^{-31}$ |
| $NiCl_2$ | $1.914\times10^{-32}$ | $1.914\times10^{-32}$ |
| O | $5.828\times10^{-37}$ | $5.828\times10^{-37}$ |
| ClO | $2.326\times10^{-38}$ | $2.326\times10^{-38}$ |
| BaO(s) | $3.158\times10^{-3}$ | $3.158\times10^{-3}$ |
| $Cr_2O_3(s)$ | $1.579\times10^{-3}$ | $1.579\times10^{-3}$ |
| $Ni(s\text{-}\alpha)$ | $1.448\times10^{-3}$ | $1.448\times10^{-3}$ |
| $ZrO_2(s\text{-}\alpha)$ | $9.318\times10^{-4}$ | $9.318\times10^{-4}$ |
| KCl(s) | $2.165\times10^{-4}$ | $2.165\times10^{-4}$ |
| $BaCl_2(s\text{-}\alpha)$ | $1.285\times10^{-21}$ | $4.498\times10^{-29}$ |

are small, it is hard to say which value is correct, except to note that an iteration matrix singularity was encountered in the run with the NASA code.

The results of the case with five condensed species included for initial consideration among the various cases tried were taken to be the accepted results of the NASA code for the delay problem, because this is the first case where a complete solution was obtained, in the sense that species like $BaCl_2$(s-$\alpha$), $NiCl_2$ and ClO were predicted. The CPU time of 2.93 s listed in table 5.6 is that required for this case.

The order of the condensed species included for initial consideration in the equilibrium mixture also affected the calculation results of the NASA code. Listed in table 5.9 are the results of four computer runs, the first two runs including five condensed species and the other two including six condensed species. But, the order of the species differ slightly, being in the descending order of abundances determined by the new code. The first column of results shown in table 5.9 was obtained by interchanging the positions of the second and fourth species, namely $Cr_2O_3$(s) and $ZrO_2$(s-$\alpha$). Iteration matrix singularities was encountered twice; and the presence of $BaCl_2$(s-$\alpha$), $NiCl_2$ and ClO were predicted, except that the amount of $BaCl_2$(s-$\alpha$) was different from that predicted when the descending order was followed according to table 5.7. The second column of results shown in table 5.9 was obtained by interchanging the fourth with the last, which is a change of $ZrO_2$(s-$\alpha$) and KCl(s). An iteration matrix singularity was encountered four times and none of $BaCl_2$(s-$\alpha$), $NiCl_2$ or ClO was predicted. The predictions of the amounts of $BaCl_2$(s-$\alpha$), $NiCl_2$ and ClO in both of these cases may have been affected by remedial steps taken when singular matrices were encountered. Furthermore, the CPU times required to converge to a solution in both cases were considerably higher than those when the descending order was followed, that is 5.43 and 4.27 s, respectively, compared to 2.93 s.

When six condensed species were included for consideration and with the second and the fourth species according to descending order of abundances interchanged, an iteration matrix singularity was encountered four times and $BaCl_2$(s-$\alpha$), $NiCl_2$ and ClO were not predicted. On the

Table 5.9: Selected NASA code results for the delay with 5 and 6 different condensed species† at a loading density of 0.2 $gm/cm^3$.

| condensed species | BaO(s), $ZrO_2$(s-$\alpha$), Ni(s-$\alpha$), $CrO_3$(s-$\alpha$), KCl(s) | BaO(s), $Cr_2O_3$(s), Ni(s-$\alpha$), KCl(s), $ZrO_2$(s-$\alpha$) | BaO(s), $ZrO_2$(s-$\alpha$), Ni(s-$\alpha$), $CrO_3$(s-$\alpha$), KCl(s), $BaCl_2$(s-$\alpha$) | BaO(s), $Cr_2O_3$(s), Ni(s-$\alpha$), $BaCl_2$(s-$\alpha$), KCl(s), $ZrO_2$(s-$\alpha$) |
|---|---|---|---|---|
| coefficient matrix singularites | 2 | 4 | 4 | 1 |
| derivative matrix singularites | 0 | 0 | 0 | 0 |
| $BaCl_2$(s-$\alpha$) abundance | $4.347\times10^{-21}$ | not predicted | not predicted | $1.193\times10^{-22}$ |
| $NiCl_2$ abundance | $1.914\times10^{-32}$ | not predicted | not predicted | $1.914\times10^{-32}$ |
| ClO abundance | $2.326\times10^{-38}$ | not predicted | not predicted | $2.326\times10^{-38}$ |
| CPU time (s) | 5.43 | 4.27 | 1.54 | 1.56 |

† The order of the condensed species in the header of this table is explained in the text.

other hand, when the fourth and the last species, $ZrO_2$(s-α) and $BaCl_2$(s-α), were interchanged, an iteration matrix singularity was encountered once and the presence of $BaCl_2$(s-α), $NiCl_2$ and ClO were predicted. However, the amount of $BaCl_2$(s-α) was different from that predicted when the descending order was followed. The prediction of the amounts of $BaCl_2$(s-α), $NiCl_2$ and ClO in both of these two cases may have also been affected by steps taken to rectify the singular iteration matrices encountered. The CPU time needed to get a converged solution in either case was not much higher than that when the descending order was followed: 1.54 and 1.56 s, respectively, compared to 1.26 s. Hence, the effects of changing the order of the condensed species on CPU time in the case when five condensed species were included were greater than when six condensed species were included.

A comparison of the results given in tables 5.7 and 5.9 indicates that interchanging the positions of the second and the fourth species had greater impact on the prediction of the abundances of $BaCl_2$(s-α), $NiCl_2$ and ClO in the case when six condensed species were included than in the case when five were included. This being the case in the sense that in the former case the number of matrix singularities encountered increased from two to four and $BaCl_2$(s-α), $NiCl_2$ and ClO were not predicted at all, while in the latter case the number of matrix singularities encountered changed from one to two and $BaCl_2$(s-α), $NiCl_2$ and ClO were predicted except that the amount of $BaCl_2$(s-α) was different. However, the trend was reversed when the fourth and the last species were interchanged. Therefore, the effects of changing the order of the condensed species included for consideration on species abundances were not predictable.

Finally, calculation results for the NASA code were affected when multiple loading densities were considered. Two calculations were performed for which five condensed species in the first and six in the second were included in descending order of abundances for initial consideration, and in both calculations the loading densities of 0.1, 0.2 and 0.3 $gm/cm^3$ were considered consecutively. The results shown in table 5.10 are those for a loading density of 0.2 $gm/cm^3$. For consistency of presentation, the results of the case when five condensed species were included were listed before those of the case when six condensed species were included. However, for the purpose of discussion, the latter are described first.

When more than one loading density is specified for consideration, the results to the first loading density are used as the initial estimates to the second and the results of the second are used as the initial estimates to the third and so on. The specification of the loading densities to be considered in the order of 0.1, 0.2 and 0.3 $gm/cm^3$ is simply solving the problem for 0.2 $gm/cm^3$ by first solving the problem for 0.1 $gm/cm^3$. In the case when six condensed species were included for consideration, no matrix singularity was encountered for all the three loading densities considered, and, for a loading density of 0.2 $gm/cm^3$, $BaCl_2$(s-α), $NiCl_2$ and ClO were all predicted. This is the only case presented so far for which no matrix singularity was encountered with the NASA code. The same trend was not observed when five condensed species were included for consideration. An iteration matrix singularity was encountered four times for a loading density of 0.1 $gm/cm^3$ and once for a loading density of 0.2 $gm/cm^3$. For a loading density of 0.2 $gm/cm^3$, $NiCl_2$ was predicted but not $BaCl_2$(s-α) and ClO. Therefore, for a loading density of 0.1 $gm/cm^3$ the inclusion of six condensed species for consideration caused the minimization process to take a different path that is free of matrix singularities; the same is true for a loading density of 0.2 $gm/cm^3$, which can be taken as the combined result of considering six condensed species and by considering the loading density of 0.1 $gm/cm^3$ first.

Based on the results presented in table 5.7, in particular the result that a complete solution was not achieved until the five most abundant condensed species were included for initial consideration, it was concluded that in general the solution of problems involving many condensed species

Table 5.10: Selected NASA code results for the delay with 5 and 6 different condensed species[†] at a set of sequential loading densities of 0.1, 0.2 and 0.3 gm/cm$^3$.

| condensed species | $BaO(s)$, $CrO_2(s\text{-}\alpha)$, $Ni(s\text{-}\alpha)$, $ZrO_2(s\text{-}\alpha)$, $KCl(s)$ | $BaO(s)$, $Cr_2O_3(s)$, $Ni(s\text{-}\alpha)$, $ZrO_2$, $KCl(s)$, $BaCl_2(s\text{-}\alpha)$ |
|---|---|---|
| number of coefficient matrix singularites | 1 | 0 |
| number of derivative matrix singularites | 0 | 0 |
| $BaCl_2(s\text{-}\alpha)$ abundance (kg-mole/kg-mixture) | not predicted | $1.324\times10^{-23}$ |
| $NiCl_2$ abundance (kg-mole/kg-mixture) | $7.040\times10^{-33}$ | $1.914\times10^{-33}$ |
| ClO abundance (kg-mole/kg-mixture) | not predicted | $2.326\times10^{-38}$ |

[†] The condensed species in the header of this table are included in descending order of their equilibrium abundances as determined by the new code.

but with very little gas present at equilibrium by the NASA code would be difficult, because generally speaking it is impossible to know which condensed species should be specified for consideration in advance.

Based on the results presented in table 5.9, it was concluded that abundances of trace species given by the NASA code are sensitive to the order that condensed species are specified for initial consideration and may have been affected. It was also concluded that abundances of trace species given by the NASA code may be affected when multiple loading densities were considered, based on the results presented in table 5.10.

Among the above three observations, the most significant is the first one, because it is about a real difficulty of the NASA code. The second and the third observations are less important because the slight differences in the abundances of the trace species usually do not affect the overall problem results, such as the equilibrium temperature and pressure. Finally, the NASA code handles singular matrices quite well, it did not seem that matrix singularities affected the convergence of the program; condensed species handling procedure seems to have more influence on this. However, matrix singularities did seem to affect the abundances of trace species.

### 5.1.3 Comparison of Results of the Bagheera and New Codes

Calculations were done using the Bagheera and new codes for the five energetic materials defined previously. For each test case, the new code was used to do calculations using models, number of species and input data matching those of the Bagheera code. Values of the equilibrium temperatures and pressures of product mixtures and the CPU times for computer runs, as determined by the Bagheera and new codes are summarized in table 5.11. These calculations were performed by assuming the gaseous products formed an Amagat type of ideal mixture, with the individual gases governed by a modified pressure-explicit truncated virial equation of state, and the condensed species were assumed to be at a constant molar volume.

Table 5.11: Comparison of the equilibrium temperatures and pressures and CPU times for the Bagheera and new codes for five sample energetic materials all at a loading density of 0.2 gm/cm$^3$.

| energetic material | mixture properties and CPU time | Bagheera code | new code | CPU ratio | temperature range (K) |
|---|---|---|---|---|---|
| Lova propellant<br>(4, 136, 7, 0,<br>0%, 0%)[†] | $T$ (K) | 2561 | 2561 | | |
| | $P$ (MPa) | 265.8 | 265.8 | | |
| | CPU time (s) | 0.89 | 4.01 | 4.5 | 2300–2700[‡] |
| propellant with lead oxide<br>(7, 165, 44, 0,<br>0%, 0%) | $T$ (K) | 2434 | 2434 | | |
| | $P$ (MPa) | 230.0 | 230.0 | | |
| | CPU time (s) | 1.26 | 6.18 | 4.9 | 2300–2700 |
| primer<br>(8, 219, 39, 2,<br>6.3%, 6.5%) | $T$ (K) | 2547 | 2547 | | |
| | $P$ (MPa) | 82.60 | 82.60 | | |
| | CPU time (s) | 3.28 | 11.10 | 3.4 | 2300–2700 |
| black powder (igniter)<br>(6, 161, 32, 2<br>18.2%, 45.9%) | $T$ (K) | 2169 | 2170 | | |
| | $P$ (MPa) | 67.82 | 67.79 | | |
| | CPU time (s) | 1.86 | 22.20 | 11.9 | 2300–2700 |
| | CPU time (s) | 1.86 | 10.52 | 5.7 | 2000–2400 |
| delay or fuse<br>(7, 29, 36, 6,<br>84.3%, 96.6%) | $T$ (K) | — | 1039 | | |
| | $P$ (MPa) | — | 1.97 | | |
| | CPU time (s) | — | 1.31 | — | 2300–2700 |
| | CPU time (s) | — | 0.68 | — | 800–1200 |

[†] The six numbers in brackets denote *(1)* number of system elements, *(2)* number of gaseous species considered, *(3)* number of condensed species considered, *(4)* number of condensed species present at equilibrium, *(5)* percentage of condensates by mole, *(6)* percentage of condensates by weight.

[‡] Temperature range used in the new code to start the equilibrium calculations.

The library of thermodynamic data of the Bagheera code is essentially that of the NASA code, but it includes data for additional species. Therefore the numbers of species selected for the test problems were slightly larger than those for the comparison with the NASA code, with the exception of the number of condensed species for the delay, which increased by seven from 29 to 36, a fair increment. These additional condensed species were found to have a significant influence on the final results.

The solutions of the first four test problems by using the Bagheera and new codes were straightforward. The predictions on the presence of condensed species were the same as those for the comparison between the NASA and new codes. For the LOVA propellant and the propellant with lead oxide, which formed gaseous products only, the values of the equilibrium temperatures and pressures predicted by the two codes agreed to four significant digits.

In the cases of the primer and black powder, both of which formed two condensed products at equilibrium, values of both the equilibrium temperatures and pressures predicted by the two codes also agreed to four significant digits in the former, but there were slight differences in the latter. These differences could be explained by the larger amount of condensed products present at equilibrium in this latter case, in conjunction with the possibly less precise values of system pressures determined as a result of the assumption of an Amagat type of ideal mixture and the fair number of gaseous species in it.

The larger amount of condensed products was considered as a factor, because this would made the black powder problem a bit harder to handle. The mixture assumption was considered as a factor because agreements to four significant digits on the values of the equilibrium temperatures and pressures for this problem were achieved when comparing the new code with both the NASA and Blake codes (results of comparison between the new and Blake codes are presented in the next subsection); the amount of condensed products determined at equilibrium were basically the same in all three comparisons, however a more tedious procedure was required to solve for the system pressure when performing calculations for this comparison then for the other two. The models used for the condensed species do not affect the results very much, as shown *before*, not withstanding the fact that there were only two condensed products.

In general the equilibrium temperatures and pressures predicted by the Bagheera code were higher than those predicted by the NASA code. The differences can be accounted for mainly by the different models used for the gaseous products. Higher temperatures were predicted because the internal energy contents of gases following the modified truncated virial equation of state used in the Bagheera code are lower than that for a perfect gas; hence, for the same initial energy contents of the energetic materials, the product gases were heated to higher temperatures at equilibrium. Also, higher pressures were predicted because, firstly, the gases were modelled as real gases (following the modified virial equation of state) in the Bagheera code and, secondly, the mixture equilibrium temperatures were higher. The difference in pressures was the largest for the LOVA propellant and decreased in the order of the energetic materials, this is because the amount of gases in the product mixture was decreasing in that order.

For the final test case of the delay, the Bagheera code had difficulties in solving the problem—either convergence was not achieved for the basic perfect-gas solution within a specified maximum number of iterations, or matrix singularities were encountered. The same problems persisted even when: firstly, the maximum number of iterations was increased; secondly, the six condensed species (determined by the new code) known to be present at equilibrium were specified to be considered at the initial stage of the solution; and thirdly, when all possible condensed product species selected from the library except these six were specified to be omitted from consideration—thereby limiting the species to be considered by the program to only these six condensed species, together with other gaseous species selected from the library.

The new code solved the delay formulation without any difficulties. All the possible species selected from the library, gaseous and condensed, were considered together; no special consideration or omission of condensed species was required. The equilibrium temperature and pressure of the product mixture were determined to be 1067 K and 2.03 MPa, respectively, which were quite different from those determined for the comparison between the NASA code and the new code. This is because the library of the Bagheera code included data for additional condensed species. As a matter of fact, the six condensed species determined to be present at equilibrium were $BaO(s)$, $NiCr_2O_4(s)$, $ZrO_2(s\text{-}\alpha)$, $K_2CrO_4(s\text{-}2)$, $BaCl_2(s\text{-}\alpha)$ and $Cr_2O_3(s)$, and these are different from those stated above.

### 5.1.4 Comparison of Results of the Blake and New Codes

Calculations were done using the Blake and new codes for the five energetic materials defined previously. For each test case, the new code was used to do calculations using models, number of species and input data matching those of the Blake code. Values of the equilibrium temperatures and pressures of product mixtures and the CPU times for computer runs, as determined by the

Blake and new codes are summarized in table 5.12. These calculations were done by assuming the mixture of gaseous products as nonideal and using the conventional, truncated, pressure-explicit virial equation of state. Also, the condensed products were assumed to have variable molar volume.

Table 5.12: Comparison of the equilibrium temperatures and pressures and CPU times for the Blake and new codes for four sample energetic materials all at a loading density of 0.2 gm/cm$^3$.

| energetic material | mixture properties and CPU time | Bagheera code | new code | CPU ratio | temperature range (K) |
|---|---|---|---|---|---|
| Lova propellant | $T$ (K) | 2563 | 2563 | | |
| (4, 24, 1, 0, | $P$ (MPa) | 257.0 | 257.0 | | |
| 0%, 0%)† | CPU time (s) | 2.37 | 1.35 | 0.6 | 2300–2700‡ |
| propellant with lead oxide | $T$ (K) | 2433 | 2433 | | |
| (7, 29, 0, 0, | $P$ (MPa) | 222.5 | 222 5 | | |
| 0%, 0%) | CPU time (s) | 4.87 | 1 99 | 0.4 | 2300–2700 |
| primer | $T$ (K) | 2564 | 2564 | | |
| (8, 28, 2, 2, | $P$ (MPa) | 81.41 | 81.41 | | |
| 6.3%, 6.9%) | CPU time (s) | 6.78 | 3.44 | 0 5 | 2300–2700 |
| black powder (igniter) | $T$ (K) | 2167 | 2167 | | |
| (6, 28, 4, 2 | $P$ (MPa) | 69.37 | 69.37 | | |
| 18.1%, 45.7%) | CPU time (s) | 12.37 | 5.82 | 0.5 | 2300–2700 |
| | CPU time (s) | 12.37 | 5.10 | 0.4 | 2000–2400 |

† The six numbers in brackets denote *(1)* number of system elements, *(2)* number of gaseous species considered, *(3)* number of condensed species considered, *(4)* number of condensed species present at equilibrium, *(5)* percentage of condensates by mole, *(6)* percentage of condensates by weight.

‡ Temperature range used in the new code to start the equilibrium calculations

The library of thermodynamic data of the Blake code is quite a bit smaller than those of the NASA and Bagheera codes. This fact is reflected by the number of possible species that could be selected. The results of the two codes agreed to four significant digits, the same as the comparison between the NASA and new codes. For the primer and the black powder, even though both the Blake and Bagheera codes used the virial equation of state, the agreement of results between the Blake and new codes was better than that between the Bagheera and new codes. This is likely due to the necessary separate treatment of large number of gaseous species as a result of the Amagat type of ideality assumed in the Bagheera code, as oppose to treating the gases like a single gas because of the nonideality assumption used in the Blake code.

For the LOVA propellant, there were only a total of 24 gaseous species and one condensed species (graphite) within the limits of the numbers of gaseous and condensed species that could be considered, and hence were all selected. The four most abundant gaseous species with independent molecular formulae, CO, $H_2$, $N_2$ and $H_2O$, based on the results of the NASA code were specified for consideration for finding the first set of components. For the propellant with lead oxide, product species were selected based on the results of the NASA code. Twenty-nine gaseous species were selected, and no condensed species. These gaseous species turned out also to be the most abundant gaseous species that could be selected based on the results of the new code when all possible products were considered. The seven most abundant gaseous species with linearly independent molecular formulae were specified for finding the first set of components.

For the primer, the most abundant gaseous species selected based on the results of the NASA code did not agree with those selected based on the results of the new code. The differences occurred among those species whose abundances were close to the cut-off limit. The most abundant gaseous species selected were then based on the results of the new code. The two condensed constituents: $MgO(lq/s)$[1] and $MgF_2(lq/s)$ were selected for consideration because $MgO(s)$ and $MgF_2(lq)$ were predicted to be present at equilibrium. In the Blake code, condensed constituents for which their condensed phases are postulated to exist at equilibrium are always chosen for component considerations. Therefore, to facilitate a solution to a problem, these two condensed constituents, together with the six most abundant gaseous species which have linearly independent formulae among themselves and with respect to these two condensed constituents, were specified for consideration for finding the first set of components. The CPU time was longer when the eight most abundant gaseous species having linearly independent formulae were specified instead. Even with these specifications of possible components, solutions were obtained only when the least abundant among the 29 gaseous species was excluded from the species list.

For the black powder, the most abundant 29 gaseous species selected based on the results of the NASA code were same as those based on the new code. The two condensed constituents $K_2CO_3(lq/s)$ and $K_2S(lq/s)$ were specified for consideration for finding the first set of components, because $K_2CO_3(lq)$ and $K_2S(lq)$ were predicted to be present at equilibrium by the NASA code. The four most abundant gaseous species which have linearly independent formulae among themselves and with respect to the two condensed constituents, $CO_2$, CO, $N_2$ and $H_2O$, were also specified for consideration for finding components. Again, Blake took longer to obtain a solution when six gaseous species having linearly independent formulae, the above four plus $H_2S$ and K, were specified instead; and the least abundant gaseous species among the 29 selected must be excluded from the species list before a solution was obtained in either case.

The gaseous species K, mentioned above, was not the most abundant gaseous species that could be specified as a possible component for expressing the formulae of product species containing potassium. The most abundant gaseous species for this purpose was KOH; K was the next most abundant gaseous species after KOH for this purpose. However, Blake was unable to find an acceptable set of components for carrying out computations, when KOH was used in the first place. Component sets were found with the replacement by K, but maximum numbers of iterations were exceeded and floating point errors encountered. A solution was not achieved until another gaseous species was excluded from consideration, as already mentioned.

After the checks on selection of species were made, for final comparison purposes, the new code was rerun using the same species as selected for the Blake code for each problem, as mentioned in the last section. The new code solved the above four problems without any difficulties. The library of Blake has no data for any chromium or nickel containing species, and it was not possible to use Blake to carry out the calculation for the delay. The most difficult case among the five test cases was the delay, as can be seen from the results of calculations of the NASA or the Bagheera code. However, even calculations for this test case were not performed, because some of the difficulties associated with using Blake had become obvious from the results of calculations of the first four test cases.

---

[1] $MgO(lq/s)$ means that $MgO(lq)$ and/or $MgO(s)$ are considered possible products in the equilibrium mixture The Blake code uses the term 'condensed constituent' and the molecular formula of a substance followed by a 'dollar sign' (e.g., MgO$) to refer collectively to the condensed phases of a substance, which may actually include both the liquid and solid phases, or only one of them depending on the availability of thermodynamic data in the library. The 'condensed constituent' term and meaning are used herein, but the 'dollar sign' notation in the Blake code is replaced by the notation '(lq/s)' to be consistent with other phase designators.

As additional examples of these difficulties, some of the findings of the preliminary calculations of the black powder problem using Blake are noted here. At the beginning, this problem was solved for 29 gaseous species and two condensed constituents. The seven least-abundant gaseous species, N, $C_2H_2$, $CH_2$, $C_2N_2$, $C_2H_4$, C and $HNO_3$, and the three condensed constituents absent at equilibrium, C(s-gr), KOH(lq/s) and $K_2SO_4$(lq/s), predicted by the NASA code were excluded. The three least-abundant gaseous species, in descending order of abundances, included for calculation were O, $CH_3$ and CN. When no species was specified for consideration for finding components, Blake did not succeed in finding an acceptable set. The same situation arose when the six most abundant gaseous species according to the results of the NASA code, $CO_2$, CO, $N_2$, $H_2O$, $H_2S$ and KOH, were specified for consideration as components. The difficulty in finding an acceptable set of components was rectified when KOH was replaced by K, which was the next most abundant gaseous species that could be selected as a component, for expressing the molecular formulae of other product species containing potassium. However, convergence was not achieved. Finally when CN, the least abundant gaseous species among the 29 in the species list, was excluded, then a solution was obtained.

In the last calculation the number of condensed constituents considered was kept to a minimum; only the two which were known to have one of their phases present at equilibrium were considered. The next calculation was performed with one more condensed constituent, $K_2SO_4$(lq/s), included for consideration, while keeping everything else unchanged. There were 28 gaseous species and three condensed constituents that are included for consideration. The two condensed constituents, C(s-gr) and KOH(lq/s), were still excluded, and the same six gaseous species, $CO_2$, CO, $N_2$, $H_2O$, $H_2S$ and K, specified for consideration as components (which helped convergence in the last calculation) were retained. In this case, convergence was not achieved at first, but when the least-abundant gaseous species among the 28 considered, that is $CH_3$, was excluded, a solution to the problem was obtained.

A second calculation on further increasing the number of condensed constituents considered was done. Of the two remaining condensed constituents, C(s-gr) and KOH(lq/s), which were excluded, C(s-gr) was retained for consideration this time, and everything else was kept the same. No convergence was achieved. (It was found that, if KOH(lq/s) was included instead of C(s-gr), a set of acceptable components could not be found.) Once again when the least-abundant gaseous species among the 27 first considered (that is O) was excluded from consideration, convergence was obtained.

Based on the calculations discussed above, it seems that when consideration of condensed constituents is required, even though the maximum number of gaseous species that can be considered in the Blake code is 29, convergence is usually achieved for a smaller number. There also seems to be some limits on the number of species that can be considered. This can be seen when one more condensed constituent was included for consideration, then one more gaseous species had to be excluded to achieve convergence.

The results of a second set of calculations demonstrating the effects of different species lists on the equilibrium results are also described here. The first calculation in this set was performed by including nineteen of the 36 possible gaseous species. Most of the seventeen gaseous species excluded were species present in small amounts at equilibrium. When all condensed constituents were included and no possible component was specified, no acceptable components were found. When the condensed constituent KOH(lg/s) was excluded and the six gaseous species CO, K, $CO_2$, $N_2$, $H_2O$ and SO, which were used by DREV for calculations on the present black powder formulation, were specified for consideration for finding an acceptable first set of components, a solution was found. The equilibrium temperature and pressure were determined to be 2163 K and

70.11 MPa, respectively, and only $K_2CO_3$(lq) and $K_2S$(lq) were predicted. These results differ slightly from the accepted final results of the black-powder problem.

The second calculation in this set included more gaseous species (24) for consideration; however, a few of the twelve gaseous species excluded were present in fair amounts at equilibrium. When the condensed constituents considered and the possible components specified were kept the same, the equilibrium temperature and pressure were determined to be 2171 K and 70.22 MPa, respectively, but this time $K_2SO_4$(lq) was predicted in addition to $K_2CO_3$(lq) and $K_2S$(lq). The results of this calculation is fairly different from the accepted final results of the black-powder problem, because of the prediction of the presence of $K_2SO_4$(lq).

For the third calculation in this set, the gaseous species excluded were those existing in the least amounts according to the NASA results. At the beginning, the seven least-abundant gaseous species were excluded, resulting in 29, the maximum number that Blake will consider, gaseous species being included. The condensed constituents considered and the possible components specified were kept the same. The only condensed constituent excluded was KOH(lq/s) and four condensed constituents were considered, of which C(s-gr) and $K_2SO_4$(lq/s) should be absent at equilibrium. No convergence was achieved. Calculations were repeated, each time with the least-abundant gaseous species of the remaining list excluded. Convergence was achieved after three more gaseous species (O, $CH_3$ and CN) were excluded, which agreed with the results of the previous calculations on increasing the number of condensed constituents considered. No $K_2SO_4$(lq) was predicted and the equilibrium temperature and pressure determined were 2167 K and 69.37 MPa, respectively. These results agree with the accepted final results of the black powder problem. Hence, when there is no knowledge about the significant species present at equilibrium and species have to be excluded, because of limitation on the maximum number of species that can be considered, the results obtained can be incorrect, as can be seen based on the results of the first two calculations in this series, unless many trials are attempted.

## 5.2 Equilibrium Calculations for a Moderate Number of Species with Melting

### 5.2.1 Comparison of Results of the NASA and New Codes

When describing the procedure adopted within the new code for treating problems involving phase transitions, in particular melting, between two neighbouring condensed phases, in section 3.11.1, two examples with $N_2S$ illustrating problems with some of the polynomial coefficients of product species used in the NASA code were given. Results of calculations of these two examples will be presented first in this section, followed by results of calculations of the example of $Na_2SO_4$ and PbO, the melting temperatures of which are 2 K apart, given in the same section. Finally, results of an extended comparison of the treatment of melting between the NASA and new codes, based on selected numerical results for the black-powder problem described in section 4.4.1 are given. Results of the first example of $N_2S$ will be referred to when discussing the results of black-powder problems.

To demonstrate that the NASA code has difficulty in solving problems involving the transition of $Na_2S$, two sets of calculations were performed for a formulation that consisted of the ingredients listed in table 5.13, both for a loading density of 0.2 gm/cm$^3$. These ingredients were selectively chosen with the aim to produce condensed $Na_2S$ as a product in the equilibrium mixture. The enthalpy of formation of $KNO_3$ was taken from Freedman's article and that of $Na_2S$ from the

Table 5.13: Test formulation used to demonstrate that the NASA code does not always converge for equilibrium problems involving transitions of $Na_2S$.

| ingredient | formula | enthalpy of formation at 298.15 K (cal/mole) |
|---|---|---|
| potassium nitrate (KN) | $K_1N_1O_3$ | −117,760 |
| sodium sulfide | $Na_2S_1$ | −87,500 |
| sulphur (S) | $S_1$ | 0 |

JANAF Thermochemical Tables. The calculations were performed on the basis of incremental changes in the weight percentages of $KNO_3$ and S.

The first set of calculations started with weight percentages of 31, 30 and 39 for $KNO_3$, $Na_2S$ and S, respectively. A total of seven calculations were performed by increasing the percentage of $KNO_3$ and decreasing the percentage of $Na_2S$ in steps of 0.5, with the final set of percentages being 34, 30 and 36. To facilitate the attainment of convergence, the four condensed species consisting of $K_2SO_4$(s-$\beta$), $Na_2S$(s-1), $Na_2SO_4$(lq) and S(lq) were specified for consideration at the beginning of a calculation as condensed products. These four species were the actual condensed products that were present later at equilibrium, with the exception that $Na_2S$(s-2) might be present instead of $Na_2S$(s-1), and in their descending order of equilibrium abundances. Results of these calculations are summarised in table 5.14. Note that, because transition temperatures dictated by polynomial coefficients are quoted to six significant digits, for consistency, equilibrium temperatures presented in this example and the following ones which are not transition temperatures are additionally quoted to six significant digits.)

This set of calculations was supposed to determine increasing equilibrium temperatures and covered cases involving the transition from $Na_2S$(s-1) to $Na_2S$(s-2) at a temperature of 1276 K. For the first calculation the equilibrium temperature was determined as 1275.45 K, which is just below the transition temperature. $Na_2S$(s-1) was present at equilibrium but not $Na_2S$(s-2). However, no further converged solutions could be achieved until the last set of percentages was used, in which case the equilibrium temperature had already reached 1333.24 K. This temperature is higher than the transition temperature and $Na_2S$(s-2) was present instead of $Na_2S$(s-1). The difficulties in obtaining a converged solution are attributed to the fact that the standard chemical potentials

Table 5.14: First set of calculations for the test formulation given in table 5.13, for a loading density of 0.2 gm/cm$^3$.

| weight (%) | | | equilibrium temperature (K) | equilibrium abundance ($10^{-3}$ kg-mole/kg-mixture) | |
|---|---|---|---|---|---|
| $KNO_3$ | $Na_2S$ | S | | | |
| 31.0 | 30.0 | 39.0 | 1275.45 | $Na_2S$(s-1) at 3.103 | $Na_2S$(s-2) absent |
| 31.5 | 30.0 | 38.5 | no convergence | | |
| 32.0 | 30.0 | 38.0 | | | |
| 32.5 | 30.0 | 37.5 | | | |
| 33.0 | 30.0 | 37.0 | | | |
| 33.5 | 30.0 | 36.5 | | | |
| 34.0 | 30.0 | 36.0 | 1333.24 | $Na_2S$(s-1) absent | $Na_2S$(s-2) at 3.046 |

of these two species determined by using their polynomial coefficients given in the NASA code never cross (see figure 3.4). As a atural consequence, the code would not be able to determine the transition at a temperature at which the chemical potentials of $Na_2S$(s-1) and $Na_2S$(s-2) were supposed to be equal.

The second set of calculations was performed similarly. The starting weight percentages were 37, 30 and 33. A total of five calculations were done, and the ending weight percentages were 39, 30 and 31. The three condensed species consisting of $K_2SO_4$(lq), $Na_2S$(lq) and $Na_2SO_4$(lq) were specified for consideration, at the beginning of a calculation, as condensed products this time. They were the actual condensed products present at equilibrium and in their descending order of equilibrium abundance for the cases in which either $Na_2S$(lq) or $Na_2S$(s-2) existed. $Na_2S$(s-2) was not specified in place of $Na_2S$(lq) for consideration as a condensed product, because no convergence could be achieved for any of the calculations in the set if it was used. This set of calculations was supposed to determine increasing equilibrium temperatures and covered the cases involving the melting of $Na_2S$(s-2) at 1452.17 K (see figure 3.3), and results of these calculations are summarized in table 5.15.

Table 5.15: Second set of calculations for the test formulation given in table 5.13, for a loading density of 0.2 gm/cm$^3$.

| weight (%) | | | equilibrium temperature (K) | equilibrium abundance ($10^{-3}$ kg-mole/kg-mixture) | |
|---|---|---|---|---|---|
| $KNO_3$ | $Na_2S$ | S | | | |
| 37.0 | 30.0 | 33.0 | 1422.72 | $Na_2S$(s-2) at 2.998 | $Na_2S$(lq) absent |
| 37.5 | 30.0 | 32.5 | oscillation without convergence | | |
| 38.0 | 30.0 | 32.0 | 1452.17 | $Na_2S$(s-2) at 1.813 | $Na_2S$(lq) at 1.171 |
| 38.5 | 30.0 | 31.5 | 1447.94 | $Na_2S$(s-2) absent | $Na_2S$(lq) at 2.968 |
| 39.0 | 30.0 | 31.0 | 1474.03 | $Na_2S$(s-2) absent | $Na_2S$(lq) at 2.968 |

The equilibrium temperature obtained in the first calculation was 1422.72 K, which is below the melting temperature of 1452.17 K dictated by the polynomial coefficients, as well as the designated melting temperature 1445 K. Hence, $Na_2S$(s-2) was present and $Na_2S$(lq) was absent. No solution was obtained for the second calculation; an oscillation occurred when $Na_2S$(lq) was added and removed alternatively. In the NASA code, a solution is obtained via a set of convergences, at each convergence a test on the inclusion and deletion of condensed species is performed. If the solid phase of a substance is present at a convergence at a temperature greater than 50 K above the designated melting temperature, it is replaced by the liquid phase and a new convergence is sought. However, the solid phase is retained and the liquid phase is added, if the solid phase is present at a temperature less than 50 K above the designated melting temperature, and both phases are considered to contribute to the possible existence of melting. If melting does occur, the melting temperature dictated by the polynomial coefficients of the two phases would become the equilibrium temperature.

The oscillation in the convergence solution occurred because the melting temperature dictated by the polynomial coefficients is different from the designated melting temperature. With the consideration of only $Na_2S$(s-2), a convergence was achieved at 1446.24 K, which is less than 50 K above the designated melting temperature, and $Na_2S$(lq) was added. When both of these two phases were considered, a convergence was reached at 1452.17 K, but $Na_2S$(lq) was found unacceptable. The second problem was not a melting problem and $Na_2S$(lq) was deleted. With only $Na_2S$(s-2) present, then a new convergence at 1446.24 K was obtained. The same process was repeated and an oscillation occurred.

In the third calculation, when only $Na_2S$(lq) was considered, a converged solution was obtained at 1421.67 K, which is less than 50 K below the designated melting temperature. Then, $Na_2S$(s-2) was included (a situation opposite to that described above) and melting was determined at 1452.17 K. In the fourth calculation, a straightforward converged solution was achieved at 1447.94 K with only $Na_2S$(lq) present in the equilibrium mixture. This time a liquid phase was present at a temperature above the designated melting temperature, therefore nothing needed to be done. However, the results of these two calculations are contradicting—the solid phase of a substance exits at a temperature higher than that of its liquid phase. This discrepancy is attributed to the fact that the melting temperature dictated by the polynomial coefficients is different than the designated melting temperature. The final calculation was similar to the fourth one, a converged solution was achieved at a temperature of 1474.03 K, which was higher than 1445 and 1452.17 K, with only $Na_2S$(lq) present at equilibrium.

Difficulties encountered by the NASA code for problems like the melting of $Na_2S$(s-2) are avoided in the new code, by replacing the designated melting temperatures by those dictated by the polynomial coefficients and by using the latter for the selection of condensed phases for consideration. The new code can also avoid problems like the case for $Na_2S$(s-1) and $Na_2S$(s-2), by keeping the original designated melting temperature of a condensed phase, when no melting temperature can be determined based on the polynomial coefficients.

To demonstrate that the NASA code has difficulty in solving problems involving melting of two substances when the melting temperatures are close together, results of calculations, using $Na_2SO_4$ and PbO as an example (see figure 3.5), from the NASA and new codes are now presented. Calculations were done for a formulation of ingredients listed in table 5.16. The ingredients were selectively chosen so that condensed $Na_2SO_4$ and PbO would be present at equilibrium. The enthalpy of formation of $NaNO_3$ was taken from the Bagheera code and that of PbO from the JANAF Thermochemical Tables. The weight percentages of $NaNO_3$ and PbO were adjusted to suit this problem.

Table 5.16: Test formulation used to demonstrate that the NASA code does not always converge for equilibrium problems involving the melting of two substances when their melting temperatures are close.

| ingredient | formula | enthalpy of formation at 298.15 K (cal/mole) |
|---|---|---|
| sodium nitrate (KN) | $Na_1N_1O_3$ | −112,450 |
| lead oxide | $Pb_1S_1$ | −52,440 |
| sulphur (S) | $S_1$ | 0 |

Results of some calculations performed by using the NASA code are summarized in table 5.17. The first set of weight percentages for $NaNO_3$, PbO and S were 5, 85 and 10, respectively. A total of five calculations were carried out for a loading density of 0.2 gm/cm$^3$, and the final set of percentages was 8, 82 and 10. To facilitate obtaining convergence, the three condensed species $Na_2SO_4$(s-I), PbO(s-yw) and PbS(s) were specified for consideration as condensed products. These were the condensed products present at equilibrium, in their descending order of equilibrium abundance for the case in which $Na_2SO_4$(s-I) but not $Na_2SO_4$(lq) and PbO(s-yw) but not PbO(lq) were

Table 5.17: First set of calculations for the test formulation given in table 5.16, for a loading density of 0.2 gm/cm$^3$.

| weight (%) | | | equilibrium temperature (K) | equilibrium abundance ($10^{-5}$ kg-mole/kg-mixture) | |
|---|---|---|---|---|---|
| $NaNO_3$ | PbO | S | | | |
| 5.0 | 85.0 | 10.0 | 1142.51 | $Na_2SO_4$(s-I) at 29.41 | PbO(s-yw) at 212.1 |
| 5.2 | 84.8 | 10.0 | 1157.00 | $Na_2SO_4$(s-I) at 24.63<br>$Na_2SO_4$(lq) at 5.961 | PbO(s-yw) at 212.8 |
| 6.0 | 84.0 | 10.0 | oscillation without convergence | | |
| 7.0 | 83.0 | 10.0 | singular matrices and oscillation | | |
| 8.0 | 82.0 | 10.0 | 1218.04 | $Na_2SO_4$(lq) at 47.06 | PbO(lq) at 222.2 |

present. For this case the melting temperatures of $Na_2SO_4$ and PbO as dictated by their polynomial coefficients were 1157.00 and 1159.00 K, respectively, which agree in for these calculations with their designated values.

A straightforward convergence was achieved in the first calculation. The equilibrium temperature that was obtained was below both the melting temperatures of $Na_2SO_4$(s-I) and PbO(s-yw), and neither $Na_2SO_4$(lq) nor PbO(lq) was present in the equilibrium mixture. In the second calculation, the first convergence was achieved at 1161.06 K, which is less than 50 K above the melting temperatures of $Na_2SO_4$(s-I) and PbO(s-yw). $Na_2SO_4$(lq) was then added and a melting condition was determined at 1157.00 K, with both $Na_2SO_4$(s-I) and $Na_2SO_4$(lq) and only PbO(s-yw) present at equilibrium.

In the third calculation, an oscillation occurred when switching between the solid and the liquid phases happened alternatively, with the cycle repeating every four convergences as follows: After the first convergence $Na_2SO_4$(s-I) was replaced by $Na_2SO_4$(lq). Then at the second convergence PbO(s-yw) was replaced by PbO(lq). $Na_2SO_4$(lq) was deleted and $Na_2SO_4$(s-I) was re-introduced after the third convergence. Finally, PbO(lq) was deleted and replaced by PbO(s-yw), at the fourth convergence. The cycle then repeated.

In addition to the oscillation, matrix singularities were encountered in the fourth calculation. Matrix singularities occurred when the NASA code tried to consider the melting of both $Na_2SO_4$ and PbO. The oscillation cycle was roughly as follows: It started with $Na_2SO_4$(lq) and PbO(lq) selected for consideration, and $Na_2SO_4$(s-I) and PbO(s-yw) were then introduced. With all four condensed species considered together, actually two melting problems were considered; matrix singularities were encountered and the NASA code determined that $Na_2SO_4$(lq) and PbO(lq) were unacceptable and deleted them. However, subsequently $Na_2SO_4$(s-I) and PbO(s-yw) were switched to $Na_2SO_4$(lq) and PbO(lq). With only $Na_2SO_4$(lq) and PbO(lq) considered, the cycle repeated. The final calculation was quite straightforward again. With convergence achieved at 1218.04 K which was above the melting temperatures of $Na_2SO_4$(s-I) and PbO(s-yw), only $Na_2SO_4$(lq) and PbO(lq) were present at equilibrium.

The same set of calculations was performed by using the new code, and the results are summarized in table 5.18. The melting conditions of $Na_2SO_4$ and PbO were readily resolved. Same solutions as those of the NASA code were obtained for the first, second, and the last calculations. For the third and the fourth calculations, for which the NASA code had difficulties in achieving the solutions, actually they both involved the melting of PbO.

Table 5.18: Second set of calculations for the test formulation given in table 5.16, for a loading density of 0.2 gm/cm$^3$.

| weight (%) | | | equilibrium temperature (K) | equilibrium abundance (kg-mole/kg-mixture) | |
|---|---|---|---|---|---|
| $NaNO_3$ | PbO | S | | | |
| 5.0 | 85.0 | 10.0 | 1142.51 | $Na_2SO_4$(s-I) at 29.41 | PbO(s-yw) at 212.1 |
| 5.2 | 84.8 | 10.0 | 1157.00 | $Na_2SO_4$(s-I) at 24.63<br>$Na_2SO_4$(lq) at 5.961 | PbO(s-yw) at 212.8 |
| 6.0 | 84.0 | 10.0 | 1159.00 | $Na_2SO_4$(s-I) at 35.30 | PbO(s-yw) at 144.5<br>PbO(s-1) at 70.96 |
| 7.0 | 83.0 | 10.0 | 1159.00 | $Na_2SO_4$(s-I) at 41.18 | PbO(s-yw) at 27.05<br>PbO(s-1) at 191.8 |
| 8.0 | 82.0 | 10.0 | 1281.04 | $Na_2SO_4$(lq) at 47.06 | PbO(lq) at 222.2 |

The NASA code was also used to solve the same set of black-powder problems, the results of which were obtained by the new code had been plotted in figure 4.5 in section 4.4.1. Selected results of these calculations obtained by the NASA and new codes are tabulated for reference in tables 5.19 and 5.20 for comparison purposes. Extremely precise values of loading densities were used only for the purpose of determining the range over which an oscillation in the addition and removal of $K_2S$(lq) occurred in the NASA code, as well as the onset and completion of the melting of $K_2S$(s-3).

For loading densities from 0.095 to 0.09563563 gm/cm$^3$, both codes achieved converged solutions and produced the same results. The equilibrium temperatures were below both 1221 and 1222.24 K and only $K_2S$(s-3) was present at equilibrium. Oscillations as in the case of $Na_2S$ described earlier occurred in the calculations obtained by using the NASA code for loading densities from 0.09563564 to 0.09726173 gm/cm$^3$. These were caused by the discrepancy between the designated melting temperature of $K_2S$(s-3), which is 1221 K, and its melting temperature dictated by the polynomial coefficients of $K_2S$(s-3) and $K_2S$(lq), which is 1222.24 K. Using the calculation for 0.096 gm/cm$^3$ as an example, with only $K_2S$(s-3) being considered, a converged solution was achieved at 1221.28 K, which is less than 50 K above 1221 K. $K_2S$(lq) was then added and both $K_2S$(s-3) and $K_2S$(lq) were considered; however, this new case was not a melting problem and $K_2S$(lq) was deleted. Once $K_2S$(s-3) only was considered, a new convergence at 1221.28 K was achieved again, and the process was repeated.

While oscillations still occurred at 0.09726173 gm/cm$^3$ for the NASA code, the new code predicted the onset of melting and an equilibrium abundance for $K_2S$(lq) of $2.7374\times10^{-9}$ kg-mole/kg-mixture. At 0.09726174 gm/cm$^3$ the NASA code determined the onset of melting. The two codes determined the same equilibrium temperature and pressure; however, while the abundances of $K_2S$(s-3) agreed to five significant digits, the abundances of $K_2S$(lq) only agreed to the same order of magnitude. Additional calculations were done from 0.09726175 to 0.0985 gm/cm$^3$ for very small increments in the loading density, mainly for the comparison of the trace amounts of $K_2S$(lq) determined by the two codes when there was little melting. Same equilibrium temperature and pressure were determined (as a matter of fact for all the remaining calculations). It can be seen that while the abundances of $K_2S$(s-3) agreed to five significant digits, there are fair differences in the trace abundances of $K_2S$(lq). At 0.0985 gm/cm$^3$ an agreement of five significant digits in the abundance of $K_2S$(lq) was obtained again.

Table 5.19: Comparison of equilibrium temperatures and pressures from the NASA and new codes for the black powder formulation given in table 4.6, for the case of $K_2S$ melting.

| loading density (gm/cm$^3$) | equilibrium temperature (K) | | equilibrium pressure (MPa) | |
|---|---|---|---|---|
| | NASA code | new code | NASA code | new code |
| 0.095 | 1220.51 | 1220.51 | 14.86 | 14.86 |
| 0.09563563 | 1221.00 | 1221.00 | 14.96 | 14.96 |
| 0.09563564 | oscillation | 1221.00 | oscillation | 14.96 |
| 0.09726173 | oscillation | 1222.24 | oscillation | 15.22 |
| 0.09726174 | 1222.24 | 1222.24 | 15.22 | 15.22 |
| 0.09726175 | 1222.24 | 1222.24 | 15.22 | 15.22 |
| 0.097262 | 1222.24 | 1222.24 | 15.22 | 15.22 |
| 0.097265 | 1222.24 | 1222.24 | 15.22 | 15.22 |
| 0.09729 | 1222.24 | 1222.24 | 15.22 | 15.22 |
| 0.0975 | 1222.24 | 1222.24 | 15.25 | 15.25 |
| 0.0985 | 1222.24 | 1222.24 | 15.37 | 15.37 |
| 0.1035 | 1222.24 | 1222.24 | 15.99 | 15.99 |
| 0.10376457 | 1222.24 | 1222.24 | 16.02 | 16.02 |
| 0.1037646 | 1222.24 | 1222.24 | 16.02 | 16.02 |
| 0.105 | 1223.10 | 1223.10 | 16.21 | 16.21 |

Table 5.20: Comparison of equilibrium abundances of $K_2S$(s-3) and $K_2S$(lq) for black powder for which the correspoinding equilibrium temperatures and pressures are listed in table 5.19.

| loading density (gm/cm$^3$) | equilibrium abundance (kg-mole/kg-mixture) | | | |
|---|---|---|---|---|
| | $K_2S$(s-3) | | $K_2S$(s-1) | |
| | NASA code | new code | NASA code | new code |
| 0.095 | $1.6731\times10^{-3}$ | $1.6731\times10^{-3}$ | absent | absent |
| 0.09563563 | $1.6698\times10^{-3}$ | $1.6698\times10^{-3}$ | absent | absent |
| 0.09563564 | oscillation | $1.6698\times10^{-3}$ | oscillation | absent |
| 0.09726173 | oscillation | $1.6615\times10^{-3}$ | oscillation | $2.7374\times10^{-9}$ |
| 0.09726174 | $1.6615\times10^{-3}$ | $1.6615\times10^{-3}$ | $1.6973\times10^{-9}$ | $5.5228\times10^{-9}$ |
| 0.09726175 | $1.6615\times10^{-3}$ | $1.6615\times10^{-3}$ | $3.6846\times10^{-9}$ | $8.2169\times10^{-9}$ |
| 0.097262 | $1.6614\times10^{-3}$ | $1.6614\times10^{-3}$ | $6.7657\times10^{-8}$ | $7.2289\times10^{-8}$ |
| 0.097265 | $1.6606\times10^{-3}$ | $1.6606\times10^{-3}$ | $8.2545\times10^{-7}$ | $8.3270\times10^{-7}$ |
| 0.09729 | $1.6539\times10^{-3}$ | $1.6539\times10^{-3}$ | $7.1521\times10^{-6}$ | $7.1578\times10^{-6}$ |
| 0.0975 | $1.5978\times10^{-3}$ | $1.5978\times10^{-3}$ | $6.0186\times10^{-5}$ | $6.0193\times10^{-5}$ |
| 0.0985 | $1.3330\times10^{-3}$ | $1.3330\times10^{-3}$ | $3.1049\times10^{-4}$ | $3.1049\times10^{-4}$ |
| 0.1035 | $6.4661\times10^{-5}$ | $6.4660\times10^{-5}$ | $1.5090\times10^{-3}$ | $1.5090\times10^{-3}$ |
| 0.10376457 | $4.5377\times10^{-9}$ | $2.8688\times10^{-9}$ | $1.5701\times10^{-3}$ | $1.5701\times10^{-3}$ |
| 0.1037646 | absent | absent | $1.5701\times10^{-3}$ | $1.5701\times10^{-3}$ |
| 0.105 | absent | absent | $1.5652\times10^{-3}$ | $1.5652\times10^{-3}$ |

The next two sets of results for the loading densities of 0.1035 and 0.10376457 gm/cm$^3$ are for the comparisons when $K_2S$(s-3) had nearly disappeared. Now the equilibrium abundances of $K_2S$(s-3) were different while those of $K_2S$(lq) were the same. At 0.1035 gm/cm$^3$, the abundances of $K_2S$(s-3) agreed to four significant digits, and at 0.10376457 gm/cm$^3$ the agreement was only to the same order of magnitude. At the final two loading densities, $K_2S$(s-3) had completely disappeared and only $K_2S$(lq) was present. The two codes obtained same results.

While the new code handled the melting problem quite well, it took much longer time than the NASA code. The new code was less efficient in solving a melting problem than a regular one which does not involve melting. This is due to the extra number of iterations required to achieve convergence in temperature when there is melting; the trial temperature would fall on either side of the melting temperature of the substance in melting in an oscillatory fashion, as mentioned before. CPU times taken by the two codes for determining equilibrium compositions are listed in table 5.21 for comparison, for a selected number of the calculations in the sets of black powder problems solved. Listed also are the numbers of iterations taken by the new code to achieve convergence in temperature in these calculations, after the equilibrium temperatures had been bracketed. The initial equilibrium temperature bracket was 2300 to 2700 K in all the calculations.

Table 5.21: CPU times for determining equilibrium compositions using the NASA and new codes, and number of iterations taken by the new code for temperature convergence after bracketing the equilibrium temperature, for some black-powder calculations for which the equilibrium temperatures and pressures are listed in table 5.19.

| loading density (gm/cm$^3$) | NASA code CPU time (s) | new code CPU time (s) | number of iterations for temperature convergence after bracketing equilibrium temperature |
|---|---|---|---|
| 0.095 | 2.18 | 37.65 | 7 |
| 0.09726174 | 2.04 | 34.59 | 7 |
| 0.097265 | 2.05 | 41.65 | 13 |
| 0.1035 | 2.10 | 58.95 | 21 |
| 0.1037646 | 2.17 | 42.36 | 10 |
| 0.105 | 2.20 | 33.70 | 6 |

At 0.095 gm/cm$^3$, the problem was a regular problem, no melting was involved, only $K_2S$(s-3) was present, seven iterations on temperature were required to achieve convergence in temperature. At 0.09726174 gm/cm$^3$, the problem was still essentially a non-melting problem, only a trace amount of $K_2S$(lq) was formed, again seven iterations were required to achieve convergence. At 0.097265 gm/cm$^3$, the problem became more like a melting problem, but the amount of $K_2S$(lq) was still relatively small in comparison to that of $K_2S$(s-3); thirteen iterations were required in this case. The CPU times required to determine equilibrium compositions were roughly the same for all the melting problems, ranging from a small amount of $K_2S$(lq) was formed to a small amount of $K_2S$(s-3) was left. The average CPU time was approximately 50 s, with the maximum occurred at 0.1035 gm/cm$^3$ at 58.95 s for 21 iterations. There was a decrease in the number of iterations needed when the amount of unmelted $K_2S$(s-3) became less and less. At 0.1037646 gm/cm$^3$ , melting had just completed and ten iterations was needed. Finally, at 0.105 gm/cm$^3$, at which only $K_2S$(lq) was present, six iterations were needed, which is similar to the case of 0.095 gm/, at which only $K_2S$(s-3) was present.

### 5.2.2 Comparison of Results of the Bagheera and New Codes

To compare the capabilities of the Bagheera and new codes in analysing mixtures involving a melting substance, two sets of calculations were carried out for two slightly different compositions of black powder (see the ingredients in table 5.4). In the first set of calculations, the composition in terms of weight percentages used was potassium nitrate at 37%, charcoal at 17%, sulphur at 27%, water at 0.5% and ash at 18.5%. The melting of $K_2S$ was analysed by doing calculations. You many recall that there were oscillations in the NASA calculations involving the melting of $K_2S$. Such oscillations arose firstly because there was a discrepancy between the designated melting temperature of $K_2S$(s-3) and $K_2S$(lq) and the melting temperature dictated by their polynomial coefficients, and secondly because the NASA code uses the transition temperature dictated by the polynomial coefficients of the two neighbouring phases, when analysing a situation involving the possibly of a substance in transition. However, the Bagheera code appears to stay with the designated transition temperature of the two phases involved when analysing a possible transition situation, which offers good computational advantages. This better feature will become evident from the results of the first set of calculations that will be presented below.

For the first set of calculations, a total of 193 possible product species, composed of 161 gaseous and 32 condensed species, were selected from the library of the Bagheera code and considered. Among the selected condensed species, there were 13 neighbouring pairs. In addition, 13 calculations were performed, covering conditions involving condensed $K_2S$ being present entirely in its solid phase, in melting, and to entirely in its liquid phase. The equilibrium temperature and pressure of the product mixture determined by the two codes are tabulated in table 5.22, and the equilibrium abundances of the two phases $K_2S$(s-3) and $K_2S$(lq) are tabulated in table 5.23. (To be consistent with the results on melting temperatures reported earlier, equilibrium temperatures determined by the new code are reported to six significant digits; however, the equilibrium temperatures determined by the Bagheera code are reported to only five significant digits, because this is the number used for the data output.)

Table 5.22: Comparison of equilibrium temperatures and pressures from the Bagheera and new codes for a black powder problem involving the melting of $K_2S$.

| loading density (gm/cm$^3$) | equilibrium temperature (K) | | equilibrium pressure (MPa) | |
|---|---|---|---|---|
| | Bagheera code | new code | Bagheera code | new code |
| 0.179 | 1220.6 | 1221.42 | 25.20 | 25.20 |
| 0.1795 | 1220.8 | 1221.64 | 25.28 | 25.28 |
| 0.1807 | no convergence | 1222.17 | no convergence | 25.46 |
| 0.18086 | no convergence | 1222.24 | no convergence | 25.49 |
| 0.1809 | no convergence | 1222.24 | no convergence | 25.49 |
| 0.181 | no convergence | 1222.24 | no convergence | 25.50 |
| 0.183 | no convergence | 1222.24 | no convergence | 25.75 |
| 0.185 | no convergence | 1222.24 | no convergence | 26.00 |
| 0.186 | 1221.3 | 1222.24 | 26.13 | 26.13 |
| 0.18605 | 1221.4 | 1222.24 | 26.13 | 26.13 |
| 0.1861 | 1221.4 | 1222.24 | 26.14 | 26.14 |
| 0.187 | 1221.8 | 1222.62 | 26.28 | 26.28 |
| 0.19 | 1223.0 | 1223.88 | 26.75 | 26.75 |

Table 5.23: Comparison of equilibrium abundances of $K_2S$(s-3) and $K_2S$(lq) for black powder for which the correspoinding equilibrium temperatures and pressures are listed in table 5.22.

| loading density (gm/cm$^3$) | equilibrium abundance (kg-mole/kg-mixture) | | | |
|---|---|---|---|---|
| | $K_2S$(s-3) | | $K_2S$(lq) | |
| | Bagheera code | new code | Bagheera code | new code |
| 0.179 | $6.053\times10^{-4}$ | $5.989\times10^{-4}$ | absent | absent |
| 0.1795 | $6.037\times10^{-4}$ | $5.973\times10^{-4}$ | absent | absent |
| 0.1807 | no convergence | $5.936\times10^{-4}$ | no convergence | absent |
| 0.18086 | no convergence | $5.928\times10^{-4}$ | no convergence | $3.101\times10^{-7}$ |
| 0.1809 | no convergence | $5.881\times10^{-4}$ | no convergence | $4.669\times10^{-6}$ |
| 0.181 | no convergence | $5.765\times10^{-4}$ | no convergence | $1.552\times10^{-5}$ |
| 0.183 | no convergence | $3.479\times10^{-4}$ | no convergence | $2.298\times10^{-4}$ |
| 0.185 | no convergence | $1.227\times10^{-4}$ | no convergence | $4.409\times10^{-4}$ |
| 0.186 | absent | $1.135\times10^{-5}$ | $5.618\times10^{-4}$ | $5.453\times10^{-4}$ |
| 0.18605 | absent | $5.938\times10^{-6}$ | $5.617\times10^{-4}$ | $5.504\times10^{-4}$ |
| 0.1861 | absent | $3.461\times10^{-7}$ | $5.616\times10^{-4}$ | $5.556\times10^{-4}$ |
| 0.187 | absent | absent | $5.592\times10^{-4}$ | $5.536\times10^{-4}$ |
| 0.19 | absent | absent | $5.514\times10^{-4}$ | $5.458\times10^{-4}$ |

The designated melting temperature of $K_2S$(s-3) and $K_2S$(lq) is 1221 K. It can bee seen that the Bagheera code was able to converge up to a temperature of 1220.8 K and predicted the presence of $K_2S$(s-3) only. No convergence was achieved for the next six runs. However, when convergence was achieved again at the loading density of 0.186 gm/cm$^3$, the Bagheera code determined an equilibrium temperature of 1221.3 K, which is below 1222.24 K, the melting temperature dictated by the polynomial coefficients of $K_2S$(s-3) and $K_2S$(lq), and predicted the presence of $K_2S$(lq) only. On the other hand, the new code converged in each case and predicted a gradual transition from $K_2S$(s-3) to $K_2S$(lq) at 1222.24 K.

CPU times for the previous equilibrium calculations are given in table 5.24. Because the architectures of the Bagheera and NASA codes are very similar, the trends in the comparison of CPU times from the Bagheera and new codes are similar to those of the NASA and new codes. In

Table 5.24: Comparison of CPU times for determining equilibrium compositions using the Bagheera and new codes for some black-powder calculations for which results are given in tables 5.22 and 5.23.

| loading density (gm/cm$^3$) | Bagheera code CPU time (s) | new code CPU time (s) | loading density (gm/cm$^3$) | Bagheera code CPU time (s) | new code CPU time (s) |
|---|---|---|---|---|---|
| 0.179 | 1.26 | 47.65 | | | |
| 0.1795 | 1.26 | 47.31 | 0.185 | no convergence | 56.37 |
| 0.1807 | no convergence | 45.86 | 0.186 | 1.80 | 61.29 |
| 0.18086 | no convergence | 43.77 | 0.18605 | 1.80 | 60.96 |
| 0.1809 | no convergence | 55.23 | 0.1861 | 2.16 | 43.04 |
| 0.181 | no convergence | 63.32 | 0.187 | 1.80 | 40.58 |
| 0.183 | no convergence | 61.73 | 0.19 | 1.80 | 41.43 |

cases where the Bagheera code converged, the new code took fairly longer CPU times. In general, these longer times resulted from iterating many times on trial temperatures falling on either side of the temperature 1224.24 K, which came as a result of the energy constraint that was hard or impossible to satisfy by considering either $K_2S$(s-3) or $K_2S$(lq) alone.

The reason the Bagheera code did not obtain a converged solution in the previous calculations is probably because of the discrepancy between the designated melting temperature of $K_2S$(s-3) and $K_2S$(lq) and the melting temperature dictated by their polynomial coefficients. A second set of calculations that involved analyzing the melting of $K_2CO_3$ was performed to add more information. The composition in terms of weight percentages used was potassium nitrate at 34%, charcoal at 17%, sulphur at 27%, water at 0.5%, and ash at 21.5%. In this case the melting temperature of 1173.99 K was dictated by the polynomial coefficients of $K_2CO_3$(s) and $K_2CO_3$(lq), and it practically coincided with the designated value of 1174 K. Six calculations were done with the same set of species used for the first set of calculations and the results are tabulated in tables 5.25 and 5.26. In these calculation both the Bagheera and new codes predicted a gradual transition from $K_2CO_3$(s) to $K_2CO_3$(lq).

Based on the results of the NASA and new codes presented in tables 5.19 and 5.20, and those of the Bagheera and new codes presented in tables 5.25 and 5.26, it is observed that the results of

Table 5.25: Comparison of equilibrium temperatures and pressures from the Bagheera and new codes for a black-powder problem involving the melting of $K_2CO_3$.

| loading density (gm/cm$^3$) | equilibrium temperature (K) | | equilibrium pressure (MPa) | |
|---|---|---|---|---|
| | Bagheera code | new code | Bagheera code | new code |
| 0.11 | 1170.6 | 1171.43 | 14.05 | 14.05 |
| 0.115 | 1173.6 | 1173.99 | 14.73 | 14.71 |
| 0.12 | 1174.0 | 1173.99 | 15.30 | 15.26 |
| 0.13 | 1174.0 | 1173.99 | 16.40 | 16.37 |
| 0.14 | 1174.0 | 1173.99 | 17.51 | 17.47 |
| 0.15 | 1174.8 | 1175.61 | 18.65 | 18.65 |

Table 5.26: Comparison of equilibrium abundances of $K_2CO_3$(s) and $K_2S$(lq) for black powder for which the corresponding equilibrium temperatures and pressures are listed in table 5.25.

| loading density (gm/cm$^3$) | equilibrium abundance (kg-mole/kg-mixture) | | | |
|---|---|---|---|---|
| | $K_2CO_3$(s) | | $K_2CO_3$(lq) | |
| | Bagheera code | new code | Bagheera code | new code |
| 0.11 | $2.436\times10^{-3}$ | $2.441\times10^{-3}$ | absent | absent |
| 0.115 | $2.453\times10^{-3}$ | $2.369\times10^{-3}$ | absent | $7.429\times10^{-6}$ |
| 0.12 | $2.070\times10^{-3}$ | $1.950\times10^{-3}$ | $4.304\times10^{-4}$ | $5.644\times10^{-4}$ |
| 0.13 | $1.261\times10^{-3}$ | $1.147\times10^{-3}$ | $1.334\times10^{-3}$ | $1.462\times10^{-3}$ |
| 0.14 | $5.376\times10^{-4}$ | $4.283\times10^{-4}$ | $2.143\times10^{-3}$ | $2.266\times10^{-3}$ |
| 0.15 | absent | absent | $2.752\times10^{-3}$ | $2.758\times10^{-3}$ |

the NASA and new codes are essentially the same, whereas there are small differences between the results of the Bagheera and new codes. These differences are likely due to the use of the Amagat-type ideal mixture model and the modified truncated virial equation of state for the gaseous species in the Bagheera code. They are less likely due to the differences of the Newton-Raphson and VCS algorithms, because both the NASA and Bagheera codes use the Newton-Raphson scheme. The same conclusions were drawn in section 5.1.1, based on the results of calculations not involving melting.

### 5.2.3 Comparison of Results of the Blake and New Codes

To facilitate the performance comparison of the new code with the Blake code, equilibrium calculations were repeated for the black-powder formulation given in table 4.8 by using the new code, but for a subset of the possible product species that could be selected from the Blake library. Only the most abundant 29 gaseous species plus the condensed phases of the substances that are known to have one of their condensed phases present at chemical equilibrium, as determined by the demonstration runs discussed in section 4.4.2 are included. This is done simply to adapt to the limitations of the Blake code. You many recall that in order to achieve a converged solution, a further reduction in the number of gaseous species that could be included for consideration was required for some of the previous calculations using the Blake code. It happened only for these calculations that a converged solution was achieved for the maximum number of gaseous species that can be handled by the Blake code.

For comparisons involving a melting component substance, calculations were done for the same nine loading densities used for the previous demonstration runs. Results of equilibrium mixture temperatures and pressures have been tabulated in table 5.27, and those of equilibrium abundances of $K_2S$(s-3) and $K_2S$(lq), the two phases of the melting substance $K_2S$, are given in table 5.28. The two codes yielded basically the same results, except that the Blake code did not converge for the case of the loading density of 0.005 gm/cm$^3$. Even after some drastic attempts were taken, such as greatly reducing the number of gaseous species considered from the beginning of the run, convergence was still not achieved. This was quite surprising because the Blake code seemed to have been working so well for the other loading densities. In particular, at this loading density

Table 5.27: Comparison of equilibrium temperatures and pressures from the Blake and new codes for black powder with a melting component given in table 4.8.

| loading density (gm/cm$^3$) | equilibrium temperature (K) | | equilibrium pressure (MPa) | |
|---|---|---|---|---|
| | Blake code | new code | Blake code | new code |
| 0.00085 | 1391 | 1391 | 0.18 | 0.18 |
| 0.00086 | 1392. | 1392. | 0.18 | 0.18 |
| 0.0009 | 1392. | 1392 | 0.19 | 0.19 |
| 0.0015 | 1392. | 1392. | 0.31 | 0.31 |
| 0.005 | no convergence | 1392 | no convergence | 1.02 |
| 0.021 | 1394. | 1394. | 4.26 | 4.26 |
| 0.042 | 1396 | 1396. | 8.60 | 8.60 |
| 0.0458 | 1396. | 1396. | 9.40 | 9.40 |
| 0.0465 | 1396. | 1396. | 9.55 | 9.55 |

Table 5.28: Comparison of equilibrium abundances of $K_2S$(s-3) and $K_2S$(lq) from0 the Blake and new codes for black powder for which the corresponding equilibrium temperatures and pressures are listed in table 5.27.

| loading density (gm/cm$^3$) | equilibrium abundance (kg-mole/kg-mixture) | | | |
|---|---|---|---|---|
| | $K_2S$(s-3) | | $K_2S$(lq) | |
| | Blake code | new code | Blake code | new code |
| 0.00085 | $3.422\times10^{-3}$ | $3.422\times10^{-3}$ | absent | absent |
| 0.00086 | $3.417\times10^{-3}$ | $3.416\times10^{-3}$ | $5.495\times10^{-6}$ | $6.406\times10^{-6}$ |
| 0.0009 | $3.373\times10^{-3}$ | $3.372\times10^{-3}$ | $4.942\times10^{-5}$ | $5.034\times10^{-5}$ |
| 0.0015 | $2.884\times10^{-3}$ | $2.883\times10^{-3}$ | $5.413\times10^{-4}$ | $5.422\times10^{-4}$ |
| 0.005 | no convergence | $1.746\times10^{-3}$ | no convergence | $1.682\times10^{-3}$ |
| 0.021 | $5.262\times10^{-4}$ | $5.242\times10^{-4}$ | $2.903\times10^{-3}$ | $2.905\times10^{-3}$ |
| 0.042 | $5.723\times10^{-5}$ | $5.548\times10^{-5}$ | $3.373\times10^{-3}$ | $3.374\times10^{-3}$ |
| 0.0458 | absent | $5.372\times10^{-6}$ | $3.430\times10^{-3}$ | $3.424\times10^{-3}$ |
| 0.0465 | absent | absent | $3.430\times10^{-3}$ | $3.430\times10^{-3}$ |

the proportions of the two phases were about equal and the case should have been a straightforward calculation.

Differences in equilibrium abundances are more noticeable for phases that exist in trace amounts. For example, for the case of the loading density of 0.058 gm/cm$^3$, while the new code determined a minute amount of $K_2S$(s-3), the Blake code determined none. These differences are attributed to the differences of the two codes in the solution algorithms and the methods for determining the proportions of each phase.

For comparisons involving a melting noncomponent substance the calculations were done for the same seven loading densities used for the previous demonstrations. For these calculations, convergence was achieved by the Blake code for all cases. Results of equilibrium mixture temperatures and pressures have been tabulated in table 5.29, and those of equilibrium abundances of $K_2CO_3$(s) and $K_2CO_3$(lq), the two phases of the melting substance $K_2CO_3$, are given in table 5.30. The trends in the results are similar to the previous case, as can be observed, except that the differences in the

Table 5.29: Comparison of equilibrium temperatures and pressures from the Blake and new codes for black powder with a melting noncomponent given in table 4.8.

| loading density (gm/cm$^3$) | equilibrium temperature (K) | | equilibrium pressure (MPa) | |
|---|---|---|---|---|
| | Blake code | new code | Blake code | new code |
| 0.0876 | 1199. | 1199 | 16.85 | 16.85 |
| 0.08764 | 1199. | 1199. | 16.86 | 16.86 |
| 0.088 | 1199 | 1199 | 16.93 | 16.92 |
| 0 0887 | 1199 | 1199. | 17.06 | 17.05 |
| 0.0895 | 1199. | 1199. | 17.20 | 17.20 |
| 0.09 | 1199. | 1199. | 17 29 | 17.29 |
| 0.091 | 1200. | 1200. | 17 49 | 17.49 |

Table 5.30: Comparison of equilibrium abundances of $K_2CO_3(s)$ and $K_2CO_3(lq)$ from the Blake and new codes for black powder for which the corresponding temperatures and pressures are listed in table 5.29.

| loading density ($gm/cm^3$) | equilibrium abundance (kg-mole/kg-mixture) | | | |
|---|---|---|---|---|
| | $K_2CO_3(s)$ | | $K_2CO_3(lq)$ | |
| | Blake code | new code | Blake code | new code |
| 0.0876 | $3.334\times10^{-4}$ | $3.335\times10^{-4}$ | absent | absent |
| 0.08764 | $3.336\times10^{-4}$ | $3.292\times10^{-4}$ | absent | $4.862\times10^{-6}$ |
| 0.088 | $3.145\times10^{-4}$ | $2.791\times10^{-4}$ | $2.242\times10^{-5}$ | $6.067\times10^{-5}$ |
| 0.0887 | $2.166\times10^{-4}$ | $1.827\times10^{-4}$ | $1.315\times10^{-4}$ | $1.681\times10^{-4}$ |
| 0.0895 | $1.064\times10^{-4}$ | $7.404\times10^{-5}$ | $2.544\times10^{-4}$ | $2.893\times10^{-4}$ |
| 0.09 | $3.845\times10^{-5}$ | $6.939\times10^{-6}$ | $3.301\times10^{-4}$ | $3.642\times10^{-4}$ |
| 0.091 | absent | absent | $3.772\times10^{-4}$ | $3 775\times10^{-4}$ |

equilibrium abundances are more noticeable for these demonstrations for all calculations involving melting. This occurs because the melting substance was present in a very small amount from the beginning.

The CPU times for running the two codes for the two sets of calculations are presented in table 5.31. The Blake code once again took a much longer time than the new code to converge because it spent lots of time iterating to find the right set of components. Furthermore, the Blake code took a longer time to solve problems involving a melting component (a more abundant substance) than problems involving a melting noncomponent (a less abundant substance), while the new code took about the same time to solve both of these types of problems. In addition, there was an increase in the CPU time for the Blake code when the proportion of the liquid phase of a melting component increased.

Table 5.31: Comparison of CPU times for determining equilibrium compositions using the Blake and new codes for some black-powder calculations for which results are given in tables 5.27, 5.28, 5.29 and 5.30.

| calculations with melting component | | | calculations with melting noncomponent | | |
|---|---|---|---|---|---|
| loading density ($gm/cm^3$) | Blake code CPU time (s) | new code CPU time (s) | loading density ($gm/cm^3$) | Blake code CPU time (s) | new code CPU time (s) |
| 0.00085 | 60 85 | 9.22 | | | |
| 0.00086 | 60 06 | 20.38 | | | |
| 0.0009 | 71.30 | 20.72 | 0 0876 | 40.62 | 7.85 |
| 0.0015 | 92.69 | 19.19 | 0.08764 | 40.62 | 16.79 |
| 0.005 | no convergence | 16.76 | 0.088 | 40.12 | 14.23 |
| 0.021 | 102.64 | 18.10 | 0 0887 | 39.90 | 15.49 |
| 0.042 | 103.79 | 19.30 | 0 0895 | 39.78 | 16.33 |
| 0.0458 | 102 91 | 16.28 | 0.09 | 38.60 | 18.73 |
| 0.0465 | 101 68 | 11.98 | 0 091 | 37.40 | 7 98 |

## 5.3 Equilibrium Calculations for a Large Number of Species Without and With Melting

In this section, results of assessment of the NASA and new codes concerning large systems are presented. A comparison between the two codes for the 18-element system described in section 4.5 was first performed. A loading density of 0.2 gm/cm$^3$ and a total of 587 species were considered. For composition 1 the NASA code did not converge, when no condensed species was specified for consideration from the very beginning. Without using the results obtained by the new code and assuming any prior knowledge of which condensed species to include, additional calculations were performed for three modifications to composition 1 in an attempt to achieve convergence. If convergence was achieved, the calculation for composition 1 could then be repeated, using the converged results to aid the specification of condensed species for consideration right from the beginning.

The three compositions called 1-a, 1-b and 1-c that were used for these calculations were obtained by modifying the weight percentages of $BaCrO_4$ and $KClO_4$. They are given in table 5.32. No condensed species was specified at the beginning for consideration. Convergence was not achieved for compositions 1-a and 1-b. For composition 1-c, convergence was achieved and there were ten condensed species present at equilibrium (see table 5.33), with $B_2O_3$(lq) and Cr(lq) being the most and the second most abundant condensed species. With composition 1-c being not very different from composition 1, the condensed species present at equilibrium in the former case might be similar to those in the latter case. Thence they could be used as a guide for specifying condensed species at the beginning for consideration for composition 1, and $B_2O_3$(lq) and Cr(lq) were specified because they were the most abundant.

At first the calculation was repeated for composition 1 with only $B_2O_3$(lq) specified for consideration right from the beginning. Once again no convergence was achieved. Convergence was achieved, however, when both $B_2O_3$(lq) and Cr(lq) were specified, indicating that 14 condensed species should be present at equilibrium. Results of this set of calculations are summarized in table 5.33, and the condensed species are listed in descending order of abundance. The condensed

Table 5.32: First of the two formulations given in table 4.11 for the consideration of equilibrium systems with a large number of species.

| ingredient | formula | enthalpy of formation at 298.15 K (cal/mole) | percentage by weight for composition | | | |
|---|---|---|---|---|---|---|
| | | | 1 | 1-a | 1-b | 1-c |
| barium chromate | $Ba_1Cr_1O_4$ | −342,200 | 45 | 40 | 35 | 30 |
| potassium perchlorate | $K_1Cl_1O_4$ | −102,800 | 5 | 10 | 15 | 20 |
| barium nitrate | $Ba_1N_2O_6$ | −238,280 | 1 | 1 | 1 | 1 |
| sodium cryolite | $Na_3Al_1F_6$ | −758,470 | 1 | 1 | 1 | 1 |
| Viton A fluoroelastomer | $C_{11}F_{14}H_8$ | −737,170 | 5 | 5 | 5 | 5 |
| magnesium carbonate | $Mg_1C_1O_3$ | −265,700 | 15 | 15 | 15 | 15 |
| potassium sulphate (KS) | $K_2S_1O_4$ | −342,660 | 5 | 5 | 5 | 5 |
| lead oxide | $Pb_1O_1$ | −52,440 | 8 | 8 | 8 | 8 |
| titanium oxide | $Ti_1O_2$ | −225,800 | 5 | 5 | 5 | 5 |
| lithium hydride | $Li_1H_1$ | −21,660 | 1 | 1 | 1 | 1 |
| boron | $B_1$ | 0 | 8 | 8 | 8 | 8 |
| zirconium | $Zr_1$ | 0 | 1 | 1 | 1 | 1 |

Table 5.33: Selected results of calculations of the first formulation of an 18-element system and derivatives from this formulation from the NASA code.

| | composition | | | | |
|---|---|---|---|---|---|
| | 1 | 1-a | 1-b | 1-c | 1 |
| condensed species considered initially | none | none | none | none | $B_2O_3$(lq)<br>Cr(lq) |
| condensed species present at equilibrium | no convergence | no convergence | no convergence | $B_2O_3$(lq)<br>Cr(lq)<br>$BaF_2$(lq)<br>$Mg_2TiO_4$(lq)<br>MgO(s)<br>$BaCl_2$(l)<br>$ZrO_2$(s-II)<br>BaS(s)<br>$MgAl_2O_4$(lq)<br>Pb(l) | $B_2O_3$(lq)<br>C(s-gr)<br>Cr(s)<br>$BaF_2$(lq)<br>MgO(s)<br>$Mg_2TiO_4$(lq)<br>BaO(s)<br>Pb(lq)<br>BaS(s)<br>$BaCl_2$(l)<br>$ZrO_2$(s-II)<br>BN(s)<br>TiC(s)<br>$MgAl_2O_4$(s) |

species present at equilibrium for composition 1 and 1-c are similar but not the same. For example, Cr(s) was present in the former case as oppose to Cr(lq) in the latter case, and it was only the third most abundant condensed species after C(s-gr).

Two conclusions may be drawn from this exercise. Firstly, when handling large systems involving many condensed species by using the NASA code, and when convergence cannot be achieved because one is not sure which condensed species to include in the calculations, the calculations can be attempted by using slightly different compositions. If an equilibrium solution is obtained, then the condensed species determined in this solution can be used as a guide for specifying condensed species for the original composition. Secondly, the fact that a converged solution was achieved for composition 1-c without the specification of any condensed species indicates that even for large systems involving numerous condensed species, the NASA code does not necessarily fail in all cases when no condensed species is specified initially.

The equilibrium solution for composition 2 was also obtained in this work, but $B_2O_3$(lq) and Cr(s) was specified to be considered. Cr(s) was used instead of Cr(lq) because it was Cr(s) that was present at equilibrium for composition 1. The equilibrium solutions for both compositions were the same as those obtained by the new code (see table 4.12). Hence, the NASA code can also solve a large system of condensed species that involves melting. The equilibrium temperatures and pressures are given in table 5.34. Listed in the table are also the CPU times required by the two codes to obtain the two equilibrium compositions. Once again, the new code took considerably longer CPU times.

A second comparison between the NASA and new codes was performed by using a 20-element system. The ingredients and two compositions of the system for this case are listed in table 5.35. The main differences between the previous system and this one are as follows: $BaN_2O_6$ was replaced by $C_3H_6O_6N_6$ while maintaining the presence of nitrogen, $TiO_2$ was dropped and the elemental metals nickel, manganese and tungsten were included to increase the number of elements to twenty.

**Table 5.34: Comparison of selected results of calculations of two formulations of the 18-element system, obtained from the NASA and new codes for a loading density of 0.2 gm/cm$^3$.**

| | | | NASA code | new code |
|---|---|---|---|---|
| composition 1 | mixture properties | T (K) | 2123 | 2123 |
| | | P (MPa) | 16.54 | 16.54 |
| | CPU time | t (s) | 39.1 | 108.1 |
| composition 2 | mixture properties | T (K) | 2130 | 2130 |
| | | P (MPa) | 16.87 | 16.87 |
| | CPU time | t (s) | 35.6 | 283.5 |

**Table 5.35: Two formulations of a 20-element system used for calculations with a large number of species by the NASA and new codes.**

| ingredient | formula | enthalpy of formation at 298.15 K (cal/mole) | percentage by weight for composition 1 | 2 |
|---|---|---|---|---|
| 1,3,5-trinitrohexahydro-*s*-triazine (RDX) | $C_3H_6O_6N_6$ | 16,760 | 4 | 4 |
| barium chromate | $Ba_1Cr_1O_4$ | −342,200 | 10 | 6 |
| potassium perchlorate | $K_1Cl_1O_4$ | −102,800 | 10 | 6 |
| sodium cryolite | $Na_3Al_1F_6$ | −758,470 | 10 | 6 |
| Viton A fluoroelastomer | $C_{11}F_{14}H_8$ | −737,170 | 20 | 20 |
| magnesium carbonate | $Mg_1C_1O_3$ | −265,700 | 5 | 9 |
| potassium sulphate (KS) | $K_2S_1O_4$ | −342,660 | 5 | 9 |
| lithium hydride | $Li_1H_1$ | −21,660 | 5 | 9 |
| lead oxide | $Pb_1O_1$ | −52,440 | 5 | 5 |
| boron | $B_1$ | 0 | 8 | 8 |
| zirconium | $Zr_1$ | 0 | 8 | 8 |
| nickel | $Ni_1$ | 0 | 8 | 8 |
| manganese | $Mn_1$ | 0 | 1 | 1 |
| tungsten | $W_1$ | 0 | 1 | 1 |

Total of 586 species: 396 gaseous and 190 condensed species.

The ingredients were arbitrarily chosen and the enthalpy of formation of $C_3H_6O_6N_6$ was taken from Freedman's article. The total number of species considered for this system was 586, consisting of 396 gaseous and 190 condensed species. Calculations were done for a loading density of 0.2 gm/cm$^3$, and the results are tabulated for convenience in table 5.36.

Both the new code and the NASA code obtained the same solution to the first composition, and the NASA code did not require the specification of any condensed species at the beginning for consideration. A total of thirteen condensed species were determined. However, different solutions were obtained by the two codes for the second composition. Also no specification of condensed species was necessary for the NASA code. While both codes determined the melting of boron at 2350 K, the equilibrium pressures were different. In addition, the amounts of solid and liquid boron were different, the NASA code determined the presence of liquid manganese but the new code did not and the amounts of gaseous manganese were also different. With liquid manganese being

Table 5.36: **Comparison of selected results of calculations of two formulations of the 18-element system, obtained from the NASA and new codes for a loading density of 0.2 gm/cm$^3$.**

| | | | NASA code | new code |
|---|---|---|---|---|
| composition 1 | mixture properties | T (K) | 2467 | 2467 |
| | | P (MPa) | 48.26 | 48.26 |
| | CPU time | t (s) | 23.4 | 626.2 |
| composition 2 | mixture properties | T (K) | 2350 | 2350 |
| | | P (MPa) | 51.15 | 51.75 |
| | species abundances (kg-mole/kg-mixture) | B(s) | $1.559\times10^{-3}$ | $2.169\times10^{-3}$ |
| | | B(lq) | $1.653\times10^{-3}$ | $1.043\times10^{-3}$ |
| | | Mn | $2.942\times10^{-5}$ | $1.820\times10^{-4}$ |
| | | Mn(lq) | $1.526\times10^{-4}$ | absent |
| | CPU time | t (s) | 32.7 | 407.5 |

the extra condensed species determined, the NASA code determined a total of sixteen condensed species, while the new code determined fifteen.

It was discovered that all these differences were due to the mishandling of Mn(lq) by the NASA code. In the library of curve-fitted coefficients for the NASA code, Mn(lq) is listed to be stable between temperatures of 1517 and 2324 K. During the course of the iterations, at one of the converged solutions at 2303. K, Mn(lq) was introduced. However, apparently the NASA code does not implement checks on upper limits of the stability of liquid phases; consequently, Mn(lq) was retained at the equilibrium temperature of 2350 K, which is higher than 2324 K. (Most often the upper limit of stability of a liquid phase is taken to be 5000 K; hence, it was not a problem. A similar problem might arise for a substance for which only the solid phase is stable.) As a check, the calculation was repeated by using the new code and with the upper limit of the stability of Mn(lq) arbitrarily set to the temperature of 3000 K, so that Mn(lq) would be included at 2350 K. Same solution as that of the NASA code was then obtained.

It took the new code a considerable longer time to converge for the first composition than for the second. However, it took only four iterations on temperature in the former case to achieve convergence after the equilibrium temperature had been bracketed, whereas sixteen were required for the latter because of oscillation due to melting, with the initial temperature bracket being 2300 to 2700 K in both cases. Hence, there is no direct correlation between the number of temperature iterations and the CPU time required to achieve convergence for a particular problem. However, comparing to the 18-element system, this system does take longer time to converge (see table 5.34).

# References

Anon., Dec. 31, 1960 to June 30, 1970, *JANAF Thermochemical Tables*, Dow Chemical Company, Midland, Michigan.

Anon., 1967, *ASME Steam Tables*, The American Society of Mechanical Engineers.

Barin, I., F. Sauert, E. Schultze-Rhonhof and S. S. Wang, 1993, *Thermochemical Data of Pure Substances*, 2nd edition, VCH, Weinheim, Federal Republic of Germany.

Benedict, M., G. B. Webb and L. C. Rubin, 1940, "An Empirical Equation for Thermodynamic Properties of Light Hydrocarbons and their Mixtures, I. Methane, Ethane, Propane and n-Butane," *Journal of Chemical Physics*, Vol. 8, No. 4, pp. 334–345.

Bird, R. B., E. L. Spotz and J. O. Hirschfelder, 1950, "The Third Virial Coefficient for Non-Polar Gases," *The Journal of Chemical Physics*, Vol. 18, No. 10, pp. 1395–1402.

Brauer, K. O., 1974, *Handbook of Pyrotechnics*, Chemical Publishing Co., Inc., New York.

Brinkley, S. R., Jr., 1947, "Calculation of the Equilibrium Composition of Systems of many Constituents," *The Journal of Chemical Physics*, Vol. 15, No. 2, pp. 107–133.

Burcat, A., 1984, "Thermochemical Data for Combustion Calculations," in W. C. Gardiner, Jr., editor, *Combustion Chemistry*, Springer-Verlag, New York, pp. 455–473.

Chase, M. W., Jr., C. A. Davis, J. R. Downey, Jr., D. J. Frurip, R. A. McDonald and A. N. Syverud, 1985, *JANAF Thermochemical Tables*, 3rd edition, Parts I and II, *Journal of Physical and Chemical Reference Data*, Vol. 14, Supplement No. 1.

Conkling, J. A., 1985, *Chemistry of Pyrotechnics: Basic Principles and Theory*, Marcel Dekker, Inc., New York.

Cruise, D. R., 1964, "Notes on the Rapid Computation of Chemical Equilibria," *The Journal of Physical Chemistry*, Vol. 68, No. 12, pp. 3797–3802.

Denbigh, K., 1981, *The Principles of Chemical Equilibrium*, 4th edition, Cambridge University Press, Cambridge.

Cowperthwaite, M., and W. H. Zwisler, 1954, "Theoretical and Mathematical Formulations for the Tiger Computer Program," Tiger Computer Program Documentation, Vol. 1, Stanford Research Institute, Menlo Park, California, AD/A–002–791.

Ellern, H., 1968, *Military and Civilian Pyrotechnics*, Chemical Publishing Co., Inc., New York.

Freedman, E., 1982, *Blake - A Thermodynamic Code Based on Tiger: User's Guide and Manual*, Technical Report ARBRL–TR–02411, Ballistic Research Laboratory, US Army Armament Research and Development Command, AD/A–121–259.

Freedman, E., 1988, "Thermodynamic Properties of Military Gun Propellants," in L. Stiefel, editor, *Gun Propulsion Technologies*, Progress in Astronautics and Aeronautic, Vol. 109, American Institute of Astronautics and Aeronautics, Washington, D. C., pp. 103–132.

Gordon, S., and B. J. McBride, 1971, *Computer Program for Calculation of Complex Chemical Equilibrium Compositions, Rocket Performance, Incident and Reflected Shocks, and Chapman-Jouguet Detonations*, Special Publication 273, National Aeronautics and Space Administration, Washington, D. C., NASA SP–273.

Gordon, S., F. J. Zeleznik and V. N. Huff, 1959, "A General Method for Automatic Computation of Equilibrium Compositions and Theoretical Rocket Performance of Propellants," NASA Technical Note D–132, National Aeronautics and Space Administration, Washington, D. C.

Hauss, I., and J. J. Gottlieb, 1997, private communications.

Gurvich, L. V., I. V. Veyts and C. B. Alcock, 1989, *Thermodynamic Properties of Individual Substances*, 4th edition, Vol. 1, Parts 1 and 2, Hemisphere Publishing Corporation.

Hirschfelder, J. O., C. F. Curtiss and R. B. Bird, 1954, *Molecular Theory of Gases and Liquids*, John Wiley and Sons, Inc., New York.

Huff, V. N., S. Gordon and V. E. Morrell, 1951, "General Method and Thermodynamic Tables for Computations of Equilibrium Composition and Temperature of Chemical Reactions," NACA Report 1037, National Advisory Committee for Aeronautics, Washington, D. C.

Kihara, T, 1948, "Determination of Intermolecular Forces from the Equation of State of Gases," *Journal of the Physical Society of Japan*, Vol. 3, No. 4, pp. 265–268.

Kihara, T, 1951, "Determination of Intermolecular Forces from the Equation of State of Gases II," *Journal of the Physical Society of Japan* Vol. 6, No. 3, pp. 184–188.

Krier, H., and M. Summerfield, editors, 1979, *Interior Ballistics of Guns*, Progress in Astronautics and Aeronautics, Vol. 66, American Institute of Aeronautics and Astronautics, New York, pp. 1–36.

Kuo, K. K., and M. Summerfield, editors., 1984, *Fundamentals of Solid-Propellant Combustion*, Progress in Astronautics and Aeronautics, Vol. 90, American Institute of Aeronautics and Astronautics, New York, pp. 1–52.

Levine, H. B., 1962, "Chemical Equilibrium in Complex Mixtures," *The Journal of Chemical Physics*, Vol. 36, No. 11, pp. 3049–3050.

Lussier, L.-S., 1991, Research Scientist, Defence Research Establishment Valcartier, Courcelette, Quebec, private communications.

Madeley, W. D., and J. M. Toguri, 1973a, "The Application of Free Energy Minimization Techniques to Determine Equilibrium Compositions in Systems of Metallurgical Interest," *Canadian Metallurgical Quarterly*, Vol. 12, No. 1, pp. 71–78.

Madeley, W. D., and J. M. Toguri, 1973b, "Computing Chemical Equilibrium Compositions in Multiphase Systems," *Industrial and Engineering Chemistry Fundamentals*, Vol. 12, No. 2, pp. 261–262.

Mahan, B. H., 1975, *University Chemistry*, 3rd edition, Addison-Wesley Publishing Company, Reading, Massachusetts.

Marsh, K. N., M. Frenkel, N. M. Gadalla, and R. C. Wilhoit, 1996, *TRC Thermodynamic Tables*, Non-hydrocarbons, Vols. I to XI, Hydrocarbons, Vols. I to XIII, Thermodynamics Research Center, Texas A and M University, College Station, Texas.

McBride, B. J., and S. Gordon, 1967, *Fortran IV Program for Calculation of Thermodynamic Data*, Technical Note D–4097, National Aeronautics and Space Administration, Washington, D. C.

McBride, B. J., and S. Gordon, 1992, *Computer Program for Calculating and Fitting Thermodynamic Functions*, Reference Publication 1271, National Aeronautics and Space Administration, Washington, D. C., NASA RP–1271.

Missen, R. W., and W. R. Smith, 1989, "A Question of Basic Chemical Literacy," *Journal of Chemical Education*, Vol. 66, No. 3, pp. 217–218.

Noble, B., 1969, *Applied Linear Algebra*, Prentice-Hall, Inc., Englewood Cliffs, New Jersey.

Orentlicher, M., and J. M. Prausnitz, 1967, "Approximate Method for Calculating the Third Virial Coefficient of a Gaseous Mixture," *Canadian Journal of Chemistry*, Vol. 45, No. 4, pp. 373–378.

Powell, E. G., G. Wilmot, L. Haar and M. Klein, 1979, "Equations of State and Thermodynamic Data for Interior Ballistics Calculations," in H. Krier and M. Summerfield, editors, *Interior Ballistics of Guns*, Progress in Aerospace Sciences and Aeronautics, Vol. 66, AIAA, Washington, D. C., pp. 325–348.

Prausnitz, J. M., R. N. Lichtenthaler and E. G. de Azevedo, 1986, *Molecular Thermodynamics of Fluid-Phase Equilibria*, 2nd edition, Prentice-Hall, Inc., Englewood Cliffs, New Jersey.

Press, W. H., B. P. Flannery, S. A. Teukolsky and W. T. Vetterling, 1986, *Numerical Recipes: the Art of Scientific Computing*, 1st edition, University of Cambridge, Cambridge.

Rabinowitz, D., 1970, *Numerical Methods for Nonlinear Algebraic Equations*, Gordon and Breach, New York.

Redlich, O., and J. N. S. Kwong, 1949, "On the Thermodynamics of Solutions V, An Equation of State, Fugacities of Gaseous Solutions," *Chemical Review*, Vol. 44, No. 1, pp. 233–234.

Reid, R. C., J. M. Prausnitz and B. E. Poling, 1987, *The Properties of Gases and Liquids*, 4th edition, McGraw-Hill, Inc., New York.

Reynolds, W. C., and H. C. Perkins, 1977, *Engineering Thermodynamics*, 2nd edition, McGraw-Hill Book Co., New York.

Sears, F. W., and G. L. Salinger, 1975, *Thermodynamics, Kinetic Theory, and Statistical Thermodynamics*, 3rd edition, Addison-Wesley Publishing Company, Reading, Massachusetts.

Soave, G., 1972, "Equilibrium Constants from a Modified Redlich-Kwong Equation of State," *Chemical Engineering Science*, Vol. 27, No. 6, pp. 1197–1203.

Smith, W. R., 1976, "Some Remarks on the Calculation of Complex Chemical Equilibria by General Methods," *Industrial and Engineering Chemistry Fundamentals*, Vol. 15, No. 3, pp. 227–229.

Smith, W.R., 1980, "Computational Aspects of Chemical Equilibrium in Complex Systems," *Theoretical Chemistry: Advances and Perspectives*, H. Eyring and D. Henderson, editors, Vol. 5, pp. 185–259, Academic Press, Inc., New York.

Smith, W.R., and R.W. Missen, 1967, "On the Two-Derivative Method of Optimization," *Canadian Journal of Chemical Engineering*, Vol. 45, No. 6, pp. 346–348.

Smith, W.R., and R.W. Missen, 1968, "Calculating Complex Chemical Equilibria by an Improved Reaction-Adjustment Method," *Canadian Journal of Chemical Engineering*, Vol. 46, No. 4, pp. 269–272.

Smith, W.R., and R.W. Missen, 1979 (winter), "What is Chemical Stoichiometry," *Chemical Engineering Education*, Vol. 13, No. 1, pp. 26–32.

Smith, W.R., and R.W. Missen, 1982, *Chemical Reaction Equilibrium Analysis: Theory and Algorithms*, John Wiley and Sons, Inc., New York.

Smith, W.R., and R.W. Missen, 1988, "Strategies for Solving the Chemical Equilibrium Problem and an Efficient Microcomputer-Based Algorithm," *The Canadian Journal of Chemical Engineering*, Vol. 66, No. 4, pp. 591–598.

Smith, J.M., and H.C. Van Ness, 1987, *Introduction to Chemical Engineering Thermodynamics*, 4th edition, McGraw-Hill, Inc., New York.

Starling, K.E., 1971, "Thermo Data Refined for LPG, Part 1: Equation of State and Computer Prediction," *Hydrocarbon Processing*, Vol. 50, No. 3, pp. 101–104.

Starling, K.E., and M.S. Han, 1972, "Thermo Data Refined for LPG, Part 14: Mixtures," *Hydrocarbon Processing*, Vol. 51, No. 5, pp. 129–132.

Stiefel, L., editor, 1988, *Gun Propulsion Technology*, Progress in Astronautics and Aeronautics, Vol. 109, American Institute of Aeronautics and Astronautics, New York, pp. 1–34.

Stull, D.R., and H. Prophet, 1971, editors, *JANAF Thermochemical Tables*, 2nd edition, NSRDS-NBS 37, U.S. Department of Commerce.

Van Wylen, G.J., and R.E. Sonntag, 1965, *Fundamentals of Classical Thermodynamics*, John Wiley and Sons, Inc., New York.

Villars, D.S., 1959, "A Method of Successive Approximations for Computing Combustion Equilibria on High Speed Digital Computers," *J. Physical Chemistry*, Vol. 63, No. 4, pp. 521–525.

Villars, D.S., 1960, "Computation of Complicated Combustion Equilibria on a High Speed Digital Computer," in G.S. Bahn and E.E. Zukoski, editors, *Kinetics, Equilibria and Performance of High Temperature Systems*, Proc. First Conference, Los Angeles, 2–5 November, 1959, Western States Section, The Combustion Institute, Butterworths, London, pp. 141–151.

Wagman, D.D., W.H. Evans, V.B. Parker, R.H. Schumm, I. Halow, S.M. Bailey, K.L. Churney, and R.L. Nuttall, 1982, *The NBS Tables of Chemical Thermodynamic Properties: Selected Values for Inorganic and $C_1$ and $C_2$ Organic Substances in SI Units, Journal of Physical and Chemical Reference Data*, Vol. 11, Supplement No. 2, National Bureau of Standards, Washington, D.C.

Walsh, G. R., 1975, *Methods of Optimization*, John Wiley and Sons Ltd., New York.

White, W. B., S. M. Johnson and G. B. Dantzig, 1958, "Chemical Equilibrium in Complex Mixtures," *Journal of Chemical Physics*, Vol. 28, No. 5, pp. 751–755.

Zeleznik, F. J., and S. Gordon, 1960, "An Analytical Investigation of Three General Methods of Calculating Chemical-Equilibrium Compostions," NASA Technical Note D–473, National Aeronautics and Space Administration, Washington, D. C.

Zeleznik, F. J., and S. Gordon, 1961, "Simultaneous Least-Squares Approximation of a Function and its First Integrals with Application to Thermodynamic Data," NASA Technical Note D–767, National Aeronautics and Space Administration, Washington, D.C.

Zeleznik, F. J., and S. Gordon, 1962, "A General IBM 704 or 7090 Computer Program for Computation of Chemical Equilibrium Compositions, Rocket Performance, and Chapman-Jouguet Detonations," NASA Technical Note D–1454, National Aeronautics and Space Administration, Washington, D. C.

# APPENDIX 2

# CHEMICAL EQUILIBRIUM ANALYSIS FOR GASEOUS AND CONDENSED COMBUSTION PRODUCTS AT CONSTANT VOLUME (Journal Paper)

by

Frederick C. H. Wong and James J. Gottlieb

# A Stoichiometric-Algorithm-Based Computational Code for Chemical Equilibrium Analysis of Combustion Products at Constant Volume

Frederick C. H. Wong[†] James J. Gottlieb[‡]
Institute for Aerospace Studies, University of Toronto
4925 Dufferin Street, Downsview, ON, Canada M3H 5T6

## Abstract

The VCS algorithm, which makes use of chemical equations and requires no matrix inversion, was applied to the development of a new computational code, for determining the equilibrium composition of combustion products at fixed mass in a constant volume vessel assuming no heat lost. The combustion products were modelled as a mixture of gases with pure condensates dispersed throughout. Five sample calculations for energetic materials forming an increasing amount of condensed products were used to demonstrate the excellant capability of this algorithm in handling these products. Of the three major computational codes: NASA, Bagheera, and Blake, which all require matrix inversion, used to solve these five problems, the Bagheera code failed because of matrix singularity in the case involving the largest amount of condensed products, while it was difficult to obtain a solution for the NASA code in the same case, and the Blake code is hard to use in general. The VCS-algorithm-based solution method succeeded in solving all five cases easily. It was also found that the new code is slower than the NASA and the Bagheera codes, but faster than the Blake code.

## 1 Introduction

For the analysis of new military gun propellants, samples of the propellants are often burnt inside a closed cylindrical vessel. Properties of a propellant can be deduced from the signature of pressure changes of the product mixture inside the vessel. Computational codes which evaluate product-mixture compositions based on chemical equilibrium principles are required for such deductions. Three existing major chemical equilibrium computational codes for propellant properties analyses are the NASA code [1], the Bagheera code [2], and the Blake code [3]. The NASA code is a well known thermodynamic code, and the Bagheera and the Blake codes are the present and the previous NATO standard codes for military propellant analyses, respectively.

For the development of the above three codes, the product mixture is modelled as a mixture of gases with pure condensates, solids and/or liquids, dispersed throughout. The solution algorithms of these three codes are of the nonstoichiometric type, and they all require matrix inversion. Sophisticated these three codes are, nonetheless, they all run into difficulties in solving systems which have a fair number of condensed products present at equilibrium.

---

[†] Research Assistant

[‡] Professor

A new chemical equilibrium computational code had been developed based on the Villar-Cruise-Smith (VCS) algorithm for analysing product compositions at constant volume. This algorithm is of the stoichiometric type and requires no matrix inversion. The purpose of this paper is to demonstrate that the new code, written based on this algorithm, is superior to the three existing major codes in handling pure condensed species. The basic differences between nonstoichiometric and stoichiometric formulations will first be described. The results of calculations of five test problems for the comparison between the new code and the three existing codes are then presented and discussed.

## 2 Constraints and Problem Definition

For the development of the new chemical equilibrium computational code, the volume of the closed vessel inside which combustion takes place is assumed to remain constant. In addition, the heat loses to the surroundings during the milliseconds of combustion is neglected. Thus, the total energy of the products must equal to that of the reactants. Consequently, the chemical equilibrium problem investigated is under the thermodynamic state constraints of constant energy and volume. In addition, because a close system is considered, mass is conserved in the system. Finally, a postulated product species must either be present (mole number being positive) or absent (mole number being zero) at equilibrium, and these two conditions consist the nonnegativity constraint which applies to all postulated products.

The VCS algorithm was developed for systems with constant temperature and pressure as the state constraints, but for the present study, it was applied to a system with constant energy and volume as the state constraints. To help in understanding the basic differences between the solution methods used in the new computational code and in the three existing major codes, the equilibrium solution to a system with constant temperature and pressure as the state constraints will first be discussed.

From the second law of thermodynamic, at equilibrium, the value of the Gibbs state function of a closed system at constant temperature and pressure is at a minimum. The chemical equilibrium problem of such a system can be expressed with the help of vector-matrix notation as

$$\text{minimize } G(\mathbf{n}) \tag{1}$$

subject to

$$\mathbf{A}\mathbf{n} = \mathbf{b} \tag{2}$$

and

$$n_i \geq 0, \quad \text{with} \quad i = 1, 2, \ldots, N, \tag{3}$$

where $G(\mathbf{n})$ indicates that the system Gibbs state function $G$ is a function of $\mathbf{n}$, the species-abundance vector, $\mathbf{A}$ is the formula matrix, $\mathbf{b}$ is the element-abundance vector and $n_i$ is the

$i$th element of $\mathbf{n}$. The elements of $\mathbf{n}$, $n_i$, $i$ equals 1 to $N$, where $N$ is the number of species considered in the system, are species mole numbers; the columns of $\mathbf{A}$, $\mathbf{a}_i$, $i$ equals 1 to $N$, are formula vectors of the $N$ species, and the elements of $\mathbf{a}_i$, $a_{ki}$, $k$ equals 1 to $M$, where $M$ is the number of atomic elements involved in the system, are numbers of atoms of the elements making up the $i$th species molecule; and the elements of $\mathbf{b}$, $b_k$, $k$ equals 1 to $M$, are the total molar amounts of the $M$ elements involved in the system, which are specified and fixed for each problem. The order of the species and the elements are immaterial; however, once they are chosen they remain fixed. Equations 2 and 3 express the mass conservation and the nonnegative constraints, respectively.

Equation 2 dictates that any acceptable compositional state of the product mixture, defined by $\mathbf{n}$, must give the same elemental abundances. It may be rewritten to express a constraint on the changes in compositional states as

$$\mathbf{A}\,\delta\mathbf{n} = \mathbf{0}, \tag{4}$$

where $\delta\mathbf{n}$ is the species-abundance-change vector whose elements, $\delta n_i$, $i$ equals 1 to $N$, are the differences in the number of moles of the species between two compositional states.

## 3 Chemical Stoichiometry

Chemical stoichiometry are book keeping techniques on the conservation of elemental abundances during physiochemical changes. Through the application of these techniques, the conservation of mass constraint can be observed. Central to chemical stoichiometry is the concept of chemical equations which, in the stoichiometric sense, are simply conservation statements and do not necessarily reflect actual reaction mechanisms. A set of chemical equations, which is not unique, relating all the product species can be determined once they have been specified [4][5, pp. 18-27] [6].

Equation 2 is a set of $M$ linear algebraic equations in the $N$ unknowns of species mole numbers. In general, the number of product species considered in a system is larger than the number of elements involved in the system; thus, $M$ is usually less than $N$. For such a case, equation 2 possesses an infinity of solutions, and its general solution can be expressed as

$$\mathbf{n} = \mathbf{n}^0 + \sum_{j=1}^{R} \boldsymbol{\nu}_j \xi_j, \tag{5}$$

where $\mathbf{n}^0$ is any particular solution (e.g., an initial composition), the $\boldsymbol{\nu}_j$'s (dimensions $N$ by 1) is any set of $R$ linearly independent solutions of the homogeneous equation corresponding to equation 2 (i.e., equation 4), and the $\xi_j$'s is a set of real parameters [7, pp. 90-92, 119-120]

Each $\boldsymbol{\nu}_j$ is called a stoichiometric vector, it is nonzero and satisfies

$$\mathbf{A}\boldsymbol{\nu}_j = \mathbf{0} \qquad (j = 1, 2, \ldots, R). \tag{6}$$

Its $i$th element $\nu_{ij}$ ($i$ equals 1 to $N$) is called the stoichiometric coefficient of the $i$th species in the $j$th stoichiometric vector. By performing partial differentiation on equation 5 with respect to $\xi_j$, it can be shown that

$$\nu_{ij} = \left(\frac{\partial n_i}{\partial \xi_j}\right)_{\xi_{k \neq j}}, \tag{7}$$

where $k$ takes on the values 1 to $R$ except $j$. That is $\nu_{ij}$ is the change in $n_i$ for a unit change in $\xi_j$, while keeping the $\xi_k$'s constant.

The quantity $R$ is the maximum number of linearly independent solutions of equation 4 and is given by

$$R = N - C, \tag{8}$$

where $C$ is the rank of $\mathbf{A}$ which is less than or equal to $M$. Usually, but not always, $C$ is equal to $M$.

The $\xi_j$'s can be recognized as the $R$ variables the values of which are to be specified in order to solve for the remaining $C$ variables in equation 4. They have also been referred to as extents of reactions.

The significance of equation 5 is that any compositional solution $\mathbf{n}$ of the system can be written in terms of any particular solution $\mathbf{n}^0$ and a linear combination of a set of $R$ linearly independent vectors $\boldsymbol{\nu}_j$'s. Hence, equation 5 may be regarded as essentially a linear transformation from the $N$ independent variables $n_i$'s to the $R$ independent variables $\xi_j$'s. However, the former are constrained by mass conservation, whereas the latter satisfy this constraint automatically (which can be proven by premultiplying equation 5 by $\mathbf{A}$ and making use of equation 6). Thus, it could be of advantage to work with the $\xi_j$'s instead.

A set of chemical equations is obtained when equation 6 is written out for the $R$ stoichiometric vectors $\boldsymbol{\nu}_j$'s, by using the column formula vectors $\mathbf{a}_i$'s of $\mathbf{A}$ as

$$\sum_{i=1}^{N} \mathbf{a}_i \nu_{ij} = \mathbf{0} \quad \text{with} \quad j = 1, 2, \ldots, R, \tag{9}$$

and replacing the formula vectors $\mathbf{a}_i$'s by their corresponding molecular formulae $A_i$'s of the species and the vector $\mathbf{0}$ by 0, such that

$$\sum_{i=1}^{N} A_i \nu_{ij} = 0 \quad \text{with} \quad j = 1, 2, \ldots, R. \tag{10}$$

Such a set of chemical equations is not unique, because the set of stoichiometric vectors is not unique. These equations are only statements of the mass conservation law, which are determined solely from the list of product species considered, and they do not imply any knowledge of actual reactions that take place. A general procedure for determining such a set of chemical equations by performing elementary operations on $\mathbf{A}$ is given by Smith and Missen [5, pp. 18-27].

A complete stoichiometric matrix, $\mathbf{N}$, of a system is composed of a set of $R$ linearly independent stoichiometric vectors, that is

$$\mathbf{N} = [\boldsymbol{\nu}_1, \boldsymbol{\nu}_2, \ldots, \boldsymbol{\nu}_R]. \tag{11}$$

Other than the requirement of linearly independence, the choice of the $R$ stoichiometric vectors, and hence N, is entirely arbitrary which can be exercised to achieve certain computational advantages. Usually, N is chosen in the canonical form shown below; the portion of N below row $C$ is an identity matrix of dimension $R$. Savings in computer memories is also achieved because only the storage of $RC$ rather than $RN$ coefficients is required.

$$\mathbf{N} = \begin{bmatrix} \nu_{11} & \nu_{12} & \cdots & \nu_{1R} \\ \nu_{21} & \nu_{22} & \cdots & \nu_{2R} \\ \vdots & \vdots & \vdots & \vdots \\ \nu_{C1} & \nu_{C2} & \cdots & \nu_{CR} \\ 1 & 0 & \cdots & 0 \\ 0 & \ddots & \ddots & \vdots \\ \vdots & \ddots & \ddots & 0 \\ 0 & \cdots & 0 & 1 \end{bmatrix}_{N\times R} . \tag{12}$$

To determine the stoichiometric vectors, a set of $C$ species, called the components, which have linearly independent formula vectors are selected from the $N$ species, and the formula vectors of each of the remaining $R$ species, called the noncomponents, is expressed as a linear combination of the formula vectors of the $C$ species. When converted into a chemical equation, each of the stoichiometric vectors in N is equivalent to requiring that one mole of the noncomponent species, with unity stoichiometric coefficient, be formed from the component species.

Making use of N and equation 5, the species-abundance vector can be expressed as

$$\mathbf{n} = \mathbf{n}^0 + \mathbf{N}\boldsymbol{\xi}, \tag{13}$$

where $\boldsymbol{\xi}$ is a column vector with its $j$th element, $j$ equals 1 to $R$, being the $\xi_j$ parameter.

## 4 Nonstoichiometric and Stoichiometric Formulations

Mathematically, the chemical equilibrium problem with the thermodynamic state constraints of constant temperature and pressure can be formulated in several ways. Depending on whether the problem is formulated directly based on the species mole numbers, or chemical stoichiometry is employed and the problem is formulated in terms of the reaction extents, a formulation can be classified as nonstoichiometric or stoichiometric, respectively [8, 9]. In the former, the mass conservation constraint would have to be treated separately, whereas in the latter this constraint is incorporated by means of chemical stoichiometry, resulting in an essentially unconstrained problem. The two formulations also suggest different numerical solution methods.

As a nonstoichiometric formulation, the system Gibbs state function, $G$, is minimized with respect to the species mole numbers subject to the mass conservation and the nonnegativity constraints. That is

$$\text{minimize } G(\mathbf{n}) \tag{14}$$

such that

$$\mathbf{A}\mathbf{n} = \mathbf{b} \quad \text{and} \quad n_i \geq 0, \quad \text{with} \quad i = 1, 2, \ldots, N, \tag{15}$$

where $G(\mathbf{n})$ indicates that $G$ is a function of $\mathbf{n}$.

At fixed temperature and pressure, $G$ is given by

$$G = \sum_{i=1}^{N} n_i \mu_i = \mathbf{n}^T \boldsymbol{\mu}, \tag{16}$$

where $\mu_i$ is the chemical potential of the $i$th species, defined as

$$\mu_i \equiv \left( \frac{\partial G}{\partial n_i} \right)_{T,P,n_{j \neq i}} . \tag{17}$$

$T$ and $P$ are the system temperature and pressure, respectively, and $j$ can assume values between 1 to $N$ except $i$. $\mathbf{n}^T$ is the transpose of $\mathbf{n}$, and $\boldsymbol{\mu}$ is a column vector with its $i$th element being $\mu_i$.

In the above formulation, $\mathbf{A}$ is assumed to have full rank of $M$. If the rank of $\mathbf{A}$ is less than $M$, then the system of equations $\mathbf{A}\mathbf{n} = \mathbf{b}$ would have to be reduced to a set of linearly independent equations before they are applied. The Lagrangian multiplier method is normally used to incorporate these linear constraints.

When the chemical equilibrium problem is formulated using the stoichiometric approach, the Gibbs state function is minimized with respect to the reaction extents instead, while subject to the nonnegativity constraint only. That is

$$\text{minimize } G(\boldsymbol{\xi}) \tag{18}$$

such that

$$n_i \geq 0 \quad \text{with} \quad i = 1, 2, \ldots, N. \tag{19}$$

The problem is only essentially unconstrained because the nonnegativity constraint still holds. The VCS algorithm uses this formulation.

When following this approach and solving the chemical equilibrium problem iteratively, corrections in the mole numbers are obtained from those in the reaction extents. Denoting the corrections in the reaction extents by $\boldsymbol{\delta\xi}$ and following equation 13, then

$$\boldsymbol{\delta}\mathbf{n} = \mathbf{N}\boldsymbol{\delta\xi}. \tag{20}$$

Provided that mole numbers which satisfy the mass conservation constraint are used to start the iterations, adjusted mole numbers at each iteration step will continue to satisfy this constraint. In addition, $\mathbf{N}$ is not unique and the VCS algorithm makes a judicious choice of it and eliminates matrix inversion from the iterations.

# 5 Chemical Potentials for Gaseous and Condensed Species

Both of the above formulations require the evaluation of chemical potentials which are the most essential quantities required for carrying out the chemical equilibrium analysis. For the present study, the product mixture was modelled to be a mixture of gases with pure liquids and/or solids dispersed throughout. The forms of the chemical potentials reflect or embody the models used for the gaseous mixture and the individual species themselves. The gaseous mixture may be modelled as an ideal or a nonideal mixture, and the gases may be modelled as perfect or imperfect gases. In addition, the liquid and solid species, can be assumed to occupy no volume or to have finite volume but can be incompressible or compressible. In the following, the forms of the chemical potential of a species in a gaseous mixture and of a pure condensed species are discussed.

## 5.1 Ideal Gaseous Mixture

An ideal mixture is one whereby the chemical potential of every species in the mixture is a linear function of the logarithm of its mole fraction [10, p. 249]. For the $i$th species,

$$\mu_i(T, P, x_i) = \mu_i^*(T, P) + RT \ln x_i, \tag{21}$$

where $\mu_i^*(T, P)$ is the standard chemical potential, the chemical potential of pure species $i$ in the same physical state and at the same temperature, $T$, and pressure, $P$, of the mixture. For an ideal gaseous mixture, the mole fraction $x_i$ is given as $n_i/n_{t_g}$, where $n_i$ and $n_{t_g}$ are the number of moles of the $i$th species and the total number of moles of gases in the mixture, respectively.

A direct consequence of the ideality assumption of a gaseous mixture is the Amagat's law, which states that at fixed temperature and pressure, the volume of the mixture is equal to the sum of the volume of the component species as pure gases at the same conditions. That is

$$V = \sum_{i=1}^{N'} n_i v_i, \tag{22}$$

where $V$ is the volume of the mixture, $N'$ is the number of species in the mixture, and $v_i$ is the molar volume of pure species $i$. Differentiating equation 22 with respect to $n_i$ and defining the partial molar volume of the $i$th species to be

$$\bar{v}_i \equiv \left(\frac{\partial V}{\partial n_i}\right)_{T,P,n_{j\neq i}}, \tag{23}$$

it can be seen that

$$\bar{v}_i = v_i. \tag{24}$$

Thus, in an ideal gaseous mixture, the partial molar volume of the $i$th species is simply its molar volume as a pure gas at the system conditions.

### 5.1.1 Perfect-gas Mixture

This is a mixture of perfect gases, gases following the perfect equation of state $pv = RT$. The chemical potential of the $i$th species in such a mixture is given by

$$\mu_i(T,P,x_i) = \mu_i^0(T) + RT\ln P + RT\ln x_i, \tag{25}$$

where $\mu_i^0(T)$ is the standard chemical potential of pure species $i$ at the reference pressure of one unit, normally chosen to be 1 bar or 1 atm, as a function of temperature only. Thus, the function $\mu_i^*(T,P)$ for the $i$th species in a perfect-gas mixture is equal to $\mu_i^0(T) + RT\ln P$, which is the chemical potential of pure species $i$ as a perfect gas at $T$ and $P$.

Equation 25 can alternatively be expressed as

$$\mu_i(T,P,x_i) = \mu_i^0(T) + RT\ln p_i, \tag{26}$$

where $p_i$ is the partial pressure of the $i$th species in the mixture and is defined to be

$$p_i \equiv x_i P. \tag{27}$$

### 5.1.2 Imperfect-gas Mixture

The components of an ideal gaseous mixture can be imperfect gases, gases following equations of state of the form $pv = zRT$, where $z$ is the compressibility factor and is different from one. In this case, $\mu_i^*(T,P)$ will contain an extra term involving the fugacity coefficient, an account of the deviation from perfect-gas behaviour, of pure species $i$, $\phi_i$, given as

$$RT\ln\phi_i(T,P) = \int_0^P \left(v_i - \frac{RT}{p}\right) \mathrm{d}p. \tag{28}$$

The chemical potential of the $i$th species can then be stated as

$$\mu_i(T,P,x_i) = \mu_i^0(T) + RT\ln P + RT\ln\phi_i(T,P) + RT\ln x_i \tag{29}$$

($\mu_i^0(T)$ remains to be the standard chemical potential of pure species $i$ at the reference pressure of one unit and in the idealized perfect gas state). This is a mixture that follows the Lewis and Randall's fugacity rule [11, pp. 28-32].

## 5.2 Nonideal Gaseous Mixture

The most general way to model a gaseous mixture is as a nonideal mixture. In this case the requirement that the chemical potential of every species in the mixture be a linear function of the logarithm of its mole fraction is relaxed, and the chemical potential of each species becomes mixture composition dependent. For the $i$th species,

$$\mu_i(T,P,\mathbf{x}) = \mu_i^0(T) + RT\ln P + RT\ln\phi_i(T,P,\mathbf{x}) + RT\ln x_i, \tag{30}$$

where $x$ is the species-mole-fraction vector, whose $i$th element, $i$ equals 1 to $N'$, is the mole fraction of the $i$th species in the mixture and

$$RT \ln\phi_i(T, P, x) = \int_0^P \left(\bar{v}_i - \frac{RT}{p}\right) \mathrm{d}p. \tag{31}$$

In general, in this case, $\bar{v}_i$ is a function of mixture composition and does not equal to $v_i$ [11, p. 28-29].

## 5.3 Pure Condensed Species

The chemical potential of a pure condensed species, solid or liquid, is given as

$$\mu(T, P) = \mu(T, P^0) + \int_{P^0}^P v \,\mathrm{d}p, \tag{32}$$

where $\mu(T, P^0)$ is the standard chemical potential of the species at $T$ and the reference pressure $P^0$ of one unit, normally chosen to be 1 bar or 1 atm. (The symbol $\mu^0(T)$ is not used which is normally reserved for gases in the idealized perfect-gas state.) There are three different models that can be used when assigning values to the molar volume $v$ for a pure condensed species.

### 5.3.1 Zero Molar Volume

In this case, the condensed species is assumed to occupy no volume or its volume is neglected. Thus the second term in equation 32 contributes nothing and

$$\mu(T, P) = \mu(T, P^0) \quad \text{with} \quad P^0 = 1\,\text{unit}. \tag{33}$$

### 5.3.2 Constant Molar Volume

In this case, the condensed species is assumed to have finite volume except that it is incompressible. Thus $v$ is nonzero but constant and the second term of equation 32 can be integrated to give

$$\mu(T, P) = \mu(T, P^0) + v(P - P^0) \quad \text{with} \quad P^0 = 1\,\text{unit}. \tag{34}$$

### 5.3.3 Variable Molar Volume

In this case, the condensed species is assumed to have finite volume and is compressible. The molar volume $v$ is a function of $T$ and $P$, and generally an equation of state is required for the evaluation of the second term in equation 32.

## 5.4 Assignment of Values to Standard Chemical Potentials

Regardless of the model used for a species, the evaluation of its chemical potential requires assigning a value to its standard chemical potential, at the reference pressure of one unit. Based on the application of equation 17 to a pure species, this quantity can be seen to be simply the standard molar Gibbs function of the species, denoted as $g^0$, which can be obtained in turn by using the relation

$$g^0 = h^0 - Ts^0 , \tag{35}$$

where $h^0$ and $s^0$ are the standard molar enthalpy and entropy, respectively. In addition, the values of $h^0$ and $s^0$ are related to $c_p^0$, the standard molar heat capacity at constant pressure.

All of the aforementioned quantities are functions of temperature only, and numerical values for $c_p^0$, $h^0$, and $s^0$ for many species are tabulated in references like the *JANAF Thermochemical Tables* [12]. Simultaneous least-square fits to the numerical data of these last three functions are normally carried out with the use of polynomials [13, 14], and the resulting coefficients are stored in the library of a computational code for evaluating $g^0$.

# 6 Brinkley, NASA, and Rand (BNR) Nonstoichiometric Algorithms

Three classical numerical algorithms for solving the chemical equilibrium problem with constant-temperature-and-pressure thermodynamic state constraints, which make use of the nonstoichiometric formulation are the Brinkley, NASA, and Rand algorithms. They are often referred to together as the BNR algorithms, because they are variations of the same basic method. Some intrinsic difficulties with these three algorithms had been discussed in detail by Smith [9] and Smith and Missen [5, pp. 204-211]. The basic method shared by these algorithms, their key differences, and an outline on their intrinsic difficulties will be given below to aid the understanding of the present comparision of nonstoichiometric and stoichiometric algorithms.

All these three algorithms can be derived by explicitly incorporating the conservation of mass constraint by using Lagrange multipliers, before the minimum to the system Gibbs function is sought and applying the Newton-Raphson method to the resulting set of equations. They differ essentially only in the way how the mole-number variables are treated and how equilibrium conditions and the conservation of mass constraint are satisfied.

The Lagrangian $\mathcal{L}$ as a function of $\mathbf{n}$ and $\boldsymbol{\lambda}$ where $\boldsymbol{\lambda}$ is a column vector of $M$ unknown Lagrange multipliers $\lambda_1, \lambda_2, \ldots, \lambda_M$ is defined to be

$$\mathcal{L}(\mathbf{n}, \boldsymbol{\lambda}) \equiv \sum_{i=1}^{N} n_i \mu_i + \sum_{k=1}^{M} \lambda_k \left( b_k - \sum_{i=1}^{N} a_{ki} n_i \right) . \tag{36}$$

Then the Kuhn-Tucker necessary conditions [15, pp. 35-39] for a minimum $\mathcal{L}$ are also conditions for finding the minimum of $G$ while satisfying the mass conservation constraint. There are $N + M$ conditions involving the $N + M$ unknowns $n_1, n_2, \ldots, n_N$ and $\lambda_1, \lambda_2, \ldots, \lambda_M$. Firstly, for the $i$th species with $i = 1, 2, \ldots, N$,

$$\mu_i - \sum_{k=1}^{M} a_{ki}\lambda_k = 0 \quad \text{if} \quad n_i > 0, \tag{37}$$

or

$$\mu_i - \sum_{k=1}^{M} a_{ki}\lambda_k \geq 0 \quad \text{if} \quad n_i = 0. \tag{38}$$

Secondly, for the conservation of mass

$$\mathbf{An} = \mathbf{b}, \tag{39}$$

which is a set of $M$ equations.

Based on the general definition of the chemical potential of a species in a mixture, it can be shown that a species will be absent at equilibrium only if the entire phase in which such a species is in is absent at equilibrium [5, pp. 57-58]. Thus, for the present system, all of the gaseous species in the presumed-to-be-present gaseous mixture would have nonzero molar amounts at equilibrium. On the other hand, it is possible that, at equilibrium, a pure condensed species may be absent and have zero molar amount. Furthermore, equation 37 is applicable to all the gaseous species and those pure condensed species present at equilibrium, while equation 38 is applicable to those condensed species that are absent at equilibrium.

For a system involving chemical reactions and for which both temperature and pressure can be specified independently, the phase rule dictates that the maximum number of phases that can be present at equilibrium is equal to the rank of $\mathbf{A}$. Thus, taken into account the gaseous phase and assuming that $\mathbf{A}$, as normally the case, has the full rank of $M$, the maximum number of pure condensed species that can normally be present at equilibrium is $M - 1$.

Often, the number of condensed species that needed to be considered is larger than the maximum possible number that can be present at equilibrium. For such cases, these three algorithms will run into difficulties, because the phase rule has been violated. To solve such problems, assumptions on the presence and absence of the condensed species at equilibrium would have to be made and consider only those that are assumed to be present at equilibrium. However, almost always which condensed species would actually be present at equilibrium is not known in advance, selections of condensed species are made through permutation and a trial and error approach would have to be taken to find the combination, the solution, that gives the lowest system Gibbs state function. This difficulty of not knowing which condensed species to choose is a major disadvantage of these algorithms.

Equation 37 is used for determining the molar amount of a gaseous species or a pure condensed species included for consideration. At the solution, whether a pure condensed species is assumed to be absent or determined to be absent through minimization must satisfy equation 38. Equation 38 can also be used as a criterion for testing whether a pure condensed species which is assumed to be absent at equilibrium might actually be present and should be included for consideration.

Equation 37 applied to the gaseous species and the condensed species considered gives a set of equilibrium conditions which are to be satisfied together with the mass conservation constraint. All the three algorithms solve this resulting set of equations by using the Newton-Raphson method.

While the three algorithms share the same basic approach, they differ slightly in the way how the mole-number variables are treated and how equilibrium conditions and the conservation of mass constraint are satisfied. The RAND algorithm [16,17] works with the variables $n_i$'s, whereas $\ln n_i$'s are used by the Brinkley [18] and the NASA [19,20] algorithms.

The RAND algorithm was originally formulated [21] as a constrained minimization method, which requires the conservation of mass constraint be satisfied at each step and iteratively minimizes the system Gibbs function. It was later modified so that the conservation of mass constraint need not necessary be satisfied at each step and iterations are carried out to satify the equilibrium conditions and conservation of mass constraint simultaneously.

Contrary to the original RAND algorithm, the Brinkley algorithm requires that the equilibrium conditions be satisfied at each step and iterations be carried out to satisfy the conservation of mass constraint. When the restriction that the equilibrium conditions be satisfied at each step is relaxed, the NASA algorithm is resulted. Thus the NASA algorithm complements the Brinkley algorithm similar to the way the modification to the RAND algorithm complements its original version. Computationally, there is little difference in the performance of the three algorithms [22].

The coefficient matrices of the linearized iterative equations of all the three algorithms obtained by the application of the Newton-Raphson method turn out to be the same; only the right hand side of the equations are different. Denoting this matrix by $\boldsymbol{\beta}$, then

$$\boldsymbol{\beta} = \left[\begin{array}{ccc} \mathbf{A}_1\boldsymbol{\Lambda}\mathbf{A}_1^T & \mathbf{b}_1 & \mathbf{A}_2 \\ \mathbf{b}_1^T & \multicolumn{2}{c}{\mathbf{Q}} \\ \mathbf{A}_2^T & & \end{array}\right], \tag{40}$$

where $\mathbf{A}_1$ and $\mathbf{A}_2$ are those portions of the formula matrix $\mathbf{A}$ referring to the multispecies phase of perfect-gas mixture and the pure condensed phases, respectively. $\boldsymbol{\Lambda} = \mathrm{diag}[n_1, n_2, \ldots, n_{N'}]$, $\mathbf{b}_1$ is the current elemental-abundance vector corresponding to the multispecies phase, that is

$$\mathbf{b}_1 = \mathbf{A}_1\mathbf{n}_1, \tag{41}$$

where $\mathbf{n}_1 = [n_1, n_2, \ldots, n_{N'}]^T$, and $\mathbf{Q}$ is the null matrix of order $\pi \times \pi$, except that $Q_{11} = -n_z$, where $\pi$ is the total number of phases and $n_z$ is the total number of moles of inert gaseous species.

The further difficulty with these three algorithms is that $\boldsymbol{\beta}$ can occasionally become singular. For example, $\boldsymbol{\beta}$ would always be singular for problems involving pure condensed species only, that is no gaseous phase is postulated, because all the entries in $\boldsymbol{\beta}$ with subscript 1 are absent. Also, $\boldsymbol{\beta}$ would be singular when too many condensed species are considered and the phase rule is violated. Furthermore, finite computer word lengths can also cause $\boldsymbol{\beta}$ to be numerically singular. A calculation will fail, whenever matrix singularity occurs, unless some corrective actions are taken.

# 7 Major Current Computational Codes

The three major current computational codes for chemical equilibrium analysis of constant-volume problems, which are based on nonstoichiometric formulations, are briefly described in this section. These are also the computational codes to which the new code had compared. All these three codes use the same product mixture model: a mixture of gases with pure condensates dispersed throughout. However, they use different models for the gaseous mixture and for the gaseous and condensed species themselves. The codes are described in the order of increasing complexity of the models.

## 7.1 The NASA Code

The NASA code [1] is a general purpose chemical equilibrium computational code, with applications not only limited to equilibrium computations for assigned thermodynamic states, but also including rocket performance, shock wave calculations, and Chapman-Jouguet detonations. For the present study, it was used to carry out constant-volume-and-energy-type calculations.

The code was written by assuming that the gaseous products form a perfect-gas mixture and that the pure condensed species occupy no volume. Thus, equations 25 and 32 are used for evaluating chemical potentials. Its solution algorithm is of the nonstoichiometric type, since the conservation of mass constraint is not treated by chemical stoichiometry but by means of Lagrangian multipliers. In addition, it uses the Newton-Raphson method for solving the set of equations (37, 39) resulting from the minimization of the Lagrangian and requires matrix inversion.

The NASA code also has a library of polynomial coefficients, which were obtained by curve fits to data in the *JANAF Thermochemical Tables*, for evaluating the standard state values of heat capacities at constant pressure, enthalpies and entropies of a large number of product species. The polynomials used are:

$$\frac{c_p^0}{R} = a_1 + a_2T + a_3T^2 + a_4T^3 + a_5T^4, \tag{42}$$

$$\frac{h^0}{RT} = a_1 + \frac{a_2}{2}T + \frac{a_3}{3}T^2 + \frac{a_4}{4}T^3 + \frac{a_5}{5}T^4 + \frac{b_1}{T}, \tag{43}$$

and

$$\frac{s^0}{R} = a_1 \ln T + a_2T + \frac{a_3}{2}T^2 + \frac{a_4}{3}T^3 + \frac{a_5}{4}T^4 + b_2, \tag{44}$$

where $a_1$ to $a_5$ and $b_1$ and $b_2$ are the constants to be determined.

There is a small discrepancy in the NASA code with regard to the reference pressure chosen and the thermodynamic data used. The reference pressure chosen for the definition of standard thermodynamic properties is one atmosphere in the NASA code. The library of polynomial coefficients was originally determined by using data in the earlier versions of the *JANAF Thermochemical Tables* [23, 24] which also use one atmosphere as the reference pressure. However, the library was later re-determined based on the data given in the third edition of the *JANAF Thermochemical Tables* [12] which is a SI edition and uses one bar as the reference pressure instead, and the reference pressure used in the NASA code has not been adjusted accordingly. The effects of this discrepancy on the results should be small. In addition, for comparision purposes, the same setting has been kept.

## 7.2 The Bagheera Code

The Bagheera code is the NATO standard code for analysing the thermodynamic properties of military propellants. It can only perform constant-volume-and-energy type of caculations. For this code, the mixture of gaseous products is assumed to be an ideal mixture of imperfect gases and obeys the Amagat's law. The gaseous species themselves are assumed to follow a modified volume-explicit virial equation of state of the form

$$v = \frac{RT}{p} + \frac{\beta_1}{1+\alpha_1 p} - \frac{\beta_2}{1+\alpha_2 p}, \tag{45}$$

where $\beta_1$ is the first term, the positive part, of the series giving the value of the second virial coefficient, $B$, in the conventional pressure-explicit virial equation of state, obtained based on the Lennard-Jones (6-12) potential for spherical molecules [25, pp. 162-163, p. 1119]. In addition,

$$\beta_2 = \beta_1 - B, \tag{46}$$

$$\alpha_1 = \frac{\beta_2^2 + B^2 - C}{\beta_1 RT}, \tag{47}$$

where $C$ is the third virial coefficient in the conventional pressure-explicit virial equation of state, obtained by a method similar to that used for $B$ [25, p. 170, p. 1119, pp. 228-230], and

$$\alpha_2 = \frac{\beta_2}{RT}. \tag{48}$$

The condensed species are assumed to have finite, constant molar volume. Their chemical potentials are obtained by using equation 34 and assuming that the value of $P$ is much larger than one, which is normally true for military propellant analysis, so that the term $P^0$ can be neglected and

$$\mu(T,P) = \mu(T,P^0) + vP \quad \text{with} \quad P^0 = 1 \text{ unit}. \tag{49}$$

The library of polynomial coefficients of the Bagheera code is essentially that of the NASA code (determined based on the third edition of the *JANAF Thermochemical Tables*) but includes coefficients for some additional species. The reference pressure chosen in the Bagheera code for the definition of standard thermodynamic properties is one bar and is consistent with that used for the thermodynamic data.

The solution method of the Bagheera code is also of the nonstoichiometric type and makes use of Lagrangian multipliers to incorporate the mass conservation constraint. Again it uses the Newton-Raphson method to solve a set of nonlinear equations and requires matrix inversion.

## 7.3 The Blake Code

The Blake code [3] was the previous NATO standard code for military propellant thermodynamic properties analysis. It was adapted from the Tiger code [26]. Applications of the Blake code involve only calculations for assigned thermodynamic states. For the present study, it was used to carry out calculations for combustions at constant volume and energy.

The Blake code uses the most general models for the gaseous mixture and the species themselves. The gases are not only assumed to be imperfect gases, they are also assumed to form a nonideal mixture; in addition, the condensates are assumed to have finite, variable molar volume.

There is a choice of four equations of state in the Blake code for describing the $p$-$v$-$T$ properties of the gaseous mixture: the perfect gas, the conventional truncated virial, the Becker-Kistiakowsky-Wilson (BKW), and the Powell-Wilmot-Haar-Klein (PWHK) [27] equations of state. For the present study, calculations were carried out by using the conventional truncated virial equation of state which is the default choice and has the following form:

$$z_{\text{mix}} = \frac{Pv}{RT} = 1 + \frac{B_{\text{mix}}}{v} + \frac{C_{\text{mix}}}{v^2}, \tag{50}$$

where $z_{\text{mix}}$ is the compressibility factor of the mixture, $v$ is the molar volume of the mixture, and $B_{\text{mix}}$ and $C_{\text{mix}}$ are the second and the third virial coefficients of the mixture respectively, determined by using the following mixing rules [3, p. 11]:

$$B_{\text{mix}} = \sum_{i=1}^{N'} \sum_{j=1}^{N'} x_i x_j B_{ij} \tag{51}$$

and

$$C_{\text{mix}} = \sum_{i=1}^{N'} x_i^3 C_{iii}. \tag{52}$$

The cross-second-virial coefficient $B_{ij}$ for the $i$th and the $j$th species are determined in a way similar to that used for determining the second virial coefficients of pure species, but by using combining rules relating their Lennard-Jones force constants. The cross-third-virial coefficient $C_{iii}$ is simply the third virial coefficient of pure species $i$ and is determined by assuming the rigid sphere model [3, p. 10].

For the condensates, a polynomial-type, empirical equation of state of the following form is used:

$$v = A_1 + A_2 p + A_3 p^2, \tag{53}$$

where the constants $A_1$, $A_2$ and $A_3$ are given by

$$A_1 = a_1 + a_2 T + a_3 T^2, \tag{54}$$

$$A_2 = a_4 + a_5 T + a_6 T^2, \tag{55}$$

$$A_3 = a_7 + a_8 T + a_9 T^2. \tag{56}$$

The nine coefficients $a_1$ to $a_9$ are empirically determined.

The classification of the solution algorithm of the Blake code is not so well defined; for the algorithm does use component species, but not in the sense of using chemical stoichiometry, and it does not use extents of reactions as independent variables. The algorithm uses a set of independent variables, the number of which is always the number of elements in the system (which would normally be the number of Lagrangian multipliers) plus two. The foundation of this algorithm was laid by S. R. Brinkley [26]; according to Smith and Missen [5, pp. 127-133], the Brinkley algorithm is of the nonstoichiometric type. This is the classification adopted in this paper. The set of nonlinear equations in the independent variables is also solved by using the Newton-Raphson method, and matrix inversion is also required.

The library of polynomial coefficients of the Blake code is much limited compared to those of the NASA and the Bagheera codes, both in terms of the number of product species and the number of elements involved, and the polynomials used for curve fits are different from those used for these two codes. Furthermore, in the Blake code, the data used for determining the coefficients are taken largely from the second edition of the *JANAF Thermodynamic Tables* [28], and the reference pressure of one atmosphere chosen for defining standard thermodynamic properties agrees with that used in this edition of the tables. However, the reference pressure chosen should be adjusted if data from later versions of these tables which use one bar as the reference pressure are used instead.

### 7.4 Potential Numerical Difficulties

The potential difficulties of singular coefficient matrix of the BNR algorithms for constant temperature and pressure problems were discussed in the previous section. These algorithms were developed for product mixtures for which the gases are assumed to form a perfect-gas mixture and the pure condensates are assumed to have no volume.

For the present study, constant-volume-and-energy type of problems were solved. In the case of the Bagheera and the Blake codes, models more general than perfect-gas mixture and zero-molar-volume condensates are used; however, the solution formulations of these two codes, and that of the NASA code, remain to be of the nonstoichiometric type and require matrix inversion. Consequently, it was expected that these three codes might encounter singularity problems and probably have difficulties in obtaining a solution for problems involving many condensed species. Some of the difficulties encountered will be addressed in section 12, where the results of calculations using these three codes and the new code for five test problems are presented.

## 8 Villar-Cruise-Smith(VCS) Stoichiometric Algorithm

This is the algorithm the new computational code is based upon. Because it eliminates the need for matrix inversion and handles the nonnegativity constraint for the condensed species straightforwardly, it is particularly suited for solving chemical equilibrium problems involving many condensed species [5, p. 144]. This algorithm was developed for ideal systems at constant temperature and pressure, and for the present study, it was applied to systems consisting of a gaseous mixture and a number of pure condensed species at constant volume and internal energy, and the system can be nonideal.

The VCS algorithm makes use of the stoichiometric formulation given by equations 18 and 19, and is named after the several workers contributed to its development. Villars [29, 30] originally viewed this algorithm as a way of using the Newton-Raphson method on the first-order necessary conditions for a minimum $G$. He used an arbitrarily chosen stoichiometric matrix $\mathbf{N}$ and adjusted the stoichiometirc equations one at a time. Later, Cruise [31] incorporated the use of an optimized $\mathbf{N}$ and advocated adjusting all equations simultanoeusly. Finally, Smith and Missen [32] reformulated the algorithm from the minimization point of view and introduced the use of a step-size parameter, resulting in improved convergence properties.

In its final form the VCS algorithm uses the second variation method for solving the unconstrained minimization problem, which involves finding the local minimum of the quadratic approximation to the system Gibbs state function at the current estimate of the equilibrium composition. The quadratic approximation is obtained by a Taylor series expansion of the system Gibbs state function as a function of the reaction extent parameters and with terms higher than the second order neglected, which can be written as

$$\delta G = \left.\frac{\partial G}{\partial \boldsymbol{\xi}}\right|^{T}_{\mathbf{n}^{(m)}} \delta\boldsymbol{\xi} + \frac{1}{2}\,\delta\boldsymbol{\xi}^{T} \left.\frac{\partial^2 G}{\partial \boldsymbol{\xi}^2}\right|_{\mathbf{n}^{(m)}} \delta\boldsymbol{\xi}, \tag{57}$$

where $\delta G$ is the change in $G$, $\partial G/\partial\boldsymbol{\xi}$ and $\delta\boldsymbol{\xi}$ are column vectors whose $j$th element, $j$ equals 1 to $R$, are the partial derivative $\partial G/\partial \xi_j$ and the change in $\xi_j$, respectively, the subscript $\mathbf{n}^{(m)}$ means that the entity on the left is evaluated at the current estimate of the equilibrium composition, and the superscript $T$ indicates the transpose of a vector. In addition, $\partial^2 G/\partial\boldsymbol{\xi}^2$ is the Hessian matrix whose $j$th element in the $i$th row is the double partial derivative $\partial^2 G/\partial\xi_i\partial\xi_j$, and both $i$ and $j$ can assume values from 1 to $R$. Finally, all changes are with respect to current values.

The amounts of reaction extents that must be adjusted to reach minimum $\delta G$ are obtained through the first order necessary conditions and given as

$$\delta\boldsymbol{\xi}^{(m)} = -\left.\frac{\partial^2 G}{\partial \boldsymbol{\xi}^2}\right|^{-1}_{\mathbf{n}^{(m)}} \left.\frac{\partial G}{\partial \boldsymbol{\xi}}\right|_{\mathbf{n}^{(m)}}, \tag{58}$$

where $m$ ($\geq 1$) is the iteration-step index and the superscript $-1$ denotes an inverse. The corresponding adjustments in mole numbers, $\delta\mathbf{n}^{(m)}$, are obtained from equation 20. Once the new estimate of the equilibrium composition is obtained the process is repeated until convergence is achieved.

For a single multispecies phase, such as a gaseous mixture, the elements of the Hessian matrix can first be written as

$$\frac{\partial^2 G}{\partial\xi_i\partial\xi_j} = \frac{\partial}{\partial\xi_j}\left(\sum_{k=1}^{N} \nu_{ki}\mu_k\right) \quad \text{with} \quad i, j = 1, 2, \ldots, R, \tag{59}$$

and $N$ is the total number of species in the phase. Equation 59 is obtained by applying the chain rule of differentiation, since $G$ is a function of the species mole numbers which in turn are dependent on $\xi_i$, and by making use of equations 7 and 17. Assuming an ideal solution, equation 21 applies. When similarily applying the chain rule for differentiating $\mu_k$ with respect to $\xi_j$ and making use of equation 21, the right hand side of equation 59 becomes

$$RT\sum_{k=1}^{N}\sum_{l=1}^{N}\nu_{ki}\nu_{lj}\left(\frac{\delta_{kl}}{n_k}-\frac{1}{n_t}\right), \tag{60}$$

where $\delta_{kl}$ is the Kronecker delta which equals to unity when $k$ and $l$ have the same value and equals zero when $k$ and $l$ are different. Further simplification yields

$$\frac{1}{RT}\frac{\partial^2 G}{\partial\xi_i\partial\xi_j}=\sum_{k=1}^{N}\frac{\nu_{ki}\nu_{kj}}{n_k}-\frac{\bar{\nu}_i\bar{\nu}_j}{n_t} \quad \text{with} \quad i,j=1,2,\ldots,R, \tag{61}$$

where

$$\bar{\nu}_i=\sum_{k=1}^{N}\nu_{ki} \quad \text{and} \quad \bar{\nu}_j=\sum_{k=1}^{N}\nu_{kj}. \tag{62}$$

Since the choice of N is arbitary, this can be effected so that the inversion of the Hessian matrix is avoided. Firstly, if N is choosen to be in the canonical form, for a noncomponent species, the product $\nu_{ki}\nu_{kj}$ is equal to one when $i$ equals $j$, ortherwise it is equal to zero, since each noncomponent species has a stoichiometric coefficient of value one only in one stoichiometric vector and zero in the remainings. Thus, when the component species are numbered from 1 to $M$ and the noncomponent species from $M$+1 to $N$, the elements of the Hessian matrix become

$$\frac{1}{RT}\frac{\partial^2 G}{\partial\xi_i\partial\xi_j}=\frac{\delta_{ij}}{n_{j+M}}+\sum_{k=1}^{M}\frac{\nu_{ki}\nu_{kj}}{n_k}-\frac{\bar{\nu}_i\bar{\nu}_j}{n_t}; \quad \text{with} \quad i,j=1,2,\ldots,R, \tag{63}$$

where only the diagonal elements will have the first term on the rght hand side.

Secondly, if the component species are chosen to be the most abundant species, the second term on the right hand side of equation 63 tends to be small compare to the first, because the $n_k$'s are larger than the $n_{j+M}$'s. The last term will also generally be small, because of the presence of the term $n_t$ in the denominator; it may even vanish if either $\bar{\nu}_i$ or $\bar{\nu}_j$ equals zero.

When N is formed meeting the above two requirements, the Hessian matrix will become diagonally dominant. Finally, if the off-diagonal terms are neglected, it can be approximated as being diagonal and be inverted directly to give

$$\frac{\partial^2 G}{\partial\xi^2}^{-1}\approx\left[\frac{1}{RT}\left(\frac{1}{n_{i+M}}+\sum_{k=1}^{M}\frac{\nu_{ki}^2}{n_k}-\frac{\bar{\nu}_i^2}{n_t}\right)^{-1}\delta_{ij}\right] \quad \text{with} \quad i,j=1,2,\ldots,R. \tag{64}$$

At the end of each iteration step, the new species mole numbers are examined to ensure that the component species remain to be the most abundant species. If this is unture, a new set of component species is selected and a new stoichiometric matrix is formed before carrying out the next iteration step.

With the inversion of the Hessian matrix eliminated, equation 58 can be rewritten giving straightforwardly corrections to the reaction extent parameters as

$$\delta\xi_j^{(m)} = -\left(\frac{1}{n_{j+M}^{(m)}} + \sum_{k=1}^{M}\frac{\nu_{kj}^2}{n_k^{(m)}} - \frac{\bar{\nu}_j^2}{n_t^{(m)}}\right)^{-1}\frac{\Delta G_j^{(m)}}{RT} \quad \text{with} \quad j = 1, 2, \ldots, R, \tag{65}$$

where the superscript $-1$ now stands for the reciprocal of a scalar quantity and

$$\Delta G_j^{(m)} = \left.\frac{\partial G}{\partial \xi_j}\right|_{\mathbf{n}^{(m)}} = \sum_{i=1}^{N}\nu_{ij}\mu_i^{(m)}. \tag{66}$$

For systems involving an ideal multispecies phase plus a number of single-species phases, equation 65 has a slightly different form. In its final form for a system consists of an ideal gaseous mixture and a number of pure condensed species, equation 65 becomes

$$\delta\xi_j^{(m)} = -\left[\frac{\delta_{j+M}}{n_{j+M}^{(m)}} + \sum_{k=1}^{M}\frac{\nu_{kj}^2\delta_k}{n_k^{(m)}} - \frac{(\sum_{k=1}^{N}\nu_{kj}\delta_k)^2}{n_{tg}^{(m)}}\right]^{-1}\frac{\Delta G_j^{(m)}}{RT}, \quad \text{with} \quad j = 1, 2, \ldots, R, \tag{67}$$

where $\delta_{j+M}$ is unity if the $(j+M)$th species is a gaseous species and is zero if it is a condensed species, the same conditions apply to $\delta_k$, and $n_{t_g}^{(m)}$ is the total number of moles of gases in the gaseous phase. This is the equation used in the present code for determining the corrections to the reaction extent parameters.

After the $\delta\xi_j$'s have been determined, changes to species abundances are obtained from equation 20. However, such changes are modified twice before they are applied. The first modification is to take into consideration the nonnegativity constraint, which is handled in general by multiplying the species-abundance-change vector obtained from equation 20 by a scaling parameter, such that

$$\delta\mathbf{n} = \kappa\mathbf{N}\delta\boldsymbol{\xi} \quad \text{with} \quad 0 < \kappa \leq 1 \tag{68}$$

and all the $n_i$'s are kept greater than zero. The second modification is to perform a minimization in the direction defined by this new $\delta\mathbf{n}$, and the final $\delta$ **n** is the one which gives minimium Gibbs state function. Details of this minimization procedure is given in the original reference by Smith and Missen [1968] and is not be repeated here.

For pure condensed species an additional procedure is required to handle the nonnegativity constraint. As a matter of fact, through the application of this and another special procedure, the VCS algorithm can consider practically as many condensed species as required. Firstly, the Kuhn-Tucker condition for the stoichiometric formulation for a noncomponent condensed species being absent at equilibrium is used to determine the deletion or introduction of such a species from or into the main calculation. This condition is similar to equation 38 and is given as

$$\frac{\partial G}{\partial n_i} \equiv \frac{\partial G}{\partial \xi_j} = \mu_i^{*} + \sum_{k=1}^{M}\nu_{kj}\mu_k \geq 0 \quad \text{if} \quad n_i = 0, \tag{69}$$

where $i$ equals to $j + M$. Equation 69 is based on N being expressed in the canonical form. $\mu_i^*$ is the standard chemical potential of the pure condensed species, which is independent of the composition of the product mixture. The quantity on the right is also recognized to be the free energy change across the $j$th reaction denoted as $\Delta G_j$. The first two terms are identical because the stoichiometric coefficient of a noncomponent species is unity. This condition implies that if the value of the system Gibbs state function will decrease with the addition of an infinitesmial amount of a condensed species (i.e., $\Delta G_j$ is negative) that is absent, the species will form. Thus, the sign of $\Delta G_j$ is checked for determining whether such a condensed species should be introduced into the main calculation.

During the course of a calculation, when the adjusted mole number (determined based on equation 20) at an iteration step of a noncomponent condensed species present in minute amount becomes negative, it is set to zero. At each subsequent step, the sign of $\Delta G_j$, $j = i - M$, based on the stoichiometric equation for this species is examined. Should $\Delta G_j$ becomes negative, the species is reintroduced into the calculation. In this way, pure condensed species may readily enter or leave the main calculation during iterations.

Secondly, when many condensed species are considered together, occasionally chemical equations are determined which involve only condensed species. These are phase-rule-violating situations, and at least one of the species in an equation like this must not be present. To delete a species, such a reaction is adjusted by an amount $\delta\xi_j$ which takes the sign of $-\Delta G_j$ and has a magnitude which reduces the amount of the limiting species to zero. That is

$$\delta\xi_j = \text{sign}(-\Delta G_j) \times \text{minimum}[n_j, n_1/|\nu_{1j}|, \ldots, n_k/|\nu_{kj}|, \ldots, n_M/|\nu_{Mj}|], \tag{70}$$

where $n_j$ is the mole number of the $j$th noncomponent species, $n_1$ to $n_M$ are the mole numbers of the component species and $|\nu_{1j}|$ to $|\nu_{Mj}|$ are the absolute values of the stoichiometric coefficients of the component species for this $j$th reaction. In this way, a phase is deleted and a degree of freedom is gained. With this phase-deletion procedure incorporated, the case where only pure condensed species are present in the product mixture and no gaseous phase is postulated can also be treated. This is a linear programming problem which cannot be handled by the BNR algorithms, as noted before.

Smith and Missen [1968] also deviced a systematic mean in determining a set of initial equilibrium estimates of species mole numbers which satisfy the mass conservation constraint. This procedure is based on solving a linear programming problem directly related to the actual problem to be solved, obtained by neglecting the composition dependent logarithmic terms in the chemical potentials and defined as follows:

$$\text{minimize } G(\mathbf{n}) = \mathbf{n}^T \boldsymbol{\mu}^*, \tag{71}$$

subject to the linear constraints

$$\mathbf{A}\mathbf{n} = \mathbf{b} \tag{72}$$

and for

$$n_i \geq 0 \quad \text{with} \quad i = 1, 2, \ldots, N. \tag{73}$$

The $\mu^*$'s are constant at constant temperature and pressure.

There are three possible outcomes to this linear programming problem. The first is that a solution exists with $M$ of the mole numbers being nonzero while the rest are. In this case the mole numbers of the remaining gaseous species are determined from the $M$ solution mole numbers. By using these $M$ species as components and the remaining $R(N-M)$ species as noncomponents, a complete stoichiometric matrix in the canonical form can be formed. The mole numbers of the gaseous noncomponents are determined by firstly assuming that their forming reactions have reached equilibrium, that is by setting the $\Delta G_j$'s of corresponding reactions to zero, and by secondly retaining the mole numbers of the component species. Thus

$$n_j = n_{t_g} \exp\left(-\mu_j^* - \sum_{k=1}^{M} \nu_{kj}\mu_k\right) \tag{74}$$

where $j$ takes on values that fall within the range from 1 to $R$ and $n_{t_g}$ is the total number of moles of the gaseous components.

These $n_j$'s are then taken to be reaction extents. Adjustments to the mole numbers of the components and the gaseous noncomponents are then made, such that the nonnegativity constraint is observed and a one-dimensional minimization is achieved, much like that for the adjustments in the main calculation. This procedure is also described in the original reference by Smith and Missen [1968] and is not repeated here. The mole numbers of the noncomponent pure condensed speices are left at zero, and they are introduced into the main calculation by following the procedure described above.

The second outcome is that a solution exits but with fewer than $M$ of the mole numbers being nonzero. In this case, all the remaining gaseous species are assigned with an arbitarily small mole number, for example, $1. \times 10^{-15}$, while the remaining condensed species are left at zero. This case happens infrequently. The last outcome is that no feasible solution is found. This means that the mass conservation constraint defines an impossible situation.

With a large number of gaseous species included in a calculation, often many of them will only exist in trace amounts at equilibrium. To correct the molar amoumts of these species, only very small iteration steps can be taken in order to satisfy the nonnegativity constraint, and convergence will be slow. To circumvent this difficulty, Smith and Missen [1982] removed these gaseous species, just like in the case of the condensed species, from the main calculaton and adjusted their amounts seperately. A similar procedure is followed in the present code and will be described in the following section.

## 9 Application of the VCS algorithm to the present problem

The thermodynamic state constraints for the present problem are constant internal energy and volume. The gaseous products can be assumed to be an ideal or a nonideal solution, such as in the NASA and Bagheera codes and the Blake code, respectively. In addition, the pure condensed species can be assumed to have zero, constant or variable molar volume such as in the cases of the NASA, the Bagheera and the Blake codes, respectively. To apply the VCS algorithm, which is an ideal-system algorithm, to a nonideal solution, the intermediate approach [5, p. 169] was used. This approach involves retaining the use of equation 67, but the chemical potentials of the gaseous species are replaced by their nonideal values. Based on equation 31, it can be seen that even at constant temperature and pressure, the fugacity coefficient, which is mixture composition dependent, would have to be re-evaluated at each iteration step. This affects the choice of the iteration scheme on pressure to satisfy the constant volume constraint.

When applying the VCS algorithm to problems with constant internal energy and volume thermodynamic state constraints, iterations on the system temperature and possibly pressure are also required. When solving a problem of such a type, a trial equilibrium temperature, $T_t$, needs to be specified in order to perform a VCS calculation. Based on the equilibrium composition found for this trial temperature, the total internal energy of the reaction products, $U_p$, can be determined. This energy must equal to that of the reactants, $U_r$, otherwise, the trial temperature assumed is incorre, a higher temperature should be assumed if $U_p$ is lower than $U_r$ and vice versa.

In the present code, the equilibrium temperature is solved for by first bracketing it and then applying the Brent root-finding method [33, pp. 251-254]. $U_p$ is a monotonically increasing function of the trial equilibrium temperature and so is $\Delta U (= U_p - U_r)$, the difference between the total internal energy of the products and of the reactants. Thus, the equilibrium temperature can be determined by finding the root to the equation

$$\Delta U(T_t) = 0, \tag{75}$$

and root bracketing is determined by detecting a sign change in $\Delta U$. The default initial bracket is 2300 to 2700 K. The bracket limits and, if necessary, the temperature range, which is nomally set at 400 K, can be adjusted until the root is bracketed.

The total internal energy of the product mixture consists of contributions from the gaseous mixture and the condensed species. Thus

$$U_p = U_g + U_c, \tag{76}$$

where $U_g$ and $U_c$ are the total internal energy of the gaseous mixture and of the condensed species, respectively. In the case of an ideal gaseous mixture, the internal energy of the mixture is equal to the sum of those of the component species as pure gases at the system conditions. That is

$$U_g = \sum_{i=1}^{N'} u_{g_i}, \tag{77}$$

where $N'$ is the number of species in the gaseous mixture and $u_{g_i}$ is the molar internal energy of the $i$th species in the gaseous mixture. On the other hand, in the case of a nonideal gaseous mixture, the entire mixture is treated like a single gas. Also, the internal energy contributed by the condensed species is the sum of the internal energy of the individual species at the system conditions. Hence

$$U_c = \sum_{i=1}^{N''} u_{c_i}, \tag{78}$$

and similarly $N''$ is the number of pure condensed species in the product mixture and $u_{c_i}$ is the molar internal energy of the $i$th condensed species in the product mixture.

The Brent method was used because it has two nice features. It combines the sureness of the bisection method, convergence is guaranteed provided the root is first bracketed, with the speed of inverse quadratic interpolation. The method requires the values of the function only, not its derivative or functional form, which are not readily available in this case for $\Delta U$. The subroutine given by Press and others [33, p. 245, pp. 253-254] for root bracketing and the Brent method had been incorporated into the present program.

To satisfy the constant volume constraint, a similar iteration on pressure could be nested within the iteration on temperature. That is for a given trial temperature, iterations on pressure is carried out until the specific volume of the product mixture is equal to the constraint value. To this end, for a given trial pressure, iterations are carried out until convergence is achieved, that is a equilibrium composition is obtained. Based on this equilibrium composition, the specific volume of the product mixture is then determined, if this specific volume is larger than that of the constraint value, a higher pressure should be assumed and vice versa. However, this was not the approach followed.

The approach followed was to determine a pressure which will lead to the conformity to the constant volume constraint at each iteration step, so that only one equilibrium calculation is required for each trial temperature. The basis for adopting this approach is that the standard chemical potentials of gaseous species in a nonideal mixture need to be re-evaluated at each iteration step in any case. Based on equations 25 and 29 it can be seen that the standard chemical potentials of the gaseous species in a perfect-gas mixture or an ideal mixture of imperfect gases need only be evaluated once for any given pair of trial temperature and pressure. However, because of the mixture-composition-dependent characteristic of these quantities (equation 30) for a nonideal mixture, they need to be re-evaluated at each iteration step, as mention above. To be in line with this requirement, the approach that a new pressure be determined at each iteration step was taken. The pressure is determined either directly or by iteration depending on the models used for the gaseous mixture and the pure condensed species.

The procedure followed in each case when comparing with the three aforementioned current computational codes is described below. In the case of the NASA code where the gaseous mixture is a perfect-gas mixture and the pure condensed species occupy no volume, the pressure is determined directly by applying the perfect equation of state. In the case of the Bagheera code where the gaseous mixture is an ideal mixture of imperfect gases following the Amagat's rule and the pure condensed species have constant molar volume, the volume occupied by the gaseous mixture is obtained by substracting the volume taken up by the condensed species from the constraint volume. The pressure then is the one at which the sum of the volume occupied by each gas as a pure gas at this pressure and the accompanying trial temperature is equal to the volume to be occupied by the mixture.

In the case of the Blake code, eventhough the gaseous mixture is a nonideal mixture, the pressure could not be evaluated directly, because the condensed species are compressible, thus the volume occupied by the mixture is a variant and is temperature and pressure dependent. The pressure is then the one at which the sum of the volume occupied by the gaseous mixture and by each pure condensed species at this pressure and the accompanying trial temperature is equal to the constraint volume. In the last two cases where the pressure is determined iteratively, the Brent method is once again employed. A few calculations using the first approach for which an iteration on pressure is nested within the iteration on temperature were performed, there does not seem to be large differences in the computational times of the two approaches.

Once a trial equilibrium temperature has been chosen, a VCS calculation is performed with a new pressure and the chemical potentials of the species evaluated at the beginning of each iteration step. The $\Delta G_j$'s are then determined and the re-introduction of condensed species are also checked. Before proceeding further, a check on chemical equations involving pure condensed species entirely is performed. This includes the case involving a noncomponent condensed species being re-introduced. The case involving a noncomponent condensed species which will continue to be absent is not a problem. The phase-deletion procedure is applied to the first chemical equation of such a type encountered, and a new iteration step is taken after a deletion.

If there is no chemical equation involving entirely pure condensed species, adjustments in the reaction extent parameters are then calculated by using equation 67. The deletion of noncomponent condensed species is checked next. Since the stoichiometric coefficient of a noncomponent species is unity, whenever the adjustment of the reaction extent for the chemical equation, associated with a pure noncomponent condensed species is negative and has a magnitude larger than the current molar amount of such a condensed species, the direct adjustment of the molar amount of such a condensed species, by using this adjustment of the reaction extent, will render the adjusted amount of the condensed species to become negative (see equation 20). In this case, if the current molar amount of the condensed species is less than one-thousandth of its least abundant forming component, it is deleted by reducing its molar amount to zero, by limiting the amount of the reaction extent adjusted to be equal in magnitude to the molar amount of the condensed species. The one-thousandth criterion is arbitarily chosen to prevent premature deletion of a condensed species.

The molar amounts of the components and other noncomponent species are adjusted accordingly based on equation 20; this includes noncomponent condensed species being re-introduced. Such changes are modified twice before they are applied, to take into consideration the nonnegativity constraint and to effect a one-dimensional minimization, as mentioned above. The Convergence criterion is that the absolute value of the fractional correction in mole number, the correction in mole number divided by the new mole number after the correction has been applied, is less than or equal to $5. \times 10^{-6}$ for each of the species present in the mixture.

In the present code, the same procedure as proposed by [32] is used for determining initial estimates of the equilibrium mole numbers for a trial equilibrium temperature, but with a modification to include the handling of trace gaseous species. Instead of removing the trace gaseous species from the main calculation and adjusting their amounts seperately, gaseous species estimated based on equation 74 to have molar amounts below a certain predefined lower limit are not considered from the outset. Deletion or re-introduction of gaseous species are carried out after a convergence of the main calculation has been achieved.

After the first convergence, all the gaseous species whose molar amounts have fallen below the pre-defined lower limit are deleted; and those that were left out at the beginning, but whose estimated amounts based on the converged mole numbers are now above or equal to the lower limit are introduced, to prepare for another round of iterations. If no deletion or introduction is necessary final convergence is taken to have achieved; otherwise, the components are adjusted to reflect such changes and iterations are continued.

From the second convergence onward, no deletion is performed; only gaseous species that were left out at the beginning and those that were deleted after previous convergences will be checked for introduction. In this way, some gaseous species present in amounts slightly smaller than the lower limit will be included, and they get included because the amounts of gaseous species are usually over estimated by equation 74. Final convergence is achieved when no more gaseous species needs to be introduced. The equilibrium solution is then obtained by carrying out one final deletion of gaseous species which present in amounts smaller than the lower limit and adjusting the component species accordingly.

The final deletion step is taken only for matching the number of gaseous species that were taken into consideration when comparing with the current codes. In the current codes, some gaseous species with amounts slightly smaller than the specified lower limits are allowed. Because of this, the lower limits specified in the new code are not equal to those specified in the current codes, but equal to the molar amounts of the least abundant gaseous species considered.[1]

For different trial equilibrium temperatures, the initial estimates of the equilibrium mole numbers are different. However, if the temperatures do not differ very much, the initial estimates should also not differ very much. At the present moment, a new set of initial estimates (noncomponent pure condensed species and noncomponent gaseous species whose estimated amounts are below the lower limit are not required) is evaluated only when a new trial equilibrium temperature is different from the current one by more than 400 K; otherwise, the equilibrium mole numbers determined for the current temperature are used as the initial estimates for the new temperature.

## 10 The Computational Code

The new computational code developed is a general code that can be applied to a wide variety of systems. It solves for the equilibrium composition of products of combustion that takes place in a closed vessel. It was assumed that the volume of the vessel is constant and there is no heat loss from the product mixture to the vessel walls. The later assumption implies that the total internal energy of the products stays constant and is equal to that of the reactants before the combustion has taken place. Thus, the core problem solved by the code is a chemical equilibrium problem with constant total volume and internal energy as the thermodynamic constraints. The solution of such a problem was achieved by adapting the VCS algorithm which was developed for solving chemical equilibrium problems with constant temperature and pressure as the constraints.

---

[1] In the NASA and the Bagheera codes, besides the lower limits used for handling trace gaseous species, there are also lower limits specified for printing results; abundances of the gaseous species, which are below the latter limits will not be printed. The limits for printing are normally chosen to be greater than the limits for handling trace species.

Different models for the gaseous mixture can be used in the code. The gaseous products can be assumed to be a mixture of perfect gases, an ideal mixture of imperfect gases or a nonideal mixture of imperfect gases, which is the most general model that a mixture of gaseous can be. If the gaseous mixture is assumed to be a mixture of perfect gases than the perfect gas equation of state should be used to describe the $p$-$v$-$T$ properties of the gases. Otherwise, an equation of state for imperfect gases is needed for describing such properties.

Depending on the typical temperature and pressure ranges that the product mixture of an application may be at, one equation of state may describe the $p$-$v$-$T$ properties of the gases more accurately than the others and should be used. The present code has the versatility that the equation of state used to describe such properties can be changed by replacing the subroutine for determining the chemical potentials of product species and the subroutine for finding the difference between the total internal energy of the product mixture and that of the original reactants.

Similarly different compressibility models can be used for the condensed species. Condensed species can be considered as compressible or incompressible. If they are considered to be incompressible, they can further be considered to have zero or constant molar volumes. On the other hand, if the condensed species are assumed to be compressible, then an equation of state is required to describe their $p$-$v$-$T$ properties. Again, the code has the versatility to allow different equations of state be used, depending on the application. This is also achieved through the replacement of existing subroutines for determining the chemical potentials of product species and the difference between the total internal energy of products and reactants, as in the case of the gaseous species.

The greatest advantage of the new code is that no specific knowledge is required on possible condensed species which may exist at equilibrium and should be included or be included in any particular order, so that convergence can be achieved in a calculation; all possible condensed species for an application can be included and the code can consider all of them together and determine which of them are present, along with their amounts, or absent at equilibrium. The new code can handle a large number of product species, gaseous and condensed. At the present moment, it has been dimensioned to include a maximum of seven hundred species in one calculation.

## 11 Test Cases and Procedure

To compare the capability of the new computational code in handling condensed species with those of the aforementioned existing major codes, five sample energetic materials were used as test cases. The first energetic material is a LOVA propellant; the second is a propellant for which DREV [2] claimed that the Blake code would not converge; the third is a primer; the fourth is a black powder which can be used as an igniter; and the last is a delay. Primers, igniters and propellants are normally used in sequence, with a primer initiating an igniter, and an igniter igniting a propellant. Delays are used for introducing time lapses between stages in pyrotechnic processes. The five test materials were chosen such that there is an increasing number and an increasing amount of condensed products present in the equilibrium product mixtures, assuming constant-volume and adiabatic combustion.

The compositions of the five energetic materials are listed in tables 1 to 5. The first four compositions were provided by DREV; the fifth one was taken from *Chemistry of Pyrotechnics* by Conkling [34, p. 130] and slightly modified. In each table, the name, molecuiar or summation formula, enthalpy of formation, and percentage by weight of each ingredient of an energetic material are given.

The name of an ingredient can be a chemical name, e.g., potasium nitrate, a common name, e.g., graphite, or a trade name, e.g., Viton A. It was chosen as what was deemed appropiate. Furthermore, many of the ingredients of the five samples are listed in Freedman's article [35], in which they have also been assigned abbreviated names. The abbreviated names of such ingredients are also provided in the tables, which are in capital letters and bracketed.

The formulae and enthalpies of formation were taken from different sources. Those for the LOVA propellant were used by DREV, and they were found to be taken mainly from the library of ingredients of the Bagheera code. Those for the second propellant and the black powder were also used by DREV and were found taken mainly from the library of ingredients of the Blake code and from Freedman's article. For the primer, the enthalpy of formation of potassium nitrate was taken from the Blake library and that of magnesium carbonate from the *JANAF Thermochemical Tables* [12], and the formula and enthalpy of formation of Viton A were provided by DREV. In the case of the delay, the enthalpy of formation of barium chromate was taken form the Bagheera library and that of potassium perchlorate from the *JANAF Thermochemical Tables*.

Enthalpies of formation of ethyl centralite used for the LOVA and the second propellant are different, because they were taken from two sources. The formulae for ingredients such as cellulose, nitrocellulose and charcoal are summation formulae. They essentially give the ratios among the types of atoms involved in forming the ingredient and could be scaled based on different bases giving different sets of numbers of atoms. Apparently the bases used for the formulae in the Bagheera and the Blake codes are different; this explains why the numbers of atoms for the 12.6% nitrocellulose are so much larger than those for the 13.15% nitrocellulose. Even though formulae and enthalpies of formation of the five samples were taken from different sources, this would not affect the consistency of the comparisions, because ingredients information of individual sample was kept the same when carrying out the comparisions.

The enthalpies of formation were required for energy considerations. When treating the conservation of energy constraint, the total internal energies of the energetic materials were needed, and they were obtained by summing the internal energies of the ingredients. Before combustion took place, the energetic materials, and thus their ingredients, were assumed to be at 298.15 K (25° C) and 1 atm. At these conditions, the internal energies of the ingredients, which are solids, can be approximated by their enthalpies, because their product terms between pressure and volume are small by comparision [??]. In addition, their enthalpies at these conditions were taken to be their enthalpies of formation at the same conditions, which is the common practice. This is why enthalpies of formation were required as input data.

According to DREV, the Blake code could not solve the second propellant problem; floating point errors were encountered. However, if lead oxide was removed from the formulation, the code worked. Therefore, it is important to keep the original composition, with lead oxide included, and enthalpies of formation for the tests. In particular, the enthalpy of formation of lead oxide was found to be in error, the value quoted in the *JANAF Thermochemical Tables* [12] is −52440. cal/mole. The value −103500. cal/mole was found both in the library of ingredients of the Blake code and in Freedman's article.

The composition of the black powder is very close to that of the black powder Du Pont 3814 quoted by Freedman [35]. The original formulation of the delay given by Conkling [34, p. 130] consisted a 17% by weight of a 50/50 zirconium-nickel alloy. Owing to the difficulty in obtaining the enthalpy of formation of this uncommon alloy, the formulation was altered to include elemental zirconium and nickel instead, for which the enthalpies of formation are simply zero. Also, for simplicity reason, an equal percentage by weight of 8.5% of each element was assumed.

The major objective of the present comparision was to demonstrate the robustness of the new code. In order to be sure that comparisions were between algorithms and to eliminate any uncertainties which may arise due to the use of different models and input data, the same gaseous mixutre model, condensates model, equations of state, and species property and thermodynamic data were all kept the same when comparing the new code with an existing code. Thus if an existing code has difficulty or fail to solve a problem while the new code succeeds, it can be attributed to the superiority of the solution algorithm of the new code. For comparision purposes, all calculations were peformed for a loading density of 0.2 gm/c.c..

Besides the capabilities of handling condensed species, the speeds of the solution algorithms of the new and the current codes were also compared in terms of CPU times. The CPU times compared were times required for the actual solution of equilibrium problems, they were the times from the initial estimation of equilibrium compositions to the convergence of iterations determining the equilibrium compositions. The times taken for the processing of ingredients data, the selection of possible product species, and the processing and printing of final outputs were not included. Furthermore, all the codes were compiled with same compiling options and run on a Hewlett-Packard 9000 series model 433s work station. In particular, no optimization of the codes performed by the compiler was specificed.

Another aspect which would affect the CPU times is the number of product species considered for a problem. In order to have a proper comparision, when solving a problem, the number of species considered by the new code was kept the same as that considered by a current code. However, the meaning of keeping the same number of species requires some elaboration.

Ingredients of an energetic material are compounds of certain elements. In the NASA or the Bagheera code, in general, the variable arrays are large enough such that all the product species which are formed from a subset of the elements defined by the ingredients and found in its library of thermodynamic data are selected for a calculation. This is the basic list of product species to be considered. And for each condensed product species there is an associated temperature range, at a temperature within which the species is considered to be a stable phase and outside an unstable phase. (For example, in the NASA code, liquid water is considered to be a stable phase between 273.15 and 500 K.) The condensed species in the basic list, which are unstable phases for a trial equilibrium temperature under consideration are eliminated and not considered. Thus, the condensed species considered at any one time are in general a subset of those in the basic list. The new code uses the same basic list of product species and selects the same stable condensed species as the NASA or the Bagheera code.

In addition, the library of the NASA or the Bagheera code is very large; the number of gaseous species in the basic list can easily be over a hundred when six to seven elements are involved in a system. Many of these gaseous species present only in trace amount, and their abundances are set to zero. The cut-off limits are different in these two codes. The new code has the option to specify a cut-off limit and can match the number of gaseous species having non-zero abundances in either of these two codes.

In the Blake code, at most twenty-nine gaseous species and the condensed species of ten substances (if data for both solid and liquid phases of a substance are available, they are selected together) can be selected for consideration; thus usually not all the possible product species in the library will be selected. The species are selected in the order they appear in the library; and by specifing which species to be omitted, control over the selection can be exercised. However, in general there is no guideline as to select which species. This is particularly true when new or uncommon energetic materials are analysed. It is possible that gaseous species existing in significant amount and condesed species that should be present at equilibrium are missed. In addition, the Blake code usually has great difficulties in choosing a set of components when condensed phases of a few substances are selected. Therefore, for comparision purposes, when selecting product species, reference was made to the results of the NASA code or the new code, so that the gaseous species selected would be the most abundant gaseous species if all the possible products were considered, and the condensed phases of substances for which one of the two phases was present at equilibrium were selected.

The use of the results of the NASA code to aid the selection of product species was suggested by Freedman [3, p. 41]. However, the NASA code and the Blake code use different models and data, the species abundances predicted by the two codes would be different. Thus the most abundant gaseous species predicted by the two codes were not necessarily the same. (Usually the same condensed species were predicted, except that the Blake code had difficulties in solving the problems which included condensed species of a few substances for consideration.) To achieve the above objective, calculations were performed by using the new code (using same models and data as the Blake code), in which *all* possible product species that could be selected from the library of the Blake code were considered.

The library of the Blake code is much smaller than that of the NASA code; thus it is possible for some gaseous species which presented in fair amount according to the NASA results were not in the Blake library. It was the most abundant gaseous species which were also found in the library of the Blake code that were selected. If these selected most abundant gaseous species were different from those selected based on the results of the new code, the latter was followed. The two selections were considered to be different only when the two sets of species selected were different, the amounts of individual species selected could be different.

Even though selection of species based on the results of other computational codes was carried out to aid the achievement of solutions in the case of the Blake code, the selection did not base on the results of the new code at the outset. This was to avoid giving the impression that results of the new code which was to be compared with the Blake code were used directly to help to obtain the results of the Blake code.

For the final comparision, especially of the CPU times, the new code was rerun using the same list of species selected for the Blake code. Furthermore, in the Blake code, all the condensed species, after they were selected from the library, were considered between 300 and 5000 K, making no further selection based on whether the phases were stable or unstable for a given trial equilibrium temperature, as in the cases of the NASA and Bagheera codes. That is which of the two condensed phases, or none, of a substance would be present at equilibrium was determined through minimization. The new code followed the same procedure.

The CPU time taken by the new code to solve a problem also depends on the initial temperature bracket for bracketing the equilibrium temperature. Since the equilibrium temperatures for many energetic materials lie between 2300 and 2700 K, these were the nominal values chosen for the initial temperature bracket. However, two of the sample energetic materials had equilibium temperatures lower than 2300 K; for these two cases, additional runs were performed by using initial temperature brackets with temperature limits at approximately 200 K above and below the equilibrium temperature.

The CPU time for solving a problem varies slightly from run to run. Thus when comparing the new code with a current code, calculations were repeated ten times and the CPU times were averaged. The errors determined in terms of standard deviations were in general smaller than one-hundredth of a second. However, it was felt that quoting results to the second decimal place was quite sufficient; consequently the errors and the CPU times were rounded to the hundredths.

## 12 Results of Calculations and Discussions

Calculations were carried out for the previously defined five energetic materials using the three current major thermodynamic codes and the new code. In particular, for each test case, the new code was used to perform calculations using models, number of species and input data matching those of each of the three major codes. Values of the equilibrium temperatures and pressures of product mixtures determined by the three current codes and the new code were tabulated in tables 6, 8 and 10.

Listed below the identification of each energetic material is information on the number of elements involved, number of gaseous and condensed species considered, the number of condensed species found to be present at equilibrium, and the percentage by mole and by weight of condensates in the equilibrium product mixture. The energetic materials were chosen such that there was an increasing number and an increasing amount of condensates present at equilibrium. Because the Bagheera code did not converge for one test case, the percentages of condensates for such a case was determined based on the results of the new code. Consequently, for consistency, all the percentages were determined based on the results of the new code. The percentages within each test case determined when comparing the new code with the three current codes varied slightly because different models and thermodynamic data were used and different number of species were considered.

Equilibrium compositions were not given except in the case of the delay when comparing with the NASA code, which are shown in table 14, because the number of species involved in the other cases are generally quite large and the main purpose of the comparisons was to demonstrate the robustness of the new code. It would only be quoted that agreements in species abundances are generally to four significant figures, as demonstrated by the results given in table 14. Agreements better than this were found in some cases; however, it was felt that results of species abundances should be quoted to at most four significant figures.

## 12.1 Comparison with the NASA code

The comparison with the NASA code is discussed first. For this comparison, calculations were performed by assuming the gaseous species to be perfect gases and the condensed species had zero molar volume. The four elements involved in the LOVA propellant were C, H, N, and O. The number of condensed species considered was small in comparison with that of the gaseous species. At equilibrium, only gaseous and no condensed species were present. The seven elements involved in the propellant with lead oxide were C, H, O, N, K, S, and Pb. The number of condensed species considered were much larger than that for the LOVA propellant. However, again, only gaseous species were present at equilibrium. The eight elements involved with the primer were B, C, F, H, K, Mg, N, and O. This was the system involving the largest number of elements; hence, the number of species considered were also the largest. Only two condensed species, liquid $MgF_2$ and solid MgO, were present at equilibrium. The black powder involved the six elements K, N, O, S, C, and H. Even though, the number of elements involved was one less than that of the propellant with lead oxide, the numbers of species considered in these two cases were very close. This is a result of the type of elements involved. At equilibrium, two condensed species were present, liquid $K_2CO_3$ and liquid $K_2S$, but in higher percentages than the two of the primer.

For the above four energetic materials, the NASA code obtained results without any difficulty, and so was the new code. The equilibrium temperatures and pressures obtained by using the two codes agreed to four significant figures. Even though the equilibrium temperatures of the product mixtures of the first three materials were roughly equal, the equilibrium pressures did decreased by fair percentages. This was due to a decrease in the predicted amount of gases present in the product mixtures.

The seven elements of the delay were Ba, Cr, O, K, Cl, Zr, and Ni. Although a fair number of elements were involved, for this combination of elements, the number of possible product species that could be selected was not large. The new code was able to consider all of them together, in particular all the twenty-nine condensed species, and determine that at equilibrium six condensed species were present. In the descending order of abundances, the six condensed species were: $BaO(s)$, $Cr_2O_3(s)$, $Ni(s,\alpha)$, $ZrO_2(s,\alpha)$, $KCl(s)$, and $BaCl_2(s,\alpha)$. (The phase designation $(s,\alpha)$ refers to the alpha-type solid of a substance.)

Even though the NASA code predicted the same equilibrium temperature and pressure given by the new code, the solution of the problem itself was not so straight forward. It was affected by factors such as whether condensed species were specified for consideration right from the beginning, the order these condensed species were specified and whether multiple loading densities were considered. It also required more iterations than normal. In addition, even if a solution was reached, singular matrices were often encountered. The delay problem makes a good test case because, first, there is a fair number of condensed species present at equilibrium, and second, many of the species, including one condensed species, are present in trace amounts. The consideration of these trace species help to illustrate some of the difficulties that may be encountered by the NASA code when solving a problem involving many condensed species.

Shown in tables 12, 13 and 15 to 17 are selected results of calculations of the delay problem obtained by using the NASA code for the loading density 0.2 gm/c.c., which include the number of matrix singularities encountered during the courses of iterations and the abundances of the trace species $BaCl_2(s,\alpha)$, $NiCl_2$, and $ClO$. The same equilibrium temperature and pressure and abundances of the remaining species other than these three species were determined by all the runs whose results are shown in these tables, and they are not listed.

The effects of the specification of condensed species to be considered from the start in order to achieve a solution are discussed first. Shown in tables 12 and 13 are selected results of calculations obtained by using the NASA code for the loading density 0.2 gm/c.c., with zero, four, five or six condensed species included in the descending order of their equilibrium abundances determined by the new code, for consideration right from the beginning. Results for the cases of one, two or three condensed species included, also in descending order of abundances, for consideration were not shown because they are the same as those for the case when no condensed species was included.

In addition, the inclusion of the condensed species according to the descending order of their equilibrium abundances as determined by the new code is entirely arbitrary. Also, equilibrium compositions are typically obtained in three to twelve iterations [1, p. 73] in the NASA code and the maximum allowable number of iterations had been set to fifty. However, the results in tables 12 and 13 were obtained by setting the maximum allowable number of iterations to be twenty thousands, an arbitrary chosen large number, because convergence was not achieved in the cases of four, five or six condensed species included for consideration when only a maximum of fifty iterations was allowed.

In the NASA code, for a problem involving condensed species and their possible presence at equilibrium, if no condensed species is specified for the initial consideration of a solution, the default is to seek a solution by first assuming the product mixture to be a mixture of perfect gases only. Upon achieving this first solution, condensed products are then tested for incorporation. However, there are occasions that when only a perfect-gas mixture is considered, a very low temperature is reached. For such cases, an error message will be printed by the code, calling for the inclusion of condensed species for the initial consideration. This was the case for the delay problem when no condensed species was included for consideration from the start as well as when one, two or three condensed species were included, in the descending order of their equilibrium abundances determined by the new code, when the maximum number of iterations was set to fifty. Thus, to sum up, when the maximum number of iterations was set to fifty, the inclusion of condensed species was called for when zero, one, two or three condensed species were included, and convergence was not achieved when four, five or all six condensed species predicted by the new code were included.

In order to see if convergence can be achieved, calculations were carried out by setting the maximum allowable number of iterations to be twenty thousands. Run-time floating-point errors were encountered and the jobs were aborted for the cases with no condensed species up to three condensed species included for consideration. A solution was first obtained when four condensed species were included. In this case, singularity of the iteration matrix was encountered three times and singularity of the derivative matrix was encountered once. The species $BaCl_2(s,\alpha)$, $NiCl_2$, and ClO were not predicted. Convergence was also achieved when five or six condensed species were included. Singularity of the coefficient matrix was encountered once in the former case and twice in the later. The species $BaCl_2(s,\alpha)$, $NiCl_2$, and ClO were predicted in trace amounts; however, the amount of $BaCl_2(s,\alpha)$ is different in the two cases, $1.285 \times 10^{-21}$ kg-mole/kg of product mixture in the former and $4.466 \times 10^{-21}$ kg-mole/kg of product mixture in the later. Also, longer CPU time, 2.93 sec versus 1.26 sec, was taken to reach a solution when only five condensed species were included.

Whenever iteration matrix singularity is encountered during the course of iteration, the NASA code may alter the elemental abundances slightly to circumvent the problem and carry on with the iteration. This slight change in elemental abundances may affect the prediction of trace species like $BaCl_2(s,\alpha)$, $NiCl_2$, and ClO and explain why these species were not predicted in the case when four condensed species were included for consideration and why the amounts of $BaCl_2(s,\alpha)$ were different when five or six condensed species were included, since iteration matrix singularity was encountered in all these three cases.

To give as examples of equilibrium species abundances determined, in table 14, the abundances determined for the case when five condensed species were included are listed along with those determined by the new code. Only seven of the twenty-seven gaseous species considered were above the cut-off limit. Agreement to four significant figures was found among all the species except $BaCl_2(s,\alpha)$; an amount of $4.498 \times 10^{-29}$ kg-mole/kg of product mixture was predicted by the new code as oppose to $1.285 \times 10^{-21}$ kg-mole/kg of product mixture quoted above. Since both these amounts are quite small, it is hard to say which value is better, except noting that iteration matrix singularity was encountered in the NASA run.

The results of the case with five condensed species included for consideration among the various cases tried were taken to be the accepted results for the delay problem, because this is the first case where a complete solution was obtained, in the sense that species like $BaCl_2(s,\alpha)$, $NiCl_2$, and ClO were predicted. Thus, the CPU time, 2.93 sec, listed in table 7 is that required for this case.

The order of the condensed species included for consideration also affected the calculation results. Listed in tables 15 and 16 are the results with five and six condensed species included respectively, but in orders different from the descending order of abundances determined by the new code. The first set of results shown in table 15 was obtained by interchanging the positions of the second and the fourth species, namely $Cr_2O_3$(s) and $ZrO_2$(s,$\alpha$). Iteration matrix singularity was encountered twice; and the presence of $BaCl_2$(s,$\alpha$), $NiCl_2$, and ClO were predicted, except that the amount of $BaCl_2$(s,$\alpha$) was different from that predicted when the descending order was followed which is shown in table 13. The second set of results shown in table 15 was obtained by interchanging the fourth and the last, which is the fifth, species that is $ZrO_2$(s,$\alpha$) and KCl(s). Iteration matrix singularity was encountered four times and none of $BaCl_2$(s,$\alpha$), $NiCl_2$, or ClO was predicted. The prediction of the amounts of $BaCl_2$(s,$\alpha$), $NiCl_2$, and ClO in both of these two cases may have been affected by remedial steps taken when singular matrices were encountered. Furthermore, the CPU time required to reach a solution in either case was considerably higher than that when the descending order was followed: 5.43 and 4.27 sec respectively compared to 2.93 sec.

In the case when six condensed species were included for consideration and with the second and the fourth species according to descending order of abundances interchanged, iteration matrix singularity was encountered four times and $BaCl_2$(s,$\alpha$), $NiCl_2$, and ClO were not predicted. On the other hand, when the fourth and the last, which is the sixth, species, $ZrO_2$(s,$\alpha$) and $BaCl_2$(s,$\alpha$), were interchanged, iteration matrix singularity was encountered once and the presence of $BaCl_2$(s,$\alpha$), $NiCl_2$, and ClO were predicted. However, the amount of $BaCl_2$(s,$\alpha$) was different from that predicted when the descending order was followed. The prediction of the amounts of $BaCl_2$(s,$\alpha$), $NiCl_2$, and ClO in both of these two cases may have also been affected by steps taken to rectify the singular iteration matrices encountered. The CPU time required to reach a solution in either case this time was not much higher than that when the descending order was followed: 1.54 and 1.56 sec respectively compared to 1.26 sec. Thus the effects of changing the order of the condensed species on CPU time in the case when five condensed species were included were greater than when six condensed species were included.

A comparison of the results given in tables 13, 15 and 16 indicates that interchanging the positions of the second and the fourth species had greater impact on the prediction of the abundances of $BaCl_2$(s,$\alpha$), $NiCl_2$, and ClO in the case when six condensed species were included than in the case when five were included. This being the case in the sense that in the former case the number of matrix singularities encountered increased from two to four and $BaCl_2$(s,$\alpha$), $NiCl_2$, and ClO were not predicted at all, while in the later case the number of matrix singularities encountered changed from one to two and $BaCl_2$(s,$\alpha$), $NiCl_2$, and ClO were predicted except that the amount of $BaCl_2$(s,$\alpha$) was different. However, the trend was reversed when the fourth and the last species were interchanged. Thus the effects of changing the order of the condensed species included for consideration on species abundances were not predictable.

Finally, calculation results were affected when multiple loading densities were considered. Two calculations were performed for which five condensed species in the first and six in the second were included in descending order of abundances for consideration, and in both calculations the loading densities 0.1, 0.2, and 0.3 gm/c.c. were considered consecutively. The results shown in table 17 are those for the loading density 0.2 gm/c.c.. For consistency of presentation, the results of the case when five condensed species were included were listed before those of the case when six condensed species were included. However, for the purpose of discussion, the later are described first.

When more than one loading density is specified for consideration, the results to the first loading density are used as the initial estimates to the second and the results of the second are used as the initial estimates to the third and so on. The specification of the loading densities to be considered in the order of 0.1, 0.2, and 0.3 gm/c.c. is simply solving the problem for 0.2 gm/c.c. by first solving the problem for 0.1 gm/c.c.. In the case when six condensed species were included for consideration, no matrix singularity was encountered for all the three loading densities considered and for loading density 0.2 gm/c.c. $BaCl_2(s,\alpha)$, $NiCl_2$, and ClO were all predicted. This is the only case presented so far for which no matrix singularity was encountered. The same trend was not observed when five condensed species were included for consideration. Iteration matrix singularity was encountered four times for loading density 0.1 gm/c.c. and once for loading density 0.2 gm/c.c.. For loading density 0.2 gm/c.c., $NiCl_2$ was predicted but not $BaCl_2(s,\alpha)$ and ClO. Thus for loading density 0.1 gm/c.c. the inclusion of six condensed species for consideration caused the minimization process to take a different path which are free from matrix singularities; and the same is true for loading density 0.2 gm/c.c., which can be taken as the combined result of considering six condensed species and by considering the loading density 0.1 gm/c.c. first.

Based on the results presented in tables 12 and 13, in particular the result that a complete solution was not achieved until the five most abundant condensed species were included, it was concluded that in general the solution of problems involving many condensed species present at equilibrium by the NASA code would be difficult, because generally speaking it is impossible to know which condensed species should be specified for consideration in advance. Based on the results presented in tables 15 and 16, it was concluded that abundances of trace species given by the NASA code are sensitive to the order condensed species are specified for consideration and may have been affected. It was also concluded that abundances of trace species given by the NASA code may be affected when multiple loading densities were considered, based on the results presented in table 17. Among the above three observations, the most significant one is the first one, because it is about a real difficulty of the NASA code. The second and the third observations are less important because the slight differences in the abundances of the trace species usually do not affect the overall results, such as equilibrium temperature and pressure, of a problem. Finally, the NASA code handles singular matrices quite well, it did not seem that matrix singularities affected the convergence of the program; condensed species handling procedure seems to have more influence on this. However, matrix singularities did seem to affect the abundances of trace species.

## 12.2 Comparison with the Bagheera code

For the comparison between the Bagheera code and the new code, calculations were performed by assuming the gaseous products forming an Amagat-type ideal mixture, with individual gases following a modified pressure-explicit truncated virial equation of state, and the condensed species to have constant molar volume.

The library of thermodynamic data of the Bagheera code is essentially that of the

NASA code but includes data for additional species. Thus the numbers of species selected for the test problems were slightly larger than those for the comparison with the NASA code, with the exception of the number of condensed species for the delay, which increased by seven from twenty-nine to thirty-six, a fair increment. It turned out that these additional condensed species had significant influence on the final results.

The solution of the first four test problems by using the Bagheera code and the new code was straight forward. The prediction results on the presence of condensed species were the same as those for the comparison between the NASA code and the new code. For the LOVA propellant and the propellant with lead oxide, which formed gaseous products only, the equilibrium temperatures and pressures agreed to four significant figures.

For the primer and the black powder, both of which formed two condensed species at equilibrium, there were slight differences in the results. For the former, there was difference in the equilibrium temperature; for the latter, differences were found both in the equilibrium temperature and pressure. This could be explained by the larger amount of condensed species present at equilibrium in the case of black powder. There were small differences in the amount of condensed species predicted by the the two codes. Because condensed species were present in larger amount in the case of black powder, the differences were also larger in this case. Changes in the amount of condensed species implied changes in the amount of gaseous species as well. The overall effect was greater differences in equilibrium temperatures and pressures.

In general equilibrium temperatures and pressures predicted by the Bagheera code were higher than those predicted by the NASA code. The differences can be accounted for mainly by the different models used for the gaseous products. Higher temperatures were predicted because internal energy contents of gases following the modified truncated virial equation of state used in the Bagheera code are lower than a perfect gas; thus for the same initial energy contents of the energetic materials, the product gases were heated to higher temperatures at equilibrium. Also, higher pressures were predicted because, first, the gases were modelled as real gases (following the modified virial equation of state) in the Bagheera code and, second, the mixture equilibrium temperatures were higher. The difference in pressures was the largest for the LOVA propellant and decreased in the order of the energetic materials, this is because the amount of gases in the product mixture was decreasing in that order.

For the final test case, the delay, the Bagheera code had difficulties in solving the problem; either convergence was not achieved for the basic perfect-gas solution within a specified maximum number of iterations, or matrix singularities were encountered. The same problems persisted even when, first, the maximum number of iterations was increased; second, the six condensed species (determined by the new code) known to be present at equilibrium were specified to be considered at the initial stage of the solution; and third, when all possible condensed product species selected from the library except these six were specified to be omitted from consideration, thus limiting the species to be considered by the program to only these six condensed species, together with other gaseous species selected from the library.

The new code solved the delay formulation without any difficulties. All the possible species selected from the library, gaseous and condensed, were considered together; no special consideration or omission of condensed species was required. The equilibrium temperature and pressure of the product mixture were determined to be 1067. K and 2.03 MPa, respectively, which were quite different from those determined for the comparison between the NASA code and the new code. This is because the library of the Bagheera code included data for additional condensed species. As a matter of fact, the six condensed species determined to be present at equilibrium were: $BaO(s)$, $NiCr_2O_4(s)$, $ZrO_2(s,\alpha)$, $K_2CrO_4(2)$, $BaCl_2(s,\alpha)$, and $Cr_2O_3(s)$, which were different from those stated above.

## 12.3 Comparison with the Blake code

When comparing the new code with the Blake code, calculations were performed by assuming the mixture of gaseous products to be nonideal and following the conventional truncated pressure-explicit virial equation of state. Also, the condensed products were assumed to have variable molar volume. The library of thermodynamic data of the Blake code is quite a bit smaller than those of the NASA and the Bagheera codes. This fact is reflected by the number of possible species that could be selected. The results of the two codes agreed to four significant figures, same as the comparison between the NASA code and the new code. For the primer and the black powder, even though both the Blake and the Bagheera codes used the virial equation of state, the agreement of results between the Blake code and the new code was better than that between the Bagheeera code and the new code. This is likely due to the necessary separate treatment of large number of gaseous species as a result of the Amagat-type ideality assumed in the Bagheera code, as oppose to treating the gases like a single gas because of the nonideality assumption used in the Blake code.

For the LOVA propellant, there were only a total of twenty-four gaseous species and one condensed species, graphite, that could be selected. They were within the limits of the numbers of gaseous and condensed species that could be considered and hence were all selected. The four most abundant gaseous species with independent molecular formulae, $CO$, $H_2$, $N_2$, and $H_2O$, based on the results of the NASA code were specified for consideration for finding the first set of components. For the propellant with lead oxide, product species were selected based on the results of the NASA code. Twenty-nine gaseous species, but no condensed species, were selected. These gaseous species turned out also to be the most abundant gaseous species that could be selected based on the results of the new code when all possible products were considered. The seven most abundant gaseous species with linearly independent molecular formulae were specified for finding the first set of components.

For the primer, the most abundant gaseous species selected based on the results of the NASA code did not agree with those selected based on the results of the new code. The differences occurred among those species whose abundances were close to the cut-off limit. The most abundant gaseous species selected were then based on the results of the new code. The two condensed constituents: $MgO\$$ and $MgF_2\$$ were selected for consideration because $MgO(s)$ and $MgF_2(l)$ were predicted to be present at equilibrium. In the Blake code, condensed constituents for which their condensed phases are postulated to exist at equilibrium are always chosen as components. And to aid the solution of the problem, these two condensed constituents, together with the six most abundant gaseous species which have linearly independant formulae among themselves and with respect to these two condensed constituents, were specified for consideration for finding the first set of components. The CPU time was longer when the eight most abundant gaseous species having linearly independant formulae were specified instead. Even with these specifications of possible components, solutions were obtained only when the least abundant, among the twenty-nine, gaseous species was excluded from the species list.

For the black powder, the most abundant twenty-nine gaseous species selected based on the results of the NASA code were same as those based on the new code. The two condensed constituents $K_2CO_3\$$ and $K_2S\$$ were specified for consideration for finding the first set of components, because $K_2CO_3(l)$ and $K_2S(l)$ were predicted to be present at equilibrium by the NASA code. The four most abundant gaseous species which have linearly independant formulae among themselves and with respect to the two condensed constituents, $CO_2$, CO, $N_2$, and $H_2O$, were also specified for consideration for finding components. Again, Blake took longer to obtain a solution when six gaseous species having linearly independant formulae, the above four plus $H_2S$ and K, were specified instead; and the least abundant gaseous species among the twenty-nine selected must be excluded from the species list before a solution was obtained in either case.

The gaseous species K, mentioned above, was not the most abundant gaseous species that could be specified as a possible component for expressing the formulae of product species containing potassium. The most abundant gaseous species for this purpose was KOH; K was the next most abundant gaseous species after KOH for this purpose. However, Blake was unable to find an acceptable set of components for carrying out computations, when KOH was used in the first place. Component sets were found with the replacement by K, but maximum numbers of iterations were exceeded and floating point errors encountered. A solution was not achieved until another gaseous species was excluded from consideration, as already mentioned.

After the checks on selection of species, for final comparision purposes, the new code was rerun using the same species as selected for the Blake code for each problem, as mentioned in the last section. The new code solved the above four problems without any difficulties. The library of Blake has no data for any chromium or nickel containing species, and it was not possible to use Blake to carry out the calculation for the delay. The most difficult case among the five test cases was the delay, as can be seen from the results of calculations of the NASA or the Bagheera code. However, even calculations for this test case was not performed, some of the difficulties associated with using Blake had become obvious from the results of calculations of the first four test cases.

As additional examples of these difficulties, some of the findings of the preliminary calculations of the black powder problem using Blake are noted here. At the beginning, this problem was solved for twenty-nine gaseous species and two condensed constituents. The seven least-abundant gaseous species, N, $C_2H_2$, $CH_2$, $C_2N_2$, $C_2H_4$, C, and $HNO_3$, and the three condensed constituents absent at equilibrium, C(s), KOH$\$$, and $K_2SO_4\$$, predicted by the NASA code were excluded. The three least-abundant gaseous species, in decending order of abundances, included for calculation were O, $CH_3$, and CN. When no species was specified for consideration for finding components, Blake did not succeed in finding an acceptable set.

The same situation arose when the six most abundant gaseous species according to the results of the NASA code, $CO_2$, CO, $N_2$, $H_2O$, $H_2S$, and KOH, were specified for consideration as components. The difficulty in finding an acceptable set of components was rectified when KOH was replaced by K, which was the next most abundant gaseous species that could be selected as a component, for expressing the molecular formulae of other product species containing potassium. However, convergence was not achieved. Finally when CN, the least abundant gaseous species among the twenty-nine in the species list, was excluded, then a solution was obtained.

In the last calculation the number of condensed constituents considered was kept to a minimum; only the two which were known to have one of their phases present at equilibrium were considered. The next calculation was performed with one more condensed constituent, $K_2SO_4\$$, included for consideration, while keeping everything else unchanged. There were twenty-eight gaseous species and three condensed constituents included for consideration. The two condensed constituents C(s) and $KOH\$$ were still excluded and the same six gaseous species, $CO_2$, CO, $N_2$, $H_2O$, $H_2S$, and K, specified for consideration as components which brought convergence in the last calculation were kept. In this case, convergence was not achieved at first, but when the least abundance gaseous species among the twenty-eight considered, $CH_3$, was excluded, solution to the problem was obtained.

A second calculation on further increasing the number of condensed constituents considered was performed. Of the two remaining condensed constituents, C(s) and $KOH\$$, which were excluded, C(s) was retained for consideration this time; and everything else was kept the same. No convergence was achieved. It was found that if $KOH\$$ was included instead of C(s), a set of acceptable components could not even be found. Once again when the least abundant gaseous species among the twenty-seven first considered, O, was excluded from consideration, convergence was achieved.

Based on the calculations discussed above, it seems that when consideration of condensed constituents is required, even though the maximum number of gaseous species that can be considered in the Blake code is twenty-nine, convergence is usually achieved for a smaller number. There also seems to be some limits on the number of constituents that can be considered. This can be seen when one more condensed constituent was included for consideration, then one more gaseous species had to be excluded to achieve convergence.

The results of a second set of calculations demonstrating the effects of different species lists on the equilibrium results are also described here. The first calculation in this set was performed by including nineteen of the thirty-six possible gasoues species. Most of the seventeen gaseous species excluded were species present in small amounts at equilibrium. When all condensed constituents were included and no possible components were specified, no acceptable components were found. When the condensed constituent $KOH\$$ was excluded and the six gaseous species CO, K, $CO_2$, $N_2$, $H_2O$, and SO, which were used by DREV for calculations on the present black powder formulation, were specified for consideration for finding an acceptable first set of components, a solution was found. The equilibrium temperature and pressure were determined to be 2163. K and 70.11 MPa, respectively, and only $K_2CO_3(l)$ and $K_2S(l)$ were predicted. These results differ slightly from the accepted final results of the black powder problem.

The second calculatioin in this set included more gaseous species, twenty-four, for consideration; however, a few of the twelve gaseous species excluded were present in fair amounts at equilibrium. When the condensed constituents considered and the possible components specified were kept the same, the equilibrium temperature and pressure were determined to be 2171. K and 70.22 MPa, respectively, but this time $K_2SO_4$(l) was predicted in addition to $K_2CO_3$(l) and $K_2S$(l). The results of this calculation is fairly different from the accepted final results of the black powder problem, because of the prediction of the presence of $K_2SO_4$(l).

For the third calculation in this set, the gaseous species excluded were those existing in the least amounts according to the NASA results. At the beginning, the seven least-abundant gaseous species were excluded, resulting in twenty-nine, the maximum number that Blake will consider, gaseous species being included. The condensed constituents considered and the possible components specified were kept the same. The only condensed constituent excluded was KOH$ and four condensed constituents were considered, of which C(s) and $K_2SO_4$$ should be absent at equilibrium. No convergence was achieved. Calculations were repeated, each time with the least-abundant gaseous species of the remaining list excluded. Convergence was achieved after three more gaseous species, O, $CH_3$, and CN, were excluded, which agreed with the results of the previous calculations on increasing the number of condensed constituents considered. No $K_2SO_4$(l) was predicted and the equilibrium temperature and pressure determined were 2167. K and 69.37 MPa, respectively. These results agree with the accepted final results of the black powder problem. Thus when there is no knowledge about the significant species present at equilibrium and species have to be excluded, because of limitation on the maximum number of species that can be considered, the results obtained can be incorrect, as can be seen based on the results of the first two calculations in this series, unless many trials are attempted.

# A Mathematical Formulae

In this appendix, additional important formulae used in the new computational code are presented. Making use of equations 45 and 28 (without using the subscript $i$ in equation 28), the fugacity coefficient of an imperfect pure gas following equation 45 and at the system temperature and pressure is given as

$$RT\ln\phi(T,P) = \frac{\beta_1}{\alpha_1}\ln(1+\alpha_1 P) - \frac{\beta_2}{\alpha_2}\ln(1+\alpha_2 P). \tag{A-1}$$

Because equation 50 is pressure explicit, the equation alternate to equation 31 but with $T$ and $V$, the total volume of a mixture, as the independent variables given as

$$RT\ln\phi_i(T,V,x) = \int_V^\infty \left[\left(\frac{\partial P}{\partial n_i}\right)_{T,V,n_{j\neq i}} - \frac{RT}{V}\right] \mathrm{d}V - RT\ln z_{\mathrm{mix}} \tag{A-2}$$

[11, p. 38] was used, to obtain the fugacity coefficient of the $i$th species in a nonideal mixture following equation 50. In the above equation, $n_i$ and $n_j$ are the number of moles of the $i$th and the *j*th speices in the mixture, and *j* can assume values from 1 to $N'$ except *i*. With the use of equations 51 and 52, the right hand side of equation A-2 can be integrated giving

$$RT \ln\phi_i(T, V, x) = \frac{2RT}{v}\sum_{j=1}^{N'} x_j B_{ij} + \frac{3RT}{2v^2} x_i^2 C_{iii} - RT \ln z_{\text{mix}}. \tag{A-3}$$

The molar internal energy of a perfect gas is a function of temperature only. Its values at different pressures in general is given by its value at the reference pressure of one unit, $u^0$, and

$$u^0 = h^0 - RT. \tag{A-4}$$

The molar internal energy of an imperfect pure gas following equation 45 can be obtained by using the general quation

$$u = \int_0^P \left[ v - T\left(\frac{\partial v}{\partial T}\right)_{p, n_{t_g}} \right] \mathrm{d}p - pv + h^0 \tag{A-5}$$

(cf. [11, p. 28]). Upon substituting equation 45 into the above equation and carrying out the mathematical manipulations then

$$\begin{aligned} u = {} & \frac{1}{\alpha_1}\ln(1+\alpha_1 P)(\beta_1 - T\beta_1') - \frac{1}{\alpha_2}\ln(1+\alpha_2 P)(\beta_2 - T\beta_2') \\ & + \frac{T\beta_1\alpha_1'}{\alpha_1^2}[\ln(1+\alpha_1 P) + \frac{1}{1+\alpha_1 P} - 1] \\ & - \frac{T\beta_2\alpha_2'}{\alpha_2^2}[\ln(1+\alpha_2 P) + \frac{1}{1+\alpha_2 P} - 1] \\ & - RT - \frac{\beta_1 P}{1+\alpha_1 P} + \frac{\beta_2 P}{1+\alpha_2 P} + h^0, \end{aligned} \tag{A-6}$$

where primed quantities are first derivatives of temperature.

The total internal energy of a nonideal mixture following equation 50, for which the rigid sphere model is used for evaluating the thrid virial coefficient, can be obtained by using the general quation

$$U = \int_V^\infty \left[ P - T\left(\frac{\partial P}{\partial T}\right)_{V, n_{t_g}} \right] \mathrm{d}V + \sum_{i=1}^{N'} n_i u_i^0 \tag{A-7}$$

[11, p. 38]. Upon substituting equation 50 into the above equation and carrying out the mathematical manipulations, and making use of equation A-4, then

$$U = -\frac{n_{t_g} R T^2 B'_{\text{mix}}}{v} + \sum_{i=1}^{N'} n_i h_i^0 - n_{t_g} RT, \tag{A-8}$$

where $B'_{\text{mix}}$ is the first derivative of $B_{\text{mix}}$ with respect to $T$ [25, p. 162, pp. 1114-1115]. The temperature derivative of $C_{\text{mix}}$ does not appear because $C_{\text{mix}}$ determined based the rigid sphere model is temperature independent.

# Nomenclature

## Alphanumeric

| | |
|---|---|
| $\mathbf{0}$ | the null vector |
| $a$ | number of atoms of an element in a species molecule,<br>coefficients of polynomials (equations 42 to 44) for fitting thermodynamic functions,<br>parameters for evaluating temperature dependent coefficients (equations 54 to 56) of empirical equation of state for condensed species |
| $\mathbf{a}$ | formula vector of a species |
| $A$ | molecular formula of a species,<br>temperature dependent coefficients of empirical equation of state (equation 53) for condensed species |
| $\mathbf{A}$ | formula matrix of a system |
| $b$ | total number of moles of an atomic element in a system,<br>coefficients of polynomials (equations 43 and 44) for fitting thermodynamic functions |
| $\mathbf{b}$ | elemental abundance vector of a system |
| $B$ | second virial coefficient |
| $c_p$ | molar heat capacity at constant pressure of a species |
| $C$ | rank of formula matrix $\mathbf{A}$,<br>third virial coefficient |
| $g$ | molar Gibbs function of a species |
| $G$ | total Gibbs function of a system |
| $\delta G$ | change in total Gibbs function of a system |
| $\Delta G$ | change of Gibbs function across a chemical reaction |
| $h$ | molar enthalpy of a species |
| $l$ | liquid phase of a substance |
| $\mathcal{L}$ | Lagrangian of a system |
| $M$ | number of atomic elements involved in a system |
| $n$ | number of moles of a species |
| $\mathbf{n}$ | species abundance vector of a system |
| $\delta\mathbf{n}$ | species abundance change vector of a system |
| $n_t$ | total number of moles of species in a multispecies phase |
| $n_{t_g}$ | total number of moles of gases in a mixture which comprises gases and pure condensates |

| | |
|---|---|
| $n_z$ | number of moles of inert gases in a gaseous mixture |
| $N$ | number of species in a system |
| $\mathbf{N}$ | stoichiometric matrix of a system |
| $N'$ | number of gaseous species in a system |
| $N''$ | number of condensed species in a system |
| $p$ | pressure,<br>partial pressure of a species |
| $P$ | system pressure |
| $\mathbf{Q}$ | a matrix whose elements are zeros except that $Q_{11}$ is equal to $-n_z$ |
| $R$ | maximum number of linearly independent chemical equations relating the species in a system,<br>universal gas constant |
| $s$ | molar entropy of a species, solid phase of a substance |
| $T$ | temperature,<br>system temperature |
| $T_t$ | trial equilibrium system temperature |
| $u_c$ | molar internal energy of a condensed species |
| $u_g$ | molar internal energy of a gaseous species |
| $U_c$ | internal energy of condensed products |
| $U_g$ | internal energy of gaseous products |
| $U_p$ | internal energy of products |
| $U_r$ | internal energy of reactants |
| $\Delta U$ | difference between internal energy of products and reactants $(U_p - U_r)$ |
| $v$ | molar volume |
| $\bar{v}$ | partial molar volume of a species |
| $V$ | volume of a gaseous mixture |
| $x$ | mole fraction of a species in a gaseous mixture |
| $\mathbf{x}$ | species mole fractions vector of a gaseous mixture |
| $z$ | compressibility factor |

## Greek

| | |
|---|---|
| $\alpha$ | phase designator,<br>parameter in modified virial equation of state (equation 45) |
| $\beta$ | phase designator,<br>parameter in modified virial equation of state (equation 45) |
| $\boldsymbol{\beta}$ | coefficient matrix of linearized equations of BNR algorithms |
| $\delta_{ij}$ | the Kronecker delta; $\delta_{ij} = 1$ if $i = j$, $\delta_{ij} = 0$ if $i \neq j$ |

| | |
|---|---|
| $\delta_k$ | a phase related parameter; $\delta_k = 1$ if the $k$th species is a gaseous species, $\delta_k = 0$ if the $k$th species is a condensed species |
| $\phi$ | fugacity coefficient |
| $\lambda$ | Lagrange multiplier |
| $\boldsymbol{\lambda}$ | Lagrange multipliers vector |
| $\Lambda$ | a diagonal matrix whose diagonal elements are $\{n_1, n_2, \ldots, n_{N'}\}$ |
| $\mu$ | chemical potential of a species |
| $\boldsymbol{\mu}$ | chemical potentials vector of species in a system |
| $\nu$ | stoichiometric coefficient |
| $\boldsymbol{\nu}$ | stoichiometric vector |
| $\pi$ | total number of phases in a system |
| $\xi$ | reaction extent parameter |
| $\boldsymbol{\xi}$ | reaction extent vector |
| $\delta\xi$ | change in reaction extent parameter |
| $\boldsymbol{\delta\xi}$ | reaction extent change vector |

## Subscripts

| | |
|---|---|
| $i$ | index for species and for chemical equations |
| $j$ | index for chemical equations and for species |
| $k$ | index for elements, for Lagrange multipliers and for species |
| $l$ | index for species |
| mix | mixture (gaseous) |

## Superscripts

| | |
|---|---|
| -1 | inverse of a scalar or of a matrix |
| 0 | standard quantity at reference presrue of one unit |
| $m$ | index of iteration steps |
| $T$ | transpose of a vector or of a matrix |
| $*$ | standard quantity at system pressure $P$ |
| ' | first derivative of temperature |

## References

[1] Gordon, S., and B. J. McBride, "Computer Program for Calculation of Complex Chemical Equilibrium Compositions, Rocket Performance, Incident and Reflected Shocks, and Chapman-Jouguet Detonations," Special Publication 273, National Aeronautics and Space Administration, Washington, D.C., 1971, (NASA SP-273).

[2] Lussier, L.-S., Research Scientist, Defence Research Establishment Valcartier (DREV), Courcelette, Quebec, Private Communications.

[3] Freedman, E., "Blake - A Thermodynamic Code Based on Tiger: User's Guide and Manual," Technical Report ARBRL-TR-02411, Ballistic Research Laboratory, US Army Armament Research and Development Command, 1982, (AD/A-121 259).

[4] Smith, W. R., and R. W. Missen, "What Is Chemical Stoichiometry," *Chemical Engineering Education*, Vol. 13, pp. 26–32, 1979.

[5] Smith, W. R., and R. W. Missen, *Chemical Reaction Equilibrium Analysis: Theory and Algorithms*, John Wiley and Sons, Inc., New York, 1982.

[6] Missen, R. W., and W. R. Smith, "A Question of Basic Chemical Literacy," *Journal of Chemical Education*, Vol. 66, pp. 217–218, 1989.

[7] Noble, B., *Applied Linear Algebra*, Prentice-Hall, Inc., Englewood Cliffs, New Jersey, 1969.

[8] Smith, W. R., and R. W. Missen, "Strategies for Solving the Chemical Equilibrium Problem and an Efficient Microcomputer-Based Algorithm," *The Canadian Journal of Chemical Engineering*, Vol. 66, pp. 591–598, 1988.

[9] Smith, W. R., "The Computation of Chemical Equilibria in Complex Systems," *Industrial & Engineering Chemistry, Fundamentals*, Vol. 19, No. 1, pp. 1–10, 1980.

[10] Denbigh, K., *The Principles of Chemical Equilibrium*, 4th edn., Cambridge University Press, Cambridge, 1981.

[11] Prausnitz, J. M., R. N. Lichtenthaler, and E. G. de Azevedo, *Molecular Thermodynamics of Fluid-Phase Equilibria*, 2nd edn., Prentice-Hall, Inc., Englewood Cliffs, New Jersey, 1986.

[12] Chase, M. W., Jr., C. A. Davis, J. R. Downey, Jr., D. J. Frurip, R. A. McDonald, and A. N. Syverud, "JANAF Thermochemical Tables, 3rd edn., Parts I and II," *Journal of Physical and Chemical Reference Data*, Vol. 14, Supplement No. 1, 1985.

[13] McBride, B. J., and S. Gordon, "Computer Program for Calculating and Fitting Thermodynamic Functions," Reference Publication 1271, National Aeronautics and Space Administration, Washington, D.C., 1992, (NASA RP-1271).

[14] McBride, B. J., and S. Gordon, "Fortran IV Program for Calculation of Thermodynamic Data," Technical Note D-4097, National Aeronautics and Space Administration, Washington, D.C., 1967, (NASA TN D-4097).

[15] Walsh, G. R., *Methods of Optimization*, John Wiley and Sons Ltd., New York, 1975.

[16] Zeleznik, F. J., and S. Gordon, "A General IBM 704 or 7090 Computer Program for Computation of Chemical Equilibrium Compositions, Rocket Performance, and Chapman-Jouguet Detonations," Technical Note D-1454, National Aeronautics and Space Administration, Washington, D.C., 1962, (NASA TN D-1454).

[17] Levine, H. B., "??? —— Check Out —— ???" *The Journal of Chemical Physics*, Vol. 36, pp. 3049–, 1962.

[18] Brinkley, S. R., Jr., "Calculation of the Equilibrium Composition of Systems of Many Constituents," *The Journal of Chemical Physics*, Vol. 15, No. 2, pp. 107–110, 1947.

[19] Huff, V. N., S. Gordon, and V. E. Morrell, "General Method and Thermodynamic Tables for Computation of Equilibrium Composition and Temperature of Chemical Reactions," NACA Report 1037, National Advisory Committee for Aeronautics, Washington, D.C., 1951.

[20] Gordon, S., F. J. Zeleznik, and V. N. Huff, "A General Method for Automatic Computation of Equilibrium Compositions and Theoretical Rocket Performance of Propellants," NASA Technical Note D-132, National Aeronautics and Space Administration, Washington, D.C., 1959, (NASA TN D-132).

[21] White, W. B., S. M. Johnson, and G. B. Dantzig, "Chemical Equilibrium in Complex Mixtures," *The Journal of Chemical Physics*, Vol. 28, No. 5, pp. 751–755, 1958.

[22] Zeleznik, F. J., and S. Gordon, "An Analytical Investigation of Three General Methods of Calculating Chemical-Equilibrium Compositions," Technical Note D-473, National Aeronautics and Space Administration, Washington, D.C., 1960, (NASA TN D-473).

[23] Anonymous, *JANAF Thermochemical Tables*, Dow Chemical Co., Midland, Michigan, Dec. 31, 1960 to Jun. 30, 1970.

[24] Anonymous, *JANAF Thermochemical Data*, Ser. A, Jun. 1963; Ser. B, Jan. 1964; Ser. C, Apr. 1965; Ser. D, Mar. 1966; Ser. E, Jan. 1967, Dow Chemical Co., Midland, Michigan.

[25] Hirschfelder, J. O., C. F. Curtiss, and R. B. Bird, *Molecular Theory of Gases and Liquids*, John Wiley and Sons, Inc., New York, 1954.

[26] Cowperthwaite, M., and W. H. Zwisler, "Theoretical and Mathematical Formulations for the Tiger Computer Program," Tiger Computer Program Documentation, Vol. 1, Stanford Research Institute, Menlo Park, California, 1974, (AD/A-002 791).

[27] Powell, E. G., G. Wilmot, L. Haar, and M. Klein, "Equations of State and Thermodynamic Data for Interior Ballistics Calculations," in H. Krier, and M. Summerfield, Eds., *Interior Ballistics of Guns*, Progress in Astronautics and Aeronautics, Vol. 66, American Institute of Astronautics and Aeronautics, Washington, D.C., 1979, pp. 325–348.

[28] Stull, D. R., and H. Prophet, Eds., *JANAF Thermochemical Tables*, 2nd edn., NSRDS-NBS 37, U.S. Department of Commerce, 1971.

[29] Villars, D. S., "A Method of Successive Approximations for Computing Combustion Equilibria on a High Speed Digital Computer," *The Journal of Physical Chemistry*, Vol. 63, No. 4, pp. 521–525, 1959.

[30] Villars, D. S., "Computation of Complicated Combustion Equilibria on a High-Speed Digital Computer," in G. S. Bahn, and E. E. Zukoski, Eds., *Kinetics, Equilibria and Performance of High Temperature Systems, Proceedings of the First Conference*, Los Angeles, 2-5 November, 1959, Western States Section, The Combustion Institute, Butterworths, London, 1960, pp. 141–151.

[31] Cruise, D. R., "Notes on the Rapid Computation of Chemical Equilibria," *The Journal of Physical Chemistry*, Vol. 68, No. 12, pp. 3797–3802, 1964.

[32] Smith, W. R., and R. W. Missen, "Calculating Complex Chemical Equilibria by an Improved Reaction-Adjustment Method," *The Canadian Journal of Chemical Engineering*, Vol. 46, pp. 269–272, 1968.

[33] Press, W. H., B. P. Flannery, S. A. Teukolsky, and W. T. Vetterling, *Numerical Recipes: the Art of Scientific Computing*, 1st edn., University of Cambridge, Cambridge, 1986.

[34] Conklin[illegible] J. A., *Chemistry of Pyrotechnics: Basic Principles and Theory*, Marcel Dekker[illegible]c., New York, 1985.

[35] Freedman, E., "Thermodynamic Properties of Military Gun Propellants," in L. Stiefel, Ed., *Gun Propulsion Technologies*, Progress in Astronautics and Aeronautic, Vol. 109, American Institute of Astronautics and Aeronautics, Washington, D.C., 1988, pp. 103–132.

[36] Wagman, D. D., W. H. Evans, V. B. Parker, R. H. Schumm, I. Halow, S. M. Bailey, K. L. Churney, and R. L. Nuttall, "The NBS Tables of Chemical Thermodynamic Properties: Slected Values for Inorganic and $C_1$ and $C_2$ Organic Substances in SI Units," *Journal of Physical and Chemical Reference Data*, Vol. 11, Supplement No. 2, 1982.

Table 1: Composition of the LOVA propellant used for code comparisons.

| ingredient | formula | enthalpy of formation at 298.15 K (cal/mole) | percentage by weight |
|---|---|---|---|
| 1,3,5-trinitrohexahydro-*s*-triazine (RDX) | $C_3H_6O_6N_6$ | 16760. | 76 |
| cellulose acetate butyrate (CAB) | $C_{4562}H_{6527}O_{2411}$ | −159400000. | 12 |
| (ATEC) | $C_{14}H_{22}O_8$ | −400000. | 7.6 |
| nitrocellulose, 12.6% of nitration (NC1260) | $C_{22027}H_{27718}O_{36345}N_{8994}$ | −619617000. | 4 |
| ethyl centralite (EC) | $C_{17}H_{20}O_1N_2$ | −35840. | 0.4 |

Table 2: Composition of the propellant with lead oxide used for code comparisons.

| ingredient | formula | enthalpy of formation at 298.15 K (cal/mole) | percentage by weight |
|---|---|---|---|
| nitrocellulose, 13.15% of nitration (NC1315) | $C_{6000}H_{7364}O_{10271}N_{2636}$ | −164650000. | 89.217 |
| amyl phthalate (AMYLPH) | $C_{18}H_{26}O_4$ | −220900. | 6.499 |
| potassium sulphate (KS) | $K_2S_1O_4$ | −342660. | 1.28 |
| ethyl centralite (EC) | $C_{17}H_{20}O_1N_2$ | −25100. | 1.231 |
| diphenylamine (DPA) | $C_{12}N_1H_{11}$ | 31070. | 0.985 |
| graphite (C) | $C_1$ | 0 | 0.591 |
| lead oxide (PBO) | $Pb_1O_1$ | −103500. | 0.197 |

Table 3: Composition of the primer used for code comparisons.

| ingredient | formula | enthalpy of formation at 298.15 K (cal/mole) | percentage by weight |
|---|---|---|---|
| potassium nitrate (KN) | $K_1N_1O_3$ | −117760. | 75 |
| magnesium carbonate | $Mg_1C_1O_3$ | −265700. | 10 |
| boron | $B_1$ | 0 | 8 |
| Viton A fluoroelastomer | $C_{11}F_{14}H_8$ | −737170. | 7 |

Table 4: Composition of the black powder used for code comparisons.

| ingredient | formula | enthalpy of formation at 298.15 K (cal/mole) | percentage by weight |
|---|---|---|---|
| potassium nitrate (KN) | $K_1N_1O_3$ | −117760. | 73.849 |
| susquehanna charcoal (SUSQ) | $C_{1221}H_{573}S_8N_4O_{100}$ | −4490000. | 15.746 |
| sulphur (S) | $S_1$ | 0 | 9.966 |
| liquid water (H2O) | $H_2O_1$ | −68315. | 0.299 |
| ash (potassium carbonate) (ASH) | $K_2C_1O_3$ | −274900. | 0.14 |

Table 5: Composition of the delay used for code comparisons.

| ingredient | formula | enthalpy of formation at 298.15 K (cal/mole) | percentage by weight |
|---|---|---|---|
| barium chromate | $Ba_1Cr_1O_4$ | −342200. | 80 |
| zirconium | $Zr_1$ | 0 | 8.5 |
| nickel | $Ni_1$ | 0 | 8.5 |
| potassium perchlorate | $K_1Cl_1O_4$ | −102800. | 3 |

Table 6: Comparison of the equilibrium temperature and pressure, $T$ and $P$, values of combustion products determined by using the NASA code and the new code, for five sample energetic materials at loading density of 0.2 gm/c.c..

| energetic material | mixture properties | NASA code | new code |
|---|---|---|---|
| LOVA propellant<br>($4^{\bullet}$, $133^{*}$, $7^{\dagger}$)<br>($0^{\bullet\bullet}$, $0\%^{**}$, $0\%^{\dagger\dagger}$) | $T$ (K)<br>$P$ (MPa) | 2551.<br>204.0 | 2551.<br>204.0 |
| propellant with lead oxide<br>(7, 160, 38)<br>(0, 0%, 0%) | $T$ (K)<br>$P$ (MPa) | 2421.<br>178.6 | 2421.<br>178.6 |
| primer<br>(8, 214, 37)<br>(2, 6.3%, 6.4%) | $T$ (K)<br>$P$ (MPa) | 2538.<br>73.37 | 2538.<br>73.37 |
| black powder (igniter)<br>(6, 156, 29)<br>(2, 17.9%, 45.1%) | $T$ (K)<br>$P$ (MPa) | 2153.<br>58.61 | 2153.<br>58.61 |
| delay, fuse<br>(7, 27, 29)<br>(6, 79.7%, 94.0%) | $T$ (K)<br>$P$ (MPa) | 361.1<br>1.12 | 361.1<br>1.12 |

$^{\bullet}$ number of elements involved in system
$^{*}$ number of gaseous species considered
$^{\dagger}$ number of condensed species considered
$^{\bullet\bullet}$ number of condensed species present at equilibrium
$^{**}$ percentage by mole of condensates in mixture
$^{\dagger\dagger}$ percentage by weight of condensates in mixture

Table 7: Comparison of CPU times required for determining chemical equilibrium compositions by using the NASA code and the new code, for five sample energetic materials at loading density of 0.2 gm/c.c..

| energetic material | CPU time, NASA code (sec) | CPU time, new code (sec) | CPU time ratio (new code to NASA code) |
|---|---|---|---|
| LOVA propellant | 0.29 | 1.67<br>(2300 K - 2700 K)[†] | 5.8 |
| propellant with lead oxide | 0.46 | 3.91<br>(2300 K - 2700 K) | 8.5 |
| primer | 1.32 | 9.97<br>(2300 K - 2700 K) | 7.6 |
| black powder (igniter) | 1.09 | 19.12<br>(2300 K - 2700 K) | 17.5 |
| | | 8.80<br>(2000 K - 2400 K) | 8.1 |
| delay, fuse | 2.93 | 2.55<br>(2300 K - 2700 K) | 0.9 |
| | | 2.19<br>(300 K - 500 K) | 0.7 |

[†] Initial bracket of temperature of combustion products at equilibrium in degrees Kelvin.

Table 8: Comparison of the equilibrium temperature and pressure, $T$ and $P$, values of combustion products determined by using the Bagheera code and the new code, for five sample energetic materials at loading density of 0.2 g-m/c.c..

| energetic material | mixture properties | Bagheera code | new code |
|---|---|---|---|
| LOVA propellant | $T$ (K) | 2561. | 2561. |
| (4, 136, 7) | $P$ (MPa) | 265.8 | 265.8 |
| (0, 0%, 0%) | | | |
| propellant with | $T$ (K) | 2434. | 2434. |
| lead oxide | $P$ (MPa) | 230.0 | 230.0 |
| (7, 165, 44) | | | |
| (0, 0%, 0%) | | | |
| primer | $T$ (K) | 2547. | 2547. |
| (8, 219, 39) | $P$ (MPa) | 82.60 | 82.60 |
| (2, 6.3%, 6.5%) | | | |
| black powder (igniter) | $T$ (K) | 2169. | 2170. |
| (6, 161, 32) | $P$ (MPa) | 67.82 | 67.79 |
| (2, 18.2%, 45.9%) | | | |
| delay, fuse | $T$ (K) | — | 1039. |
| (7, 29, 36) | $P$ (MPa) | — | 1.97 |
| (6, 84.3%, 96.6%) | | | |

Table 9: Comparison of CPU times required for determining chemical equilibrium compositions by using the Bagheera code and the new code, for five sample energetic materials at loading density of 0.2 gm/c.c..

| energetic material | CPU time, Bagheera code (sec) | CPU time, new code (sec) | CPU time ratio (new code to Bagheera code) |
|---|---|---|---|
| LOVA propellant | 0.89 | 4.01<br>(2300 K - 2700 K) | 4.5 |
| propellant with lead oxide | 1.26 | 6.18<br>(2300 K - 2700 K) | 4.9 |
| primer | 3.28 | 11.10<br>(2300 K - 2700 K) | 3.4 |
| black powder (igniter) | 1.86 | 22.20<br>(2300 K - 2700 K) | 11.9 |
|  |  | 10.52<br>(2000 K - 2400 K) | 5.7 |
| delay, fuse | — | 1.31<br>(2300 K - 2700 K) | — |
|  |  | 0.68<br>(800 K - 1200 K) | — |

Table 10: Comparison of the equilibrium temperature and pressure, $T$ and $P$, values of combustion products determined by using the Blake code and the new code, for four sample energetic materials at loading density of 0.2 gm/c.c..

| energetic material | mixture properties | Blake code | new code |
|---|---|---|---|
| LOVA propellant<br>(4, 24, 1)<br>(0, 0%, 0%) | $T$ (K)<br>$P$ (MPa) | 2563.<br>257.0 | 2563.<br>257.0 |
| propellant with lead oxide<br>(7, 29, 0)<br>(0, 0%, 0%) | $T$ (K)<br>$P$ (MPa) | 2433.<br>222.5 | 2433.<br>222.5 |
| primer<br>(8, 28, 2)<br>(2, 6.3%, 6.9%) | $T$ (K)<br>$P$ (MPa) | 2564.<br>81.41 | 2564.<br>81.41 |
| black powder (igniter)<br>(6, 28, 4)<br>(2, 18.1%, 45.7%) | $T$ (K)<br>$P$ (MPa) | 2167.<br>69.37 | 2167.<br>69.37 |

Table 11: Comparison of CPU times required for determining chemical equilibrium compositions by using the Blake code and the new code, for four sample energetic materials at loading density of 0.2 gm/c.c..

| energetic material | CPU time, Blake code (sec) | CPU time, new code (sec) | CPU time ratio (new code to Blake code) |
|---|---|---|---|
| LOVA propellant | 2.37 | 1.35<br>(2300 K - 2700 K) | 0.6 |
| propellant with lead oxide | 4.87 | 1.99<br>(2300 K - 2700 K) | 0.4 |
| primer | 6.78 | 3.44<br>(2300 K - 2700 K) | 0.5 |
| black powder (igniter) | 12.37 | 5.82<br>(2300 K - 2700 K) | 0.5 |
| | | 5.10<br>(2000 K - 2400 K) | 0.4 |

Table 12: Selected results of calculation of the delay formulation obtained by using the NASA code with zero or four condensed species included, in the decending order of their equilibrium abundances determined by the new code, for consideration right from the beginning.

| condensed species included | none | BaO(s), $Cr_2O_3$(s)<br>Ni(s,$\alpha$), $ZrO_2$(s,$\alpha$) |
|---|---|---|
| loading density considered (gm/c.c.) | 0.2 | 0.2 |
| number of coefficient matrix singularities encountered | none | three |
| number of derivative matrix singularities encountered | none | one |
| abundance of $BaCl_2$(s,$\alpha$) (kg-mole/kg of product mixture) | floating exception | not predicted (zero) |
| abundances of $NiCl_2$, ClO (kg-mole/kg of product mixture) | floating exception | not predicted (zero) |

Table 13: Selected results of calculation and the CPU time required for determining the equilibrium composition of the delay by using the NASA code with five or six condensed species included, in the decending order of their equilibrium abundances determined by the new code, for consideration right from the beginning.

| condensed species included | $BaO(s)$, $Cr_2O_3(s)$ $Ni(s,\alpha)$, $ZrO_2(s,\alpha)$ $KCl(s)$ | $BaO(s)$, $Cr_2O_3(s)$ $Ni(s,\alpha)$, $ZrO_2(s,\alpha)$ $KCl(s)$, $BaCl_2(s,\alpha)$ |
|---|---|---|
| loading density considered (gm/c.c.) | 0.2 | 0.2 |
| number of coefficient matrix singularities encountered | one | two |
| number of derivative matrix singularities encountered | none | none |
| CPU time required (sec) | $2.93 \pm 0.01$ | $1.26 \pm 0.01$ |
| abundance of $BaCl_2(s,\alpha)$ (kg-mole/kg of product mixture) | $1.285 \times 10^{-21}$ | $4.466 \times 10^{-21}$ |
| abundances of $NiCl_2$, $ClO$ (kg-mole/kg of product mixture) | $1.914 \times 10^{-32}$<br>$2.326 \times 10^{-38}$ | $1.914 \times 10^{-32}$<br>$2.326 \times 10^{-38}$ |

Table 14: Comparison of equilibrium species abundances of the delay at the loading density of 0.2 gm/c.c. determined by using the NASA code and the new code, with results of the NASA code obtained by including the five most abundant condensed species determined by the new code in decending order of abundances for consideration right from the beginning.

| product species | NASA code (kg-mole/kg of product mixture) | new code (kg-mole/kg of product mixture) |
|---|---|---|
| $O_2$ | $1.870 \times 10^{-3}$ | $1.870 \times 10^{-3}$ |
| $O_3$ | $3.695 \times 10^{-27}$ | $3.695 \times 10^{-27}$ |
| KCl | $1.870 \times 10^{-28}$ | $1.870 \times 10^{-28}$ |
| $K_2Cl_2$ | $1.042 \times 10^{-31}$ | $1.042 \times 10^{-31}$ |
| $NiCl_2$ | $1.914 \times 10^{-32}$ | $1.914 \times 10^{-32}$ |
| O | $5.828 \times 10^{-37}$ | $5.828 \times 10^{-37}$ |
| ClO | $2.326 \times 10^{-38}$ | $2.326 \times 10^{-38}$ |
| BaO(s) | $3.158 \times 10^{-3}$ | $3.158 \times 10^{-3}$ |
| $Cr_2O_3$(s) | $1.579 \times 10^{-3}$ | $1.579 \times 10^{-3}$ |
| Ni(s,$\alpha$) | $1.448 \times 10^{-3}$ | $1.448 \times 10^{-3}$ |
| $ZrO_2$(s,$\alpha$) | $9.318 \times 10^{-4}$ | $9.318 \times 10^{-4}$ |
| KCl(s) | $2.165 \times 10^{-4}$ | $2.165 \times 10^{-4}$ |
| $BaCl_2$(s,$\alpha$) | $1.285 \times 10^{-21}$ | $4.498 \times 10^{-29}$ |

Table 15: Selected results of calculations and the CPU times required for determining the equilibrium compositions of the delay by using the NASA code with five condensed species included, in orders modified from the decending order of their equilibrium abundances determined by the new code, for consideration right from the beginning.

| condensed species included | $BaO(s)$, $ZrO_2(s,\alpha)$<br>$Ni(s,\alpha)$, $Cr_2O_3(s)$<br>$KCl(s)$ | $BaO(s)$, $Cr_2O_3(s)$<br>$Ni(s,\alpha)$, $KCl(s)$<br>$ZrO_2(s,\alpha)$ |
|---|---|---|
| loading density considered (gm/c.c.) | 0.2 | 0.2 |
| number of coefficient matrix singularities encountered | two | four |
| number of derivative matrix singularities encountered | none | none |
| CPU time required (sec) | 5.43 ± 0.01 | 4.27 ± 0.01 |
| abundance of $BaCl_2(s,\alpha)$ (kg-mole/kg of product mixture) | $4.347 \times 10^{-21}$ | not predicted (zero) |
| abundances of $NiCl_2$, $ClO$ (kg-mole/kg of product mixture) | $1.914 \times 10^{-32}$<br>$2.326 \times 10^{-38}$ | not predicted (zero) |

Table 16: Selected results of calculations and the CPU times required for determining the equilibrium compositions of the delay by using the NASA code with six condensed species included, in orders modified from the decending order of their equilibrium abundances determined by the new code, for consideration right from the beginning.

| condensed species included | $BaO(s)$, $ZrO_2(s,\alpha)$<br>$Ni(s,\alpha)$, $Cr_2O_3(s)$<br>$KCl(s)$, $BaCl_2(s,\alpha)$ | $BaO(s)$, $Cr_2O_3(s)$<br>$Ni(s,\alpha)$, $BaCl_2(s,\alpha)$<br>$KCl(s)$, $ZrO_2(s,\alpha)$ |
|---|---|---|
| loading density considered (gm/c.c.) | 0.2 | 0.2 |
| number of coefficient matrix singularities encountered | four | one |
| number of derivative matrix singularities encountered | none | none |
| CPU time required (sec) | $1.54 \pm 0.01$ | $1.56 \pm 0.01$ |
| abundance of $BaCl_2(s,\alpha)$ (kg-mole/kg of product mixture) | not predicted (zero) | $1.193 \times 10^{-22}$ |
| abundances of $NiCl_2$, $ClO$ (kg-mole/kg of product mixture) | not predicted (zero) | $1.914 \times 10^{-32}$<br>$2.326 \times 10^{-38}$ |

Table 17: Selected results of calculation of the delay for the loading density 0.2 gm/c.c., obtained by using the NASA code when the loading densities 0.1, 0.2, and 0.3 gm/c.c. were considered sequentially in that order in a single run and with five or six condensed species included, in the decending order of their equilibrium abundances determined by the new code, for consideration right from the beginning.

| condensed species included | $BaO(s)$, $Cr_2O_3(s)$<br>$Ni(s,\alpha)$, $ZrO_2(s,\alpha)$<br>$KCl(s)$ | $BaO(s)$, $Cr_2O_3(s)$<br>$Ni(s,\alpha)$, $ZrO_2(s,\alpha)$<br>$KCl(s)$, $BaCl_2(s,\alpha)$ |
|---|---|---|
| loading densities considered (gm/c.c.) | 0.1, 0.2, 0.3 | 0.1, 0.2, 0.3 |
| number of coefficient matrix singularities encountered | one | none |
| number of derivative matrix singularities encountered | none | none |
| abundance of $BaCl_2(s,\alpha)$ (kg-mole/kg of product mixture) | not predicted (zero) | $1.324 \times 10^{-23}$ |
| abundances of $NiCl_2$, $ClO$ (kg-mole/kg of product mixture) | $7.040 \times 10^{-33}$<br>not predicted (zero) | $1.914 \times 10^{-32}$<br>$2.326 \times 10^{-38}$ |

# APPENDIX 3

# NUMERICAL MODEL FOR GAS AND PARTICLE MOTIONS IN A CLOSED VESSEL

by

**Grant W. C. Tisdall**

# A Numerical Model of Reactive Gas-Particulate Complex Turbulent Flow in a Constant Volume Vessel

by

**Grant W.C. Tisdall**

**Department of Aerospace Science and Engineering**

**A Thesis submitted in conformity with the requirements for the**
**Degree of Master of Applied Science in the**
**University of Toronto**

# Abstract

This report is concerned with improving granular propellant burn rate laws. Basic attributes of constant volume vessels containing burning propellant are presented. The vessel's physical phenomena and flowfield characteristics are discussed and non-ideal phenomena highlighted. A review of current gas-particulate models is given and a new gas-particulate model, compatible with compressible turbulent flow, is proposed. The model includes non-ideal effects of wall convective heat transfer and turbulent diffusion of propellant grains. Discussions are given of: 1) various required constitutive laws; 2) state dependent property equations and 3) convective wall heat transfer, which is used to select an appropriate Nusselt correlation. A review of common turbulence models is presented and an appropriate model is chosen based on vessel flow characteristics.

# Acknowledgments

I would like to expressly thank my supervisor Prof. J.J. Gottlieb, who provided guidance and insight into this research. His unlimited understanding over the past few months and his willingness to give substantial flexibility and leeway in the preparation time of this report is gratefully appreciated.

I wish to particularly thank Cathleen for her unconscious influence which prompted me to continue on in Graduate studies after Waterloo and for her continued support throughout this past year.

I would also like to acknowledge the much appreciated financial support obtained from Defense Research Establishment Valcartier, Courcelette, Quebec.

# Nomenclature

## Alpha-Numeric Symbols

| | |
|---|---|
| $a(\varepsilon)$ | rate of propagation of $R$ in solid phase [m/s] |
| $a_t$ | experimentally measured propagation rate [m/s] |
| $a, b$ | Van der Waals equation constants |
| $c$ | specific heat [J/kg·K] |
| $\dot{d}$ | rate of grain surface regression due to combustion [m/s] |
| $e$ | internal energy [J/kg] |
| $f$ | velocity dependent interphase drag [N/m$^3$] |
| $g$ | gravity [m/s$^2$] |
| $g_o$ | unit constant |
| $h$ | heat transfer coefficient [kg/K·s] |
| $k$ | turbulent kinetic energy [m$^2$/s$^2$] |
| $k$ | thermal conductivity [N/K·s] |
| $l_m$ | turbulent mixing length [m] |
| $\dot{m}$ | mass flow rate of propellant gas [kg/s] |
| $m, n$ | Nusselt correlation constants |
| $q$ | heat transfer flux [J/m$^2$·s] |
| $t$ | time [s] |
| $u$ | instantaneous longitudinal velocity component [m/s] |
| $v$ | instantaneous transverse velocity component [m/s] |
| $w$ | instantaneous tangential velocity component [m/s] |
| $\overline{u}$ | time averaged mean longitudinal velocity component [m/s] |
| $\overline{v}$ | time averaged mean transverse velocity component [m/s] |
| $\overline{w}$ | time averaged mean tangential velocity component [m/s] |
| $\tilde{u}$ | mass averaged mean longitudinal velocity component [m/s] |
| $\tilde{v}$ | mass averaged mean transverse velocity component [m/s] |
| $\tilde{w}$ | mass averaged mean tangential velocity component [m/s] |
| $z, r, \theta$ | longitudinal, transverse and tangential cylindrical coordinates |
| $A$ | surface area [m$^2$] |
| $C$ | turbulence model constant |
| $C$ | total CVV propellant charge weight [kg] |
| $D$ | diameter [m] |
| $H$ | arbitrary parameter |
| $L$ | length [m] |
| $M$ | total mass of phase [kg] or [kg·mole] |
| $N$ | number of perforations in a propellant grain |
| Nu | Nusselt number |
| $P$ | ambient pressure [MPa] |
| Pe | Pecklet number |
| Pr | Prandtl number |
| $\mathrm{Pr}_{t\infty}$ | turbulent Prandtl number model constant |
| $Q$ | total heat transfer [J] |

| | |
|---|---|
| $Q, R, S$ | functions in algebraic stress model |
| $R$ | intergranular stress [N/m$^2$] |
| $R$ | radius of curvature [m] |
| Re | Reynolds number |
| $S_p$ | total surface area of solid phase in control volume [m$^2$] |
| $T$ | temperature [K] |
| $U$ | instantaneous gas phase velocity [m/s] |
| $V$ | volume [m$^3$] |
| $V_p$ | total volume of solid phase in control volume [m$^3$] |
| $Z(t)$ | fraction of propellant consumed at time $t$ |

## Greek Symbols

| | |
|---|---|
| $\alpha$ | thermal diffusivity [m/s$^2$] |
| $\beta$ | burn rate coefficient |
| $\delta$ | channel half width [m] |
| $\delta$ | Kronecker delta |
| $\eta$ | gas covolume [m$^3$/kg] |
| $\varepsilon$ | porosity |
| $\varepsilon_0$ | settling porosity |
| $\varepsilon_1$ | porosity above which grain bed is completely fluidized |
| $\varepsilon_2$ | porosity above which $a(\varepsilon)$ is zero |
| $\gamma$ | ratio of specific heats |
| $\kappa$ | stress attenuation factor |
| $\mu$ | viscosity [N-s/m$^2$] |
| $\nu$ | kinematic viscosity [m$^2$/s] |
| $\psi$ | igniter gas mass flow rate [kg/s] |
| $\psi(P)$ | coefficient function of pressure |
| $\Re$ | universal gas constant [J/mole·K] |
| $\rho$ | density [kg/m$^3$] |
| $\sigma$ | shear or normal stress on a fluid particle [N/m$^2$] |
| $\sigma$ | constant effective Prandtl-Schmidt number |
| $\Sigma$ | solid-gas interface |
| $\theta$ | correction functions in $\epsilon$ equation |
| $\xi$ | inverse viscosity [m$^2$/N·s] |
| $\epsilon$ | dissipation rate of turbulent kinetic energy [m$^2$/s$^3$] |

## Superscripts

| | |
|---|---|
| $exp$ | experimental |
| $th$ | theoretical |
| $tot$ | total |
| $'$ | Reynolds averaged fluctuation |
| $''$ | Favre averaged fluctuation |

## Subscripts

| | |
|---|---|
| $c$ | critical |
| $cell$ | grid cell |
| $ch$ | chamber |
| $conv$ | convective |
| $e$ | free stream |
| $\varepsilon_1, \varepsilon_2$ | represents constants in $\epsilon$ equation |
| $f$ | fluid |
| $g$ | gas |
| $gr$ | grain |
| $ig$ | ignition solid or gas |
| $i, j, k$ | cylindrical tensor indicies |
| $l$ | local |
| $max$ | maximum |
| $\mu$ | specific constants or turbulence correction functions |
| $o$ | initial |
| $p$ | solid phase or constant pressure |
| $prop$ | propellant solid or gas |
| $s$ | surface |
| $t$ | turbulent |
| $tot$ | total |
| $v$ | constant volume |
| $w$ | wall |
| $wt$ | molecular weight |
| $1, 2$ | represents specific constants or turbulence correction functions |

# Contents

1 Introduction 1
- 1.1 The Constant Volume Vessel . . . . . 1
- 1.2 Vessel Convective Heat Transfer . . . . . 1
- 1.3 Goals and Objectives . . . . . 2

2 Constant Volume Vessel 3
- 2.1 The Vessel Experiment . . . . . 3
- 2.2 Granular Propellant . . . . . 5

3 Flow Characteristics 7
- 3.1 Isotropy . . . . . 7
- 3.2 Separation and Recirculation . . . . . 8
- 3.3 Curvature . . . . . 11
- 3.4 Heat Transfer . . . . . 13
- 3.5 Compressibility . . . . . 15
- 3.6 Two-Phase Flow . . . . . 15

4 Two-Phase Mathematical Modeling 17
- 4.1 Two-Phase Flow . . . . . 17
- 4.2 CVV Conservation Equations . . . . . 19

5 Constitutive Laws 23
- 5.1 Interphase Heat Transfer . . . . . 23
- 5.2 Propellant Burn Rate . . . . . 24
- 5.3 Interphase Drag . . . . . 26
- 5.4 Intergranular Stress . . . . . 27
- 5.5 Equation of State . . . . . 28
- 5.6 State-Dependent Property Variation . . . . . 29
- 5.7 Grain Form Functions . . . . . 31

6 Turbulent Heat Transfer 33
- 6.1 Convective . . . . . 33
- 6.2 Conductive . . . . . 35

7 Turbulence Modeling 37
- 7.1 Gas Phase . . . . . 37
  - 7.1.1 Zero Equation Model . . . . . 38
  - 7.1.2 One Equation Model . . . . . 39
  - 7.1.3 Two Equation Model . . . . . 40
  - 7.1.4 Reynolds Stress Model . . . . . 42

7.1.5 Algebraic Stress Model . . . . . . . . . . . . . . . . . . . . . . . . . 43
7.1.6 Energy Fluctuation . . . . . . . . . . . . . . . . . . . . . . . . . . . 44
7.2 Solid Phase . . . . . . . . . . . . . . . . . . . . . . . . . . . . . . . . 44
7.3 CVV Turbulence Model . . . . . . . . . . . . . . . . . . . . . . . . . . 45

**8 Future Work** **48**

**A Governing Equations** **54**
A.1 Conservation of Mass for the Gas Phase . . . . . . . . . . . . . . . . 55
A.2 Conservation of Mass for the Solid Phase . . . . . . . . . . . . . . . 56
A.3 Conservation of Momentum for the Gas Phase . . . . . . . . . . . . . 58
A.4 Conservation of Momentum for the Solid Phase . . . . . . . . . . . . 61
A.5 Conservation of Energy for the Gas Phase . . . . . . . . . . . . . . . 62

**B Favre-Reynolds Decomposition** **67**
B.1 Conservation of Mass for the Gas Phase . . . . . . . . . . . . . . . . 68
B.2 Conservation of Mass for the Solid Phase . . . . . . . . . . . . . . . 68
B.3 Conservation of Momentum for the Gas Phase . . . . . . . . . . . . . 69
B.4 Conservation of Momentum - Solid Phase . . . . . . . . . . . . . . . . 70
B.5 Conservation of Energy for the Gas Phase . . . . . . . . . . . . . . . 71

**C CVV Turbulence Model Equations** **74**
C.1 Kinetic Energy Equation . . . . . . . . . . . . . . . . . . . . . . . . . 74

**D Viscosity Relation** **79**

# 1 Introduction

## 1.1 The Constant Volume Vessel

The essential design elements of any ballistic model are the rate of consumption (burn rate), maximum generated peak pressure of a particular propellant and the muzzle velocity of the projectile. Some of this information is usually obtained through a constant volume vessel (CVV), which is used as an experimental tool to record the pressure verses time data created by the combustion cycles of different granular propellant grains.

It is important, for any modeling effort, to understand the basic phenomena that occurs. The principal events that occur during the transient, turbulent combustion cycle of a CVV (approximately 5–20 ms) are as follows: 1) primer ignition (usually black powder) which vents hot gas into the quiescent propellant bed, 2) ignition of the nearest propellant grains through convective heating, 3) creation of localized high pressure regions by the generation of combustion gases, 4) the initiation of a flowfield by the movement and compaction of the individual grains and 5) acceleration of a flame (or ignition) front through the propellant bed. It must be recognized that inherently included in this combustion cycle are the non-ideal effects of dynamic burning due to extreme pressures and rapid pressure increases, non uniform ignition of propellant grains, expansion of the vessel walls (usually negligible) and time dependent energy losses in the form of heat transfer to the vessel walls.

The CVV pressure data can also be used to determine an optimum propellant by calculating "Quickness" values,[1] where optimum is defined as the largest "Quickness" value. Note that, due to the above mentioned non-ideal effects, it impossible to compare the "Quickness" of different propellants on an absolute basis (they are only compared on a relative scale) and the theoretical maximum pressure of a propellant is not equal to its experimental value.

## 1.2 Vessel Convective Heat Transfer

Of all the non-ideal effects occuring in the combustion cycle of a CVV, convective wall heat transfer is the easiest to quantify. The following is a description of the present common technique used to model CVV convective wall heat transfer.

In the past, CVV heat transfer calculations have been performed on a simplistic level. The total heat transfer of the combustion cycle was deemed proportional to the difference in maximum theoretical and experimental pressures ($Q^{tot} \propto P^{th}_{max} - P^{exp}_{max}$) and the heat transfer rate proportional to total heat transfer and the time derivative of pressure ($q_w \propto Q^{tot}\partial P/\partial t$) [ROBBINS 76]. This type of analysis is not accurate and gives only an approximate result since energy losses due to vessel wall expansion and $P^{exp}_{max}$ measurement error are implicitly (and mistakenly) included in the constants of the above mentioned $Q^{tot}$ expression, which in turn makes the $q_w$ expression an even further approximation. Also $q_w$ is calculated in the above expression as a lumped parameter, which does not allow for the determination of variation in $q_w$ along the vessel surface.

The above mentioned heat transfer models do not result in a very satisfactory determination of CVV heat transfer and, since the calculation of propellant burn rates is coupled to the vessels heat loss, a new method for the calculation of CVV heat transfer is desirable. This conclusion initiated the more recent work of Berger [BERGER 90], where the combustion cycle of one large propellant grain in a two dimensional geometry was modeled and the main focus was on obtaining a vessel wall convective heat transfer coefficient. The results of Berger's model only produced trends of the actual CVV combustion cycle and Berger therefore concluded that a more complex CVV model would be required in order to better determine convective wall heat transfer.

---

[1] "Quickness" values are determined by averaging the pressure data's time derivatives, which are taken at specified intervals during the experiment.

## 1.3 Goals and Objectives

The main objective of this project is to formulate a new mathematical model of the turbulent flowfield inside a CVV, in order to give an accurate and reliable prediction of the non-ideal effect of convective wall heat transfer, as a function of position and time, based on true scientific principles and physical processes rather than on empirical and semi-empirical relations.

Convective wall heat transfer that occurs throughout a CVV combustion cycle is a portion of the available propellant energy, which is lost as heat, and this is reflected in the CVV experimental pressure measurements. This in turn affects the determination of empirical propellant burn rates because they are based on the pressure measurement. A better prediction of convective wall heat transfer should enable the determination of more accurate propellant burn rates and contribute to the realization of "Quickness" comparisons made on an absolute scale.

In order to more accurately predict heat transfer rates and thereby improve upon the determination of propellant burn rate laws, this project will therefore attempt to include more physics into the prediction of a CVV three dimensional flowfield through the use of Favre averaged mass conservation, energy conservation and Navier-Stokes (momentum conservation) equations. The inclusion of fluid turbulence effects will allow the characteristics of the mechanical boundary layer of the vessel wall to be resolved in greater detail and thereby enable the convective wall heat transfer rate to be calculated by an appropriate Nusselt number correlation. Also included in the new model will be: 1) non-uniform ignition of the propellant bed and individual propellant grain movement and distribution, since these effects will affect maximum and minimum wall heat transfer rates and 2) a simple model for turbulent diffusion of propellant grains, since diffusion is thought to have an effect on grain motion and distribution [HARLOW 75].

Section 2 of this report describes the basic attributes of a CVV. Section 3 is an investigation into and a description of the various flow characteristics thought to be present in a CVV, which then gives a better understanding of the nature of a CVV flowfield. This discussion is used later on to facilitate the selection of an appropriate turbulence model for the prediction of a CVV turbulent flowfield. In section 4, the theory of two phase modeling is presented and a brief description of current two phase models is presented in order to propose and formulate a new model more compatible with the two phase characteristics of a CVV. Section 5 presents, discusses and selects constitutive laws needed to represent indeterminable terms in the conservation equations that arise from two phase modeling. A presentation of state dependent property relations is also included. In section 6, a discussion of turbulent convective wall and conductive heat transfer is presented, an investigation into the determination of convective wall heat transfer based on Nusselt correlations for the geometry of a CVV is performed and an appropriate correlation is selected. Finally in section 7 a literature review of various existing turbulence models is performed and a particular model is selected based on CVV flow characteristics. Also included is a discussion of solid phase turbulent diffusion and a model is presented for its determination.

# 2 Constant Volume Vessel

The main purpose of a CVV is to test the performance characteristics of a selected granular propellant. One of the more important characteristics of a propellant is its burn rate, which is a key design parameter in interior ballistics and has a direct influence on gun system performance. The only stumbling block is an exact analytical expression for the burn rate of granular propellant cannot be derived theoretically because of the complex interaction of, the not completely understood, different phenomena involved (see sections 2.2 and 5.2). Due to this unknown interaction, it is generally accepted that propellant burn rates are dependent on the surrounding pressure, partly on the initial temperature and somewhat on the undetermined flowfield. Therefore a CVV is used to record pressure data measured during the combustion cycle of a selected propellant, with a particular geometry and chemical composition, in order to characterize empirically the effect of pressure on a propellant's burn rate.

## 2.1 The Vessel Experiment

Constant volume vessels are heavy walled devices, cylindrical in shape and composed of an alloy steel construction capable of withstanding pressures up to 700 MPa. The length to diameter ratio is usually around two, in order to reduce the available surface area where the non-ideal heat losses occur. Typical CVV volumes are approximately 200–2400 $cm^3$.

A CVV contains a large number of propellant grains (figure 1), randomly oriented, which are closely packed in a silk bag around a center core igniter charge typically containing black powder (more commonly know as gun powder). The igniter charge usually consists of a thick walled brass tube perforated with small holes along its length, which displays the important characteristics of a high adiabatic flame temperature and a relatively quick burn rate. The bagged charge is located in the center of the vessel by suspending it on thin support rods. The centercore charge is normally ignited at one end, which then causes hot igniter combustion gas

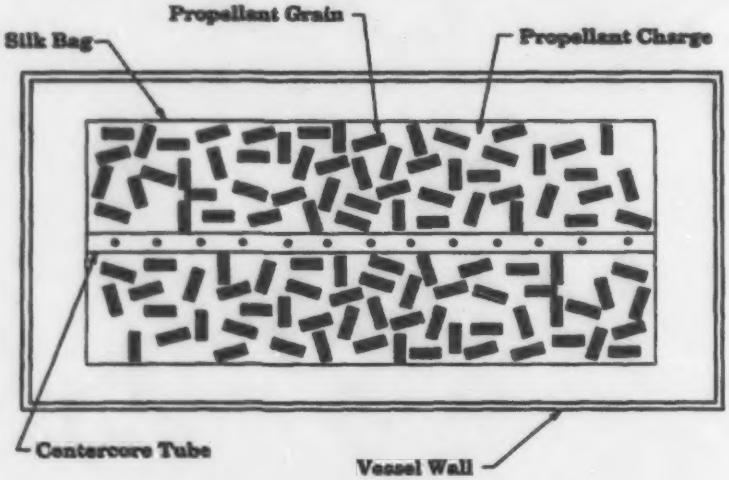

Figure 1: Cross section of a loaded CVV.

to be vented succesively through the small holes along its length and into the initially quiescent granular propellant bed. This relatively gradual and controlled ignition process is preferred over the case of a sudden shock delivered to the main propellant charge because the shock would result in an instantaneous detonation of the whole charge, which would be detrimental to the structural integrity of the gun breech.

Much of the overall events that occur during the transient combustion cycle of a CVV have been previously determined, which are as follows; 1) the propellant grains are loaded quite close together in what is formally known as a "packed bed", 2) a blow from the firing pin detonates a small sensitive explosive at one end of the igniter charge, 3) the black powder ignites and discharges hot combustion gas into the quiescent and relatively insensitive granular propellant bed, 4) a combination of heat from hot igniter gas and adiabatically compressed air close to the burning igniter charge raises the surface temperature of the nearest grains to the ignition temperature (through convective heat transfer) and the grains begin to burn, 5) a chain reaction is the set up and the combined heat of propellant and igniter gases ignite the next closest grains, 6) as more propellant grains begin to combust, a localized region of high pressure is created due to the low initial permeability of the grain bed to the combustion gases, 7) the interphase drag initializes the movement of the grain bed due to the localized high pressure region and compaction of the grain bed begins, 8) a flamefront is accelerated along with the moving grain bed and effectively spreads granular combustion throughout the rest of the propellant charge and 9) the grain bed is propelled through the CVV and impacts the opposite end of the chamber. It has been observed experimentally that the propellant bed can impact the wall at several hundred meters per second. All of these events are responsible for creating an unsteady viscous, compressible flowfield, which is assumed to exhibit a highly turbulent and multi-dimensional nature. The diagram in figure 2 helps visualize the movement and ignition of the propellant bed.

The pressure variation of the above described combustion cycle is recorded for a particular propellant simultaneously throughout the cycle at predetermined standard intervals. The data is then plotted on a pressure curve and the propellant's covolume and burn rate law constants

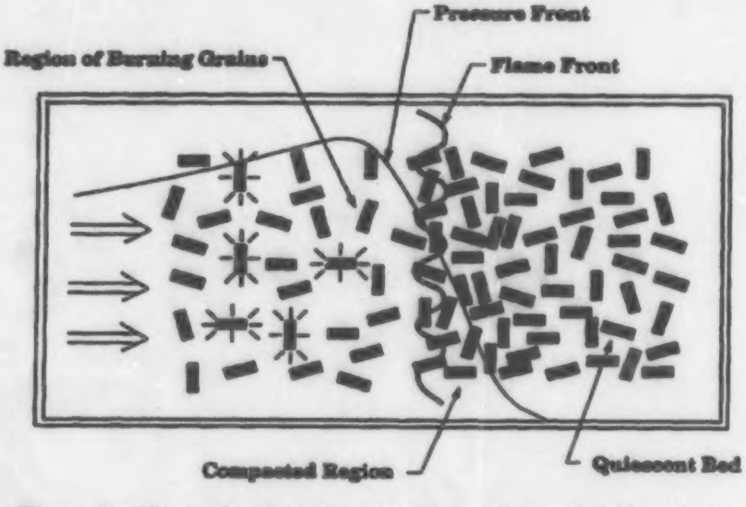

Figure 2: Flame front progression through a propellant bed.

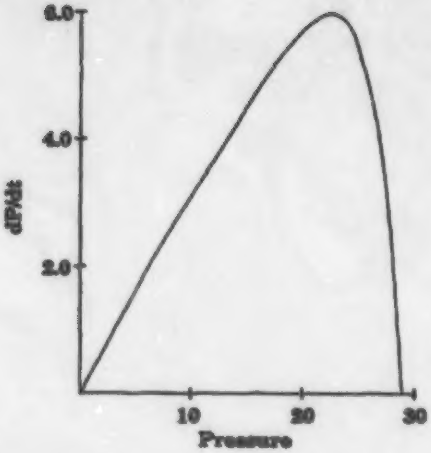

Figure 3: CVV experimental pressure curve.

are calculated. Figure 3 shows a typical pressure time derivative verses pressure curve of a CVV, where it can be seen that pressure increases until it reaches a peak (normally when 75% of charge is combusted) and then decreases to its final value because at this point the amount of heat loss due to wall convection is greater than the amount gained by combustion. The non-ideal effect of heat transfer occurs throughout a CVV combustion cycle and effects every pressure measurement since part of the available energy from combustion is not reflected in the pressure measurements but is lost in the form of heat. The calculation of covolume and burn rate constants is usually done neglecting the heat losses, where the error in maximum peak pressure is normally 7–14%. A correction factor, based on the difference between the theoretical and experimental peak pressure, must then be applied to account for these losses.

When the burn rates, calculated from a CVV experiment, are applied to a particular gun system, adjustments often have to be made to the burn rate constants on a trial and error basis in order to match the propellant burn rate to the performance characteristics of the gun system. This procedure is often necessary because of the non-ideal effects, such as bore friction, erosive burning and heat transfer, which were not considered during the determination of the propellant's burn rate law. This matching procedure reflects the importance of this project in helping to omit this totally empirical and tedious task of fitting propellant burn rates to individual gun systems.

## 2.2 Granular Propellant

CVV propellant grains are all identical (allowing for slight manufacturing irregularities), uniformly shaped particles typically in the shape of a cylinder with the dimensions of $D \approx 1$ cm and $L \approx 2$ cm. Each grain normally contains several perforations usually 1 mm in diameter which are used to control the amount of propellant surface area during the combustion cycle (see figure 4).

The dimensions of the above propellant grain play an important role during a CVV combustion cycle and the following is just an example of important grain characteristics: 1) size; 2) shape; 3) number of perforations and the amount of material between the perforations (web size) and 4) the ratio of volatile material, inert material and moisture contained in the grain.

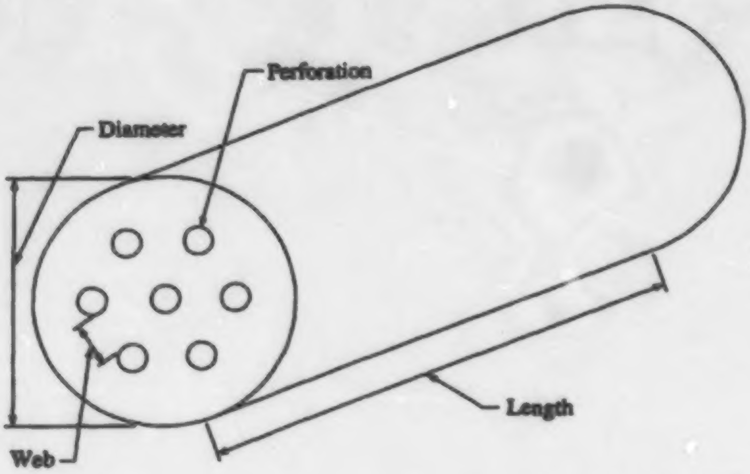

Figure 4: Diagram of a typical seven perforated cylindrical grain.

All these characteristics act simultaneously during a combustion cycle to affect the granular burn rate. This interaction combined with the ambient temperature and pressure conditions is presently indeterminable and therefore it is more convenient to determine propellant burn rates from a CVV pressure curve.

All propellants fall into one of two different categories, namely singlebase or multibase. For single based propellants the only explosive material used is nitrocellulose and all the remaining ingredients are used to control storage stability and burn rates. Multibase propellants utilize, in addition to nitrocellulose, nitroglycerine to facilitate the dissolving of the nitrocellulose, which helps enhance the explosive qualities of the propellant. Nitroguanidine is another compound added to keep the combustion cool, in order not to waste propellant energy in disassociating the combustion gases.

Typical combustion products generated by CVV propellant are $CO_2$, $H_2O$, $CO$, $H_2$ and $N_2$. A representative ratio of the different combustion gases is 0.024, 0.109, 0.39, 0.259 and 0.213 respectively. This represents a mixture of polar and nonpolar gases which play an important role in the determination of state dependent parameters such as fluid viscosity (see section 5.6 and Appendix D).

# 3 Flow Characteristics

The flow characteristics of a CVV must be visualized in order to choose the most efficient turbulence model for the prediction of the turbulent flowfield (i.e., the best prediction with the least amount of computation). The three dimensional, turbulent flowfield inside of a CVV experiment is very complex. The two-phase flowfield, consisting of solid propellant grains and a gas mixture of air and combustion products, has unsteady and developing features which could give rise to significant areas of anisotropic and inhomogeneous turbulence inside a CVV.

The developing flowfield can be divided into two regions consisting of a main or center flow and a wall boundary layer, where the turbulent boundary layer is dominated by viscous effects. In the main or center region the flow is dominated by inviscid effects but significant viscous effects may be present due to the formation of grain boundary layers. The principle structure of the combined flowfield consists of numerous separation points along the wall boundaries combined with subsequent zones of recirculation in both regions.

The turbulent boundary layer is further complicated by the fact that in certain areas it is formed along a concave curved surface which could introduce curvature effects into the boundary layer development. Other complexities arise since the burning of propellant grains cause an increase of temperature and pressure inside of a CVV. These increases result in the evolution of heat transfer to the chamber walls and cause compressibility effects to become non-negligible. There is also the possibility of the perfect gas relation becoming less valid and real gas effects becoming increasingly important as combustion takes place. The above mentioned flow characteristics are discussed in greater detail in the following sections.

## 3.1 Isotropy

Isotropy is an important consideration in turbulent flow prediction since almost all practical turbulence models assume isotropic conditions in order to simplify the modeling equations. It is important to note that if large regions of strong nonisotropic flow are present in a modeled flowfield, isotropic turbulence models will not adequately predict the turbulent flow structure.

Isotropic turbulence is defined as turbulence that has statistically steady mean velocity values and is independent of any externally imposed conditions [TENNEKES 72]. Therefore any point in the flow is independent of influence from other points in the flowfield by the transport of turbulence quantities, or from an earlier time via history effects. Isotropy can be visualized as a severely scrambled flowfield in which any sense of directionality is lost and in which the mean velocity fluctuations are equal ($\overline{u'^2} = \overline{v'^2} = \overline{w'^2}$). It should be recognized that in practice, turbulence can only be generated by flow velocity gradients and in the domain of these gradients the flow is considered anisotropic (see Figure 5). The outer boundary layer is the only isotropic region in the flat plate flow of Figure 5. Close to the plate, in the inner boundary layer, there is considerable anisotropic behavior due to the inhibiting nature of the wall. The flow is also anisotropic in the mean flow region because of already existing velocity gradients and the basic one dimensional nature of the incoming flow.

For a CVV, mean velocity gradients (or average shear stresses) are found in the core flow region and close to the walls. In the core region, large eddies are assumed to be the dominant flow structure (see Section 3.2) and it is common knowledge that the strain rates of large eddies are comparable to the strain rate of a mean flow. In addition, for a developing flowfield the strain

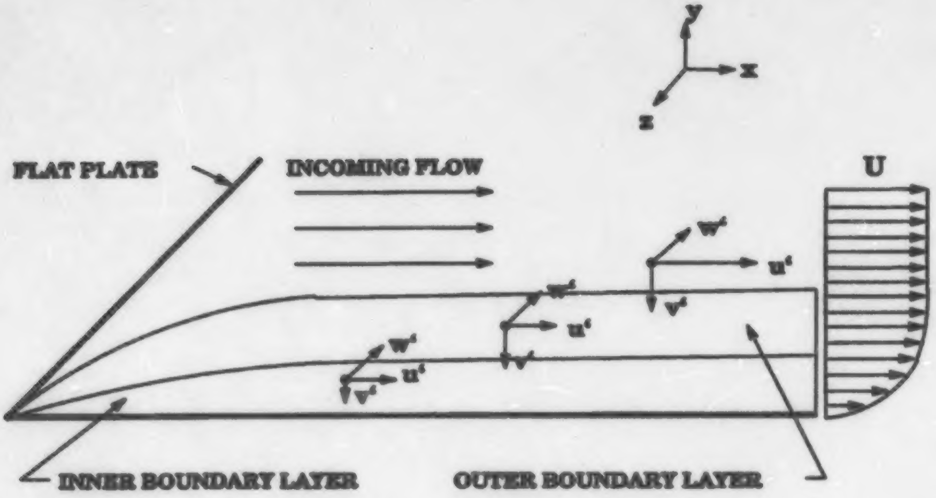

Figure 5: Turbulent flow over a flat plate.

rates are constantly shifting in magnitude and direction. Therefore by the definition of isotropy, large eddies in a CVV have steady anisotropy (nonisotropy) due to the shifting strain rate of the mean flow.

As eddy size in a flow becomes smaller, there is a permanent decrease of anisotropy in that region. In a CVV this reduction occurs in energy dissipation regions of the flow, such as in the outer boundary layer near the wall. The small eddies that exist in these regions are very responsive to changing flow conditions and they can be thought of as in approximate equilibrium with the local conditions. Therefore at the smaller scales the strain rate field can be considered isotropic in the mean.

## 3.2 Separation and Recirculation

The complex developing structure inside of a CVV creates various separation points along the vessel walls which are coupled to their accompanying zones of recirculation. A separation region can be defined as consisting of the three distinct areas of a free stream, a shear layer and a recirculation zone (refer to Figure 6). The recirculation zone can be refined further in to an inner layer close to the wall, an outer layer that is part of the larger scale free stream flow and an overlap region between the inner and outer layers shown in figure 7.

The reason why flow separation occurs is because the mean wall shear stress decreases to a zero value. This is accomplished inside a CVV when the mean velocity parallel to the wall reduces to zero and the mean velocity perpendicular to the wall increases proportionately. Serpa et al. [SERPA 87] discovered that the turbulent separation process extends over considerable surface area and is unlike laminar separation which occurs at a fixed point or line. They also found that the separation process is very intermittent, where intermittancy is defined as the fraction of time at a certain surface position that the local flow is opposite to the free stream direction (a value of 0 represents attached flow and 1 represents fully separated flow). Their results indicate that during an experiment, the intermittancy value never reaches or remains at

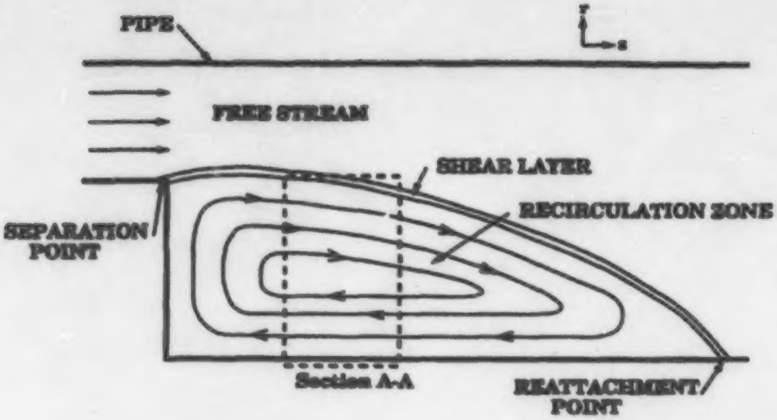
PIPE
r
z
FREE STREAM
SHEAR LAYER
RECIRCULATION ZONE
SEPARATION POINT
Section A-A
REATTACHMENT POINT

Figure 6: Separated flow over a backward facing step.

unity one hundred percent of the time. This result is clearly indicative of the unsteady nature of turbulent separation (even during fully developed flow) and shows the turbulent separation inside of a CVV is of an extremely unsteady nature since the flow is rarely (if at all) fully developed. Serpa et al. also found that during separation momentum and energy thicknesses fall initially, then rise through the recirculation zone (plateauing in the middle of the zone) and then rise significantly more at the reattachment point before falling to their initial value before separation occurred. This result is an excellent indication that separation will directly affect the very nature of a CVV's boundary layer structure.

The near wall area in a separation region is defined as a layer of fluid flowing in a reversed direction to the mean flow and is located between a solid surface and the maximum reversed velocity, which occurs slightly away from the wall (see Figure 7). The inner layer is known to be dominated by viscous and unsteady turbulence effects and to contain very high velocity fluctuations [SIMPSON 81a]. Simpson et al. found the intensity of velocity fluctuations parallel

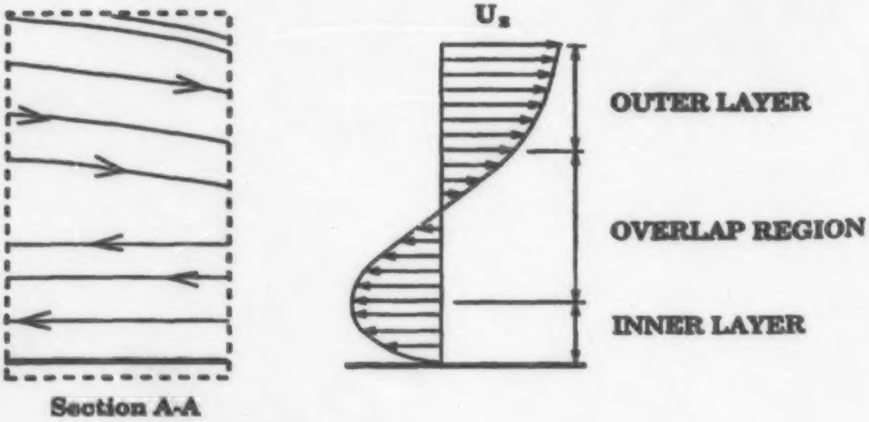
$U_z$
OUTER LAYER
OVERLAP REGION
INNER LAYER
Section A-A

Figure 7: Detailed sketch of a recirculation zone.

to the wall were an order of magnitude larger and perpendicular to the wall an order of magnitude smaller than the local mean velocity. In the case of a CVV these unequal velocity fluctuations could enhance the already existing anisotropic flowfield. Simpson et al. also determined that mean velocities in the backflow region result from time averages of large velocity fluctuations and are not really related to the source of turbulence. The structure of the stresses in the near wall region were found to be very different from a normal boundary layer. These Reynolds shear stresses ($\overline{u'_i u'_j}$) remain very small (almost negligible) and do not play a major role in the near wall momentum exchange [ADAMS 88]. Simpson et al. found the existence of large normal stresses ($\overline{u'_i u'_i}$) and determined that they were not generated locally near the wall, but in the free shear layer or at the reattachment point. All these observations show that for a CVV flowfield to be correctly predicted, separation effects should be included in any turbulence model.

Simpson et al. also investigated the effects of separation on eddy viscosity and Prandlt's mixing length. They found that when starting above the separation region and then moving downstream, though and below the separation point, the mixing length and eddy viscosity in the outer layer continuously decrease with respect to $z$. They also found there are no areas of constant mixing length or eddy viscosity in the separated outer region. Values of both the mixing length and the eddy viscosity are much lower than values in a comparable attached turbulent flow, which is understandable since a large part of momentum transport is due to normal stresses. In general, the mixing length and eddy viscosity become physically meaningless in the inner layer of a flow. The mixing length is undefined when the velocity gradient becomes negative and the eddy viscosity is undefined when the velocity gradient equals zero. These results have a direct effect on the type of turbulence model that can be used to predict the flowfield of a CVV and will be discussed in Section 7.

In part two of the experiment on a separating turbulent boundary layer, Simpson et al. [SIMPSON 81b] discovered that there is little production (by shear and advection) or convection of turbulent kinetic energy in the near wall region. This discovery leads to the conclusion that in the near wall region, turbulent dissipation balances turbulent diffusion, not turbulent production. The turbulent energy of the flow is produced mainly by shear and normal stresses in the outer and free shear layers and is then diffused in to the free stream and inner layer regions of the flow by large scale eddies. In fact the backflow region appears to be controlled by these large scale eddies and not by the wall shear stresses since the eddies provide the mechanism for turbulent energy diffusion. This result indicates the important role that turbulent transport and diffusion play inside of a CVV.

In part three of the experiment, Shiloh et al. [SHILOH 81] investigated the three dimensional aspects of a turbulent separating boundary layer. They found that in the outer 90 percent of a shear layer region, $\overline{w'^2}$ is equal to $\overline{v'^2}$. In the near wall region, their results indicate that $\overline{w'^2}$ and $\overline{u'^2}$ are greater than $\overline{v'^2}$ at all locations. They conclude that as the fluid is carried to the wall by large scale eddies, velocity fluctuations in the $r$ direction decrease towards the wall (becoming zero at the wall) and because of continuity requirements, the fluid is deflected and the $u$ and $w$ velocity fluctuations increase. This result portrays the expected anisotropic behavior of separated flow in the near wall region of a CVV.

## 3.3 Curvature

Forced curvature of flow streamlines by curved surfaces and/or by recirculation, in the plane of mean shear, can greatly affect the structure of shear flow turbulence. Inside a CVV, forced curvature occurs when the combustion gases flow along the periphery of the vessel and when the gases are contained in a recirculation region.

Curvature in general is capable of producing two very opposite effects on a turbulent structure. A stabilizing effect which merely attenuates an existing turbulent eddy structure is produced in flow over a *convex* surface. In the case of a CVV a destabilizing effect, which creates Taylor-Görtler (T-G) vorticies, is produced in flow over a *concave* surface and the strength of the vorticies is limited by the Reynolds stress gradients they generate. This shows that concave curvature can introduce further unsteadiness and turbulence effects into a CVV flowfield.

The destabilizing effects on turbulent concave flow are brought about by two different but interconnected phenomena. The first is curvature itself, which induces destabilizing effects directly by the creation of centripetal body forces. These body forces decrease the angular momentum of fluid elements outward from the wall and make fluid particles more susceptible to outside influences (i.e., more anisotropic). The decaying angular momentum also affects turbulent length scales by continually increasingly them as one moves further from the wall [SMITS 79] in the outer region of the boundary layer. These centripetal effects can be seen in Figure 8.

Smits et al. found that mean velocity gradients predicted from the local-equilibrium formula tend to be lower than the standard value. From these results one can postulate that the local-equilibrium formula (production equals dissipation) is not entirely valid in a boundary layer region. In the work of Hoffmann et al. [HOFFMANN 85], the T-G vortex structure was fixed so that primary effects of surface curvature could be distinguished from the secondary effect of vorticies. From their experiments they found that predicted values of mean velocity gradients are lower than standard values and presented a different explanation for this discrepancy. They argued that destabilizing curvature increases turbulent mixing and that the velocity difference between points decreases as a result of this mixing, that is a lower velocity gradient is produced. Both of the above explanations are consistent with experimental evidence and therefore decreases

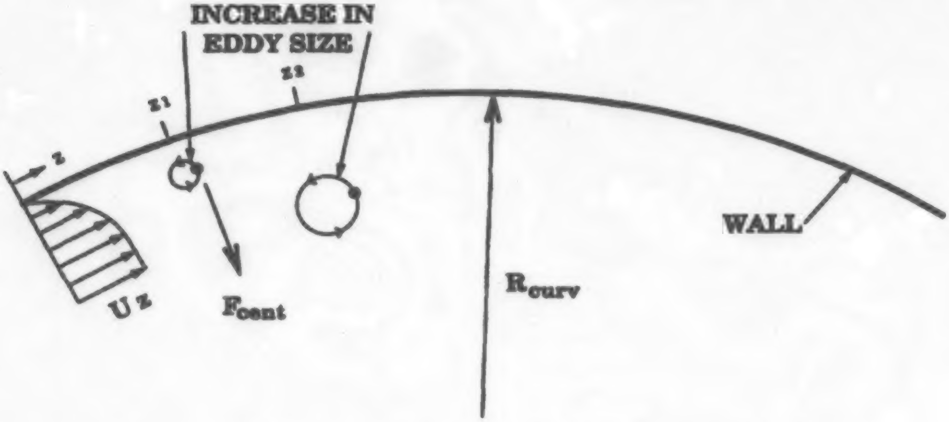

Figure 8: Enlargement of turbulent eddy size in curved flow.

in mean velocity gradients are probably a combination of each result. As for a CVV, these results indicate curvature will definitely increase the anisotropic nature of the flowfield and the heat transfer rate through the boundary layer.

The formation of T-G vorticies is the secondary cause of destabilizing effects on concave flow. As was first shown by Görtler [GÖRTLER 40], laminar flow over a concave surface becomes unstable at high Reynolds numbers and this can lead to the formation of a system of large longitudinal roll cells (T-G vorticies). This same roll cell pattern has also been observed in turbulent flow [HUNT 79].

The T-G vorticy structure is of a contra-rotating nature and causes a repeatable stationary pattern of spanwise variation in mean velocity profiles. The vorticies wander from side to side (spanwise) in turbulent flow because of turbulence contained in the shear layer and larger scale turbulence or unsteadiness in the free stream (see Figure 9).

A direct result of vorticy formation is a spanwise variation in boundary layer thickness and wall shear stresses. These variations give rise to a secondary flow strain rate, which is further evidence that a CVV flowfield is fully three dimensional. The vorticies also cause the boundary layer growth on concave walls to be much faster than that on convex walls [MOSER 87]. Since the vorticies are contra-rotating, the greatest change in the turbulence quantities is located at the boundary between roll cells where the bulk fluid motion is directed away from the walls. This is the area where the boundary layer is at it's thickest and the wall shear stresses are at their lowest. The above discussion demonstrates that T-G vorticies will affect the nature of the turbulent boundary layer in a CVV.

The destabilizing effects on turbulence quantities in concave flow have been documented by the above mentioned authors as well as Richmond et al. [RICHMOND 91]. It has been found that very close to a wall, mean velocity and wall shear stresses obey law of the wall profiles and at larger distances from the wall (in the outer boundary layer) $u_x$ is less than that of flat plate profiles. The degree of reduction is dependent upon the curvature magnitude, which is measured by the parameter $\delta/R$ (0.01 is weak curvature), where $\delta$ is the channel halfwidth and $R$ is the

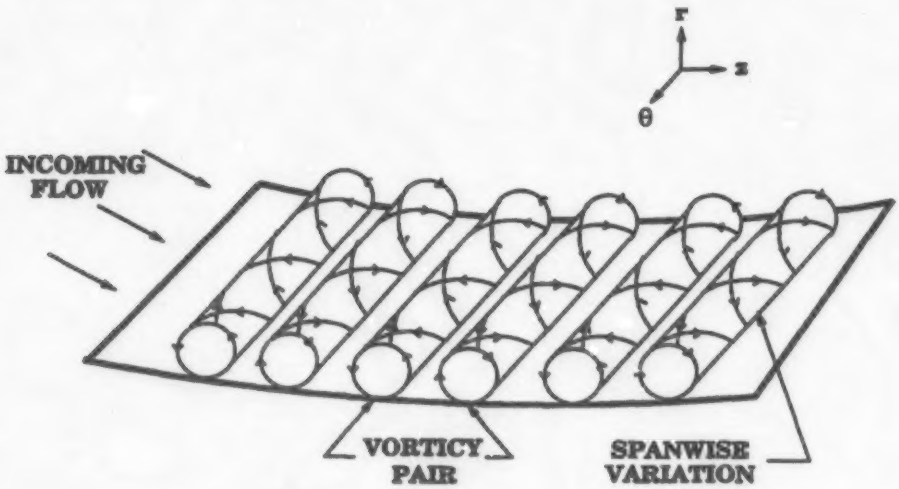

Figure 9: T-G vorticy effects in concave curved flow.

radius of curvature measured from the centerline. In strong curvature ($\delta/R = 0.1$), turbulence intensities and wall shear stresses are twice that of flat plate values. As mentioned before, the production of large shear stress gradients in the outer boundary layer (normal to the surface) greatly reduce $\partial u_i/\partial x_j$ values and this results in a slight decrease in the peak production values of $\overline{u_i'u_j'}$, that is flattening of the curve. The CVV curvature can be described as strong since $\delta/R \approx 0.5$ and therefore the previous results are a good indication of the expected basic nature of a CVV flowfield.

It has also been shown that T-G vorticies are primarily responsible for the creation of high wall shear stresses. In fact, T-G vorticies account for nearly half of the difference between convex and concave wall shear stress where viscous (laminar) stress and the underlying turbulence structure account for the rest. The calculation of secondary flow streamlines (of T-G vorticies) [MOSER 87] show that, although vorticies fill the entire flowfield (a channel in this case), they are concentrated more on the concave side. This result indicates significant secondary flow (and therefore 3-D effects) can be expected in the concave regions of CVV flowfield. The T-G vorticies affect underlying turbulence by convecting it along secondary streamlines and introducing a secondary strain field ($\partial u_z/\partial r\theta$), which contributes to the production of underlying turbulence. This result is self evident since any increase in shear strain will, in principle, tend to raise the level of transfer of mean kinetic energy to turbulence energy and increase shear stresses through the generation and/or redistribution process. In fact, Moser et al. determined that similar to recirculating flow, turbulent diffusion contributes significantly to the transfer of kinetic energy and is as much as 40 percent higher in concave than in convex flow. They also determined that, unlike recirculating flow, streamwise convection and production were strongest near the wall and contributed about 10 percent to the turbulent energy production in the region. These results indicate the definite contribution of T-G vorticies to a turbulent structure and demonstrate that increased turbulent mixing and diffusion will be present in a CVV boundary layer.

The largest effects of curvature, in general, are found in the outer layer, where the ratio of the extra strain rate ($\partial u_r/\partial z$) to simple shear ($\partial u_z/\partial r$) is the largest and because of this extra strain rate, a CVV will have a highly three dimensional flow in the outer boundary layer region.

### 3.4 Heat Transfer

To determine the heat transfer characteristics of a given flowfield, complete and accurate descriptions of velocity, temperature, pressure and shear stress patterns are required since convective heat transfer always involves a transfer of momentum. This was illustrated by Grant [GRANT 58], whose experimental results imply that boundary layer heat transfer occurs by the convection of macroeddies and by turbulent fluctuations due to microeddies. The major difficulty in modeling the heat transfer of a CVV is the already complex flowfield is further complicated by the largely unknown and misunderstood interactions between heat transfer and the developing flow.

The unknown effects of heat transfer on a turbulent flowfield (and vice versa) have been observed by a number of experimenters and their observations have helped demonstrate the interdependence between heat transfer and the structure of a flowfield. The influence of turbulent separated flow on heat transfer was discussed by Gooray et al. [GOORAY 85]. They found the presence of separation (accompanied by recirculation) greatly influences the process of energy transfer. The heat transfer coefficient in a recirculating region is larger than that of an attached flow and this is attributed to the increase of streamwise turbulent kinetic energy in the shear layer of a separation region, which is due to the existence of large shear stresses and a low rate of turbulent energy dissipation in the shear layer.

The effects of heat transfer on a turbulent flow structure was studied by Inger [INGER 77]. His experiment was conducted in a three dimensional flowfield consisting of vorticies which he found caused lateral periodic variations in shear stress, velocity, pressure and heat transfer, that is an indication of T-G vorticies. Inger's observations are important since his flow structure is extremely similar to that of the possible structure inside of a CVV. He determined the effects of heat transfer on a turbulence field become significant about halfway in to a boundary layer (outward from the wall), where heat transfer serves to partially dampen out lateral periodic variations in flow variables (i.e., turbulent fluctuations). Inger also determined that highly cooled walls enhance streamwise shear stress and heat transfer fluctuations, increase wall pressure values and decrease spanwise shear stress. Even though the vessel walls of a CVV are not considered highly cooled, they are still cooler than that of the interior and therefore, the turbulent flowfield could experience highly cooled heat transfer effects to a lesser degree.

Mabey also investigated the effects of heat transfer on turbulent flow [MABEY 90]. He determined that for attached flow along cool walls, turbulent separation is delayed and decreases in temperature throughout the boundary layer increase its density and decrease its overall thickness. The velocity profile ($u/U_e$) of the boundary layer becomes more "full", which is representative of a boundary layer at a higher Reynolds number or one further from separation (i.e., larger positive near wall velocity) at the same Reynolds number (see Figure 10).

The combined effects of an increased boundary layer thickness and a more "full" velocity profile result in a larger velocity gradient at the wall. This larger gradient combined with a slight increase in the molecular viscosity gives a small increase in the value of the local wall shear stress. For separated flow, Mabey was uncertain of the influence of heat transfer in the inner layer of a separated region. He postulated that due to large mixing rates and rapidly changing signs of velocity gradients close to the wall, the static temperature characteristics are roughly approximate to that of an attached, fully turbulent region. He also postulated that subject to the previous assumption, the maximum reverse flow velocity should increase due to cool vessel walls. The above mentioned results indicate the flow characteristics of a CVV boundary layer could be at a higher Reynolds number than for a similar flow without heat transfer and that

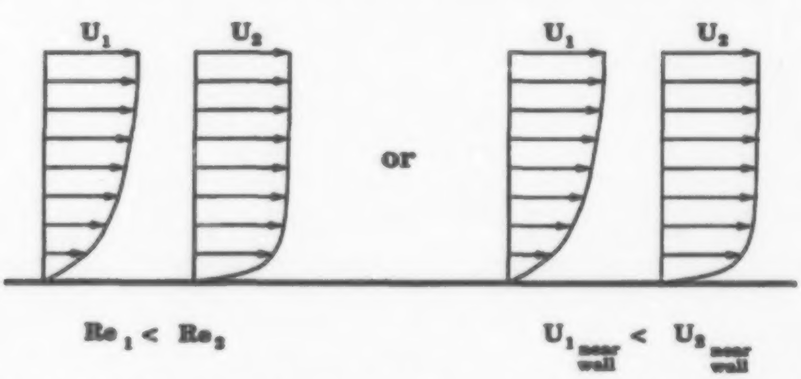

Figure 10: The effect of heat transfer on a turbulent velocity profile.

heat transfer greatly affects the turbulent structure of a boundary layer. Therefore when testing the predictions of a CVV mathematical model, data should be used from an experiment that involved heat transfer.

Žukauskas et al. [ŽUKAUSKAS 87] investigated two different types of energy transport in flows containing heat transfer, namely molecular and turbulent transport. They determined that close to a wall, in the viscous sublayer, energy is transported primarily by molecular diffusion and with low conductivity fluids (Pr$>$ 1), most of the resistance to heat transfer occurs in this region. They also found that the importance of turbulent energy transport increases over that of molecular transport further away from the wall. It is in this region that most of the resistance to heat transfer occurs for fluids with high conductivity (Pr$<$ 1), which is the case for a CVV (Pr$\approx$ 0.7). Other significant results of Žukauskas et al. are that as the thickness of a turbulent boundary layer increases, the heat transfer rate decreases and that wall shear stress is a combination of molecular, turbulent and thermal effects. These results of clearly show the interdependence between heat transfer and the turbulent flowfield inside of a CVV.

## 3.5 Compressibility

The flow inside of a CVV is significantly compressed during the combustion process. In fact, for most CVV experiments, the maximum pressure can reach 300 MPa or more towards the end of the combustion cycle. A direct effect of this compressibility is a reduction in stream tube area, which helps produce a three dimensional flow by introducing secondary strains to the flowfield. The following presentation of experimental results indicate that compressibility can affect the basic turbulence structure of a CVV flowfield.

In studing the effects of compressibility on a fully turbulent shear layer [PAPAMOSCH 88], it was shown that the growth rate of a shear layer decreases with increasing Mach number. This growth rate reduction starts at the subsonic level and continues in to the supersonic level, which implies that the compression effect on a flow is separate from shock or expansion wave effects and that compression is a stabilizing force on a turbulent flow structure.

Petrie et al. [PETRIE 86] also found similar results for internal separated flow off a backward facing step. The entrainment rate and the mixing layer growth were much less than what has been observed in previous incompressible flow experiments. Petrie et al. also determined that compressibility effects cause a decrease in the transverse component turbulence intensity ($\sqrt{\overline{u_r'^2}}/U_r$) and in the Reynold shear stresses ($\overline{u_i'u_j'}$) when results are compared to incompressible flows. Therefore the obvious conclusion is that reduced transverse transport capability results in a decrease in the Reynolds shear stress. In addition, it was found that the turbulent field of a compressible mixing layer is considerably more anisotropic than a comparable incompressible mixing layer because of decreased transverse turbulence intensity. These results indicate that compressibility might have a reducing effect on the heat transfer rate of the CVV by decreasing the turbulent mixing quantities of transverse turbulence intensity and Reynold shear stresses.

## 3.6 Two-Phase Flow

In general, two-phase flow can be defined as the existence of two distinct substances, solid, liquid or gas, that differ in material properties (e.g., density), velocity and/or temperature. These two phases are always in complete and continuous contact with each other and interact through certain physical phenomena such as drag and chemical reactions.

The two-phase flow inside of a CVV consists of highly compressible combustion gases along with incompressible but deformable solid particles (i.e., propellant grains). The grains at the start of the combustion cycle are situated quite close together in what is formally known as a packed bed. The discharge of hot igniter gas in to the quiescent propellant bed initiates propellant combustion through the combined effects of convective heat transfer (between igniter gas and grains) and the poor thermally conductive nature of the propellants. These two effects allow for a rapid increase, from an ambient to a critical ignition temperature, of the individual grains surface temperature.

Granular combustion usually starts predominantly at one end of the bed and then moves successively through to the other end in the form of a flame (or ignition) front. The packed bed is permeable to the generated hot combustion gases but the gas flow is considerably impeded due to drag exerted on it by the grains. This drag creates a local region of larger pressure behind the flame front and results in the formation of a large pressure gradient. The pressure gradient affects the flow by accelerating the combusting grains (and therefore also the flame front) in to the noncombusting region. This accelerated motion helps to initiate a totally three dimensional flowfield in which grains are distributed in a heterogeneous fashion. Grain movement also helps to fluidize (disperse) the packed bed, where fluidization is commonly defined as a collection of particles in a fluid stream moving at velocities sufficiently large enough, so that the drag exerted on the grains exceeds their net buoyant weight and they are free to move [HOMSY 83].

Since the unsteady motion of the two phases has the potential for unequal velocities and temperatures, an allowance must be made for these inequalities by deriving conservation laws separately for each phase rather than modeling the flow as a mixture. This is also self evident since the particle phase is not neutrally buoyant and therefore because of the large differences in density between the two phases, the inertia of the particle phase cannot be ignored.

The conservation laws of each phase are in turn coupled through the interaction of drag forces, convective heat transfer and combustion. The drag forces permit relative motion between the phases, convective heat transfer models the ignition of the grains by hot gases and combustion (or phase transition) permits the interchange of mass, momentum and energy. A model for the turbulent diffusion of grains must also be included in any flow model since the influence of turbulent fluctuations, which are certainly important inside a CVV, are thought to have an effect on grain motion and distribution [HARLOW 75].

# 4 Two-Phase Mathematical Modeling

## 4.1 Two-Phase Flow

One unavoidable consequence must be considered when modeling a heterogeneous two-phase flow, consisting of variable size particles, with non-negligible inertia (relatively large). Since two separate continuity equations are required, one for each phase, an accurate mass balance between the two phases in each control volume must be taken into account. In other words, the amount of each phase in each cell must be known at all times in order to satisfy conservation of mass requirements.

There are three different fundamental cases to the problem of mass conservation. The first case is when the solid particles are always smaller than any control volume. This implies that a porosity function ($\varepsilon$), ranging from zero to one, must be defined such that it represents the fraction of unit microscopic volume occupied by one phase and conversely one minus the porosity function ($1-\varepsilon$) represents the remaining volume cell fraction of the other phase. The second case occurs when a control volume is always the same size as a solid particle. This is not practical for a CVV since all the moving propellant grains are of variable size (non-uniform grain burning) during the combustion cycle and this would result in a severe distortion of the computational grid. Also the propellant grains are relatively large compared to the size of computational cells needed in the boundary layer and therefore proper resolution of flow near the vessel wall would be impossible. The third case is when particles are always larger than any control volume. For this case a porosity function would still be required since the amount of particle overlap in an adjacent cell would require the knowledge of the volume fractions in that adjacent cell. Another practical complication with this third case is that constant reduction rate in propellant grain size during the combustion cycle would eventually result in grains becoming smaller than the existing cell size.

For a CVV, or any flow with combusting particles for that matter, large particles modeled by a collection of small particles in a computational cell is deemed the most practical. This is especially true for a CVV since multi-perforated grains are the most common type of propellant. A collection of small particles in each cell is more representative since gas can flow through the collection, which is similar to what happens to multi-perforated grains in an actual flowfield (figure 11). Also with particles always smaller than the grid size, proper resolution of boundary layer flows is possible.

A common assumption given for individual small particles is that they are always incompressible [PANTON], which is a valid approximation for any CVV granular propellant. For the general form of this particle collection model, the gas phase can enter or leave a control volume through the cell boundaries (at the gas phase velocity) and can also enter by vaporization or leave by condensation through the holes (note: condensation does not occur inside a CVV). Figure 12 gives a comprehensive picture of this gas phase model. The particle phase, consisting of a finite number of spheres, lies completely inside the control volume and also has truncated portions along the cell boundaries. Similar to the gas phase, solid matter can enter or leave the control volume through cell boundaries (at the solid phase velocity) and can also leave by vaporization from or enter by condensation to the spheres.

All current two-phase flow models, using the above solid and gas phase representations, formulate governing equations based on the assumption that mass, momentum and energy are

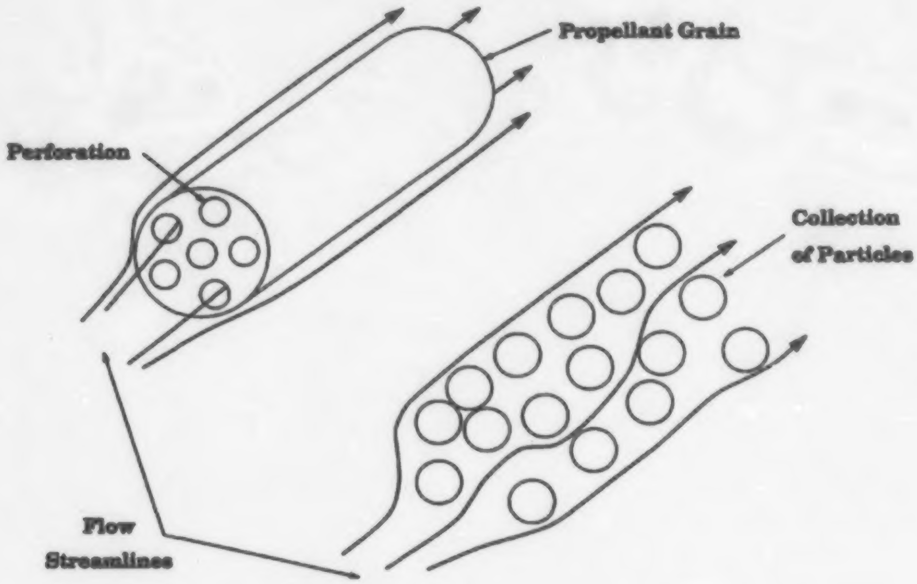

Propellant Grain
Perforation
Collection of Particles
Flow Streamlines

Figure 11: Particle collection model.

balanced over control volumes occupied separately by each phase. Other common current modeling assumptions include; 1) the interface between gas and solid matter is a surface of zero thickness which contains no mass, momentum and energy (i.e. combustion takes place only at the surface of a particle), 2) each phase can be isolated from the mixture for calculation purposes so long as all phase interactions are included, 3) the modeled particles in reality do not break up or fragment and 4) vaporized grain surface material takes with itself its own momentum and energy. Combustion is also considered uniform around a particle and that there is no net reaction force due to the production of combustion gases. Note that if the particles did not have a rapid combustion rate (which is contrary to a CVV), the assumption of zero burning thickness would be largely incorrect. This is because combustion could take place away from the particles surface,

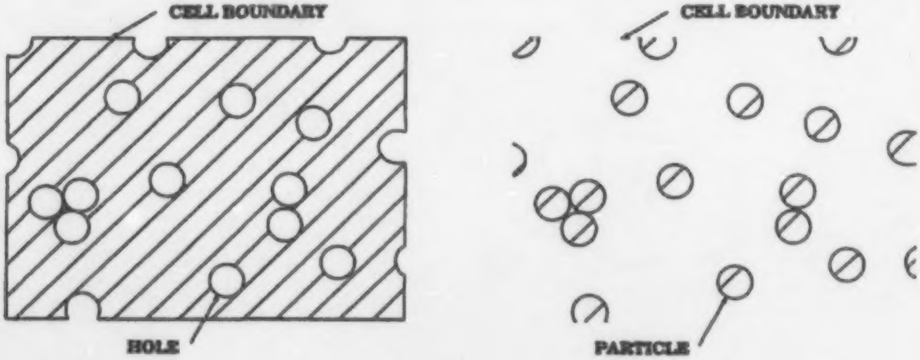

CELL BOUNDARY
HOLE
CELL BOUNDARY
PARTICLE

Figure 12: Two-dimensional control volumes for gas phase (left) and solid phase (right).

which would result in the more complicated problem of a higher phase (>2) *reacting* mixture.

Presently there are two different types of two-phase flow models; continuum and formal averaged. The continuum approach (e.g., [PANTON] and [KRIER 76]), which uses a differential derivation, assumes that all phases are present simultaneously at all points in space (coexistence), the control volume can go to zero in the limit and that the mixture is homogeneous. The formal averaged approach (e.g., [GOUGH 79b] and [HARLOW 75]), which uses an integral derivation of the microflow equations combined with specified boundary conditions at the phase interface, assumes that each phase is discrete and should be modeled as such, the control volume is finite and that the mixture is heterogeneous.

The advantage of a continuum model is that the existence of turbulent stresses is included, which therefore enables the boundary layer flowfield and heat transfer coefficient to be determined. The main disadvantage is that since a homogeneous flowfield is assumed, the model equations do not result in a static equilibrium solution when heterogeneous flow is present (explained further in [GOUGH 79b]). Also, erroneous results are obtained when a continuum model is applied to a heterogeneous flowfield. The particle phase of the model tries to force a homogeneous solution by effectively diffusing or smearing the dense particle regions (i.e., individual grains) into flowfield regions less populated by particles, which thereby results in an even distribution of the particle phase. This does not realistically model the discrete particle regions present in the CVV and is therefore not satisfactory for the determination of individual grain movement and clustering.

The advantage of a formal averaged model is since each phase is modeled discretely, the smearing effect is less evident and the determination of grain movement and clustering is possible. Also, a discrete formulation allows for the validity of a porosity variable since each cell is finite, which is not the case in a continuum model since for a control volume of zero volume, the theory of porosity is questionable. The main disadvantage of current formal averaged models is diffusive mechanisms (viscosity and turbulent stresses) are not present and therefore boundary layer heat transfer can not be fundamentally modeled.

It should be remembered, in the above discussion, that the objective of a CVV two-phase, flow model is to accurately predict the heat transfer coefficient and grain distribution during a combustion cycle. Therefore, the most obvious way to accomplish this goal is to combine the advantages of both model types by modeling the gas phase with the continuum approach and the solid phase with the formal averaged approach. It is recognized that the continuum modeled gas phase of the new model also contradicts the before mentioned porosity theory but, for a numerical solution, the control volumes are always finite and therefore this model does not *practically* contradict the idea of porosity. This new hybrid two-phase model, along with an appropriate representation of turbulent particle diffusion, will represent the physics of the CVV more closely and allow for heterogeneous grain movement, turbulent effects and heat transfer determination. The new proposed two phase model for CVV flow is presented in the following section.

## 4.2 CVV Conservation Equations

Flowfields that involve significant heat transfer, such as a CVV, require the equations of motion and energy for compressible flow in order to quantify the heat transfer rate [LAKSHMINAR 86]. It is well known that the instantaneous velocity field of single phase turbulent flow can be described by the Navier-Stokes (N-S) equation

$$\rho\left(\frac{\partial u_i}{\partial t}+u_j\frac{\partial u_i}{\partial x_j}\right)=-\frac{\partial P}{\partial x_i}+\frac{\partial}{\partial x_j}\left[\mu\left(\frac{\partial u_i}{\partial x_j}+\frac{\partial u_j}{\partial x_i}-\frac{2}{3}\delta_{ij}\frac{\partial u_k}{\partial x_k}\right)\right]$$

and the instantaneous temperature field by the thermal energy equation

$$\begin{aligned}\rho\left(\frac{\partial e}{\partial t}+u_i\frac{\partial e}{\partial x_i}\right)+P\frac{\partial u_i}{\partial x_i} &= +\dot{S}_{gen}+\frac{\partial}{\partial x_i}\left(k\frac{\partial T}{\partial x_i}\right)\\ &\quad +\mu\left(\frac{\partial u_i}{\partial x_j}+\frac{\partial u_j}{\partial x_i}-\frac{2}{3}\delta_{ij}\frac{\partial u_k}{\partial x_k}\right)\frac{\partial u_i}{\partial x_j}.\end{aligned}$$

These equations, along with the equation describing the conservation of mass

$$\frac{\partial \rho}{\partial t}+\frac{\partial \rho U_i}{\partial x_i}=0\,,$$

an equation of state and an empirical equation giving $\mu$ as a function of pressure and temperature adequately describe most turbulent, non-combusting, instantaneous flowfields.

The exact numerical simulation of instantaneous turbulent flow at low Reynolds numbers is possible. The problem is as the turbulent Reynolds number increases, the number of different length scales contained in the flow also increase and the storage capacity of present and foreseeable computers, needed to store and keep track of the length scales, is rapidly exceeded. Even for the simplest of problems the amount of computer time and memory is prohibitively expensive for applications other than research and because of the numerous calculations performed in a practical problem, truncation and numerical error become increasingly significant. Another difficulty in the application of instantaneous equations is the solutions are extremely sensitive to minute changes in the boundary and initial conditions. Also, averaged flow variables are more easily measured than instantaneous values.

One method of circumventing these difficulties is the introduction of time (or Reynolds) averaging [SCHLICHTING 87] to the equations, since flow averages are not overly sensitive to slight changes in the boundary conditions and they also substantially reduce the number of length scales in the flow. The time averaging method has become very common in the solution of engineering problems because it is usually only the average value that is of importance. The period of a time average is selected to be long compared with the turbulence time scale but short compared with that of the mean flow.

For highly compressible flows such as in a CVV, the density variation must also be included in the above equations. Density fluctuation makes the Reynolds averaged form of the equations more complex and therefore it is more common to use the mass (or Favre) averaging technique instead [FAVRE 65]. The following is a presentation of two phase mass averaged conservation equations that will be utilized in the present CVV analysis. Derivation and mass averaging of the gas and solid phase equations can be found in Appendices A and B. It should be noted however that a simplified derivation of Gough's equations is included only for completeness and a more detailed derivation of formal averaging functions and boundary conditions, if needed, can be found in [GOUGH 79b].

**Balance of Mass**

Gas Phase

$$\frac{\partial}{\partial t}(\varepsilon\overline{\rho}) + \frac{\partial}{\partial x_i}(\varepsilon\overline{\rho}\widetilde{u_i}) = \varepsilon_p\rho_p^2\dot{d}\frac{S_p}{M_p} \tag{1}$$

Solid Phase

$$\frac{\partial}{\partial t}(\varepsilon_p) + \frac{\partial}{\partial x_i}(\varepsilon_p\overline{u_{i_p}}) = -\varepsilon_p\rho_p\dot{d}\frac{S_p}{M_p} \tag{2}$$

Because of the incompressibility assumption of the solid phase, equation 2 is in effect a p.d.e. describing the variation of $\varepsilon_p$.

**Balance of Momentum**

Gas Phase

$$\frac{\partial}{\partial t}(\varepsilon\overline{\rho}\widetilde{u_i}) + \frac{\partial}{\partial x_i}(\varepsilon\overline{\rho}\widetilde{u_i}\widetilde{u_j}) = -\overline{\rho}\bar{\tilde{f}}_i - \varepsilon\frac{\partial\overline{P}}{\partial x_i} + \frac{\partial}{\partial x_i}[\varepsilon(\overline{\sigma}_{ij} - \overline{\rho u_i'' u_j''})]$$

$$+ \varepsilon_p\rho_p^2\overline{u_{i_p}}\dot{d}\frac{S_p}{M_p} \tag{3}$$

where

$$\overline{\sigma}_{ij} = \mu\left[\left(\frac{\partial\widetilde{u_i}}{\partial x_j} + \frac{\partial\widetilde{u_j}}{\partial x_i}\right) - \frac{2}{3}\delta_{ij}\frac{\partial\widetilde{u_k}}{\partial x_k}\right]$$

Solid Phase

$$\frac{\partial}{\partial t}(\varepsilon_p\overline{u_{i_p}}) + \frac{\partial}{\partial x_i}(\varepsilon_p\overline{u_{i_p}}\,\overline{u_{j_p}}) = \frac{\overline{\rho}}{\rho_p}\tilde{f}_i - \frac{1}{\rho_p}\frac{\partial}{\partial x_i}(\varepsilon_p\overline{R}) - \frac{\varepsilon_p}{\rho_p}\frac{\partial\overline{P}}{\partial x_i}$$

$$+ \varepsilon_p g_i - \varepsilon_p\rho_p\overline{u_{i_p}}\dot{d}\frac{S_p}{M_p} \tag{4}$$

On comparison of the instantaneous momentum equation and equation 3, it is obvious that application of Favre averaging is not without consequence. Additional unknowns of the form $\overline{\rho u_i'' u_j''}$ have now been introduced and in order to resolve these new unknowns a semi-empirical turbulence model must be employed. The selection of an appropriate turbulence model is discussed in section 7.

**Balance of Energy**

Gas Phase

$$\begin{aligned}\varepsilon\left(\overline{\rho}\frac{\partial\tilde{e}}{\partial t}+\overline{\rho}\widetilde{u_i}\frac{\partial\tilde{e}}{\partial x_i}+\frac{\mu_t}{\sigma_t}\frac{\partial\tilde{e}}{\partial x_i}\right) &= -\overline{P}\frac{\partial}{\partial x_i}(\varepsilon\widetilde{u_i})+\overline{\rho}(\tilde{f}_i(\tilde{u}-\overline{u_p})+\varepsilon\overline{\sigma}_{ij}\frac{\partial\widetilde{u_i}}{\partial x_j}\\ &+\frac{\partial}{\partial x_i}\left[\varepsilon\left(\frac{\mu c_p}{\mathrm{Pr}}+\frac{\mu_t c_p}{\mathrm{Pr}_t}\right)\frac{\partial\overline{T}}{\partial x_i}\right]-\varepsilon_p\rho_p^2\overline{q_i}\frac{S_p}{M_p}\\ &+\varepsilon_p\rho_p^2\dot{d}\left(\overline{e_p}+\frac{P}{\rho_p}+\frac{\overline{u_{i_p}}^2}{2}\right)\frac{S_p}{M_p}+\widetilde{u_i}\varepsilon_p\rho_p^2\overline{u_{i_p}}\dot{d}\frac{S_p}{M_p}\\ &+\varepsilon_p\rho_p^2\dot{d}\frac{S_p}{M_p}\left(\tilde{e}-\frac{\widetilde{u_i}^2}{2}\right) \qquad (5)\end{aligned}$$

Note, due to the incompressibility of the solid phase, the bulk temperature of the propellant is unaffected by motion and the kinetic energy of the particles is considered negligible compared to internal energy. Therefore the solid phase energy equation is represented by a one dimensional heat conduction equation which is coupled to convective heat transfer at the particle surface. A discussion of this equation is presented in section 5.1.

# 5 Constitutive Laws

The nine derived conservation equations contain the variables (not including turbulent flux terms) $\tilde{u}$, $\tilde{v}$, $\tilde{w}$, $\overline{u_p}$, $\overline{v_p}$, $\overline{w_p}$, $\overline{\rho}$, $\overline{P}$, $\overline{T}$, $\tilde{e}$, $e_p$, $\tilde{f}_s$, $\varepsilon$, $\overline{R}$, $S_p$, $V_p$ and $\dot{d}$. The term $e_p$ is commonly taken as a constant and is defined as the chemical energy released for the combustion of a solid propellant. Therefore since there are sixteen variables, seven constitutive laws are required in order to close the equation set. The following sections describe the seven relations needed and also the relations needed for state-dependent parameters such as molecular weight, specific heats, viscosity and thermal conductivity.

## 5.1 Interphase Heat Transfer

The combustion cycle of a CVV begins with the ignition of a primer charge which is distributed through the center of the granular propellant bed. The primer discharges hot combustion gas at various locations into the quiescent propellant bed and heat generated by the primer combustion and adiabatic expansion of gases near the burning primer raises the bulk temperature of the nearest solid propellant grains. Due to the low thermal conductivity of CVV solid propellant, grain surfaces reach the ignition temperature long before the transferred thermal energy penetrates to the center of the grains. The surface of the grains closest to the burning primer rapidly rise to the ignition temperature, which allows self sustained granular combustion to begin. Then the combined igniter and propellant combustion gases further propagate through and ignite the remaining propellant bed in the form of a flame front.

The transfer of heat from the hot combustion gases to the propellant grains occurs through the combined processes of convection and radiation energy transfer. Heat conduction energy transfer is also present but is considered negligible compared to the other two mechanisms. The complicated radiation energy transfer between propellant grains and between propellant grains and the gas phase is impractical to model at the present time due to unknown shape factor relationships for large conglomerations of moving particles and the emissivity and absorbsion characteristics of the combustion products. Therefore it is common procedure to assume that convection dominates over radiation energy transfer in a CVV and this interphase convective heat transfer is commonly referred to as convective deflagration.

Convective deflagration was first modeled by Kuo [KUO 76] for the case of a stationary bed of ball propellant. Kuo defined the total heat transfer coefficient of a grain surface as consisting of both convective and radiative components

$$h_{tot} = h_{conv} + \varepsilon_p \sigma (T + T_{ps})(T^2 + T_{ps}^2),$$

where $\varepsilon_p$ represents the emissivity of the particle phase (set to unity), $h_{conv}$ represents the convective heat transfer coefficient and $T_{ps}$ is the surface temperature of a propellant grain. This equation is then used as a boundary condition for a transient solid phase heat conduction o.d.e., which is then coupled to an algebraic expression for the penetration depth of the thermal wave into the grain's interior. From this set of equations, the propellants surface temperature and temperature gradient can be determined.

Kuo then used a complex ignition criterion where particle ablation (gasification of surface material) occurs at a lower temperature and self sustained granular combustion occurs at the higher ignition temperature. The heat transfer to a propellant grain is modeled to reduce linearly to zero as the grain surface temperature increases from the ablation to the ignition temperature. This analysis is more detailed than is practically necessary and Gough proposed a much simpler model based solely on convective heat transfer.

Gough [GOUGH 79b] assumed the energy transfer to a propellant grain to end and the ignition of a propellant grain to begin only when the specified ignition temperature is exceeded. Radiation energy transfer is neglected and the convective heat transfer coefficient is calculated from the following existing correlations for a packed propellant bed

$$\mathrm{Nu}_p = 0.4\mathrm{Pr}^{\frac{1}{3}}\mathrm{Re}_p^{0.7}, \tag{6}$$

where the value of porosity is less than the settling condition ($\varepsilon < \varepsilon_0$) and for a fluidized bed

$$\mathrm{Nu}_p = 0.4\mathrm{Pr}^{\frac{1}{3}}\mathrm{Re}_p^{\frac{2}{3}}, \tag{7}$$

where the porosity is greater than the settling condition ($\varepsilon_0 < \varepsilon < 1$). The particle Reynolds number is defined as $\mathrm{Re}_p = \frac{\rho|u-u_p|D_p}{\mu}$, the fluid properties are calculated at the film temperature and the heat transfer rate to the particle is determined from Newtons Law of Cooling.

Gough [GOUGH 79b] also adopted a simpler model for calculation of the transient propellant grains temperature variation. He assumed that a particle's temperature follows a cubic profile and proposed the following algebraic equation for propellant grain surface temperature

$$T_{ps} = T_{po} - \frac{2}{3}\frac{h_l H}{k_p^2} + \left[\left(T_{po} - \frac{2}{3}\frac{h_l H}{k_p}\right)^2 + \frac{4}{3}\frac{h_l T H}{k_p^2} - T_{po}\right]^{0.5}, \tag{8}$$

where the depth of thermal penetration is assumed one dimensional due to the low solid phase thermal conductivity. The variation of $H$ is given by

$$\frac{DH}{Dt_p} = \alpha_p q_p, \tag{9}$$

where $H$ is an arbitrary parameter used is used to calculate the propellant surface temperature, $\frac{D}{Dt_p}\left(= \frac{\partial}{\partial t} + u_{i_p}\frac{\partial}{\partial x_i}\right)$ represents the convective derivative along the macroscopic particle phase stream line and $q_p$ is the convective particle heat transfer rate.

The above equations are assumed to predict convective heat transfer in both the igniter and propellant charges and Gough reported that they predicted satisfactory approximations of convective flame spreading rates.

## 5.2 Propellant Burn Rate

At the start of a CVV combustion cycle, heat is transferred to the propellant grains from the gas phase. This energy transfer continues until the surface temperature of the grains reach the ignition temperature and then combustion begins. The burn rate of particle combustion $\dot{d}$ is very important and needs to be accurately modeled in order to refrain from violating the pressure constraints of a particular gun system.

The rate at which a particular granular propellant burns is dependent on numerous parameters, such as shape of the propellant particle (flakes, strips, balls, perforated cylinders) and its chemical composition. It is commonly known that a particle's geometry has a direct effect on the degree of exposed surface area (constant, increasing or decreasing) as combustion progresses. At constant pressure the rate of combustion is proportional to the amount of surface area exposed (as $A_s$ increases, $\dot{d}$ increases). Numerous experiments have determined that the burn rate is also dependent on temperature and strongly on pressure (as $T_{po}$ and $P$ increase, $\dot{d}$ increases). It is because of this complex and not completely understood parameter dependent combustion process that an exact analytical expression can not be theoretically derived for the propellant burn rate. Therefore experimental measurements are performed in order to provide simple empirical burn rate laws.

It has been experimentally observed that propellant particles continue to decrease in size throughout their combustion cycle. It is assumed the rate of regression of all surfaces of a propellant grain are equal and that the grain retains its original shape during combustion, which is commonly known as Piobert's Law. It is generally accepted that for a simple model of the burn rate, $\dot{d}$ depends primarily on the initial temperature of the grain $T_{po}$ and strongly on the ambient pressure. In particular, $\dot{d}$ is found to vary exponentially with respect to pressure ($P^n$ where $n < 1$).

The most common empirical steady-state burn rate law demonstrating pressure effects was proposed by De Saint Roberts [AMC 64]

$$\frac{Dd}{Dt_p} = \dot{d} = \frac{dx_i}{dt} = \beta P^n,$$

where $x_i$ represents the unit dimensions of a grain, $\beta$ is a burn rate coefficient and $n$ is the burn rate index. The constants $\beta$ and $n$ are determined by CVV experimental data.

Gough [GOUGH 79b] employed a slightly more complex steady-state burn rate law, also dependent exponentially on ambient pressure, which gave a better curve fit to the data.

$$\dot{d} = \beta_1 + \beta_2 P^n,$$

where $\beta_1$, $\beta_2$ and $n$ are also constants for a particular propellant determined by experiment.

The effect of temperature on the burn rate is obvious since combustion begins when the propellant surface reaches the ignition temperature, which can be reached sooner if the initial temperature of the propellant is higher. This effect has been observed experimentally and is commonly included in burn rate calculations by the relation

$$\dot{d} = \frac{\beta P^n}{T_{ig} - T_{po}},$$

where $T_{ig}$ is the combustion temperature. The effect of temperature is normally considered negligible compared to the effect of pressure on the burn rate for a CVV and therefore this relation will not be used.

All the burn rate laws previously discussed have been based on steady state combustion experiments, where transient effects on the burn rate were not taken in to account. Krier [KRIER 79] tried to include transient combustion effects by including the pressure time derivative in the following relation

$$\dot{d} = \beta P^n \left[ 1 + \psi(P) \frac{\alpha_s n}{\beta^2 P^{2n+1}} \frac{dP}{dt} \right],$$

where $\psi(P)$ represents a coefficient function of pressure (usually set to unity) and $\alpha_s$ is the thermal diffusivity of the solid phase. For a CVV, transient effects due to pressure are known to be negligible at higher pressures and therefore this relation is not required.

The burn rate laws are often derived through experiments conducted under conditions very different from those found in a typical gun system and therefore empirical adjustments must be made in order to account for the dynamic effects that are actually encountered during granular combustion. The actual burn rate of a propellant is influenced by the flow of gas over (and within for perforated grains) its surface, which acts to destroy the symmetry of the grain during combustion. The effect of erosive burning was investigated by Kuo [KUO 76] where he determined that the burn rate is normally directly proportional to the flow velocity and he proposed the semiempirical burn rate law

$$\dot{d} = aP^n + K_e h \exp\left( -\frac{\beta \dot{d} \rho_p}{\rho |u_i - u_{i_p}|} \right), \tag{10}$$

where $h$ is the convective heat transfer coefficient, $K_e$ and $\beta$ are erosive burn constants and $a$ and $n$ are calculated according to the values of the drag coefficient at the grain surface.

## 5.3 Interphase Drag

The propellant charge of a CVV is permeable to the gas phase, but during gas flow through the propellant bed considerable flow resistance is produced by the mechanism of drag. The interphase drag results in the generation of a large pressure gradient between the region of burning and inert propellant during the combustion cycle, which in turn forces the particle bed into motion. At the start of the CVV combustion cycle the state of the propellant particles is referred to as a "packed bed". As the drag on the particles increase and the individual particles begin to move, the propellant bed begins to disperse (or compact) and the moving collection of particles is then referred to (in the case of dispersion) as a "fluidized bed".

The interphase drag force acts to strongly couple the solid and gas phase conservation equations and, in particular, influences the transfer of momentum and energy between the phases. The interphase drag can be defined as the force of the gas phase on the solid phase (or vice versa) per unit wetted area and it acts at the gas-particle interface ($\Sigma$). Gough [GOUGH 79b] proposed the following interphase drag relation based on experimental data

$$f_i = f_{i_s} + \beta \varepsilon_p \left( \frac{Du_i}{Dt} - \frac{Du_{i_p}}{Dt_p} \right), \tag{11}$$

where $f_{i_s}$ is the steady state drag and $\beta$ is the virtual mass coefficient added to account for the contribution of unsteady effects ($\beta = \frac{1}{2}$ for spheres). The empirical steady state drag dependence on the flowfield for a packed bed is given by

$$f_{s_s} = \frac{\varepsilon_p}{D_p}(u_s - u_{s_p})^2 \left\{1.75 + 150\frac{\varepsilon_p}{\varepsilon \mathrm{Re}_{s_p}}\right\}, \tag{12}$$

where $D_p = \frac{6M_p}{\rho_p S_p}$ and $\mathrm{Re}_{i_p} = \frac{\rho|u_s - u_{s_p}|\varepsilon D_p}{\mu}$.

Gough reports that typical values of $\mathrm{Re}_{s_p}$ are on the order of approximately $10^5$ and therefore the $\mathrm{Re}_{s_p}$ term representing viscous drag in the above expression might only be of consequence close to the vessel walls. The interphase drag force is known to vary as the propellant bed changes from a packed to a fluidized state and therefore Gough defined the following constitutive law to represent the manner in which particle drag decreases as the degree of fluidization increases

$$\frac{f_{s_s}}{\frac{\varepsilon_p}{D_p}\rho(u_s - u_{s_p})^2} = \begin{cases} 1.75 + 150\frac{\varepsilon_p}{\varepsilon \mathrm{Re}_{s_p}} & \varepsilon \leq \varepsilon_0 \\ \left(1.75 + 150\frac{\varepsilon_p}{\varepsilon \mathrm{Re}_{s_p}}\right)\left(\frac{\varepsilon_p}{1-\varepsilon_1}\frac{\varepsilon_1}{\varepsilon}\right)^{0.45} & \varepsilon_0 \leq \varepsilon \leq \varepsilon_1, \\ 0.3 & \varepsilon_1 \leq \varepsilon \leq 1 \end{cases} \tag{13}$$

where $\varepsilon_0$ is the propellant bed settling porosity and $\varepsilon_1 = \left[1 + 0.02\left(\frac{1-\varepsilon_0}{\varepsilon_0}\right)\right]^{-1}$ which represents the point at which the bed becomes completely fluidized. In a fluidized bed, the particle drag acts only on single particles and is no longer influenced by packed bed conditions.

These empirical relations provide good agreement with the measurements of transient flow in a noncombusting bed of inert multiperforated cylindrical propellant [GOUGH 79b] (same as CVV propellant type) and they are assumed to apply to both the main propellant and the centercore igniter charges.

## 5.4 Intergranular Stress

During a CVV combustion cycle, the granular propellant bed is penetrated by the heated combustion products of the primer and propellant charge. This penetration is resisted by particle drag, which leads to the compaction of the propellant bed and the initiation of a stress load in the incompressible but deformable solid phase. Increasing gas pressure and collisions between particles also contribute to this stress load. Therefore, the intergranular stress term $R$ must be included in the solid phase momentum equation to reflect the loads carried by the solid phase alone (i.e., the difference between stress in the solid and gas phases). The intergranular stress acts only on the surface area of the particles ($A_p$) since the stresses in the solid phase correspond to those in the gas phase at the interface $\Sigma$.

Gough [GOUGH 79a] assumes $R$ is isotropic and a function of porosity only ($R = R(\varepsilon)$). He proposed the rate of propagation of intergranular disturbances can be represented by

$$\frac{D(\varepsilon_p R)}{Dt_p} = -\rho_p \frac{a(\varepsilon)^2}{g_0}\frac{D\varepsilon}{Dt_p}, \tag{14}$$

where $g_0$ is a constant and $a(\varepsilon)$ represents the intergranular stress rate of propagation through the solid phase.

Gough then defined the constitutive law

$$a(\varepsilon) = \begin{cases} a_l \frac{\varepsilon_0}{\varepsilon} & \varepsilon \leq \varepsilon_0 \\ a_l \exp(-\kappa(\varepsilon - \varepsilon_0)) & \varepsilon_0 \leq \varepsilon \leq \varepsilon_2, \\ 0 & \varepsilon_2 \leq \varepsilon \leq 1 \end{cases} \tag{15}$$

where $\kappa$ is the stress attenuation factor which controls the exponential decay of $R$ with respect to $\varepsilon$ as the bed fluidizes and $\varepsilon_2$ is the value of the porosity above which $a(\varepsilon) = 0$. The values of $a_l$ and $\varepsilon_0$ are given by experiment and vary according to the type of propellant. Typical values are $\varepsilon_0 \approx 0.4$ and $a_l \approx 450$ m/s. The stress attenuation factor $\kappa$ is given as being physically equal to infinity but a finite value can be interpreted as representing particle collisions in the dispersed state.

## 5.5 Equation of State

For most combusting flowfields of lower density, the ideal gas law accurately describes the pressure exerted on the walls of a container in relation to the temperature and density characteristics of the flow. The gas molecules in a lower density flow are modeled as non-interacting point mass particles in thermal equilibrium with one another and since the chamber volume is many orders of magnitude larger than the total volume occupied by the gas molecules, the ideal gas law is a good approximation.

The main thermodynamic characteristics of a CVV are high temperature, high pressure and high density flow since typical CVV propellant loading densities are relatively large ($\approx 0.3$ g/cm$^3$). For higher loading densities, the ideal gas approximation begins to break down and can lead to large errors because the gas molecules begin to interact with one another. These interactions create intermolecular forces which affect the relationship between energy and pressure. The interaction forces are composed of two different phenomena. A repulsive force accounts for the nonnegligible molecular volume of each molecule and an attractive force accounts for the cohesiveness between the molecules.

Van der Waals tried to approximate real gas behavior by incorporating two additional correctional constants in the ideal gas law, which are species specific. The equation proposed by Van der Waals is

$$\left(P - \frac{a}{V^2}\right)(V - b) = \Re T,$$

where $a$ represents the effect of attractive forces and $b$ represents the decrease in total volume available to the gas molecules (i.e. covolume).

A simplified version of the Van der Waals equation is the Nobel-Abel dense gas law which is commonly written as

$$P = \frac{\rho \Re T}{1 - \rho\eta},$$

where $\eta$ represents the covolume of the gas phase. This simplified equation neglects the effect of intermolecular attraction forces since CVV flow takes place at high temperatures ($\approx 3000K$) and the attraction forces are assumed negligible compared to the kinetic energy of the molecules.

Gough [GOUGH 79b] used a different version of the Noble-Abel equation for two phase flow which relates $e = e(P, \rho)$

$$e = \frac{P}{(\gamma - 1)\rho}(1 - \eta\rho), \tag{16}$$

where $\gamma$ is the ratio of specific heats. The covolume for a particular propellant is determined graphically by combusting a series of different mass charges and measuring the corresponding maximum pressure. It was found by Krier [KRIER 78] that the covolume effect becomes, as expected, increasingly important at higher pressures and the above relation is usually not valid at $P > 50 - 100$ MPa. In order to improve upon the equations predictive capabilities, Krier [KRIER 78] recommended that a variable covolume ($\eta = \eta(\rho)$) could be used to match the predictions of other more complex equations of state valid at much higher pressures.

One other factor must be included with Gough's equation in order to predict CVV two phase flow correctly. The gas phase density is not only dependent on temperature and pressure but also on the amount of phase transformation from the solid to gas phase during the combustion cycle. The gas phase density of a CVV can be defined as the ratio of the gas mixture molecular weight to it's volume and the increase in mass of the gas phase is equal to the mass of the combusted solid propellant, according to conservation of mass principles.

Krier [KRIER 79] defined the above relationships in mathematical terms as

$$M_g = CZ(t),$$

$$V_g = V_{ch} - \frac{C}{\rho_p}[1 - Z(t)],$$

which gives

$$\rho = \frac{CZ(t)}{V_{ch} - \frac{C}{\rho_p}[1 - Z(t)]},$$

where $C$ is the propellant charge weight, $V_{ch}$ is the volume of a CVV and $Z(t)$ represents the fraction of propellant consumed at time $t$.

Krier's density equation is not particularly useful for the present microscopic CVV analysis because the variable gas phase volume is defined for the macroscopic dimensions of the whole CVV ($V_{ch}$). This results in the calculation of one average gas phase density over the entire CVV. The equation also does not allow for the non-uniform ignition of the propellant grain bed.

It is more appropriate to define a relation applicable to a microscopic CVV analysis. The time dependent gas phase molecular weight can be better approximated by Gough's equation 18 given in section 5.6. The volume available to the gas phase is simply the computational cell volume minus the volume of solid phase present in the cell. The above arguments can be used to define a new proposed CVV equation for density as

$$\rho = \frac{M_{wt}}{V_{cell} - \varepsilon_p V_{cell}}. \tag{17}$$

## 5.6 State-Dependent Property Variation

The gas phase of a CVV is subjected to large variations in the ambient pressure (≈0.1–300 MPa), temperature (≈273–3000 K) and density (≈1.3–500 kg/m$^3$). Therefore it is normal to assume state-dependent variables, such as molecular weight and viscosity, do not remain constant and provisions must be made for their variation.

Gough [GOUGH 83] considered the variation in gas phase molecular weight and specific heats only with respect to time. He defined the variation in the gas phase molecular weight and specific heats as due to the mixing of the igniter and combustion gases with the ambient gas without further chemical reaction. Gough proposed the following local relation for gas phase molecular weight

$$\frac{DM_{wt}}{Dt} = \frac{M_{wt}}{\varepsilon\rho}\left[\left(1 - \frac{M_{wt}}{M_{ig}}\right)\psi + \left(1 - \frac{M_{wt}}{M_{prop}}\right)\dot{m}\right], \tag{18}$$

where the initial $M_{wt}$ is that for air, $M_{ig}$ is the igniter charge molecular weight, $M_{prop}$ is the propellant molecular weight, $\psi$ represents the rate of injection of the igniter charge per unit volume (usually in tabular form) and $\dot{m}$ $(= \varepsilon_p\rho_p\frac{S_p}{V_p}\dot{d})$ represents the rate of mass production of propellant combustion per unit volume.

Gough also proposed the following local relation for gas phase specific heats

$$\frac{Dc}{Dt} = \frac{1}{\varepsilon\rho}\left[(c_{ig} - c)\,\psi + (c_{prop} - c)\,\dot{m}\right], \tag{19}$$

where $c$ represents either constant pressure or volume specific heat, $c_{ig}$ is the igniter gas specific heat and $c_{prop}$ is the specific heat of the propellant combustion gases. Once the $c_p$ and $c_v$ variation has been determined, the ratio of specific heats can be calculated by $\gamma = \frac{c_p}{c_v}$.

The variation of CVV gas phase viscosity must also be taken into account and is particularly important because it is used to calculate: 1) convective wall heat transfer; 2) viscous boundary layer stress terms in the momentum and energy equations and 3) interphase convective heat transfer, which is used to determine propellant ignition. Gough [GOUGH 83] used a Sutherland type viscosity correlation

$$\mu = 0.134064\frac{\left(\frac{T}{296}\right)^{1.5}}{T + 110},$$

which was derived from the kinetic theory of gases for a dilute gas which neglects the pressure variation.

Gough's relation is not appropriate for CVV flow because it applies only to dilute gases and does not take pressure variations into account or allow for the variation of gas phase molecular weight. At high pressure, the gas phase molecules internal spacing begins to become small enough that simple kinetic theory assumptions become inaccurate. Reid et al. [REID 87] presents these ideas clearly by the graphical results in figure 13. It can be seen at low pressures the viscosity increases proportionally with temperature, at higher pressures the viscosity increases inversely proportional with temperature (representative of liquid behavior) and at very high temperatures pressure has little effect and viscosity again increases proportionally with temperature.

More accurate predictions of viscosity are available through well tested algebraic dense gas correlations, where nonideal effects due to pressure are empirically included. One of the most accurate models (≈ 6% error) recommended by Reid et al. [REID 87] for polar and nonpolar gases is the model by Lucas. A dimensionless viscosity is defined as

$$\mu_r = \mu\xi = f(T_r), \tag{20}$$

where $\xi$ represents an inverse viscosity related to the gas phase molecular weight, critical pressure and temperature and $f(T_r)$ represents a function of reduced temperature (note $T_r = \frac{T}{T_c}$). For a detailed description of the model see Appendix D.

Unfortunately there are no similar accurate correlations available at the present time for

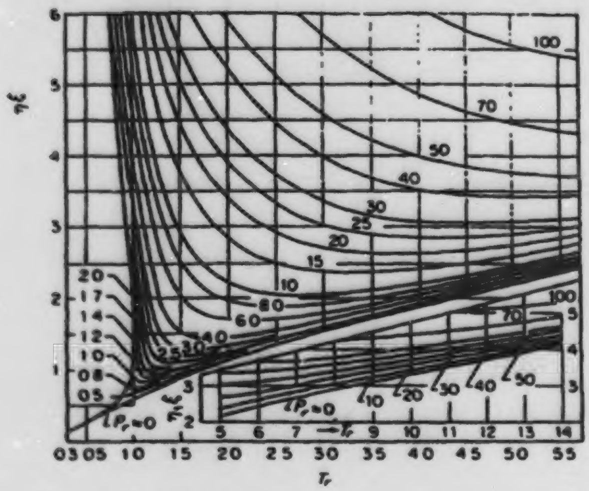

Figure 13: Variation of viscosity with pressure and temperature.

determining the thermal conductivity of a dense polar or nonpolar gas [REID 87]. Therefore for the lack of a better relation, the Prandlt number is used to determine the gas phase thermal conductivity, where the Prandlt number is estimated by the perfect gas polyatomic relation [BURMEISTER 83]

$$\mathrm{Pr} = \frac{4\gamma}{9\gamma - 5}. \tag{21}$$

It is recognized that the above relation is not an appropriate equation to use to represent *Pr* in a CVV but at least the ratio of specific heats is determined by Gough's equation which is suited for two phase flow.

## 5.7 Grain Form Functions

Propellant grain surface area and volume variations during a CVV combustion cycle can be related to the initial grain geometry and the propellant surface regression *d*. Grain volume decreases continually during the combustion cycle and a common relation given by Gough [GOUGH 83] for multiperforated cylinders is

$$V_{gr} = \frac{\pi}{4}(L_o - 2d)[(D_o - 2d)^2 - N(d_o + 2d)^2], \tag{22}$$

where $N$ is the number of perforations, $L_o$ is the initial length, $D_o$ is the external diameter and $d_o$ is the perforation diameter.

The direction of variation (increasing or decreasing) of grain surface area depends heavily on it's geometry. Spherical propellant decrease, single perforated cylinders remains constant and multiperforated cylinders increase in surface area as combustion progresses. This is shown quite clearly in figure 14.

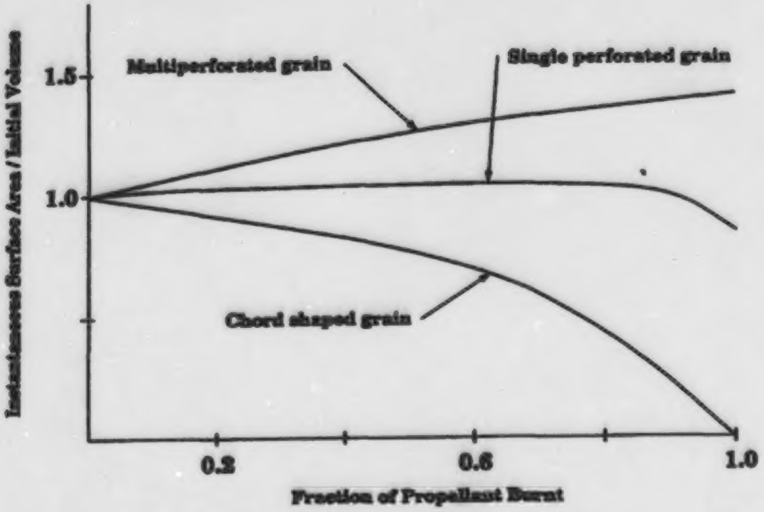

Figure 14: Comparison of different shaped grains surface area variation.

Gough also gives the following surface area relation for multiperforated cylinders

$$S_{gr} = \pi(L_o - 2d)[(D_o - 2d) + N(d_o + 2d)] + \frac{\pi}{2}[(D_o - 2d)^2 + N(d_o + 2d)^2]. \qquad (23)$$

Both of the above functions are only valid until the regressing perforation surfaces intersect and then the grain breaks up into slivers. This behavior is demonstrated in figure 15. Once slivering occurs, the grain form functions are quite complicated for $N > 1$. Form functions predicting the slivering of a seven perforation grain can be found in Krier [KRIER 73].

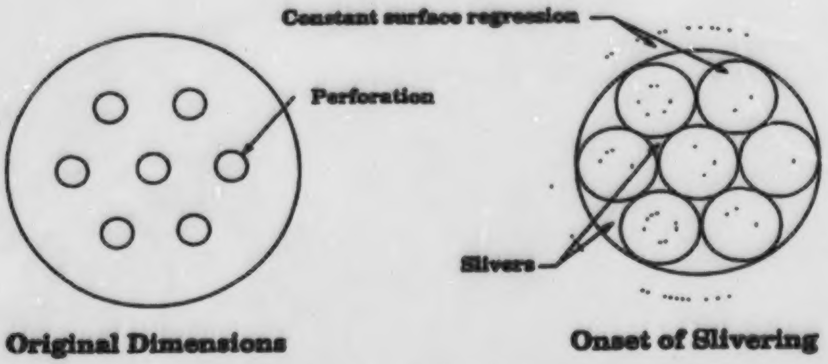
Constant surface regression
Perforation
Slivers
Original Dimensions
Onset of Slivering

Figure 15: Cross section of a cylindrical grain during combustion.

# 6 Turbulent Heat Transfer

The gas phase turbulent flow inside of a CVV is an example of *coupled* fluid flow because of the significant variations present in fluid properties (such as $\rho$ and $\mu$) with respect to temperature and therefore, the flowfield and heat transfer cannot be evaluated at any single reference temperature. The large temperature gradients present result in a nonlinear description of the temperature field, which is coupled to the velocity field equations, due to the flow properties being a function of temperature.

Heat transfer, through the gas phase of a CVV, is due to the presence of these temperature gradients and is thought to be a combination of mainly conductive in the interior of a CVV and mainly convective along the inside surface of the vessel wall. Radiative energy transfer, in general, always coexists with convection and conduction but in the case of the CVV, it is assumed that the combustion gases have a high absorbtivity and therefore radiative energy transfer to the vessel wall is negligible. The presence of high velocities, in a CVV, makes forced convection (over natural convection) the dominant mode of convective wall heat transfer. The following section describes the physical nature of convective and conductive heat transfer and also presents the methods that will be used to model them.

## 6.1 Convective

Convective heat transfer, from the hot combustion gases to the cooler vessel walls, can be thought of as being comprised of two different mechanisms. The first mechanism, which dominates energy transfer very close to the vessel wall surface in the region of low velocity, is due to the random molecular motion of the fluid. The second mechanism, which dominates energy transfer away from the wall in the outer boundary layer, is due to the bulk or macroscopic motion of the fluid. The total convective vessel wall heat transfer is then the superposition of energy transport by the random molecular motion and the bulk fluid motion which, combined with the existing temperature gradients, leads to the creation of a turbulent thermal boundary layer along the inside perimeter of the CVV (see Figure 16).

In order to determine convective wall heat transfer, Newton's Law of Cooling can be used to represent the transfer of heat through the boundary layer, which is usually written as

$$q_{conv} = h_l(T_w - T_g), \tag{24}$$

where $q_{conv}$ is the convective heat transfer per unit area, $T_w$ is the gas phase temperature at the wall surface, $T_g$ is the temperature of the gas phase outside of the boundary layer and $h_l$ is the local convective wall heat transfer coefficient. The heat transfer coefficient depends strongly on the character of the boundary layer, surface geometry, nature of the fluid motion and thermo and fluid dynamic transport properties. In particular, the coefficient depends on the state of the flowfield (laminar or turbulent) because turbulent fluctuations are commonly known to greatly enhance energy transfer. It can also be expected that $q_{conv}$ and $h_l$ will vary with respect to distance and time along the CVV surface due to the ever changing flow conditions.

There are two main methods that can be used to determine the heat transfer coefficient of a boundary layer. The first is to equate $h_l$ to conductive heat transfer at the wall by using the

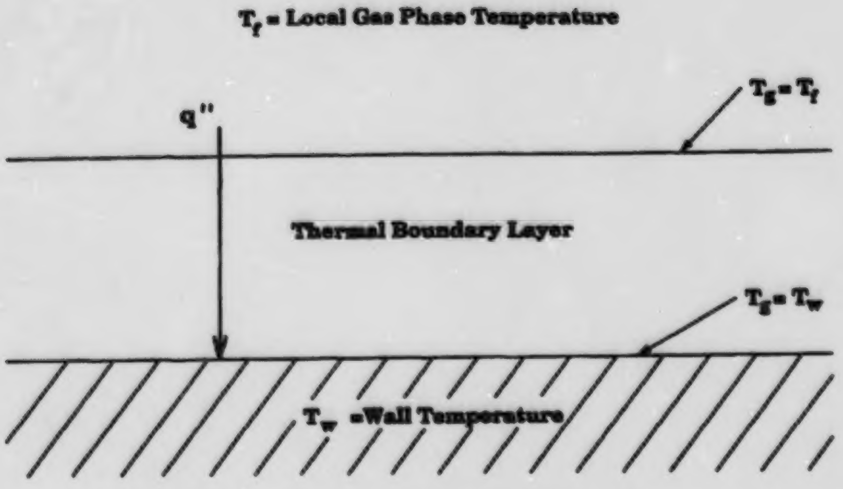

Figure 16: Convective wall heat transfer.

boundary condition $q_{conv} = q_{cond}$

$$h_l(T_w - T_g) = k_g \left.\frac{\partial T_g}{\partial x_i}\right|_{x_i=0} \longrightarrow h_l = \frac{k_g \left.\frac{\partial T_g}{\partial x_i}\right|_{x_i=0}}{(T_w - T_g)},$$

where $k_g$ is the thermal conductivity of the gas phase. The difficulty with this method is it requires a thorough description of the mechanical *and* thermal boundary layers in order to determine the temperature gradient at the wall. This is usually a very computationally intensive task and requires the inclusion of additional equations for turbulent heat fluxes in a complex turbulent flow. Many different models for turbulent heat fluxes have been formulated and examples of models applicable to complex flow have been proposed by Nagano et al. [NAGANO 88], which uses two additional p.d.e.s for heat flux determination analogous to the $k-\epsilon$ model, and by Launder [LAUNDER 88], which uses transport p.d.e.s for the turbulent heat fluxes themselves and model approximations for the unknown turbulent correlations. Both of these models require numerous additional modeling constants and since the CVV is not a well investigated flow geometry, it is best at the present time not to use these additional modeling equations and leave the required modeling constants at a minimum.

The second, more preferred, method is to use $h_l$ to define a dimensionless temperature gradient term near the wall surface and then empirically relate the dimensionless quantity to various fluid and thermodynamic properties of the flowfield. This type of analysis commonly uses the Nusselt number, which is defined as

$$\mathrm{Nu} = \frac{h_l D}{k_g}, \tag{25}$$

where $L$ is the characteristic length of a flow (in the case of a CVV, $D = D_{ch}$ is the most convenient). The Nusselt number is known to be a function of $L$, Re and Pr and Nusselt correlations are commonly given for turbulent flow in the form

$$\mathrm{Nu} = C\mathrm{Re}_D^m \mathrm{Pr}^n,$$

where C, m and n are constants that vary with surface geometry and flow characteristics. For the case of a CVV, the temperature gradient of the boundary layer is large and therefore the fluid properties should be evaluated at the film temperature, defined as

$$T_f = \frac{T_w + T_g}{2}, \tag{26}$$

where $T_w$ is expected to vary throughout the combustion cycle of a CVV. This time dependent variation of $T_w$ can be deduced through a simple heat dissipation analysis of the CVV walls to outside ambient conditions.

For a CVV, a correlation is needed for highly turbulent developing flow based on the easily defined characteristic length of the vessel diameter. There are very few Nusselt correlations available with the above mentioned characteristics but an empirical one was proposed by Heiney [HEINEY 78]. Heiney performed experiments with aircraft cannon systems, where ballistic cycles were typically less than 5ms and the cannon walls were rifled. This resulted in a highly turbulent flowfield which never reached steady state conditions and the correlation was based on the cannon diameter. The correlation presented by Heiney was

$$\mathrm{Nu} = 0.05\mathrm{Re}^{0.8}\mathrm{Pr}^{0.4}. \tag{27}$$

This correlation is thought to be particularly suited to CVV wall convective heat transfer because the cannon's ballistic cycle was relatively short and therefore the correlation should also implicitly include some effects due to two phase flow. Most other correlations used in gun system convective heat transfer calculations are applied to single phase, fully developed turbulent flow along the gun barrel after the combustion cycle has finished. A nonideal condition (for CVVs) of Heiney's correlation is that it was determined for one dimensional experimental flow conditions along the cannon barrel. It is assumed the short ballistic cycle did not allow the flow to become fully one dimensional and that three dimensional effects are also implicitly included.

## 6.2 Conductive

The conductive mode of energy transfer occurs whenever there is a conducting medium present combined with temperature gradients. In the gas phase of a CVV's interior, energy transfer is assumed to occur mainly through conduction. This energy transfer can be represented in the gas phase thermal energy equation by Fourier's Law of Conduction

$$q_{cond} = -k_g \frac{\partial T}{\partial x_i}.$$

Similar to the Nusselt number for convective heat transfer, a dimensionless quantity representing the ratio of kinematic viscosity to thermal diffusivity can be prescribed for conductive heat transfer. This quantity is commonly referred to as the Prandtl number

$$\mathrm{Pr} = \frac{\mu c_p}{k_g} \longrightarrow k_g = \frac{\mu c_p}{\mathrm{Pr}}, \tag{28}$$

where $\mu$ is the viscosity and $c_p$ is the constant pressure specific heat of the gas phase. This Prandtl number relation represents a relative measure of momentum and energy transfer. For fluids with $Pr < 1$, temperature diffusion occurs more rapidly than momentum diffusion and vice versa [KAYS 80].

In turbulent flow, a turbulent component of conductive energy transfer exists and the total conductive energy term is defined as

$$\overline{q_{cond}} = -(k_g + k_{g_t})\frac{\partial \overline{T}}{\partial x_i}. \tag{29}$$

This turbulent thermal conductivity can be approximated by the expression

$$k_{g_t} = \frac{\mu_t c_p}{\mathrm{Pr}_t}, \tag{30}$$

where turbulent viscosity $\mu_t$ is determined by the velocity turbulence model and $\mathrm{Pr}_t$ represents the turbulent Prandtl number.

The turbulent Prandtl number has been extensively studied experimentally and was found to remain relatively constant. Typical values are $\mathrm{Pr}_t \approx 0.7$ in the center of pipe flow and $\mathrm{Pr}_t \approx 2$ very close to bounding surfaces [KAYS 80]. The following empirical relationship is commonly used to approximate $\mathrm{Pr}_t$

$$\mathrm{Pr}_t = \frac{1}{\frac{1}{2\mathrm{Pr}_{t\infty}} + C\mathrm{Pe}_t\sqrt{\frac{1}{\mathrm{Pr}_{t\infty}}} - (C\mathrm{Pe}_t)^2\left[1 - \exp\left(-\frac{1}{C\mathrm{Pe}_t\sqrt{\mathrm{Pr}_{t\infty}}}\right)\right]}, \tag{31}$$

where $C = 0.2$ and $\mathrm{Pr}_{t\infty} = 0.86$ for air and $\mathrm{Pe}_t = \frac{\mu_t}{\nu}$ [KAYS 80].

# 7 Turbulence Modeling

Turbulence modeling must be included in a CVV flow model because, in the mass averaged formulation of the gas and solid phase momentum equations, additional unknowns ($\overline{\rho u_i' u_j'}$ and $\overline{u_{i_p}' u_{j_p}'}$) are introduced. These new second order terms, called Reynolds stresses, are responsible for the turbulent transport of momentum and heat and create a situation known as the "Closure Problem".[2]

The following section reviews four main types of turbulence models for the determination of the gas phase Reynolds stresses. The relationship between CVV flow characteristics and the predictive capabilities of different turbulence models is discussed, in order to ascertain the degree of applicability of each reviewed model to a CVV flowfield. The discussion is then used to select an appropriate turbulence model, in the third section, to represent turbulent CVV gas phase motion.

The second section discusses the topic of solid phase turbulent diffusion and a method is selected in order to represent this phenomena in a CVV.

## 7.1 Gas Phase

An infinite set of mean transport equations is required in order to reproduce all the information contained in the instantaneous Navier-Stokes equations and therefore they must be truncated by using experimental data and/or educated guesses. To close the new system of equations (i.e., same number of equations as unknowns), turbulence models must be devised in order to account for the new unknowns in terms of known quantities.

Reynolds averaged turbulence model equations are usually formulated under the incompressibility assumption because if compressibility were to be included in the equations, the result would be more complicated than the incompressible case ($\overline{\rho u_i'}$ correlations appear) and additional turbulence modeling assumptions and equations would be required. For the present CVV analysis the application of Favre (or mass) averaging results in a simpler form for the equations (no $\overline{\rho u_i'}$ terms), which allows for the inclusion of compressibility in the mass averaged turbulence modeling equations without the generation of these additional terms. Therefore the effects of compressibility are included in the conservation equations *and* the turbulence model equations of the present model through mass averaging.

Common turbulence models used to close equation sets are divided in to two main groups. The first group, which consists of Zero, One, Two equation and Algebraic Reynolds Stress Models, assumes a Bousinesque eddy viscosity concept to formulate equations for the Reynolds stresses. The second group, which includes models such as the Reynolds Stress Model, obtains Reynolds stresses from differential equations and uses assumptions to model the resulting third order correlations and unmeasureable quantities. The following review, of the above mentioned turbulence model types, is conducted using the more common Reynolds averaged equations, but it should be recognized that the selected model will be rederived in mass averaged quantities.

---

[2] When transport equations are derived for the second order terms, additional third order unknowns ($\bar{\rho}\overline{u_i' u_j' u_k'}$) appear and so on.

### 7.1.1 Zero Equation Model

Bousinesque argued that random molecular motion, which gives rise to stresses in laminar flow, somewhat superficially resembles velocity fluctuations in turbulent flow. He then suggested turbulent flow could be modeled similar to laminar flow but with a greatly increased viscosity determined by experiment. By using this concept, Reynolds stresses can be related to the local gradient of mean flow quantities by the following equation [RODI 80]

$$-\overline{u_i'u_j'} = \nu_t \left( S_{ij} - \frac{2}{3} k \delta_{ij} \right) , \tag{32}$$

where

$$S_{ij} = \left( \frac{\partial \overline{u_i}}{\partial x_j} + \frac{\partial \overline{u_j}}{\partial x_i} \right) .$$

The term involving the Kronecker delta $\delta_{ij}$ ensures the sum of the three normal stresses is equal to twice the turbulent kinetic energy $k$ (defined as $\frac{1}{2}\overline{u_i'u_i'}$) and the term $S_{ij}$ is commonly referred to as the strain rate tensor.

The turbulent viscosity $\nu_t$ is related to the mean velocity gradient by Prandtl's mixing length hypothesis, which states that $\nu_t$ can be represented by a velocity scale multiplied by a length scale ($\nu_t \propto VL$). His hypothesis employs an algebraic equation for the eddy viscosity which is written as

$$\nu_t = C_\mu l_m^2 \left| \frac{\partial \overline{u_z}}{\partial r} \right| , \tag{33}$$

where empirical data is used to prescribe the distribution of the mixing length $l_m$ over an entire flowfield and the value of the flow constant $C_\mu$.

Many of the assumptions used in the formation of the zero equation model (ZEM), which is comprised of equations 32 and 33, make it inadequate to describe the complex turbulent flowfield inside of a CVV. The basic theoretical flaw is that molecular viscosity is a property of a fluid, but turbulence is a property of a flow. Therefore a laminar description of turbulence will not create a general model of turbulent flow but will instead create a highly empirical one. This is not an acceptable method for turbulent modeling in the case of a CVV because, since it is not a well investigated flow geometry, it would be difficult to include a general description of the complex effects of curvature, separation and heat transfer on the flow constants $C_\mu$ and $l_m$. Also, since the eddy viscosity is not constant across a boundary layer, further empirical modification must be added to the constant $C_\mu$ in order to account for it's variation.

The main drawback of the ZEM is the empirical evaluation of $l_m$ for a specific flowfield. A further drawback is the assumption of isotropic conditions, which is inherent in the model since the eddy viscosity is defined in equation 33 as a scalar quantity. This means that history effects and the convective and diffusive transport of turbulent kinetic energy, which are important in recirculating and curved regions, would not be included in this turbulence model. The assumption of isotropy also implies that strong secondary flows or strain rates, which are also present in regions of recirculation and high curvature, would not represented by the model (note: the development of secondary strain originates from anisotropic flow behavior).

Experimental analysis has also shown difficiencies in the ZEM for complex turbulent flow prediction. As discussed in Section 3.2, Simpson et al. [SIMPSON 81a] determined from experimental data that R-S must be modeled in separated recirculating flow by relating it to the turbulence structure and not to the local mean velocity, which is not the case in the present model. There is also the basic difficulty that the eddy viscosity becomes physically meaningless (i.e. negative) in the backflow region of separated flow. This is further compounded by the ZEM prediction that close to the separation point, where $\partial \overline{u_z}/\partial r$ and $\partial \overline{u_{r\theta}}/\partial r$ go to zero, the eddy viscosity approaches a zero value and therefore R-S also decreases to zero. This is grossly in error since all experiments have show an increase in turbulent transport as the separation point is approached.

The results of the present analysis, which point out the inadequacy of the ZEM for the complex flow of a CVV, were echoed by Lakshminarayana [LAKSHMINAR 86]. He recommended the model should be used only for attached two dimensional boundary layers with mild pressure gradients (i. e. no separation) and felt there was little value for the ZEM in three dimensional complex flows where turbulent transport effects are important.

### 7.1.2 One Equation Model

In order to improve the predictions of the eddy viscosity model, a partial differential equation was devised in order to account for the transport of turbulent kinetic energy $k$. This equation can be derived by simple manipulations of the N-S equations and for simplicity is written in the high Reynolds number form

$$\frac{\partial k}{\partial t} + \overline{Uuk}\frac{\partial k}{\partial x_k} = \frac{1}{\rho}\frac{\partial}{\partial x_j}\left(\frac{\mu_t}{\sigma_k}\frac{\partial k}{\partial x_j}\right) + \frac{\mu_t}{\rho}\left(\frac{\partial \overline{u_i}}{\partial x_j} + \frac{\partial \overline{u_j}}{\partial x_i}\right)\frac{\partial \overline{u_i}}{\partial x_j} - \epsilon\,, \tag{34}$$

where $\sigma_k$ is the effective Prandtl-Schmit number, $\epsilon$ is the isotropic dissipation rate given by $\epsilon \equiv \nu(\overline{\partial u_i'/\partial x_j})^2$ and the turbulent dynamic viscosity $\mu_t$ is given by $\mu_t = \nu_t \rho$.

The above equation allows for the specification of a turbulent velocity scale ($\sqrt{k}$) that does not explicitly rely on the local velocity gradient, but it should be noted that inherent in the above equation is the assumption that the local state of turbulence is characterized by only one velocity scale. The new velocity scale combined with Prandtl's concept of an algebraic equation for mixing length results in the following expression [RODI 80]

$$\nu_t = C_\mu l_m \sqrt{k}\,, \tag{35}$$

where like the ZEM, the distribution of the mixing length ($l_m$) over the entire flowfield and the value of the flow constant ($C_\mu$) are determined empirically.

The one equation model (OEM), which is comprised of equations 32, 34 and 35, still retains the basic drawback of the ZEM (i.e., the algebraic specification of $l_m$). Experimental data must still be used to specify $l_m$ as a function of position over an entire flowfield, thereby creating a turbulence model that is applicable only to specific well investigated flow geometries. This empirical specification of $l_m$ becomes increasingly more complex as one goes from two to three dimensional geometry. Therefore, determination of $l_m$ inside a CVV would be extremely difficult since the flow geometry is neither two dimensional or well investigated. Another difficiency that restricts the present model to simple turbulent flow is the assumption of isotropy because $\nu_t$

is defined as a scalar in equation 35. Also all turbulent transport ($\overline{u_i'u_j'}$) is based on only one velocity scale and all kinetic energy dissipation is isotropic, which is not true in the highly viscous region of near wall flow. Similar to the ZEM definition of $\nu_t$ the OEM definition does not allow for the existence of turbulent secondary flows or strain rates, which are assumed to be present in a CVV.

Still the OEM is an improvement over the previous model because it allows for the turbulent transport of $k$, which means the recirculating regions of separated flow (which contain substantial $k$ diffusion) can be somewhat predicted by the present model. The substitution of $\sqrt{k}$ for the velocity scale also allows the OEM to prescribe a finite positive value to the eddy viscosity in the backflow region of separated flow. Encouraged by this Johnson et al. [JOHNSON 84] investigated and compared the predictions of the ZEM and OEM for a two dimensional separated flow. Their results showed the prediction of the mean velocity profile was better by the OEM than the ZEM, which is to be expected since the transport of $k$ is included in the present model. But since the improvement was only marginal for the additional effort of solving a differential equation, the present model is not commonly used.

The above discussion indicates that the present model can be applied only to one or two dimensional simple flows with or without separation and is not suitable for a CVV.

### 7.1.3 Two Equation Model

Researchers and experimenters recognize the characterization of turbulence by one transport equation is not adequate for the prediction of complex turbulent flow. An additional differential equation is required for the turbulent length scale ($l_m$), in order to eliminate the need of specifying $l_m$ as a function of position throughout a flow because $l_m$ is subject to transport processes and history effects similar to $k$. An example of this dependence is mesh generated turbulence, where eddies produced by flow through a fine mesh are convected downstream and their size at any arbitrary downstream position depends on their initial size.

Many groups (e.g., Imperial College and Stanford) have experimented with transport equations for $l_m$ but have met with limited success. Launder et al. [LAUNDER 74] experimented with three different kinds of two equation models. They determined a differential equation based on the kinetic energy dissipation rate $\epsilon$ gave the best results since this equation had practical advantages over length scale based equations and was better behaved when applied to near wall flow. The $\epsilon$ equation for isotropic dissipation can be derived from the N-S equations by appropriate manipulation and is commonly written in the following form

$$\frac{\partial \epsilon}{\partial t} + \overline{u_k}\frac{\partial \epsilon}{\partial x_k} = \frac{1}{\rho}\frac{\partial}{\partial x_j}\left(\frac{\mu_t}{\sigma_\epsilon}\frac{\partial \epsilon}{\partial x_j}\right) + \frac{C_1\mu_t}{\rho}\frac{\epsilon}{k}\left(\frac{\partial \overline{u_i}}{\partial x_j} + \frac{\partial \overline{u_j}}{\partial x_i}\right)\frac{\partial \overline{u_i}}{\partial x_j} - C_2\frac{\epsilon^2}{k}, \tag{36}$$

where $\sigma_\epsilon, C_1$ and $C_2$ are modeling constants.

The turbulent eddy viscosity can then be related to $k$ and $\epsilon$ by the following equation [LAKSHMINAR 86]

$$\nu_t = C_\mu \frac{k^2}{\epsilon}, \tag{37}$$

where $l_m = k^{3/2}/\epsilon$ and the velocity scale is $\sqrt{k}$. The standard $k-\epsilon$ model (hereafter referred to as the TEM) consists of equations 32, 34, 36 and 37 and is the most commonly used version of two equation models.

The main problem with the TEM is that Reynolds stress is modeled in terms of $k$ and $\nu_t$ (equation 32), which therefore forces the principal axes of $\overline{u_i'u_j'}$ and $S_{ij}$ to be aligned. This means that any sudden magnitude change in the strain rate results in an equal magnitude change in the R-S without the eddy viscosity having time to respond. This type of reaction is true in pure strain flow [TUCKER 68] but not in pure shear flow [CHAMPAGNE 70]. The CVV flowfield is a combination of both flow types, strain in the near wall region due to the presence of the wall and shear in the core region due to the presence of separated shear layers. Tucker et al. determined the TEM underpredicted turbulent production in strain flow and does not produce enough anisotropy in the $\overline{u_i'u_j'}$ terms, which is to be expected since $\nu_t$ is calculated the same for all $\overline{u_i'u_j'}$. Champagne et al. determined that the TEM did not adequately predict shearing and normal stresses in shear flow, which is to be expected due to the assumption of aligned axes in equation 32. Reynolds stated that due to the previous results, the TEM should not be expected to be a general model but it might work well in specific cases by using experimental data to modify the model constants.

There have been a number of TEM modifications introduced in the literature to try to account for the characteristics of complex turbulent flow. These corrections are adequate in many circumstances as long as the turbulent transport terms in the modeling equations are not the dominant physical mechanism [LUMLEY 83]. When turbulent transport terms become the dominant force, the turbulent mechanism in the flow is too complex to be adequately described by a simplifying eddy viscosity assumption.

The complexity of a turbulence model depends upon the relative importance of the turbulent transport terms. For a flow in which transport is not the dominant mechanism, the inertial terms on the left hand side of the N-S equations are balanced mainly by pressure gradients and/or the buoyancy term. Examples of this are natural convection over a vertical flat plate and pressure driven, fully developed pipe flow. For a flowfield in which turbulent transport is the dominant mechanism, the inertial terms are balanced mainly by turbulent transport terms. Examples of this are flows containing severe separation, curvature and also heat transfer, since the thermal energy equation does not contain any pressure or buoyancy terms. It is obvious from the above discussion that a CVV can be defined as a flowfield in which turbulent transport is the dominant mechanism.

The reviews of the TEM predictions compared to experimental data are not encouraging. Nallasamy [NALLASAMY 85] investigated application of the TEM to internal flows and came to the conclusion that model performance becomes poorer as one goes from attached to recirculating, swirling and combusting flows, in that order. Lakshminarayana [LAKSHMINAR 86] reported the following conclusions: 1) the TEM without modification to the model constants fails to capture many of the features associated with complex flow (i.e., curvature, separation, etc...); 2) predicted velocity profiles are not accurate around a separation point (i.e., suddenly applied strain); 3) the model is not good for severely separated and recirculating flow (only mild) and 4) the model is good for attached two dimensional boundary layers. One reason that may account for the TEMs difficulty in predicting separated flow is since little production or convection of $k$ occurs within the near wall region, these terms in the $k$ equation have a negligible influence and therefore $k$ ceases to be dependent on the local mean velocity gradient. The TEM is tied to the mean velocity gradient (see equation 32) and therefore the TEM in the near wall region of separated flow is not very accurate.

The main reason why the TEM is problematic in being successfully applied to complex three dimensional flow is that the model makes the broad assumptions of isotropic dissipation rate and eddy viscosity (equations 32 and 36). The isotropic assumption is widely known to be adequate only for two and three dimensional flows that are mildly complex and therefore in the environment of a CVV, this assumption is not valid. One way for the TEM to account for anisotropic effects is to couple the $k-\epsilon$ equations to algebraic representations of the Reynolds stress equations. This enables more physics to be introduced in to the constants of the TEM without significant additional computational effort. Nallasamy reported [NALLASAMY 85] the TEM performed poorly in simple separated flow over a backward facing step and suggested that the Algebraic Stress Model (ASM) should be used along with a modified TEM in order to account for curvature effects in complex separated flow. The starting point for formulating an algebraic representation of the Reynolds stresses is the Reynolds Stress Model itself.

### 7.1.4 Reynolds Stress Model

In turbulent shear flow, energy is usually produced in one component (e.g., $u_x$ velocity) and then transferred to other components by turbulent processes. This type of energy transfer is present in a CVV since it contains separated shear layers and recirculating regions. The Reynold stresses, which play an important role in energy transfer, develop differently in complex turbulent flow because of the existence of multiple velocity scales [RODI 80] and this should be represented in any general turbulence model. In order to account for the different development of individual Reynolds stresses (i.e., anisotropy) and their transport, an equation has been formulated for the $\overline{u_i'u_j'}$ terms. The exact equation, which can be derived from the N-S equations, is commonly written in the following form [BRADSHAW 81]

$$\begin{aligned}\frac{\partial\overline{u_i'u_j'}}{\partial t}+\overline{u_k}\frac{\partial\overline{u_i'u_j'}}{\partial x_k} &= -\frac{\partial}{\partial x_k}\left(\overline{u_i'u_j'u_k'}+\delta_{ik}\frac{\overline{u_i'P'}}{\rho}+\delta_{ik}\frac{\overline{u_j'P'}}{\rho}-\nu\frac{\partial\overline{u_i'u_j'}}{\partial x_k}\right)\\ &\quad -\left(\overline{u_i'u_k'}\frac{\partial\overline{u_j}}{\partial x_k}+\overline{u_j'u_k'}\frac{\partial\overline{u_i}}{\partial x_k}\right)-2\nu\overline{\frac{\partial u_i'}{\partial x_k}\frac{\partial u_j'}{\partial x_k}}\\ &\quad +\overline{\frac{P'}{\rho}\left(\frac{\partial u_i'}{\partial x_j}+\frac{\partial u_j'}{\partial x_i}\right)}. \qquad (38)\end{aligned}$$

Equation 38 and a modified version of equation 36 forms the basic Reynolds Stress Model (RSM).

The obvious difficiency of the RSM is the need to use an isotropic dissipation equation to determine length scales, but it is commonly assumed anisotropy will be adequately represented by the Reynolds stress equations themselves. Another disadvantage of the RSM is that terms other than the dependent variables (second moments) are generated and they must be approximately modeled in order to close the equation set. These new terms represent the diffusive transport of turbulent fluctuations ($\overline{u_i'u_j'u_k'}$), the dissipation of fluctuations by viscosity ($2\nu\overline{\partial u_i'\partial u_j'}/\partial x_k^2$) and the distribution of fluctuations by pressure ($\overline{u'P'}$ and $\overline{P'\partial u'}/\partial x$ terms). The unknown terms have been modeled by many people but the models of Launder et al. [LAUNDER 75] and Hanjalic et al. [HANJALIC 76] are the most commonly used. The generation or stress production ($\overline{u_k}\partial\overline{u_i'u_j'}/\partial x_k$) does not have to be modeled since in theory it can be measured.

The Reynolds Stress Model (RSM) has a key theoretical advantage over eddy viscosity models since the assumption of alignment of the principal axes ($\overline{u_i'u_j'}$ and $S_{ij}$) is removed (i.e., equation 38 replaces 32). The stress and strain rates are allowed to develop at different rates and this produces a more general turbulence model. Another advantage of the RSM is that terms accounting for curvature, anisotropy and other effects on the Reynold stresses are automatically included (in principle) in the Reynolds stress transport equations. These terms are not included in the TEM scalar equations and must be explicitly added to that model.

There have been many reviews and investigations into the performance of the RSM. The model of Launder et al. has been applied to numerous flow situations, such as turbulence driven secondary flows and curvature induced extra strain rates and they were all well predicted [RODI 80]. In [LAKSHMINAR 86], Lakshminarayana concluded that the RSM should be used in complex flow situations where severe extra strain, large separation, curvature and/or three dimensionality are present, which is important since these characteristics are similar to that inside of a CVV. Nallasamy [NALLASAMY 85] determined, in flow subjected to a sudden pipe expansion, the RSM provided better results than a modified two equation model and that the RSM improved the prediction of heat transfer rates in the redevelopment region. This is an important result since the flow structure of a CVV is of a developing nature. Wilcox et al. [WILCOX 80] determined that the RSM gave a better prediction than a modified TEM in flows with suddenly applied strain and/or shear rates (i.e. separation). He also concluded that the rate of approach to equilibrium and the equilibrium state were accurately predicted.

The main technical difficulty of the RSM is that computational effort can be excessive due to the convection and diffusion terms in the Reynolds stress transport equation. The computational effort can be reduced by replacing these terms in the equation by approximations which in turn result in an algebraic form of the Reynolds stress equation.

### 7.1.5 Algebraic Stress Model

Rodi [RODI 76] recognized the rate of change, convection and diffusion terms in the modeled Reynolds stress equation contained gradients of the Reynolds stresses. He proposed that if the gradients were eliminated by model approximations, equation 38 could be simplified into an algebraic expression and would therefore be easier to solve. Rodi assumed the transport of $\overline{u_i'u_j'}$ was proportional to the transport of $k$, which resulted in a proportionality factor of $\overline{u_i'u_j'}/k$, and he used this assumption to derive the following expression

$$\frac{\overline{u_i'u_j'}}{k} = \frac{2}{3}\delta_{ij} + \frac{1-C_2}{C_1}\left[\frac{\frac{P_{ij}}{\epsilon} - \frac{2}{3}\delta_{ij}\frac{P}{\epsilon}}{1+\frac{1}{C_1}\left(\frac{P}{\epsilon}-1\right)}\right] , \tag{39}$$

where

$$P_{ik} = -\rho\left(\overline{u_i'u_j'}\frac{\partial \overline{u_k}}{\partial x_j} + \overline{u_k'u_j'}\frac{\partial \overline{u_i}}{\partial x_j}\right) \quad , \quad P = -\rho\overline{u_i'u_j'}\frac{\partial \overline{u_i}}{\partial x_j} ,$$

and $C_1$ and $C_2$ represent model constants.

Using the above equation, the following expression for $C_\mu$ (from equation 37) can be derived in order to incorporate into the TEM anisotropy and curvature effects [POURAHMADI 83]

$$C_\mu = (2\sqrt{Q}\cos[(I/3)\cos^{-1}(RQ^{-2/3})] - S/3)^2 , \tag{40}$$

where $Q$, $R$ and $S$ are complicated functions of $P$, $\epsilon$ and velocity gradients. The complete Algebraic Stress Model (ASM) consists of equations 32, 34, 36, 37 and 40.

Many reviews of the predictive capabilities of the ASM have been made. Lakshimarayana [LAKSHMINAR 86] and Nallasamy [NALLASAMY 85] determined that mean velocities, turbulent quantities, curvature and separation predictions are improved over that of the TEM and even regions of secondary and anisotropic three dimensional flow are predicted. They therefore concluded that the best form of the $k-\epsilon$ equations is the ASM.

But even with the above results, the ASM still has some inadequacies. The ASM uses the isotropic dissipation equation but, like the RSM, it is assumed the algebraic stress relation will compensate for any anisotropic behavior. The main drawback of the ASM is the continued use of the eddy viscosity assumption. The isotropic nature of $\nu_t$ is compensated for by equation 40 but the stress and strain rate axes are still aligned and this causes the interaction between stress, strain and eddy viscosity to be ill represented. In flows where turbulent transport (advection and diffusion) of Reynolds stresses is important, the simplifying assumptions of equation 32 and algebraic Reynolds stress modeling can result in poor turbulent flowfield prediction. This means the ASM may not perform well for turbulent developing flow where the local equilibrium assumption is not valid ($P = \epsilon$). This makes the ASM problematic for use in a CVV even though the model is capable of predicting complex turbulent effects. For turbulent flows of a developing nature, both Lakshminarayana and Nallasamy agreed the RSM would be the best choice.

### 7.1.6 Energy Fluctuation

The Reynolds stresses have a counterpart in the averaged energy equation, namely

$$\overline{\rho u_i'' \frac{\partial e''}{\partial x_i}},$$

which represents a local energy flux. This turbulent correlation represents an unknown quantity and turbulent flow experiments have shown that turbulent energy diffusion is substantially larger than laminar diffusion in many regions of the flow. Therefore this term can not be neglected and must also be empirically modeled.

There are many different approaches, similar to the those for $\overline{\rho u_i'' u_j''}$, that can be used to solve for the unknown energy flux in terms of known quantities. Higher order models such as the $k-\epsilon$ model of Nagano et al. [NAGANO 88] for energy flux or the energy flux p.d.e. of Launder [LAUNDER 88] provide a more detailed description but their main drawback for CVV flow is the need for numerous additional modeling constants. At the present time, the structure of CVV flow is largely unmeasured and there is little experimental data to help determine correct values of the constants. Therefore the simpler approach of using a turbulent Prandtl number model [BRADSHAW 81] will be implemented for a CVV, which is presented in section 7.3.

## 7.2 Solid Phase

It is only natural to assume the turbulent nature of the CVV must initiate, to a certain degree, turbulence in the solid phase as well. In particular, gas phase turbulence could result in the dispersion of the discrete solid phase due to diffusion [HARLOW 75], which in turn would have an effect on grain motion and distribution.

There are very few existing turbulence models available for the determination of solid phase turbulent velocity fluctuations. One such model was proposed by Abbas et al. [ABBAS 81] where a solid phase diffusion velocity was calculated by an approximate method and added to the mean particle velocity. This model has not been extensively tested and does not accurately reproduce the driving mechanism for particle turbulent diffusion. Therefore turbulent velocity fluctuation is neglected in the momentum equations of the solid phase for the present CVV analysis.

The main objective of solid phase turbulence modeling is to determine the degree of particle turbulent diffusion and a much simpler and more fundamental method, which bypasses the determination of solid phase velocity fluctuation, can be employed. Dukowicz [DUKOWICZ] and Madabhushi et al. [MADABHUSHI 91] recommend modeling the turbulent diffusion of the particle phase by subjecting it to the instantaneous rather than the mean velocity field of the gas phase. The instantaneous velocity can then be employed in the interphase drag force, which represents the driving mechanism for particle motion. The interphase drag relation of section 5.3 including turbulent diffusion effects is presented in the following section.

## 7.3 CVV Turbulence Model

The previous review of common gas phase turbulence models indicates the ASM is the most economical choice for a CVV. The RSM and the ASM are both expected to give superior predictions, in CVV complex turbulent flow, when compared to the other presented turbulence models but the ASM is of a less computational nature than the RSM. The one problem with the ASM is that since a CVV is not a well investigated flow geometry, the numerous turbulence modeling constants can not be easily validated for CVV flow. Therefore it is more practical to first apply a less complicated turbulence model which relys on fewer modeling constants.

The TEM is the next obvious choice for a CVV because it still allows somewhat for the prediction of flow separation and recirculation. One further advantage of initially applying the TEM is it can be easily modified into the ASM without major structural changes to the existing code. Therefore by first employing the TEM, the potential for a higher degree of modeling exists, which can easily be incorporated by the addition of the ASM assumptions.

The TEM of section 7.1.3 can be applied to the CVV gas phase by rederiving the equations in terms of Favre averaged quantities. The Bousinesque relation 32 in mass averaged variables is achieved by multiplying both sides of the equation by $\rho$ and then mass averaging to get

$$-\overline{\rho u_i'' u_j''} = \mu_t \left( \frac{\partial \widetilde{u_i}}{\partial x_j} + \frac{\partial \widetilde{u_j}}{\partial x_i} - \frac{2}{3}\bar{\rho} k \delta_{ij} \right) \tag{41}$$

where the density weighted turbulent kinetic energy is defined as $k = \frac{\overline{\rho u_i'' u_i''}}{2}$

The two equation model selected for a CVV is the low Reynolds number formulation proposed by Nagano et al. [NAGANO 88]. The following set of equations is the mass averaged version of Nagano's model. For a derivation see Appendix C.

$k$ Equation

$$\frac{\partial}{\partial t}(\epsilon \bar{\rho} k) + \frac{\partial}{\partial x_i}(\epsilon \bar{\rho} \widetilde{u_i} k) = -\varepsilon \overline{\rho u_i'' u_j''} \frac{\partial \widetilde{u_j}}{\partial x_i} + \frac{\partial}{\partial x_i}\left[ \varepsilon \left( \mu + \frac{\mu_t}{\sigma_k} \right) \frac{\partial k}{\partial x_i} \right] - \varepsilon \epsilon$$

$$- 2\mu\varepsilon \left( \frac{\partial \sqrt{k}}{\partial x_i} \right)^2 \tag{42}$$

### $\varepsilon$ Equation

$$\frac{\partial}{\partial t}(\varepsilon\overline{\rho}\epsilon) + \frac{\partial}{\partial x_i}(\varepsilon\overline{\rho}\widetilde{u_i}\epsilon) = -C_{\epsilon 1}\theta_1 \frac{\epsilon}{k} \varepsilon\overline{\rho u_i'' u_j''} \frac{\partial \widetilde{u_j}}{\partial x_i} + \frac{\partial}{\partial x_i}\left[\varepsilon\left(\mu + \frac{\mu_t}{\sigma_\epsilon}\right)\frac{\partial \epsilon}{\partial x_i}\right]$$
$$- C_{\epsilon 2}\theta_2 \varepsilon \frac{\epsilon^2}{k} + \mu\mu_t(1-\theta_\mu)\varepsilon\overline{\rho}\left(\frac{\partial^2 \widetilde{u_j}}{\partial x_i \partial x_k}\right)^2 \tag{43}$$

where

$$\mu_t = C_\mu \theta_\mu \frac{k^2}{\epsilon}$$

and $C_\mu = 0.09$, $C_{\epsilon 1} = 1.45$, $C_{\epsilon 2} = 1.9$, $\sigma_k = 1.0$, $\sigma_\epsilon = 1.3$, $\theta_1 = 1.0$, $\theta_\mu = \left(1 - \exp\left(\frac{-\mathrm{Re}_y}{26.5}\right)\right)^2$, $\theta_2 = 1 - 0.3\exp\left(-\mathrm{Re}_t\right)^2$, $\mathrm{Re}_y = \frac{u_* y}{\nu}$ and $\mathrm{Re}_t = \frac{k^2}{\nu\epsilon}$.

### Energy Fluctuation

$$\overline{\rho u_i'' \frac{\partial e''}{\partial x_i}} = \frac{\mu_t}{\mathrm{Pr}_t}\frac{\partial \widetilde{e}}{\partial x_i}, \tag{44}$$

where the turbulent Prandtl number is modeled by the simple algebraic expression given in section 6.2.

### Turbulent Particle Diffusion

The interphase drag relation can be redefined to include the effects of turbulent diffusion on the solid phase by the relation

$$f_i = f_{i_s} + \beta\varepsilon_p \left( \frac{DU_i}{Dt} - \frac{Du_{i_p}}{Dt_p} \right). \tag{45}$$

The empirical steady state drag dependence on the flowfield for a packed bed is given by

$$f_{i_s} = \frac{\varepsilon_p}{D_p}(U_i - u_{i_p})^2 \left\{ 1.75 + 150\frac{\varepsilon_p}{\varepsilon \mathrm{Re}_{i_p}} \right\}, \tag{46}$$

where $U_i (= \widetilde{u_i} + u_i'')$ represents the instantaneous gas phase velocity and $\mathrm{Re}_{i_p} = \frac{\rho|U_i - u_{i_p}|\varepsilon D_p}{\mu}$.

The constitutive law which represents the manner in which particle drag decreases as the degree of fluidization increases can also be redefined by

$$\frac{f_{i_s}}{\frac{\varepsilon_p}{D_p}\rho(U_i - u_{i_p})^2} = \begin{cases} 1.75 + 150\frac{\varepsilon_p}{\varepsilon \mathrm{Re}_{i_p}} & \varepsilon \leq \varepsilon_0 \\ \left(1.75 + 150\frac{\varepsilon_p}{\varepsilon \mathrm{Re}_{i_p}}\right)\left(\frac{\varepsilon_p}{1-\varepsilon_1}\frac{\varepsilon_0}{\varepsilon}\right)^{0.45} & \varepsilon_0 \leq \varepsilon \leq \varepsilon_1, \\ 0.3 & \varepsilon_1 \leq \varepsilon \leq 1 \end{cases} \quad (47)$$

where the porosity values ($\varepsilon_0$ and $\varepsilon_1$) are the same as in section 5.3.

# 8 Future Work

A complete model for the determination of CVV convective wall heat transfer has now been formulated. The next step of the project is to determine appropriate boundary conditions which can represent a CVV experiment, decide upon a particular numerical scheme for the model equations, select a grid configuration for the CVV interior and produce a computer program of the model. This program will then be used to predict desired CVV characteristics such as vessel wall heat transfer, propellant burn rates and propellant grain distribution.

## References

[ABBAS 81] Abbas, A.S., Kous, S.S. and Lockwood, F.C., 1981, *The Prediction of Particle Laden Gas Flows*, Proceedings of the 18th Symposium on Combustion, Combustion Institute, Pittsburg, PA, pp. 1427–1438.

[ADAMS 88] Adams, E.W. and Johnston, J.P., 1988, *Flow Structure in the Near-Wall Zone of a Turbulent Separated Flow*, AIAA Journal, Vol. 26, pp. 932–939.

[AMC 64] AMC, 1964, *The Engineering Design Handbook — Explosive Series — Solid Propellants Part One*, AAMC Pamphlet, AMCP 706–175.

[BERGER 90] Berger, F.C., 1990, *Heat Transfer from Propellant Burning in a Constant Volume Chamber*, Masters Thesis, UTIAS.

[BRADSHAW 81] Bradshaw, P., Cebeci, T. and Whitelaw, J.H., 1981, *Engineering Calculation Methods for Turbulent Flow*, The London Academic Press.

[BURMEISTER 83] Burmeister, L.C., 1983, *Convective Heat Transfer*, John Wiley and Sons, p. 63.

[CHAMPAGNE 70] Champagne, F.H., Harris, V.G. and Corrsin, S., 1970, *Experiments on nearly Homogeneous Turbulent Shear Flow*, Journal of Fluid Mechanics, Vol. 41, pp. 81–139.

[DUKOWICZ] Dukowicz, J.K., 1980, *A Particle-Fluid Numerical Model for Liquid Sprays*, Journal of Computational Physics, Vol. 35, pp. 229–253.

[FAVRE 65] Favre, A., 1965, *Equations des Gaz Turbulents Compressibles*, Journal de Mechanique, Vol. 4, pp. 361–390 and 392–421.

[GOORAY 85] Gooray, A.M., Watkins, C.B. and Aung, W., 1985, *Turbulent Heat Transfer Computations for Rearward Facing Steps and Sudden Pipe Expansions*, Journal of Heat Transfer, Vol. 107, pp. 70–76.

[GÕRTLER 40] Görtler, H., 1940, *On the Three Dimensional instability of Laminar Boundary Layers on Concave Walls*, NACA TM 137.

[GOUGH 79a] Gough, P.S., 1978, *Modeling of Two-Phase Flow in Guns*, Interior Ballistics of Guns, Progress in Astronautics and Aeronautics, Vol. 66, pp. 176–196.

[GOUGH 79b] Gough, P.S. and Zwarts, F.J., 1979, *Modeling Heterogeneous Two-Phase Reacting Flow*, AIAA Journal, Vol. 17, pp. 17–25.

[GOUGH 83] Paul Gough Associates Inc., 1983, *Two-Dimensional, Two-Phase Modeling of Multi-Increment Bagged Artillery Charges*, ARBRL–CR–00503.

[GRANT 58] Grant, H., 1958, *The Large Eddies of Turbulent Motion*, Journal of Fluid Mechanics, Vol. 4, pp. 149–190.

[HANJALIC 76] Hanjalic, K. and Launder, B.E., 1976, *Contribution Towards a Reynolds Stress Closure for Low Reynolds Number Turbulence*, Journal of Fluid Mechanics, Vol. 74, pp. 593–610.

[HARLOW 75] Harlow, F.H. and Amsden, A.A., 1975, *Numerical Calculation of Multiphase Fluid Flow*, Journal of Computational Physics, Vol. 17, pp. 19–52.

[HEINEY 78] Heiney, O.K., 1978, *Ballistics Applied to Rapid-Fire Guns*, Interior Ballistics of Guns, Progress in Astronautics and Aeronautics, Vol. 66, pp. 87–109.

[HOFFMANN 85] Hoffmann, P.H., Muck, K.C. and Bradshaw, P., 1985, *The Effect of Concave Surface Curvature on Turbulent Boundary Layers*, Journal of Fluid Mechanics, Vol. 161, pp. 371–403.

[HOMSY 83] Homsy, G.M., 1983, *A Survey of Some Results in the Mathematical Theory of Fluidization*, Theory of Dispersed Multiphase Flow, Academic Press, pp. 57–71.

[HUNT 79] Hunt, I.A. and Joubert, P.N., 1979, *Effects of Small Streamline Curvature on Turbulent Duct Flow*, Journal of Fluid Mechanics, Vol. 91, pp. 633–659.

[INGER 77] Inger, G.R., 1977, *Three Dimensional Heat and Mass Transfer Effects across High Speed Reattaching Flows*, AIAA Journal, Vol. 15, pp. 383–389.

[JOHNSON 84] Johnson, D. A. and King, L. S., 1984, *A New Turbulence Closure Model for Boundary Layer Flows with Strong Adverse Pressure Gradients and Separation*, AIAA Paper 84–0175.

[KAYS 80] Kays, W.M. and Crawford, M.E., 1980, *Convective Heat and Mass Transfer*, McGraw-Hill Series in Mechanical Engineering, pp. 105, 226–228.

[KRIER 73] Krier, H., Shimpi, S.A. and Adams, M.J., 1973, *Interior Ballistic Predictions Using Data from Closed and Variable Volume Simulators*, TR–AAE–73–6.

[KRIER 76] Krier, H., Rajan, S. and Van Tassell, W.F., 1976, *Flame-Spreading and Combustion in Packed Beds of Propellant Grains*, AIAA Journal, Vol. 14, pp. 301–309.

[KRIER 78] Krier, H. and Gokhale, S.S., 1978, *Modeling of Convective Mode Combustion Through Granulated Propellant to Predict Detonation Transition*, AIAA Journal, Vol. 16, pp. 177–183.

[KRIER 79] Krier, H. and Adams, M.J., 1979, *An Introduction to Gun Interior Ballistics and a Simplified Ballistic Code*, AIAA Journal, Vol. 17, pp. 1–40.

[KUO 76] Kuo, K.K., Koo, J.H., Davis, T.R. and Coates, G.R., 1976, *Transient Combustion in Mobile Gas-Permeable Propellants*, Acta Astronautica, Vol. 3, pp. 573–591.

[LAKSHMINAR 86] Lakshminarayana, B., 1986, *Turbulence Modeling for Complex Shear Flows*, AIAA Journal, Vol. 24, pp. 1900–1917.

[LAUNDER 74] Launder, B.E. and Spalding, D.B., 1974, *The Numerical Computation of Turbulent Flow*, Computational Methods in Applied Mechanics and Engineering, Vol. 3, pp. 269–289.

[LAUNDER 75] Launder, B.E., Reece, G.J. and Rodi, W., 1975, *Progress in the Development of a Reynolds Stress Turbulence Closure*, Journal of Fluid Mechanics, Vol. 68, pp. 537–566.

[LAUNDER 88] Launder, B.E., 1988, *On the Computation of Convective Heat Transfer in Complex Turbulent Flows*, Journal of Heat Transfer, Vol. 110, pp. 1112–1128.

[LUMLEY 83] Lumley, J.L., 1983, *Turbulence Modeling*, Journal of Applied Mechanics, Vol. 50, pp. 1097–1103.

[MABEY 90] Mabey, D.G., 1990, *Effects of Heat Transfer on Aerodynamics and Possible Implications for Wind Tunnel Tests*, Progress in Aerospace Science, Vol. 27, pp. 267–303.

[MADABHUSHI 91] Madabhushi, R.K., Sabnis, J.S., de Jong, F.J. and Gibeling, H.J., 1991, *Calculation of the Two-Phase Aft-Dome Flowfield in the Solid Rocket Motors*, AIAA Journal of Propulsion, Vol. 7, pp. 178–184.

[MOSER 87] Moser, R.D. and Moin, P., 1987, *The Effects of Curvature in Wall-Bounded Turbulent Flows*, Journal of Fluid Mechanics, Vol. 175, pp. 479–510.

[NAGANO 88] Nagano, Y. and Kim, C., 1988, *A Two-Equation Model for Heat Transport in Wall Turbulent Shear Flows*, Journal of Heat Transfer, Vol. 110, pp. 583–589.

[NALLASAMY 85] Nallasamy, M., 1985, *A Critical Evaluation of Various Turbulence Models as Applied to Internal FLuid Flows*, NASA TP 2474.

[PANTON] Panton, R., 1968, *Flow Properties for the Continuum Viewpoint of a Non-Equilibrium Gas-Particle Mixture*, Journal of Fluid Mechanics, Vol. 31, pp. 273–303.

[PAPAMOSCH 88] Papamoschou, D. and Roshko, A., 1988, *The Compressible Turbulent Shear Layer: an Experimental Study*, Journal of Fluid Mechanics, Vol. 197, pp. 453–477.

[PETRIE 86] Petrie, H.L., Samimy, M. and Addy, A.L., 1986, *Compressible Separated Flows*, AIAA Journal, Vol. 24, pp. 1971–1978.

[POURAHMADI 83] Pourahmadi, F. and Humphrey, J.A.C., 1983, *Prediction of Curved Channel Flow with an Extended $k$–$\epsilon$ Model of Turbulence*, AIAA Journal, Vol. 21, pp. 1365–1373.

[RICHMOND 91] Richmond, M.C. and Patel, V.C., 1991, *Convex and Concave Surface Curvature Effects in Wall-Bounded Turbulent Flows*, AIAA Journal, Vol. 29, pp. 895–902.

[REID 87] Reid, R.C., Prausnitz, J.M. and Poling, B.E., 1987, *The Properties of Gases and Liquids–Fourth Edition*, Ch. 9–10, McGraw-Hill.

[ROBBINS 76] Robbins, F.W. and Horst, A.W., 1976, *Numerical Simulation of Closed Bomb Performance based on BLAKE Code Thermodynamic Data*, Naval Ordinance Station, Indian Head, Md.

[RODI 76] Rodi, W., 1976, *A New Algebraic Relation for Calculating Reynolds Stresses*, ZAMM, Vol. 56, pp. 219–221.

[RODI 80] Rodi, W., 1980, *Turbulence Models for Environmental Problems*, Prediction Methods for Turbulent Flows, The Hemisphere Publishing Corporation, pp. 259-350.

[SCHLICHTING 87] Schlichting, H., 1987, *Boundary-Layer Theory*, A McGraw-Hill Classic Textbook.

[SERPA 87] Serpa, J.M., Lessmann, R.C. and Haigist, W.M., 1987, *Turbulent Separated and Reattached Flow over a Curved Surface*, Journal of Fluids Engineering, Vol. 109, pp. 403–409.

[SHILOH 81] Shiloh, K., Shivaprasad, B.G. and Simpson, R. L., 1981, *The Structure of a Separating Turbulent Boundary Layer. Part 3: Transverse Velocity Measurements*, Journal of Fluid Mechanics, Vol. 113, pp. 75–90.

[SIMPSON 81a] Simpson, R.L., Chew, Y.T. and Shivaprasad, B.G., 1981, *The Structure of a Separating Turbulent Boundary Layer. Part: Mean Flow and Reynolds Stresses*, Journal of Fluid Mechanics, Vol. 113, pp. 23–51.

[SIMPSON 81b] Simpson, R.L., Chew, Y.T. and Shivaprasad, B.G., 1981, *The Structure of a Separating Turbulent Boundary Layer. Part 2: Higher Order Turbulence Results*, Journal of Fluid Mechanics, Vol. 113, pp. 53–73.

[SMITS 79] Smits, A.J., Young, S.T.B. and Bradshaw, P., 1979, *The Effect of Short Regions of High Surface Curvature on Turbulent Boundary Layers*, Journal of Fluid Mechanics, Vol. 94, pp. 209–242.

[TENNEKES 72] Tennekes, H. and Lumley, J.L., 1972, *A First Course in Turbulence*, The MIT Press.

[TUCKER 68] Tucker, H.J. and Reynolds, A.J., 1968, *The Distortion of Turbulence by Irrotational Plane Strain*, Journal of Fluid Mechanics, Vol. 32, pp. 657–673.

[WILCOX 80] Wilcox, D.C. and Rubesin, M.W., 1980, ***Progress in Turbulence Modeling for Complex Flow Fields Including Effects of Compressibility***, NASA–TP–1517.

[ŽUKAUSKAS 87] Žukauskas, A., Šlančiauskas, A. and Karni, J., 1987, ***Heat Transfer in Turbulent Fluid Flows***, The Hemisphere Publishing Corporation.

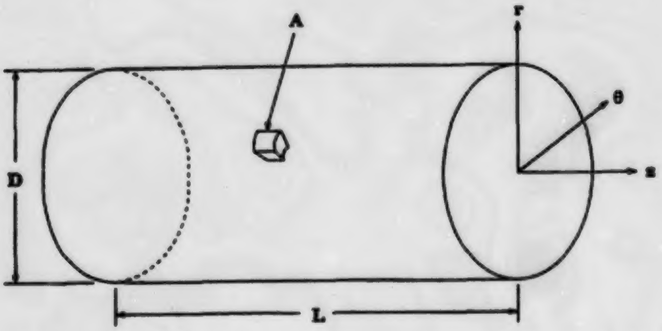

Figure 17: Constant Volume Vessel.

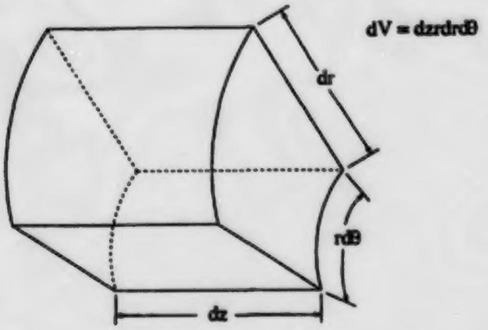

Figure 18: Elemental Control Volume A.

# A Governing Equations

### Nomenclature of Following Derivations

i) $\varepsilon$ — fraction of gas phase contained in control volume (C.V.)

ii) $\varepsilon_p = (1-\varepsilon)$ — fraction of solid phase contained in C.V.

iii) $\rho$ — variable gas phase density

iv) $\rho_p$ — constant solid phase density

v) $\sigma_i$ — stress on solid phase at interface surface

vi) $\Sigma_i$ — interface surface between phases

vii) $A_i$ — external boundary surface of gas phase C.V.

viii) $A_{i_p}$ — external boundary surface of solid phase C.V.

ix) $\dot{d}$ — rate of regression of solid phase surface due to combustion

x) $f_i$ — velocity dependent interphase drag

xi) $M_p$ — total mass of solid phase in C.V.

xii) $n$ — outward pointing unit normal to surface

xiii) $R$ — stress tensor reflecting solid phase load due to external pressure

xiv) $s_i$ — velocity of boundary surface $A_i$ or interface surface $\Sigma_i$

xv) $S_p$ — total surface area of solid phase in C.V.

xvi) $\dot{S}_{mass}$ — source of mass due to grain burning
xvii) $\dot{S}_{mom}$ — source of momentum due to grain burning
xviii) $\dot{S}_{ht}$ — source of energy due to interphase heat transfer
xix) $\dot{S}_{ch}$ — source of energy due to chemical combustion
xx) $u_t$ — instantaneous velocity of gas phase
xxi) $u_{t_p}$ — instantaneous velocity of solid phase
xxii) $V_g = \varepsilon V$ — volume of gas phase in C.V.
xxiii) $V_p = \varepsilon_p V$ — volume of solid phase in C.V.
xxiv) $(X)_{z+dz} = (X)_z + \frac{\partial}{\partial z}(X)_z dz$

## A.1 Conservation of Mass for the Gas Phase

i) write the mass conservation equation

$$\sum(mass)_{in} - \sum(mass)_{out} + (mass\ source\ term) = d(mass\ increase)$$

ii) insert corresponding terms from figure 19 in to the above expression

$$\begin{aligned}(\varepsilon\rho u dr r d\theta)_z + (\varepsilon\rho v dz r d\theta)_r + (\varepsilon\rho w dz dr)_\theta - (\varepsilon\rho u dr r d\theta)_{z+dz} - (\varepsilon\rho v dz r d\theta)_{r+dr} \\ - (\varepsilon\rho w dz dr)_{\theta+d\theta} + \dot{S}_{mass} dz dr r d\theta = \frac{\partial}{\partial t}(\varepsilon\rho dz dr r d\theta)\end{aligned}$$

iii) expand terms and simplify

$$\begin{aligned}-\frac{\partial}{\partial z}(\varepsilon\rho u) dr r d\theta dz - \frac{\partial}{\partial r}(\varepsilon\rho v r) dz d\theta dr - \frac{\partial}{\partial \theta}(\varepsilon\rho w) dz dr d\theta \\ + \dot{S}_{mass} dz dr r d\theta = \frac{\partial}{\partial t}(\varepsilon\rho) dz dr r d\theta\end{aligned}$$

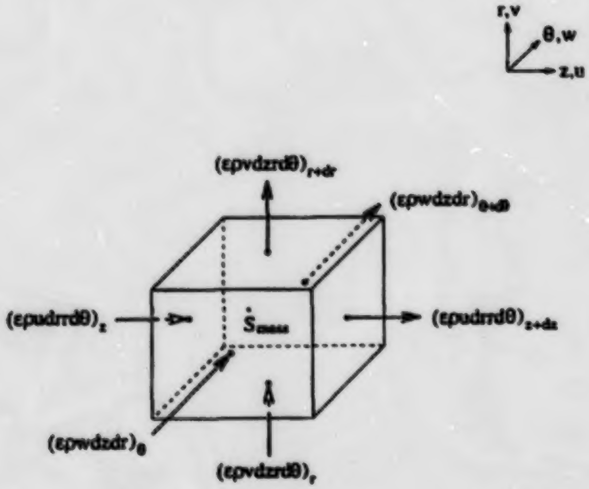

Figure 19: Mass Flux Through Control Volume.

iv) substitute Gough's definition of $\dot{S}_{mass}$

$$\dot{S}_{mass} = \varepsilon_p \rho_p^2 \dot{d} \frac{S_p}{M_p}$$

v) divide by $dzrdrd\theta$ to get

$$\frac{\partial}{\partial t}(\varepsilon\rho) + \frac{\partial}{\partial z}(\varepsilon\rho u) + \frac{1}{r}\frac{\partial}{\partial r}(\varepsilon\rho v r) + \frac{\partial}{r\partial\theta}(\varepsilon\rho w) = \varepsilon_p \rho_p^2 \dot{d} \frac{S_p}{M_p} \tag{48}$$

## A.2 Conservation of Mass for the Solid Phase

i) write the mass conservation equation

$$d(mass\ increase) = \sum (mass)_{in} - \sum (mass)_{out}$$

ii) noting that solid phase in C.V. is bounded by $(A_p U \Sigma)$,

$$\begin{aligned} \frac{d}{dt}\int_{V_p} \rho_p dV = \int_{(A_p U\Sigma)_z} \rho_p (s_z - u_p) n dA + \int_{(A_p U\Sigma)_r} \rho_p (s_r - v_p) n dA \\ + \int_{(A_p U\Sigma)_\theta} \rho_p (s_\theta - w_p) n dA \end{aligned}$$

LHS
iii) using $\int_{V_p} \rho_p dV = \varepsilon_p \rho_p dzrdrd\theta$ gives

$$+\rho_p \frac{\partial}{\partial t}(\varepsilon_p) dzrdrd\theta \tag{49}$$

RHS
iv) expansion of integrals gives

$$\begin{aligned} &+ \int_{A_{z_p}} \rho_p (s_z - u_p) n dA + \int_{A_{r_p}} \rho_p (s_r - v_p) n dA + \int_{A_{\theta_p}} \rho_p (s_\theta - w_p) n dA \\ &+ \int_{\Sigma_z} \rho_p (s_z - u_p) n dA + \int_{\Sigma_r} \rho_p (s_r - v_p) n dA + \int_{\Sigma_\theta} \rho_p (s_\theta - w_p) n dA \end{aligned}$$

v) integrating $A_{i_p}$ integrals and recognizing $s_i = 0$ at $A_{i_p}$ gives

$$-\rho_p \frac{\partial}{\partial z}(\varepsilon_p u_p) dzrdrd\theta - \rho_p \frac{\partial}{\partial r}(\varepsilon_p v_p r) drdzd\theta - \rho_p \frac{\partial}{\partial \theta}(\varepsilon_p w_p) d\theta dzdr \tag{50}$$

vi) integrating $s_i = u_{i_p} + n\dot{d}$ at $\Sigma_i$ reduces 3 $\int_{\Sigma_i}$ to one mass sink term

$$-\varepsilon_p \rho_p^2 \dot{d} \frac{S_p}{M_p} dzrdrd\theta \tag{51}$$

vii) combining eqns 49, 50, 51 and dividing by $\rho_p dzrdrd\theta$ gives

$$\frac{\partial}{\partial t}(\varepsilon_p) + \frac{\partial}{\partial z}(\varepsilon_p u_p) + \frac{1}{r}\frac{\partial}{\partial r}(\varepsilon_p v_p r) + \frac{\partial}{r\partial\theta}(\varepsilon_p w_p) = -\varepsilon_p \rho_p \dot{d}\frac{S_p}{M_p} \tag{52}$$

which is in effect a P.D.E. for $\varepsilon_p$

## A.3 Conservation of Momentum for the Gas Phase

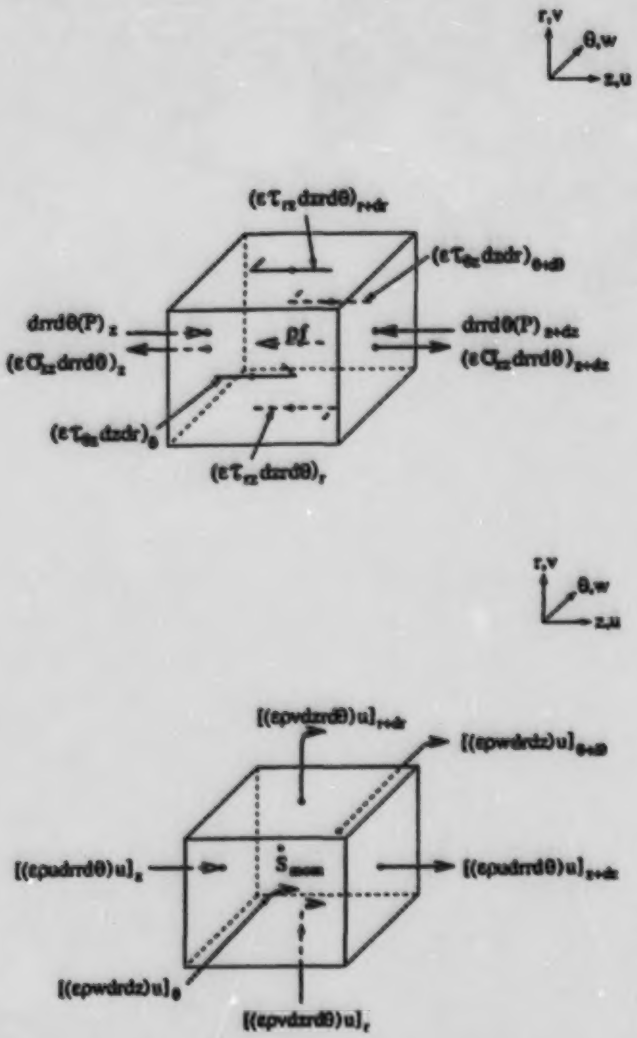
r,v
θ,w
z,u
(ετ_rz dzrdθ)_r+dr
(ετ_θz dzdr)_θ+dθ
drrdθ(P)_z
(εσ_zz drrdθ)_z
ρf
drrdθ(P)_z+dz
(εσ_zz drrdθ)_z+dz
(ετ_θz dzdr)_θ
(ετ_rz dzrdθ)_r
r,v
θ,w
z,u
[(ερvdzrdθ)u]_r+dr
[(ερwdrdz)u]_θ+dθ
[(ερudrrdθ)u]_z
Ṡ_mom
[(ερudrrdθ)u]_z+dz
[(ερwdrdz)u]_θ
[(ερvdzrdθ)u]_r

Figure 20: *Z* Momentum Flux Through Control Volume.

i) write the momentum conservation equation for the $z$ direction

$$\begin{aligned}\sum(momentum)_{in} - \sum(momentum)_{out} + (momentum\ source\ term)\\ = d(momentum\ increase) - \sum(forces)_{C.V.}\end{aligned}$$

LHS
ii) insert corresponding terms from figure 20 in LHS of conservation equation

$$\begin{aligned}&[(\varepsilon\rho u drrd\theta)u]_z + [(\varepsilon\rho v dzrd\theta)u]_r + [(\varepsilon\rho w dzdr)u]_\theta - [(\varepsilon\rho u drrd\theta)u]_{z+dz}\\ &- [(\varepsilon\rho v dzrd\theta)u]_{r+dr} - [(\varepsilon\rho w dzdr)u]_{\theta+d\theta} + \dot{S}_{zmom}dzdrrd\theta\end{aligned}$$

iii) expand terms and simplify

$$\begin{aligned}&-\frac{\partial}{\partial z}(\varepsilon\rho u^2)drrd\theta dz - \frac{\partial}{\partial r}(\varepsilon\rho uvr)dzd\theta dr - \frac{\partial}{\partial\theta}(\varepsilon\rho uw)dzdrd\theta\\ &+ \dot{S}_{zmom}dzdrrd\theta\end{aligned}$$

iv) substitute Gough's definition of $\dot{S}_{zmom}$

$$\dot{S}_{zmom} = \varepsilon_p\rho_p^2 u_p\dot{d}\frac{S_p}{M_p}$$

v) divide by $dzrdrd\theta$ to get

$$-\frac{\partial}{\partial z}(\varepsilon\rho u^2) - \frac{1}{r}\frac{\partial}{\partial r}(\varepsilon\rho uvr) - \frac{\partial}{r\partial\theta}(\varepsilon\rho uw) + \varepsilon_p\rho_p^2 u_p\dot{d}\frac{S_p}{M_p} \tag{53}$$

RHS
vi) insert corresponding terms from figure 21 in RHS of conservation equation

$$\begin{aligned}&\frac{\partial}{\partial t}[(\varepsilon\rho dzdrrd\theta)u] + \rho f_z dzdrrd\theta + \int_{V_g}(\nabla P)_z dV + (\varepsilon\sigma_{zz}drrd\theta)_z\\ &+ (\varepsilon\tau_{rz}dzrd\theta)_r + (\varepsilon\tau_{\theta z}dzdr)_\theta - (\varepsilon\sigma_{zz}drrd\theta)_{z+dz}\\ &- (\varepsilon\tau_{rz}dzrd\theta)_{r+dr} - (\varepsilon\tau_{\theta z}dzdr)_{\theta+d\theta}\end{aligned}$$

vii) expand terms and simplify

$$\begin{aligned}&\frac{\partial}{\partial t}(\varepsilon\rho u)dzdrrd\theta + \rho f_z dzdrrd\theta + \varepsilon\frac{\partial P}{\partial z}dzdrrd\theta - \frac{\partial}{\partial z}(\varepsilon\sigma_{zz})drrd\theta dz\\ &- \frac{\partial}{\partial r}(\varepsilon\tau_{rz}r)dzd\theta dr - \frac{\partial}{\partial\theta}(\varepsilon\tau_{\theta z})dzdrd\theta\end{aligned}$$

Figure 21: $Z$ Forces on Control Volume.

viii) divide by $dzrdrd\theta$ to get

$$\frac{\partial}{\partial t}(\varepsilon\rho u) + \rho f_z + \varepsilon\frac{\partial P}{\partial z} - \frac{\partial}{\partial z}(\varepsilon\sigma_{zz}) - \frac{1}{r}\frac{\partial}{\partial r}(\varepsilon\tau_{rz}r) - \frac{\partial}{r\partial\theta}(\varepsilon\tau_{\theta z}) \tag{54}$$

## MOMENTUM EQUATIONS

ix) combine equations 53 and 54 to get

$$\begin{aligned}\frac{\partial}{\partial t}(\varepsilon\rho u) + \frac{\partial}{\partial z}(\varepsilon\rho u^2) + \frac{1}{r}\frac{\partial}{\partial r}(\varepsilon\rho uvr) + \frac{\partial}{r\partial\theta}(\varepsilon\rho uw) &= -\rho f_z - \varepsilon\frac{\partial P}{\partial z} \\ &+ \frac{\partial}{\partial z}(\varepsilon\sigma_{zz}) + \frac{1}{r}\frac{\partial}{\partial r}(\varepsilon\tau_{rz}r) + \frac{\partial}{r\partial\theta}(\varepsilon\tau_{\theta z}) + \varepsilon_p\rho_p^2 u_p\dot{d}\frac{S_p}{M_p}\end{aligned} \tag{55}$$

x) similar equations can be derived for the $r$ and $\theta$ directions to get

$$\begin{aligned}\frac{\partial}{\partial t}(\varepsilon\rho v) + \frac{\partial}{\partial z}(\varepsilon\rho uv) + \frac{1}{r}\frac{\partial}{\partial r}(\varepsilon\rho v^2 r) + \frac{\partial}{r\partial\theta}(\varepsilon\rho vw) &= -\rho f_r - \varepsilon\frac{\partial P}{\partial r} \\ &+ \frac{\partial}{\partial z}(\varepsilon\tau_{rz}) + \frac{1}{r}\frac{\partial}{\partial r}(\varepsilon\sigma_{rr}r) + \frac{\partial}{r\partial\theta}(\varepsilon\tau_{r\theta}) + \varepsilon_p\rho_p^2 v_p\dot{d}\frac{S_p}{M_p}\end{aligned} \tag{56}$$

$$\begin{aligned}\frac{\partial}{\partial t}(\varepsilon\rho w) + \frac{\partial}{\partial z}(\varepsilon\rho uw) + \frac{1}{r}\frac{\partial}{\partial r}(\varepsilon\rho vwr) + \frac{\partial}{r\partial\theta}(\varepsilon\rho w^2) &= -\rho f_\theta - \varepsilon\frac{\partial P}{r\partial\theta} \\ &+ \frac{\partial}{\partial z}(\varepsilon\tau_{\theta z}) + \frac{1}{r}\frac{\partial}{\partial r}(\varepsilon\tau_{\theta r}r) + \frac{\partial}{r\partial\theta}(\varepsilon\sigma_{\theta\theta}) + \varepsilon_p\rho_p^2 w_p\dot{d}\frac{S_p}{M_p}\end{aligned} \tag{57}$$

where stress terms are given by [SCHLICHTING 87]:

$$\begin{aligned}\sigma_{zz} &= -\frac{2}{3}\mu\left[\frac{\partial u}{\partial z} + \frac{1}{r}\frac{\partial(vr)}{\partial r} + \frac{\partial w}{r\partial\theta}\right] + 2\mu\frac{\partial u}{\partial z} \\ \sigma_{rr} &= -\frac{2}{3}\mu\left[\frac{\partial u}{\partial z} + \frac{1}{r}\frac{\partial(vr)}{\partial r} + \frac{\partial w}{r\partial\theta}\right] + 2\frac{\mu}{r}\frac{\partial(vr)}{\partial r} \\ \sigma_{\theta\theta} &= -\frac{2}{3}\mu\left[\frac{\partial u}{\partial z} + \frac{1}{r}\frac{\partial(vr)}{\partial r} + \frac{\partial w}{r\partial\theta}\right] + 2\mu\frac{\partial w}{r\partial\theta} \\ \tau_{z\theta} = \tau_{\theta z} &= \mu\left(\frac{\partial w}{\partial z} + \frac{\partial u}{r\partial\theta}\right) \\ \tau_{zr} = \tau_{rz} &= \mu\left(\frac{1}{r}\frac{\partial(ur)}{\partial r} + \frac{\partial v}{\partial z}\right) \\ \tau_{r\theta} = \tau_{\theta r} &= \mu\left(\frac{1}{r}\frac{\partial(wr)}{\partial r} + \frac{\partial v}{r\partial\theta}\right)\end{aligned}$$

## A.4 Conservation of Momentum for the Solid Phase

i) write the momentum conservation equation for $z$ direction

$$(momentum\ increase) + \sum(momentum)_{out} - \sum(momentum)_{in} = \\ + \sum(forces)_{C.V.}$$

ii) noting that solid phase in C.V. is bounded by $(A_p U \Sigma)$, gives

$$\frac{d}{dt}\int_{V_p} \rho_p u_p dV - \int_{(A_p U\Sigma)_z} \rho_p(s_z - u_p) n dA - \int_{(A_p U\Sigma)_r} \rho_p(s_r - v_p) n dA \\ - \int_{(A_p U\Sigma)_\theta} \rho_p(s_\theta - w_p) n dA = \int_{\Sigma_z} \sigma_z n dA \\ - \int_{(A_p U\Sigma)_z} R n dA - \int_{(A_p U\Sigma)_z} P n dA + \int_{V_p} \rho_p g_z dV$$

LHS
iii) integrating first term similar to section A.2 gives

$$\rho_p \frac{\partial}{\partial t}(\epsilon_p u_p) dz r dr d\theta$$

iv) expansion of integrals of last 3 terms gives

$$- \int_{A_{z_p}} \rho_p u_p(s_z - u_p) n dA - \int_{A_{r_p}} \rho_p u_p(s_r - v_p) n dA - \int_{A_{\theta_p}} \rho_p u_p(s_\theta - w_p) n dA \\ - \int_{\Sigma_z} \rho_p u_p(s_z - u_p) n dA - \int_{\Sigma_r} \rho_p u_p(s_r - v_p) n dA - \int_{\Sigma_\theta} \rho_p u_p(s_\theta - w_p) n dA$$

v) integrating $A_{i_p}$ integrals and recognizing $s_i = 0$ at $A_{i_p}$ gives

$$\rho_p \frac{\partial}{\partial z}(\epsilon_p u_p^2) dz r dr d\theta + \rho_p \frac{\partial}{\partial r}(\epsilon_p u_p v_p r) dr dz d\theta + \rho_p \frac{\partial}{\partial \theta}(\epsilon_p u_p w_p) d\theta dz dr$$

vi) integrating $s_i = u_{i_p} + n\dot{d}$ at $\Sigma_i$ reduces 3 $\Sigma_i$ integrals to one momentum sink term

$$+\epsilon_p \rho_p^2 u_p \dot{d} \frac{S_p}{M_p} dz r dr d\theta$$

vii) addition of all LHS terms gives

$$\rho_p \frac{\partial}{\partial t}(\epsilon_p u_p) dz r dr d\theta + \rho_p \frac{\partial}{\partial z}(\epsilon_p u_p^2) dz r dr d\theta + \rho_p \frac{\partial}{\partial r}(\epsilon_p u_p v_p r) dr dz d\theta \\ + \rho_p \frac{\partial}{\partial \theta}(\epsilon_p u_p w_p) d\theta dz dr + \epsilon_p \rho_p^2 u_p \dot{d} \frac{S_p}{M_p} dz r dr d\theta \tag{58}$$

**RHS**

viii) first term is considered analytically intractable and is replaced by

$$\rho f_z dzrdrd\theta$$

ix) the second term is integrated to give

$$-\frac{\partial}{\partial z}(\varepsilon_p R)dzrdrd\theta$$

x) the third term can be rewritten and integrated to give

$$-\int_{V_g}(\nabla P)_z dV = -\varepsilon_p \frac{\partial P}{\partial z}dzrdrd\theta$$

xi) the last term can be integrated to give

$$\varepsilon_p \rho_p g_z dzrdrd\theta$$

xii) addition of all RHS terms gives

$$\rho f_z dzrdrd\theta - \frac{\partial}{\partial z}(\varepsilon_p R)dzrdrd\theta - \varepsilon_p \frac{\partial P}{\partial z}dzrdrd\theta + \varepsilon_p \rho_p g_z dzrdrd\theta \tag{59}$$

xiii) combining eqns 58, 59 and dividing by $\rho_p dzrdrd\theta$ gives

$$\begin{aligned}\frac{\partial}{\partial t}(\varepsilon_p u_p) + \frac{\partial}{\partial z}(\varepsilon_p u_p^2) + \frac{1}{r}\frac{\partial}{\partial r}(\varepsilon_p u_p v_p r) + \frac{\partial}{r\partial\theta}(\varepsilon_p u_p w_p) = \\ + \frac{\rho}{\rho_p}f_z - \frac{1}{\rho_p}\frac{\partial}{\partial z}(\varepsilon_p R) - \frac{\varepsilon_p}{\rho_p}\frac{\partial P}{\partial z} + \varepsilon_p g_z - \varepsilon_p \rho_p u_p \dot{d}\frac{S_p}{M_p}\end{aligned} \tag{60}$$

xiv) similar equations can be derived for $r$ and $\theta$ directions to get

$$\begin{aligned}\frac{\partial}{\partial t}(\varepsilon_p v_p) + \frac{\partial}{\partial z}(\varepsilon_p u_p v_p) + \frac{1}{r}\frac{\partial}{\partial r}(\varepsilon_p v_p^2 r) + \frac{\partial}{r\partial\theta}(\varepsilon_p v_p w_p) = \\ + \frac{\rho}{\rho_p}f_r - \frac{1}{\rho_p r}\frac{\partial}{\partial r}(\varepsilon_p r R) - \frac{\varepsilon_p}{\rho_p}\frac{\partial P}{\partial r} + \varepsilon_p g_r - \varepsilon_p \rho_p v_p \dot{d}\frac{S_p}{M_p}\end{aligned} \tag{61}$$

$$\begin{aligned}\frac{\partial}{\partial t}(\varepsilon_p w_p) + \frac{\partial}{\partial z}(\varepsilon_p u_p w_p) + \frac{1}{r}\frac{\partial}{\partial r}(\varepsilon_p v_p w_p r) + \frac{\partial}{r\partial\theta}(\varepsilon_p w_p^2) = \\ + \frac{\rho}{\rho_p}f_\theta - \frac{1}{\rho_p}\frac{\partial}{r\partial\theta}(\varepsilon_p R) - \frac{\varepsilon_p}{\rho_p}\frac{\partial P}{r\partial\theta} + \varepsilon_p g_\theta - \varepsilon_p \rho_p w_p \dot{d}\frac{S_p}{M_p}\end{aligned} \tag{62}$$

## A.5 Conservation of Energy for the Gas Phase

i) write the energy conservation equation neglecting radiation

$$\sum d(energy)_{adv} + \sum d(energy)_{con} + \sum d(stress\ and\ pressure\ work)$$

$$- (\textit{interphase drag work}) - (\textit{heat transfer source term})$$
$$+ (\textit{chemical energy source term}) = d(\textit{energy storage})$$

ENERGY ADVECTION

ii) insert corresponding terms from figure 22 in to change in advection term (energy in - energy out)

$$(\varepsilon \dot{q}_{adv} drrd\theta)_z + (\varepsilon \dot{q}_{adv} dzrd\theta)_r + (\varepsilon \dot{q}_{adv} dzdr)_\theta - (\varepsilon \dot{q}_{adv} drrd\theta)_{z+dz}$$
$$- (\varepsilon \dot{q}_{adv} dzrd\theta)_{r+dr} - (\varepsilon \dot{q}_{adv} dzdr)_{\theta+d\theta}$$

iii) substituting $\dot{q}_{adv} = \rho u_i(e + \frac{u_i^2}{2})$ and simplifying gives

$$-\frac{\partial}{\partial z}[(\varepsilon \rho u(e + \frac{u^2+v^2+w^2}{2})drrd\theta)]dz - \frac{\partial}{\partial r}[(\varepsilon \rho v(e + \frac{u^2+v^2+w^2}{2})dzrd\theta)]dr$$
$$-\frac{\partial}{\partial \theta}[(\varepsilon \rho w(e + \frac{u^2+v^2+w^2}{2})dzdr)]d\theta$$

iv) divide by $dzdrrd\theta$ to get

$$-\frac{\partial}{\partial z}[\varepsilon \rho u(e + \frac{u^2+v^2+w^2}{2})] - \frac{1}{r}\frac{\partial}{\partial r}[\varepsilon \rho v r(e + \frac{u^2+v^2+w^2}{2})]$$
$$- \frac{\partial}{r\partial \theta}[\varepsilon \rho w(e + \frac{u^2+v^2+w^2}{2})] \qquad (63)$$

ENERGY CONDUCTION

v) insert corresponding terms from figure 22 in to change in conduction term

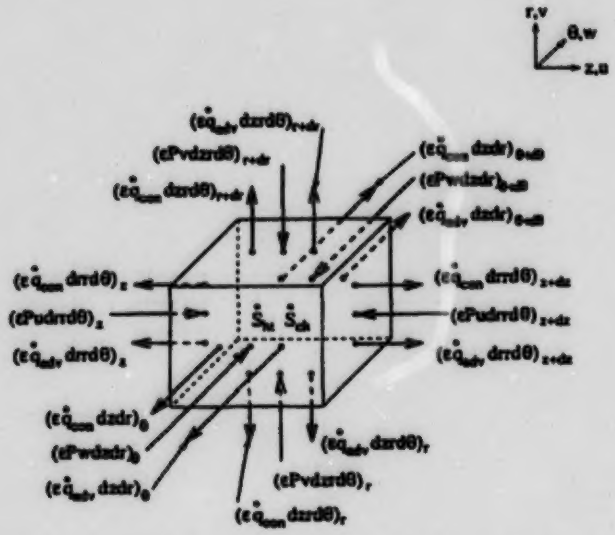
r,v
θ,w
z,u
(εq̇adv dzrdθ)r+dr
(εPvdzrdθ)r+dr
(εq̇con dzrdθ)r+dr
(εq̇con dzdr)θ+dθ
(εPwdzdr)θ+dθ
(εq̇adv dzdr)θ+dθ
(εq̇con drrdθ)z
(εPudrrdθ)z
(εq̇adv drrdθ)z
Ṡht Ṡch
(εq̇con drrdθ)z+dz
(εPudrrdθ)z+dz
(εq̇adv drrdθ)z+dz
(εq̇con dzdr)θ
(εPwdzdr)θ
(εq̇adv dzdr)θ
(εq̇adv dzrdθ)r
(εPvdzrdθ)r
(εq̇con dzrdθ)r

Figure 22: Energy Flux and Pressure Terms on Control Volume.

(energy in - energy out)

$$(\varepsilon\dot{q}_{con}drrd\theta)_z + (\varepsilon\dot{q}_{con}dzrd\theta)_r + (\varepsilon\dot{q}_{con}dzdr)_\theta - (\varepsilon\dot{q}_{con}drrd\theta)_{z+dz}$$
$$- (\varepsilon\dot{q}_{con}dzrd\theta)_{r+dr} - (\varepsilon\dot{q}_{con}dzdr)_{\theta+d\theta}$$

vi) substituting $\dot{q}_{con} = (-k_g\frac{\partial T}{\partial x_i})$ and simplifying gives

$$+\frac{\partial}{\partial z}[(\varepsilon\left(k_g\frac{\partial T}{\partial z}\right)drrd\theta)]dz + \frac{\partial}{\partial r}[(\varepsilon\left(k_g\frac{\partial T}{\partial r}\right)dzrd\theta)]dr$$
$$+ \frac{\partial}{\partial \theta}[(\varepsilon\left(k_g\frac{\partial T}{r\partial \theta}\right)dzdr)]d\theta$$

vii) substitute $k_g \equiv \frac{\mu c_p}{\Pr}$ and divide by $dzdrrd\theta$ to get

$$\frac{\partial}{\partial z}\left[\varepsilon\frac{\mu c_p}{\Pr}\frac{\partial T}{\partial z}\right] + \frac{1}{r}\frac{\partial}{\partial r}\left[\varepsilon\frac{\mu c_p}{\Pr}r\frac{\partial T}{\partial r}\right] + \frac{\partial}{r\partial\theta}\left[\varepsilon\frac{\mu c_p}{\Pr}\frac{\partial T}{r\partial\theta}\right] \tag{64}$$

## STRESS AND PRESSURE WORK

viii) insert corresponding terms from figures 22, 23 in stress and pressure terms

$$(\varepsilon\sigma_{zz}udrrd\theta)_{z+dz} + (\varepsilon\tau_{zr}vdrrd\theta)_{z+dz} + (\varepsilon\tau_{z\theta}wdrrd\theta)_{z+dz} - (\varepsilon\sigma_{zz}udrrd\theta)_z$$
$$- (\varepsilon\tau_{zr}vdrrd\theta)_z - (\varepsilon\tau_{z\theta}wdrrd\theta)_z + (\varepsilon\sigma_{rr}vdzrd\theta)_{r+dr}$$
$$+ (\varepsilon\tau_{rz}udzrd\theta)_{r+dr} + (\varepsilon\tau_{r\theta}wdzrd\theta)_{r+dr} - (\varepsilon\sigma_{rr}vdzrd\theta)_r$$
$$- (\varepsilon\tau_{rz}udzrd\theta)_r - (\varepsilon\tau_{r\theta}wdzrd\theta)_r + (\varepsilon\sigma_{\theta\theta}wdzdr)_{\theta+d\theta}$$
$$+ (\varepsilon\tau_{\theta z}udzdr)_{\theta+d\theta} + (\varepsilon\tau_{\theta r}vdzdr)_{\theta+d\theta} - (\varepsilon\sigma_{\theta\theta}wdzdr)_\theta$$

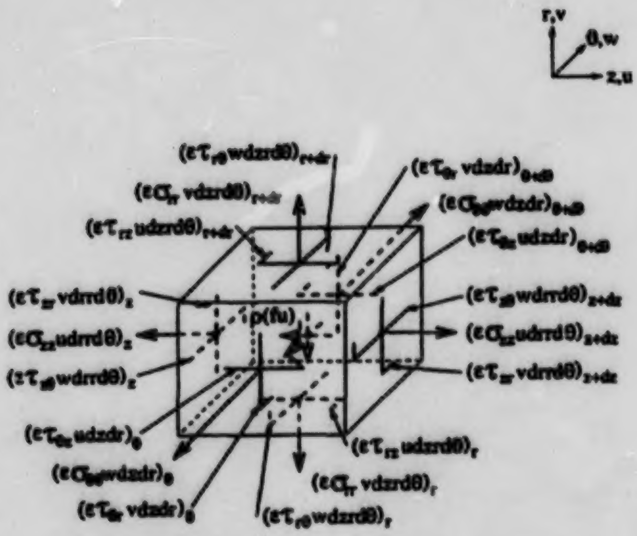
r,v
θ,w
z,u
$(\varepsilon\tau_{r\theta}wdzrd\theta)_{r+dr}$
$(\varepsilon\tau_{\theta r}vdzdr)_{\theta+d\theta}$
$(\varepsilon\sigma_{rr}vdzrd\theta)_{r+dr}$
$(\varepsilon\sigma_{\theta\theta}wdzdr)_{\theta+d\theta}$
$(\varepsilon\tau_{rz}udzrd\theta)_{r+dr}$
$(\varepsilon\tau_{\theta z}udzdr)_{\theta+d\theta}$
$(\varepsilon\tau_{zr}vdrrd\theta)_z$
$(\varepsilon\tau_{z\theta}wdrrd\theta)_{z+dz}$
p(fu)
$(\varepsilon\sigma_{zz}udrrd\theta)_z$
$(\varepsilon\sigma_{zz}udrrd\theta)_{z+dz}$
$(z\tau_{z\theta}wdrrd\theta)_z$
$(\varepsilon\tau_{zr}vdrrd\theta)_{z+dz}$
$(\varepsilon\tau_{\theta z}udzdr)_\theta$
$(\varepsilon\tau_{rz}udzrd\theta)_r$
$(\varepsilon\sigma_{\theta\theta}wdzdr)_\theta$
$(\varepsilon\sigma_{rr}vdzrd\theta)_r$
$(\varepsilon\tau_{\theta r}vdzdr)_\theta$
$(\varepsilon\tau_{r\theta}wdzrd\theta)_r$

Figure 23: Work Terms on Control Volume.

$$
\begin{aligned}
&- (\varepsilon\tau_{\theta z} udzdr)_\theta - (\varepsilon\tau_{\theta r} vdzdr)_\theta + (\varepsilon Pudrrd\theta)_z \\
&+ (\varepsilon Pvdzrd\theta)_r + (\varepsilon Pwdzdr)_\theta - (\varepsilon Pudrrd\theta)_{z+dz} \\
&- (\varepsilon Pvdzrd\theta)_{r+dr} - (\varepsilon Pwdzdr)_{\theta+d\theta}
\end{aligned}
$$

ix) expand terms and simplify

$$
\begin{aligned}
&\frac{\partial}{\partial z}(\varepsilon\sigma_{zz} udrrd\theta dz + \varepsilon\tau_{zr} vdrrd\theta dz + \varepsilon\tau_{z\theta} wdrrd\theta dz) \\
&\qquad + \frac{\partial}{\partial r}(\varepsilon\sigma_{rr} vdzrd\theta dr + \varepsilon\tau_{rz} udzrd\theta dr + \varepsilon\tau_{r\theta} wdzrd\theta dr) \\
&\qquad + \frac{\partial}{\partial\theta}(\varepsilon\sigma_{\theta\theta} wdzdrd\theta + \varepsilon\tau_{\theta z} udzdrd\theta + \varepsilon\tau_{\theta r} vdzdrd\theta) \\
&\qquad - \frac{\partial(\varepsilon Pu)}{\partial z} dzdrrd\theta - \frac{\partial(\varepsilon Pvr)}{\partial r} dzdrd\theta - \frac{\partial(\varepsilon Pw)}{\partial\theta} dzdrrd\theta
\end{aligned}
$$

x) divide by $dzrdrd\theta$ to get

$$
\begin{aligned}
&\frac{\partial}{\partial z}(\varepsilon\sigma_{zz} u + \varepsilon\tau_{zr} v + \varepsilon\tau_{z\theta} w) + \frac{1}{r}\frac{\partial}{\partial r}(\varepsilon\sigma_{rr} vr + \varepsilon\tau_{rz} ur + \varepsilon\tau_{r\theta} wr) \\
&\qquad + \frac{\partial}{r\partial\theta}(\varepsilon\sigma_{\theta\theta} w + \varepsilon\tau_{\theta z} u + \varepsilon\tau_{\theta r} v) \\
&\qquad - \frac{\partial(\varepsilon Pu)}{\partial z} - \frac{1}{r}\frac{\partial(\varepsilon Pvr)}{\partial r} - \frac{\partial(\varepsilon Pw)}{r\partial\theta}
\end{aligned} \tag{65}
$$

## SOURCE TERMS AND INTERPHASE DRAG

xi) insert corresponding terms from figures 22, 23 in drag and source terms

$$
-\rho(f_z u_p + f_r v_p + f_\theta w_p)dzdrrd\theta - \dot{S}_{ht} dzdrrd\theta + \dot{S}_{ch} dzdrrd\theta
$$

xii) substitute Gough's definition of $\dot{S}_{ch}$ and $\dot{S}_{ht}$

$$
\begin{aligned}
\dot{S}_{ch} &= \varepsilon_p \rho_p^2 \dot{d}\left(e_p + \frac{P}{\rho_p} + \frac{u_p^2 + v_p^2 + w_p^2}{2}\right)\frac{S_p}{M_p} \\
\dot{S}_{ht} &= \varepsilon_p \rho_p^2 q \frac{S_p}{M_p}
\end{aligned}
$$

xiii) divide by $dzrdrd\theta$ to get

$$
-\rho(f_z u_p + f_r v_p + f_\theta w_p) - \varepsilon_p \rho_p^2 q \frac{S_p}{M_p} + \varepsilon_p \rho_p^2 \dot{d}\left(e_p + \frac{P}{\rho_p} + \frac{u_p^2 + v_p^2 + w_p^2}{2}\right)\frac{S_p}{M_p} \tag{66}
$$

## ENERGY STORAGE

xiv) write the energy storage term

$$
\frac{\partial}{\partial t}[\varepsilon\rho(e + \frac{u^2 + v^2 + w^2}{2})dzdrrd\theta]
$$

**xv)** divide by $dzrdrd\theta$ to get

$$\frac{\partial}{\partial t}[\varepsilon\rho(e+\frac{u^2+v^2+w^2}{2})] \tag{67}$$

## ENERGY EQUATION

**xvi)** combine equations 63, 64, 65, 66 and 67 to get

$$\begin{aligned}
&\frac{\partial}{\partial t}[\varepsilon\rho(e+\frac{u^2+v^2+w^2}{2})]+\frac{\partial}{\partial z}[\varepsilon\rho u(e+\frac{u^2+v^2+w^2}{2})]\\
&\quad+\frac{1}{r}\frac{\partial}{\partial r}[\varepsilon\rho vr(e+\frac{u^2+v^2+w^2}{2})]+\frac{\partial}{r\partial\theta}[\varepsilon\rho w(e+\frac{u^2+v^2+w^2}{2})]=\\
&\quad-\frac{\partial(\varepsilon Pu)}{\partial z}-\frac{1}{r}\frac{\partial(\varepsilon Pvr)}{\partial r}-\frac{\partial(\varepsilon Pw)}{r\partial\theta}+\frac{\partial}{\partial z}\left[\varepsilon\frac{\mu c_p}{\mathrm{Pr}}\frac{\partial T}{\partial z}\right]\\
&\quad+\frac{1}{r}\frac{\partial}{\partial r}\left[\varepsilon\frac{\mu c_p}{\mathrm{Pr}}r\frac{\partial T}{\partial r}\right]+\frac{\partial}{r\partial\theta}\left[\varepsilon\frac{\mu c_p}{\mathrm{Pr}}\frac{\partial T}{r\partial\theta}\right]-\rho(f_z u_p+f_r v_p+f_\theta w_p)\\
&\quad+\frac{\partial}{\partial z}(\varepsilon\sigma_{zz}u+\varepsilon\tau_{zr}v+\varepsilon\tau_{z\theta}w)+\frac{1}{r}\frac{\partial}{\partial r}(\varepsilon\sigma_{rr}vr+\varepsilon\tau_{rz}ur+\varepsilon\tau_{r\theta}wr)\\
&\quad+\frac{\partial}{r\partial\theta}(\varepsilon\sigma_{\theta\theta}w+\varepsilon\tau_{\theta z}u+\varepsilon\tau_{\theta r}v)-\varepsilon_p\rho_p^2 q\frac{S_p}{M_p}\\
&\quad+\varepsilon_p\rho_p^2\dot{d}\left(e_p+\frac{P}{\rho_p}+\frac{u_p^2+v_p^2+w_p^2}{2}\right)\frac{S_p}{M_p}
\end{aligned}$$

**xvii)** subtract eqns 48, $u$ times 55, $v$ times 56 and $w$ times 57 from above equation to get the thermal energy equation

$$\begin{aligned}
&\rho\varepsilon\left(\frac{\partial e}{\partial t}+u\frac{\partial e}{\partial z}+\frac{v}{r}\frac{\partial(er)}{\partial t}+w\frac{\partial e}{r\partial\theta}\right)=P\left(\frac{\partial}{\partial z}(\varepsilon u)+\frac{1}{r}\frac{\partial}{\partial r}(\varepsilon vr)+\frac{\partial}{r\partial\theta}(\varepsilon w)\right)\\
&\quad+\rho(f_z(u-u_p)+f_r(v-v_p)+f_\theta(w-w_p))+\frac{\partial}{\partial z}\left[\varepsilon\frac{\mu c_p}{\mathrm{Pr}}\frac{\partial T}{\partial z}\right]\\
&\quad+\frac{1}{r}\frac{\partial}{\partial r}\left[\varepsilon\frac{\mu c_p}{\mathrm{Pr}}r\frac{\partial T}{\partial r}\right]+\frac{\partial}{r\partial\theta}\left[\varepsilon\frac{\mu c_p}{\mathrm{Pr}}\frac{\partial T}{r\partial\theta}\right]+\varepsilon\tau_{zr}\left(\frac{\partial v}{\partial z}+\frac{1}{r}\frac{\partial(ur)}{\partial r}\right)\\
&\quad+\varepsilon\tau_{z\theta}\left(\frac{\partial w}{\partial z}+\frac{\partial u}{r\partial\theta}\right)+\varepsilon\tau_{\theta r}\left(\frac{\partial v}{r\partial\theta}+\frac{1}{r}\frac{\partial(wr)}{\partial r}\right)\\
&\quad+\varepsilon\left(\sigma_{zz}\frac{\partial u}{\partial z}+\frac{\sigma_{rr}}{r}\frac{\partial(vr)}{\partial r}+\sigma_{\theta\theta}\frac{\partial w}{r\partial\theta}\right)-\varepsilon_p\rho_p^2 q\frac{S_p}{M_p}\\
&\quad+\varepsilon_p\rho_p^2\dot{d}\left(e_p+\frac{P}{\rho_p}+\frac{u_p^2+v_p^2+w_p^2}{2}\right)\frac{S_p}{M_p}+\varepsilon_p\rho_p^2\dot{d}\frac{S_p}{M_p}\left(e-\frac{u^2+v^2+w^2}{2}\right)\\
&\quad+u\varepsilon_p\rho_p^2 u_p\dot{d}\frac{S_p}{M_p}+v\varepsilon_p\rho_p^2 v_p\dot{d}\frac{S_p}{M_p}+w\varepsilon_p\rho_p^2 w_p\dot{d}\frac{S_p}{M_p}
\end{aligned} \tag{68}$$

## B Favre-Reynolds Decomposition

TIME AVERAGING RULES

$u_{i_p} = \overline{u_{i_p}} + u'_{i_p}$

$\rho = \overline{\rho} + \rho'$

$P = \overline{P} + P'$

$T = \overline{T} + T'$

$\overline{f + g} = \overline{f} + \overline{g}$

$\overline{f\overline{g}} = \overline{f}\overline{g}$

$\overline{\frac{\partial f}{\partial x_i}} = \frac{\partial \overline{f}}{\partial x_i}$

$\overline{u'_i} = 0$

$\overline{\overline{u_i}} = \widetilde{u_i}$

MASS AVERAGING RULES

$u_i = \widetilde{u_i} + u''_i$

$e = \tilde{e} + e''$

$f = \tilde{f} + f''$

$\widetilde{u_i} = \frac{\overline{\rho u_i}}{\overline{\rho}}$

$\overline{\rho u''_i} = 0$

$\overline{u''_i} = -\frac{\overline{\rho' u'_i}}{\overline{\rho}}$

$\overline{u_i} + u'_i = \widetilde{u_i} + u''_i$

$\widetilde{\rho u_i} = \overline{\rho u_i} + \overline{\rho' u'_i}$

Note: fluctuation of $\varepsilon$ and $\mu$ are neglected

## B.1 Conservation of Mass for the Gas Phase

i) use equation 48 derived in Appendix A

$$\frac{\partial}{\partial t}(\epsilon\rho) + \frac{\partial}{\partial z}(\epsilon\rho u) + \frac{1}{r}\frac{\partial}{\partial r}(\epsilon\rho v r) + \frac{\partial}{r\partial\theta}(\epsilon\rho w) = \epsilon_p\rho_p^2\dot{d}\frac{S_p}{M_p}$$

ii) decompose equation according to averaging rules

$$\begin{aligned}\frac{\partial}{\partial t}\epsilon(\overline{\rho}+\rho') + \frac{\partial}{\partial z}\epsilon(\overline{\rho}+\rho')(\tilde{u}+u'') + \frac{1}{r}\frac{\partial}{\partial r}\epsilon r(\overline{\rho}+\rho')(\tilde{v}+v'')\\ + \frac{\partial}{r\partial\theta}\epsilon(\overline{\rho}+\rho')(\tilde{w}+w'') = \epsilon_p\rho_p^2\dot{d}\frac{S_p}{M_p}\end{aligned}$$

iii) time average the above equation

$$\begin{aligned}\overline{\frac{\partial}{\partial t}\epsilon(\overline{\rho}+\rho') + \frac{\partial}{\partial z}\epsilon(\overline{\rho}+\rho')(\tilde{u}+u'') + \frac{1}{r}\frac{\partial}{\partial r}\epsilon r(\overline{\rho}+\rho')(\tilde{v}+v'')}\\ \overline{+\frac{\partial}{r\partial\theta}\epsilon(\overline{\rho}+\rho')(\tilde{w}+w'')} = \epsilon_p\rho_p^2\dot{d}\frac{S_p}{M_p}\end{aligned}$$

iv) simplify equation using time averaging rules

$$\begin{aligned}\frac{\partial}{\partial t}(\epsilon\overline{\rho}) + \frac{\partial}{\partial z}\epsilon(\overline{\overline{\rho}\tilde{u}} + \overline{\overline{\rho}u''} + \overline{\rho'u''}) + \frac{1}{r}\frac{\partial}{\partial r}\epsilon r(\overline{\overline{\rho}\tilde{v}} + \overline{\overline{\rho}v''} + \overline{\rho'v''})\\ + \frac{\partial}{r\partial\theta}\epsilon(\overline{\overline{\rho}\tilde{w}} + \overline{\overline{\rho}w''} + \overline{\rho'w''}) = \epsilon_p\rho_p^2\dot{d}\frac{S_p}{M_p}\end{aligned}$$

v) using the relation $\overline{\overline{\rho}u_i''} + \overline{\rho'u_i''} = \overline{\rho u_i''} = 0$ gives

$$\frac{\partial}{\partial t}(\epsilon\overline{\rho}) + \frac{\partial}{\partial z}(\epsilon\overline{\rho}\tilde{u}) + \frac{1}{r}\frac{\partial}{\partial r}(\epsilon\overline{\rho}\tilde{v}r) + \frac{\partial}{r\partial\theta}(\epsilon\overline{\rho}\tilde{w}) = \epsilon_p\rho_p^2\dot{d}\frac{S_p}{M_p} \qquad (69)$$

## B.2 Conservation of Mass for the Solid Phase

i) use equation 52 derived in Appendix A

$$\frac{\partial}{\partial t}(\epsilon_p) + \frac{\partial}{\partial z}(\epsilon_p u_p) + \frac{1}{r}\frac{\partial}{\partial r}(\epsilon_p v_p r) + \frac{\partial}{r\partial\theta}(\epsilon_p w_p) = -\epsilon_p\rho_p\dot{d}\frac{S_p}{M_p}$$

ii) decompose equation according to averaging rules

$$\frac{\partial}{\partial t}(\epsilon_p) + \frac{\partial}{\partial z}\epsilon_p(\overline{u_p}+u_p') + \frac{1}{r}\frac{\partial}{\partial r}\epsilon_p r(\overline{v_p}+v_p') + \frac{\partial}{r\partial\theta}\epsilon_p(\overline{w_p}+w_p') = -\epsilon_p\rho_p\dot{d}\frac{S_p}{M_p}$$

iii) expand terms and use averaging rules to get

$$\frac{\partial}{\partial t}(\varepsilon_p) + \frac{\partial}{\partial z}(\varepsilon_p \overline{u_p}) + \frac{1}{r}\frac{\partial}{\partial r}(\varepsilon_p \overline{v_p} r) + \frac{\partial}{r\partial\theta}(\varepsilon_p \overline{w_p}) = -\varepsilon_p \rho_p \dot{d} \frac{S_p}{M_p} \tag{70}$$

## B.3 Conservation of Momentum for the Gas Phase

i) use equation 55 derived in Appendix A

$$\begin{aligned}
\frac{\partial}{\partial t}(\varepsilon\rho u) + \frac{\partial}{\partial z}(\varepsilon\rho u^2) + \frac{1}{r}\frac{\partial}{\partial r}(\varepsilon\rho u v r) + \frac{\partial}{r\partial\theta}(\varepsilon\rho u w) &= -\rho f_z - \varepsilon\frac{\partial P}{\partial z} \\
&+ \frac{\partial}{\partial z}(\varepsilon\sigma_{zz}) + \frac{1}{r}\frac{\partial}{\partial r}(\varepsilon\tau_{rz} r) + \frac{\partial}{r\partial\theta}(\varepsilon\tau_{\theta z}) + \varepsilon_p\rho_p^2 u_p \dot{d}\frac{S_p}{M_p}
\end{aligned}$$

ii) decompose equation according to averaging rules

$$\begin{aligned}
\frac{\partial}{\partial t}\varepsilon(\overline{\rho} + \rho')(\tilde{u} + u'') + \frac{\partial}{\partial z}\varepsilon(\overline{\rho} + \rho')(\tilde{u} + u'')^2 + \frac{1}{r}\frac{\partial}{\partial r}\varepsilon r(\overline{\rho} + \rho')(\tilde{u} + u'')(\tilde{v} + v'') \\
+ \frac{\partial}{r\partial\theta}\varepsilon(\overline{\rho} + \rho')(\tilde{u} + u'')(\tilde{w} + w'') = -(\overline{\rho} + \rho')(\tilde{f}_z + f_z'') \\
- \varepsilon\frac{\partial}{\partial z}(\overline{P} + P') + \frac{\partial}{\partial z}(\varepsilon\sigma_{zz}) + \frac{1}{r}\frac{\partial}{\partial r}(\varepsilon\tau_{rz} r) + \frac{\partial}{r\partial\theta}(\varepsilon\tau_{\theta z}) \\
+ \varepsilon_p\rho_p^2(\overline{u_p} + u_p')\dot{d}\frac{S_p}{M_p}
\end{aligned}$$

iii) expand terms and use the averaging method of B.1 to get

$$\begin{aligned}
\frac{\partial}{\partial t}(\varepsilon\overline{\rho}\tilde{u}) + \frac{\partial}{\partial z}(\varepsilon\overline{\rho}\tilde{u}^2) + \frac{1}{r}\frac{\partial}{\partial r}(\varepsilon\overline{\rho}\tilde{u}\tilde{v} r) + \frac{\partial}{r\partial\theta}(\varepsilon\overline{\rho}\tilde{u}\tilde{w}) &= -\overline{\rho}\tilde{f}_z - \varepsilon\frac{\partial\overline{P}}{\partial z} \\
&+ \frac{\partial}{\partial z}[\varepsilon(\overline{\sigma}_{zz} - \overline{\rho u''^2})] + \frac{1}{r}\frac{\partial}{\partial r}[\varepsilon(\overline{\tau}_{rz} - \overline{\rho u'' v'' r})] \\
&+ \frac{\partial}{r\partial\theta}[\varepsilon(\overline{\tau}_{\theta z} - \overline{\rho u'' w''})] + \varepsilon_p\rho_p^2\overline{u_p}\dot{d}\frac{S_p}{M_p}
\end{aligned} \tag{71}$$

iv) similar equations can be derived for the $r$ and $\theta$ directions to get

$$\begin{aligned}
\frac{\partial}{\partial t}(\varepsilon\overline{\rho}\tilde{v}) + \frac{\partial}{\partial z}(\varepsilon\overline{\rho}\tilde{u}\tilde{v}) + \frac{1}{r}\frac{\partial}{\partial r}(\varepsilon\overline{\rho}\tilde{v}^2 r) + \frac{\partial}{r\partial\theta}(\varepsilon\overline{\rho}\tilde{v}\tilde{w}) &= -\overline{\rho}\tilde{f}_r - \varepsilon\frac{\partial\overline{P}}{\partial r} \\
&+ \frac{\partial}{\partial z}[\varepsilon(\overline{\tau}_{rz} - \overline{\rho u'' v''})] + \frac{1}{r}\frac{\partial}{\partial r}[\varepsilon(\overline{\sigma}_{rr} - \overline{\rho v''^2 r})] \\
&+ \frac{\partial}{r\partial\theta}[\varepsilon(\overline{\tau}_{r\theta} - \overline{\rho v'' w''})] + \varepsilon_p\rho_p^2\overline{v_p}\dot{d}\frac{S_p}{M_p}
\end{aligned} \tag{72}$$

$$\frac{\partial}{\partial t}(\varepsilon\overline{\rho}\tilde{w}) + \frac{\partial}{\partial z}(\varepsilon\overline{\rho}\tilde{u}\tilde{w}) + \frac{1}{r}\frac{\partial}{\partial r}(\varepsilon\overline{\rho}\tilde{v}\tilde{w} r) + \frac{\partial}{r\partial\theta}(\varepsilon\,\overline{\rho}\tilde{w}^2) = -\overline{\rho}\tilde{f}_\theta - \varepsilon\frac{\partial\overline{P}}{r\partial\theta}$$

$$
\begin{aligned}
&+ \frac{\partial}{\partial z}[\varepsilon(\overline{\tau}_{\theta z} - \overline{\rho u''w''})] + \frac{1}{r}\frac{\partial}{\partial r}[\varepsilon(\overline{\tau}_{\theta r} - \overline{\rho v''w''}r)] \\
&+ \frac{\partial}{r\partial\theta}[\varepsilon(\overline{\sigma}_{\theta\theta} - \overline{\rho w''^2})] + \varepsilon_p\rho_p^2\overline{w_p}\dot{d}\frac{S_p}{M_p}
\end{aligned}
\tag{73}
$$

where

$$
\begin{aligned}
\overline{\sigma}_{zz} &= -\frac{2}{3}\mu\left[\frac{\partial\tilde{u}}{\partial z} + \frac{1}{r}\frac{\partial(\tilde{v}r)}{\partial r} + \frac{\partial\tilde{w}}{r\partial\theta}\right] + 2\mu\frac{\partial\tilde{u}}{\partial z} \\
&\quad -\frac{2}{3}\mu\left[\frac{\partial\overline{u''}}{\partial z} + \frac{1}{r}\frac{\partial(\overline{v''}r)}{\partial r} + \frac{\partial\overline{w''}}{r\partial\theta}\right] + 2\mu\frac{\partial\overline{u''}}{\partial z} \\
\overline{\sigma}_{rr} &= -\frac{2}{3}\mu\left[\frac{\partial\tilde{u}}{\partial z} + \frac{1}{r}\frac{\partial(\tilde{v}r)}{\partial r} + \frac{\partial\tilde{w}}{r\partial\theta}\right] + 2\frac{\mu}{r}\frac{\partial(\tilde{v}r)}{\partial r} \\
&\quad -\frac{2}{3}\mu\left[\frac{\partial\overline{u''}}{\partial z} + \frac{1}{r}\frac{\partial(\overline{v''}r)}{\partial r} + \frac{\partial\overline{w''}}{r\partial\theta}\right] + 2\frac{\mu}{r}\frac{\partial(\overline{v''}r)}{\partial r} \\
\overline{\sigma}_{\theta\theta} &= -\frac{2}{3}\mu\left[\frac{\partial\tilde{u}}{\partial z} + \frac{1}{r}\frac{\partial(\tilde{v}r)}{\partial r} + \frac{\partial\tilde{w}}{r\partial\theta}\right] + 2\mu\frac{\partial\tilde{w}}{r\partial\theta} \\
&\quad -\frac{2}{3}\mu\left[\frac{\partial\overline{u''}}{\partial z} + \frac{1}{r}\frac{\partial(\overline{v''}r)}{\partial r} + \frac{\partial\overline{w''}}{r\partial\theta}\right] + 2\mu\frac{\partial\overline{w''}}{r\partial\theta} \\
&\overline{\tau}_{z\theta} = \overline{\tau}_{\theta z} = \mu\left(\frac{\partial\tilde{w}}{\partial z} + \frac{\partial\tilde{u}}{r\partial\theta}\right) + \mu\left(\frac{\partial\overline{w''}}{\partial z} + \frac{\partial\overline{u''}}{r\partial\theta}\right) \\
&\overline{\tau}_{zr} = \overline{\tau}_{rz} = \mu\left(\frac{1}{r}\frac{\partial(\tilde{u}r)}{\partial r} + \frac{\partial\tilde{v}}{\partial z}\right) + \mu\left(\frac{1}{r}\frac{\partial(\overline{u''}r)}{\partial r} + \frac{\partial\overline{v''}}{\partial z}\right) \\
&\overline{\tau}_{r\theta} = \overline{\tau}_{\theta r} = \mu\left(\frac{1}{r}\frac{\partial(\tilde{w}r)}{\partial r} + \frac{\partial\tilde{v}}{r\partial\theta}\right) + \mu\left(\frac{1}{r}\frac{\partial(\overline{w''}r)}{\partial r} + \frac{\partial\overline{v''}}{r\partial\theta}\right)
\end{aligned}
$$

**note:** viscous terms containing velocity fluctuations are expected to be small and will therefore be neglected on the basis of order of magnitude arguments

## B.4 Conservation of Momentum - Solid Phase

i) use equation 60 derived in Appendix A

$$
\begin{aligned}
\frac{\partial}{\partial t}(\varepsilon_p u_p) + \frac{\partial}{\partial z}(\varepsilon_p u_p^2) + \frac{1}{r}\frac{\partial}{\partial r}(\varepsilon_p u_p v_p r) + \frac{\partial}{\partial r\theta}(\varepsilon_p u_p w_p) &= \frac{\rho}{\rho_p} f_z \\
- \frac{1}{\rho_p}\frac{\partial}{\partial z}(\varepsilon_p R) - \frac{\varepsilon_p}{\rho_p}\frac{\partial P}{\partial z} + \varepsilon_p g_z - \varepsilon_p\rho_p u_p\dot{d}\frac{S_p}{M_p}
\end{aligned}
$$

ii) decompose equation according to averaging rules

$$
\frac{\partial}{\partial t}(\varepsilon_p(\overline{u_p} + u_p')) + \frac{\partial}{\partial z}(\varepsilon_p(\overline{u_p} + u_p')^2) + \frac{1}{r}\frac{\partial}{\partial r}(\varepsilon_p(\overline{u_p} + u_p')(\overline{v_p} + v_p')r)
$$

$$
\begin{aligned}
&+ \frac{\partial}{\partial r\theta}(\varepsilon_p(\overline{u_p} + u_p')(\overline{w_p} + w_p')) = +\frac{(\overline{\rho} + \rho')}{\rho_p}(\widetilde{f}_z + f_z'') \\
&- \frac{1}{\rho_p}\frac{\partial}{\partial z}(\varepsilon_p(\overline{R} + R')) - \frac{\varepsilon_p}{\rho_p}\frac{\partial(\overline{P} + P')}{\partial z} \\
&+ \varepsilon_p g_z - \varepsilon_p \rho_p(\overline{u_p} + u_p')\dot{d}\frac{S_p}{M_p}
\end{aligned}
$$

**iii) expand terms and use the averaging method of B.1 to get**

$$
\begin{aligned}
&\frac{\partial}{\partial t}(\varepsilon_p\overline{u_p}) + \frac{\partial}{\partial z}(\varepsilon_p(\overline{u_p}^2 + \overline{u_p'}^2)) + \frac{1}{r}\frac{\partial}{\partial r}(\varepsilon_p(\overline{u_p}\,\overline{v_p} + \overline{u_p'v_p'})r) \\
&\quad + \frac{\partial}{\partial r\theta}(\varepsilon_p(\overline{u_p}\,\overline{w_p} + \overline{u_p'w_p'})) = +\frac{\overline{\rho}}{\rho_p}\widetilde{f}_z - \frac{1}{\rho_p}\frac{\partial}{\partial z}(\varepsilon_p\overline{R}) - \frac{\varepsilon_p}{\rho_p}\frac{\partial\overline{P}}{\partial z} \\
&\quad + \varepsilon_p g_z - \varepsilon_p\rho_p\overline{u_p}\dot{d}\frac{S_p}{M_p}
\end{aligned} \tag{74}
$$

**iv) similar equations can be derived for the $r$ and $\theta$ directions to get**

$$
\begin{aligned}
&\frac{\partial}{\partial t}(\varepsilon_p\overline{v_p}) + \frac{\partial}{\partial z}(\varepsilon_p(\overline{u_p}\,\overline{v_p} + \overline{u_p'v_p'})) + \frac{1}{r}\frac{\partial}{\partial r}(\varepsilon_p(\overline{v_p}^2 + \overline{v_p'}^2)r) \\
&\quad + \frac{\partial}{\partial r\theta}(\varepsilon_p(\overline{v_p}\,\overline{w_p} + \overline{v_p'w_p'})) = +\frac{\overline{\rho}}{\rho_p}\widetilde{f}_r - \frac{1}{\rho_p r}\frac{\partial}{\partial r}(\varepsilon_p\overline{R}r) - \frac{\varepsilon_p}{\rho_p}\frac{\partial\overline{P}}{\partial r} \\
&\quad + \varepsilon_p g_r - \varepsilon_p\rho_p\overline{v_p}\dot{d}\frac{S_p}{M_p}
\end{aligned} \tag{75}
$$

$$
\begin{aligned}
&\frac{\partial}{\partial t}(\varepsilon_p\overline{w_p}) + \frac{\partial}{\partial z}(\varepsilon_p(\overline{u_p}\,\overline{w_p} + \overline{u_p'w_p'})) + \frac{1}{r}\frac{\partial}{\partial r}(\varepsilon_p(\overline{v_p}\,\overline{w_p} + \overline{v_p'w_p'})r) \\
&\quad + \frac{\partial}{\partial r\theta}(\varepsilon_p(\overline{w_p}^2 + \overline{w_p'}^2)) = +\frac{\overline{\rho}}{\rho_p}\widetilde{f}_\theta - \frac{1}{\rho_p}\frac{\partial}{\partial r\theta}(\varepsilon_p\overline{R}) - \frac{\varepsilon_p}{\rho_p}\frac{\partial\overline{P}}{\partial r\theta} \\
&\quad + \varepsilon_p g_\theta - \varepsilon_p\rho_p\overline{w_p}\dot{d}\frac{S_p}{M_p}
\end{aligned} \tag{76}
$$

**note: source terms containing velocity fluctuations are expected to be small and will therefore be neglected on the basis of order of magnitude arguments**

## B.5 Conservation of Energy for the Gas Phase

i) use equation 68 derived in Appendix A

$$
\begin{aligned}
&\rho\varepsilon\left(\frac{\partial e}{\partial t} + u\frac{\partial e}{\partial z} + \frac{v}{r}\frac{\partial(er)}{\partial t} + w\frac{\partial e}{r\partial\theta}\right) = P\left(\frac{\partial}{\partial z}(\varepsilon u) + \frac{1}{r}\frac{\partial}{\partial r}(\varepsilon vr) + \frac{\partial}{r\partial\theta}(\varepsilon w)\right) \\
&+\rho(f_z(u - u_p) + f_r(v - v_p) + f_\theta(w - w_p)) + \varepsilon\tau_{zr}\left(\frac{\partial v}{\partial z} + \frac{1}{r}\frac{\partial(ur)}{\partial r}\right)
\end{aligned}
$$

$$
\begin{aligned}
&+\varepsilon\tau_{z\theta}\left(\frac{\partial w}{\partial z}+\frac{\partial u}{r\partial\theta}\right)+\varepsilon\tau_{\theta r}\left(\frac{\partial v}{r\partial\theta}+\frac{1}{r}\frac{\partial(wr)}{\partial r}\right)+\frac{\partial}{\partial z}\left[\varepsilon\frac{\mu c_p}{\mathrm{Pr}}\frac{\partial T}{\partial z}\right]\\
&+\frac{1}{r}\frac{\partial}{\partial r}\left[\varepsilon\frac{\mu c_p}{\mathrm{Pr}}r\frac{\partial T}{\partial r}\right]+\frac{\partial}{r\partial\theta}\left[\varepsilon\frac{\mu c_p}{\mathrm{Pr}}\frac{\partial T}{r\partial\theta}\right]+\varepsilon\left(\sigma_{zz}\frac{\partial u}{\partial z}+\frac{\sigma_{rr}}{r}\frac{\partial(vr)}{\partial r}+\sigma_{\theta\theta}\frac{\partial w}{r\partial\theta}\right)\\
&-\varepsilon_p\rho_p^2 q\frac{S_p}{M_p}+\varepsilon_p\rho_p^2\dot{d}\left(e_p+\frac{P}{\rho_p}+\frac{u_p^2+v_p^2+w_p^2}{2}\right)\frac{S_p}{M_p}+u\varepsilon_p\rho_p^2 u_p\dot{d}\frac{S_p}{M_p}\\
&+v\varepsilon_p\rho_p^2 v_p\dot{d}\frac{S_p}{M_p}+w\varepsilon_p\rho_p^2 w_p\dot{d}\frac{S_p}{M_p}+\varepsilon_p\rho_p^2\dot{d}\frac{S_p}{M_p}\left(e-\frac{u^2+v^2+w^2}{2}\right)
\end{aligned}
$$

**ii) decompose equation according to averaging rules**

$$
\begin{aligned}
&\varepsilon(\bar{\rho}+\rho')\left(\frac{\partial(\tilde{e}+e'')}{\partial t}+(\tilde{u}+u'')\frac{\partial(\tilde{e}+e'')}{\partial z}\right.\\
&\quad\left.+\frac{(\tilde{v}+v'')}{r}\frac{\partial(\tilde{e}+e'')r}{\partial r}+(\tilde{w}+w'')\frac{\partial(\tilde{e}+e'')}{r\partial\theta}\right)\\
&\quad=(\bar{P}+P')\left(\frac{\partial}{\partial z}\varepsilon(\tilde{u}+u'')+\frac{1}{r}\frac{\partial}{\partial r}\varepsilon(\tilde{v}+v'')r+\frac{\partial}{r\partial\theta}\varepsilon(\tilde{w}+w'')\right)\\
&\quad+(\bar{\rho}+\rho')((\bar{f}_z+f_z'')((\tilde{u}+u'')-(\overline{u_p}+u_p'))\\
&\quad+(\bar{f}_r+f_r'')((\tilde{v}+v'')-(\overline{v_p}+v_p'))+(\bar{f}_\theta+f_\theta'')((\tilde{w}+w'')-(\overline{w_p}+w_p')))\\
&\quad+\varepsilon\left(\sigma_{zz}\frac{\partial(\tilde{u}+u'')}{\partial z}+\frac{\sigma_{rr}}{r}\frac{\partial(\tilde{v}+v'')r}{\partial r}+\sigma_{\theta\theta}\frac{\partial(\tilde{w}+w'')}{r\partial\theta}\right)\\
&\quad+\varepsilon\tau_{zr}\left(\frac{\partial(\tilde{v}+v'')}{\partial z}+\frac{1}{r}\frac{\partial(\tilde{u}+u'')r}{\partial r}\right)+\varepsilon\tau_{z\theta}\left(\frac{\partial(\tilde{w}+w'')}{\partial z}+\frac{\partial(\tilde{u}+u'')}{r\partial\theta}\right)\\
&\quad+\varepsilon\tau_{\theta r}\left(\frac{\partial(\tilde{v}+v'')}{r\partial\theta}+\frac{1}{r}\frac{\partial(\tilde{w}+w'')r}{\partial r}\right)+\frac{\partial}{\partial z}\left[\varepsilon\left(\frac{\mu c_p}{\mathrm{Pr}}+\frac{\mu_t c_p}{\mathrm{Pr}_t}\right)\frac{\partial(\bar{T}+T'')}{\partial z}\right]\\
&\quad+\frac{1}{r}\frac{\partial}{\partial r}\left[\varepsilon\left(\frac{\mu c_p}{\mathrm{Pr}}+\frac{\mu_t c_p}{\mathrm{Pr}_t}\right)r\frac{\partial(\bar{T}+T'')}{\partial r}\right]+\frac{\partial}{r\partial\theta}\left[\varepsilon\left(\frac{\mu c_p}{\mathrm{Pr}}+\frac{\mu_t c_p}{\mathrm{Pr}_t}\right)\frac{\partial(\bar{T}+T'')}{r\partial\theta}\right]\\
&\quad+\varepsilon_p\rho_p^2\dot{d}\left((\overline{e_p}+e_p')+\frac{P}{\rho_p}+\frac{(\overline{u_p}+u_p')^2+(\overline{v_p}+v_p')^2+(\overline{w_p}+w_p')^2}{2}\right)\frac{S_p}{M_p}\\
&\quad-\varepsilon_p\rho_p^2(\bar{q}+q')\frac{S_p}{M_p}+(\tilde{u}+u'')\varepsilon_p\rho_p^2(\overline{u_p}+u_p')\dot{d}\frac{S_p}{M_p}\\
&\quad+(\tilde{v}+v'')\varepsilon_p\rho_p^2(\overline{v_p}+v_p')\dot{d}\frac{S_p}{M_p}+(\tilde{w}+w'')\varepsilon_p\rho_p^2(\overline{w_p}+w_p')\dot{d}\frac{S_p}{M_p}\\
&\quad+\varepsilon_p\rho_p^2\dot{d}\frac{S_p}{M_p}\left((\tilde{e}+e'')-\frac{(\tilde{u}+u'')^2+(\tilde{v}+v'')^2+(\tilde{w}+w'')^2}{2}\right)
\end{aligned}
$$

**iii) expand terms and use the averaging method of B.1 to get**

$$
\varepsilon\left(\bar{\rho}\frac{\partial\tilde{e}}{\partial t}+\bar{\rho}\tilde{u}\frac{\partial\tilde{e}}{\partial z}+\overline{\rho u''\frac{\partial e''}{\partial z}}+\bar{\rho}\frac{\tilde{v}}{r}\frac{\partial(\tilde{e}r)}{\partial r}+\overline{\rho\frac{v''}{r}\frac{\partial(e''r)}{\partial r}}+\bar{\rho}\tilde{w}\frac{\partial\tilde{e}}{r\partial\theta}+\overline{\rho w''\frac{\partial e''}{r\partial\theta}}\right)=
$$

$$
\begin{aligned}
&-\left(\overline{P}\frac{\partial}{\partial z}(\varepsilon\tilde{u}) + \frac{\overline{P}}{r}\frac{\partial}{\partial r}(\varepsilon\tilde{v}r) + \overline{P}\frac{\partial}{r\partial\theta}(\varepsilon\tilde{w})\right) \\
&-\left(\overline{+P\frac{\partial}{\partial z}(\varepsilon u'')} + \overline{\frac{P}{r}\frac{\partial}{\partial r}(\varepsilon v''r)} + \overline{P\frac{\partial}{r\partial\theta}(\varepsilon w'')}\right) \\
&+\overline{\rho}(\tilde{f}_z(\tilde{u} - \overline{u_p} - \overline{\rho' u_p'}) + \tilde{f}_r(\tilde{v} - \overline{v_p} - \overline{\rho' v_p'}) + \tilde{f}_\theta(\tilde{w} - \overline{w_p} - \overline{\rho' w_p'})) \\
&+\varepsilon\left(\overline{\sigma}_{zz}\frac{\partial\tilde{u}}{\partial z} + \overline{\sigma_{zz}\frac{\partial u''}{\partial z}} + \frac{\overline{\sigma}_{rr}}{r}\frac{\partial\tilde{v}r}{\partial r} + \overline{\frac{\sigma_{rr}}{r}\frac{\partial v''r}{\partial r}} + \overline{\sigma}_{\theta\theta}\frac{\partial\tilde{w}}{r\partial\theta} + \overline{\sigma_{\theta\theta}\frac{\partial w''}{r\partial\theta}}\right) \\
&+\varepsilon\overline{\tau}_{zr}\left(\frac{\partial\tilde{v}}{\partial z} + \frac{1}{r}\frac{\partial\tilde{u}r}{\partial r}\right) + \overline{\varepsilon\tau_{zr}\left(\frac{\partial v''}{\partial z} + \frac{1}{r}\frac{\partial u''r}{\partial r}\right)} \\
&+\varepsilon\overline{\tau}_{z\theta}\left(\frac{\partial\tilde{w}}{\partial z} + \frac{\partial\tilde{u}}{r\partial\theta}\right) + \overline{\varepsilon\tau_{z\theta}\left(\frac{\partial w''}{\partial z} + \frac{\partial u''}{r\partial\theta}\right)} \\
&+\varepsilon\overline{\tau}_{\theta r}\left(\frac{\partial\tilde{v}}{r\partial\theta} + \frac{1}{r}\frac{\partial\tilde{w}r}{\partial r}\right) + \overline{\varepsilon\tau_{\theta r}\left(\frac{\partial v''}{r\partial\theta} + \frac{1}{r}\frac{\partial w''r}{\partial r}\right)} \\
&+\frac{\partial}{\partial z}\left[\varepsilon\left(\frac{\mu c_p}{\mathrm{Pr}} + \frac{\mu_t c_p}{\mathrm{Pr}_t}\right)\frac{\partial\overline{T}}{\partial z}\right] + \frac{1}{r}\frac{\partial}{\partial r}\left[\varepsilon\left(\frac{\mu c_p}{\mathrm{Pr}} + \frac{\mu_t c_p}{\mathrm{Pr}_t}\right)r\frac{\partial\overline{T}}{\partial r}\right] \\
&+\frac{\partial}{r\partial\theta}\left[\varepsilon\left(\frac{\mu c_p}{\mathrm{Pr}} + \frac{\mu_t c_p}{\mathrm{Pr}_t}\right)\frac{\partial\overline{T}}{r\partial\theta}\right] - \varepsilon_p\rho_p^2\overline{q}\frac{S_p}{M_p} \\
&+\varepsilon_p\rho_p^2\dot{d}\left(\overline{e_p} + \frac{\overline{P}}{\rho_p} + \frac{(\overline{u_p}^2 + \overline{u_p'^2}) + (\overline{v_p}^2 + \overline{v_p'^2}) + (\overline{w_p}^2 + \overline{w_p'^2})}{2}\right)\frac{S_p}{M_p} \\
&+(\tilde{u} + \overline{u''})\varepsilon_p\rho_p^2\overline{u_p}\dot{d}\frac{S_p}{M_p} + (\tilde{v} + \overline{v''})\varepsilon_p\rho_p^2\overline{v_p}\dot{d}\frac{S_p}{M_p} + (\tilde{w} + \overline{w''})\varepsilon_p\rho_p^2\overline{w_p}\dot{d}\frac{S_p}{M_p} \\
&+\varepsilon_p\rho_p^2\dot{d}\frac{S_p}{M_p}\left(\tilde{e} + \overline{e''} - \frac{(\tilde{u} + \overline{u''})^2 + (\tilde{v} + \overline{v''})^2 + (\tilde{w} + \overline{w''})^2}{2}\right) \qquad (77)
\end{aligned}
$$

note: on the basis of order of magnitude arguments, viscous terms and source terms containing velocity fluctuations will be neglected

# C CVV Turbulence Model Equations

## C.1 Kinetic Energy Equation

In this section the conservation equations, for mean and turbulent kinetic energy, are derived using the following equations and relations for a compressible two phase flow with negligible body forces and source terms:

Conservation of Mass

$$\frac{\partial}{\partial t}(\varepsilon\rho) + \frac{\partial}{\partial z}(\varepsilon\rho u) + \frac{1}{r}\frac{\partial}{\partial r}(\varepsilon\rho v r) + \frac{\partial}{r\partial\theta}(\varepsilon\rho w) = 0$$

Conservation of Momentum

$$\begin{aligned}\frac{\partial}{\partial t}(\varepsilon\rho u) + \frac{\partial}{\partial z}(\varepsilon\rho u^2) + \frac{1}{r}\frac{\partial}{\partial r}(\varepsilon\rho u v r) + \frac{\partial}{r\partial\theta}(\varepsilon\rho u w) &= \frac{\partial}{\partial z}(\varepsilon\sigma_{zz}) \\ &+ \frac{1}{r}\frac{\partial}{\partial r}(\varepsilon\tau_{rz} r) + \frac{\partial}{r\partial\theta}(\varepsilon\tau_{\theta z})\end{aligned}$$

$$\begin{aligned}\frac{\partial}{\partial t}(\varepsilon\rho v) + \frac{\partial}{\partial z}(\varepsilon\rho u v) + \frac{1}{r}\frac{\partial}{\partial r}(\varepsilon\rho v^2 r) + \frac{\partial}{r\partial\theta}(\varepsilon\rho v w) &= \frac{\partial}{\partial z}(\varepsilon\tau_{rz}) \\ &+ \frac{1}{r}\frac{\partial}{\partial r}(\varepsilon\sigma_{rr} r) + \frac{\partial}{r\partial\theta}(\varepsilon\tau_{r\theta})\end{aligned}$$

$$\begin{aligned}\frac{\partial}{\partial t}(\varepsilon\rho w) + \frac{\partial}{\partial z}(\varepsilon\rho u w) + \frac{1}{r}\frac{\partial}{\partial r}(\varepsilon\rho v w r) + \frac{\partial}{r\partial\theta}(\varepsilon\rho w^2) &= \frac{\partial}{\partial z}(\varepsilon\tau_{\theta z}) \\ &+ \frac{1}{r}\frac{\partial}{\partial r}(\varepsilon\tau_{\theta r} r) + \frac{\partial}{r\partial\theta}(\varepsilon\sigma_{\theta\theta})\end{aligned}$$

where stress terms are defined as in section A.3.

General Differential Relations

$$\rho u_i \frac{\partial u_i}{\partial t} = \frac{\partial}{\partial t}\left(\frac{\rho u_i^2}{2}\right)$$

$$\rho u_i \frac{\partial u_i u_j}{\partial x_j} = \frac{\partial}{\partial x_j}\left(\rho u_j \frac{u_i^2}{2}\right)$$

$$\rho u_i \frac{\partial u_j}{\partial x_j} = \frac{\partial}{\partial x_j}(\rho u_i u_j) - u_j \frac{\partial}{\partial x_j}(\rho u_i)$$

$$\epsilon \equiv \mu\overline{\rho\frac{\partial u_i''}{\partial x_j}\frac{\partial u_i''}{\partial x_j}} \equiv \mu\overline{\rho\frac{\partial u_i''}{\partial x_j}\left(\frac{\partial u_i''}{\partial x_j} + \frac{\partial u_j''}{\partial x_i}\right)}$$

## MEAN KINETIC ENERGY

**The mean kinetic energy equation can be derived from the above equations using the following steps:**

**LHS**

**i) multiply LHS of $z$ momentum eqn by $\rho\tilde{u}$ to get**

$$\rho\tilde{u}\frac{\partial}{\partial t}(\epsilon\rho u) + \rho\tilde{u}\frac{\partial}{\partial z}(\epsilon\rho u^2) + \rho\tilde{u}\frac{1}{r}\frac{\partial}{\partial r}(\epsilon\rho uvr) + \rho\tilde{u}\frac{\partial}{r\partial\theta}(\epsilon\rho uw)$$

**ii) substitute $\rho = \overline{\rho} + \rho'$ and $u = \tilde{u} + u''$ and time average to get**

$$\overline{\rho}\tilde{u}\frac{\partial}{\partial t}\epsilon(\overline{\rho}\tilde{u}) + \overline{\rho}\tilde{u}\frac{\partial}{\partial z}\epsilon(\overline{\rho}\tilde{u}^2 + \overline{\rho u''^2}) + \overline{\rho}\tilde{u}\frac{1}{r}\frac{\partial}{\partial r}\epsilon r(\overline{\rho}\tilde{u}\tilde{v} + \overline{\rho u''v''})$$
$$+ \overline{\rho}\tilde{u}\frac{\partial}{r\partial\theta}\epsilon(\overline{\rho}\tilde{u}\tilde{w} + \overline{\rho u''w''})$$

**iii) rearrange according to relations**

$$\frac{\partial}{\partial t}\epsilon\overline{\rho}\left(\overline{\rho}\frac{\tilde{u}^2}{2}\right) + \frac{\partial}{\partial z}\epsilon\overline{\rho}\left(\tilde{u}\overline{\rho}\frac{\tilde{u}^2}{2} + \tilde{u}\overline{\rho u''^2}\right) + \frac{1}{r}\frac{\partial}{\partial r}\epsilon r\overline{\rho}\left(\tilde{v}\overline{\rho}\frac{\tilde{u}^2}{2} + \tilde{u}\overline{\rho u''v''}\right)$$
$$+ \frac{\partial}{r\partial\theta}\epsilon\overline{\rho}\left(\tilde{w}\overline{\rho}\frac{\tilde{u}^2}{2} + \tilde{u}\overline{\rho u''w''}\right) - \epsilon\overline{\rho u''^2}\frac{\partial}{\partial z}(\overline{\rho}\tilde{u}) - \epsilon\frac{\overline{\rho u''v''}}{r}\frac{\partial}{\partial r}(\overline{\rho}\tilde{u}r)$$
$$- \epsilon\overline{\rho u''w''}\frac{\partial}{r\partial\theta}(\overline{\rho}\tilde{u})$$

**RHS**

**iv) multiply RHS of $z$ momentum eqn by $\rho\tilde{u}$ to get**

$$\rho\tilde{u}\frac{\partial}{\partial z}\epsilon\left[2\mu\frac{\partial u}{\partial z} - \frac{2}{3}\mu\left(\frac{\partial u}{\partial z} + \frac{1}{r}\frac{\partial(vr)}{\partial r} + \frac{\partial w}{r\partial\theta}\right)\right] + \frac{\rho\tilde{u}}{r}\frac{\partial}{\partial r}\epsilon r\left[\mu\left(\frac{1}{r}\frac{\partial(ur)}{\partial r} + \frac{\partial v}{\partial z}\right)\right]$$
$$+\rho\tilde{u}\frac{\partial}{r\partial\theta}\epsilon\left[\mu\left(\frac{\partial w}{\partial z} + \frac{\partial u}{r\partial\theta}\right)\right]$$

**v) substitute $\rho = \overline{\rho} + \rho'$ and $u = \tilde{u} + u''$ and time average to get**

$$\overline{\rho}\tilde{u}\frac{\partial}{\partial z}\epsilon\left[2\mu\frac{\partial\tilde{u}}{\partial z} - \frac{2}{3}\mu\left(\frac{\partial\tilde{u}}{\partial z} + \frac{1}{r}\frac{\partial(\tilde{v}r)}{\partial r} + \frac{\partial\tilde{w}}{r\partial\theta}\right)\right] + \frac{\overline{\rho}\tilde{u}}{r}\frac{\partial}{\partial r}\epsilon r\left[\mu\left(\frac{1}{r}\frac{\partial(\tilde{u}r)}{\partial r} + \frac{\partial\tilde{v}}{\partial z}\right)\right]$$
$$+\overline{\rho}\tilde{u}\frac{\partial}{r\partial\theta}\epsilon\left[\mu\left(\frac{\partial\tilde{w}}{\partial z} + \frac{\partial\tilde{u}}{r\partial\theta}\right)\right]$$

vi) rearrange using relations to get

$$
\begin{aligned}
2\frac{\partial}{\partial x}\left(\varepsilon\overline{\rho}\mu\tilde{u}\frac{\partial\tilde{u}}{\partial z}\right) - 2\overline{\rho}\varepsilon\mu\left(\frac{\partial\tilde{u}}{\partial z}\right)^2 - \frac{2}{3}\frac{\partial}{\partial z}\left[\varepsilon\overline{\rho}\mu\tilde{u}\left(\frac{\partial\tilde{u}}{\partial z} + \frac{1}{r}\frac{\partial(\tilde{v}r)}{\partial r} + \frac{\partial\tilde{w}}{r\partial\theta}\right)\right]& \\
+ \frac{2}{3}\overline{\rho}\varepsilon\mu\frac{\partial\tilde{u}}{\partial z}\left(\frac{\partial\tilde{u}}{\partial z} + \frac{1}{r}\frac{\partial(\tilde{v}r)}{\partial r} + \frac{\partial\tilde{w}}{r\partial\theta}\right)& \\
+ \frac{1}{r}\frac{\partial}{\partial r}\left[\varepsilon\overline{\rho}\mu r\tilde{u}\left(\frac{\partial\tilde{v}}{\partial z} + \frac{1}{r}\frac{\partial(\tilde{u}r)}{\partial r}\right)\right] - \overline{\rho}\frac{\varepsilon\mu}{r}\frac{\partial\tilde{u}r}{\partial r}\left(\frac{\partial\tilde{v}}{\partial z} + \frac{1}{r}\frac{\partial(\tilde{u}r)}{\partial r}\right)& \\
+ \frac{\partial}{r\partial\theta}\left[\varepsilon\overline{\rho}\mu\tilde{u}\left(\frac{\partial\tilde{w}}{\partial z} + \frac{\partial\tilde{u}}{r\partial\theta}\right)\right] - \overline{\rho}\varepsilon\mu\frac{\partial\tilde{u}}{r\partial\theta}\left(\frac{\partial\tilde{w}}{\partial z} + \frac{\partial\tilde{u}}{r\partial\theta}\right)&
\end{aligned}
$$

## TURBULENT KINETIC ENERGY

**The turbulent kinetic energy equation can be derived from the conservation equations and differential relations using the following steps:**

### LHS

i) multiply LHS of $z$ momentum eqn by $\rho u$ and use relations to get

$$
\frac{\partial}{\partial t}\varepsilon\rho\left(\rho\frac{u^2}{2}\right) + \frac{\partial}{\partial z}\varepsilon\rho\left(\rho u\frac{u^2}{2}\right) + \frac{1}{r}\frac{\partial}{\partial r}\varepsilon r\rho\left(v\rho\frac{u^2}{2}\right) + \frac{\partial}{r\partial\theta}\varepsilon\rho\left(w\rho\frac{u^2}{2}\right)
$$

ii) substitute $\rho = \overline{\rho} + \rho'$ and $u = \tilde{u} + u''$ and time average to get

$$
\begin{aligned}
\frac{\partial}{\partial t}\varepsilon\overline{\rho}\left(\overline{\rho}\frac{\tilde{u}^2}{2} + \frac{\overline{\rho u''^2}}{2}\right) + \frac{\partial}{\partial z}\varepsilon\overline{\rho}\left(\tilde{u}\overline{\rho}\frac{\tilde{u}^2}{2} + \tilde{u}\overline{\rho u''^2} + \tilde{u}\frac{\overline{\rho u''^2}}{2} + \frac{\overline{\rho u''^3}}{2}\right)& \\
+ \frac{1}{r}\frac{\partial}{\partial r}\varepsilon r\overline{\rho}\left(\tilde{v}\overline{\rho}\frac{\tilde{u}^2}{2} + \tilde{u}\overline{\rho u''v''} + \tilde{v}\frac{\overline{\rho u''^2}}{2} + \frac{\overline{\rho u''^2 v''}}{2}\right)& \\
+ \frac{\partial}{r\partial\theta}\varepsilon\overline{\rho}\left(\tilde{w}\overline{\rho}\frac{\tilde{u}^2}{2} + \tilde{u}\overline{\rho u''w''} + \tilde{w}\frac{\overline{\rho u''^2}}{2} + \frac{\overline{\rho u''^2 w''}}{2}\right)&
\end{aligned}
$$

iii) subtract LHS of mean kinetic energy equation and neglect triple correlations (the diffusion terms are modeled empirically later) to get

$$
\begin{aligned}
\frac{\partial}{\partial t}\varepsilon\overline{\rho}\left(\frac{\overline{\rho u''^2}}{2}\right) + \frac{\partial}{\partial z}\varepsilon\overline{\rho}\left(\tilde{u}\frac{\overline{\rho u''^2}}{2}\right) + \frac{1}{r}\frac{\partial}{\partial r}\varepsilon r\overline{\rho}\left(\tilde{v}\frac{\overline{\rho u''^2}}{2}\right) + \frac{\partial}{r\partial\theta}\varepsilon\overline{\rho}\left(\tilde{w}\frac{\overline{\rho u''^2}}{2}\right)& \\
+ \varepsilon\overline{\rho u''^2}\frac{\partial}{\partial z}(\overline{\rho}\tilde{u}) + \varepsilon\frac{\overline{\rho u''v''}}{r}\frac{\partial}{\partial r}(\overline{\rho}\tilde{u}r) + \varepsilon\overline{\rho u''w''}\frac{\partial}{r\partial\theta}(\overline{\rho}\tilde{u})& \qquad (78)
\end{aligned}
$$

iv) similar equations can be written for the $r$ and $\theta$ directions

$$
\begin{aligned}
\frac{\partial}{\partial t}\varepsilon\overline{\rho}\left(\frac{\overline{\rho v''^2}}{2}\right) + \frac{\partial}{\partial z}\varepsilon\overline{\rho}\left(\tilde{u}\frac{\overline{\rho v''^2}}{2}\right) + \frac{1}{r}\frac{\partial}{\partial r}\varepsilon r\overline{\rho}\left(\tilde{v}\frac{\overline{\rho v''^2}}{2}\right) + \frac{\partial}{r\partial\theta}\varepsilon\overline{\rho}\left(\tilde{w}\frac{\overline{\rho v''^2}}{2}\right)& \\
+ \varepsilon\overline{\rho u''v''}\frac{\partial}{\partial z}(\overline{\rho}\tilde{v}) + \varepsilon\frac{\overline{\rho v''^2}}{r}\frac{\partial}{\partial r}(\overline{\rho}\tilde{v}r) + \varepsilon\overline{\rho v''w''}\frac{\partial}{r\partial\theta}(\overline{\rho}\tilde{v})& \qquad (79)
\end{aligned}
$$

$$
\begin{aligned}
&\frac{\partial}{\partial t}\varepsilon\overline{\rho}\left(\frac{\overline{\rho w''^2}}{2}\right)+\frac{\partial}{\partial z}\varepsilon\overline{\rho}\left(\tilde{u}\frac{\overline{\rho w''^2}}{2}\right)+\frac{1}{r}\frac{\partial}{\partial r}\varepsilon r\overline{\rho}\left(\tilde{v}\frac{\overline{\rho w''^2}}{2}\right)+\frac{\partial}{r\partial\theta}\varepsilon\overline{\rho}\left(\tilde{w}\frac{\overline{\rho w''^2}}{2}\right)\\
&\qquad+\varepsilon\overline{\rho u''w''}\frac{\partial}{\partial z}(\overline{\rho}\tilde{w})+\varepsilon\frac{\overline{\rho v''w''}}{r}\frac{\partial}{\partial r}(\overline{\rho}\tilde{w}r)+\varepsilon\overline{\rho w''w''}\frac{\partial}{r\partial\theta}(\overline{\rho}\tilde{w}) \qquad (80)
\end{aligned}
$$

v) addition of eqns 78, 79 and 80 gives LHS of turbulent kinetic energy eqn

$$
\begin{aligned}
&\frac{\partial}{\partial t}(\varepsilon\overline{\rho}k)+\frac{\partial}{\partial z}(\varepsilon\overline{\rho}\tilde{u}k)+\frac{1}{r}\frac{\partial}{\partial r}(\varepsilon\overline{\rho}\tilde{v}kr)+\frac{\partial}{r\partial\theta}(\varepsilon\overline{\rho}\tilde{w}k)+\varepsilon\overline{\rho u''^2}\frac{\partial}{\partial z}(\overline{\rho}\tilde{u})\\
&\qquad+\varepsilon\frac{\overline{\rho u''v''}}{r}\frac{\partial}{\partial r}(\overline{\rho}\tilde{u}r)+\varepsilon\overline{\rho u''w''}\frac{\partial}{r\partial\theta}(\overline{\rho}\tilde{u})+\varepsilon\overline{\rho u''v''}\frac{\partial}{\partial z}(\overline{\rho}\tilde{v})\\
&\qquad+\varepsilon\frac{\overline{\rho v''^2}}{r}\frac{\partial}{\partial r}(\overline{\rho}\tilde{v}r)+\varepsilon\overline{\rho v''w''}\frac{\partial}{r\partial\theta}(\overline{\rho}\tilde{v})+\varepsilon\overline{\rho u''w''}\frac{\partial}{\partial z}(\overline{\rho}\tilde{w})\\
&\qquad+\varepsilon\frac{\overline{\rho v''w''}}{r}\frac{\partial}{\partial r}(\overline{\rho}\tilde{w}r)+\varepsilon\overline{\rho w''w''}\frac{\partial}{r\partial\theta}(\overline{\rho}\tilde{w}) \qquad (81)
\end{aligned}
$$

RHS

vi) multiply RHS of $z$ momentum eqn by $\rho u$ and use relations to get

$$
\begin{aligned}
&2\frac{\partial}{\partial z}\left(\varepsilon\rho\mu u\frac{\partial u}{\partial z}\right)-2\rho\varepsilon\mu\left(\frac{\partial u}{\partial z}\right)^2-\frac{2}{3}\frac{\partial}{\partial z}\left[\varepsilon\rho\mu u\left(\frac{\partial u}{\partial z}+\frac{1}{r}\frac{\partial(vr)}{\partial r}+\frac{\partial w}{r\partial\theta}\right)\right]\\
&\qquad+\frac{2}{3}\rho\varepsilon\mu\frac{\partial u}{\partial z}\left(\frac{\partial u}{\partial z}+\frac{1}{r}\frac{\partial(vr)}{\partial r}+\frac{\partial w}{r\partial\theta}\right)\\
&\qquad+\frac{1}{r}\frac{\partial}{\partial r}\left[\varepsilon\rho\mu r u\left(\frac{\partial v}{\partial z}+\frac{1}{r}\frac{\partial(ur)}{\partial r}\right)\right]-\rho\frac{\varepsilon\mu}{r}\frac{\partial(ur)}{\partial r}\left(\frac{\partial v}{\partial z}+\frac{1}{r}\frac{\partial(ur)}{\partial r}\right)\\
&\qquad+\frac{\partial}{r\partial\theta}\left[\varepsilon\rho\mu u\left(\frac{\partial w}{\partial z}+\frac{\partial u}{r\partial\theta}\right)\right]-\rho\varepsilon\mu\frac{\partial u}{r\partial\theta}\left(\frac{\partial w}{\partial z}+\frac{\partial u}{r\partial\theta}\right)
\end{aligned}
$$

vii) substitute $\rho=\overline{\rho}+\rho'$ and $\mathrm{u}=\tilde{\mathrm{u}}+\mathrm{u}''$ and time average to get

$$
\begin{aligned}
&2\frac{\partial}{\partial z}\left(\varepsilon\overline{\rho}\mu\tilde{u}\frac{\partial\tilde{u}}{\partial z}\right)+\overline{2\rho\frac{\partial}{\partial z}\left(\varepsilon\mu u''\frac{\partial u''}{\partial z}\right)}-2\varepsilon\mu\left(\overline{\rho}\left(\frac{\partial\tilde{u}}{\partial z}\right)^2+\overline{\rho\left(\frac{\partial u''}{\partial z}\right)^2}\right)\\
&-\frac{2}{3}\frac{\partial}{\partial z}\left[\varepsilon\overline{\rho}\mu\tilde{u}\left(\frac{\partial\tilde{u}}{\partial z}+\frac{1}{r}\frac{\partial(\tilde{v}r)}{\partial r}+\frac{\partial\tilde{w}}{r\partial\theta}\right)\right]\\
&+\overline{\frac{2}{3}\frac{\partial}{\partial z}\left[\varepsilon\mu\rho u''\left(\frac{\partial u''}{\partial z}+\frac{1}{r}\frac{\partial(v''r)}{\partial r}+\frac{\partial w''}{r\partial\theta}\right)\right]}\\
&+\frac{2}{3}\overline{\rho}\varepsilon\mu\frac{\partial\tilde{u}}{\partial z}\left(\frac{\partial\tilde{u}}{\partial z}+\frac{1}{r}\frac{\partial(\tilde{v}r)}{\partial r}+\frac{\partial\tilde{w}}{r\partial\theta}\right)\\
&+\frac{2}{3}\varepsilon\mu\overline{\rho\frac{\partial u''}{\partial z}\left(\frac{\partial u''}{\partial z}+\frac{1}{r}\frac{\partial(v''r)}{\partial r}+\frac{\partial w''}{r\partial\theta}\right)}\\
&+\frac{1}{r}\frac{\partial}{\partial r}\left[\varepsilon\overline{\rho}\mu r\tilde{u}\left(\frac{\partial\tilde{v}}{\partial z}+\frac{1}{r}\frac{\partial(\tilde{u}r)}{\partial r}\right)\right]+\overline{\frac{1}{r}\frac{\partial}{\partial r}\left[\varepsilon\mu r\rho u''\left(\frac{\partial v''}{\partial z}+\frac{1}{r}\frac{\partial(u''r)}{\partial r}\right)\right]}
\end{aligned}
$$

$$
-\bar{\rho}\frac{\varepsilon\mu}{r}\frac{\partial(\tilde{u}r)}{\partial r}\left(\frac{\partial\tilde{v}}{\partial z}+\frac{1}{r}\frac{\partial(\tilde{u}r)}{\partial r}\right)-\frac{\varepsilon\mu}{r}\overline{\rho\frac{\partial(u''r)}{\partial r}\left(\frac{\partial v''}{\partial z}+\frac{1}{r}\frac{\partial(u''r)}{\partial r}\right)}
$$

$$
+\frac{\partial}{r\partial\theta}\left[\varepsilon\bar{\rho}\mu\tilde{u}\left(\frac{\partial\tilde{w}}{\partial z}+\frac{\partial(\tilde{u}r)}{r\partial\theta}\right)\right]+\overline{\frac{\partial}{r\partial\theta}\left[\varepsilon\mu\rho u''\left(\frac{\partial w''}{\partial z}+\frac{\partial(u''r)}{r\partial\theta}\right)\right]}
$$

$$
-\bar{\rho}\varepsilon\mu\frac{\partial\tilde{u}}{r\partial\theta}\left(\frac{\partial\tilde{w}}{\partial z}+\frac{\partial\tilde{u}}{r\partial\theta}\right)-\overline{\varepsilon\mu\rho\frac{\partial u''}{r\partial\theta}\left(\frac{\partial w''}{\partial z}+\frac{\partial u''}{r\partial\theta}\right)}
$$

**viii) subtract RHS of mean kinetic energy eqn and use continuity to get**

$$
\begin{aligned}
&\overline{2\frac{\partial}{\partial z}\left(\varepsilon\mu\rho u''\frac{\partial u''}{\partial z}\right)}-\overline{2\varepsilon\mu\rho\left(\frac{\partial u''}{\partial z}\right)^2}+\overline{\frac{1}{r}\frac{\partial}{\partial r}\left[\varepsilon\mu r\rho u''\left(\frac{\partial v''}{\partial z}+\frac{1}{r}\frac{\partial(u''r)}{\partial r}\right)\right]}\\
&\quad+\overline{\frac{\partial}{r\partial\theta}\left[\varepsilon\mu\rho u''\left(\frac{\partial w''}{\partial z}+\frac{\partial u''}{r\partial\theta}\right)\right]}-\overline{\varepsilon\mu\rho\frac{\partial u''}{r\partial\theta}\left(\frac{\partial w''}{\partial z}+\frac{\partial u''}{r\partial\theta}\right)}\\
&\quad-\frac{\varepsilon\mu}{r}\overline{\rho\frac{\partial(u''r)}{\partial r}\left(\frac{\partial v''}{\partial z}+\frac{1}{r}\frac{\partial(u''r)}{\partial r}\right)}
\end{aligned}
\tag{82}
$$

**ix) similar equations can be written for the $r$ and $\theta$ directions**

$$
\begin{aligned}
&\overline{2\frac{1}{r}\frac{\partial}{\partial r}\left(\varepsilon\mu\rho r v''\frac{1}{r}\frac{\partial(v''r)}{\partial r}\right)}-2\frac{\varepsilon\mu}{r}\overline{\rho\left(\frac{\partial(v''r)}{\partial r}\right)^2}+\overline{\frac{\partial}{\partial z}\left[\varepsilon\mu\rho v''\left(\frac{\partial v''}{\partial z}+\frac{1}{r}\frac{\partial(u''r)}{\partial r}\right)\right]}\\
&\quad+\overline{\frac{\partial}{r\partial\theta}\left[\varepsilon\mu\rho v''\left(\frac{\partial v''}{r\partial\theta}+\frac{1}{r}\frac{\partial(w''r)}{\partial r}\right)\right]}-\overline{\varepsilon\mu\rho\frac{\partial v''}{r\partial\theta}\left(\frac{1}{r}\frac{\partial(w''r)}{\partial r}+\frac{\partial v''}{r\partial\theta}\right)}\\
&\quad-\overline{\varepsilon\mu\rho\frac{\partial v''}{\partial z}\left(\frac{\partial v''}{\partial z}+\frac{1}{r}\frac{\partial(u''r)}{\partial r}\right)}
\end{aligned}
\tag{83}
$$

$$
\begin{aligned}
&\overline{2\frac{\partial}{r\partial\theta}\left(\varepsilon\mu\rho w''\frac{\partial w''}{r\partial\theta}\right)}-\overline{2\varepsilon\mu\rho\left(\frac{\partial w''}{r\partial\theta}\right)^2}+\overline{\frac{1}{r}\frac{\partial}{\partial r}\left[\varepsilon\mu\rho r w''\left(\frac{\partial v''}{r\partial\theta}+\frac{1}{r}\frac{\partial(w''r)}{\partial r}\right)\right]}\\
&\quad+\overline{\frac{\partial}{\partial z}\left[\varepsilon\mu\rho w''\left(\frac{\partial w''}{\partial z}+\frac{\partial u''}{r\partial\theta}\right)\right]}-\overline{\varepsilon\mu\rho\frac{\partial w''}{\partial z}\left(\frac{\partial w''}{\partial z}+\frac{\partial u''}{r\partial\theta}\right)}\\
&\quad-\frac{\varepsilon\mu}{r}\overline{\rho\frac{\partial(w''r)}{\partial r}\left(\frac{\partial v''}{r\partial\theta}+\frac{1}{r}\frac{\partial(w''r)}{\partial r}\right)}
\end{aligned}
\tag{84}
$$

**x) addition of eqns 82, 83, 84, rearranging and modeling turbulent kinetic energy diffusion as $\mu_{total}=\mu+\mu_t$ gives RHS of turbulent kinetic energy eqn**

$$
\begin{aligned}
&\frac{\partial}{\partial z}\left[\varepsilon\left(\mu+\frac{\mu_t}{\sigma_k}\right)\frac{\partial k}{\partial z}\right]+\frac{1}{r}\frac{\partial}{\partial r}\left[\varepsilon r\left(\mu+\frac{\mu_t}{\sigma_k}\right)\frac{1}{r}\frac{\partial(kr)}{\partial r}\right]+\frac{\partial}{r\partial\theta}\left[\varepsilon\left(\mu+\frac{\mu_t}{\sigma_k}\right)\frac{\partial k}{r\partial\theta}\right]\\
&\quad-\varepsilon\epsilon-2\mu\varepsilon\left[\left(\frac{\partial\sqrt{k}}{\partial z}\right)^2+\left(\frac{1}{r}\frac{\partial(\sqrt{k}r)}{\partial r}\right)^2+\left(\frac{\partial\sqrt{k}}{r\partial\theta}\right)^2\right]
\end{aligned}
\tag{85}
$$

# D Viscosity Relation

The following is a detailed description of the dense gas viscosity model by Lucas that will be applied to the CVV analysis.

Using the equation for viscosity derived from the kinematic theory of gases gives

$$\mu = 26.69\frac{(M_{wt}T)^{0.5}}{\sigma^2\Omega_v},$$

where $\Omega_v$ represents the collision integral set to unity if the molecules do not attract one other and $\sigma$ is the diameter of a gas molecule. By assuming $\sigma = 0.809V_c$ and $V_c \propto \frac{RT_c}{P_c}$, a dimensionless viscosity is written as

$$\mu_r = \xi\mu^{\circ} = f(T_r), \tag{86}$$

where

$$\xi = 0.176\left[\frac{T_c}{M_{wt}^3 P_c^4}\right]. \tag{87}$$

The low pressure viscosity is $\mu^{\circ}$, $T_c$ and $P_c$ are the critical pressure and temperature of the combustion products and $\xi$ can be thought of as an inverse viscosity. The reduced temperature function as defined by Lucas is

$$\begin{aligned} f(T_r) = [&0.807T_r^{0.618} - 0.357exp(-0.449T_r) + 0.340\exp(-4.058T_r) \\ &+ 0.018]F_P^{\circ}F_Q^{\circ}, \end{aligned} \tag{88}$$

where $F_P^{\circ}$ represents a low pressure correction factor accounting for polarity and $F_Q^{\circ}$ represents a correction factor accounting for the quantum effects of He, $N_2$ and $D_2$ gases. For the purposes of a CVV, $F_Q^{\circ}$ will be set to unity.

In order to obtain $F_P^{\circ}$ values a reduced dipole moment of the gas molecule is required, which is defined as

$$di_r = 52.46\frac{di^2 P_c}{T_c^2}. \tag{89}$$

The variation of $F_P^{\circ}$ with respect to $di_r$ is defined by the relation

$$F_P^{\circ} = \begin{cases} 1 & 0.0 \le di_r < 0.022 \\ 1 + 30.55(0.292 - Z_c)^{1.72} & 0.022 \le di_r < 0.075, \\ 1 + 30.55(0.292 - Z_c)^{1.72}\lvert 0.96 + 0.1(T_r - 0.7)\rvert & 0.075 \le di_r \end{cases} \tag{90}$$

where $Z_c = \frac{P_c V_c}{RT_c}$ is the critical compressibility factor.

At high pressures additional correctional parameters must be included in order to account for the increased molecular interaction. The first additional parameter $Z_1$ is defined as

$$Z_1 = \mu^{\circ}\xi = f(T_r). \tag{91}$$

The second additional dense gas parameter $Z_2$ is defined as

$$Z_2 = 0.6 + 0.76P_r^{\alpha} + (6.99P_r^{\beta} - 0.6)(1 - T_r), \quad \text{if } T_r \leq 1.0 \text{ and } P_r < \frac{P_{vp}}{P_c} \tag{92}$$

or

$$Z_2 = \mu^{\circ}\xi \left[\frac{1 + aP_r^{e}}{bP_r^{f} + (1 + cP_r^{d})^{-1}}\right], \quad 1 < T_r < 40 \text{ and } 0 < P_r \leq 100, \tag{93}$$

where $P_{vp}$ is the combustion gas vapor pressure and $\alpha$, $\beta$, $a$, $b$, $c$, $d$, $e$ and $f$ are constants given by the relations

$$\begin{aligned}
\alpha &= 3.262 + 14.98P_r^{5.508} \\
\beta &= 1.390 + 5.746P_r \\
a &= \frac{1.245\text{x}10^{-3}}{T_r} \exp(5.1726T_r^{-0.3286}) \\
b &= a(1.6553T_r - 1.2723) \\
c &= \frac{0.4489}{T_r} \exp(3.0578T_r^{-37.7332}) \\
d &= \frac{1.7368}{T_r} \exp(2.2310T_r^{-7.6351}) \\
e &= 1.3088 \\
f &= 0.9425 \exp(-0.1853T_r^{0.4489}).
\end{aligned}$$

After calculating $Z_1$ and $Z_2$ another parameter relating the two is defined as

$$Y = \frac{Z_2}{Z_1} \tag{94}$$

and a new high pressure correlation factor can then be defined as

$$F_P = \frac{1 + (F_P^{\circ} - 1)Y^{-3}}{F_P^{\circ}}. \tag{95}$$

Finally the dense gas viscosity correlation can be defined as

$$\mu = \frac{Z_2F_P}{\xi}. \tag{96}$$

It is interesting to note that at low pressures $Y$ is essentially unity, $F_P = 1$ and $Z_2 = \mu^{\circ}\xi$. Therefore at low pressures $\mu \longrightarrow \mu^{\circ}$ as expected. This is a very straightforward method to program and it only requires the input values of $T_c$, $P_c$, $Z_c$ and $di$ from tables in Reid as well as the CVV $P$ and $T$.

|  | $T_c$ | $P_c$ | $Z_c$ | di |
|---|---|---|---|---|
| species | (K) | (bar) | — | (debye) |
| $H_2O$ | 647.3 | 221.2 | 0.235 | 1.8 |
| $CO_2$ | 304.1 | 73.8 | 0.274 | 0.0 |
| CO | 132.9 | 35.0 | 0.295 | 0.1 |
| NO | 180 | 64.8 | 0.250 | 0.2 |
| $NO_2$ | 431 | 101 | 0.473 | 0.4 |
| $H_2$ | 33.2 | 13 | 0.306 | 0.0 |
| $N_2$ | 126.2 | 33.9 | 0.290 | 0.0 |

Table 1: Flowfield inside of a constant volume vessel.

There is a more involved method pertaining to gas mixtures involving the summation of fractional quantities but this requires a detailed analysis of the combustion products for the particular propellant. The computation of this gas mixture is outside the scope of this analysis and therefore a representative combustion component from the above table will be used for viscosity calculations of the propellant combustion gases.

# APPENDIX 4

# PREDICTION OF HEAT TRANSFER FROM PROPELLANT BURNING AT THE WALLS OF A CLOSED VESSEL

by

Florence C. Berger

# HEAT TRANSFER FROM PROPELLANT BURNING IN A CONSTANT-VOLUME CHAMBER

by

**F.C. Berger**

**Department of Aerospace Science and Engineering**

**A thesis submitted in conformity with the requirements for the Degree of Master of Applied Science in the University of Toronto**

# Abstract

In this work, a simple model for the flow and the heat transfer during the burning of solid propellant grains in a closed vessel is developed. The first part is dedicated to a theoretical description of the processes involved during burning, and to a review of the existing models. Following this, a computer program that models the burning of a single large solid propellant grain in two dimensions is presented. The model used neglects radiative heat transfer and focuses rather on convective heat transfer. Although the numerical results only reproduce trends of the experiments, they bring to light a few points that are of importance to the interior ballistician. Indeed, they show that velocities as high as 10 times the burning rate can be encountered in the vessel and that many vortices are present in the flow. Moreover, it appears that the temperature is not uniform (small areas where it is higher than the adiabatic flame temperature exist), and that the convective heat loss rate is neither constant nor proportional to the time-derivative of the average pressure. It is concluded that a more detailed three dimensional analysis of the flow in the vessel should be undertaken.

# Acknowledgments

The author would like to thank Dr J.J.Gottlieb who supervised this research. His constant interest and enthusiasm as well as useful guidance have greatly facilited the production of this work.

Clinton Groth, PhD student at UTIAS, is especially acknowledged for the great help and patience he provided, in particular for the implementation of Roe's method.

Thanks, too, to Mrs. Nora Burnett whose assistance was much appreciated during the literature search phase of this work.

# Table of Contents

Page

Title Page ........ i

Abstract ........ ii

Acknowledgments ........ iii

Table of Contents ........ iv

List of Symbols ........ vi

1.0 INTRODUCTION ........ 1

2.0 THE CLOSED BOMB EXPERIMENT ........ 2

2.1 Burning rate ........ 2

2.1.1 Effect of pressure ........ 3

2.1.2 Effect of temperature ........ 3

2.1.3 Effect of cross flow ........ 4

2.2 Closed vessel experiment ........ 4

2.3 Energy losses ........ 7

2.3.1 Heat transfer ........ 8

2.3.2 A simple model ........ 17

3.0 EXISTING MODELS ........ 18

3.1 Before 1950 (first approaches) ........ 19

3.2 Vest [1953] ........ 20

3.3 DREV [1989] ........ 22

3.4 Krier [March 1976] ........ 25

3.5 Robin and Horst [December 1976] ........ 26

3.6 Large Caliber Weapon Systems Laboratory ........ 27

3.7 Price and Juhasz [September 1977] ........ 27

3.8 Cohen and Strand [1978] ........ 29

3.9 De Soto [1965] ........ 29

3.10 Conclusion ........ 30

4.0 NUMERICAL ANALYSIS ........ 31

4.1 Governing equations ........ 32

4.2 Boundary conditions ........ 32

4.3 Initial conditions ........ 34

4.4 Heat transfer model ........ 35

4.5 Numerical method .......... 39
4.6 2D computer program .......... 40
5.0 NUMERICAL RESULTS AND DISCUSSION .......... 42
5.1 Reference computation .......... 43
5.1.1 Wall flow .......... 43
5.1.2 Core flow .......... 43
5.2 Grain geometry .......... 44
5.3 Grain motion .......... 44
5.3.1 Free motion .......... 44
5.3.2 Imposed motion .......... 45
5.4 Initial temperature .......... 45
5.5 Heat loss rate .......... 45
6.0 CONCLUDING REMARKS .......... 47
7.0 REFERENCES .......... 50
Figures
Appendix A: SIMPLE MODEL
Appendix B: INPUT PARAMETERS
Appendix C: RADIATIVE HEAT TRANSFER
Appendix D: HYBRID SCHEMES
Appendix E: ROE'S METHOD

# List of Symbols

## Alphanumeric Symbols

| | |
|---|---|
| $A$ | area [m$^2$] |
| $c_v$,$c_p$ | specific heats at constant volume and constant pressure [W·m$^{-2}$·K$^{-1}$] |
| $D$ | diameter [m] |
| $f$ | form factor |
| $h^c$ | convective heat transfer coefficient [W·m$^{-2}$·K$^{-1}$] |
| $h^r$ | radiative heat transfer coefficient [W·m$^{-2}$·K$^{-4}$] |
| $k$ | thermal conductivity [W·m$^{-1}$·K$^{-1}$] |
| $m$ | mass [kg] |
| $n$ | burning index |
| $n_x, n_y$ | number of nodes in the $x$ and $y$ directions |
| $\mathrm{Nu}_L$ | $= hL/k$ Nusselt number |
| $p$ | pressure [Pa] |
| $\mathrm{Pr}$ | $= \mu c_p/k$ Prandtl number |
| $q$ | heat loss rate [W] |
| $Q$ | instantaneous heat loss [J] |
| $r$ | burning rate [m·s$^{-1}$] |
| $R$ | gas constant [J·kg$^{-1}$·K$^{-1}$], radius [m] |
| $\mathrm{Re}_L$ | $= \rho v L/\mu$ Reynolds number |
| RF | $= p_{max}/p_{max}^{std}$ relative force |
| RQ | $= (\frac{dp}{dt})/(\frac{dp}{dt})^{std}$ relative quickness |
| $T$ | temperature [K] |
| $T_{fl}$ | adiabatic flame temperature [K] |
| $u$,$v$ | velocities in $x$ and $r$ directions respectively |
| $V$ | volume [m$^3$] |
| $w$ | web [m] |
| $x$ | length of propellant burnt measured inwards [m] |
| $Z$ | mass fraction of propellant burnt |

## Greek Symbols

| | |
|---|---|
| $\beta$ | burning coefficient [m·s$^{-1}$·Pa$^{-1}$] |
| $\epsilon$ | emissivity |
| $\eta$ | co-volume [m$^{-3}$] |
| $\varphi_\nu$ | monochromatic radiative flux [W·m$^{-2}$·s$^{-1}$] |
| $\phi_\nu$ | total monochromatic radiative flux [W·s$^{-1}$] |
| $\varphi$ | heat transfer flux [W·m$^{-2}$] |
| $\Phi$ | total heat transfer flux [W] |

| | |
|---|---|
| $\lambda$ | length to web ratio of the solid propellant grain |
| $\mu$ | viscosity [$kg \cdot m^{-1} \cdot s^{-1}$] |
| $\rho$ | density [$kg \cdot m^{-3}$] |
| $\sigma$ | $= 1.567\ 10^{-8}\ W \cdot m^{-2} \cdot K^{-4}$ Stephan-Boltzmann constant |

### Subscripts

| | |
|---|---|
| $a$ | air, ambient gases |
| $bs$ | burning surface |
| $cb$ | combustion |
| $ch$ | chamber, vessel |
| $fl$ | flame |
| $g$ | gas |
| $gr$ | solid propellant grain |
| $i$ | inner node |
| $ig$ | igniter gases, ignition |
| $load$ | loading |
| $m$ | mean |
| $p$ | propellant gas |
| $s$ | solid propellant |
| $t$ | transient |
| $w$ | wall |
| $wg$ | gaseous wall node |

### Superscripts

| | |
|---|---|
| $c$ | convective |
| $cd$ | conductive |
| $cc$ | conducto-convective |
| $exp$ | experimental |
| $fin$ | final |
| $ini$ | initial |
| $r$ | radiative |
| $th$ | theoretical |
| $tot$ | total |
| $-$ | time averaged |

## 1.0 INTRODUCTION

The need for rapid ballistic assessment for propellant acceptance or rejection has led to the development of analytical methods by which one may theoretically predict the interior ballistics of a given gun-propellant system. A key element in any such ballistic model is the representation of the rate at which the propellant grains in the charge are consumed. One can infer such rates from pressure-time data recorded during propellant burning in a pressure vessel, commonly referred to as a closed bomb. The purpose of this work is to develop a simple model for the flow and the heat transfer during the burning of the charge in such a chamber. It is part of the development of a new computer program intended to determine, as accurately as possible, the overall combustion properties and burning rate law of new propellants used in military and experimental guns at DREV.

The process involved during burning is quite complicated. Several non-ideal effects occur, which are difficult to include in the analysis. They are:

- non-uniform ignition of the grains,
- dynamic burning effects due to the high pressure and rapid pressure rise in the chamber, and
- sizable heat losses to the chamber walls.

Only the modeling of the last effect is discussed in this work. Indeed, heat losses from the hot combustion gases to the cooler vessel walls are significant even though the combustion time is very short (5 to 20 ms). It is therefore necessary to develop a realistic model based on the three modes of heat transfer rather than use semi-empirical corrections as has been done up to now. Again, various difficulties arise. They are:

- solid grains move about,
- gas motion is driven by burning and solid grains motion, both of which result in a complex, probably turbulent flow,
- conduction and convection might evolve from laminar flow at the beginning of burning to turbulent flow later on,
- free and forced convection might both be important, and
- transport and radiative properties of the gases and of the solid particles are required.

Due to the complexity of the analysis, all the aspects of the problem cannot be considered. Thus the burning of one big solid grain in a 2D geometry is modeled and radiative heat transfer is neglected. The main objective is to obtain a convective heat transfer coefficient $h^c$, as a function of both space and time, based on the fundamental equations of physics rather than on semi-empirical formulations. After describing some of the processes involved in the closed vessel experiment in chapter 2, chapter 3 reviews models that have been developed and used since the middle of the century. Finally, a new model describing the flow and a simple way to account for heat transfer are proposed and the results discussed. They reproduce trends of the actual experiment and show that this model constitutes a first step to a much more complex one, involving grain movement and turbulent gas motion.

## 2.0 THE CLOSED BOMB EXPERIMENT

In this section, first a general view on the closed bomb experiment is presented. Questions are: what was it set up for? What can be obtained from it? How do the energy losses affect the results? The processes involved during heat transfer, are then explained from a theoretical point of view, in order to get acquainted with the problem.

### 2.1 BURNING RATE

When studying the combustion of a solid propellant, one of the major concerns is to determine its burning rate. In guns, solid propellants are used as propelling charges for the projectile. When they deflagrate, they burn from the surface inwards. Experimentally it is observed that the surface recedes parallel to itself at a definite rate. This is known as Piobert's law. The major purpose of solid propellant deflagration theories is to find the dependence of this burning rate on the ambient pressure, propellant temperature and chemical composition. The knowledge of the burning rate is not only of fundamental interest but also of importance to the design of guns that employ solid propellants. In fact, it is a key element to any interior ballistics model of a gun system. From the given properties of the charge (the adiabatic flame temperature, co-volume, burning rate, etc.), the performance of the gun can be obtained. The most important are the projectile's muzzle velocity and the maximum pressure developed in the gun. Depending on the specifications, one type of solid propellant may be selected to optimize gun performance.

An exact analytical expression for the burning rate cannot be derived theoretically because the phenomena involved are both very complex and not yet entirely understood. The burning process involves at least three different phases: a solid phase, a mixed phase (solid and gas) and a gaseous phase. In the simplest model there would be no mixed phase and the following mechanisms would occur subsequently:

- heat conduction from the reaction zone to the solid raising its temperature high enough (about 700 K) so that gasification (or a more complex reaction) occurs,
- diffusion and convection of the gases to the reaction zone where the final products are formed. The combustion zone is illustrated in the diagram below.

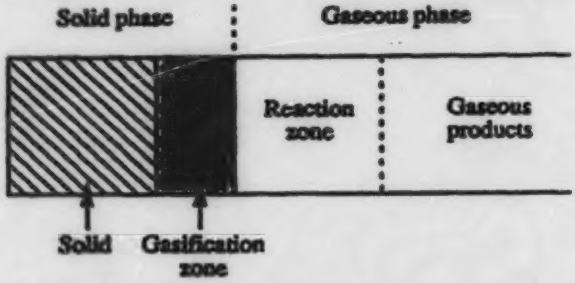

Schematic diagram of the combustion zone at the solid surface.

Depending on which process controls the burning velocity (the gasification, the solid reactions or the gaseous reactions), various expressions can be derived for the burning rate, $r$. They are not simple and may contain several unknown parameters. Experimental measurements are therefore required in order to ascertain deflagration mechanisms and also to provide a simpler empirical expression for $r$. It is generally accepted that, for a given solid propellant, $r$ depends only on two parameters, the initial solid temperature, $T_s$, and the ambient pressure in the vessel, $p$.

### 2.1.1 Effect of Pressure

Empirically the burning rate is usually found to increase with pressure in proportion to p raised to a power less than unity. Many relations between $r$ and $p$ have been proposed. For example, one of the most prevalent is De Saint Robert's [AMC 64]:

$$r = \beta p^n , \quad n < 1.$$

$\beta$ is called the burning rate coefficient and $n$ the burning rate index. This simple relation is in common use because it is closely followed by most propellants for a pressure ranging from 50 to 250 MPa. Two different expressions, one by Muraour and one by Summerfield, are also widely used. Muraour [CORNER 50] assumed an affine relationship between $r$ and $p$:

$$r = a + bp.$$

This was later modified to include De Saint Robert's relation to

$$r = a + bp^n.$$

Summerfield's relation [PRICE 68], applicable to low pressures (below 10 MPa), differs significantly:

$$\frac{1}{r} = \frac{A}{p} + B\left(\frac{1}{p}\right)^{\frac{1}{3}}.$$

The first of the above expressions is often referred to as a steady state burning rate law, as opposed to unsteady burning rate laws where transient effects are taken into account. For example, Krier [KRIER 72] included the effect of the pressure time derivative using an additional factor:

$$r = \beta p^n \left[1 + \Psi(p)\frac{n a_s}{\beta^2 p^{2n+1}}\frac{dp}{dt}\right].$$

$\Psi(p)$ is a coefficient function of pressure, although it is usually set to unity, and $a_s$ is the thermal diffusivity of the solid. At high pressures such as are encountered in a closed vessel, transient effects are minor. Indeed the error in neglecting the time derivative term is around 4 % at most ( $| \Delta r/r | \approx dp/dt \cdot \lambda_s / r\rho_s c_s p \approx 4$ % ), and therefore, only steady state burning rates are relevant to this work.

### 2.1.2 Effect of Temperature

The combustion of solid propellant begins when enough hot material is present near the solid's surface. Burning starts when the surface has reached a certain temperature. Thus, it is expected that the burning rate is higher when the solid is warmer to start with. Actually this effect has been observed experimentally and can be included in the $r$-$p$ relationship in a simple manner:

$$r = \frac{\beta p^n}{T_e - T_{si}} ,$$

where $T_e$ is the explosion temperature and $T_{si}$ is the initial temperature of the propellant. Fisher and Trippe [FISHER 73] proposed a different expression:

$$r = (\alpha T_{si} + \beta)p^n + \gamma T_{si}.$$

The effect of $T_{si}$ can be accounted for in many different ways. All the expressions used are, however, empirical, and the various coefficients introduced must be obtained using curve fitting with experimental data.

### 2.1.3 Effect of Cross Flow

If the propellant grain burns in the presence of a cross flow, the burning rate normally increases as the velocity of the flow increases. The velocity dependent contribution to $r$ is called "erosive burning". The first model was developed in 1957 by Lenoir and Robillard for cylindrically perforated grains. An erosive burning rate was added to $r$, giving

$$r = \beta p^n + \frac{\alpha}{L^{0.2}} G^{0.8} \exp(\frac{-\beta r \rho_s}{G}) ,$$

where $G$ is the mass flow rate of the gaseous products in the perforated tube and $L$ is the distance downstream from the stagnation point. It is widely used because of its simplicity. Many other correlations have been derived since, based on boundary layer analysis at the surface of the grain. In the present work, burning of the solid propellant is modeled using a local burning rate, i.e. local pressure near the burning surface as opposed to the average pressure in the vessel, and therefore an expression for $r$ including erosive burning is not relevant.

For a wide range of solid propellants, $r$ lies between 0.5 and 7.5 cm·s$^{-1}$.

## 2.2 CLOSED VESSEL EXPERIMENT

The measurement of burning rates is usually done by burning a sample of propellant in a closed vessel or a strand burner and simultaneously recording the pressure in the chamber. Devices for doing this date from the 16$^{th}$ century and generally consist of a chamber with a heavy lid and a small hole to ignite the charge. Rapid burning of the propellant caused the lid to rise upwards. The height to which the lid rose was an indication of the relative strength of the propellant. Closed vessels are nowadays significantly more sophisticated. They have been in use for about 100 years and have undergone constant improvement, particularly since the discovery of the piezo-electric gauge around 1918.

Closed bombs are cylindrical constant volume devices (figure 1), mainly made of an alloy steel (Nickel-chrome molybdenum steel) that can withstand pressures up to 700 MPa (typical gun pressures). Standard bomb volumes are 200 cm$^3$, 700 cm$^3$ and 2400 cm$^3$ with a length of twice the diameter in order to reduce the available surface area for heat losses to occur.[1] Facilities are provided to ignite the charge and record the pressure. Gases are released after combustion is complete.

The strand burner has also a constant combustion chamber but, unlike in the closed vessel, the sample of propellant is shaped in a cylindrical form with burning inhibited on all sides except one of those normal to the axis. The combustion wave therefore propagates as a 1D wave throughout the entire length of the propellant. Fine fuse wires are placed in small holes along the propellant at suitable intervals, and connected to an external timing device. From the record of the position of the flame front $x_{fl}$ at the different times, $r$ is fairly easily obtained by

$$r = \frac{dx_{fl}}{dt}.$$

However, the disadvantage of the strand burner, which makes it less useful for internal ballistics purposes, is that it does not simulate the actual conditions in a gun system as well as a closed vessel. Its usefulness comes in providing a check for closed bomb burning rates and information for the theoretical understanding of propellant combustion. Note that combustion in a closed vessel also differs from combustion in a gun due to the variable volume nature of the gun. When a burning rate, calculated from the closed vessel analysis is used as an input in a gun code, some adjustments have to be made on the burning rate constants (fixing the gun parameters: the muzzle velocity and the peak pressure), in order to meet experiments better. Trial and error procedures are used to determine best fit burning rates. In fact the burning rate constants are used to help account for factors not explicitly treated in interior ballistics models, such as erosive burning, bore friction and heat loss.

The principal disadvantage of the closed bomb method is the complexity of the data reduction technique. Closed bomb test data, because of the non-ideal effects mentioned earlier, should only be used on a relative basis. Even then, theoretically, they can only acceptably predict propellant variability if the relative quickness RQ[2] is within 10 % of some standard. These facts led to the development of a scaled ballistic simulator, the Dynagun by Krier et al. at the College of Engineering at the University of Illinois in 1975, to evaluate combustion and ballistic properties of several propellants. As it provides the same pressure environment that is found in an actual gun, burning rates derived from Dynagun should give a more reasonable representation of the rate of propellant consumption in a gun system. The results showed that, during the rapid pressure rise of the ballistic cycle, $r$ could be represented by $\beta p^n$, but that a significant burning rate undershoot was calculated during the pressure drop.

Typical pressure and pressure time derivative curves obtained from a closed vessel test are sketched on the following page. As mass is added by burning, the pressure rises more and more quickly in the vessel until it reaches a peak. At this time only 75 % (in mass) of the charge has burnt. Burnout occurs slightly afterward (less than 1 ms).

---

[1] For a fixed volume, the sphere has the minimum surface area, but spherical vessels are not as practical to use.

[2] Quickness is computed by averaging the values of the time derivative of pressure taken at specified fractions of the pressure developed in the experiment. It is useful for quality control purpose. The relative quickness is the ratio of the quickness of the propellant to a standard propellant quickness.

Finally, it decays almost exponentially to a final pressure, higher than the initial pressure because of the extra mass added.

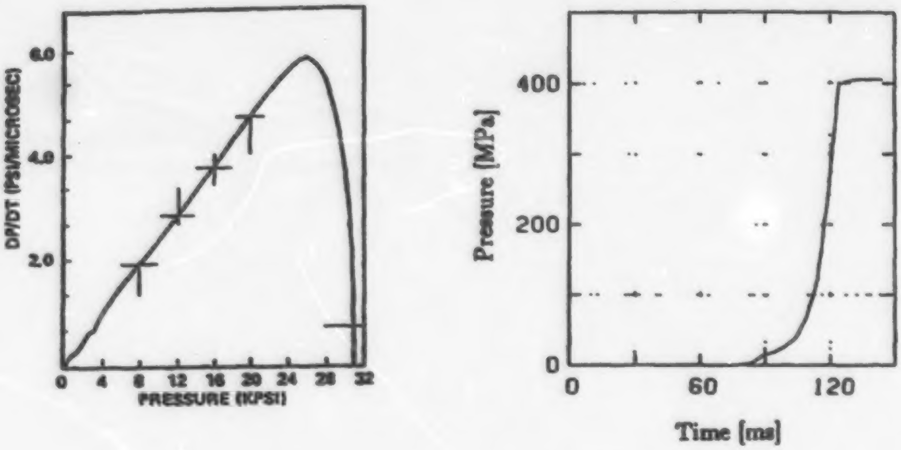

Closed bomb curve (from Juhasz).

From the pressure record, physical information on the propellant can be obtained, such as:

- the co-volume $\eta_p$,
- the impetus $F$,[3]
- the burning rate constants $\beta$ and $n$ defined as in De Saint Robert's equation.

The first two properties of the solid propellant are obtained from the maximum pressure in the vessel. Consider the equation of state just after burnout. If losses are neglected, then

$$p_{max} = \frac{m_s F}{V_{ch} - m_s \eta_p},$$

or

$$v = \eta_p + \frac{1}{p_{max}} F,$$

where $v = V_{ch}/m_s$. By plotting $v$ versus $1/p_{max}$ for various charge weights, one can obtain $\eta_p$ (ordinate at the origin) and $F$ (slope). In order to obtain $\beta$ and $n$, theory must be used in conjunction with the data because the experiment does not give a continuous record of the propellant grain size. Briefly, the mass fraction of propellant burnt, $Z$, is related to $p$ and $dp/dt$ by taking the derivative of the equation of state, and to $x$ by the grain form function. From both expressions one can obtain $dx/dt$ as a function of $p$ and $dp/dt$. $\beta$ and $n$ are estimated using curve fit techniques. Numerous extraction techniques have been employed. They will be described in chapter 3. The following assumptions are generally made:

---

[3] Also called "force constant" (although it does not have the dimensions of a force but of an energy per unit mass) because it is a measure of the intrinsic energy or strength of the propellant.

1. the propellant gas mixture follows the Noble-Able equation of state
$$p = \frac{m_p R_p T}{V_g - m_p \eta},$$
2. the molecular weight of the gases is constant (i.e., the gases mix well), as well as the co-volume,
3. all burning surfaces recede at the same rate,
4. initially the igniter is completely burnt and produces a known pressure in the vessel (approximately 0.5 MPa depending on the igniter gases' mass),
5. a steady state burning law can be used to describe the regression rate of the propellant grains
$$r = \frac{dx}{dt} = \beta p^n,$$
6. all variables are averaged in space, and hence only depend on time,
7. there are no heat losses to the chamber walls, and the effect of the initial air in the chamber is negligible.

With the heat losses being neglected in the analysis the predictions of the maximum pressure are significantly greater (7 % to 14 %). In practice corrections must be applied to the previous results to account for energy losses. This results in better agreement between theories using different extraction methods, and experiments.

### 2.3 ENERGY LOSSES

There are two reasons for the energy losses. They are slight expansion of the vessel walls (approximately 2 % in volume at 200 MPa and 7 % at 1000 MPa) and heat transfer from the hot combustion gases to the cooler vessel walls. The expansion of the combustion chamber is responsible for pressure measurements that are about 1.5 % low at gas pressures of 200 MPa, and the discrepancy increases up to 12 % at higher pressures. However, in most experiments where the maximum pressure does not exceed 300 MPa, this type of energy loss is neglected. Very few specific studies to account for the heat transfer loss are still being conducted. Most of them date from the 1970s. It is generally argued that, as only relative test information is needed, if the heat loss conditions remain the same during two tests, the error made in neglecting them is very small. However, if the RQ of the propellant is very different from the reference one, this does not hold anymore. For example, if it is smaller, there will be more time for heat losses to occur. This causes an error in determining the value of the peak pressure, and hence of the relative force RF.[4] Moreover, it is not valid to compare two experiments conducted in two different bombs.

A recent study on the effects of variable surface area to volume ratio on closed bomb burning rates for single perforated grains [TOMPKINS 85], revealed that the heat loss aspect of the reduction does not seem to be a very sensitive area provided that the ratio is less than unity and that the propellant has a fairly rapid burning rate. It is also added that more experiments should be conducted in order to generalize this statement. Nevertheless, in order to determine RF accurately and the gun performances with data obtainable from closed bombs or strand burner experiments, a proper insertion of the heat loss aspect in the analysis is necessary.

It is instructional to review the heat transfer processes applicable to closed bombs before illustrating the effects of heat losses on the pressure and temperature curves using a simple model.

### 2.3.1 Heat Transfer

There are three modes of heat transfer, namely conduction, convection and radiation. Conduction occurs at an atomic or molecular scale. It is the fundamental mode of heat transfer, and appears in any system where a temperature gradient exists. Convection occurs when one part of a non-isothermal system moves relative to another part of that system. The mass transfer results in a heat transfer on a macroscopic scale, which is coupled to the conductive transfer on a microscopic scale. Radiative transfer coexists, in most practical cases, with conduction and convection. It is an irreversible exchange between a material system and a radiative field. When burning a solid propellant in a closed bomb, the three modes of heat transfer are present, although it is generally accepted that convection is the dominant process.

Conduction:

Atoms and molecules are characterized by translational, rotational, vibrational and electronic energies. Consider a surface inside a gas, being crossed by a very high number of particles. Conductive heat transfer corresponds to the situation in which the total mass flux through the surface is zero and the total energy flux summed over all particles is not zero. The convective flux through the surface can be represented phenomenologically on a macroscopic scale by the conductive flux vector

$$\vec{\varphi}^{cd} - k(T)\vec{\nabla}T.$$

This is known as Fourier's law, and $k$ is called the thermal conductivity. It varies from $10^{-2}$ to $10^{4}$ W·m$^{-1}$·K$^{-1}$. Gases, in general, have a low conductivity roughly proportional to the square root of temperature and strongly dependent on pressure at low and high pressures. Typically, for combustion gases, $k_p = 0.2\,\mathrm{W{\cdot}m^{-1}{\cdot}K^{-1}}$.

---

[4] RF is the ratio of the maximum pressure developed by a unit weight of propellant to the one developed by a standard propellant

## Convection:

A convective transfer is consecutive to a mass transfer in an anisothermal medium. Consider an elementary surface $dS$ centered around a point M inside a fluid, as shown below. The mass flow rate through $dS$ is given by

$$dm = \rho\vec{v}.\vec{n}\, dS.$$

It is associated with the convective flux

$$d\Phi^{cv} = dm\, h(T_M)\, dS = \rho\vec{v}.\vec{n}\, h(T_M)\, dS,$$

where $h$ is the local enthalpy per unit mass of the fluid.

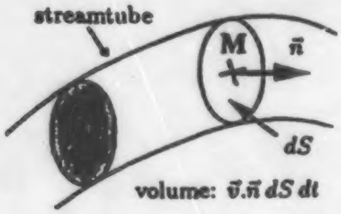

Convective heat flux through an area $dS$.

Three types of convective transfer are defined:

- forced convection applies when the movement of the fluid is imposed by an external intervention,
- free or natural convection (applies inside a fluid where a temperature gradient exists) occurs when the movement of the fluid is generated by gravity action due to the variation of density with temperature and,
- mixed convection corresponds to the coupling of the two above processes.

## Conducto-convective flux at a wall:

The heat transfer from the combustion gases to the vessel walls is given by the heat flux at the wall. A wall and a semi-transparent gas as shown on the figure below, are considered.

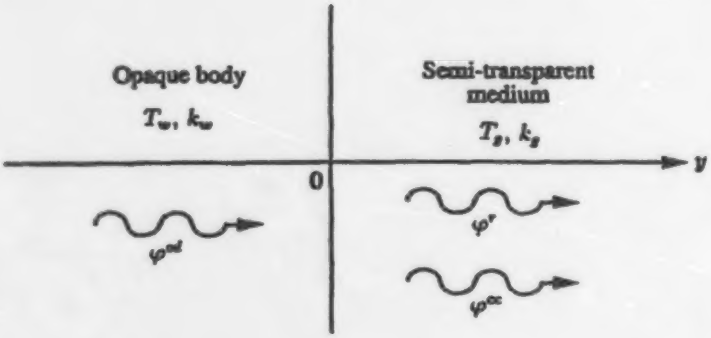

Interface between an opaque body and a semi-transparent medium: heat transfer fluxes.

The boundary condition at the wall is given by

$$-k_w \left(\frac{\partial T_w}{\partial y}\right)_{y=0} = -k_g \left(\frac{\partial T_g}{\partial y}\right)_{y=0} + \varphi^{r}_{w}$$

The first term on the right hand side of the equation is the conductive flux at the wall $\varphi_w^{cd}$, whereas the left hand side is the heat loss rate at the wall per unit surface area $dq_w/dS$. The major problem is to calculate the temperature gradient at the wall in the gas

$$\left(\frac{\partial T_g}{\partial y}\right)_{y=0}.$$

A complete analysis of the mechanical and thermal boundary layers is necessary to obtain it rigorously. A convenient short cut is to introduce a convective heat transfer coefficient $h^c[\,\mathrm{W \cdot m^{-2} \cdot K^{-1}}\,]$ such that the heat flux is equal to

$$\varphi_w^{cc} = h^c(T_w - T_g) = -k_g \left(\frac{\partial T_g}{\partial y}\right)_{y=0}.$$

This is called a conducto-convective flux ("conducto" because the flux at the wall is really conductive as the fluid's velocity is zero there and convective because it has the same expression as a convective flux). The problem is now to evaluate $h^c$. The usual correlation, valid for internal turbulent flows with a main directional flow, is

$$\mathrm{Nu}_{D_h} = 0.023\,\mathrm{Re}_{D_h}^{0.8}\,\mathrm{Pr}^{0.33},$$

where Pr is the Prandtl number, $D_h$ the hydraulic diameter (in the case of a cylindrical vessel, $D_h = D_{ch}$). The Nusselt number is

$$\mathrm{Nu}_{D_h} = \frac{hD_h}{k}.$$

Many different correlations are available depending on the type of flow and on the geometry. But in the closed bomb, there is no net flow and $D_h = D_{ch}$ is not a representative length, hence it is not strictly valid to apply these types of correlations. The diameter of the vortices in the flow or the effective depth of the radiative gas layer might be a better characteristic length. The order of magnitude of the convective transfer coefficient is given in the table below, depending on the process involved.

Table 1: Typical convective heat transfer coefficients.

| physical process | medium | $h^c[\,\mathrm{W \cdot m^{-2} \cdot K^{-1}}\,]$ |
|---|---|---|
| free convection | gas | 5–30 |
| | water | 100–1,000 |
| forced convection | gas | 10–300 |
| | water | 300–12,000 |
| | oil | 50–1,700 |
| | liquid metal | 6,000–110,000 |
| phase change | | 3,000–110,000 |

No accurate value for $h^c$ exists but it can be estimated[5] by $10^4\,\mathrm{W \cdot m^{-2} \cdot K^{-1}}$ and is generally found to vary in the same range as the convective coefficient for phase change does.

In the present study, a simple estimation of the type of convection that will drive the heat transfer can be done using typical orders of magnitude found in closed bombs. The Richardson number, $\mathrm{Ri} = \mathrm{Gr}/\mathrm{Re}^2$, is introduced. It is the ratio between the free convection and forced convection driving terms. If $\mathrm{Ri} \ll 1$, forced convection is the dominant process, if $\mathrm{Ri} \gg 1$, free convection dominates and $\mathrm{Ri} \approx 1$ corresponds to the mixed convection regime. Forced convection, here, applies to convection due to the burning of the propellant grains as opposed to convection due to gas buoyancy forces in the vessel. The velocity of the gases near the walls can be estimated using the method of Nordheim et al. [VEST 53] as

$$v_g \approx \frac{2h^c}{\rho_{load} f c_{pg}} ,$$

where $h^c$ is the convective heat transfer coefficient, $\rho_{load} = m_s/V_{ch}$ is the loading density, $f$ is the roughness factor ($0.002 \leq f \leq 0.005$) and $c_{pg}$ is the specific heat of the gases at constant pressure. With $c_{pg} = 1500\,\mathrm{J \cdot kg \cdot K^{-1}}$, $f = 0.003$ and $\rho_{load} = 200\,\mathrm{kg \cdot m^{-3}}$, the gases velocity is

$$v_g \approx \frac{h^c}{450} .$$

Using a typical value for the convective heat transfer coefficient, $h_c = 10^4\ \mathrm{W \cdot m^{-2} \cdot K^{-1}}$, the velocity of the gases can be approximated by $20\,\mathrm{m \cdot s^{-1}}$. The flow Reynolds number, based on the vessel diameter, is

$$\mathrm{Re} = \frac{\rho_g v_g D_{ch}}{\mu_g} .$$

If $\rho_g$ ranges from $0.1\ \mathrm{g \cdot cm^{-3}}$ to $100\,\mathrm{kg \cdot m^{-3}}$, $\mu_g = 4 \times 10^{-5}\ \mathrm{kg \cdot m^{-1} \cdot s^{-1}}$, $D_{ch} = 0.1$ m and $v_g = 20\ \mathrm{m \cdot s^{-1}}$, then

$$\mathrm{Re} = 5000 \text{ to } 5 \times 10^6 .$$

Under Boussinesq's[6] approximation, one can define the Grashoff number Gr, equivalent to the Reynolds number for free convection

$$\mathrm{Gr} = \frac{\rho_0^2 g \beta \delta(T) D_{ch}^3}{\mu_g^2} ,$$

where $\beta\ \delta(T)$ is the relative variation of density with temperature. Using the previous numerical values, $\beta = 4 \times 10^{-4}\ \mathrm{K^{-1}}$ and $\delta(T) = T_g - T_w = 3000$ K, the Grashoff number can be evaluated as

$$\mathrm{Gr} = 7.5 \times 10^4 \text{ to } 7.5 \times 10^8 .$$

From Re and Gr, Ri is obtained as

$$\mathrm{Ri} = \frac{\mathrm{Gr}}{\mathrm{Re}^2} \approx 1\% .$$

---

[5] From experiments conducted at DREV.

[6] Assumes small temperature variations, and variations of density with temperature only accounted for in the gravity term (Archimède's force). This is equivalent to assuming that $\rho = \rho_0[1 - \beta\ \delta(T)]$ with $\beta\ \delta(T) \ll 1$.

Since this is very small compared to unity, as a first approximation Forced convection can be considered to be the dominant process in the vessel. This is also enhanced by the fact that the velocities at the walls are relatively large for the dimension of the vessel.

**Radiation:**

Energy is constantly exchanged between any system and the radiative field by two means: emission (thermal energy is transformed into radiative energy), and absorption (radiative energy is transformed into thermal energy). There are two ways by which radiative heat losses can occur: radiation from the propellant gases and possibly the solid particles, and radiation by chemi-luminescence from the flame zone. The former is dependent upon the fact that water vapor and carbon dioxide, which are almost always contained in the combustion gases, are capable of both emitting and absorbing radiation. The solid walls of the vessel are also likely to take part in the heat transfer by means of their own radiation. The latter may occur only in the early stages of burning when the vessel is not entirely filled with the combustion gases. It has, to the author's knowledge, never been modeled. The following discussion is therefore restricted to the radiative heat transfer between the vessel walls and the combustion gases. Unless some reasonable assumptions are made concerning their radiative properties, no simple analytical expression for the radiative flux falling onto the walls can be obtained.

The vessel walls are assumed opaque, that is, the depth of penetration of radiation, $d$, is small compared to the thickness of the walls, $e$. Indeed, for metals, $d$ ranges from 1 Å to $10^2$ Å depending on the wavelength of the radiation, and $e$ is about 1 centimeter in a closed bomb. Any incident radiation is therefore either absorbed or reflected as illustrated below.

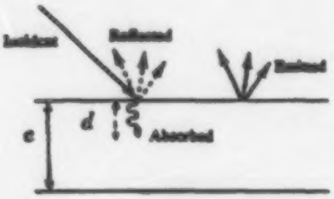

Radiative fluxes on an opaque body.

The next approximation concerns the directional character of their radiative properties. For the vast majority of opaque bodies, the reflectivity (and therefore the emissivity and the absorptivity) tends to become partially isotropic for two reasons. The first one is that the surface of the material is never perfectly smooth. Reflection becomes less and less specular when the rugosity of the surface increases. The evolution from specular to quasi isotropic reflection can be illustrated by the following diagram:

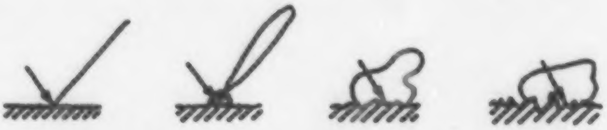

Evolution from specular to quasi isotropic reflection.

Even in the case of an optically smooth material (the asperities of the surface do not exceed one tenth of the wavelength), $\epsilon'_\nu$ and $\alpha'_\nu$ are largely independent of the direction. The second is that actual materials generally possess some diffusive properties. Due to the accumulation of successive diffusions, a fraction of an incident radiation will be reflected with a complex distribution of directions, as illustrated below.

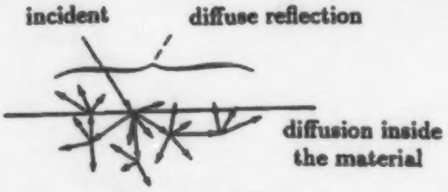

Diffuse reflection.

Therefore, the radiative properties of the walls are also assumed isotropic.

From the above discussion, it results that, only the superficial layers of the material are to be taken into account when evaluating its radiative properties. For polished materials, it is reasonable to assume that emissivity is independent of the wavelength, that is, that they radiate as grey bodies. Closed bombs are generally covered with a polished nickel-chrome-molybdenum steel liner to facilitate repair. Therefore, $\alpha'_{\nu w}$ is assumed independent of the wavelength. It can be estimated by $\alpha_w = 0.5$.

The radiative properties of the combustion gases are not well known. Very few precise measurements of their absorptivity have been made. In all current studies they are assumed opaque for simplicity. According to Klingenberg, it is likely that their absorptivity is very high [KLINGENBERG 76]. This justifies the assumption that their emissivity approaches that of a black body, that is $\alpha'_{\nu g} = \epsilon'_{\nu g} = 1$. However, to remain more general, the gases are assumed semi-transparent and non-diffusive. That is, they reflect, transmit and absorb any incident radiation. No assumption concerning the directionality and the dependence on the wavelength of their radiative properties is made.

Finally, both the vessel walls and the combustion gases are assumed to have a uniform and constant temperature.

Under the above assumptions, it can be shown (appendix C) that the total radiative flux at the vessel walls is equal to

$$\Phi^r_w = \int_0^{+\infty} \phi^r_\nu \, d\nu = \pi A_{ch} \int_0^{+\infty} \frac{\epsilon_w \bar{\bar{\epsilon}}_{\nu g}(L^\circ_\nu(T_g) - L^\circ_\nu(T_w))}{1 - (1 - \epsilon_w)(1 - \bar{\bar{\epsilon}}_{\nu g})} \, d\nu. \tag{1}$$

If the emissivity of the combustion gases is assumed independent of the wavelength, this expression simplifies into

$$\Phi^r_w = A_{ch} \frac{\epsilon_w \bar{\bar{\epsilon}}_g \sigma(T_g^4 - T_w^4)}{1 - (1 - \epsilon_w)(1 - \bar{\bar{\epsilon}}_g)}. \tag{2}$$

$\Phi^r_w$ as given by the above equation and $\Phi^r_w$ as given by equation (1) differ by the factor $1/(1 - (1 - \epsilon_w)(1 - \bar{\bar{\epsilon}}_g))$, which varies between unity and infinity for $0 \le \epsilon_w, \bar{\bar{\epsilon}}_g \le 1$. For $\epsilon_w = 0.5$, it is equal to $2/(1 + \bar{\bar{\epsilon}}_g)$. Consequently, when evaluating the total radiative heat loss at the vessel walls without taking the reflections on the walls into account, it is underestimated by the factor $2/(1+\bar{\bar{\epsilon}}_g)$.

For water and carbon dioxide, the emissivity $\bar{\bar{\epsilon}}_{\nu g}$ generally strongly depends on the wavelength. It can be written as

$$\bar{\bar{\epsilon}}_{\nu g} = 1 - \exp(\kappa_\nu R),$$

where $R$ is the effective depth of the radiative gas layer, and $\kappa_\nu$ is the monochromatic absorption coefficient. For a cylindrical vessel, $R$ is equal to

$$R = \frac{4V_{ch}}{A_{ch}} \approx R_{ch}.$$

For a given medium, $\kappa_\nu$ depends on the wavelength, the temperature and the gas pressure. The factor $T_g^4 - T_w^4$ will, in fact, rarely appear in the expression for $\Phi_w^r$, which will significantly differ from that given by equation (2). There is no simple analytical expression for the emissivity as a function of pressure, temperature and wavelength. Shack's equation takes the dependence upon the first two into account. $\bar{\bar{\epsilon}}_g$ is given by

$$\bar{\bar{\epsilon}}_g = 0.7(p_{\mathrm{CO_2}}\frac{R}{101.3})^{0.5}(\frac{T}{100.0})^{-0.5} + 7.0(p_{\mathrm{H_2O}}\frac{R}{101.3})^{0.8}(\frac{T}{100.0})^{-1},$$

where $p_{\mathrm{CO_2}}$ and $p_{\mathrm{H_2O}}$ are the partial pressures of carbon dioxide and water expressed in kiloPascals, and $T$ the temperature is in degrees Kelvin. For high pressures such as encountered in a closed vessel, this expression leads to $\bar{\bar{\epsilon}}_g = 1$.

It is generally accepted that radiation only contributes by a few percent to the total heat losses, and therefore can be neglected. The total radiative heat loss is given by

$$Q^{rad} = \int_0^{t_{cb}} \Phi_w^r \, dt.$$

The maximum radiative heat flux (equation (1)) is obtained when $\epsilon_w = \bar{\bar{\epsilon}}_{\nu g} = 1$, therefore,

$$Q_{max}^{rad} = t_{cb} A_{ch} \sigma (T_g^4 - T_w^4).$$

The total heat loss can be estimated by

$$Q^{tot} = \frac{V_{ch}}{\gamma_p - 1}\Delta p,$$

where

$$\Delta p = p_{max}^{th} - p_{max}^{exp}.$$

For a chamber volume of 700 $\mathrm{cm}^3$, a surface area of 500 $\mathrm{cm}^2$ ($A_{ch}/V_{ch} = 0.65\ \mathrm{cm}^{-1}$), a combustion time of 10 ms ($\rho_{load} = 0.2\ \mathrm{g{\cdot}cm^{-3}}$), and for an adiabatic flame temperature of 3000 K, the ratio of the maximum radiative heat loss to the total heat loss is given by[7]

$$\frac{Q_{rad}^{max}}{Q^{tot}} = 0.36\frac{(1-\Delta p/p)^4}{\Delta p/p}\%.$$

---

[7] The gases temperature, $T_g$, is estimated by $T_{fl}\ p_{max}^{exp}\ /\ p_{max}^{th}$

This expression is only for a ratio, $Q^{max}_{rad}/Q^{tot}$, smaller than 100 %. For typical pressure drops of 14 % or more, it does not exceed 1.5 %. However, for larger surface area to chamber volume ratios and smaller loading densities, for example $A_{ch}/V_{ch} = 10$ cm$^{-1}$ and $\rho_{load} = 0.15$ g·cm$^{-3}$, the percentage increases up to 29 %.

Considering the general case of a compressible fluid in the presence of a radiative field, the equations for the conservation of momentum and of energy are modified. However, even at high temperatures, only the effect on the energy equation is important. If the medium is local thermodynamic equilibrium, the energy equation becomes

$$\rho\frac{dh}{dt} = -\vec{\nabla}\cdot\vec{q} + \frac{dp}{dt},$$

where $h$ is the local enthalpy and $\vec{q} = \vec{q}^{cd} + \vec{q}^{r}$. Using Fourier's law to express the conductive flux vector $\vec{q^{cd}}$, it can be rewritten as

$$\rho\frac{dh}{dt} = \vec{\nabla}\cdot(k\vec{\nabla}T) + \frac{dp}{dt} - \vec{\nabla}\cdot\vec{q}^{r}.$$

The term $\vec{\nabla}\cdot\vec{q}^{r}$ disappears in two extreme cases: when the medium is entirely transparent ($\kappa_\nu = 0$), or when it is opaque to radiation ($\kappa_\nu \to \infty$), in which case $\vec{q}^{r} = \vec{0}$. In the general case of a semi-transparent diffusive medium, the expression of $\vec{q^{r}}$ requires to solve coupled nonlinear integro-differential equations, and is very complex. However, it can be simplified in several cases. For example, when the medium is optically thick, that is when the mean free path of the photons is very small compared to a characteristic length of the geometry of the vessel ($\kappa_\nu R \gg 1$), an analytical expression exists. This is very likely to be the case in a closed bomb, as the combustion gases have a very high absorptivity ($\bar{\bar{\alpha}}_{\nu_g} \approx 1$). The expression for the radiative flux is then similar to that for the conductive flux,

$$\vec{q}^{r} = -k^{r}(T)\vec{\nabla}T,$$

where

$$k^{r}(T) = \frac{16}{3}\sigma T^{3} l_\nu,$$

and $l_\nu$ is the mean free path of the photons. For a non-diffusive medium, it can be approximated by 1 / $\kappa_\nu$. The ratio of the conductive term to the radiative term can be estimated by

$$\frac{\vec{\nabla}\cdot\vec{q}^{r}}{\vec{\nabla}\cdot\vec{q}^{cd}} \approx \frac{16}{3}\frac{\sigma l_\nu T^{3}}{k_p^{cd}}\left(1 + 3\frac{||\vec{\nabla}T||}{T\vec{\nabla}^{2}T}\right) \approx \frac{16}{3}\frac{\sigma l_\nu}{k_p^{cd}}T^{3}.$$

For $k_p^{cd} = 0.2$ W·m$^{-1}$·K$^{-1}$, $\sigma = 5.678\times10^{-8}$, $T = 3000$ K and $l_\nu$ ranging from 0 to 4 $\mu$m, the ratio is less than 15 %. For a lower gas emissivity, $\bar{\bar{\epsilon}}_{\nu_g} = 0.8$, that is $l_\nu = 6$ mm, the ratio exceeds 50 %. Therefore, unless the combustion gases are entirely transparent or opaque to radiation, the radiative term should not be neglected if conductive effects are accounted for.

From the above discussion, it results that, the radiative heat losses are negligible compared to the total heat losses in vessels having a surface area to volume ratio smaller than unity. For high $A_{ch}/V_{ch}$ ratios, for example above 10 cm$^{-1}$, they can contribute to more than 30 % to the total heat losses. Convection, due to solid propellant burning, is therefore the dominant process of heat transfer in a closed bomb. The convective heat transfer coefficient is expected to be very high, around $10^4$ W·m$^{-2}$K$^{-1}$. Indeed, the total heat loss can be estimated by

$$Q^{tot} = \frac{V_{ch}}{\gamma_p - 1}\Delta p.$$

It is roughly equal to the total convective heat loss. The latter can be estimated using a constant convective heat transfer coefficient, $h_c$,

$$Q^{conv} = A_{ch} t_{cb} h^c (T_g - T_w).$$

Therefore, $h^c$ is given by

$$h^c = 4.6\times 10^5 \frac{\Delta p/p}{1 - \Delta p/p}\,\mathrm{W\cdot m^{-2}\cdot K^{-1}},$$

where the same numerical values as in chapter 1.3 have been used. For a pressure drop of 14 %, $h^c = 7.5\times10^4$ W·m$^{-2}$K$^{-1}$. Moreover, unless the combustion gases have a very high absorptivity, the contribution of the radiative term in the equation for the conservation of energy, can be as important as that of the conductive term. Hence, it should not be neglected if conductive effects are to be taken into account. However, near the vessel walls (boundary layer flow), both term are negligible compared to the convective term.

In the present work, the combustion gases are assumed to have a very high absorptivity. This enables to neglect the effect of radiative losses everywhere in the vessel.

From the analysis just presented, the main properties of the three different modes of heat transfer can be summarized. The rate of heat loss by convection is proportional to the mass rate of burning of the gases $\rho_s r$, and consequently convective losses are proportional to the total mass burnt,

$$q^c \propto \int \rho u\,dt \propto \int \rho_s r\,dt \propto \rho_s \int dx \propto m_s.$$

This results in reducing the adiabatic flame temperature, $T_{fl}$, by a fixed amount. The global shape of the temperature curve remains unchanged. Radiative losses are proportional to the time of burning, and hence to the size of the grain,

$$q^r \propto t \propto w.$$

In this case (constant rate heat loss) a slower increase of temperature is observed at the beginning of burning ($Z = 30$ %). Then the temperature reaches a maximum and starts to decay exponentially just before burnout ($Z = 90$ %). For slow burning propellants, the gases velocities will be very small and their component tangential to the walls even smaller. In this case, losses by simple conduction at a constant rate might be relevant. Total heat losses are therefore not directly proportional to the time of burning. This was observed experimentally in the early 1930s. To conclude this section, it should be added that forced convection will be assumed to be the dominant mode of heat transfer during the combustion of solid propellant grains in a closed vessel. This relies upon a high absorptivity of the combustion gases and a low surface area to chamber volume ratio (less than unity). Its effects on the pressure and temperature curves can be illustrated by the following simple model.

### 2.3.2 A Simple Model

A given mass of propellant, $m_s$, burning in a constant volume, $V_{ch}$, as shown below, is considered.

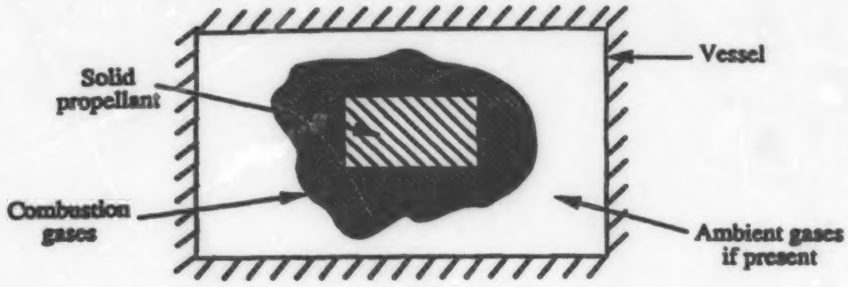

Geometry used in the simple example.

The physical properties of the propellant used are given in appendix A. The vessel's pressure and temperature time variations are obtained under the same simplifying assumptions mentioned earlier (section 2.2). Only the seventh one is dropped and replaced by the following:

- heat loss by conduction and radiation is taken into account using constant heat transfer coefficients,
- the grains are cylindrical.

The effect of the initial presence of air in the vessel is studied. No mixing nor heat transfer between the combustion gases and the air are allowed. Heat transfer by convection is accounted for in the following way: when no air is present initially, it is assumed to occur at a rate given by

$$q^c_{wp} = h^c_p A_{ch}(T_p - T_w). \tag{3}$$

The value of the convective heat transfer coefficient $h^c_p$ is chosen so that the pressure drop is about 7 %, which is what has been observed experimentally at DREV, giving $1.5 \times 10^4$ W·m$^{-2}$·K$^{-1}$. When air is present, only heat transfer between air and the vessel walls is taken into account. This can be seen as if the combustion gases evolved from the center of the vessel and never reached the walls, being always surrounded by air (as illustrated in the above figure). The rate at which the loss occurs is given by

$$q^c_{wa} = h^c_a A_{ch}(T_a - T_w). \tag{4}$$

The convective heat transfer coefficient $h^c_a$ is constant and equal to $10^2$ W·m$^{-2}$·K$^{-1}$.

In order to obtain the order of magnitude of the maximum contribution of the radiative heat loss to the total heat loss, radiative heat transfer is added (only when the effect of air is neglected) at the following rate:

$$q^r_{wp} = \epsilon_p \epsilon_w \sigma A_{ch} (T_p^4 - T_w^4). \tag{5}$$

The two emissivities, $\epsilon_p$ and $\epsilon_w$, are constant and respectively equal to unity (corresponds to maximum possible radiative heat loss) and 0.5 (common value used for polished steel). The governing equations are summarized in appendix A.

Results from all possible cases (no heat transfer: no air, or air present initially, and heat transfer: no air, or air present initially) are now discussed (figure 2). When heat losses are neglected, the pressure and the temperature increase in the vessel and then remain constant after burnout. When the effect of air is neglected, the combustion gases evolve at the adiabatic flame temperature, $T_{fl}$. The maximum pressure reached, $p_{max}$, is about 280 MPa. When air is present, the temperature rises asymptotically towards $T_{fl}$. Air undergoes an adiabatic compression, and therefore its temperature increases from 293 K (initial temperature in the vessel) to 1300 K. It remains much lower than that of the combustion gases.

When heat losses are introduced, all maxima are lower. When the presence of air is neglected, $p_{max}$ is about 260 MPa and the pressure drop is about 7 %. Both values can be adjusted by varying the convective heat transfer coefficient: the larger $h^c_p$ is, the larger the pressure drop is and the lower $p_{max}$ is. The corresponding total heat loss, $Q^{tot}_{wp}$, is approximately 53 kJ. This has the same order of magnitude as that found at DREV. As expected, radiative heat losses appear to contribute only by a few percent to the total losses: $Q^r_w/Q^{tot}_w = 5$ %. When air is present, no significant drop in pressure is observed. Indeed, the value of the air's convective heat transfer coefficient is lower than that of the combustion gases and the air reaches lower temperatures, resulting in a much smaller total heat loss, $Q^{tot}_{wa} \approx 1$ kJ. The temperature of the combustion gases is not affected. This is consistent with the assumption that only heat transfer between the air and the vessel walls occurs. On the other hand the temperature of the air drops (significantly) by about 8 %.

Using this simple model, it has been shown that the effect of heat loss should not be neglected and that convective losses are indeed dominant. But, more importantly, it appears that there must be significant mixing between the propellant gases and the ambient gases, or that the former reach the walls very quickly. Indeed, if only heat transfer between air and the vessel walls is allowed, no pressure drop and a significantly lower total heat loss is found, both of which are inconsistent with experimental results.

## 3.0 EXISTING MODELS

The existing models taking heat transfer into account, are now reviewed and discussed.

Ballisticians first introduced the effect of heat loss in internal ballistic models for guns. This dates to the very end of the 18th century. It was done simply by subtracting some fraction of the total available propellant energy. This could be accomplished by adjusting the value of the specific heat upwards by a constant $\beta$ leading to the following equation for the conservation of energy:[8]

$$\underbrace{c_v m_s Z T}_{\text{internal energy of the propellant gases}} = \underbrace{c_v m_s Z T_{fl}}_{\text{total available energy}} - \underbrace{\tfrac{1+\beta}{2}\left(M_{piston} + \tfrac{m_s}{3}\right) v_{piston}^2}_{\text{kinetic energy of the piston and of the propellant gases}}.$$

The magnitude of the heat loss coefficient was estimated by adjusting the actual and calculated peak pressures in the barrel. It varied between 0.17 and 0.23. However, this method is not applicable to the closed bomb test because the piston velocity is zero. In most existing models, even currently in use, heat loss is neglected in the analysis. This means that the temperature of the combustion gases is kept constant and equal to the adiabatic flame temperature ($T_{fl}$).

It was only in the 1970s, with the development of increasingly sophisticated gun codes which sought to include more of the physics involved, that a strong interest arose in evaluating the burning rate as an intrinsic property of a propellant as opposed to purely empirical information, and therefore in inserting a proper analysis of the heat losses. However up to now, only semi-empirical corrections have been applied in internal ballistics codes (either to the total or to the instantaneous heat loss).

## 3.1 BEFORE 1950 (FIRST APPROACHES)

All the methods used in the first half of the 20th century corrected for the maximum pressure only and did not consider in detail the heat loss during burning. Roughly, it was considered that heat transfer takes place by radiation and convection. Radiative losses were considered to be proportional to the web of the grain and convective losses to the mass of propellant burnt. Several experiments were conducted, varying the web and the ratio of the surface area and the volume of the chamber. From the pressure data, a correlation was obtained between the maximum pressure corrected for heat loss, $p_{max}^{th}$, and the web $w$. They were usually expressed in terms of the adiabatic flame temperature as shown in the table below (web is in centimeters).

Table 2: Pressure drop for various adiabatic flame temperatures.

| $T_{fl}$ [K] | $p_{max}^{th}$ [% of $p_{max}^{exp}$] |
|---|---|
| 2400 | $3.7 + 38.1w$ |
| 2800 | $2.5 + 38.1w$ |
| 3200 | $0.9 + 38.1w$ |
| 3600 | $0.9 + 38.1w$ |

---

[8] See [HUNT 51] for further details on all the assumptions used to derive this equation.

Corrections that fit equally well were used, where the heat loss was assumed proportional to the square root or the third power of the web. Work of this type by Muraour et al. led to a correlation of the form

$$p_{max}^{th} - p_{max}^{exp} = \frac{A_{ch}}{V_{ch}} t_{cb}^{r} ,$$

where $r \approx 0.25$.

### 3.2 VEST [1953]

A first attempt was made by Vest to calculate the heat transfer coefficients in terms of measurable parameters and to estimate the relative contribution of the radiative heat loss. The various heat losses are assumed to have the following form:

- total: $Q_w^{tot} = m_s c_v (T_{fl} - T_{max}^{exp}) = Q_w^c + Q_w^r$,
- convective: $Q_w^c = A_{ch} h^c t_{cb} \left( \frac{T_{fl}+T_{max}^{exp}}{2} - T_w \right)$,
- radiative: $Q_w^r = A_{ch} \epsilon_p \epsilon_w \sigma t_{cb} \left[ \left( \frac{T_{fl}+T_{max}^{exp}}{2} \right)^4 - T_w^4 \right]$,

where $T_{max}^{exp} = T_{fl} p_{max}^{exp} / p_{max}^{th}$ and $p_{max}^{th}$ is obtained from the plot of $p_{max}^{exp}$ versus $A_{ch}/V_{ch}$.[9] Further assumptions are:

- the fourth power of the wall temperature is negligible compared to the fourth power of the average gas temperature,

$$T_w^4 \ll \left[ \frac{T_{fl} + T_{max}^{exp}}{2} \right]^4 ,$$

- $T_w \approx 600$ K depending on the type of propellant,
- the emissivity of the propellant gases is equal to unity,

$$\epsilon_p = 1,$$

- and that of the walls is given by

$$\epsilon_w = 0.5 \quad \text{(polished steel) or} \quad \epsilon_w = 1.$$

---

[9] A relation of the form $p_{max}^{th} - p_{max}^{exp} = K \frac{A_{ch}}{V_{ch}}$ is found. $p_{max}^{th}$ is taken as the ordinate at the origin in the plot of $p_{max}^{exp}$ versus $\frac{A_{ch}}{V_{ch}}$.

Radiative and total losses are estimated in a straightforward manner. $Q^r_w/Q^{tot}_w$ is calculated for various loading densities ($\rho_{load} = 0.05, 0.10, 0.15\,\mathrm{g{\cdot}cm^{-3}}$) and surface area to chamber volume ratio ($A_{ch}/V_{ch}$ varies from 2.67 to 10.00 cm$^{-1}$). It is found that the ratio of the radiative heat loss to the total heat loss, $Q^r_w/Q^{tot}_w$, is inversely proportional to the loading density and the surface area to volume ratio. It ranges from 6 % to 67 % for $\epsilon_w = 1$, and from 3 % to 34 % for $\epsilon_w = 0.5$ (which is more realistic). For a higher density of loading, $\rho_{load} = 0.2\,\mathrm{g{\cdot}cm^{-3}}$, and a lower $A_{ch}/V_{ch}$ (less than unity), the data can be interpolated and the percentage does not exceed 6 % (figure 3). Convective loss is given by the difference between the radiative loss and the total loss. The convective heat transfer coefficient is then obtained for various charge weights and $A_{ch}/V_{ch}$. The main assumption used to obtain a correlation for $h^c$, is that the Nusselt number is a function of the Reynolds number and of the Prandtl number only, that is,

$$\mathrm{Nu} = f(\mathrm{Re}, \mathrm{Pr}),$$

where

$$\mathrm{Nu} = \frac{h^c D_{ch}}{k_g}, \quad \mathrm{Re} = \frac{\rho_g v_g D_{ch}}{\mu_g}, \quad \mathrm{Pr} = \frac{\mu_g c_{pg}}{k_g}.$$

If $\mu_g$, $k_g$ and $c_{pg}$ are assumed constant over the temperature range concerned, this relation simplifies to

$$h^c = f_1(\rho_g v_g)$$

for a given propellant and chamber diameter. The mass flow rate, $\rho_g v_g$, is approximated by its average value.[10] The author then obtains

$$h^c = A\left[\frac{m_s}{t_{cb}}\right]^B.$$

If the mass is expressed in grams and the combustion time in milliseconds, $A \approx 4{,}000\,\mathrm{W{\cdot}m^{-2}{\cdot}K^{-1}{\cdot}g^{-B}{\cdot}cm^{-B}}$ and $B \approx 0.8$. For a loading density ranging from 0.05 to 0.15 g·cm$^{-3}$, values ranging from 2,000 to 30,000 W·m$^{-2}$·K$^{-1}$ are obtained. They correspond to convective heat transfer coefficients found in phase change. From the value of $h^c$, the velocity of the gases at the wall can be estimated using

$$v_g = \frac{2h^c}{f c_{pg} \rho_{load}}.$$

Typical values range from 10 m·s$^{-1}$ to 80 m·s$^{-1}$, which are very high compared to the burning velocities encountered.

The present work by Vest suggests the following remarks. Only a few points are used to interpolate the data (about three) and obtain a correlation for $h^c$, which is also only valid for propellants having a burning velocity that is almost linear with pressure. Moreover, as the chamber is covered with a liner that contains nickel molybdenum, the

---

[10] If one assumes that the burning rate is a linear function of pressure and that pressure is also a linear function of time, then

$$\overline{\rho_g v_g} = \frac{m_s}{t_{cb}}.$$

emissivity of the walls is more likely to be less than 0.5. If it is taken as 0.1, the percentage of the contribution of the radiative loss is decreased by a factor of 5 and does not exceed 14 % for all loading densities.

The general similarity relation for steady compressible laminar flow is

$$\mathrm{Nu} = f(\mathrm{Re}, \mathrm{Pr}, \mathrm{Ec}, \mathrm{Gr}),$$

where

$$\mathrm{Ec} = \frac{U_\infty^2}{c_p(T_w - T_\infty)}, \quad \mathrm{Gr} = \frac{g\beta(T_w - T_\infty)D_{ch}^3}{\nu_g},$$

and the subscript $\infty$ corresponds to reference conditions. For moderate velocities (flow Mach number $\leq 0.5$) and large temperature differences ($\geq 100\ K$), the effect of the Eckert number is negligible. The same applies to the Grashoff number, when buoyancy forces are small compared to inertia forces. Hence

$$\mathrm{Nu} = f(\mathrm{Re}, \mathrm{Pr}),$$

as stated by Vest. However, in the case of a turbulent flow, the Nusselt number is found to be a strong function of the turbulence intensity, $k$ [SCHLICHTING 1979]:

$$\mathrm{Nu} = f(\mathrm{Re}, \mathrm{Pr}, k), \quad \text{with} \quad k = \frac{\sqrt{\frac{1}{3}(u'^2 + v'^2 + w'^2)}}{U_\infty}.$$

For a turbulence intensity of 2.5 % (high), an increase of 80 % (compared to a zero intensity) in the local heat flux has been calculated. The flow in the chamber is said to be highly turbulent but this is not taken into account in the heat transfer analysis.

Using the results of the present study, $h^c$ can be estimated to be $1.6\times10^4\,\mathrm{W{\cdot}m^{-2}{\cdot}K^{-1}}$, which is of the same order of magnitude as the value found in recent studies at DREV, although lower by a factor of 4. This may be due to the fact that turbulent effects are neglected when obtaining a correlation for $h^c$.

### 3.3 DREV [1989]

During the year 1989, an analysis of the sensitivity of the total heat loss to the walls to several parameters was conducted at DREV. Experimental pressure records from firings of a 700 cm$^3$ vessel and a simple theoretical analysis of the combustion process in the vessel were used to estimate the total heat loss as well as the total energy released for each test:

$$Q_w^{tot} = \frac{p_{max}^{th} - p_{max}^{exp}}{\gamma - 1}(V_{ch} - m_s\eta_p - m_a\eta_a - m_{ig}\eta_{ig}),$$

$$Q_e = \sum_{\text{species } k} \int_{T_{ik}}^{T_{fk}} m_{gk} c_{vk}\, dT.$$

$Q_e$, $Q_w^{tot}$, $Q_w^{tot}/Q_e$ are computed for five different propellants and various loading densities. They are plotted against the combustion time, $t_{cb}$, the burning rate (at an average pressure) and the loading density. It is concluded that there exists an affine relationship between the ratio $Q_w^{tot}/Q_e$ and the combustion time, $t_{cb}$. The linear regression coefficient obtained was about 0.91.

Extending the analysis done by DREV further, the next logical question concerns the general shape of the curves for $Q_w^{tot}$, $Q_e$ and $Q_w^{tot}/Q_e$. When the combustion time goes to zero, the loading density reaches $\rho_s$, $Q_w^{tot}$ goes to zero and therefore $Q_w^{tot}/Q_e$ as well. In the range of observation ($t_{cb}$ between 3 ms and 6 ms) experimental results show that the ratio $Q_w^{tot}/Q_e$ increases with $t_{cb}$ and that the loading density decreases with the combustion time. The total energy released decreases with $t_{cb}$, and always exceeds the total heat loss. It is also likely that, for large combustion times, ie low loading densities the total heat loss approaches the total energy released, and therefore the following curves are expected for $Q_w^{tot}$, $Q_e$ and $Q_w^{tot}/Q_e$ versus $t_{cb}$.

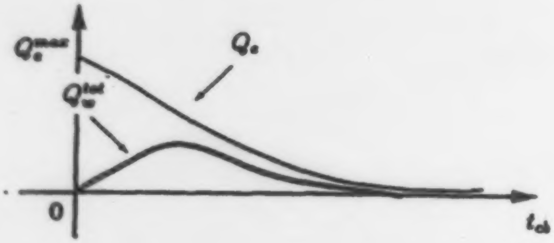

Total energy released and total heat loss versus combustion time.

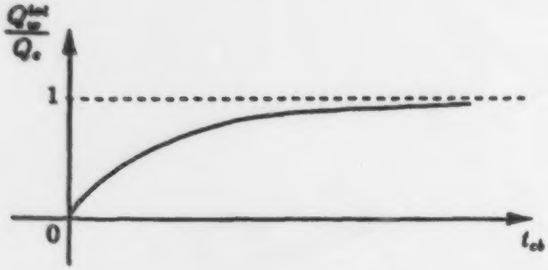

Ratio of total heat loss to total energy released versus combustion time.

In the range of observation the variables can be fitted with linear relations. The total energy released ($Q_e$) is found to be a decreasing function of $t_{cb}$ with a regression coefficient of 0.99. The following curve fit applies:

$$Q_e = Q_e^{max} - ct_{cb}, \tag{6}$$

where c is a positive constant. The heat loss ratio $Q_w^{tot}/Q_e$ is an affine function of $t_{cb}$, that is,

$$\frac{Q_w^{tot}}{Q_e} = at_{cb} + b, \tag{7}$$

where $b$ is non-zero. Both coefficients, $a$ and $b$, are shown in table 3. The analysis not including the point $(Q_w^{tot}/Q_e = 0,\ t_{cb} = 0)$ already done by DREV is repeated for comparison. If the point (0,0) is taken into account, as it should be because the theoretical curve goes through the origin, the linear regression coefficient is improved, except for propellant FNH-P. However the overall slope of the curves is quite satisfactory for all three propellants (figure 4).

Table 3: Linear regression analysis for the ratio of the total heat loss to the total energy released [%] as a function of the combustion time [ms] for various propellants.

| propellant | without (0,0) | | with (0,0) | |
|---|---|---|---|---|
| | $r$ | curve fit | $r$ | curve fit |
| FNH-P | 0.950 | $5.245t_{cb} - 18.708$ | 0.857 | $1.573t_{cb} - 0.768$ |
| B19T98 | 0.947 | $2.767t_{cb} - 2.494$ | 0.996 | $2.349t_{cb} - 0.060$ |
| M10 | 0.845 | $0.883t_{cb} - 0.452$ | 0.944 | $0.989t_{cb} - 0.089$ |

For the total heat loss, $Q_w^{tot}$, the regression coefficient and the corresponding curve fit are summarized in table 4. The origin is not included in the analysis because the slope of the data points for propellant B19T98 is negative (figure 5).

Table 4: Results of a linear regression analysis for the total heat loss [kJ] as a function of the combustion time [ms] for various propellants.

| propellant | $r$ | curve fit without (0,0) |
|---|---|---|
| FNH-P | 0.917 | $14.762t_{cb} - 41.422$ |
| B19T98 | 0.842 | $-10.159t_{cb} + 146.563$ |
| M10 | 0.180 | $-0.562t_{cb} + 14.492$ |

The linear regression coefficient is very low except for propellant FNH-P. Thus, it seems that a higher order polynomial should be used to express $Q_w^{tot}$ as a function of $t_{cb}$. However no definitive conclusion should be made because of the lack of a sufficient number of data points. Note that the total heat loss is not necessarily an increasing function of the combustion time. Equations (7) and (8) suggest that a quadratic function should be fitted instead of an affine function, at least in the combustion time range involved. This is also enhanced by the fact that $Q_w^{tot}$ should be exactly zero at the origin. Using least squares analysis and including the origin in the data points, the following curve fit is obtained for propellant B19T98 (figure 5):

$$Q_w^{tot} = 0.011 + 40.506t_{cb} - 4.361t_{cb}^2,$$

where, $Q_w^{tot}$ is in kiloJoules and $t_{cb}$ in milliseconds. For propellant FNH-P, a negative heat loss is found for low combustion times. The corresponding curve fit is given by

$$Q_w^{tot} = 0.039 - 2.655t_{cb} - 1.815t_{cb}^2.$$

No regression analysis was done for M10 because not enough data points are available.

From the above results it can be concluded that no reasonable regression analysis can be done unless more data points are available. More experiments should be conducted, especially around low and high combustion times (1 ms and 8 ms). This would allow a better estimate of the shape of the heat loss versus combustion time curve. Indeed, the knowledge of the slope would facilitate the choice between a first order and higher order polynomial to fit the data. However it should be emphasized that the total heat loss as a function of the combustion time cannot give any information on the instantaneous heat loss, or on the convective heat transfer coefficient. For a given experiment, $Q_w^{tot}$ represents the heat loss at a constant specific time: the combustion time $t_{cb}$. It is equal to

$$Q_w^{tot} = Q_w(t_{cb}) = A_{ch}\int_0^{t_{cb}} h^c(T_g - T_w)\,dt.$$

The time derivative of this expression cannot be taken, as it only applies at time $t_{cb}$. Thus, no information can be obtained about the integrand. A correlation of the type sought by DREV, can only be used to estimate the total heat loss, with an analysis that is simple to use.

## 3.4 KRIER [MARCH 1976]

Krier considered another way to insert heat loss in the analysis which would more accurately account for the non-adiabatic process. He assumed that during the burning of the propellant in the closed bomb the average temperature of the propellant gases decreased according to the relation

$$c_v m_s \frac{dT}{dt} = -V_{ch}\beta\frac{dp}{dt}\,, \tag{8}$$

where $\beta$ is again estimated by comparing peak experimental and theoretical pressures. The assumptions are that the presence of the ambient gases and igniter gases are negligible and the co-volume and the molecular weight of the gases are constant. An explicit expression for the parameter $\beta$, is now obtained. From

$$p_{max}^{th} = \frac{m_s R_p T_{fl}}{V_{ch} - m_s\eta_p}\,, \quad p_{max}^{exp} = \frac{m_s R_p T_{max}^{exp}}{V_{ch} - m_s\eta_p}\,,$$

one obtains

$$\frac{p_{max}^{th}}{p_{max}^{exp}} = \frac{T_{fl}}{T_{max}^{exp}}\,. \tag{9}$$

By integrating equation (9), the temperature is given by

$$T = -\frac{V_{ch}\beta(\gamma - 1)}{m_s R_p}p + \mathrm{K}, \tag{10}$$

where $K$ is an integrating constant. When $\beta = 0$, no heat losses occur, therefore $T_{max}^{exp} = T_{fl}$ and

$$K = T_{fl}. \tag{11}$$

By applying equation (11) at the maximum experimental pressure and by using equation (12), the following relation between $T_{max}^{exp}$ and $p_{max}^{exp}$ is deduced:

$$T_{max}^{exp} = T_{fl} - \frac{V_{ch}\beta}{m_s R_p}p_{max}^{exp}(\gamma + 1). \tag{12}$$

By combining equations (8) and (11), one obtains

$$\beta = \frac{1}{\gamma - 1}\frac{m_s}{V_{ch}}\left[\frac{R_p T_{fl}}{p_{max}^{exp}} - (\frac{V_{ch}}{m_s} - \eta_p)\right].$$

Note that, as in DREV's analysis, an accurate value for $p_{max}^{exp}$ is necessary.

Expressions for the heat loss rate and the total heat loss are now derived. Using equation (9), the heat loss rate is equal to

$$q_w = \beta V_{ch}\frac{dp}{dt}.$$

$Q_w^{tot}$ is calculated by integrating the above equation where $\beta$ and $V_{ch}$ are constant. Knowing that the initial pressure is negligible compared to the maximum pressure reached, the total heat loss can be estimated by

$$Q_w^{tot} = \beta\ V_{ch}\ p_{max}^{exp}.$$

Therefore, using the previous expression for $\beta$, $q_w$ is given by

$$q_w = \frac{Q_w^{tot}}{p_{max}^{exp}}\frac{dp}{dt} \quad \text{and} \quad Q_w^{tot} = \frac{p_{max}^{th} - p_{max}^{exp}}{\gamma - 1}(V_{ch} - m_s\eta_p).$$

This last expression is similar to the one given by DREV, except for the effect of the ambient and the igniter gases, which is neglected here. The heat loss rate at a given time is proportional to the time derivative of pressure. This results in a larger fraction of propellant consumed ($Z$ being a fraction where $R_pT$ appears in the denominator in the equation of state) and, consequently, a larger burning rate. In this analysis, burning rates estimated under the assumption of heat loss differ significantly from the ones estimated neglecting the loss (table and figure 6). These rates are also much closer to best fit burning rates (estimated using an internal ballistic code, fixing the gun parameters), although still lower by 25 %. Krier concludes that one must resort to a different model than proposed or drop one of the following assumptions:

- uniform ignition,
- uniform regression rate,
- Noble-Able equation of state.

## 3.5 ROBIN AND HORST [DECEMBER 1976]

Robin and Horst have used a very similar heat loss model in their code SIMPCB. From the experimental and theoretical (assuming no heat loss) pressures, the total heat loss is estimated by

$$Q_w^{tot} = \frac{p_{max}^{th} - p_{max}^{exp}}{\gamma - 1}(V_{ch} - m_s\eta_p - m_a\eta_a - m_{ig}\eta_{ig}),$$

as by DREV. Then, assuming a constant rate (relative to pressure) for the heat loss, a constant $K$ is defined so that

$$-K = \frac{\Delta H}{\Delta p} = m_s c_v \frac{\Delta T}{\Delta p} = -\frac{Q_w^{tot} - Q_w^{ini}}{p_{max}^{exp} - p^{exp,\,ini}}. \tag{13}$$

$K$ represents the heat lost per unit pressure. The instantaneous heat loss is simply given by

$$Q_w = K(p - p^{exp,\,ini}) + Q_w^{ini},$$

and hence the heat loss rate, if $Q_w^{ini}$ is set to zero (as is done in the code), is given by

$$q_w = K\frac{dp}{dt} = \frac{Q_w^{tot}}{p_{max}^{exp} - p^{exp,\,ini}}\frac{dp}{dt} \approx \frac{Q_w^{tot}}{p_{max}^{exp}}\frac{dp}{dt},$$

as the initial pressure is negligible compared to the maximum pressure. The heat loss factor $K$ is equivalent to the factor $\beta V_{ch}$ in Krier's model. Indeed, from equation (14),

$$-K = m_s c_v \frac{dT/dt}{dp/dt} \qquad \text{or} \qquad m_s c_v \frac{dT}{dt} = -K\frac{dp}{dt},$$

to compare with equation (9).

## 3.6 LARGE CALIBER WEAPON SYSTEMS LABORATORY

At LCWSL, another code was developed (NCBOMB). Heat loss is indirectly taken into account by dividing the pressure by the maximum of the experimental pressure in the burning rate,

$$r = \beta\left[\frac{p}{p_{max}^{exp}}\right]^n.$$

Unfortunately, no further information could be obtained about the details of this code.

## 3.7 PRICE AND JUHASZ [SEPTEMBER 1977]

Another possible way to account for heat loss is to solve an energy equation for the combustion gas' temperature. Defining the total heat loss as the difference between the total available energy and the propellant gas' internal energy, $Q_w^{tot} = m_s c_v Z(T_{fl} - T)$, and taking the time derivative of this relation one can obtain the energy equation as

$$m_s c_v Z \frac{dT}{dt} = m_s c_v (T_{fl} - T)\frac{dZ}{dt} - q_w.$$

The above equation is solved in the code developed by Price and Juhasz (CBRED).

Two options are available for evaluating $q_w$. In the first one, $q_w$ is constant, and hence is given by

$$q_w = \frac{Q_w^{tot}}{t_{max} - t_{ig}},$$

where the total heat loss is estimated as

$$Q_w^{tot} = \frac{p_{max}^{th} - p_{max}^{exp}}{\gamma - 1}(V_{ch} - m_s \eta_p)$$

as in Krier's model. In the second option, the heat loss rate is decomposed into convective and radiative components before burnout, and is strictly radiative after burnout:

$$q_w = \begin{cases} q_w^r + q_w^c & \text{for} \quad Z \le 1 \\ q_w^r & \text{for} \quad Z > 1. \end{cases}$$

The radiative heat loss rate, $q_w^r$, is assumed proportional to the experimental time derivative of pressure,

$$q_w^r = \frac{(V_{ch} - m_s\eta_p)}{\gamma - 1}\frac{dp}{dt} = \frac{Q_w^{tot}}{p_{max}^{th} - p_{max}^{exp}}\frac{dp}{dt}\,.$$

The convective heat loss rate, $q_w^c$, is estimated using a convective heat transfer coefficient, $h^c$, similar to the one derived for turbulent flows through pipes,

$$h^c = F^c\left[\frac{dm}{dt}\right]^{\frac{4}{5}},$$

where $F^c$ is a constant, and $m$ is the mass burning rate. A radiative heat transfer coefficient is introduced so that the total heat loss rate can be written in the form

$$q_w = A_{ch}[h^c(T - T_w) + \overline{h^r}(T^4 - T_w^4)].$$

$\overline{h^r}$, the average (in time) constant radiative coefficient and $F^c$ are obtained using curve fitting techniques, based on the experimental pressure curve after burnout, as follows:

- from $p^{exp}$ and $(dp/dt)^{exp}$, one can obtain using the ideal gas law, $T^{exp} = p^{exp}V_{ch}/R_g$ (all the solid has burnt) and $q_w^r$, giving $h^r$ and $\overline{h^r}$,
- $F^c$ is estimated using an averaged mass flow rate and heat loss rate.

Finally,

$$q_w = \begin{cases} A_{ch}[\overline{h^r}(T^4 - T_w^4) + F^c\left(m_s\frac{dZ}{dt}\right)^{0.8}(T - T_w)] & \text{for} \quad Z \le 1 \\ A_{ch}\overline{h^r}(T^4 - T_w^4) & \text{for} \quad Z > 1. \end{cases}$$

To conclude, several remarks on the present analysis should be made. Unlike in the previous models, $p_{max}^{exp}$ does not appear explicitly in the expression for the heat loss rate. This one also differs significantly after burnout. Indeed, $q_w$ is proportional to the pressure time derivative, but here the proportionality constant includes the pressure difference, $p_{max}^{th} - p_{max}^{exp}$, instead of simply the pressure $p_{max}^{exp}$. Furthermore, the assumption that after burnout only radiative losses occur is questionable as it is very probable that combustion gases are opaque, hence that radiation cannot reach the walls, being absorbed on its way. However, in fact, the heat loss rate after burnout can be estimated by taking the derivative of the equation of state $(p(V_{ch} - m_s\eta_p) = R_gT)$:

$$q_w = m_s c_v \frac{dT}{dt} = \frac{(V_{ch} - m_s\eta_p)}{\gamma - 1}\frac{dp}{dt}.$$

This rate is identical to the radiative rate given by Price and Juhasz. Thus, the expression for $q_w$ after burnout is valid. But, although it is likely that convective losses are negligible after burnout, because the velocities decrease very rapidly towards zero, it is not known whether radiative or conductive losses dominate. Therefore, the heat loss rate after burnout should not be called radiative, especially because radiative losses generally occur at a constant rate. Finally, and more importantly, heat transfer coefficients are estimated from observations of the pressure decrease in the vessel after burnout. It is not obvious that the rate at which it occurs is identical to the one which occurs during burning.

### 3.8 COHEN AND STRAND [1978]

Heat losses to the wall are accounted for using constant convective and radiative coefficients:

$$q_w = A_{ch}[h^c(T - T_w) + \epsilon_p \sigma (T^4 - T_w^4)].$$

The value of $h^c$ is not given in the article.

### 3.9 DE SOTO [1965]

In this paper, an analysis is made of grain ignition and flame spreading in the engine to obtain chamber pressure as a function of time. Although the flow in a solid propellant rocket motor differs from that in a closed bomb they have some similarities because they are both driven by solid propellant burning. It is, therefore, interesting to report this model,[11] which accounts for heat loss in the combustion chamber of the rocket. The geometry in the following figure is considered.

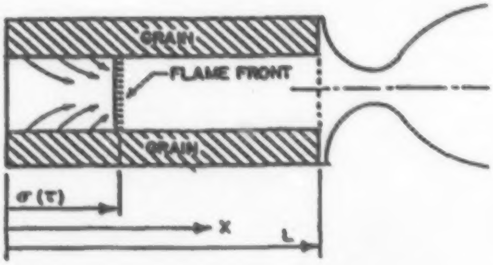

Schematic diagram of motor (from De Soto).

The heat transfer analysis is based on a statement by Kreith: for very short tubes, with initial uniform velocity and temperature distributions, the flow conditions along the wall approach those along a flat plate. The expression used for the convective heat transfer coefficient at the unburnt surface of the grain, is similar to the one given by Davey for a turbulent boundary layer over a flat plate with uniform temperature,

$$\frac{hx}{k} = 0.036 \mathrm{Re}_x^{0.8} \mathrm{Pr}^{0.4} \left(\frac{T_{fl}}{T_w}\right)^{0.18},$$

---

[11] Another more recent model, not presented in this report, can be found in PERETZ 73.

but is only valid for steady flows. To account for transient effects, the above expression was then modified to

$$h^c(x,t) = a\frac{k_g}{[x-\sigma(t)]}\left[\frac{\rho_g(t)(x-\sigma(t))u_g(x,t)}{\mu_g}\right]^b\left[\frac{c_{pg}\mu_g}{k_g}\right]^{0.33},$$

where the gas properties, $k_g$ and $\mu_g$, are assumed constant. $a$ is varied by a factor 10, and $b$ is taken as being equal to 0.5. The effect of increasing $a$ is to increase the pressure rise rate in the chamber.

To express $h^c$ as a function of space and time, a similar approach to the one used by De Soto will be presented later in the fourth chapter of this report.

## 3.10 CONCLUSION

All of these methods make use of the fact that the total heat losses to the walls are known and can be approximated by

$$Q_w^{tot} = \frac{p_{max}^{th} - p_{max}^{exp}}{\gamma - 1}(V_{ch} - m_s\eta_p - m_a\eta_a - m_{ig}\eta_{ig}).$$

Depending on the model, the initial mass of the igniter or the ambient gases is neglected. This expression suggests two remarks. First of all, it assumes that heat loss is the only type of loss that occurs. Effects such as the expansion of the vessel walls or change in the molecular mass of the gases are not taken into account. Secondly, it relies on an accurate value for the experimental pressure. Indeed, an error of only 1 % in the measurement of $p_{max}^{exp}$ causes an error of $1\times(p/\Delta p - 1)$ % on the total heat loss, that is of about 9 % for a typical pressure drop of 10 %. Semi-empirical expressions based on the value of $Q_w^{tot}$ and on experimental data after burnout are used to predict the heat loss rate. $q_w$ is either assumed constant or proportional to the time derivative of pressure:

$$q_w \propto \frac{dp}{dt} \quad \text{or} \quad q_w = \text{constant}.$$

The proportionality constant is the same in all the models and given by

$$\frac{Q_w^{tot}}{p_{max}^{exp}},$$

except in CBRED where it is equal to

$$\frac{Q_w^{tot}}{p_{max}^{th} - p_{max}^{exp}}.$$

An error in the measurement of $p_{max}^{exp}$ does not affect the heat loss analysis in this case. Finally, radiative heat transfer is treated in a very simple way. Neither the variations of the emissivity of the combustion gases with wavelength and temperature, nor the reflections of radiation on the walls are taken into account. A more accurate estimation of the heat loss rate has never been made because it has never been the main purpose of the analysis.

## 4.0 NUMERICAL ANALYSIS

In order to obtain more rigorous relations and a better understanding of the mechanisms involved, a new approach to the problem should be taken. The only way to do so is to actually model the flow in the vessel and take space variations into account. Now, the heat loss rate will be found using a turbulent boundary layer analysis. Depending on how well the theory matched the experiments, another type of loss might have to be accounted for using more rigorous expressions, or a more sophisticated model for the flow may have to be used.

A first step to this new approach is the modeling of the core flow, both inviscid and non-conductive. The present work deals with this problem as well as a simple way to account for heat loss. The first sections (4.1 to 4.3) describe the mathematical formulation of the equations. A new way to account for heat transfer is presented in section 4.4. Section 4.5 deals with the numerical method used, and section 4.6 describes the computer program.

The underlying idea of the analysis is to divide the actual flow in the vessel in two different zones, a main zone (core flow), where viscous terms are negligible and a smaller zone (wall flow), where viscous effects are dominant and where heat losses occur. In view of the complexity of the problem, the present work is restricted to the modeling of the core flow. The gases are inviscid and non-conductive.

First, a 1D computer program was written in order to decide on an appropriate numerical method. Then, from the results of a 2D code modeling the burning of a single propellant grain,[12] a semi-empirical convective coefficient was added to account for heat loss. The burning process is simulated by the injection of hot combustion gases into the vessel, through a "burning surface" that remains stationary with time. Keeping track of the position of the actual burning surface would involve the use of an adaptative grid, a large number of nodes and a much more realistic model for the combustion zone. Inert and combustion gases are assumed to follow the equation of state for perfect gases. Thermophysical parameters ( $\lambda$, $\mu$, $c_v$, $c_p$ ) are assumed constant with pressure and temperature. The effect of igniter and ignition-aid is not taken into account and the combustion zone is assumed to be infinitely small. This allows the generation of a simple set of equations that can be solved using a fixed grid. Further assumptions are:

- De Saint Robert's equation applies for the burning rate,

$$r = \beta p^n,$$

- combustion gases enter the chamber at a constant temperature equal to the adiabatic flame temperature ($T_{fl}$) and at a mass flow rate equal to the mass burning rate ($\rho_s r$).

---

[12] In the case of a 2D analysis, it would be unrealistic to model the burning of more than one grain. Indeed, in order to respect the 2D constraint, all the grains should have the symmetry axis of the vessel as their axis of symmetry. Considering the dimensions of the vessel, it is physically impossible to place the entire charge (between 50 and 100 grains with a length of about 1 cm) that way. Moreover, there would be little interest in modeling the burning of even a few grains in such an unrealistic configuration.

- Initially, the ambient gases are at rest, and the pressure and temperature in the vessel are uniform,
- no mixing is allowed between the two gases,
- they are both inviscid ($\mu_p = 0$, $\mu_a = 0$) and non-conductive ($k_p = 0$, $k_a = 0$).

## 4.1 GOVERNING EQUATIONS

To simulate the flow in the vessel, the unsteady inviscid equations of fluid dynamics, plus two additional equations for the transport of the gas constant, $R$, and the ratio of the specific-heats, $\gamma$, are solved. They can be written in vector form as

$$\frac{\partial U}{\partial t} + \frac{\partial F}{\partial z} + \frac{\partial G}{\partial r} + S = 0, \tag{15}$$

where $U$, $F$, $G$ and $S$ are vectors given by

$$U = \begin{pmatrix} \rho \\ \rho u \\ \rho v \\ e \\ \rho R \\ \rho\gamma \end{pmatrix}, \quad F = \begin{pmatrix} \rho u \\ \rho u^2 + p \\ \rho uv \\ (e+p)u \\ \rho uR \\ \rho u\gamma \end{pmatrix},$$

$$G = \begin{pmatrix} \rho v \\ \rho uv \\ \rho v^2 + p \\ (e+p)v \\ \rho vR \\ \rho v\gamma \end{pmatrix}, \quad S = \begin{pmatrix} \rho v/r \\ \rho uv/r \\ \rho v^2/r \\ (e+p)v/r \\ \rho vR/r \\ \rho v\gamma/r \end{pmatrix}.$$

Finally, the pressure is related to the internal energy, $\epsilon$, and the density, $\rho$, by the equation of state:

$$p = p(\epsilon, \rho) = (\gamma - 1)\epsilon\rho,$$

where

$$\epsilon = e - \rho\frac{u^2 + v^2}{2}.$$

Equation (15) is written in conservation law form, the source term, $S$, occurs because cylindrical coordinates are used. In order to obtain a closed set of equations, boundary and initial conditions must be specified. They are described in the two following sections.

## 4.2 BOUNDARY CONDITIONS

For the inviscid calculations of this work, there were three distinct types of boundaries – two at the edge of the overall mesh (along the walls and the axis of symmetry of the vessel) and a third one at the burning surface.

At the wall and along the axis of symmetry, the normal velocity is set to zero and the tangential velocity equal to the tangential velocity of the adjacent inner node. The pressure and temperature are computed by solving a Riemann problem between the two nodes with only one reflected wave, as illustrated in the diagram below. When heat transfer is taken into account, a different type of boundary condition applies at the wall nodes. It will be described in section 4.4, when the heat transfer model is introduced.

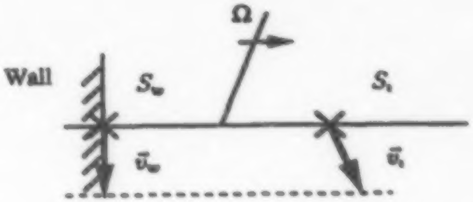

Wave pattern in the solution of a Riemann problem at a wall.

At the burning surface the temperature is set to the adiabatic flame temperature, $T_{fl}$, and the velocity is normal to the burning surface. The pressure and velocity are obtained by solving a Riemann problem with a contact surface and a reflected wave, as illustrated below.

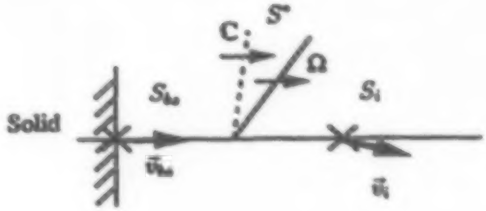

Wave pattern in the solution of a Riemann problem at the burning surface.

By guessing the middle state pressure, $p^*$, the type of the reflected wave, Ω, can be deduced (it is a shock wave if $p^* \geq p_i$, a rarefaction wave otherwise). The middle state, $S^*$, can then be computed as well as state $S_{bs}$ from the conditions at the contact surface ($p_{bs} = p^*$ and $u_{bs} = u^*$). The pressure, $p^*$, is modified until the velocity at the burning surface, $u_{bs}$, satisfies the burning rate law,

$$\rho_{bs} u_{bs} = \beta p_{bs}^n .$$

At the solid's corners, the above Riemann problem is solved by alternatively using the two neighbor gas points. The velocity is set parallel to the radial/ axial direction during the $y$-sweep/$x$-sweep. The way the corner is treated should not affect the flow pattern in the vessel, except in the vicinity of this corner node. This was confirmed by trying several options, such as keeping the velocity parallel to the radial direction, or at a 45° angle with the burning surface, setting the velocity to zero. The option chosen can be justified as follows: if the corner node is placed just outside of the solid, during the axial sweep node ① sees the flow as if it was leaving the burning surface at a velocity parallel to the $x$ (or $z$) axis (figure below). Thus, node ① should be used to compute the flow variables at the solid's corner. On the other hand, during the radial sweep, node ② sees it leaving with a velocity parallel to the $y$ (or $r$) axis, therefore node ② should be used, instead.

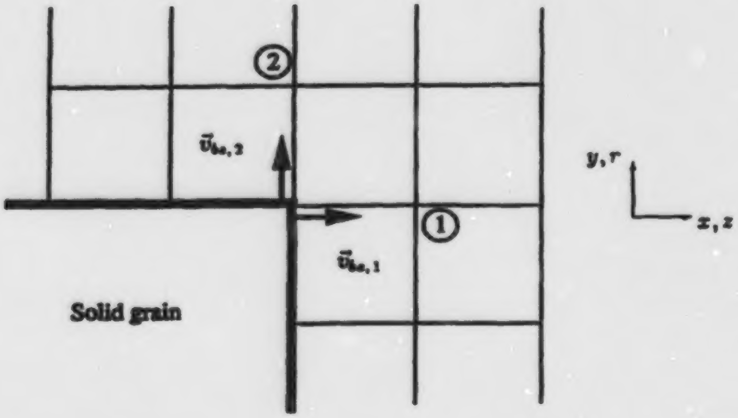

Schematic diagram of the boundary condition applied at the corner of the grain.

After burnout, no more combustion gases enter the chamber and the burning surface is replaced by a solid wall. The burning surface nodes are, therefore, treated as the wall nodes are.

## 4.3 INITIAL CONDITIONS

In an actual firing, the propellant grains are assembled in silk bags and placed in the vessel on top of the cooling rods. One end of each bag contains an igniter charge (fast burning propellant with a high adiabatic flame temperature, usually nitrocellulose) in contact with a wire which is used to initiate combustion (figure 7). Once enough time has been left so that any temperature difference smoothes out (a tolerance of plus or minus 2° F is generally accepted), the vessel is evacuated and filled with air to bring the pressure up to 0.1013 MPa. The wires are then heated using an appropriate voltage input. As the igniter burns, the propellant's surface temperature rises, enough so that the solid's melting point is reached (between 600 K and 800 K). The charge then starts to burn. At the commencement of burning, therefore, the vessel is filled by almost cold gas of similar composition to the propellant's and with a mass of about 1 % of the charge's. The effect of packaging is to minimize the distance that the flame must spread in order to obtain as uniform an ignition as possible.

Modeling of the propellant burning is done in a straightforward manner, ignoring the phenomena occurring during ignition. Computations are started when the igniter has completely burnt and mixed with the ambient gases (air here), leaving a uniform pressure, $p^{ini}$, and temperature, $T^{ini}$, in the vessel. This implies that the beginning of the pressure rise cannot be predicted accurately. The problem can be handled by starting the computations at a higher pressure than the ambient pressure when the igniter effects have become minor. $p^{ini}$ was varied between 2 MPa and 10 MPa. $T^{ini}$ is equal to 293 K, which is also the ambient temperature in the vessel, $T_w$. Initially, the vessel is filled with a mixture of air and igniter gases[13] at rest. Its composition and properties are given in appendix B. Ignition of the solid propellant grain is instantaneous and uniform.

## 4.4 HEAT TRANSFER MODEL

A simple heat transfer model has been developed to account for heat loss in the vessel. It is now described. The combustion gases are assumed to have a very high absorptivity, therefore only the effect of convective and conductive heat transfer are taken into account. As inviscid and non-conductive gases are purposely used, a proper analysis of the thermal and mechanical boundary layers cannot be included. Both are assumed to lie between the wall nodes and the first inner nodes adjacent to them, as illustrated in the diagram below.

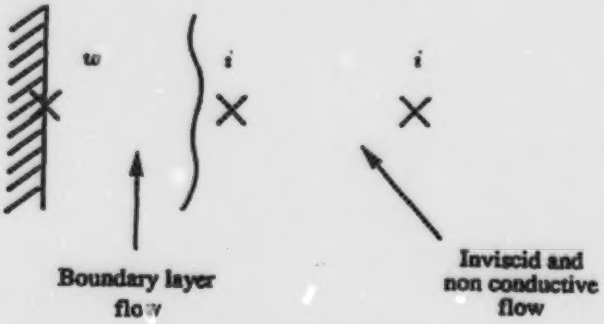

Wall and core flow models.

The strong temperature and velocity gradients are confined into a small region located near the gaseous wall nodes. Viscous terms are neglected everywhere in the flow, and conductive terms, in the inner flow only. Thus , with two additional assumptions, the heat loss can be accounted for by applying a pressure correction at the gaseous wall node. This will be explained later in this section. The heat loss rate per unit surface area is

$$\frac{dq_w}{dS_{ch}} = \varphi_w^{cc} = h^c(T_w - T_m),$$

where $T_m$ is the mean temperature in the vessel. Rigorously, $T_m$ should be the mean temperature of the gas at the boundary layer edge. The convective heat transfer coefficient, $h^c$, is estimated using correlations for turbulent flows along a flat plate, as the boundary layer thickness is expected to be small compared with the dimensions of the vessel. Let the Nusselt number be $\mathrm{Nu}_L = h^c L/k$, where $L$ is a characteristic length to be chosen, and let the Reynolds number be $\mathrm{Re}_L = \rho v^{\perp} L/\mu$, where $v^{\perp}$ is the velocity in the direction perpendicular to the wall. The following correlation is assumed:

---

[13] The mixture will be referred to as inert gases in this report, as both air and igniter gases are assumed inert, that is, they do not react chemically with the propellant gases.

$$\mathrm{Nu}_L = \begin{cases} \mathrm{Nu}_L^{min} & \text{for} \quad \mathrm{Re}_L \leq \mathrm{Re}_L^{crit} \\ \max\left(\mathrm{Nu}_L^{lam}, \mathrm{Nu}_L^{tur}\right) & \text{for} \quad Re_L \geq \mathrm{Re}_L^{crit}, \end{cases}$$

where $\mathrm{Nu}_L^{min}$ is the Nusselt number evaluated at the critical Reynolds number, $\mathrm{Re}_L^{crit}$. The laminar and turbulent Nusselt numbers are taken as

$$\mathrm{Nu}_L^{lam} = 0.664\mathrm{Pr}^{0.33}\mathrm{Re}_L^{0.5} \quad \text{and} \quad \mathrm{Nu}_L^{tur} = 0.035\mathrm{Pr}^{0.33}\mathrm{Re}_L^{0.8}.$$

The critical Reynolds number is set to the value of the critical Reynolds number for the transition from laminar to turbulent flow over flat plates, that is $5.0 \times 10^5$. The Nusselt-Reynolds relationship can be summarized by the following figure:

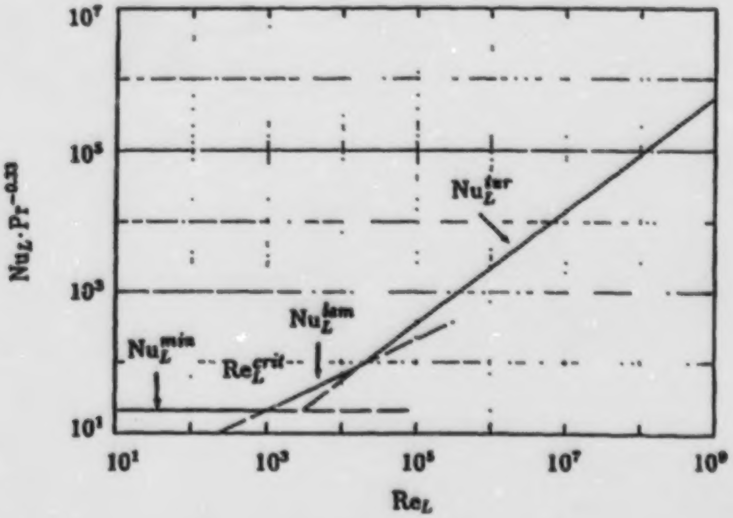

Dependence of the heat transfer coefficient $\mathrm{Nu}_L\ \mathrm{Pr}^{-0.33}$ on the Reynolds number $\mathrm{Re}_L$ according to the present model.

Many different choices for the characteristic length exist. It can be taken as a characteristic length of the vessel (for example its radius), or it can be the length of a vortex or the effective radiative gas layer length. Since these are all of the order of a few centimeters, $L = 6$ cm was chosen as a standard value.

The boundary condition applied at the gaseous wall nodes to account for heat loss, is now described in more detail. Starting from the general equations of fluid dynamics in the case of inviscid but conductive gases, the boundary layer flow between the gaseous wall node and the first node adjacent to it, is solved. Using the same notation as in equation (15), the governing equations are:

$$\frac{\partial U}{\partial t} + \frac{\partial F}{\partial z} + \frac{\partial G}{\partial r} + S = S_e, \qquad (16)$$

where $S_e$ is an energy source term which accounts for conductive losses,

$$S_e = {}^t(0, 0, 0, -\vec{\nabla}.\vec{\varphi}^{cd}) \quad \text{where} \quad \vec{\varphi}^{cd} = -k_p \vec{\nabla} T.$$

The numerical procedure applied between time step $n$ and time step $n+1$, consists of the three following steps:

1. set $S_e$ to zero, solve equation (16) using operator splitting and obtain a solution at time step $*$
2. evaluate the source term $S_e$ at time step $*$
3. set both radial and axial gradients to zero, solve equation (16), and obtain the flow variables at time step $n+1$.

Each step is now examined more specifically. The first one is described in appendix E. Equation (16) reduces to equation (15) in this case. To perform step 2 an expression for $S_e$ at each gaseous wall node is needed. During the axial sweep, equation (16) is solved at constant radius and the derivative with respect to $r$ is null. Thus, the source term reduces to

$$S_{ez} = -\frac{\partial \varphi_z^{cd}}{\partial z} \quad \text{where} \quad \varphi_z^{cd} = -k_p \frac{\partial T}{\partial z}.$$

Using first order forward differences at the gaseous wall node, the energy source term at that node is obtained as

$$S_{ezwg} = \frac{\varphi_{zwg}^{cd} - \varphi_{zi}^{cd}}{\Delta x}.$$

In order to proceed further, two more assumptions must be made. Firstly, the conductive terms in the inner flow are assumed to be negligible compared with the ones at the wall, that is to say

$$\varphi_{zi}^{cd} \ll \varphi_{zwg}^{cd}.$$

Secondly, the distance between the gaseous wall node and the wall is considered to be infinitely small, and therefore conductive terms at the gaseous wall nodes are identical to the ones at the wall, that is

$$\varphi_{zwg}^{cd} = \varphi_{zw}^{cd}.$$

The following expression for $S_{ezwg}$ is deduced:

$$S_{ezwg} = \frac{\varphi_{zw}^{cd}}{\Delta x} = -\frac{k_p}{\Delta x}\left(\frac{\partial T}{\partial z}\right)_w.$$

Let $h_z^c$ be such that

$$-k_p \left(\frac{\partial T}{\partial z}\right)_w = h_z^c (T_w - T_m) = \varphi_{zw}^{cc}.$$

$h_z^c$ represents the convective heat transfer coefficient at the wall, and $\varphi_{zw}^{cc}$ the conducto-convective flux there. The final expression for the energy source term at the gaseous wall node along the flat walls of the vessel at time step $*$ is:

$$S_{ezwg}^{*} = \frac{\varphi_{wz}^{cc*}}{\Delta x}.$$

During the radial sweep, the derivative with respect to $z$ is dropped, and therefore the source term reduces to

$$S_{er} = -\frac{\partial \varphi_r^{cd}}{\partial r} + \frac{\varphi_r^{cd}}{r} \quad \text{where} \quad \varphi_r^{cd} = -k_p \frac{\partial T}{\partial r}\,.$$

Using the same assumptions and reasoning as before, it is given by

$$S_{erwg} = -\frac{\varphi_{rw}^{cd}}{\Delta y} - \frac{\varphi_{zw}^{cd}}{r} = -k_p \left(\frac{\partial T}{\partial r}\right)_w \left(\frac{1}{r} + \frac{1}{\Delta y}\right) \quad \text{where} \quad r = (n_y - 1)\Delta y.$$

Let $h_r^c$ be such that

$$k_p \left(\frac{\partial T}{\partial r}\right)_w = h_r^c (T_w - T_m) = \varphi_{wr}^{cc}.$$

Then the energy source term at the gaseous wall node along the curved walls of the vessel at time step $*$ is:

$$S_{erwg}^{*} = \varphi_{wr}^{cc*}\left(\frac{1}{r} + \frac{1}{\Delta y}\right) \quad \text{where} \quad r = (n_y - 1)\Delta y.$$

The third step reduces to an energy (or pressure) correction, because the only remaining terms in equation (16) are the time derivative and the energy source term. The new equation is

$$\frac{\partial e}{\partial t} = S_e. \tag{17}$$

All of the conservative variables, except for the energy, remain unchanged, and therefore

$$\rho_{wg}^{n+1} = \rho_{wg}^{*},$$

$$u_{wg}^{n+1} = u_{wg}^{*}\,, \quad v_{wg}^{n+1} = v_{wg}^{*},$$

$$R_{wg}^{n+1} = R_{wg}^{*}, \quad \text{and} \quad \gamma_{wg}^{n+1} = \gamma_{wg}^{*}.$$

Equation (17) can be discretized at the gaseous wall node using first order differences to obtain

$$e_{wg}^{n+1} = e_{wg}^{*} + \Delta t S_{ewg}^{*}, \tag{18}$$

where $\Delta t$ is the time interval between time steps $*$ and $n+1$. $S_{ewg}^{*}$ has been evaluated during step 2, and $e_{wg}^{*}$ during step 1. This equation can be further simplified by introducing the pressure, $p_{wg}$, instead of the energy, $e_{wg}$. They are related by

$$p_{wg} = (\gamma_{wg} - 1)\left[e_{wg} - \rho_{wg}\frac{u_{wg}^2 + v_{wg}^2}{2}\right].$$

At the gaseous wall node the normal velocity is null. Moreover, it has been shown that the density, tangential velocity and the ratio of the specific-heats are identical between time steps $*$ and $n+1$, and therefore

$$e_{wg}^{n+1} - e_{wg}^{*} = \frac{p_{wg}^{n+1} - p_{wg}^{*}}{\gamma_{wg}^{*} - 1} .$$

Thus, dropping the subscript $_{wg}$ for simplicity, equation (18) reduces to

$$p^{n+1} = p^{*} + (\gamma_w - 1)\varphi_w^{c} \frac{\Delta t}{\Delta x^{\perp}} ,$$

where $\varphi_w^{cc}$ is the conducto-convective heat loss rate per unit area, defined earlier as

$$\varphi_w^{cc} = h^{c}(T_w - T_m),$$

and where $\Delta x^{\perp} = \Delta x$ along the flat walls, and $\Delta x^{\perp} = \Delta y(n_y - 1)/n_y$ along the curved walls.

## 4.5 NUMERICAL METHOD

Having described the mathematical formulation of the closed set of equations relevant to our model, an appropriate numerical method to solve the time-dependent flow in the closed vessel is required. Due to the strong discontinuities imposed by the boundary conditions (initial large temperature difference between the combustion gases at the burning surface and the inert gases), one-dimensional calculations were first performed in order to determine an appropriate numerical method. The following simple geometry is considered:

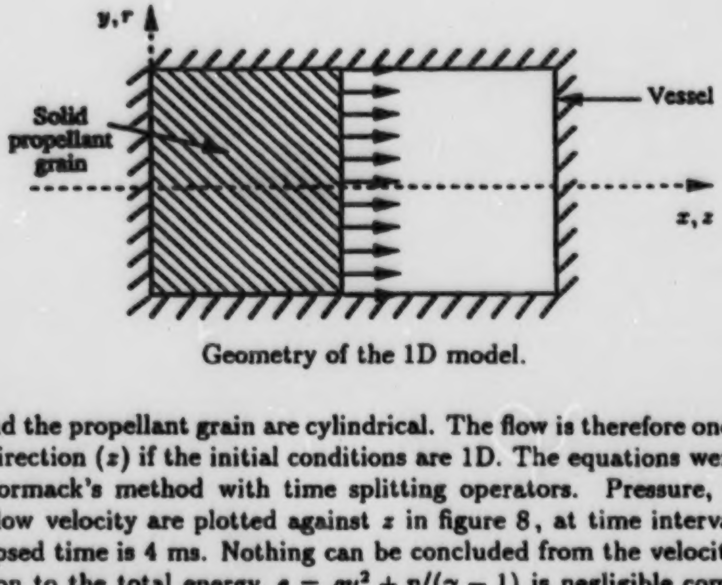

Geometry of the 1D model.

The vessel and the propellant grain are cylindrical. The flow is therefore one dimensional in the axial direction ($z$) if the initial conditions are 1D. The equations were first solved using Mac Cormack's method with time splitting operators. Pressure, temperature, density and flow velocity are plotted against $z$ in figure 8, at time intervals of 0.5 ms. The total elapsed time is 4 ms. Nothing can be concluded from the velocity diagram as its contribution to the total energy, $e = \rho u^2 + p/(\gamma - 1)$ is negligible compared to the one of the pressure term, and a lot of oscillations are present. The overall results are correct, but need to be improved. In order to remove the oscillations, numerical viscosity was added using a self-adjusting hybrid scheme (appendix D). At first the scheme was applied at all inner nodes, but this led to unrealistic results, such as decreasing pressure in the vessel. Next, the node near the burning surface was excluded, and a standard value for the numerical viscosity of $\mu_{num} = 0.125$ was chosen (figure 9). Oscillations were removed but the contact surface almost disappeared. This suggested that the numerical viscosity should be decreased to $\mu_{num} = 0.001$ (figure 10). Oscillations now appeared, but a sharper discontinuity was obtained.

In view of the previous results due to the numerical scheme, it was decided to use a more powerful numerical technique that would handle surface discontinuities better. From the numerous methods available, Roe's method, which uses approximate Riemann solvers and a flux limiting technique, was chosen. The difference scheme is described in appendix E. The new results obtained are plotted in figures 11 and 12. They are much more satisfactory. Velocity profiles are smoother and the overall predicted variables are correct.

## 4.6 2D COMPUTER PROGRAM

The two-dimensional computer program for the simulation of the combustion of a single solid propellant grain in a closed vessel is presented. The relevant differential equations were described in section 4.1. They are solved, along with their corresponding boundary and initial conditions (sections 4.2 and 4.3), using Roe's method (appendix E). The geometry is the same as in the one-dimensional case, although the grain now burns in two directions as illustrated below.

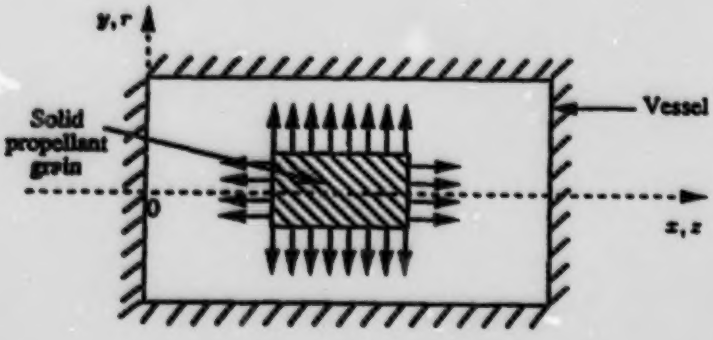

Geometry of the 2D model.

The main input parameters of the code are given in appendix B. Several types of grains can be modeled. Typically, a perfect cylindrical or monoperforated grain is burnt. In addition, to simulate the effect of imperfections in the grain's geometry, a cylindrical grain with a hole on one side and one with a reduced diameter at one location along its axis (right most grain in the figure on the next page) can be used.

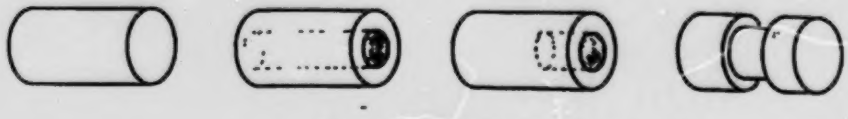

Grain geometries.

Such imperfections could be introduced by variability in size during manufacturing or by non-uniform ignition, leading to a higher burning rate, that is, a faster regression of the burning surface in some places along the grain.

The study is restricted to the burning of a single grain. In reality it is not a single propellant grain that burns, but a collection of small ones. While burning they might move chaotically in the chamber due to the expanding gases and to the ignition procedure. It is almost impossible to model this situation. An idea of the influence of the grains' motion on the flow pattern can be obtained by letting the grain move along the symmetry axis (in order to maintain the 2D symmetry). Two possibilities are offered in the code. The motion of the grain can be either imposed or free. In the first case, the movement of the center of gravity of the grain is sinusoidal and given by the equation

$$x_{gr} = x_{gr}^{eq} + a \sin(\omega t + \phi), \quad \text{where} \quad x_{gr}^{eq} = x_{gr}^{ini} - a \sin \phi.$$

The equilibrium position of the grain ($x_{gr}^{eq}$), the amplitude of the oscillations ($a$) and the frequency ($\omega$) must be specified. In the second case, the grain is assumed to move under the pressure difference and the expanding gases on both of its sides. The resulting force is shown on the diagram below.

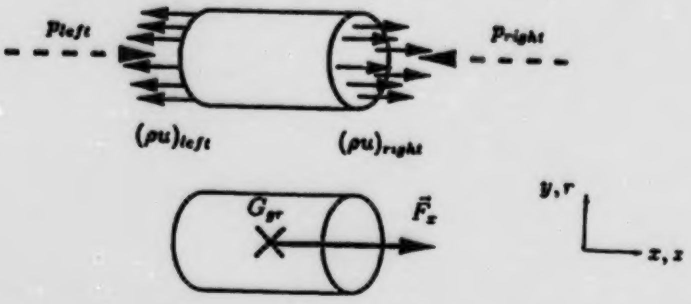

Representation of the external force acting on the grain.

It is equal to

$$F_x = \int_{S_{left}} (p + \rho u) \, d\Sigma - \int_{S_{right}} (p + \rho u) \, d\Sigma. \tag{19}$$

The position of the center of gravity of the grain, $x_{gr}$, is obtained by solving the momentum equation along the $x$ axis

$$m_{gr} \frac{d^2 x_{gr}}{dt^2} = F_x,$$

where $m_{gr}$ is the instantaneous mass of the grain:

$$m_{gr} = m_{gr}^{ini} - \int_S \int_0^t \rho u \, d\Sigma \, d\tau.$$

The above model leads to an overestimation of the acceleration applied to the grain. Indeed, in the actual process the surface of the grain recedes with time, resulting in a smaller force than the one calculated above (equation (19)), and therefore, in a smaller acceleration.

The amount of heat transfer to the vessel walls is controlled by two parameters, the characteristic length, $L$, and the critical Reynolds number, $\mathrm{Re}_L^{crit}$. A switch parameter allows the user to neglect the heat losses, whereby an adiabatic calculation is done. The effect of decreasing $L$ is to increase the heat loss rate by the factor $L^{0.2}$. If $\mathrm{Re}_L^{crit}$ is greater than $1.8\times10^4$, only turbulent heat transfer occurs. The value of the instantaneous heat loss, the average temperature in the vessel and the average convective heat transfer coefficient along the vessel walls are given at constant time intervals specified by the user.

## 5.0 NUMERICAL RESULTS AND DISCUSSION

The validity of the main assumption concerning the boundary layer flow is discussed first. The model relies on the fact that gases are inviscid and non-conductive in the inner flow. Therefore, it must be determined whether viscous and conductive terms are indeed negligible. They can be estimated using a constant viscosity ($\mu_p = \mu_a = 4.0\times10^{-5}\ \mathrm{kg\cdot m^{-1}\cdot s^{-1}}$) and a constant conductivity ($k_p = k_a = 0.227\ \mathrm{W\cdot m^{-1}\cdot K^{-1}}$), and the flow velocity and temperature at every node. Three nodes are used to obtain the derivatives at each node. As expected, the ratio of the viscous terms to the inertia terms does not exceed 5 % in the vessel except near the walls, where it can reach 50 %. "Near the wall" means on one of the 6 nodes nearest to it, out of a total of 31 nodes in the normal direction. This represents about 18 % of the radius of the vessel. For the conductive terms the ratio does not exceed 20 % either.

The above results confirm that the core flow is indeed inviscid and non-conductive and that the boundary layer height is less than 20 %. It is therefore not similar to boundary layers that develop in pipes, their height being equal to 100 % of the radius. The expression for the heat transfer coefficient as a function of the Reynolds number should be based on results from flat plate theory rather than from pipe flows.

In order to determine how variations in certain parameters affect the results of the mathematical model of the closed bomb presented in the previous chapter, a sensitivity analysis was performed on the 2D computer program. It is presented here. First, in section 5.1, the results obtained when a monoperforated solid propellant grain burns under adiabatic conditions, are given and discussed. The corresponding numerical computation serves as a reference for all of the other ones. It is referred to as "reference computation." Then, the effects of small variations in the grain geometry (section 5.2), the grain motion (section 5.3), the initial temperature of the gases (section 5.4) and the heat loss rate (section 5.5) are considered. All computer calculations were performed using the data given in appendix B.

The accuracy of the solution depends on the spacing interval of the mesh. The smaller the spacing is, the more accurate the solution is. However, the main drawback of a fine grid, is that the computational time increases very rapidly with the number of nodes. As the general aspect of the flow and trends of the results, are the main concern of this work, a relatively small number of nodes was used (31 by 21 grid) in order to save computational time. The corresponding space intervals in the axial and radial directions are: $\Delta x = 0.509\,\text{cm}$ and $\Delta y = 0.191\,\text{cm}$. The time interval between two time steps ($\Delta t$) is approximately 1 microsecond. For information, one calculation using a finer grid (101 by 26) was performed. The corresponding velocity field at two different times during combustion is shown in figure 13. For comparison, figure 14 shows the results of the same calculation performed using a 31 by 21 grid. With a finer grid, a higher number of vortices can be resolved at the early stages of burning, when they are still small. The order of magnitude of the velocities along the walls is similar.

## 5.1 REFERENCE COMPUTATION

The burning of a single monoperforated grain placed in the center of the vessel is considered. Its position does not change with time. No heat losses to the walls are allowed. The pressure, temperature, ratio of the specific-heats contours and the velocity field are plotted on figure 15 and discussed below.

### 5.1.1 Wall Flow

The knowledge of the flow pattern near the walls is of importance to the heat transfer process. Depending on the flow velocity and temperature profiles at the edge of the inner flow, the type of the boundary layer that develops along the walls can be deduced. Figure 16 shows the time variations of the flow velocity at six different locations along the curved and flat parts of the vessel. The velocity varies rapidly at the beginning of burning, reaches an almost steady peak value of about $5\,\text{m}\cdot\text{s}^{-1}$ until burnout, and then decreases to zero as no more combustion gases are injected. The largest velocities are reached along the curved part of the vessel. This is due to the grain-vessel configuration used; the grain and the vessel have the same axis of symmetry and approximately the same length to diameter ratio. They can be larger than the ones at the burning surface by a factor 10. The direction of the flow at a given point along the wall remains roughly constant with time.

The wall temperature is almost uniform along all surfaces and very high (3500 K) except where the inert gases are present, in which case it is lower (1800 K).

From the above results, it can be concluded that the boundary layer that develops when burning a solid propellant in a closed vessel is quite complex. It is undoubtedly compressible and unsteady, probably turbulent, and contains many separation points. This last point will be emphasized in sections 5.2 and 5.3.

### 5.1.2 Core Flow

The pressure contour in the vessel, as shown in figure 15, is almost uniform (a maximum difference of 0.2 MPa between any two points in the vessel is noted), especially at the burning surface. This means that the grain burns uniformly. The velocity field shows a large vortex on one side of the grain. Since the flow is faster near the axis of symmetry of the vessel, a circulation towards the upper walls develops. The general aspect of the temperature field is much alike that of the velocity field in terms of contours and vortices. The temperature is highly non-uniform and peaks as high as 5300 K are encountered. It is interesting to note that these very high temperature pockets of combustion gases are located near the inert gases. The combustion gases are formed under practically constant pressure conditions. Their initial temperature corresponds to combustion under those conditions. When evolving from the burning surface of the grain, they make room for themselves by compressing the gases previously burnt. Subsequently they are compressed adiabatically by the new coming gases. Different elements of gas start at almost the same temperature ($T_{fl}$) but attain a final temperature given by

$$T^{fin} = T_{fl} \left( \frac{p^{fin}}{p^{ini}} \right)^{\frac{\gamma_p - 1}{\gamma_p}} .$$

In our model, the first gases entering the chamber, have an initial pressure of 2.05 MPa. For a final pressure of 280 MPa, for example, their final temperature will be approximately equal to

$$T^{fin} \approx 8440\,\mathrm{K},$$

which is much higher than the the adiabatic flame temperature. For the next gases formed under a higher pressure of 200 MPa,

$$T^{fin} \approx 3935\,\mathrm{K}.$$

The first gases formed under a very low pressure will attain a very high temperature indeed and will be located near the inert gases, while the last ones will suffer no compression and remain at their initial temperature. These effects are very well reproduced by the present model. Figure 17 shows the average temperature in the vessel for the present calculation. It increases from 293 K to about 4250 K during combustion and then remains constant after burnout as it was assumed that the process was adiabatic. Of course, during an actual firing, both gas mixing and heat transfer will tend to equalize the temperature throughout the vessel to $T_{fl}$. However, it is not known how quickly and how well this equalization occurs.

## 5.2 GRAIN GEOMETRY

The geometry of the grain is modified in order to assess its influence on the velocity pattern. Figure 18 shows the effect of burning a grain with a large radius to length ratio. In figure 19 an imperfect grain is burnt. In both cases a larger number of vortices and separation points are present, as the grain burns in a less ordered manner. This result suggests that, in the actual process, where many grains burn, all having different orientations, a highly rotational and chaotic flow must develop.

## 5.3 GRAIN MOTION

### 5.3.1 Free Motion

The intensity of the force developed when the grain is left free to move under the action of the expanding gases, and the pressure difference on both of its sides, is shown in figure 20. Its maximum value does not exceed 50 N. This is not large enough to induce any movement, since the frequency of its time variations is too high. It can, therefore, be concluded that the grain does not have time to respond to the rapid changes in the flow. However, in an actual firing the grains do not burn uniformly, which can result in major changes to their original shape. Thus a non-ideal grain with a side hole was used to look for a possible difference in the force intensity. It turned out that the grain moved about 2 nodes away from its initial position ($\approx 1$ cm), which is not significant considering that the force has been overestimated (section 4.6, page 40).

### 5.3.2 Imposed Motion

The motion of the grain is imposed using low frequency sinusoidal oscillations ($\omega = \pi/5\,\mathrm{rad{\cdot}ms^{-1}} = 628.32\,\mathrm{rad{\cdot}s^{-1}}$) to describe the movement of the center of gravity, as shown in figure 21. Figure 22 shows the corresponding velocity field. It is plotted at time intervals of 5 ms, from 5 ms after combustion started, until 40 ms (just after burnout which occurs at approximately 37.5 ms). Vortices are numerous and their position unsteady. Note the periodicity of the flow pattern due to the sinusoidal motion of the grain. Figure 23 shows the flow velocities at several different locations along the curved part of the vessel walls. The direction of the flow at one point along the wall is no longer constant, and the flow velocity varies strongly with time. The average temperature of the gases in the vessel is shown in figure 24. The slope of the curve is larger at the beginning of burning, and the maximum temperature reached is lower by a few percent, because "mixing" of the combustion gases (due to the grain motion) is now more important.

From the above results it can be concluded that the effect of the grain motion on the velocity field, and consequently on the convective heat transfer process, is significant. However it has also been shown that it is very unlikely that the grains will move on their own unless they are given an initial motion. When the charge starts to burn, the silk bags in which it is confined break and the grains are projected in random directions into the vessel. This initial motion, due to the ignition procedure, certainly affects the heat transfer, at least at the beginning of burning.

## 5.4 INITIAL TEMPERATURE

The initial temperature of the inert gases in the vessel is increased from 293 K to 1000 K. Figure 25 shows the temperature contour obtained. As in the reference computation, similar high temperature pockets of combustion gases are found. The inert gases undergo the same adiabatic compression, but their initial temperature is now much higher, and so they reach a considerably higher temperature at burnout ($T_a^{fin} \approx 8000$ K).

## 5.5 HEAT LOSS RATE

The critical Reynolds number is kept equal to $5 \times 10^5$. The characteristic length $L$ is progressively set equal to infinity (no heat loss), 6 cm, 1.2 cm and 0.5 cm. The average pressure and temperature in the vessel are shown in figure 26, for the case of a slow and a fast burning grain. By varying $L$, the pressure drop can be adjusted. With a standard value of 6 cm, it is about 1 % (higher when a slower burning grain is used, because the pressures reached are smaller). If it is decreased by a factor 5 to 1.2 cm, the percentage increases to about 3 %. The pressure drops are summarized in table 5, along with the corresponding heat loss ($Q_w^{tot}$) estimated at burnout. The faster the grains burns, the smaller the pressure drop is. Indeed, the pressure reached in this case is higher. Thus, the pressure rise rate due to burning becomes much larger than the pressure decrease rate due to heat losses, which have less time to occur. The heat loss rate is plotted in figure 27. The pressure rate of change, $dp/dt$, is also shown for comparison. They are not proportional during burning, unlike what has been assumed in all previous models (chapter 3). $q_w^c$ varies considerably. It reaches a maximum at burnout and then, after combustion is complete, it drops to its minimum value determined by $\mathrm{Nu}_L^{min}$, as the flow velocity decreases towards zero. In the actual process the heat loss rate is expected to vary but may be not exactly as predicted by the model. In the early stages of combustion, the gases near the walls have a very high temperature, and therefore lose heat very quickly. When combustion proceeds their temperature decreases, due to gas mixing, and hence the heat loss rate decreases.

Table 5: Total heat losses obtained according to the model and corresponding pressure drop for various characteristic lengths.

| type of grain burning time | $L$ | $Q_w^{tot}$ [kJ - % $Q_e$] | $\Delta p/p$ [%] |
|---|---|---|---|
| slow burning grain<br>$t_{cb} = 19.8\,\mathrm{ms}$ | $L = 6\,\mathrm{cm}$ | 24.23 - 3.10 | 1.31 |
| | $L = 1.2\,\mathrm{cm}$ | 92.96 - 11.90 | 2.98 |
| | $L = 0.5\,\mathrm{cm}$ | 244.87 - 31.35 | 8.55 |
| fast burning grain<br>$t_{cb} = 10.0\,\mathrm{ms}$ | $L = 6\,\mathrm{cm}$ | 13.26 - 1.69 | 0.71 |
| | $L = 1.2\,\mathrm{cm}$ | 50.61 - 7.05 | 1.65 |
| | $L = 0.5\,\mathrm{cm}$ | 130.97 - 16.89 | 5.57 |

As a consequence, the maximum heat loss rate should be reached at some time before burnout, when the temperature has been equalized throughout the vessel. In our model, no mixing between the gases is allowed, therefore this effect cannot be reproduced and the maximum is shifted towards burnout. Figure 28 shows the average convective heat transfer coefficient along the vessel walls for a characteristic length of 6 cm. It varies between $3\,\mathrm{kW{\cdot}m^{-1}{\cdot}K^{-1}}$ at the beginning of burning and $6\,\mathrm{kW{\cdot}m^{-1}{\cdot}K^{-1}}$ at the end. For a higher heat loss rate ($L = 1.2$ cm), $h^c$ varies between $13.5\,\mathrm{kW{\cdot}m^{-1}{\cdot}K^{-1}}$ and $16\,\mathrm{kW{\cdot}m^{-1}{\cdot}K^{-1}}$. These last values are closer to the experimental ones given by DREV [MAILLETTE 90].

Before concluding this chapter, a comment on the pressure rise history as predicted by the model is presented. The actual dimensions of the burning surface cannot be modeled because only one grain is burning. A typical value for the burning surface area in an actual firing is $600\,\mathrm{cm^2}$. Using a single grain, this value can be obtained only if it has a volume of $1000\,\mathrm{cm^3}$, which is larger than the vessel's volume ($700\ \mathrm{cm^3}$). The ratio of the surface area used to the actual one is around 15 % only, which results in a smaller pressure rate. For the same time interval, the mass flow rate, because it is proportional to burning surface area, is smaller. This slows down the burning of the grain as well as the pressure increase. Moreover, as the grain's surface does not recede with time, the flow evolves in a vessel whose volume is smaller than the it actually should be ($V_{ch}^{code}/V_{ch}^{actual} = 88$ %), resulting in a larger maximum pressure. Both realistic pressure rate and maximum pressure cannot be obtained simultaneously in the current model. If the grain's volume is decreased, it will result in a more accurate maximum pressure together with a less accurate pressure rate as the grain's surface area will be smaller. Figure 29 illustrates these effects. The pressure rises obtained while burning a non-perforated and a monoperforated grain are shown. The best possible accuracy can be obtained using a monoperforated grain because it represents the best compromise between a small volume and a large burning surface area. However predicted burning times and maximum pressures are still larger than the ones obtained in an actual firing. Finally, it should be pointed out that for the same total heat loss ratio $(Q_w^{tot}/Q_e)$, predicted pressure drops are lower than the experimental ones calculated at DREV [MAILLETTE 90]. This can be explained by the simplicity of the model; heat loss is not accounted for accurately, and turbulent effects are neglected although it has been shown that they can have a strong influence on the heat loss rate (section 3.2, page 22).

## 6.0 CONCLUDING REMARKS

A brief review of the closed bomb data reduction techniques modified to include heat loss has been presented, and a new 2D model to describe the flow and account for the non-adiabatic pressurization process in the vessel has been introduced. A proper analysis of the combustion of solid propellant grains in a closed vessel should include the effect of the three space dimensions. Using a 2D model, as done herein, only trends of the experiments can be reproduced. The major drawback of a 2D analysis is that the actual value of the burning surface area cannot be kept as the burning of only one grain can be modeled. As a result, the predicted peak pressures and combustion times are higher than the ones obtained in an actual firing. In addition, in our model, the pressure drops due to heat loss are underestimated, the main reason being that turbulent effects have been neglected in the analysis.

However, using this simple model, some interesting facts were brought to light. They are summarized below.

1. The velocities encountered in the vicinity of the vessel walls can be as high as 10 times the burning rate, and even larger at the center of the vessel.

2. Many vortices are present in the flow. Their number increases when the surface of the solid propellant grains presents some irregularities (they could be due to manufacturing defects or to non-uniform ignition) and especially when the grains move (they are however only likely to do so just after ignition).

3. The gas temperature in the vessel is not uniform. Small pockets of combustion gases at a higher temperature than the adiabatic flame temperature are found. This has two important consequences. One is that, during burning, the heat loss rate is not constant but, on the contrary, varies considerably, especially at the beginning of burning. The other is that it would be impossible to give any precise meaning to measurements of gas temperature by optical or any other physical methods.

4. Finally, forced convection, driven by propellant burning and solid grain motion, is the dominant process of heat transfer. It occurs on a small scale ($L \leq 5$ mm) and is very likely to be turbulent.

In order to obtain a more accurate closed vessel behaviour, a more detailed 3D analysis is required. Additional areas for future investigations are recommended as follows:

- A proper incorporation of the compressible unsteady turbulent boundary layer developing along the vessel walls is necessary.
- A study of random grain motion after ignition should be made, as its influence on the heat loss rate is not negligible.
- A proper incorporation of the actual number of grains, as well as a better modeling of the regression of the burning surface should be made, to obtain an accurate pressure rise history in the vessel.
- A proper estimation of the radiative properties of the combustion gases and of the solid propellant grains, to obtain an accurate radiative flux.

The first of the above points, concerning the modeling of the wall flow, is briefly expanded here, since it is the most critical one.

There are two methods to solve for wall flows. One can use numerical solutions (or differential methods), or analytical solutions (integral methods). In integral methods, the momentum equation in the direction parallel to the flow is integrated across the boundary layer resulting in an integro-differential equation. If a velocity profile is assumed inside the shear layer, the only unknown is the boundary layer height, from which, with further assumptions (Reynolds and Colburn analogies), the wall shear stress and the local heat flux can be derived. There are two main reasons why this method cannot be applied to closed bomb analysis. The first one is that near the many separation points along the walls, the theory is not valid. The second is that no information on the boundary layer is available, but an assumed velocity profile that is valid inside it is necessary. For unsteady boundary layers, an analytical expression does not exist and one usually assumes a steady profile, for example using a $1/n$ power law. The validity of this approximation degrades rapidly when turbulence comes into effect. Another analytical approach is to use wall functions. They are introduced to model the internal zone of the boundary layer (viscous and inertial layer) as opposed to the external zone where turbulent effects dominate. The near-wall mesh point is placed in the fully turbulent fluid, and wall functions connect the wall conditions (temperature, heat flux, shear stress) to the dependent variables just outside the viscous sublayer by assuming a velocity and a temperature profile. They allow avoidance of the use of numerous mesh points to resolve the very steep gradients in the viscous sublayer and the introduction of low Reynolds number corrections to the turbulence model.

In the differential approach, the inviscid core behavior is approximated prior to a solution of the boundary layer equations. Inviscid core properties supply the boundary conditions for the numerical solution of the shear layer conservation equations. The method offers more details on the inside of the layer but at the expense of numerical simplicity. Again, there are several reasons that make this method useless here. Indeed, the velocities at the edge of the inviscid core strongly vary with time in an unpredictable manner, and the assumption used to derive boundary layer equations (gradients in the direction parallel to the wall are negligible compared with gradients in the direction perpendicular to it) is not valid near separation points and corners. A solution would be to divide the flow along the wall into several flows where the velocity direction is uniform, but the logic involved, due to the time dependency of all variables, would be too complex, and interface solutions would still be necessary.

If viscous and conductive effects are to be added, the full Reynolds averaged Navier-Stokes equations should be solved to model the external part of the boundary layer and wall functions should be used to resolve the internal part of the layer. However, in this case, in order to remain consistent with the level of approximations used everywhere in the flow, a better modeling of the combustion zone would be necessary. To model the main flow, Euler's equations should be used, as it has been shown that viscous and conductive effects were negligible there.

## 7.0 REFERENCES

AGARD, 1985, *Interior ballistics in guns*, AGARD Conference Proceedings No. 392, held in Florence, Italy

AMC, 1964, *Engineering Design Handbook - Explosives Series - Solid Propellants Part One*, AAMC Pamphlet, AMCP 706–175

Anderson, D.A., Tannehill, J.C., Pletcher, R.H., 1984, *Computational fluid mechanics and heat transfer*, Mac Graw-Hill

Baer, H.R. and Nunziato, J,W., 1988, *Multiphase flow model for the initiation and combustion of granular explosives*, 88-3898-CP, pp. 1463–1470

Bicen, A.F., Khezzar, L., and Whitelaw, J.H., 1988, *Subsonic single phase flow in a gun simulator*, AIAA Vol. 25, No. 1, pp.47–51

Caveny, Leonard H. et al., 1974, *Ignition transients and pressurization in closed chambers*, CPIA Publication No. 261, Proceedings of the $11^{th}$ JANNAF Combustion Meeting

Celmins, A., 1974, *Solid propellant burning rate measurement in a closed bomb*, Combustion and flame, Vol. 23, pp. 381–397

Cohen, Norman S. and Strand, Leon D., 1978, *Analytical model of high pressure burning rates in a transient environment*, AIAA Vol. 18, No. 8, pp. 968–972

Corner, J., 1950, *Theory of Interior Ballistics of Guns*, New York, Wiley

Desoto, S. and Friedman, H.A., 1965, *Flame spreading and ignition transients in solid grain propellants*, AIAA Vol. 3, No. 3, pp. 405–412

Fayon, A.H. and Goldstein, J.B., 1966, *Evaluation of solid propellant ballistic properties by constant volume burning*, Combustion and flame, No. 10, pp. 23–28

Fisher, E.B. and Trippe, A. P., 1973, *Development of a basis for the acceptance of continuously produced propellant*, Calspan Report No. VQ-5163-D-1, Picatinny Arsenal Contract No. DAAA 21-72-C-0577

Ghoniem, A.F. and Knio, O.M., 1986, *Numerical simulation of flame propagation in constant volume chambers*, 21th symposium (international) on combustion pp. 1313–1320

Grune, D., 1987, *The influence of the variation of combustion chamber volume under pressure load on the determination of thermodynamic characteristics of solid propellants in pressure bonbs*, Propellants, Explosives and Pyrotechniques, Vol. 12, pp. 8–12

Hunt, F.R.W., 1951, *Internal ballistics*, His Majesty's Stationery Office, London

Juhasz, Arpad A. and Price, Channon F., 1978, *The closed bomb technique for burning rate measurement at high pressure*, AIAA Experimental diagnostis in combustion of solids, pp. 129–151

Juhasz, Arpad A., 1982, *Round Robin results of the closed bomb and strand burner*, CPIA Publication No. 361

Klingenberg, G. and Mach, H., 1976, *Experimental study of non-steady phenomena associated with the combustion of solid gun propellants*, 16th symposium (international) on combustion pp. 1193–1200

Krier, Herman, 1978, *Extracting burning rates for multiperforated grain propellant from closed bomb testing*, University of Illinois, AAE report No. 78-2

Krier, Herman and Adams, M.J., 1974, *Predicting uniform gun interior ballistics: Part II*, University of Illinois, AAE report No. 74-6

Krier, Herman and Black, J., 1974, *Predicting uniform gun interior ballistics: Part III*, University of Illinois, AAE report No. 74-7

Krier, Herman and Nietzke, T.G., 1975, *Solid propellant burning evaluation with the Dynagun ballistic simulator*, University of Illinois Technical Report, AAE 75-8

Krier, Herman and Shimpi, S.H., 1974, *Predicting uniform gun interior ballistics: Part I*, University of Illinois, AAE report No. 74-5

Krier, Herman and Shimpi, S.A., 1975, *The closed bomb test for the assessment of solid propellant grains utilized in guns*, Combustion and flame, Vol. 25, pp. 229–240

Krier,H., T'ien, J.S., Sirignano, W.A. and Summerfield, M, 1965, *Non-steady burning phenomena of solid propellants theory and experiments*, AIAA Vol. 3, No. 3, pp. 405–412

Kuo, K.K. et al., 1984, Fundamentals of solid propellant combustion, Progress in astronautics and aeronautics, Vol 90, Ed. by Kuo, K.K. and Summerfield, M.

MacCormack R.W., 1971, *Numerical solution of the interaction of a shock wave with a laminar boundary layer*, Lecture notes in physics, Vol. 8, Springer-Verlag, p.151

MacCormack R.W. and Baldwin, B.S., 1975, *A numerical method for solving the Navier-Stokes equations with application to shock-boundary layer interactions*, AIAA Paper No. 75-1

MacCormack R.W. and Puallay, A.J., 1972, *Computational efficiency achieved by time splitting of finite difference operators*, AIAA Paper No. 72–154

Maillette, Josée, 1989, *Interior ballistic analysis of the high-low pressure gun*, University of Toronto Institute for Aerospace Studies, Master's thesis, Toronto

Maillette, Josée, Lussier, L.S. and Lavigne, J., 1990, *Some observations on the total heat loss during closed vessel firings*, DREV Memorandum 3033/90

Osborn, J.R., 1973, *Evaluation of solid propellant ballistic properties*, Combustion and flame, Vol. 20, pp. 193–197

Peretz, A., Kuo, K.K., Caveny, L.H. and Summerfield, M., 1973, *Starting transient of solid propellant rocket motors with high internal gas velocities*, AIAA Vol. 11, No. 12, pp. 1719–1727

Price, Channon F. and Culick, F. E. C., 1968, *Combustion of solid rocket propellants* AIAA Professional Study Series

Price, Channon F. and Juhasz, Arpad A., 1977, *A versatile user-oriented closed bomb data reduction program CBRED*, Ballistic Research Laboratory, Aberdeen Proving Groun, Md, Report 2018

Robbins, F.W. and Horst, A.W., 1976, *Numerical simulation of closed bomb performance based on BLAKE code thermodynamic data*, Naval Ordonance Station, Indian Head, Md

Roe, P.L., 1981, *Numerical modeling of shockwave and other discontinuities*, Numerical methods in aeronautical fluid dynamics, pp. 211–243

Roe, P.L., 1981, *Approximate Riemann solvers, parameter vectors and difference schemes*, Journal of Computational physics, Vol. 43, pp. 357–372

Roe, P.L. and Pike, J., 1984, *Efficient construction and utilization of approximate Riemann solutions*, Computing methods in Applied Sciences and Engineering, pp. 499–518

Schlichting, 1979, *Boundary layer theory*, Mc Graw-Hill series in Mechanical Engineering

Sod, G.A., 1978, *A survey of several finite difference methods for systems of nonlinear hyperbolic conservative laws*, Journal of Computational Physics, Vol. 27, pp. 1–31

Sweby, P.K., 1983, *High resolution schemes using flux limiters for hyperbolic conservation laws*, SIAM Journal of Numerical Analysis, Vol. 21, No. 5, pp. 995–1011

Tanaka, Yutaka, 1989, *Numerical simulations for combustion of quiescent and turbulent mixtures in confined vessels*, Combustion and Flame, Vol. 75, No. 2, pp 123–138

Tompkins, Robert E., Bowman, Roger E. and Juhasz, Arpad A., 1985, *A study on the effect of surface area to volume ratio on closed bomb burning rates*, Ballistic Research laboratory, Aberdeen Proving Ground, Md, Technical Report TR 2685

Vest, Douglas Carter, 1953, *On the transfer of heat in high pressure combustion chambers*, Johns Hopkins University, Master's thesis, Baltimore

Williams, F.A., 1973, *Quasi-steady gas-phase flame theory in unsteady burning of a homogeneous solid propellant*, AIAA Technical notes, Vol. 11, No. 9, pp.1328–1330

Williams, F.A., 1985, *Combustion theory*, Ed. by Benjamin/Cummings Pub. Co.

Yee, H.C., 1987, *Construction of explicit and implicit symmetric TVD schemes and their applications*, Journal of Computational Physics, Vol. 68, No. 1, pp. 151–179

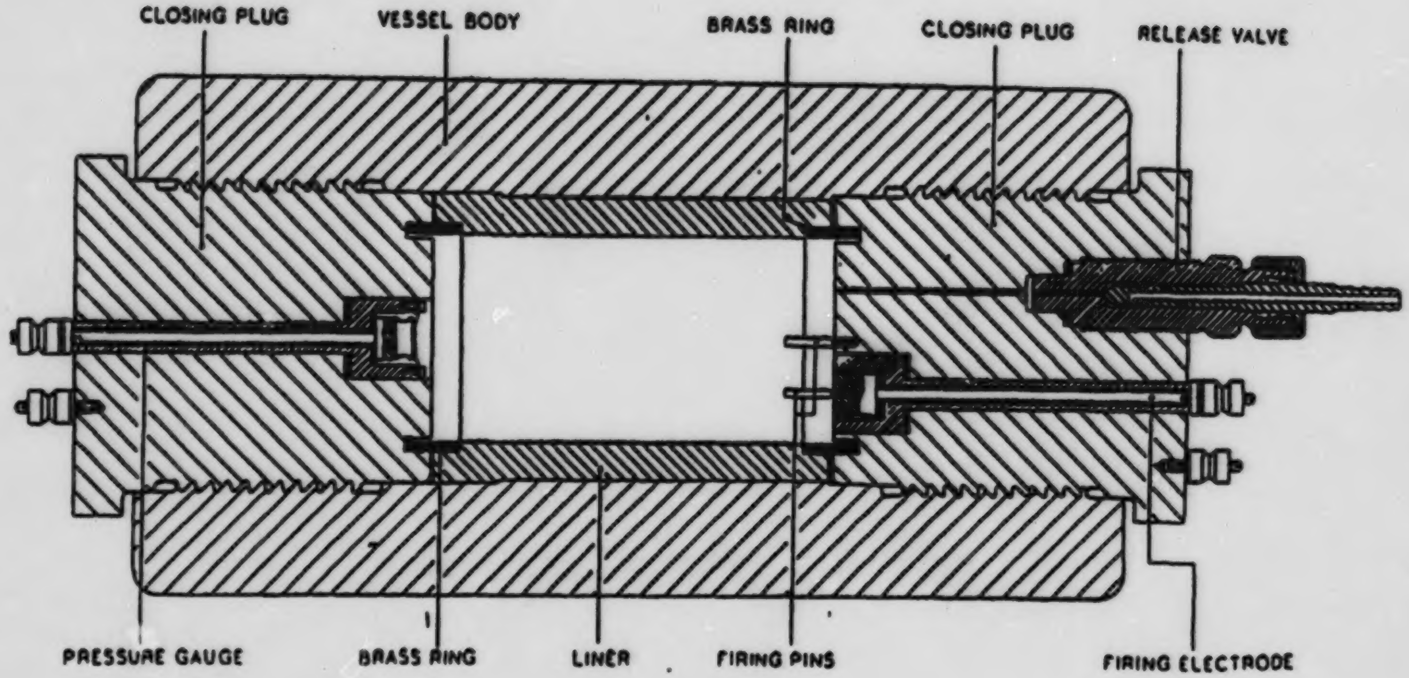
CLOSING PLUG
VESSEL BODY
BRASS RING
CLOSING PLUG
RELEASE VALVE
PRESSURE GAUGE
BRASS RING
LINER
FIRING PINS
FIRING ELECTRODE

Figure 1: Closed vessel.

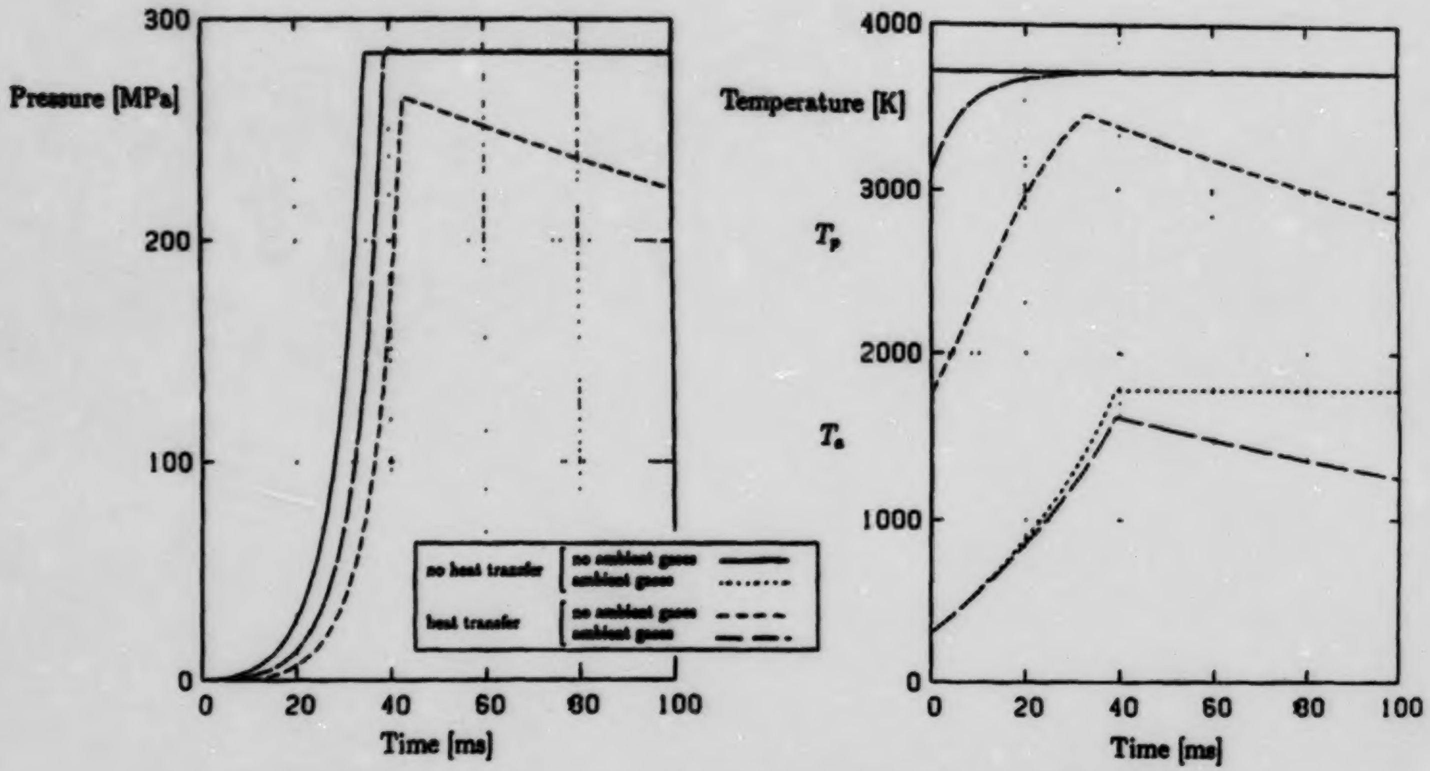

Figure 2: Pressure and temperature rise histories as predicted by the simple model.

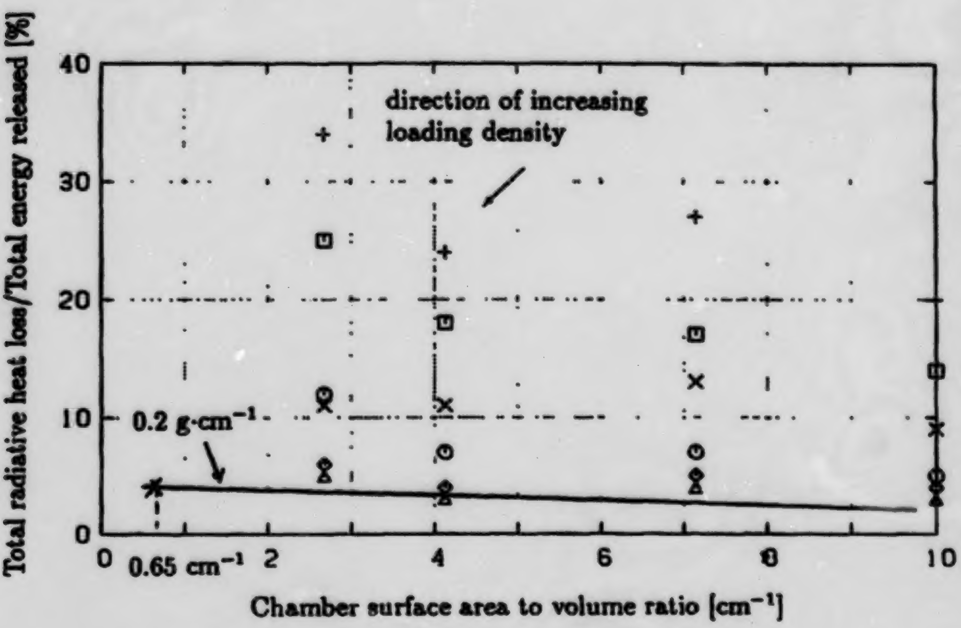

Figure 3: Maximum percentage of radiative heat loss for various loading densities and chamber area to volume ratios (from Vest).

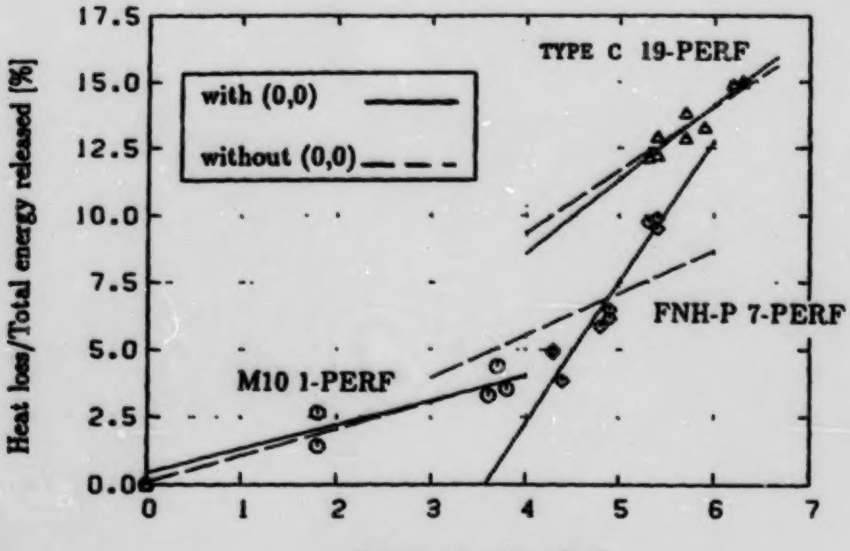

Figure 4: Linear regression between ratio of total heat loss to total energy released and combustion time (using DREV).

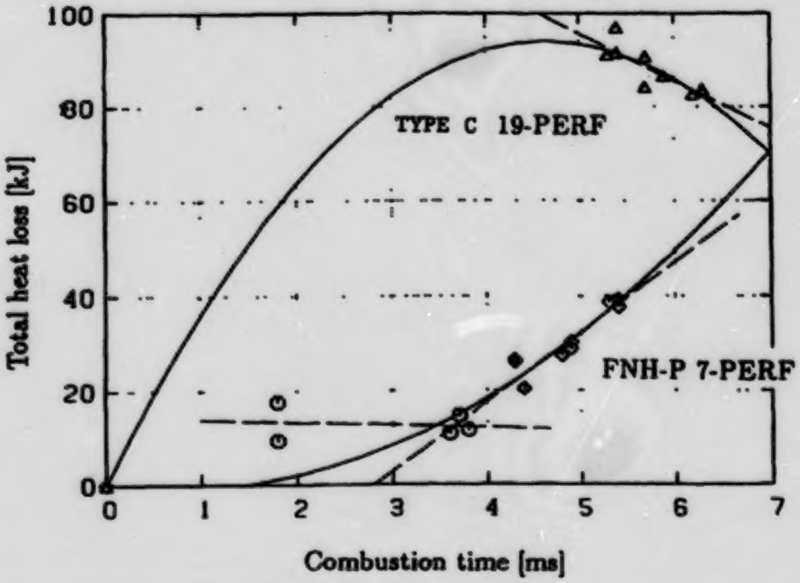

Figure 5: Quadratic and linear regression between total heat loss and combustion time (using DREV).

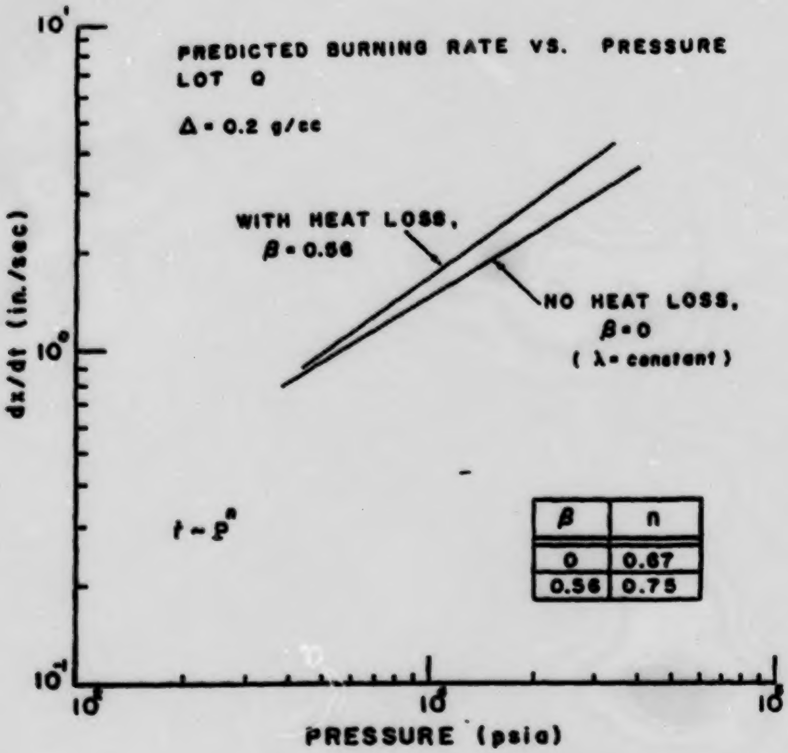

**CLOSED BOMB EXTRACTION PREDICTIONS FOR PROPELLANT LOTS P-W**

| | | With Finite β | | β = 0.0 | |
|---|---|---|---|---|---|
| Lot # | β | a $(10^{-3})$ | n | a $(10^{-3})$ | n |
| P | .225 | 1.98 | .733 | 3.18 | .677 |
| Q | .559 | 1.60 | .751 | 4.01 | .639 |
| R | .246 | 2.33 | .718 | 3.16 | .679 |
| S | .217 | 4.53 | .637 | 6.10 | .600 |
| T | .317 | 2.75 | .699 | 4.70 | .634 |
| U | .311 | .540 | .847 | 1.05 | .769 |
| V | .267 | 3.82 | .668 | 6.33 | .608 |
| W | .278 | 1.81 | .730 | 3.18 | .664 |

**Figure 6:** Predicted burning rate versus pressure with and without heat loss (from Krier).

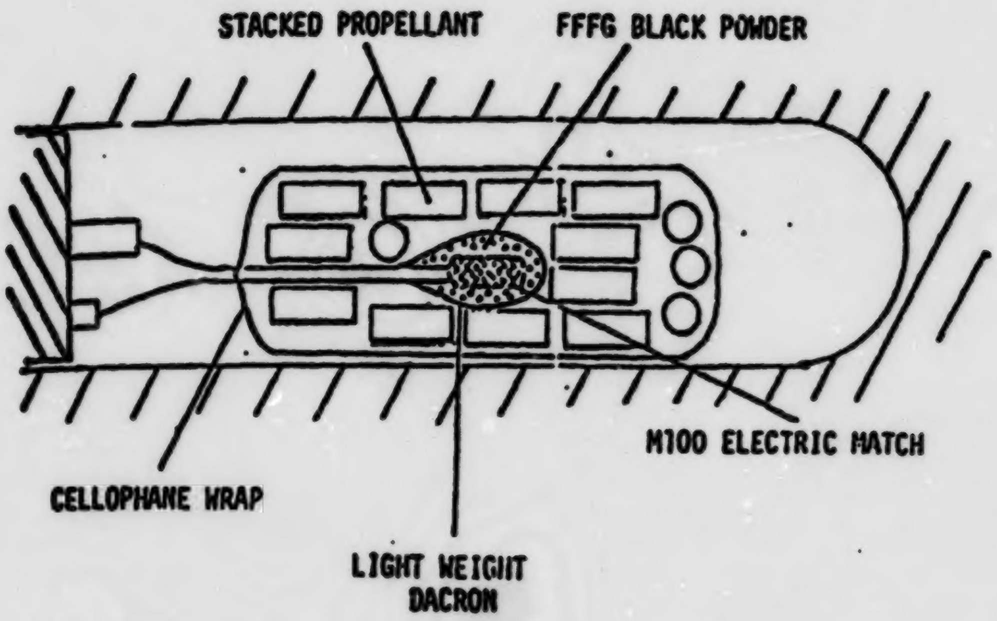
STACKED PROPELLANT
FFFG BLACK POWDER
M100 ELECTRIC MATCH
CELLOPHANE WRAP
LIGHT WEIGHT DACRON

Figure 7: Standard charge configuration adopted for Jannaf closed bomb Round Robin (from Juhasz).

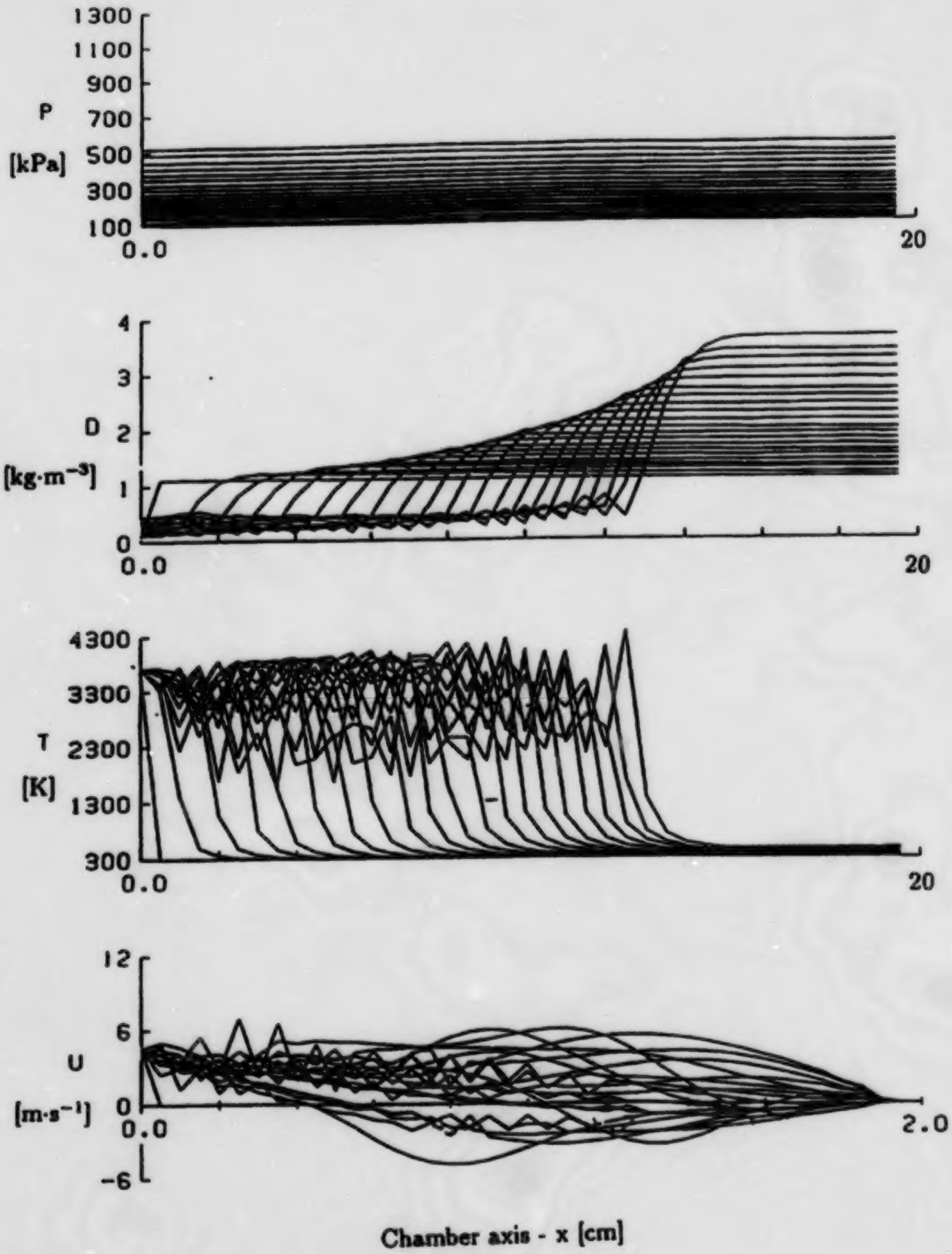

**Figure 8:** 1D model using Mac Cormack's method and $\mu_{num} = 0$
(spatial distributions, time $t = 0$ to $t = 3.5\,\text{ms}$)

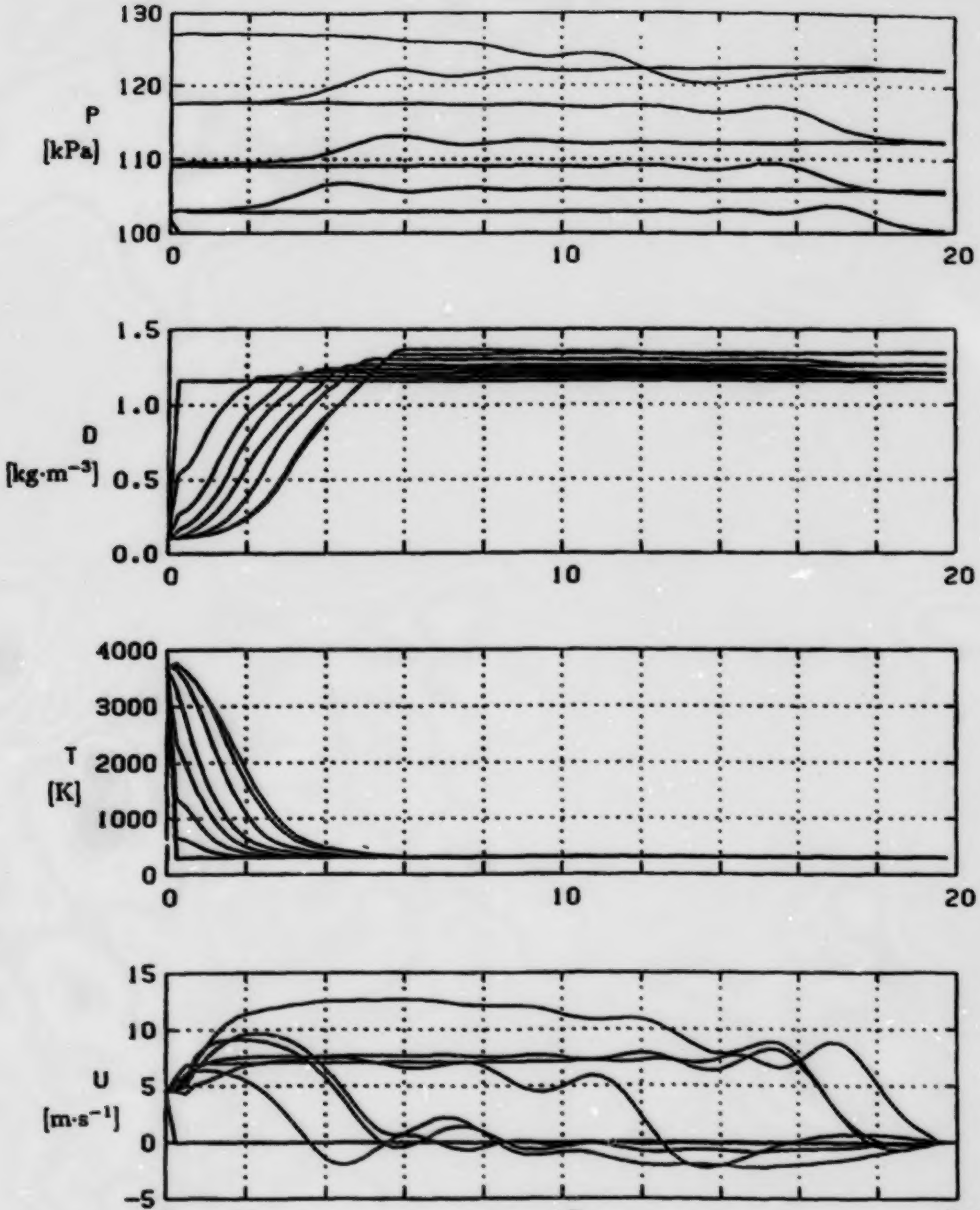

**Figure 9: 1D model using Mac Cormack's method and $\mu_{num} = 0.125$ (spatial distributions, time $t = 0$ to $t = 3.5\,\mathrm{ms}$)**

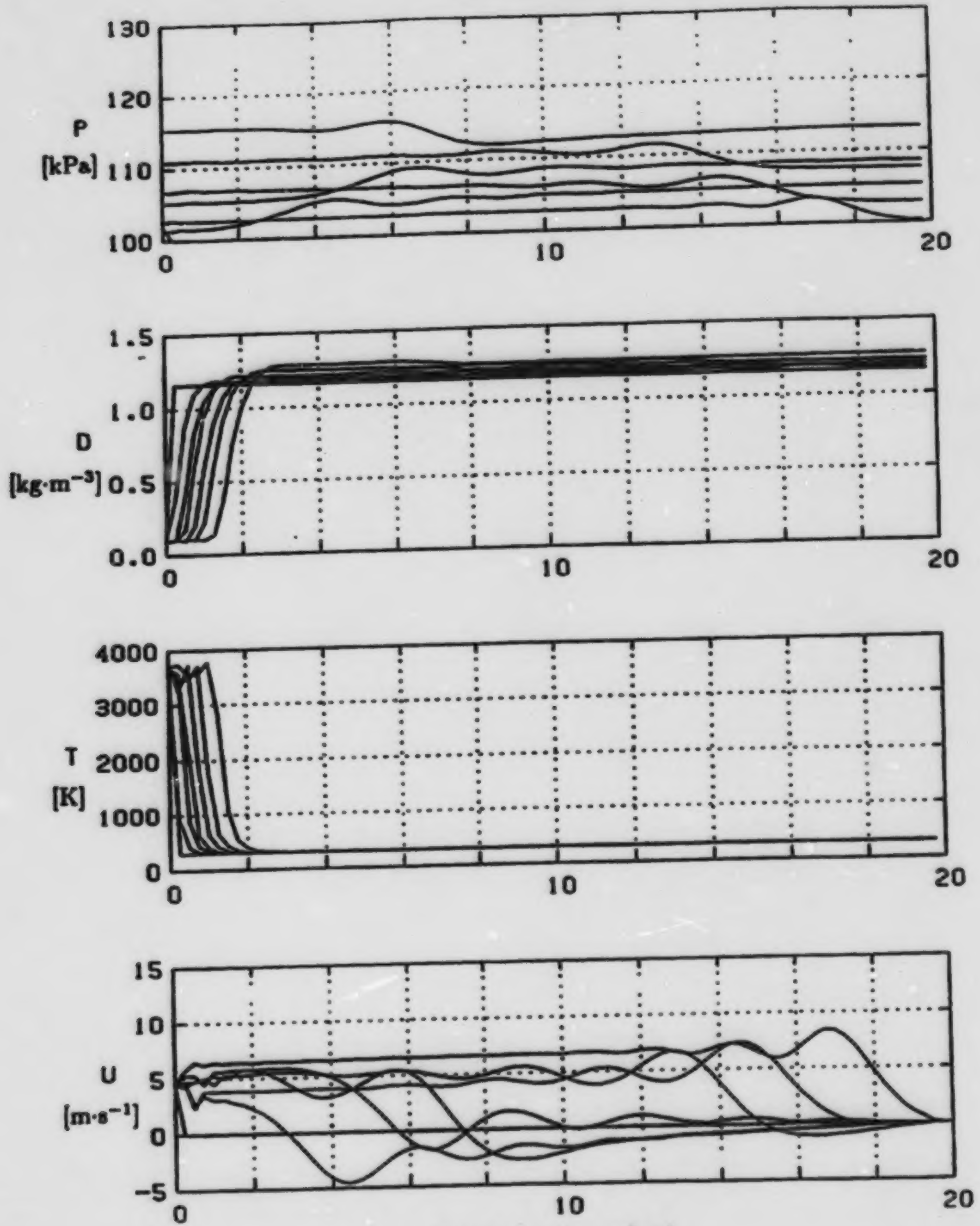

**Figure 10:** 1D model using Mac Cormack's method and $\mu_{num} = 0.001$ (spatial distributions, time $t = 0$ to $t = 3.5\,\text{ms}$)

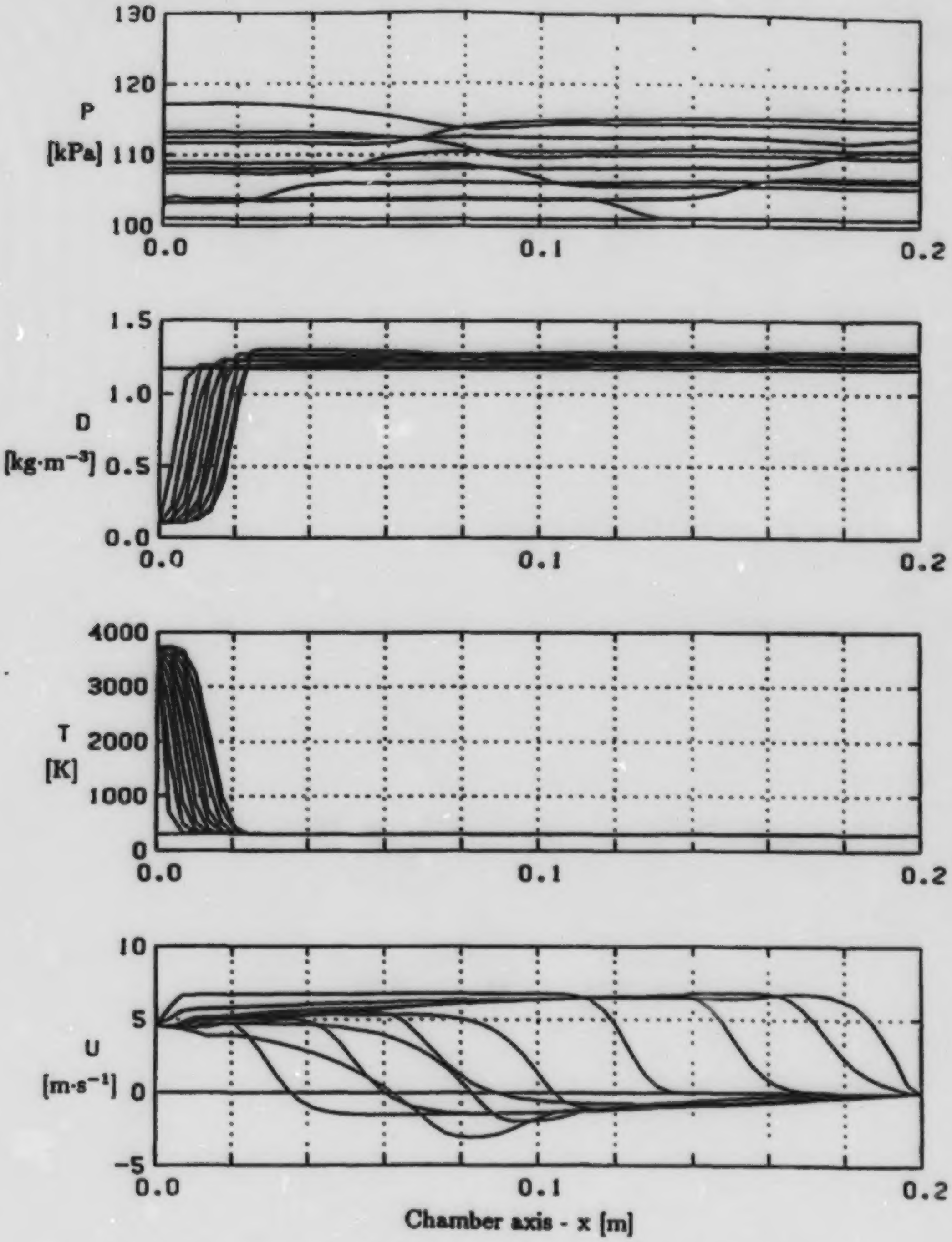

**Figure 11:** 1D model using Roe's method (overlapped spatial distributions, time $t = 0$ to $t = 3.5\,\mathrm{ms}$)

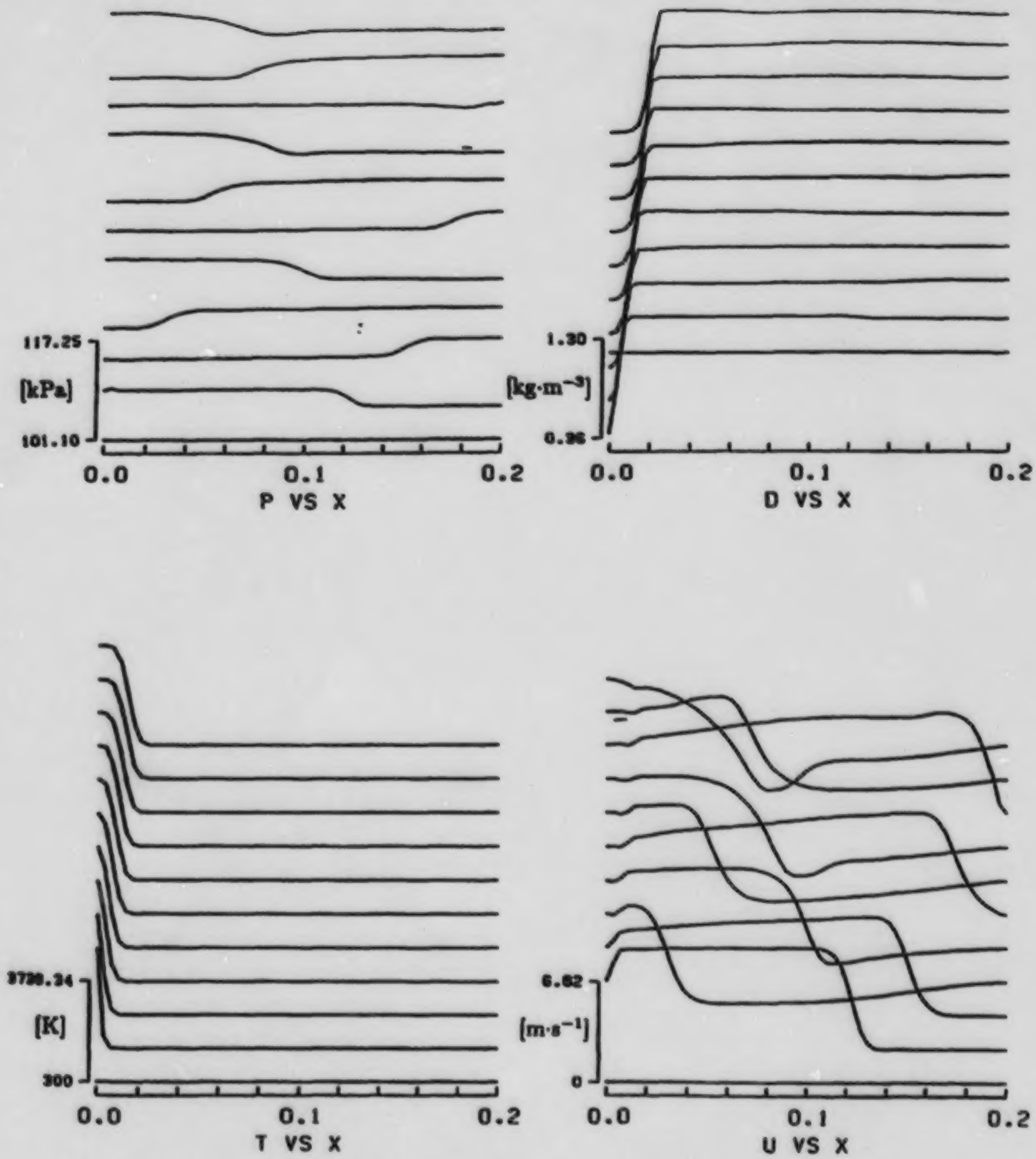

Figure 12: 1D model using Roe's method (non-overlapped spatial distributions, time $t = 0$ to $t = 3.5\,\mathrm{ms}$)

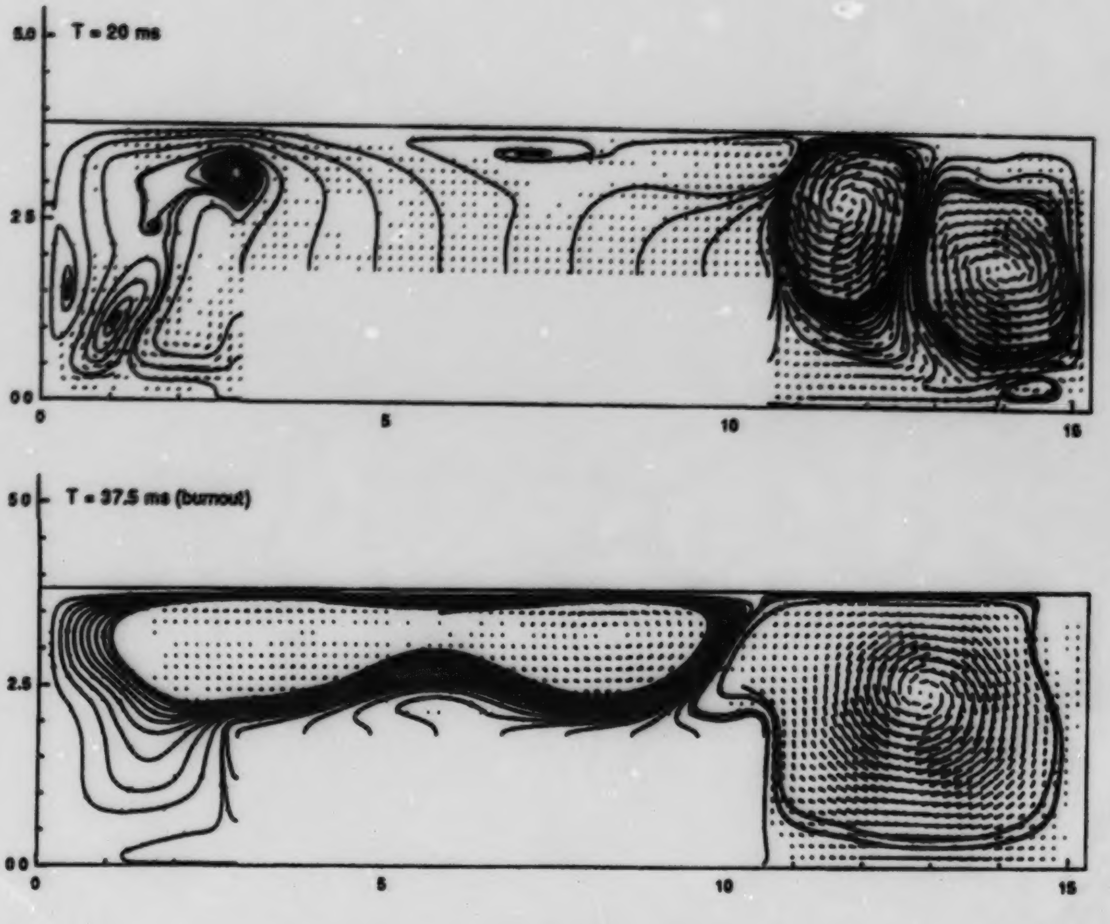

Figure 13: Velocity field using a 101 by 26 grid.

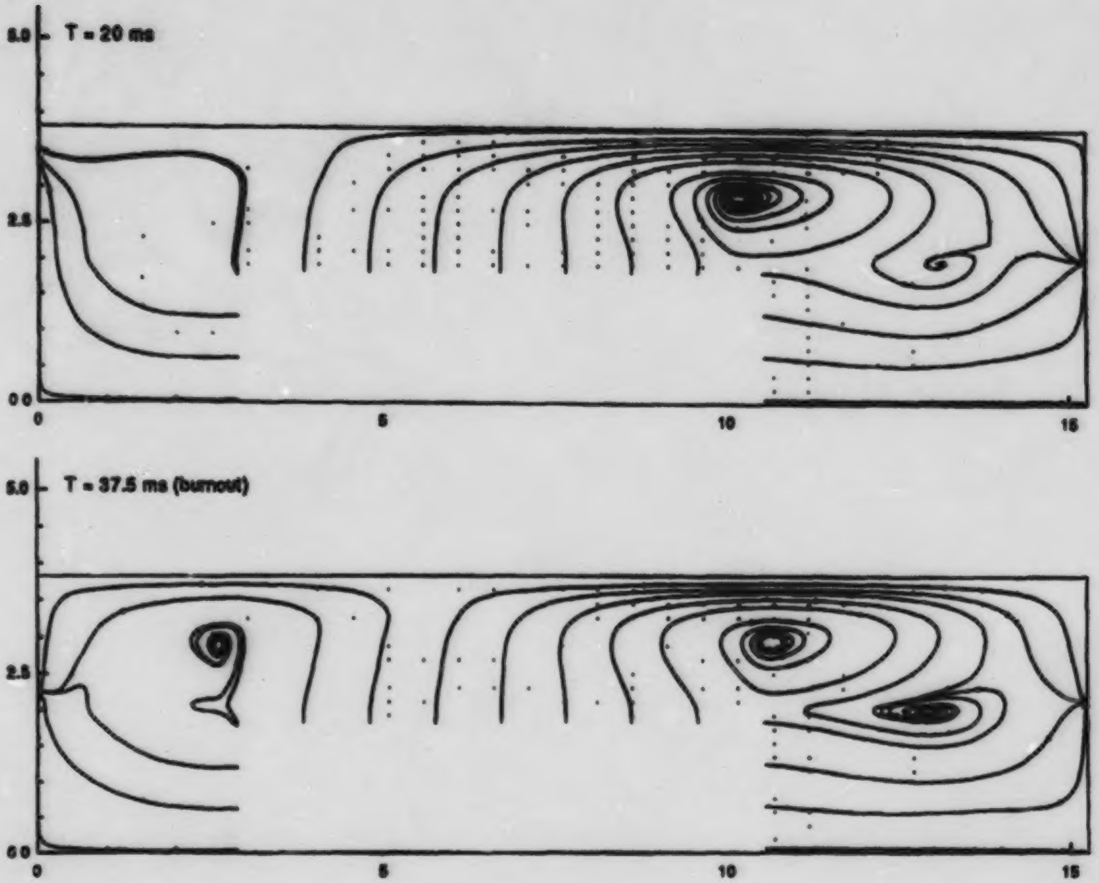

Figure 14: Velocity field using a 31 by 21 grid.

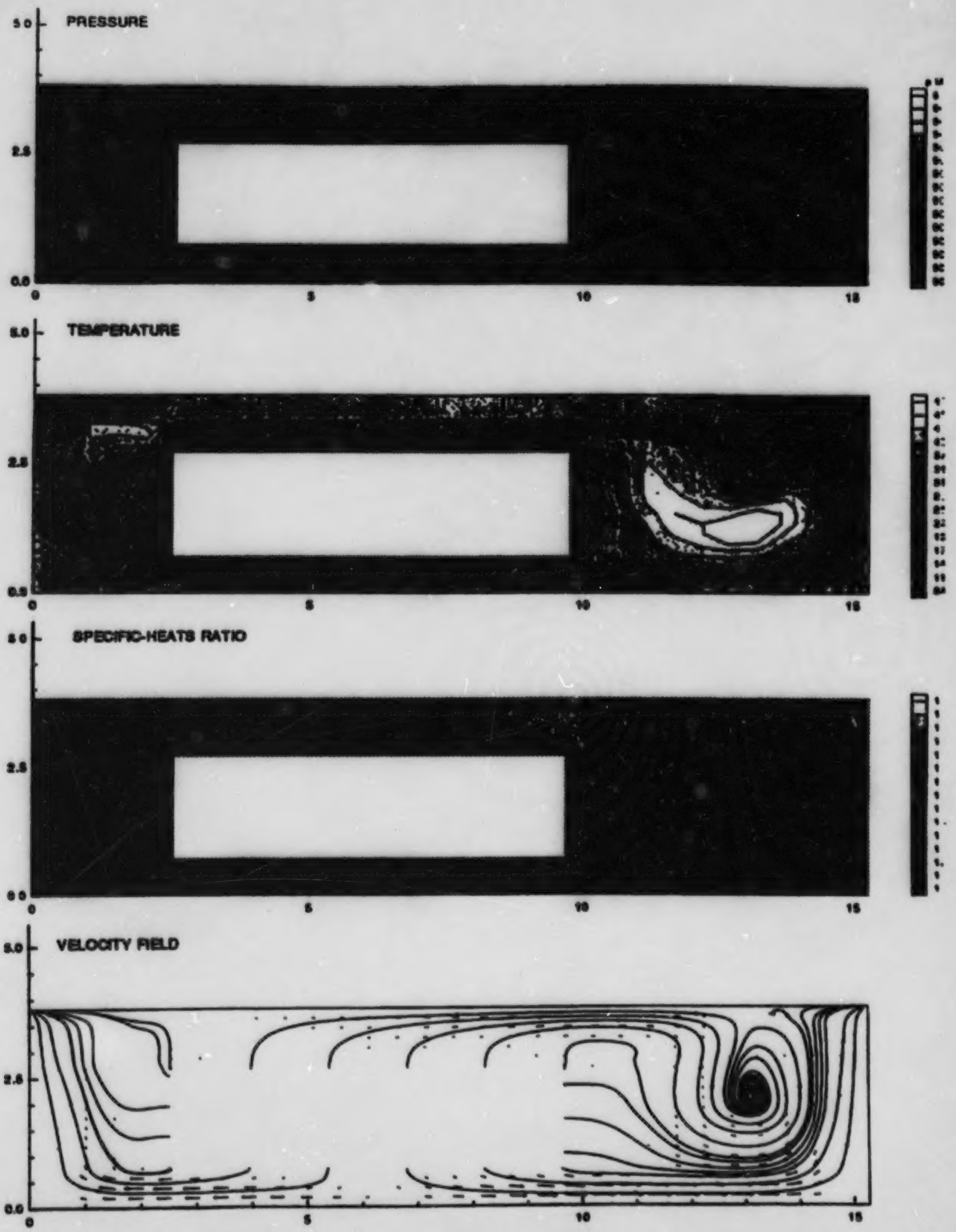

Figure 15: Typical pressure, temperature, specific-heats ratio contours and velocity field as predicted by the reference computation at time $t$ = 20 ms (Burnout at time $t$ = 37.96 ms).

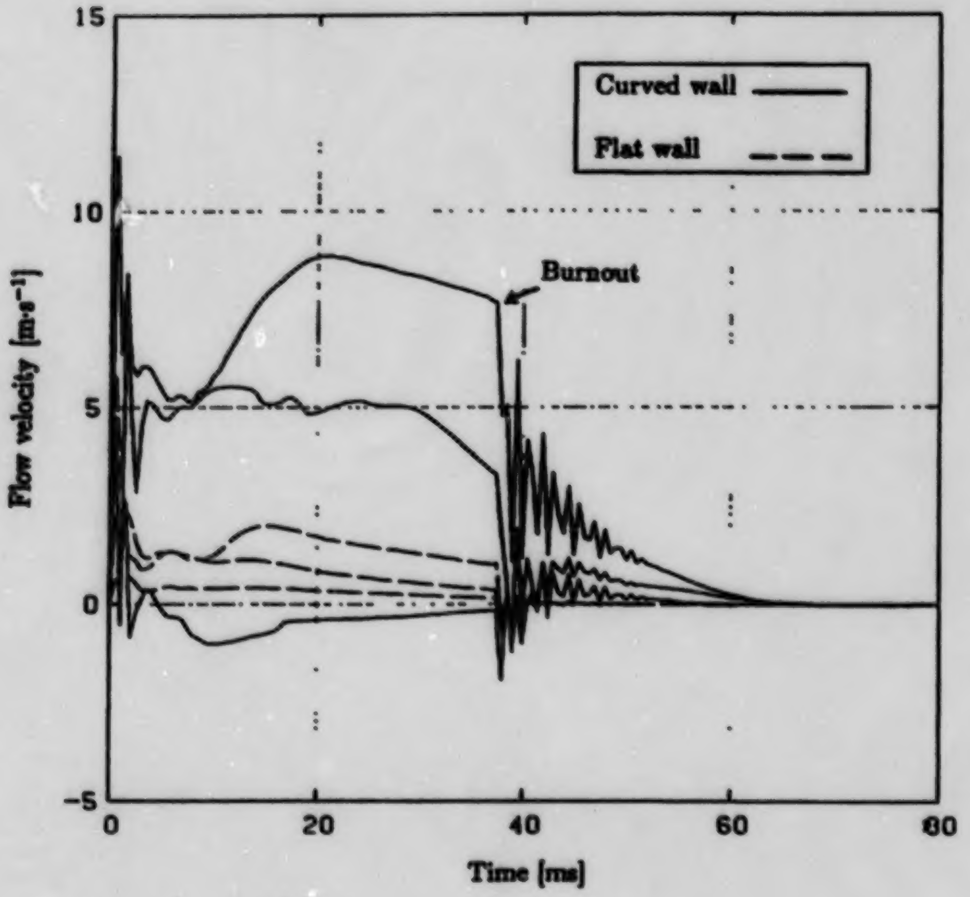

Figure 16: Variations of the flow velocity with time at six different locations along the vessel walls as predicted by the reference computation.

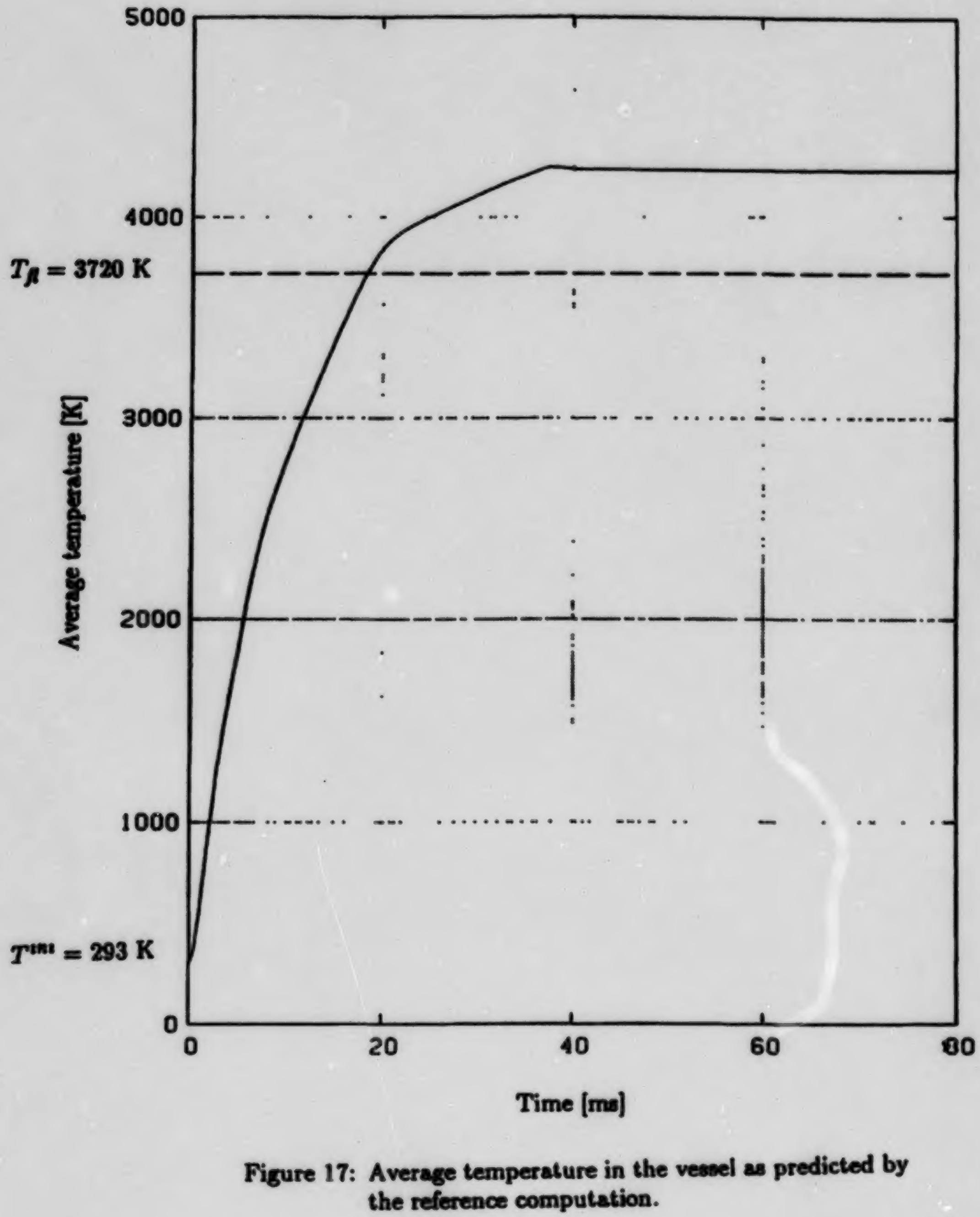

Figure 17: Average temperature in the vessel as predicted by the reference computation.

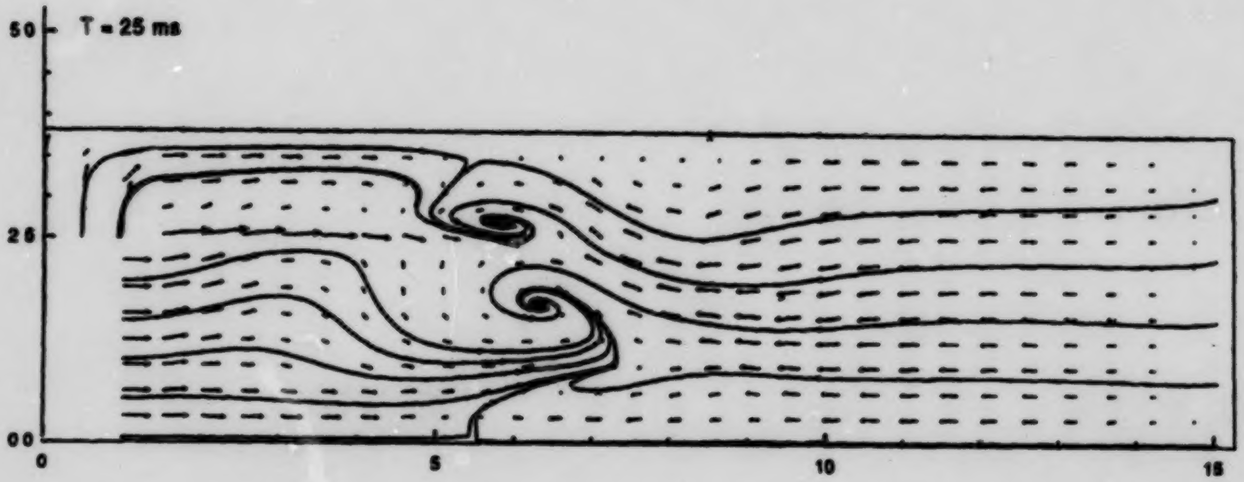

Figure 18: Velocity field obtained when burning a grain with a large radius to length ratio.

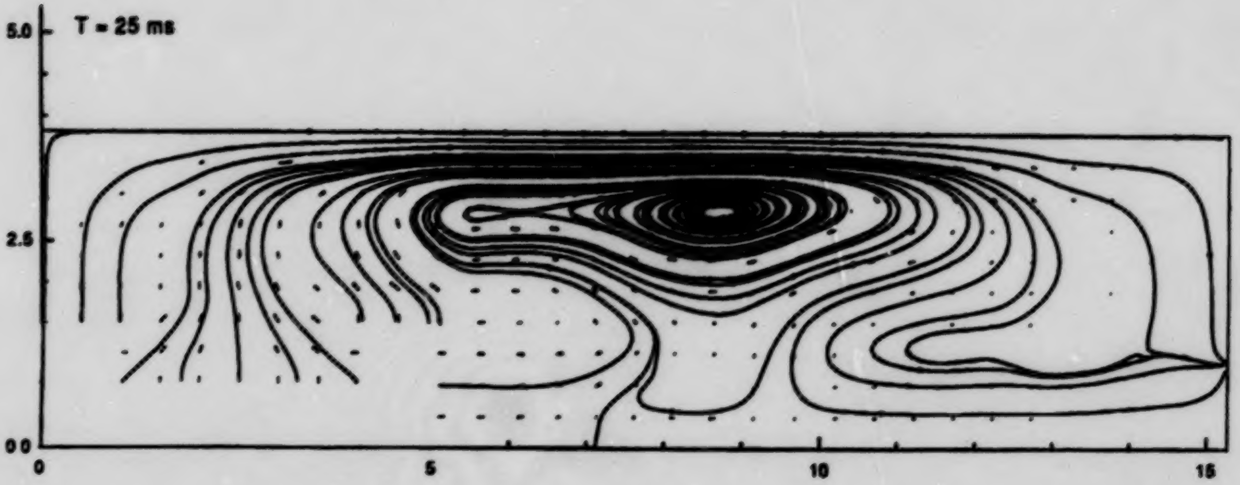

Figure 19: Velocity field obtained when burning an imperfect grain.

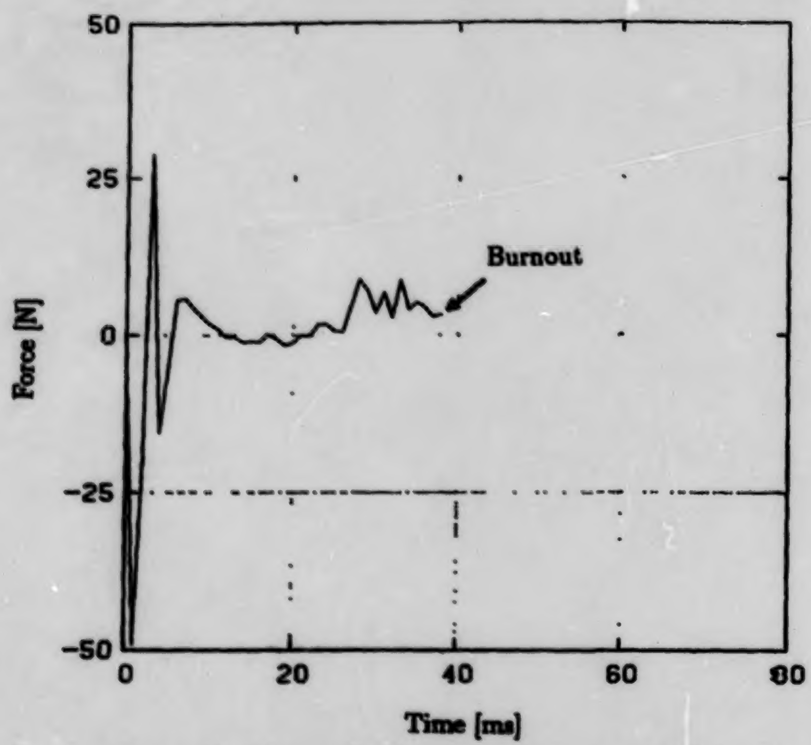

**Figure 20:** Time variations of the intensity of the force acting on the grain in the case of free motion.

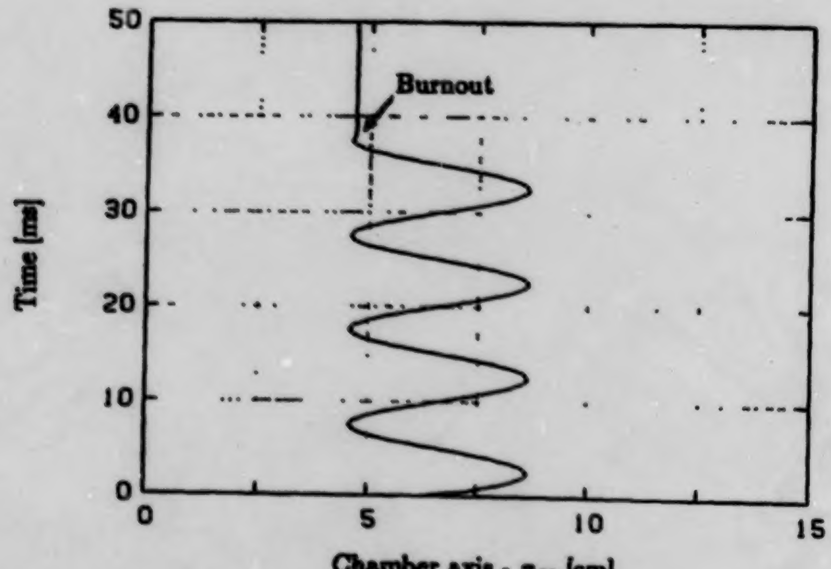

**Figure 21:** Position of the center of gravity of the grain when its motion is imposed.

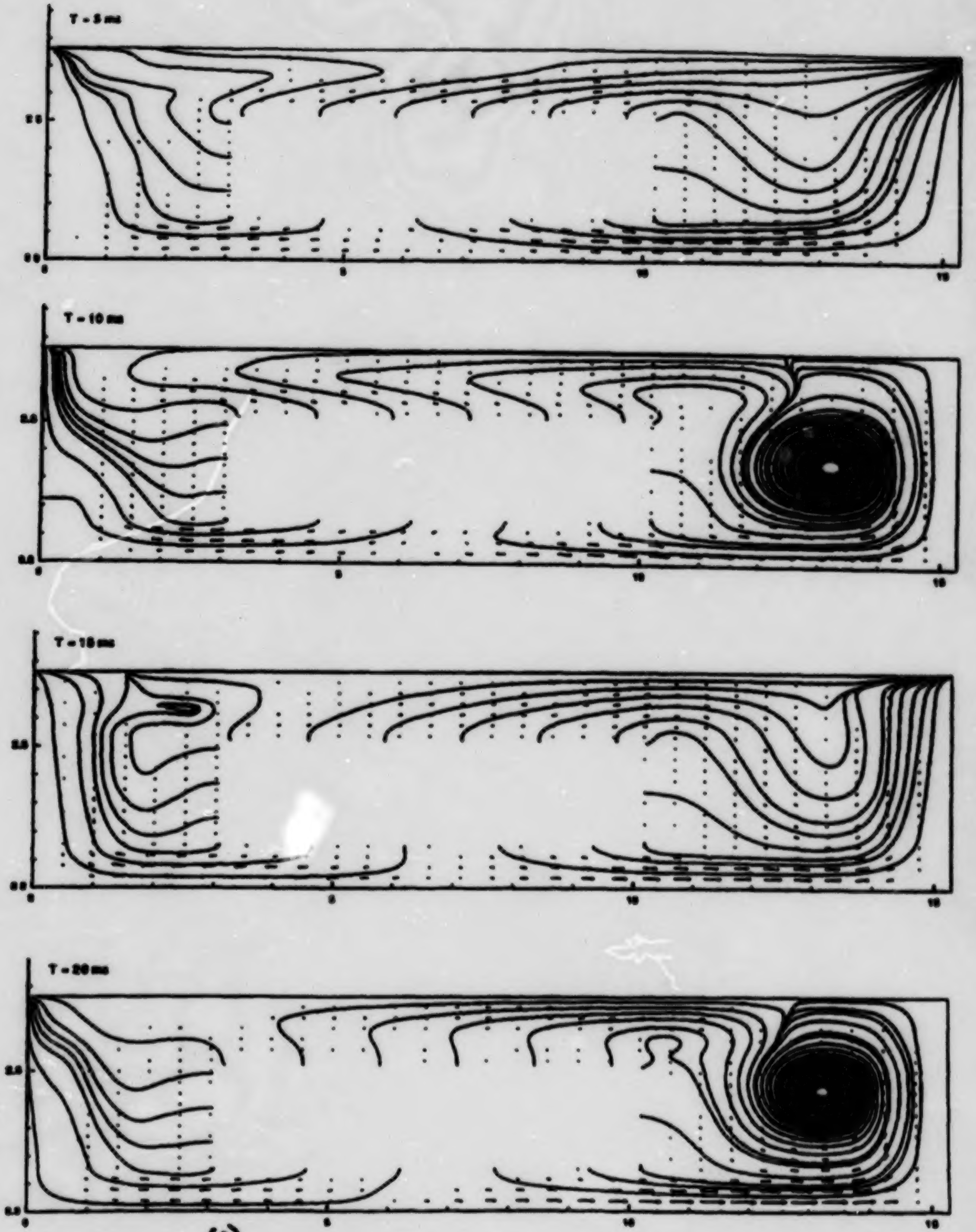

(a)

Figure 22: Velocity field obtained when burning a monoperforated grain moving sinusoidally along the vessel's axis (imposed motion).

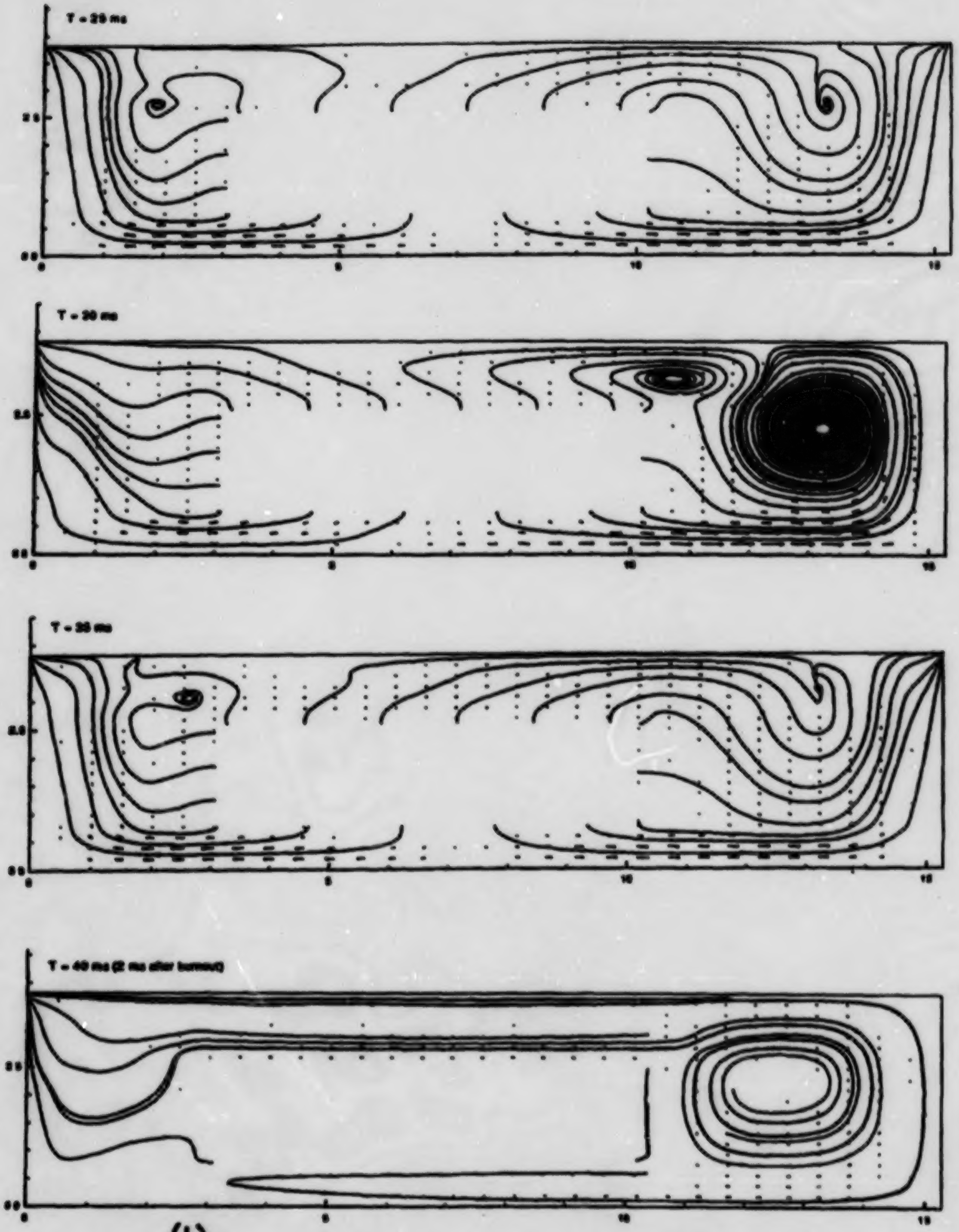

(b)

**Figure 22: Velocity field obtained when burning a monoperforated grain moving sinusoidally along the vessel's axis (imposed motion).**

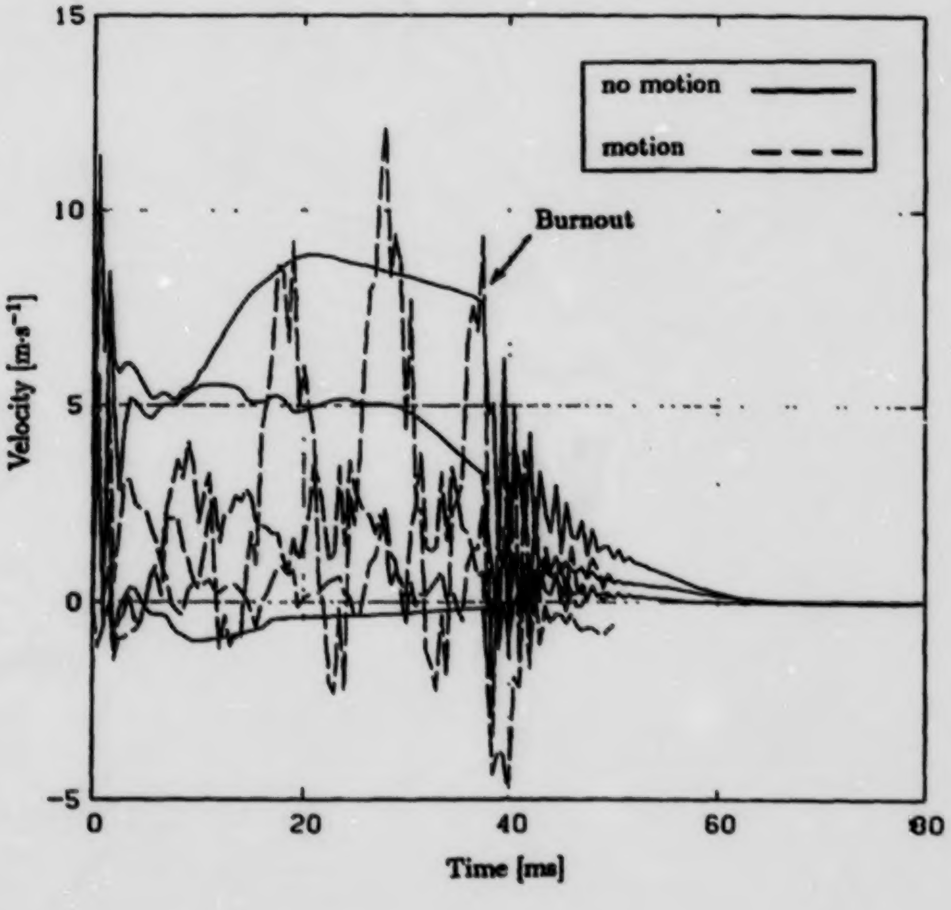

Figure 23: Variations of the flow velocity with time at three different locations along the vessel walls in the case of a fixed grain (reference computation) and a moving grain (imposed motion).

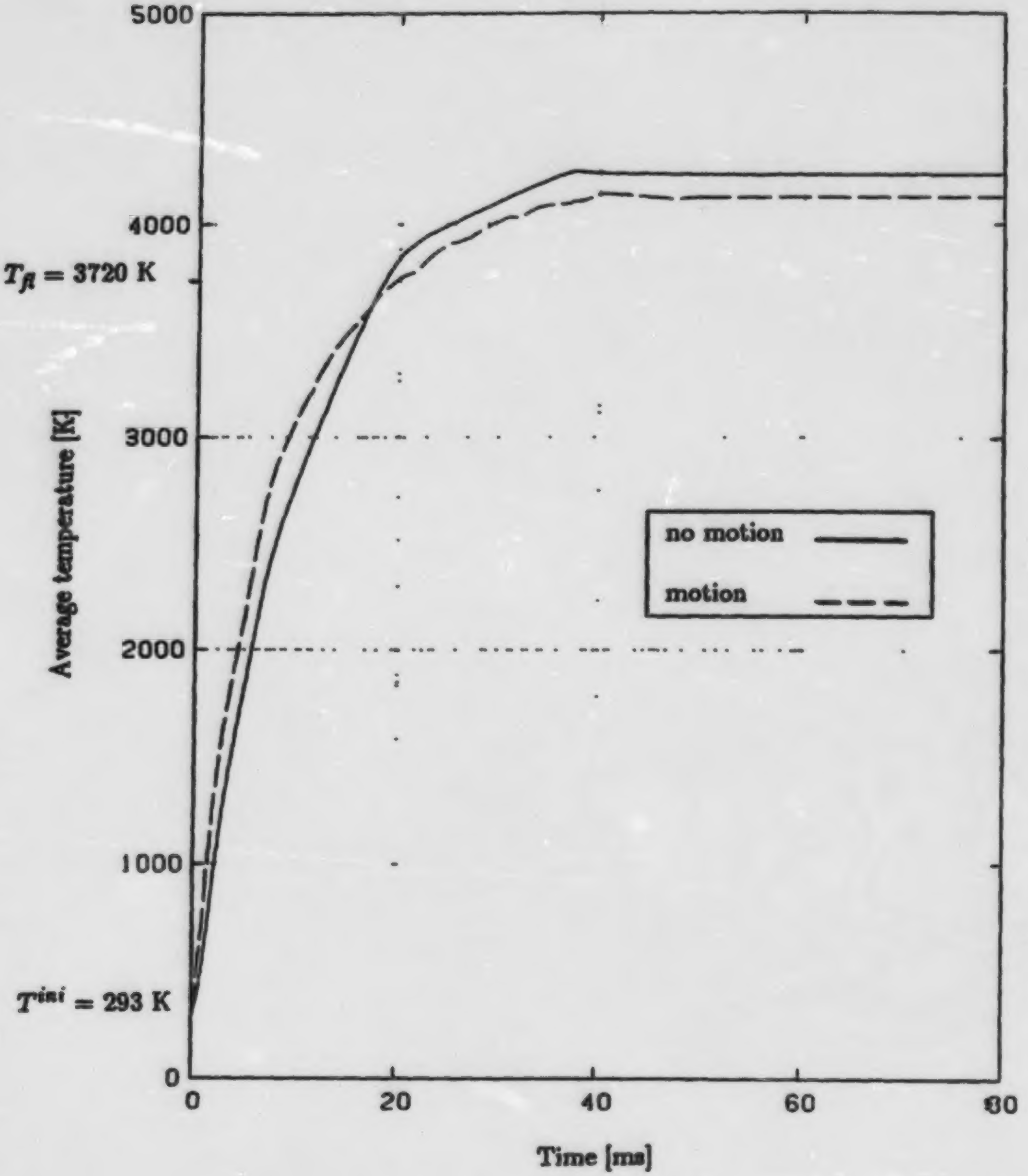

Figure 24: Average temperature in the vessel in the case of a fixed grain (reference computation) and a moving grain (imposed motion).

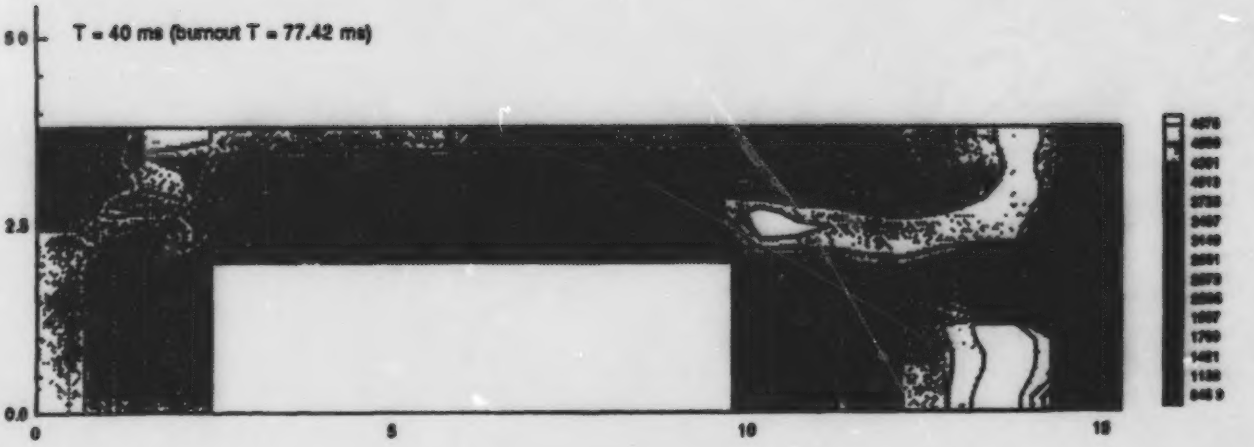

Figure 25: Predicted temperature contour for an initial inert gas temperature of 1000 K.

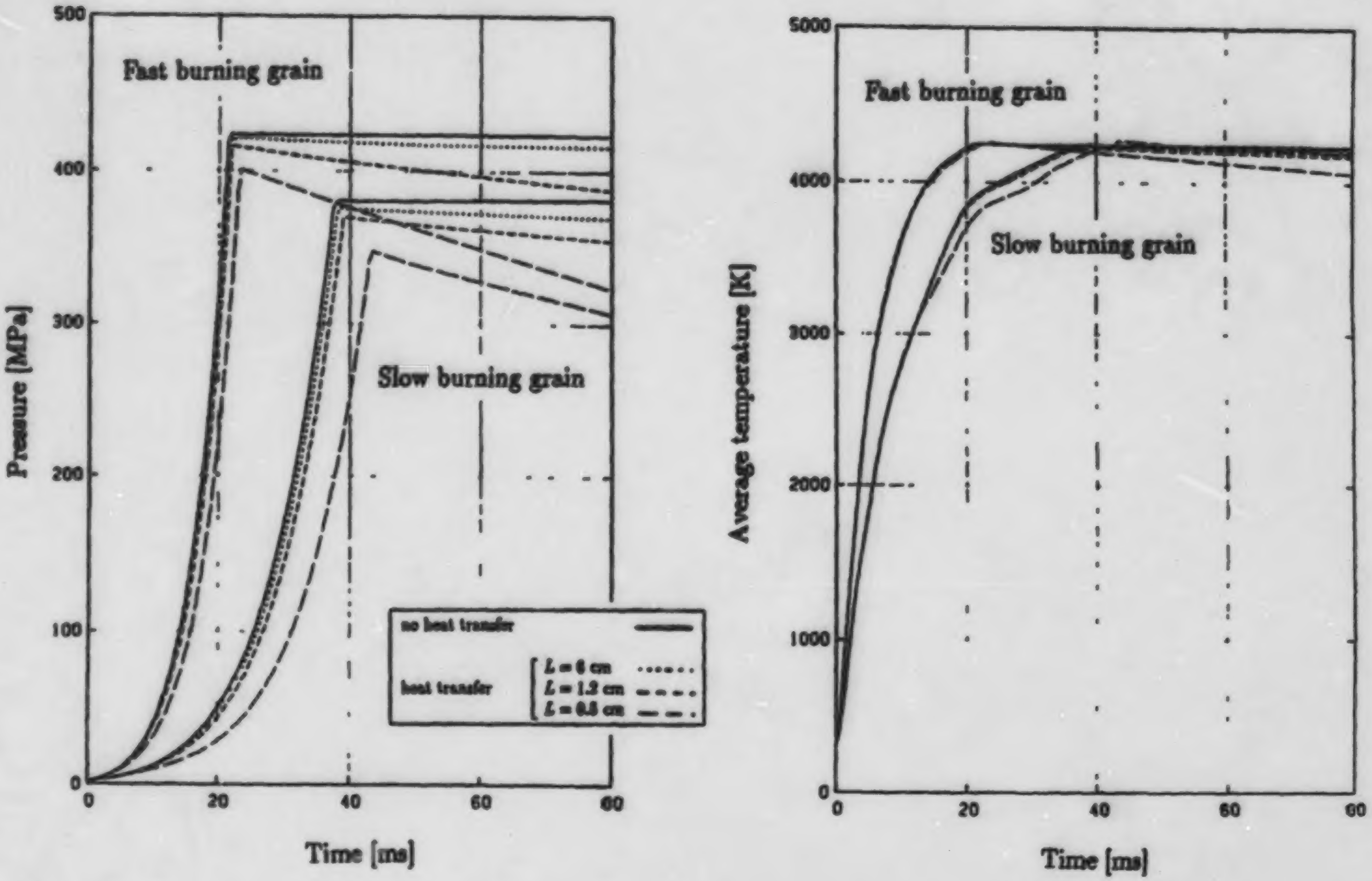

Figure 26: Average temperature and pressure in the vessel when convective heat transfer is taken into account.

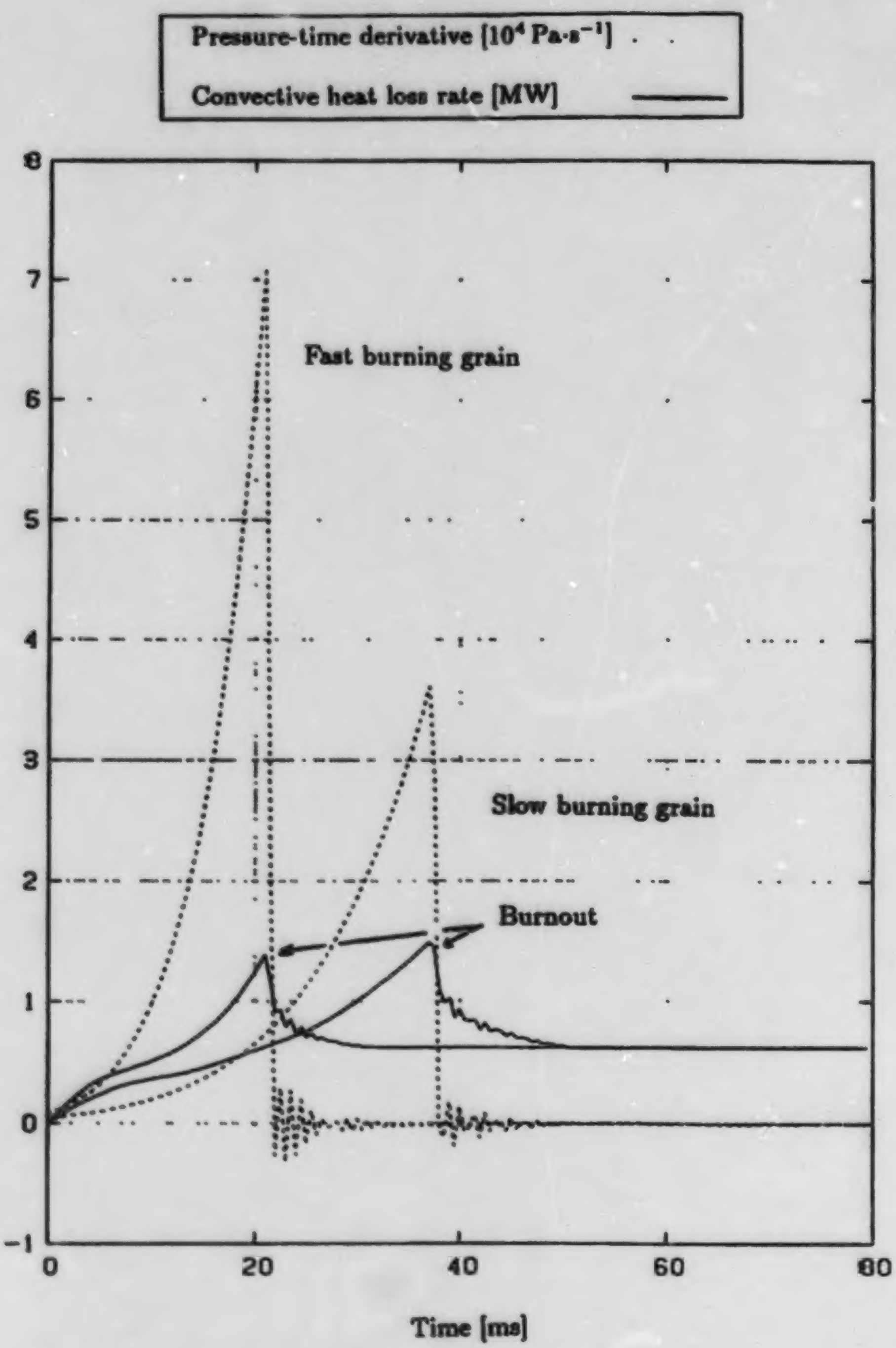

Figure 27: Typical time variations of the convective heat loss rate and pressure time-derivative.

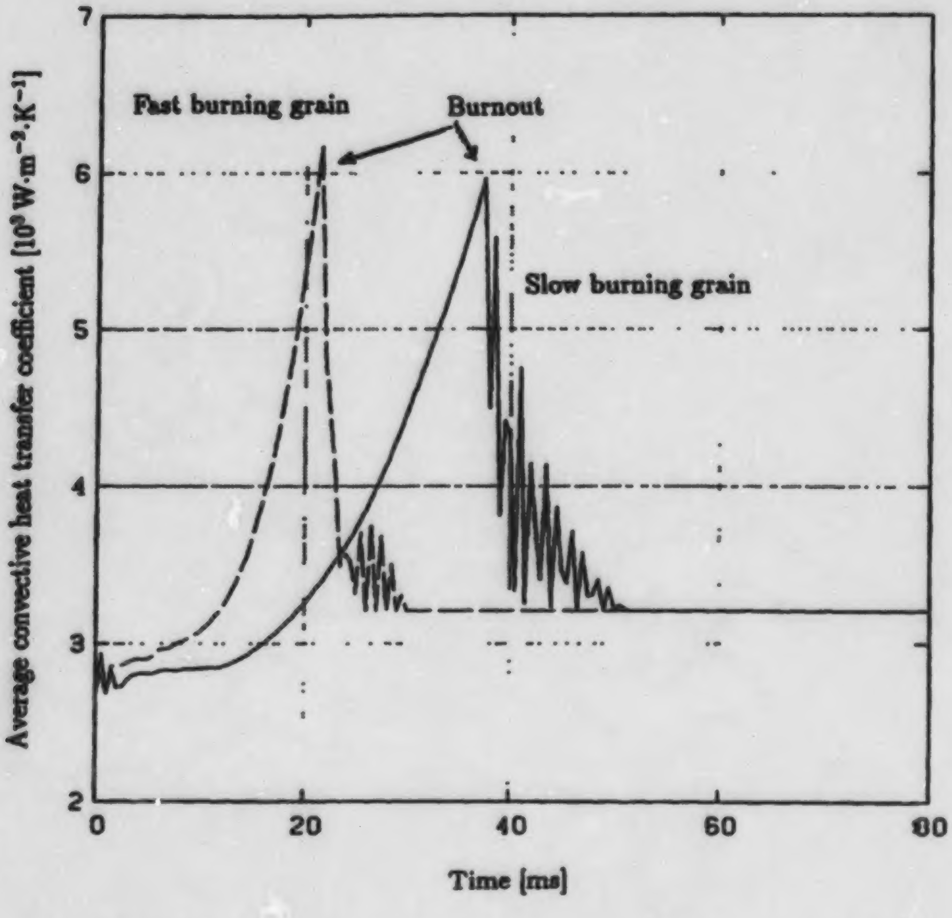

Figure 28: Typical time variations of the average convective heat transfer coefficient.

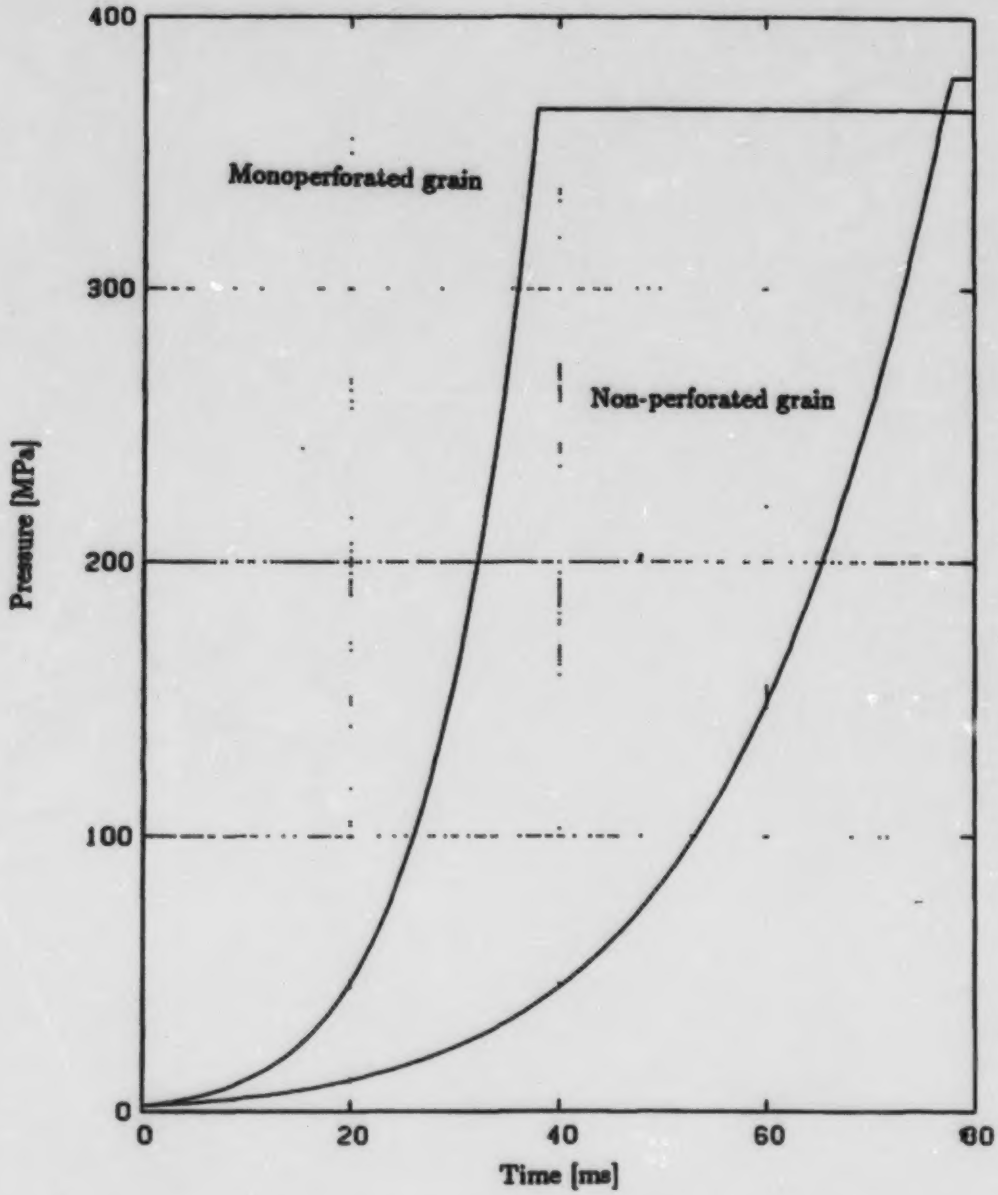

Figure 29: Pressure rise history as predicted by the model when burning a non-perforated and a monoperforated grain.

# APPENDIX A
# SIMPLE MODEL

A computer program has been written to show the effect of heat loss on the pressure and temperature rise histories in a closed vessel (section 2.3.2). The input parameters and the governing equations are described in this appendix. This simple model simulates the burning of single perforated grains of solid propellant in a constant-volume chamber $V_{ch} = 700\ \mathrm{cm}^2$.

## Input Parameters

The geometrical properties of the grains are the following:

- web: $w = 0.2$ cm,
- length to web ratio: $\lambda = 13.7$.

The solid has a density $\rho_s$ of 0.2 $\mathrm{g \cdot cm^{-3}}$. The propellant gases have constant properties. They are:

- molecular weight: $M_p = 27.7$ g,
- gas constant: $R_p = 300\ \mathrm{J \cdot kg^{-1} \cdot K^{-1}}$,
- co-volume: $\eta_p = 1.08 \times 10^{-3}\ \mathrm{cm^3 \cdot g^{-1}}$,
- ratio of the specific-heats: $\gamma_p = 1.2$,
- adiabatic flame temperature: $T_{fl} = 3720$ K.

The burning parameters are:

- index: $n = 0.89$,
- coefficient: $\beta = 2.036\ \mathrm{mm \cdot s^{-1} \cdot MPa^{-n}}$.

The radiative properties of the propellant gases and the vessel walls are:

- $\epsilon_p = 1$,
- $\epsilon_w = 0.5$.

The properties of air are as follows:

- molecular weight: $M_a = 28.96$ g,
- gas constant: $R_a = 287.06\ \mathrm{J \cdot kg^{-1} \cdot K^{-1}}$,
- co-volume: $\eta_a = 1.37 \times 10^{-3}\ \mathrm{cm^3 \cdot g^{-1}}$,

- ratio of the specific-heats: $\gamma_a = 1.4$.

An initial mass $m_s$ of 140 g is burnt. The loading density is thus 0.2 g·cm$^{-3}$.

### Governing Equations

The differential equations solved to obtain the pressure and temperature histories are described here. All gases are assumed to the follow the Noble-Able equation of state. When the effect of initial air in the chamber is neglected, the only gases present are the combustion gases. Before burnout, that is for $t \leq t_{cb}$ and $Z \leq 1$, the corresponding equation of state is

$$p = \frac{m_s Z R_p T_p}{V_{ch} - \frac{m_s}{\rho_s}(1 - Z) - m_s Z \eta_p} . \tag{A-1}$$

The burning rate law is that of De Saint Robert:

$$\frac{dx}{dt} = \beta p^n. \tag{A-2}$$

The mass fraction, $Z$, and the length, $x$, of propellant burnt are related using the the grain form function (page A-4),

$$Z = \frac{x}{\omega/2}[1 - (1 - \frac{1}{\lambda})\frac{x}{\omega/2}] . \tag{A-3}$$

By applying the first principle of thermodynamics to the closed system consisting of the solid and the propellant gases, the equation for the conservation of energy is obtained. It is

$$m_s c_{vp}(T_p - T_{fl})\frac{dZ}{dt} + m_s c_{vp} Z \frac{dT_p}{dt} = q_{wp}, \tag{A-4}$$

where $q_{wp}$ is the rate of heat loss to the walls. It can be zero, simply convective and equal to

$$q^c_{wp} = h^c_p A_{ch}(T_p - T_w),$$

or the sum of a convective and a radiative term

$$q^c_{wp} + q^r_{wp} = h^c_p A_{ch}(T_p - T_w) + \epsilon_p \epsilon_w \sigma A_{ch}(T^4_p - T^4_w).$$

The above expressions correspond to equations (4), (5) and (6) of section 2.3.2.

After burnout ($t \leq t_{cb}$, $Z \leq 1$), only gases are present in the chamber and $x = \omega/2$. The equation of state reduces to

$$p = \frac{m_s R_p T_p}{V_{ch} - m_s \eta_p} , \tag{A-5}$$

and the conservation of energy to

$$m_s c_{vp} \frac{dT_p}{dt} = q_{wp}. \tag{A-6}$$

The initial conditions corresponding to the above system (equations (A-1) to (A-6)) are:

$$p^i = 0.5 \text{ MPa},$$

$$T^i = \begin{cases} T_{fl} & \text{for} \quad q_{wp} = 0 \\ \dfrac{h_p^c A_{ch} T_w + m_s R_p T_{fl} (\lambda - 1) \frac{\beta (p^i)^n}{(\gamma_p - 1)\lambda w/2}}{h_p^c A_{ch} + m_s R_p (\lambda - 1) \frac{\beta (p^i)^n}{(\gamma_p - 1)\lambda w/2}} & \text{otherwise.} \end{cases}$$

Rigorously, the initial pressure should be zero as no gases are present in the chamber. But, in order for combustion to begin, a small (compared to the maximum pressure reached) initial pressure is assumed. The initial value for the temperature is found using the energy equation in the limit $t \to 0^+$ and assuming that $T_p$ is continuous at time 0 i.e., $T_p(0^-) = T_p(0^+)$.

When air is taken into account, additional equations to the previous system are needed. Before burnout, $t \le t_{cb}$, $Z \le 1$, two equations of state apply:

$$p = \frac{m_s Z R_p T_p}{V_{ch} - V_a - \frac{m_s}{\rho_s}(1 - Z) - m_s Z \eta_p}, \tag{A-7}$$

$$p = \frac{m_a R_a T_a}{V_a - m_a \eta_a}. \tag{A-8}$$

The conservation of energy applied to the entire system (solid + propellant gases + air) and to air only, gives

$$m_s c_{pp} (T_p - T_{fl}) \frac{dZ}{dt} + m_s c_{pp} Z \frac{dT_p}{dt} + m_a c_{pa} \frac{dT_a}{dt} = q_{wa}, \tag{A-9}$$

$$m_a c_{pa} \frac{dT_a}{dt} = -p \frac{dV_a}{dt}. \tag{A-10}$$

The heat loss rate, $q_{wa}$, is either zero or convective and given by

$$q_{wa}^c = h_a^c A_{ch} (T_a - T_w),$$

as explained in section 2.3.2. Both the grain form function and the burning rate law still apply.

After burnout, $t \ge t_{cb}$, $Z = 1$, only equations (A-7) and (A-9) are changed to

$$p = \frac{m_s R_p T_p}{V_{ch} - V_a - m_s \eta_p} \tag{A-11}$$

and

$$m_a c_{pa} \frac{dT_a}{dt} + m_s c_{pp} \frac{dT_p}{dt} = q_{wa}. \tag{A-12}$$

In this case, the initial conditions are:

$$p^i = 0.1013 \text{ MPa},$$

$$T_a^i = T_w = 293 \text{ K},$$

$$T_p' = \frac{T_{fl}}{\gamma_p} + \frac{m_s' R_s T_s'}{V_{ch} - m_s/\rho_s}(\frac{1}{\rho_s} - \eta_p)\frac{1}{c_{pp}}.$$

As before, the initial temperature of the propellant gases is found using equations (A-9) and (A-10) in the limit $t \rightarrow 0^+$, and the continuity of $T_p$ at time 0: $T_p(0^-) = T_p(0^+) = T_{ip}$.

The two above systems of first order equations were solved using a fifth order Runge-Kutta method.

## Grain Form Function

In order to solve for interior ballistics problems, one must express the way the grain's geometry changes as a function of the distance of propellant burnt. The mathematical expression of this relationship is called the form function. More specifically it relates $Z$, the mass fraction of propellant burnt

$$Z = 1 - \frac{V_{gr}^i}{V_{gr}},$$

and $x$, the length of propellant burnt (measured inwards). For complex grain geometries, such as multi-perforated grains, no exact expression for the entire range $Z = 0$ to 1 has been calculated. In the case of a single perforated grain, the derivation is simple. Consider a cross section of the grain as shown below.

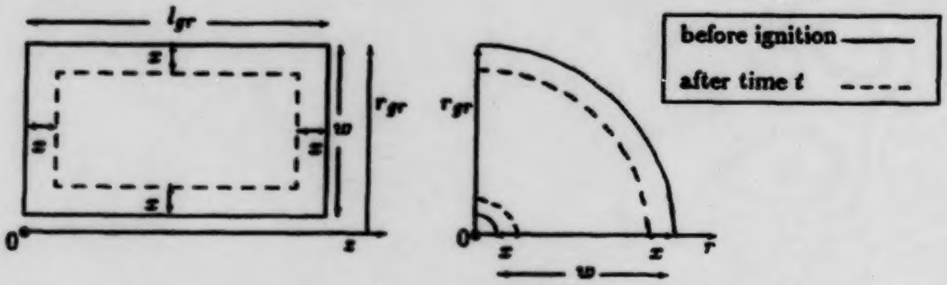

Radial and axial views of grain before ignition and at time $t$.

The initial volume of the grain is

$$V_{gr}^i = \pi[r_{gr}^2 - (r_{gr} - \omega)^2]l_{gr} = \pi l_{gr}\omega(2r_{gr} - \omega),$$

After time $t$, all surfaces recede by a distance $x$, so the radius of the grain is reduced to $r_{gr} - x$ and its length to $l_{gr} - 2x$. Thus, the grain's volume at time $t$ is

$$V_{gr} = \pi[(r_{gr} - x)^2 - (r_{gr} - \omega - x)^2](l_{gr} - 2x) = \pi(l_{gr} - 2x)(2r_{gr} - \omega)(\omega - 2x),$$

and

$$Z = 1 - (1 - 2\frac{x}{l_{gr}})(1 - 2\frac{x}{\omega_{gr}}).$$

Introducing the length to web ratio of the grain, $\lambda$, the mass fraction $Z$ is

$$Z = 1 - (1 - \frac{2}{\lambda}\frac{x}{\omega_{gr}})(1 - 2\frac{x}{\omega_{gr}}),$$

or

$$Z = \frac{x}{\omega/2}[1 - (1 - \frac{1}{\lambda})\frac{x}{\omega/2}].$$

# APPENDIX B

# INPUT PARAMETERS

Chapter 4 deals with numerical computations to study heat losses to the chamber walls, during the burning of a propellant in a constant-volume. To perform them, a number of input parameters are required. They are summarized below.

## Vessel Geometry

The constant-volume vessel considered is cylindrical with a length of twice the diameter. Its geometrical properties are:

- length: $L_{ch} = 15.27$ cm,
- diameter: $R_{ch} = 3.82$ cm,
- volume: $V_{ch} = 700$ cm$^3$,
- wall surface area: $A_{ch} = 458.2$ cm$^2$.

## Gases and Solid Properties

The molecular weight, gas constant, ratio of the specific-heats and flame or initial temperature of various gases are summarized in the table given below.

Table B-1: Properties of the gases

| | combustion | air | igniter | ambient |
|---|---|---|---|---|
| $M$ [g] | 27.71 | 28.96 | 47.26 | 40.59 |
| $R$ [J·kg$^{-1}$·K$^{-1}$] | 300.00 | 287.06 | 175.92 | 205.80 |
| $\gamma$ | 1.20 | 1.40 | 1.21 | 1.25 |
| $T$ [K] | 3720 | 293 | 1167 | 293 |

Both air and igniter gases are assumed inert. Ambient gases refer to the gases initially present in the chamber when the combustion of the solid propellant grain begins. They consist of a mixture of 4.16 g of igniter gases ( $\approx 3\%$ of the mass of the charge) and 0.84 g of air (corresponds to a pressure of 0.1013 MPa at 293 K).

A total mass $m_s = 140$ g is burnt. The solid has a density $\rho_s$ of 1.6 g·cm$^{-3}$. The burning rate parameters are the same as in the simple model:

- index: $n = 0.89$,
- coefficient: $\beta = 2.036\,\mathrm{mm{\cdot}s^{-1}{\cdot}MPa^{-n}}$.

The geometrical characteristics of the grain are the following:

- length: $l_{gr} = 7.13$ cm,
- radius: $r_{gr} = 2.10$ cm,
- web: $w = 1.34$ cm.

# APPENDIX C
# RADIATIVE HEAT TRANSFER

When burning a solid propellant in a closed bomb several types of heat losses occur. Radiative losses, although often neglected, is one of them. In this appendix, basic definitions concerning radiative heat transfer are reviewed and the derivation of the radiative flux falling onto the vessel walls is done. The result was given in section 2.3.1, equation (1).

## Basic Definitions

Absorption, emission, reflection and transmission are characterized by monochromatic and directional coefficients, called absorptivity $\alpha'_\nu$, emissivity $\epsilon'_\nu$, reflectivity $\rho'_\nu$ and transmitivity $\tau'_\nu$. They are defined by

$$\alpha'_\nu = \frac{\varphi^{a'}_\nu}{\varphi^{i'}_\nu}, \quad \rho'_\nu = \frac{\varphi^{r'}_\nu}{\varphi^{i'}_\nu}, \quad \tau'_\nu = \frac{\varphi^{t'}_\nu}{\varphi^{i'}_\nu}.$$

The monochromatic coefficients are related to one another by two equations. Drude's law states that the emission and the absorption coefficients are equal:

$$\epsilon'_\nu = \alpha'_\nu,$$

and it can be easily shown that to ensure conservation, one must have,

$$\alpha'_\nu + \rho'_\nu + \tau'_\nu = 1,$$

as illustrated in the figure below.

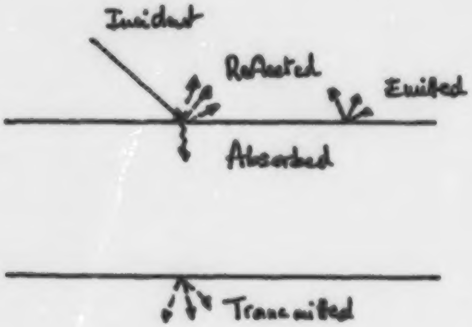

Radiative fluxes in a semi transparent non-diffusive medium.

The flux emitted from a surface $dS$, under conditions of local thermodynamic equilibrium, is

$$d\varphi^{e'}_\nu = \epsilon'_\nu L^{o}_\nu(T)\, dS,$$

where $L_\nu^\circ(T)$ is the luminance of equilibrium radiation at temperature $T$. A black body, by definition, absorbs all radiation whatever its wavelength and its direction ($\alpha'_\nu = \epsilon'_\nu = 1$). The flux emitted by a black body is then equal to

$$\varphi^e = \int_0^{+\infty} \pi L_\nu^\circ \, d\nu = \sigma T^4.$$

A grey body is an opaque body whose radiative properties are independent of the wavelength, that is, $\epsilon'_\nu = \epsilon$ and $\alpha'_\nu = \alpha$. In this case the emitted flux is given by

$$\varphi^e = \epsilon \sigma T^4.$$

In the present radiative transfer analysis, the radiative flux at the surface of the opaque vessel walls is needed. $\varphi^r$ is given by the difference between the emitted flux $\varphi^e$, and the absorbed flux $\varphi^a$. However for most calculations it is simpler to introduce a leaving flux $\varphi^p$ and an incident flux $\varphi^i$, as

$$\varphi^p = \varphi^e + \varphi^{ref},$$

$$\varphi^i = \varphi^a + \varphi^{ref},$$

where $\varphi^{ref}$ is the reflected flux. Thus, $\varphi^r$ is obtained by

$$\varphi^r = \varphi^p - \varphi^i.$$

An expression for the total flux falling onto the vessel walls, $\Phi^r_w$, is now derived.

## Radiative Flux Between a Semi-Transparent Gas and their Opaque Enclosure

First, for simplicity, two grey spheres $S_1$ and $S_2$ with surface areas $A_1$ and $A_2$, separated by a semi-transparent medium as shown in the figure below, are considered.

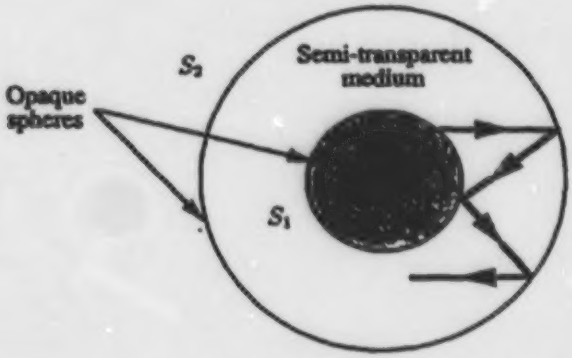

Radiative flux in a semi transparent medium confined between two opaque spheres.

If the radiative coefficients are isotropic, the following equations apply:

$$\varphi_1^r = \varphi_1^p - \varphi_1^i$$

$$\varphi_2^r = \varphi_2^p - \varphi_2^i$$

$$\varphi_1^p = \varphi_1^e + \varphi_1^r = \epsilon_1 \pi L^\circ(T_1) + (1 - \epsilon_1)\varphi_1^i$$

$$\varphi_2^p = \varphi_2^e + \varphi_2^r = \epsilon_2 \pi L^\circ(T_2) + (1 - \epsilon_2)\varphi_2^i$$

$$\varphi_1^i = \varphi_2^p$$

$$\varphi_2^i = f\varphi_1^p + (1 - f)\varphi_2^p$$

$f$ is a form factor, which takes into account the reflections of the radiation on both surfaces. Here $f = A_1/A_2$. Solving for the above system the flux on sphere $S_2$ is obtained as

$$\varphi_2^r = f\frac{\epsilon_1\epsilon_2\sigma(T_1^4 - T_2^4)}{1 - (1 - \epsilon_2)(1 - f\epsilon_1)}.$$

The total flux falling onto $S_2$ is obtained by integrating $\varphi_2^r$ over the entire surface of the sphere, to give

$$\Phi_2^r = \int_{S_2} \varphi_2^r \, d\Sigma = A_2\varphi_2^r.$$

Consider an enclosure filled with a semi-transparent gas, as shown below.

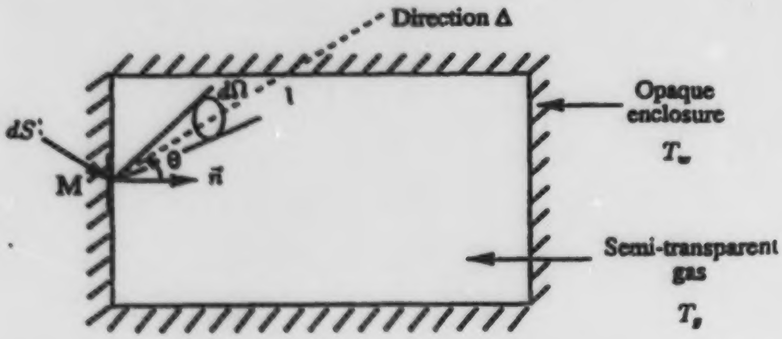

Radiative flux in an opaque enclosure filled with a semi-transparent gas.

The walls are opaque and grey. They emit and reflect isotropically. The temperatures of the walls and of the gases are assumed uniform and constant. First, the emitted radiative fluxes are obtained without taking the reflexions from the walls into account. The monochromatic radiative flux absorbed by the wall and emitted by the gases, $\varphi_{\nu g}^r$ is given by

$$\varphi_{\nu g}^e = \varphi_{\nu w}^a = \epsilon_w L_\nu^\circ(T_g) \int_0^{2\pi} \epsilon_{\nu g}(M, \Delta) \cos\theta \, d\Omega,$$

where $\epsilon_{\nu g}(M, \Delta)$ is the emission coefficient of the gases at point $M$ in the direction $\Delta$,

$$\epsilon_{\nu g}(M, \Delta) = 1 - \exp(-\kappa_\nu l).$$

Let $\bar{\epsilon}_{\nu g}(M)$ be the average emission coefficient, with respect to direction, of the gases at $M$,

$$\bar{\epsilon}_{\nu g}(M) = \frac{1}{\pi}\int_0^{2\pi} \epsilon_{\nu g}(M,\Delta)\cos\theta\, d\Omega.$$

Then

$$\varphi^a_{\nu w} = \pi\epsilon_w\bar{\epsilon}_{\nu g}(M)L^\circ_\nu(T_g),$$

Introducing an additional average on all points $M$ belonging to the surface of the vessel,

$$\bar{\bar{\epsilon}}_{\nu g} = \frac{1}{A_w}\int_{A_w} \bar{\epsilon}_{\nu g}(M)\, d\Sigma = 1 - \exp(-\kappa_\nu R),$$

the total monochromatic flux absorbed by the walls is written as

$$\phi^a_{\nu w} = \pi A_w \epsilon_w \bar{\bar{\epsilon}}_{\nu g} L^\circ_\nu(T_g).$$

Applying the above reasoning and using Drude's law, $(\alpha'_{\nu g}(M,\Delta) = \epsilon'_{\nu g}(M,\Delta))$, the monochromatic radiative flux emitted by the wall and absorbed by the gas is given by

$$\phi^e_{\nu w} = \epsilon_w L^\circ_\nu(T_w)\int_0^{2\pi}\int_A \alpha_{\nu g}(M,\Delta)\cos\theta\, d\Omega\, d\Sigma = \phi^a_{\nu g} = \pi A_w \epsilon_w \bar{\bar{\epsilon}}_{\nu g} L^\circ_\nu(T_w).$$

Finally the total radiative flux at the wall is

$$\Phi^r_w = \int_0^{+\infty}(\phi^e_{\nu w} - \phi^a_{\nu w})\, d\nu = \int_0^{+\infty} \epsilon_{\nu w}\bar{\bar{\epsilon}}_{\nu g}\pi A_w[L^\circ_\nu(T_g) - L^\circ_\nu(T_w)]\, d\nu.$$

If the radiative properties of the gases are assumed independent of the wavelength, this expression simplifies into

$$\Phi^r_w = \pi A_w \epsilon_w \bar{\bar{\epsilon}}_g \sigma(T_g^4 - T_w^4), \tag{C-1}$$

It is the common expression used in most studies.

To obtain the exchange flux between the gas and the enclosure, one must account for the various reflections on the wall. A method similar to the one presented in the case of two opaque bodies is applied. The leaving flux $\varphi_p$ is replaced by the radiosity $J_\nu$, and the incident flux $\varphi_i$ by the eclairement $E_\nu$, giving

$$J_{\nu w} = \underset{\overset{\swarrow}{\text{emitted}}}{\epsilon_w \pi L^\circ_\nu(T_w)} + \underset{\overset{\searrow}{\text{reflected}}}{\rho_w J_{\nu g}}$$

$$J_{\nu g} = \underset{\overset{\swarrow}{\text{emitted}}}{\bar{\bar{\epsilon}}_{\nu g}\pi L^\circ_\nu(T_g)} + \underset{\overset{\searrow}{\text{transmitted}}}{\tau_{\nu g} J_{\nu w}}$$

$$E_{\nu w} = J_{\nu g} \quad E_{\nu g} = J_{\nu w}$$

$$\bar{\bar{\rho}}_w = 1 - \bar{\bar{\epsilon}}_w \quad \bar{\bar{\tau}}_{\nu g} = 1 - \bar{\bar{\epsilon}}_{\nu g}$$

By definition, the monochromatic radiative flux falling onto the walls is given by

$$\phi^r_{\nu w} = A_w(J_{\nu w} - E_{\nu w}).$$

Solving for the above system, $\phi^r_{\nu w}$ is obtained as

$$\phi^r_{\nu w} = \pi A_w \epsilon_w \frac{\bar{\bar{\varepsilon}}_{\nu g}(L^\circ_\nu(T_g) - L^\circ_\nu(T_w))}{1 - (1 - \epsilon_w)(1 - \bar{\bar{\varepsilon}}_{\nu g})}.$$

The total flux is simply given by the integral of $\phi^r_{\nu w}$ over the entire wavelength spectrum

$$\Phi^r_w = \int_0^{+\infty} \phi^r_{\nu w}\, d\nu = \pi A_w \int_0^{+\infty} \frac{\epsilon_w \bar{\bar{\varepsilon}}_{\nu g}(L^\circ_\nu(T_g) - L^\circ_\nu(T_w))}{1 - (1 - \epsilon_w)(1 - \bar{\bar{\varepsilon}}_{\nu g})}\, d\nu. \qquad \text{(C–2)}$$

$\bar{\bar{\varepsilon}}_{\nu g}$ generally strongly depends on $\nu$, therefore, the factor $T_g^4 - T_w^4$ will rarely appear and $\Phi^r_w$ will significantly differ from that, assuming no reflections (equation (C-1)).

# APPENDIX D
# HYBRID SCHEMES

In chapter 4, a new model representing the burning of a single grain in a closed vessel, was introduced. The equations were first solved using Mac Cormack's scheme. However due to the poor numerical results obtained, artificial viscosity was added to the scheme. This is now explained.

There are many different ways of adding artificial viscosity to a numerical scheme. In self-adjusting hybrid schemes, a viscous term is added whenever strong discontinuities are encountered. The underlying idea is to switch to a non-oscillatory first order scheme when discontinuities are present and keep a higher order solution otherwise. Many switch parameters are available. The one chosen here is based on density variation. When solving the equations between two adjacent nodes $i$ and $i+1$, a switch parameter is computed as:

$$\theta_{i+\frac{1}{2}} = max(\theta_i, \theta_{i+1}),$$

where

$$\theta_i = \begin{cases} \frac{|\Delta_{i+\frac{1}{2}}|-|\Delta_{i-\frac{1}{2}}|}{|\Delta_{i+\frac{1}{2}}|+|\Delta_{i-\frac{1}{2}}|} & \text{for} \quad |\Delta_{i+\frac{1}{2}}| + |\Delta_{i-\frac{1}{2}}| > \epsilon\, \rho_i \\ 0 & \text{otherwise.} \end{cases}$$

$\Delta$ is set to the variation in density and $\epsilon$ equal to a negligible measure of it:

$$\Delta_{i+\frac{1}{2}} = \rho_{i+1} - \rho_i \quad \text{and} \quad \epsilon = 10^{-5}.$$

In the present model, the 1D Mac Cormack scheme is hybridized as follows:

$$U_i^* = U_i^n - \frac{\Delta t}{\Delta x}(F_{i+1}^n - F_i^n)$$

$$U_i^{n+1} = \frac{1}{2}(U_i^* + U_i^n) - \frac{\Delta t}{2\Delta x}(F_{i+1}^* - F_i^*)$$

$$\underbrace{+\mu_{num}[\theta_{i+\frac{1}{2}}^n(U_{i+1}^n - U_i^n) - \theta_{i-\frac{1}{2}}^n(U_i^n - U_{i-1}^n)]}_{\text{viscous term}}$$

The new stability condition for this type of scheme is more restrictive than the CFL condition. It is:

$$\Delta t \leq \frac{\sqrt{3}}{2}\frac{\Delta x}{\max(|\,u\,| + a)}.$$

# APPENDIX E

# ROE'S METHOD

In this appendix the numerical method used to solve the equations given in chapter 4, is reviewed and described. The method is an example of a total variation diminishing (TVD) scheme. These were first introduced by Harten in 1981. The main property of a TVD scheme is that, unlike monotonous schemes, it can be accurate to second order and oscillation-free across discontinuities (when applied to nonlinear scalar hyperbolic conservation laws and constant coefficient hyperbolic systems). To satisfy TVD conditions, some kind of limiting procedure is necessary.

Before introducing the method, some general properties of finite difference schemes for hyperbolic systems are reviewed.

## Dispersion and Dissipation

The notion of dispersion and dissipation can be introduced using a simple scalar hyperbolic equation:

$$\frac{\partial u}{\partial t} + a\frac{\partial u}{\partial x} = 0 \quad \text{with} \quad u(x,0) = f(x). \tag{E–1}$$

The solution of equation (E-1) is $u = f(x - at)$, where $f$ can be any function. However not all numerical schemes are able to propagate any $f$ without altering its amplitude (dissipation) or its frequency distribution (dispersion). Using a simple calculus (using $f(x) = \exp(j\omega x)$) it can be shown that high frequencies will not be properly propagated (important phase error) unless $2\pi/\omega\Delta x \geq 10$. The effect of dissipation (using a step function) is illustrated in the following figure:

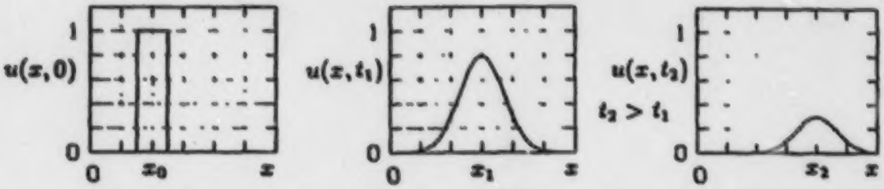

Effect of dissipation in a numerical scheme using a step function.

But even if each frequency is propagated at the correct speed, the amplitude may not be conserved, as shown below.

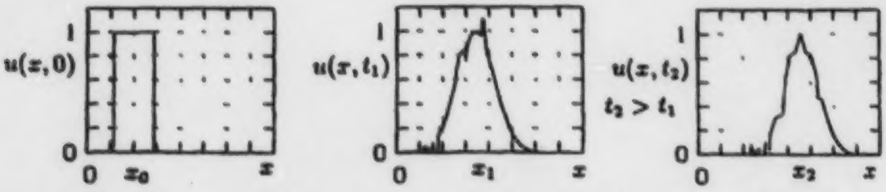

Effect of dispersion in a numerical scheme using a step function.

Here time discretization is important. Again, using a solution to (E-1) of the form $u_i^n = S^n \exp(j\omega x^n)$, the modulus of the amplification factor can be obtained. It is:

$$| A | = | \frac{S^{n+1}}{S^n} | = \frac{1}{1 + 2(1 - \cos\omega\Delta x) a \frac{\Delta t}{\Delta x}(1 + a\frac{\Delta t}{\Delta x})} .$$

Now $| A | \leq 1$, otherwise the scheme would be unstable. It can be shown that a slightly dissipative scheme is more stable. From a physical point of view, a dissipative scheme damps oscillations introduced by boundary or initial conditions that are too sharp. If one can write

$$| A | \leq 1 - \sigma(\omega\Delta x)^{2s},$$

the scheme is said to be dissipative of order $2s$. In the above example $s = 1$ and $\sigma = \lambda(\lambda + 1)$. The previous inequality is illustrated on the graph below, where both $| A |$ and the parabola $1 - \sigma(\omega\Delta x)^{2s}$ are plotted against $\omega\Delta x$.

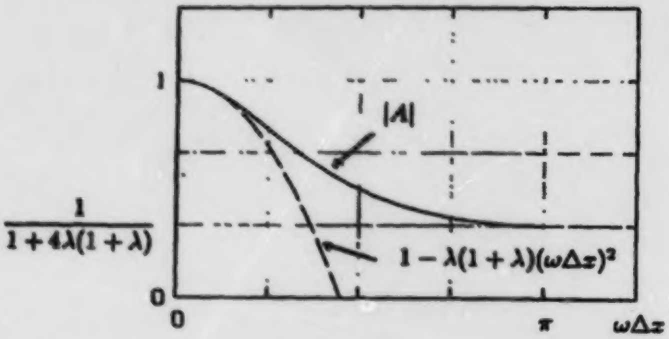

Modulus of the amplification factor.

### Modern Schemes

Modern schemes have been developed to obtain high dispersive and diffusive qualities. These include TVD schemes. Roe's method is a mixture of Riemann solvers and TVD schemes. It is based on earlier work from Godunov. His algorithm is summarized below and illustrated on the next page, for a 1D problem.

1. Given a finite difference grid and the values of $u$ at time $n\Delta t$, $u_i^n$,
2. construct, from $u_i^n$, a step function representing the solution $u^n$ at that time.
3. At each point of abscissa $(i + \frac{1}{2})\Delta x$, the problem is the same as a Riemann problem if the time step $\Delta t$ is small enough to ensure no interaction with the neighboring points. Solve N Riemann problems and obtain the solution at time $(n + 1)\Delta t$.
4. From solution $u^{n+1}$, the new values $u_i^{n+1}$ are calculated by integrating $u^{n+1}$.

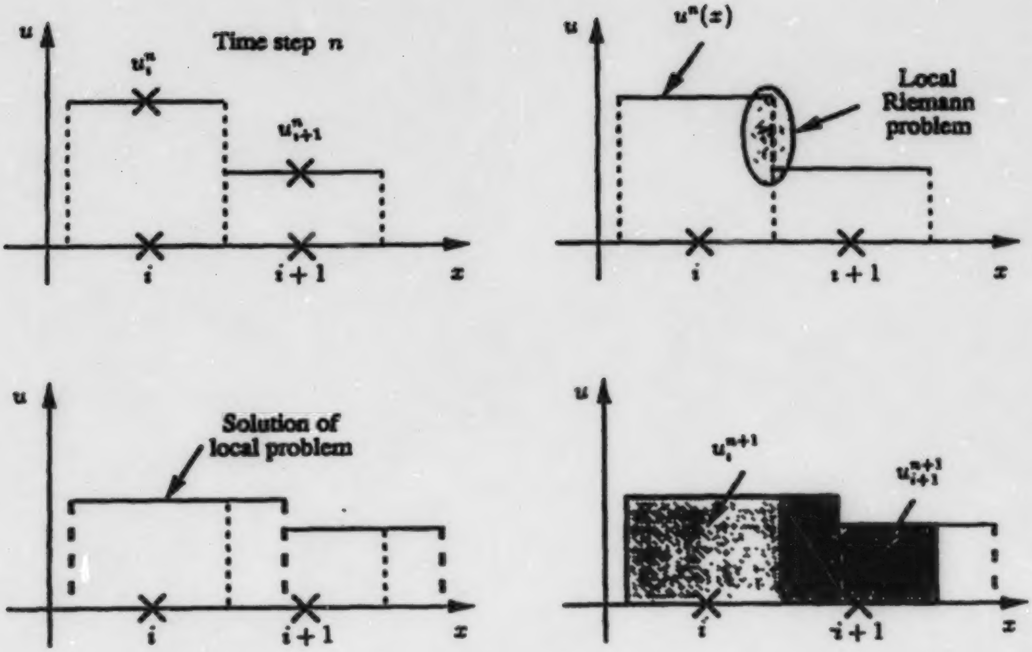
u
Time step $n$
$u_i^n$
$u_{i+1}^n$
$i$
$i+1$
$x$
$u^n(x)$
Local Riemann problem
Solution of local problem
$u_i^{n+1}$
$u_{i+1}^{n+1}$

Illustration of Godunov's algorithm.

The previous algorithm has some disadvantages. It does not ensure the conservation of sharp shocks and uses an iterative procedure to solve each Riemann problem (by definition). This often requires excessive computational time to obtain a very accurate solution, considering the truncation error made during step 4. Hence, Roe and others devised an approximate Riemann solver using an average state to compute the fluxes across each wave:

$$\overline{\rho} = \sqrt{\rho_i \rho_{i+1}},$$

$$\overline{u} = \frac{\sqrt{\rho_i}u_i + \sqrt{\rho_{i+1}}u_{i+1}}{\sqrt{\rho_i} + \sqrt{\rho_{i+1}}},$$

$$\overline{H} = \frac{\sqrt{\rho_i}H_i + \sqrt{\rho_{i+1}}H_{i+1}}{\sqrt{\rho_i} + \sqrt{\rho_{i+1}}},$$

$$\overline{a} = (\gamma - 1)(\overline{H} - \frac{\overline{u}^2}{2}).$$

The flux is linearized using the average state

$$F = \overline{A}U,$$

and the solution at the next time level is obtained by

$$U^{n+1} = U^n - \frac{\Delta t}{\Delta x} F.$$

From this, he developed a first order algorithm [ROE 1984] that includes an entropy correction to ensure physical solutions only. This basic scheme is an upwind first order scheme and, therefore, has the common defect of being diffusive. Then, Roe attempted to reduce diffusivity by going to a higher order scheme with an additional anti-diffusive term, in order to remove the oscillations associated with classical high order methods.

It has been shown that viscosity is necessary to stabilize the computations but has to be minimized to reduce the dissipative nature of the scheme. There are many types of limiting procedures. They are divided into two categories, slope and flux limiting procedures. Roe uses a flux limiter. For this type of method, it can be shown [SWEBY 1984], that the flux limiter coefficient must lie in a specific region in order to ensure positivity and TVD inequalities. This region is illustrated below.

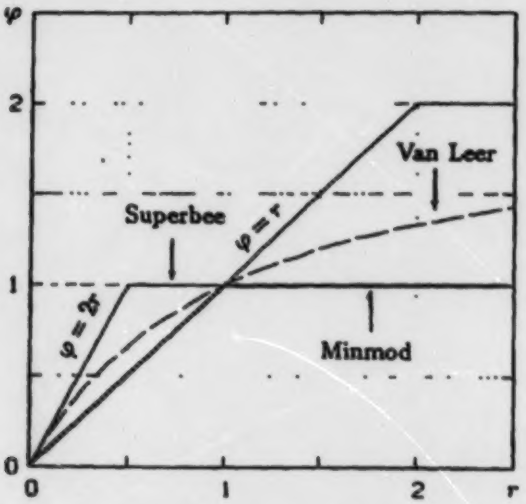

TVD, flux limiters region (from Sweby).

The upper boundary corresponds to Roe's function Superbee, the lower to his function Minmod. Van Leer's function lies in-between. The same study, revealed that Superbee should be used in the case of contact discontinuities and Van Leer's function for the remaining waves. In the present work, Roe's method with second order corrections, as described previously, was used, and the above remark concerning the choice of an appropriate flux limiter, was taken into account.

# APPENDIX 5

# SOME NOTES ON RADIATIVE HEAT TRANSFER IN A CLOSED VESSEL

by

Florence C. Berger and James J. Gottlieb

# SOME NOTES ON RADIATIVE HEAT TRANSFER IN CLOSED BOMBS

### by

### Florence Berger and James Gottlieb

## 1.0 RADIATIVE HEAT TRANSFER

### 1.1 Introduction

When burning a solid propellant in a closed vessel or bomb several types of heat losses occur. Radiative losses, although often neglected, is one of them. There are two ways by which radiative heat losses can occur: radiation from the propellant gases and possibly the solid particles, and radiation by chemi-luminescence from the flame zone. The former is dependent upon the fact that water vapor and carbon dioxide, which are almost always contained in the combustion gases, are capable of both emitting and absorbing radiation. The solid walls of the vessel are also likely to take part in the heat transfer by means of their own radiation. The latter may occur only in the early stages of burning when the vessel is not entirely filled with the combustion gases. It has, to the author's knowledge, never been modeled. The following discussion is therefore restricted to the radiative heat transfer between the vessel walls and the combustion gases.

### 1.2 Basic Definitions

Energy is constantly exchanged between any system and the radiative field by two means: emission (thermal energy is transformed into radiative energy), and absorption (radiative energy is transformed into thermal energy). Three types of media are distinguished:

- transparent medium, which does not interact with the radiative field,
- opaque bodies which absorb, emit and reflect an incident radiation, and
- semi-transparent medium which absorb, emit, reflect and transmit an incident radiation.

Absorption, emission, reflection and transmission are characterized by monochromatic and directional coefficients, called absorptivity $\alpha'_\nu$, emissivity $\epsilon'_\nu$, reflectivity $\rho'_\nu$ and transmitivity $\tau'_\nu$. They are defined by

$$\alpha'_\nu = \frac{\varphi^{a'}_\nu}{\varphi^{i'}_\nu}, \quad \rho'_\nu = \frac{\varphi^{r'}_\nu}{\varphi^{i'}_\nu}, \quad \tau'_\nu = \frac{\varphi^{t'}_\nu}{\varphi^{i'}_\nu},$$

where $\varphi'_\nu$ is a directional monochromatic radiative flux ($[\mathrm{W \cdot m^{-2} s^{-1}}]$). The monochromatic coefficients are related to one another by two equations. Drude's law states that the emission and the absorption coefficients are equal ($\epsilon'_\nu = \alpha'_\nu$), and it can be easily shown that to ensure conservation, one must have $\alpha'_\nu + \rho'_\nu + \tau'_\nu = 1$, as illustrated in the figure below.

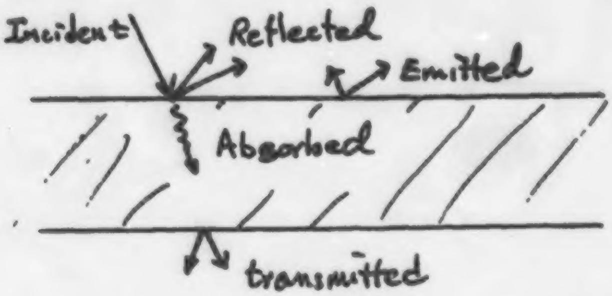

Radiative fluxes in a semi transparent non-diffusive medium.

The flux emitted from a surface $dS$, under conditions of local thermodynamic equilibrium, is

$$d\varphi^{e'}_\nu = \epsilon'_\nu L^o_\nu(T)\,dS,$$

where $L^o_\nu(T)$ is the luminance of equilibrium radiation at temperature $T$. A black body, by definition, absorbs all radiations whatever its wavelength and its direction ($\alpha'_\nu = \epsilon'_\nu = 1$). The flux emitted by a black body is then equal to

$$\varphi^e = \int_0^{+\infty} \pi L^o_\nu(T)\,d\nu = \sigma T^4.$$

A grey body is an opaque body whose radiative properties are independent of the wavelength, that is, $\epsilon'_\nu = \epsilon$ and $\alpha'_\nu = \alpha$. In this case the emitted flux is given by

$$\varphi^e = \epsilon\sigma T^4.$$

### 1.3 Assumptions

Unless some reasonable assumptions are made concerning the radiative properties, of the vessel walls and of the combustion gases, no simple analytical expression for the radiative flux falling onto the walls can be obtained.

The vessel walls are assumed opaque, that is, the depth of penetration of radiation, $d$, is small compared to the thickness of the walls, $e$. Indeed, for metals, $d$ ranges from 1 Å to $10^2$ Å depending on the wavelength of the radiation, and e is about one centimeter in a closed bomb. Any incident radiation is therefore either absorbed or reflected as illustrated below.

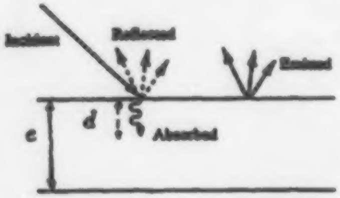

Radiative fluxes on an opaque body.

The next approximation concerns the directional character of their radiative properties. For the vast majority of opaque bodies, the reflectivity (and therefore the emissivity and the absorptivity) tends to become partially isotropic for two reasons. The first one is that the surface state of the material is never perfectly smooth. Reflection becomes less and less specular when the rugosity of the surface increases. The evolution from specular to quasi isotropic reflection can be illustrated by the following diagram:

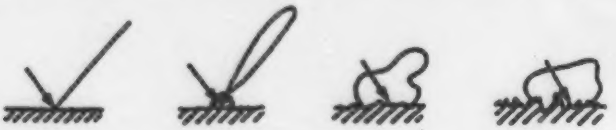

Evolution from specular to quasi isotropic reflection.

Even in the case of an optically smooth material (the asperities of the surface do not exceed one tenth of the wavelength), $\epsilon'_\nu$ and $\alpha'_\nu$ are largely independent of the direction. The second is that actual materials generally possess some diffusive properties. Due to the accumulation of successive diffusions, a fraction of an incident radiation will be reflected with a complex distribution of directions, as illustrated below.

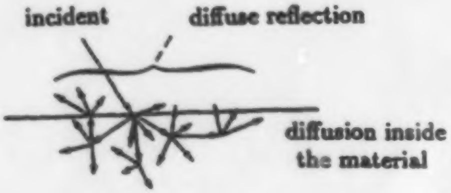

Diffuse reflection.

Therefore, the radiative properties of the walls are also assumed isotropic.

From the above discussion, it results that, only the superficial layers of the material are to be taken into account when evaluating its radiative properties. For polished materials, it is reasonable to assume that emissivity is independent of the wavelength, that is, that they radiate as grey bodies. Closed bombs are generally covered with a polished nickel-chrome-molybdenum steel liner to facilitate repair. Therefore, $\alpha'_{\nu w}$ is assumed independent of the wavelength. It can be estimated by $\alpha_w = 0.5$.

The radiative properties of the combustion gases are not well known. Very few precise measurements of their absorptivity have been made. In all current studies they are assumed opaque for simplicity. According to Klingenberg[1] it is likely that their absorptivity is very high. This justifies the assumption that their emissivity approaches that of a black body, that is $\alpha'_{\nu g} = \epsilon'_{\nu g} = 1$. However, to remain more general, the gases are assumed semi-transparent and non-diffusive. That is, they reflect, transmit and absorb an incident radiation. No assumption concerning the directionality and the dependence on the wavelength of their radiative properties is made.

---

[1] Klingenberg, G. and Mach, H., 1976, ***Experimental study of non-steady phenomena associated with the combustion of solid gun propellants***, 16th symposium (international) on combustion pp 1193–1200.

Finally, both the vessel walls and the combustion gases are assumed to have a uniform and constant temperature.

### 1.4 Estimation of the Maximum Radiative Heat Loss

Under the above assumptions, a simple derivation of the total radiative flux at the vessel walls can be done. It is now presented. Consider an enclosure filled with a semi-transparent gas, as shown on the diagram below.

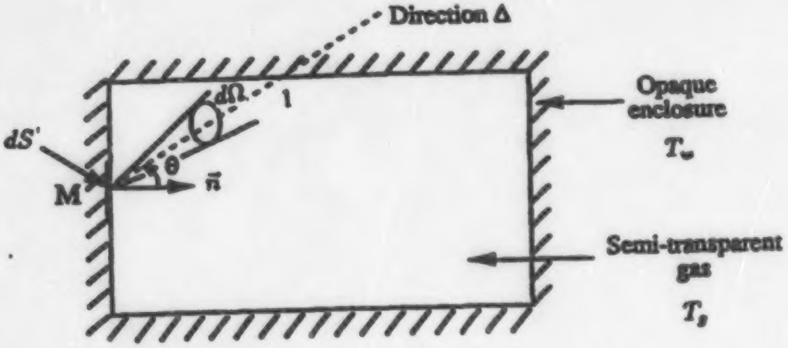

Radiative flux in an opaque enclosure filled with a semi-transparent gas.

The walls are opaque and grey. They emit and reflect isotropically. The temperatures of the walls and of the gases are assumed uniform and constant. First, the emitted radiative fluxes are obtained without taking the reflexions by the walls into account. The monochromatic radiative flux absorbed by the wall and emitted by the gases, $\varphi^e_{\nu g}$ is given by

$$\varphi^e_{\nu g} = \varphi^e_{\nu w} = \epsilon_w L^o_\nu(T_g) \int_0^{2\pi} \epsilon_{\nu g}(M,\Delta) \cos\theta \, d\Omega,$$

where $\epsilon_{\nu g}(M,\Delta)$ is the emission coefficient of the gases at point $M$ in the direction $\Delta$,

$$\epsilon_{\nu g}(M,\Delta) = 1 - \exp(-\kappa_\nu l).$$

Let $\overline{\epsilon}_{\nu g}(M)$ be the average emission coefficient, with respect to direction, of the gases at $M$,

$$\overline{\epsilon}_{\nu g}(M) = \frac{1}{\pi} \int_0^{2\pi} \epsilon_{\nu g}(M,\Delta) \cos\theta \, d\Omega.$$

Then

$$\varphi^e_{\nu w} = \pi \epsilon_w \overline{\epsilon}_{\nu g}(M) L^o_\nu(T_g),$$

Introducing an additional average on all points $M$ belonging to the surface of the vessel,

$$\overline{\overline{\epsilon}}_{\nu g} = \frac{1}{A_w} \int_{A_w} \overline{\epsilon}_{\nu g}(M) \, d\Sigma,$$

the total monochromatic flux absorbed by the walls is written as

$$\phi^e_{\nu w} = \pi A_w \epsilon_w \overline{\overline{\epsilon}}_{\nu g} L^o_\nu(T_g).$$

Applying the above reasoning and using Drude's law, $(\alpha'_{\nu g}(M,\Delta) = \epsilon'_{\nu g}(M,\Delta))$, the monochromatic radiative flux emitted by the wall and absorbed by the gas is given by

$$\phi^e_{\nu w} = \phi^a_{\nu g} = \epsilon_w L^\circ_\nu(T_w) \int_0^{2\pi} \int_{A_w} \alpha_{\nu g}(M,\Delta) \cos\theta \, d\Omega \, d\Sigma = \pi A_w \epsilon_w \bar{\bar{\epsilon}}_{\nu g} L^\circ_\nu(T_w).$$

Finally the total radiative flux at the wall is

$$\Phi^r_w = \int_0^{+\infty} (\phi^e_{\nu w} - \phi^a_{\nu w}) \, d\nu = \int_0^{+\infty} \epsilon_{\nu w} \bar{\bar{\epsilon}}_{\nu g} \pi A_w [L^\circ_\nu(T_g) - L^\circ_\nu(T_w)] \, d\nu.$$

If the radiative properties of the gases are assumed independent of the wavelength, this expression simplifies into

$$\Phi^r_w = \pi A_w \epsilon_w \bar{\bar{\epsilon}}_g \sigma (T_g^4 - T_w^4), \tag{1}$$

It is the common expression used in most studies.

To obtain the exchange flux between the gas and the enclosure, one must account for the various reflections on the wall. The following equations apply:

$$J_{\nu w} = \underbrace{\epsilon_w \pi L^\circ_\nu(T_w)}_{\text{emitted}} + \underbrace{\rho_w J_{\nu g}}_{\text{reflected}}$$

$$J_{\nu g} = \underbrace{\bar{\bar{\epsilon}}_{\nu g} \pi L^\circ_\nu(T_g)}_{\text{emitted}} + \underbrace{\tau_{\nu g} J_{\nu w}}_{\text{transmitted}}$$

$$E_{\nu w} = J_{\nu g} \quad E_{\nu g} = J_{\nu w}$$

$$\bar{\bar{\rho}}_w = 1 - \bar{\bar{\epsilon}}_w \quad \bar{\bar{\tau}}_{\nu g} = 1 - \bar{\bar{\epsilon}}_{\nu g}$$

$J_\nu$ is called the radiosity. It corresponds to the leaving flux from opaque body. $E_\nu$ is the eclairement and corresponds to the incident flux on an opaque body. By definition, the monochromatic radiative flux falling onto the walls is given by

$$\phi^r_{\nu w} = A_w (J_{\nu w} - E_{\nu w}).$$

Solving for the above system, $\phi^r_{\nu w}$ is obtained as

$$\phi^r_{\nu w} = \pi A_w \epsilon_w \frac{\bar{\bar{\epsilon}}_{\nu g}(L^\circ_\nu(T_g) - L^\circ_\nu(T_w))}{1 - (1 - \epsilon_w)(1 - \bar{\bar{\epsilon}}_{\nu g})}.$$

The total flux is simply given by the integral of $\phi^r_{\nu w}$ over the entire wavelength spectrum

$$\Phi^r_w = \int_0^{+\infty} \phi^r_{\nu w} \, d\nu = \pi A_w \int_0^{+\infty} \frac{\epsilon_w \bar{\bar{\epsilon}}_{\nu g}(L^\circ_\nu(T_g) - L^\circ_\nu(T_w))}{1 - (1 - \epsilon_w)(1 - \bar{\bar{\epsilon}}_{\nu g})} \, d\nu. \tag{2}$$

If the emissivity of the combustion gases is assumed independent of the wavelength, this expression simplifies into

$$\Phi^r_w = A_w \frac{\epsilon_w \bar{\bar{\epsilon}}_g \sigma (T_g^4 - T_w^4)}{1 - (1 - \epsilon_w)(1 - \bar{\bar{\epsilon}}_g)}. \tag{3}$$

$\Phi^r_w$ as given by the above equation and $\Phi^r_w$ as given by equation (1) differ by the factor $1/(1-(1-\epsilon_w)(1-\bar{\bar{\epsilon}}_g))$, which varies between unity and infinity for $0 \leq \epsilon_w, \bar{\bar{\epsilon}}_g \leq 1$. For $\epsilon_w = 0.5$, it is equal to $2/(1+\bar{\bar{\epsilon}}_g)$. Consequently, when evaluating the total radiative heat loss at the vessel walls without taking the reflections on the walls into account, it is underestimated by the factor $2/(1+\bar{\bar{\epsilon}}_g)$.

For water and carbon dioxide, the emissivity $\bar{\bar{\epsilon}}_{\nu g}$ generally strongly depends on the wavelength. It can be written as

$$\bar{\bar{\epsilon}}_{\nu g} = 1 - \exp(\kappa_\nu R), \tag{4}$$

where $R$ is the effective depth of the radiative gas layer and $\kappa_\nu$ is the monochromatic absorption coefficient. For a cylindrical vessel, $R$ is equal to

$$R = \frac{4V_w}{A_w} \approx R_w.$$

For a given medium, $\kappa_\nu$ depends on the wavelength, the temperature and the gas pressure. The factor $T_g^4 - T_w^4$ will, in fact, rarely appear in the expression for $\Phi^r_w$, which will significantly differ from that given by equation (3). There is no simple analytical expression for the emissivity as a function of pressure, temperature and wavelength. Shack's equation takes the dependence upon the first two into account. $\bar{\bar{\epsilon}}_g$ is given by

$$\bar{\bar{\epsilon}}_g = 0.7(p_{CO_2}\frac{R}{101.3})^{0.5}(\frac{T}{100.0})^{-0.5} + 7.0(p_{H_2O}\frac{R}{101.3})^{0.8}(\frac{T}{100.0})^{-1},$$

where $p_{CO_2}$ and $p_{H_2O}$ are the partial pressures of carbon dioxide and water expressed in kiloPascals, and $T$ the temperature is in degrees Kelvin. For high pressures such as encountered in a closed vessel, this expression leads to $\bar{\bar{\epsilon}}_g = 1$.

It is generally accepted that radiation only contributes by a few percent to the total heat losses, and therefore can be neglected. The total radiative heat loss is given by

$$Q^{rad} = \int_0^{t_{cb}} \Phi^r_w \, dt.$$

The maximum radiative heat flux (equation (2)) is obtained when $\epsilon_w = \bar{\bar{\epsilon}}_{\nu g} = 1$, therefore

$$Q^{rad}_{max} = t_{cb} A_w \sigma (T_g^4 - T_w^4).$$

The total heat loss can be estimated by

$$Q^{tot} = \frac{V_w}{\gamma_p - 1}\Delta p,$$

where

$$\Delta p = p^{th}_{max} - p^{exp}_{max}.$$

For a chamber volume of 700 cm$^3$, a surface area of 500 cm$^2$ ($A_w/V_w = 0.65$ cm$^{-1}$), a combustion time of 10 ms ($\rho_{load} = 0.2$ g·cm$^{-3}$), and for an adiabatic flame temperature of 3000 K, the ratio of the maximum radiative heat loss to the total heat loss is given by[2]

$$\frac{Q_{rad}^{max}}{Q^{tot}} = 0.36\frac{(1-\Delta p/p)^4}{\Delta p/p}\%.$$

This expression is only valid for $Q_{rad}^{max}/Q^{tot}$ smaller than unity. For typical pressure drops of 14 % or more, it does not exceed 1.5 %. However, for larger surface area to volume chamber ratios and smaller loading densities, for example $A_w/V_w = 10$ cm$^{-1}$ and $\rho_{load} = 0.15$ g·cm$^{-3}$, the percentage increases up to 29 %.

### 1.5 Importance of the Radiative Term for Conservation of Energy

Considering the general case of a compressible fluid in the presence of a radiative field, the equations for the conservation of momentum and of energy are modified. However, even at high temperatures, only the effect on the energy equation is important. If the medium is local thermodynamic equilibrium, the energy equation becomes

$$\rho\frac{dh}{dt} = -\vec{\nabla}\cdot\vec{q} + \frac{dp}{dt},$$

where $h$ is the local enthalpy and $\vec{q} = \vec{q}^{cd} + \vec{q}^{r}$. Using Fourier's law to express the conductive flux vector $\vec{q}^{cd}$, it can be rewritten as

$$\rho\frac{dh}{dt} = \vec{\nabla}\cdot(k\vec{\nabla}T) + \frac{dp}{dt} - \vec{\nabla}\cdot\vec{q}^{r},$$

where $k$ is the thermal conductivity of the gases. The term $\vec{\nabla}\cdot\vec{q}^{r}$ disappears in two extreme cases: when the medium is entirely transparent ($\kappa_\nu = 0$), or when it is opaque to radiation ($\kappa_\nu \rightarrow \infty$), in which case $\vec{q}^{r} = \vec{0}$. In the general case of a semi-transparent diffusive medium, the expression of $\vec{q}^{r}$ requires to solve coupled nonlinear integro-differential equations, and is very complex. However, it can be simplified in several cases. For example, when the medium is optically thick, that is when the mean free path of the photons is very small compared to a characteristic length of the geometry of the vessel ($\kappa_\nu R \gg 1$), an analytical expression exists. This is very likely to be the case in a closed bomb, as the combustion gases have a very high absorptivity ($\overline{\overline{\alpha}}_{\nu g} \approx 1$). The expression for the radiative flux is then similar to that for the conductive flux,

$$\vec{q}^{r} = -k^{r}(T)\vec{\nabla}T,$$

where

$$k^{r}(T) = \frac{16}{3}\sigma T^3 l_\nu,$$

and $l_\nu$ is the mean free path of the photons. For a non-diffusive medium, it can be approximated by $1/\kappa_\nu$. The ratio of the conductive term to the radiative term can be estimated by

$$\frac{\vec{\nabla}\cdot\vec{q}^{r}}{\vec{\nabla}\cdot\vec{q}^{cd}} \approx \frac{16}{3}\frac{\sigma l_\nu T^3}{k_p^{cd}}\left(1 + 3\frac{||\vec{\nabla}T||}{T\vec{\nabla}^2 T}\right) \approx \frac{16}{3}\frac{\sigma l_\nu}{k_p^{cd}}T^3.$$

---

[2] The gases temperature, $T_g$, is estimated by $T_{fl}\, p_{max}^{exp} \,/\, p_{max}^{th}$.

For $k_p^{cd} = 0.2$ W·m$^{-1}$·K$^{-1}$, $\sigma = 5.678\times10^{-8}$, $T = 3000$ K and $l_\nu$ ranging from 0 to 4 μm, the ratio is less than 15 %. If the mean free path of the photons is larger, the ratio can exceed 50 %. Therefore, unless the combustion gases are entirely transparent or opaque to radiation, the radiative term should not be neglected if conductive effects are accounted for.

### 1.6 Conclusions

From the above discussion, it results that, the radiative heat losses are negligible compared to the total heat losses in vessels having a surface area to volume ratio smaller than unity. For high $A_w/V_w$ ratios, for example above 10 cm$^{-1}$, they can contribute to more than 30 % to the total heat losses. Convection, due to solid propellant burning, is therefore the dominant process of heat transfer in a closed bomb. The convective heat transfer coefficient is expected to be very high, around $10^4$ W·m$^{-2}$K$^{-1}$. Indeed, the total heat loss can be estimated by

$$Q^{tot} = \frac{V_w}{\gamma_p - 1}\Delta p.$$

It is roughly equal to the total convective heat loss. The latter can be estimated using a constant convective heat transfer coefficient, $h_c$,

$$Q^{conv} = A_w t_{cb} h^c (T_g - T_w).$$

Therefore, $h^c$ is given by

$$h^c = 4.6\times10^5 \frac{\Delta p/p}{1 - \Delta p/p} \mathrm{W\cdot m^{-2}\cdot K^{-1}},$$

where the same numerical values as in chapter 1.3 have been used. For a pressure drop of 14 %, $h^c = 7.5\times10^4$ W·m$^{-2}$K$^{-1}$.

Moreover, unless the combustion gases have a very high absorptivity, the contribution of the radiative term in the equation for the conservation of energy, can be as important as that of the conductive term. Hence, it should not be neglected if conductive effects are to be taken into account. However, near the vessel walls (boundary layer flow), both term are negligible compared to the convective term.

# 2.0 RADIATIVE HEAT TRANSFER IN CLOSED BOMBS

## 2.1 Introduction

We now review and discuss the existing models taking heat transfer into account.

Ballisticians, at first, introduced the effect of heat loss in internal ballistic models for guns. This goes back to the very end of the 18th century. It was done simply by subtracting some fraction of the total available propellant energy. This could be accomplished by adjusting the value of the specific heat upwards by a constant $\beta$ leading to the following equation for the conservation of energy[3]:

$$\underset{\substack{\text{internal energy}\\ \text{of the propellant}\\ \text{gases}}}{c_v m_s Z T} = \underset{\substack{\text{available}\\ \text{energy}}}{c_v m_s Z T_{fl}} - \underset{\substack{\text{kinetic energy of the}\\ \text{piston and of the}\\ \text{propellant gases}}}{\frac{1+\beta}{2}(M_{piston} + \frac{m_s}{3})v_{piston}^2}$$

The magnitude of the heat loss coefficient was estimated by adjusting the actual and calculated peak pressure in the barrel. It varied between 0.17 and 0.23.

However, this method can not be applied to model the closed bomb test because the piston velocity is zero. In most existing models, even currently in use, heat loss is neglected in the analysis. This means that the temperature of the combustion gases is kept constant and equal to the adiabatic flame temperature, $T_{fl}$.

It is only in the 1970s that, with the development of increasingly sophisticated gun codes, which sought to include more of the physics involved, that a strong interest arose in evaluating the burning rate as an intrinsic property of a propellant as opposed to an empirical information, therefore in modeling heat loss.

Two types of corrections are applied (for the total or the instantaneous heat loss), but in all cases, heat loss is accounted for empirically.

## 2.2 Before 1950—early approaches

All the methods used in the first half of the 20th century correct for the maximum pressure only and do not consider in detail the heat loss during burning. Roughly, it is considered that heat transfer takes place by radiation and convection. Radiative losses are proportional to the web of the grain and convective losses to the mass of propellant burnt. Several experiments are conducted, varying the web and the ratio of the surface area and the volume of the chamber. From the pressure data, a correlation is obtained between the maximum pressure corrected for heat loss, $p^{th}_{max}$, and the web $w$. They are usually given for various adiabatic flame temperature, where the web is in cm:

| $T_{fl}$ [K] | $p^{th}_{max}$ [% of $p^{exp}_{max}$] |
|---|---|
| 2400 | $3.7 + 38.1w$ |
| 2800 | $2.5 + 38.1w$ |
| 3200 | $0.9 + 38.1w$ |
| 3600 | $0.9 + 38.1w$ |

---

[3] See [HUNT 1951] for further details on all the assumptions used to derive this equation.

Corrections, that fit equally well, have been used, where the heat loss is assumed proportional to the square root or the third power of the web. Work of this type by Muraour et al., leads to a correlation of the form:

$$p_{max}^{th} - p_{max}^{exp} = \frac{S_{ch}}{V_{ch}} t_{cb}^{r}$$

where $r \approx 0.25$.

## 2.3 DOUGLAS (1953)

A first attempt is made here to calculate the heat transfer coefficients in terms of measurable parameters and to estimate the relative contribution of the radiative heat loss. The various heat losses are taken as:

Total: $Q_w^{tot} = m_s c_v (T_{fl} - T_{max}^{exp}) = Q_w^c + Q_w^r$

Convective: $Q_w^c = A_{ch} h^c t_{cb} (\frac{T_{fl}+T_{max}^{exp}}{2} - T_w)$

Radiative: $Q_w^r = A_{ch} \epsilon_p \epsilon_w \sigma t_{cb} ((\frac{T_{fl}+T_{max}^{exp}}{2})^4 - T_w^4)$

where $T_{max}^{exp} = T_{fl} \frac{p_{max}^{exp}}{p_{max}^{th}}$ and $p_{max}^{th}$ is obtained from the plot of $p_{max}^{exp}$ versus $A_{ch}/V_{ch}$[4]. Further assumptions are as follows:

- the fourth power of the wall temperature is negligible compared to the fourth power of the average gas temperature:

$$T_w^4 \ll (\frac{T_{fl} + T_{max}^{exp}}{2})^4$$

- $T_w \approx 600$ K depending on the type of propellant,
- $\epsilon_p = 1$,
- $\epsilon_w = 0.5$ (polished steel) or 1.

Radiative and total losses are estimated in a straightforward manner. $Q_w^r/Q_w^{tot}$ is calculated for various loading densities ($\rho_{load}$ = 0.05, 0.10, 0.15 g·cm−3) and $A_{ch}/V_{ch}$ (from 2.67 to 10.0 $\text{cm}^{-1}$). It is found that:

$$\frac{Q_w^r}{Q_w^{tot}} \propto \frac{1}{\rho_{load}} \frac{1}{\frac{A_{ch}}{V_{ch}}}$$

and ranges from 6 % to 67 % for $\epsilon_w = 1$ and from 3 % to 34 % for $\epsilon_w = 0.5$ (which is more realistic). For a higher density of loading, $\rho_{load} = 0.2\ \text{kg}\cdot\text{m}^{-3}$ and lower $A_{ch}/V_{ch}$ (less than unity), the data can be interpolated within 6 percent.

Convective loss is given by the difference between the radiative loss and the total loss. The convective heat transfer coefficient is then obtained for various charge weights and $A_{ch}/V_{ch}$. The main assumption to obtain a correlation for $h^c$, is that the Nusselt number $Nu$ is a function of the Reynolds number and of the Prandtl number only:

$$Nu = f(Re, Pr),$$

---

[4] A relation of the form: $p_{max}^{th} - p_{max}^{exp} = K\frac{A_{ch}}{V_{ch}}$ is found. $p_{max}^{th}$ is taken as the ordinate at the origin in the plot of $p_{max}^{exp}$ versus $\frac{A_{ch}}{V_{ch}}$.

where

$$Nu = \frac{h^c D_{ch}}{\lambda_g}, \quad Re = \frac{\rho_g v_g d_{ch}}{\mu_g}, \quad Pr = \frac{\mu_g c_{pg}}{\lambda_g}.$$

If $\mu_g$, $\lambda_g$ and $c_{pg}$ are assumed constant over the temperature range concerned, this relation simplifies to

$$h^c = f_1(\rho_g v_g)$$

for a given propellant and chamber diameter. The mass flow rate $\rho_g v_g$ is approximated by its average value.[5] The author then obtains

$$h^c = A(\frac{m_s}{t_{cb}})^B.$$

where $A \approx 4000$ and $B \approx 0.8$.[6] Values ranging from 2000 to 30000 W·m$^{-2}$·K$^{-1}$ (for $\rho_{load} = 0.05$ to 0.15 kg·m$^{-3}$ ) are found.

The value of $h^c$ is used to estimate the velocity of the gases at the wall from

$$v_g = \frac{2h^c}{f c_{pg} \rho_{load}}$$

Typical values range from 10 m·s$^{-1}$ to 80 m·s$^{-1}$ , which are very high compared to the burning velocities encountered.

Only a few points are used to interpolate the data (about three) and obtain a correlation for $h^c$, which is also only valid for propellants having a burning velocity almost linear with pressure. Moreover, the emissivity of steel is more likely to be equal to 0.1 than to 0.5 whereby the percentage of the contribution of the radiative loss is decreased by a factor of 5 and do not exceed 14 % for all loading densities.

The general similarity relation for steady compressible laminar flow is:

$$Nu = f(Re, Pr, Ec, Gr)$$

where

$$Ec = \frac{U_\infty^2}{c_p(T_w - T_\infty)}, \qquad Gr = \frac{g\beta(T_w - T_\infty)d_{ch}^3}{\nu_g}.$$

For moderate velocities ($M \leq 0.5$) and large temperature differences ($\geq 100\ K$), the effect of the Eckert number is negligible. The same applies to the Grashoff number, when buoyancy forces are small compared to inertia forces. Whence

$$Nu = f(Re, Pr),$$

as stated by Douglas.

---

[5] If one assumes that the burning rate is a linear function of pressure and that pressure is also a linear function of time, then:

$$\overline{\rho_g v_g} = \frac{m_s}{t_{cb}}$$

[6] if all variables are expressed in S I units.

However, in the case of a turbulent flow, the Nusselt number is found to be a strong function of the turbulence intensity $k$[7] [SCHLICHTING 1979]. Whereby:

$$Nu = f(Re, Pr, k)$$

For a turbulence intensity of 2.5 % (high) an increase of 80 % (compared to a zero intensity) in the local heat flux has been calculated. The flow in the chamber is said to be highly turbulent but this is not taken into account in the heat transfer analysis.

Using the results of the present study, $h^c$ can be estimated by $1.610^4$ W·m$^{-2}$·K$^{-1}$, which is of the same order of magnitude as the value found in recent studies at DREV (lower by a factor of 4).

### 2.4 DREV 1989

During the year 1989, a sensitivity analysis was conducted at DREV on the total heat loss to the walls. From experimental pressure records from firings of a 700 cm$^3$ vessel and a simple theoretical analysis of the combustion process in the vessel, the total heat loss as well as the total energy released are estimated for each test:

$$Q_w^{tot} = \frac{p_{max}^{th} - p_{max}^{exp}}{\gamma - 1}(V_{ch} - m_s\eta_p - m_a\eta_a - m_s\eta_s)$$

$$Q_e = \sum_{species\ k} \int_{T_{sk}}^{T_{Fk}} m_{gk} c_{vk}\, dT$$

$Q_e$, $Q_w$, $\frac{Q_w}{Q_e}$ are computed for five different propellants and various loading densities, and plotted against the combustion time $t_{cb}$, the burning rate (at an average pressure) and the loading density. We conclude that an affine relationship exists between the ratio $Q_w^{tot}/Q_e$ and combustion time $t_{cb}$, with a linear regression coefficient of about 0.91.

Let us extend the analysis further, what should the general shape of the curves $Q_w^{tot}$, $Q_e$ and $Q_w^{tot}/Q_e$ be ? When the combustion time goes to zero, the loading density reaches $\rho_s$, $Q_w^{tot}$ goes to zero and therefore $Q_w^{tot}/Q_e$ as well. In the range of observation ($t_{cb}$ between 3 ms and 6 ms) experimental results show that the ratio $Q_w^{tot}/Q_e$ is increasing with $t_{cb}$ and that the loading density decreases with the combustion time. As the energy released decreases with $t_{cb}$, a curve of the type below is expected for $Q_e$ versus $t_{cb}$.

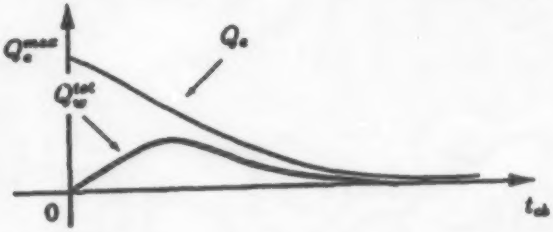

As the total heat loss can never exceed the energy released, we expect for $Q_w^{tot}$

---

[7] $k = \frac{\sqrt{\frac{1}{3}(u'^2+v'^2+w'^2)}}{U_\infty}$

versus $t_{cb}$ as shown at the top of the next page.

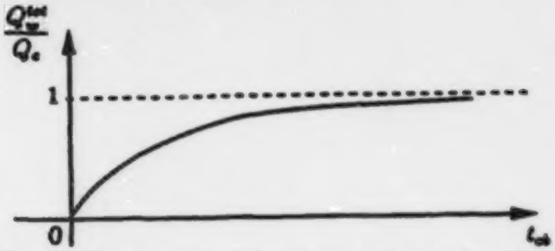

It is probable that for large combustion times, that is, low loading densities that the total heat loss approaches the energy released.

In the range of observation the variables can be fitted into linear relations. For the heat ratio:

$$\frac{Q_w^{tot}}{Q_e} = at_{cb} + b \tag{5}$$

If the point (0,0) is included in the analysis, as it should be, the linear regression coefficient is improved on average:

| propellant | without (0,0) | with (0,0) |
|---|---|---|
| FNH-P | 0.950 | 0.857 |
| B19T98 | 0.947 | 0.996 |
| M10 | 0.845 | 0.944 |

$Q_e$ is found to be a linear function of $t_{cb}$ with a coefficient of 0.99:

$$Q_e = Q_e^{max} - ct_{cb} \tag{6}$$

For the total heat loss $Q_w^{tot}$ a linear regression yields, if the origin is not included:

| propellant | r |
|---|---|
| FNH-P | 0.917 |
| B19T98 | 0.842 |
| M10 | 0.180 |

which is not very conclusive. Equations qqq and qqq suggest that a quadratic should be fitted instead of an affine function, at least in the combustion time range involved. This is also enhanced by the fact that $Q_w^{tot}$ should be exactly zero at the origin. If the origin is included for propellant B19T98, the following fit is obtained (using least squares analysis):

$$Q_w^{tot} = 0.0114861 + 40.5063t_{cb} - 4.36086t_{cb}^2$$

For propellant FNH-P, negative heat loss is found for low combustion times if the origin is included and for M10 not enough data points are available.

It is felt that more experiments should be conducted in order to obtain more specific curve fits, especially for low and high combustion times (1 ms and 8 ms), to obtain a better estimate on the shape of the curve, more particularly on its slope.

Now, the total heat loss function of the combustion time can not give any information on the instantaneous heat loss, neither on the convective heat transfer coefficient as, it is the heat loss at a specific time, constant for a given experiment:

$$Q_w^{tot} = Q_w(t_{cb}) = A_{ch} \int_0^{t_{cb}} h^c (T_g - T_w)\, dt$$

We can not take the time derivative of this expression, and therefore no information can be obtained on the integrand. A correlation of the type seeked by DREV, can only be used to estimate the total heat loss in a rapid manner.

### 2.5 KRIER March 1976

KRIER considered another form which would more accurately account for the non adiabatic process. He assumed that during the burning of the propellant in the closed bomb the average temperature of the propellant gases decreased according to the relation:

$$c_v m_s \frac{dT}{dt} = V_{ch} \beta \frac{dp}{dt}$$

$\beta$ again was estimated comparing peak experimental and theoretical pressures. The assumptions are that inert gases and ignition gases are negligible, the co-volume and the molecular weight of the gases constant. From:

$$p_{max}^{th} = \frac{m_s R_p T_{fl}}{V_{ch} - m_s \eta_p} \qquad p_{max}^{exp} = \frac{m_s R_p T_{max}^{exp}}{V_{ch} - m_s \eta_p} \tag{7}$$

one obtains:

$$\frac{p_{max}^{th}}{p_{max}^{exp}} = \frac{T_{fl}}{T_{max}^{exp}} \tag{8}$$

Integrating (qqq):

$$T = -\frac{V_{ch} \beta (\gamma - 1)}{m_s R_p} p + \text{cste}$$

$$T_{max}^{exp} = -\frac{V_{ch} \beta (\gamma - 1)}{m_s R_p} p_{max}^{exp} + \text{cste}$$

For $\beta = 0$, $T_{max}^{exp} = T_{fl}$, hence:

$$T_{max}^{exp} = T_{fl} - \frac{V_{ch} \beta}{m_s R_p} p_{max}^{exp} (\gamma + 1) \tag{9}$$

Combining equalities (qqq) and (qqq):

$$\beta = \frac{1}{\gamma - 1} \frac{m_s}{V_{ch}} \left( \frac{R_p T_{fl}}{p_{max}^{exp}} - \left( \frac{V_{ch}}{m_s} - \eta_p \right) \right)$$

Note that an accurate value of $p_{max}^{exp}$ is necessary. The heat loss rate and the total heat loss to the walls are given by:

$$q_w = \beta V_{ch} \frac{dp}{dt} \qquad Q_w^{tot} = \beta V_{ch}\, p_{max}^{exp} \tag{10}$$

From:

$$q_w = \frac{Q_w}{p_{max}^{exp}} \frac{dp}{dt}$$

and if the co-volume is neglected, one has:

$$Q_w^{tot} = V_{ch} \frac{p_{max}^{th} - p_{max}^{exp}}{\gamma - 1}$$

The heat loss rate at time t is proportional to the pressure time derivative. This results in a larger fraction of propellant consumed ($Z$ being a fraction where $R_pT$ appears at the denominator in the equation of state), hence a larger burning rate. In this analysis, burning rates estimated under the assumption of heat loss differ significantly from the ones estimated neglecting the loss. This is illustrated in the table and figure below:

These rates are also much closer to best fit burning rates (estimated using an internal ballistic code, fixing the gun parameters), although still lower by 25 %. It is concluded that one must resort to a different model than proposed or drop one of the following assumptions:

- uniform ignition,
- uniform regression rate,
- Noble-Able equation of state.

## 2.6 ROBIN and HORST December 1976

ROBBINS and HORST have used a very similar heat loss model. From the experimental and theoretical (assuming no heat loss) pressures, the total heat loss is estimated:

$$Q_w^{tot} = c_{v_g} V_g \frac{p_{max}^{th} - p_{max}^{exp}}{R_g}$$

Then, assuming a constant rate (relative to pressure) for the heat loss, a constant $K$ is defined so that:

$$-K = \frac{\Delta H}{\Delta p} = m_s c_v \frac{\Delta T}{\Delta p} = -\frac{Q_w^{tot} - Q_w^{ini}}{p_{max}^{exp} - p_{ini}^{exp}} \tag{11}$$

It represents the heat lost per unit Pascal. The instantaneous heat loss is simply given by:

$$Q_w = K(p - p_{ini}^{exp}) + Q_w^{ini}$$

hence the heat loss rate, if $Q_w^{ini}$ is set to zero (as in the actual code), is given by:

$$q_w = K\frac{dp}{dt} = \frac{Q_w^{tot}}{p_{max}^{exp} - p_{ini}^{exp}}\frac{dp}{dt}$$

The heat loss factor $K$ is equivalent to the factor $\beta V_{ch}$ in Krier's model. Indeed, from equation qqq:

$$-K = m_s c_v \frac{\frac{dT}{dt}}{\frac{dp}{dt}}$$

$$m_s c_v \frac{dT}{dt} = -K\frac{dp}{dt}$$

to compare with equation qqq.

## 2.7 Large Caliber Weapon Systems Laboratory

At LCWSL, they used the code NCBOMB where the heat loss rate is indirectly taken into account by dividing the pressure by the maximum of the experimental pressure in the burning rate:

$$r = \beta\left(\frac{p}{p_{max}^{exp}}\right)^n$$

Unfortunately, no further information could be obtained on this code.

## 2.8 PRICE and JUHASZ September 1977

Another possible way to account for heat loss is to solve an energy equation for the combustion gases temperature. In the code developed here (CBRED)[8]:

$$m_s c_v Z\frac{dT}{dt} = m_s c_v(T_{fl} - T)\frac{dZ}{dt} - q_w$$

Two options are available for evaluating $q_w$. In the first one, $q_w$ is constant, hence given by:

$$q_w = \frac{Q_w^{tot}}{t_{max} - t_{ign}}$$

where the total heat loss is estimated by:

$$Q_w^{tot} = V_{ch}\frac{p_{max}^{th} - p_{max}^{exp}}{\gamma - 1}$$

---

[8] Defining the total heat loss by the difference between the total available energy and the propellant gases internal energy, $Q_w^{tot} = m_s c_v Z(T_{fl} - T)$, and taking the time derivative of the above relation one can obtain the heat loss rate as given by this equation.

as in KRIER's model.

In the second option, the heat loss rate is decomposed in convective and radiative components with a difference before and after burnout:

$$\begin{aligned} q_w &= q_w^r + q_w^c \quad \text{for } Z \leq 1 \\ &= q_w^r \quad \text{for } Z > 1 \end{aligned}$$

$q_w^r$ is assumed proportional to the experimental pressure time derivative:

$$q_w^r = \frac{V_{ch}}{\gamma - 1}\frac{dp}{dt} \qquad q_w^r = \frac{Q_w^t}{p_{max}^{th} - p_{max}^{exp}}\frac{dp}{dt}$$

$q_w^c$ is estimated using a convective heat transfer coefficient $h^c$ similar to the one derived for turbulent flows through pipes:

$$h^c = F^c(\frac{dm}{dt})^{\frac{4}{5}}$$

where $F^c$ is a constant, and $m$ the mass burning rate. The total heat loss rate is written in the form:

$$q_w = A_{ch}(h^c(T - T_w) + \overline{h^r}(T^4 - T_w^4))$$

$\overline{h^r}$, the average (in time) constant radiative coefficient and $F^c$ are obtained using curve fit techniques, based on the experimental pressure curve after burnout:

- from $p^{exp}$ and $(dp/dt)^{exp}$, one can obtain, using the ideal gas law, $T^{exp} = \dfrac{p^{exp}V_{ch}}{R_g}$ (as all the solid has burned) and $q_w^r$, giving $h^r$ and $\overline{h^r}$.
- $F^c$ is estimated using an averaged mass flow rate and heat loss rate.

Finally:

$$\begin{aligned} q_w &= \frac{Q_w^{tot}}{p_{max}^{th} - p_{max}^{exp}}\frac{dp}{dt} + F^c(m_s\frac{dZ}{dt})^{0.8}(T - T_w)A_{ch} \quad \text{for } Z \leq 1 \\ &= \frac{Q_w^{tot}}{p_{max}^{th} - p_{max}^{exp}}\frac{dp}{dt} \quad \text{for } Z > 1 \end{aligned}$$

The assumption that after burnout only radiative losses occur is discutable as:

- it is very probable that combustion gases are opaque hence radiation cannot reach the walls, being absorbed on its way,
- radiative losses are negligible compared to convective losses.

But, noting that, after burnout the heat loss rate can be estimated by[9]:

$$q_w = m_s c_v \frac{dT}{dt} = \frac{V_{ch}}{\gamma - 1}\frac{dp}{dt} = q_w^r$$

---

[9] Taking the derivative of the equation of state. $pV_{ch} = m_s R_p T$.

as given in the analysis above. Therefore the expression given for $q_w$ seems valid after burnout. It just might not be called a radiative heat loss. But, more important the heat transfer coefficients are estimated from observing the pressure decrease in the vessel after burnout. It is not obvious that the rate at which it occurs is identical to the one which occurs during burning.

### 2.9 COHEN and STRAND 1978

Heat losses to the wall are accounted for using constant convective and radiative coefficients:

$$q_w = A_{ch}(h^c(T - T_w) + \epsilon_p \sigma (T^4 - T_w^4))$$

The value of $h^c$ is not given in the article.

### 2.10 Conclusions

All these methods make use of the fact that the total heat losses to the walls are known and can be approximated by:

$$Q_w^{tot} = V_{ch} \frac{p_{max}^{th} - p_{max}^{exp}}{\gamma - 1}$$

They are based on semi-empirical expressions for the heal loss rate $q_w$. It is either assumed constant or proportional to the time derivative of pressure:

$$q_w \propto \frac{dp}{dt} \qquad \text{or} \qquad q_w = \text{cst}$$

Radiative heat transfer is treated in a very simple way. Neither the variations of the emissivity of the combustion gases with wavelength and temperature, nor the reflections of radiation on the walls are taken into account. A more accurate estimation of the heat loss rate has never been made because it has never been the main purpose of the analysis.

In order to obtain more rigorous relations and a better understanding of the mechanisms involved, a new approach to the problem should be taken. The only way to do so, is to actually model the flow in the vessel and take space variations into account. Now, the heat loss rate will be given from a turbulent boundary layer analysis. Depending on how well the theory will match the experiments, radiative heat transfer might have to be accounted for using more rigorous expressions (see chapter qqq), or a more sophisticated model for the flow.

A first step to this new approach is the modeling of the core flow, both inviscid and non conductive. The present work deals with this problem as well as a simple way to account for heat loss. Assumptions and results are given in the following chapter.

# APPENDIX 6

# STUDY OF EQUATIONS OF STATE FOR COMBUSTION PRODUCTS IN A CLOSED VESSEL

by

**Ilja Hauss**

# A STUDY OF EQUATIONS OF STATE FOR THE DENSITY RANGE FROM DILUTE GASES TO COMPRESSED LIQUIDS

by

Ilja Hauss

Thesis Document

# Abstract

Important classical equations of state for the relationship between pressure, volume and temperature are reviewed and their predictions of state properties are compared to experimental results for carbon dioxide ($CO_2$), in order to assess their predictive capabilities over the large range of densities from dilute gases to compressed liquids. Because most equations of state are restricted in application, such as only to dilute gases or only to dense liquids, more than one equation of state is required to cover the entire density range from dilute gases to compressed liquids if prediction accuracy is important. The present work considers the possibility of blending (or combining) equations of state that are accurate for low-density gases with those that are accurate for high-density gases and liquids in an attempt to produce one expression that is accurate over the entire density range from dilute gases to compressed liquids. Experimental data for $CO_2$ is used to illustrate capabilities and limitations of various equations of state.

# Acknowledgements

I would like to thank Professor J. J. Gottlieb for his support and patience during the preparation of this paper. I also would like to express my thanks to all of the students of the Gasdynamic Group of UTIAS for their help and for their interest and encouragement. I especially appreciate their efforts to create a comfortable, creative and fertile atmosphere.

# Table of Contents

Title Page ........ i
Abstract ........ ii
Acknowledgements ........ iii
Table of Contents ........ iv
1 INTRODUCTION ........ 1
2 REVIEW OF SOME EQUATIONS OF STATE ........ 3
  2.1 Introductory Information ........ 3
  2.2 Ideal Gas Law ........ 6
  2.3 Clausius' Equation of State ........ 7
  2.4 Virial Equations of State ........ 8
    2.4.1 Two-Term Truncated Virial Equation of State ........ 11
    2.4.2 Three-Term Truncated Virial Equation of State ........ 11
    2.4.3 Beattie and Bridgeman's Equation of State ........ 12
  2.5 Extended Clausius' Equation of State ........ 14
  2.6 Cubic Equations of State ........ 16
  2.7 Hankinson, Brobst and Thomson's Equation of State ........ 20
  2.8 Comparison of Results from Different Equations of State ........ 22
  2.9 Summary of Results for Different Equations of State ........ 44
3 BLENDED LIQUID AND GASEOUS EQUATION OF STATE ........ 53
  3.1 Blending Two Equations of State ........ 53
  3.2 Blending the Equations of State of Hankinson, Brobst and Thomson with that of Redlich and Kwong ........ 54
4 SUMMARY AND PROSPECT ........ 66
References ........ 67
APPENDIX A: METHOD OF IMPLEMENTING MAXWELL'S RULE 68
APPENDIX B: SECOND AND THIRD VIRIAL COEFFICIENTS ........ 74

# 1 INTRODUCTION

Searching for and suggesting better equations of state have extended over a period of more than a century. Dozens of equations of state have been proposed by past researchers of international stature like Van der Waals; Redlich and Kwong; Soave; Benedict, Webb and Rubin; Onnes; and Beattie and Bridgeman (see references 1 to 10). The motivation for their efforts is justified by the rewards of having the exceptional power and utility of a good equation of state for predicting the behaviour of compressible gases and liquids. A well-behaved equation combined with appropriate thermodynamic relationships can predict, with high precision, important thermodynamic properties like heat capacity, enthalpy, entropy, fugacity, vapour pressure, activity coefficients, and vapour-liquid equilibria in mixtures. Despite enormous efforts over the last century, nobody has invented a single relationship that is truly good over a wide range of densities from that for dilute gases to compressed liquids. Overall, the high precision of various proposed equations of state is simply restricted to a narrow range of densities, like that for the dilute gaseous state only, or for the liquid state only, or for both ranges simultaneously with poor accuracy over the intermediate range.

The state of a pure substance under equilibrium conditions without special force fields is normally specified in general terms by a relationship involving the gas pressure ($p$), specific (or molar) volume ($v$), and temperature ($T$). This relationship that describes the volumetric behaviour of a substance as a function of both the pressure and temperature is called an equation of state; it can be expressed symbolically in the form

$$f(p, v, T) = 0 \,.$$

There are usually two different approaches in developing a specific volumetric relationship between $p$, $v$ and $T$. One approach is theoretical and uses the concepts of kinetic theory and/or statistical mechanics in conjunction with intermolecular force fields. The most common examples of this approach yield the equations of state of Lennard, Jones and Devonshire in one case and that of Hirschfelder in another. The other approach is empirical or semi-theoretical (i.e., a mix of theory and empiricism). This approach is exemplified by the equations of state from Clausius; Benedict, Webb and Rubin; Redlich and Kwong, and Soave, in which they postulate equation of state or corrections to them involving free parameters that are determined by a fit to experimental and/or theoretical data. The empirical approach has been the most successful in representing data with high precision over a fairly wide range of density values.

After the formulation of the ideal gas law, $pv = RT$ or $p = \rho RT$, which was the first important correlation to accurately predict the volumetric behaviour of gases at low densities, investigators suggested relationships that stemmed from different objectives. On one hand there are equations designed for special $pvT$-regions, like the equation of state from Benedict, Webb and Rubin that reproduces hydrocarbon data with high precision for low-density gases to high-density gases at critical-point conditions, or like the equations of state of Flory, Orwell, and Lennard and Jones which are restricted to the liquid density range. On the other hand there are suggested equations to represent data over the entire range of densities, from that of infinitely diluted gas to compressed liquids, as exemplified by both Van der Waals' and Redlich and Kwong's equations of state. It is worth emphasizing that in using these equations fairly high deviations from experimental results must be accepted.

Other equations of state first proposed by Onnes suggested an open ended equation, the virial equation of state, by calculating the pressure as a power expansion in density, in which the coefficients are functions only of the temperature. To cover a large density range in Onnes' work with high precision requires a virial equation with some theoretical and many arbitrary coefficients. Relatively simple and short equations are sufficient only for the range of low densities, whereas to cover the larger range from low to high densities requires an equation of state with a long expansion and a method of specifying the coefficients. For example, a virial equation of state with two coefficients can represent experimental data fairly precisely up to one fiftieth of the critical density, whereas a longer equation of state with five coefficients typically achieves only one half the critical density [10].

To predict gas properties with high accuracy over a wide range of densities from dilute gases to liquids, it is still unavoidable today to use different equations of state and their constants to handle different $pvT$-regions specific to certain conditions and individual substances. In this study the possibility of a new method of using different equations of state is considered, in which separate equations of state for liquids and gases are combined. The basic idea is to combine two existing equations of state based on the understanding that one gives accurate results for the liquid region and the other accurately covers the low-density gas range. The objective is to produce a combined relationship that is applicable continuously over both ranges, such that thermodynamic properties are accurately predicted over the entire range from compressed liquid to dilute gas densities. Classical equations of state are reviewed first in the next chapter to gain experience, with emphasis placed on their form, regions of applicability and special limitations.

# 2 REVIEW OF SOME EQUATIONS OF STATE

## 2.1 Introductory Information

The formulation of the ideal gas law and related knowledge of its strong restriction to the range of low-density gases stimulated many investigators to search for a more generally valid equation of state, as mentioned in chapter 1. One should distinguish between different types of equations of state. There are so-called virial equations of state that consist of expansions in terms of specific volume or density; there are so-called cubic equations of state that contain volume terms raised to the first, second and third powers; and there are complex closed equations of state like that of Bendedict, Webb and Rubin. In this chapter, the most common ideal gas law, four typical virial equations of state, the virial equation of state of Bendedict, Webb and Rubin, the simplest and most successful cubic equations of state, and the technique of Hankinson, Thomson and Probst for compressed liquids are introduced. It is important to emphasize that this study is confined to investigating the most common and well-known equations of state.

A number of these well-known equations of state include the effects of repulsion and attraction between molecules during collisions but do not automatically account for the co-existence of liquid and vapour as a mixture at pressures and temperatures below those of the critical point. Isotherms that are plotted in terms of the pressure versus specific volume usually exhibit both a local minimum and maximum between the dense liquid and dilute vapour equilibrium conditions, and this is illustrated in figure (1) for the case of Van der Waals' equation of state. This combined minimum and maximum variation of the isotherm is obviously not physically realistic, because a gas-liquid system with a derivative $\left.\frac{\partial^2 p}{\partial v^2}\right|_T > 0$ should generally not exist in the general case of normal fluids.[1] For the occurrence of vapour and liquid equilibrium conditions, changes in density under isothermal conditions occur only at constant pressure, that is the saturation vapour pressure $p = p_{sat}$ is a constant. This situation has a well-known correction procedure that is described here and required later in this report for a number of equations of state.

Maxwell's [4] correction produces a realistic estimation of the constant saturation pressure $p_{sat}$ at a given isotherm temperature $T = T_{sat}$. At equilibrium the Gibb's free energy is at a minimum, and when this information is combined with the knowledge that $T_{sat}$ and $p_{sat}$ are both constant at saturation, Maxwell was able to deduce a method of

---

[1] Some exotic fluids do exhibit strange behaviour with $\left.\frac{\partial^2 p}{\partial v^2}\right|_T > 0$ around the triple point.

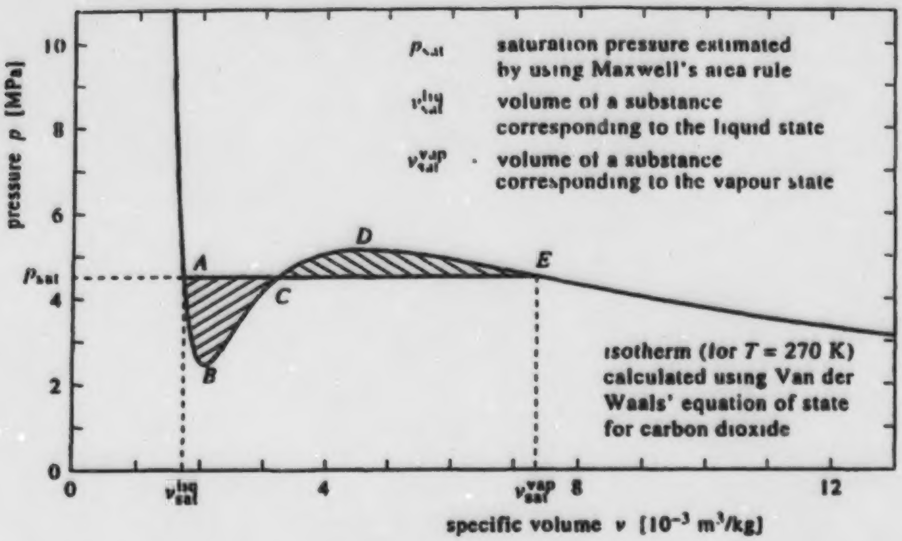

Figure 1: Illustration of Maxwell's rule for an isotherm: the horizontal line $AE$ is drawn such that areas $ABCA$ and $CDEC$ are equal, thereby eliminating the aphysical minimum at $B$ and maximum at $D$ in the original isotherm (constructed using Van der Waals' equation of state for $CO_2$) and thereby producing a constant saturation pressure (line $AE$).

revising the isotherm such that the two areas $ABCA$ and $CDEC$ would be equal as depicted in figure (1). His well-known rule therefore corrects the physically unrealistic curve with the minimum and maximum separated by an inflection point to become more realistic with a horizontal saturation portion given by $AE$ in which liquid and vapour coexist as a mixture. A practical method of implementing Maxwell's procedure to obtain saturation properties, which is iterative for the complicated equations of state, is presented in appendix A.

This study is confined to the most common and well-known equations of state, as mentioned earlier, and their predictions are compared to experimental data for $CO_2$, and this is done to illustrate their range of applicability and many of their limitations.

The choice and use of carbon-dioxide data only are qualified further. The molecule $CO_2$ is nonpolar; it is therefore quite suitable to use in a preliminary evaluation of almost any equation of state. A polar molecule is unbalanced with respect to both negativity and positivity, a physical feature caused by electrons circulating in an irregular distribution around the nucleus. Although the molecule has no net charge the separation of the charge molecular weight: $M^{CO_2} = 44.01$ kg/kmole

specific gas constant: $R^{CO_2} = 188.92$ J/kg·K

experimental critical-point pressure: $p_{cp}^{CO_2} = 7.3815$ MPa

experimental critical-point temperature: $T_{cp}^{CO_2} = 304.15$ K

experimental critical-point density: $\rho_{cp}^{CO_2} = 468.2$ kg/m$^3$

experimental critical-point specific volume: $v_{cp}^{CO_2} = 2.136\times10^{-3}$ m$^3$/kg

theoretical critical-point temperature: $T_{cp^*}^{CO_2} = 304.19$ K

theoretical critical-point specific volume: $v_{cp^*}^{CO_2} = 2.136\times10^{-3}$ m$^3$/kg

sublimination temperature: $T_{sublim}^{CO_2} = 194.65$ K (at 760 mm Hg)

melting temperature: $T_{melt}^{CO_2} = 216.55$ K

acentric factor: $\omega^{CO_2} = 0.239$

special accentricity factor: $\omega_*^{CO_2} = 0.2373$

Table 1: Some properties of carbon dioxide.

center from the molecule geometric center yields a polar molecule. It is obvious that this kind of polarity affects interactions between the same and other molecules, and therefore it is difficult for an equation of state to predict the correct $pvT$-behaviour when the polarity is not carefully considered. Nonetheless, it is useful and convenient to consider $CO_2$ data in this study, because a broad base of experimental data exists, including all of the coefficients and constants required for the various proposed equations of state used in this investigation. For a thorough study it would ideally be important to scrutinize the majority of all proposed equations of state, with any special attention given to their form and range of applicability, as well as to compare the equation-of-state predictions to a multitude of experimental data gathered from a variety of different gases and liquids. However, the present investigation is limited to one of proving feasibility only, because the extent of this work must be kept practicable. Therefore, in this investigation, the most important equations of state are considered and only the data for $CO_2$ are incorporated for comparison purposes.

Some data for $CO_2$ that are required for using and testing various equations of state and are provided in tables (1) and (2) for future reference. Table (1) contains typical and other information gathered from Reid, Prausnitz and Poling [3] and Lide and Kehiaian [8] on the properties of $CO_2$, such as molecular weight, specific gas constant and experimental and theoretical critical-point properties, acentricity factors and other data, whereas table (2) is taken from Lide and Kehiaian [8] and includes data for the pressure, tempera-

| $T_{sat}$ (K) | $p_{sat}$ (MPa) | $v_{sat}^{liq}$ ($10^{-3}$ $m^3/kg$) | $v_{sat}^{vap}$ ($10^{-3}$ $m^3/kg$) |
|---|---|---|---|
| 216.55 | 0.518 | 0.848 | 72.464 |
| 220 | 0.600 | 0.857 | 63.291 |
| 225 | 0.734 | 0.871 | 50.943 |
| 230 | 0.891 | 0.885 | 48.103 |
| 235 | 1.075 | 0.901 | 36.232 |
| 240 | 1.282 | 0.918 | 30.581 |
| 245 | 1.518 | 0.936 | 25.773 |
| 250 | 1.787 | 0.956 | 21.787 |
| 255 | 2.085 | 0.978 | 18.450 |
| 260 | 2.421 | 1.002 | 15.723 |
| 265 | 2.787 | 1.029 | 13.387 |
| 270 | 3.203 | 1.059 | 11.287 |
| 273.15 | 3.4839 | 1.078 | 10.310 |
| 274 | 3.5633 | 1.084 | 10.040 |
| 275 | 3.6576 | 1.092 | 9.728 |
| 276 | 3.7543 | 1.099 | 9.416 |
| 277 | 3.8521 | 1.107 | 9.116 |
| 278 | 3.9520 | 1.115 | 8.818 |
| 279 | 4.0547 | 1.123 | 8.525 |
| 280 | 4.1588 | 1.132 | 8.244 |
| 281 | 4.2654 | 1.141 | 7.968 |
| 282 | 4.3732 | 1.150 | 7.704 |
| 283 | 4.4831 | 1.160 | 7.452 |
| 284 | 4.5956 | 1.170 | 7.210 |
| 285 | 4.7096 | 1.181 | 6.974 |
| 286 | 4.8261 | 1.193 | 6.738 |
| 287 | 4.9450 | 1.204 | 6.502 |
| 288 | 5.0666 | 1.217 | 6.262 |
| 289 | 5.1895 | 1.229 | 6.035 |
| 290 | 5.3148 | 1.243 | 5.817 |
| 291 | 5.4432 | 1.258 | 5.605 |
| 292 | 5.5732 | 1.273 | 5.397 |
| 293 | 5.7066 | 1.290 | 5.187 |
| 294 | 5.8421 | 1.309 | 4.980 |
| 295 | 5.9802 | 1.329 | 4.778 |
| 296 | 6.1205 | 1.350 | 4.574 |
| 297 | 6.2639 | 1.374 | 4.372 |
| 298 | 6.4098 | 1.401 | 4.168 |
| 299 | 6.5598 | 1.433 | 3.964 |
| 300 | 6.7115 | 1.479 | 3.733 |
| 301 | 6.8661 | 1.515 | 3.504 |
| 302 | 7.0246 | 1.573 | 3.259 |
| 303 | 7.1858 | 1.656 | 2.978 |
| 304.19 | 7.3815 | 2.136 | 2.136 |

Table 2: Saturation liquid and vapour properties for carbon dioxide.

ture, liquid specific volume and vapour specific volume that defines the liquid and vapour saturation curves from the melting temperature of 216.55 K at the pressure 0.518 MPa to the critical-point temperature of 304.19 K at the critical-point pressure of 7.3815 MPa. Other data for $CO_2$ will be given as needed in the report.

## 2.2 Ideal Gas Law

The equation of state for ideal gases is normally called the ideal gas law. The ideal gas law [7] was the first important correlation of thermodynamic properties. This law combines the rule of both Boyle and Mariotte, that is the product of pressure $p$ and volume $v$ is constant for isothermal changes ($pv$ = constant), with another law due to Charles ($p/T$ = constant), and another law due to Gay and Lussac ($v/T$ = constant) The ideal gas law can be written in the following ways:

$$\frac{pv}{T} = \text{constant}, \qquad pv = RT, \qquad \text{or} \qquad p = \rho RT, \tag{1}$$

where $p$ denotes the pressure, $v$ is the specific volume, $\rho = 1/v$ denotes density, $T$ is the absolute temperature and $R$ denotes the specific gas constant. This law is valid only for the range of very low-density gases—for the case of ideal-gas conditions when $p \rightarrow 0$. It generally applies with good accuracy for gas densities less than one hundredth of that at the critical point ($\rho_{cp} = 468.2$ kg/m$^3$ for $CO_2$).

The ideal gas law becomes exact for dilute gases with diminishing molecular interactions (fewer collisions), although such a gas is only a theoretical concept. The ideal gas law is not applicable at high gas and liquid densities typical of the critical point. Despite these strong limitations the ideal gas law is, owing to its simplicity, very important as the first approximation for predicting thermodynamic properties of gases at relatively low densities and high temperatures. One advantage of the ideal gas law is that it is simple, and it can often be considered as the starting point for developing equations of state that apply to gases at higher densities and lower temperatures. For example, Clausius' equation of state, the virial equations of state, Beattie and Bridgeman's equation of state and the extended Clausius equation of state to be presented in chapters 2.3–2.5 are essentially extensions of the ideal gas law to better apply to gases at higher densities, without explicitly considering their applicability in the region of the critical point.

In using the ideal equation of state to do calculations for carbon dioxide ($CO_2$) that are presented later in this report, we use molecular weight $M^{CO_2} = 44.01$ kg/kmole and the specific gas constant $R^{CO_2} = 188.92$ J/kg·K from table (1).

## 2.3 Clausius' Equation of State

The equation of state of Clausius is an early attempt about 1870 to improve the ideal gas law by considering the effects of repulsive forces between molecules during collisions. At the time when kinetic theory concepts were just being accepted, he realized that substances do not have an unlimited compressibility, because repulsive force fields between molecules become stronger as they are pushed closer together. This is referred to as a limiting volume effect of finite-sized molecules, an effect that acts much like a reduction in the total volume available for molecular translational motion, because of the actual volume occupied by a molecule and its electrons. Clausius suggested that the volume available for translational gas motion be reduced by this limiting volume, and his equation of state can is expressed in present-day notation as

$$p = \frac{RT}{v - \dot{b}} = \frac{\rho RT}{1 - \dot{b}\rho} . \tag{2}$$

Parameter $\hat{b}$ includes the volume reduction as might be imagined for a small impenetrable volume. For a specific volume $v$ equal to $\hat{b}$ this equation has an asymptote with an infinite gas pressure. Also, the pressure is negative for $v < \hat{b}$ and this is not meaningful physically; however, this range of negative pressures is neither required nor used.

The equation of state of Clausius is applicable for low-density gases and moderately high-temperature and high-density gases, possibly up to a fiftieth of the density of gases and liquids at the critical point ($\rho_{cp} = 468.2$ kg/m$^3$ for $CO_2$). It providing thereby a worthwhile extension of the ideal equation of state from dilute gas densities to sightly higher density gases. However, in spite of this worthwhile extension, the Clausius equation of state is not applicable in the high-density range of gases and liquids in the vicinity of the critical point of substances. Nevertheless, this was the first significant effort of including the effects of an increased gas pressure from repulsive forces of molecular collisions in an equation of state.

In using Clausius' equation of state to perform calculations for $CO_2$ that are presented later in this report, we use $M^{CO_2} = 44.01$ kg/kmole and $R^{CO_2} = 188.92$ J/kg·K from table (1), and we use $\hat{b}^{CO_2} = 29.67$ cm$^3$/mole $= 0.6746\times10^{-3}$ m$^3$/kg. An expression for $\hat{b}^{CO_2}$ is taken directly from Redlich and Kwong's equation of state, which is given by $\hat{b} = 0.08664RT_{cp}/p_{cp}$ in chapter 2.6, and the value of $\hat{b}^{CO_2}$ is calculated by using $R^{CO_2}$ given above and the critical-point properties $T_{cp}^{CO_2} = 304.19$ K and $p_{cp}^{CO_2} = 73.82$ bar $= 7.382$ MPa from table (1).

## 2.4 Virial Equations of State

The first virial equation of state was proposed by Onnes [1] at the turn of the century (1900). He realized that the ideal gas law gave unsatisfactory predictions for higher density gases, especially for those near the critical point. The virial equation of state he proposed is an open ended relationship that expresses the gas pressure as an series expansion in terms of the specific volume (or density). Virial equations of state are often expressed in the form

$$p = \frac{RT}{v}\left[1 + \frac{B(T)}{v} + \frac{C(T)}{v^2} + \frac{D(T)}{v^3} + \ldots\right] \tag{3}$$

as a series expansion in terms of the specific volume $v$, or in the alternative form

$$p = \rho RT\left[1 + B(T)\rho + C(T)\rho^2 + D(T)\rho^3 + \ldots\right] \tag{4}$$

as a series expansion in terms of the density $\rho$. In these equations, $p$, $T$ and $R$ denote the pressure, temperature and gas constant, respectively. The coefficients 1, $B(T)$, $C(T)$,

$D(T)$, etc., are commonly referred to as the first, second, third, fourth, etc., virial coefficients, respectively. All but the first one ($A = 1$) are normally temperature dependent. Furthermore, the series expansion is often truncated as a convenience approximation to include one, two, three or four virial coefficients, depending on the degree of sophistication, accuracy required, and availability of data to define the temperature-dependent coefficients. Truncating the expansion to include only the first virial coefficient $A = 1$ reduces the virial equation of state to the ideal gas law. The second, third and following virial coefficients dictate deviations from ideality, that is deviations from the ideal gas law, or alternatively extensions to the ideal gas law. The virial coefficients can be estimated by using either theoretical methods like statistical mechanics or experimental methods based on experimental data.

In theoretical approaches a knowledge of quantum mechanics is used, and the potential governing molecular collisions is often assumed to stem from the well-known Lennard and Jones' and Stockmayer's theories [2]. These potentials are coupled to analyses or computer calculations to produce the temperature-dependent second, third, and possibly higher virial coefficients.

In experimental approaches the second and higher virial coefficients are determined from experimental pressure, volume and temperature data. To facilitate this procedure, the virial equation of state is expressed in the form $p = \frac{ZRT}{v}$ or $Z = \frac{pv}{RT}$, where $Z$ is the real-gas compressibility factor. Equation (3) is rewritten as

$$(Z-1)v = B(T) + \frac{C(T)}{v} + \frac{D(T)}{v^2} + \dots , \tag{5}$$

and the virial coefficients $B(T)$, $C(T)$, $D(T)$, etc., are defined by the relationships

$$B(T) = \lim_{v^{-1}\to 0} [(Z-1)v]_T ,$$

$$C(T) = \lim_{v^{-1}\to 0} [(Z-1)v - B(T)]_T ,$$

$$D(T) = \lim_{v^{-1}\to 0} \left[(Z-1)v^2 - B(T)v - C(T)\right]_T ,$$

etc. Then, $B(T)$, $C(T)$, $D(T)$, etc., can be approximated from experimental data plotted in the form of $[(Z-1)v]$, $[(Z-1)v - B(T)]$, $[(Z-1)v^2 - B(T)v - C(T)]$, etc., versus the inverse volume $v^{-1}$ or density $\rho$.

The second virial coefficient $B(T)$ stems from the overall effects of repulsion and attraction between molecules during a binary collision (two molecules), whereas the third virial coefficient $C(T)$ includes the overall ffects of repulsion and attraction of molecules during a trimolecular collision (three molecules) [1], [2]. Theoretical considerations for a specified force field yield expressions for $B(T)$ and $C(T)$. In the special case of the Lennard-Jones 6–12 potential, series expressions for $B(T)$ and $C(T)$ as a function of temperature are reviewed and presented in appendix B, and their series coefficients are re-evaluated for increased accuracy and listed in tables therein.

The second virial coefficient used in this report is given by a curve fit to experimental data for $CO_2$. The general curve fit is given by

$$B(T) = \sum_{i=0}^{2} a_i \left(\frac{T_{ref}}{T} - 1\right)^i \tag{6}$$

from Lide and Kehiaian [8], the values of the three coefficients for $CO_2$ are given by

$$a_0^{CO_2} = -127.3 \text{ cm}^3/\text{mole} = -2.893\times10^{-3} \text{ m}^3/\text{kg},$$

$$a_1^{CO_2} = -287.6 \text{ cm}^3/\text{mole} = -6.535\times10^{-3} \text{ m}^3/\text{kg},$$

$$a_2^{CO_2} = -118.3 \text{ cm}^3/\text{mole} = -2.688\times10^{-3} \text{ m}^3/\text{kg},$$

and the reference temperature $T_{ref}^{CO_2} = 298.15$ K for $CO_2$. This correlation for the second virial coefficient is in fairly good agreement with predictions based on the Lennard-Jones 6–12 potential (see appendix B for details).

The third virial coefficient used in this report is also given by a curve fit to experimental data for $CO_2$. The general curve fit is given

$$C(T) = b_o^2 \left[0.4 \left(\frac{T_{ref}}{T}\right)^m - 0.0072 \left(\frac{T_{ref}}{T}\right)^7\right] \tag{7}$$

with the exponent

$$m = \frac{1}{2} + \frac{1.85}{1 + \left(\frac{T}{T_{ref}}\right)^2},$$

for which $b_o^{CO_2} = 85.05\times10^{-3}$ cm$^3$/mole $= 1.933\times10^{-3}$ m$^3$/kg and $T_{ref}^{CO_2} = 400$ K for $CO_2$. This correlation for the third virial coefficient is also in fairly good agreement with theoretical predictions of $C(T)$ based on the Lennard-Jones 6–12 potential (see appendix B for additional details).

Empirical equations in form of the virial equation of state have been extensively used and much experience has been gained. This study considers three representative virial equations of state, that is a seldom used two-term truncated virial equation of state, an often-used three-term truncated virial equation of state, and Beattie and Bridgeman's four-term truncated virial equation of state. These virial equations of state are summarized in sections 2.4.1 to 2.4.3.

### 2.4.1 Two-Term Truncated Virial Equation of State

The two-term truncated virial equation of state is obtained by retaining the first two terms on the right-hand side of equation (3), that is up to and including the second virial coefficient $B(T)$. This simple version of the virial equation of state is

$$p = \frac{RT}{v}\left[1 + \frac{B(T)}{v}\right] = \rho RT\left[1 + B(T)\rho\right]. \tag{8}$$

The second virial coefficient $B(T)$ is obtained from a curve fit to experimental data that was given earlier by equation (6).

This two-term truncated form of the virial equation of state is valid for gases only at fairly low densities, that is for densities lower than about a fiftieth the critical-point density of a substance ($\rho_{cp} = 468.2$ kg/m$^3$ for $CO_2$). Including only the second virial coefficient in this equation of state helps essentially to include more accurately the effects of repulsive and attractive forces between molecules during collisions. This is clear by considering the variation of $B(T)$ with temperature. One can show that $B(T)$ given by equation (6) is positive for temperatures larger than 713.34 K, the so-called Boyle temperature, and in this positive range it includes the overall effects of repulsion for binary collisions. On the other hand, $B(T)$ is negative at temperatures lower than the Boyle temperature, and in this range the effects of attraction during binary collisions are included in the equation of state. See appendix B for more information.

Despite including the effects of repulsion and attraction of binary collisions via $B(T)$ in the two-term truncated virial equation of state, this equation of state is not sufficiently flexible with only the second virial coefficient to apply in the vicinity of the critical-point of substances. However, the temperature dependent coefficient $B(T)$ in the two-term truncated virial equation of state proves advantageous in range of applicability over Clausius's equation of state with a constant $\hat{b}$, because Clausius' equation includes only the effects of repulsion, and generally near the upper limit—the maximum value of $B(T)$. This advantage of the two-term virial equation of state over Clausius' equation of state is obvious if equation (8) is written as $p \approx \dfrac{RT}{v - B(T)}$ for the typical case when $B(T) \ll v$ and $v[1 + B(T)/v]^{-1} \approx v - B(T)$. The role of the temperature-dependent co-volume term is then obvious.

The two-term truncated virial equation of state is valid typically when $|\rho B(T)| < 1/3$ approximately, and the Clausius equations of state is valid when $|\rho \hat{b}| < 1/3$ approximately. These are useful rules that are necessary, but they are not sufficient for all cases.

### 2.4.2 Three-Term Truncated Virial Equation of State

The three-term truncated virial equation of state is obtained by retaining the first three terms on the right-hand side of equation (3), that is up to and including the third virial coefficient $C(T)$. This version of the virial equation of state can be expressed as

$$p \;=\; \frac{RT}{v}\left[1+\frac{B(T)}{v}+\frac{C(T)}{v^2}\right] \;=\; \rho RT\left[1+B(T)\rho+C(T)\rho^2\right]. \tag{9}$$

The second and third virial coefficients $B(T)$ and $C(T)$ are obtained from curve fits to experimental data given earlier as equations (6) and (7), respectively.

The advantage of the three-term truncated virial equation of state over the simpler two-term version is that the effects of repulsion and attraction between molecules is taken into account for trimolecular collisions by the third virial coefficient $C(T)$. This is a minor perturbation at low gas densities and high gas temperatures when $C(T)$ is positive, typically less than the effects from binary collisions from the second virial coefficient $B(T)$, but this latter effect becomes more important for densities and temperatures approaching that of the critical point, and at temperatures lower than the critical-point temperature. Note that $C(T)$ is positive for temperatures greater than 132.54 K (see appendix B).

### 2.4.3 Beattie and Bridgeman's Equation of State

Beattie and Bridgeman [1] proposed an equation of state that is semiempirical[2] and consists of a series expansion in terms of the specific volume $v$ up to the fourth power. Their truncated virial equation of state has the form $p = \frac{RT}{v}\left[1+\frac{B(T)}{v}+\frac{C(T)}{v^2}+\frac{D(T)}{v^3}\right]$ in terms of $v$ or $p = \rho RT\left[1+B(T)\rho+C(T)\rho^2+D(T)\rho^3\right]$ in terms of $\rho$. This conventional expansion form is considered somewhat inconvenient; as a consequence, Beattie and Bridgeman use the compact form

$$p \;=\; \frac{RT\,(1-\epsilon)\,(v+B)}{v^2}-\frac{A}{v^2} \;=\; \rho RT\,(1-\epsilon)\,(1+B\rho)-A\rho^2\,, \tag{10}$$

---

[2] This equation of state is semitheoretical in the sense that the theoretical virial equation of state in truncated form is used with virial coefficients determined empirically by means of the best fit to available experimental data

which is now widely accepted in the literature. This form features three primary parameters, $A$, $B$ and $\epsilon$ in equation (10), expressed as

$$A = A_0\left(1 - \frac{a}{v}\right), \qquad B = B_0\left(1 - \frac{b}{v}\right), \qquad \text{and} \qquad \epsilon = \frac{c}{vT^3}, \tag{11}$$

with five secondary constants $A_0$, $B_0$, $a$, $b$ and $c$. These secondary constants are substance specific. Values for these five constants have been determined previously for a large number of gases, and these values are listed for reference in tables available in the literature [1]. For the specific case of carbon dioxide,

$$A_0^{CO_2} = 5.0065\times10^6 \text{ atm·cm}^6/\text{mole}^2 = 261.91 \text{ N·m}^4/\text{kg}^2 ,$$

$$B_0^{CO_2} = 104.76 \text{ cm}^3/\text{mole} = 2.3804\times10^{-3} \text{ m}^3/\text{kg} ,$$

$$a^{CO_2} = 71.32 \text{ cm}^3/\text{mole} = 1.6205\times10^{-3} \text{ m}^3/\text{kg} ,$$

$$b^{CO_2} = 72.35 \text{ cm}^3/\text{mole} = 1.6439\times10^{-3} \text{ m}^3/\text{kg} ,$$

$$c^{CO_2} = 660\times10^6 \text{ cm}^3\text{·K}^3/\text{mole} = 14,997 \text{ m}^3\text{·K}^3/\text{kg} ,$$

provide values for the five coefficients for Beattie and Bridgeman's equation of state, that is for equations (10) and (11).

Beattie and Bridgeman's equation of state can easily be reorganized in the standard form of $p = \rho RT\left[1 + B(T)\rho + C(T)\rho^2 + D(T)\rho^3\right]$, and then the empirical second, third and fourth virial coefficients are given as

$$B(T) = B_o - \frac{A_o}{RT} - \frac{c}{T^3}, \quad C(T) = -bB_o + \frac{aA_o}{RT} - \frac{cB_o}{T^3}, \quad \text{and} \quad D(T) = \frac{bcB_o}{T^3}. \tag{12}$$

These empirical virial coefficients are temperature dependent, as might be expected. Beattie and Bridgeman's $B(T)$ an $C(T)$ differ somewhat from the corresponding theoretical values based on the Lennard-Jones 6–12 potential, especially for the case of $B(T)$ which has surprisingly high positive values ($B_o$ is unusually large). Additional information is available for interest in appendix B.

Beattie and Bridgeman's equation of state is sufficiently flexible in terms of the number of virial coefficients that the $pvT$-properties exhibit a minimum and maximum at sufficiently low temperatures and specific volumes, and Maxwell's rule introduced in chapter 2 and illustrated in figure (1) can be used to determine the liquid and vapour saturation curves and the critical-point properties at its extreme.

The predicted critical-point properties from Beattie and Bridgeman's equation of state are obtained first. The isotherm through the critical point features the coalescence of a minimum, maximum and point of inflection. Hence, $\left.\frac{\partial p}{\partial v}\right|_{T=T_c} = 0$ and $\left.\frac{\partial^2 p}{\partial v^2}\right|_{T=T_c} = 0$ must be satisfied simultaneously at the critical point. By differentiating Beattie and Bridgeman's equation of state as indicated, these two requirements result in the simultaneous solution of $v^3 + 2B(T)v^2 + 3C(T)v + 4D(T) = 0$ and $v^3 + 3B(T)v^2 + 6C(T)v + 10D(T) = 0$ for $v_c$ and $T_c$, in which $B(T)$, $C(T)$ and $D(T)$ are given by equation (12), and then $p_c$ follows from the equation of state. The final results for the case $CO_2$ are $p_c = 5.11$ MPa, $T_c = 280.4$ K and $v_c = 3.644 \times 10^{-3}$ m$^3$/kg. On comparing these predictions with the experimental values of $p_c = 7.382$ MPa, $T_c = 304.19$ K and $v_c = 2.136 \times 10^{-3}$ m$^3$/kg for $CO_2$, these critical-point values are in error by −31%, 8% and −71%, respectively.

Such large errors at the critical point were so surprising that we suspected originally an error in one of the coefficients. However, Beattie and Bridgeman's equation of state is essentially fitted to experimental data for gases and liquids without special consideration for the critical-point properties, and it is really an extension of the ideal gas law to have a larger range of applicability to higher densities. Thesse considerations can result in large errors near the critical point, in spite of the flexibility of using many virial coefficients in the equation of state.

The liquid and vapour saturation curves are determined using Maxwell's rule and the iteration procedure given in appendix A, and the numerical results are summarized in table (3).

Beattie and Bridgeman's equation of state has been used quite successfully in the chemical industry, in regards to the storage of many different compressed gases and liquids in tanks at temperatures typical of the atmosphere, that is from summer to winter conditions. Their use for combustion and explosion gases at high temperatures is not necessarily recommended.

## 2.5 Extended Clausius Equations of State

The Clausius equation of state introduced earlier as equation (2) can be improved considerably in terms of its range of application from low density to higher density gases. An initial approach is to simply modify the co-volume coefficient from $\hat{b}$ that is constant to $\hat{b}(T)$ that is temperature dependent. This yields what we call the partially extended Clausius equation of state $p = \frac{RT}{v - \hat{b}(T)} = \frac{\rho RT}{1 - \hat{b}(T)\rho}$. This partially extended equation of state is consistent with the two-term truncated virial equation of state given by equation (8) for the case of low densities, because this virial equation $p = \rho RT\,[1 + B(T)\rho] \approx \dfrac{\rho RT}{1 - B(T)\rho}$ for the case of $B(T)\rho \ll 1$. This suggests that the temperature-dependent parameter $\hat{b}(T)$ be defined for simplicity as the second virial coefficient $B(T)$ for this partially extended equation of state, and this is what we use.

To further improve the range of application of the partially extended Clausius equation of state to higher densities, we begin with the three-term truncated virial equation of state given previously as $p = \dfrac{RT}{v}\left[1 + \dfrac{B(T)}{v} + \dfrac{C(T)}{v^2}\right] = \rho RT\left[1 + B(T)\rho + C(T)\rho^2\right]$ by equation (9). This equation is rewritten in the Clausius-like form as

$$p = \frac{RT}{v - B(T) - [C(T) - B(T)^2]\,\dfrac{1}{v}} = \frac{\rho RT}{1 - B(T)\rho - [C(T) - B(T)^2]\,\rho^2}\,, \tag{13}$$

| $T$ (K) | $p_{sat}$ (MPa) | $v_{sat}^{liq}$ ($10^{-3}$ m$^3$/kg) | $v_{sat}^{vap}$ ($10^{-3}$ m$^3$/kg) |
|---|---|---|---|
| 216.55 | 1.0419 | 1.6465 | 32.7961 |
| 218 | 1.0935 | 1.6566 | 31.2405 |
| 220 | 1.1674 | 1.6709 | 29.2440 |
| 223 | 1.2842 | 1.6934 | 26.5387 |
| 225 | 1.3660 | 1.7091 | 24.9063 |
| 228 | 1.4949 | 1.7339 | 22.6818 |
| 230 | 1.5850 | 1.7512 | 21.3320 |
| 233 | 1.7266 | 1.7787 | 19.4829 |
| 235 | 1.8253 | 1.7980 | 18.3549 |
| 238 | 1.9800 | 1.8287 | 16.8019 |
| 240 | 2.0876 | 1.8505 | 15.8497 |
| 243 | 2.2558 | 1.8853 | 14.5322 |
| 245 | 2.3726 | 1.9101 | 13.7203 |
| 248 | 2.5549 | 1.9501 | 12.5911 |
| 250 | 2.6812 | 1.9789 | 11.8917 |
| 253 | 2.8780 | 2.0257 | 10.9136 |
| 255 | 3.0141 | 2.0598 | 10.3042 |
| 256 | 3.0837 | 2.0778 | 10.0112 |
| 257 | 3.1543 | 2.0965 | 9.7254 |
| 258 | 3.2259 | 2.1160 | 9.4466 |
| 259 | 3.2985 | 2.1364 | 9.1744 |
| 260 | 3.3721 | 2.1576 | 8.9084 |
| 261 | 3.4468 | 2.1799 | 8.6484 |
| 262 | 3.5225 | 2.2032 | 8.3939 |
| 263 | 3.5993 | 2.2276 | 8.1447 |
| 264 | 3.6771 | 2.2534 | 7.9004 |
| 265 | 3.7560 | 2.2807 | 7.6606 |
| 266 | 3.8359 | 2.3095 | 7.4250 |
| 267 | 3.9170 | 2.3402 | 7.1931 |
| 268 | 3.9991 | 2.3729 | 6.9646 |
| 269 | 4.0823 | 2.4079 | 6.7390 |
| 270 | 4.1666 | 2.4456 | 6.5157 |
| 271 | 4.2520 | 2.4865 | 6.2941 |
| 272 | 4.3385 | 2.5311 | 6.0735 |
| 273 | 4.4261 | 2.5801 | 5.8530 |
| 273.15 | 4.5009 | 2.6347 | 5.6313 |
| 274 | 4.5149 | 2.6347 | 5.6313 |
| 275 | 4.6047 | 2.6963 | 5.4069 |
| 276 | 4.6957 | 2.7672 | 5.1773 |
| 277 | 4.7879 | 2.8510 | 4.9388 |
| 278 | 4.8812 | 2.9545 | 4.6844 |
| 279 | 4.9757 | 3.0929 | 4.3989 |
| 280 | 5.0713 | 3.3228 | 4.0255 |
| 280.43 | 5.1123 | 3.6442 | 3.6442 |

Table 3: Saturation liquid and vapour properties for carbon dioxide predicted by using Beattie and Bridgeman's equation of state.

in which three terms up to order $\rho^2$ are retained. The temperature-dependent coefficients $B(T)$ and $C(T) - B(T)^2$ are composed of the second and third virial coefficients give by equations (6) and (7).

The new extended equation of state of Clausius is useful for moderately high-density and high-temperature gases, possibly up to one fifth of the density of liquids, thereby providing worthwhile improvements in extending the range of applicability for the ideal gas law and Clausius' original equation of state from the case of dilute gases towards more dense gases typical of those at the critical point. To give one example of the capability of the extended equation of state, when the critical-point temperature of 304.19 K and specific volume of $2.136\times10^{-3}$ m$^3$/kg are substituted into this equation, the prediction of the critical-point pressure is 7.350 MPa. This prediction is only 0.4% lower than the experimental value of 7.382 MPa, but this good agreement is somewhat fortuitous, because the extended equation of state feature a maximum rather than a point of inflection near the critical point. In spite of increased range of application of the extended equation of state of Clausius, this equation of state is not generally valid in the high-density range of gases and liquids at the critical point of substances or in the compressed liquid region.

## 2.6 Cubic Equations of State

Cubic equations of state [3] that are introduced in this chapter are all of the Van der Waals form; they express the pressure of a system in terms of the sum of repulsive and attractive forces, that is $p = p_{\text{repulsive}} + p_{\text{attractive}}$. The generic form of cubic equations of state suggested by Helmertz and Schwarzmann [6] is

$$p = \frac{RT}{v-b} - \frac{a}{v^2+ubv+wb^2} = \frac{\rho RT}{1-b\rho} - \frac{a\rho^2}{1+ub\rho+wb^2\rho^2}\,, \tag{14}$$

where $p$ denotes pressure, $v$ is the specific volume, $\rho = 1/v$ denotes density, $T$ is the temperature and $R$ denotes the gas constant. The first term on the right side of equation (14) is the same as that of Clausius' equation of state – equation (2), and the gas-specific positive parameter $b$ includes influences of repulsive forces between molecules during collisions. The effects of molecular attraction is accounted for by second term on the right side of equation (2), by incorporating the gas-specific positive parameter $a$ and two additional constants $u$ and $w$

The magnitude of the attractive force between molecules and the magnitude of the gas pressure determine the phase of a substance (i.e., gas, liquid or solid). For the case of relatively low density gases the influence of molecular attraction is small and not important,

| equation of state | $a$ | $b$ | $u$ | $w$ |
|---|---|---|---|---|
| Van der Waals | $\frac{27R^2T_c^2}{64p_c} = \frac{0.42188R^2T_c^2}{p_c}$ | $\frac{RT_c}{8p_c} = \frac{0.125RT_c}{p_c}$ | 0 | 0 |
| Redlich and Kwong | $\frac{0.42748R^2T_c^2}{p_c}\left[\frac{1}{T_r^{1/2}}\right]$ | $\frac{0.08664RT_c}{p_c}$ | 1 | 0 |
| Soave | $\frac{0.42748R^2T_c^2}{p_c}\left[1+f_\omega(1-T_r^{1/2})\right]^2$<br>$f_\omega = 0.480 + 1.574\omega - 0.176\omega^2$ | $\frac{0.08664RT_c}{p_c}$ | 1 | 0 |
| Peng and Robinson | $\frac{0.45724R^2T_c^2}{p_c}\left[1+f_\omega(1-T_r^{1/2})\right]^2$<br>$f_\omega = 0.37464 + 1.54226\omega - 0.26992\omega^2$ | $\frac{0.07780RT_c}{p_c}$ | 2 | −1 |

Table 4: Parameters $a$ and $b$ and constants $u$ and $w$ for some fundamental cubic equations of state.

whereas the opposite is true for gases near the critical point and for the case of liquids. Attractive forces become more significant with increasing density or diminishing specific volume. If the specific volume is increasing, that is $v \to \infty$ and molecular collisions between molecules become unimportant, this implies that both $a \to 0$ and $b \to 0$. Hence, the cubic equation of state is consistent with the ideal gas law and applicable to low-density gases.

If the parameters $a$ and $b$ and the constants $u$ and $w$ are defined appropriately, many classical cubic equations of state can be obtained, as illustrated by the results summarized in table (4) for Van der Waals; Redlich and Kwong; Soave; and Peng and Robinson. In this table, $R$, $T$, $p_c$, $T_c$ and $T_r = T/T_c$ denote the specific gas constant, temperature, pressure, temperature at the critical point, and reduced temperature, respectively. Redlich and Kwong, Soave and also Peng and Robinson include a term in square brackets for parameter $a$ to include the effects of nonsphericity of molecules, and this term is temperature dependent by means of $T$ in the reduced temperature $T_r = T/T_c$. In the case of Soave's and Peng and Robinson's nonsphericity corrections, $f_\omega$ is introduced as a second-degree polynomial in terms of standard acentric factor $\omega$. Note that $f_\omega$ may be considered as zero for Van der Waals' equation of state (i.e., no molecular-nonsphericity correction).

In using Van der Waals', Redlich and Kwong's, Soave's, and Peng and Robinson's cubic equations of state with parameters listed in table (4) to perform calculations for CO$_2$, we use the data $M^{CO_2} = 44.01$ kg/kmole, $R^{CO_2} = 188.92$ J/kg·K, $T_c^{CO_2} = 304.19$ K.

$p_c^{CO_2} = 73.82$ bar $= 7.382$ MPa, and $\omega^{CO_2} = 0.239$. Furthermore, note that the critical-point volume is given by $v_c^{CO_2} = 94.05$ cm$^3$/mole $= 2.136\times10^{-3}$ m$^3$/kg and the critical-point density is given by $\rho_c = 10.66\times10^{-3}$ moles/cm$^3$ $= 468.0$ kg/m$^3$.

The standard procedure of determining the two parameters $a$ and $b$ in equation (14) makes use of the characteristics of the critical point of a substance, and this method was applied to produce all of the equations for $a$ and $b$ listed in table (4). In this method the first and second derivatives of the pressure with respect to the volume at a constant temperature are set equal to zero, that is $\left.\frac{\partial p}{\partial v}\right|_{T=T_c} = 0$ and $\left.\frac{\partial^2 p}{\partial v^2}\right|_{T=T_c} = 0$, because the isotherm through the critical point features the coalescence of a minimum, maximum and point of inflection. These two conditions are sufficient[3] for the determination of the two parameters $a$ and $b$ in equation (14).

It is remarkable that the parameter $b$ depends on critical-point properties only and is therefore constant for a specific gas, and furthermore that its form is similar for all equations of state. In contrast, the parameter $a$ is constant only for Van der Waals' equation of state, is temperature dependent for the others equations of state, and changes in form considerably because of the temperature dependence in Redlich and Kwong's equation and owing to the nonsphericity corrections for both Soave's and Peng and Robinson's equations of state.

The cubic equations of state can be expressed as a series expansion in terms of both $v$ and $\rho$. If this is done, then the first five empirical virial coefficients are given by

$$A(T) = 1\,, \qquad B(T) = b - \frac{a}{RT}\,, \qquad C(T) = b^2 - u\frac{ab}{RT}\,,$$

$$D(T) = b^3 - \left(u^2 - w\right)\frac{ab^2}{RT}\,, \qquad \text{and} \qquad E(T) = b^4 + \left(u^3 - 2uw\right)\frac{ab^3}{RT}\,,$$

---

[3] For the case of the Van der Waals' equation of state, for which u and $w$ of equation (14) are zero, we can use the derivative conditions $\left.\frac{\partial p}{\partial v}\right|_{T=T_c} = 0$ and $\left.\frac{\partial^2 p}{\partial v^2}\right|_{T=T_c} = 0$ to define the parameters $a$ and $b$ as

$$a(v_c, T_c) = \frac{9RT_cv_c}{8} \qquad \text{or} \qquad a(p_c, T_c) = \frac{27R^2T_c^2}{64p_c}\,, \qquad \text{or} \qquad a(p_c, v_c) = 3p_cv_c^2\,,$$

and

$$b(v_c) = \frac{v_c}{3}\,, \qquad \text{or} \qquad b(p_c, T_c) = \frac{RT_c}{8p_c}\,.$$

where $v_c$, $p_c$, and $T_c$ correspond to known critical-point data, and $R$ denotes the gas constant We note that the parameters $a$ and $b$ are normally determined by using the known critical-point data $p_c$ and $T_c$, and the third critical-point value $v_c$ is not used Hence, Van der Waals' equation of state is incapable of reproducing the known value of $v_c$ in the general case for the case when $b\rho < 1$. For the special case of Van der Waals' equation of state with $u = 0$ and $w = 0$, only the second virial coefficient is temperature dependent and all others are constants. For the other equations of state of Redlich and Kwong, Soave, and Peng and Robinson, the second and higher virial coefficients are a function of the temperature. This temperature dependence should be expected because an equation of state that is applicable with good accuracy over a large range of gas densities from dilute gases to highly compressed gases near the critical point must have such dependencies.

The cubic equations of state are not sufficiently flexible to define the three properties $p_c$, $T_c$ and $v_c$ independently at the critical point. The experimental values of $p_c$ and $T_c$ are normally used to determine $a$ and $b$, as mentioned previously. The predicted value of $v_c$ is a by-product of the specific cubic equation of state, and the value of $v_c$ is permitted to be in error. In the case of Van der Waals' equation of state, the predicted value is $v_c^{CO_2} = 3b = 2.919\times10^{-3}$ m$^3$/kg for CO$_2$, which is 37% higher than the experimental value $v_c^{CO_2} = 2.136\times10^{-3}$ m$^3$/kg. In the cases of both Redlich and Kwong's and Soave's equations of state, $v_c$ is solve iteratively from the cubic equation $(v_c/b)^3 - 3(v_c/b)^2 - 3(v_c/b) - 1 = 0$ and given by $v_c = 3.84736$, which results in $v_c = 2.597\times10^{-3}$ m$^3$/kg for CO$_2$, which is 22% higher than the experimental value. In the last case of Peng and Robinson's equation of state, $v_c$ is solve iteratively from a similar cubic equation $(v_c/b)^3 - 3(v_c/b)^2 + 3(v_c/b) - 3 = 0$ and given by $v_c = 3.9514b$, which results in $v_c = 2.393\times10^{-3}$ m$^3$/kg for CO$_2$, which is only 12% higher than the experimental value.

Cubic equations of state are designed in a sense, owing to the determination of the coefficients $a$ and $b$ on the basis of critical-point properties, to give reasonable predictions of $pvT$-data for higher densities and lower temperatures typical of the critical-point conditions. On the other hand, they do possess the correct behaviour in the limit of low-density gases by converging to predictions of the ideal gas law. Nevertheless, they are not necessarily sufficiently flexible to give good predictions over the entire range of all densities and temperatures ranging from the critical point to ideal gas behaviour of dilute gases. One example of their deficiencies is their inability to predict the critical-point specific volume. However, cubic equations of state were the first means of including useful predictions in the vicinity of, or at least somewhat near, the critical point, the first of which was Van der Waals' equation of state. Redlich and Kwong's, Soave's and Peng and Robinson's equations of state are often used today, in spite of their deficiencies, because better equations are not available.

Cubic equations of state can be applied directly to an individual gaseous substance or indirectly to a mixture of gases. Empirical mixing rules for determining $a$ and $b$ are

$$a = \sum_{i=1}^{m} \sum_{j=1}^{m} Y_i Y_j a_{ij} \qquad \text{and} \qquad b = \sum_{i=1}^{m} Y_i b_i$$

for a nonideal gas mixture, for which $Y_i$ and $Y_j$ are the mole ratios for the mixture components $i$ and $j$, and the interaction parameter $a_{ij} = a_i a_j (1 - \delta_{ij} k_{ij})$, where $\delta_{ij}$ denotes the Kronecker delta function (1 if $i \neq j$, 0 if $i = j$) and $k_{ij}$ is usually a small experimentally determined species interaction constant for species $i$ and $j$. A good theoretical explanation for these empirical mixture rules is not available, but if the chemical structure of different components of a mixture are similar, these rules give representative mixture results.

## 2.7 Hankinson, Brobst and Thomson's Equation of State

Hankinson, Brobst and Thomson [3] developed one of the most accurate methods for predicting the properties of pure liquids that are compressed beyond the liquid saturation values. Their method is fairly involved, and it also has some unfortunate limitations, so a summary of their method in the context of this report takes some space and effort.

Hankinson, Brobst and Thomson's method is based on using one of Tait's equations of state for liquids to relate the pressure and specific volume of a liquid along a given isotherm that intersects the liquid saturation curve. Hence, the liquid temperature $T$ is specified to define the isotherm, and we must have $T$ less than the critical-point temperature $T_c$ for this isotherm to intersect the liquid saturation curve. This is the first unfortunate limitation of their method to temperatures less than $T_c$.

Once the isotherm temperature $T$ is specified, one can then obtain the corresponding vapour pressure $p_{\mathrm{sat}}$, the liquid saturation specific volume $v_{\mathrm{sat}}^{\mathrm{liq}}$ and the vapour saturation specific volume $v_{\mathrm{sat}}^{\mathrm{vap}}$ from tables of experimental data in the literature, if these tables are available. Such data from a published table in reference [3] for the specific case of $CO_2$ is reproduced in table (2) for convenient usage herein.

Although experimental values of the liquid saturation specific volume $v_{\mathrm{sat}}^{\mathrm{liq}}$ might be available in the literature, Hankinson, Brobst and Thomson's method does not rely on this particular item but instead estimates the liquid saturation volume, and this estimated volume is denoted by $v_{\mathrm{sat}*}^{\mathrm{liq}}$. Their method uses

$$v_{\mathrm{sat}*}^{\mathrm{liq}} = v_{r*} v_R^{(0)} \left(1 - \omega_* v_R^{(\delta)}\right) , \tag{15}$$

for which a number of new parameters needs to be defined.

| | |
|---|---|
| $v_1^{(0)}$ | $-1.52816$ |
| $v_2^{(0)}$ | $1.43907$ |
| $v_3^{(0)}$ | $-0.81446$ |
| $v_4^{(0)}$ | $0.190454$ |
| $v_0^{(\delta)}$ | $-0.296123$ |
| $v_1^{(\delta)}$ | $0.386914$ |
| $v_2^{(\delta)}$ | $-0.0427258$ |
| $v_3^{(\delta)}$ | $-0.0480645$ |
| $v_4^{(\delta)}$ | $1.00001$ |

| | |
|---|---|
| $\alpha_0$ | $0.0861488$ |
| $\alpha_1$ | $0.0344483$ |
| $\beta_0$ | $1.0$ |
| $\beta_1$ | $-9.070217$ |
| $\beta_2$ | $62.45326$ |
| $\beta_3$ | $-135.1102$ |
| $\beta_4$ | $4.79594$ |
| $\beta_5$ | $0.250047$ |
| $\beta_6$ | $1.14188$ |

Table 5: Values of nondimensional constants used with Hankinson, Brobst and Thomson's equation for predicting compressed liquid properties.

In equation (15), $\omega_*$ denotes a special acentric factor that forces Soave's equation of state to fit experimental or other vapour-pressure data [3]. This acentric factor is available in the literature for many substances; $\omega_*^{CO_2} = 0.2374$ for $CO_2$ [3], which is close to the standard acentric factor $\omega^{CO_2} = 0.2390$. If $\omega_*$ are unavailable in the literature, then it should be replaced by the standard acentric factor $\omega$.

In equation (15), the nondimensional parameters $v_R^{(0)}$ and $v_R^{(\delta)}$ are calculated by

$$\begin{aligned} v_R^{(0)} &= 1 + v_1^{(0)}(1 - T_{r*})^{\frac{1}{3}} + v_2^{(0)}(1 - T_{r*})^{\frac{2}{3}} \\ &\quad + v_3^{(0)}(1 - T_{r*}) + v_4^{(0)}(1 - T_{r*})^{\frac{4}{3}} \qquad \text{if} \quad 0.25 < T_{r*} < 0.95\,. \end{aligned} \tag{16}$$

$$v_R^{(\delta)} = \frac{v_0^{(\delta)} + v_1^{(\delta)}T_{r*} + v_2^{(\delta)}T_{r*}^2 + v_3^{(\delta)}T_{r*}^3}{T_{r*} - v_4^{(\delta)}} \qquad \text{if} \quad 0.25 < T_{r*} < 1.0\,, \tag{17}$$

and the corresponding nondimensional coefficients are listed in table (5). In these equations, $T_{r*} = T/T_{c*}$ is a special reduced temperature in which $T_{c*}$ is a theoretical critical-point temperature that can differ slightly from the experimental value $T_c$. From tables in reference [3], $T_{c*}^{CO_2} = 304.15$ K for the case of $CO_2$, which differs slightly from $T_c^{CO_2} = 304.19$ K. If $T_{c*}$ is unavailable from the literature, then it may be replaced the experimental value $T_c$. We note that equation (16) is valid only in the range $0.25 < T_{r*} < 0.95$, which places unfortunate limits the method of Hankinson, Brobst and Thomson.

In equation (15), $v_{c*}$ is the theoretical volume of the pure liquid at the critical point, and it is available for several substances in the literature [1]. For the specific case of $CO_2$, $v_{c*}^{CO_2} = 2.131 \times 10^{-3}$ m$^3$/kg, which is slightly lower than the experimental critical-point value of $v_c^{CO_2} = 2.136\times10^{-3}$ m$^3$/kg. If $v_{c^*}$ is unavailable in the literature, it may be replaced by the experimental critical-point specific volume $v_c$.

The specification of the liquid saturated specific volume for an isotherm specified by temperature $T$ and at the vapour pressure $p_{sat}$ is now done. To obtain the compressed liquid volume on the same isotherm at a higher pressure $p$. Hankinson, Brobst and Thomson's method uses one of Tait's equations specialized for pur liquids, which is a relationship between the liquid pressure and volume on an isotherm. Their generalize equation is

$$v = v_{sat}^{liq}\left[1 - \alpha \ln\left(\frac{p - \beta p_c}{p_{sat} - \beta p_c}\right)\right] \tag{18}$$

for the case when the volume $v$ is a function of the pressure $p$, and as

$$p = \beta p_c + (p_{sat} - \beta p_c)\exp\left[\frac{1}{\alpha}\left(1 - \frac{v}{v_{sat}^{liq}}\right)\right] \tag{19}$$

for the opposite case when the pressure is a function of the volume $v$. In equations (18) and (19), $v_{sat}^{liq}$ is the liquid saturation specific volume given by table (2) or equation (15), $p_{sat}$ is the vapour pressure at temperature $T$ from table (2), $p_c$ is the experimental critical-point pressure, and the nondimensional parameters $\alpha$ and $\beta$ are defined as

$$\begin{aligned} \alpha &= \alpha_0 + \alpha_1\omega_* \,, \\ \beta &= \beta_0 - \beta_1(1-T_{r^*})^{1/3} - \beta_2(1-T_{r^*})^{2/3} - \beta_3(1-T_{r^*}) \\ &\quad - \exp\left(\beta_4+\beta_5\omega_*+\beta_6\omega_*^2\right)(1-T_{r^*})^{4/3} \,, \end{aligned} \tag{20}$$

in which the special reduced temperature $T_{r^*}$ has been previously, and the nondimensional coefficients are listed in table (5). In spite of $v_{sat}^{liq}$ not being linked to tablulated data in table (2), we observe that the use of the vapour pressure $p_{sat}$ is inherently linked to table (2). This is an unfortunate limitation of using the method of Hankinson, Brobst and Thomson.

Hankinson. Brobst and Thomson's method of predicting the volume of compressed liquids is valid only for the limited range of reduced temperatures given by $0.25 < T_r < 0.90$ However, within this range the compressed liquid volume or the resulting compressed liquid pressure are given accurately by equations (15) and (19).

## 2.8 Comparison of Results from Different Equations of State

Well-known. classical equations of state have been introduced previously in this chapter and also reviewed in regards to their analytical form. These equations of state are now compared graphically in terms of selected plots of pressure versus specific volume and temperature in figures (2-18) distributed over pages 27–43. Also included in these figures are experimental data for $CO_2$ [9] to facilitate comparisons of results from different equations of state and experimental data, and these comparisons also facilitate the ensuing discussion.

The presentation of results in figures (2–18) is organized in the following manner. Because the equations of state are explicit in terms of the pressure and implicit in terms of the specific volume and temperature, the results of these different equations of state are given for comparison purposes in terms of two-dimensional plots of pressure versus specific volume for a constant temperature (isotherm) in figures (2–13), and separately in terms of two-dimensional plots of pressure versus temperature for a constant specific volume (isochor) in figures (14–18). Three dimensional graphs of pressure versus both specific volume and temperature are not presented because the data would be too complex and cluttered.

The data are also presented in four main groups consisting of *(a)* pressure-volume graphs for gases at low to moderate densities, *(b)* pressure-volume graphs for liquids (at liquid densities), *(c)* pressure-volume graphs for vapours and liquids in equilibrium at densities typical of the critical-point density, and *(d)* pressure-temperature graphs for vapours and liquids in equilibrium at densities typical of the critical-point density. A fifth grouping consists of seven graphs showing the errors between measured $pvT$ data for $CO_2$ and predictions by different equations of state; these are presented in figures (19–25) mainly for interest.

Comparisons of various equations of state (EOS) for the case of gases at low to moderate densities and constant temperatures of 400, 600, 1000, 1400 and 1800 K are given in figures (2–6), respectively, on pages 27–31. From this first set of results, one sees that the ideal gas law overpredicts the pressure at low temperatures (under 600 K) in comparison to the experimental data, predicts the pressure well at a temperature of 600 K, and underpredicts the experimental data more and more at increasing temperatures (greater than 600 K). This illustrates that the ideal gas law has severe limitations, stemming primarily from not including the effects of either molecular repulsion and attraction), although this law can certainly be used as a first approximation to predict the behaviour of real gases, especially for the case of low densities

The Clausius equation of state fails rather badly at low temperatures (under 600 K), because molecular attraction is ignored. However, this equation, despite its simplicity, is remarkably good for temperatures greater than 600 K, where molecular repulsion becomes most important. The agreement is almost exact for the case of isotherms of 1400 and 1800 K given in figures (5-6)

The two virial equations of state (i.e., Beattie and Brideman's and the truncated virial equation) give better predictions than the perfect gas law and Clausius' equation of state, primarily because they include the effects of both molecular repulsion and attraction. The truncated virial equation of state is almost exact for increasing temperatures (above 600 K), whereas the Beattie and Bridgeman's equation represents the experimental data accurately only for the mid-tempeature range. At low temperatures (less than 600 K) these two equations of state represent the experimental data accurately only if the specific volume is larger than five times the critial volume.

Predictions by cubic equations of state (i.e., Van der Waals', Redlich and Kwong's, Soave's, Peng and Robinson's) are all similar for the case of high temperatures and large specific volumes. However, the basic trends that emerge are as follows: *(a)* both Van der Waals' and Redlich and Kwong's equations underpredict the pressure, *(b)* Soave's equation of state overpredicts the pressure, and *(c)* Peng and Robinson's equation of state is almost exact for all of the temperatures and specific volumes given in figures (2–6).

Comparisons of various equations of state for the case of liquids at compressed liquid densities and constant temperatures of 240, 260, 280 and 300 K are given in figures (7–10), respectively, on pages 32–35. From this second set of results, the cubic equations of state and the technique of Hankinson, Brobst and Thomson are most applicable in obtaining predictions of the pressure of compressed liquids. Hence, results from these equations of state are the only ones shown in the figures. Van der Waals equation of state is also excluded because it does not yield good results.

The technique of Hankinson, Brobst and Thomson gives the best agreement with the experimental data for $CO_2$, except for temperatures higher than 280 K. This might have been expected because the results in figure (7) for 300 K exceed range of applicability ($T_r < 0.95$) of their equation of state for saturated and compressed liquids.

Redlich and Kwong's and Soave's equations of state give similar results in that the predictions lie on the right side of the experimental data, but Soave's equation is generally in better agreement. Peng and Robinson's equation of state give results that lie on the left side of the experimental data, with about the same margin of error as the predictions of Soave's results.

Comparisons of various equations of state for the case of gases and liquids in equilibrium at near critical-point densities and constant temperatures of 280, 290 and 300 K are given in figures (11-13), respectively, on pages 36-38. In addition to the data for liquid $CO_2$ the saturation line for $CO_2$ is also shown (dotted). From this third set of results, the ideal gas law, Clausius' equation of state, and the virial equations of state all fail to give good estimations of vapour and liquid equilibria data. Van der Waals' equation of state is at best an approximation. Peng and Robinson's equation of state is nearly exact for lower temperatures (less than 290 K), whereas Redlich and Kwong's and Soave's equations of state deviate quite noticeably from the experiental data. All of the cubic equations of state tend to predict pressures higher than the experimental data. This becomes worse for higher temperatures that approach the critical point (304.19 K), especially on the liquid side of the saturation line.

Comparisons of various equations of state in terms of pressure versus temperature for constant specific volumes of 0.90, 2.136, 3.00, 7.50 and 15.0 $m^3/kg$ are presented in figures (14-18), respectively, on pages pages 39-43. From this fourth set of results, we see that the ideal gas law and the Clausius' equation of state do not yield any useful results for the cases of low specific volumes of 0.90 and $2.136\times10^{-3}$ $m^3/kg$, corresponding to compressed liquids and critical-point values, because these equations of state do not apply to compressed liquids ($0.90\times10^{-3}$ $m^3/kg$) or directly at the critical point ($2.136\times10^{-3}$ $m^3/kg$). These equations give more accurate predictions in comparison to experimental data for $CO_2$ only in the range of large specific volumes (above five times the critical volume of $2.136\times10^{-3}$ $m^3/kg$) and for higher temperatures (above 400 K). Similar remarks can also be made concerning the virial equations of state, except that the limit of applicability in regards to the specific volume is somewhat lower, that is about three to four times the critical volume of $2.136\times10^{-3}$ $m^3/kg$.

Errors between measured pressure data for $CO_2$ and predictions from different equations of state are presented in figures (19-25). The results in these graphs help illustrate the magnitude of the error and some trends of these errors for various equations of state. Figures (19-22) contain results for the case when pressure is plotted versus specific volume for isotherms with $T$ = 400 600, 1000 and 1800 K, respectively, whereas figures (23-25) contain other results when the pressure is plotted versus temperature for isochors with $v$ = 3.0, 7.5 and $15\times10^{-3}$ $m^3/kg$, respectively. From these results in figures (19-22), one can see that errors in the pressure from 1 to 5% are typical for when the specific volume is large, whereas from figures (23-25) one sees that these errors are much higher at 5 to 20%

for the case of small specific volumes of saturated and compressed liquids.

Only the cubic equations of state give reasonable results for specific volumes equal to and smaller than the critical volume; see the results in figures (15 and 16). Soaves' and Redlich and Kwong's equations of state represent the experimental data best. However, Redlich and Kwong's equation-of-state predictions are better for lower temperatures and pressures, whereas the better accuracy shifts to Soave's equation of state as the pressure increases.

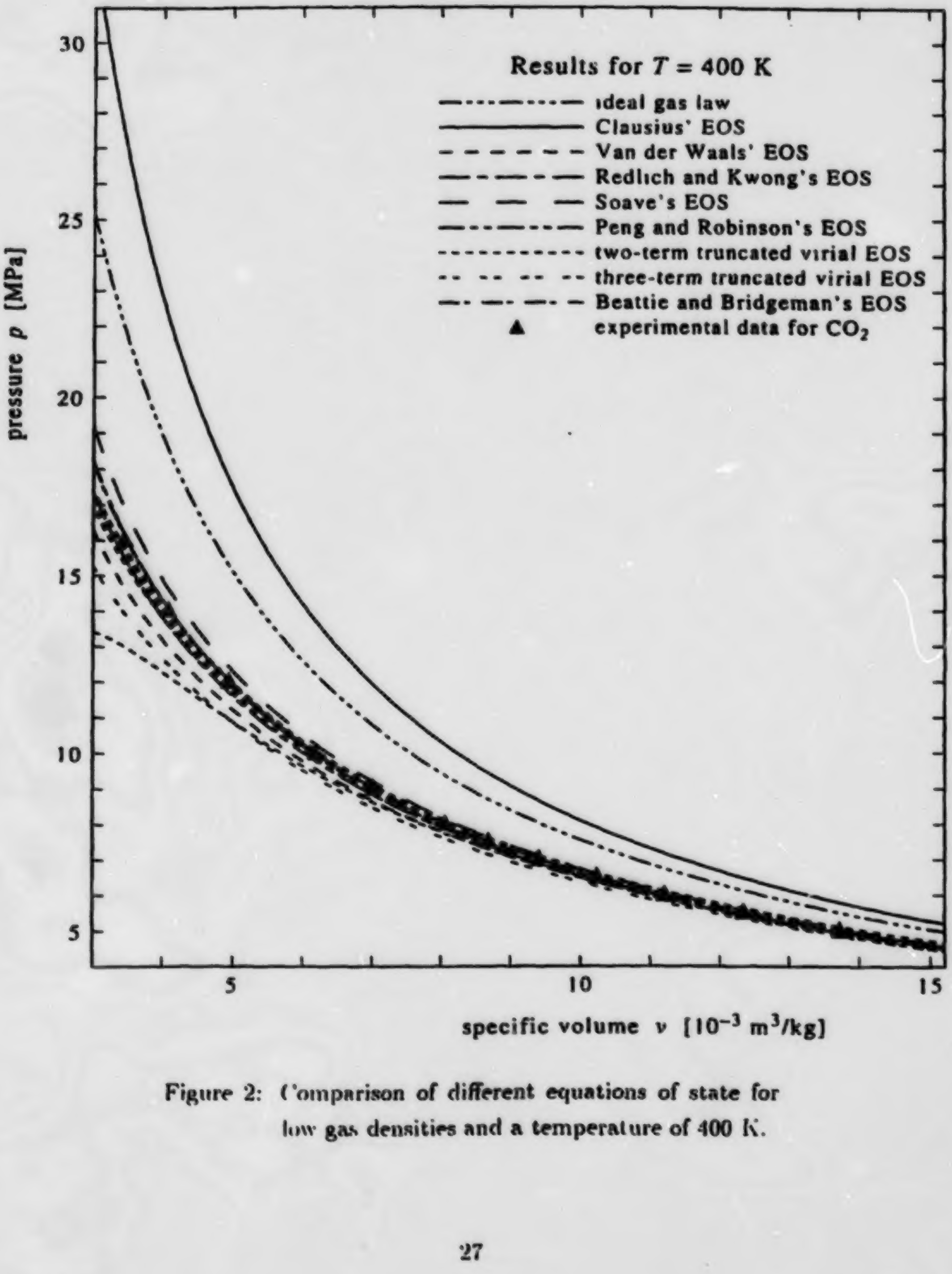

Figure 2: Comparison of different equations of state for low gas densities and a temperature of 400 K.

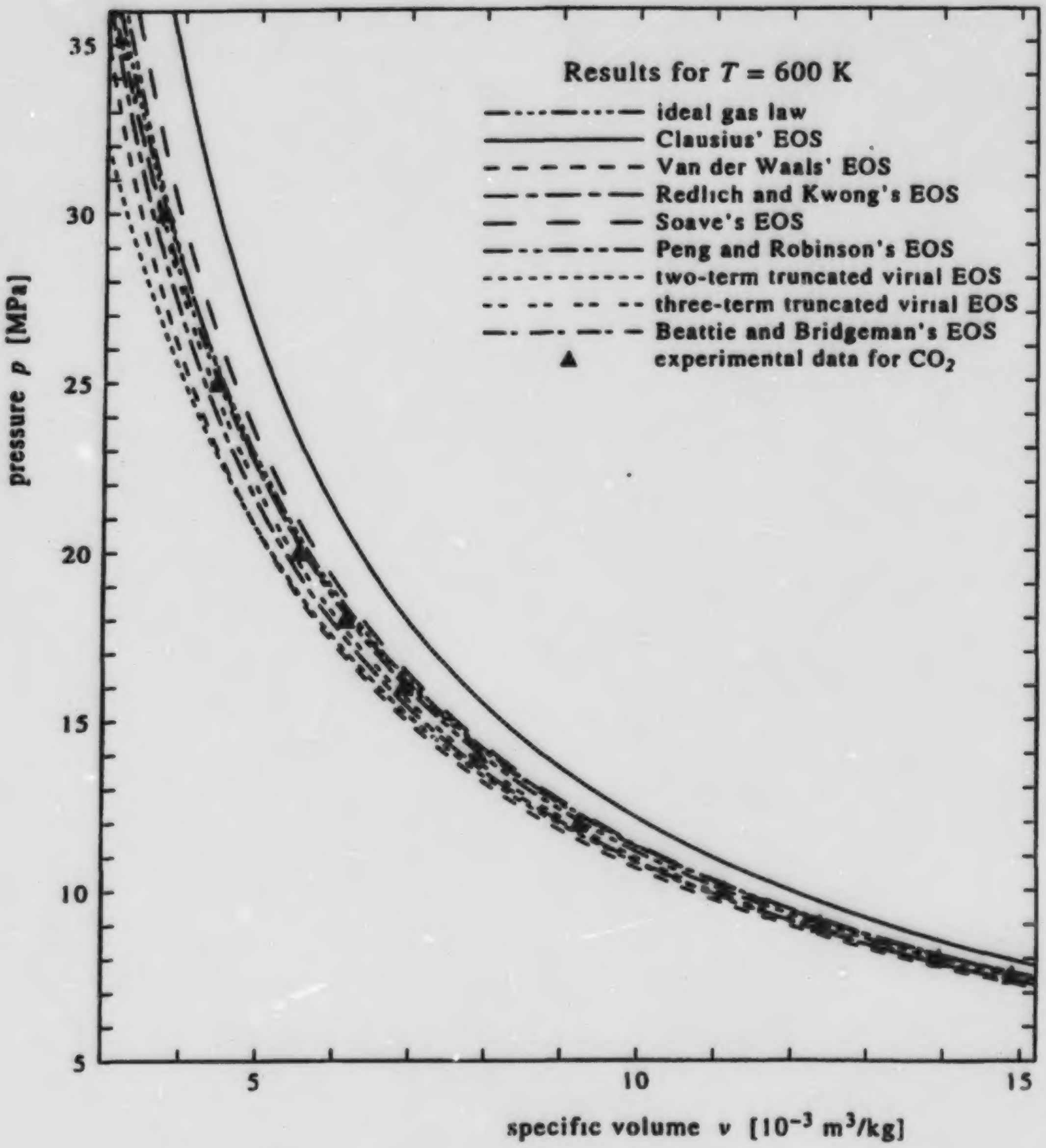

Figure 3: Comparison of different equations of state for low gas densities and a temperature of 600 K.

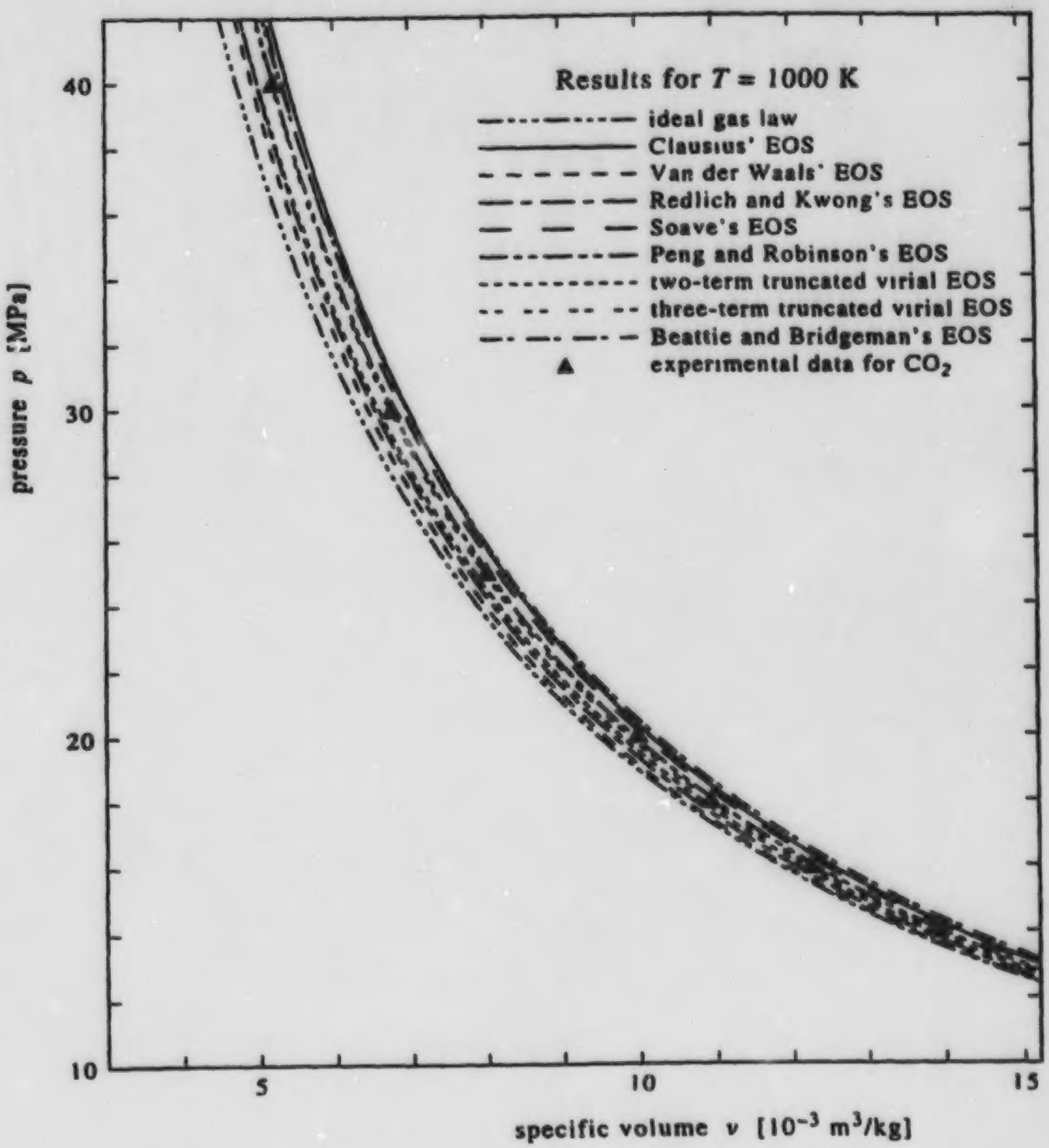

Figure 4: Comparison of different equations of state for low gas densities and a temperature of 1000 K.

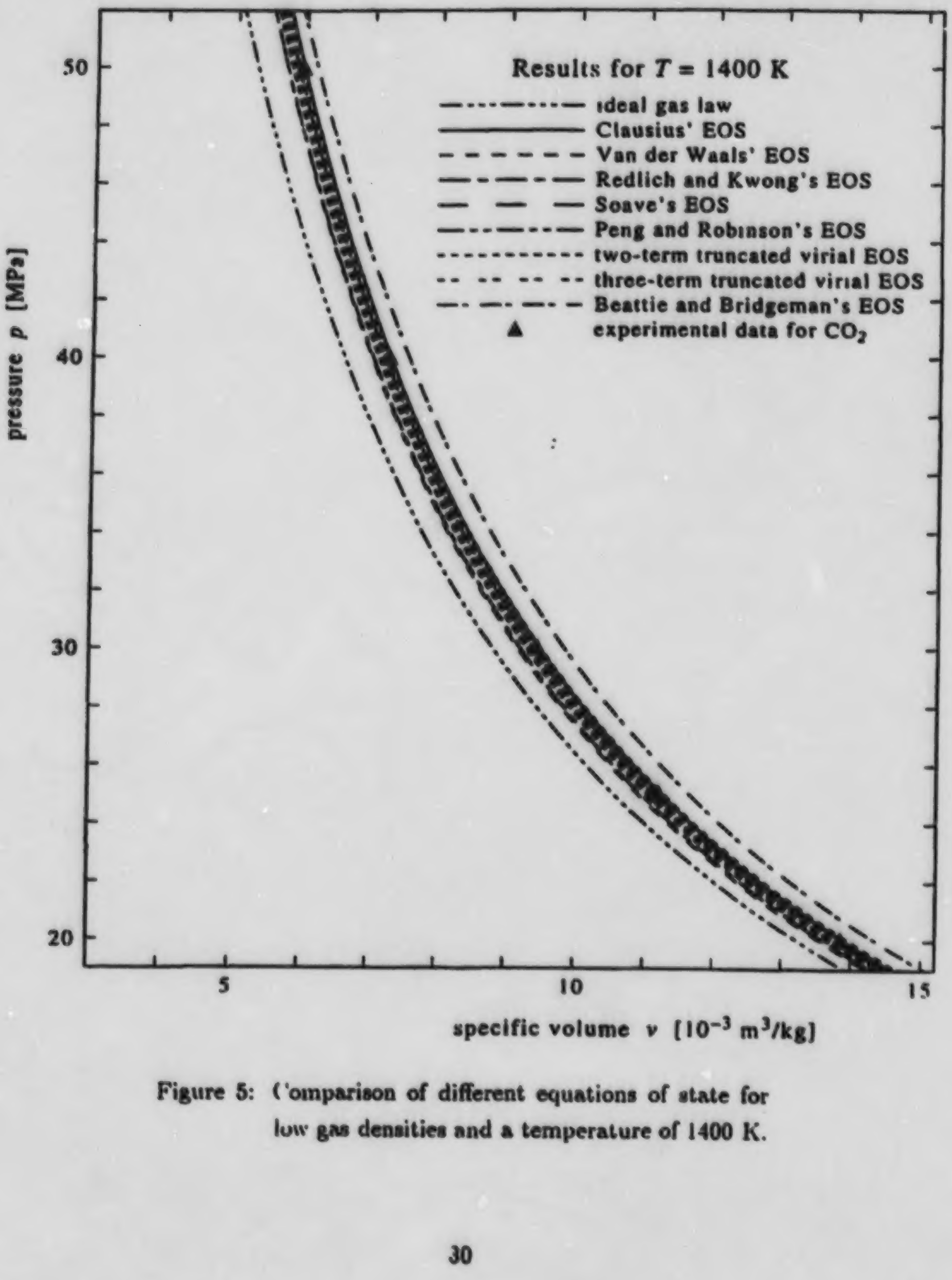

Figure 5: Comparison of different equations of state for low gas densities and a temperature of 1400 K.

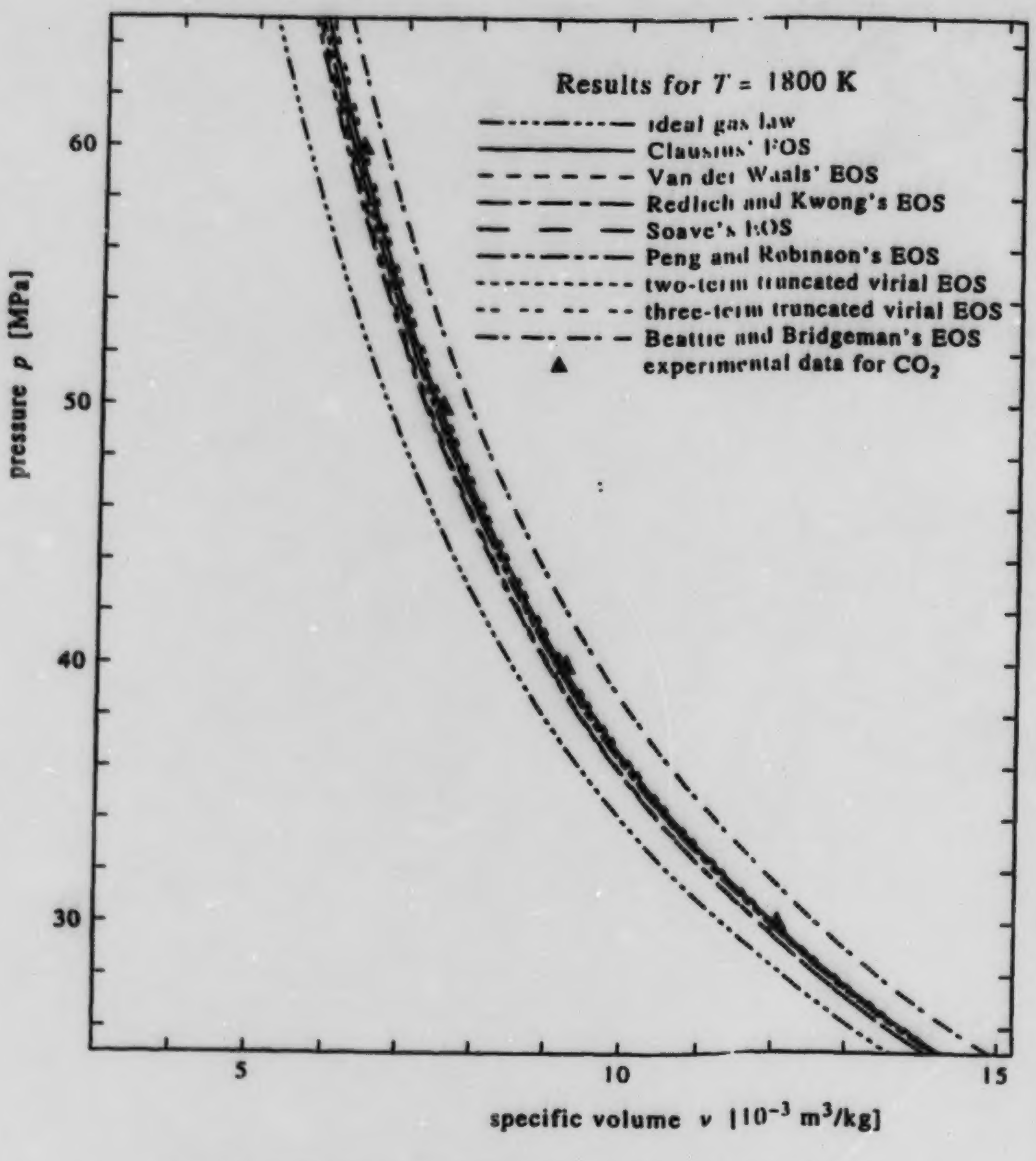

Figure 6: Comparison of different equations of state for low gas densities and a temperature of 1800 K.

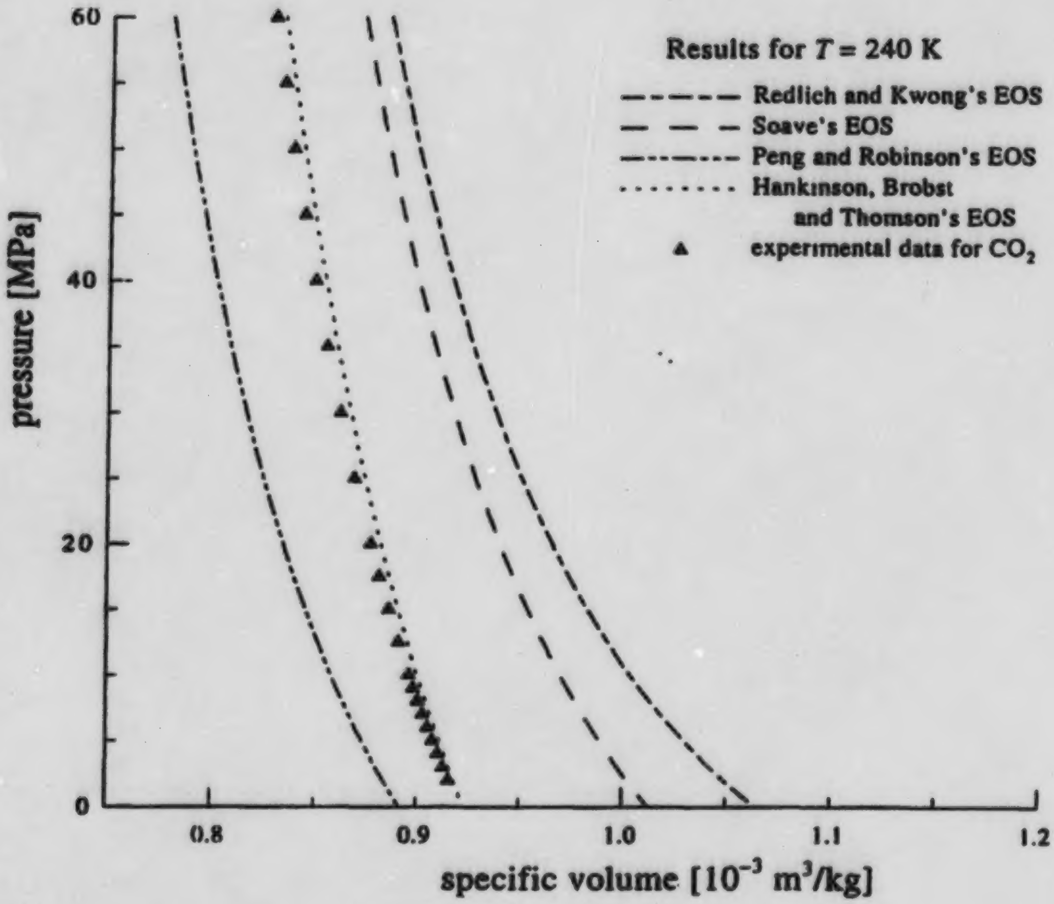

Figure 7: Comparison of different equations of state for near liquid densities and a temperature of 240 K.

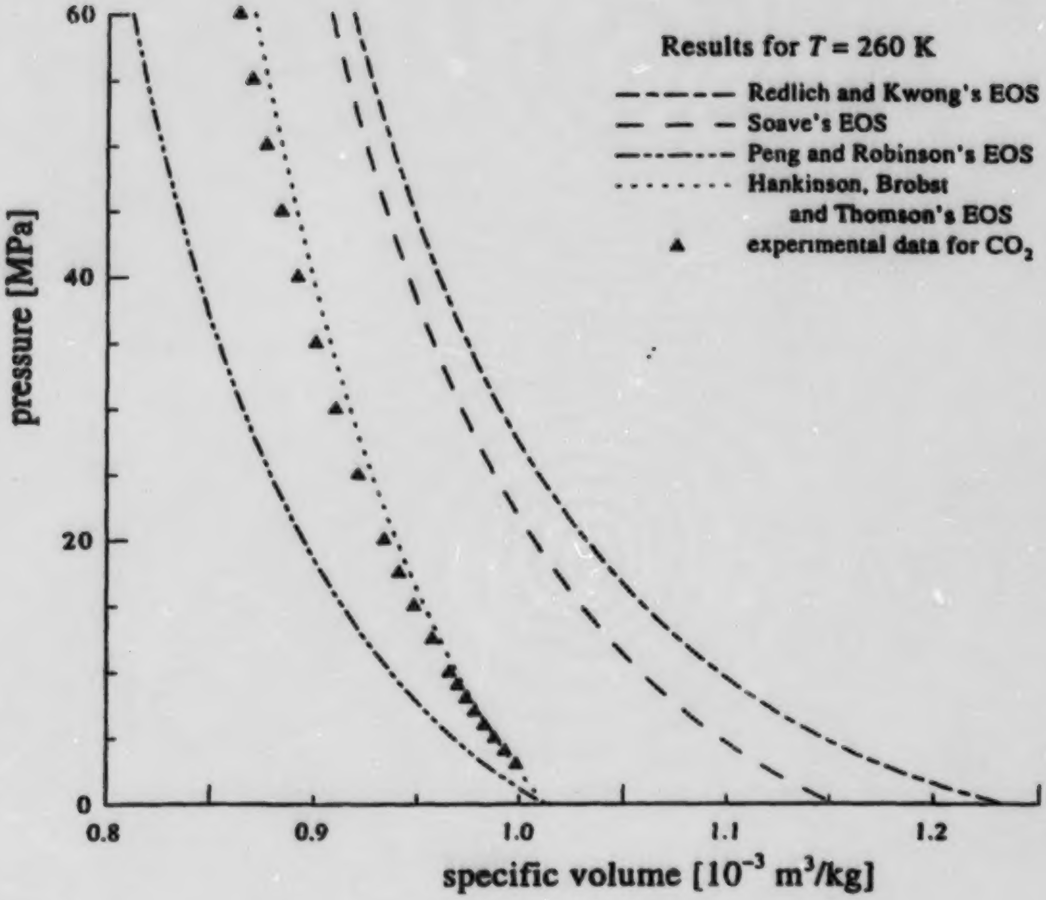

Figure 8: Comparison of different equations of state for near liquid densities and a temperature of 260 K.

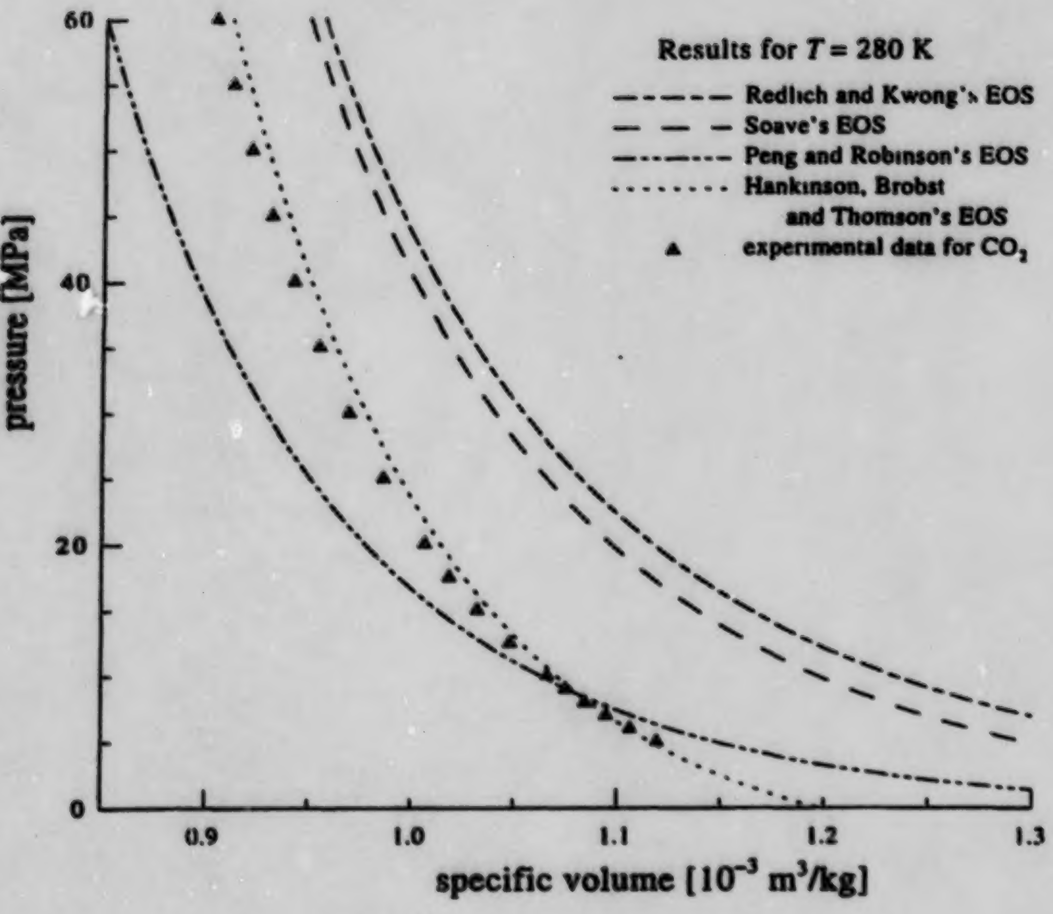

Figure 9: Comparison of different equations of state for near liquid densities and a temperature of 280 K.

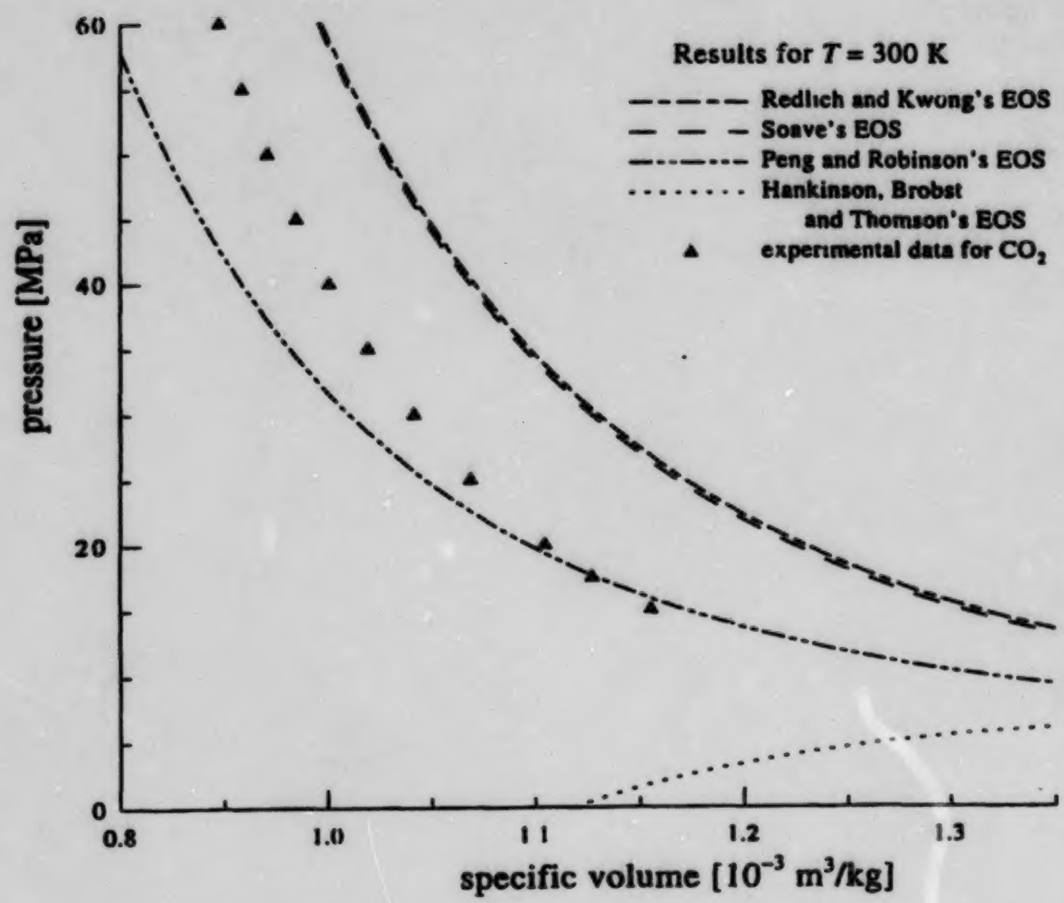

Figure 10: Comparison of different equations of state for near liquid densities and a specific volume of 300 K.

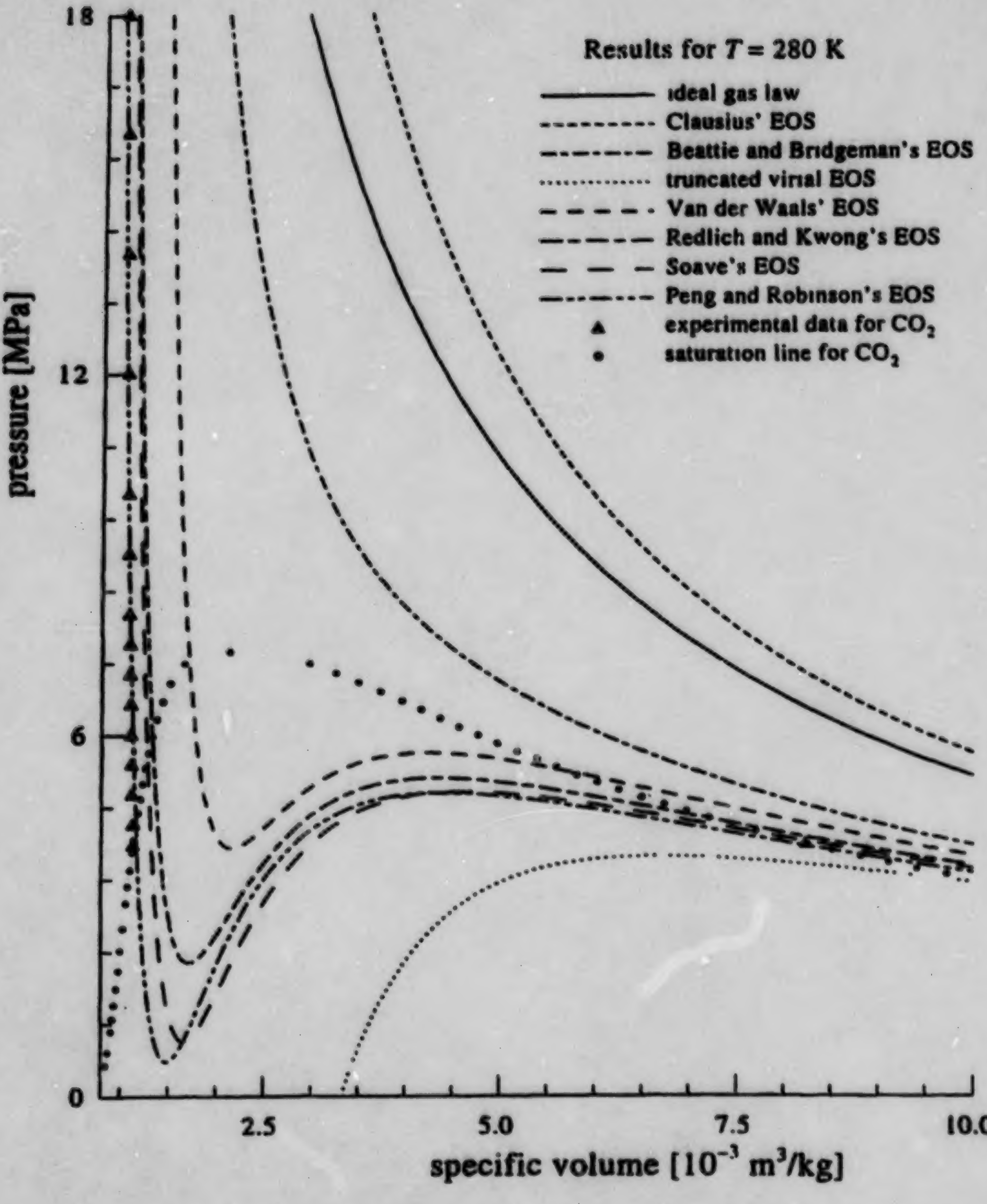

Figure 11: Comparison of different equations of state for near critical-point densities and a temperature of 280 K.

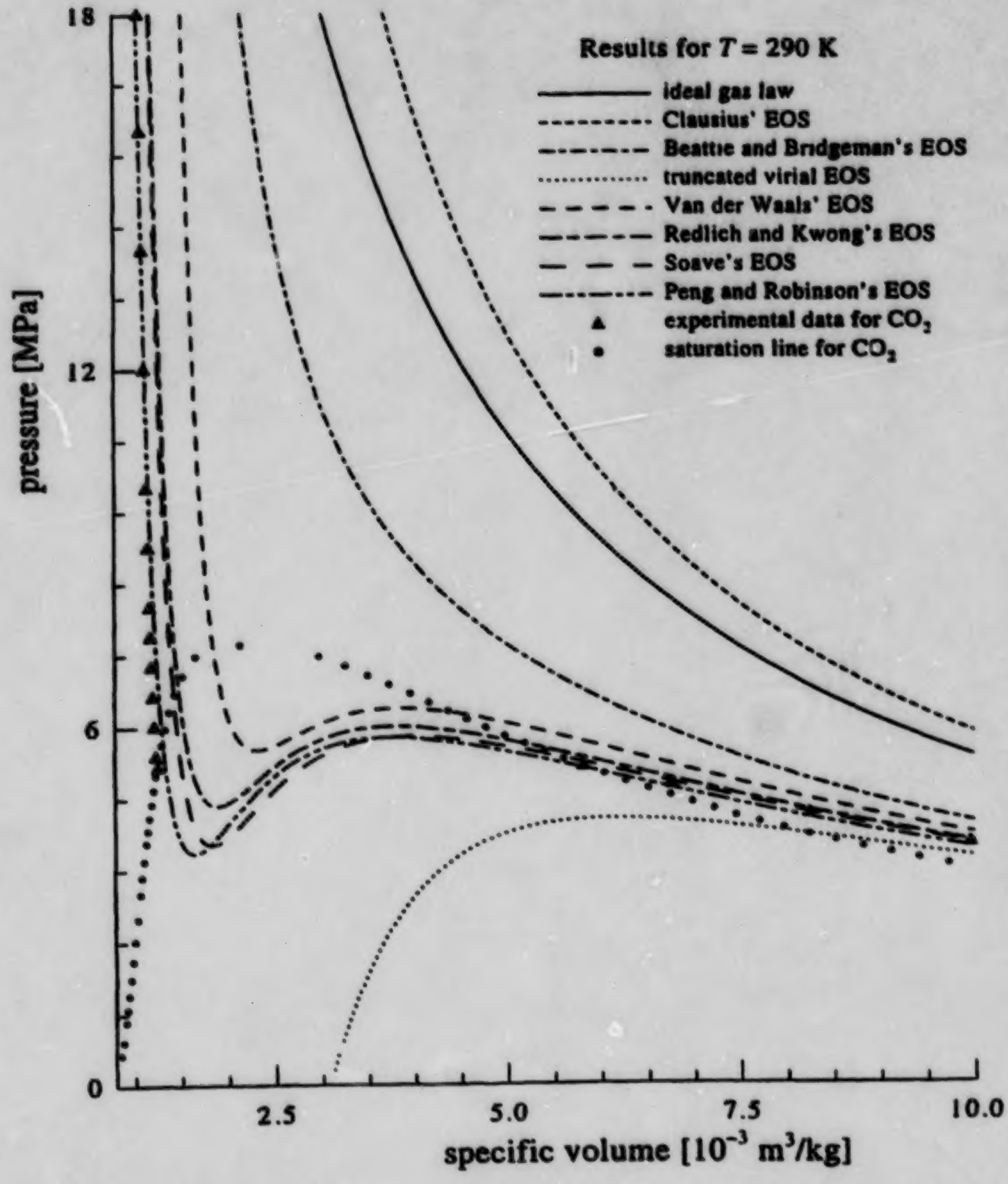

Figure 12: Comparison of different equations of state for near critical-point densities and a temperature of 290 K.

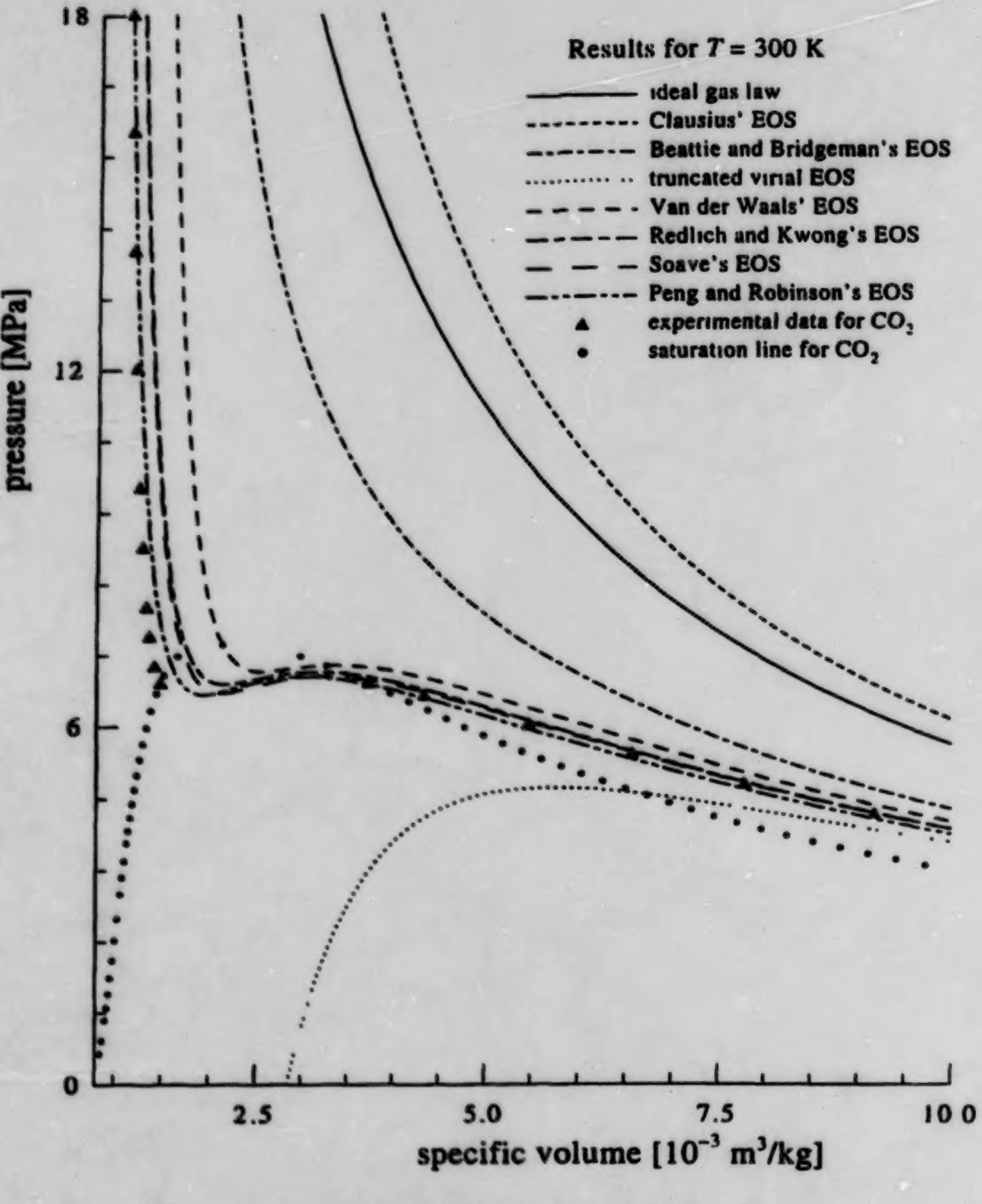

Figure 13: Comparison of different equations of state for near critical-point densities and a temperature of 300 K.

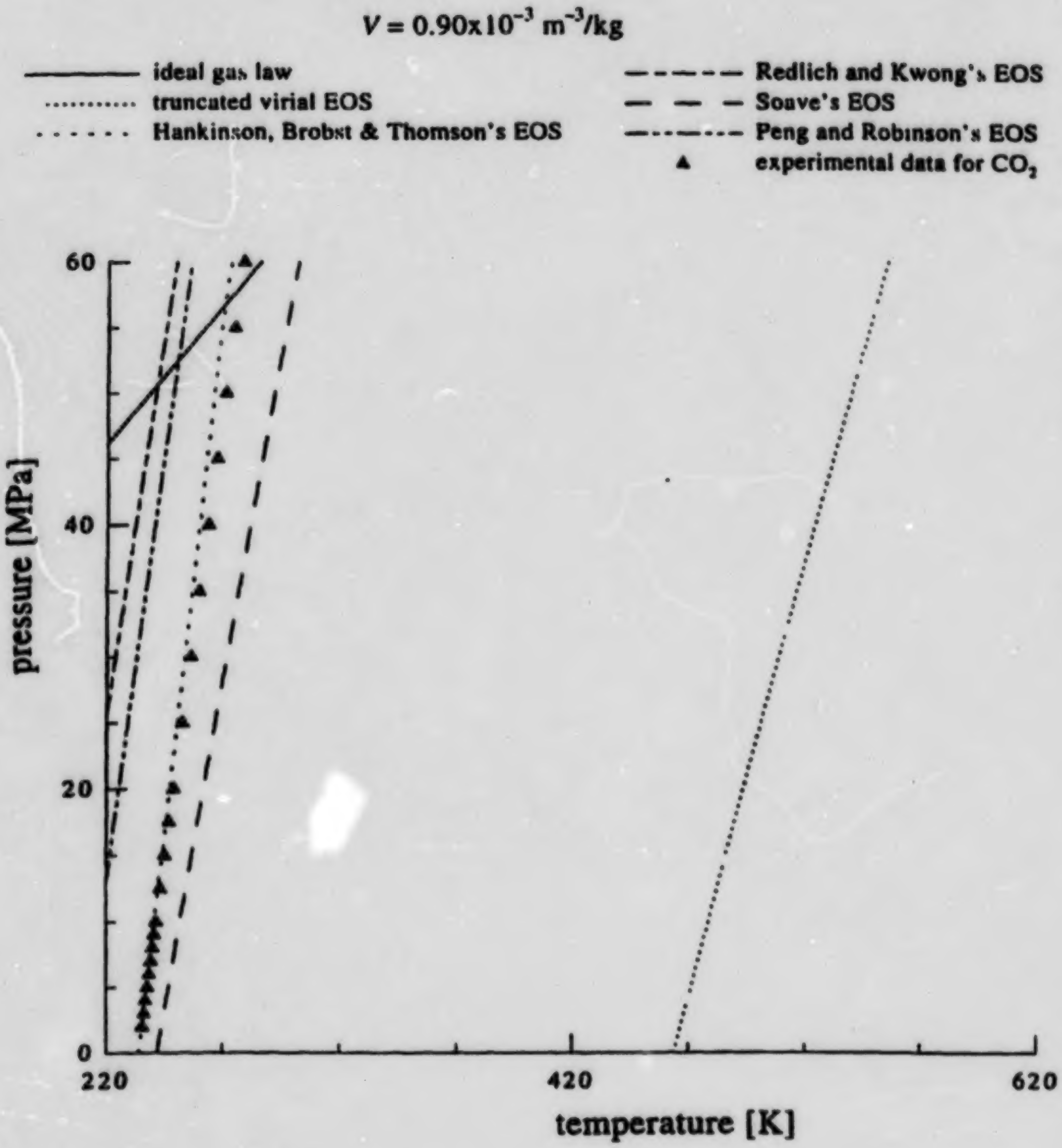

Figure 14: Comparison of different equations of state for a specific volume of $0.90 \times 10^{-3}$ m$^3$/kg.

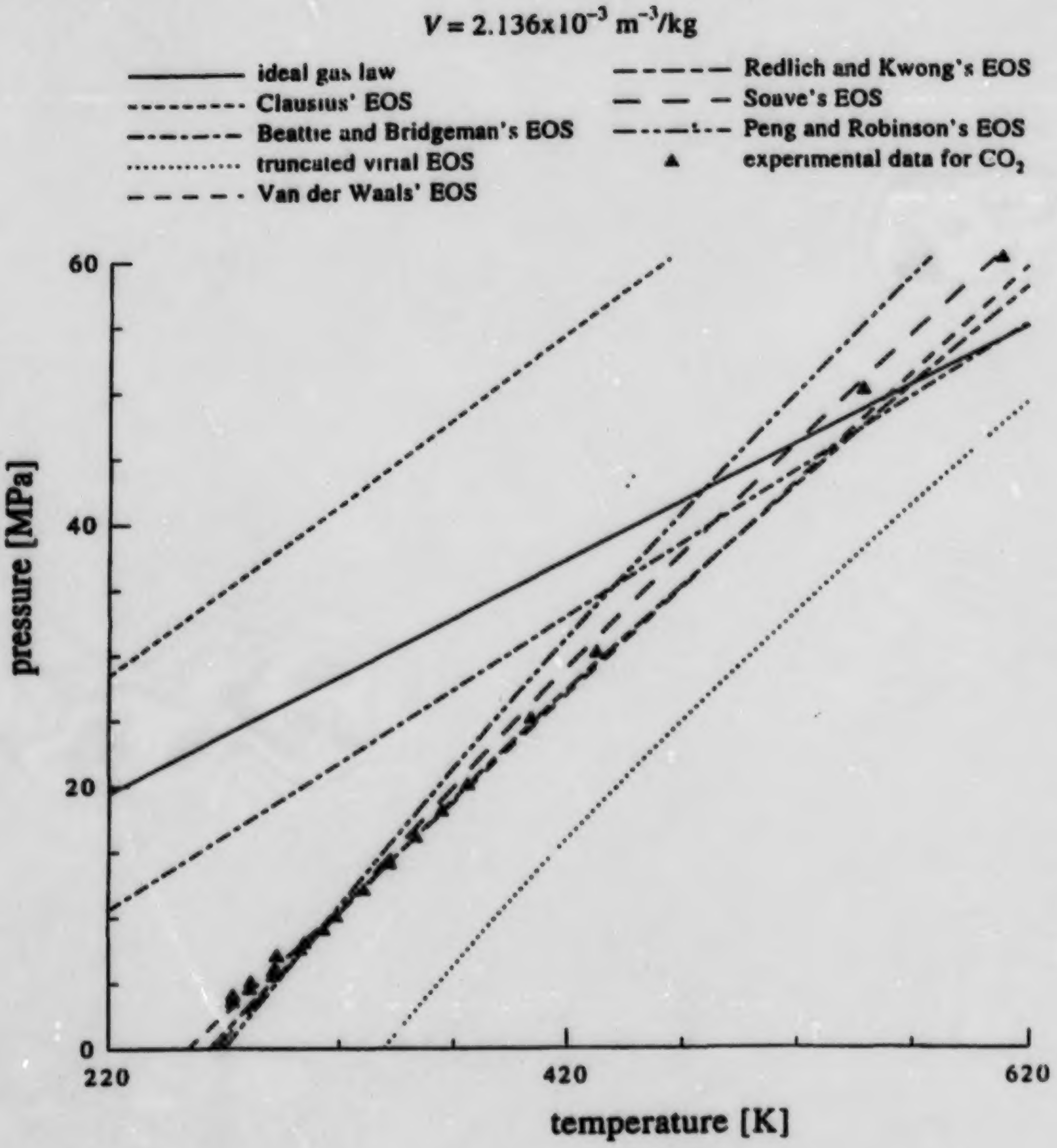

Figure 15: Comparison of different equations of state for a specific volume of $2.136 \times 10^{-3}$ m$^3$/kg.

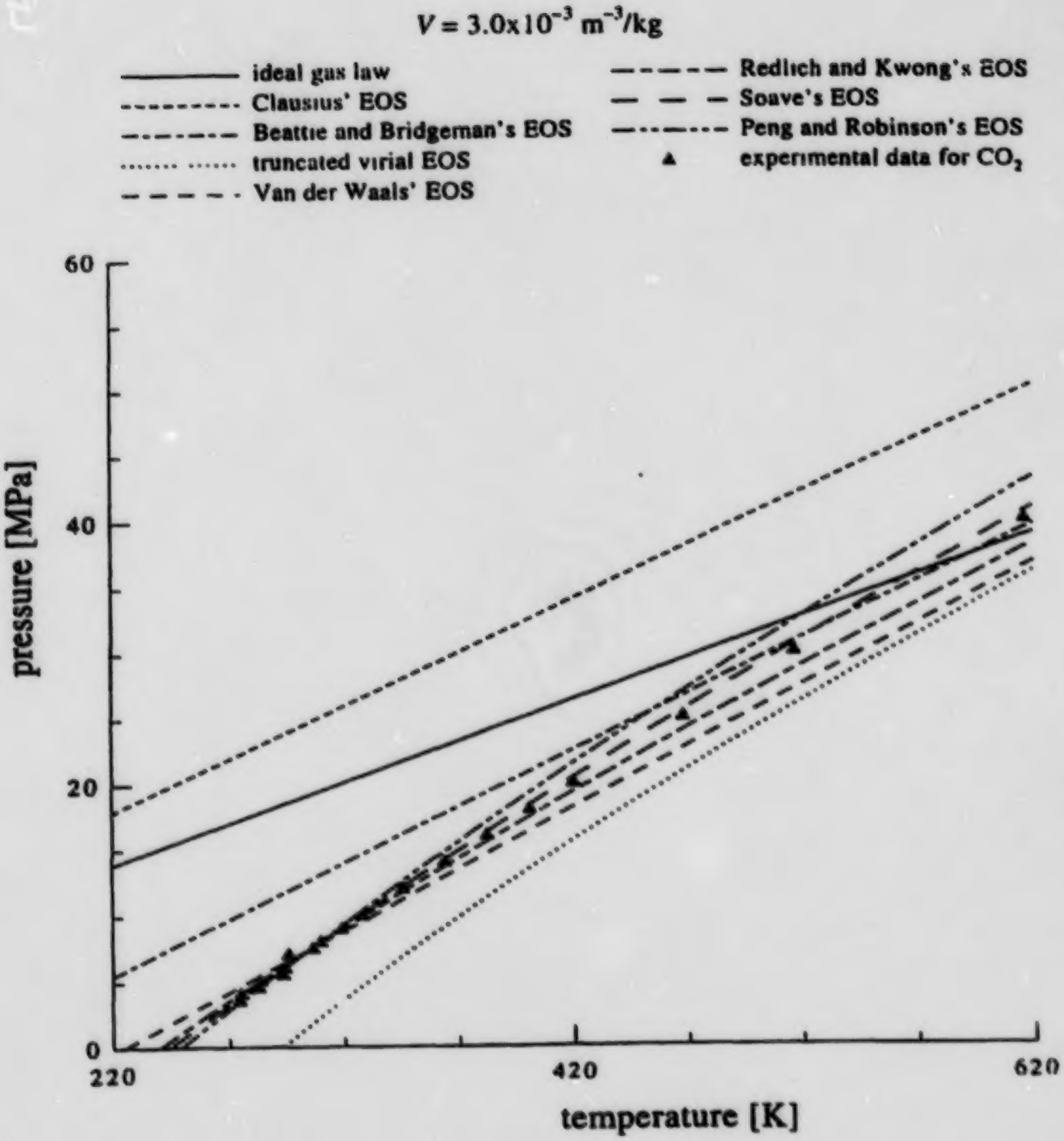

Figure 16: Comparison of different equations of state for a specific volume of $3.00\times10^{-3}$ m$^3$/kg.

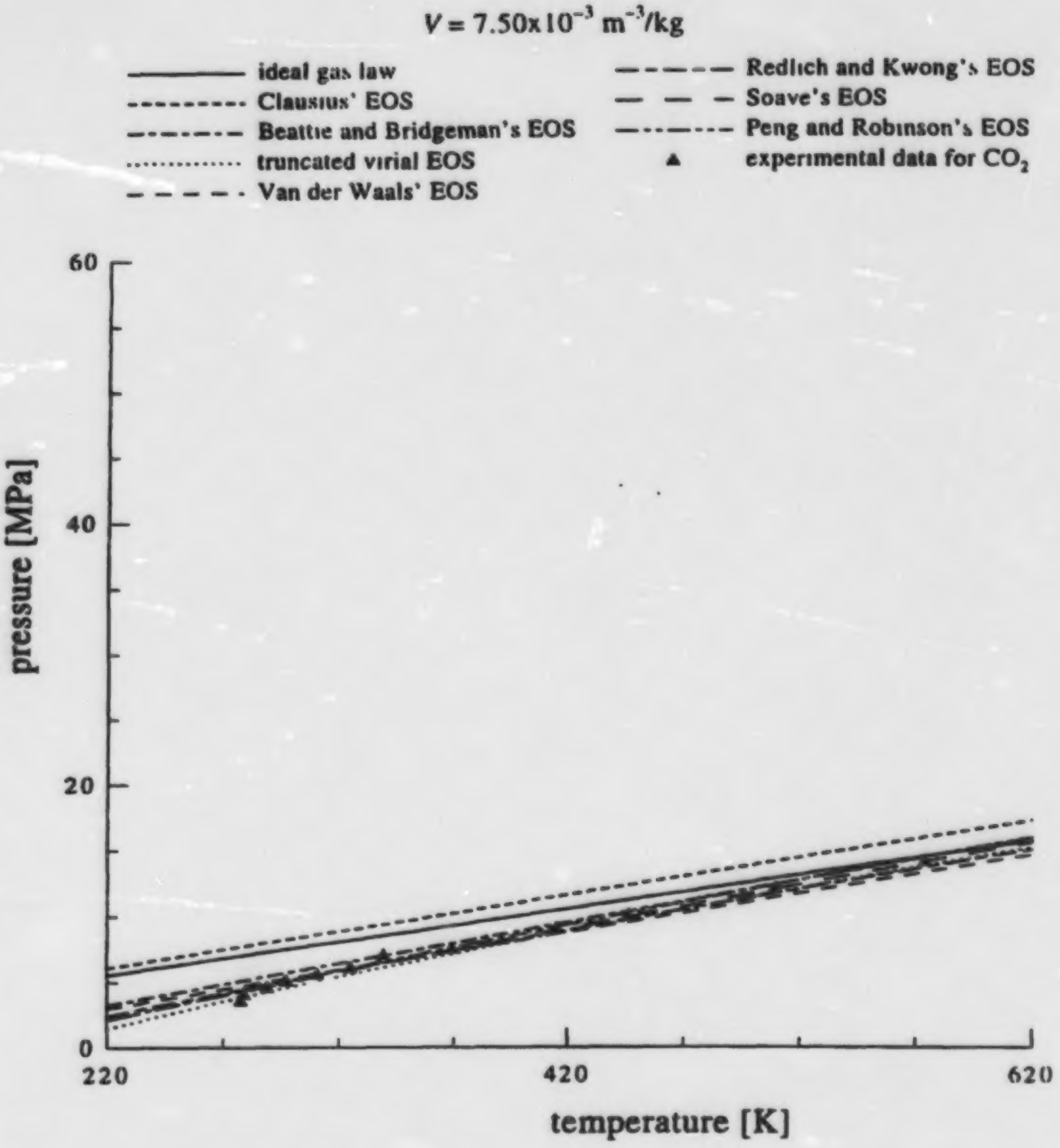

Figure 17: Comparison of different equations of state for a specific volume of $7.50\times10^{-3}$ m$^3$/kg

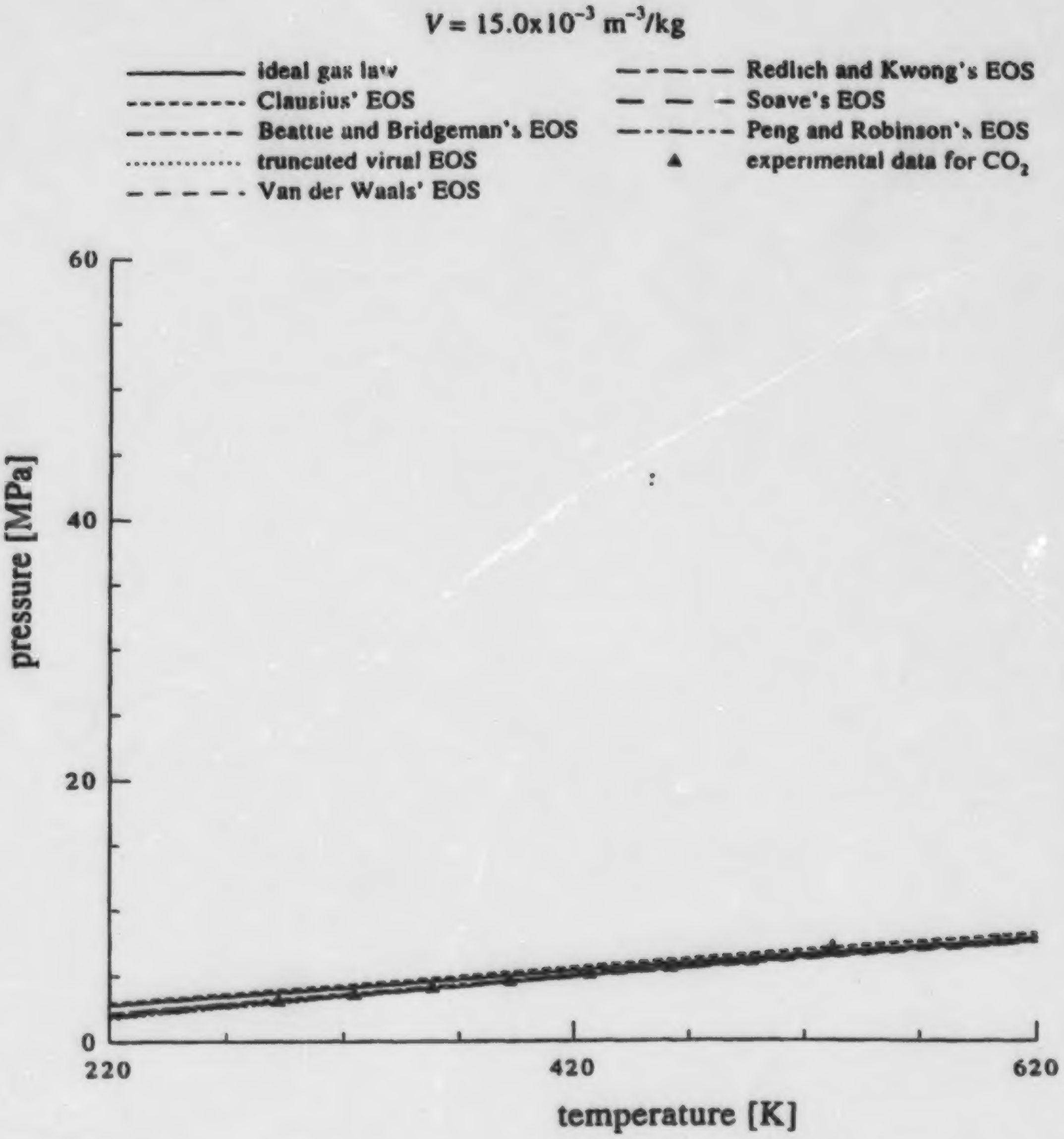

Figure 18: Comparison of different equations of state for a specific volume of $15.0 \times 10^{-3}\ m^3/kg$.

## 2.9 Summary of Results for Different Equations of State

The results of comparing different equations of state and exprimental data for $CO_2$ are summarized below:

- The ideal gas law gives good predictions of gas properties only when the gas density is low. Hence, realistic pressure-volume-temperature ($pvT$) properties of real substances like $CO_2$ at moderate densities can be predicted only as a first approximation, and predicted $pvT$ properties at densities near the critical-point value are hopelessly inaccurate.
- The Clausius equation of state gives better predictions of $pvT$ properties than the ideal gas law, that is it is applicable for the case of lower specific volumes and higher temperatures. Like the ideal gas law, Clausius' predicted $pvT$ data at densities near the critical-point value are also hopelessly inaccurate.
- Beattie and Bridegeman's equation of state gives good $pvT$ predictions only for a medium range of temperatures for $CO_2$ typical of atmospheric conditions (summer and winter). Predictions for substances other than carbon dioxide, like hydrocarbons used in the petroleum industry, may be more accurate over a wider range of temperatures and specific volumes.
- The truncated virial equation gives accurate results for gaseous $pvT$ properties for specific volumes larger than $3v_c$, and this is especially true for increasing temperatures.
- Van der Waals' equation of state makes a first attempt in predicting $pvT$ properties over the range of densities from liquids and gases. However, the results are not accurate for densities approaching the critical-point value, so this equation of state cannot be taken seriously for practical useage.
- Redlich and Kwong's equation of state is reasonably accurate in predicting $pvT$ properties over a wide range of densities from that of liquids to fairly dilute gases, and also for the case of low to high temperatures. However, fairly high deviations from experimental data for liquid-density conditions must be tolerated
- Soave's equation of state is an improvement of Redlich and Kwong's equation of state, and $pvT$ properties are predicted more accurately, expecially at increasing temperatures and pressures. However, these are only marginal improvements.

- Peng and Robinson's equation of state covers the whole range of volumes and temperatures from compressed liquids to dilute gases, and predictions of $pvT$ properties is fairly good, even for the case of saturated conditions. However, Peng and Robinson's equation does not have the desired uniform accuracy for all $pvT$ conditions.
- Hankinson, Brobst and Thomson's technique of predicting the properties of saturated and compressed liquids is remarkable. However, this equation of state is highly specialized for saturated and compressed liquids in a restricted range of reduced temperatures (i.e., $0.25 < T_r < 0.95$). This equation of state is not applicable to gases.

Not one equation of state predicts $pvT$ properties with acceptably accuracy over the entire range of specific volumes from compressed liquids to dilute gases. This was mentioned earlier in the Chapter 1 (Introduction) and confirmed here in Chapter 2. The search for a more comprehensive equation of state for the accurate prediction of $pvT$ properties of liquids and gases continues.

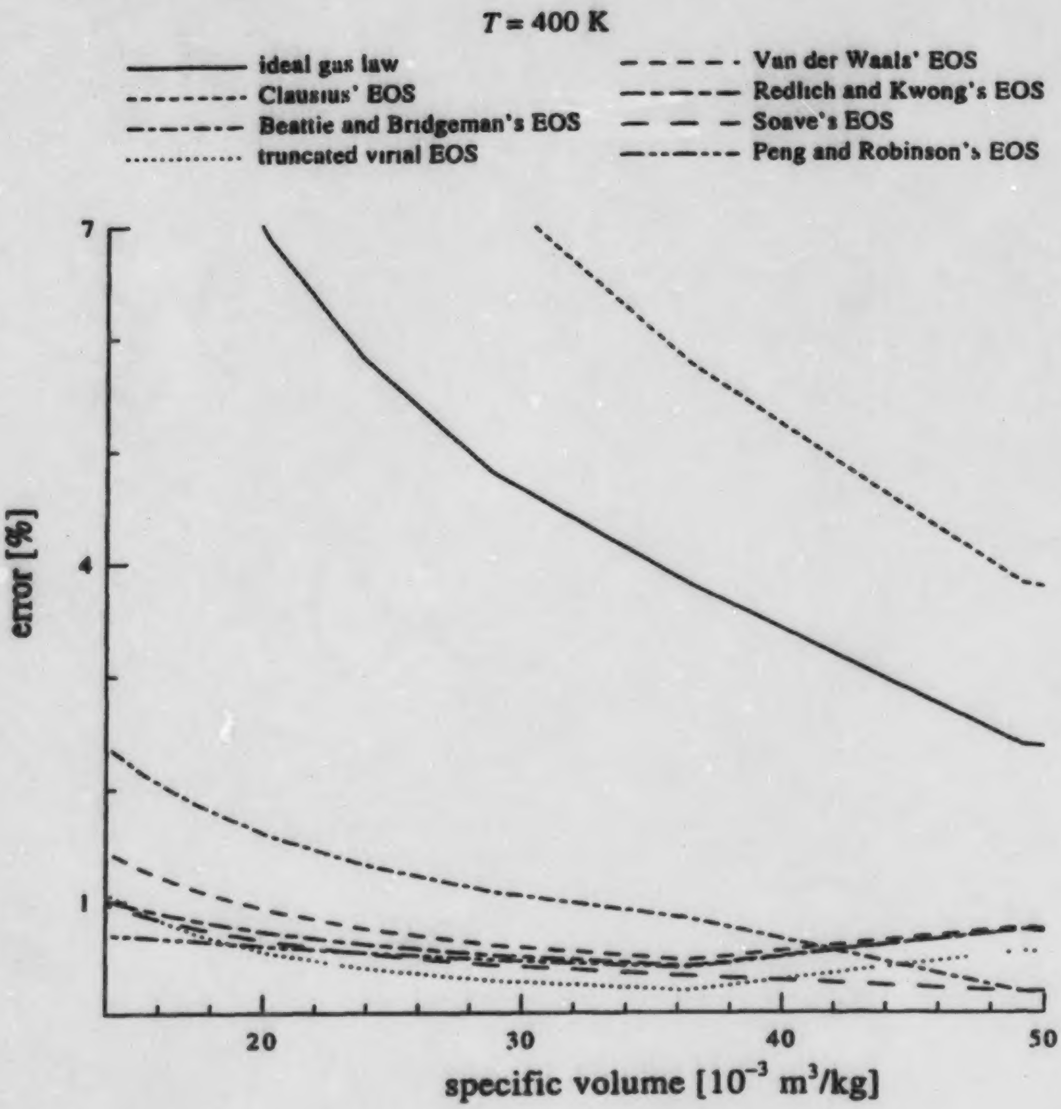

Figure 19: Errors from different equations of state for low gas densities and a temperature of 400 K.

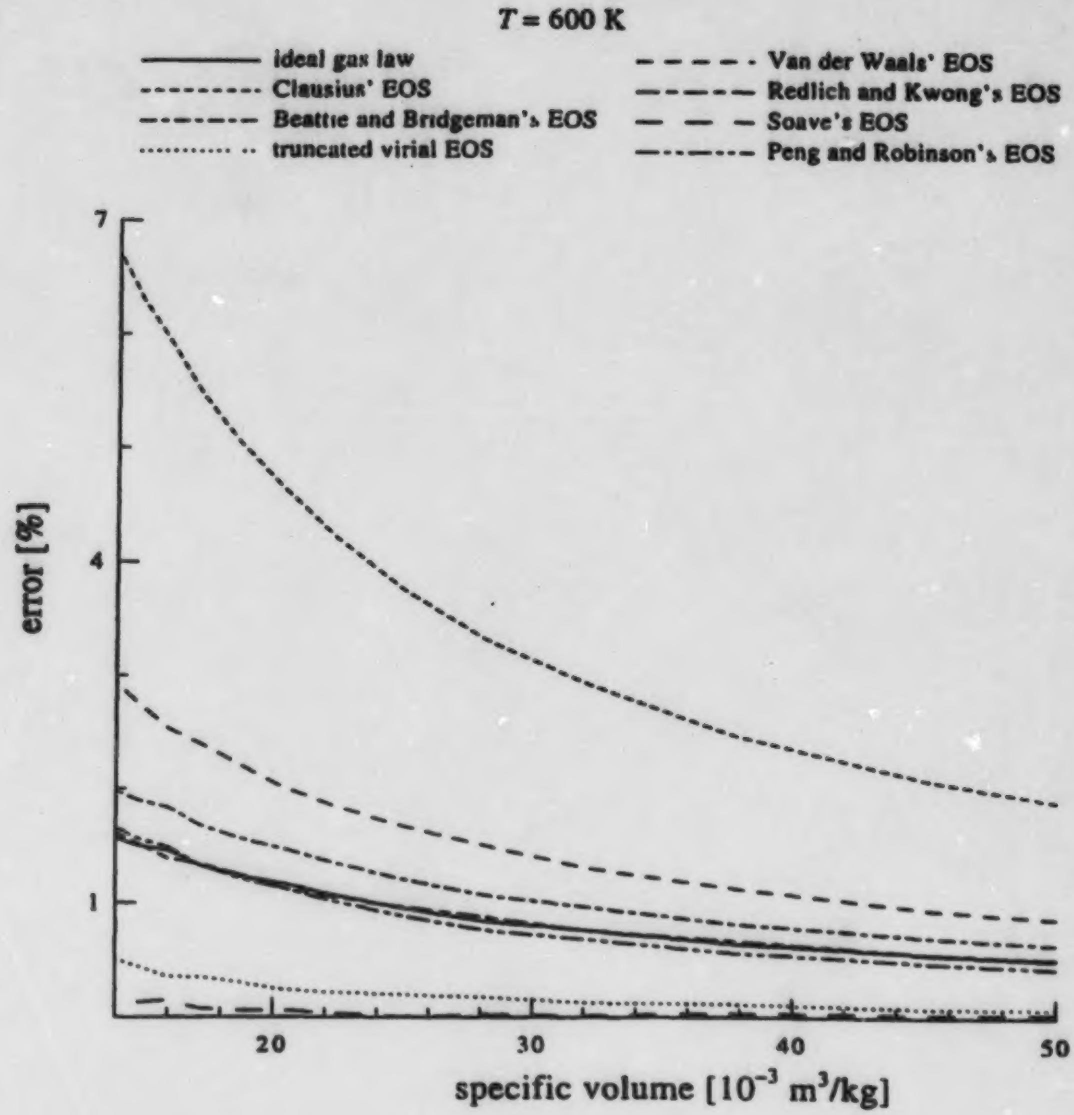

Figure 20: Errors from different equations of state for low gas densities and a temperature of 600 K.

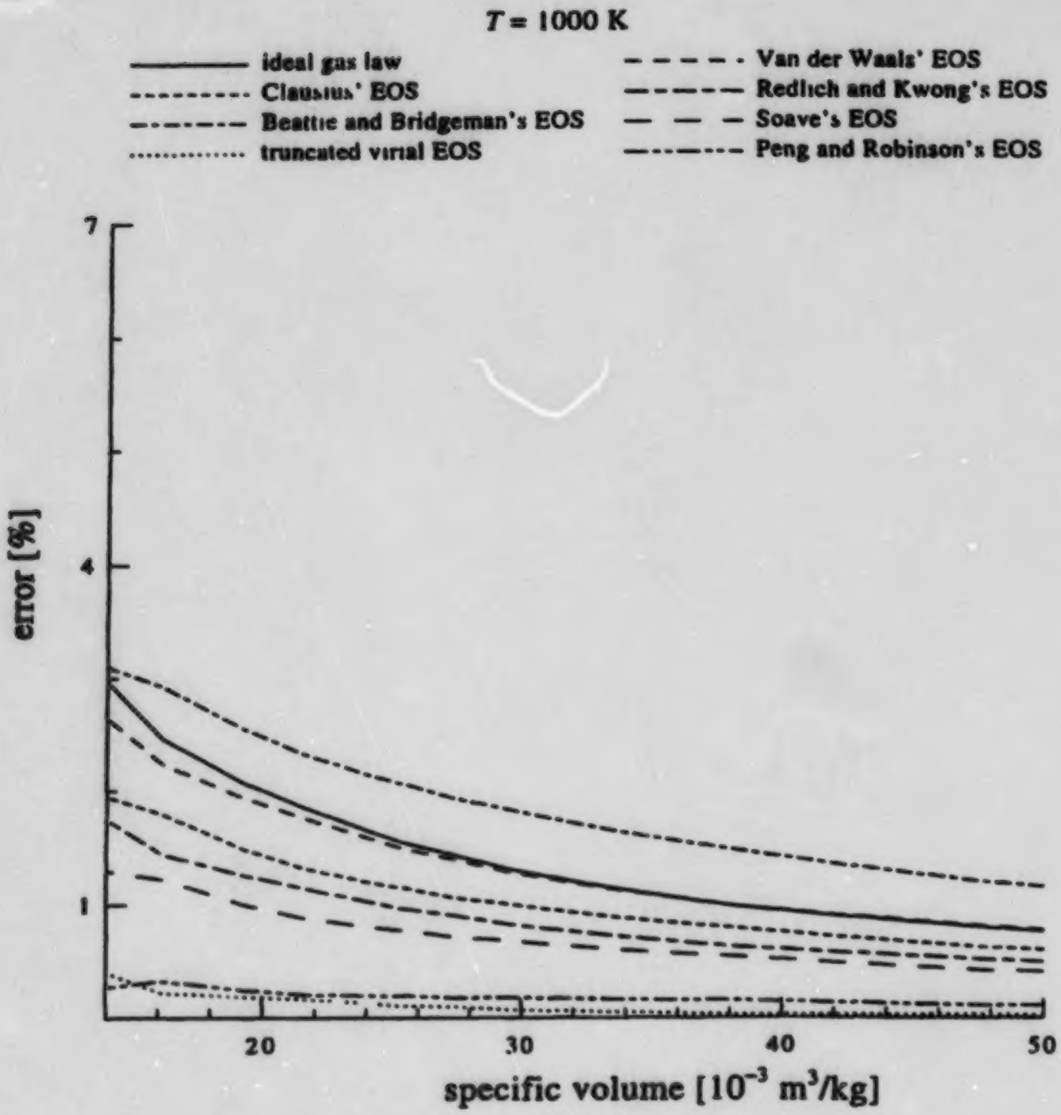

Figure 21: Errors from different equations of state for low gas densities and a temperature of 1000 K.

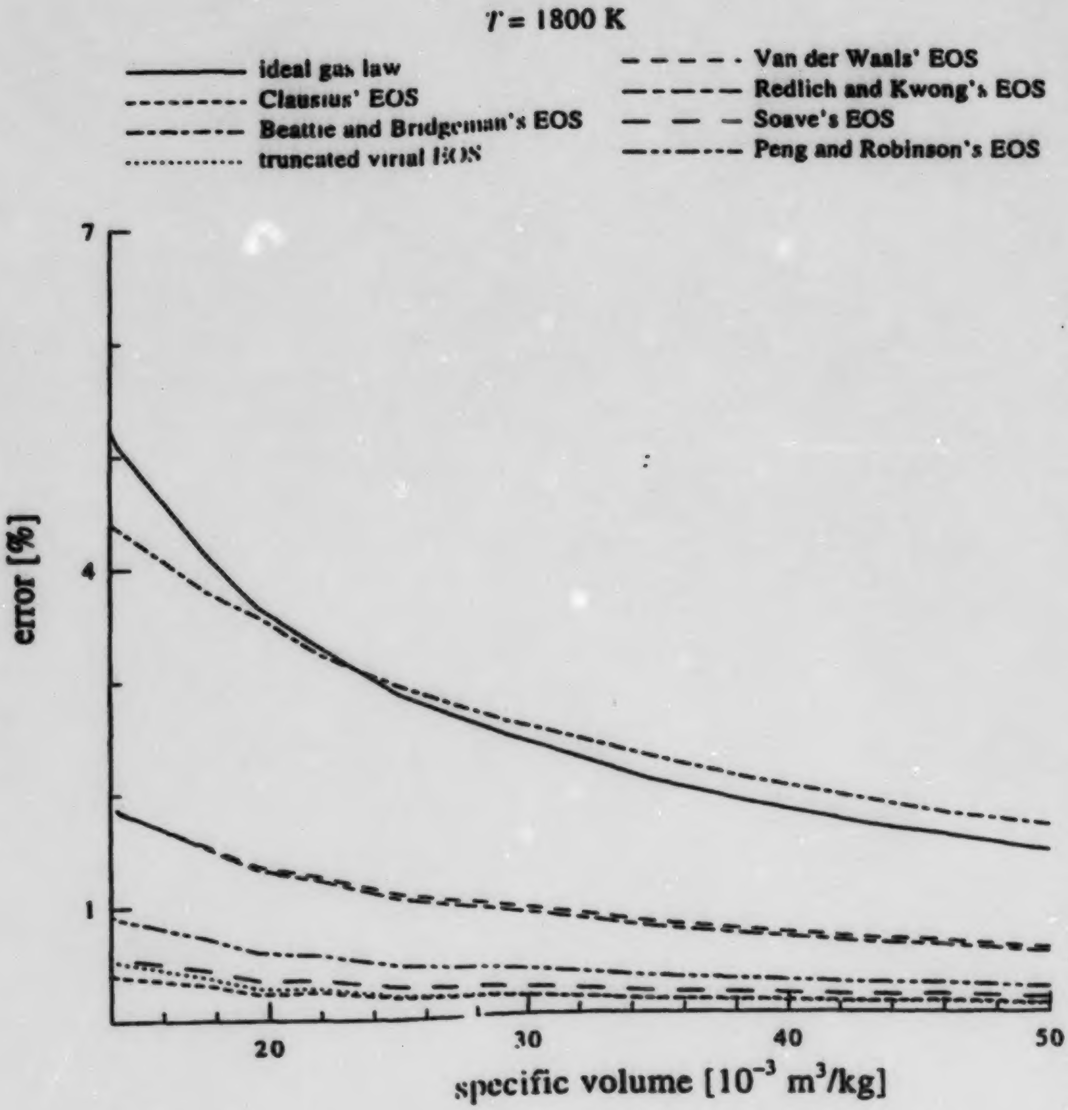

Figure 22: Errors from different equations of state for low gas densities and a temperature of 1800 K

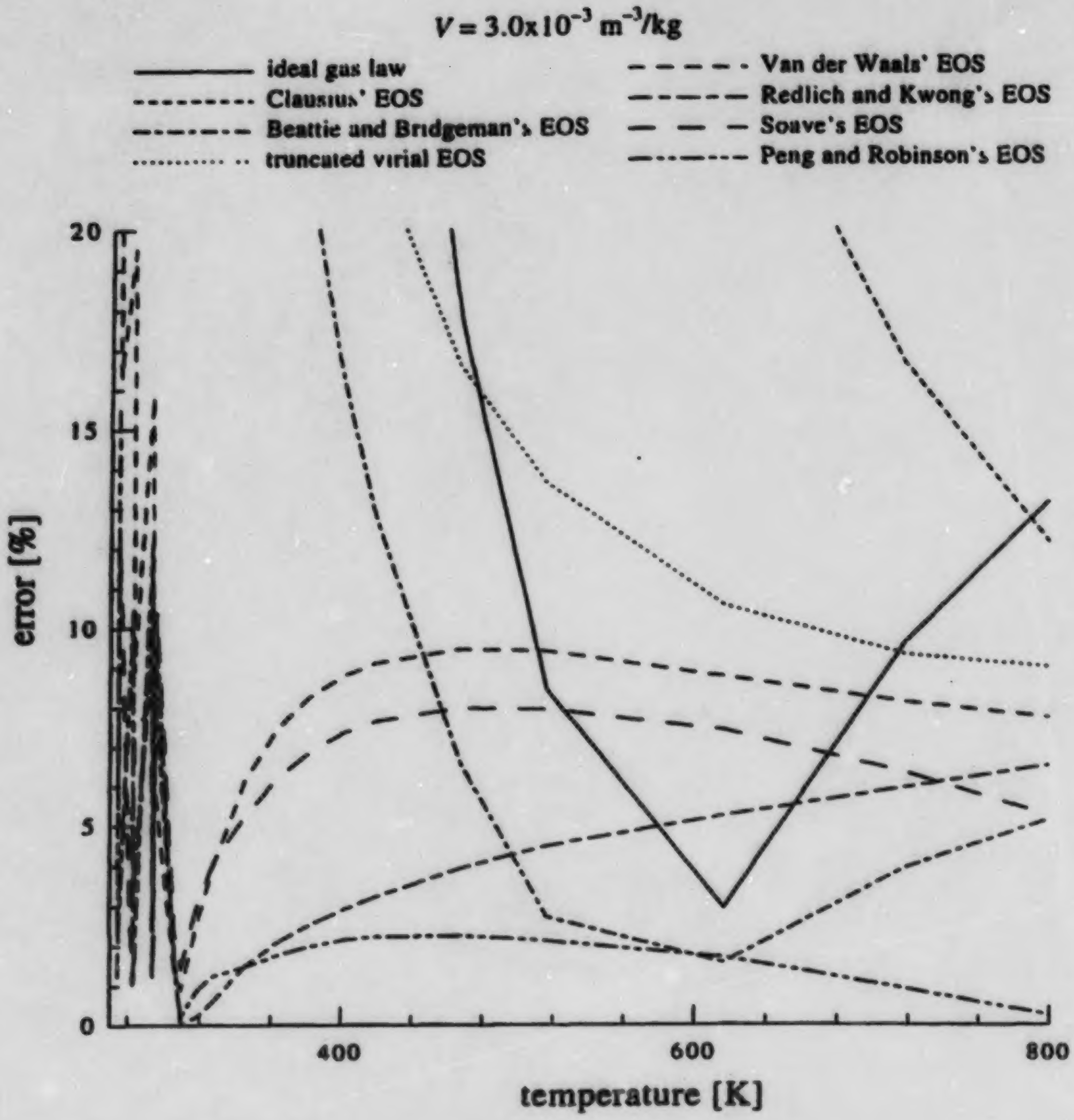

Figure 23: Errors from different equations of state for a specific volume of $3.0\times10^{-3}$ m$^3$/kg.

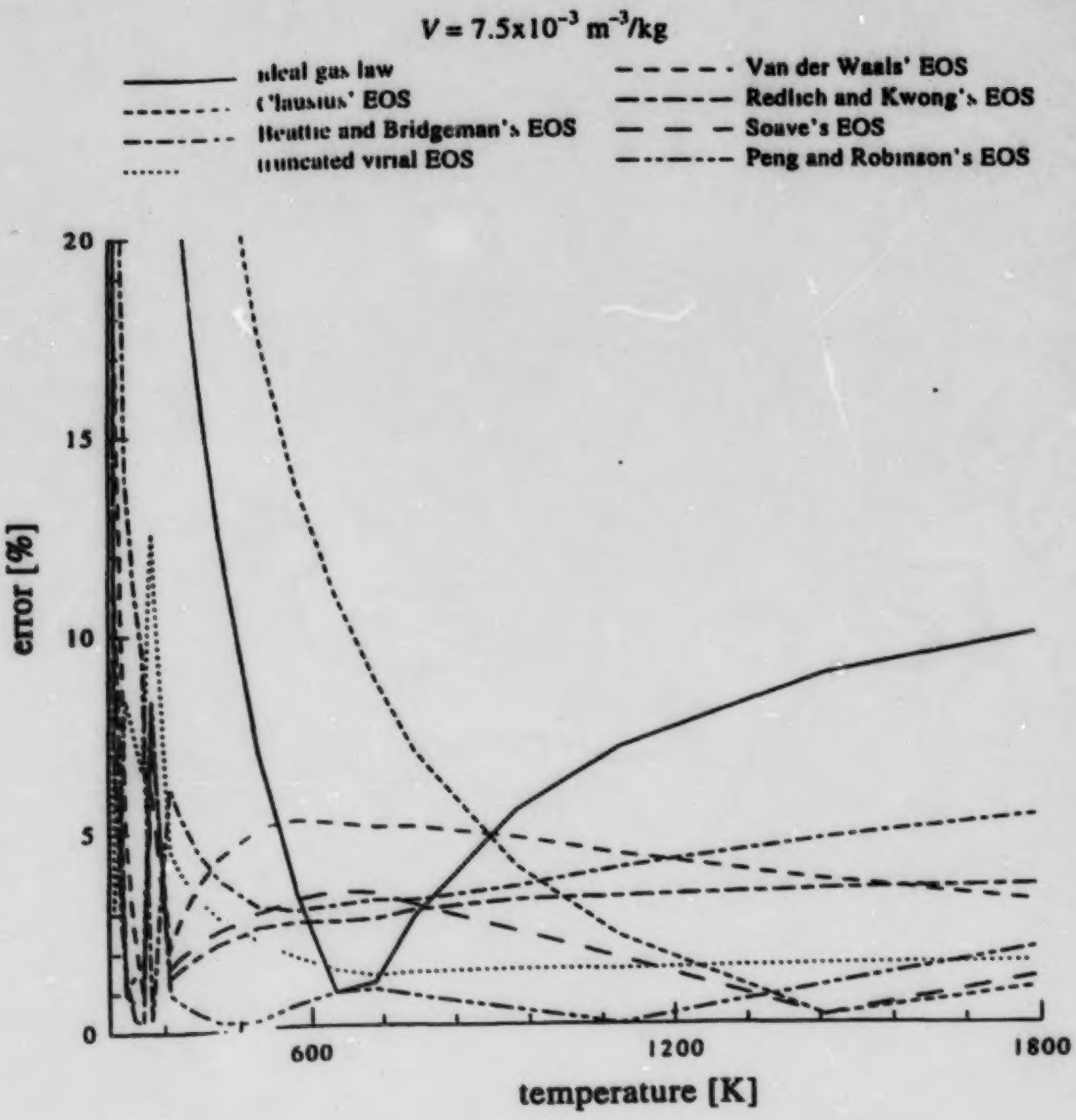

Figure 24. Errors from different equations of state for a specific volume of $7.5\times10^{-3}$ $m^3/kg$.

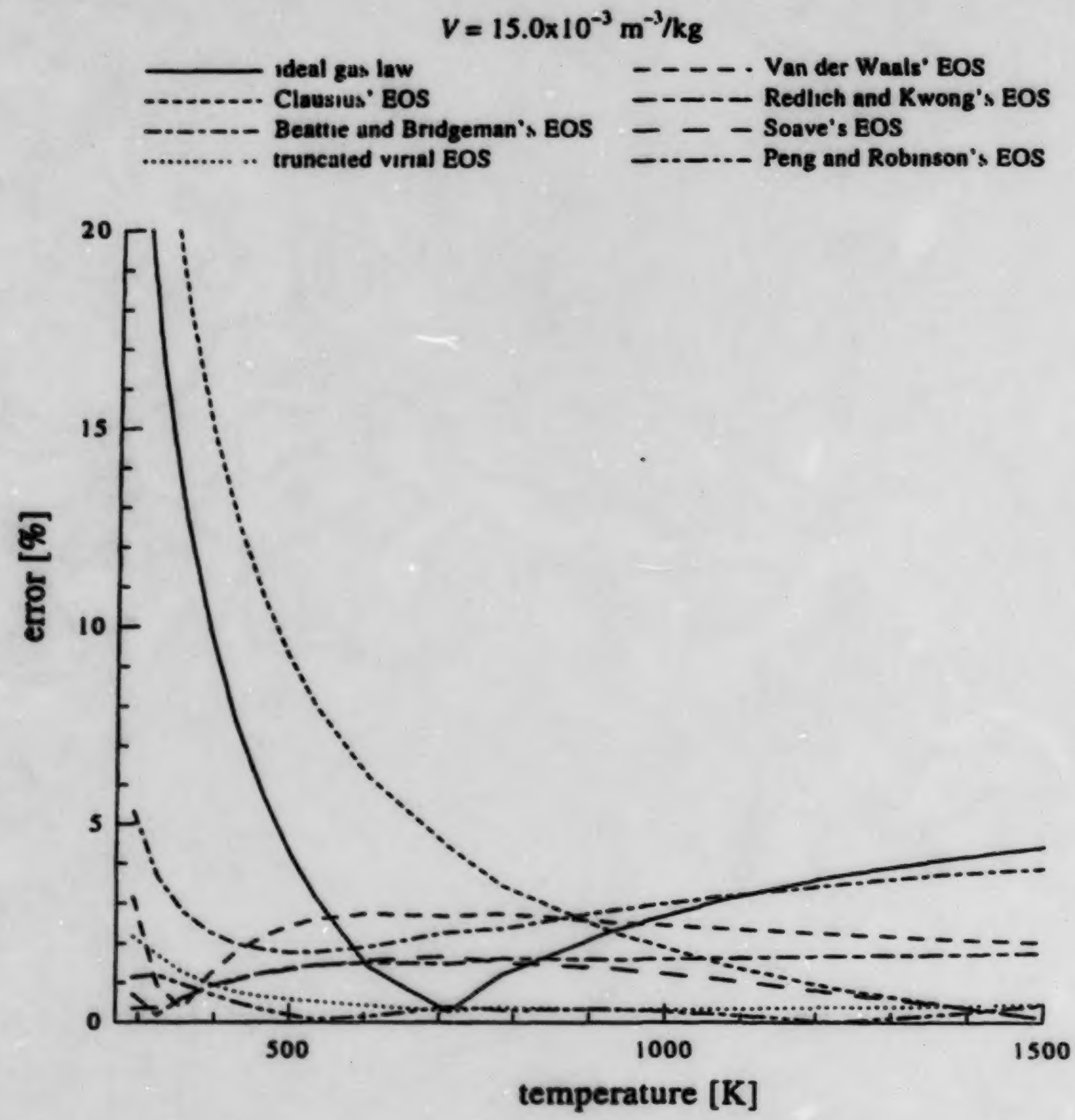

Figure 25. Errors from different equations of state for a specific volume of $15\times10^{-3}$ m$^3$/kg

# 3 BLENDED EQUATIONS OF STATE

Several well-known and classical equations of state were introduced and reviewed in chapters 1 and 2. These results illustrate that, in spite of the highly developed cubic equations of state like that of Peng and Robinson, the high-accuracy prediction of the volumetric behaviour of a real substance over a large range of pressures, specific volumes and temperatures still requires a specialized equation that is dedicated or restricted to a particular range of pressures, volumes and temperatures. This is exemplified further by the technique of Hankinson, Thomson and Brobst for predicting the volumetric properties of saturated and compressed liquids only in the restricted range of reduced temperatures given by $0.25 < T_r < 0.95$.

A new method of developing a single equation of state for predicting more comprehensive volumetric properties of gases and liquids for a large range of densities from that of the compressed liquid to that of dilute gases is proposed and tested in this chapter. The method is based on blending or combining a good equation of state for compressed liquids with a good equation of state for gases such that the resulting prediction of the combined equation of state for pressure-volume-temperature ($PVT$) properties is good over the entire range from compressed liquids to dilute gases.

## 3.1 Method of Blending Two Equations of State

The present method of blending two equations of state, one that is supposedly accurate for saturated and compressed liquids with one that is supposedly accurate for gases, is achieved by blending or combining the pressures from these two equations of state in the following manner:

$$p^{\mathrm{EOS}}_{\mathrm{blended}}(v,T) = p^{\mathrm{EOS}}_{\mathrm{liquid}}(v,T) + C(v,T)\left[p^{\mathrm{EOS}}_{\mathrm{gas}}(v,T) - p^{\mathrm{EOS}}_{\mathrm{liquid}}(v,T)\right], \tag{21}$$

where $p^{\mathrm{EOS}}_{\mathrm{liquid}}$, $p^{\mathrm{EOS}}_{\mathrm{gas}}$ and $p^{\mathrm{EOS}}_{\mathrm{blended}}$ denote the pressures of the compressed liquid, gaseous and blended equations of state, and $C(v,T)$ is a blending function that is permitted to depend on the specific volume $v$ and temperature $T$

The blending function can be formulated in different ways; in this work it is defined as follows: Firstly, $C(v,T)$ is restricted to the range $0 \leq C(v,T) \leq 1$, and

$$p^{\mathrm{EOS}}_{\mathrm{blended}}(v,T)\Big|_{C(v,T)\to 0} \to p^{\mathrm{EOS}}_{\mathrm{liquid}}(v,T),$$

$$p^{\mathrm{EOS}}_{\mathrm{blended}}(v,T)\Big|_{C(v,T)\to 1} \to p^{\mathrm{EOS}}_{\mathrm{gas}}(v,T),$$

at these two limits. Secondly, the specific form chosen for the blending function is

$$C(X) \equiv C(v,T) = \frac{\left(\frac{X}{X_0}\right)^s}{1+\left(\frac{X}{X_0}\right)^s}, \tag{22}$$

where $X$ can be set to the specific volume $v$, the temperature $T$, or some appropriate combination of $v$ and $T$. The symbol $X_0$ denotes a reference value for $X$ and $s$ is a pure-number exponent, respectively.

The mid-point of the blending transition from one equation of state to the other is controlled by the parameter $X_0$: when $X = X_0$ the contribution to $p^{\mathrm{EOS}}_{\mathrm{blended}}(v,T)$ is one-half of $p^{\mathrm{EOS}}_{\mathrm{liquid}}(v,T)$ and one-half of $p^{\mathrm{EOS}}_{\mathrm{gas}}(v,T)$. The width of the transition is controlled by the exponent $s$; the transition is spread widely for small $s$ values ($\ll 1$) and narrowly confined for a large $s$ value ($\gg 1$).

Convenient choices for $X$ and $X_0$ might appear initially to be the specific volume $v$ and critical volume $v_c$, respectively. For low values of $v$ corresponding to compressed liquids the blended equation-of-state pressure is virtually the liquid equation-of-state pressure. For large values of $v$ corresponding to low-density gases the blended equation-of-state pressure is then virtually the gaseous equation-of-state pressure. In the intermediate range near the critical point, the blended equation-of-state pressure is a blended combination of liquid and gaseous equation-of-state pressures. These three results are summarized for interest below:

$$p^{\mathrm{EOS}}_{\mathrm{blended}}(v,T)\Big|_{v\to 0} \to p^{\mathrm{EOS}}_{\mathrm{liquid}}(v,T),$$

$$p^{\mathrm{EOS}}_{\mathrm{blended}}(v,T)\Big|_{v\to v_c} \to \frac{1}{2}p^{\mathrm{EOS}}_{\mathrm{liquid}}(v,T) + \frac{1}{2}p^{\mathrm{EOS}}_{\mathrm{gas}}(v,T),$$

$$p^{\mathrm{EOS}}_{\mathrm{blended}}(v,T)\Big|_{v\to\infty} \to p^{\mathrm{EOS}}_{\mathrm{gas}}(v,T),$$

The choices of $X = v$ and $X_0 = v_c$ are premature at this stage; these and others need to be verified, which is the subject of the next sections.

## 3.2 Blending the Equations of State of Hankinson, Brobst and Thomson with that of Redlich and Kwong

The review in chapter 2 of classical equations of state showed that Hankinson, Thomson and Brobst technique of representing compressed and saturated liquid states for carbon dioxide was one of the most accurate equations of state. Therefore, Hankinson, Thomson and Brobst equation of state was selected first to be the equation of state for compressed and saturated liquids, even if their technique is limited to the reduced temperature range of $0.25 < T_r < 0.95$. Their equation of state given previously by equation (19) is repeated as

$$p^{\mathrm{EOS}}_{\mathrm{liquid}}(v, T) = \beta p_c + (p_{\mathrm{sat}} - \beta p_c) \exp\left[\frac{1}{\alpha}\left(1 - \frac{v}{v^{\mathrm{liq}}_{\mathrm{sat}}}\right)\right], \tag{23}$$

in which $p$ has been replaced by $p^{\mathrm{EOS}}_{\mathrm{liquid}}(v, T)$ to conform to the notation of the blended equation of state. Expressions for $v^{\mathrm{liq}}_{\mathrm{sat}}$, $\alpha$ and $\beta$ follow from equations (15) and (20), respectively, whereas $p_c$ is the critical pressure and $p_{\mathrm{sat}}$ denotes saturation-line data (see section 2.5 for more information).

The review in chapter 2 of classical equations of state showed that the Redlich and Kwong's equation of state for gases is quite simple and fairly accurate for predicting $pvT$ data compared to Soave's and Peng and Robinson's. Hence, Redlich and Kwong's equation of state was first selected for the equation of state for the gases. Their equation of state given in general form by equation (14) can be combined with the data given in table (2) and expressed in the final form

$$p^{\mathrm{EOS}}_{\mathrm{gas}}(v, T) = \frac{RT}{v - 0.08664\dfrac{RT_c}{p_c}} - \frac{0.42748 R^2 T_c^{5/2}}{p_c T^{1/2}\left(v^2 + 0.08664\dfrac{RT_c}{p_c} v\right)} \tag{24}$$

for blending with the previous equation of state for liquids by using equation (21).

The blending parameter is specified in the manner given earlier by equation (22) as

$$C(X) \equiv C(v) = \frac{\left(\dfrac{v}{v_0}\right)^s}{1 + \left(\dfrac{v}{v_0}\right)^s}, \tag{25}$$

in which $s = 3$ and $v_0 = 2.6\times10^{-3}$ kg/m$^3$ (after some trial-and-error testing with experimental data for $CO_2$). Note that the blended equation of state is, of course, restricted to the range $0.25 < T_r < 0.95$, because this restriction stems directly from Hankinson, Thomson and Brobst equation of state.

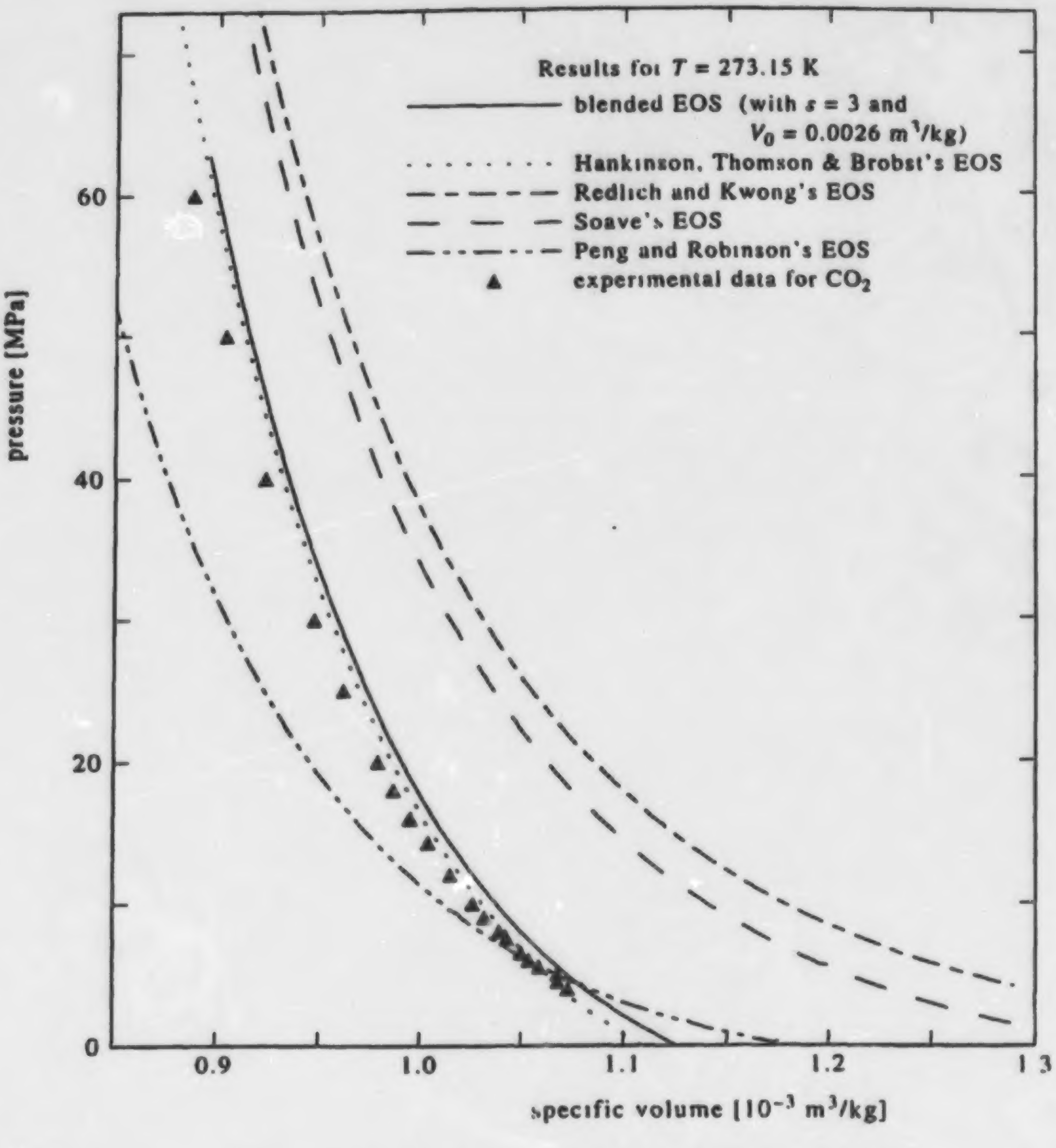

Figure 26: Comparison of the blended equation of state from Hankinson, Thomson and Brobst's and Redlich and Kwong's equations of state (with $s = 3$ and $v_0 = 0.0026$ m³/kg) to other single equations of state, for small specific volumes (liquids) and the temperature $T = 273.15$ K.

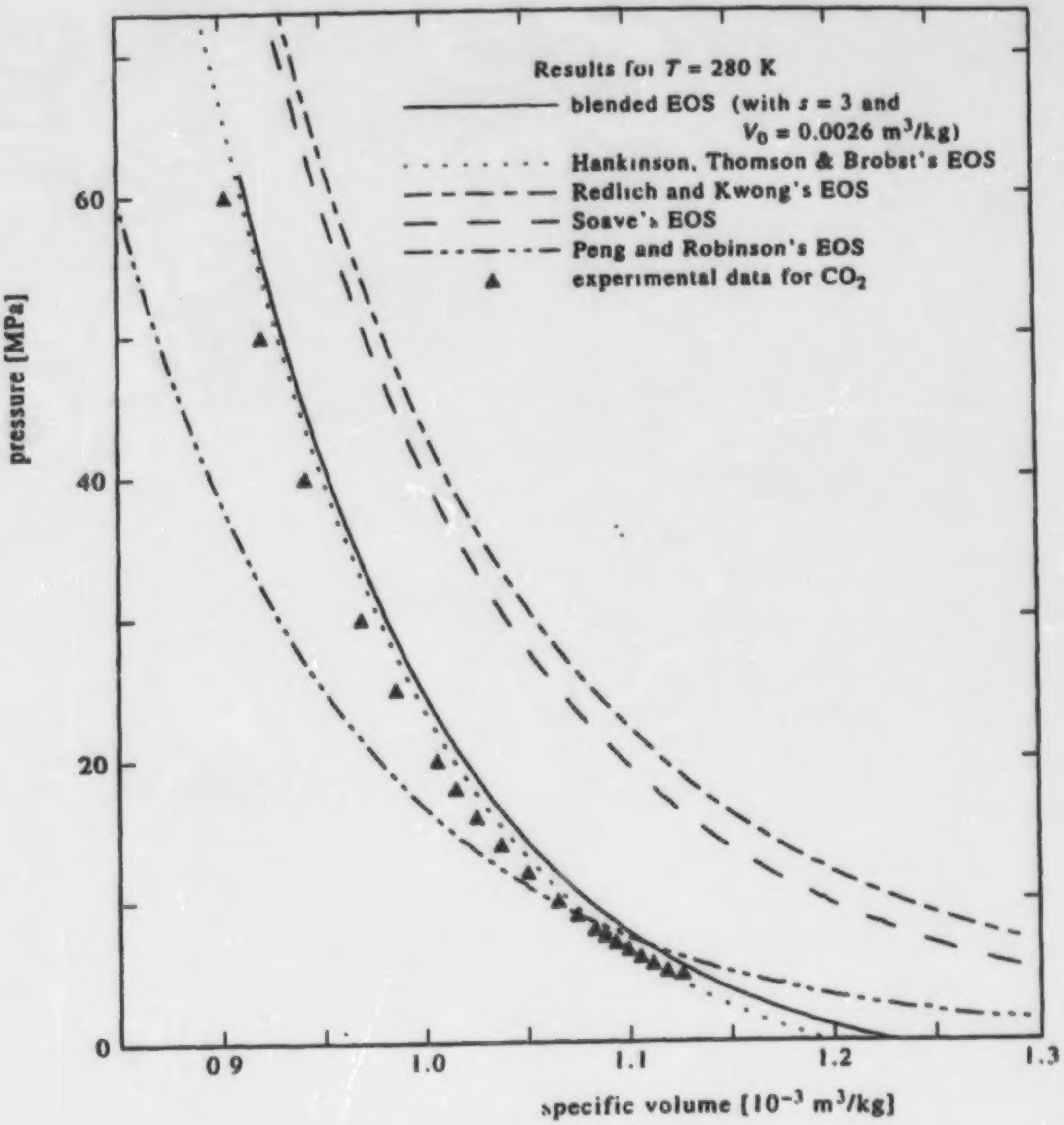

Figure 27· Comparison of the blended equation of state from Hankinson, Thomson and Brobst's and Redlich and Kwong's equations of state (with $s = 3$ and $v_0 = 0.0026$ m$^3$/kg) to other single equations of state, for small specific volumes (liquids) and the temperature $T = 280$ K.

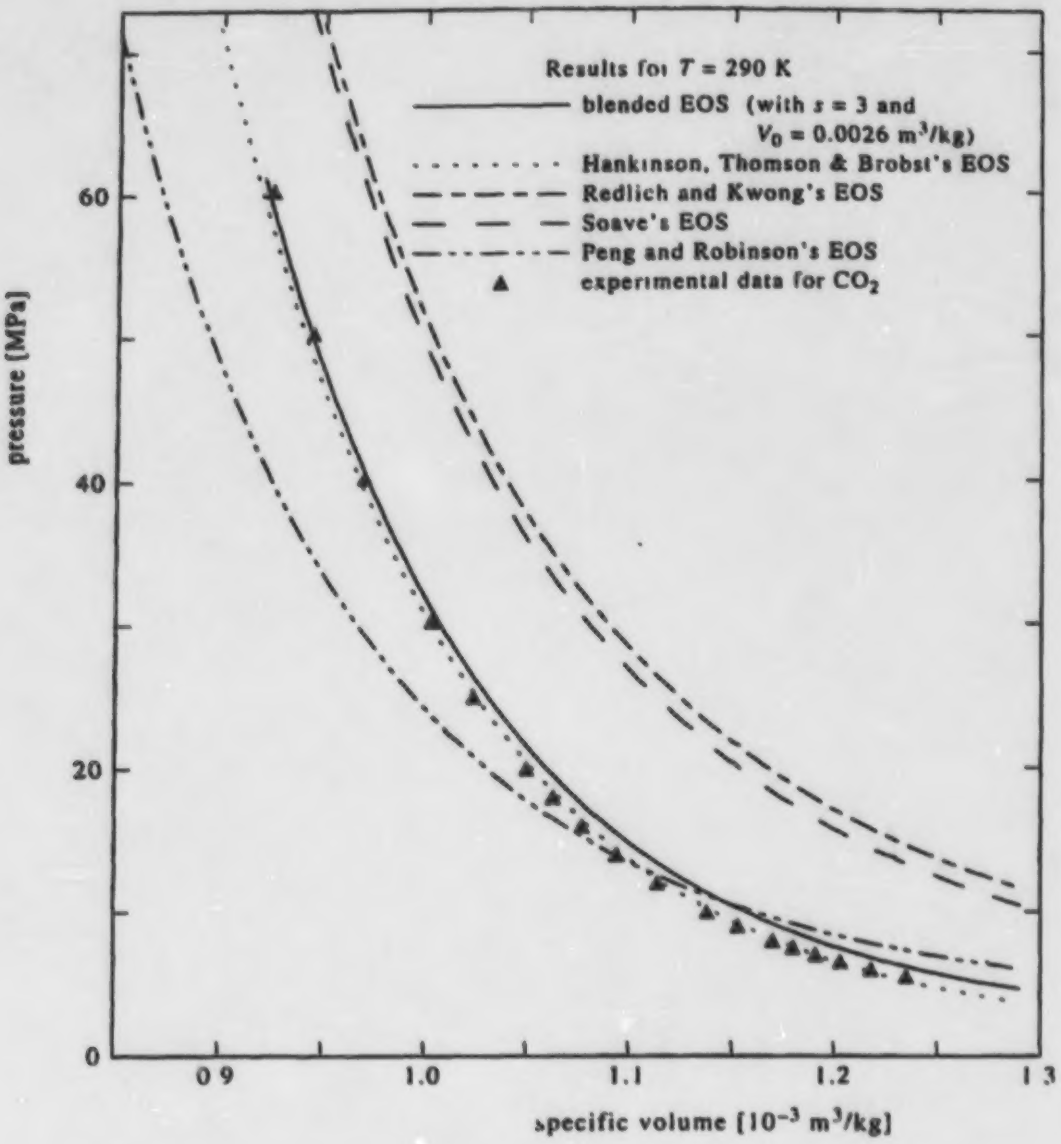

Figure 28: Comparison of the blended equation of state from Hankinson, Thomson and Brobst's and Redlich and Kwong's equations of state (with $s = 3$ and $v_0 = 0.0026$ m$^3$/kg) to other single equations of state, for small specific volumes (liquids) and the temperature $T = 290$ K.

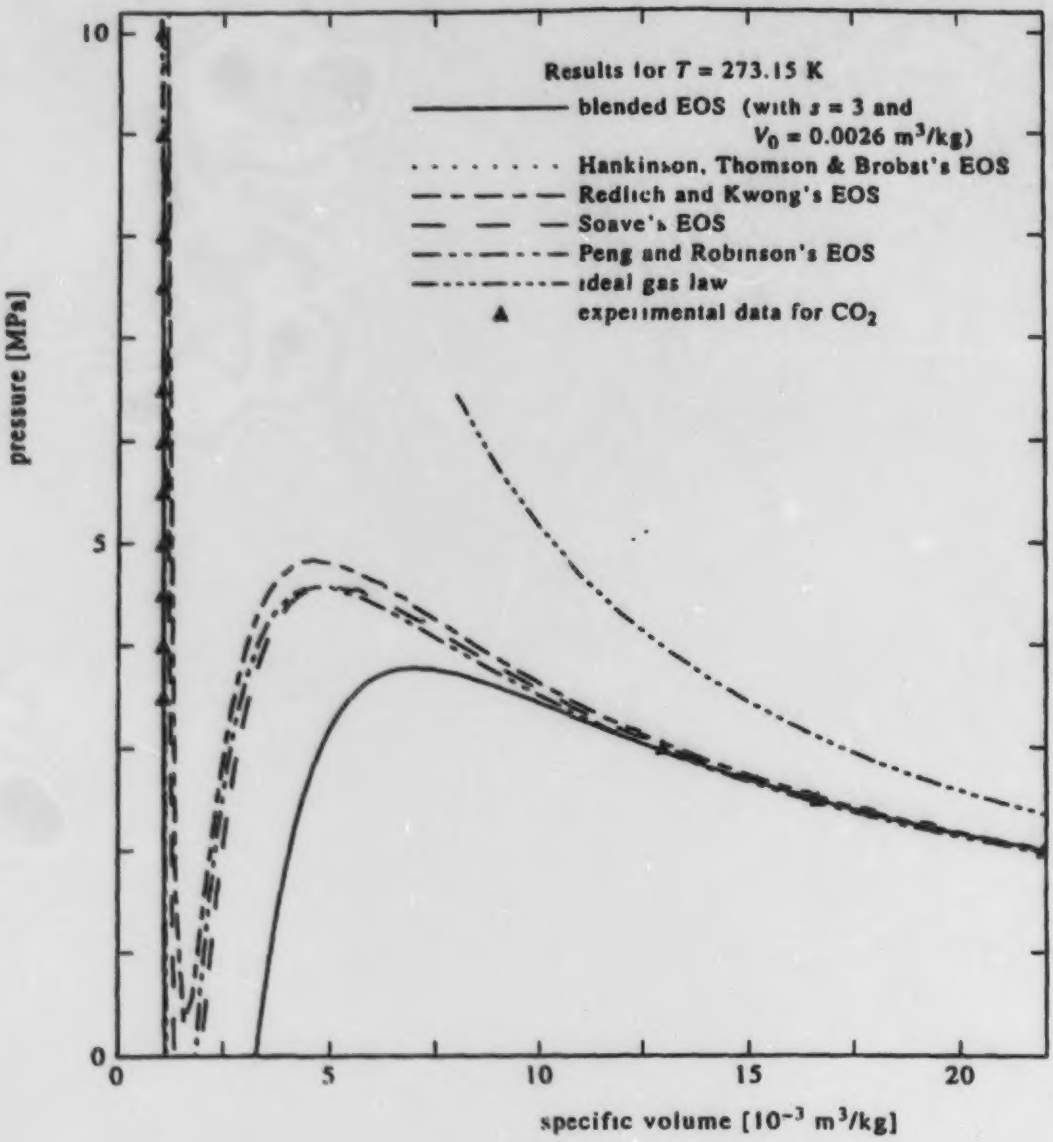

Figure 29: Comparison of the blended equation of state from Hankinson, Thomson and Brobst's and Redlich and Kwong's equations of state (with $s = 3$ and $v_0 = 0.0026$ $m^3$/kg) to other single equations of state, for large specific volumes (gases) and the temperature $T = 273.15$ K.

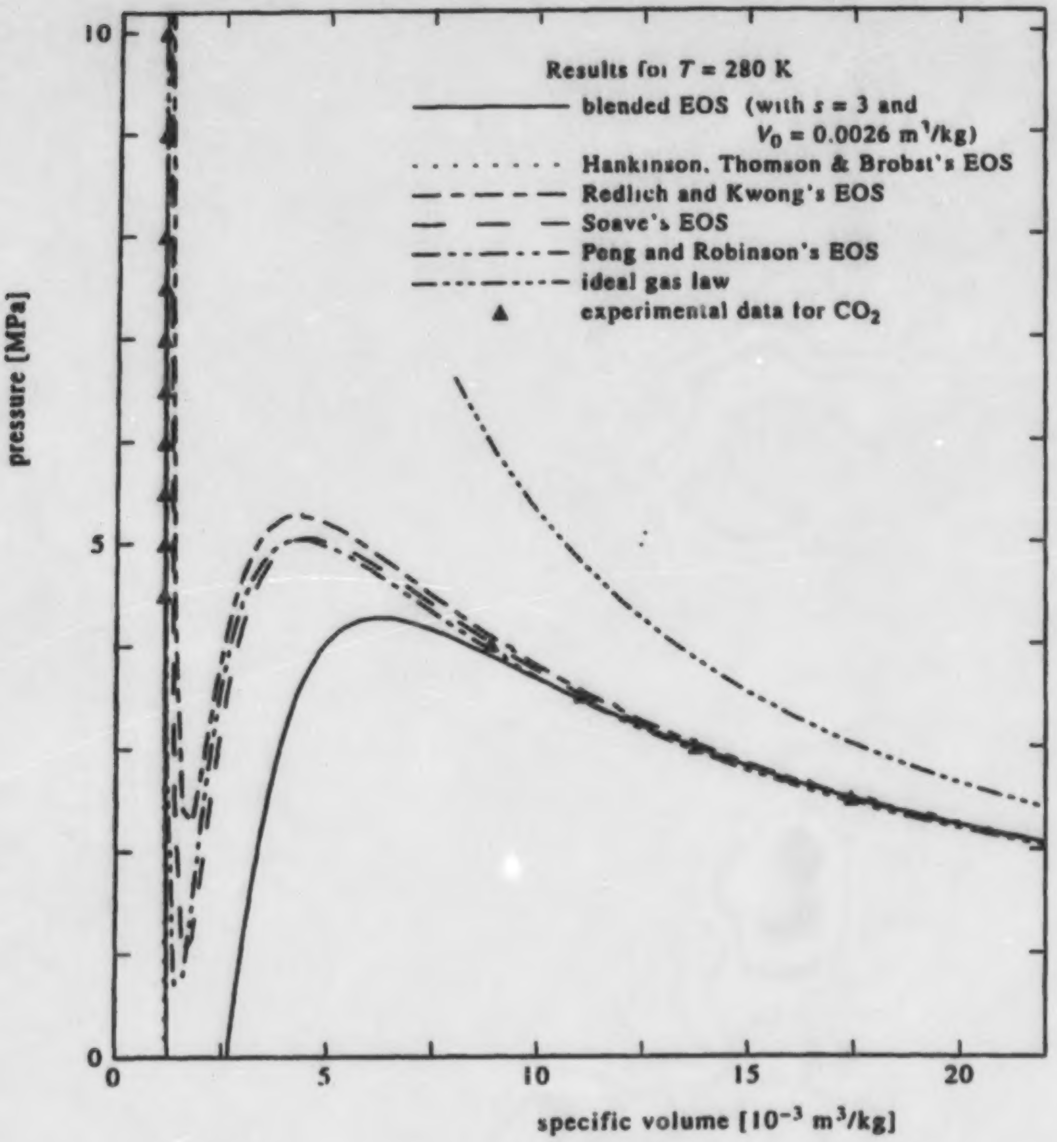

Figure 30: Comparison of the blended equation of state from Hankinson, Thomson and Brobst's and Redlich and Kwong's equations of state (with $s = 3$ and $v_0 = 0.0026$ m$^3$/kg) to other single equations of state, for large specific volumes (gases) and the temperature $T = 280$ K.

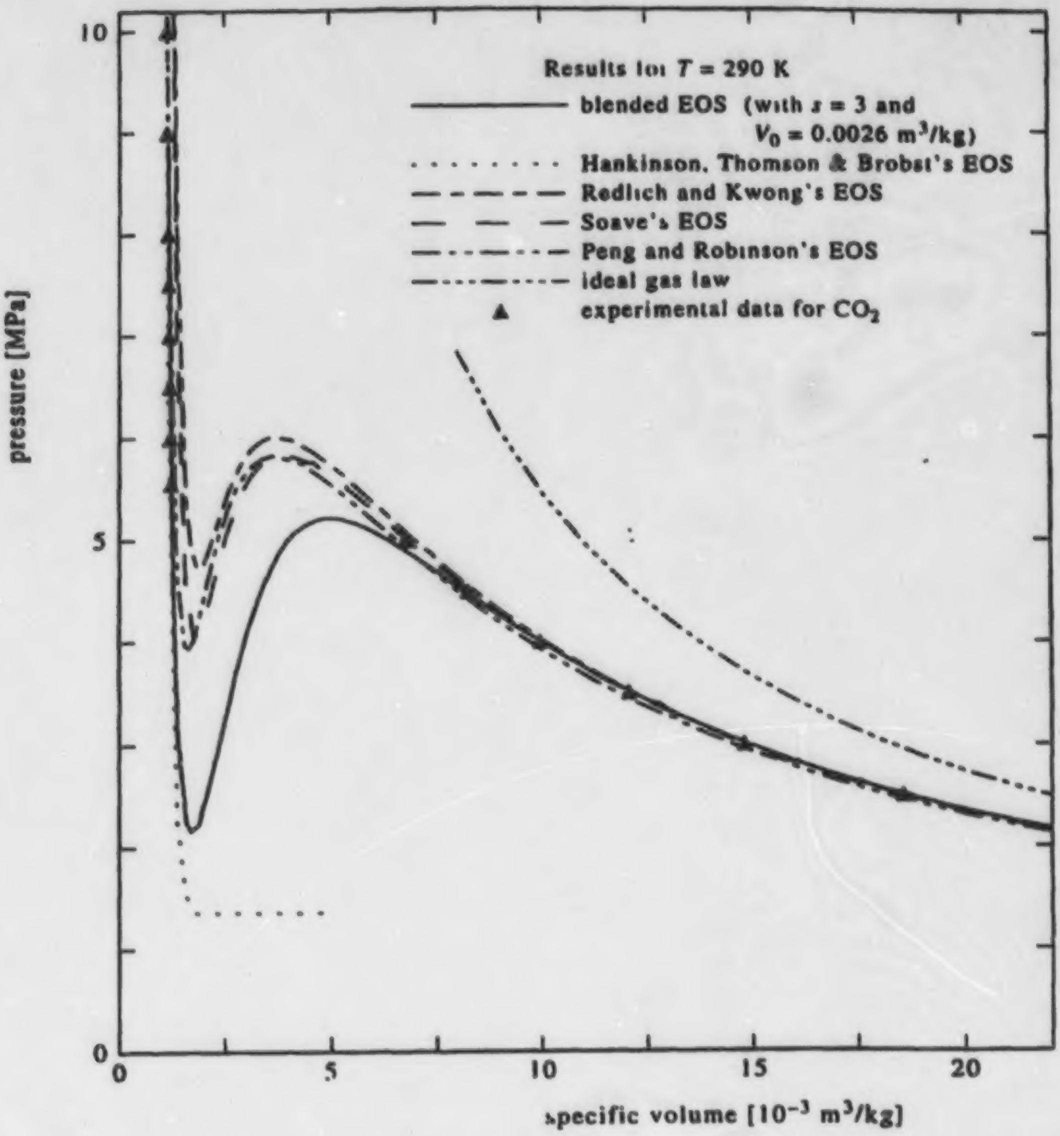

Figure 31: Comparison of the blended equation of state from Hankinson, Thomson and Brobst's and Redlich and Kwong's equations of state (with $s = 3$ and $v_0 = 0.0026$ m$^3$/kg) to other single equations of state, for large specific volumes (gases) and the temperature $T = 290$ K.

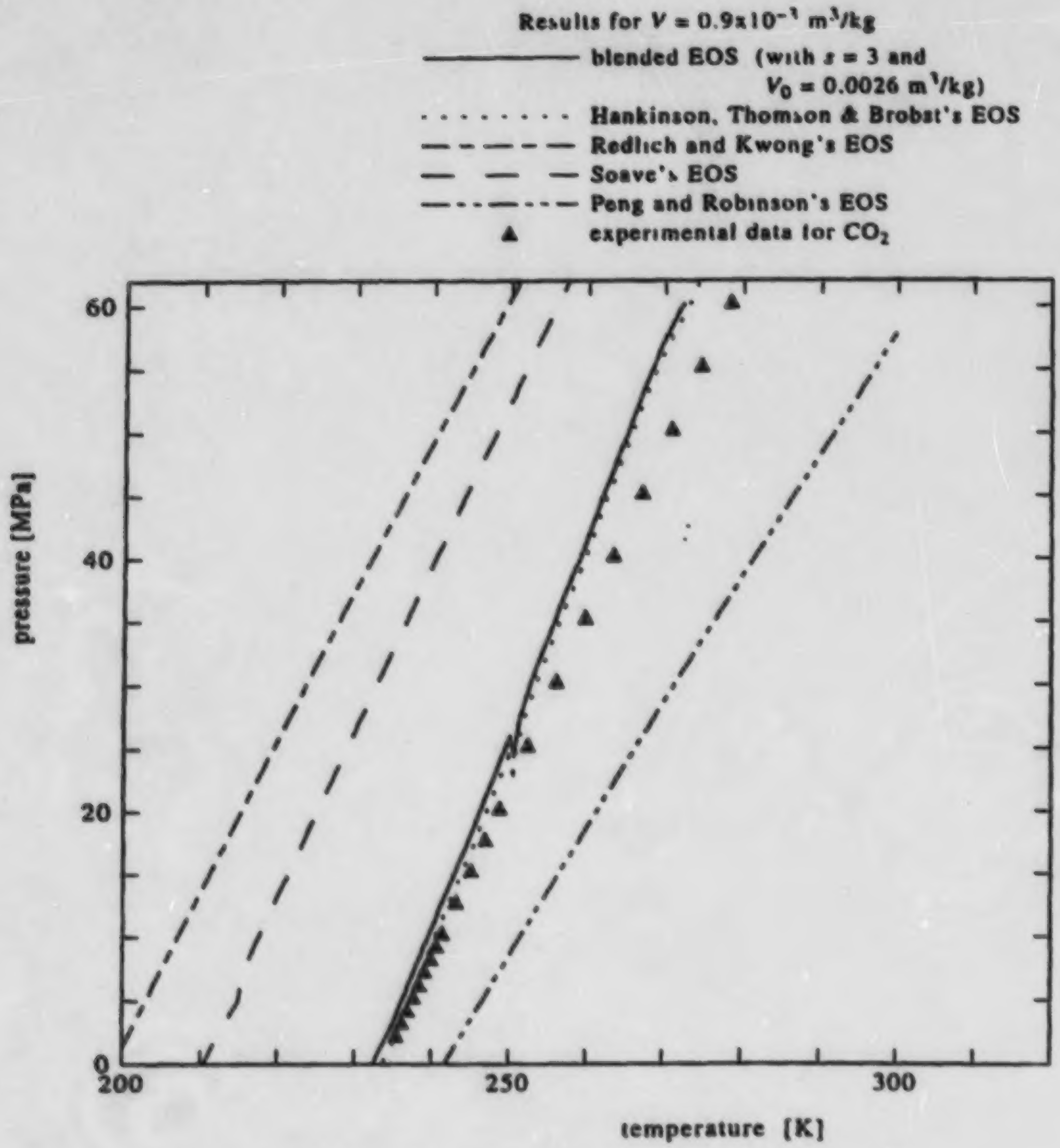

Figure 32: Comparison of the blended equation of state from Hankinson, Thomson and Brobst's and Redlich and Kwong's equations of state (with $s = 3$ and $v_0 = 0.0026$ m$^3$/kg) to other single equations of state, for moderate temperatures and the specific volume $V = 0.9\times10^{-3}$ m$^3$/kg.

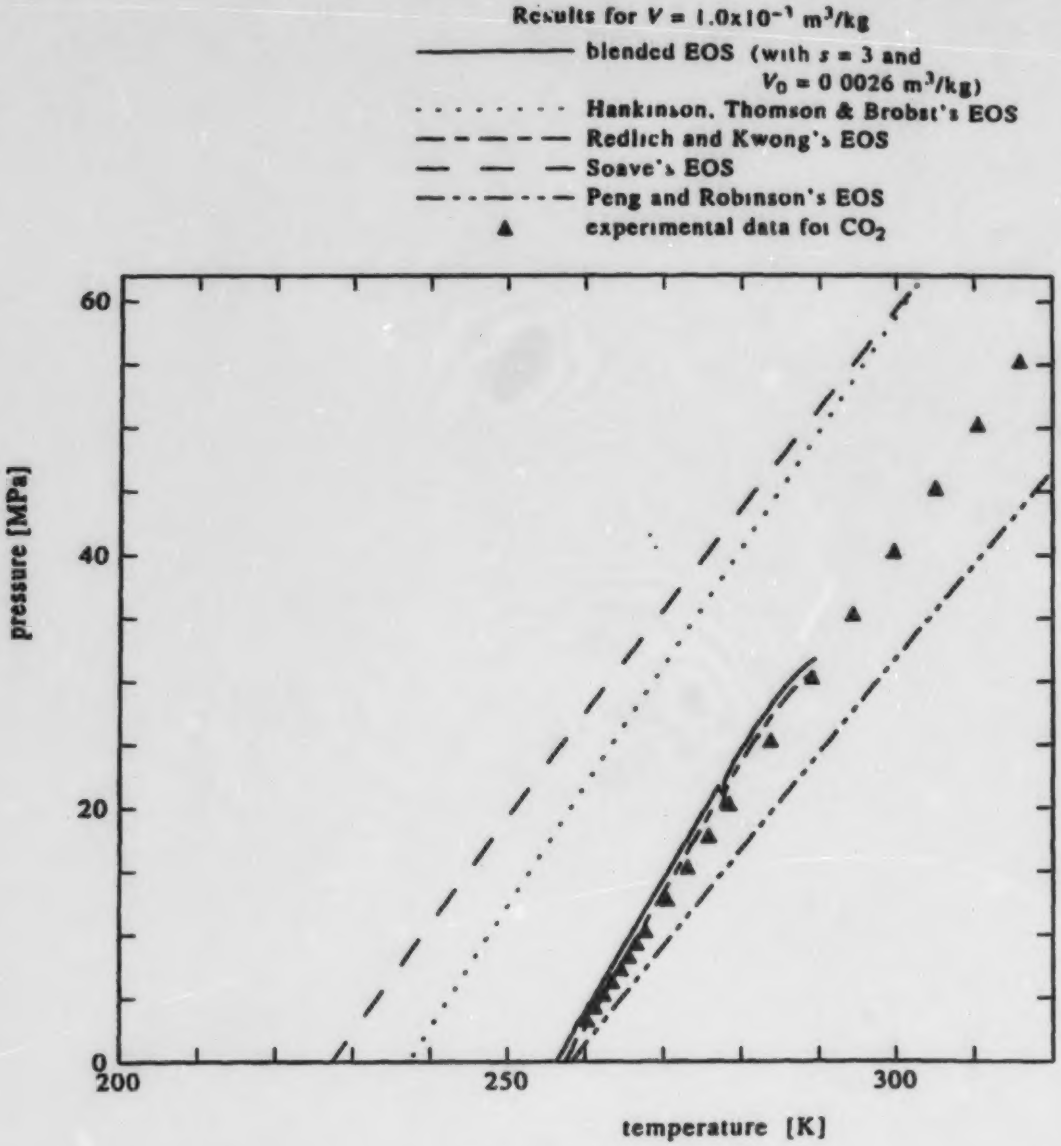

Figure 33: Comparison of the blended equation of state from Hankinson, Thomson and Brobst's and Redlich and Kwong's equations of state (with $s = 3$ and $v_0 = 0.0026$ m$^3$/kg) to other single equations of state, for moderate temperatures and the specific volume $V = 1.0\times10^{-3}$ m$^3$/kg.

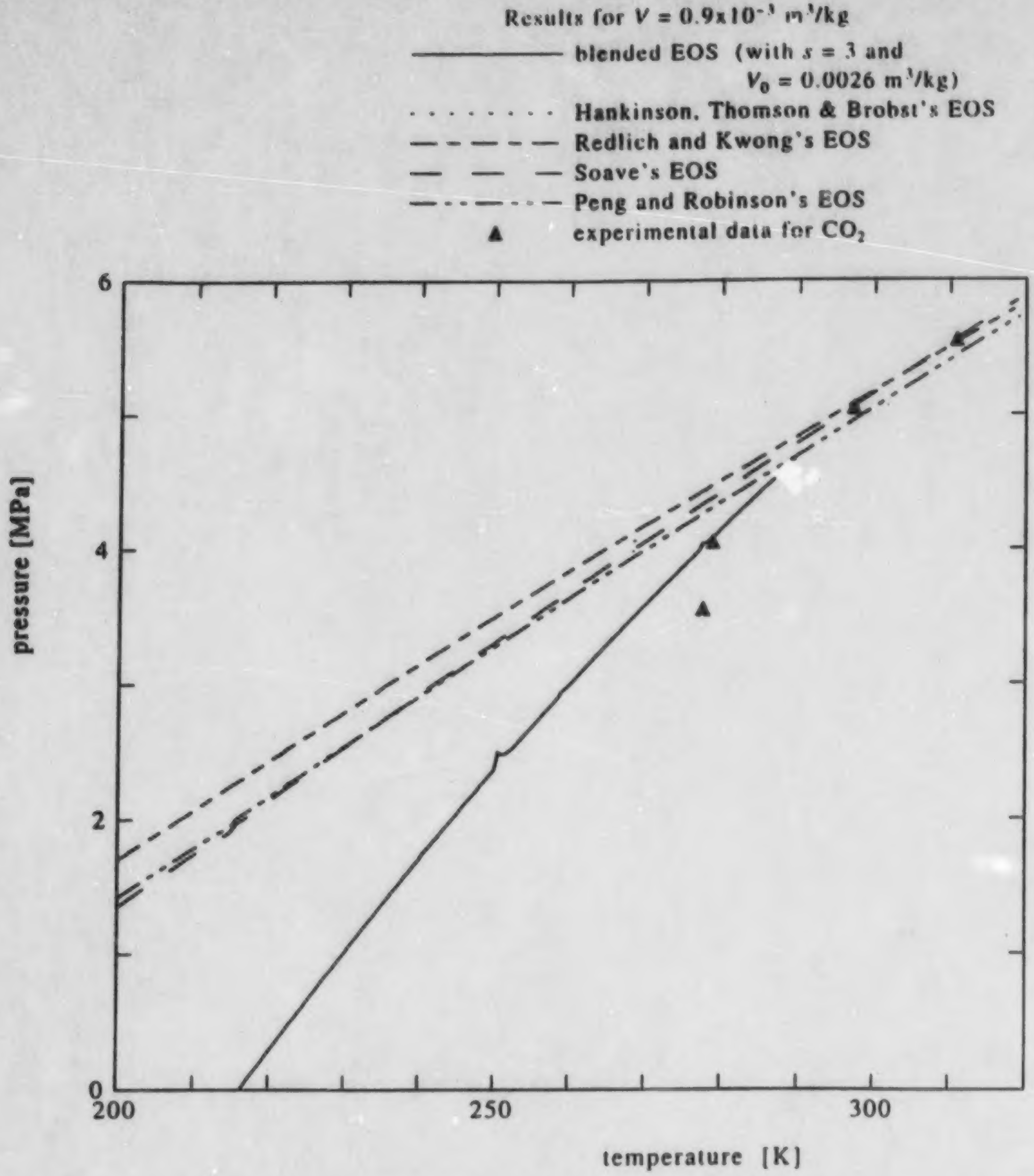

Figure 34: Comparison of the blended equation of state from Hankinson, Thomson and Brobst's and Redlich and Kwong's equations of state (with $s = 3$ and $v_0 = 0.0026$ m$^3$/kg) to other single equations of state, for moderate temperatures and the specific volume $V = 7.5\times10^{-3}$ m$^3$/kg.

The results of this combining are presented in the pressure-volume graphs (26 – 31) for several constant temperatures (isotherms) and in the pressure-temperature graphs (32 – 34) for several specific volumes (isochors). The combined equation of state is compared to the original built-in equations of state and to the equations of Soave, and Peng and Robinson, as well as to experimental data of $CO_2$.

Enlarged for liquid densities, see figures (26, 27, 28), the conformity of the combined equation of state with the results of the Hankinson, Thomson and Brobst Technique is illustrated. Only for lower pressure small deviations are possible, but it is remarkable that the results are quite better than all of the cubic equations of state. The technique of Hankinson, Thomson and Brobst does not yield results for the prediction of gaseous states. The combining with the equation of Redlich and Kwong abolish this restriction. It is demonstrated in the figures (29, 30, 31) that the new equation of state gives very good results for gaseous densities and close to saturated conditions the accuracy is even better than the original equation of Redlich and Kwong and nearly as good as the equation of Peng and Robinson.

The PT-behaviour for constant volume is shown in the figures (32 – 34). The curve of the Combined Equation of State is for liquid densities quite similar to the results of the technique of Hankinson, Thomson and Brobst and represents therefore the experimental data very good. The results for high volume are senseless because the thechnique of Hankinson, Thomson and Brobst doesn't give results for liquid densities, compare figure (34).

Sumed up, the combined equation of state gives good results and in some cases the results can be better than the predictions of the original built-in equations. Also deviations compared to the built-in equations of state have to be expected in the transition area, depending on the values of the factors $s$ and $v_0$ which are included in the combing factor $C(v)$. But it is necessary to emphasize that the new relation has a relative complicated analytical form.

## 4 Summary and Prospect

Many equations of state have been proposed over a period of the last century in order to provide an analytical approach to determine important thermodynamical properties. In chapter 2 some well-known and common equations of state have been reviewed. It is necessary to emphasize that these equations are only a selection. there are much more equations proposed and often the described equations are adjusted and improved to cover specific conditions and substances more accurate. But the reviewed equations are representing the several classes of equations of state and especially their are very appropriate to demonstrate and discuss general characteristics and limitations.

Existing equations of state are not sufficient applicable to predict $pvT$-Data accurate for a large range of densities, from dilute gases to compressed liquids. Therefore the method of Blending of Two Equations of State has been introduced in chapter 3 and has been applied for the combination of the Hankinson, Thomson and Brobst Technique with Redlich and Kwong's Equation of State. The results of the combination encourage to pursue further the idea of blending two equations of state. It could be demonstrated in chapter 3.2 that in principal the range of applicability and the accuracy can be extended and improved, but at the expense of a large extent of complexitiy.

This report is confined to introduce the method and to evaluate the validity in principle. The next steps to continue and to extend the work include the evaluation of further suitable combinations of equations of state considering different and possibly polar substances. Besides, in this report the analytical form of the blending function is permitted to depend only on the volume $C_{(X)} = C_{(v)}$, but it is likely that the accuracy of the blended equation of state can be increased by extending the blending function to be temperature dependend $C_{(X)} = C_{(T)}$ or both temperature and volume dependend $C_{(X)} = C_{(T,v)}$

Further the blended equations of state have to be evaluated concerning to thermodynamical properties like the specific heat capacity, enthalpy and entropy. that means to scrutinize the differentiations $\mathrm{d}h = c_p \mathrm{d}T$ and $\mathrm{d}s = (\mathrm{d}h - V\mathrm{d}p)/T$

# References

[1] F. D. Rossini (1955), *Thermodynamics and physics of matter*, Vol. 1, Princeton University Press.

[2] J. O. Hirschfelder, C. F. Curtiss, R. B. Bird (1954), *Molecular Theory of gases and liquids*, John Wiley & Sons, Inc.

[3] R. C. Reid, J. M. Prausnitz, B. E. Poling (1987), *The properties of gases and liquids*, fourth edition, McGraw-Hill Book Co.

[4] Schaum (1987), *Technische Thermodynamik*, HAAG+HERRCHEN Verlag.

[5] S. Eliezer (1986), *An introduction to equations of state: theory and applications*, Cambridge University Press.

[6] K. C. Chao, R. L. Robinson, Jr. (1979), *Equations of state: theories and application*, American Chemical Society.

[7] E. Hering, R. Martin, M. Stohrer (1992), *Physik für Ingenieure*, VDI Verlag GmbH.

[8] D. R. Lide, H. V. Kehiaian (1994), *CRC Handbook of thermophysical and thermodchemical Data*, CRC Press.

[9] N. B. Vargaftik (1975), *Tables on the thermophysical properties of liquids and gases in normal and dissociated states*, second edition, John Wiley & Sons, Inc.

[10] J. J. Martin (1988), *Equations of state*, Vol. 59, No. 12, Journal of Industrial and Engineering Chemistry.

[11] J. H. Dymond, E. B. Smith (1980), *The virial coefficients of pure gases and mixtures*, Clarendon Press, Oxford.

# APPENDIX A:
# METHOD OF IMPLEMENTING MAXWELL'S RULE

Many sophisticated equations of state take into account the overall effects of the repulsion and attraction of molecules during bi- and tri-molecular collisions. These equations of state consequently exhibit a minimum and maximum separated by a point of inflection when the pressure $p$ is plotted versus the specific volume $v$ at a constant temperature $T$ (isotherm in the $pv$-plane), if the isotherm temperature is sufficiently low. This feature is illustrated in figure A–1 for Van der Waals equation of state.

Maxwell's rule [4] is essentially a straightforward correction to an isotherm such that the minimum and maximum are altered (or collapsed) into a horizontal line ($AE$ in figure A–1), that is a line of constant saturation pressure $p_{sat}$. This is done simply by making the areas $ABCA$ and $CDEC$ equal, which corresponds to the liquid and vapour having the same Gibb's free energy at a constant pressure and temperature, regardless of their concentrations. The saturation pressure $p_{sat}$ is thereby defined for the constant isotherm temperature $T$, and the liquid and its vapour can thereby co-exist as a mixture.

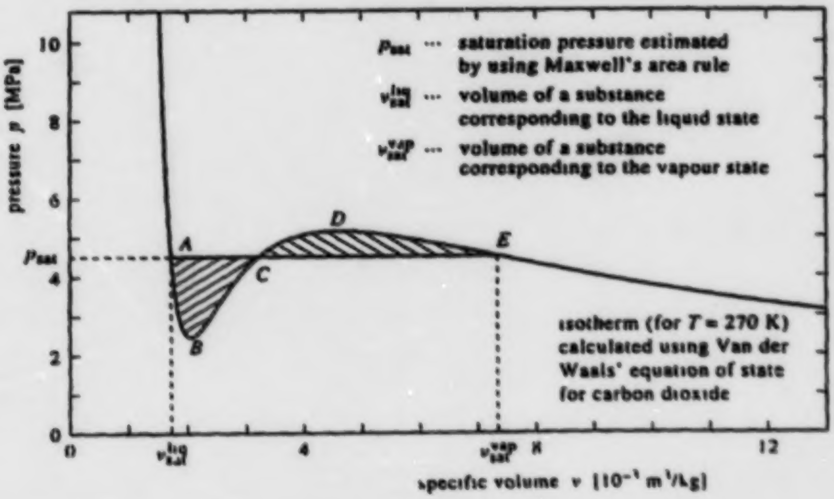

Figure A–1: Illustration of Maxwell's rule for an isotherm: the horizontal line $AE$ is drawn such that areas $ABCA$ and $CDEC$ are equal, thereby eliminating the aphysical minimum at $B$ and maximum at $D$ in the original isotherm (constructed using Van der Waals' equation of state for $CO_2$) and thereby producing a constant saturation pressure (line $AE$).

Maxwell's rule is simple to understand, but the practical implementation of this rule to general equations of state denoted by $p = p(v, T)$ does have some difficulties. Most methods involve *(a)* specifying an isotherm temperature $T$, *(b)* guessing a initial constant pressure (e.g., $p_1$ which will eventually become $p_{sat}$), and *(c)* performing some iteration procedure that makes the areas more equal between the horizontal line $p_1$ and the isotherm originating from some general equation of state $p = p(v, T)$, *(d)* repeating the iterative procedure until the two areas become equal and *(c)* extracting the final values of $p_{sat}$, $v_{sat}^{liq}$ and $v_{sat}^{vap}$ for the given isotherm temperature $T$.

Implicit in this iterative procedure is an often tedious task of repeatedly using the equation of state $p = p(v, T)$ at the pressure $p_1$ and given isotherm temperature $T$ to determine two roots (of three or more) for the specific volume of the saturated liquid $v_{sat}^{liq}$ and saturated vapour $v_{sat}^{vap}$, which usually introduces another iterative process. A practical method of the implementation of Maxwell's rule is introduced herein that has the advantage of not requiring any determination of the roots of the equation of state $p = p(v, T)$ for a specific volume (e.g., $v_{sat}^{liq}$ and $v_{sat}^{vap}$) at a given $p$ and $T$.

An overview of the new method is given first, and mathematical details follow. Two different coordinate points $(p_1, v_1)$ and $(p_2, v_2)$ are selected on the same isotherm of given temperature $T$ with the provisions that $(p_1, v_1)$ must lie on the left branch of the isotherm and $(p_2, v_2)$ must lie on the right branch, as shown in figure A–2. The slopes of the isotherm are negatively valued at points 1 and 2, and $p_1$ and $p_2$ are not necessarily equal. Values of $v_1$ and $v_2$ are specified such that $v_1 < v_{cp}$ and $v_2 > v_{cp}$, where $v_{cp}$ is the critical volume from the equation of state. The values of $p_1$ and $p_2$ are calculated directly from the equation of state $p = p(v, T)$ by using $v_1$ and $v_2$, respectively, and the common temperature $T$.

These two coordinates $(p_1, v_1)$ and $(p_2, v_2)$ on the same isotherm are joined by a straight line, and by using the coordinate point $(p_1, v_2)$ a right-angled triangle is produced with an area denoted by $A_{tri}$. The straight line joining points $(p_1, v_1)$ and $(p_2, v_2)$ also defines another area denoted by $A_{curv}$ between this line and the isotherm. The new method essentially involves changing $v_1$ and $v_2$ simultaneously in an efficient iterative procedure such that both areas $A_{tri}$ and $A_{curv}$ diminish simultaneously to zero. When $A_{tri} = 0$ and $A_{curv} = 0$, the final solution is then $p_{sat} = p_1 = p_2$, $v_{sat}^{liq} = v_1$ and $v_{sat}^{vap} = v_2$, as depicted in figure A–2.

The procedure of iteratively changing $v_1$ and $v_2$ results in the straightforward determination of the corresponding $p_1$ and $p_2$ using a general equation of state $p = p(v, T)$, which is an advantage over the reverse procedure that generally requires a root solving procedure.

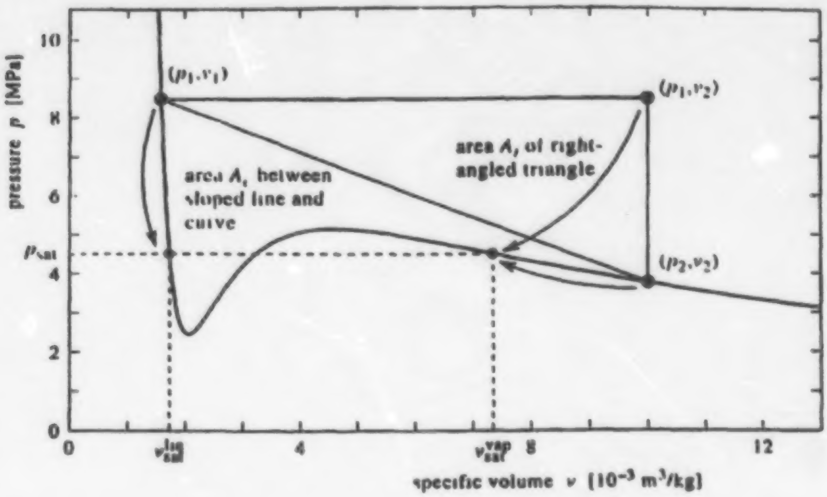

Figure A–2: Illustration of two areas $A_{curv}$ and $A_{tri}$ and three coordinate points $(p_1, v_1)$, $(p_1, v_2)$ and $(p_2, v_2)$ used in the iterative procedure to determine $p_{sat}$, $v_{sat}^{liq}$ and $v_{sat}^{vap}$.

The disadvantage of the new method is that it involves the use of two iterates ($v_1$ and $v_2$), instead of only one iterate $p_1$ in other methods, but this is not much of a handicap.

The new method begins by defining two abutting areas in the $pv$-plane that are directly related to a selected isotherm of temperature $T$ for which $p_{sat}$, $v_{sat}^{liq}$ and $v_{sat}^{vap}$ are to be determined by iteration, as discussed and illustrated in figure A–2. The right-angled triangle with the three vertices or coordinate points $(p_1, v_1)$, $(p_1, v_2)$ and $(p_2, v_2)$ has an area $A_{tri}$ and total derivative $\mathrm{d}A_{tri}$ given by

$$A_{tri} = \frac{1}{2}(p_1 + p_2)(v_2 - v_1) \qquad \text{and} \qquad \mathrm{d}A_{tri} = a_{tri}\,\mathrm{d}v_1 + b_{tri}\,\mathrm{d}v_2 \, ,$$

respectively, in which the coefficients $a_{tri}$ and $b_{tri}$ are defined by

$$a_{tri} = \left.\frac{\partial A_{tri}}{\partial v_1}\right|_{v_2} = \frac{1}{2}\left.\frac{\partial p(v,T)}{\partial v}\right|_1 (v_2 - v_1) - \frac{1}{2}(p_1 + p_2) \, ,$$

$$b_{tri} = \left.\frac{\partial A_{tri}}{\partial v_2}\right|_{v_1} = \frac{1}{2}\left.\frac{\partial p(v,T)}{\partial v}\right|_2 (v_2 - v_1) + \frac{1}{2}(p_1 + p_2) \, ,$$

respectively. In these expressions, $(\partial p(v,T)/\partial v)_i$ is the partial derivative of an equation of state with respect to specific volume at the isotherm constant temperature, and this partial derivative is evaluated at coordinate point $i$, that is by using $p_i$ and $v_i$ (for the two coordinates $i = 1$ and 2).

The other area $A_{\mathrm{curv}}$ between the curve and sloped line joining points $(p_1, v_1)$ and $(p_2, v_2)$, and its total derivative $\mathrm{d}A_{\mathrm{curv}}$ can be expressed in equivalent manner as

$$A_{\mathrm{curv}} = \frac{1}{2}(p_1 + p_2)(v_2 - v_1) - \int_{v_1}^{v_2} p(v, T)\,\mathrm{d}v \qquad \text{and} \qquad \mathrm{d}A_{\mathrm{curv}} = a_{\mathrm{curv}}\,\mathrm{d}v_1 + b_{\mathrm{curv}}\,\mathrm{d}v_2 \,,$$

respectively, in which the coefficients $a_{\mathrm{curv}}$ and $b_{\mathrm{curv}}$ are also defined similarly as

$$a_{\mathrm{curv}} = \left.\frac{\partial A_{\mathrm{curv}}}{\partial v_1}\right|_{v_2} = \frac{1}{2}\left.\frac{\partial p(v,T)}{\partial v}\right|_1 (v_2 - v_1) + \frac{1}{2}(p_1 - p_2) \,,$$

$$b_{\mathrm{curv}} = \left.\frac{\partial A_{\mathrm{curv}}}{\partial v_2}\right|_{v_1} = \frac{1}{2}\left.\frac{\partial p(v,T)}{\partial v}\right|_2 (v_2 - v_1) + \frac{1}{2}(p_1 - p_2) \,,$$

respectively. The integral of the equation of state $\int_{v_1}^{v_2} p(v, T)\,\mathrm{d}v$ can generally be evaluated in closed form for most equations of state, because the integration is over the specific volume at a constant isotherm temperature.

The two equations $\mathrm{d}A_{\mathrm{tri}} = a_{\mathrm{tri}}\,\mathrm{d}v_1 + b_{\mathrm{tri}}\,\mathrm{d}v_2$ and $\mathrm{d}A_{\mathrm{curv}} = a_{\mathrm{curv}}\,\mathrm{d}v_1 + b_{\mathrm{curv}}\,\mathrm{d}v_2$ can be combined to give $\mathrm{d}A_{\mathrm{curv}} - \mathrm{d}A_{\mathrm{tri}} = p_1\,\mathrm{d}v_1 - p_2\,\mathrm{d}v_2$, which is shorter and could be used to replace one of the previous and longer expressions. This is not done herein.

The two equations $\mathrm{d}A_{\mathrm{tri}} = a_{\mathrm{tri}}\,\mathrm{d}v_1 + b_{\mathrm{tri}}\,\mathrm{d}v_2$ and $\mathrm{d}A_{\mathrm{curv}} = a_{\mathrm{curv}}\,\mathrm{d}v_1 + b_{\mathrm{curv}}\,\mathrm{d}v_2$ can be solved for $\mathrm{d}v_1$ and $\mathrm{d}v_2$ in terms of the differential areas $\mathrm{d}A_{\mathrm{tri}}$ and $\mathrm{d}A_{\mathrm{curv}}$, that is

$$\mathrm{d}v_1 = \frac{1}{a_{\mathrm{tri}}b_{\mathrm{curv}} - a_{\mathrm{curv}}b_{\mathrm{tri}}}\left(b_{\mathrm{curv}}\,\mathrm{d}A_{\mathrm{tri}} - b_{\mathrm{tri}}\,\mathrm{d}A_{\mathrm{curv}}\right) ,$$

$$\mathrm{d}v_2 = \frac{1}{a_{\mathrm{tri}}b_{\mathrm{curv}} - a_{\mathrm{curv}}b_{\mathrm{tri}}}\left(-a_{\mathrm{curv}}\,\mathrm{d}A_{\mathrm{tri}} + a_{\mathrm{tri}}\,\mathrm{d}A_{\mathrm{curv}}\right) ,$$

provided the determinant $a_{\mathrm{tri}}b_{\mathrm{curv}} - a_{\mathrm{curv}}b_{\mathrm{tri}}$ is nonsingular. For a linear problem we could set $\mathrm{d}A_{\mathrm{tri}} = -A_{\mathrm{tri}}$ and $\mathrm{d}A_{\mathrm{curv}} = -A_{\mathrm{curv}}$ and solve directly for the values of $\mathrm{d}v_1$ and $\mathrm{d}v_2$ as

$$\mathrm{d}v_1 = \frac{-1}{a_{\mathrm{tri}}b_{\mathrm{curv}} - a_{\mathrm{curv}}b_{\mathrm{tri}}}\left(b_{\mathrm{curv}}\,A_{\mathrm{tri}} - b_{\mathrm{tri}}\,A_{\mathrm{curv}}\right) ,$$

$$\mathrm{d}v_2 = \frac{-1}{a_{\mathrm{tri}}b_{\mathrm{curv}} - a_{\mathrm{curv}}b_{\mathrm{tri}}}\left(-a_{\mathrm{curv}}\,A_{\mathrm{tri}} + a_{\mathrm{tri}}\,A_{\mathrm{curv}}\right)$$

to provide $v_{\mathrm{sat}}^{\mathrm{liq}} = v_1 + \mathrm{d}v_1$ and $v_{\mathrm{sat}}^{\mathrm{vap}} = v_2 + \mathrm{d}v_2$. However, because the problem is generally nonlinear, this step only provides values of $\mathrm{d}v_1$ and $\mathrm{d}v_2$ which have the correct sign but not necessarily the correct magnitude. Hence, the new values are considered as approximations, because they should be closer to the solution for the saturation properties.

These new values for $\mathrm{d}v_1$ and $\mathrm{d}v_2$ are then used to generate new values of $v_1 = v_1 + \mathrm{d}v_1$ and $v_2 = v_2 + \mathrm{d}v_1$ for the next step in an iterative procedure to produce more accurate values of $v_{sat}^{liq}$ and $v_{sat}^{vap}$. The iteration is continued until convergence is obtained, that is until $dv_1 \to 0$ and $dv_2 \to 0$ and correspondingly $v_1 \to v_{sat}^{liq}$, $v_2 \to v_{sat}^{vap}$ and $p_1 \to p_2 \to p_{sat}$.

If the initial guesses of $v_1$ and $v_2$ are highly inaccurate, then the predicted linear changes $dv_1$ and $dv_2$ might be too large and need to be restricted. One suggestion is to use $dv_1 = \text{sign}(dv_1)\min[|dv_1|, (v_2 - v_1)/100]$ and $dv_2 = \text{sign}(dv_2)\min[|dv_2|, (v_2 - v_1)/100]$, which produces the desired results. However, this restriction is seldom required.

The saturation curve for carbon dioxide was obtained for Van der Waals' equation of state, by using Maxwell's correction and the iterative scheme given in this appendix, and numerical results appear in table A-1. Van der Waals' equation of state is given by $p = RT/(1 - bv) - a/v^2$ (see chapter 2.6), for which $a = 27R^2T_c^2/64p_c$ and $b = RT_c/8p_c$, and $p_c = 7.3815$ MPa and $T_c = 304.15$ K are the critical pressure and temperature.

| $T$ (K) | $p_{sat}$ (MPa) | $v_{sat}^{liq}$ ($10^{-3}$ m$^3$/kg) | $v_{sat}^{vap}$ ($10^{-3}$ m$^3$/kg) |
|---|---|---|---|
| 216.55 | 1.6116 | 1.3784 | 21.0529 |
| 220 | 1.7442 | 1.3928 | 19.5390 |
| 225 | 1.9488 | 1.4149 | 17.5808 |
| 230 | 2.1682 | 1.4384 | 15.8618 |
| 235 | 2.4029 | 1.4637 | 14.3450 |
| 240 | 2.6531 | 1.4910 | 12.9999 |
| 245 | 2.9193 | 1.5206 | 11.8013 |
| 250 | 3.2017 | 1.5528 | 10.7279 |
| 255 | 3.5007 | 1.5881 | 9.7621 |
| 260 | 3.8165 | 1.6272 | 8.8885 |
| 265 | 4.1495 | 1.6708 | 8.0941 |
| 270 | 4.4999 | 1.7199 | 7.3673 |
| 272 | 4.6450 | 1.7415 | 7.0931 |
| 273.15 | 4.7297 | 1.7545 | 6.9394 |
| 274 | 4.7929 | 1.7643 | 6.8275 |
| 275 | 4.8679 | 1.7762 | 6.6976 |
| 276 | 4.9437 | 1.7886 | 6.5697 |
| 277 | 5.0202 | 1.8013 | 6.4435 |
| 278 | 5.0974 | 1.8144 | 6.3191 |
| 279 | 5.1753 | 1.8280 | 6.1964 |
| 280 | 5.2539 | 1.8420 | 6.0752 |
| 281 | 5.3333 | 1.8566 | 5.9555 |
| 282 | 5.4131 | 1.8717 | 5.8372 |

| $T$ (K) | $p_{sat}$ (MPa) | $v_{sat}^{liq}$ ($10^{-3}$ m$^3$/kg) | $v_{sat}^{vap}$ ($10^{-3}$ m$^3$/kg) |
|---|---|---|---|
| 283 | 5.4942 | 1.8875 | 5.7202 |
| 284 | 5.5757 | 1.9038 | 5.6044 |
| 285 | 5.6580 | 1.9209 | 5.4898 |
| 286 | 5.7411 | 1.9388 | 5.3761 |
| 287 | 5.8248 | 1.9575 | 5.2634 |
| 288 | 5.9093 | 1.9771 | 5.1514 |
| 289 | 5.9946 | 1.9977 | 5.0400 |
| 290 | 6.0805 | 2.0195 | 4.9292 |
| 291 | 6.1673 | 2.0425 | 4.8186 |
| 292 | 6.2547 | 2.0670 | 4.7082 |
| 293 | 6.3429 | 2.0931 | 4.5976 |
| 294 | 6.4319 | 2.1211 | 4.4866 |
| 295 | 6.5216 | 2.1513 | 4.3749 |
| 296 | 6.6121 | 2.1840 | 4.2620 |
| 297 | 6.7033 | 2.2199 | 4.1473 |
| 298 | 6.7953 | 2.2597 | 4.0302 |
| 299 | 6.8880 | 2.3044 | 3.9094 |
| 300 | 6.9815 | 2.3555 | 3.7834 |
| 301 | 7.0758 | 2.4159 | 3.6496 |
| 302 | 7.1708 | 2.4905 | 3.5027 |
| 303 | 7.2665 | 2.5916 | 3.3305 |
| 304 | 7.3631 | 2.7799 | 3.0723 |
| 304.19 | 7.3815 | 2.9195 | 2.9195 |

Table A-1: Saturation liquid and vapour properties for carbon dioxide predicted by using Van der Waals equation of state.

Isotherms for Van der Waals' equation of state can be plotted in the $pv$-plane, including the co-existence of the liquid and vapour in the saturation region, by using the results in table A–1 and the equation of state. These results are shown in figure A–3 for interest.

Corresponding results in the $pT$-plane for lines of constant $v$ are also shown for interest in figure A–4. The saturation properties collapse to one line because $p_{sat} = p_{sat}(T)$

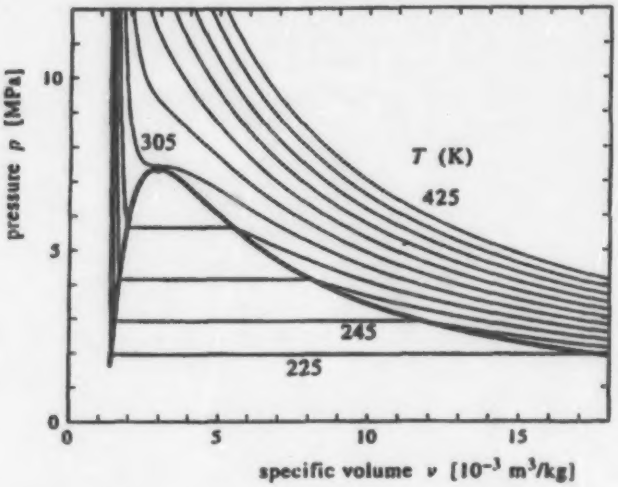

Figure A–3: Isotherms for Van der Waals equation of state.

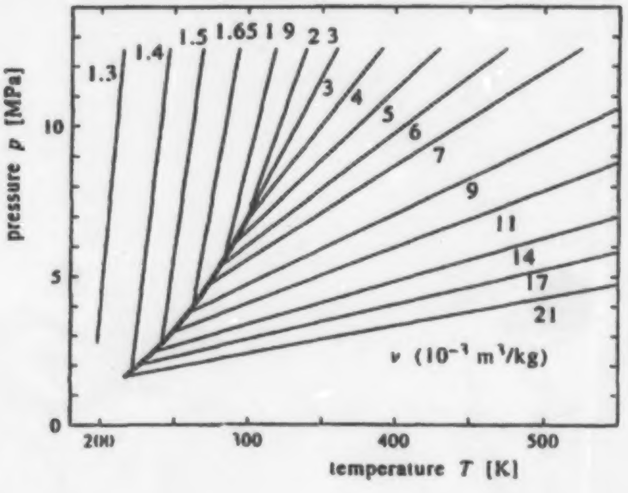

Figure A–4: Constant-volume lines for Van der Waals equation of state.

# APPENDIX B:
# SECOND AND THIRD VIRIAL COEFFICIENTS

The theory for the second and third virial coefficients $B(T)$ and $C(T)$ based on the Lennard and Jones 6-12 potential is well known and summarized in the book by Hirschfelder, Curtiss and Bird [2]. $B(T)$ and $C(T)$ are given therein in tables as a function of the temperature $T$, appropriate series representations for $B(T)$ and $C(T)$ are presented as a function of temperature, and numerical values for the two sets of series coefficients are also listed in tables (see pages 1114–1119). The two series for $B(T)$ and $C(T)$ with known coefficients are a convenient means of using $B(T)$ and $C(T)$ in computer codes for calculations involving virial and some other equations of state. However, the two sets of series coefficients for $B(T)$ and $C(T)$ have recently been checked and determined to be somewhat inaccurate, especially for the case of $C(T)$. Consequently, updated values of the series coefficients for both $B(T)$ and $C(T)$ are documented in this appendix. Experimental data for $B(T)$ and $C(T)$ and curve fits to these are also presented and discussed.

### Second Virial Coefficient

The series respresentation for the second virial coefficient $B(T)$ has the form [2]

$$B(T) = b_o \sum_{j=0}^{\infty} b_j \left(\frac{T}{T_o}\right)^{-j/2-1/4} \qquad \text{with} \qquad b_j = -\frac{2^{j+1/2}}{4j!}\,\Gamma\left(\frac{2j-1}{4}\right),$$

in which $b_j$ is the $j^{th}$ series coefficient, $b_o$ and $T_o$ are gas specific constants, and $\Gamma(x)$ denotes the gamma function. Values for $b_o$ and $T_o$ for the case of $CO_2$ are recommended by Hirschfelder, Curtiss and Bird as $b_o^{CO_2} = 85.05\ \mathrm{cm^3/mole} = 1.933\times10^{-3}\ \mathrm{m^3/kg}$ and $T_o^{CO_2} = 205$ K.

The series coefficients $b_j$ can be evaluated quickly and accurately today by using well-known computer software tools like MAPLE, MATHEMATICA or MATHLAB. The updated values for the coefficients $b_j$, from $j = 0$ to $j = 41$, are presented for convenience in table B–1 on the next page. These values for the most part are in good agreement with those listed on page 1119 of the book by Hirschfelder, Curtiss and Bird [2].

The second virial coefficient $B(T)$ and its first and second derivatives $B'(T)$ and $B''(T)$ with respect to temperature $T$ can be computed efficiently for a given temperature, on the basis of the series representation just given and values of the coefficients presented in table B–1, by making using of Hoerner's rule for computing polynomial equations efficiently. One convenient algorithm in FORTRAN for doing such calculations is shown in table B–2.

| $j$ | $b_j$ |
|---|---|
| 0 | $1.7330009\times10^{0}$ |
| 1 | $-2.5636934\times10^{0}$ |
| 2 | $-0.8665005\times10^{0}$ |
| 3 | $-4.2728222\times10^{-1}$ |
| 4 | $-2.1662512\times10^{-1}$ |
| 5 | $-1.0682056\times10^{-1}$ |
| 6 | $-5.0545860\times10^{-2}$ |
| 7 | $-2.2890119\times10^{-2}$ |
| 8 | $-9.9286511\times10^{-3}$ |
| 9 | $-4.1329382\times10^{-3}$ |
| 10 | $-1.6547752\times10^{-3}$ |
| 11 | $-6.3872681\times10^{-4}$ |
| 12 | $-2.3818734\times10^{-4}$ |
| 13 | $-8.5982455\times10^{-5}$ |

| $j$ | $b_j$ |
|---|---|
| 14 | $-3.0100598\times10^{-5}$ |
| 15 | $-1.0236007\times10^{-5}$ |
| 16 | $-3.3863172\times10^{-6}$ |
| 17 | $-1.0913389\times10^{-6}$ |
| 18 | $-3.4305828\times10^{-7}$ |
| 19 | $-1.0530463\times10^{-7}$ |
| 20 | $-3.1597473\times10^{-8}$ |
| 21 | $-9.2768368\times10^{-9}$ |
| 22 | $-2.6673192\times10^{-9}$ |
| 23 | $-7.5168046\times10^{-10}$ |
| 24 | $-2.0778030\times10^{-10}$ |
| 25 | $-5.6376034\times10^{-11}$ |
| 26 | $-1.5024114\times10^{-11}$ |
| 27 | $-3.9350793\times10^{-12}$ |

| $j$ | $b_j$ |
|---|---|
| 28 | $-1.0135315\times10^{-12}$ |
| 29 | $-2.5684631\times10^{-13}$ |
| 30 | $-6.4073830\times10^{-14}$ |
| 31 | $-1.5742193\times10^{-14}$ |
| 32 | $-3.8108427\times10^{-15}$ |
| 33 | $-9.0935017\times10^{-16}$ |
| 34 | $-2.1397780\times10^{-16}$ |
| 35 | $-4.9670388\times10^{-17}$ |
| 36 | $-1.1378185\times10^{-17}$ |
| 37 | $-2.5730156\times10^{-18}$ |
| 38 | $-5.7457404\times10^{-19}$ |
| 39 | $-1.2674098\times10^{-19}$ |
| 40 | $-2.7623752\times10^{-20}$ |
| 41 | $-5.9506437\times10^{-21}$ |

Table B–1: Nondimensional values of the series coefficients $b_j$ ($j = 0$ to 41) for the second virial coefficient $B(T)$, for the specific case of the Lennard-Jones 6–12 potential.

```
JMAX=41 42
A=TEMP**(-0.25D0)
B=A*A
C=DBLE(2*JMAX-1)
BLJ=COEFLJ(JMAX)
BLJP=C*COEFLJ(JMAX)
BLJPP=C*(C+4D0)*COEFLJ(JMAX)
DO J=1,JMAX-1
      C=C-2D0
      BLJ=COEFLJ(JMAX-J)+BLJ*B
      BLJP=C*COEFLJ(JMAX-J)+BLJP*B
      BLJPP=C*(C+4D0)*COEFLJ(JMAX-J)+BLJPP*B
ENDDO
BLJ=BLJ*A
BLJP=-0.25D0*BLJP*A
BLJPP=0.0625D0*BLJPP*A
```

Table B–2: Algorithm in FORTRAN for computing the second virial coefficient $B(T)$ and its first and second derivatives.

The mathematical operations consist essentially of one exponentiation, 42 multiplications and 81 additions for the evaluation of the series of 42 terms for $B(T)$.

Theoretical results for the second virial coefficient are shown as a function of temperature in figure B-1 for the specific case of $CO_2$, that is by using the specific values of $b_v^{CO_2} = 85.05 \cancel{\times 10^{-3}}$ cm$^3$/mole $= 1.933 \times 10^{-3}$ m$^3$/kg and $T_0^{CO_2} = 205$ K to convert the normalized theoretical results to dimensional values for $CO_2$. Also shown in the figure are $CO_2$ data taken from Dymond and Smith [11] and a curve fit to their experimental data. The following curve fit was taken from the physics handbook of Lide and Kehiaian [8]:

$$B(T) = \sum_{i=0}^{2} a_i \left( \frac{T_{ref}}{T} - 1 \right)^i ,$$

in which $T_{ref}^{CO_2} = 298.15$ K for $CO_2$ and the values of the three coefficients are

$$a_0^{CO_2} = -127.3 \text{ cm}^3/\text{mole} = -2.893 \times 10^{-3} \text{ m}^3/\text{kg} ,$$
$$a_1^{CO_2} = -287.6 \text{ cm}^3/\text{mole} = -6.535 \times 10^{-3} \text{ m}^3/\text{kg} ,$$
$$a_2^{CO_2} = -118.3 \text{ cm}^3/\text{mole} = -2.688 \times 10^{-3} \text{ m}^3/\text{kg} ,$$

for $CO_2$. The agreement between the theoretical and experimental results is fairly good considering the theoretical assumption of the Lennard-Jones 6–12 potential for the force

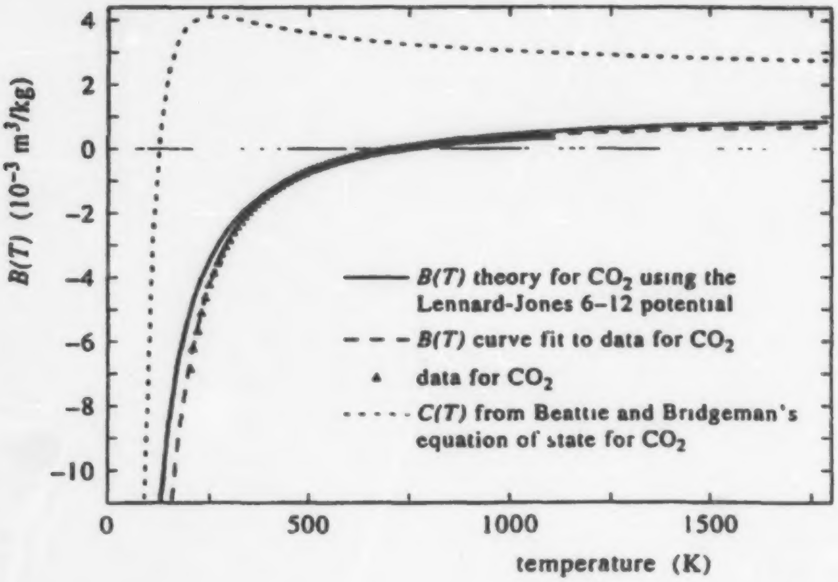

Figure B–1. Comparison of theoretical and experimental results for the second virial coefficient $B(T)$ for the case of $CO_2$.

field between molecules. Because the curve fit represents $CO_2$ data for $B(T)$ better than the theoretical results for $B(T)$ using the Lennard-Jones 6–12 potential, and the curve-fit trends appear correct outside the data range, the curve fit is recommended for use.

The variation of second virial coefficient with temperature for the case of $B(T)$ derived from Beattie and Bridgeman's equation of state is also shown in figure B–1. Their equation of state is given as $p = \rho RT(1-\varepsilon)(1+B\rho) - A\rho^2$, in which $A = A_0(1-a\rho)$, $B = B_0(1-b\rho)$ and $\varepsilon = c\rho/T^3$ (see equation (10) for details). This equation can be manipulated to yield an expression for the second virial coefficient given as $B(T) = B_0 - \frac{A_0}{RT} - \frac{c}{T^3}$. From these results shown in figure B–1, the shape and trends of Beattie and Bridgeman's $B(T)$ are essentially correct but the curve is higher than the experimental data.

The temperature-dependent second virial coefficient has the physical significance of accounting for the repulsion and attraction of molecules during bimolecular (binary) collisions. At temperatures above the Boyle temperature 713.34 K, $B(T)$ is positive and the dominant effect of intermolecular forces during the collision is that of bimolecular repulsion, resulting in higher gas pressures than those predicted by the ideal gas law ($p = \rho RT$). At lower temperatures $B(T)$ is negative and the dominant effect of intermolecular forces during the collision process is that of bimolecular attraction, resulting in lower gas pressures than those predicted by the ideal gas law. At the Boyle temperature of 713.34 K when $B(T)$ is zero the effect of these binary collision forces is balanced and the ideal gas law can predict the correct gas pressure, albeit fortuitiously.

For gases at higher temperatures for which $B(T)$ is positive and at sufficiently low gas densities the effects of bimolecular repulsion is often negligible and therefore ignored. However, for slightly higher gas densities that intermolecular repulsion forces have some influence, the initial effects of this repulsion are often included by modifying the ideal gas law, $p = \rho RT$, to the Clausius equation of state, $p = \rho RT/[1 - \hat{b}\rho]$, with a constant co-volume coefficient $\hat{b}$. The value of $\hat{b}$ is taken as some average value of the positive part of spectrum of values of $B(T)$. For example, for $CO_2$ one might well select the value $\hat{b}^{CO_2} = 29.67$ cm$^3$/mole $= 0.6744\times10^{-3}$ m$^3$/kg, which is in the upper-range of the positive $B(T)$ values shown graphically in figure B–1. This is a fairly good approximation at higher temperatures because $B(T)$ does not change appreciably thereat.

One can also compare the constant coefficient $b = RT_c/8p_c = 0.9729\times10^{-3}$ m$^3$/kg in Van der Waals' equation of state, $p = \rho RT/[1 - b\rho] - a\rho^2$, and furthermore compare $b = 0.08664RT_c/8p_c = 0.6744\times10^{-3}$ m$^3$/kg in Redlich and Kwong's equation of state,

$p = \rho RT/[1 - b\rho] - a\rho^2/[1 + b\rho]$, to the spectrum of positive values of $B(T)$ displayed in figure B-1. These values for $b$ also lie in the upper range of the positive values for $B(T)$. Consequently, this comparison helps deduce that the existence of $b$ in Clausius', Van der Waals', and Redich and Kwong's equations of state is to help account for the intermolecular forces of bimolecular repulsion.

This is a simple interpretation of how a constant $\hat{b}$ value might be selected for the Clausius and possibly other equations of state. In addition, it clearly illustrates that that the use of the Clausius equation of state is limited to the high-temperature region in which $B(T)$ is large and reasonably constant, which is a disadvantage stemming directly from oversimplification, that is ignoring the actual variation of $B(T)$ with temperature, especially in the case of lower gas temperatures when $B(T)$ is near zero or negative.

### Third Virial Coefficient

The series respresentation for the third virial coefficient $C(T)$ has the form [2]

$$C(T) = b_o^2 \sum_{j=0}^{\infty} c_j \left(\frac{T}{T_o}\right)^{-j/2-1/2},$$

in which $c_j$ is the $j^{\text{th}}$ series coefficient and $b_o$ and $T_o$ are gas specific constants. Recommended values in Hirschfelder, Curtiss and Bird's book for the case of carbon dioxide $CO_2$ are $b_o^{CO_2} = 85.05$ cm$^3$/mole $= 1.933 \times 10^{-3}$ m$^3$/kg and $T_o^{CO_2} = 205$ K, as mentioned earlier. Note that the series representation of $C(T)$ is quite similar to that for $B(T)$, but the coefficients $c_j$, as we will see, are much more complicated.

The $j^{\text{th}}$ coefficient of the series representation of $C(T)$ is the double integral equation

$$c_j = -6\,\frac{2^j}{j!}\,\Gamma\left(\frac{j-1}{2}\right) \int_0^{\sqrt{3/4}} \int_{1/2}^{\sqrt{1-y^2}} y A_j \, dx \, dy$$

for the specific case of the Lennard-Jones 6–12 potential [2]. In this equation, $\Gamma(x)$ is the gamma function, and the coefficient $-6\,\frac{2^j}{j!}\,\Gamma\left(\frac{j-1}{2}\right)$ preceding the double integral can be evaluated easily by using the software MAPLE, MATHEMATICA or MATHLAB The part of the integrand $A_j$ in the previous equation is given by the expression

$$A_j = \left(1 + \xi^2 + \eta^2\right) + \sqrt{1 + \xi^2 + \eta^2}\left[\frac{1 + \xi + \eta}{\sqrt{1 + \xi^2 + \eta^2}}\right]^j$$
$$-\sqrt{1 + \xi^2}\left[\frac{1 + \xi}{\sqrt{1 + \xi^2}}\right]^j - \sqrt{1 + \eta^2}\left[\frac{1 + \eta}{\sqrt{1 + \eta^2}}\right]^j - \sqrt{\xi^2 + \eta^2}\left[\frac{\xi + \eta}{\sqrt{\xi^2 + \eta^2}}\right]^j.$$

for the specific case of the Lennard-Jones 6 12 potential. In this expression,

$$\xi = \left[\frac{1}{x^2 + y^2}\right]^3 \qquad \text{and} \qquad \eta = \left[\frac{1}{(1-x)^2 + y^2}\right]^3$$

are functions of $x$ and $y$.

The exact solution for the double integral is not known, although an approximate solution exists when the value of $j$ becomes large [2]. The integration must be done numerically; however, this integration is not straightforward for three reasons: *(a)* numerical round-off errors are detrimental to high accuracy in the vicinity of the point $x = 1$ and $y = 0$ ($\eta \to \infty$ when $y \to 0$ and $x \to 1$ simultaneously) even though the integrand is well behaved; *(b)* the special case of $j = 1$ is ill-posed because the gamma function and double-integral are both unbounded although their product is finite; and *(c)* the region of integration is bounded on one side by a curve—the radius of the circle $x^2 + y^2 = 1$. These integration problems can be overcome by using the following method of integration.

For the special case of $j = 0$ the integrand part $A_{j=0}$ is calculated accurately by using

$$A_0 = \begin{cases} (1+\xi+\eta) - \sqrt{1+\xi^2+\eta^2} - \sqrt{1+\xi^2} - \sqrt{1+\eta^2} - \sqrt{\xi^2+\eta^2} & \text{if } \eta < 10^6, \\ (1+\xi) - \sqrt{1+\xi^2} - \dfrac{\xi^2}{4\eta^3} + \dfrac{3\xi^2\,(1+\xi^2)}{16\eta^5} - \dfrac{5\xi^2\,(2+3\xi^2+2\xi^4)}{64\eta^7} - \cdots & \text{if } \eta \geq 10^6. \end{cases}$$

to make round-off errors insignificant. The second part of this equation is an expansion of the first part for the case when $\eta$ is large (e.g., $\eta \geq 10^6$). In terms of the $x$ and $y$ domain, this corresponds to the case of $(1-x)^2 + y^2 \leq 10^{-2}$. Note that the last term in the expansion, that is $5\xi^2\,(2+3\xi^2+2\xi^4)/64\eta^7$, is short and included mainly for interest. This term is not needed for computational accuracy because terms up to $\eta^{-5}$ are sufficient.

For the specific case of $j = 1$ the part of the integrand $A_1$ multiplied by $\Gamma(0)$ has the limiting form given by

$$\Gamma(0)A_1 = \begin{cases} \ln\left[\dfrac{(1+\xi^2)(1+\eta^2)}{1+\xi^2+\eta^2}\right] + \xi\ln\left[\dfrac{(1+\xi^2)(\xi^2+\eta^2)}{\xi^2(1+\xi^2+\eta^2)}\right] \\ \qquad + \eta\ln\left[\dfrac{(1+\eta^2)(\xi^2+\eta^2)}{\eta^2(1+\xi^2+\eta^2)}\right] & \text{if } \eta < 10^6, \\ \ln\left(1+\xi^2\right) + \xi\ln\left(\dfrac{1+\xi^2}{\xi^2}\right) - \dfrac{\xi(1+\xi)}{\eta^2} + \dfrac{\xi^2}{\eta^3} \\ \qquad + \dfrac{\xi(1+\xi)(1+\xi+\xi^2)}{2\eta^4} - \dfrac{\xi^2(1+\xi^2)}{\eta^5} \\ \qquad - \dfrac{\xi(1+\xi)(1+2\xi+\xi^2+2\xi^3+\xi^4)}{3\eta^6} \\ \qquad + \dfrac{\xi^2(2+3\xi^2+2\xi^3)}{2\eta^7} + \cdots & \text{if } \eta \geq 10^6, \end{cases}$$

and the use of these results gives accurate calculations of the modified part of the integrand $\Gamma(0)A_1$ such that round-off errors are not detrimental. The last part of the equation is again an expansion of the first part for the case when $\eta$ is large (e.g., $\eta \geq 10^6$). Note that the last term in this expansion, $\xi^2(2+3\xi^2+2\xi^3)/2\eta^7$, is rather short and included here for interest. This term is not necessarily required to maintain accuracy during calculations because terms up to $\eta^{-5}$ are sufficient.

For the more general case of $j \geq 2$, the integrand part $A_j$ is calculated accurately by

$$A_j = \begin{cases} \left(1+\xi^2+\eta^2\right) + \sqrt{1+\xi^2+\eta^2}\left[\dfrac{1+\xi+\eta}{\sqrt{1+\xi^2+\eta^2}}\right]^j - \sqrt{1+\xi^2}\left[\dfrac{1+\xi}{\sqrt{1+\xi^2}}\right]^j \\ \qquad -\sqrt{1+\eta^2}\left[\dfrac{1+\eta}{\sqrt{1+\eta^2}}\right]^j - \sqrt{\xi^2+\eta^2}\left[\dfrac{\xi+\eta}{\sqrt{\xi^2+\eta^2}}\right]^j & \text{if } \eta < 10^6. \\ (1+\xi) - \sqrt{1+\xi^2}\left[\dfrac{1+\xi}{\sqrt{1+\xi^2}}\right]^j + \dfrac{j(j-1)\xi}{\eta} + \dfrac{j(j-1)(j-3)\xi(1+\xi)}{2\eta^2} \\ \quad + \dfrac{(j-1)\xi\left[2j(j^2-8j+9)(1+\xi^2)+3(j^3-7j^2+9j+1)\xi\right]}{12\eta^3} \\ \quad + \dfrac{j(j-1)^2\xi(1+\xi)\left[(j-3)(j-11)(1+\xi^2)+(j-5)^2\xi\right]}{24\eta^4} \\ \quad + \dfrac{(j-1)\xi\left[6jJ_1(1+\xi^4)+15(j-1)J_2\xi(1+\xi^3)+20jJ_3\xi^2\right]}{720\eta^5} + \cdots & \text{if } \eta \geq 10^6. \end{cases}$$

in which $J_1 = j^4 - 24j^3 + 146j^2 - 264j + 165$, $J_2 = j^4 - 20j^3 + 102j^2 - 132j + 9$ and $J_3 = j^5 - 20j^4 + 116j^3 + 116j^2 - 220j + 147$. The use of the original equation and its expansion helps eliminate the adverse effect of round-off errors.

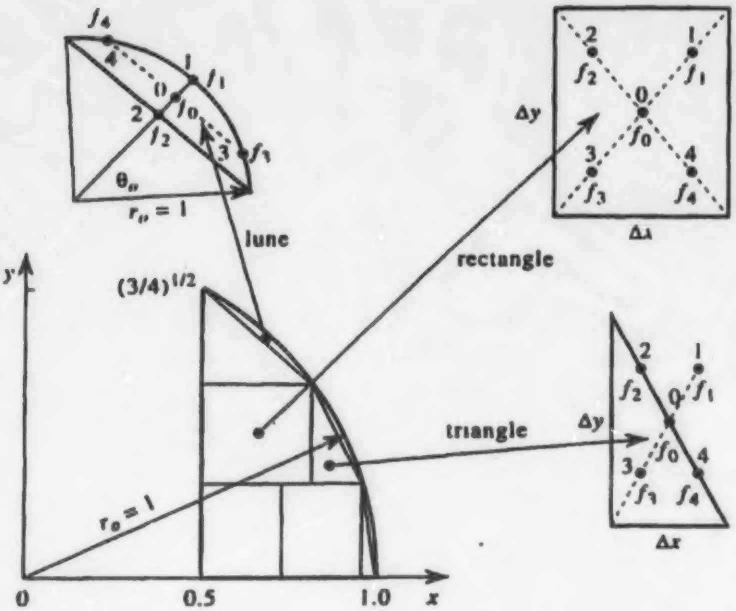

Figure B–2. Region of integration covered by a coarse grid of finite elements consisting of rectangles, triangles and lunes.

Performing the double integration accurately, as mentioned previously, not only requires an accurate calculation of the integrand (as introduced) but also involves an accurate numerical integration scheme over the integration domain. This domain is bounded at the bottom by the horizontal line $y = 0$, at the left side by the vertical line $x = 1/2$, and at the right and upper side by the circular arc $x^2 + y^2 = 1$, as illustrated in figure B–2. The integration scheme is based on high-order finite elements in the form of rectangles, right-angled triangles and lunes of a circle, and these are also depicted in the figure

The high-order finite elements are designed to fit a quadratic equation in two dimensions to the actual integrand and thereby capture exactly the resulting area under the quadratic equation. This quadratic equation is defined by

$$f(\hat{x}, \hat{y}) = a_1 + a_2\hat{x} + a_3\hat{y} + a_4\hat{x}\hat{y} + a_5\hat{x}^2 + a_6\hat{y}^2.$$

in which $\hat{x}$ and $\hat{y}$ are local and often normalized values of $x$ and $y$ with respect to a point within an element (e.g., center of the rectangle). Finite-element rectangles, triangles and lunes are required in the analysis and special results for these are now presented.

Consider the case of the rectangle first. Let the local coordinate origin be the center of the rectangle, and let the rectangular width and height be given by $\Delta x$ and $\Delta y$, respectively. Define five interior coordinates $(\hat{x}, \hat{y})$ as $(0,0)$, $(\beta/2, \beta/2)$, $(-\beta/2, \beta/2)$, $(-\beta/2, -\beta/2)$, and $(\beta/2, -\beta/2)$ at which the evaluated functions are defined as $f_0$, $f_1$, $f_2$, $f_3$ and $f_4$, respectively. The parameter $\beta$ controls the distance of the nodal coordinates from the center of the rectangle, and these nodal points lie on the diagonals of the rectangle. These details are illustrated for the rectangle with $\beta = 1/\sqrt{3}$ in figure B-2. The coefficients of $f(\hat{x}, \hat{y})$ can be evaluated as $a_1 = f_0$, $a_2 = (f_1 - f_2 - f_3 + f_4)/2\beta$, $a_3 = (f_1 + f_2 - f_3 - f_4)/2\beta$, $a_4 = (f_1 - f_2 + f_3 - f_4)/\beta^2$ and $a_5 + a_6 = (f_1 - f_2 + f_3 - f_4 - 4f_0)/\beta^2$.

The integration $I_{\text{rectangle}} = \Delta x \Delta y \int_{-1/2}^{-1/2} \int_{-1/2}^{-1/2} f(\hat{x}, \hat{y})\, d\hat{x}\, d\hat{y}$ is done and we obtain $I_{\text{rectangle}} = \left[a_1 + \frac{1}{12}(a_5 + a_6)\right] \Delta x \Delta y$. On replacing $a_1$ and $a_5 + a_6$ by their previous results in terms of $f_0$, $f_1$, $f_2$, $f_3$ and $f_4$, and selecting $\beta = 1/\sqrt{3}$, we obtain

$$I^{\beta=1/\sqrt{3}}_{\text{rectangle}} = \frac{1}{4}(f_1 + f_2 + f_3 + f_4)\, \Delta x \Delta y$$

as the final results. The selection of $\beta = 1/\sqrt{3}$ eliminates the need to evaluate $f_0$, yields an equal weighting for $f_1$, $f_2$, $f_3$ and $f_4$, and produces a simple result. Note that the alternate selection of $\beta = 1/2$ yields $I^{\beta=1/2}_{\text{rectangle}} = \frac{1}{3}(f_1 + f_2 + f_3 + f_4 - f_0)\, \Delta x \Delta y$.

Now consider the case of the right-angled triangle. Let the local coordinate origin be the center of the diagonal and let the base and height of the triangle be defined by $\Delta x$ and $\Delta y$, respectively. Define five interior and exterior coordinates $(\hat{x}, \hat{y})$ as $(0,0)$, $(\beta/2, \beta/2)$, $(-\beta/2, \beta/2)$, $(-\beta/2, -\beta/2)$ and $(\beta/2, -\beta/2)$ at which the evaluated functions are defined as $f_0$, $f_1$, $f_2$, $f_3$ and $f_4$, respectively. The parameter $\beta$ controls the distance of the nodal coordinates from the center of the rectangle around the triangle, and these nodal points lie on the diagonals of this rectangle. These details are illustrated for the triangle with $\beta = 1/2$ in figure B-2. The coefficients of $f(\hat{x}, \hat{y})$ can be evaluated as $a_1 = f_0$, $a_2 = (f_1 - f_2 - f_3 + f_4)/2\beta$, $a_3 = (f_1 + f_2 - f_3 - f_4)/2\beta$, $a_4 = (f_1 - f_2 + f_3 - f_4)/\beta^2$ and $a_5 + a_6 = (f_1 - f_2 + f_3 - f_4 - 4f_0)/\beta^2$, the same as for the case of the rectangle.

The integration $I_{\text{triangle}} = \Delta x \Delta y \int_{-1/2}^{-1/2} \int_{-1/2}^{-\hat{y}} f(\hat{x}, \hat{y})\, d\hat{x}\, d\hat{y}$ is now performed and the result is $I_{\text{triangle}} = \left[\frac{1}{2}a_1 - \frac{1}{12}(a_2 + a_3) + \frac{1}{24}(a_5 + a_6)\right] \Delta x \Delta y$. We now replace $a_1$, $a_2 + a_3$ and $a_5 + a_6$ by their previous results in terms of $f_0$, $f_1$, $f_2$, $f_3$ and $f_4$, and we also select $\beta = 1/2$. Then,

$$I^{\beta=1/2}_{\text{triangle}} = \frac{1}{6}(f_2 + 2f_3 + f_4 - f_0)\, \Delta x \Delta y$$

is the final result of the integration. The specific selection of the value of $\beta = 1/2$ eliminates the determination and use of $f_1$ that lies outside the triangle.

Consider the final case of the lune of a circle. The geometrical location and attributes of this lune are defined first. The straight side segment of this lune is attached to the slanted side of the previous triangle of width $\Delta x$ and height $\Delta y$, and the center of this straight side is at the coordinate point $(x, y)$, which is apparent from the sketches of triangles and lunes in figure B-2. Then, the angle of the line from the origin ($x = 0$, $y = 0$) through the point $(x, y)$, which cuts the lune symmetrically, is given by $\theta_{oo} = \tan^{-1}(y/x)$. The half angle that defines the lune is given by $\theta_o = \sin^{-1}\left(\sqrt{(\Delta x/2r_o)^2 + (\Delta y/2r_o)^2}\right)$, where in general $r_o$ is the radius of the circle (even if $r_o = 1$ in our specific case). The distance from the origin ($x = 0$, $y = 0$) to $(x, y)$ is $r_o \cos(\theta_o)$, the general result for a lune with a radius $r_o$. The maximum thickness of this lune along the radial line is $r_o - r_o \cos(\theta_o)$.

A local coordinate system $(\hat{x}, \hat{y})$ is centered in the lune, and this origin ($\hat{x} = 0, \hat{y} = 0$) is located at $x = \left[\frac{r_o}{2} + \frac{r_o}{2}\cos(\theta_o)\right]\cos(\theta_{oo})$ and $y = \left[\frac{r_o}{2} + \frac{r_o}{2}\cos(\theta_o)\right]\sin(\theta_{oo})$. The coordinate $\hat{x}$ is parallel the straight side of the lune and the coordinate $\hat{y}$ is along a radial line. Five local coordinate points $(\hat{x}, \hat{y})$ are defined on the boundary of the lune as $(0,0)$, $(0, \Delta\hat{y})$, $(0, -\Delta\hat{y})$, $(\Delta\hat{x}, 0)$ and $(-\Delta\hat{x}, 0)$, in which $\Delta\hat{y} = \frac{r_o}{2} - \frac{r_o}{2}\cos(\theta)$ and $\Delta\hat{x} = \sqrt{r_o^2 - (r_0 - \Delta\hat{y})^2}$. At these five coordinate points the evaluated functions are denoted by $f_0$, $f_1$, $f_2$, $f_3$ and $f_4$, respectively. These details are apparent from the sketch of the lune in figure B-2. The coefficients of $f(\hat{x}, \hat{y})$ can be evaluated as $a_1 = f_0$, $a_2 = (f_3 - f_4)/2\Delta\hat{x}$, $a_3 = (f_1 - f_2)/2\Delta\hat{y}$, $a_4$ is undefined (and not needed), $a_5 = (f_3 + f_4 - 2f_0)/2\Delta\hat{x}^2$ and $a_6 = (f_1 + f_2 - 2f_0)/2\Delta\hat{y}^2$, and the particular locations of $f_0$, $f_1$, $f_2$, $f_3$ and $f_4$ within and on the periphery of the lune are shown in figure B-2.

The integration $I_{\text{lune}} = \int_{r_o\cos(\theta_o)}^{r_o} \int_{-\sqrt{1-y^2}}^{\sqrt{1-y^2}} f(\hat{x}, \hat{y})\, dx\, dy$ is now performed in terms of $x$ and $y$, not $\hat{x}$ and $\hat{y}$, by using $\hat{x} \equiv x$ and $\hat{y} \equiv y - \frac{r_o}{2} - \frac{r_o}{2}\cos\theta_o$ in the integrand $f(\hat{x}, \hat{y})$ or $f(x, y - \frac{r_o}{2} - \frac{r_o}{2}\cos\theta_o)$. This integration is tedious but straightforward, yielding the result

$$\begin{aligned} I_{\text{lune}} = \;& a_1 r_o^2 \mathcal{A} + a_3 \frac{r_o^3}{6}\left[4\sin^3(\theta_o) - 3\mathcal{A} - 3\mathcal{A}\cos(\theta_o\right] + a_5 \frac{r_o^4}{12}\left[3\mathcal{A} - 2\cos(\theta_o)\sin^3(\theta_o)\right] \\ & + a_6 \frac{r_o^4}{12}\left[3\mathcal{A} + 3\mathcal{A}\{1 + cos(\theta_o)\}^2 - 8\sin^3(\theta_o) - 2\cos(\theta_o)\sin^3(\theta_o)\right]. \end{aligned}$$

in which $\mathcal{A} = \theta_o - \frac{1}{2}\sin(\theta_o)$. Note that $r_o^2\mathcal{A} = r_o^2\left[\theta_o - \frac{1}{2}\sin(\theta_o)\right]$ is the area of the lune.

The previous results for $a_1$, $a_3$, $a_5$ and $a_6$ in terms of $f_0$, $f_1$, $f_2$, $f_3$, $f_4$ and $f_5$ are now substituted into the previous equation. We also determine the limiting form of the equation for the case of small angles for $\theta_o$. The final results can be summarized as

$$I_{\rm lune} = \begin{cases} f_0 r_o^2 \mathcal{A} + \dfrac{(f_1 - f_2) r_o^3}{12 \Delta \hat{y}} \left[ 4 \sin^3(\theta_o) - 3\mathcal{A} - 3\mathcal{A} \cos(\theta_o) \right] \\ \quad + \dfrac{(f_3 + f_4 - 2 f_0) r_o^3}{24 \Delta \hat{x}^2} \left[ 3\mathcal{A} - 2 \cos(\theta_o) \sin^3(\theta_o) \right] + \dfrac{(f_1 + f_2 - 2 f_0) r_o^4}{24 \Delta \hat{y}^2} \\ \quad \times \left[ 3\mathcal{A} + 3\mathcal{A} \{ 1 + \cos(\theta_o) \}^2 - 8 \sin^3(\theta_o) - 2 \cos(\theta_o) \sin^3(\theta_o) \right] & \text{if } \theta_o \geq 10^{-3}. \\ \\ \dfrac{55 f_0 + 4 f_1 + 18 f_2 + 14 f_3 + 14 f_4}{105} \left[ \dfrac{2}{3} r_o^2 \theta_o^3 \right] & \text{if } \theta_o < 10^{-3}, \end{cases}$$

in which the last result is for the case of small angles. For an accurate integration with many cells, the use of the results for the small angle approximation eliminates round-off errors. For the case of small angles the area of the lune is given simply as $\frac{2}{3} r_o^2 \theta_o^3$.

The results of the integration for the coefficients $c_j$ of the third virial coefficient $C(T)$ are presented in table B–3. The first 42 coefficients are listed, that is for $j = 0$ to $j = 41$. These values are more accurate than those listed on page 1119 of the book by Hirschfelder, Curtiss and Bird [2] by as much as a factor of three for higher values of $j$. However, the agreement of the calculated values from the present series with tabulated values presented on page 1116 of their book is quite good. It seems clear that their tabulated values must have been calculated by using a set of different and better series coefficients than those presented in their book.

The third virial coefficient $C(T)$ and its first and second derivatives $C'(T)$ and $C''(T)$ with respect to temperature $T$ can be computed efficiently for a given temperature, on the basis of the series representation just given and values of the coefficients presented in table B–3, by making using of Hoerner's rule for computing polynomial equations efficiently. One convenient algorithm written in the FORTRAN language for doing such calculations is presented in table B–4. The mathematical operations consist essentially of one exponentiation, 42 multiplications and 81 additions for the evaluation of the series of 42 terms for $C(T)$

Theoretical results for the third virial coefficient are shown as a function of temperature in figure B–3 for the specific case of $CO_2$, that is by using the specific values of $b_o^{CO_2} = 85.05 \times 10^{-3}$ cm$^3$/mole $= 1.933 \times 10^{-3}$ m$^3$/kg and $T_o^{CO_2} = 205$ K to convert the normalized theoretical results to dimensional values for $CO_2$. Also shown in the figure are $CO_2$ data taken from the reference book by Dymond and Smith [11]. A short and simple curve fit was also developed to fit the experimental data, and the results are shown in

| $j$ | $c_j$ |
|---|---|
| 0 | $1.72851902 \times 10^{0}$ |
| 1 | $-3.19323258 \times 10^{0}$ |
| 2 | $1.51546862 \times 10^{0}$ |
| 3 | $9.52918462 \times 10^{-1}$ |
| 4 | $4.26974091 \times 10^{-1}$ |
| 5 | $5.74994320 \times 10^{-2}$ |
| 6 | $-1.42030080 \times 10^{-1}$ |
| 7 | $-2.12691253 \times 10^{-1}$ |
| 8 | $-2.07334814 \times 10^{-1}$ |
| 9 | $-1.68491111 \times 10^{-1}$ |
| 10 | $-1.22580998 \times 10^{-1}$ |
| 11 | $-8.24353661 \times 10^{-2}$ |
| 12 | $-5.21630474 \times 10^{-2}$ |
| 13 | $-3.14068217 \times 10^{-2}$ |
| 14 | $-1.81305135 \times 10^{-2}$ |
| 15 | $-1.00906042 \times 10^{-2}$ |
| 16 | $-5.43690978 \times 10^{-3}$ |
| 17 | $-2.84526379 \times 10^{-3}$ |
| 18 | $-1.44995136 \times 10^{-3}$ |
| 19 | $-7.21046276 \times 10^{-4}$ |
| 20 | $-3.50521399 \times 10^{-4}$ |
| 21 | $-1.66821065 \times 10^{-4}$ |
| 22 | $-7.78254360 \times 10^{-5}$ |
| 23 | $-3.56287785 \times 10^{-5}$ |
| 24 | $-1.60214785 \times 10^{-5}$ |
| 25 | $-7.08255888 \times 10^{-6}$ |
| 26 | $-3.08024974 \times 10^{-6}$ |
| 27 | $-1.31879472 \times 10^{-6}$ |
| 28 | $-5.56188467 \times 10^{-7}$ |
| 29 | $-2.31181559 \times 10^{-7}$ |
| 30 | $-9.47506664 \times 10^{-8}$ |
| 31 | $-3.83091203 \times 10^{-8}$ |
| 32 | $-1.52858590 \times 10^{-8}$ |
| 33 | $-6.02155031 \times 10^{-9}$ |
| 34 | $-2.34265582 \times 10^{-9}$ |
| 35 | $-9.00389934 \times 10^{-10}$ |
| 36 | $-3.41983926 \times 10^{-10}$ |
| 37 | $-1.28397444 \times 10^{-10}$ |
| 38 | $-4.76648344 \times 10^{-11}$ |
| 39 | $-1.75000683 \times 10^{-11}$ |
| 40 | $-6.35600841 \times 10^{-12}$ |
| 41 | $-2.28417914 \times 10^{-12}$ |

**Table B–3:** Nondimensional values of the series coefficients $c_j$ $(j = 0$ to $41)$ for the third virial coefficient $C(T)$, for the specific case of the Lennard-Jones 6–12 potential.

```
JMAX=41
A=1D0/DSQRT(TEMP)
C=DBLE(JMAX)
CLJ=COEFLJ(JMAX)
CLJP=C*COEFLJ(JMAX)
CLJPP=C*(C+2D0)*COEFLJ(JMAX)
DO J=1,JMAX-1
      C=C-1D0
      CLJ=COEFLJ(JMAX-J)+CLJ*A
      CLJP=C*COEFLJ(JMAX-J)+CLJP*A
      CLJPP=C*(C+2D0)*COEFLJ(JMAX-J)+CLJPP*A
ENDDO
CLJ=CLJ*A
CLJP=-0.5D0*CLJP*A
CLJPP=0.25D0*CLJPP*A
```

**Table B–4:** Algorithm in FORTRAN for computing the third virial coefficient $C(T)$ and its first and second derivatives.

figure B-3. The general curve fit is given by

$$C(T) = b_o^2\left[0.40\left(\frac{T_{ref}}{T}\right)^m - 0.0072\left(\frac{T_{ref}}{T}\right)^7\right]$$

with the exponent

$$m = \frac{1}{2} + \frac{1.85}{1 + \left(\frac{T}{T_{ref}}\right)^2}\,.$$

where $b_o^{CO_2} = 85.05\times\cancel{10^{-3}}$ cm$^3$/mole $= 1.933\times10^{-3}$ m$^3$/kg and $T_{ref}^{CO_2} = 400$ K for $CO_2$.The agreement between the theoretical and experimental results in figure B-3 is fairly good considering the theoretical assumption of the Lennard-Jones 6-12 potential for the force field between molecules and the scatter in the experimental data for $CO_2$. There appears little preference for using the theoretical equation or the curve fit to reproduce $C(T)$ for $CO_2$, because the amount of data and its visible trends are really insufficient to make a definitive choice. However, one straightforward advantage of using the curve fit is that it simpler to program.

The variation of third virial coefficient with temperature for the case of $C(T)$ derived from Beattie and Bridgeman's equation of state is also shown in figure B-3. Their equation

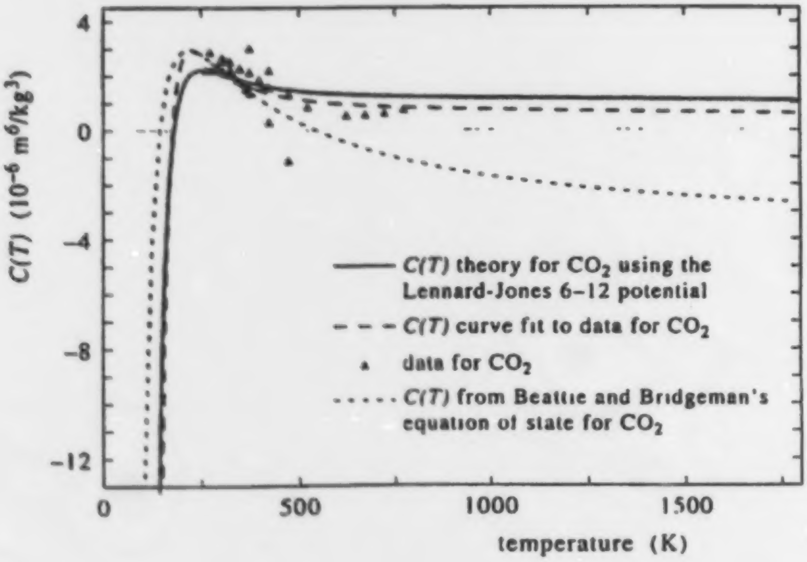

Figure B-3. Comparison of theoretical and experimental results for the third virial coefficient $C(T)$ for the case of $CO_2$.

of state is given as $p = \rho RT(1-\varepsilon)(1+B\rho) - A\rho^2$, in which $A = A_0(1-a\rho)$, $B = B_0(1-b\rho)$ and $\varepsilon = c\rho/T^3$ (see equation (10) for details). This equation can be manipulated to yield an expression for the third virial coefficient that is given by $C(T) = -bB_0 + \frac{aA_0}{RT} - \frac{cB_0}{T^3}$. The fourth virial coefficent is $D(T) = bcB_0/T^3$. From the results shown in figure B–3, the shape and trends of Beattie and Bridgeman's $C(T)$ are essentially correct, the curve cuts through the data quite well, but the results at high temperatures are unfortunately negatively valued.

The temperature-dependent third virial coefficient has the physical significance of accounting for the effects of repulsion and attraction of molecules during trimolecular collisions. At temperatures higher than 132.54 K, $C(T)$ is positive and the dominant effect of the intermolecular force during the collision process is that of trimolecular repulsion, resulting in higher gas pressures than those predicted by the ideal gas law ($p = \rho RT$). At lower temperatures $C(T)$ is negative and the dominant effect of the intermolecular force during the collision process is that of trimolecular attraction, resulting in lower gas pressures than those predicted by the ideal gas law. At the temperature 132.54 K when $C(T)$ is zero the effects of these trimolecular forces counteract or are balanced.

# APPENDIX 7

# SPLINE REPRODUCTION OF THERMOCHEMICAL DATA FOR FLOW COMPUTATIONS FOR A CLOSED VESSEL

by

Antonio Mandatori

# Abstract

## A SPLINE METHOD OF REPRODUCING JANAF THERMOCHEMICAL DATA

Master of Applied Science

Antonio Mandatori

University of Toronto Institute for Aerospace Studies

University of Toronto

A spline method is presented for reproducing JANAF thermochemical data for specific heat $\left(C_p^\circ\right)$, enthalpy $(H^\circ)$, entropy $(S^\circ)$ and Gibbs free energy $(G^\circ)$ of gaseous species as a function of temperature $(T)$, and at the reference pressure of 1 bar. The interpolant is $C_p^\circ = \sum_{i=1}^{8} a_i T^{i-5}$, from which $H^\circ$, $S^\circ$ and $G^\circ$ are obtained using relevant differential equations and simple integration. The eight coefficients are evaluated directly from thermochemical data for $C_p^\circ$, $H^\circ$, $S^\circ$ and $G^\circ$, such that $C_p^\circ$, $C_p^{\circ\prime}$, $C_p^{\circ\prime\prime}$, $H^\circ$, $H^{\circ\prime}$, $H^{\circ\prime\prime}$, $H^{\circ\prime\prime\prime}$, $S^\circ$, $S^{\circ\prime}$, $S^{\circ\prime\prime}$, $S^{\circ\prime\prime\prime}$, $G^\circ$, $G^{\circ\prime}$, $G^{\circ\prime\prime}$, $G^{\circ\prime\prime\prime}$ and $G^{\circ\prime\prime\prime\prime}$ are satisfied at each end of the spline (knots), where the prime denotes differentiation with respect to $T$. Values for $C_p^\circ$, $H^\circ$, $S^\circ$ and $G^\circ$ and their derivatives are obtained directly from the thermodynamic functions that are used to produce the JANAF tabulated data. The present spline method does not use a least-squares method. On comparison to the best previous method that uses least-squares fits, the accuracy of reproducing JANAF data is nearly comparable.

# Acknowledgements

I would like to thank Professor J.J. Gottlieb, my supervisor, for suggesting the problem and for guidance during my thesis studies.

Funding, in terms of student assistantship, from the Defense Research Establishment Valcartier for this type of work is much appreciated.

## Table of Contents

1.0 INTRODUCTION . . . . . . . . . . 1
    1.1 Background Information . . . . . . . . . . 1
    1.2 Previous Reproduction Methods . . . . . . . . . . 4
    1.3 Project Objectives . . . . . . . . . . 5
2.0 RELEVANT THERMODYNAMIC RELATIONSHIPS . . . . . . . . . . 7
3.0 DERIVATIVES OF SPECIFIC HEAT AT CONSTANT PRESSURE . . . . . . . . . . 10
    3.1 Introduction . . . . . . . . . . 10
    3.2 Results for Monatomic Gases . . . . . . . . . . 10
    3.3 Results for Diatomic and Polyatomic Gases . . . . . . . . . . 11
4.0 VERIFICATION OF PRESENT METHOD OF REPRODUCING JANAF DATA . . . . . . . 19
5.0 CONCLUDING REMARKS . . . . . . . . . . 21
6.0 REFERENCES . . . . . . . . . . 22

# 1.0 INTRODUCTION

## 1.1 Background Information

The JANAF thermochemical tables[1] present thermodynamic data for about 1796 gaseous, liquid and solid species. Tabulated as a function of temperature, at a pressure of 1 bar, are

a. specific heat at constant pressure $\left(C_p^\circ\right)$, in units of J·K⁻¹·kg⁻¹,

b. entropy $(S^\circ)$, in units of J·K⁻¹·kg⁻¹,

c. Gibbs free energy $\left(G^\circ - H^\circ_{298.15}\right)$, in units of J·kg⁻¹,

d. enthalpy $\left(H^\circ - H^\circ_{298.15}\right)$, in units of kJ·kg⁻¹,

e. heat of formation of the substance from its reference elements in their standard state $(\Delta_f H^\circ)$, in units of kJ·kg⁻¹,

f. Gibbs energy of formation $(\Delta_f G^\circ)$, in units of kJ·kg⁻¹, and

g. the logarithm to the base 10 of the equilibrium constant $(\log K_f)$.

The temperature range is 0 to 6000 K, and the data is presented at steps of approximately 100 K. See table 1 for an example page of the JANAF tables for the gaseous carbon dioxide ($CO_2$). All data correspond to a pressure of 1 bar, and this is the reason for the superscript (°). Values of $C_p$, $H$, $S$ and $G$ at other pressures normally depend on the equation of state. In the simplest case of a thermally perfect gas ($p = \rho RT/M$), the data applies at all temperatures (no dependence on the pressure or equation of state).

Tabulated values of $C_p^\circ$, $H^\circ$, $S^\circ$ and $G^\circ$ in JANAF tables are computed using equations from statistical mechanics and thermodynamics, and these involve partition functions. Relevant equations from McBride and Gordon[2] (1992) are listed below for interest.

$$\frac{C_p^\circ}{R} = \frac{1}{R}\frac{d\left(H^\circ - H^\circ_{298.15}\right)}{dT} = \frac{T}{R}\frac{dS^\circ}{dT} = -\frac{T}{R}\frac{d^2\left(G^\circ - H^\circ_{298.15}\right)}{dT^2} = T^2\frac{d^2(\ln Q)}{dT^2} + 2T\frac{d(\ln Q)}{dT} + \frac{5}{2} \qquad 1.1$$

$$\frac{H^\circ - H^\circ_{298.15}}{RT} = \frac{G^\circ - H^\circ_{298.15}}{RT} - \frac{1}{R}\frac{d\left(G^\circ - H^\circ_{298.15}\right)}{dT} = T\frac{d(\ln Q)}{dT} + \frac{5}{2} \qquad 1.2$$

$$\frac{S^\circ}{R} = -\frac{1}{R}\frac{d\left(G^\circ - H^\circ_{298.15}\right)}{dT} = T\frac{d(\ln Q)}{dT} + \ln Q + \frac{3}{2}\ln M + \frac{5}{2}\ln T + S_c \qquad 1.3$$

$$-\frac{G^\circ - H^\circ_{298.15}}{RT} = \frac{S^\circ}{R} - \frac{H^\circ - H^\circ_{298.15}}{RT} = \ln Q + \frac{3}{2}\ln M + \frac{5}{2}\ln T + S_c - \frac{5}{2} \qquad 1.4$$

$Q$ is the partition function that depends on $T$ only, $p$ is the gas pressure, $R$ is the universal gas constant (8.31451 kJ·kg-mol⁻¹·K⁻¹), $M$ is the molecular weight of the species in units of kg-mass/kg-mol, and $S_c$ is the Sackur-Tetrode parameter[3] that depends on the pressure ($S_c = -1.151693$ at $p = 1$ bar). These four relationships illustrate the interdependence of $C_p^\circ$, $H^\circ$, $S^\circ$ and $G^\circ$. The partition function depends on the translational, rotational, vibrational and electrical excitation of an atom or a molecule. Note that in equations 1.1 to 1.4, $\frac{dS^\circ}{dT} = \left.\frac{dS}{dT}\right|_{p=1\,\text{bar}}$,

$$\frac{d\left(H^{\circ}-H^{\circ}_{298.15}\right)}{dT}=\left.\frac{d\left(H-H_{298.15}\right)}{dT}\right|_{p=1\,\mathrm{bar}}, \text{ and } \frac{d\left(G^{\circ}-H^{\circ}_{298.15}\right)}{dT}=\left.\frac{d\left(G-H_{298.15}\right)}{dT}\right|_{p=1\,\mathrm{bar}}.$$

The heat of formation $\Delta_f H^{\circ}_T$, the Gibbs free energy of formation $\Delta_f G^{\circ}_T$, and the equilibrium constant $(\log K_f)$ are also presented in the JANAF tables. At temperature $T$, they can be calculated by means of the equations[3]

$$\left(\Delta_f H^{\circ}_T\right)_{species}=\left(H^{\circ}_T\right)_{species}-\sum_{i=1}^{I}\frac{\left(H^{\circ}_T\right)_{\mathcal{F}_i}}{\beta}\ , \tag{1.5}$$

$$\left(\Delta_f G^{\circ}_T\right)_{species}=\left(G^{\circ}_T\right)_{species}-\sum_{i=1}^{I}\frac{\left(G^{\circ}_T\right)_{\mathcal{F}_i}}{\beta}\ , \tag{1.6}$$

$$\log K_f=\frac{-\Delta_f G^{\circ}_T}{2.3025851\,RT}\ . \tag{1.7}$$

In the above equations, $i$ denotes the $i^{th}$ atom of the species, $I$ denotes the number of atoms in the species, $\mathcal{F}_i$ denotes $i^{th}$ element or "building block" of the species and $\beta$ denotes the number of atoms in the element. For example,

$$\begin{aligned}\left(\Delta_f H^{\circ}_T\right)_{H_2SO_4}=\left(H^{\circ}_T\right)_{H_2SO_4}&-\frac{1}{2}\left(H^{\circ}_T\right)_{H_2(g)}-\frac{1}{2}\left(H^{\circ}_T\right)_{H_2(g)}-\frac{1}{1}\left(H^{\circ}_T\right)_{S(\alpha)}\\&-\frac{1}{2}\left(H^{\circ}_T\right)_{O_2(g)}-\frac{1}{2}\left(H^{\circ}_T\right)_{O_2(g)}-\frac{1}{2}\left(H^{\circ}_T\right)_{O_2(g)}-\frac{1}{2}\left(H^{\circ}_T\right)_{O_2(g)}\end{aligned} \tag{1.8}$$

or

$$\left(\Delta_f H^{\circ}_T\right)_{H_2SO_4}=\left(H^{\circ}_T\right)_{H_2SO_4}-\frac{2}{2}\left(H^{\circ}_T\right)_{H_2(g)}-\frac{1}{1}\left(H^{\circ}_T\right)_{S(\alpha)}-\frac{4}{2}\left(H^{\circ}_T\right)_{O_2(g)} \tag{1.9}$$

is the heat of formation of sulphuric acid.

Thermochemical data is used frequently and advantageously in the scientific community. The continuing study of improving combustion systems depends strongly on using thermochemical properties of hydrocarbons to calculate gas mixture properties and efficiencies of flow processes. Efficiency is improved when the appropriate fuels are mixed in the proper proportions and flow process is controlled to achieve preset goals. In the automotive industry, for example, efficiency is usually related to fuel consumption with rapid burning and no detonation inside the combustion chambers. In the aircraft industry, there is a stronger focus on increasing engine thrust while reducing fuel consumption. Computations using thermochemical data is both common and extensively used today.

The tables have been used frequently in their original hard copy format. When only a few values are needed, it is quite easy to look up these values directly, or use interpolation to find values not directly listed. However, if many values are required, or if the properties of a large mixture of gases need to be determined, the task of looking up values becomes quite tedious and time consuming. With the integration of computers into our modern day environment, an accurate and automatic numerical process of reproducing and interpolating the thermochemical data is highly desirable to rapidly compute complex thermochemistry calculations.

One obvious way of accomplishing this task is to incorporate the tables directly into the program and perform an automated look up and interpolation each time a value is needed. Methods of interpolation can be divided into categories defining their level of sophistication. Direct interpolation of tabulated data is called category I. It is characterized by various local methods of interpolation (e.g., linear, parabolic, cubic and higher order). In each of these cases, the interpolation range covers only part of the data set, and the accuracy in the reproduction of the data is dependent only on the interpolation technique. Note that, in regards to the $C_p^\circ$, $H^\circ$, $S^\circ$ and $G^\circ$ data sets, independent interpolations with temperature in each data set to yield values of $C_p^\circ$, $H^\circ$, $S^\circ$ and $G^\circ$ result in inconsistencies, because equations 1.1 to 1.4 are independently, but not simultaneously satisfied.

A second category can be defined as global methods of interpolation. (Incorporating a global method provides a quicker, more automatic approach.) In this category II, either a single curve is fitted to an entire data set (e.g., $C_p^\circ = C_p^\circ(T)$), or the data is subdivided into a number of ranges, and each is approximated by an interpolant with different coefficients. In this case, the accuracy is improved by increasing the number of segments as well as choosing an appropriate interpolant. An example of methods in category II are segmented least-squares splines. In regards to $C_p^\circ$, $H^\circ$, $S^\circ$ and $G^\circ$, if each are curve fitted with an independent interpolant, then the results at a given temperature will normally be inconsistent, because equations 1.1 to 1.4 are not satisfied simultaneously.

Category III exploits the interdependence of the data columns of $C_p^\circ$, $H^\circ$, $S^\circ$ and $G^\circ$. A curve is applied to only one of the columns in the JANAF tables (e.g., $H^\circ$), and the other thermodynamic properties are obtained by using equations 1.1 to 1.4 (e.g., $C_p^\circ = H^{\circ\prime}$). Here, the accuracy of reproduction can depend on which column, or property, is interpolated, as well as the choice of interpolant and the number of segments. This approach does avoid the problem of inconsistencies in the $C_p^\circ$, $H^\circ$, $S^\circ$ and $G^\circ$ data sets, because equations 1.1 to 1.4 are satisfied simultaneously.

A fourth category can also be defined. One interpolant is selected so that it is consistent with the $C_p^\circ$, $H^\circ$, $S^\circ$ and $G^\circ$ relationships through integration and/or differentiation. The coefficients are obtained by using a least-squares fit to all data for $C_p^\circ$, $H^\circ$, $S^\circ$ and $G^\circ$ simultaneously, and this distributes the error more uniformly among the data sets and thereby minimizes error throughout the four data sets. Note, there are no inconsistencies in the reproduction of $C_p^\circ$, $H^\circ$, $S^\circ$ and $G^\circ$ data, because equations 1.1 to 1.4 are satisfied simultaneously. Current methods for reproducing $C_p^\circ$, $H^\circ$, $S^\circ$ and $G^\circ$ data normally fall into category IV.

## 1.2 Previous Reproduction Methods

Yuan and Mok,[3] in 1968, selected the curve fit $C_p^\circ = A + B\exp(-C/T^n)$ to fit to the specific heat at constant pressure, and they tested its accuracy in the range of 298.15 K to 1500 K. The particular selection of an exponential function is based on the structure of the partition function $Q$ (consists of exponentials). This selection may be helpful to obtain better accuracy for a fit to $C_p^\circ$ data, but it is not helpful in reproducing the $C_p^\circ$, $H^\circ$, $S^\circ$ and $G^\circ$ data quickly or effectively. $H^\circ$, $S^\circ$ and $G^\circ$ require numerical integrations because there is no explicit result (a severe disadvantage). Although Yuan and Mok's approach falls into the category III defined above, providing consistent results for $C_p^\circ$, $H^\circ$, $S^\circ$ and $G^\circ$ because equations 1.1 to 1.4 are satisfied, the method is not practical owing to the numerical integrations required to obtain the $H^\circ$, $S^\circ$ and $G^\circ$ data.

Thinh, Duran, Ramalho and Kaliaguine,[4] in 1971, selected the polynomial $C_p^\circ = \sum_{i=1}^{4} a_i T^{i-1}$ to least-square fit to the specific heat at constant pressure. He proposed that the accuracy could be improved if the sum of the squares of the percentage deviation was minimised instead of the sum of the squares of the actual deviation. Thinh et al. compared their method to both the standard polynomial least-squares based on older data and the exponential model of Yuan and Mok. Although they claimed their method was much more accurate than that of Yuan & Mok, on careful inspection of all sources, the same magnitude of error was found in their work. Thinh et al. do not fit their equation simultaneously to the $H^\circ$, $S^\circ$ and $G^\circ$ data sets. However, they can obtain $H^\circ$, $S^\circ$ and $G^\circ$ by using equations 1.2 to 1.4. Therefore, this method falls into category III.

Thompson,[5] in 1977, proposed a more physically oriented equation to represent the specific heat at constant volume. Symbolically, $C_p^\circ = a\frac{x^2}{1+x^2} + R$, with $x = b(T-c)$, where there are three constants $a$, $b$ and $c$ to be evaluated over a wide temperature range. $C_p^\circ$, $H^\circ$, $S^\circ$ and $G^\circ$ are obtained by integration, and explicit results can be found. This method falls into category III because $a$, $b$ and $c$ are obtained from a fit to $C_p^\circ$ only. The method can be accurate (0–4%) over a wide range because the equation for $C_p^\circ$ has some physical significance. However, the logarithm and inverse tan functions in $H^\circ$, $S^\circ$ and $G^\circ$ make this reproduction method slow computationally. Furthermore, polynomials over short segmented ranges provide more accurate reproductions of the $C_p^\circ$, $H^\circ$, $S^\circ$ and $G^\circ$ data.

In 1961, Zeleznik and Gordon[6] of NASA proposed a method whereby they selected a polynomial $C_p^\circ = \sum_{i=1}^{7} a_i T^{i-3}$ as a fit to the specific heat at constant pressure. This equation can be used to obtain $H^\circ$, $S^\circ$ and $G^\circ$ in a consistent manner by suitable integrations. The coefficients were evaluated by using a least-squares fit to all data for $C_p^\circ$, $H^\circ$, $S^\circ$ and $G^\circ$, and tested for accuracy of reproduction. Only one interval from 1000 to 5000 K was used. This method falls into the category IV because the $C_p^\circ$, $H^\circ$, $S^\circ$ and $G^\circ$ data are consistent in terms of equations 1.1 to 1.4. The method can also be applied to the range 300 to 1000 K, and $C_p^\circ$, $H^\circ$, $S^\circ$ and $G^\circ$ can be made consistent at the joint (knot).

In 1969, Prothero[7] suggested that the accuracy of NASA's simultaneous fit to the $C_p^\circ$, $H^\circ$, $S^\circ$ and $G^\circ$ data sets could be increased if the joint at 1000 K was altered so that the least-squares errors for the intervals on either side were made equal. By doing so, the accuracy of the higher temperature range was improved at the expense of accuracy in the lower temperature range, but overall the fit is better. This method is still in category IV.

Passut and Danner,[8] in 1972, emulated NASA's approach.[2,6] They chose to define $H^\circ = \sum_{i=1}^{6} a_i T^{i-1}$, which is differentiated to obtain $C_p^\circ$. $S^\circ$ and $G^\circ$ can then be obtained from $C_p^\circ$ by appropriate integrations. The coefficients were evaluated by using a least-squares fit to all data for $C_p^\circ$, $H^\circ$, $S^\circ$ and $G^\circ$. Although this method falls into category IV, and it should reproduce thermochemical properties with comparable accuracy to the methods of Yuan and Mok, Thinh et al. and NASA, the tabulated results shown in Passut and Danner's paper illustrate that their accuracy is slightly worse. The reasons are not known.

In 1992, McBride and Gordon[9] updated the previous methods of Zeleznik and Gordon,[6] Prothero,[7] and Passut and Danner.[8] Firstly, JANAF thermochemical data for $C_p^\circ$, $H^\circ$, $S^\circ$ and $G^\circ$ are computed directly from partition functions (equations 1.1 to 1.4), which helps eliminate round-off errors of tabulated data. Secondly, the polynomial curve for $C_p^\circ$ can have a maximum of eight coefficients, the powers on the temperature do not need to be integers, and the basis functions do not need to be sequenced or ordered. Thirdly, the same curve for $C_p^\circ$ is used to obtain $H^\circ$, $S^\circ$ and $G^\circ$, and the least-squares fit is applied to all data sets simultaneously (category IV). Finally, the data set for $C_p^\circ$, $H^\circ$, $S^\circ$ and $G^\circ$ can be subdivided into many intervals, to improve the accuracy of the data reproduction. However, McBride and Gordon typically use two or three temperature intervals. This method supersedes all previous approaches in reproducing JANAF thermochemical data both quickly and accurately.

### 1.8 Project Objectives

The NASA approach of McBride and Gordon[9] in reproducing the $C_p^\circ$, $H^\circ$, $S^\circ$ and $G^\circ$ data from JANAF thermochemical tables by using splined polynomials over a few intervals and a least-squares fit is clever and straightforward. The data can be reproduced quickly with high accuracy, as mentioned previously.

The simultaneous least-squares fit of the polynomials to the $C_p^\circ$, $H^\circ$, $S^\circ$ and $G^\circ$ data can be eliminated in the NASA approach. The coefficients of a polynomial representing $C_p^\circ$, $H^\circ$, $S^\circ$ and $G^\circ$ consistently, can be evaluated directly from $C_p^\circ$, $H^\circ$, $S^\circ$ and $G^\circ$ data and its derivatives at the two endpoints of an interval of the data. For example, let $C_p^\circ = \sum_{i=1}^{8} a_i T^{i-3}$ represent the specific heat data over the temperature interval from $T_1$ to $T_2$. $H^\circ$, $S^\circ$ and $G^\circ$ can be obtained in a consistent manner by using equations 1.1 to 1.4. The eight coefficients $(a_i, i = 1, \ ,8)$ can be determined directly from the conditions $C^\circ_{P_1}$, $C^{\circ\prime}_{P_1}$ and $C^{\circ\prime\prime}_{P_1}$ at the start of the interval and $G^\circ_2$, $S^\circ_2$, $C^\circ_{P_2}$, $C^{\circ\prime}_{P_2}$ and $C^{\circ\prime\prime}_{P_2}$ at the end of the interval. (Note that $G^\circ_1$ and $S^\circ_1$ define two additional constants of integration.)

Values of $C^{\circ\prime}_P$ and $C^{\circ\prime\prime}_P$ are not available in the JANAF tabulated data, but they can be determined fairly easily by differentiating the statistical mechanics expression for $C_P = C_P(Q)$, because $Q = Q(T)$ is known. (Note that expressions for $Q$ are used to produce the JANAF thermochemical tables.) This method makes $C^\circ_P$, $C^{\circ\prime}_P$, $C^{\circ\prime\prime}_P$, $H^\circ$, $H^{\circ\prime}$, $H^{\circ\prime\prime}$, $H^{\circ\prime\prime\prime}$, $S^\circ$, $S^{\circ\prime}$, $S^{\circ\prime\prime}$, $S^{\circ\prime\prime\prime}$, $G^\circ$, $G^{\circ\prime}$, $G^{\circ\prime\prime}$, $G^{\circ\prime\prime\prime}$ and $G^{\circ\prime\prime\prime\prime}$ all continuous across both ends of the interval, if more than one interval is being used (significant advantage). However, the elimination of the least-squares fit procedure is offset partly by the need to determine $C^{\circ\prime}_P$ and $C^{\circ\prime\prime}_P$. Another consideration is whether this alternative method is comparable or less accurate.

This alternative method and the resulting accuracy of reproducing the $C^\circ_P$, $H^\circ$, $S^\circ$ and $G^\circ$ data sets are the subject of this thesis. The primary objective is to study and validate this alternate method.

## 2.0 RELEVANT THERMODYNAMIC RELATIONSHIPS

The thermodynamic properties $C_p^\circ$, $H^\circ$, $S^\circ$ and $G^\circ$ (at a pressure of 1 bar) are coupled or interrelated. When an interpolating equation is selected for one of these properties, the corresponding equations for the other three properties can be obtained from the original by either differentiation or integration. These interrelationships are presented herein, for easy application in the following chapters.

The specific heat at constant pressure is defined in terms of the enthalpy[9] as

$$C_p^\circ = \frac{d\left(H^\circ - H_{298.15}^\circ\right)}{dT} \ . \tag{2.1}$$

If $H^\circ - H_{298.15}^\circ$ was specified as a polynomial interpolant, then $C_p^\circ$ can be obtained by differentiation. Alternatively, if $C_p^\circ$ is specified as a polynomial interpolant, then

$$H_T^\circ = H_{298.15}^\circ + \int_{298.15}^{T} C_p^\circ \, dT \tag{2.2}$$

produces the corresponding equation for enthalpy.

The first law of thermodynamics can be expressed in the form[9] $dH = TdS + \frac{1}{\rho}dp$, or alternatively, in the form $\frac{dH}{dT} = T\frac{dS}{dT} + \frac{1}{\rho}\frac{dp}{dT}$. Since the data in the JANAF tables all correspond to the case of $p = 1$ bar, we obtain $\left.\frac{dH}{dT}\right|_p = T\left.\frac{dS}{dT}\right|_p$, or $\frac{d\left(H^\circ - H_{298.15}^\circ\right)}{dT} = T\frac{dS^\circ}{dT}$. Hence,

$$C_p^\circ = T\frac{dS^\circ}{dT} \tag{2.3}$$

is an important relationship for the present work. If $S^\circ$ is specified as a polynomial interpolant, then the corresponding equation for $C_p^\circ$ can be obtained by differentiation. If $C_p^\circ$ is represented as a polynomial, then

$$S_T^\circ = S_{298.15}^\circ + \int_{298.15}^{T} \frac{C_p^\circ}{T} dT \tag{2.4}$$

provides the corresponding expression for $S_T^\circ$.

Gibbs free energy[9] is defined as $G = H - TS$. This relationship can be rewritten as

$$G^\circ - H_{298.15}^\circ = H^\circ - H_{298.15}^\circ - TS^\circ \tag{2.5}$$

for the work in this thesis. If $C_p^\circ$ is specified as a polynomial interpolant, we can find corresponding equations for $H^\circ - H_{298.15}^\circ$ and $S^\circ$ first, and then the corresponding equation for $G^\circ - H_{298.15}^\circ$.

Another useful thermodynamic relationship can be derived as follows. By differentiating equation 2.5 with respect to temperature,

$$\frac{d\left(G^\circ - H_{298.15}^\circ\right)}{dT} = \frac{d\left(H^\circ - H_{298.15}^\circ\right)}{dT} - T\frac{dS}{dT} - S^\circ = C_p^\circ - C_p^\circ - S^\circ = -S^\circ \ . \tag{2.6}$$

Hence,

$$S^\circ = -\frac{d\left(G^\circ - H^\circ_{298.15}\right)}{dT} = -G^{\circ\prime} \qquad 2.7$$

and the higher derivatives $S^{\circ\prime}$, $S^{\circ\prime\prime}$, etc., can be obtained easily. Furthermore, we can show that

$$\begin{aligned} C_p^\circ &= -TG^{\circ\prime\prime} \\ C_p^{\circ\prime} &= -TG^{\circ\prime\prime\prime} - G^{\circ\prime\prime} \\ C_p^{\circ\prime\prime} &= -TG^{\circ\prime\prime\prime\prime} - 2G^{\circ\prime\prime\prime}, \text{ etc.,} \end{aligned} \qquad 2.8$$

providing a set of relationships between the specific heat at constant pressure and Gibbs free energy.

In the present work, the data for specific heat at constant pressure is represented by a "polynomial" of the form $C_p^\circ = a_1\frac{1}{T^4} + a_2\frac{1}{T^3} + a_3\frac{1}{T^2} + a_4\frac{1}{T} + a_5 + a_6(T-T_1) + a_7(T-T_1)^2 + a_8(T-T_1)^3$. All of the other thermodynamic relationships for $C_p^{\circ\prime\prime}$, $C_p^{\circ\prime}$, $C_p^\circ$, $H^\circ$, $S^\circ$ and $G^\circ$ can be obtained from the preceding equations and thermodynamic relationships. These are listed below.

$$\frac{d^2C_p^\circ}{dT^2} = a_1\frac{20}{T^6} + a_2\frac{12}{T^5} + a_3\frac{6}{T^4} + a_4\frac{2}{T^3} + 2a_7 + 6a_8(T-T_1) \qquad 2.9$$

$$\frac{dC_p^\circ}{dT} = -a_1\frac{4}{T^5} - a_2\frac{3}{T^4} - a_3\frac{2}{T^3} - a_4\frac{1}{T^2} + a_6 + 2a_7(T-T_1) + 3a_8(T-T_1)^2 \qquad 2.10$$

$$C_p^\circ = a_1\frac{1}{T^4} + a_2\frac{1}{T^3} + a_3\frac{1}{T^2} + a_4\frac{1}{T} + a_5 + a_6(T-T_1) + a_7(T-T_1)^2 + a_8(T-T_1)^3 \qquad 2.11$$

$$\begin{aligned} H^\circ = H_1^\circ &- a_1\frac{1}{3}\left(\frac{1}{T^3} - \frac{1}{T_1^3}\right) - a_2\frac{1}{2}\left(\frac{1}{T^2} - \frac{1}{T_1^2}\right) - a_3\left(\frac{1}{T} - \frac{1}{T_1}\right) + a_4\ln\frac{T}{T_1} + a_5(T-T_1) \\ &+ a_6\left[\frac{1}{2}(T^2 - T_1^2) - T_1(T-T_1)\right] + a_7\left[\frac{1}{3}(T^3 - T_1^3) - T_1(T^2 - T_1^2) + T_1^2(T-T_1)\right] \\ &+ a_8\left[\frac{1}{4}(T^4 - T_1^4) - T_1(T^3 - T_1^3) + \frac{3}{2}T_1^2(T^2 - T_1^2) + T_1^3(T-T_1)\right] \end{aligned} \qquad 2.12$$

$$\begin{aligned} S^\circ = S_1^\circ &- a_1\frac{1}{4}\left(\frac{1}{T^4} - \frac{1}{T_1^4}\right) - a_2\frac{1}{3}\left(\frac{1}{T^3} - \frac{1}{T_1^3}\right) - a_3\frac{1}{2}\left(\frac{1}{T^2} - \frac{1}{T_1^2}\right) - a_4\left(\frac{1}{T} - \frac{1}{T_1}\right) \\ &+ a_5\ln\frac{T}{T_1} + a_6\left[(T-T_1) - T_1\ln\left(\frac{T}{T_1}\right)\right] + a_7\left[\frac{1}{2}(T^2-T_1^2) - 2T_1(T-T_1) + T_1^2\ln\left(\frac{T}{T_1}\right)\right] \\ &+ a_8\left[\frac{1}{3}(T^3-T_1^3) - \frac{3}{2}T_1(T^2-T_1^2) + 3T_1^2(T-T_1) - T_1^3\ln\left(\frac{T}{T_1}\right)\right] \end{aligned} \qquad 2.13$$

$$
\begin{aligned}
G^\circ = G_1^\circ - S_1^\circ(T-T_1) &- a_1\frac{1}{4}\left[\frac{1}{3}\left(\frac{1}{T^3}-\frac{1}{T_1^3}\right)+\frac{(T-T_1)}{T_1^4}\right] \\
&- a_2\frac{1}{3}\left[\frac{1}{2}\left(\frac{1}{T^2}-\frac{1}{T_1^2}\right)+\frac{(T-T_1)}{T_1^3}\right] - a_3\frac{1}{2}\left[\left(\frac{1}{T}-\frac{1}{T_1}\right)+\frac{(T-T_1)}{T_1^2}\right] + a_4\left[\ln\frac{T}{T_1}-\frac{(T-T_1)}{T_1}\right] \\
&+ a_5\left[(T-T_1)-T\ln\frac{T}{T_1}\right] - a_6\left[\frac{1}{2}(T^2-T_1^2)-T_1(T-T_1)+T_1\left[(T-T_1)-T\ln\left(\frac{T}{T_1}\right)\right]\right] \\
&- a_7\left[\frac{1}{2}\left[\frac{1}{3}(T^3-T_1^3)-T_1^2(T-T_1)\right]-2T_1\left[\frac{1}{2}(T^2-T_1^2)-T_1(T-T_1)\right]-T_1^2\left[(T-T_1)-T\ln\left(\frac{T}{T_1}\right)\right]\right] \\
&- a_8\Bigg[\ \frac{1}{3}\left[\frac{1}{4}(T^4-T_1^4)-T_1^3(T-T_1)\right]-\frac{3}{2}T_1\left[\frac{1}{3}(T^3-T_1^3)-T_1^2(T-T_1)\right] \\
&\qquad + 3T_1^2\left[\frac{1}{2}(T^2-T_1^2)-T_1(T-T_1)\right]+T_1^3\left[(T-T_1)-T\ln\left(\frac{T}{T_1}\right)\right]\ \Bigg]
\end{aligned}
\qquad 2.14
$$

Given the polynomial interpolant for $C_P^\circ$, these equations for $C_P^\circ$, $H^\circ$, $S^\circ$ and $G^\circ$ provide a means of interpolating JANAF data over a general temperature interval $T_1$ to $T_2$. These equations also provide a consistent interpolation; equations 1.1 to 1.4 are satisfied simultaneously. The eight coefficients need to be determined for the specific interval in question. These coefficients are obtained from $C_P^\circ$, $C_P^{\circ\prime}$ and $C_P^{\circ\prime\prime}$ at $T_1$ and $G^\circ$, $S^\circ$, $C_P^\circ$, $C_P^{\circ\prime}$ and $C_P^{\circ\prime\prime}$ at $T_2$. The method of obtaining $C_P^{\circ\prime}$ and $C_P^{\circ\prime\prime}$ are illustrated in the next chapter.

Equations 2.9, 2.10 and 2.11 applied at both $T = T_1$ and $T = T_2$, and equations 2.12 and 2.13 applied at $T = T_2$, yield eight equations to solve for eight unknown coefficients ($a_i$, $i = 1,..,8$). These equations take the following matrix form.

$$
\begin{bmatrix} \\ \text{8 by 8 matrix} \\ \text{of basis functions} \\ \text{calculated at} \\ T_1 \text{ and } T_2 \\ \\ \end{bmatrix}
\cdot
\begin{bmatrix} a_1 \\ a_2 \\ a_3 \\ a_4 \\ a_5 \\ a_6 \\ a_7 \\ a_8 \end{bmatrix}
=
\begin{bmatrix} (C_P^{\circ\prime\prime})_1 \\ (C_P^{\circ\prime\prime})_2 \\ (C_P^{\circ\prime})_1 \\ (C_P^{\circ\prime})_2 \\ (C_P^\circ)_1 \\ (C_P^\circ)_2 \\ H_2^\circ \\ S_2^\circ \end{bmatrix}
. \qquad 2.15
$$

These are linear algebraic equations, and $a_i$ can be obtained by a standard method (IMSL routines).

## 3.0 DERIVATIVES OF SPECIFIC HEAT AT CONSTANT PRESSURE

### 3.1 Introduction

The PAC91 code from NASA by McBride and Gordon[2] provides a method for calculating thermochemical data for $C_p^\circ$, $H^\circ$, $S^\circ$ and $G^\circ$ based on partition functions ($Q$). Equations for the partition functions are presented in their report and additional details are embedded inside the coded equations in their FORTRAN program.

The specific heat at constant pressure is related to the partition function as follows

$$\frac{C_p}{R} = T^2\frac{d^2(\ln Q)}{dT^2} + 2T\frac{d(\ln Q)}{dT} + \frac{5}{2} \;, \qquad 3.1$$

where the partition function ($Q$) is the summation of the internal partition functions for each electronic state, that is

$$Q = \sum_{m=1}^{L} Q^m \;, \qquad 3.2$$

where $Q^m$ is the $m^{th}$ electronic state and $L$ is the number of electronic states.

The specific heat equation can be differentiated twice with respect to temperature to obtain $C_p'$, and $C_p''$ in terms of $Q$. These results are

$$C_p' = R\left(T^2\frac{d^3(\ln Q)}{dT^3} + 4T\frac{d^2(\ln Q)}{dT^2} + 2\frac{d(\ln Q)}{dT}\right) \;, \qquad 3.3$$

$$C_p'' = R\left(T^2\frac{d^4(\ln Q)}{dT^4} + 6T\frac{d^3(\ln Q)}{dT^3} + 6\frac{d^2(\ln Q)}{dT^2}\right) \;. \qquad 3.4$$

The problem of finding the first and second derivative of specific heat is hereby reduced to another problem of finding the third and fourth derivative of the natural logarithm of the partition function. The first and second derivatives of the natural logarithm of the partition function are already calculated in PAC91.

### 3.2 Results for Monatomic Gases

For monatomic gases, the partition function for each electronic state is

$$Q^m = g_m e^{-\epsilon/kT} \;. \qquad 3.5$$

The first, second, third and fourth derivatives of this equation are summarized below.

$$\frac{d\ln Q^m}{dT} = \frac{1}{Q^m}\frac{dQ^m}{dT} \qquad 3.6$$

$$\frac{d^2(\ln Q^m)}{dT^2} = -\frac{1}{(Q^m)^2}\left(\frac{dQ^m}{dT}\right)^2 + \frac{(x-2)}{T}\frac{dQ^m}{dT} \qquad 3.7$$

$$\frac{d^3(\ln Q^{\mathrm{int}})}{dT^3} = \frac{2}{(Q^{\mathrm{int}})^3}\left(\frac{dQ^{\mathrm{int}}}{dT}\right)^3 - \frac{3}{(Q^{\mathrm{int}})^2 T}\left(\frac{dQ^{\mathrm{int}}}{dT}\right)^2 (x-2) + \frac{1}{Q^{\mathrm{int}} T^2}\frac{dQ^{\mathrm{int}}}{dT}\left[(x-2)^2 - (x-2) - x\right] \qquad 3.8$$

$$\frac{d^4(\ln Q^{\mathrm{int}})}{dT^4} = -\frac{6}{(Q^{\mathrm{int}})^4}\left(\frac{dQ^{\mathrm{int}}}{dT}\right)^4 + \frac{6}{(Q^{\mathrm{int}})^3 T}\left(\frac{dQ^{\mathrm{int}}}{dT}\right)^3 (x-2) + \frac{1}{(Q^{\mathrm{int}})^2 T^2}\left(\frac{dQ^{\mathrm{int}}}{dT}\right)^2 \left[-7(x-2) + 4(x-2) + 4x\right] + \frac{1}{Q^{\mathrm{int}} T^3}\frac{dQ^{\mathrm{int}}}{dT}\left[(x-2)^3 - 3(x-2)^2 - 3x(x-2) + 2(x-2) + 4x\right] \qquad 3.9$$

Note that $x = \epsilon/kT$ is used in PAC91. Hence, $C_p^{\circ\prime}$ and $C_p^{\circ\prime\prime}$ are given as

$$C_p^{\circ\prime} = R\left[2\frac{T^2}{Q^3}\left(\frac{dQ}{dT}\right)^3 + \frac{T}{Q^2}\left(\frac{dQ}{dT}\right)^2 (2-3x) + \frac{1}{Q}\frac{dQ}{dT}(x^2-2x)\right] \qquad 3.10$$

$$C_p^{\circ\prime\prime} = R\left[-6\frac{T^2}{Q^4}\left(\frac{dQ^{\mathrm{int}}}{dT}\right)^4 + 6\frac{T}{Q^3}\left(\frac{dQ}{dT}\right)^3 x + \frac{1}{Q^2}\left(\frac{dQ}{dT}\right)^2 (-7x^2 + 18x - 6x) + \frac{1}{QT}\left(\frac{dQ}{dT}\right)(x^3 - 6x^2 + 6x)\right] \qquad 3.11$$

for monatomic gases.

### 3.3 Results for Diatomic and Polyatomic Molecules

For diatomic and polyatomic molecules, there are several contributions and corrections to the internal partition function. $Q^{\mathrm{int}}$ is written as

$$Q^{\mathrm{int}} = Q_e^{\mathrm{int}} Q_V^{\mathrm{int}} Q_R^{\mathrm{int}} Q_\rho^{\mathrm{int}} Q_\theta^{\mathrm{int}} Q_W^{\mathrm{int}} Q_c^{\mathrm{int}} \quad . \qquad 3.12$$

the product of the various contributions (electric excitation, vibration and rotation) and corrections (rotational stretching, low temperature rigid rotation, Fermi resonance, and a combination of anharmonicity and vibrational-rotational interaction).

Consider $Q_e^{\mathrm{int}}$ first. In PAC91, $Q_e^{\mathrm{int}}$ is defined as

$$\ln Q_e^{\mathrm{int}} = \ln g_m - \frac{c_2 T_0}{T} \quad , \qquad 3.13$$

and

$$\frac{d(\ln Q_e^{\mathrm{int}})}{dT} = \frac{c_2 T_0}{T^2} \quad , \qquad 3.14$$

$$\frac{d^2(\ln Q_e^{\mathrm{int}})}{dT^2} = -\frac{2c_2 T_0}{T^3} \quad , \qquad 3.15$$

$$\frac{d^3(\ln Q_e^{\mathrm{int}})}{dT^3} = \frac{6c_2 T_0}{T^4} \quad . \qquad 3.16$$

$$\frac{d^4\left(\ln Q_e^m\right)}{dT^4} = -\frac{24 c_2 T_0}{T^5} \quad . \tag{3.17}$$

are its first four derivatives.

Now consider $Q_V^m$. In order to simplify the following differentiations, it is convenient to first define another variable $s_{i,k}$. Let

$$\begin{aligned} s_{i,1} &= \frac{1}{1 - r_{i,1}} \ , \\ s_{i,2} &= T\frac{d(\ln s_{i,1})}{dT} \ , \\ s_{i,3} &= T\frac{ds_{i,2}}{dT} \ , \\ &\cdot \quad \cdot \quad \cdot \\ &\cdot \quad \cdot \quad \cdot \\ &\cdot \quad \cdot \quad \cdot \\ s_{i,5} &= T\frac{ds_{i,4}}{dT} \ , \end{aligned} \tag{3.18}$$

where $r_{i,1} = \exp(-c_2\, \nu_i/T)$. In terms of these variables, $Q_V^m$ is then defined as

$$\ln Q_V^m = \sum_{i=1}^{n} d_i \ln(s_{i,1}) \quad , \tag{3.19}$$

where $n$ is the number of unique frequencies. Then,

$$T\frac{d\left(\ln Q_V^m\right)}{dT} = \sum_{i=1}^{n} d_i s_{i,2} \quad , \tag{3.20}$$

$$T^2\frac{d^2\left(\ln Q_V^m\right)}{dT^2} = \sum_{i=1}^{n} d_i s_{i,3} - T\frac{d\ln Q_V^m}{dT} \quad , \tag{3.21}$$

$$T^3\frac{d^3\left(\ln Q_V^m\right)}{dT^3} = \sum_{i=1}^{n} d_i s_{i,4} - T\frac{d\ln Q_V^m}{dT} - 3T^2\frac{d^2\ln Q_V^m}{dT^2} \quad , \tag{3.22}$$

$$T^4\frac{d^4\ln Q_V^m}{dT^4} = \sum_{i=1}^{n} d_i s_{i,5} - T\frac{d\ln Q_V^m}{dT} - 7T^2\frac{d^2\ln Q_V^m}{dT^2} - 6T^3\frac{d^3\ln Q_V^m}{dT^3} \quad , \tag{3.23}$$

are the first four derivatives.

Now consider $Q_R^m$. For diatomic and linear polyatomic molecules, $Q_R^m$ is defined as

$$\ln Q_R^m = -\ln\frac{c_2 \sigma B_0}{T} \quad , \tag{3.24}$$

and

$$T\frac{d\left(\ln Q_R^m\right)}{dT} = 1 \quad , \tag{3.25}$$

$$T^2 \frac{d^2(\ln Q_R^m)}{dT^2} = -1 \ , \tag{3.26}$$

$$T^3 \frac{d^3(\ln Q_R^m)}{dT^3} = 2 \ , \tag{3.27}$$

$$T^4 \frac{d^4(\ln Q_R^m)}{dT^4} = -6 \ , \tag{3.28}$$

are the first four derivatives. For non-linear molecules, $Q_R^m$ is defined as

$$\ln Q_R^m = \frac{1}{2} \ln\left[\frac{\pi}{\sigma^2 A_0 B_0 C_0}\left(\frac{T}{c_2}\right)^3\right] \ . \tag{3.29}$$

and

$$T \frac{d(\ln Q_R^m)}{dT} = \frac{3}{2} \ , \tag{3.30}$$

$$T^2 \frac{d^2(\ln Q_R^m)}{dT^2} = -\frac{3}{2} \ , \tag{3.31}$$

$$T^3 \frac{d^3(\ln Q_R^m)}{dT^3} = 3 \ , \tag{3.32}$$

$$T^4 \frac{d^4(\ln Q_R^m)}{dT^4} = -9 \ , \tag{3.33}$$

are the first four derivatives.

Now consider $Q_\rho^m$. It is defined as

$$\ln Q_\rho^m = \rho_4 r_f^4 + \rho_3 r_f^3 + \rho_2 r_f^2 + \rho_1 r_f + \rho_5 + r_s \ , \tag{3.34}$$

where $r_f = \rho_6 T$, $\rho_1$ to $\rho_6$, are constants and $r_s = \frac{c_2 D_0}{16T}$ or $r_s = 0$ depending on the symmetry of the molecule. Then,

$$T \frac{d(\ln Q_\rho^m)}{dT} = 4\rho_4 r_f^4 + 3\rho_3 r_f^3 + 2\rho_2 r_f^2 - r_s \ , \tag{3.35}$$

$$T^2 \frac{d^2(\ln Q_\rho^m)}{dT^2} = 2(6\rho_4 r_f^4 + 3\rho_3 r_f^3 + \rho_2 r_f^2 + r_s) \ . \tag{3.36}$$

$$T^3 \frac{d^3(\ln Q_\rho^m)}{dT^3} = 6(4\rho_4 r_f^4 + \rho_3 r_f^3 - r_s) \ . \tag{3.37}$$

$$T^4 \frac{d^4(\ln Q_\rho^m)}{dT^4} = 24(\rho_4 r_f^4 + r_s) \ , \tag{3.38}$$

are the first four derivatives. If the molecule has a symmetrical top geometry, then a correction factor must be added. In this case,

$$\ln(Q_\rho^m)_c = \frac{2\rho_2 - \rho_1^2}{2} T^2 \ , \tag{3.39}$$

and

$$T\frac{d\ln\left(Q_\rho^m\right)_c}{dT} = \left(2\rho_2 - \rho_1^2\right)T^2 \quad , \qquad 3.40$$

$$T^2\frac{d^2\ln\left(Q_\rho^m\right)_c}{dT^2} = \left(2\rho_2 - \rho_1^2\right)T^2 \quad , \qquad 3.41$$

$$T^3\frac{d^3\ln\left(Q_\rho^m\right)_c}{dT^3} = 0 \quad , \qquad 3.42$$

$$T^4\frac{d^4\ln\left(Q_\rho^m\right)_c}{dT^4} = 0 \quad , \qquad 3.43$$

are the first four derivatives.

The second class of corrections deals with low-temperature rigid rotation, and

$$\ln Q_\theta^m = \ln\left(1 + \frac{\theta_1}{T} + \frac{\theta_2}{T^2} + \frac{\theta_3}{T^3}\right) \quad . \qquad 3.44$$

Then,

$$T\frac{d\left(\ln Q_\theta^m\right)}{dT} = \frac{T}{Q_\theta^m}\frac{dQ_\theta^m}{dT} \quad , \qquad 3.45$$

$$T^2\frac{d^2\left(\ln Q_\theta^m\right)}{dT^2} = \frac{T^2}{Q_\theta^m}\frac{d^2Q_\theta^m}{dT^2} - \left[T\frac{d\left(\ln Q_\theta^m\right)}{dT}\right]^2 \quad . \qquad 3.46$$

$$T^3\frac{d^3\left(\ln Q_\theta^m\right)}{dT^3} = \frac{T^3}{Q_\theta^m}\left(\frac{d^3Q_\theta^m}{dT^3}\right) - T\frac{d\left(\ln Q_\theta^m\right)}{dT}\left[\left(T\frac{d\left(\ln Q_\theta^m\right)}{dT}\right)^2 + 3T^2\frac{d^2\left(\ln Q_\theta^m\right)}{dT^2}\right] \quad . \qquad 3.47$$

$$\begin{aligned}T^4\frac{d^4\left(\ln Q_\theta^m\right)}{dT^4} = {} & \frac{T^4}{Q_\theta^m}\frac{d^4Q_\theta^m}{dT^4} - \left(T\frac{d\left(\ln Q_\theta^m\right)}{dT}\right)^4 - 4\left(T^3\frac{d^3\left(\ln Q_\theta^m\right)}{dT^3}\right)\left(T\frac{d\left(\ln Q_\theta^m\right)}{dT}\right) \\ & - 3T^2\frac{d^2\left(\ln Q_\theta^m\right)}{dT^2}\left[T^2\frac{d^2\left(\ln Q_\theta^m\right)}{dT^2} + 2\left(T\frac{d\left(\ln Q_\theta^m\right)}{dT}\right)^2\right] \quad . \end{aligned} \qquad 3.48$$

are the first four derivatives.

The remaining contributions are due to Fermi resonance $\left(Q_W^m\right)$ and a combination of anharmonicity and vibrational-rotational interaction $\left(Q_c^m\right)$. These contributions can be handled by a common equation. Once again, in order to simplify the derivation, it is convenient to recall the previous definition of $s_{i,k}$. Furthermore, the remaining terms $r_{i,k}$ are also needed, as given below.

$$\begin{aligned} r_{i,1} &= \exp\left(-\frac{c_2 \nu_i}{T}\right) \\ r_{i,2} &= T\frac{d(\ln r_{i,1})}{dT} \\ r_{i,3} &= T\frac{dr_{i,2}}{dT} \\ &\cdot \quad \cdot \quad \cdot \\ &\cdot \quad \cdot \quad \cdot \\ &\cdot \quad \cdot \quad \cdot \\ r_{i,5} &= T\frac{dr_{i,4}}{dT} \end{aligned} \qquad 3.49$$

In terms of these variables, $Q_W^m$ and $Q_c^m$ are then defined by $Q_\psi^m$, $\psi = W \; or \; C$, so that

$$\ln Q_\psi^m = \left(\frac{c_2}{T}\right)^p C \prod_{i=1}^{n} r_{k_i,1}^{n_i} s_{k_i,1}^{m_i} \quad . \qquad 3.50$$

and

$$T\frac{d\left(\ln Q_\psi^m\right)}{dT} = \ln Q_\psi^m S \quad , \qquad 3.51$$

$$T^2\frac{d^2\left(\ln Q_\psi^m\right)}{dT^2} = \ln Q_\psi^m \left[S^2 + \sum_{i=1}^{n}\left(n_i r_{k_i,3} + m_i s_{k_i,3}\right)\right] - T\frac{d\left(\ln Q_\psi^m\right)}{dT} \quad . \qquad 3.52$$

$$\begin{aligned} T^3\frac{d^3\left(\ln Q_\psi^m\right)}{dT^3} = \ln Q_\psi^m &\left[\sum_{i=1}^{n}\left(n_i r_{k_i,4} + m_i s_{k_i,4}\right) + S\left(3\sum_{i=1}^{n}\left(n_i r_{k_i,3} + m_i s_{k_i,3}\right) + S^2\right)\right] \\ &- 3T^2\frac{d^2\left(\ln Q_\psi^m\right)}{dT^2} - T\frac{d\left(\ln Q_\psi^m\right)}{dT} \quad , \end{aligned} \qquad 3.53$$

$$\begin{aligned} T^4\frac{d^4\left(\ln Q_\psi^m\right)}{dT^4} = \ln Q_\psi^m &\left[\sum_{i=1}^{n}\left(n_i r_{k_i,5} + m_i s_{k_i,5}\right) + 3\left(\sum_{i=1}^{n}\left(n_i r_{k_i,3} + m_i s_{k_i,3}\right)\right)^2\right. \\ &\left. + S\left(4\sum_{i=1}^{n}\left(n_i r_{k_i,4} + m_i s_{k_i,4}\right) + S\left(6\sum_{i=1}^{n}\left(n_i r_{k_i,3} + m_i s_{k_i,3}\right) + S^2\right)\right)\right] \\ &- 6T^3\frac{d^3\left(\ln Q_\psi^m\right)}{dT^3} - 7T^2\frac{d^2\left(\ln Q_\psi^m\right)}{dT^2} - T\frac{d\left(\ln Q_\psi^m\right)}{dT} \quad . \end{aligned} \qquad 3.54$$

are the first four derivatives, where $S = \sum_{i=1}^{n}\left(n_i r_{k_i,2} + m_i s_{k_i,2}\right) - p$.

Finally, internal rotation is also accounted for. In the case of a free rotor,

$$\ln Q_c^m = \frac{1}{2}\ln(VT) \quad . \qquad 3.55$$

and

$$T\frac{d\left(\ln Q_c^m\right)}{dT} = \frac{1}{2} \quad . \qquad 3.56$$

$$T^2\frac{d^2\left(\ln Q_c^m\right)}{dT^2} = -\frac{1}{2} \quad , \tag{3.57}$$

$$T^3\frac{d^3\left(\ln Q_c^m\right)}{dT^3} = 1 \quad , \tag{3.58}$$

$$T^4\frac{d^4\left(\ln Q_c^m\right)}{dT^4} = -3 \quad , \tag{3.59}$$

are the first four derivatives. For a constrained rotor, $Q_c^m$ is given by

$$\ln Q_c^m = \ln\sum_{i=1}^{N_e} e^{-\frac{\eta_i c_2}{T}} \quad , \tag{3.60}$$

where $\eta_i$ is the energy level and $N_e$ is the number of energy levels. Then,

$$T\frac{d\left(\ln Q_c^m\right)}{dT} = \sum_A \quad , \tag{3.61}$$

and

$$T^2\frac{d^2\left(\ln Q_c^m\right)}{dT^2} = \sum_B - \sum_A^2 - \sum_A - T\frac{d\left(\ln Q_c^m\right)}{dT} \quad , \tag{3.62}$$

$$\begin{aligned} T^3\frac{d^3\left(\ln Q_c^m\right)}{dT^3} = {} & \sum_C - 3\sum_B - 3\sum_B\sum_A + 2\sum_A^3 + 3\sum_A^2 + \sum_A \\ & - 3T^2\frac{d^2\left(\ln Q_c^m\right)}{dT^2} - T\frac{d\left(\ln Q_c^m\right)}{dT} \quad , \end{aligned} \tag{3.63}$$

$$\begin{aligned} T^4\frac{d^4\left(\ln Q_c^m\right)}{dT^4} = {} & \sum_D - 6\sum_C - 4\sum_C\sum_A - 3\sum_B^2 + 7\sum_B + 12\sum_B\sum_A^2 \\ & + 18\sum_B\sum_A - 6\sum_A^4 - 12\sum_A^3 - 6\sum_A^2 - \sum_A \\ & - 6T^3\frac{d^3\left(\ln Q_c^m\right)}{dT^3} - 7T^2\frac{d^2\left(\ln Q_c^m\right)}{dT^2} - T\frac{d\left(\ln Q_c^m\right)}{dT} \quad , \end{aligned} \tag{3.64}$$

are its first four derivatives. Note that

$$\begin{aligned} \sum_A &= \frac{\sum_{i=1}^{N_e}\left[e^{\frac{-\eta_i c_2}{T}}\eta_i c_2\right]}{TQ_c^m} , & \sum_B &= \frac{\sum_{i=1}^{N_e}\left[e^{\frac{-\eta_i c_2}{T}}(\eta_i c_2)^2\right]}{T^2Q_c^m} , \\ \sum_C &= \frac{\sum_{i=1}^{N_e}\left[e^{\frac{-\eta_i c_2}{T}}(\eta_i c_2)^3\right]}{T^3Q_c^m} , & \sum_D &= \frac{\sum_{i=1}^{N_e}\left[e^{\frac{-\eta_i c_2}{T}}(\eta_i c_2)^4\right]}{T^4Q_c^m} , \end{aligned} \tag{3.65}$$

for brevity

All of the previous contributions to the internal partition function are calculated for each electronic state and then summed together. This summation is trivial if there is only one electronic state. In the case for which there is more than one, we obtain

$$T\frac{dQ^m}{dT} = Q^m T\frac{d(\ln Q^m)}{dT} \quad . \tag{3.66}$$

$$T^2\frac{d^2Q^m}{dT^2} = Q^m\left[T^2\frac{d^2(\ln Q^m)}{dT^2} + \left(T\frac{d(\ln Q^m)}{dT}\right)^2\right] \quad . \tag{3.67}$$

$$T^3\frac{d^3Q^m}{dT^3} = Q^m\left[T^3\frac{d^3(\ln Q^m)}{dT^3} + T\frac{d(\ln Q^m)}{dT}\left(\left(T\frac{d(\ln Q^m)}{dT}\right)^2 + 3T^2\frac{d^2(\ln Q^m)}{dT^2}\right)\right] \quad . \tag{3.68}$$

$$\begin{aligned} T^4\frac{d^4Q^m}{dT^4} = Q^m\Bigg[&T^4\frac{d^4(\ln Q^m)}{dT^4} + \left(T\frac{d(\ln Q^m)}{dT}\right)^4 + 4T^3\frac{d^3(\ln Q^m)}{dT^3}T\frac{d(\ln Q^m)}{dT} \\ &+ T^2\frac{d^2(\ln Q^m)}{dT^2}\left(3T^2\frac{d^2(\ln Q^m)}{dT^2} + 6\left(T\frac{d(\ln Q^m)}{dT}\right)^2\right)\Bigg] \quad . \end{aligned} \tag{3.69}$$

are the derivatives of the partition function. Equations 3.66 to 3.69 are calculated for each electronic state and summed together to obtain the derivatives of the partition function $Q$. The required derivatives of the natural logarithms of the partition function are obtained from equations similar to equations 3.66 to 3.69 without the superscript $m$, that is,

$$T\frac{dQ}{dT} = QT\frac{d(\ln Q)}{dT} \quad , \tag{3.70}$$

$$T^2\frac{d^2Q}{dT^2} = Q\left[T^2\frac{d^2(\ln Q)}{dT^2} + \left(T\frac{d(\ln Q)}{dT}\right)^2\right] \quad . \tag{3.71}$$

$$T^3\frac{d^3Q}{dT^3} = Q\left[T^3\frac{d^3(\ln Q)}{dT^3} + T\frac{d(\ln Q)}{dT}\left(\left(T\frac{d(\ln Q)}{dT}\right)^2 + 3T^2\frac{d^2(\ln Q)}{dT^2}\right)\right] \quad . \tag{3.72}$$

$$\begin{aligned} T^4\frac{d^4Q}{dT^4} = Q\Bigg[&T^4\frac{d^4(\ln Q)}{dT^4} + \left(T\frac{d(\ln Q)}{dT}\right)^4 + 4T^3\frac{d^3(\ln Q)}{dT^3}T\frac{d(\ln Q)}{dT} \\ &+ T^2\frac{d^2(\ln Q)}{dT^2}\left(3T^2\frac{d^2(\ln Q)}{dT^2} + 6\left(T\frac{d(\ln Q)}{dT}\right)^2\right)\Bigg] \quad . \end{aligned} \tag{3.73}$$

are intermediate equations.

Finally, we can obtain $C_p^{\circ}$, $C_p^{\circ\prime}$ and $C_p^{\circ\prime\prime}$ as follows:

$$C_p^{\circ} = R\left[\frac{T^2}{Q}\frac{d^2Q}{dT^2} + \left(2 - T\frac{d(\ln Q)}{dT}\right)T\frac{d(\ln Q)}{dT}\right] \quad . \tag{3.74}$$

$$\begin{aligned} C_p^{\circ\prime} = \frac{R}{T}\Bigg[&\frac{T^3}{Q}\frac{d^3Q}{dT^3} + 4T^2\frac{d^2(\ln Q)}{dT^2} \\ &+ T\frac{d(\ln Q)}{dT}\left(2 - \left(T\frac{d(\ln Q)}{dT}\right)^2 - 3T^2\frac{d^2(\ln Q)}{dT^2}\right)\Bigg] \quad . \end{aligned} \tag{3.75}$$

$$C_p^{\circ\prime\prime} = \frac{R}{T^2}\Bigg[\frac{T^4}{Q}\frac{d^4Q}{dT^4} - \left(T\frac{d(\ln Q)}{dT}\right)^4$$

$$+ T^2\frac{d^2(\ln Q)}{dT^2}\left(3T^2\frac{d^2(\ln Q)}{dT^2} + 6\left(T\frac{d(\ln Q)}{dT}\right)^2\right) \qquad 3.76$$

$$- 4T^3\frac{d^3(\ln Q)}{dT^3}T\frac{d(\ln Q)}{dT} + 6T^3\frac{d^3(\ln Q)}{dT^3} + 6T^2\frac{d^2(\ln Q)}{dT^2}\Bigg] .$$

Note that after $H^\circ - H^\circ_{298.15}$ is obtained in PAC91, $T\frac{d(\ln Q)}{dT}$ is computed next in PAC91, and $T^2\frac{d^2(\ln Q)}{dT^2}$ is obtained from equation 3.71. By using $C_p^\circ$ from equation 3.74, we can then obtain $T^2\frac{d^2(\ln Q)}{dT^2}$, which is used in equation 3.75. Then, $C_p^{\circ\prime}$ is obtained and then $T^3\frac{d^3(\ln Q)}{dT^3}$ can be computed, which is then used in equation 3.76 to get $C_p^{\circ\prime\prime}$. This completes the work in computing $C_p^\circ$, $C_p^{\circ\prime}$ and $C_p^{\circ\prime\prime}$.

## 4.0 VERIFICATION OF PRESENT METHOD OF REPRODUCING JANAF DATA

One approach in verifying the present method is to determine how it reproduces data in the JANAF Thermochemical Tables. This is done with four different gaseous species (Ar, $C_5H_{11}$, $H_2O$, MgO) for the thermodynamic variables $C_p^\circ$, $H^\circ$, $S^\circ$ and $G^\circ$. Three intervals with knots at temperatures of approximately 75, 298.15, 1000 and 6000 K will be used in these verifications. For each gas, the eight coefficients are determined separately for each of the three temperature ranges, using thermodynamic data for $C_p^{\circ\prime\prime}$, $C_p^{\circ\prime}$, $C_p^\circ$, $H^\circ$, $S^\circ$ and $G^\circ$ at the knot temperatures only. Hence, the thermochemical data at the knot is reproduced exactly, and the data reproduction between the knots is not exact (in general). These errors should be small if the reproduction of the data is accurate.

Errors in the reproduction of JANAF data for Ar, $C_5H_{11}$, $H_2O$, and MgO are shown in figures 1 to 4, for $C_p^\circ$, $H^\circ$, $S^\circ$ and $G^\circ$. Error plots are shown in contrast to the comparisons between actual and reproduced data, because theses data sets overlap and obscure the small differences (i.e. errors are small) and some salient features. The knot locations are indicated in the figures by vertical lines. At the knots, the errors in $C_p^\circ$, $H^\circ$, $S^\circ$ and $G^\circ$ can be seen to be zero, which is typical of this data reproduction method. Errors in reproducing $G^\circ$ are the smallest, and those in reproducing $C_p^\circ$ are the largest, because $C_p^\circ$, is obtained from $G^\circ$ by differentiation. (Although differentiation reduces the positive powers on the temperature, it correspondingly decreases the negative powers.)

The errors in adjacent intervals are not uniform, because the knots have not been selected or adjusted to achieve this. One can optimize knot locations so that the maximum error in each interval is nearly the same (as suggested by Prothero[7]). For example, if the temperature interval 1000 to 6000 K is reduced to 2000 to 6000 K, by about 20%, then the maximum error can be reduced markedly by a factor of about 50. This is illustrated by the two sets of results for gaseous $H_2O$ in figures 3 and 5. Note that including more knots in the reproduction method also reduces the error.

The NASA PAC91 code was used to reproduce the $C_p^\circ$, $H^\circ$, $S^\circ$ and $G^\circ$ data for the same four gases (Ar, $C_5H_{11}$, $H_2O$, MgO), using the same polynomial interpolant and the same knot locations. The results are presented in figures 6 to 10. Most of the qualitative features are similar, and in many cases the errors are smaller. PAC91 and the present results are plotted on the same diagrams in figures 11 to 15 to facilitate their comparisons. It appears that relaxing the criterion of making the derivatives exact at the knots results in lower overall errors within the intervals.

Additional comparisons of PAC91 and present results are given in tables 2 to 13.

Maximum and average errors for each temperature range are presented. The average error is defined as the sum of the absolute differences (percentage) divided by the number of data points. These tabulated results, show the same trends as found from the comparisons in figures 11 to 15.

## 5.0 CONCLUDING REMARKS

A spline method of reproducing the JANAF thermochemical tables has been presented. This method uses a spline to interpolate the data instead of the commonly used least-squares fit. The accuracy in reproducing the JANAF tables is less than the best methods available to date. This is unfortunate because the present method has some advantages (e.g. elimination of the least-squares), and it is both a local and global interpolation.

## 6.0 REFERENCES

1. Chase, W.M., et al., 1985, *JANAF Thermochemical Tables*, Third Edition, Vol. 14, Suppl. 1, Dow Chemical Company, Thermal Research Laboratory, American Chemical Society & American Institute of Physics, Midland Michigan.

2. McBride, Bonnie J., and Sanford Gordon, November 1992, *Computer Program for Calculating and Fitting Thermodynamic Functions*, NASA Reference Publication 1271.

3. Yuan, S.C., and Y.I. Mok, March 1968, *A New Look at Heat Capacity Prediction*, Hydrocarbon Processing, Vol. 47, No. 3, pp. 133-6.

4. Thinh, T.P., J.L. Duran, R.S. Ramalho and S. Kaliaguine, January 1971, *Equations Improve $C_p^\circ$ Predictions*, Hydrocarbon Processing, Vol. 50, No. 1, pp. 98-104.

5. Thompson, Philip A., 1977, *A Simple Formula for the Heat Capacity of Polyatomic Gases, with Constants for 143 Substances*, Journal of Chemical and Engineering Data, Vol. 22, No. 4, pp. 431-6.

6. Zeleznik, Frank J., and Sanford Gordon, May 1961, *Simultaneous Least-Squares Approximation of a Function and its First Integrals with Application to Thermodynamic Data*, NASA Technical Note D-767.

7. Prothero, A., August 1969, *Computing with Thermochemical Data*, Combustion Flame, Vol. 13, pp. 399-408.

8. Passut, Charles A., and Ronald P. Danner, 1972, *Correlation of Ideal Gas Enthalpy, Heat Capacity, and Entropy*, Industrial Engineering and Chemical Process Design and Development, Vol. 11, No. 4, pp. 543-6.

9. Adkins, C.J., 1988, *Equilibrium Thermodynamics*, Third Edition, Cambridge University Press, Great Britain.

# Table 1
# Example of a JANAF Thermochemical Table (for $CO_2$)

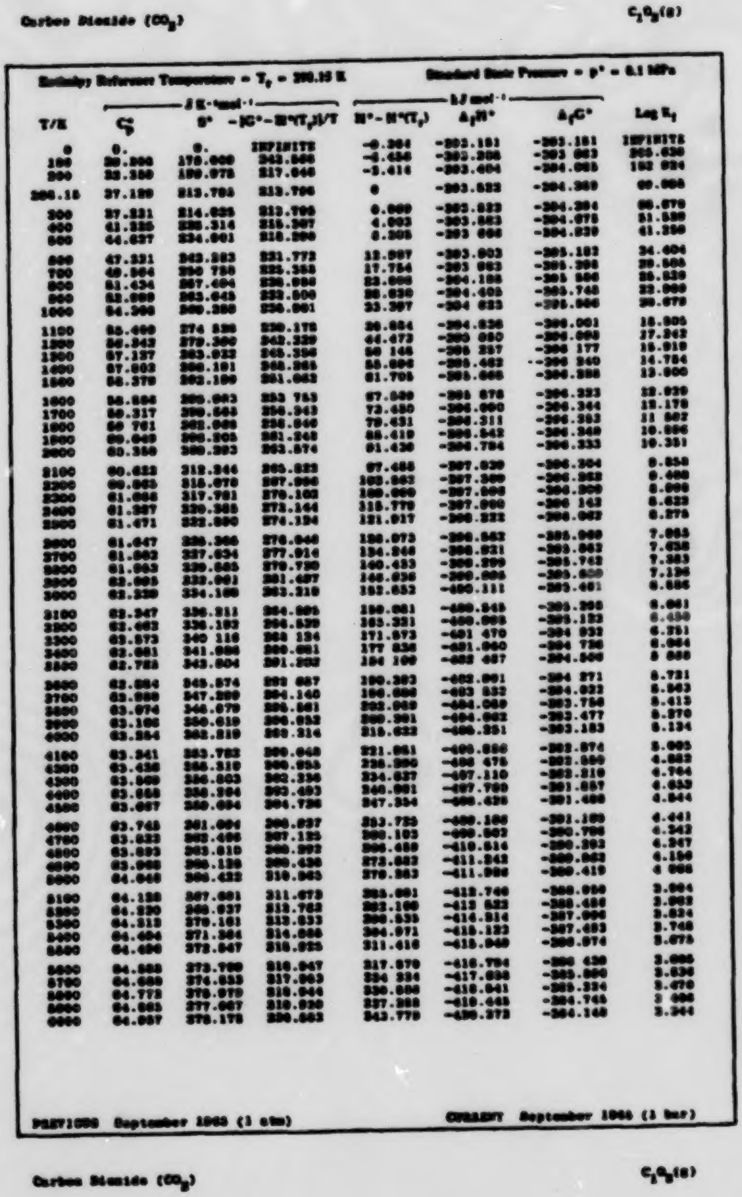

**Table 2**
**Percent Error for Argon**
**25 K to 298.15 K**

| Argon Ar(g) | PAC91 | | | Current Method | | |
|---|---|---|---|---|---|---|
| | Maximum % Error | $T$ (K) | Average % Error | Maximum % Error | $T$ (K) | Average % Error |
| $C_p^\circ$ | 0.0000 | 25 | 0.0000 | 0.0000 | 51 | 0.0000 |
| $H^\circ - H_0^\circ$ | 0.0000 | 297 | 0.0000 | 0.0000 | 71 | 0.0000 |
| $S^\circ$ | 0.0000 | 298 | 0.0000 | 0.0000 | 35 | 0.0000 |
| $G^\circ$ | 0.0000 | 25 | 0.0000 | 0.0000 | 191 | 0.0000 |

**Table 3**
**Percent Error for Argon**
**298.15 K to 2000 K**

| Argon Ar(g) | PAC91 | | | Current Method | | |
|---|---|---|---|---|---|---|
| | Maximum % Error | $T$ (K) | Average % Error | Maximum % Error | $T$ (K) | Average % Error |
| $C_p^\circ$ | 0.0000 | 2000 | 0.0000 | 0.0000 | 520 | 0.0000 |
| $H^\circ - H_0^\circ$ | 0.0000 | 351 | 0.0000 | 0.0000 | 713 | 0.0000 |
| $S^\circ$ | 0.0000 | 1927 | 0.0000 | 0.0000 | 843 | 0.0000 |
| $G^\circ$ | 0.0000 | 2000 | 0.0000 | 0.0000 | 940 | 0.0000 |

**Table 4**
**Percent Error for Argon**
**2000 K to 6000 K**

| Argon Ar(g) | PAC91 | | | Current Method | | |
|---|---|---|---|---|---|---|
| | Maximum % Error | $T$ (K) | Average % Error | Maximum % Error | $T$ (K) | Average % Error |
| $C_p^\circ$ | 0.0000 | 2087 | 0.0000 | 0.0000 | 3609 | 0.0000 |
| $H^\circ - H_0^\circ$ | 0.0000 | 2236 | 0.0000 | 0.0000 | 4276 | 0.0000 |
| $S^\circ$ | 0.0000 | 2247 | 0.0000 | 0.0000 | 2975 | 0.0000 |
| $G^\circ$ | 0.0000 | 3870 | 0.0000 | 0.0000 | 3531 | 0.0000 |

## Table 5
## Percent Error for Tert-Pentyl Rad
## 75 K to 298.15 K

| Tert-Pentyl rad $C_5H_{11}(g)$ | PAC91 | | | Current Method | | |
|---|---|---|---|---|---|---|
| | Maximum % Error | $T$ (K) | Average % Error | Maximum % Error | $T$ (K) | Average % Error |
| $C_p^\circ$ | 0.0029 | 75 | 0.0008 | 0.0499 | 164 | 0.0203 |
| $H^\circ - H_0^\circ$ | 0.0002 | 119 | 0.0001 | 0.0089 | 126 | 0.0042 |
| $S^\circ$ | 0.0000 | 189 | 0.0000 | 0.0018 | 129 | 0.0007 |
| $G^\circ$ | 0.0000 | 75 | 0.0000 | 0.0004 | 162 | 0.0002 |

## Table 6
## Percent Error for Tert-Pentyl Rad
## 298.15 K to 1000 K

| Tert-Pentyl rad $C_5H_{11}(g)$ | PAC91 | | | Current Method | | |
|---|---|---|---|---|---|---|
| | Maximum % Error | $T$ (K) | Average % Error | Maximum % Error | $T$ (K) | Average % Error |
| $C_p^\circ$ | 0.0043 | 309 | 0.0008 | 0.0359 | 548 | 0.0155 |
| $H^\circ - H_0^\circ$ | 0.0004 | 330 | 0.0001 | 0.0101 | 436 | 0.0041 |
| $S^\circ$ | 0.0001 | 330 | 0.0000 | 0.0024 | 447 | 0.0009 |
| $G^\circ$ | 0.0000 | 555 | 0.0000 | 0.0006 | 543 | 0.0003 |

## Table 7
## Percent Error for Tert-Pentyl Rad
## 1000 K to 6000 K

| Tert-Pentyl rad $C_5H_{11}(g)$ | PAC91 | | | Current Method | | |
|---|---|---|---|---|---|---|
| | Maximum % Error | $T$ (K) | Average % Error | Maximum % Error | $T$ (K) | Average % Error |
| $C_p^\circ$ | 0.0017 | 1000 | 0.0001 | 0.0220 | 1333 | 0.0092 |
| $H^\circ - H_0^\circ$ | 0.0001 | 1158 | 0.0000 | 0.0079 | 1619 | 0.0030 |
| $S^\circ$ | 0.0000 | 1162 | 0.0000 | 0.0028 | 1696 | 0.0008 |
| $G^\circ$ | 0.0000 | 1292 | 0.0000 | 0.0012 | 2244 | 0.0004 |

**Table 8**
**Percent Error for Steam**
**75 K to 298.15 K**

| Steam $H_2O(g)$ | PAC91 | | | Current Method | | |
|---|---|---|---|---|---|---|
| | Maximum % Error | $T$ (K) | Average % Error | Maximum % Error | $T$ (K) | Average % Error |
| $C_p^\circ$ | 0.0012 | 75 | 0.0003 | 0.0053 | 151 | 0.0021 |
| $H^\circ - H_0^\circ$ | 0.0001 | 104 | 0.0000 | 0.0008 | 118 | 0.0003 |
| $S^\circ$ | 0.0000 | 174 | 0.0000 | 0.0002 | 120 | 0.0001 |
| $G^\circ$ | 0.0000 | 77 | 0.0000 | 0.0000 | 149 | 0.0000 |

**Table 9**
**Percent Error for Steam**
**298.15 K to 1000 K**

| Steam $H_2O(g)$ | PAC91 | | | Current Method | | |
|---|---|---|---|---|---|---|
| | Maximum % Error | $T$ (K) | Average % Error | Maximum % Error | $T$ (K) | Average % Error |
| $C_p^\circ$ | 0.0016 | 1000 | 0.0004 | 0.0089 | 563 | 0.0035 |
| $H^\circ - H_0^\circ$ | 0.0001 | 334 | 0.0000 | 0.0011 | 675 | 0.0005 |
| $S^\circ$ | 0.0000 | 336 | 0.0000 | 0.0002 | 462 | 0.0001 |
| $G^\circ$ | 0.0000 | 559 | 0.0000 | 0.0001 | 555 | 0.0000 |

**Table 10**
**Percent Error for Steam**
**1000 K to 6000 K**

| Steam $H_2O(g)$ | PAC91 | | | Current Method | | |
|---|---|---|---|---|---|---|
| | Maximum % Error | $T$ (K) | Average % Error | Maximum % Error | $T$ (K) | Average % Error |
| $C_p^\circ$ | 0.0055 | 1056 | 0.0010 | 0.0231 | 2304 | 0.0082 |
| $H^\circ - H_0^\circ$ | 0.0005 | 1147 | 0.0001 | 0.0061 | 1690 | 0.0022 |
| $S^\circ$ | 0.0001 | 1155 | 0.0000 | 0.0012 | 1745 | 0.0003 |
| $G^\circ$ | 0.0000 | 2333 | 0.0000 | 0.0004 | 2260 | 0.0001 |

### Table 11
### Percent Error for Magnesium Oxide
### 75 K to 298.15 K

| Magnesium Oxide MgO(g) | PAC91 | | | Current Method | | |
|---|---|---|---|---|---|---|
| | Maximum % Error | $T$ (K) | Average % Error | Maximum % Error | $T$ (K) | Average % Error |
| $C_p^\circ$ | 0.0048 | 75 | 0.0008 | 0.0140 | 140 | 0.0047 |
| $H^\circ - H_0^\circ$ | 0.0002 | 102 | 0.0001 | 0.0020 | 112 | 0.0008 |
| $S^\circ$ | 0.0000 | 103 | 0.0000 | 0.0004 | 114 | 0.0001 |
| $G^\circ$ | 0.0000 | 75 | 0.0000 | 0.0000 | 141 | 0.0000 |

### Table 12
### Percent Error for Magnesium Oxide
### 298.15 K to 1000 K

| Magnesium Oxide MgO(g) | PAC91 | | | Current Method | | |
|---|---|---|---|---|---|---|
| | Maximum % Error | $T$ (K) | Average % Error | Maximum % Error | $T$ (K) | Average % Error |
| $C_p^\circ$ | 0.0135 | 1000 | 0.0030 | 0.0990 | 583 | 0.0386 |
| $H^\circ - H_0^\circ$ | 0.0004 | 648 | 0.0002 | 0.0148 | 472 | 0.0068 |
| $S^\circ$ | 0.0001 | 657 | 0.0000 | 0.0024 | 481 | 0.0010 |
| $G^\circ$ | 0.0000 | 715 | 0.0000 | 0.0006 | 573 | 0.0002 |

### Table 13
### Percent Error for Magnesium Oxide
### 1000 K to 6000 K

| Magnesium Oxide MgO(g) | PAC91 | | | Current Method | | |
|---|---|---|---|---|---|---|
| | Maximum % Error | $T$ (K) | Average % Error | Maximum % Error | $T$ (K) | Average % Error |
| $C_p^\circ$ | 0.0257 | 1049 | 0.0083 | 0.0845 | 2441 | 0.0281 |
| $H^\circ - H_0^\circ$ | 0.0031 | 1148 | 0.0007 | 0.0146 | 1848 | 0.0055 |
| $S^\circ$ | 0.0005 | 1158 | 0.0001 | 0.0027 | 1890 | 0.0008 |
| $G^\circ$ | 0.0001 | 2333 | 0.0000 | 0.0009 | 2396 | 0.0003 |

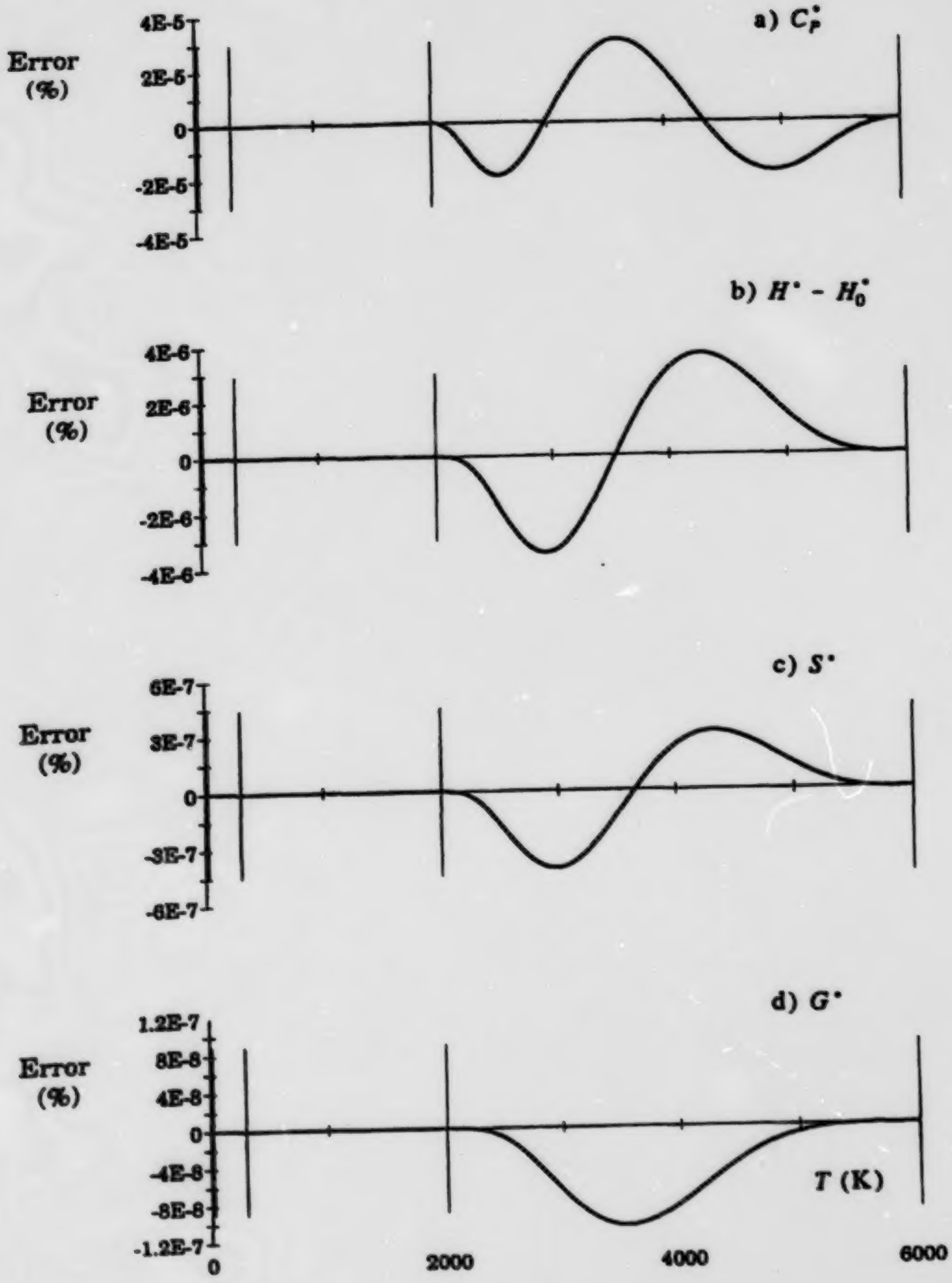

**Figure 1:** Errors for reproducing JANAF data for argon (Ar), for three temperature intervals with knots at 25, 298.15, 2000 and 6000 K.

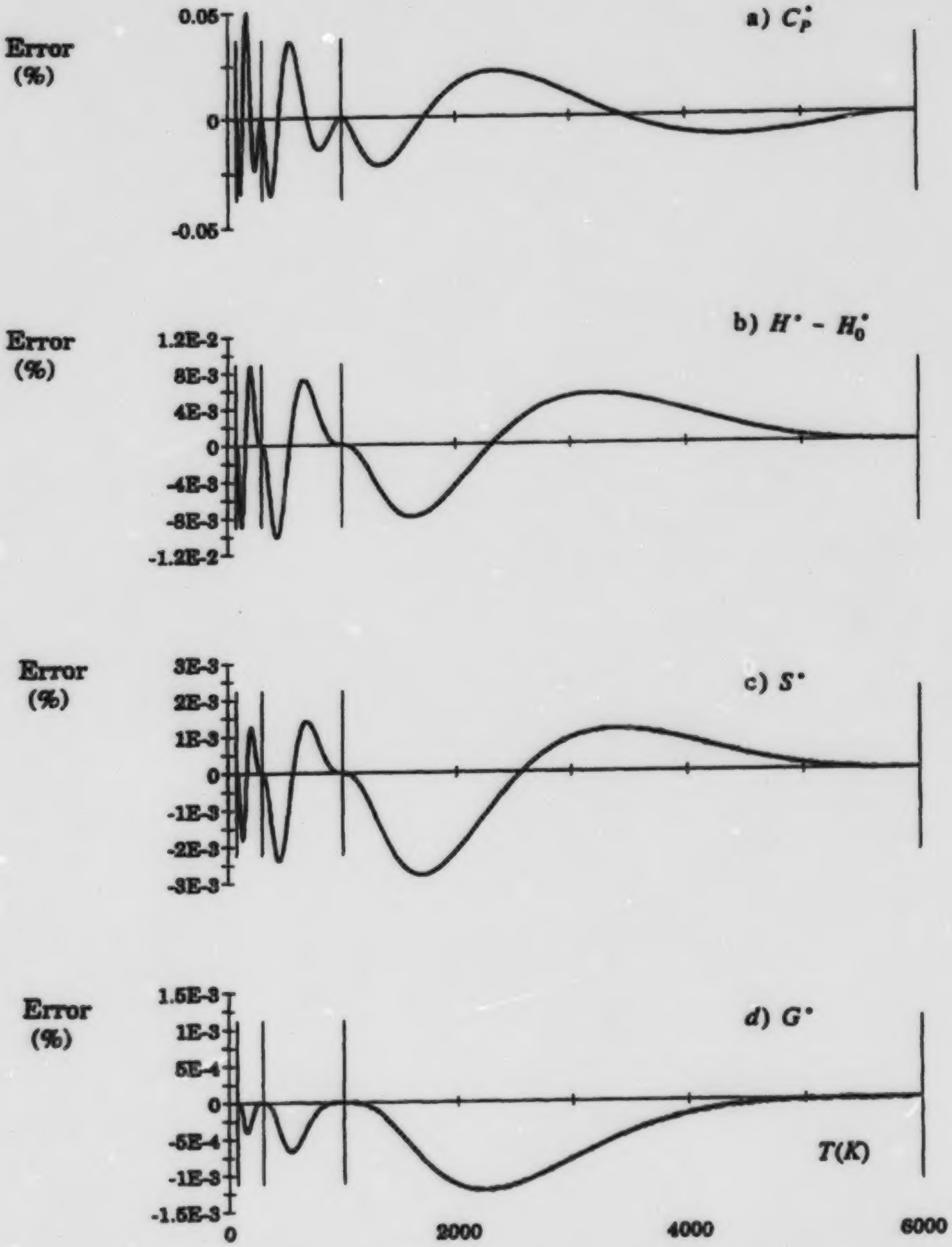

**Figure 2**: : Errors for reproducing JANAF data for $C_9H_{11}$, for three temperature intervals with knots at 75, 298.15, 1000 and 6000 K

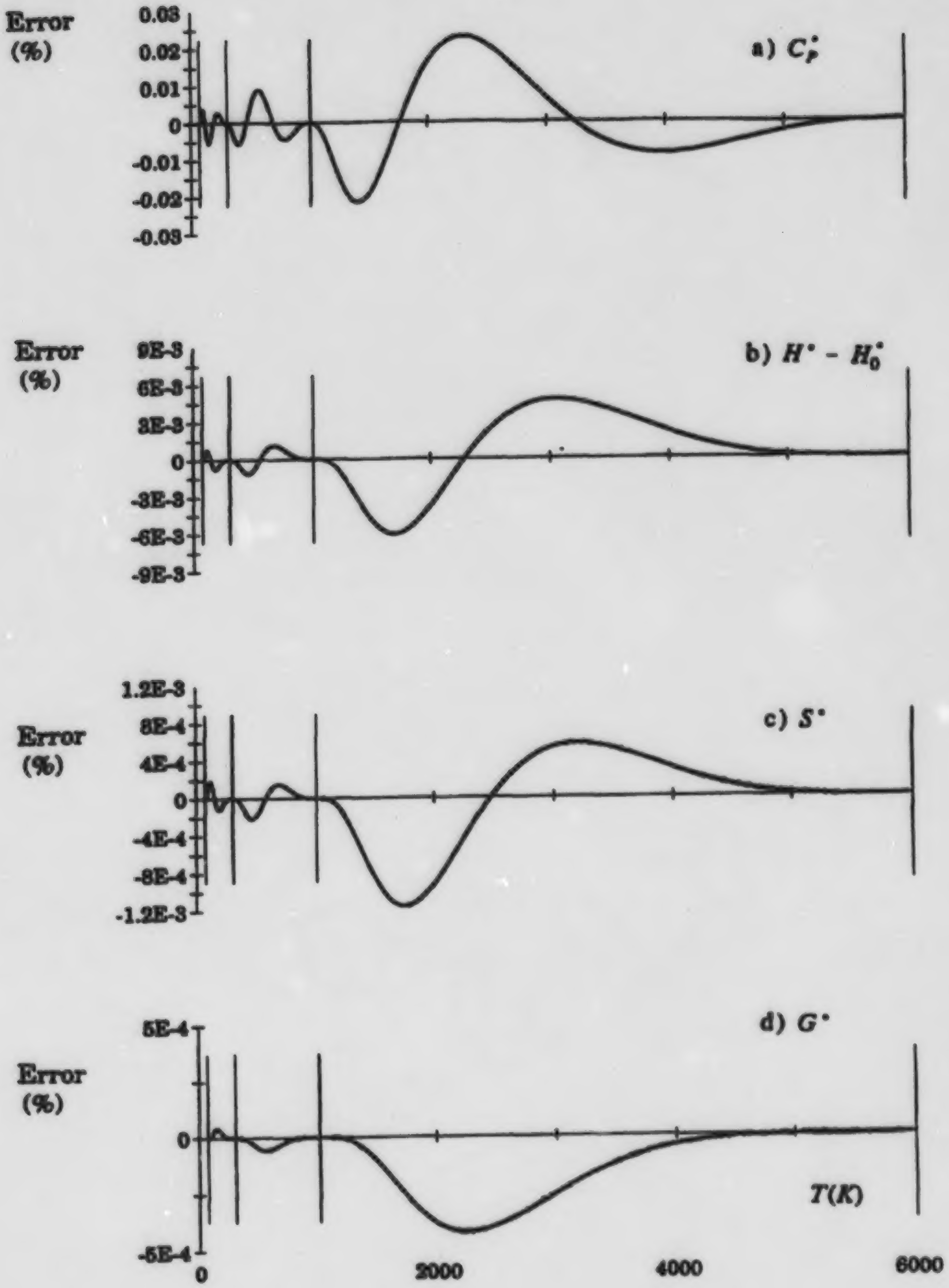

**Figure 3: : Errors for reproducing JANAF data for $H_2O$, for three temperature intervals with knots at 75, 298.15, 1000 and 6000 K.**

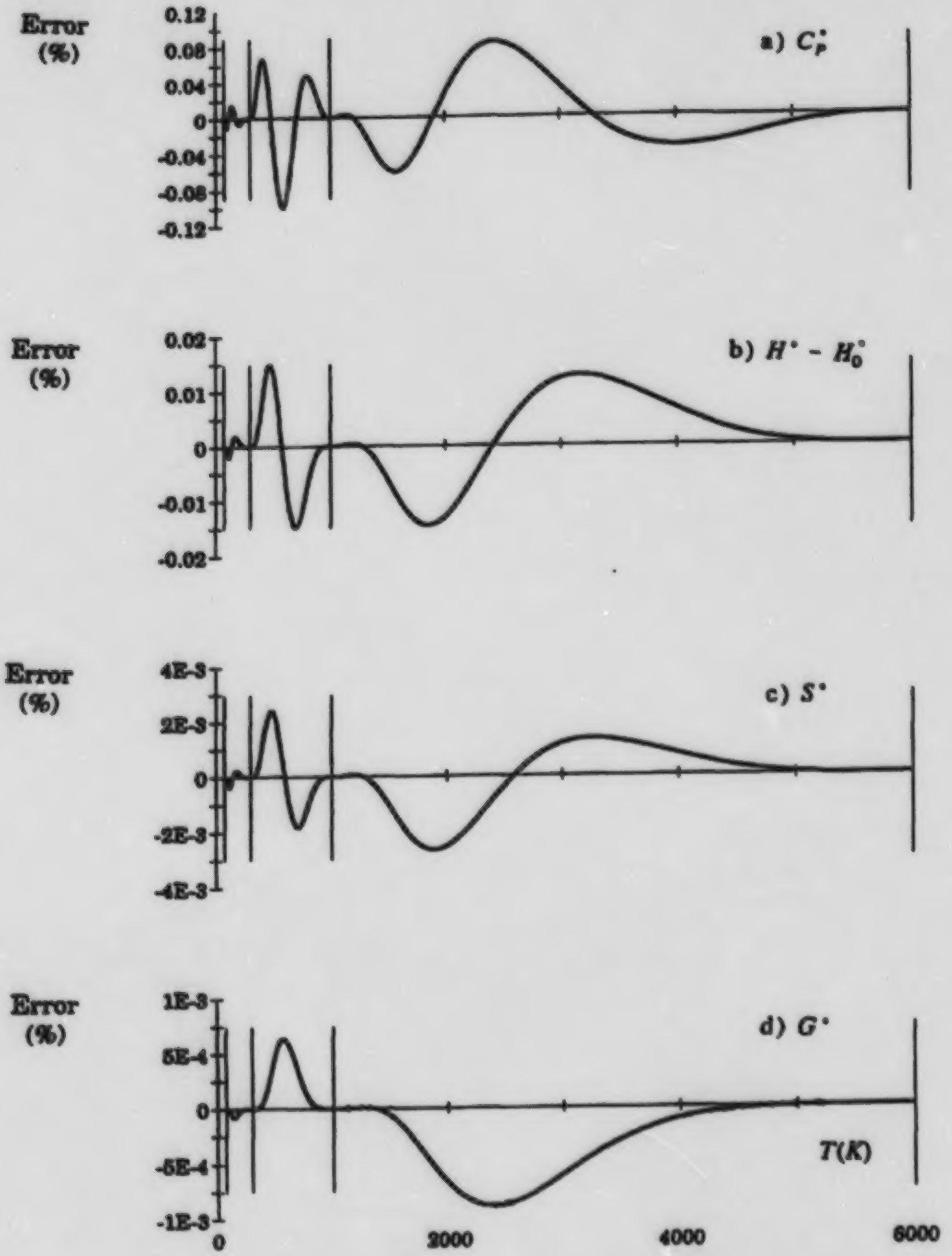

**Figure 4: Errors for reproducing JANAF data for magnesium oxide (MgO), for three temperature intervals with knots at 75, 298.15, 1000 and 6000 K.**

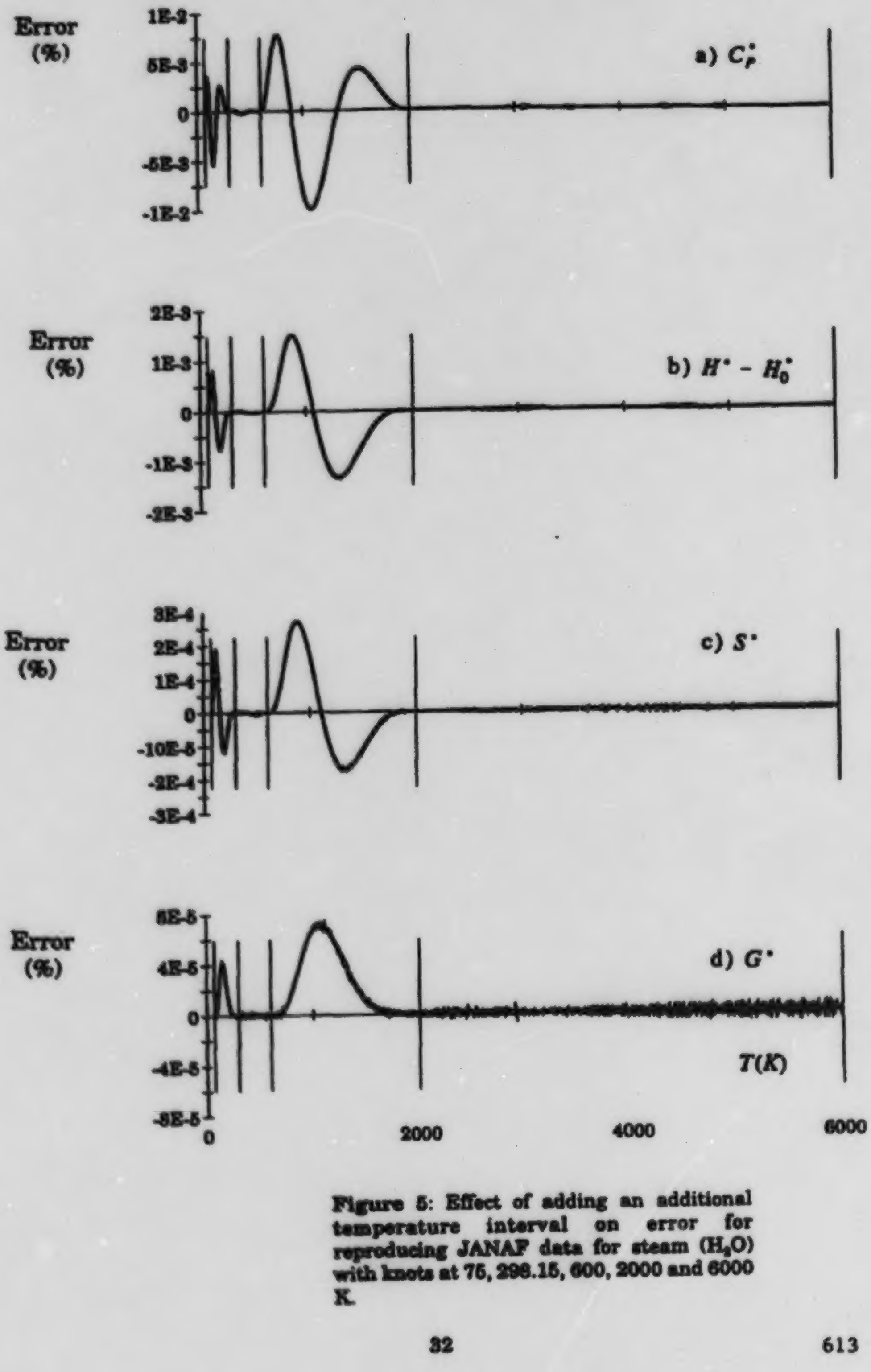

**Figure 5**: Effect of adding an additional temperature interval on error for reproducing JANAF data for steam ($H_2O$) with knots at 75, 298.15, 600, 2000 and 6000 K.

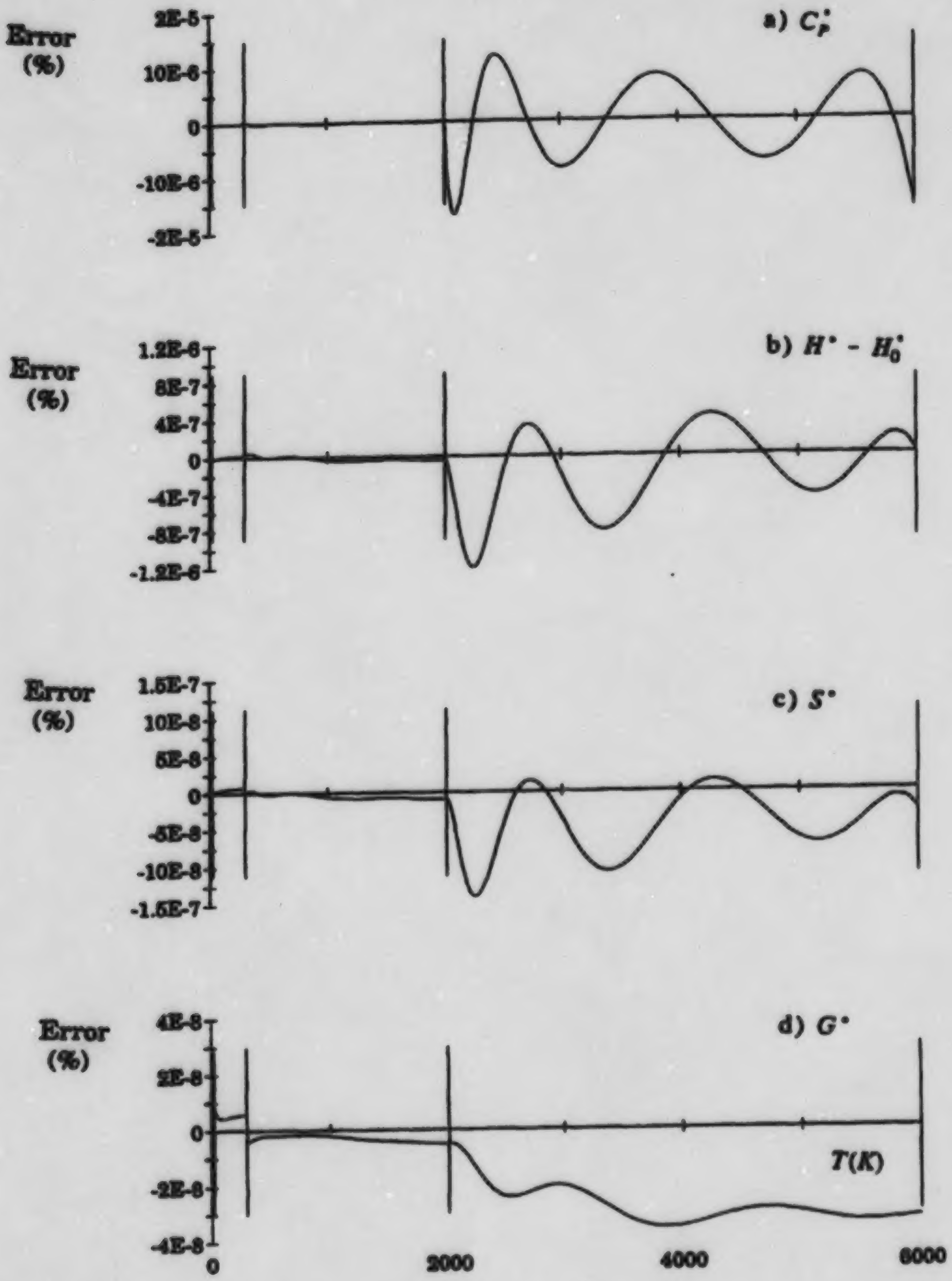

**Figure 6**: Errors for reproducing JANAF data from PAC91 for argon (Ar), for three temperature intervals with knots at 25, 298.15, 2000 and 6000 K.

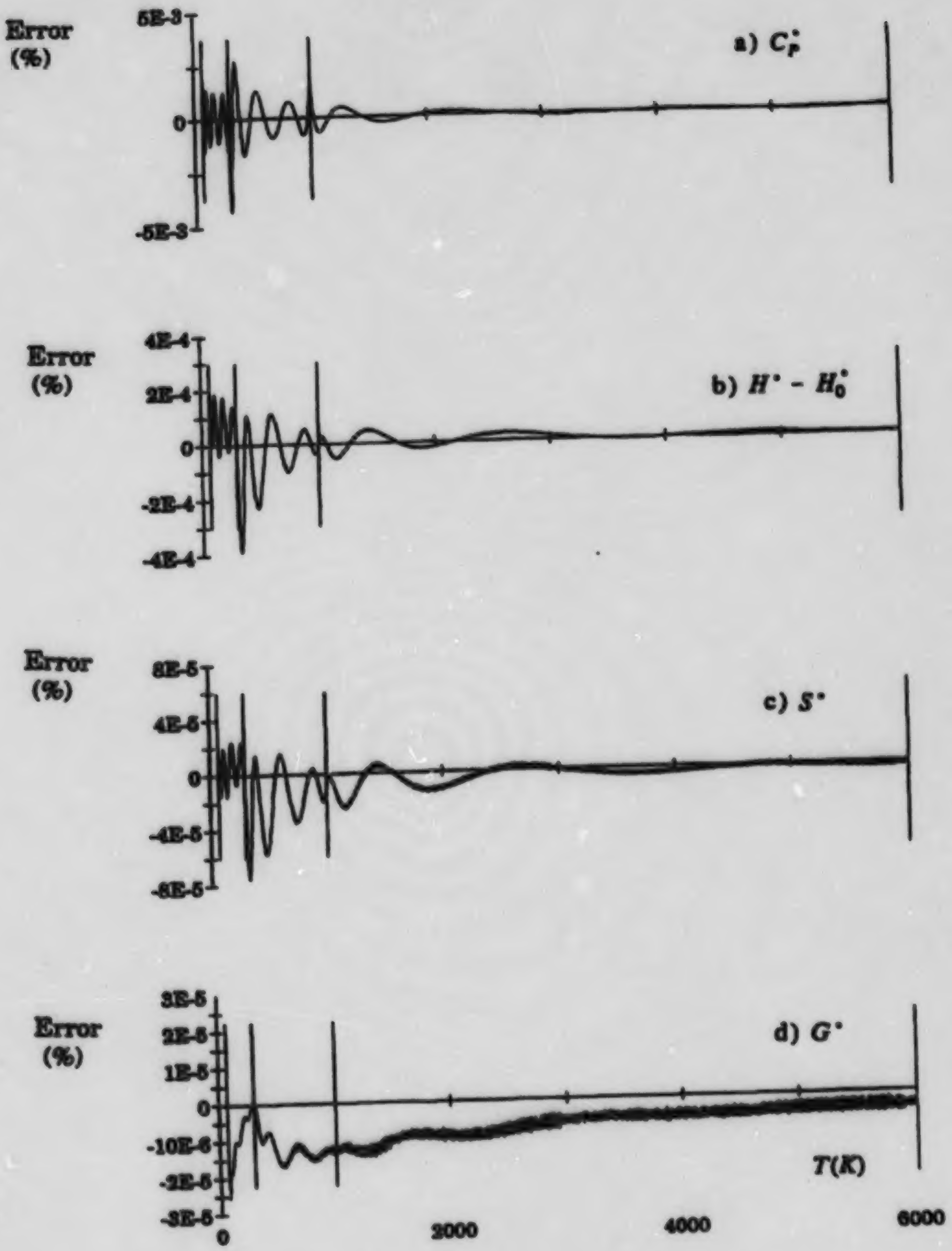

**Figure 7:** Errors for reproducing JANAF data from PAC91 for $C_5H_{11}$, for three temperature intervals with knots at 75, 298.15, 1000 and 6000 K.

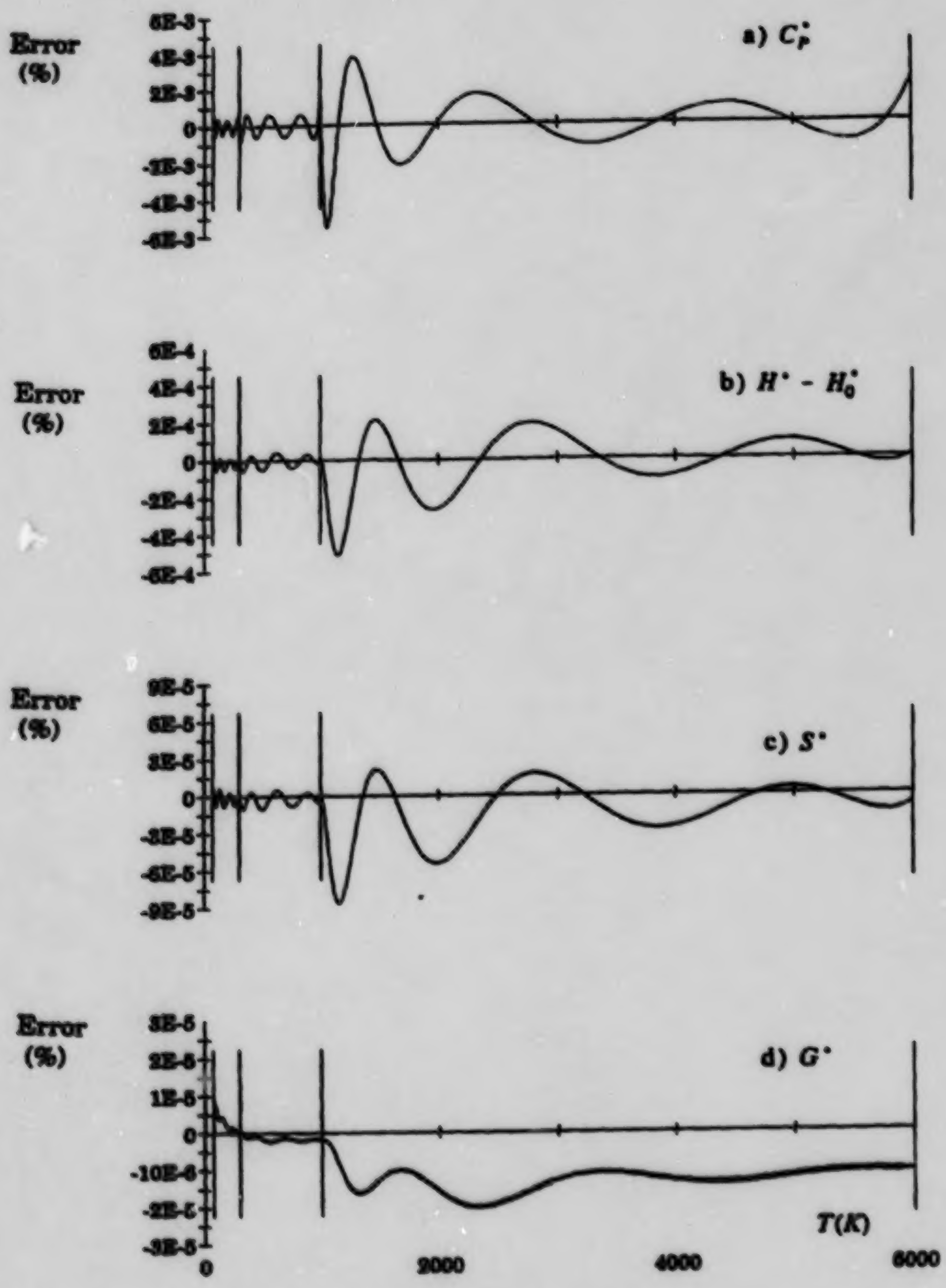

Figure 8: Errors for reproducing JANAF data from PAC91 for steam ($H_2O$), for three temperature intervals with knots at 75, 298.15, 1000 and 6000 K.

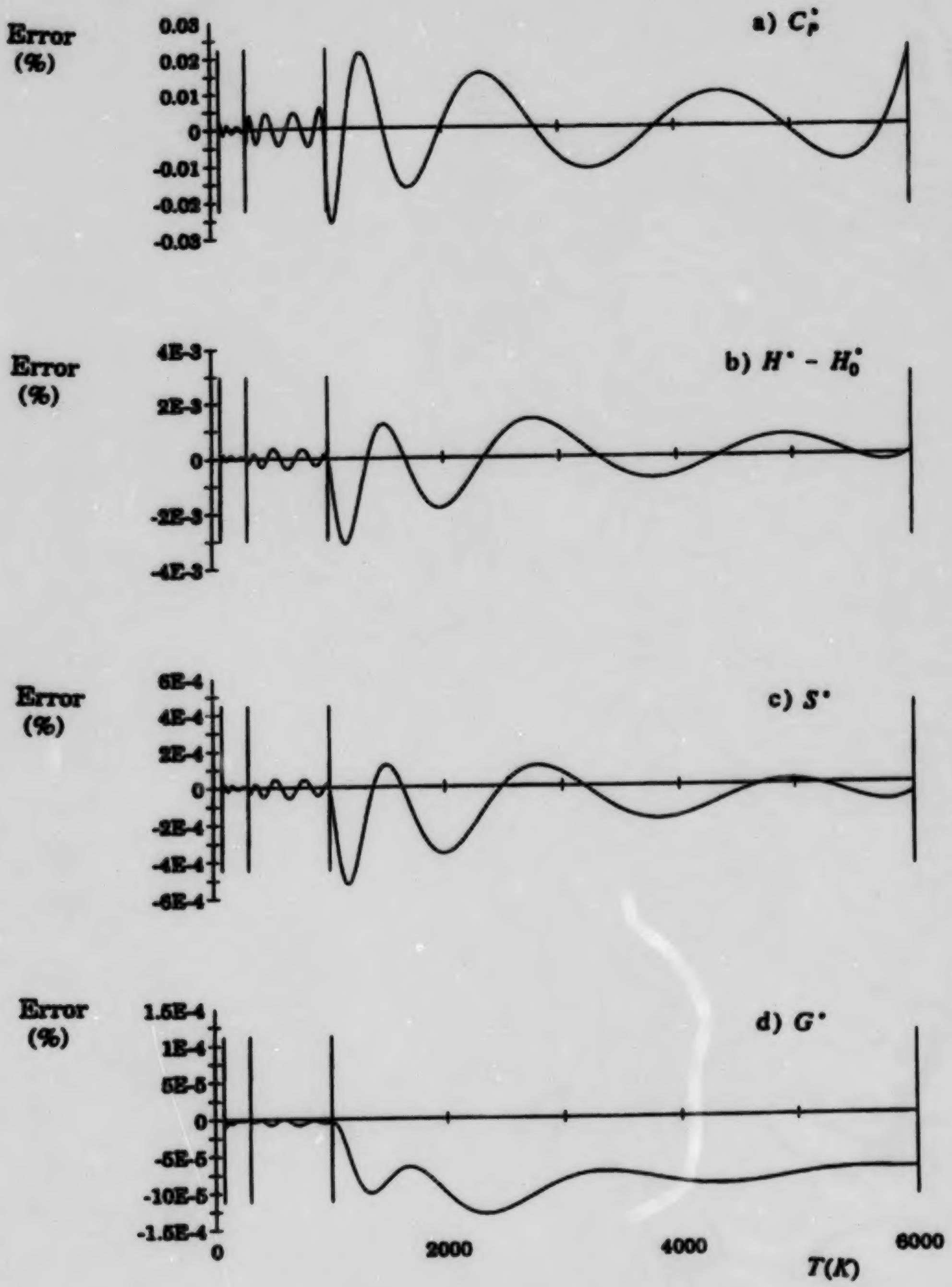

**Figure 9: Errors for reproducing JANAF data from PAC91 for Magnesium Oxide (MgO), for three temperature intervals with knots at 75, 298.15, 1000 and 6000 K.**

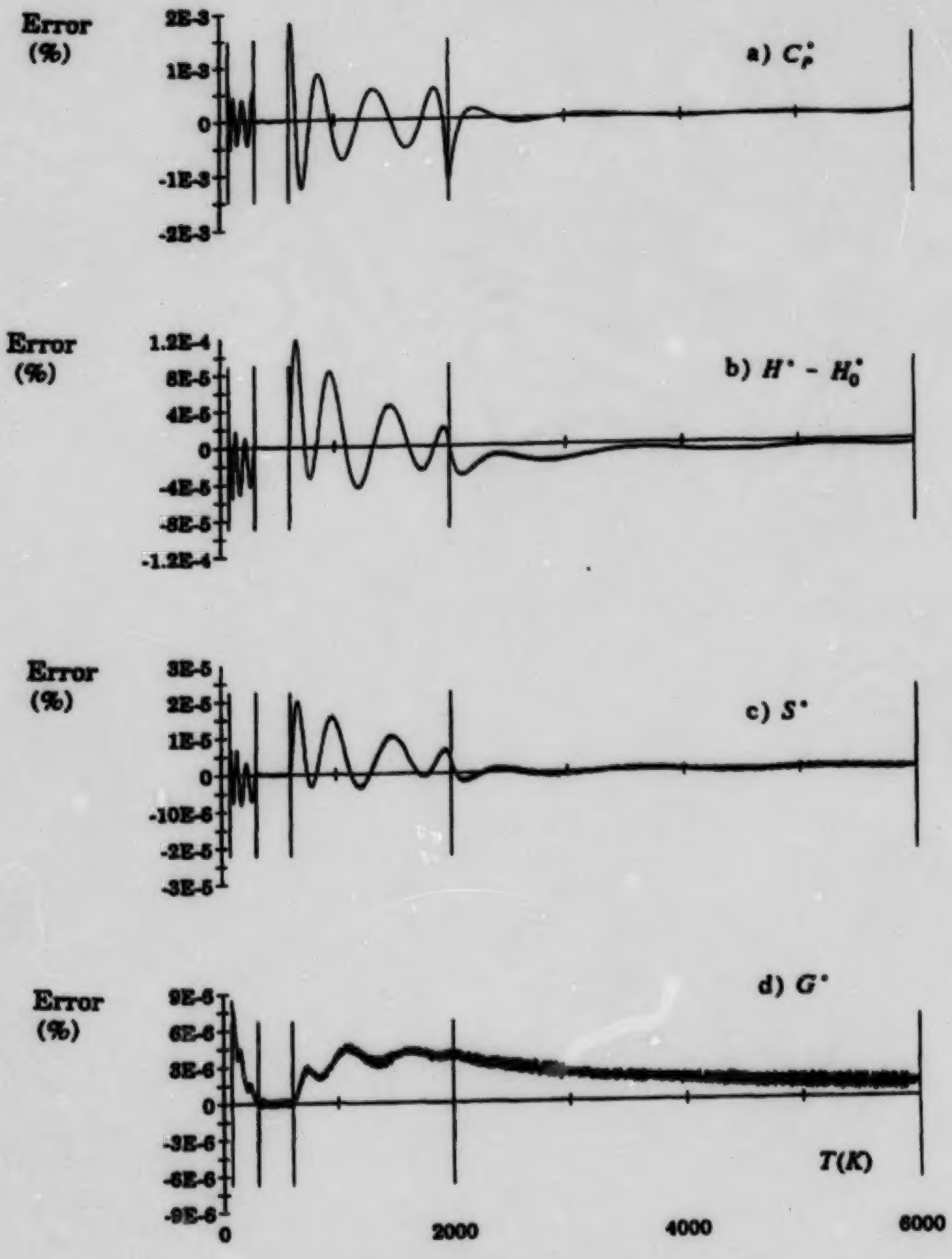

**Figure 10**: Effect of adding an additional temperature interval on error for reproducing JANAF data for steam ($H_2O$) from PAC91 with knots at 75, 298.15, 600, 2000 and 6000 K.

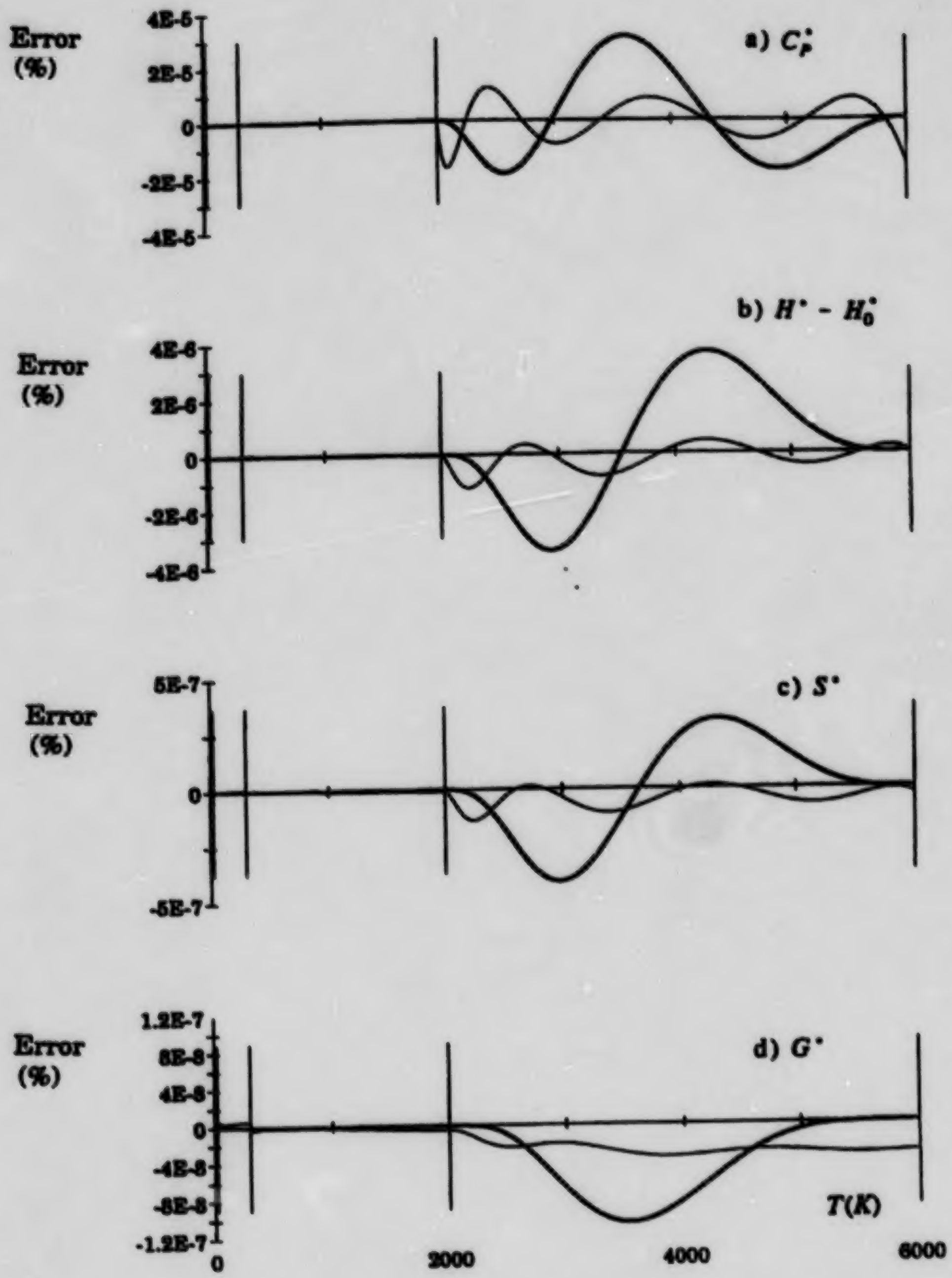

**Figure 11: Comparison of errors between PAC91 and current method for reproducing JANAF data for argon (Ar), for three temperature intervals with knots at 25, 298.15, 2000 and 6000 K.**

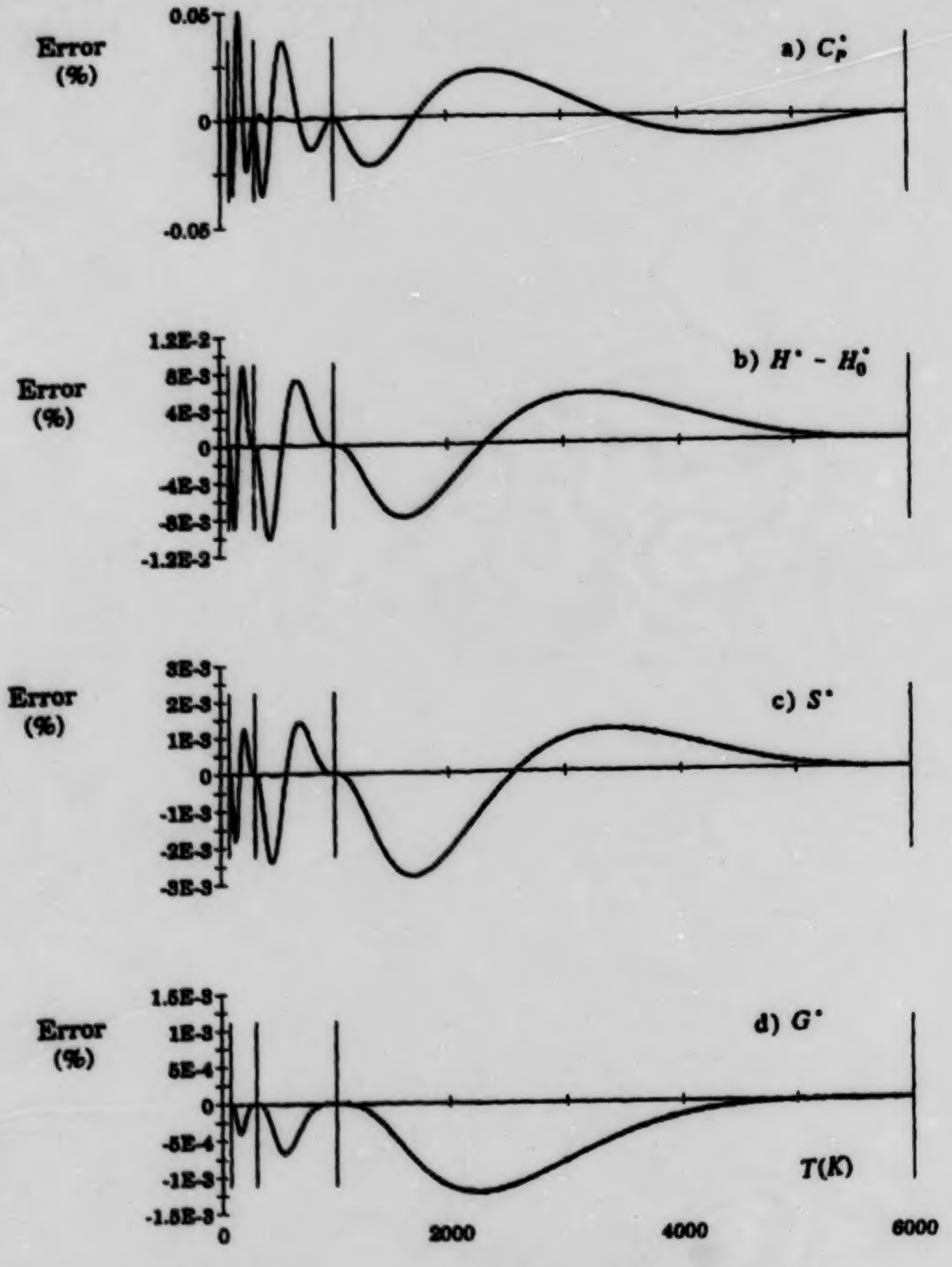

**Figure 12**: Comparison of errors between PAC91 and current method for reproducing JANAF data for $C_5H_{11}$, for three temperature intervals with knots at 75 K, 298.15 K, 1000 K and 6000 K.

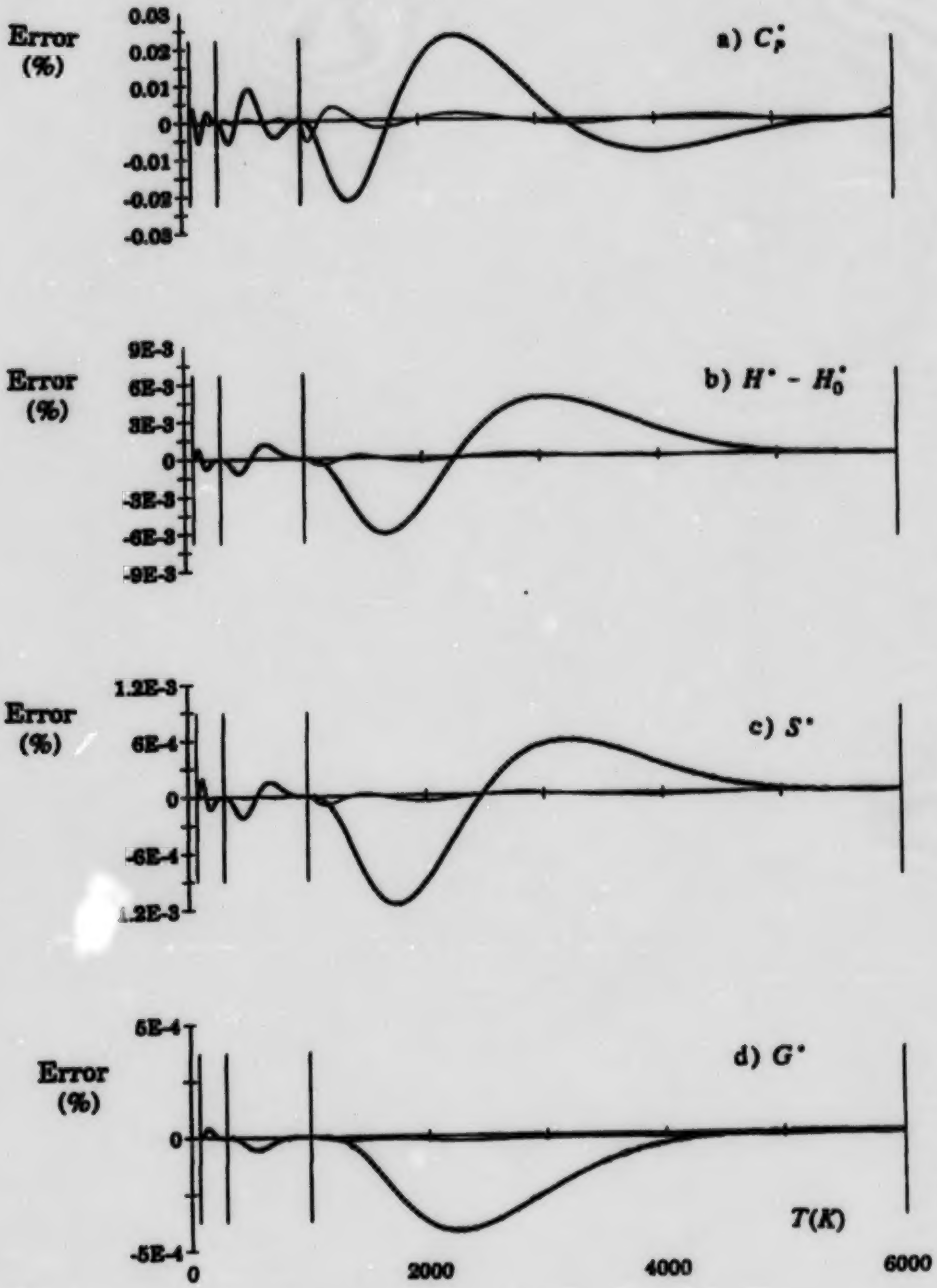

**Figure 18:** Comparison of errors between PAC91 and current method for reproducing JANAF data for $H_2O$, for three temperature ranges with knots at 75K, 298.15 K, 1000K and 6000 K.

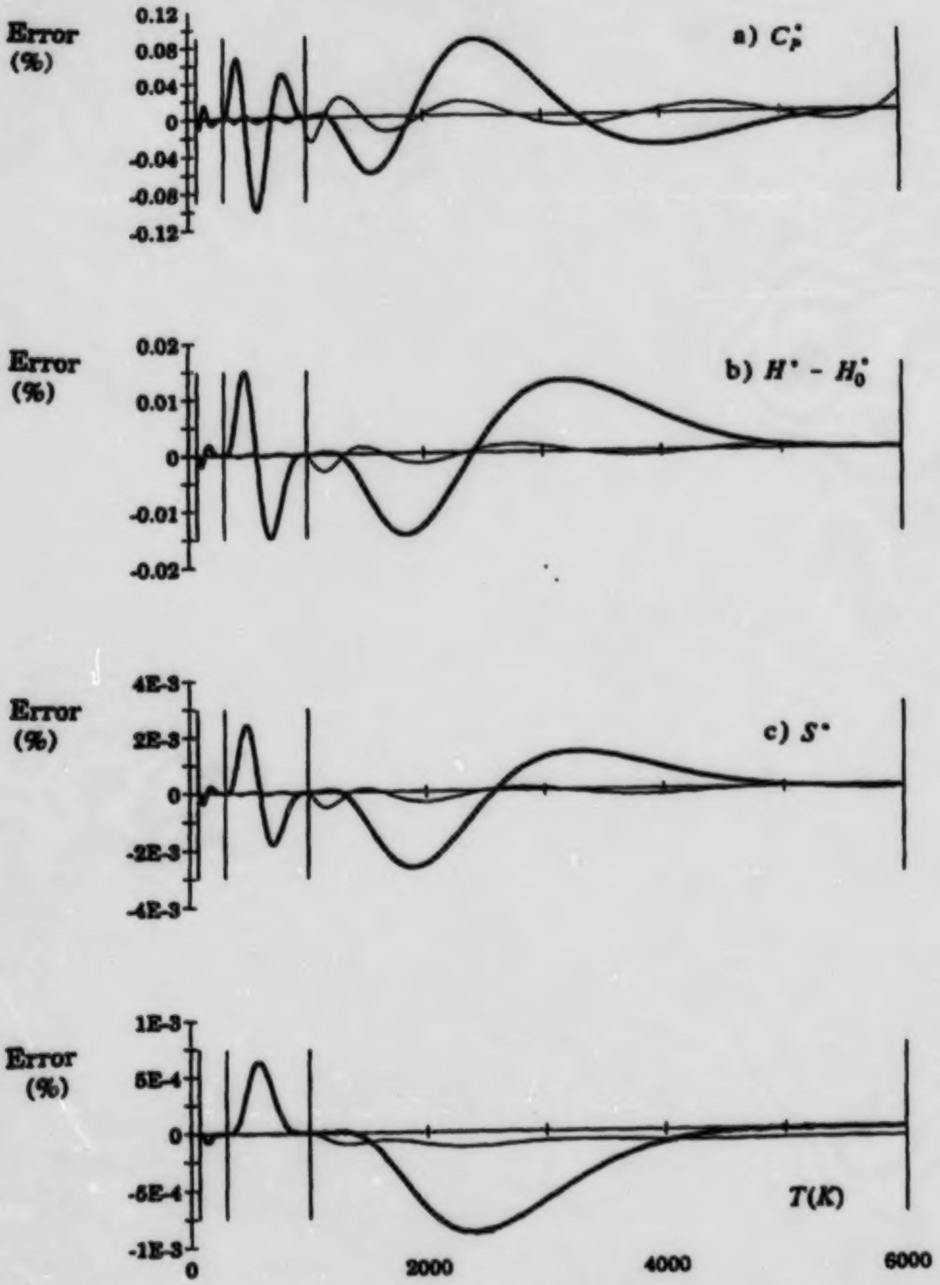

**Figure 14: Comparison of errors between PAC91 and current method for reproducing JANAF data for magnesium oxide (MgO), for three temperature intervals with knots at 75, 298.15, 1000 and 6000 K.**

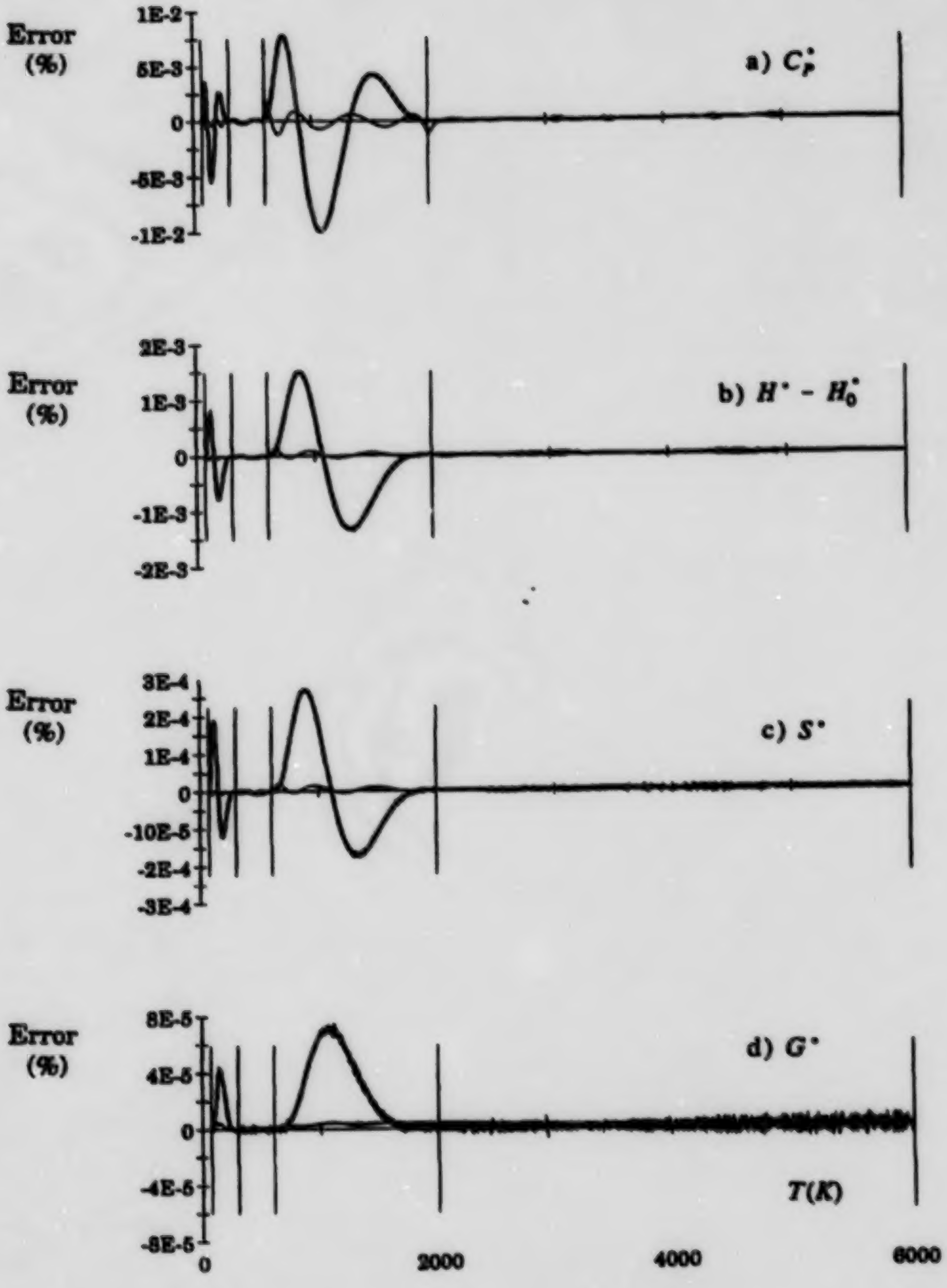

**Figure 15**: Comparison of effects of adding an additional temperature interval on error for reproducing JANAF data for steam ($H_2O$) with knots at 75, 298.15, 600, 2000 and 6000 K.

# APPENDIX 8

# COMPUTATIONAL MODEL FOR GAS-PARTICLE FLOWS USING PARTICLES WITH DISTRIBUTED SURFACES

by

Chak M. Tsui

# A Computational Model for Gas-Particle Flows with Distributed Phase Interfaces

by

**Chak M. Tsui**

A thesis submitted in conformity with the requirements
for the degree of Master of Applied Science
Graduate Department of Aerospace Science and Engineering
University of Toronto

# Abstract

A new method of computing unsteady gas-particle flows with smoothly distributed phase interfaces is introduced to facilitate computations in which the gas flow a continuum about particles that have independent paths (non-continuum). However, a viscous-flow resistance is imposed such that flow restricted more strongly further inside the particle interface where the particle become solid. The resulting force on the moving particle from the viscous-flow resistance and gas pressure around the particle is used to determine its acceleration and trajectory. Two unsteady one-dimensional problems are solved to assess the advantages and limitations of the new model. The first involves the reflection of a shock wave from a closed duct end for which the wall has a stationary distributed interface, and the second involves the acceleration of a projectile in a duct by a high-pressure gas, for which the projectile has smoothly distributed interfaces with the gas.

# Acknowledgements

The author would like to express his appreciation to his thesis supervisor Prof. J. J. Gottlieb for providing encouragement, support, and guidance throughout the course of this study. Acknowledgements are also given to members of the gasdynamics group and structural dynamics group for their support and friendship.

The author would like to acknowledge and thank Dr. Fan Zhang of Combustion Dynamics Ltd., Medicine, Hat, Alberta for his advice in regard to procuring and using the VODE software package. Discussions with Dr. Kazuhito Fujiwara of Kumamoto University, Japan, are very much appreciated.

The author would like to express a special thanks for his family for all of their encouragement and support.

# Contents

Abstract i

Acknowledgements ii

Contents iii

Nomenclature iv

1 Introduction 1

2 Model for Gas-Particle Flows with Distributed Phase Interfaces 10

2.1 Governing Equations for Gas Flows . . . . . . . . . . . . . . . . . . . . . . 10

2.2 Governing Equations for Particle Motions . . . . . . . . . . . . . . . . . . 11

2.3 Equations for Smoothly Distributing an Interface . . . . . . . . . . . . . . 13

2.4 Equations for Viscous-Flow Resistance . . . . . . . . . . . . . . . . . . . 14

3 Computational Solution Procedure 16

3.1 Grid for Numerical Computations . . . . . . . . . . . . . . . . . . . . . . 16

3.1.1 Flux Estimations . . . . . . . . . . . . . . . . . . . . . . . . . . . 16

3.2 Godunov's First-Order Scheme . . . . . . . . . . . . . . . . . . . . . . . 17

3.3 Variable-Coefficient ODE Solver . . . . . . . . . . . . . . . . . . . . . . 19

3.3.1 System of ODEs . . . . . . . . . . . . . . . . . . . . . . . . . . . 19

3.3.2 Jacobian Matrix for the ODE System . . . . . . . . . . . . . . . . 20

3.3.3 VODE Usage . . . . . . . . . . . . . . . . . . . . . . . . . . . . . 21

3.4 Particle Motion . . . . . . . . . . . . . . . . . . . . . . . . . . . . . . . 22

4 Test Problems 23

4.1 Shock Reflection at a Distributed Interface . . . . . . . . . . . . . . . . . . . . 23

4.1.1 Problem Definition . . . . . . . . . . . . . . . . . . . . . . . . 23

4.1.2 Analytical Solution . . . . . . . . . . . . . . . . . . . . . . . . 24

4.1.3 Initial Conditions . . . . . . . . . . . . . . . . . . . . . . . . . 25

4.1.4 Results . . . . . . . . . . . . . . . . . . . . . . . . . . . . . . 25

4.2 Projectile Acceleration . . . . . . . . . . . . . . . . . . . . . . . . . . . . 27

4.2.1 Problem Definition . . . . . . . . . . . . . . . . . . . . . . . . 27

4.2.2 Analytical Solution . . . . . . . . . . . . . . . . . . . . . . . . 27

4.2.3 Initial Conditions . . . . . . . . . . . . . . . . . . . . . . . . . 28

4.2.4 Results . . . . . . . . . . . . . . . . . . . . . . . . . . . . . . 29

5 Concluding Remarks 30

Bibliography 32

# Nomenclature

## Alphanumeric Letters

| | |
|---|---|
| $a$ | speed of sound of the gas flow [m/s], acceleration [m/s$^2$] |
| $\vec{a}$ | vector acceleration [m/s$^2$] |
| $A$ | cross-sectional area [m$^2$] |
| $B(x)$ | dimensionless modification term in viscous-flow resistance |
| $c_{visc}$ | second dimensionless coefficient of viscous-flow resistance |
| $C_{visc}$ | first coefficient of viscous-flow resistance [m$^{-1}$] |
| $C_p$ | specific heat of the material at constant pressure [J/kg·K] |
| $C_d$ | dimensionless drag coefficient |
| $d$ | equivalent diameter of the particle [m] |
| $e$ | energy per unit volume [J/m$^3$] |
| $f_{visc}$ | viscous-flow resistance per unit volume [N/m$^3$] |
| $F_{back}$ | gas pressure force on the rear surface of a projectile [N] |
| $F_{front}$ | gas pressure force on the frontal surface of a projectile [N] |
| $\vec{F}_{drag}$ | aerodynamic drag force [N] |
| $\vec{F}_{grav}$ | gravitational force [N] |
| $\mathbf{F}(\mathbf{U})$ | flux term in $x$ direction |
| $\mathbf{G}(\mathbf{U})$ | flux term in $y$ direction |
| $\bar{\mathbf{G}}$ | modified spatial derivatives of flux term in chapter 3 |
| $\mathbf{H}(\mathbf{U})$ | term of spatial derivatives |
| $k$ | thermal conductivity of the gas phase [J/m·s·K] |
| $m$ | mass [kg] |
| $M_i$ | incident shock Mach number |
| $M_r$ | reflected shock Mach number |
| $n$ | exponent in viscous-flow resistance |
| $N$ | total number of cells |
| Nu | Nusselt number |
| $p$ | static pressure of the gas flow [N/m$^2$] |
| Pr | Prandtl number |
| $\dot{q}$ | heat transfer [J/m$^3$·s] |
| $R$ | gas constant [J/kg·K] |
| Re | Reynolds number |

| | |
|---|---|
| $\mathcal{R}$ | Riemann solver operator |
| $\mathbf{S}(\mathbf{U}_g, \mathbf{U}_p)$ | source term in the Euler's equations |
| $\tilde{\mathbf{S}}$ | modified source term in chapter 3 |
| $t$ | time |
| $T$ | temperature [K] |
| $\mathbf{T}(\mathbf{V})$ | source term in the **VODE** subroutine |
| $u$ | velocity in $x$ direction [m/s] |
| $\vec{u}$ | vector velocity [m/s] |
| $\mathbf{U}$ | conservative variables |
| $\tilde{\mathbf{U}}$ | modified conservative variables in chapter 3 |
| $v$ | velocity in $y$ direction [m/s] |
| $V$ | volume [m$^3$] |
| $\mathbf{V}$ | independent variable array used in the **VODE** subroutine |
| $x$ | displacement [m] |
| $\vec{x}$ | vector displacement [m] |

## Greek Letters

| | |
|---|---|
| $\gamma$ | ratio of specific heats |
| $\delta t$ | time between successive plotted spatial distributions of variables [s] |
| $\Delta t$ | time step [s] |
| $\Delta x$ | width of a cell [m] |
| $\eta$ | normalized free parameter in the Bézier's polynomial ($0 \leq \eta \leq 1$) |
| $\zeta$ | normalized free parameter in the Bézier's polynomial ($0 \leq \zeta \leq 1$) |
| $\epsilon$ | volume fraction |
| $\epsilon_{g_{min}}$ | minimum allowed gas-volume fraction |
| $\mu$ | viscosity [N·s/m$^2$] |
| $\rho$ | density [kg/m$^3$] |
| $\sigma$ | partial phase density [kg/m$^3$] |

## Superscripts

| | |
|---|---|
| $+$ | left side of this location |
| $-$ | right side of this location |
| init | initial condition |
| old | state at the last time level |
| new | state at the next time level |
| $T$ | matrix transpose |

## Subscripts

| | |
|---|---|
| 1 | first point for Bézier's polynomials, also used in cell indexing, and the gas state in front of the incoming shock |
| 2 | second point for Bézier's polynomials, also used in cell indexing, and the gas state behind the incoming shock |

| | |
|---|---|
| 3 | third point for Bézier's polynomials, also used in cell indexing, and the gas state behind the reflected shock |
| 4 | fourth point for Bézier's polynomials, also used in cell indexing |
| $i$ | index for the $i^{th}$ cell |
| $i-1/2$ | index for the left boundary of the $i^{th}$ cell |
| $i+1/2$ | index for the right boundary of the $i^{th}$ cell |
| $g$ | gas phase |
| $l$ | at the left side of the projectile |
| $o$ | at a reference condition |
| $p$ | particle phase, projectile |
| $r$ | at the right side of the projectile |
| sphere | property of a sphere |
| $x$ | $x$ direction |
| $y$ | $y$ direction |

## VODE Parameters

| | |
|---|---|
| NEQ | number of variables |
| T | current time |
| TOUT | time for the output |
| ITOL | an indicator for the type of error control |
| RTOL | relative error tolerance parameter |
| ATOL | absolute error tolerance parameter |
| ITASK | an index specifying the task to be performed |
| ISTATE | an index to specify the state of the calculation |
| IOPT | an indicator for optional input |
| LRW | size of the double precision work array |
| LIW | size of the integer work array |
| ML | number of sub-diagonals under the main diagonal |
| MU | number of sub-diagonals above the main diagonal |
| MF | method flag |
| RPAR | user specified double-precision scalar or array variable |
| IPAR | user specified integer scalar or array variable |
| H0 | the step size to be used on the first step |
| HMAX | maximum step size allowed |
| HMIN | minimum step size allowed |
| MAXORD | maximum order allowed |
| MXSTEP | maximum number of steps allowed |
| MXHNIL | maximum number of message printed |

# Chapter 1

# Introduction

Flows of a dusty-gas or gas-particle mixture constitute a subclass of two-phase flows [Soo, 1967; Rudinger, 1980; Hetsroni, 1982] in which one phase consists of small particles that are solid or rigid. These particles are normally suspended and transported by the second gaseous phase (carrier gas). Gas-particle flows occur naturally in the form of smoke, haze, pollen, pollutants and volcanic ash in the atmosphere, and also in the form of sand, hail and snow storms. In industrial engineering gas-particle flows are used as fluidized beds, for particulate conveyance in pipes, and to separate particles from the carrier gas. Some common aerospace applications include the solid-propellant rocket motor, flight through a particle-laden gas, and sand erosion of helicopter blades and jet-engine compressor fans. Furthermore, gas-particle flows are inherent to grain-elevator and coal-mine explosions, and they also occur in the detonation of some heterogeneous explosives.

Some gas-particle mixtures undergo essentially equilibrium flow, that is the gas and particles move in unison at essentially the same velocity and also essentially with the same temperature, when viscous-drag (from boundary-layer shear) and heat-transfer processes are dominant over flow processes [Rudinger, 1980]. Most mixtures undergo nonequilibrium flow in which slip occurs between the gas and particle phases and when heat is transferred from the hot to cold phase, because viscous-drag and heat-transfer processes are normally slow compared to velocity and temperature changes of the gas phase, although the effects of viscosity and heat transfer always act in the direction of establishing equilibrium flow. A prime example of nonequilibrium flow is the shock-induced motion of a gas-particle mixture in accidental explosions and laboratory shock tubes.

Particles in gas-particle mixtures are frequently of different sizes, shapes and possibly material properties (e.g., a mixture of sand and soil), and they therefore move at different velocities because the viscous-drag acceleration varies with particle shape, size and density. Consequently, some neighbouring particles on collision paths undergo collisions and path deflections [Hetsroni, 1982], while some of these might simply agglomerate owing to electrostatic or other effects [Hetsroni, 1982], whereas other neighbouring particles only experience near misses and one particle passes another. Particle-particle collisions, path deflections, and passing events may be considered as another version of nonequilibrium flow.

Predictions of gas-particle flows with nonequilibrium behaviour are important to understanding flow phenomena and in providing better aerodynamic and industrial designs of equipment that may result in increased safety in the workplace. Numerical prediction models are reviewed herein with the intent of establishing a good perspective for understanding present and future computational developments for solving difficult gas-particle flow problems involving gas-particle slip, heat transfer, and particle-particle collisions. After reviewing a number of different gas-particle flow models, commencing with simple early treatments and progressing chronologically to sophisticated recent models, the objectives and scope of the this study are then given.

The method of particle-trajectory tracing is reviewed first because of its simplicity, and it is one of the first models used in predicting the influence of the gas on particle motions. In some problems involving bird strikes with aircraft, large particles ingested by aircraft engines [Tabakoff & Hamed, 1989], the separation of large particle from the carrier gas by means of a particle separator [Svarovsky, 1981; Hetsroni, 1982; Ogawa, 1984], and flows of particles in solid-propellant rocket motors [Carrier, Fendell, Brent, Kimbrough, Loucks, Hess, & Acosta, 1991; Sabnis, Jong, & Gibeling, 1992], only a few discrete particles normally move through a steady two- or three-dimensional flow field. Their particle trajectories are usually required to determine or control the particle impact location. The standard model for particle trajectory tracing is done in two steps. In the first step, the steady two- or three-dimensional flow without particles is computed numerically, for example by solving Euler's continuity, momentum and energy equations

$$\frac{\partial \mathbf{F}(\mathbf{U}_g)}{\partial x} + \frac{\partial \mathbf{G}(\mathbf{U}_g)}{\partial y} = 0 \tag{1.1}$$

for two space dimensions, for which the perfect equation of state $p_g = \rho_g R_g T_g$ is required to close these equations. In this expression the vectors are given by

$$\begin{aligned} \mathbf{U}_g &= [\rho_g \quad \rho_g u_g \quad \rho_g v_g \quad e_g]^T, \\ \mathbf{F}(\mathbf{U}_g) &= \left[\rho_g u_g \quad \rho_g u_g^2 + p_g \quad \rho_g u_g v_g \quad u_g(e_g + p_g)\right]^T, \\ \mathbf{G}(\mathbf{U}_g) &= \left[\rho_g v_g \quad \rho_g u_g v_g \quad \rho_g v_g^2 + p_g \quad v_g(e_g + p_g)\right]^T, \end{aligned} \tag{1.2}$$

and $R_g$, $p_g$, $\rho_g$, $u_g$, $v_g$, $e_g = \frac{1}{\gamma-1}p_g + \frac{1}{2}\rho_g(u_g^2 + v_g^2)$, and $T_g$ denote the gas constant, pressure, density, flow velocities in the $x$ and $y$ directions, energy per unit volume, and temperature, respectively. In the last step, particle trajectories through this computed flow field are calculated by using the known flow-field results, for the case of different trajectories originating from various starting locations. Particle-path calculations are based on flow-field properties along the particle trajectory where the equation of motion of an individual particle is used in the form

$$\vec{a}_p = \frac{d\vec{u}_p}{dt} = \frac{d^2\vec{x}_p}{dt^2} = \frac{1}{m_p}\left[\vec{F}_{drag} + \vec{F}_{grav}\right], \tag{1.3}$$

where $\vec{F}_{grav} = m_p\vec{g}$ is the gravitational force on the particle and the aerodynamic drag force on the particle is given by

$$\vec{F}_{drag} = \frac{1}{2} C_d A_p \rho |\vec{u}_g - \vec{u}_p| (\vec{u}_g - \vec{u}_p) \,. \tag{1.4}$$

In the preceding equations, the vectors $\vec{a}_p$, $\vec{u}_p$, and $\vec{x}_p$ denote particle acceleration, velocity, and position, respectively. Also, $m_p$, $C_d$, $A_p = \pi d^2/4$, and $\vec{u}_g$ designate particle mass, coefficient of viscous drag, particle cross-sectional area where $d$ is the diameter of the particle, and vector flow velocity. Note that $\vec{u}_g = \hat{i}u_g + \hat{j}v_g$, where $\hat{i}$ and $\hat{j}$ are the unit vectors in $x$ and $y$ direction, respectively; the correlation for the drag coefficient is normally given by $C_d = 0.48 + 28\mathrm{Re}^{-0.85}$, where $\mathrm{Re} = \rho_g d |\vec{u}_g - \vec{u}_p| / \mu_g$ is the Reynolds number, $d$ is the equivalent diameter of the spherical particle, and Sutherland's approximation for the dynamic viscosity of the air is given by $\mu_g = \mu_{g_o}(T/T_{g_o})^{0.77}$, in which $\mu_{g_o} = 1.71 \times 10^{-5}$ N·s/m$^2$ and $T_{g_o} = 273$ K.

In this simple model of particle-trajectory tracing, the gas is treated as a continuum using Eq. (1.1), and the particles are treated as independent bodies moving through the gas using Eq. (1.3). A direct advantage is that discrete particles starting from different locations have independent trajectories through the flow field such that particles can pass one another. Another advantage is that particle-particle collisions can also be incorporated into the predictions, if the conservation of linear momentum, angular momentum, and energy with or without losses are applied as particle paths are evaluated. In addition, particle collisions with walls can be included similarly, because a wall can be considered as a large stationary particle. On the other hand, there are certain disadvantages of this simple model. There is no influence of both the particle volume and particle motion on the gas flow field, and heat transfer between the gas and particles is usually ignored. Another disadvantage is that unsteady gas-particle flows cannot normally be solved. Although this simple model of particle-trajectory tracing applies well for some applications mentioned earlier, additional models are required for other applications (e.g., for unsteady flows of dusty gases).

The method of dual gas and particle continua with negligible particle volume is reviewed next, because this more complicated model was needed historically to solve important problems involving numerous small particles in unsteady flows with viscous and heat-transfer interactions between the phases. Such flows include, for example, the migration of smoke, pollutants, and volcanic ash in the Earth's atmosphere [Zlatev, Dimov, & Georgiev, 1994] and shock-induced dusty-gas flows in ducts and explosions [Rudinger, 1980; Miura & Glass, 1982 & 1985]. The unsteady flow equations of mass, momentum, and energy for the gas and particle phases are coupled in terms of mass transfer (if chemical reactions occur), momentum transfer (viscous drag), and heat transfer (between the gas and particle phases). These equations are given by

$$\frac{\partial \mathbf{U}_g}{\partial t} + \frac{\partial \mathbf{F}(\mathbf{U}_g)}{\partial x} + \frac{\partial \mathbf{G}(\mathbf{U}_g)}{\partial y} + \mathbf{H}(\mathbf{U}_g) = \mathbf{S}(\mathbf{U}_g, \mathbf{U}_p) \,, \tag{1.5}$$

$$\frac{\partial \mathbf{U}_p}{\partial t} + \frac{\partial \mathbf{F}(\mathbf{U}_p)}{\partial x} + \frac{\partial \mathbf{G}(\mathbf{U}_p)}{\partial y} + \mathbf{H}(\mathbf{U}_p) = -\mathbf{S}(\mathbf{U}_g, \mathbf{U}_p) \,, \tag{1.6}$$

for the case where particle volume is neglected only in the gas-phase equations. In these equations the vectors for the gas phase are given by

$$\begin{aligned} \mathbf{U}_g &= [\rho_g \quad \rho_g u_g \quad \rho_g v_g \quad e_g]^T, \\ \mathbf{F}(\mathbf{U}_g) &= \left[\rho_g u_g \quad \rho_g u_g^2 \quad \rho_g u_g v_g \quad u_g(e_g + p_g)\right]^T, \\ \mathbf{G}(\mathbf{U}_g) &= \left[\rho_g v_g \quad \rho_g u_g v_g \quad \rho_g v_g^2 \quad v_g(e_g + p_g)\right]^T, \\ \mathbf{H}(\mathbf{U}_g) &= \left[0 \quad \frac{\partial p_g}{\partial x} \quad \frac{\partial p_g}{\partial y} \quad 0\right]^T, \\ \mathbf{S}(\mathbf{U}_g, \mathbf{U}_p) &= [0 \quad f_x \quad f_y \quad f_x u_p + f_y v_p + \dot{q}]^T, \end{aligned} \tag{1.7}$$

and the vectors for the particle phase are given by

$$\begin{aligned} \mathbf{U}_p &= [\varepsilon_p \rho_p \quad \varepsilon_p \rho_p u_p \quad \varepsilon_p \rho_p v_p \quad \varepsilon_p e_p]^T, \\ \mathbf{F}(\mathbf{U}_p) &= \left[\varepsilon_p \rho_p u_p \quad \varepsilon_p \rho_p u_p^2 \quad \varepsilon_p \rho_p u_p v_p \quad \varepsilon_p u_p(e_p + p_g)\right]^T, \\ \mathbf{G}(\mathbf{U}_p) &= \left[\varepsilon_p \rho_p v_p \quad \varepsilon_p \rho_p u_p v_p \quad \varepsilon_p \rho_p v_p^2 \quad \varepsilon_p v_p(e_p + p_g)\right]^T, \\ \mathbf{H}(\mathbf{U}_p) &= \left[0 \quad \varepsilon_p \frac{\partial p_g}{\partial x} \quad \varepsilon_p \frac{\partial p_g}{\partial y} \quad 0\right]^T. \end{aligned} \tag{1.8}$$

The perfect equation of state $p_g = \rho_g R_g T_g$ is required to help close this set of equations. The subscripts $g$ and $p$ denote the properties of gas and particle phases, respectively, and the particle energy per unit volume is $e_p = C_{p_p} T_p + \frac{1}{2}\rho_p(u_p^2 + v_p^2)$, where $C_{p_p}$ is the specific heat of the particle material. The drag-force components in $x$ and $y$ directions are given by $f_x = -\hat{\imath} \cdot \vec{F}_{\mathrm{drag}} \varepsilon_p / V_p$ and $f_y = -\hat{\jmath} \cdot \vec{F}_{\mathrm{drag}} \varepsilon_p / V_p$ in units of Newtons per unit of volume, for which the centre dot designates the vector dot product and $V_p = (1/6)\pi d^3$ is the volume of a particle of diameter $d$. The symbol $\varepsilon_p$ denotes the particle-volume fraction, $\rho_p$ is the material density of the particle which is normally considered constant [Gough, 1979]. The heat transfer per unit volume between the gas and particle phases is given by $\dot{q} = -6\mu_g C_{p_g} \mathrm{Nu}(T_g - T_p)/(d^2 \mathrm{Pr})$, where $\mathrm{Nu} = 2.0 + 0.6\mathrm{Pr}^{1/3}\mathrm{Re}^{1/2}$ is the Nusselt number correlation, $\mathrm{Pr} = \mu_g C_{p_g}/k_g \simeq 0.75$ is the Prandtl number for air, $d$ is the equivalent diameter of the spherical particle, $\mu_g$ is the viscosity of the gas defined by a previous equation, $C_{p_g} = \frac{\gamma}{\gamma - 1} R_g$ is the gas specific heat at constant pressure, and $k_g$ is the gas thermal conductivity.

Two primary advantages of the dual gas and particle continua model are that interactions between the two phases are included within the approximation of the continuum mixture and unsteady gas-particle flows can be solved. One disadvantage is that particle volume effects on the gas phase are ignored because the gaseous volume fraction $\varepsilon_g = 1 - \varepsilon_p \simeq 1$; hence, the equations for the gaseous phase are valid only for sparsely populated particles. Other disadvantages are that the particle continuum prohibits realistic computations of particle-particle collisions and the passing of one particle by another.

The method of dual gas and particle continua including particle-volume effects is reviewed next, so that problems involving dense particle clouds can be solved computationally. One example is the motion of propellant grains in laboratory projectile launchers used for studying projectile impacts on targets [Krier & Summerfield, 1979; Stiefel, 1988]. The unsteady flow equations of mass, momentum, and energy for the gas and particle phases are given by Eqs. (1.5) and (1.6), but the vectors for the gaseous phase in Eq. (1.7) are now replaced by

$$\begin{aligned}
\mathbf{U}_g &= [\varepsilon_g\rho_g \quad \varepsilon_g\rho_g u_g \quad \varepsilon_g\rho_g v_g \quad \varepsilon_g e_g]^T,\\
\mathbf{F}(\mathbf{U}_g) &= \left[\varepsilon_g\rho_g u_g \quad \varepsilon_g\rho_g u_g^2 \quad \varepsilon_g\rho_g u_g v_g \quad \varepsilon_g u_g(e_g+p_g)\right]^T,\\
\mathbf{G}(\mathbf{U}_g) &= \left[\varepsilon_g\rho_g v_g \quad \varepsilon_g\rho_g u_g v_g \quad \varepsilon_g\rho_g v_g^2 \quad \varepsilon_g v_g(e_g+p_g)\right]^T,\\
\mathbf{H}(\mathbf{U}_g) &= \left[0 \quad \varepsilon_g\frac{\partial p_g}{\partial x} \quad \varepsilon_g\frac{\partial p_g}{\partial y} \quad 0\right]^T,\\
\mathbf{S}(\mathbf{U}_g,\mathbf{U}_p) &= [0 \quad f_x \quad f_y \quad f_x u_p + f_y v_p + \dot{q}]^T,
\end{aligned} \tag{1.9}$$

because $\varepsilon_g = 1 - \varepsilon_p$ is no longer approximated as unity. The vectors for the particle phase remains as given by Eq. (1.8). The obvious advantage is that the particle volume is taken into account in the gas phase equations. This makes predictions more relevant for mixture flows when numerous particles occupy a significant volume of the two-phase flow, but particle-particle collisions are still not handled in a realistic manner. In the continuum model of particles, the concentration of particles decreases or increases in various parts of the flow field, but actual particle-particle collisions are simply not treated realistically and the possible passing of one particle by another are neglected.

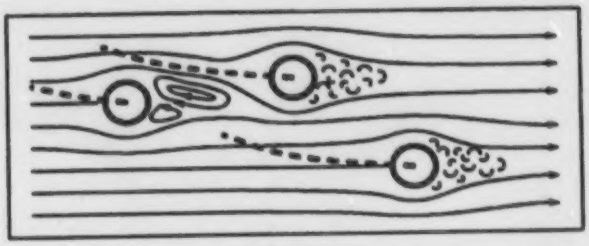

The most advanced method of a gas continuum and particle non-continuum is now reviewed. The gas is treated as a continuum and particles are allowed to move as individuals. This is illustrated in the adjoining figure where particles are swept along with the flow and are also falling slowly in the flow field. Notice that flow separation and vortex shedding are shown at the rear of these spherical particles. Each particle is accelerated by both the gas pressure and viscous shear of the gas acting around its surface. If the relative velocity is supersonic, then a bow shock and other waves would also be formed. In the case of inviscid and unsteady flow, the equations of gas motion of continuity, momentum, and energy are given by

$$\frac{\partial \mathbf{U}_g}{\partial t} + \frac{\partial \mathbf{F}(\mathbf{U}_g)}{\partial x} + \frac{\partial \mathbf{G}(\mathbf{U}_g)}{\partial y} + \mathbf{H}(\mathbf{U}_g) = 0 \tag{1.10}$$

in two space dimensions, where the vectors

$$\begin{aligned}
\mathbf{U}_g &= [\rho_g \quad \rho_g u_g \quad \rho_g v_g \quad e_g]^T,\\
\mathbf{F}(\mathbf{U}_g) &= \left[\rho_g u_g \quad \rho_g u_g^2 \quad \rho_g u_g v_g \quad u_g(e_g+p_g)\right]^T,\\
\mathbf{G}(\mathbf{U}_g) &= \left[\rho_g v_g \quad \rho_g u_g v_g \quad \rho_g v_g^2 \quad v_g(e_g+p_g)\right]^T,
\end{aligned} \tag{1.11}$$

$$H(U_g) = \left[0 \quad \frac{\partial p_g}{\partial x} \quad \frac{\partial p_g}{\partial y} \quad 0\right]^T .$$

The equation of state $p_g = \rho_g R_g T_g$ is required to close these equations, and *slip* boundary conditions need to be applied around the surface of each moving particle during computations. Because the gas flows around individual particles within the space available to the gas, $\epsilon_g$ is unity and not needed in the equations. The motion of the particle is due to form drag, that is the integrated effects of the pressure around the particle dictate the total force and Newton's second law is normally used to calculate the movement of each particle on an individual basis. If the particle is unsymmetric in shape, then particle rotation should also be included for more credible predictions. Note that the Reynolds-averaged Navier-Stokes equations with a turbulence model for the gas flow could also be solved, and then both the form and viscous drag would be simultaneously included along with the rotation of symmetrical particles from viscous effects.

The primary advantage of the method of a gas continuum and particle non-continuum two-phase flows with a definitive gas-particle interface is that it allows more realistic computations of interactions between the gas and particle motions. For example, a bow shock and other waves are induced if the relative velocity between the gas and particle is nearly equal or larger than the sound speed, and these gas-particle interactions can be predicted accurately only if particles are represented individually. This method also allows particle-particle collisions to be computed realistically, as well as particle-particle passings to be handled according to Newton's laws of motion as individual particles moving along separate paths.

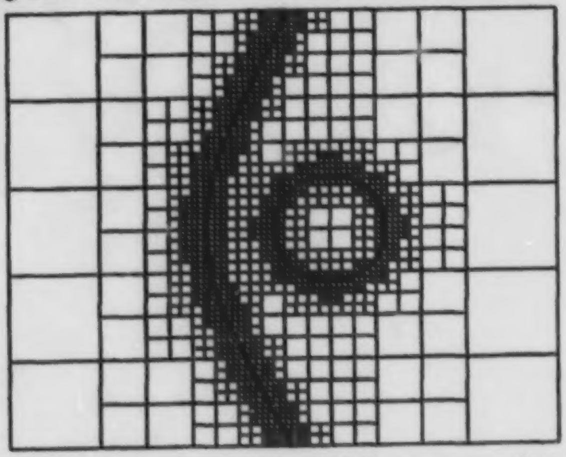

There are many difficulties in computing flow fields of gases moving around individual particles. A first difficulty is that a fine computational grid is required to resolve the flow field around small particles accurately, and this normally results in much computational effort on supercomputers. The use of grid adaption or refinement can help reduce the effort. For example, the grid subdivision method used by Colella [1985 & 1990] and Pember, Bell, Colella, Crutchfield, & Welcome [1993] illustrated in the adjacent figure is a modern approach. Where flow gradients are large and also near and at surfaces of bodies, a large rectangular cell is subdivided into two or four smaller cells for grid refinement. These small cells are further subdivided if necessary, that is when gradients of flow properties are very large. Typically up to 7 to 10 levels of cell subdivisions may be required for accurate flow representation and a significant reduction in computational effort.

A second difficulty in computing flow fields of gases moving around individual particles is that grid refinement requires locating neighbouring cells in subdivided regions, which typically involves quad- and octal-tree data structures for two- and three-dimensional flows, respectively. Such tree structures and their usage increases the computational overhead. Bayyuk, Powell, & Van Leer [1993] conducted a detail study of the quad-tree data structure required for locating the neighbours of any particular cell. Berger & LeVeque [1989] showed how to apply such grid refinement techniques to compute flows around arbitrary shaped bodies, and Davis & Dannenhoffer [1993] developed techniques of adaptive grid refinements for Navier-Stokes equations such that viscous drag can be included in the determination of the motion of the particle.

A third difficulty in computing flow fields of gases moving around individual particles is that the piece of a cell not overlapped by a particle (the shaded piece in the adjacent figure) can cause a reduction in the time step based on the Courant-Friedrichs-Lewy (CFL) criterion. In updating the gas flow properties of all cells, the common time step for all cells is limited by the shortest exposed side of all cells partly covered by particles. For complicated flows there is at least one exposed cell with an arbitrarily small exposed side; hence, the time step is correspondingly arbitrarily small.

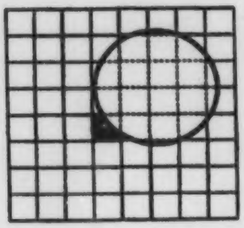

The limiting time-step problem can usually be overcome by two methods. One method is that of cell merging and unmerging, which is illustrated in the adjacent figure. This is sometimes called local h-refinement [Powell, Roe, & Quirk, 1993]. In this h-refinement method, cells partly covered by particles are treated as specially shaped cells when all sides of an exposed cell are longer than one-half of their respective lengths. The overlapped particle surface is normally replaced by a straight line joining the two intersection points of the particle and cell boundaries. This special cell can have three, four, or five sides. In the other case when a particle covers more than one half the length of any cell side, the exposed part of the cell is merged with a neighbouring cell.

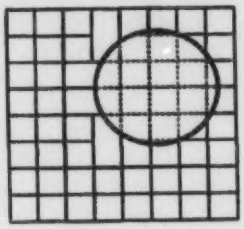

Another method of overcoming this limiting time-step problem is that of changing or adjusting cell corners. Needham [1994] implemented this scheme in solving defence problems involving the fracturing and dispersion of materials (e.g., concrete bulker walls) from explosions. This scheme is illustrated in the adjacent figure. In this case, the cell corners are adjusted to lie on the particle surface. Hence, these special cells all have four sides but these sides are normally not rectangular, and they therefore require special computational effort.

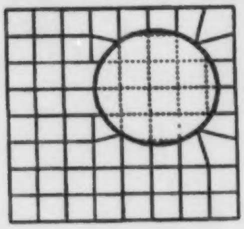

A fourth difficulty in computing flow fields of gases moving around individual particles occurs when two particles collide and many adjacent cells (e.g., part of a column of cells) are covered simultaneously, and when two particles separate and uncover many adjacent cells simultaneously. Cell merging and unmerging and cell corner alternations required additional corrections (fixups) such that the gas mass, momentum, and energy is neither created nor destroyed, and anomalous pressure excursions (zero or infinity) are not introduced.

A fifth difficulty in computing flow fields of gases moving around individual particles is that realistic handling of multiple particle collisions for flows with numerous particles. In numerical predictions, firstly, one must keep track of the boundaries of all the individual particles in the flow field and ensure that no overlapping of particles occurs. Secondly, if two particles have an impending collision then this collision process must be handled in a special manner such that they make contact and either rebound elastically or inelastically (or simply stick together). Triple or even multiple particle collisions pose additional difficulties in modelling. Note that cell mergings, corner alternations, and particle-particle collisions required complicated algorithm and computational overhead to implement. Typically, 5% to 15% of the cells in two-phase flow problems are simultaneously affected and need special computational care.

The present study introduces and assesses a new method of computing two-phase gas-particle flows with gas-particle interactions and particle-particle collisions. This method of computing two-phase flows introduces slightly smoothed interfaces between the phases, and this helps overcome most of the previous difficulties but introduces very few others. The interfaces between the gas and each solid-phase particle are slightly distributed in space and the two phases overlap at their common interface. For example, the particle-volume fraction $\varepsilon_p$ decreases rapidly at the body surface from unity within the body to zero outside the body. This is shown in the adjacent diagram for a spherical particle, where the thickness of the distributed particle surface is exaggerated greatly for illustration proposes. The gas-volume fraction $\varepsilon_g = 1 - \varepsilon_p$ decreases rapidly at its distributed interface with the particle from unity in the pure gas region to zero inside the solid particle. In addition to solving conventional gas-particle flow problems, this new method can also be used to solve other problems such as gas flows around airfoils (see the adjoining figure), but the primary advantage is obtained when solving two-phase flows with numerous moving particles that have a variety of shape and sizes.

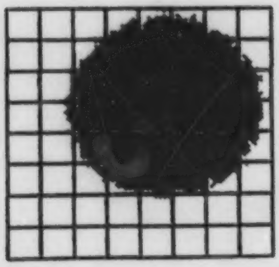

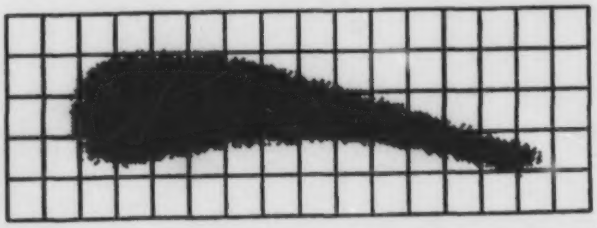

The motion of the gas is computed throughout the entire flow field as flow through a mixture of free space (outside particles) and moving porous media (inside interfaces and particles). Euler's equations given by Eqs. (1.5) and (1.9) are used, in which $f_x$ and $f_y$ denote the viscous-flow resistances in $x$ and $y$ directions, respectively. Note that $\varepsilon_g = 1$ for the gas flow outside particles and $\varepsilon_g$ varies inside the distributed interfaces of particles and possibly also inside particles (e.g., $\varepsilon_g$ is set to a minimum value such as $10^{-4}$). Within interfaces and inside particles, large viscous forces are introduced such that gas-particle slip causes retarding interaction forces that helps diminish slip rapidly to zero as $\varepsilon_g$ becomes very small. The distributed interface eliminates the need for cell merging and unmerging, and it also regularizes the computations for cells into a standard unified procedure. However, a suitable viscous-force function is needed to achieve this goal with sophistication.

The integrated effect of distributed viscous forces and gas pressure within the interface about a particle can be used as the driving forces in Newton's laws to predict the motion of a particle. During particle-particle collisions the distributed surfaces of these particles are allowed to overlap. However, overlapping porosity distributions are then used to invoke repulsive forces which slow down the collision process and also repel the particles. A repulsive force model needs to be proposed to achieve this behaviour. Note that particle collisions with walls can be handled similarly by slightly distributing the wall surface; the wall is simply considered as a large stationary particle.

Grid adaption is still required to increase computational accuracy with reduced computational effort. Cell subdivision is now performed only where high gradients of flow properties and volume fraction occur in the flow field. No special grid subdivisions are required to help define particle surfaces as in previous methods. However, strong source terms involving the viscous and repulsive forces are introduced into Euler's equations, and these cause difficulties in obtaining numerical solutions.

The primary objective of this study is to assess the advantages and difficulties of applying this newly proposed method of distributed interfaces between phases in gas-particle flows. One-dimensional flow problems involving *(a)* the reflection of a moving shock wave at a closed duct end and *(b)* the launching of a projectile by a high-pressure gas are solved for this propose. This is a preliminary step before solving more complicated two- and three-dimensional problems, because algorithms for the viscous forces and particle-particle collisions can be proposed, tested and refined by using these simple problems.

The governing equations of motion of gas-particle flow with distributed interfaces are introduced and discussed in chapter 2. The computational solution procedure is then described in chapter 3, and this is followed by a presentation of test-problem results. These test problems involve the reflection of a shock wave at a closed duct end and the launching of a projectile by a high-pressure gas in chapter 4. The thesis ends with concluding remarks in chapters 5 and reference follow.

# Chapter 2

# Model for Gas-Particle Flows with Distributed Phase Interfaces

## 2.1 Governing Equations for Gas Flows

Euler's continuity, momentum, and energy equations for unsteady, one-space-dimensional, compressible, inviscid flow of the continuum gaseous phase of a two-phase flow can be written in the form

$$\frac{\partial}{\partial t}\begin{bmatrix} \varepsilon_g \rho_g \\ \varepsilon_g \rho_g u_g \\ \varepsilon_g e_g \end{bmatrix} + \frac{\partial}{\partial x}\begin{bmatrix} \varepsilon_g \rho_g u_g \\ \varepsilon_g \rho_g u_g^2 \\ \varepsilon_g u_g (e_g + p_g) \end{bmatrix} + \begin{bmatrix} 0 \\ \varepsilon_g \dfrac{\partial p_g}{\partial x} \\ p_g \dfrac{\partial \varepsilon_g}{\partial t} \end{bmatrix} = \begin{bmatrix} 0 \\ f_{\text{visc}} \\ f_{\text{visc}} u_p \end{bmatrix} \tag{2.1}$$

with viscous losses due to gas flow through a porous medium. These equations have been adapted from Gough [1979] for the present case of gas-particle flows with distributed phase interfaces and viscous losses therein. The gas- and particle-volume fractions are denoted by $\varepsilon_g$ and $\varepsilon_p = 1 - \varepsilon_g$, respectively. The viscous-flow resistance $f_{\text{visc}}$ has units of Newtons per unit of mixture volume and stems from the relative motion between the gas and porous medium in the distributed phase interface. Also, $u_p$ is the velocity of the particle material, $e_g = \rho_g C_{v_g} T_g + \frac{1}{2}\rho_g u_g^2$ is the gas energy per unit volume, and $f_{\text{visc}} u_p$ is the work done per unit mixture volume by the gas on a moving particle. There are no source terms for mass and energy in the continuity and energy equation because mass transfer and its corresponding energy transfer between the two phases are not considered in this work. Furthermore, heat transfer between the phases is not included in this preliminary study, so a heat transfer term does not occur as a source term in the energy equation.

The form of the term $\varepsilon_g \partial p_g / \partial x$ in the momentum equation and the presence of the term $p_g \partial \varepsilon_g / \partial x$ in the energy equation are both important. The term $\varepsilon_g \partial p_g / \partial x$ gives the correct pressure force around a particle, whereas $\partial(\varepsilon_g p_g)/\partial x$ does not. The term $p_g \partial \varepsilon_g / \partial t$

is required to balance a similar term $p_g \partial \varepsilon_p / \partial t$ in the particle equations such that the work between the moving phase boundaries is treated properly. Both terms are included correctly in the work of Gough [1979].

Equations (2.1) can be written in vector notation as

$$\frac{\partial \mathbf{U}_g}{\partial t} + \frac{\partial \mathbf{F}(\mathbf{U}_g)}{\partial x} + \mathbf{H}(\mathbf{U}_g) = \mathbf{S}(\mathbf{U}_g, \mathbf{U}_p) \tag{2.2}$$

for brevity, where

$$\mathbf{U}_g = \begin{bmatrix} \varepsilon_g \rho_g \\ \varepsilon_g \rho_g u_g \\ \varepsilon_g e_g \end{bmatrix}, \qquad \mathbf{F}(\mathbf{U}_g) = \begin{bmatrix} \varepsilon_g \rho_g u_g \\ \varepsilon_g \rho_g u_g^2 \\ \varepsilon_g u_g (e_g + p_g) \end{bmatrix},$$

$$\mathbf{H}(\mathbf{U}_g) = \begin{bmatrix} 0 \\ \varepsilon_g \dfrac{\partial p_g}{\partial x} \\ p_g \dfrac{\partial \varepsilon_g}{\partial t} \end{bmatrix}, \qquad \mathbf{S}(\mathbf{U}_g, \mathbf{U}_p) = \begin{bmatrix} 0 \\ f_{\mathrm{visc}} \\ f_{\mathrm{visc}} u_p \end{bmatrix} \tag{2.3}$$

are the vectors.

The thermally perfect equation of state $p_g = \rho_g R_g T_g$ is used to help close the previous gas-flow equations. The variables $R_g$, $p_g$, $\rho_g$, and $T_g$ designate the gas constant, pressure, density, and temperature, respectively. Expressions given later for $f_{\mathrm{visc}}$, and other results obtained from solving the equations of motion of the other phase for $\varepsilon_p = 1 - \varepsilon_g$ and $u_p$ complete the closure of the preceding equations. Note that the energy of the gas can be expressed as $e_g = \rho_g C_{v_g} T_g + \frac{1}{2}\rho_g u_g^2 = \frac{1}{\gamma-1} p_g + \frac{1}{2}\rho_g u_g^2$.

It is important to distinguish the difference between the density and partial density of both phases in a gas-particle mixture. The density $\rho_g$ of a gas is defined as the gas mass divided by the gas volume and the particle density $\rho_p$ (constant) is defined as the particle mass divided by the volume it occupies. On the other hand, the partial densities (or concentrations) $\sigma_g = \varepsilon_g \rho_g$ and $\sigma_p = \varepsilon_p \rho_p$ are defined as the gas mass and particle mass divided by the volume of the mixture, respectively. Similarly, the partial gas- and particle-phase momenta are defined by $\varepsilon_g \rho_g u_g$ and $\varepsilon_p \rho_p u_p$, respectively, and partial gas- and particle-phase energies are defined by $\varepsilon_g e_g$ and $\varepsilon_p e_p$, respectively. Note that $e_p = \rho_p C_{p_p} T_p + \frac{1}{2}\rho_p u_p^2$, in which $C_{p_p}$ and $T_p$ is the specific heat and temperature of the particle material, respectively.

## 2.2 Governing Equations for Particle Motions

Euler's equivalent continuity, momentum, and energy equations for unsteady, one-dimensional, compressible, inviscid flow of the continuum particle phase of a two-phase flow can be expressed in the form

$$\frac{\partial}{\partial t}\begin{bmatrix} \varepsilon_p\rho_p \\ \varepsilon_p\rho_p u_p \\ \varepsilon_p e_p \end{bmatrix} + \frac{\partial}{\partial x}\begin{bmatrix} \varepsilon_p\rho_p u_p \\ \varepsilon_p\rho_p u_p^2 \\ \varepsilon_p u_p(e_p + p_g) \end{bmatrix} + \begin{bmatrix} 0 \\ \varepsilon_p \dfrac{\partial p_g}{\partial x} \\ p_g \dfrac{\partial \varepsilon_p}{\partial t} \end{bmatrix} = \begin{bmatrix} 0 \\ -f_{\text{visc}} \\ -f_{\text{visc}} u_p \end{bmatrix} \tag{2.4}$$

with viscous losses due to gas flow through a porous medium. These equations have been adapted from Gough [1979] for the present case of gas-particle phase interfaces and viscous flow losses therein. The viscous flow losses $-f_{\text{visc}}$ in these particle-phase equations are identical but opposite in sign to that in the gaseous equations, because these are the interaction effects occurring between the two phases. The term $p_g \partial\varepsilon_p/\partial t$ in the energy equation is important. Without this term the temperature of the particle would change even though there is no heat transfer to cause this effect.

The conservation equations (2.4) can be expressed in vector notation as

$$\frac{\partial \mathbf{U}_p}{\partial t} + \frac{\partial \mathbf{F}(\mathbf{U}_p)}{\partial x} + \mathbf{H}(\mathbf{U}_p) = -\mathbf{S}(\mathbf{U}_g, \mathbf{U}_p) \tag{2.5}$$

for convenience, where

$$\mathbf{U}_p = \begin{bmatrix} \varepsilon_p\rho_p \\ \varepsilon_p\rho_p u_p \\ \varepsilon_p e_p \end{bmatrix}, \qquad \mathbf{F}(\mathbf{U}_p) = \begin{bmatrix} \varepsilon_p\rho_p u_p \\ \varepsilon_p\rho_p u_p^2 \\ \varepsilon_p u_p(e_p + p_g) \end{bmatrix},$$

$$\mathbf{H}(\mathbf{U}_p) = \begin{bmatrix} 0 \\ \varepsilon_p \dfrac{\partial p_g}{\partial x} \\ p_g \dfrac{\partial \varepsilon_p}{\partial t} \end{bmatrix}, \qquad \mathbf{S}(\mathbf{U}_g, \mathbf{U}_p) = \begin{bmatrix} 0 \\ f_{\text{visc}} \\ f_{\text{visc}} u_p \end{bmatrix} \tag{2.6}$$

are the vectors. Note that mass and heat transfer between the phases are absent as source terms because these effects are not included in this study.

The previous equations describe the motion of the particle phase as a continuum. In this study, this assumption of a continuum is relaxed and the motions of non-continuum independent particles are considered. This change in methodology is achieved by making the assumption that each particle is both incompressible and rigid. The effects of these changes is illustrated below.

Firstly, consider the continuity equation $\frac{\partial(\varepsilon_p\rho_p)}{\partial t} + \frac{\partial(\varepsilon_p\rho_p u_p)}{\partial x} = 0$ for the particle phase. The material density $\rho_p$ is constant (incompressible) and the velocity $u_p$ is spatially constant within each particle (rigid and $\partial u_p/\partial x = 0$). The continuity equation reduces to

$$\frac{D\varepsilon_p}{Dt} = \frac{\partial \varepsilon_p}{\partial t} + u_p \frac{\partial \varepsilon_p}{\partial x} = 0\,. \tag{2.7}$$

Hence, the particle-volume fraction $\varepsilon_p$ for each particle is constant along its path through space with time, and independent particles can have their own $\varepsilon_p$ distributions and move at their own velocities.

Secondly, consider the momentum equation $\frac{\partial(\varepsilon_p\rho_p u_p)}{\partial t} + \frac{\partial(\varepsilon_p\rho_p u_p^2)}{\partial x} + \varepsilon_p\frac{\partial p_g}{\partial x} = -f_{\text{visc}}$. For particles that are incompressible (constant $u_p$) and rigid ($\partial u_p/\partial x = 0$), this equation reduces to

$$\rho_p\varepsilon_p\frac{\mathrm{D}u_p}{\mathrm{D}t} + \varepsilon_p\frac{\partial p_g}{\partial x} + u_p\frac{\mathrm{D}\varepsilon_p}{\mathrm{D}t} = -f_{\text{visc}}\,, \tag{2.8}$$

with the last term $u_p\mathrm{D}\varepsilon_p/\mathrm{D}t$ being zero by virtue at the earlier continuity equation. By integrating over a mixture volume that includes an entire particle (i.e., $\int\cdots\mathrm{d}V_m$), and letting $\mathrm{d}V_m = A_m\mathrm{d}x$ for one-dimensional flows and using Newton's second law, the acceleration of a particle in the gas flow is given by

$$a_p = \frac{\mathrm{D}u_p}{\mathrm{D}t} = -\frac{A_m}{m_p}\int_{\text{particle}}\varepsilon_p\frac{\partial p_g}{\partial x}\,\mathrm{d}x - A_m\int_{\text{particle}} f_{\text{visc}}\,\mathrm{d}x\,, \tag{2.9}$$

where $A_m$ is the mixture cross-sectional area for a one-dimensional flow. This equation governs the velocity of a particle along its trajectory from the influence of the forces from both the flow pressure gradient and viscous-flow losses in the distributed phase interface around the particle.

Thirdly, the energy equation $\frac{\partial(\varepsilon_p e_p)}{\partial t} + \frac{\partial[\varepsilon_p u_p(e_p + p_g)]}{\partial x} + p_g\frac{\partial\varepsilon_p}{\partial x} = -f_{\text{visc}}u_p$ can be reduced to the following form

$$\frac{\mathrm{D}T_p}{\mathrm{D}t} = 0\,, \tag{2.10}$$

by using the assumptions of particle incompressibility and rigidity and previous results from the continuity and momentum equations. The above equation illustrates that the temperature $T_p$ of a particle remains constant along its path. This result should be expected because heat transfer and external work are not included in the energy equation.

## 2.3 Equations for Smoothly Distributing an Interface

Smoothly distributed interfaces between the gas and particle phases are introduced such that the thickness of the interface is small compared to particle size dimensions and the average distance between particles in which the gas flows. In these thin interfaces the porosity of the solid is rapidly changed from a particle-volume fraction $\varepsilon_p$ of zero outside the particle to unity within the particle. The gas-volume fraction $\varepsilon_g = 1 - \varepsilon_p$ changes correspondingly from unity in the gaseous phase to zero within the solid-particle phase. The thickness of phase interface is problem dependent, and the numerical modeller or computer-code user must set this thickness for the particular problem being solved. In this section, a convenient transition shape function is suggested for smoothly distributing $\varepsilon_p$ and $\varepsilon_g$ with distance at the periphery of the particle. Note that variations in gas flow properties (e.g., pressure, density, gas-flow velocity) through the distributed interface are the outcome of the flow computations that depend on the viscous-flow losses within the interface.

A Bézier's cubic polynomial [Sarfraz, 1994] is used to simultaneously distribute smoothly the particle- and gas-volume fractions $\varepsilon_p$ and $\varepsilon_g$ through the distributed phase interface. A convenient parametric representation is given below for both $\varepsilon_g$ and $\varepsilon_p$ as

$$\varepsilon_g = \varepsilon_{g_1} + 3(\varepsilon_{g_2} - \varepsilon_{g_1})\eta(1-\eta)^2 + 3(\varepsilon_{g_3} - \varepsilon_{g_1})\eta^2(1-\eta) + (\varepsilon_{g_4} - \varepsilon_{g_1})\eta^3 \,, \tag{2.11}$$

$$\varepsilon_p = \varepsilon_{p_1} + 3(\varepsilon_{p_2} - \varepsilon_{p_1})\eta(1-\eta)^2 + 3(\varepsilon_{p_3} - \varepsilon_{p_1})\eta^2(1-\eta) + (\varepsilon_{p_4} - \varepsilon_{p_1})\eta^3 \,, \tag{2.12}$$

$$x = x_1 + 3(x_2 - x_1)\eta(1-\eta)^2 + 3(x_3 - x_1)\eta^2(1-\eta) + (x_4 - x_1)\eta^3 \,, \tag{2.13}$$

for which the free parameter $\eta$ has the range $0 \leq \eta \leq 1$. This Bézier curve begins at the $\varepsilon_{g_1} = 1$, $\varepsilon_{p_1} = 0$, and $x = x_1$ when $\eta = 0$, changes smoothly as $\eta$ increases, and ends at the location $\varepsilon_{g_4} = 0$, $\varepsilon_{p_4} = 1$, and $x = x_4$ when $\eta = 1$. The shape is controlled by specifying two control coordinates $\varepsilon_{g_2}$ or $\varepsilon_{p_2}$ at $x_2$ and $\varepsilon_{g_3}$ or $\varepsilon_{p_3}$ at $x_3$. For a symmetrically shaped interface with zero slopes for $\varepsilon_g$ and $\varepsilon_p$ at both ends, we set $x_2 - x_1 = x_4 - x_3$, $\varepsilon_{g_2} = 1$ or $\varepsilon_{p_2} = 0$ and $\varepsilon_{g_3} = 0$ or $\varepsilon_{p_3} = 1$. In this study we also set $x_2 - x_1 = x_4 - x_3 = \frac{3}{10}(x_4 - x_1)$.

The interfacial variation of $\varepsilon_g$ and $\varepsilon_p$ versus normalized distance are both illustrated on the adjacent figure for interest. The four coordinates defining the $\varepsilon_g$ curve are indicated by black dots and the corresponding coordinates for the $\varepsilon_p$ curve are shown as open circles.

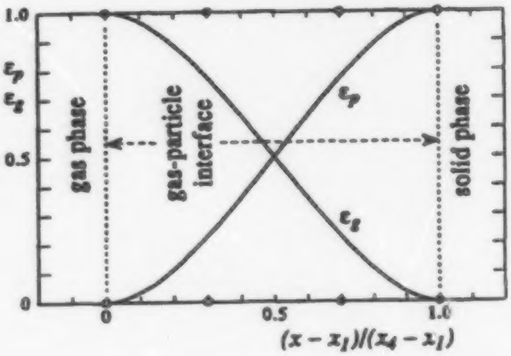

## 2.4 Equations for Viscous-Flow Resistance

The viscous-flow resistance is specified in the form

$$f_{\text{visc}} = -C_{\text{visc}} B(x) \left[ \frac{1}{2} c_{\text{visc}} \rho_g a_g (u_g - u_p) + \frac{1}{2} \rho_g (u_g - u_p) |u_g - u_p| \right] \tag{2.14}$$

for the present work. The coefficient $C_{\text{visc}}$ is set to a value of 0.52. The coefficient $c_{\text{visc}}$ in the "linear dynamic-slip pressure" term is set to a value of about $3.02\times10^{-2}$, and in this term $a_g$ is the sound speed (normally set to a constant value of 331.32 m/s). The last term in the viscous-flow resistance is the "quadratic dynamic-slip pressure". The variable $B(x)$ denotes the function which depends on $x$; it is zero where particle material is absent ($\varepsilon_p = 0$) and it rises to a maximum value where particle material occupies the entire mixture volume ($\varepsilon_p = 1$). $B$ versus $x$ is shown in the adjoining figure (below). The parametric equations for setting up $B(x)$ are given by

$$\begin{aligned} B(x) &= B_1 + 3(B_2 - B_1)\zeta(1-\zeta)^2 + 3(B_3 - B_1)\zeta^2(1-\zeta) + (B_4 - B_1)\zeta^3 \,, & (2.15) \\ x &= x_{b_1} + 3(x_{b_2} - x_{b_1})\zeta(1-\zeta)^2 + 3(x_{b_3} - x_{b_1})\zeta^2(1-\zeta) + (x_{b_4} - x_{b_1})\zeta^3 \,, & (2.16) \end{aligned}$$

where $\zeta$ is a parameter with $0 \leq \zeta \leq 1$ and $(x_{b_i}, B_i)$ are four control points for which $(x_{b_1}, B_1) = (0,0)$, $(x_{b_2}, B_2) = (1,0)$, $(x_{b_3}, B_3) = (0.5, 1.0)$, and $(x_{b_4}, B_4) = (1,1)$. This function $B(x)$ is related to the particle-volume fraction $\varepsilon_p$ via Eqs. (2.12) and (2.13). Hence, $B(x)$ is directly related to the particle-volume fraction in this sense. $B$ versus $\varepsilon_p$ is shown in the adjoining figure (below).

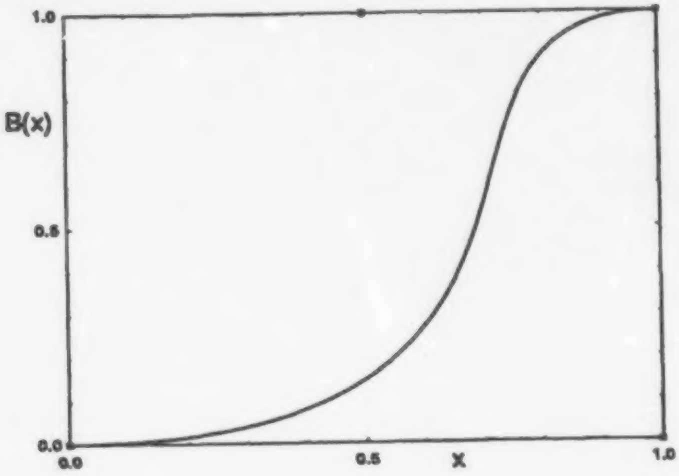

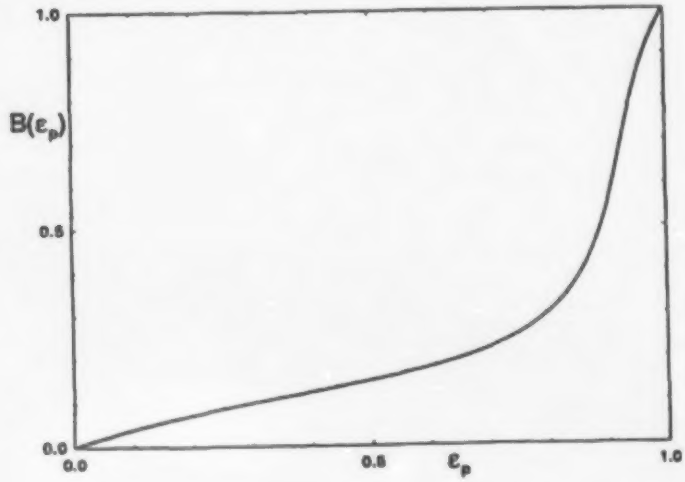

# Chapter 3

# Computational Solution Procedure

The computational procedure outlined in this chapter begins by defining the grid and cells used in the numerical computations. Then the method of estimating fluxes into and out of cells by means of solving Riemann problems is described. Godunov's scheme for solving the partial differential equations for the motion of the gaseous phase of the two-phase mixture is introduced next. The gas motion is solved independently of the particle-phase motion by using a special integration software package called VODE. A description of this commercially available package and its use is presented next. After outlining the solution procedure using the VODE software for the gaseous motion, the description of the method of solving the motion of the particle phase is finally presented.

## 3.1 Grid for Numerical Computations

The grid used for the present numerical computations consists of equally sized cells in one space dimension, and nodes are located at the centres of each cell. This node-centered grid is illustrated in the following figure. The nodes are numbered from 1 to $N$ and the cell width is equal to $\Delta x$.

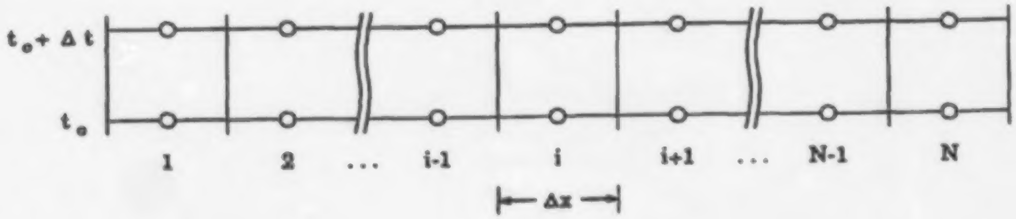

### 3.1.1 Flux Estimations

Flux evaluation at cell boundaries consists of solving a Riemann problem, and the Riemann problem is now discussed. It is a problem which deals with the fluid's behaviour at a discontinuity. The adjoining figure shows a typical wave pattern of a Riemann problem. The average conservative variables in a cell (e.g., $\varepsilon_g \rho_g$, $\varepsilon_g \rho_g u_g$, and $\varepsilon_g e_g$) are indicated by a dash line. Average variables in adjoining cells may be different and this produces a discontinuity at the cell boundaries. The discontinuity at the boundary $(i-1/2)$ produces a shock wave (S) that travels to the left and a rarefaction wave (R) that travels to the right. A contact surface (C) is also produced and it is shown as travelling to the left. To obtain the states between various waves in the Riemann problem, a Riemann solver is required. The Riemann solver of Gottlieb & Groth [1988] for unsteady, one-dimensional, compressible, inviscid flow of perfect gases is used. It is important to notice that their Riemann solver does not apply directly to solving the conservation equation (2.1)[1] because it does not include the effects of gas-volume fraction $\varepsilon_g$ and all source terms directly in its solution. However, the application of this Riemann solver is used to estimate the solution of the Riemann problem and then extract the flux at the cell boundary.

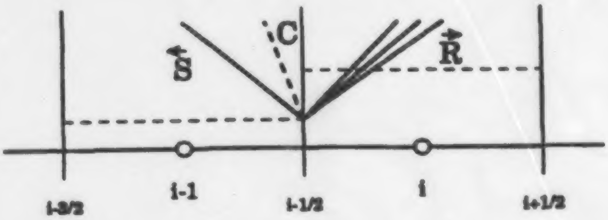

## 3.2 Godunov's First-Order Scheme

The gas-phase conservation equations were given previously by Eq. (2.2) as

$$\frac{\partial \mathbf{U}_g}{\partial t} + \frac{\partial \mathbf{F}(\mathbf{U}_g)}{\partial x} + \mathbf{H}(\mathbf{U}_g) = \mathbf{S}(\mathbf{U}_g, \mathbf{U}_p) \tag{3.1}$$

where the vectors follow in Eq. (2.3), but are redefined slightly below:

$$\mathbf{U}_g = \begin{bmatrix} \varepsilon_g \rho_g \\ \varepsilon_g \rho_g u_g \\ \varepsilon_g e_g \end{bmatrix}, \qquad \mathbf{F}(\mathbf{U}_g) = \begin{bmatrix} \varepsilon_g \rho_g u_g \\ \varepsilon_g (\rho_g u_g^2 + p_g) \\ \varepsilon_g u_g (e_g + p_g) \end{bmatrix},$$

---

[1] The Riemann solver applys directly, to the one-dimensional compressible, inviscid, flow of perfect gases for which the conservation equations are given by

$$\frac{\partial}{\partial t}\begin{bmatrix} \rho_g \\ \rho_g u_g \\ e_g \end{bmatrix} + \frac{\partial}{\partial x}\begin{bmatrix} \rho_g u_g \\ (\rho_g u_g^2 + p_g) \\ u_g(e_g + p_g) \end{bmatrix} = 0$$

without change in flow area.

$$\mathbf{H}(\mathbf{U}_g) = \begin{bmatrix} 0 \\ p_g \dfrac{\partial \varepsilon_g}{\partial x} \\ p_g \dfrac{\partial \varepsilon_g}{\partial t} \end{bmatrix}, \qquad \mathbf{S}(\mathbf{U}_g, \mathbf{U}_p) = \begin{bmatrix} 0 \\ f_{\text{visc}} \\ f_{\text{visc}} u_p \end{bmatrix} \tag{3.2}$$

To solve this set of partial differential equations, Godunov's first-order scheme is used because it deals directly with the physics of fluid motions from one cell to the next. Also it is one of the simplest to apply in its first-order form. In Godunov's first-order scheme, the spatial derivatives at the $i^{\text{th}}$ cell are written in terms of the fluxes at the cell boundaries as

$$\frac{\partial \mathbf{F}(\hat{\mathbf{U}}_{g_i})}{\partial x} \simeq \frac{\mathbf{F}\left[\mathcal{R}(\hat{\mathbf{U}}^-_{g_{i+1/2}}, \hat{\mathbf{U}}_{g_{i+1/2}})^+)\right] - \mathbf{F}\left[\mathcal{R}(\hat{\mathbf{U}}^-_{g_{i-1/2}}, \hat{\mathbf{U}}^+_{g_{i-1/2}})\right]}{\Delta x}, \tag{3.3}$$

where

$$\hat{\mathbf{U}}_g = \begin{bmatrix} \rho_g \\ \rho_g u_g \\ e_g \end{bmatrix}, \quad \mathbf{F}(\hat{\mathbf{U}}_g) = \begin{bmatrix} \rho_g u_g \\ \rho_g u_g^2 + p_g \\ u_g(e_g + p_g) \end{bmatrix} \tag{3.4}$$

are the vectors. In the above equations, $\mathbf{F}\left[\mathcal{R}(\hat{\mathbf{U}}^-_{g_{i-1/2}}, \hat{\mathbf{U}}^+_{g_{i-1/2}})\right]$ denotes the flux evaluated at the left boundary $(i-1/2)$ from the Riemann solution $\mathcal{R}(\hat{\mathbf{U}}^-_{g_{i-1/2}}, \hat{\mathbf{U}}^+_{g_{i-1/2}})$ between states $\hat{\mathbf{U}}^-_{g_{i-1/2}}$ and $\hat{\mathbf{U}}^+_{g_{i-1/2}}$. Notice that $\hat{\mathbf{U}}^-_{g_{i-1/2}}$ denotes the state on the left side of the left boundary $(i-1/2)$ and $\hat{\mathbf{U}}^+_{g_{i-1/2}}$ denotes the state on the right side of the left boundary $(i-1/2)$. Similarly, $\mathbf{F}\left[\mathcal{R}(\hat{\mathbf{U}}^-_{g_{i+1/2}}, \hat{\mathbf{U}}^+_{g_{i+1/2}})\right]$ denotes the flux evaluated at the right boundary $(i+1/2)$ from the Riemann solution $\mathcal{R}(\hat{\mathbf{U}}^-_{g_{i+1/2}}, \hat{\mathbf{U}}^+_{g_{i+1/2}})$ between states $\hat{\mathbf{U}}^-_{g_{i+1/2}}$ and $\hat{\mathbf{U}}^+_{g_{i+1/2}}$. Notice that $\hat{\mathbf{U}}^-_{g_{i+1/2}}$ denotes the state on the left side of the right boundary $(i+1/2)$ and $\hat{\mathbf{U}}^+_{g_{i+1/2}}$ denotes the state on the right side of the right boundary $(i+1/2)$. For Godunov's first-order scheme we use

$$\hat{\mathbf{U}}^-_{g_{i-1/2}} = \hat{\mathbf{U}}_{g_{i-1}} \quad , \quad \hat{\mathbf{U}}^+_{g_{i-1/2}} = \hat{\mathbf{U}}_{g_i} \, , \tag{3.5}$$

$$\hat{\mathbf{U}}^-_{g_{i+1/2}} = \hat{\mathbf{U}}_{g_i} \quad , \quad \hat{\mathbf{U}}^+_{g_{i+1/2}} = \hat{\mathbf{U}}_{g_{i+1}} \, , \tag{3.6}$$

because state extrapolations to the boundaries is not incorporated. Then Euler's equations (2.2) for the $i^{\text{th}}$ cell can be expressed as

$$\frac{\partial \mathbf{U}_{g_i}}{\partial t} = \mathbf{S}(\mathbf{U}_{g_i}, \mathbf{U}_{p_i}) - \mathbf{H}(\mathbf{U}_{g_i}) - \frac{\mathbf{F}\left[\mathcal{R}(\mathbf{U}_{g_i}, \mathbf{U}_{g_{i+1}})\right] - \mathbf{F}\left[\mathcal{R}(\mathbf{U}_{g_{i-1}}, \mathbf{U}_{g_i})\right]}{\Delta x} \tag{3.7}$$

in vector form.

The term $p_g \partial \varepsilon_g / \partial x$ in the vector $\mathbf{H}(\mathbf{U}_g)$ in the conservation equation (3.7) is approximated by a second-order central-difference formula

$$p_g \left(\frac{\partial \varepsilon_g}{\partial x}\right)_i \simeq p_{g_i} \frac{\varepsilon_{g_{i+1}} - \varepsilon_{g_{i-1}}}{2\Delta x}, \tag{3.8}$$

where the subscript $i$ denotes the $i^{\text{th}}$ cell. The term $p_g \partial \varepsilon_g / \partial t$ is ignored in the present work.

## 3.3 Variable-Coefficient ODE Solver

The heart of the solution procedure for solving the partial differential equations for the gaseous phase is the usage of a double-precision variable-coefficient ordinary differential equation solver called VODE. The primary reason for using this solver is that the conservation equations (2.2) contains strong source terms. Strong source terms produce large changes in the flow variables during a flow time step; hence, sub time steps are required to properly integrate into the solution in the influence of the source terms with more accuracy and to even maintain solution stability. The VODE subroutine treats the set of partial differential equations (PDEs) as if they were a set of ordinary differential equations (ODEs) for the purpose of integration.

### 3.3.1 System of ODEs

The set of partial differential equations for the gaseous phase can be written in the form

$$\frac{\partial \mathbf{V}}{\partial t} = \mathbf{T}(\mathbf{V})\,, \tag{3.9}$$

for solution by the VODE subroutine, where

$$\mathbf{V} = \begin{bmatrix} \tilde{\mathbf{U}}_1 \\ \tilde{\mathbf{U}}_2 \\ \vdots \\ \tilde{\mathbf{U}}_{i-1} \\ \tilde{\mathbf{U}}_i \\ \tilde{\mathbf{U}}_{i+1} \\ \vdots \\ \tilde{\mathbf{U}}_{N-1} \\ \tilde{\mathbf{U}}_N \end{bmatrix}, \quad \mathbf{T}(\mathbf{V}) = \begin{bmatrix} 0 \\ \tilde{\mathbf{S}}_2 \\ \vdots \\ \tilde{\mathbf{S}}_{i-1} \\ \tilde{\mathbf{S}}_i \\ \tilde{\mathbf{S}}_{i+1} \\ \vdots \\ \tilde{\mathbf{S}}_{N-1} \\ 0 \end{bmatrix} - \frac{1}{\Delta x} \begin{bmatrix} 0 \\ \tilde{\mathbf{G}}_2 \\ \vdots \\ \tilde{\mathbf{G}}_{i-1} \\ \tilde{\mathbf{G}}_i \\ \tilde{\mathbf{G}}_{i+1} \\ \vdots \\ \tilde{\mathbf{G}}_{N-1} \\ 0 \end{bmatrix}, \tag{3.10}$$

with

$$\tilde{\mathbf{U}}_i = \begin{bmatrix} \mathbf{U}_{g_i} \\ \varepsilon_{g_i} \end{bmatrix}, \quad \tilde{\mathbf{S}}_i = \begin{bmatrix} \mathbf{S}(\mathbf{U}_{g_i}, \mathbf{U}_{p_i}) - \mathbf{H}(\mathbf{U}_{g_i}) \\ \left(\dfrac{\partial \varepsilon_g}{\partial t}\right)_i \end{bmatrix}, \tag{3.11}$$

$$\tilde{\mathbf{G}}_i = \begin{bmatrix} \mathbf{F}\left[\mathcal{R}(\mathbf{U}_{g_i}, \mathbf{U}_{g_{i+1}})\right] - \mathbf{F}\left[\mathcal{R}(\mathbf{U}_{g_{i-1}}, \mathbf{U}_{g_i})\right] \\ 0 \end{bmatrix}. \tag{3.12}$$

Notice that each $\tilde{\mathbf{U}}_i$, for $1 \leq i \leq N$, contains three conservative variables $\varepsilon_{g_i}\rho_{g_i}$, $\varepsilon_{g_i}\rho_{g_i}u_{g_i}$, and $\varepsilon_{g_i}e_{g_i}$ for the gas. The gas-volume fraction $\varepsilon_{g_i}$ is the fourth entry for the $i^{th}$ cell, such that the dimension of $\tilde{\mathbf{V}}$ is $4N\times1$. The source vector $\tilde{\mathbf{S}}_i$ of the $i^{th}$ cell consists of $\mathbf{S}(\mathbf{U}_g,\mathbf{U}_p)$ and $\mathbf{H}(\mathbf{U}_g)$ in Eq. (3.2) and with a fourth entry

$$\left(\frac{\partial\epsilon_g}{\partial t}\right)_i \simeq \frac{\epsilon_{g_i}^{new}-\epsilon_{g_i}^{old}}{\Delta t}\,, \tag{3.13}$$

is a first order approximation of the time derivative of the gas-volume fraction. $\tilde{\mathbf{G}}_i$ is a $4\times1$ vector consists of three entries that are an approximation of the spatial derivative of the flux vector given by the Riemann solution and the last entry is zero. Each entry inside the square bracket in Eq. (3.10) is a $4\times1$ vector and $\mathbf{0}$ is a $4\times1$ null vector.

The first and the last cell in the source terms of the ODE system in Eq. (3.10) are forced to be zero, which is equivalent to having zero time derivative for the conservative variables in the first and last cells of the grid. These is stem from the application of non-reflecting boundary conditions at the grid ends. However, this is only half of the picture. The other step in applying non-reflecting boundary conditions [Gottlieb, Zhang, & Groth, -] is that the states at the first and last cells are set equal to the states at their adjacent cell. Hence, no wave can be reflected back into the flow field.

### 3.3.2 Jacobian Matrix for the ODE System

The Jacobian for the ODE system is a banded matrix given by

$$\frac{\partial\mathbf{T}(\mathbf{V})}{\partial\mathbf{V}} = \begin{bmatrix} \frac{\partial\mathbf{T}_1}{\partial\tilde{\mathbf{U}}_1} & \frac{\partial\mathbf{T}_1}{\partial\tilde{\mathbf{U}}_2} & \mathbf{0} & \cdots & \cdots & \cdots & \mathbf{0} \\ \frac{\partial\mathbf{T}_2}{\partial\tilde{\mathbf{U}}_1} & \frac{\partial\mathbf{T}_2}{\partial\tilde{\mathbf{U}}_2} & \frac{\partial\mathbf{T}_2}{\partial\tilde{\mathbf{U}}_3} & \mathbf{0} & \cdots & \cdots & \mathbf{0} \\ \mathbf{0} & \frac{\partial\mathbf{T}_3}{\partial\tilde{\mathbf{U}}_2} & \frac{\partial\mathbf{T}_3}{\partial\tilde{\mathbf{U}}_3} & \frac{\partial\mathbf{T}_3}{\partial\tilde{\mathbf{U}}_4} & \mathbf{0} & \cdots & \mathbf{0} \\ \vdots & \ddots & \ddots & \ddots & \ddots & \ddots & \vdots \\ \mathbf{0} & \cdots & \mathbf{0} & \frac{\partial\mathbf{T}_{N-2}}{\partial\tilde{\mathbf{U}}_{N-3}} & \frac{\partial\mathbf{T}_{N-2}}{\partial\tilde{\mathbf{U}}_{N-2}} & \frac{\partial\mathbf{T}_{N-2}}{\partial\tilde{\mathbf{U}}_{N-1}} & \mathbf{0} \\ \mathbf{0} & \cdots & \cdots & \mathbf{0} & \frac{\partial\mathbf{T}_{N-1}}{\partial\tilde{\mathbf{U}}_{N-2}} & \frac{\partial\mathbf{T}_{N-1}}{\partial\tilde{\mathbf{U}}_{N-1}} & \frac{\partial\mathbf{T}_{N-1}}{\partial\tilde{\mathbf{U}}_{N}} \\ \mathbf{0} & \cdots & \cdots & \cdots & \mathbf{0} & \frac{\partial\mathbf{T}_{N}}{\partial\tilde{\mathbf{U}}_{N-1}} & \frac{\partial\mathbf{T}_{N}}{\partial\tilde{\mathbf{U}}_{N}} \end{bmatrix}. \tag{3.14}$$

**Because of the definitions of V and T(V) in Eq. (3.10), there are a major diagonal, 7 upper, and 7 lower sub-diagonals in the Jacobian. The Jacobian is evaluated internally by the VODE subroutine.**

### 3.3.3 VODE Usage

**Inputs of the VODE subroutine consist of both standard and optional inputs, input constants, and variables. Specific values are listed below:**

$$\begin{aligned}
\mathrm{NEQ} &= 2004\,, \\
\mathrm{T} &= 0.0\,, \\
\mathrm{TOUT} &= 0.0\,, \\
\mathrm{ITOL} &= 1\,, \\
\mathrm{RTOL} &= 1.0\times10^{-5}\,, \\
\mathrm{ATOL} &= 1.0\times10^{-6}\,, \\
\mathrm{ITASK} &= 1\,, \\
\mathrm{ISTATE} &= 1\,, \\
\mathrm{IOPT} &= 1\,, \\
\mathrm{LRW} &= 62146\,, \\
\mathrm{LIW} &= 2034\,, \\
\mathrm{ML} &= 7\,, \\
\mathrm{MU} &= 7\,, \\
\mathrm{MF} &= -25\,, \\
\mathrm{RPAR} &= 0.0\,, \\
\mathrm{IPAR} &= 0\,, \\
\mathrm{H0} &= 0.0\,, \\
\mathrm{HMAX} &= 0.0\,, \\
\mathrm{HMIN} &= 0.0\,, \\
\mathrm{MAXORD} &= 0\,, \\
\mathrm{MXSTEP} &= 10000\,, \\
\mathrm{MXHNIL} &= 20\,.
\end{aligned}$$

**To use the VODE package, in addition to the setting up input parameters, one needs to decide which differencing method is used, the corresponding sizes of double-precision variables and integer work-arrays in LRW and LIW, the size of the upper and lower sub-diagonals of the Jacobian in ML and MU, etc. Please refer to the internal documentation of the VODE package for more details. Also, see Byrne & Hindmarsh, 1975; Jackson & Sacks-Davis, 1980; Hindmarsh, 1983; Byrne & Hindmarsh, 1987; Brown, Byrne, & Hindmarsh, 1989; and Byrne, 1992.**

## 3.4 Particle Motion

The acceleration of a particle was given by Eq. (2.9) as

$$a_p = -\frac{A_m}{m_p}\int_{\text{particle}} \varepsilon_p \frac{\partial p_g}{\partial x}\,\mathrm{d}x - A_m \int_{\text{particle}} f_{\text{visc}}\,\mathrm{d}x\ , \tag{3.15}$$

for which the integration is over the entire particle. This integration is done by using finite differencing, and

$$a_p^{\text{new}} \simeq -\frac{A_m}{m_p}\sum_i \varepsilon_{p_i}\frac{p_{g_{i+1}} - p_{g_{i-1}}}{\Delta x} - A_m \sum_i f_{\text{visc}_i}\Delta x \tag{3.16}$$

is used in the computer code. The superscript 'new' is used because the variables in the above equation are the updated flow properties from the last time level. Hence, the displacement and velocity of a particle with distributed interface are given by

$$x_p^{\text{new}} = x_p^{\text{old}} + u_p^{\text{old}}\Delta t + \frac{1}{2}a_p^{\text{old}}\Delta t^2\ , \tag{3.17}$$

$$u_p^{\text{new}} = u_p^{\text{old}} + a_p^{\text{old}}\Delta t\ , \tag{3.18}$$

where $x_p$, $u_p$, and $\Delta t$ denote the particle displacement, velocity, and time step between the last time level (the superscript 'old') and the current time level (the superscript 'new'). In particular, $a_p^{\text{old}}$ is the particle acceleration evaluated in Eq. (3.16) in which the gas properties in that equation are obtained from the last time level.

# Chapter 4

# Test Problems

In this chapter, two test problems are discussed and results are shown by applying the concept of distributed phase interfaces between the gas and particles. The first problem is the numerical prediction of the reflection of a moving shock wave by a stationary closed duct end that has a distributed interface with the gas. The second problem is the numerical prediction of the motion of a projectile by a high-pressure gas on one side and a low-pressure gas on the other. Each problem is first defined, followed by a discussion of the known analytical solution, and the required application of initial conditions. The computational results for each problem are then discussed.

## 4.1 Shock Reflection at a Distributed Interface

### 4.1.1 Problem Definition

As a first trial of the concept of distributed phase interface, an unsteady one-space-dimensional prediction of the interaction between perfect gases and a stationary distributed interface is completed, so that the effects of the gas-volume fraction and the viscous-flow resistance as sources in the Euler's equations can be studied. This prediction involves the reflection of a shock wave by a distributed interface in a constant area duct with compressible, inviscid flows of perfect gases. Three assumptions are made. Firstly, the end of the constant area duct is slightly distributed over a number of cells while the side surface of the duct remains well-defined. Secondly, there is no heat transfer between the gas and the constant area duct. Thirdly, the distributed interface of the duct end is non-deformable. The

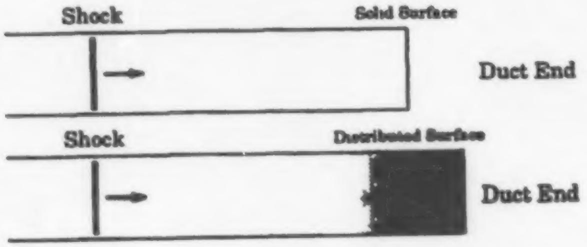

reflection of a shock wave by a duct end shown in the adjoining figure (top) is solved analytically. The solution of this problem is well known, and it can be predicted theoretically by using gasdynamic theory [Zucrow, 1976; Anderson, 1982]. The interface of the duct end and the gas is slightly distributed in the adjoining figure (bottom). Notice that both figures are aligned at the average end of the duct and the exaggerated length of shading illustrateds the distributed phase interface for illustration purposes only. A number of numerical predictions are completed by applying Godunov's first order scheme with **VODE** to the appropriate Euler's equations.

### 4.1.2 Analytical Solution

The analytical solution of the one-dimensional reflection of a shock wave by a duct end is well known and can be obtained via gasdynamic theory [Zucrow, 1976; Anderson, 1982].

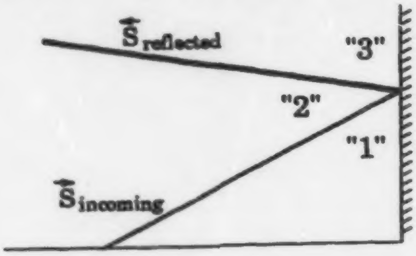
$\overleftarrow{S}_{\text{reflected}}$
"3"
"2"
"1"
$\overleftarrow{S}_{\text{incoming}}$

In the above figure, a moving shock is reflected by a stationary closed duct end and regions of interest are marked numerically. For an incoming shock with a shock Mach number $M_i$, the relations between the states in front of and behind the shock are given by

$$\frac{p_2}{p_1} = \frac{2\gamma}{\gamma+1} M_i^2 - \frac{\gamma-1}{\gamma+1}\,, \tag{4.1}$$

$$\frac{\rho_2}{\rho_1} = \frac{\frac{\gamma+1}{2} M_i^2}{1 + \frac{\gamma-1}{2} M_i^2}\,, \tag{4.2}$$

$$\frac{u_2}{a_1} = \frac{2}{\gamma+1} \frac{M_i^2 - 1}{M_i}\,, \tag{4.3}$$

$$\left(\frac{a_2}{a_1}\right)^2 = \frac{p_2}{p_1}\left[\frac{\gamma-1}{\gamma+1} + \frac{2}{(\gamma+1)M_i^2}\right]. \tag{4.4}$$

Knowing that the gas flow velocity $u_3$ behind the reflected shock is zero, one can determine the shock Mach number $M_r$ of the reflected shock from the following quadratic equation,

$$M_r^2 + \frac{\gamma+1}{2}\frac{u_2}{a_2} M_r - 1 = 0\,. \tag{4.5}$$

Notice that for the above quadratic equation, one root is positive while the other one is negative because the product equals $-1$. The positive solution is dropped because the reflected shock is moving to the left. Thus,

$$M_r = -\frac{1}{2}\left[\left(\frac{\gamma+1}{2}\frac{u_2}{a_2}\right) + \sqrt{\left(\frac{\gamma+1}{2}\frac{u_2}{a_2}\right)^2 + 4}\,\right] . \tag{4.6}$$

Hence, the state after the reflected shock is given by

$$\frac{p_3}{p_2} = \frac{2\gamma}{\gamma+1}M_r^2 - \frac{\gamma-1}{\gamma+1} , \tag{4.7}$$

$$\frac{\rho_3}{\rho_2} = \frac{\frac{\gamma+1}{2}M_r^2}{1+\frac{\gamma-1}{2}M_r^2} , \tag{4.8}$$

$$u_3 = 0 , \tag{4.9}$$

$$\left(\frac{a_3}{a_2}\right)^2 = \frac{p_3}{p_2}\left[\frac{\gamma-1}{\gamma+1} + \frac{2}{(\gamma+1)M_r^2}\right] , \tag{4.10}$$

where the subscripts 1, 2, and 3 refer to the gaseous state in front of and behind the incoming shock, and the gaseous state behind the reflected shock, respectively. Notice that the subscript $g$ is dropped in the above equations.

### 4.1.3 Initial Conditions

In the numerical prediction of shock moves into a perfect gas at atmospheric conditions. A grid of 200 evenly distributed nodes are used. The full length of the grid is 10 m such that each cell is 0.05 m in width. From $x = 0$ m to $x = 2.5$ m, the grid is in the gas phase where $\varepsilon_g = 1$. The distributed phase interface of the closed duct end starts at $x = 2.5$ m to $x = 7.5$ m and $\varepsilon_g$ is defined via the method described in section 2.3. From $x = 7.5$ m to $x = 10$ m, the grid is in the solid phase where $\varepsilon_g = \varepsilon_{g_{min}}$.

The initial conditions for the gas properties are as follows. In front of the shock, the pressure is 101.3 kPa, 1.293 kg/m$^3$ in the density, 0 m/s in flow velocity, 287 J/kg·K in gas constant, and 1.4 in ratio of specific heats.

Initially, the incoming shock is located at $x = 1$ m. The shock Mach number is 2 in one trial and 4 in a different trial. The gas properties behind the incoming shock are evaluated by using the shock relations from Eq. (4.1) to Eq. (4.4).

### 4.1.4 Results

In solving this problem, numerous results are obtained with different parameters. In this report, some of the best are shown. In the following results, there is a 0.5 millisecond difference in time between successive profiles shown.

In Fig. 4.1, the gas-volume fraction profile is shown. The distributed phase interfaces starts at $x/\Delta x = 50$ and ends at $x/\Delta x = 150$. The minimum of the gas-volume fraction is given by $\varepsilon_{g_{min}} = 10^{-4}$. Notice that the four control points used to generate the profile are shown as hollow squares. In Fig. 4.2, the second-order central-differencing of the spatial derivative $\partial \varepsilon_g / \partial x$ and the term in the viscous-flow resistance $B(x)$ are shown. Notice that the four control points used to generate the profile are shown as hollow squares. From Fig. 4.3 to Fig. 4.6, the gas pressure, density, sound speed, and flow Mach number are shown, respectively, for the case of $M_i = 2$. The incoming and reflected shock wave can be easily identified and a dashed line is shown as the incoming starts to interact with and reflected by the distributed phase interface. Notice that the theoretical prediction of state after the reflected shock wave is marked by a horizontal line. In Fig. 4.3, the pressure after the reflected shock is slowly rising to the theoretical prediction.

In Figs. 4.7 and 4.8, the pressure and density profile are shown for the incoming shock Mach number at 4, respectively. The pressure and density rises more rapidly, but a larger overshoot also occurs. This is illustrated in the Fig. 4.7.

From Figs. 4.9 to 4.11, the minimum of gas-volume fraction is given by $\varepsilon_{g_{min}} = 10^{-2}$ which is two orders in magnitude larger than before. The pressure and density profile are shown in Figs. 4.10 and 4.11, respectively. It is interesting to notice that there are smaller overshoots in this setup compared to previous results.

## 4.2 Projectile Acceleration

### 4.2.1 Problem Definition

The second problem involves the interactions between the compressible, inviscid, flow of a perfect gas and the launching projectile with distributed phase interfaces in one space dimension. Four assumptions are made for this numerical prediction. Firstly, the projectile is of the shape of a cylinder, and the frontal and rear surfaces of the projectile are slightly distributed. Secondly, the projectile fits perfectly inside the constant area duct. Thirdly, there is neither heat transfer nor friction between the duct and the projectile. Finally, the projectile and the constant area duct are non-deformable. The motion of a projectile in the adjacent figure (top) can be predicted with a rarefaction wave at the back and a compression wave at the front of the projectile by using gasdynamic theory. The frontal and rear surfaces of the projectile are distributed artificially in the adjoining figure (bottom), where the form of the distribution is pre-defined. Notice that in both figures the projectile are aligned at the average of the projectile surface. A number of numerical predictions are completed by applying Godunov's first-order scheme with VODE, a variable-coefficient ODE solver.

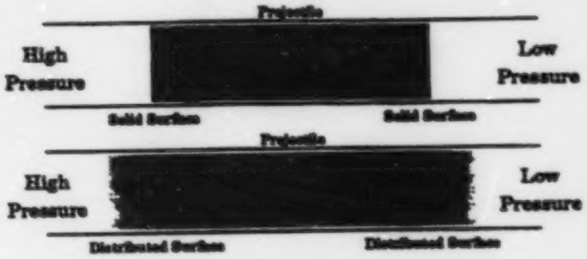

### 4.2.2 Analytical Solution

The equation of motion of the projectile in a constant-area duct is given by the Newton's second law

$$a_p = \frac{du_p}{dt} = \frac{d^2x_p}{dt^2} = \frac{1}{m_p}\left(F_{\text{front}} + F_{\text{back}}\right) , \tag{4.11}$$

where $a_p$, $u_p$, $x_p$, and $m_p$ designate the particle acceleration, velocity, displacement, and mass, respectively. The variables $F_{\text{front}}$ and $F_{\text{back}}$ denote the force acting on the projectile. The forces can be derived by using gasdynamic theory. At the frontal surface of the projectile, a compression wave is formed. By crossing this compression wave using the method of characteristics [Zucrow, 1976; Anderson, 1982], the force acting on the frontal surface of the projectile is given by

$$F_{\text{front}} = -A_p p_{g,r}\left(1 + \frac{\gamma_r - 1}{2a_{g,r}}u_p\right)^{\frac{2\gamma_r}{\gamma_r - 1}} \tag{4.12}$$

as the forces on the frontal surface of the projectile. The symbol $A_p$ denotes the cross-sectional area of the projectile and the subscript $r$ designates the gaseous properties on the right side of the projectile. Notice that this force has a minus sign because the direction is to the left. Similarly, the force acting on the back of the projectile can be determined by assuming a rarefaction wave is formed at the back of the projectile. The force acting on the back of the projectile is given by

$$F_{\text{back}} = A_p p_{g_l} \left(1 - \frac{\gamma_l - 1}{2a_{g_l}} u_p\right)^{\frac{2\gamma_l}{\gamma_l - 1}} . \tag{4.13}$$

Hence, the projectile velocity can be written as an ordinary differential equation

$$\frac{\mathrm{d}u_p}{\mathrm{d}t} = \frac{A_p}{m_p}\left[p_{g_l}\left(1 - \frac{\gamma_l - 1}{2a_{g_l}} u_p\right)^{\frac{2\gamma_l}{\gamma_l - 1}} - p_{g_r}\left(1 + \frac{\gamma_r - 1}{2a_{g_r}} u_p\right)^{\frac{2\gamma_r}{\gamma_r - 1}}\right] , \tag{4.14}$$

which is solved numerically for $u_p$. The displacement and acceleration of the projectile are then calculated according to Eq. (4.11).

### 4.2.3 Initial Conditions

In this problem a projectile with a diameter of about 5 inches and mass of about 40 kg (steel, 7860 kg/m$^3$) is moved from one end of the grid of 4 meters long by high-pressure gas. The state at the high-pressure end of the projectile is 25 MPa in pressure, 249.5 kg/m$^3$ in density, 0 m/s in flow velocity, 287 J/kg·K in gas constant, and 1.4 in ratio of specific heats. The state at the other side of the projectile is 101.3 kPa in pressure, 1.293 kg/m$^3$ in density, 0 m/s in flow velocity, 287 J/kg·K in gas constant, and 1.4 in ratio of specific heats.

Due to the fact that the projectile moves very fast after a short time, which makes the time step very small and slows down the prediction, the gas quantities at the high pressure end of the projectile are "relaxed" such that it is 1013.0 kPa in pressure, 12.93 kg/m$^3$ in density, 0 m/s in flow velocity, 287 J/kg·K in gas constant, and 1.4 in ratio of specific heats at the high-pressure end. Notice that in section 4.2.4, the first set of initial condition denotes the relaxed one while the second set denotes the original one.

In this numerical prediction, an equally spaced 250-node grid is used. With 0.005 m as the width of the cells, the total length of the grid is then 1.25 m. The first 40 cells denotes a space of length 0.2 m before the projectile inside the gun tube for the propellant. The total length of the projectile is 0.6 m or 120 cells, and divided into three regions of equal length. The first region denotes the distributed interface at the rear of the projectile while the last region denotes the distributed interface at the frontal surface of the projectile, and the middle section denotes the body of the projectile.

To set up the above initial conditions for this problem, the following is done. Knowing that if the projectile is held stationary and let the gas flow through it, the steady state solution can be obtained, which is having a linear profile for pressure and density inside the projectile. With this steady-state profile, the projectile will then let go and begin the numerical prediction.

### 4.2.4 Results

In this study, many results are obtained for this problem but only a few are shown here. Two sets of results are shown in this report for the numerical prediction of the launching of a projectile. From Fig. 4.12 to Fig. 4.15, the "relaxed" initial condition is used, whereas from Fig. 4.16 to Fig. 4.18, the realistic initial conditions are used.

In Fig. 4.12, the gas-volume fraction $\varepsilon_g$ profile, spatial derivative of the gas-volume fraction $\partial\varepsilon_g/\partial x$, and the term $B(x)$ is shown. Notice that the four control points in generating the profile via Bézier's polynomials are shown as hollow squares. In Figs. 4.13, 4.14, and 4.15, the acceleration, velocity, and displacement of the projectile are shown, respectively. Notice that in the percentage difference in acceleration illustrated in Fig. 4.13, the error first rises as the projectile starts picking up speed, and eventually drops to a finite value before it rises linearly. It is interesting to notice that there are small sudden drops in the percentage difference wherever the boundaries of the distributed phase interface crosses a cell boundary, and the crossings of boundaries at the high pressure end are responsible for the larger drops whereas the crossings of boundaries at the low pressure end are responsible to the smaller drops.

From Fig. 4.16 to Fig. 4.18, the realistic setup for the problem of launching a projectile is used. In Fig. 4.16, the projectile acceleration is over-predicted by about 7% at the end of 10 milliseconds which is very large compare to the case where a "relaxed" initial condition is used. Similar conclusion can be drawn from the projectile velocity and displacement profile.

# Chapter 5

# Concluding Remarks

A new model of distributing phase interfaces in predicting two-phase flows of gas and particles was introduced. Two one-space-dimensional problems were solved numerically using this new model; they are the reflection of a shock wave at a distributed phase interface (closed duct end) and the acceleration of a projectile for which the surfaces were distributed.

The study of the computational fluid dynamics (CFD) solution procedure and the implementation of the **VODE** software package took a lot of effort. The primary difficulty was accurately handling the strong source terms in Euler's equations, for which the **VODE** subroutine was incorporated. Also, the problem became extremely time consuming to solve computationally. This appeared to be the results of the strong source terms, but may also be the result of the initial setups of the equations or possibly improper software usage. If one-dimensional flow problems are solved for real times that are short but take hours to solve on a modern workstation, then realistic two- and three-dimensional flow problems are impractical to solve by the **VODE** software.

Very few definitive conclusions can be made from the present preliminary work for the following reasons. Firstly, the **VODE** subroutine package took too long computatiuonally to give meaningful flow solutions over realistic flow times. Secondly, a first-order scheme may not have been sufficiently high-order to produce accurate results, and high order solutions may help reduce run time using the **VODE** software. Thirdly, the terms $p_g \partial \varepsilon_g / \partial t$ and $p_g \partial \varepsilon_p / \partial t$ in the gas and particle energy equations were not used in solving the projectile problem, as they are not used in many computations of gas-particle flows, because they were brought to the attention to the author in the writing of this thesis. Including such terms may improve the accuracy of predictions, but they would not solve the long run time using the **VODE** software. Fourthly, the partial decoupling of the gas and particle equations may have resulted in degraded accuracy of the numerical predictions, but they would not solve the long run time using the **VODE** software. Fifthly, the Riemann solver used in this study to estimate the fluxes at cell boundaries is only a first-order scheme and this also contribute to the inefficiency of the **VODE** software but this is questionable.

The present study, however, does identify specific problems and difficulties that must be overcome in order to determine if the concept of distributed phase interface is worthwhile.

The following are recommend by the author on what should be done in the future. Firstly, either the **VODE** software package has to be made more efficient or another solution procedure must be used. Secondly, a second- or even higher-order numerical scheme should be developed to increase the solution accuracy. Thirdly, the conservation equations should be studied such that all terms are to be included in future predictions. Fourthly, a fully coupled gas- and particle-phase solution procedure should be incorporated to increase accuracy. Fifthly, a more relevant Riemann solver should be incorporated for calculating fluxes at cell boundaries, and the generalized Riemann porblem of Matania Ben-Artiz might provide such solution.

# Bibliography

[1] Anderson, John D., Jr., 1982, *Modern Compressible Flow with Historical Perspective*, McGraw-Hill Book Company, New York.

[2] Bayyuk, Sami A., Powell, Kenneth G., & Van Leer, Bram, 1993, A Simulation Technique for 2-D Unsteady Inviscid Flows Around Arbitrary Moving and Deforming Bodies of Arbitrary Geometry, *AIAA Paper 93-3391*.

[3] Berger, Marsha J., & LeVeque, Randall J., 1989, An Adaptive Cartesian Mesh Algorithm for the Euler Equations in Arbitrary Geometries, *AIAA Paper 89-1930*.

[4] Brown, P. N., Byrne, G. D., & Hindmarsh, A. C., 1989, Vode: A Variable-Coefficient ODE Solver, *SIAM J. Sci. Stat. Comput.* 10, pp. 1038–1051. Also *LLNL Report UCRL-98412*, June 1988.

[5] Byrne, George D., 1992, The Solution of a Co-Polymerization Model with VODE, *Recent Developments in Numerical Methods for ODEs/DAEs/PDEs*, pp. 137–197.

[6] Byrne, George D., & Hindmarsh, Alan C., 1987, Stiff ODE Solvers: A Review of Current and Coming Attractions, *J. Comput. Phys.* 70, pp. 1–62.

[7] Byrne, G. D., & Hindmarsh, A. C., 1975, A Polyalgorithm for the Numerical Solution of Ordinary Differential Equations, *ACM Trans. Math. Software* 1, pp. 71–96.

[8] Carrier, G., Fendell, F., Brent, D., Kimbrough, C., Loucks, S., Hess, E., & Acosta, P., 1991, Simple Modeling of Particle Trajectories in Solid Rocket Motors, *J. Peopulsion* 7, No. 2, pp. 185–195.

[9] Colella, Phillip, 1985, A Direct Eulerian MUSCL Scheme for Gas Dynamics, *SIAM J. Sci. Stat. Comput.* 6, pp. 104–117.

[10] Colella, Phillip, 1990, A Multidimensional Second Order Godunov Scheme for Conservation Laws, *J. Comput. Phys.* 87, pp. 171–200.

[11] Davis, Roger L., & Dannenhoffer III, John J., 1993, Decomposition and Parallelization Strategies for Adaptive Grid-Embedding Techniques, *Comput. Fluid Dyn.* 1, pp. 79–93.

[12] Gottlieb, J.J., & Groth, C.P.T., 1988, Assessment of Riemann Solvers for Unsteady One-Dimensional Inviscid Flows of Perfect Gases, *J. Comput. Phys.* 78, pp. 437–458.

[13] Gottlieb, J.J., & Coskunses, C.E., 1985, Effects of Particle Volume on the Structure of a Partly Dispersed Normal Shock Wave in a Dusty Gas, *UTIAS Report 295*, University of Toronto.

[14] Gottlieb, J.J., Zhang, Kun Yuan, & Groth, Clinton P.T., Dirichlet Boundary Conditions for One-Dimensional Unsteady Flows of Perfect Gases. (In Press)

[15] Gough, P.S., 1979, Modeling of Two-Phase Flow in Guns, *Progress in Astronautics and Aeronautics* 66, pp. 176–196.

[16] Greatix, D.R., & Gottlieb, J.J., 1982, An Analytical and Numerical Study of a Shock Wave Interaction with an Area Change, *UTIAS Report 268*, University of Toronto.

[17] Groth, Clinton P.T., 1993, TVD Flux-Difference Split Methods for High-Speed Thermochemical Nonequilibrium Flows with Strong Shocks, *UTIAS Report 350*, University of Toronto.

[18] Hetsroni, Gad, 1982, *Handbook of Multiphase Systems*, McGraw-Hill Book Company, New York.

[19] Hindmarsh, A. C., 1983, ODEPACK, A Systematized Collection of ODE Solvers, *Scientific Computing*, R. S. Stepleman et al., eds., North-Holland, Amsterdam, pp. 55–64.

[20] Hirsch, C., 1988, *Numerical Computation of Internal and External Flows* 1 & 2, Wiley, New York.

[21] Idel'Chik, I. E., 1960, *Handbook of Hydraulic Resistance Coefficients of Local Resistance and of Friction*, translated from Russian in 1966 by the Israel Program for Scientific Translations Ltd., U.S. Atomic Energy Commission Report No. AEC–tr–6630 available from U.S. Department of Commerce, Clearinghouse for Federal Scientific and Technical Information, Springfield, Virgina 22151, U.S.A.

[22] Jackson, K. R., & Sacks-Davis, R., Sept. 1980, Vode: An Alternate Implementation of Variable Step-Size Multistep Formulas for Stiff ODEs, *ACM Trans. Math. Software* 6, pp. 295–318.

[23] Krier, Herman & Summerfield, Martin, 1979, *Interior Ballistics of Guns, Progress in Astronautics and Aeronautics* 66, American Institute of Aeronautics and Astronautics, Inc., Washington, D.C.

[24] Miura, H., & Glass, I. I., 1982, On a dusty-gas shock tube, *Proc. R. Soc. Lond.* **A 382**, pp. 373–388.

[25] Miura, H., & Glass, I. I., 1985, Development of the flow induced by a piston moving impulsively in a dusty gas, *Proc. R. Soc. Lond.* **A 397**, pp. 295–309.

[26] Needham, C. E., 1994, private communication with Prof. J. J. Gottlieb.

[27] Ogawa, Akira, 1984, *Separation of Particles from Air and Gases* I & II, CRC Press, Inc.

[28] Pember, Richard B., Bell, John B., Colella, Phillip, Crutchfield, William Y., & Welcome, Michael L., 1993, Adaptive Cartesian Grid Methods for Representing Geometry in Inviscid Compressible Flow, *AIAA Paper 93-3385.*

[29] Powell, Kenneth G., Roe, Philip L., & Quirk, James, 1993, Adaptive-Mesh Algorithms for Computational Fluid Dynamics, *Algorithmic Trends in Computational FLuid Dynamics*, Springer-Verlag, New York.

[30] Rudinger, G., 1980, *Fundamentals of Gas-Particle Flow*, Elsevier Scientific Publishing Company, New York.

[31] Sabnis, Jayant S., de Jong, Frederik J. & Gibeling, Howard J., 1992, Calculation of Particle Trajectories in Solid-Rocket Motors with Arbitrary Aceleration, *Journal of Propulsion and Power* 8, No. 5, pp. 961–967.

[32] Sarfraz, Muhammad, 1994, Cubic Spline Curves with Shape Control, *Comput. & Graphics* 18, No. 5, pp. 707–713.

[33] Martin Sommerfield, 1988, Numerical Simulation of Supersonic Two-Phase Gas-Particle Flows, *Shock Tubes and Waves*, pp. 235-241.

[34] Soo, S. L., 1967, *Fluid Dynamics of Multiphase System*, Blaisdell Publishing Company, Ginn amd Company (Xerox Corp.), Lexington, Massachusetts (formerly Blaisdell, Waltham, Massachusetts).

[35] Stiefel, Ludwig, 1988, *Gun Propulsion Technology, Progress in Astronautics and Aeronautics* 109, American Institute of Aeronautics and Astronautics, Inc., Washington, D.C.

[36] Svarovsky, L., 1981, *Solid-Gas Separation*, Elsevier Scientific Publishing Company, New York.

[37] Tabakoff, W., & Hamed, A., 1989, Effect of Environmental Particles on a Radial Compressor, *J. Propulsion* 5, No. 6, pp. 731–737.

[38] Zlatev, Zabari, Dimov, Ivan, & Georgiev, Krassimir, 1994, Modeling the Long-Range Transport of Air Pollutants, *IEEE Computational Science & Engineering* 1, pp. 45–52.

[39] Zucrow, 1976, *Gasdynamics* 1, Wiley, New York.

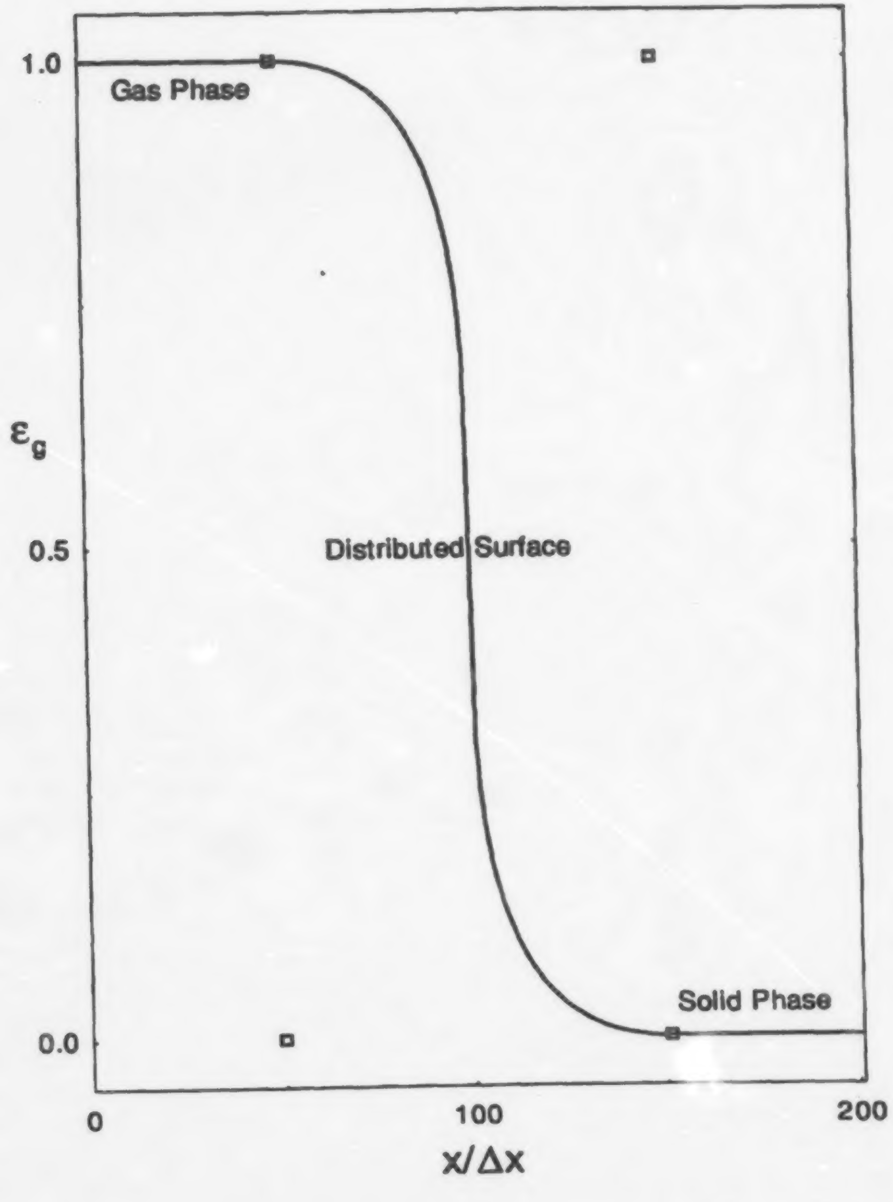

Figure 4.1: Gas-volume fraction profile with $M_s = 2.0$, $\varepsilon_{g_{min}} = 10^{-4}$.

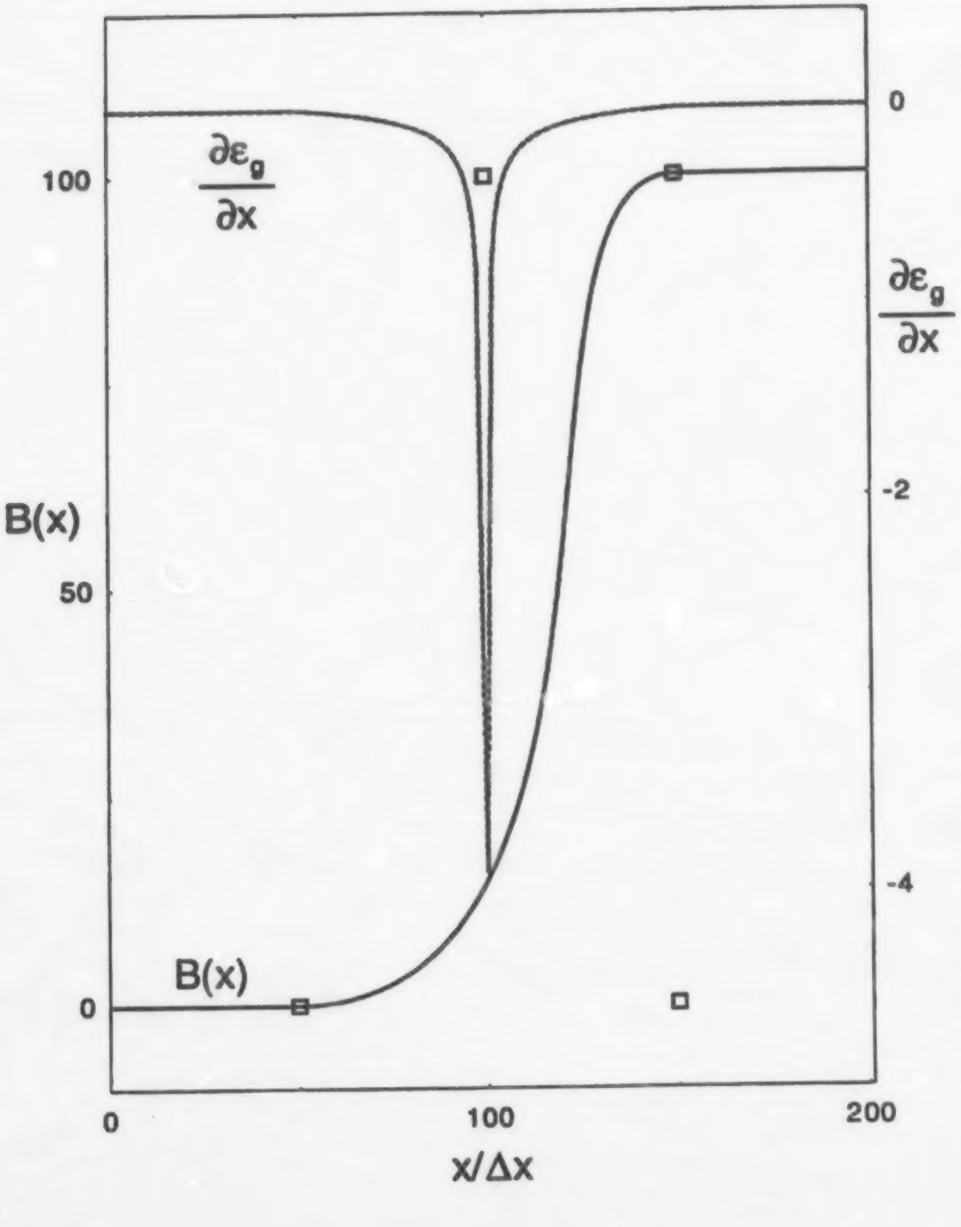

Figure 4.2: Terms in viscous-flow resistance with $M_s = 2.0$, $\varepsilon_{g_{min}} = 10^{-4}$.

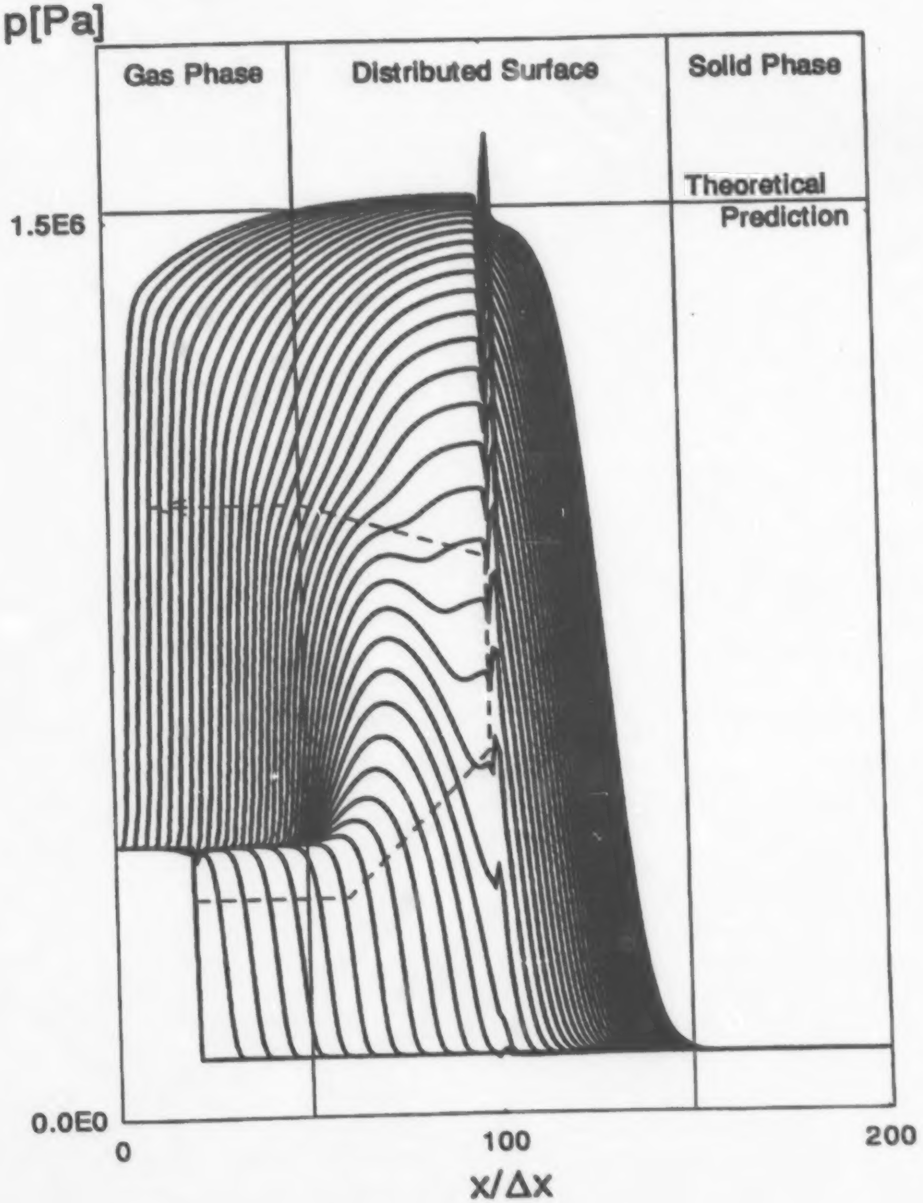

Figure 4.3: Pressure profile with $M_i = 2.0$, $\varepsilon_{g_{min}} = 10^{-4}$.

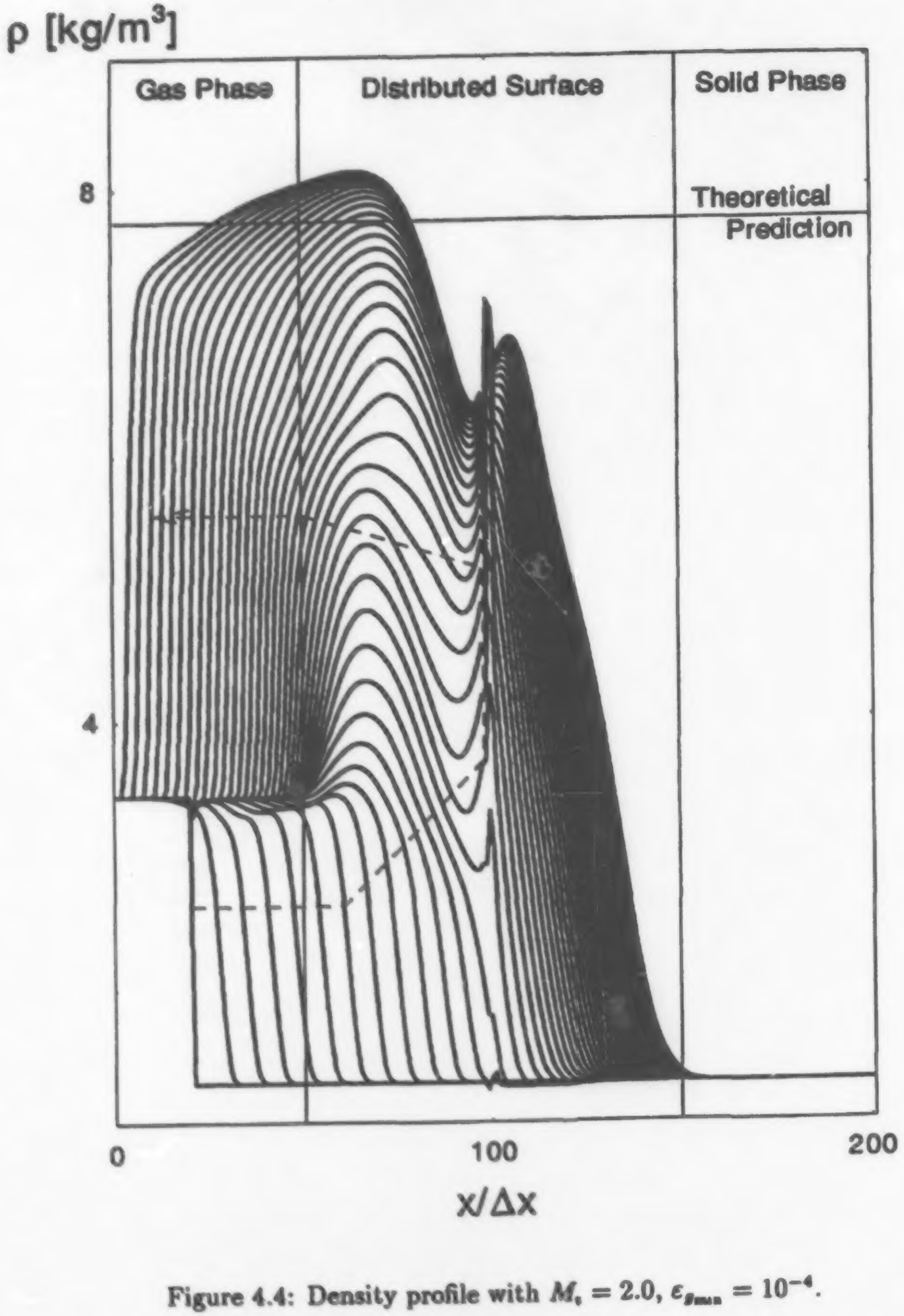

Figure 4.4: Density profile with $M_s = 2.0$, $\varepsilon_{g_{min}} = 10^{-4}$.

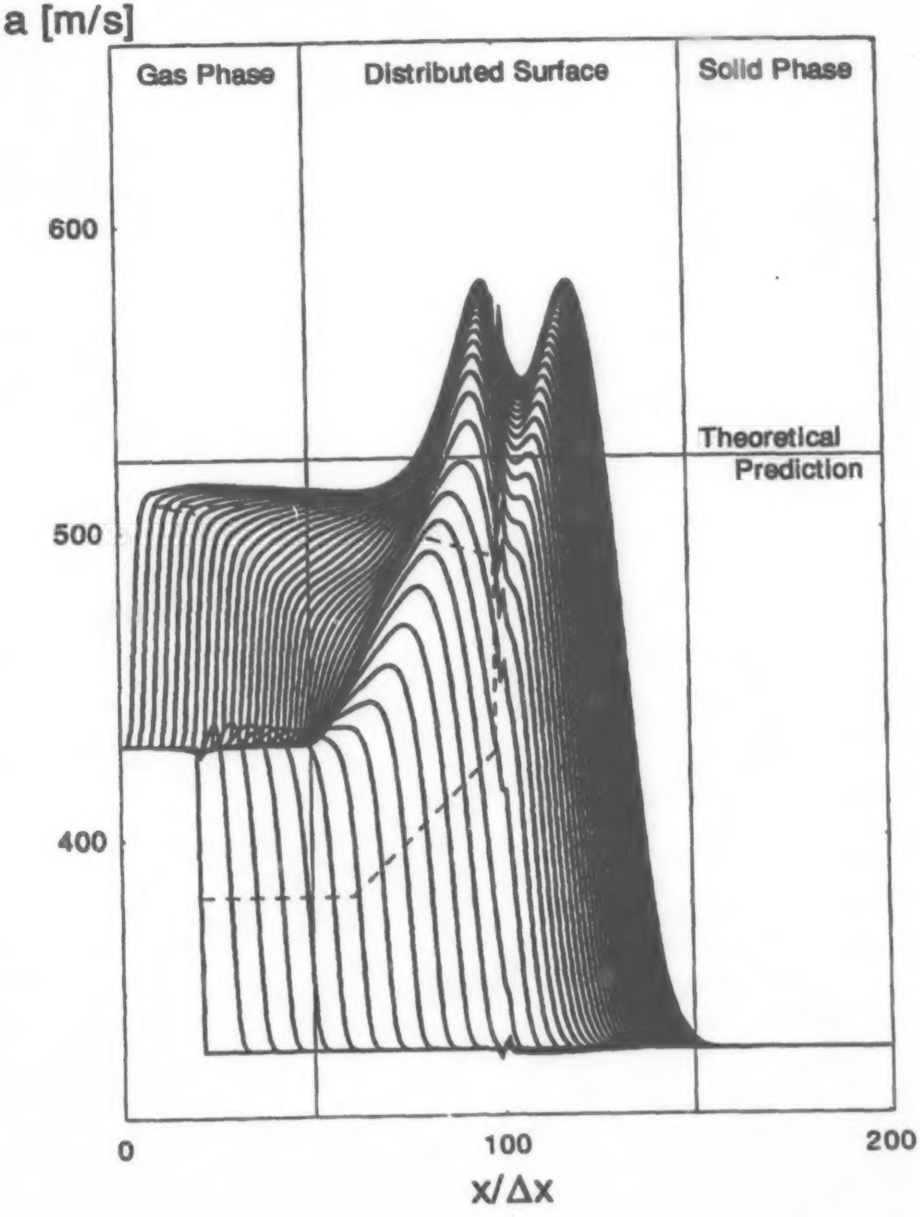

Figure 4.5: Sound speed profile with $M_s = 2.0$, $\varepsilon_{g_{min}} = 10^{-4}$.

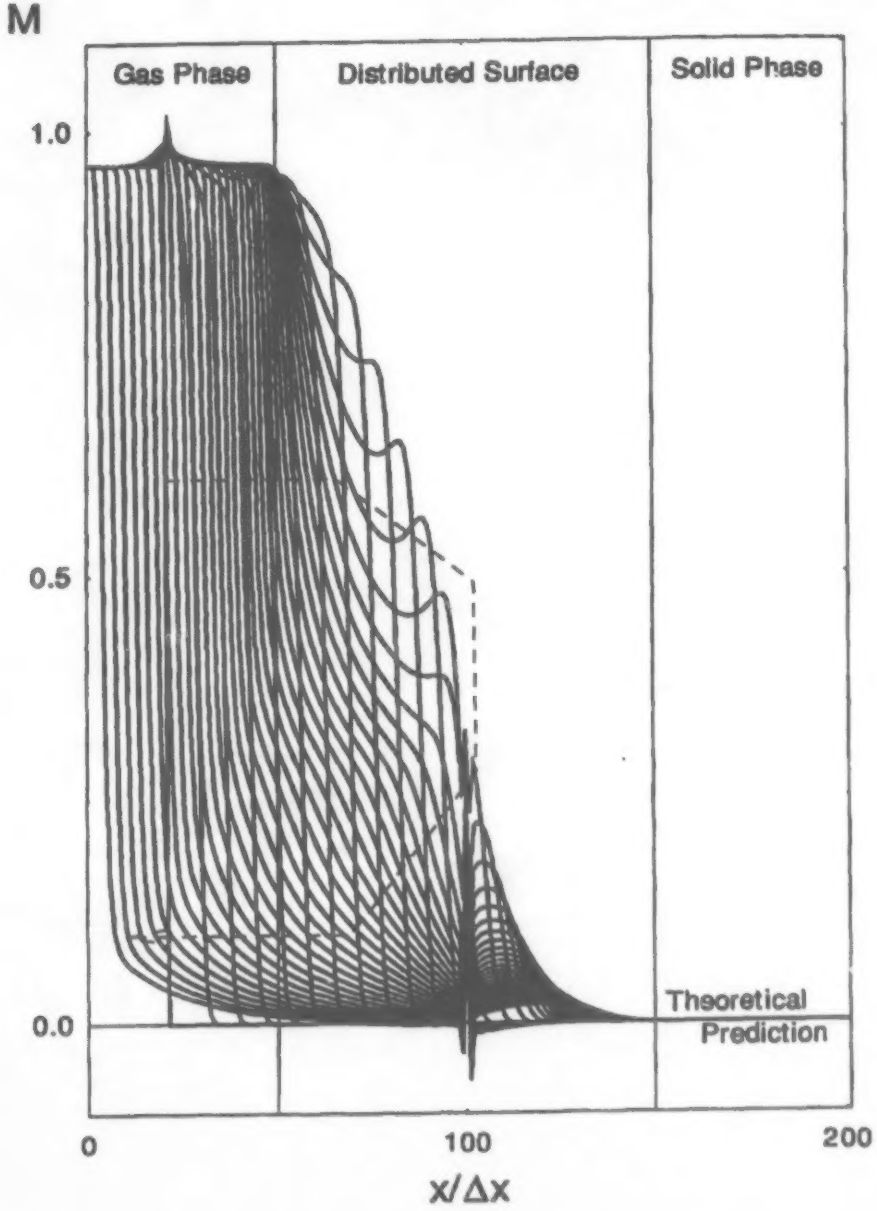

Figure 4.6: Flow mach number profile with $M_i = 2.0$, $\epsilon_{g_{min}} = 10^{-4}$.

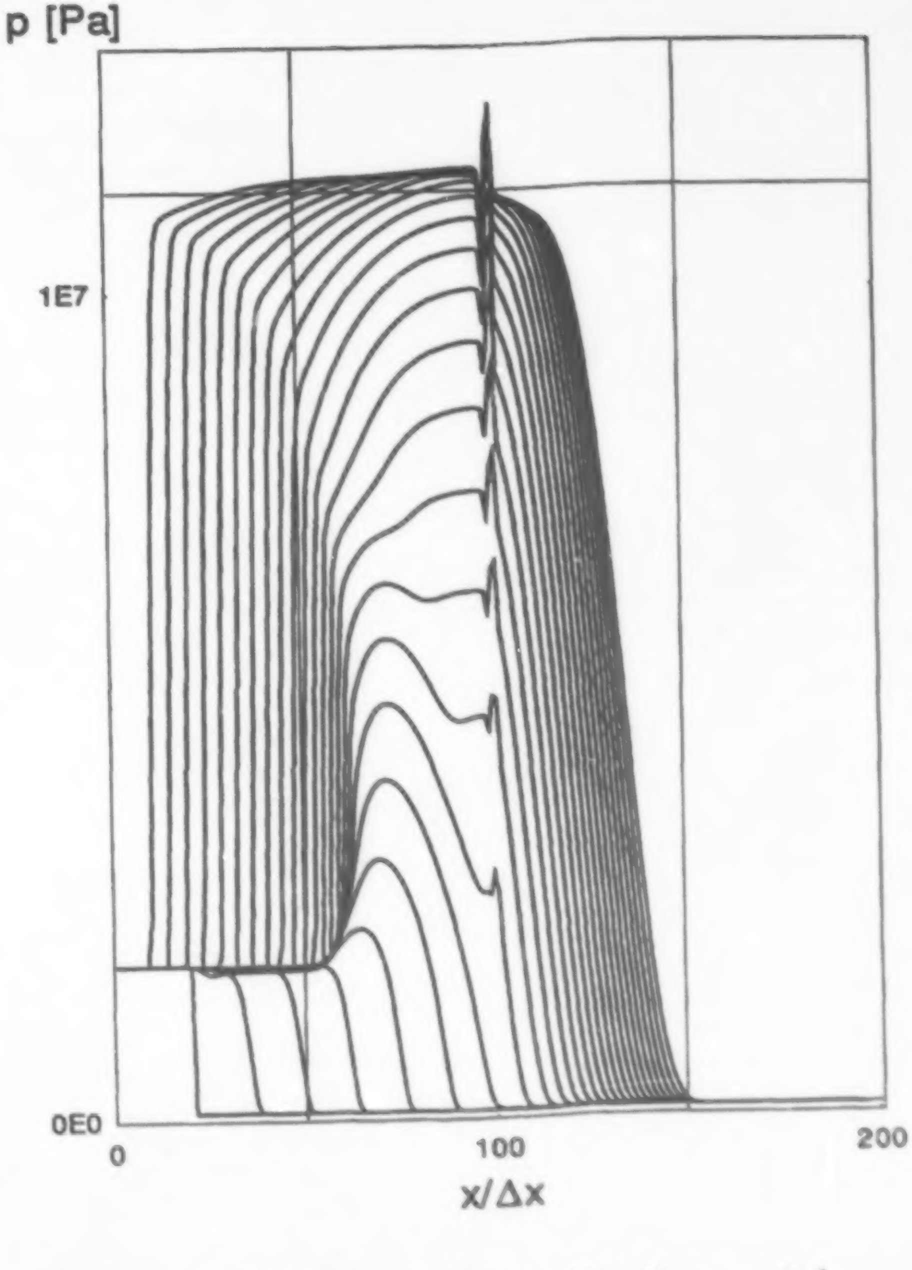

Figure 4.7: Pressure profile with $M_s = 4.0$, $\epsilon_{\beta max} = 10^{-4}$.

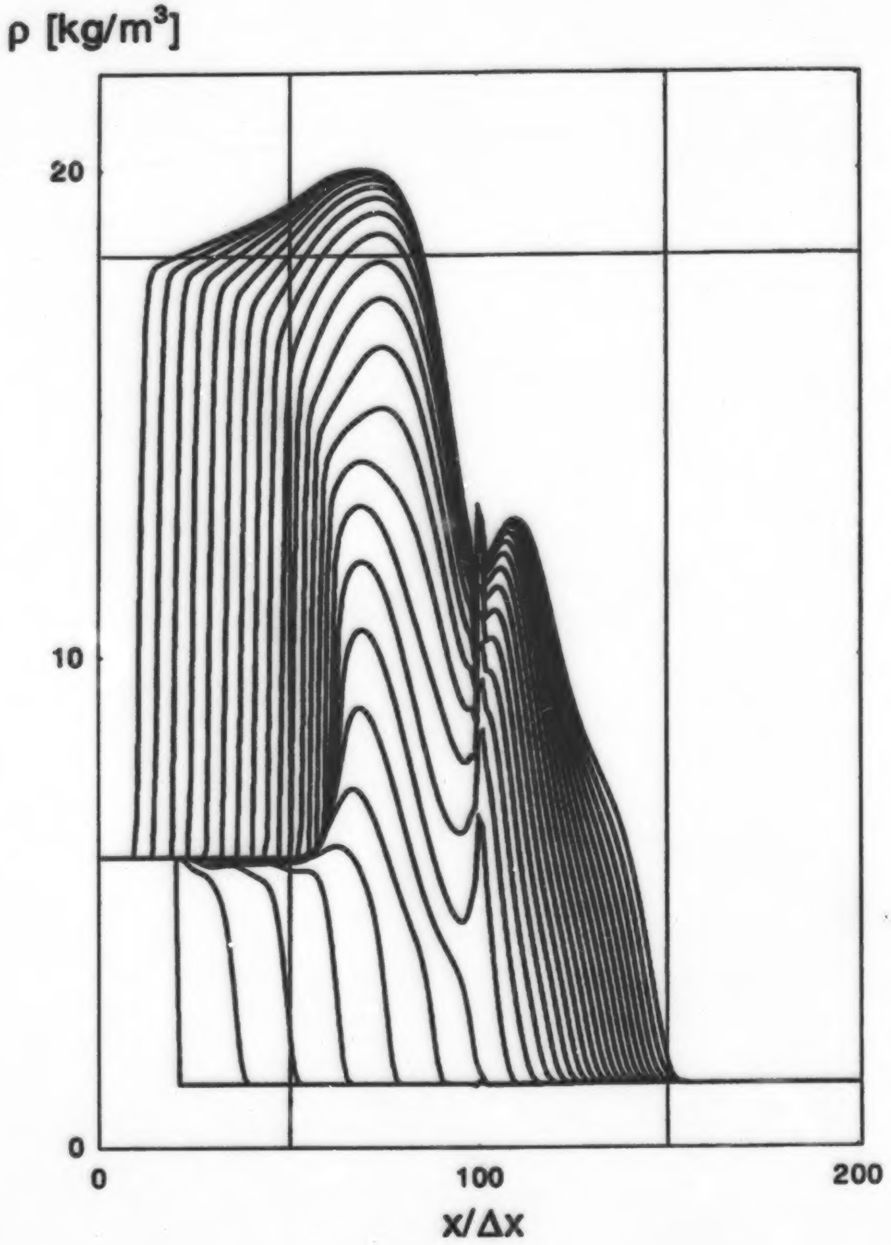

Figure 4.8: Density profile with $M_i = 4.0$, $\varepsilon_{\theta_{min}} = 10^{-4}$.

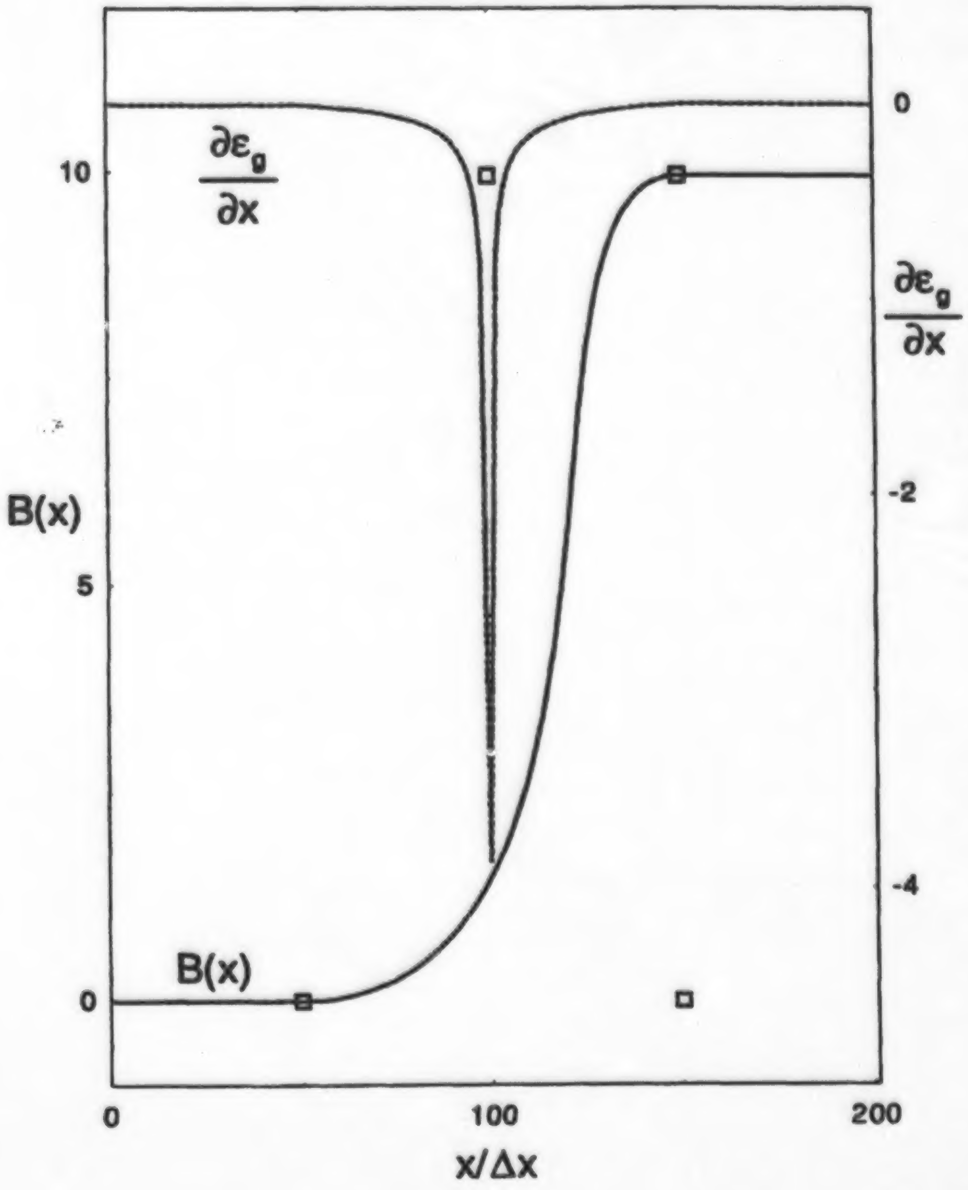

Figure 4.9: Terms in viscous-flow resistance with $M_s = 2.0$, $\varepsilon_{g_{min}} = 10^{-2}$.

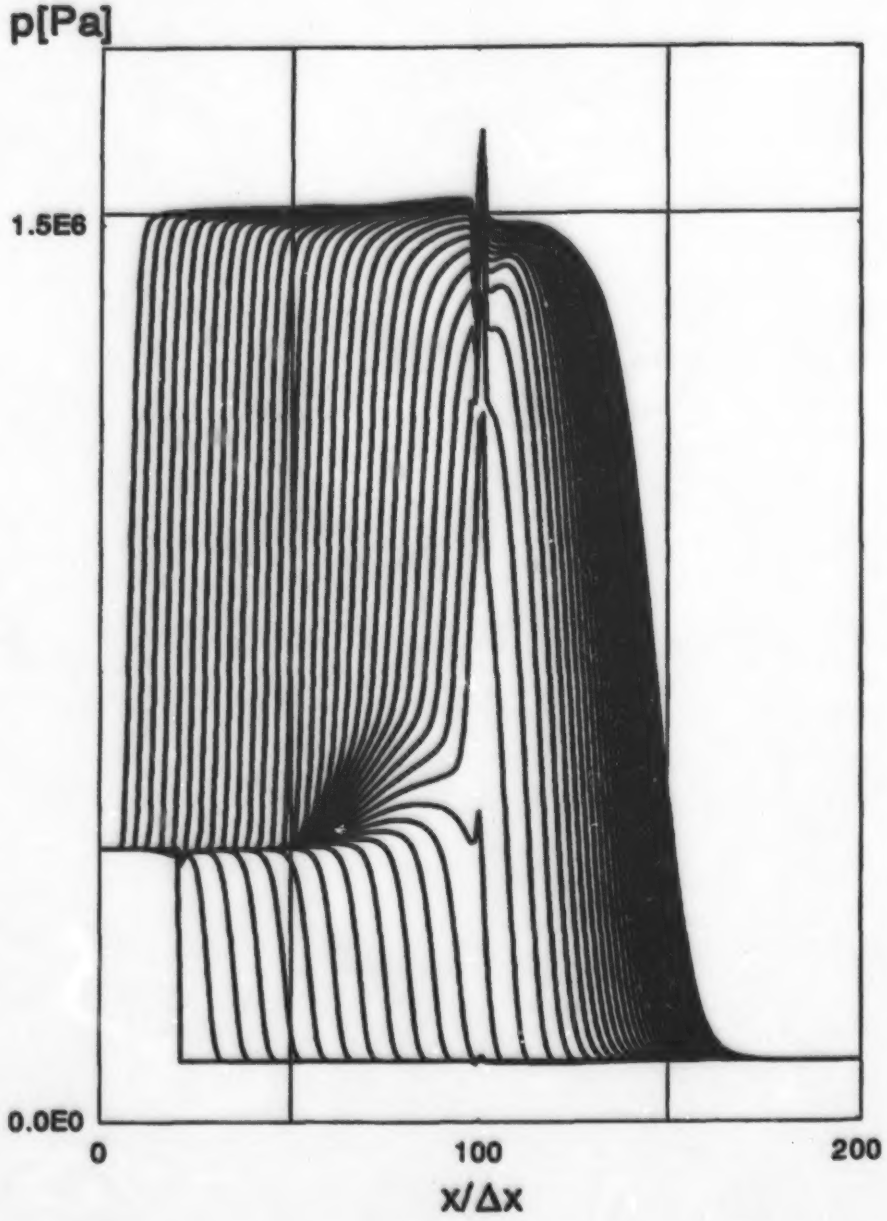

Figure 4.10: Pressure profile with $M_i = 2.0$, $\varepsilon_{g_{min}} = 10^{-2}$.

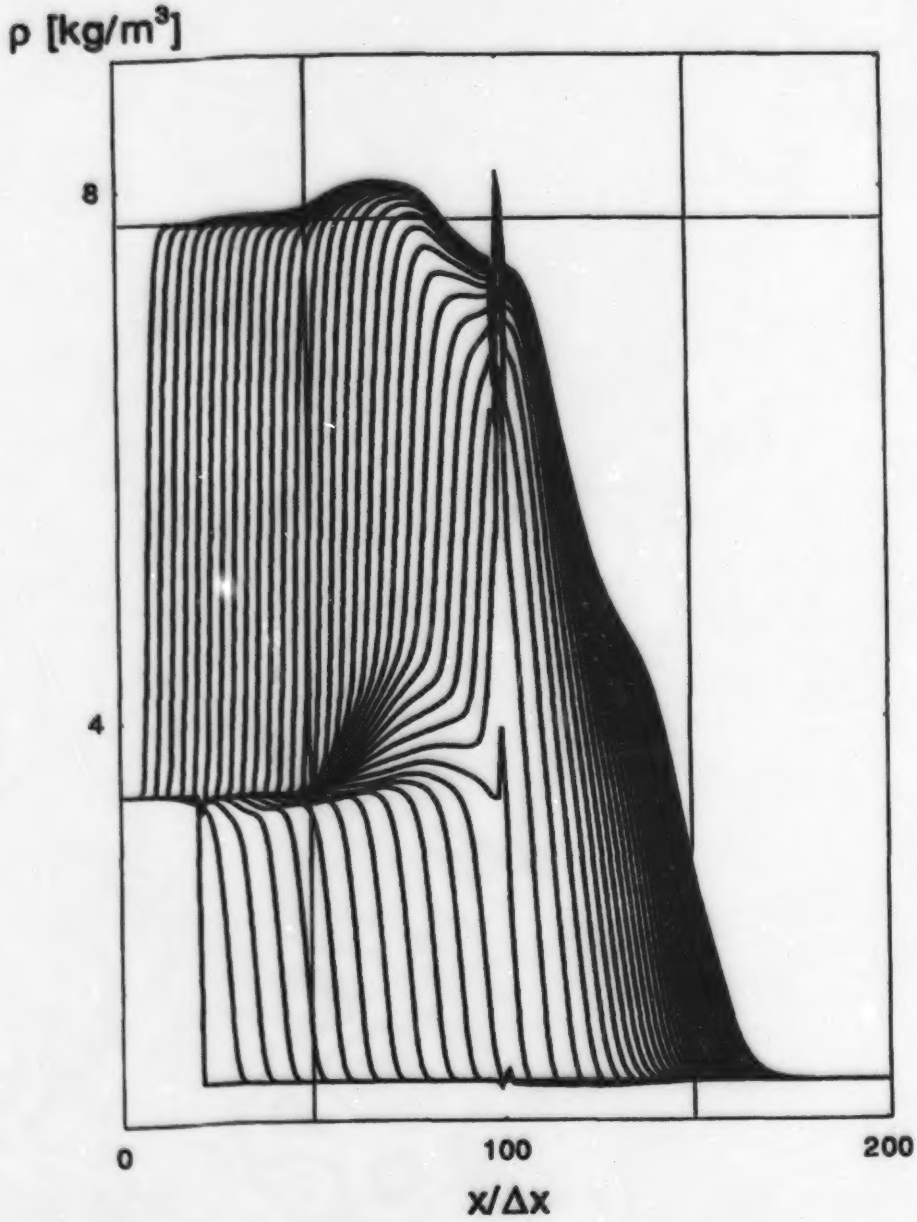

Figure 4.11: Density profile with $M_s = 2.0$, $\varepsilon_{g_{min}} = 10^{-2}$.

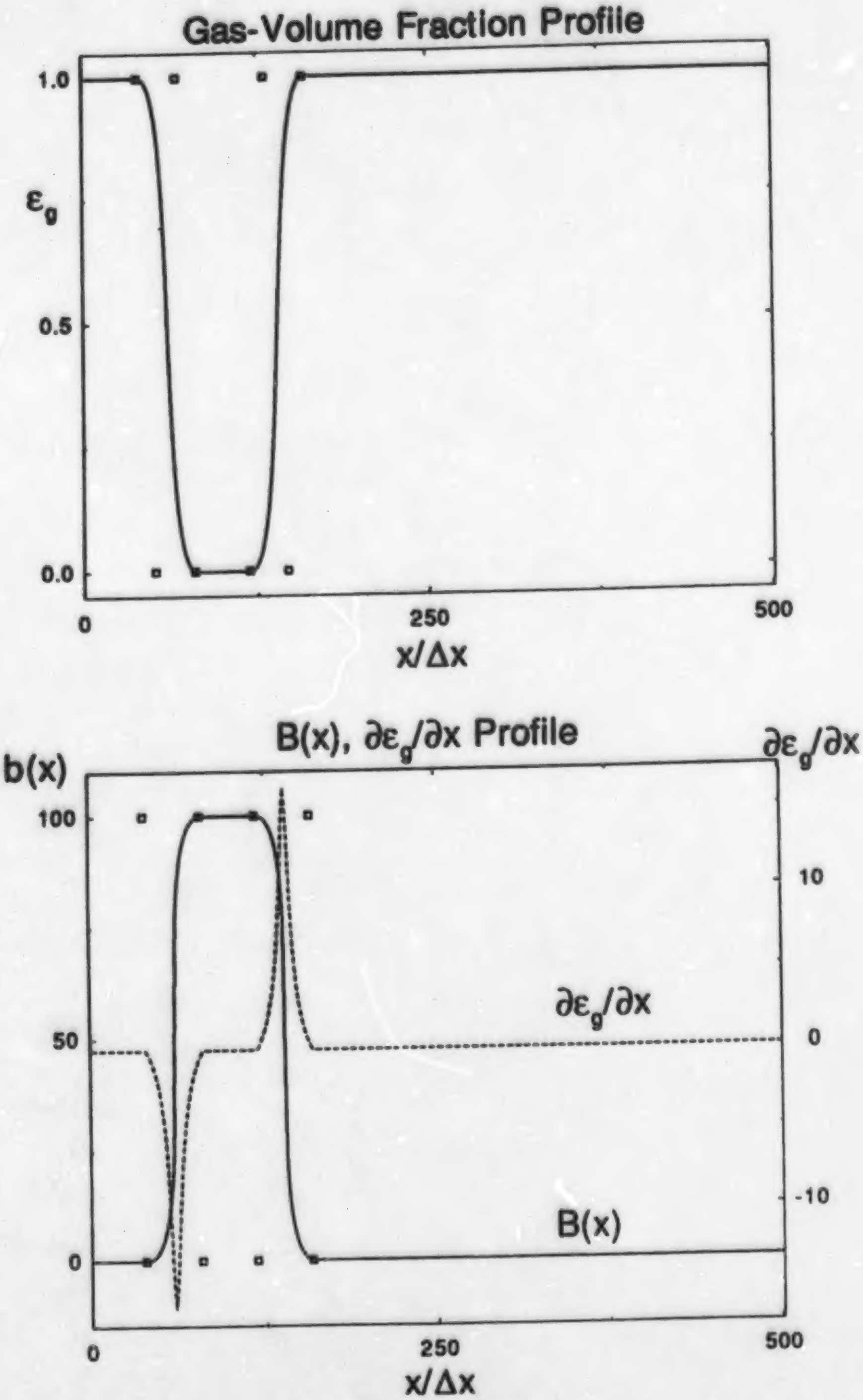

Figure 4.12: Gas-volume fraction profile at $t = 0$s

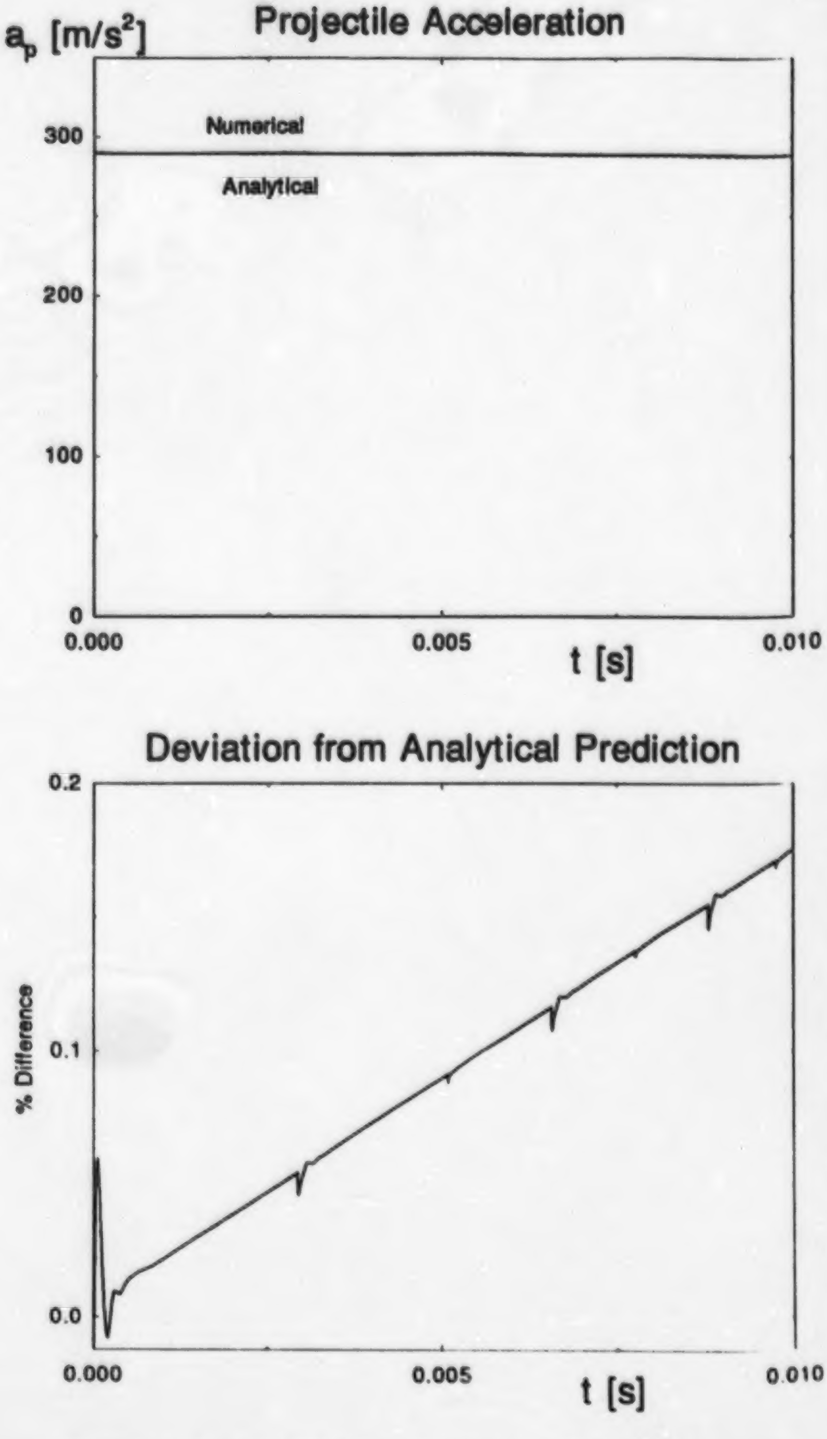

Figure 4.13: Projectile acceleration for the "relaxed" setup.

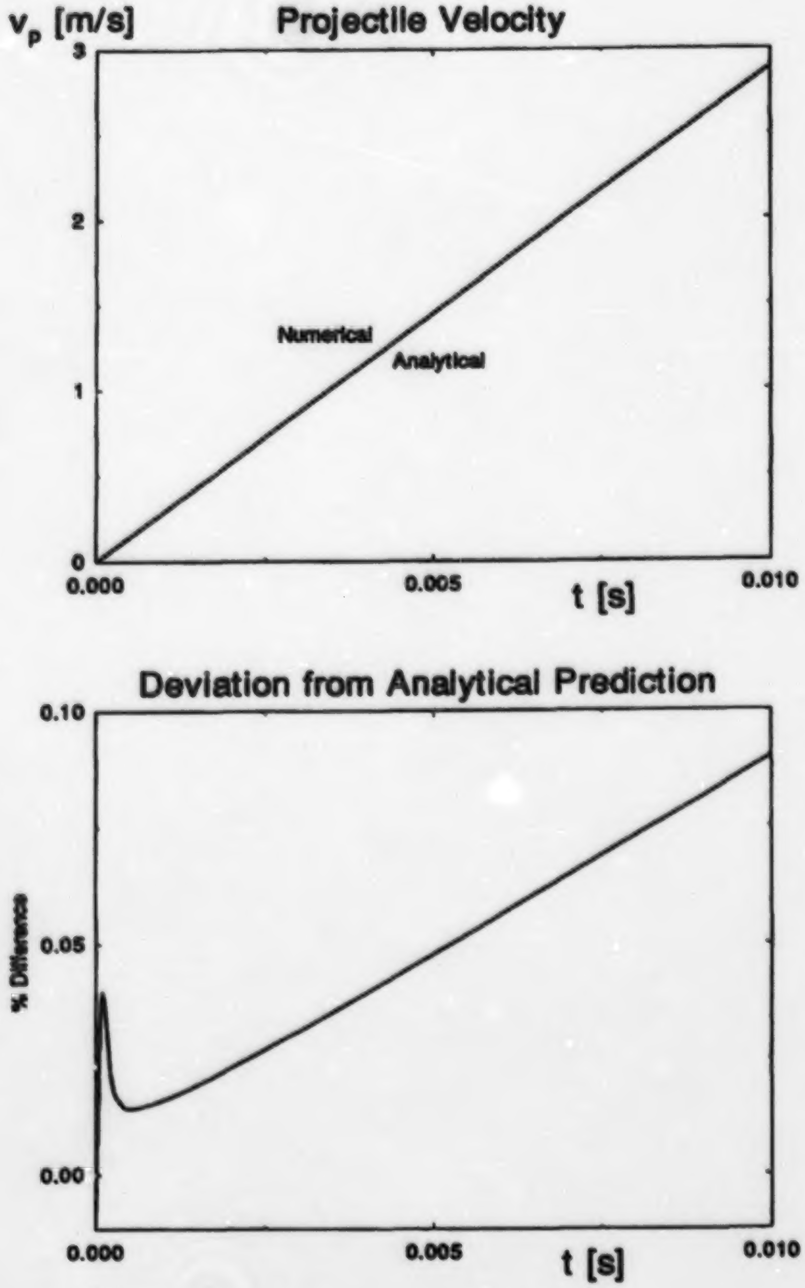

Figure 4.14: Projectile velocity for the "relaxed" setup.

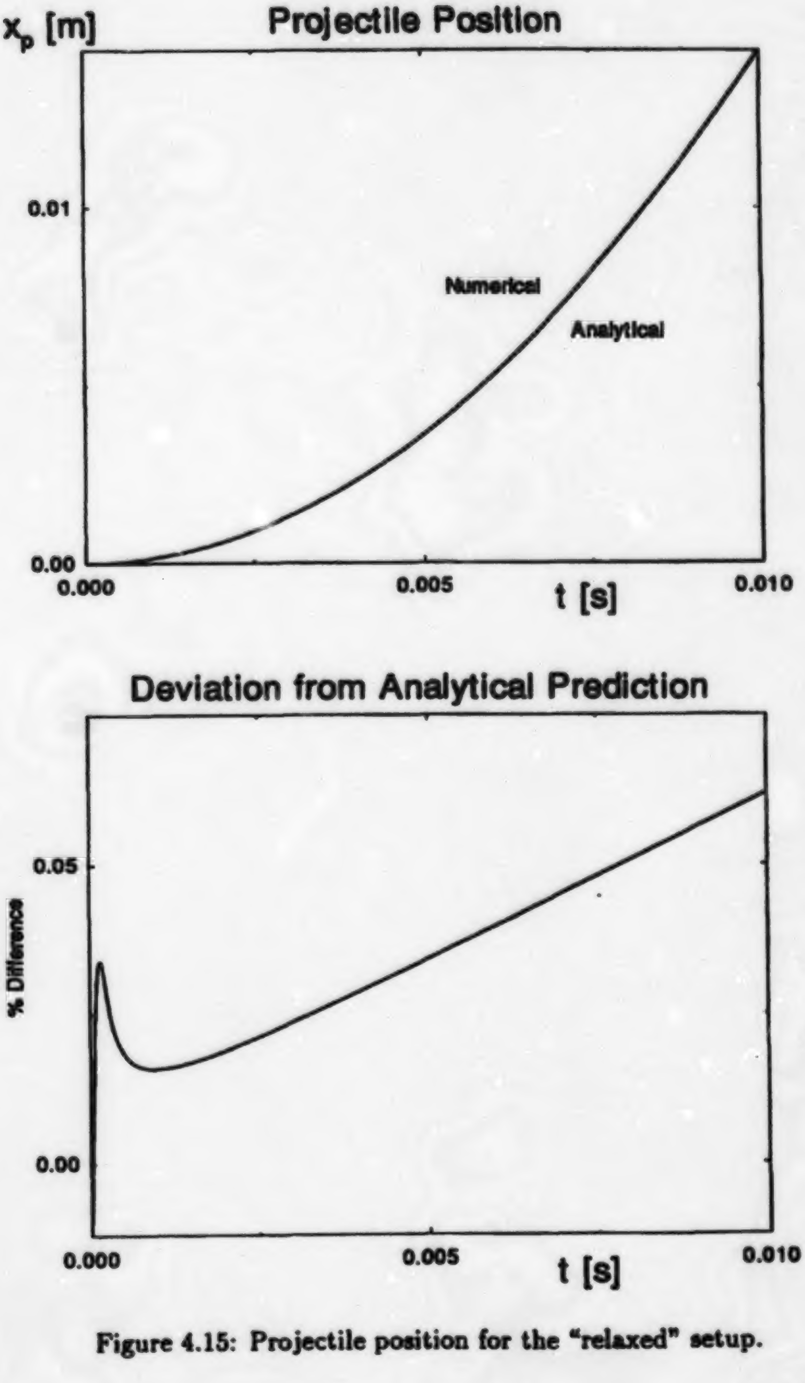

Figure 4.15: Projectile position for the "relaxed" setup.

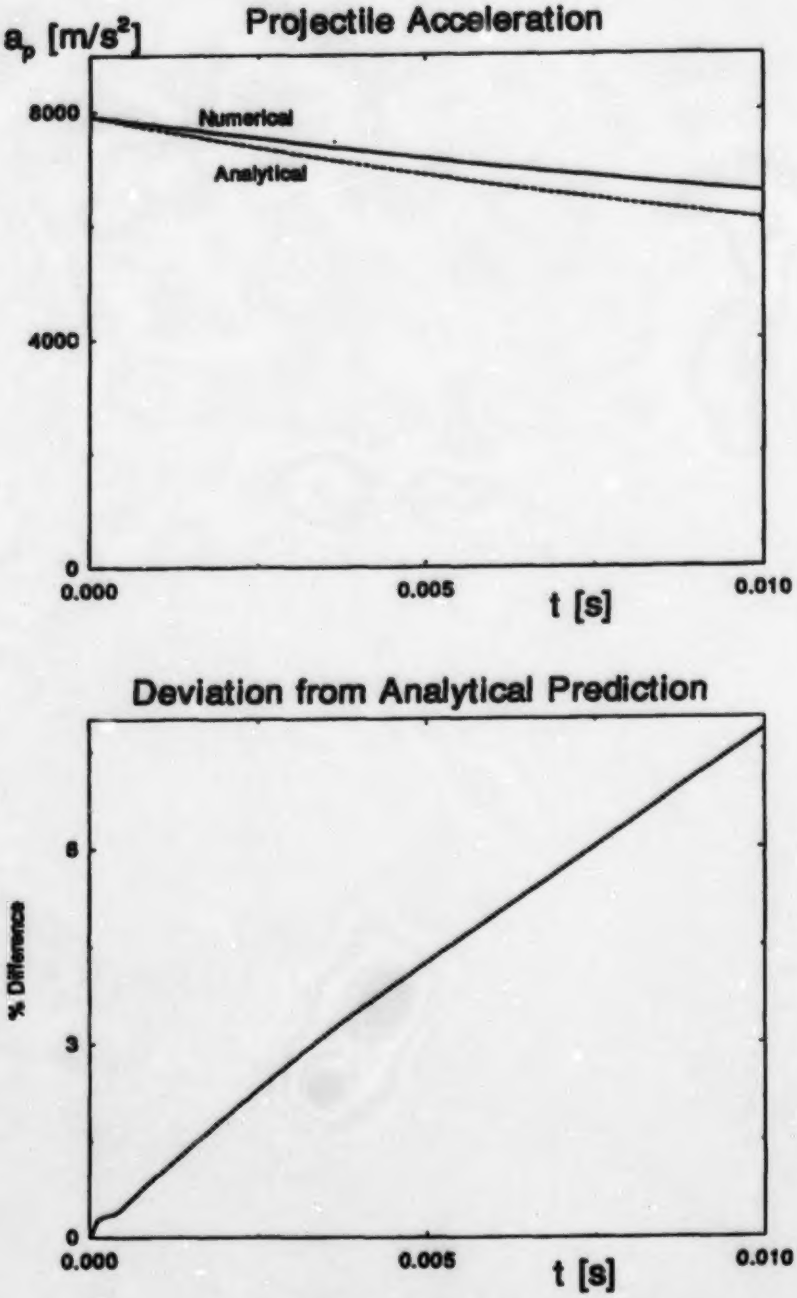

Figure 4.16: Projectile acceleration for the realistic setup.

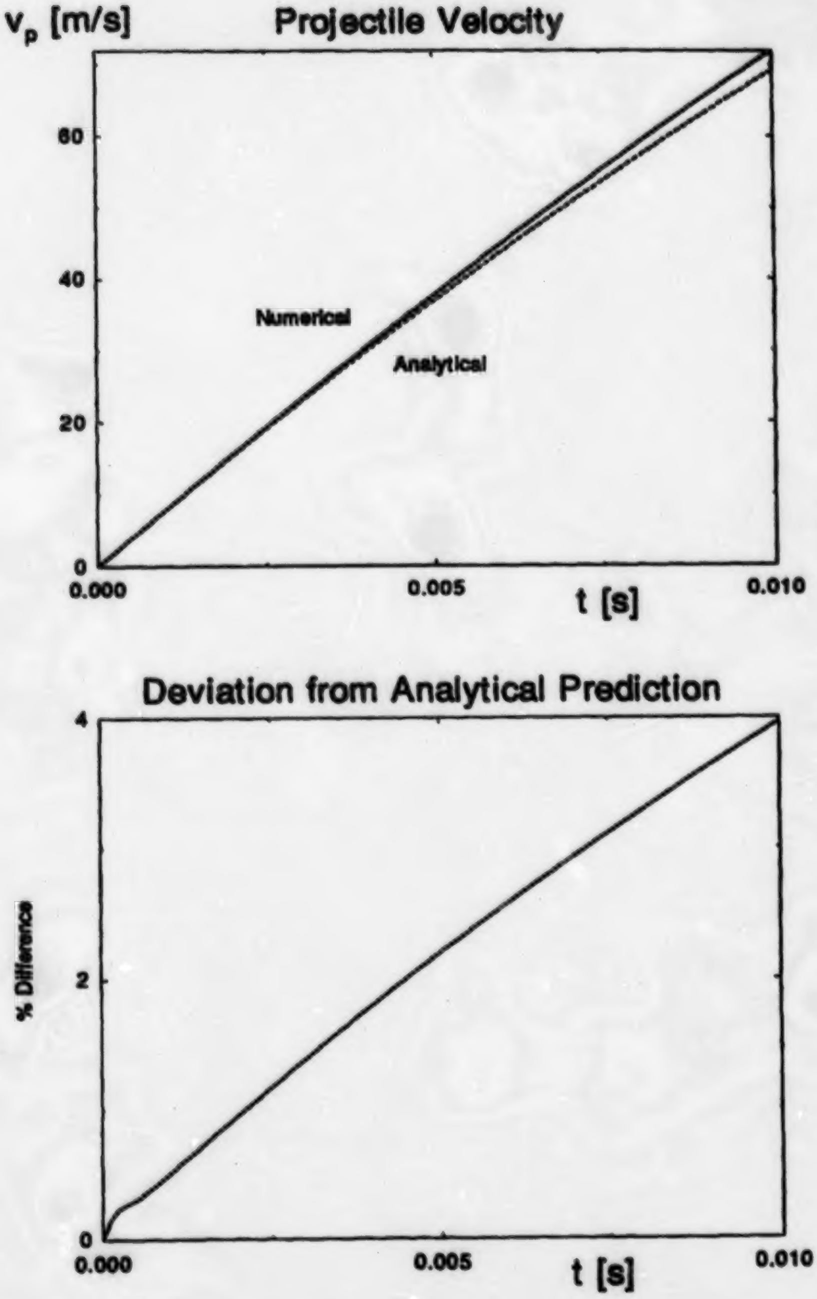

Figure 4.17: Projectile velocity for the realistic setup.

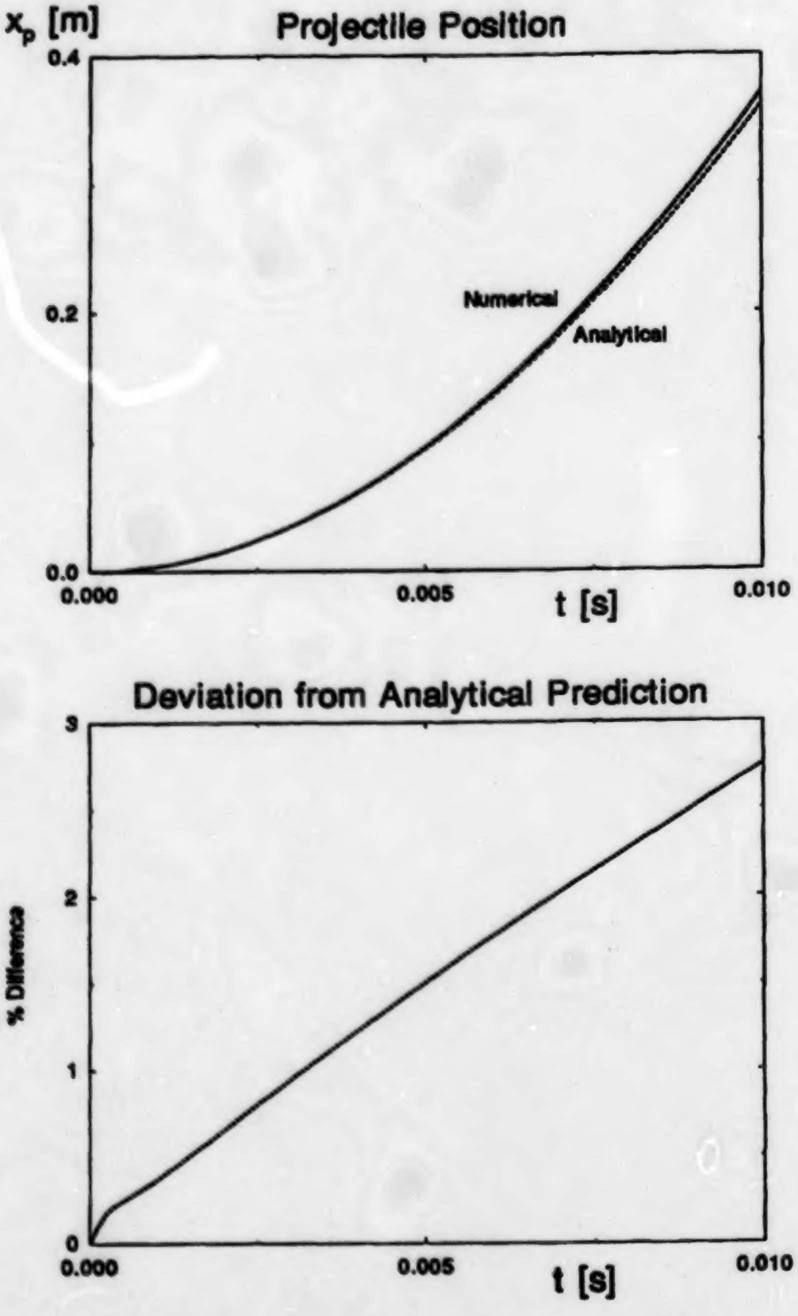

Figure 4.18: Projectile position for the realistic setup.

# APPENDIX 9

# NUMERICAL STUDY OF PARTICLE-PARTICLE COLLISIONS USING PARTICLES WITH DISTRIBUTED SURFACES

by

Vlad Vainberg

# The Numerical Study of Particle-Particle Collisions Using a Distributed Particle Surface Model

by

V. Vainberg

DIVISION OF ENGINEERING SCIENCE

FACULTY OF APPLIED SCIENCE AND ENGINEERING
UNIVERSITY OF TORONTO

Supervisor. Dr J. J. Gottlieb

# Abstract

A numerical method of simulating particle-particle interactions is explored in which the particles are assumed to be incompressible and have smoothly distributed, thin, porous surfaces A one-dimensional problem involves motion of a particle having a distributed surface inside a duct. The two particle collision is modelled as a collision between one particle having a distributed surface and a wall with a similarly distributed surface. The two surfaces are allowed to overlap slightly, resulting in a force build-up on a moving particle from the porous overlap with the wall. The resulting force slows the particle down and also can reverse its motion. Several numerical models of the process are analysed and their respective advantages and disadvantages are assessed.

# Acknowledgements

The author would like to express his gratitude to his thesis supervisor Dr. J. J Gottlieb for providing guidance and support throughout the duration of this project. The acknowledgements are also extended to the author's friends and family for their support during the project

# Contents

Abstract i

Acknowledgements ii

Contents iii

Nomenclature v

1 Introduction 1

2 Model for Particle Collisions with Distributed Surfaces

2.1 Principal Equations for Particle Motion 4

2.2 Equation for Smoothly Distributing a Particle Surface 5

2.3 Equations for Resistance Force 5

3 Numerical Solution Procedure

3.1 Grid Configuration for Numerical Calculations 7

3.2 First Order Solution Methods 7

3 3 Second and Third Order Solutions

3.2 1 Attempted Solution 9

3.2 2 Alternate Solution 10

3 4 Particle Motion 11

4 Test Problem - Particle Reflection Off The Wall

4.1 Problem Statement .... 12
4.2 Initial Conditions .... 12
4 3 Results.... 13

5 Concluding Remarks 14

Bibliography 15

Appendices

# Nomenclature

## Alphanumeric Letters

| | |
|---|---|
| $A$ | cross-sectional area [m$^2$] |
| $C_D$ | drag coefficient |
| $e$ | energy per unit volume [J/m$^3$] |
| $f_{vsc}$ | viscous-flow resistance force per unit volume [N/m$^3$] |
| $F$ | force [N] |
| $\vec{F}_{drag}$ | aerodynamic drag force [N] |
| $\vec{F}_{grav}$ | gravitational force [N] |
| $F(U)$ | flux term in $x$ direction |
| $G(U)$ | flux term in $y$ direction |
| $m$ | mass [kg] |
| $N$ | total number of cells |
| $p$ | static pressure [N/m$^2$] |
| $t$ | time [s] |
| $\vec{u}$ | velocity vector [m/s] |
| $u$ | velocity in $x$ direction [m/s] |
| $u_0$ | initial particle velocity in $x$ direction [m/s] |
| $V_{filled}$ | occupied portion of cell volume [m$^3$] |
| $V_{avail}$ | free portion of cell volume [m$^3$] |
| $W$ | number of cells occupied by the wall |
| $x$ | displacement [m] |
| $\vec{x}$ | displacement vector [m] |

## Greek Letters

| | |
|---|---|
| $\partial t$ | time differential [s] |
| $\partial x$ | space differential [m] |
| $\Delta t$ | time step [s] |
| $\Delta x$ | width of a cell [m] |
| $\varepsilon$ | volume fraction |
| $\rho$ | density [kg/m$^3$] |

## Superscripts

| | |
|---|---|
| old | properties at previous time level |
| new | properties at next time level |
| right | right side of location |
| left | left side of location |
| T | matrix transpose |

## Subscripts

| | |
|---|---|
| $i$ | index for $i^{th}$ cell |
| $i-\frac{1}{2}$ | index for left boundary of $i^{th}$ cell |
| $i+\frac{1}{2}$ | index for right boundary of $i^{th}$ cell |

# Chapter 1

# Introduction

Particle-particle collisions in gas-particle flows are a common occurrence in nature as well as in man-made environments. The interactions between particles in gas flows, their collisions in particular, have a profound effect on the dynamics of the gaseous substances they make up. The study of gas flows and their behaviour are vitally important to many fields of engineering and science. Some aerospace applications include rocket motors using particle-laden propellants and jet engines on vertical take-off aircraft ingesting sand particles Military applications include granular propellants used in high velocity guns

Studying gas particle collisions is important to be able to provide better predictions for behaviour of non-steady flows, and by doing so create more efficient and better performing engineering designs. This study is aimed at introducing several numerical models for particle collisions and comparing their respective results in order to establish a good understanding of some of the methods and common problems encountered when studying gas particle collisions.

The method utilised in this study is the method of particle-trajectory tracing, which was one of the first models in predicting the influence of the gas on particle motions. In several problems involving large particle strikes with aircraft during frozen rain, this model is used, due to the fact that only a few discrete particles usually move through a steady two- or three-dimensional flow field The trajectories of such particles are required to determine and control the particle impact locations The standard model for trajectory tracing of such particles is done in two steps In the first step, the steady two- and three-dimensional flow field without particles is computed numerically by solving Euler's continuity, momentum and energy equations

$$\frac{\partial F(U)}{\partial x} + \frac{\partial G(U)}{\partial y} = 0$$

for two-dimensional space, where the perfect gas equation of state ($p = \rho R T$) is required In the above expression

$$U = [\rho \quad \rho u \quad \rho \upsilon \quad e]^T,$$

$$F(U) = [\rho u \quad \rho u^2 \quad \rho u v \quad u(e+p)]^T ,$$

$$G(U) = [\rho v \quad \rho u v \quad \rho v^2 + p \quad v(e+p)]^T ,$$

where $p,\ \rho,\ v,\ e = \frac{1}{\gamma - 1}p + \frac{1}{2}\rho(u^2 + v^2)$, R, and T denote pressure, density, flow velocity in the x direction and y direction, energy per unit volume, gas constant, and temperature of the gas, respectively Then, particle trajectories through the given flow field are computed using the flow field parameters Particle-path calculations are flow-field properties along the trajectory, where the equation of motion for an individual particle is given by

$$\vec{a}_p = \frac{d\vec{u}_p}{dt} = \frac{d^2\vec{x}_p}{dt^2} = \frac{1}{m_p}[\vec{F}_a + \vec{F}_g] ,$$

where $\vec{F}_g = m_p \vec{g}$ is the gravitational force, and the aerodynamic force is given by

$$\vec{F}_a = \frac{1}{2}A_p C_D \rho \, |\vec{u} - \vec{u}_p|(\vec{u} - \vec{u}_p) .$$

In the above equations, $\vec{a}_p$, $\vec{u}_p$, $\vec{x}_p$, $m_p$, $C_D$, $A_p$, $\vec{u}$ denote vector particle acceleration, velocity, position, particle mass, coefficient of viscous drag, particle cross-sectional area, and vector flow velocity.

In this model, the gas is assumed to be a continuum, and the particles are treated as independent solid bodies moving through the gas An advantage of this model is that the particle paths can be evaluated using the conservation of linear momentum, angular momentum, and energy Particle collisions with walls can be regarded as collisions with large stationary particles

A more advanced method of studying particle-particle collisions introduces slightly smoothed interfaces between the gas phase and the particle phase. The particles are still considered to be individual small bodies moving independently in a gas continuum The repulsion forces are not caused by impact itself, but rather by viscous forces that are small where the particle volume fraction is small and become very large inside particles These viscous forces can be used as the driving forces in Newtonian equations to predict particle motion

During particle-particle collisions the smoothly distributed surfaces are allowed to overlap, and the overlapping porosity is what triggers the viscous forces that slow down the colliding particles and eventually repel the particles away from each other A model for such a force is introduced in this study

The primary objective of this study is to create a one-space-dimensional model of an incompressible particle with a distributed interface colliding with a wall with a similar interface and designing a model for a force that, with no losses, would satisfy Newton's laws of motion The modelling is done by creating a numerical program in C language.

The equations for gas-particle flow with distributed surface and the force model are provided in Chapter 2 The numerical solution methods are discussed in Chapter 3 The test problem is presented in Chapter 4. The study ends with some concluding remarks in Chapter 5.

# Chapter 2

# Model for Particle Collisions with Distributed Surfaces

## 2.1 Principal Equations of Particle Motion

Euler's continuity and momentum equations for the motion of the non-continuum independent particles can be written as

$$\frac{\partial}{\partial t}\begin{bmatrix}\varepsilon\rho \\ \\ \varepsilon\,\rho\,u\end{bmatrix}+\frac{\partial}{\partial x}\begin{bmatrix}\varepsilon\,\rho\,u \\ \\ \varepsilon\,\rho\,u^2\end{bmatrix}+\begin{bmatrix}0 \\ \varepsilon\,\dfrac{\partial p}{\partial x}\end{bmatrix}=\begin{bmatrix}0 \\ \\ -f_{vsc}\end{bmatrix} \qquad (2\ 1)$$

Each one of the moving particles is incompressible and rigid. The general unknowns in the continuity equation are $\varepsilon$, $u$, and $p$, where $p$ is constant, since there is no change in material properties of the particle while it is in motion Further evaluation of the above equations results in

$$\frac{\partial(\varepsilon\rho)}{\partial t}+\varepsilon\rho\frac{\partial u}{\partial x}+u\frac{\partial(\varepsilon\rho)}{\partial x}=0 \quad \text{, and} \qquad (2\ 2)$$

$$\varepsilon\rho\frac{\partial u}{\partial t}+u\frac{\partial(\varepsilon\rho)}{\partial t}+\varepsilon\rho u\frac{\partial u}{\partial x}+u\frac{\partial(\varepsilon\rho u)}{\partial x}=-f_{vsc} \qquad (2\ 3)$$

Since this study only considers the incompressible case, $\rho = const$, the expressions $u\frac{\partial(\varepsilon\rho u)}{\partial x}$ and $u\frac{\partial(\varepsilon\rho)}{\partial t}$ are both reduced to zero, and the above equations are then further reduced to

$$\frac{\partial (\varepsilon\rho)}{\partial t}+\varepsilon\rho\frac{\partial u}{\partial x}+u\frac{\partial (\varepsilon\rho)}{\partial x}=0\ , \tag{2.4}$$

$$\varepsilon\rho\frac{\partial u}{\partial t}+\varepsilon\rho u\frac{\partial u}{\partial x}=-f_{visc} \tag{2.5}$$

All heat transfer and external work are ignored here

## 2.2 Equation for Smoothly Distributing a Particle Surface

In order to model the particle-particle (or particle-wall) collisions, the interfaces between the particle and gas continuum phases are smoothened. The particle-gas interface is smoothly distributed in such a manner that the size of the interface is small compared to the size of the entire particle (or wall). The particle volume fraction $\varepsilon$ changes smoothly from zero to one, as the distributed surface ends and the 'core' of the particle begins

On a grid of uniform spacing the smoothening function is

$$\varepsilon_i=\frac{\varepsilon_{i-1}+\varepsilon_i+\varepsilon_{i+1}}{3}\ , \tag{2.6}$$

where the left $\varepsilon_i$ are the new smoothed volume fractions of the particle and the $\varepsilon_i$ on the right are the initial values The function described above can be applied several times to the particle in order to increase the size of the distributed interface An example of a distributed particle interface is shown in Fig 2 1

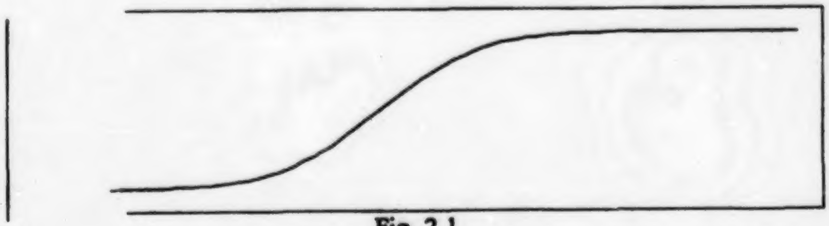

Fig 2 1

## 2.3 Equations for Resistance Force

When a particle-particle or a particle-wall collision occurs, the two objects exert a resistance force upon each other In case of a particle-wall collision, one only need to consider the force acting on the particle, since the wall is of infinitely larger mass than the particle and is completely stationary.

Upon contact, the distributed surfaces of two particles or those of a moving particle and a stationary wall begin to overlap. That overlap causes a viscous flow resistance force, and thus the resistance force is modelled. The force model used by this study is

$$f_{visc_{cell}} = \left( \frac{V_{filled}}{V_{avail}^{2} - V_{filled} \cdot V_{avail}} \right) \cdot 10^{(1.2+i-W/2)} , \qquad (2.7)$$

where $f_{visc_{cell}}$ is the viscous resistance force applied by an individual cell of the wall affected by the overlap, $V_{filled}$ is the volume portion of the cell originally occupied by the wall, $V_{avail}$ is the volume portion of the cell available to be filled by the particle, and $W$ is the number of cells the wall occupies on the grid.

# Chapter 3

# Computational Solution Procedure

## 3.1 Space Grid for Numerical Calculations

The grid used for the numerical calculations in this study consists of a collection of equally sized cells in one dimension of space, with the nodes positioned at the centres of each cell. This configuration can be seen in the figure following this paragraph. The cell width is equal to $\Delta x$ and the time step is equal to $\Delta t$.

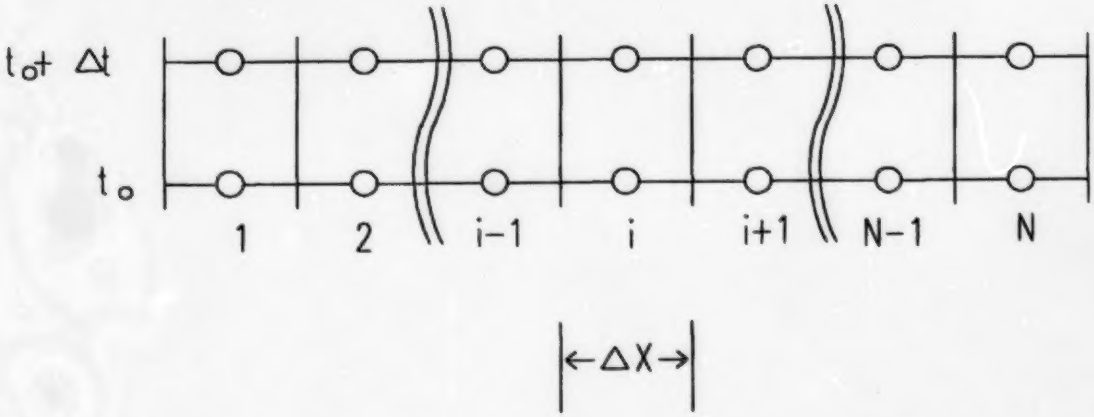

The time step $\Delta t$ is set to

$$\Delta t = \beta \frac{\Delta x}{u_0} \quad , \tag{3.1}$$

where $u_0$ is the initial velocity of the particle and $\beta \leq \frac{1}{2}$

## 3.2 First Order Solution

The computation of new volume fraction in a given cell at a given time can be done in two ways In the first method, the new volume fractions are computed without calculating cell wall fluxes, but directly from the volume fractions of the adjacent cells.

$$\begin{aligned} \varepsilon\rho_i^{new} &= \varepsilon\rho_i^{old} - \frac{\varepsilon\rho_i - \varepsilon\rho_{i-1}}{\Delta x}(u\Delta t) \quad u>0\,, \\ \varepsilon\rho_i^{new} &= \varepsilon\rho_i^{old} - \frac{\varepsilon\rho_{i+1} - \varepsilon\rho_i}{\Delta x}(u\Delta t) \quad u<0\,, \end{aligned} \qquad (3.2)$$

where $\varepsilon\rho^{old}$ are the cell volume fractions in the previous time step and $\varepsilon\rho^{new}$ is the cell volume fraction in the current time step. The variable on the right hand side of the equation (3.2) all belong to the last time step

## 3.3 Second Order Solutions

Another method of computing the new cell volume fraction as the particle is moving across the grid involves calculating the cell wall fluxes. From equations (2 4 - 2.5)

$$\frac{\partial(\varepsilon\rho)}{\partial t} + u\frac{\partial(\varepsilon\rho u)}{\partial x} = 0 \qquad (3\ 3)$$

$$\frac{\partial(u\varepsilon\rho)}{\partial t} + \frac{\partial(\varepsilon\rho u^2)}{\partial x} = \sum_i f_i \qquad (3\ 4)$$

By replacing derivatives with Δ's, the equations become

$$\frac{\Delta(\varepsilon\rho)}{\Delta t} + u\frac{\Delta(\varepsilon\rho u)}{\Delta x} = 0, \text{ etc}$$

The differences in cell volume fractions can be expressed in time and space as

$$\Delta(\varepsilon\rho) = (\varepsilon\rho)^{new} - (\varepsilon\rho)^{old} \text{ in time, and} \qquad (3\ 5)$$

$$\Delta(\varepsilon\rho u)=(\varepsilon\rho u)^{right}-(\varepsilon\rho u)^{left} \quad \text{in space} \tag{3 6}$$

Thus, the main equations of cell volume fraction change are

$$(\varepsilon\rho)^{new}=(\varepsilon\rho)^{old}-\frac{\Delta t}{\Delta x}[(\varepsilon\rho u)^{right}-(\varepsilon\rho u)^{left}] \ , \tag{3 7}$$

$$(\varepsilon\rho u)^{new}=(\varepsilon\rho u)^{old}-\frac{\Delta t}{\Delta x}[(\varepsilon\rho u^2)^{right}-(\varepsilon\rho u^2)^{left}]+\sum_i f_i \ , \tag{3.8}$$

$$u^{new}=u^{old}+\frac{F}{m}\Delta t \ , \tag{3 9}$$

where $\sum_i f_i$ and F are the total force acting on the particle during the impact.

### 3.3.1 Attempted Solution

Several methods of obtaining the cell wall fluxes were introduced throughout the course of this study. One of the first attempts to calculate the cell wall flux was to fit a third degree polynomial through four cell volume fraction values, two on each side of the cell wall.

$$\varepsilon_i=\varepsilon_0+a\left(\frac{1}{2}\Delta x\right)+b\left(\frac{1}{2}\Delta x\right)^2+c\left(\frac{1}{2}\Delta x\right)^3 \ , \tag{3 11}$$

where $\varepsilon_0$ is the value sought Then

$$\varepsilon_{i+2}=\varepsilon_0+\left(\frac{3}{2}a\right)+\left(\frac{9}{4}b\right)+\left(\frac{27}{8}c\right) \ ,$$

$$\varepsilon_{i+1}=\varepsilon_0+\left(\frac{1}{2}a\right)+\left(\frac{1}{4}b\right)+\left(\frac{1}{8}c\right) \ ,$$

$$\varepsilon_{i-1}=\varepsilon_0-\left(\frac{1}{2}a\right)+\left(\frac{1}{4}b\right)-\left(\frac{1}{8}c\right) \ ,$$

$$\varepsilon_{i-2}=\varepsilon_0-\left(\frac{3}{2}a\right)+\left(\frac{9}{4}b\right)-\left(\frac{27}{8}c\right)$$

These equations reduce to

$$\varepsilon_0 = \frac{1}{16}\left[-1, -9, 9, -1\right]\left[\varepsilon_{i-2}, \varepsilon_{i-1}, \varepsilon_i, \varepsilon_{i+1}\right]^T \quad . \tag{3.12}$$

This equation, although a good third degree polynomial fit, has a serious flaw with respect to the problem being discussed in this study Owing to its span over four cells, it returns non-zero flux values for some cell walls where flux should be zero, such as in a situation where $\varepsilon_{i-2}, \varepsilon_{i-1}, \varepsilon_i$ are all zero, and $\varepsilon_{i+1}$ is a positive value. Theoretically, the flux from cell 'i-1' to cell 'i ' should be zero However, the above equation will indeed return a negative value While the problem described above can easily be fixed by setting negative fluxes to zero, another problem arises when $\frac{1}{16}\left(\varepsilon_{i+1} + \varepsilon_{i-2}\right) > \frac{9}{16}\left(\varepsilon_i + \varepsilon_{i-1}\right)$, in which case $\varepsilon_0$ turns out to be a negative value. A few errors of that kind completely cripple the numerical computations and render them entirely useless Thus, another method is needed to compute the cell wall fluxes A correct method must have positivity control for the same errors not to reoccur

### 3.3.2 Alternate Solution

In order to avoid the previously encountered problems with positivity, a new method for computing the cell wall fluxes is introduced In this case, second degree terms are introduced first and third degree terms are added later. Extrapolating linearly to the adjacent cell

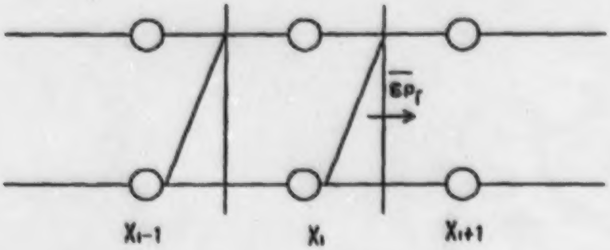

the following equation is obtained

$$\varepsilon\rho = \varepsilon\rho_i + \frac{\varepsilon\rho_{i+1} - \varepsilon\rho_i}{\Delta x}\left(x - x_i\right) \tag{3 13}$$

Integrating the above equation with respect to $(x-x_i)$, the following relation is derived

$$\bar{\varepsilon\rho}_{right}=\frac{\displaystyle\int_{x_i+\frac{1}{2}\Delta x-u\Delta t-x_i}^{x_i+\frac{1}{2}\Delta x-x_i}\varepsilon\rho\, d(x-x_i)}{\displaystyle\int_{x_i+\frac{1}{2}\Delta x-u\Delta t-x_i}^{x_i+\frac{1}{2}\Delta x-x_i}d(x-x_i)}=\frac{\varepsilon\rho_i(u\Delta t)+\dfrac{\varepsilon\rho_{i+1}-\varepsilon\rho_i}{\Delta x}\cdot\dfrac{1}{2}(u\Delta t)^2}{(u\Delta t)} \qquad (3\ 14)$$

From the above expression, the following expressions for right cell wall fluxes are derived

$$\overline{\varepsilon\rho_{right}}=\varepsilon\rho_i+\frac{\varepsilon\rho_{i+1}-\varepsilon\rho_i}{2\Delta x}u\Delta t \qquad (3.15)$$

Similarly, for the left side the expression is

$$\overline{\varepsilon\rho_{left}}=\varepsilon\rho_{i-1}+\frac{\varepsilon\rho_i-\varepsilon\rho_{i-1}}{2\Delta x}u\Delta t \qquad (3.16)$$

Substituting these values into equation (3.7),

$$\varepsilon\rho_i^{new}=\varepsilon\rho_i^{old}-\frac{u\Delta t}{\Delta x}\left(\varepsilon\rho_i-\varepsilon\rho_{i-1}\right)-\frac{1}{2}\left(\frac{u\Delta t}{\Delta x}\right)^2\left(\varepsilon\rho_{i+1}-2\varepsilon\rho_i+\varepsilon\rho_{i-1}\right)\ ,\ u>0 \quad (3.17)$$

$$\varepsilon\rho_i^{new}=\varepsilon\rho_i^{old}-\frac{u\Delta t}{\Delta x}\left(\varepsilon\rho_{i+1}-\varepsilon\rho_i\right)-\frac{1}{2}\left(\frac{u\Delta t}{\Delta x}\right)^2\left(2\varepsilon\rho_i-\varepsilon\rho_{i+1}-\varepsilon\rho_{i-1}\right)\ ,\ u<0 \quad (3\ 18)$$

By introducing higher order terms into equation (3 13), it becomes

$$\varepsilon\rho=\varepsilon\rho_i+\frac{\varepsilon\rho_{i+1}-\varepsilon\rho_i}{\Delta x}(x-x_i)+\frac{1}{2}\frac{\varepsilon\rho_{i+1}-2\varepsilon\rho_i+\varepsilon\rho_{i-1}}{(\Delta x)^2}(x-x_i)^2 \qquad (3\ 19)$$

Taking the higher order terms into account, the final equations become third order and yield

$$\begin{aligned}\varepsilon\rho_i^{new}&=\varepsilon\rho_i^{old}-\frac{u\Delta t}{\Delta x}\left(\varepsilon\rho_i-\varepsilon\rho_{i-1}\right)-\frac{1}{2}\left(\frac{u\Delta t}{\Delta x}\right)^2\left(\varepsilon\rho_{i+1}-2\varepsilon\rho_i+\varepsilon\rho_{i-1}\right)\\&-\frac{1}{6}\left(\frac{u\Delta t}{\Delta x}\right)^3\left(\varepsilon\rho_{i+1}-3\varepsilon\rho_i+3\varepsilon\rho_{i-1}-\varepsilon\rho_{i-2}\right)\ ,\ u>0\end{aligned} \qquad (3\ 20)$$

$$\begin{aligned}\varepsilon\rho_i^{new} = \varepsilon\rho_i^{old} &- \frac{u\Delta t}{\Delta x}\left(\varepsilon\rho_{i+1} - \varepsilon\rho_i\right) - \frac{1}{2}\left(\frac{u\Delta t}{\Delta x}\right)^2\left(2\varepsilon\rho_i - \varepsilon\rho_{i+1} - \varepsilon\rho_{i-1}\right) \\ &- \frac{1}{6}\left(\frac{u\Delta t}{\Delta x}\right)^3\left(\varepsilon\rho_{i+2} - 3\varepsilon\rho_{i-1} + 3\varepsilon\rho_i - \varepsilon\rho_{i+1}\right), \ u<0\end{aligned} \quad , \qquad (3\ 21)$$

which are the equations used in the computational program A pattern emerges and all higher order terms can be deduced, if desired

## 3.4 Particle Motion

The particle in the problem is moving in one-dimensional space. It starts with a velocity of $u_0$. The velocity remains unchanged unless the particle encounters an obstacle. Upon encountering a wall with distributed interface, the viscous resistance force starts changing the velocity of the particle. Eventually, the particle is reflected from the wall, and, since there are no losses due to friction or heat transfer, assumes a velocity that is equal in magnitude and opposite in direction to the original velocity $u_0$.

# Chapter 4

# Test Problem - Particle Reflection From The Wall

## 4.1 Problem Statement

In order to test the concept of collision of particles with distributed surfaces, the following problem is set up. A particle with smoothly distributed surface interface travels at constant velocity down a one-dimensional duct. The duct ends with a wall, that has a slightly distributed surface in a way similar to that of the particle. In this problem, the validity of the numerical equations developed from Euler's equations is studied, as well as the viscous resistance force effect based on the amount of physical overlap between the distributed interfaces of the moving particle and that of a stationary wall

Several assumptions are made in this problem. First, the particle is considered incompressible, i.e. the density $\rho$ across the entire length of the particle is constant Second, there are no energy or momentum losses associated with the particle-wall impact. Third, the distributed surface of the wall does not change its shape at any time Finally, the density of the wall is identical to that of the particle

The solution of this problem is quite simple, for with no losses the particle must simply rebound from the wall and continue its motion with the same speed as before the impact, but in the opposite direction (simple Newtonian theory).

## 4.2 Initial Conditions

The particle is travelling in a one dimensional duct with a fixed end Initial velocity of the particle is set to be 1 0 m/s The size of the duct is 0.3 m, and the initial size of the particle is 0 01 m A grid of 300 nodes is used in the numerical calculation, each cell is 0 001 m in length The distributed surface of the wall occupies 30 cells, or 0 03 m

## 4.3 Results and Discussion

The results obtained in this problem have been largely satisfactory. The charts representing the motion of the particle in time and space are available in Appendix A

The original velocity of the particle $u_0$ is set to 1 m/s The velocity of the particle following the impact with the wall is -0.997 m/s. The magnitude of velocity of the particle bouncing off the wall is within 1% from the magnitude of the original velocity. This small error is attributed to the rounding that occurs during the numerical computations done by the computer code written by the author to solve the problem in this study.

The particle seems to undergo diffusion, which occurs due to the way that the governing equations are formulated The amount of diffusion largely depends on the size of the distributed surface, and the relative amount of diffusion with respect to the size of the particle decreases when the distributed surface is made much smaller than the size of the entire particle The amount of diffusion is larger when the method discussed in Section 3.3.2 is utilised Such diffusion is the reason the main bulk of the particle never reaches the wall when that method is used, and the particle is repelled from the wall by the viscous forces acting on the thin distributed porous surface that has grown in size by the time the particle has reached the wall. The representative charts are available in Appendices A 1 and A.2.

When a less precise but a simpler method discussed in Section 3.2 is utilised and $\beta$ is set to 0.98, the overlap between the particle and the wall can be clearly seen (Appendices A.3 and A.4).

The author's conclusion is that the models introduced in this study for both particle motion and viscous force build-up are both feasible and return good results The particle mass is conserved throughout the problem, which is an indication of the fact that the numerical code is working correctly.

# Chapter 5

# Concluding Remarks

This study introduced a numerical model for studying particle-particle collisions using distributed surface interfaces. A one space dimensional problem was solved using this model - particle reflection off a wall, both with distributed interfaces.

The numerical software, written in C language by the author of this study, returns reasonably good results, and most of the original problems associated with instability of original cell wall flux estimation routine have been solved The software is reasonably efficient with respect to processor time it requires and can run both on DOS based and faster workstations.

The study identified a very serious issue that concerns anyone attempting to do computational fluid dynamics (CFD). There has to be definitive positivity control in CFD codes. Since the particles considered in this study were incompressible, it was very easy to see when the code gave the wrong answers, because a change in volume is a direct violation of the original incompressibility assumption

It would be worthwhile to take this study beyond one dimensional and incompressible problem The method has potential which must be explored further

## Bibliography

[1] Zucrow, 1976, Gasdynamics 1, Wiley, New York

# Appendix A.1

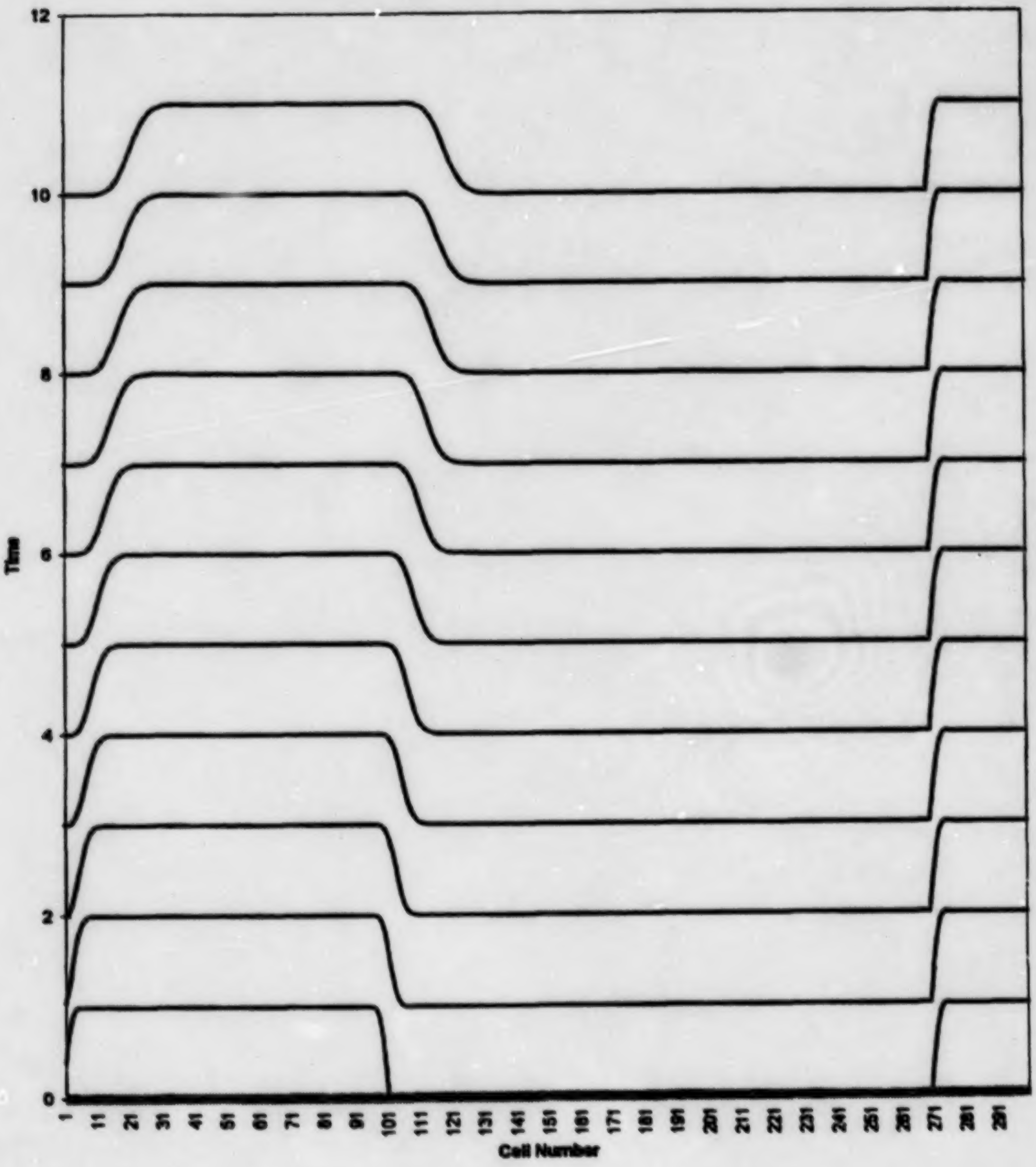

Particle Motion at Constant Velocity (Beta=0.48)

# Appendix A.2

**Particle Reflection Off The Wall (Beta = 0.48)**

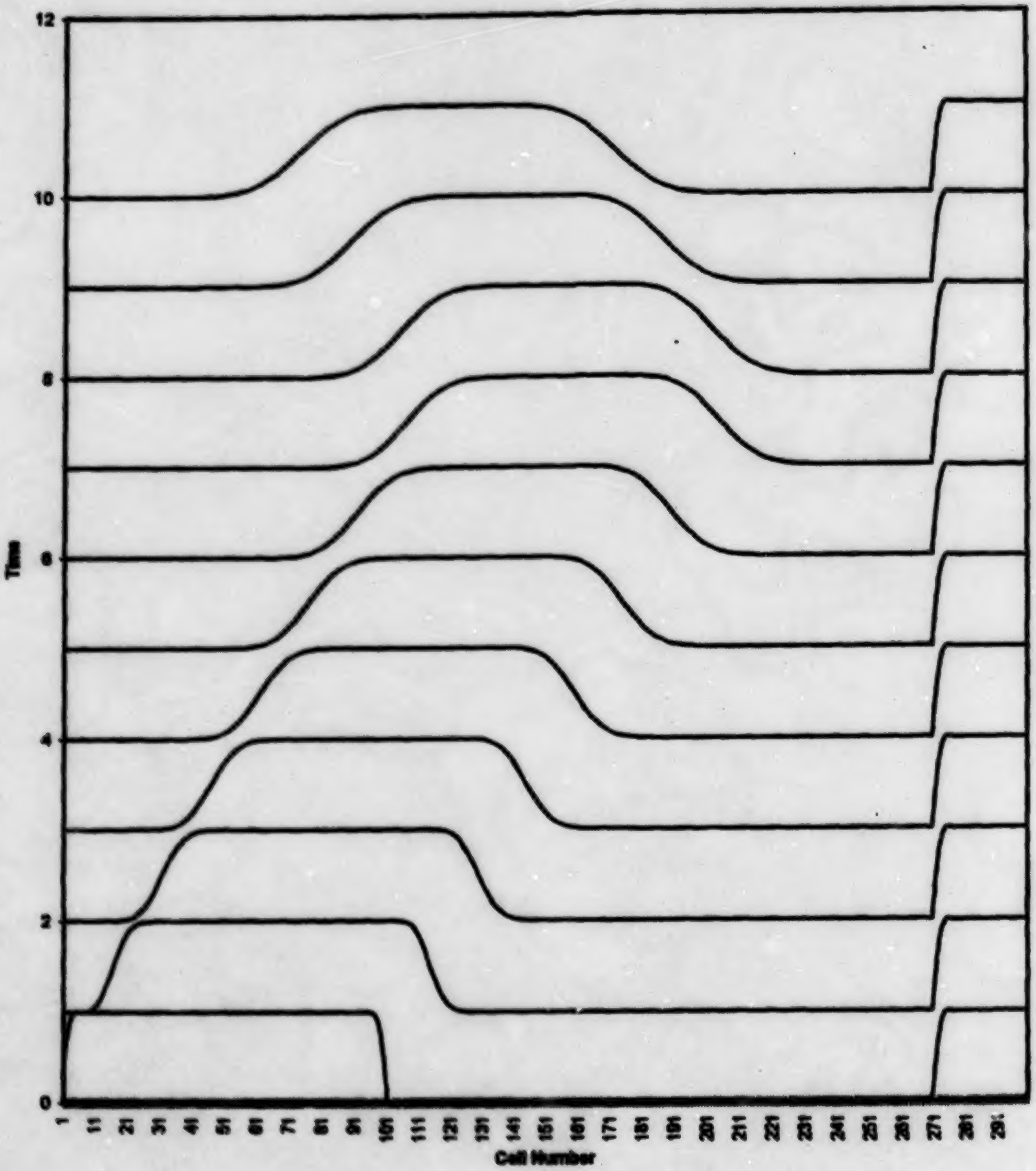

# Appendix A.3

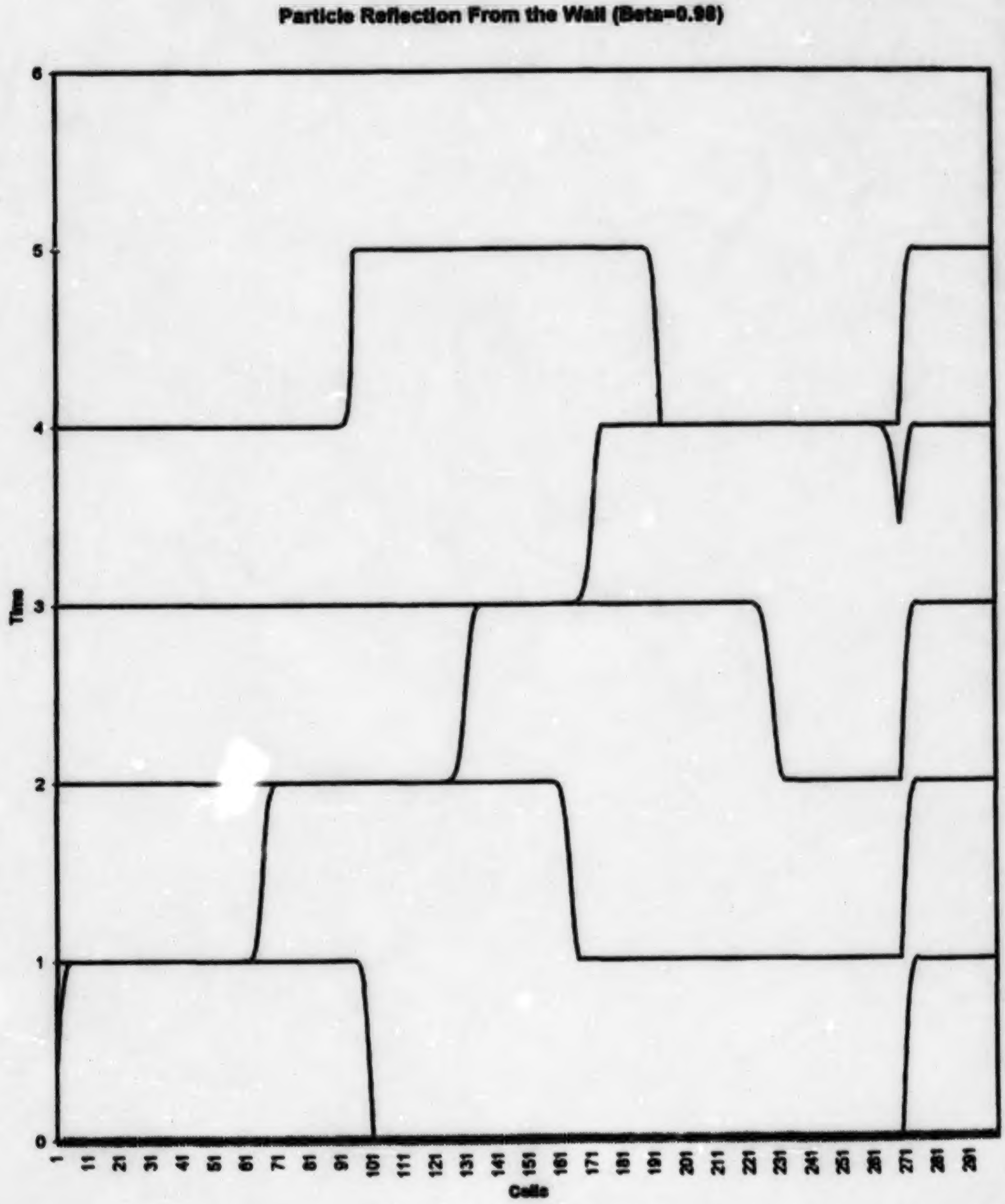
Particle Reflection From the Wall (Beta=0.98)
Time
0
1
2
3
4
5
6
Cells
1
11
21
31
41
51
61
71
81
91
101
111
121
131
141
151
161
171
181
191
201
211
221
231
241
251
261
271
281
291

# Appendix A.4

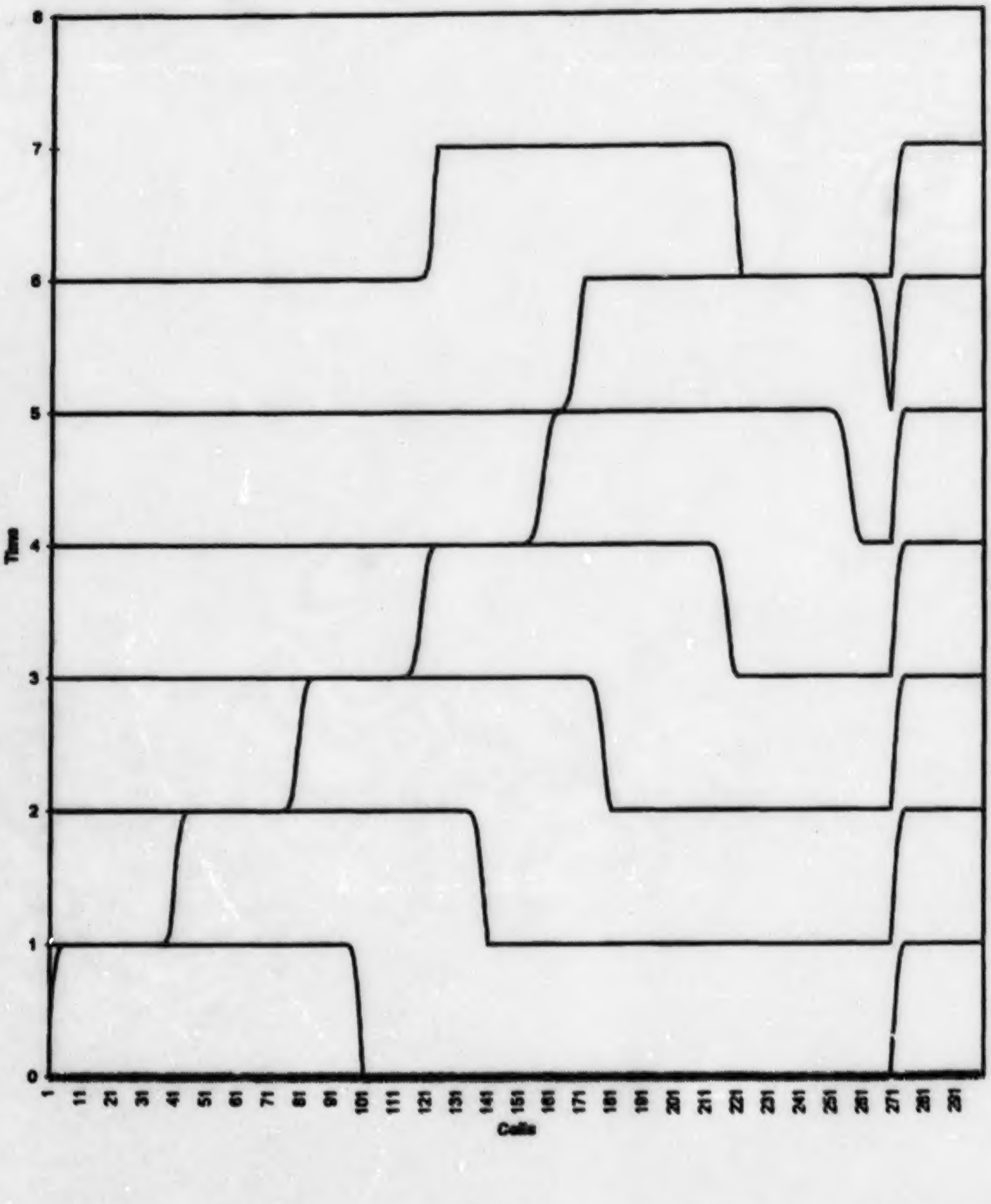

Motion and Reflection of The Particle (Beta=0.98)

# Appendix B

## The Numerical Software
## (written in C, compilable both in UNIX and MS-DOS/Win95 environment).

```
#include "vlad.h"

const double p0 = 1.225;
const double u0 = 1.0;
const double delta_x = 0.001;
const double Beta = 0.5;
const double MinDen = 0.0001;
const int CellsPerWave = 100;
const int CellsPerTube = 300;
const int CellsPerWall = 30;


CInfo **C_Mat_Alloc (int row, int col);
double *Vec_Alloc (int size);
/****************************************************************
/**********************Tools************************************
/****************************************************************
CInfo **C_Mat_Alloc (int row, int col)
{
 CInfo **temp_Mat;
 int i, j;

 temp_Mat = (CInfo **) malloc ((row+1)*sizeof(CInfo*));
 temp_Mat[0] = (CInfo *) malloc ((row*(col+1)+1)*sizeof(CInfo));

 temp_Mat[1] = temp_Mat[0] + 1;
 for (i=2; i <= row; i++)
 {
  temp_Mat[i] = temp_Mat[i-1] + col + 1;
 }

 temp_Mat[0][0].e = row;
 temp_Mat[0][0].v_e = col;

 for (i=1; i <= row; i++)
 {
  for (j=1; j <= col; j++)
  {
           temp_Mat[i][j].e = 0.0;
           temp_Mat[i][j].v_e = 0.0;
           temp_Mat[i][j].p = p0;
           temp_Mat[i][j].u = 0.0;
  }
 }

 return temp_Mat;
}
/****************************************************************
double *Vec_Alloc (int size)
{
 double *temp_Vec;
 int i;

 temp_Vec = (double *) malloc ((size+1)*sizeof(double));

 temp_Vec[0] = size;

 for (i=1; i <= size; i++)


 {
  temp_Vec[i] = 0.0;
 }

 return temp_Vec;
}
/*************************************************************
void C_ViewMat (CInfo **temp_mat)
{
 int i, j, row, col;

 row = (int) temp_mat[0][0].e;
 col = (int) temp_mat[0][0].v_e;

 printf ("row = %d, col = %d\n", row, col);

 for (i=1; i <= row; i++)
 {
  for (j=1; j <= col; j++)
  {
          printf ("p=%1.3lf u=%1.3lf e=%1.10lf ve=%1.10lf ",
  }
  printf ("\n");                      temp_mat[i][j].p, temp_mat[i][j].u,
 }
 printf ("\n");                      temp_mat[i][j].e, temp_mat[i][j].v_e);
}
/*************************************************************
void C_ViewMatS (CInfo **temp_mat, int shot)
{
 int i, j, row, col;

 row = (int) temp_mat[0][0].e;
 col = (int) temp_mat[0][0].v_e;

 printf ("row = %d, col = %d\n", row, col);

 for (i=1; i <= row; i++)
 {
  printf ("p=%1.3lf u=%1.3lf e=%1.3lf ve=%1.3lf\n", temp_mat[i][shot].p,
temp_mat[i][shot].v_e);         temp_mat[i][shot].u, temp_mat[i][shot].e,
 }
 printf ("\n");
}
/***************************************************************
void ViewShots (CInfo **temp_mat)
{
 int i, j, row, col;
 row = (int) temp_mat[0][0].e;
 col = (int) temp_mat[0][0].v_e;

 printf ("row = %d, col = %d\n", row, col);

 for (i=1; i <= row; i++)
 {
  for (j=1; j <= col; j++)
  {
            printf ("%1.3lf ", temp_mat[i][j].e);
  }
  printf ("\n");
 }
 printf ("\n");
}
/*****************************************************************************/
void ViewVec (double *temp_vec)
{
 int i, size;

 size = (int) temp_vec[0];

 printf ("%d\n", size);

 for (i=1; i <= size; i++)
 {
  printf ("%d %1.3lf\n", i, temp_vec[i]);
 }
 printf ("\n");
}
/*****************************************************************************/
/**********************Equation Functions*********************************/
/*****************************************************************************/
CInfo ConMassEqIP (CInfo OldCell, CInfo RightCell, CInfo LeftCell, CInfo
            Right2Cell, CInfo Left2Cell, double u)

{
 const double delta_t = (Beta * delta_x) / u0;

 CInfo new_cell;
 double temp_e;

 if (u >= 0.0)
 {
  temp_e = OldCell.e - ((u * delta_t / delta_x) * (OldCell.e - LeftCell.e));
  temp_e = temp_e - 0.5 * pow((u*delta_t/delta_x), 2.0) * (RightCell.e - 2.0 * OldCell.e + LeftCell.e);
  temp_e = temp_e - (1.0/6.0) * pow((u*delta_t/delta_x), 3.0) * (RightCell.e - 3.0*OldCell.e + 3.0*LeftCell.e - Left2Cell.e);
 }
 else
 {
  temp_e = OldCell.e - ((u * delta_t / delta_x) * (RightCell.e - OldCell.e));
  temp_e = temp_e - 0.5 * pow((u*delta_t/delta_x), 2.0) * (2.0 * OldCell.e - LeftCell.e - RightCell.e);
  temp_e = temp_e - (1.0/6.0) * pow((u*delta_t/delta_x), 3.0) * (Right2Cell.e - 3.0*RightCell.e + 3.0*OldCell.e - LeftCell.e);
 }
```

```
 if (temp_e > 1.0)
 {
  new_cell.v_e = temp_e;
  new_cell.e = 1.0;
  new_cell.p = p0;
  new_cell.u = 0.0;
 }
 else
 {
  new_cell.p = p0;
  new_cell.e = temp_e;
  new_cell.v_e = temp_e;
  new_cell.u = 0.0;
 }

 return new_cell;
}

/*****************************************************************************
CInfo ConMassEq (CInfo OldCell, CInfo RightCell, CInfo LeftCell, double u)
{
 const double delta_t = (Beta * delta_x) / u0;

 CInfo new_cell;
 double temp_ep;

 if (u >= 0.0)
 {
  temp_ep = OldCell.e - ((u * delta_t / delta_x) * (OldCell.e - LeftCell.e));
 }
 else
 {
  temp_ep = OldCell.e + ((u * delta_t / delta_x) * (RightCell.e - OldCell.e));
 }

 if (temp_ep/p0 > 1.0)

 {
  new_cell.v_e = temp_ep/p0;
  new_cell.e = 1.0;
  new_cell.p = temp_ep;
  new_cell.u = 0.0;
 }
 else
 {
  new_cell.p = OldCell.p;
  new_cell.e = temp_ep/p0;
  new_cell.v_e = new_cell.e;
  new_cell.u = 0.0;
 }
 return new_cell;
}
/*************************************************************************/
CInfo ConMomEq (CInfo old, CInfo right, CInfo left, CInfo temp_new_cell, double *forces)
{
 const double delta_t = 1.0;
 const double delta_x = 1.0;

 CInfo new_cell;
 double temp_epu;
 int force_num, i;

 force_num = forces[0];

 temp_epu = old.e * old.p * old.u - delta_t * ((right.e * right.p * right.u * right.u)

 for (i=1; i <= force_num; i++)                    -(left.e * left.p * left.u * left.u))/delta_x;
 {
  temp_epu = temp_epu + forces[i]*delta_t;
 }

 new_cell.p = temp_new_cell.p;
 new_cell.e = temp_new_cell.e;
 new_cell.v_e = temp_new_cell.v_e;
 new_cell.u = temp_epu/(temp_new_cell.e * temp_new_cell.p);

 return new_cell;
}
/*************************************************************************/
/***********************Wave Functions************************************/
/*************************************************************************/
void InitWaveShape (CInfo **Wave)
{
 const int SmoothIter = 5;
 int i, j;
 CInfo **Temp_Wave;

 Temp_Wave = C_Mat_Alloc (CellsPerWave, 1);

 for (i=1; i <= CellsPerWave; i++)
 {
  Wave[i][1].e = 1.0;
  Wave[i][1].p = p0;
  Wave[i][1].u = u0;
  Temp_Wave[i][1].e = 1.0;
 }

 for (i=1; i <= SmoothIter; i++)
 {
  Temp_Wave[1][1].e = (Wave[1][1].e + Wave[2][1].e) / 3.0;

  for (j=2; j < CellsPerWave; j++)
  {
        Temp_Wave[j][1].e = (Wave[j-1][1].e + Wave[j][1].e + Wave[j+1][1].e) / 3.0;
  }
```

```
  Temp_Wave[CellsPerWave][1].e = (Wave[CellsPerWave-1][1].e

  for (j=1; j <= CellsPerWave; j++)      + Wave[CellsPerWave][1].e) / 3.0;
  {
        Wave[j][1].e = Temp_Wave[j][1].e;
  }
 }

 Mat_Free(Temp_Wave);
}
/**********************************************************************
CInfo **InitTube (CInfo **OrgWave)
{
 CInfo **Temp_Tube;
 int i, size;

 Temp_Tube = C_Mat_Alloc (CellsPerTube, 1);

 size = (int) OrgWave[0][0].e;

 for (i=1; i <= size; i++)
  Temp_Tube[i][1] = OrgWave[i][1];

 return Temp_Tube;
}
/**********************************************************************
CInfo **InitWall (CInfo **OrgWave)
{
 CInfo **TempWall;
 int i;

 TempWall = C_Mat_Alloc(CellsPerWall, 1);

 for (i=1; i <= CellsPerWall; i++)
 {
  TempWall[i][1] = OrgWave[i][1];
  TempWall[i][1].u = 0.0;

  if (TempWall[i][1].e == 1.0)
        TempWall[i][1].e = 0.99;
 }

 return TempWall;
}
/**********************************************************************
void WaveMove (CInfo **Tube, double u)
{
 const double Round_Off = 0.5;
 const double Some_Number = 1.0;
 const double delta_t = (Beta * delta_x) / u0;

 CInfo **TempTube, right, right2, left, left2;
 int i;
```

```
TempTube = C_Mat_Alloc (CellsPerTube, 1);
right.e = right.v_e = right.u = right.p = 0.0;
left.e = left.v_e = left.u = left.p = 0.0;

for (i=1; i <= CellsPerTube; i++)
{
 if (i == 1)
 {
        left2.e = 0.0;
        left2.p = p0;
        left2.u = u0;
        left.e = 0.0;
        left.p = p0;
        left.u = u0;

        right.e = Tube[2][1].e;
        right.p = Tube[2][1].p;
        right.u = Tube[2][1].u;
        right2.e = Tube[3][1].e;
        right2.p = Tube[3][1].p;
        right2.u = Tube[3][1].u;
 }
 else if (i == 2)
 {
        left2.e = 0.0;
        left2.p = p0;
        left2.u = u0;
        left.e = Tube[1][1].e;
        left.p = Tube[1][1].p;
        left.u = Tube[1][1].u;
        right.e = Tube[3][1].e;
        right.p = Tube[3][1].p;
        right.u = Tube[3][1].u;
        right2.e = Tube[4][1].e;
        right2.p = Tube[4][1].p;
        right2.u = Tube[4][1].u;
 }
 else if (i == CellsPerTube - 1)
 {
        left2.e = Tube[CellsPerTube - 3][1].e;
        left2.p = Tube[CellsPerTube - 3][1].p;
        left2.u = Tube[CellsPerTube - 3][1].u;
        left.e = Tube[CellsPerTube - 2][1].e;
        left.p = Tube[CellsPerTube - 2][1].p;
        left.u = Tube[CellsPerTube - 2][1].u;
        right.e = Tube[CellsPerTube][1].e;
        right.p = Tube[CellsPerTube][1].p;
        right.u = Tube[CellsPerTube][1].u;
        right2.e = 0.0;
        right2.p = p0;
        right2.u = u0;
 }
 else if (i == CellsPerTube)
 {
        left2.e = Tube[CellsPerTube - 2][1].e;
        left2.p = Tube[CellsPerTube - 2][1].p;
        left2.u = Tube[CellsPerTube - 2][1].u;
        left.e = Tube[CellsPerTube - 1][1].e;
        left.p = Tube[CellsPerTube - 1][1].p;
        left.u = Tube[CellsPerTube - 1][1].u;
        right.e = 0.0;
        right.p = p0;
        right.u = u0;
        right2.e = 0.0;
        right2.p = p0;
        right2.u = u0;
 }
 else
 {
        left2.e = Tube[i-2][1].e;
        left2.p = Tube[i-2][1].p;
        left2.u = Tube[i-2][1].u;
        left.e = Tube[i-1][1].e;
        left.p = Tube[i-1][1].p;
        left.u = Tube[i-1][1].u;
        right.e = Tube[i+1][1].e;
        right.p = Tube[i+1][1].p;
        right.u = Tube[i+1][1].u;
        right2.e = Tube[i+2][1].e;
        right2.p = Tube[i+2][1].p;
        right2.u = Tube[i+2][1].u;
 }

 TempTube[i][1] = ConMassEqIP (Tube[i][1], right, left, right2, left2, u);

  if (TempTube[i][1].e < 0.0)
  {
        TempTube[i][1].e = TempTube[i][1].v_e = 0.0;
  }
 }

 for (i=1; i <= CellsPerTube; i++)
 {
  Tube[i][1] = TempTube[i][1];

  if (Tube[i][1].e > MinDen)
        Tube[i][1].u = u;
 }

 Mat_Free (TempTube);
}
/*************************************************************************
void NewVelocity (CInfo **Tube,  CInfo **Wall, CInfo **OrgWave, double *U)
{
 const double delta_t = (Beta * delta_x) / u0;

 double Force, TempForce, eFill, eVol, Mass, TempMass;
 int i;

 Force = 0.0;
 for (i=1; i <= CellsPerWall; i++)
 {
  eFill = Tube[CellsPerTube-CellsPerWall+i][1].e;
  eVol = 1.0 - Wall[i][1].e;

  if (eFill != eVol)
  {
          TempForce = ((eFill)/(eVol * eVol - eVol * eFill)) * pow(10.0, 1.2+i-(int)(CellsPerWall/2.0));
  }
  else if (eFill != 0.0)
  {
          TempForce = ((eFill*0.99)/(eVol * eVol - eVol * eFill*0.99)) * pow(10.0, 1.2+i-(int)(CellsPerWall/2.0));
  }
  else
  {
          TempForce = 0.0;
  }

  if (TempForce < 0.0)
  {
          TempForce = TempForce * -1.0;
  }

  Force = Force + TempForce;
 }

 Mass = 0.0;
 for (i=1; i <= CellsPerWave; i++)
 {
  Mass = Mass + OrgWave[i][1].e * OrgWave[i][1].p;
 }

 TempMass = 0.0;
 for (i=1; i <= CellsPerTube; i++)
  TempMass = TempMass + Tube[i][1].e * Tube[i][1].p;

 *U = *U - (Force * delta_t)/Mass;

/*  printf ("%lf, %lf %lf %lf %lf\n", Force, Mass, TempMass, delta_t, *U);
 getch(); */
}
/*************************************************************************/

void ShotsWrite (CInfo **Shots, int ShotNum)
{
 const char *filename = "Ushots.out";
 const double High_Heels = 1.0;
 FILE *file_ptr;
 int i, j;

 file_ptr = fopen(filename, "w");
```

```
 for (i=1; i <= CellsPerTube; i++)
 {
  for (j=1; j <= ShotNum+1; j++)
  {
          fprintf (file_ptr, "%1.5lf ", Shots[i][j].e + (j-1) * High_Heels);
  }
  fprintf (file_ptr, "\n");
 }
 fclose (file_ptr);
}
/*************************************************************************
int main ()
{
 const int ShotNum = 10;
 const int MovePerShot = 40;

 CInfo **OrgWave, **Tube, **Shots, **Wall;
 double *forces;
 double delta_t, u;
 double Mass, TempMass;
 int i, MoveCounter, ShotCounter;
 char bounce, end;

 OrgWave = C_Mat_Alloc (CellsPerWave, 1);
 InitWaveShape (OrgWave);
 Tube = InitTube (OrgWave);
 Wall = InitWall (OrgWave);

 Shots = C_Mat_Alloc (CellsPerTube, ShotNum+1);
 for (i=1; i <= CellsPerTube; i++)
  Shots[i][1] = Tube[i][1];
 for (i=1; i <= CellsPerWall; i++)
  Shots[CellsPerTube-CellsPerWall+i][1].e += Wall[i][1].e;

 bounce = end = 0;
 MoveCounter = 0;
 ShotCounter = 1;
 u = u0;

 while (!end)
 {
  WaveMove (Tube, u);
  MoveCounter += 1;

  if (Tube[CellsPerTube-CellsPerWall+1][1].e > 0.0)
  {
          NewVelocity (Tube, Wall, OrgWave, &u);
  }

  if ((!bounce) && (u < 0.0))
  {
          bounce = 1;
          hi;
  }
 If ((bounce) && (Tube[1][1].e > MinDen))
 {
         end = 1;
 }

 If ((MoveCounter % MovePerShot) == 0)
 {
         ShotCounter += 1;
         If (ShotCounter <= ShotNum + 1)
         {
          for (i=1;  i<= CellsPerTube; i++)
                  Shots[i][ShotCounter] = Tube[i][1];

          for (i=1; i <= CellsPerWall; i++)
                  Shots[CellsPerTube-CellsPerWall+i][ShotCounter].e += Wall[i][1].e;
         }
 }
}

 ShotsWrite(Shots, ShotNum);
/*  ViewShots (Shots);
 getch(); */
 C_ViewMat (Tube);

 Mass = TempMass = 0.0;
 for (i=1; i <= CellsPerWave; i++)
  Mass = Mass + OrgWave[i][1].e * OrgWave[i][1].p;
 for (i=1; i <= CellsPerTube; i++)
  TempMass = TempMass + Tube[i][1].e * Tube[i][1].p;
 printf ("%lf %lf\n", Mass, TempMass);

 printf ("%lf\n", t);
 return 0;
}
```